DOE/ER-0313/14

Fusion Reactor Materials

Semiannual Progress Report for Period Ending March 31, 1993

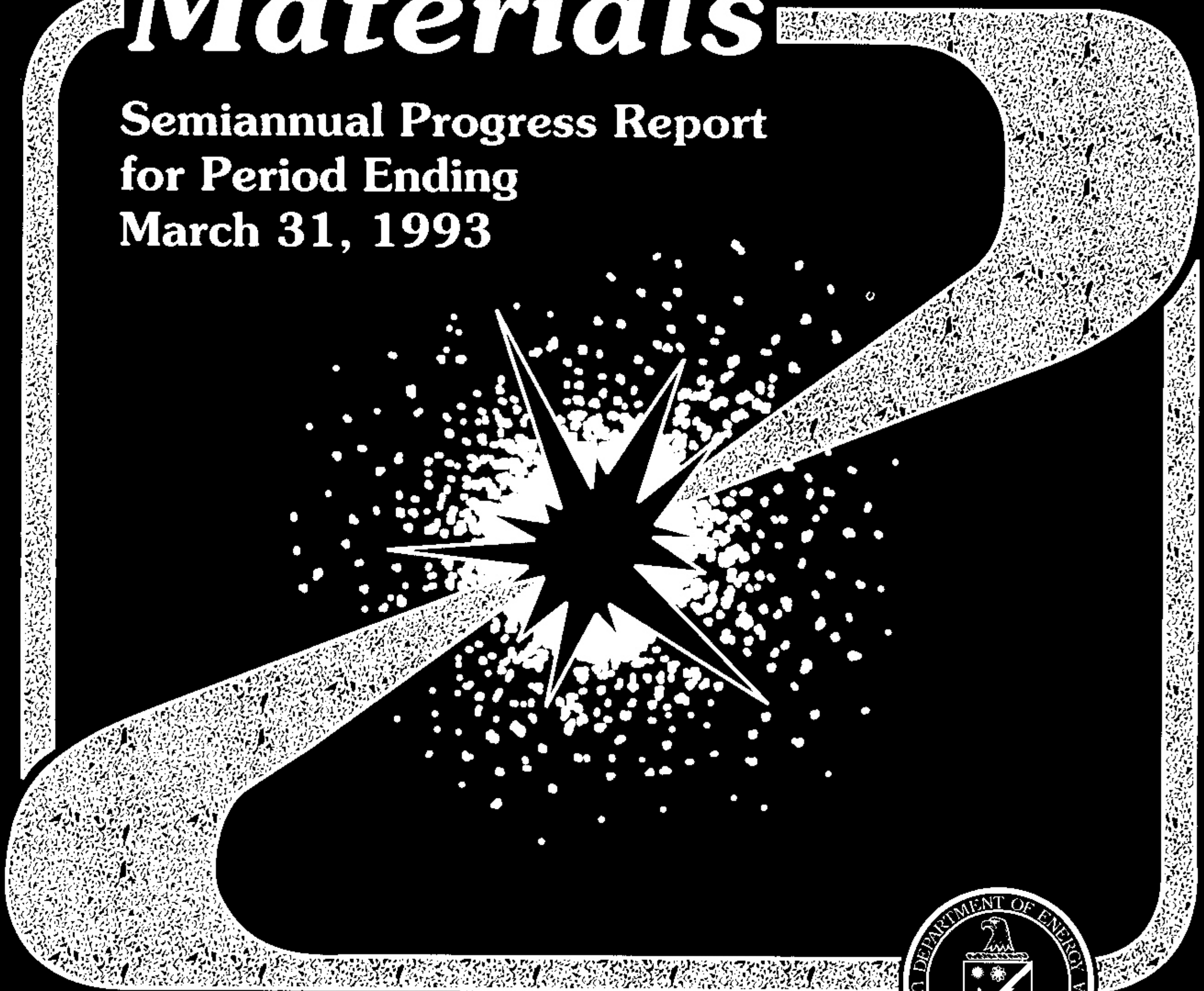

U. S. Department of Energy
Office of Fusion Energy

This report has been reproduced directly from the best available COPY

Available to DOE and DOE contractors from the Office of Scientific and Technical Information. P.O. Box 62, Oak Ridge. TN 37831; prices available from (615) 576-8401. FTS 626-8401.

Available to the public from the National Technical Information Service, U.S Department of Commerce. 5265 Port Royal Rd.. Springfield, VA 22161.

This report was prepared as an account of work sponsored by an agency of the United States Government. Neither the United States Government nor any agency thereof, nor any of their employees. makes any warranty. express or implied, or assumes any legal liability or responsibility for the accuracy. completeness, or usefulness of any information. apparatus. product. or process disclosed. or represents that its use would not infringe privately owned rights. Reference herein to any specific commercial product, process. or service by trade name, trademark. manufacturer, or otherwise, does not necessarily constitute or imply its endorsement. recommendation, or favoring by the United States Government or any agency thereof. The views and opinions of authors expressed herein do not necessarily state or reflect those of the United States Government or any agency thereof.

DOE/ER-0313/14
Distribution
Categories
UC-423, -424

FUSION REACTOR MATERIALS
SEMIANNUAL PROGRESS REPORT
FOR THE PERIOD ENDING
MARCH 31, 1993

Prepared for
DOE Office of Fusion Energy
(AT 15 02 03 A)

DATE PUBLISHED: **July** 1993

Prepared for
OAK RIDGE NATIONAL LABORATORY
Oak Ridge, Tennessee 37831
Managed by
MARTIN MARIETTA ENERGY SYSTEMS, **INC.**
for the
U.S. DEPARTMENT OF ENERGY
under Contract DE-AC05-84OR21400

FOREWORD

This is the fourteenth in a series of semiannual technical progress reports on fusion reactor materials. This report combines research and development activities which were previously reported separately in the following progress reports:

Alloy Development for Irradiation Performance

Damage Analysis and Fundamental Studies

Special Purpose Materials

These activities arc concerned principally with the effects of the neutronic and chemical environment on the properties and performance of reactor materials; together they form one element **of** the overall materials programs being conducted in support of the Magnetic Fusion Energy Program of the U.S. Department of Energy. The other major element of the program is concerned with the interactions bctween reactor materials and the plasma and is reported separately.

The Fusion Reactor Materials Program is a national effort involving several national laboratories, universities, and industries. The purpose of this series of reports is to provide a working technical record for the use **of** the program participants, and to provide a means of communicating the efforts of materials scientists to the rest of the fusion community, both nationally and worldwide.

This report has been compiled and edited under the guidance of A. F. Rowcliffe, G. L. Burn, and **S. S.** Knee', *Oak* Ridge National Laboratory. Their efforts, and the efforts of the many persons who made technical contributions, are gratefully acknowledged.

F. W. Wiffen
Division of Advanced Physics
and Technology

Reports previously listed in this series are **as follows:**

WEER-0313/1	Period ending September 30,1986
DOEER-0313/2	Period ending March 31, 1987
DOE/ER-0313/3	Period ending September 30,1987
WEER-0313/4	Period ending March 31.1988
DOE/ER-0313/5	Period ending September 30,1988
WEER-0313/6	Period ending March 31,1989
DOE/ER-0313/7	Period ending September 30,1989
DOE/ER-0313/8	Period ending March 31, 1990
WEER-0313/9	Period ending September 30,1990
DOE/ER-0313/10	Period ending March 31. 1991
DOE/ER-0313/11	Period ending September 30,1991
DOE/ER-0313/12	Period ending March 31.1992
DOE/ER-0313/13	Period ending September 30,1992
DOE/ER-0313/14	Period ending March 31, 1993

CONTENTS

1.0 IRRADIATION FACILITIES, TEST MATRICES, AND EXPERIMENTAL METHODS. . . . 1

1.1 PREPARATION OF COBRA 1A FOR INSERTION INTO EBR-II -- M. L. Hamilton and R. M. Ermi (Pacilic NorUiwest Laboratory) and C. R. Eiholzer (Westinghouse Hanford Company) 3

COBRA 1A was built to support the research and development efforts of the U.S. DOE Neutron Interactive Materials (NIMs) program. COBRA was inserted into the EBR-II for **irradiation** beginning in run 162. The specimen loading **is** documented here.

1.2 FABRICATION AND OPERATION OF HFIR-MFE RB* SPECTRALLY TAILORED IRRADIATION CAPSULES -- A. **W.** Longest, J. E. Pawel, D. W. Heatherly, R. G. Sitterson, and R. L. Wallace *(Oak* Ridge National Laboratory) 14

Fabrication and operation of four HFIR-MFE RB* capsules (60, 200, 330, and 400°C) to accommodate MFE specimens previously irradiated in spectrally tailored experiments in the ORR are proceeding satisfactorily. Irradiation of the 60 and 330°C capsules. which started on July 17, 1990, wiis completed on November 14, 1992, after 24 cycles of irradiation to an incremental damage level of approximately 10.9 displacements per **atom** (dpa). Assembly **nf** die follow-up 200 and 400°C capsules was completed in November 1992, and their planned 20-cycle irradiation to approximately 9.1 incremental dpa wiis started on November 21, 1992. As of February 11, 1993, the 200 and 400°C **capsules** had successfully complctcd three cycles of irradiation to approximately 1.4 incremental dpa.

1.3 STATUS OF U.S./JAPAN COLLABORATIVE PROGRAM PHASE II HFIR TARGET CAPSULES --J. E. Pawel and R. L. Senn (Oak Ridge National Laboratory and K. Shiba (Japan Atomic Energy Research Institute **41**

Capsules JP9 through JP 16 were installed in die High **Flux** Isolope Reactor (HFIR) target July 20, 1990, for irradiation beginning with HFIR fuel cycle 289. Of these eight target capsules, JP10, 11, 13, and 16 completed their scheduled number of cycles (11) and were removed from the reactor in September 1991. In addition, JP14 was removed from the reactor **at** the end of cycle 310 (9/18/92) **after 21** cycles.

Three new **capsules in this** series, JP20, 21, and **22,** have been **designed.** The new capsules will contain transmission electron microscope (TEM) **disks** and **SS-3** llat tensile specimens at 300-600°C and will achieve doses of 8, 18, and 35 dpa, respectively.

2.0 DOSIMETRY, DAMAGE PARAMETERS, AND ACTIVATION CALCULATIONS.. 45

2.1 HELIUM MEASUREMENTS FOR THE MOTA 1G DISCHARGE OF THE ^{59}Ni ISOTOPIC TAILORING EXPERIMENT--F. A. Gamer (Pacific Northwest Laboratory) and B. M. Oliver (Rockwell International) 47

The **final** measurements **of** helium generalion in specuncns used in the ^{59}Ni isotopic tailoring experiment havc been completed. Tbe results show that the target generation rates were sustained throughout the experimental series. It was **also** demonstrated that helium generation **rates** grow continuously in undoped specimens,,reaching levels substantially larger than usually quoted in most other studies.

Neutron fluence and spectral measurements and radiation damage calculations are reported for the MOTA-1G experiment in the Fast Flux Test Facility (FFTF). The irradiation was conducted from January 4, 1990, to March 19, 1991, for a total exposure of 299.7 EFPD. The maximum fluence was 15.8 x 10^{22} n/cm^2, 10.0 x 10^{22} above 0.1 MeV producing 43.0 dpa in iron. Neutron fluence and radiation damage maps are presented for the entire MOTA assembly based on the analysis of ten neutron spectral measurements and seven additional flux gradient measurements.

V-B and V-5Cr-B alloys have been irradiated in FFTF to assess the impact of helium generation rate on microstructural evolution of vanadium-base alloys. Using this method it is somewhat difficult to separate the various effects of the original boron as well as the lithium and helium products of the ^{10}B (n, a) reaction. Post-irradiation measurements of helium concentrations have been completed for two sets of V-B alloys, one irradiated in-core and one below core. It appears that the boron doping technique used to produce the various alloys was reasonably successful in reaching the desired helium/dpa variations.

New nuclear section libraries (known as USACT92) have been created for activation calculations. A point-wise file was created from merging the previous version of the activation library, the U.S. Nuclear Data Library (ENDF/B-VI), and the European Activation File (EAF-2). 175 and 99 multi-group versions were also created. All the data are available at the National Energy Research Supercomputer Center.

Tungsten has been used in a variety of low activation ferritic alloys and also in copper composite alloys, both currently being irradiated in various fusion materials experiments. It has been proposed as an armor material also. However. in a manner that is strongly dependent on neutron spectra, tungsten transmutes strongly to rhenium and then osmium. This adds significant complexity to the interpretation of data developed in one spectral environment hut intended for application to another environment

Calculations have been performed to estimate the ionizing and displacive irradiation fields that will occur in ceramics during irradiation in accelerators and fission and fusion reactors. A useful measure of the relative strength of ionizing vs. displacive radiation is the ratio of the absorbed ionizing dose to the displacement damage dose. which in the case of ion irradiation is equal to the ratio of the electronic stopping power to the nuclear stopping power. In ceramics such as Al_2O_3, this ratio is about 20 at a fusion reactor first wall, and has a typical value of about 100 in a fusion reactor blanket region and in mixed spectrum reactors such as HFIR. Particle accelerator sources typically have much higher ionizing to displacive radiation ratios, ranging from about 2000 for 1 MeV protons to >10,000 for 1 MeV electrons.

2.7 IMPROVEMENT OF DECAY AND CROSS-SECTION DATA LIBRARIES FOR ACTIVATION CALCULATIONS--H. Attaya (Argonne National Laboratory) 79

A new decay data library has been completed. The new library contains up-to-date decay information (half-lives, branching ratios, decay energies, γ's energies and intensities). Activation responses such as the air and water biological hazard potentials, the waste disposal rating, and the biological dose are also included in this library. Recently developed cross-section libraries have been acquired to be used together with the decay data library.

2.8 ACTIVATION ANALYSES FOR DIFFERENT STRUCTURAL ALLOYS CONSIDERED FOR ITER--H. Attaya and D. Smith (Argonne National Laboratory) 85

Activation calculations have been made for the austenitic steel 316SS, the ferritic alloys HT-9, the titanium alloy Ti6Al4V, and the vanadium alloy V5Cr5Ti in a liquid metal (Na) design suggested recently for ITER. The calculations show that the vanadium alloy has the minimum short and long-term radioactivity and BHP. It also has the minimum decay heat all the time. The titanium alloy has less radioactivity than the austenitic and the ferritic alloys. However, the decay heat of this alloy could exceed that of the conventional alloys.

3.0 MATERIALS ENGINEERING AND DESIGN REQUIREMENTS 91

No contributions

4.0 FUNDAMENTAL MECHANICAL BEHAVIOR 93

4.1 MECHANICAL PROPERTIES ALONG INTERFACES OF BONDED STRUCTURES IN FUSION REACTORS -- M. H. Hassan and G. L. Kulcinski (University of Wisconsin) 95

Proper assessment of the mechanical properties along interfaces of bonded structures currently used in many fusion reactor designs is essential to compare the different fabrication techniques. A Mechanical Properties Microprobe (MPM) was used to measure hardness and Young's modulus along the interfaces of Be/Cu bonded structure, The MPM was able to distinguish different fabrication techniques by a direct measurement of the hardness, Young's modulus, and H/E^2 which reflects the ability of deformation of the interfacial region.

4.2 GREENS FUNCTION METHODOLOGY FOR FRACTURE MECHANICS OF Sic-Sic COMPOSITE STRUCTURES -- A. El-Azab and N. M. Ghoniem (University of California. Los Angeles) 104

A fundamental solution of plane elasticity in a finite domain is developed in this paper. A closed-form Green's function for the elastic field of an edge dislocation of arbitrary Burger's vector at an arbitrary point in an orthotropic finite electric domain, that is free of traction, is presented. the method is based on the classical theory of potential fields, with an additional distribution of surface dislocations to satisfy the free traction boundary conditions. A solution is first developed for a dislocation in a semi-infinite half-plane. The resulting field is composed of two parts: a singular contribution from the original dislocation, and a regular component associated with the surface distribution. The Schwarz-Christoffel transformation is then utilized to map the field quantities to a finite, polygonal domain. A closed form solution containing Jacobi elliptic functions is developed for rectangular domains, and applications of the method to problems of fracture and plasticity are emphasized

In agreement with limited earlier studies. a comprehensive irradiation experiment conducted in EBR-II demonstrates that while cold-working decreases swelling of Fe-15Cr-XNi (X=12-45 wt%) alloys at relatively low irradiation temperatures, it increases swelling at higher temperatures. Aging of cold-worked specimens to produce polygonized dislocation networks tends to further increase swelling, especially at higher nickel (>25%) levels. Swelling at lower nickel levels also appears to be sensitive to details of the annealing treatment.

Pure copper has been irradiated in a variety of starting conditions by either 1.0 MeV electrons or fast neutrons in FFTF-MOTA. Electron irradiation at 250 and 350°C produces a non-monotonic swelling behavior as a function of cold work level, increasing swelling at lower cold work levels and decreasing swelling at higher cold-work levels. In FFTF at 365 and 430°C, however, 10% cold-work reduces swelling initially, with little additional influence at higher cold-work levels. Swelling at 520 and 600°C is less than 1% at 35.9 and 13.6 dpa, respectively, with little effect of cold work level.

Microstructurally-oriented irradiation experiments are shown in this paper to be strongly dependent on details of reactor history that frequently are not brought to the experimenter's attention. In some cases, these details can dominate the experiment so as to produce very misleading results. To aid in the design and interpretation of microstructurally-oriented experiments, a number of studies are reviewed to highlight history effects and then guidelines are presented to minimize the impact of reactor history in new experiments.

The second and last phase of the EBR-II AA-14 experiment confirms many of the trends observed in Phase I of the experiment. Phase I reached 12 to 14 dpa for pure nickel and nickel-binary alloys at 425. 500, and 600°C. Phase II reached 31.1 to 31.8 dpa at the same temperatures.

Our knowledge of the processes involved in creating defects during cascade-producing irradiations is reviewed. Molecular dynamics simulations within the past few years have led to an understanding of the creation and survival of point defects in the critical first picoseconds of the cascade process, through the quenching of the thermal spike. The concept that "freely migrating defects" arise only from isolated Frenkel pairs produced in a cascade is critically discussed.

The Molecular Dynamics (MD) method **is** used to calculate defect energetics in ß-silicon carbide. Many-body interaction effects in **this** covalent material are accounted for by using a hybrid of two-body and three-body potentials. Calculated bulk properties of ß-SiC based on this potential are in agreement with experimental data to within 17%. **A** micro-crystal **is** constructed to represent the computational cell and external forces are applied to **the** micro-crystal so that it behaves as a part of an infinite medium. The potential energy for the **unperturbed** computational cell **is first** calculated. The cell **is** then set at a defect configuration and relaxed, and the potential energy of the relaxed cell is calculated. The difference between the potential energy of the unperturbed cell and that of the defect-containing cell **is** used to calculate the formation and binding energies of point defects, defect clusters, and helium-vacancy clusters in SiC.

The full spectrum of fracture toughness (J integrals), including pure mode I, different mixed mode I/III and pure mode III, will be examined for a ferritic/martensitic stainless steel with 0.1C-8Cr-2W-0.2V-0.04Ta-Fe (by wt%), designated as F-82H. The J integrals of pure mode I (J_{IC}) and mixed mode I/III (J_{mixed}) are determined with single specimen method using standard compact tension specimens and modified compact tension specimens, respectively. The pure mode III integral is measured with multiple specimen method using "triple-pantleg" specimens. Effects of hydrogen on the J integrals of pure **mode** I and mixed mode I/III are also going to be studied. 9 ppm H (about 500 appm) is pre-charged into specimens cathodically. The preliminary results showed that addition of **mode** III Stress (shear stress) to mode I loading had a significant negative effect on the fracture toughness of F-82H.

The irradiation creep behavior of the fusion heats of HT9 and 9Cr-1Mo at -400°C has been **measured** to exposures **as** large **as** 208 dpa. HT9 **is** somewhat nonlinear in its response to hoop **stress** level in the range 0-200 MPa, but 9Cr-1Mo **exhibits** only slightly greater than linear behavior **with** stress level. The strain **data** of both alloys appear **to** include some contributions from precipitate-related density changes. Swelling may have occurred in 9Cr-1Mo.

Tensile and Charpy impact tests were made on three normalized-and-tempered *2* 1/4Cr-2WV (0.1% C) steels with 0.1, *0.25.* and 0.5% V (all concentrations are in weight percent). Increasing vanadium from 0.1 to 0.25% increased the yield stress up to twenty percent. **A** higher ductile-brittle transition temperature (DBTT) accompanied the higher strength of the 0.25% V steel when both were tempered at 700°C. Tempering at 750°C gave similar DBTTs. Increasing vanadium from 0.25 to 0.5% caused a slight increase in strength with a large decrease in toughness. Thus a balance between strength and impact toughness is achieve with an intermediate vanadium concentration. Addition of 0.02% Ti to 2 1/4Cr-0.25V, 2 1/4Cr-2W, and 2 1/4Cr-2W-0.25V (0.1% C) steels caused a yield stress decrease of 10 to 30%, which was attributed to the effect of titanium on the MC precipitate distribution. The strength loss was accompanied by an increase in impact toughness, which may also have been affected by a decrease in prior austenite grain size. Furthermore, there was little difference in the DBTT of the Ti-modified steels tempered at 700 or 750°C. If it were possible to use a Ti-modified steel tempered at 700°C, this might offset the strength advantage of steels without titanium, which have to be tempered at the higher temperature.

Experiments have shown that Type 316 stainless steel is susceptible to heat-affected-zone (HAZ) cracking upon cooling when welded using the gas tungsten arc (GTA) process under lateral constraint. The cracking has been hypothesized to be caused by stress-assisted helium bubble growth and rupture at grain boundaries. This study utilized an experimental welding setup, which enabled different compressive stresses to be applied to the plates during welding. Autogeneous GTA welds were produced in Type 316 stainless steel doped with 256 appm helium. The application of a compressive stress. 55 MPa, during welding suppressed the previously observed catastrophic cracking. Detailed examinations conducted after welding showed a dramatic change in helium bubble morphology. Grain boundary bubble growth along directions parallel to the weld was suppressed. The results suggest that stress-modified welding techniques may be used to suppress or eliminate helium-induced cracking during joining of irradiated materials.

At 178 dpa and ~400°C, the irradiation creep behavior of 20% cold-worked PCA has become dominated by the creep disappearance phenomenon. The total diametral deformation rate has reached the limiting value of 0.33%/dpa at the three highest stress levels. The stress-enhancement of swelling tends to camouflage the onset of creep disappearance, however.

Pure molybdenum and Mo-41wt% Re, in both the 20% cold-worked and aged and the annealed and aged conditions, were irradiated in FFTF/Mota to exposures as high as 111 dpa. Pure molybdenum appears to approach a saturation swelling level that is independent of the starting state. Cold-worked and aged molybdenum initially swells at a higher rate than that of solution-annealed and aged molybdenum and overshoots the saturation level at lower irradiation temperatures. This requires that part of the accumulated swelling be removed to approach saturation. probably by void shrinkage. The alloy Mo-41Re exhibits a more complex behavior with the annealed and aged condition initially swelling faster, but eventually the density change of both conditions begins to turn downward and tends toward densification. The role of solid transmutation to Tc, Re, and Os is thought to be very important in the irradiation behavior of these two metals. Calculations of transmutant generation are provided for FFTF, HFIR and STARFIRE spectra.

Irradiation has been completed in MOTA-2B lor creep tubes constructed from a candidate reduced activation austenitic alloy supplied by the Baikov Institute in Moscow. The total swains are strongly dependent on irradiation temperalure in the range 425-600°C, but are not completely linear with stress level.

Density change measurements have been complctcd on the Ispra second generation AMCR alloys irradiated in MOTA-2A. The various compositional modifications induce a wide **variation** of swelling behavior in the range 423-600°C at 32-36 dpa.

Previous **work** on a series of experimental high-manganese reduced-activation austenitic stainless steels demonstrated that they had improved tensile properties relative to type 316 stainless steel in both the annealed and 20% cold-worked conditions. Steels were tested with an Fe-20Mn-12Cr-0.25C (in weight percent) base composition, to which various combinations of Ti, W, V, P, and B were added. Tensile tests have now been completed on these steels after thermal aging at 600°C. Thermal suability varied with composition, but the alloys were as stable or more stable than type 316 stainless steel. The strength of *the* annealed stcels increased slightly after aging to 5000 h, while a strength decrease occurred **for** the cold worked steel. In both conditions, a steel containing a combination of **all** the alloying elements was most stable **and had** the best strength after thermal aging 5000 h at 600°C. Despite having much higher strength than 316 stainless steel after aging, the ductility of the strongest experimental alloy was **still** as good as that of316 stainless steel.

The effects of He/dpa ratio on swelling behavior were examined on three austenitic stainless steels. Materials were solution-annealed JPCA and two low carbon containing alloys **(C and K)** modified with titanium and niobium. These steels were neutron-irradiated in ORR and HFIR with and without spectrally tailoring, respectively. Achieved damage level was 7.4 **dpa** in ORR irradiation with average He/dpa of about 21 appm/dpa. In case of HFIR irradiation, they were **33** dpa and 76 appm/dpa, respectively. Alloy to alloy variation and temperature dependence of swelling behavior are far more distinctively detected in ORR irradiation than in HFIR irradiation, in spite of the lower damage level of ORR irradiation. In the case **of** ORR-irradiation. **JPCA** exhibited small swelling values of <0.01 **and** 0.03% at *603* and 673 K. respectively, while a low carbon alloy K showed relatively larger swelling: 0.2% at 603 K and 0.6% at 673 K. Number densities of cavities in HFIR-irradiated alloys were larger than those observed in ORR by one to two orders. On the other band, number densities **and** sizes of dislocation loops produced by ORR irradiation were two to live tunes **as** large **as** those by HFIR irradiation. These facts suggest that in ORR condition with closer He/dpa to that of fusion, mutual annihilation rate of point defects was reduced and then bias driven cavity growth might be enhanced compared with HFIR condition.

6.2.8 MICROSTRUCTURES OF A WELDED JOINT USING AN IRRADIATED WRAPPER TUBE--S. Hamada, K. Watanabe, A. Hishinuma, I. Takahashi and T. Kikuchi (Japan Atomic Energy Research Institute) 241

The behavior of helium in welded joint fabricated using tungsten inert gas (TIG) welding process for a type 316 stainless steel wrapper tube irradiated in a fast reactor was investigated. The wrapper tube was irradiated to (1.5 - 4.2) x 10^{26} n/m^2 (helium level of 3 to 9 appm) at 395 - 410°C. All welded joints fractured in the heat-affected zone (HAZ). The microstructures of each portion of the base metal, the HAZ and the fusion zone in a welded joint were examined through a transmission electron microscope. Small helium bubbles were observed in number density of 2 x 10^{20} m^{-3} in the matrix and rarely found on the grain boundaries of the base metal. In the HAZ, small and large helium bubbles mixed and lined up along the grain boundaries. In particular, some of them elongated along the grain boundary. In the matrix of the fusion zone, delta-ferrite phases and unresolved carbides were scattered. Large cavities were attached to these precipitates and also occurred along grain boundaries. These results suggest that the failure in the HAZ of welded joints is attributed to the preferential growth and coalescence of helium bubbles in the grain boundaries of the HAZ caused by weld heat input and stress during welding

6.29 DOSE DEPENDENCE OF THE MICROSTRUCTURAL EVOLUTION IN NEUTRON-IRRADIATED AUSTENITIC STAINLESS STEEL -- S. J. Zinkle, P. J. Maziasz, and R. E Stoller (Oak Ridge National Laboratory) 251

Microstructural data on the evolution of the dislocation loop, cavity, and precipitate populations in neutron-irradiated austenitic stainless steels are reviewed in order to estimate the displacement damage levels needed to achieve the "steady state" condition. The microstructural data can be conveniently divided into two temperature regimes. In the low temperature regime (below about 300°C) the microstructure of austenitic stainless steels is dominated by "black spot" defect clusters and faulted interstitial dislocation loops. The dose needed to approach saturation of the loop and defect cluster densities is generally on the order of 1 displacement per atom (dpa) in this regime. In the high temperature regime (~300 to 700°C). cavities, precipitates, loops in excess of 10 dpa are generally required to approach a "steady state" microstructural conditions. Due to complex interactions between the various microstructural components that form during irradiation, a secondary transient regime is typically observed in temperatures. This slowly evolving secondary transient may extend to damage levels in excess of 50 dpa in typical 300-series stainless steels, and to >100 dpa in radiation-resistant developmental steels. The detailed evolution of any given microstructural component in the high-temperature regime is sensitive to slight variations in numerous experimental variables, including heat-to-heat composition changes and neutron spectrum.

6.2.10 FRACTURE TOUGHNESS OF IRRADIATED CANDIDATE MATERIALS FOR ITER FIRST WALL/BLANKET STRUCTURES: PRELIMINARY RESULTS -- D. J. Alexander, I. E. Pawel. M. L. Grossbeck. and A. F. Rowcliffe (Oak Ridge National Laboratory) 277

Candidate materials for first wall/blanket structures in ITER have been irradiated to damage levels of about 3 dpa at temperatures of either 60 or 250°C. Preliminary results have been obtained for several of these materials irradiated at 60°C. The results show that irradiation at this temperature reduces the fracture toughness of austenitic stainless steels, but the toughness remains quite high. The unloading compliance technique developed for the subsize disk compact specimens works quite well, particularly for materials with lower toughness. Specimens of materials with very high toughness deform excessively. and this results in experimental difficulties.

6.3.1 DENSITY CHANGES INDUCED BY NEUTRON IRRADIATION IN DYNAMICALLY COMPACTED TUNGSTEN AND PCA -- F. A. Garner (Pacific Northwest Laboratory) and J. Megusar (Massachusetts Institute of Technology) 289

Dynamically compacted tungsten with a starting density of 95.3% of the theoretical value densified 2 to 3% when irradiated in FFTF/MOTA-2A at three temperatures between 423 and 600°C and displacement levels corresponding to 32 and 36 dpa in stainless steel. Rapidly solidified and dynamically compacted PCA with high levels of titanium and carbon were also irradiated at these conditions. The density changes were small enough to determine that significant swelling had not occurred but, microscopy is necessary to determine whether void growth occurred in addition to precipitate-related strains.

6.3.2 DENSITY CHANGES OBSERVED IN Nb-1Zr AFTER IRRADIATION IN FFTF-MOTA -- F. A. Garner (Pacific Northwest Laboratory) 291

Nb-1Zr has been proposed for potential application to ITER. Whereas previous irradiation studies on Nb-1Zr were focused on the annealed condition, this study involved a comparative irradiation of both the annealed and aged, and the cold-worked and aged conditions. Based on measurements of density change, the cold-worked and aged condition appears to first undergo a phase-related dilation prior to the onset of void swelling. while the annealed condition densified prior to swelling and in some cases does not swell at all.

6.3.3 ASSESSMENT OF NIOBIUM-BASE ALLOYS FOR STRUCTURAL APPLICATIONS IN THE ITER DIVERTOR--I. M. Purdy (Argonne National Laboratory) 294

The corrosion and embrittlement of pure Nb, Nb-1Zr, Nb-5Mo-1Zr, and Nb-5V-1.25Zr (alloy elements in wt.%) were evaluated in high-purity (HP) deoxygenated water at 300°C for up to 120 days. One heat of the Nb-5V-1.25Zr alloy ("O" lot) exhibited both a modest corrosion rate and good resistance to embrittlement relative to other Nb-base alloys. At present, Nb-5V-1.25Zr is the most promising Nb-base alloy on the basis of both corrosion and embrittlement characteristics in HP deoxygenated water at 300°C.

6.3.4 MICROSTRUCTURAL EVOLUTION INDUCED BY BORON TRANSMUTATION IN NEUTRON-IRRADIATED VANADIUM-BASE ALLOYS--H. M. Chung (Argonne National Laboratory) 299

Microstructural evolution associated with transmutation of ^{10}B to helium and lithium has been characterized to provide a better understanding of the boron-doping technique, frequently used to simulate the effect of helium generation under fusion reactor conditions. Transmission electron microscopy (TEM) was used to examine specimens of V-20Ti alloy after irradiation at 600°C to ≈44-80 dpa in the Fast Flux Test Facility (FFTF). In the earlier stage of irradiation to low fluence, concentric shells of He-damage and Li-damage zones are produced around a V_3B_2 precipitate or a ^{10}B-rich cluster. On further irradiation, helium atoms diffuse away from the damage shell either to be dissolved in the matrix or to form microcavities, leaving a shell rich in Li, defect clusters, and dislocations. Oxygen atoms in solid solution migrate toward the Li-rich shells, and γ-LiV$_2$O$_5$ shells precipitate subsequently. In view of this behavior. neither boron nor Li produced from the transmutation is likely to result in a detrimental weakening of grain boundaries.

Irradiation of the seven DHCE capsules was completed in the Materials Open Test Assembly (MOTA)-2B at the end of Cycle 12B in the Fast Flux Test Facility (FFTF). The accrued exposure was 203.3 effective full-power days (EFPDs), vis-a-vis the target exposure of 300 EFPDs. Peak damage in the samples was ≈29 displacement per atom (dpa). All seven capsules have been discharged from the FFTF and are being shipped to Argonne National Laboratory (ANL), where the samples will be retrieved from the capsules and distributed to the experimenters. including Monbusho of Japan, for examination and testing. A substantial effort is underway at ANL to retrieve the samples from the highly tritiated capsules.

The thermal creep rates and stress-rupture life of V-5Cr-5Ti and V-10Cr-5Ti alloys were determined at 600°C and the impurity composition and microstructural characteristics of creep-tested specimens were analyzed and correlated with the measured creep properties. The results of these tests show that V-5Cr-5Ti, which contains impurity compositions typical of a commercial vanadium-base alloy, exhibits creep strength substantially superior to that of V-20Ti, HT-9, or Type 316 stainless steel. The V-10Cr-5Ti alloy exhibits creep strength somewhat higher than that of V-5Cr-5Ti.

Ductile-brittle transition temperatures (DBTTs) were determined by Charpy-impact tests for dehydrogenated and hydrogenated V-3Ti, V-5Cr-3Ti, and V-5Cr-5Ti alloys. These DBTT data complement the data previously obtained by Loomis et al. on Charpy-impact testing of unalloyed V, V-1Ti, V-3Ti-1Si, V-5Ti, V-10Ti, V-18Ti, V-4Cr-4Ti, V-8Cr-6Ti, V-9Cr-5Ti, V-10Cr-9Ti, V-14Cr-5Ti, V-15Cr-5Ti, V-7Cr-15Ti, and Vanstar-7 alloys. The results show that V alloys with Ti additions (0-18 wt.%) have a minimum DBTT (≈-250°C) in an alloy containing 3-5 wt.% Ti, that addition of 4 to 15 wt.% Cr to V-(4-6)Ti alloy results in a substantial increase (25-215°C) of the DBTT, and that 0.5 and 1.0wt.% Si additions to V-3Ti alloy result in a significant increase (-100°C) in DBTT. In addition, the results show that the presence of 400-1200 appm H in unalloyed V and V-base alloys causes a significant increase (≈400 ppm O, ≈200 ppm C, and ≈900 ppm Si for use as structural material in a fusion reactor.

Irradiation continues in the EBR-II and DR-3 reactors of pure copper and GlidCop CuAl25 in the form of subsize tensile fatigue specimens. The first phase of the EBR-II irradiation sequence has been completed. A size effects experiment conducted on unirradiated CuAl25 fatigue specimens is nearing completion. Early results on the fatigue behavior of subsize specimens are presented in this report.

6.4.2 The Response of Dispersion-Strengthened Copper Alloys to High Fluence Neutron Irradiation at 415°C -- D. J. Edwards, J. W. Newkirk (Univ. of MO-Rolla), F. A. Garner, M. L. Hamilton (Pacific Northwest Laboratory), A. Nadkarni, and P. Samal (SCM Metal Products) 331

Various oxide-dispersion-strengthened copper alloys have been irradiated to 150 dpa at 415°C in the Fast Flux Test Facility (FFTF). The Al_2O_3-strengthened GlideCop^{TM} alloys, followed closely by a HfO_2-strengthened alloy, displayed the best swelling resistance, electrical conductivity, and tensile properties. The conductivity of the HfO_2-strengthened alloy reached a plateau at the higher levels of irradiation, instead of exhibiting the steady decrease in conductivity observed in the other alloys. A high initial oxygen content resulted in significantly higher swelling for a series of castable oxide-dispersion-strengthened alloys, while a Cr_2O_3-strengthened alloy showed poor resistance to radiation.

6.4.3 NEUTRON-INDUCED SWELLING OBSERVED IN COPPER ALLOYS IRRADIATED IN MOTA's 2A AND 2B -- F. A. Garner (Pacific Northwest Laboratory), D. J. Edwards (University of Missouri-Rolla), B. N. Singh (Risø National Laboratory), and H. Watanabe (Kyushu University) 34s

Density measurements have been completed on copper alloys irradiated in MOTA 2A and MOTA 2B at (375°C, 12.7 dpa and 21.2 dpa) and (423°C, 48.0 and 95.4 dpa). While most of the density changes observed are consistent with those of earlier studies, there were several surprises. Addition of 5% Ni appears to accelerate the swelling rate initially at 423°C, but depresses swelling at 375°C. The suppressing action of cold work on swelling of Cu-5Ni is relatively small, and Cu-5Mn resists swelling very strongly in both the annealed and cold-worked conditions.

6.4.4 IRRADIATION OF COPPER ALLOYS IN THE SM-3 REACTOR--S. J. Zinkle (Oak Ridge National Laboratory), F. A. Garner (PNL), V. R. Barabash (D.V. Efremov), S. A. Fahritsiev (D. V. Efremov) and A. S. Pokrovsky (SRIAR) 347

A total of 74 alloys of varying composition and thermomechanical condition have been prepared for a joint US-Russia irradiation experiment in the SM-3 reactor in Dimitrovgrad, Russia. The alloys will be irradiated in the form of TEM disks and sheet tensile specimens at temperatures of about 120, 250, and 340°C for one 45-day cycle in the core and Channel 2 irradiation positions. This will produce damage levels of about 7 and 1 dpa, respectively. Cadmium shielding will be used in the Channel 2 position to shield the thermal neutrons and thereby reduce the amount of solid transmutation products in copper.

6.4.5 EFFECT OF ION IRRADIATION ON THE STRUCTURAL STABILITY OF DISPERSION-STRENGTHENED COPPER ALLOYS -- S. J. Zinkle (Oak Ridge National Laboratory), E. V. Nesterova, and V. V. Rybin (Central Research Institute for Structural Materials). and V. R. Barabash and A. V. Naberenkov (D. V. Efremov Scientific Research Institute of Electrophysical Apparatus).. 352

Transmission electron microscopy was used to compare the microstructure and particle distributions of two commercial oxide dispersion-strengthened copper alloys, GlidCop A125 and MAGT 0.2. Measurements were made on specimens in their as-wrought condition, after thermal annealing for 1 h at 900°C, and after 3 MeV Ar^+ ion irradiation at 180 and 350°C to damage levels of 20 to 30 displacements per atom (DPA). All of the annealed and ion-irradiated specimens were found to be resistant to recrystallization. In addition, void formation was not observed in any of the irradiated specimens. The GlidCop oxide particle geometry was transformed from triangular platelets to circular disks by the ion irradiation. The MAGT particle geometry consisted of circular disks and spheres before and after irradiation. The oxide particle edge length in the unirradiated GlidCop alloy was about 10 nm, whereas the mean particle diameter in both the MAGT and GlidCop alloys was about 6 nm.

Various oxide-dispersion-strengthened copper alloys have been irradiated **to** 150 dpa at **415°C** in the Fast Flux Test Facility (FFTF). The Al_2O_3-strengthened GlideCop^{TM} alloys, followed closely by a HfO_2-strengthened alloy, displayed the best swelling resistance, electrical conductivity, and tensile properties. The conductivity of the HfO_2-strengthened alloy reached a plateau at the higher levels of irradiation, instead of exhibiting the steady decrease in conductivity observed in the other alloys. **A** high initial oxygen content resulted in significantly higher swelling for a series of castable oxide-dispersion-strengthened alloys. while a Cr_2O_3-strengthened alloy showed poor resistance to radiation.

Density measurements have been **completed** on copper alloys irradiated in MOTA **2A** and MOTA 2B **at** (375°C, 12.7 dpa and 21.2 dpa) and (423°C, 48.0 and 95.4 dpa). While most of the density changes observed are consistent with those of earlier studies, there were several surprises. **Addition** of 5% Ni appears to accelerate the swelling rate initially at 423°C. **but** depresses swelling at 375°C. The suppressing action of cold **work** on swelling of Cu-5Ni is relatively small, and Cu-5Mn resists swelling very strongly in both the annealed and cold-worked conditions.

A total of 74 alloys of varying composition and thermomechanical condition have **been** prepared for a joint ITS-Russia irradiation experiment in the SM-3 reactor in Dimitrovgrad, Russia. The alloys will be irradiated in the form of TEM **disks** and sheet tensile specimens at temperatures **of** about 120, 250, and 340°C for one 45-day cycle in the core and Channel 2 irradiation positions. This will produce damage levels of about 7 and 1 dpa, respectively. Cadmium shielding will be used in the Channel 2 position to shield the thermal neutrons and thereby reduce the amount of solid transmutation products in copper.

Transmission electron microscopy was used to compare the microstructure and particle distributions **of** two commercial oxide dispersion-strengthened copper alloys. GlidCop A125 and MAGT 0.2. Measurements were made on specimens in their as-wrought condition, after thermal annealing for 1 h **at** 900°C, and after 3 MeV Ar^+ ion irradiation **at** 180 and 350°C to damage levels of 20 to 30 displacements per atom (DPA). All of the annealed and ion-irradiated specimens were found to be resistant to recrystallization. In addition, void formation was not observed in any of the irradiated specimens. The GlidCop oxide particle geometry was transformed from triangular platelets to circular disks by the ion irradiation. The MAGT particle geometry consisted of circular disks and spheres before and after irradiation. The **oxide** particle edge length in the unirradiated GlidCop alloy was about 10

The plugged pipe removed from the cold-trap purification loop of the forced-circulation lithium system was examined to study mass transfer/deposition behavior and to establish the cause of plugging. Several intermetallic compounds were identified in residue collected from the plugged cold-trap pipe. Plugging was caused by deposition of calcium/zinc/nickel crystals in the pipe sections within the pump coil and flow-meter magnet. Addition of calcium as a getter to reduce the concentration of nitrogen in the lithium leads to formation of (Ca,Zn)Ni_5 crystals and subsequent plugging of the cold-trap loop. Deposits of manganese/iron/nickel globules and manganese/zinc/nickel dendrites, as well as Li_9CrN_5 and possibly Ca_3N_2, were also identified in the residue. These phases may have reduced flow through the cold-trap loop but were not abundant enough to plug the loop. The results indicate that the use of a dissolved getter, such as calcium, to reduce nitrogen content in an austenitic stainless steel loop may not be effective. Elements in the lithium from structural alloys (e.g., due to corrosion) and those added (e.g., calcium) to reduce the concentration of nonmetallic impurities (e.g., nitrogen) play an important role in the mass transfer/deposition behavior in circulating lithium systems.

Scoping tests were conducted on compatibility of gallium with candidate structural materials. e.g., Type 316 SS, Inconel 625, and Nb-5 Mo-1 Zr alloy, as well as Armco iron, Nickel 270, and pure chromium. Type 316 stainless steel is least resistant and Nb-5 Mo-1 Zr alloy is most resistant to corrosion in static gallium. At 400°C, corrosion rates are ≈4.0, 0.5, and 0.03 mm/y for Type 316 SS, Inconel *625*, and Nb-5 Mo-1 Zr alloy, respectively. The pure metals react rapidly with gallium. In contrast to findings in earlier studies, pure iron shows greater corrosion than does nickel. The corrosion rates at 400°C are ≥90 and 17 mm/y, respectively, for Armco iron and Nickel 270. The results indicate that at temperatures up to 400°C, corrosion occurs primarily by dissolution accompanied by formation of metal/gallium intermetallic compounds.

Susceptibility of crevice-weldment specimens of Types 316L and 316NG stainless steel (SS) to SCC was investigated in slow-strain-rate-tensile (SSRT) tests in water that simulates important parameters anticipated in first-wall/blanket systems. The SSRT tests were performed in oxygenated water containing 0.06-10 ppm chloride at temperatures of 95 to 225°C to establish the effects of water purity and temperature on SCC resistance. These steels, including weldments, exhibit good resistance to SCC under crevice conditions at temperatures of <150°C in water containing ≤0.1 ppm chloride. It appears that Type 316NG SS is somewhat more resistant to SCC than Type 316L SS at temperatures >150°C in oxygenated water containing 0.1-10 ppm chloride. Most specimens fractured in the base metal, and several others fractured in the heat-affected zone (HAZ) of the weld, but none failed in the weld metal.

Aluminide coatings were produced on vanadium and vanadium-base alloys by exposure of the materials to liquid lithium that contained 3-5 at.% dissolved *aluminum in* sealed capsules at temperatures between 775 and 880°C. Reaction of the aluminide layer with dissolved nitrogen in liquid lithium provides a means of developing an in-situ electrical insulator coating on the surface of the alloys. The electrical resistivity of AIN coatings on **aluminided V** and V-20 wt.% Ti was determined in-situ.

Crack-growth-rate (CGR) tests were performed on 1-in.-thick (1T) compact-tension (CT) specimens of Types 316NG and 3161. stainless steel (SS) in oxygenated water conraining 0-5 ppin C1$^-$ at 150, 185, and 225°C. The results obtained under cyclic loading conditions at stress intensity factors of ≈27 to 39 MPa·m$^{1/2}$ indicate that environmental enhancement of the rates increases with C1$^-$ concentrations >0.1 ppm at 150°C in comparison with calculated rates in *air under the specific loading* conditions. lo contrast, at the higher temperatures the CGRs were not affected hy C1$^-$ in oxygenated water hut were greater than the predicted rates *in* air by one order of magnitude.

Aluminide coatings were produced on vanadium and vanadium-base alloys by exposure of the materials to liquid lithium that contained 3-5 at.% dissolved aluminum in sealed V and **V-20** wt.% Ti capsules at temperatures between 775 atid 880°C. After each test, the **capsules** werc opened and llic *samples* were examined by optical microscopy and scanning electron microscopy (SEM), and analyzed by electron-energy-dispersive spectroscopy (EDS) and X-ray diffraction. *Hardness* of the *coating layers* and hulk alloys was determined by microindentation techniques. The nature of the coatings, i.e., surface coverage, thickness, and composition, varied with *exposure time* and temperature, solute concentration in lithium, and alloy composition. Solute elements that yielded adherent coatings on various substrates can provide a means of developing *in-situ* electrical insulator coatings by reaction of the reactive layers with dissolved nitrogen in liquid lithium.

No *contributions*

The key radiation effects issues associated with the successful operation of ceramic materials in components of the planned International Thermonuclear Experimental Rcactor (ITER) are discussed. *Radiation-induced volume* changes **and** degradation of the mechanical properties should not hc **a** serious issue for die fluences planned for ITER. On the other hand. radiation-induced electrical degradation effects rnny severely limit allowable the exposure of ceramic insulators. Degradation of the loss tangent and thermal conductivity may also restrict the location of some components such as ICRH feedthrough insulators to positions far away from the first wall. In-situ measurements suggest that the degradation of physical properties in ceramics during irradiation is greater than that measured in postirradiation tests. Additional in-situ data during neutron irradiation are needed before engineering designs for ITER can be finalized.

8.2 EFFECT OF IRRADIATION SPECTRUM ON THE MICROSTRUCTURAL EVOLUTION IN OXIDE CERAMICS -- S.J. Zinkle *(Oak* Ridge National Laboratory) 426

Cross section transmission electron microscopy was utilized to examine the radiation-induced microstructural changes in oxide ceramics after irradiation with a wide variety of ion beams. The microstructure showed a strong dependence on ion mass and energy. The microstructural results have been correlated with the calculated depth-dependent partitioning between ionization and displacement damage. This correlation indicates that defect clusters do not form in $MgAl_2O_4$ if the ratio of energy deposited into electronic ionization to atomic displacements is greater than about 10. The corresponding ratio needed to suppress defect cluster formation in MgO and Al_2O_3 is 500 to 1000. Additional microstructural evidence obtained on the ion irradiated ceramic specimens suggests that the physical mechanism responsible for the lack of defect clusters in highly ionizing radiation environments is associated with ionization-enhanced diffusion (IED), which promotes annihilation of the point defects created by displacement damage during the irradiation. The most important parameter for IED is the ratio of ionizing to displacive radiation, since this is roughly proportional to the amount of ionization per dpa. However, the absolute magnitude of the ionizing radiation flux is also important.

8.3 ELECTRICAL CONDUCTIVITY OF CERAMIC INSULATORS DURING EXTENDED ION IRRADIATION WITH AN APPLIED ELECTRIC FIELD -- S. J. Zinkle (Oak Ridge National Laboratory) and W. Kesternich (Forschungszentrum Juelich) 437

The initial results are presented from a cyclotron ion irradiation program investigating radiation-induced conductivity (RIC) and radiation-induced electrical degradation (RIED) of ceramic insulators. Polycrystalline specimens of Al_2O_3, $MgAl_2O_4$, AlN and Si_3N_4 were irradiated with either 28 MeV He^{++} or 20 MeV H^+ ions at temperatures between 150 and 600°C with an applied dc electric field of 100 to 500 V/mm. A large prompt increase in the electrical conductivity was observed in all of the specimens during irradiation. However, there was no evidence for permanent electrical degradation in any of the specimens for damage levels up to about 5×10^{-3} displacements per atom.

8.4 IRRADIATION OF $MgAl_2O_4$ SPINEL IN FFTF-MOTA -- F. A. Garner and G. W. Hollenberg (Pacific Northwest Laboratory), C. A. Black and R. C. Bradt (University of Nevada-Reno) 447

$MgAl_2O_4$ spinel specimens irradiated in FFTF-MOTA at temperatures between 385 and 750°C to fluences ranging from 2.2 to 24.0 x 10^{22} n cm^{-2} (E>0.1 MeV) darken significantly, but do not develop any loss in weight or change in dimensions. Measurements of Knoop hardness and its dependence on crystalline orientation, neutron fluence and irradiation temperature are in progress. Measurements of elastic properties are also nearing completion.

8.5 HIGH-TEMPERATURE PROPERTIES OF SiC/SiC FOR FUSION APPLICATIONS -- R. H. Jones and C. H. Henager, Jr. (Pacific Northwest Laboratory) 451

Si/SiC composites exhibit novel mechanical properties relative to their monolithic counterparts. The crack velocity (da/dt) versus stress intensity (K) relationship for monolithic ceramics can be described by a simple power law relationship where SiC/SiC was found to exhibit a multi-stage da-dt versus K relationship similar to that for stress corrosion of metals. A K independent stage II was followed by a *strongly* K dependent state III, which paralleled the monolithic behavior. Experiments to determine the threshold K or stage I were not conducted; however, it **is** expected that they *exist* for *these* materials. There **is** also evidence that the fracture resistance of these materials **is** greater if **cracks** are produced by subcritical growth processes relative to machined notches. Oxygen was found to increase da/dt **and** decrease the K for *the* stage II to stage III transition while cyclic loads produced little damage at low K values but there was some evidence for increasing damage with increasing number of cycles **and** K.

8.6 MEASUREMENT OF DC ELECTRICAL CONDUCTIVITY OF ALUMINA DURING SPALLATION-NEUTRON IRRADIATION -- E. H. Farnum, F. W. Clinard, Jr., J. C. Kennedy, III, W. F. Sommer, and M. D. Dammeyer (Los Alamos National Laboratory) . . . 457

An irradiation experiment was carried out during the summer of 1992 at the Los Alamos Spallation Radiation Effects Facility (LASREF). *In situ* measurements of electrical conductivity in alumina, sapphire, and mineral-insulated electrical cables were made at 640°C, 590°C, and 400°C. Both DC and **AC** (100 Hz to 1 MHz) measurements were made to a fluence of approximately 3 x 10^{23} n/m^2. Optical absorption from 300 nm to 800 nm was measured in pure silica- and OH-doped silica-core optical fibers during the irradiation. A large number of passive samples were included in the irradiation, some **at** the furnace temperatures and some at ambient temperature. This report describes preliminary analysis of the DC conductivity measurements. The AC measurements are analyzed in the companion report.

8.7 MEASUREMENT OF AC ELECTRICAL CONDUCTIVITY OF SINGLE CRYSTAL Al_2O_3 DURING SPALLATION-NEUTRON IRRADIATION -- J. C. Kennedy, III, E. H. Farnum, W. F. Sommer, and F. W. Clinard, Jr. (Los Alamos National Laboratory) 465

Samples of **single** crystal Al_2O_3, commonly known as sapphire, and polycrystalline Al_2O_3 were irradiated with spallation neutrons **at** the Los Alamos Spallation Radiation Effects Facility (LASREF) under various temperature conditions and with a continuously applied alternating electric **field.** This paper describes **the** results **of** measurements on the sapphire samples. Neutron fluence and flux values are estimated values pending recovery and analysis of dosimetry **packages.** The conductivity increased approximately with the square root of the neutron flux **at** fluences less than 3 x 10^{19} n/m^2 at fluxes less than 1 x 10^{16} n/m^2-sec. Conductivity initially decreased at low fluences with minimums near fluences of 1 x 10^{20} n/m^2. Incubation periods with a gradual increase in conductivity preceded the onset of an accelerated increase in conductivity beginning at fluences as low as 10^{21} n/m^2. The increase in conductivity reached saturation levels as high as 2 x 10^{-2} (ohm-m)$^{-1}$ at fluences as low as 2 x 10^{22} n/m^2. Frequency swept impedance measurements indicated a change in the electrical properties from capacitive to resistive behavior with increasing fluence.

8.8 IRRADIATION EFFECTS IN CERAMICS: TRANSITION FROM LOW TO HIGH DOSE BEHAVIOR -- F. W. Clinard, Jr., and E. H. Farnum (Los Alamos National Laboratory) 475

Ceramics subjected to irradiation show a wide variety of damage responses. depending on composition, nature of bonding, crystal structure, impurity levels, starting microstructure, number of phases, and type **of** bombarding particle. As doses reach high levels (a condition that varies in magnitude **from** one material to another) major **changes** in physical **properties** can occur, and atomic **arrangements** may even change from crystalline to disordered. However. some ceramics show marked resistance to damage, and some properties may improve. More work **is** needed to fully understand these phenomena, but it **is** currently possible in many cases to predict at least qualitatively both microstructural damage response and observed property changes.

8.9 THE EFFECT OF RADIATION INDUCED ELECTRICAL CONDUCTIVITY (RIC) ON THE THERMAL CONDUCTIVITY OF SAPPHIRE AT 77K -- D. P. White (Oak Ridge National Laboratory) 480

Microwave heating of plasmas in fusion reactors requires the development of microwave windows through which the microwaves can pass without great losses. The degradation of the thermal conductivity of alumina in a radiation environment is an important consideration in reliability studies of these microwave windows. Several recent papers have addressed this question at higher temperatures and at low temperatures. The current paper extends the low temperature calculations to determine the effect of phonon-electron scattering on the thermal conductivity at 77 K due to RIC. These low temperature calculations are of interest because the successful application of high power (>1 MW) windows for electron cyclotron heating systems in fusion reactors will most likely require cryogenic cooling to take advantage of the low loss tangent and higher thermal conductivity of candidate window materials at these temperatures.

8.10 SURFACE PREPARATION EFFECTS IN NEAR SURFACE MODULUS MEASUREMENT FOR CVD SiC -- M. Osborne (Rensselaer Polytechnic Institute), L. L. Snead (Oak Ridge National Laboratory), and D. Steiner (Rensselaer Polytechnic Institute) 484

Surface preparation has an observable effect on the data obtained from the Nanoindenter for shallow (20 nm) indents on CVD SiC when polished with Syton™. This observed effect is significantly less for 1/2 micron diamond polished CVD SiC and for deep (160 nm) indents. These effects were manifested by the relative variations in the experimental modulus and hardness data. An analytical analysis of the anticipated variation in the modulus and hardness is performed and shown to correlate well with the observed trends. The observed variations appear to be the result of SiC material properties, as well as surface preparation, since the predicted variations are much smaller than the observed variations.

8.11 MICROMECHANICS OF FIBER PULL-OUT AND CRACK BRIDGING IN SCS-6 SiC-CVD SiC COMPOSITE SYSTEM AT HIGH-TEMPERATURE -- A. El-Azab and N. M. Ghoniem (University of California, Los Angeles) 495

A micro mechanical model is developed to study fiber pull-out and crack bridging in fiber reinforced SiC-SiC composites with time dependent thermal creep. By analyzing the creep data for monolithic CVD SiC (matrix) and the SCS-6 SiC fibers in the temperature range 900-1250°C, it is found that the matrix creep rates can be ignored in comparison to those of fibers. Two important relationships are obtained: (1) a time dependent relation between the pull-out stress and the relative sliding distance between the fiber and matrix for the purpose of analyzing pull-out experiments, and (2) the relations between the bridging stress and the crack opening displacement to be used in studying the mechanics and stability of matrix crack bridged by fibers at high temperatures. The present analysis can be also applied to Nicalon-reinforced CVD SiC matrix system since the Nicalon fibers exhibit creep characteristics similar to those of the SCS-6 fibers.

1.0 IRRADIATION FACILITIES, TEST MATRICES, AND EXPERIMENTAL METHODS

PREPARATION OF COBRA 1A FOR INSERTION INTO EBR-II - M. L. Hamilton and R. M. Ermi (Pacific Northwest Laboratory)[1] and C. R. Eiholzer (Westinghouse Hanford Company)

OBJECTIVE

The purpose of this effort is to document the preparation of the COBRA 1A experiment for irradiation in the Experimental Breeder Reactor II (EBR-II) for irradiation beginning in run 162.

SUMMARY

COBRA 1A was built to support the research and development efforts of the U.S. DOE Neutron Interactive Materials (NIMs) program and the Japanese university fusion materials program. COBRA was inserted into the EBR-II for irradiation beginning in run 162. The specimen loading is documented here.

PROGRESS AND STATUS

Introduction

The anticipated shutdown of the Fast flux Test Facility (FFTF) necessitates a transfer of the Fusion Materials irradiation programs from the FFTF to EBR-II. This requires the development of a MOTA-type vehicle for EBR-II, i.e.. one that is capable of performing instrumented, temperature controlled irradiations in a fast neutron environment. The assembly being developed will be referred to as a Materials Instrumented Test Assembly, or MITA. Due to the two year lead time required for the development of such a vehicle and the desire to continue accumulating neutron exposure in the interim. another irradiation vehicle that utilizes existing technology is being used in the meantime. It is referred to as a Cold B7A Radiation Assembly, or COBRA. The first irradiation of the first COBRA will be referred to as COBRA 1A. Reconstituted irradiations of the first COBRA will increment the letter designation, i.e., 1B, 1C. etc., where the "CO" in COBRA will then refer to "continuing" irradiations. A new COBRA-type of irradiation vehicle will increment the number designation, i e.. 2A.

The U.S. Neutron Interactive Materials (NIMs) program and the Japanese university fusion materials community (funded by the US/Japan Collaborative Program on Fundamental Studies of Irradiation Effects in Fusion Materials Utilizing Fission Reactors) are partners in the MITA and COBRA efforts. The goal of there two programs is to develop improved materials for use in many different components of proposed fusion devices and to facilitate the prediction of their performance limits in a fusion environment. These programs focus on metallic or ceramic specimens for post-irradiation determination of swelling, mechanical properties and microstructure.

COBRA loading

Experiment Description. COBRA 1A is referred to by ANL-W as subassembly X-516. It comprises seven B7A capsules in a standard B7A assembly. The PNL and WHC identification codes for the seven capsules, A through G, correspond to the ANL-W identification codes. B-388 through E-394. Three capsules (D, F and G) are filled with inert gas to provide irradiation at elevated temperatures (800, 500 and 600°C respectively). The remaining four capsules (A, B, C and E) are weeper capsules designed to maintain the test specimens at ambient temperature (~400°C). The capsules are being irradiated in a hexagonal duct with capsule C (B-390) located at the center, as shown in Figure 1.

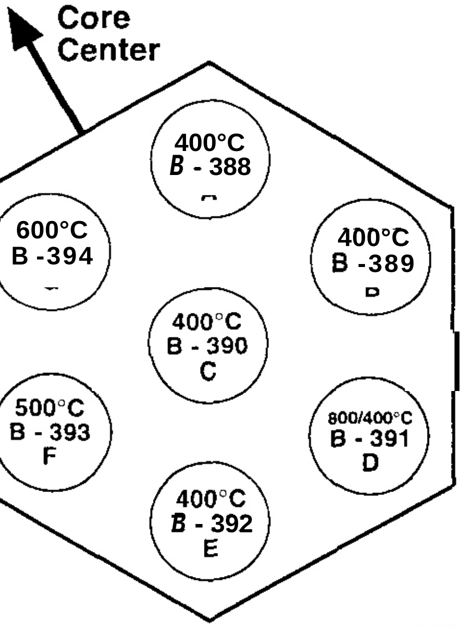

Figure 1. Capsule arrangement in COBRA 1A (subassembly X516).

The temperature of the inerted subcapsules is controlled by the size of the gap between the outer wall of the subcapsule and the inner wall of the capsule, as well as

---

[1] Pacific Northwest Laboratory is operated for the U.S. Department of Energy by Battelle Memorial Institute under Contract DE-AC06-76RLO 1830.

the composition of the insulating gas that fills this gap. Direct contact with sodium will maintain the temperature of the specimens in the weeper capsules as close as possible to ambient. Some of the subcapsules in the 800°C capsule (D) will be gas gapped in such a way as to achieve a temperature as close as possible to the ambient weeper temperature. Specimens provided by the two partners are being irradiated above and below as well as within the core region. Three capsules (E, F and G) will be irradiated for about 150 EFPD, while the remaining four (A through D) will be irradiated for approximately twice as long. The B7A capsules were designed, fabricated and assembled by Westinghouse Hanford Company. Standard B7A assembly hardware was supplied by EBR-II.

COBRA 1A will be irradiated in row 2, sector B, position 2B1 in EBR-II. A core map for run 162 is shown in Figure 2. The estimated nominal flux at reactor midplane in this position is $2.339 \times 10^{\text{[illegible]}}$ n/cm^2/sec (E > 0.111 MeV) for run 162, based on reactor physics calculations. The most recent flux normalization profile for row 2 was determined in 1978 after run 75D. It is shown in Figure 3.

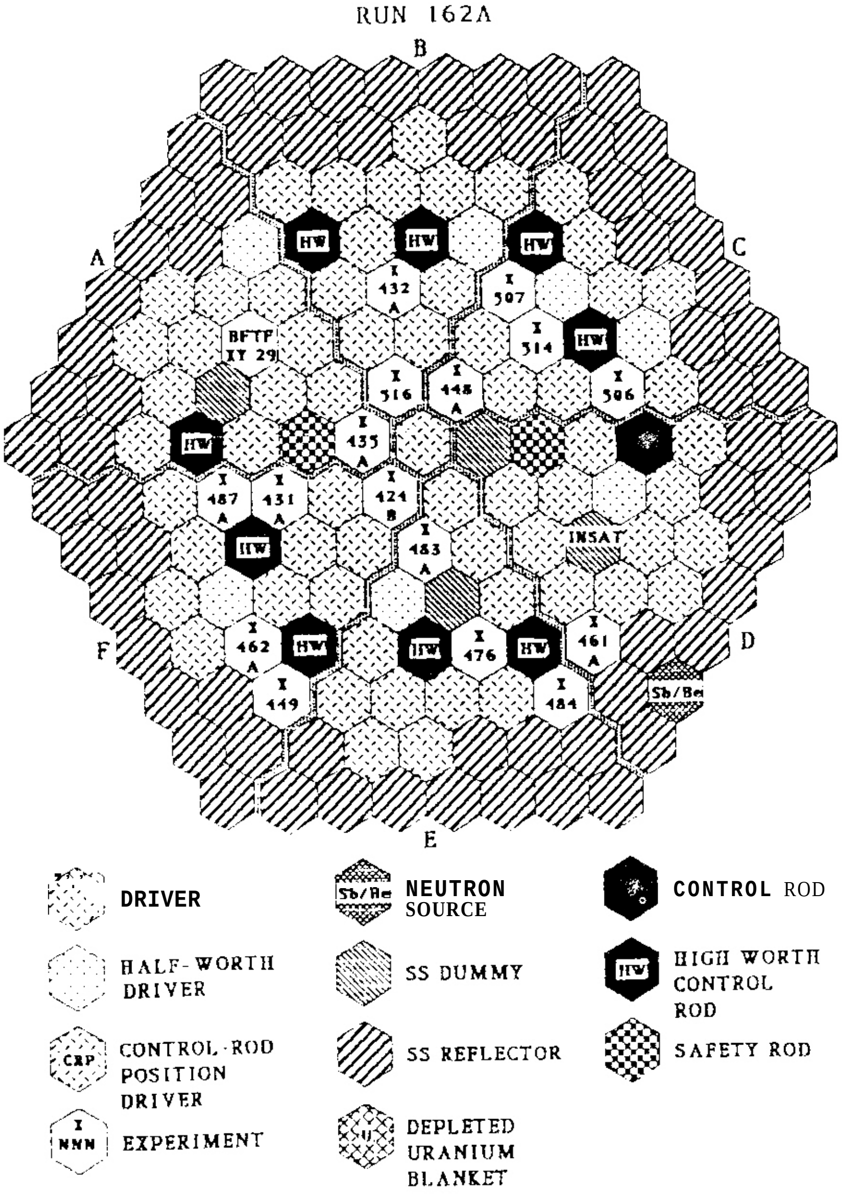

Figure 2. Core map for EBR II run 162.

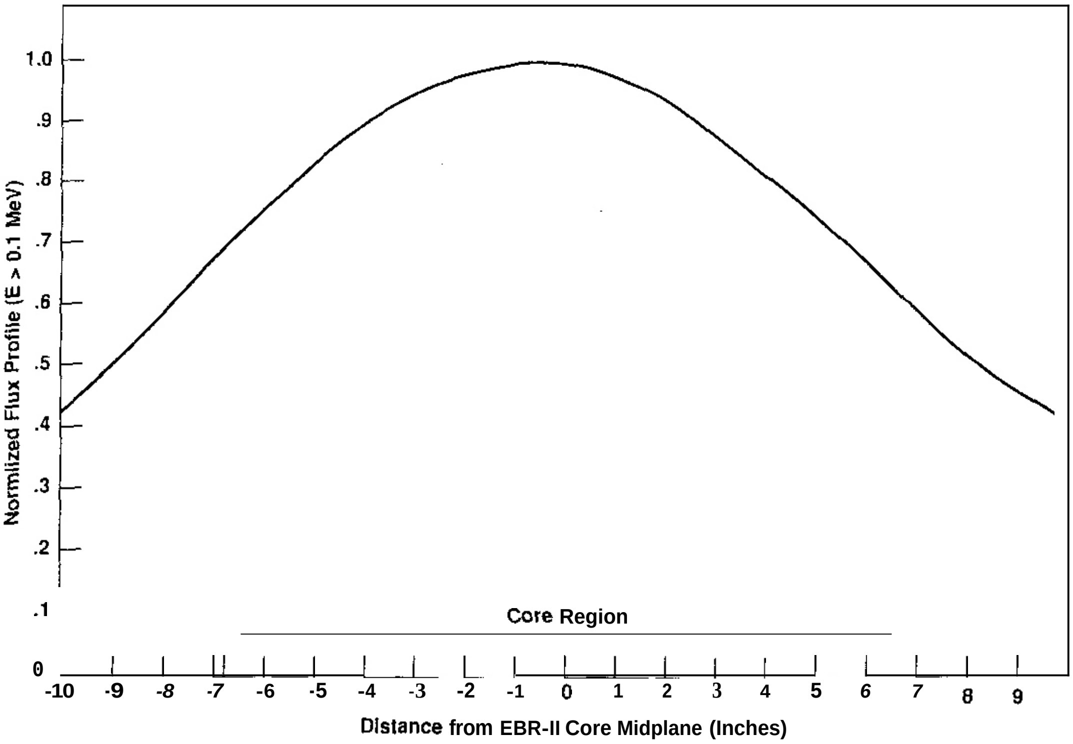

Figure 3. Flux normalization profile for row 2 (from 1978).

Capsule Allocation. The capsule matrix for COBRA 1A is shown in Figure 4 as a function of the division of each capsule into subcapsules or baskets. The codes given in the upper left corner of each element of the matrix designate the basket or subcapsule identification. The letters "S" or "B" in the lower left corner indicate whether the element refers to a subcapsule or a basket. The number immediately below the "S" or "B" is the length of the subcapsule or basket. The number in parentheses in the lower right corner of each element indicates the position of the bottom of the subcapsule or basket. i.e., the location of the bottom of the specimens, relative to the middle of the core. Both dimensions are given in inches. the units in which the Components were specified.

Baskets allow sodium to flaw through them and are typically used for irradiation under weeper conditions, while subcapsules are sealed and are typically used for irradiation under gas gapped conditions. Subcapsules are also used for specimens to be irradiated under weeper conditions that cannot be allowed to come into contact with the reactor sodium. All baskets and subcapsules are made of stainless steel except for those subcapsules with a superscripted asterisk next to the "S"; these are made of TZM.

The letters given in the upper right corner of some elements indicate the presence of dosimetry packages (8-spectral set. G=gradient wire) or thermal measuring devices (TED = thermal expansion device, T-MON = rectangular SiC bar used as a thermal monitor). Both types of dosimetry were packaged in helium-filled, stainless steel, sealed containers. TEDs are sodium-filled stainless steel or Inconel tubes that acquire a permanent deformation that corresponds to the maximum temperature to which they are exposed during Irradiation. The thermal monitors are extra SiC bars that will be analyzed for thermal exposure.

Specimen Matrix. The objective of the U.S. NIMs program is to develop improved materials for use in fusion devices and predict their performance limits in a fusion environment. The long term effort focuses on providing an increased understanding of damage mechanisms through experiment, data analysis and modelling. A short term effort is focussed on meeting the near-term materials needs for the International Thermonuclear Experimental Reactor (ITER).

The emphasis in the U.S. is primarily on (but is not limited to) alloys for first wall/blanket applications. Major areas include 1) supplying high fluence. engineering data for current or potential fusion candidate heats of ferritic steels. 2) exploring reduced activation alloys of several types (ferritic iron-based steels as well as vanadium alloys and SiC/SiC). 3) developing copper alloys for high neat flux applications and an understanding of their fundamental radiation response. and 4) clarifying the role of helium. Smaller efforts are directed toward the development of beryllium for neutron multiplier or plasma interactive components. and the development of composite materials far high heat flux applications.

The Japanese university program for the development of fusion reactor materials is using the FFTF/MOTA as part of a larger program to attain an understanding of the various radiation responses that control materials' behavior. Specifically. their program is designed 1) to establish correlations between high and low exposure irradiations in fission and fusion neutrons and 2) to determine the mechanisms governing microstructural and microchemical evolution and their relation to property changes in materials

Six sub-groups have been designated responsible far such efforts in Japan for different classes of materials:

a) Ferrous materials,
b) Refractory metals and alloys. high heat flux materials
c) Pure metals and model alloys for fundamental studies,
d) Isotopic tailoring experiments.
e) Ceramics and composite materials. and
f) Dosimetry

A summary of the combined U.S. and .Japanese specimen matrix is shown in Table 1. arranged by alloy type. The geometries of the U.S. and Japanese specimens are listed in Table 2. Table 1 shows the programmatic affiliation (U.S., Japanese. or collaborative) of each specimen as well as the specimen type and COBRA 1A position. U.S. programmatic affiliations are broken down to show the distribution between laboratories. No collaborative affiliations are shown in this table other than with the US/Japan Collaborative Program on Fundamental Studies of Irradiation Effects in fusion Materials Utilizing fission Reactors.

CONCLUSIONS

The COBRA 1A experiment was successfully prepared and inserted into EBR-II for irradiation starting with run 162.

FUTURE WORK

Planning will continue for the development of both COBRA 1B and MITA

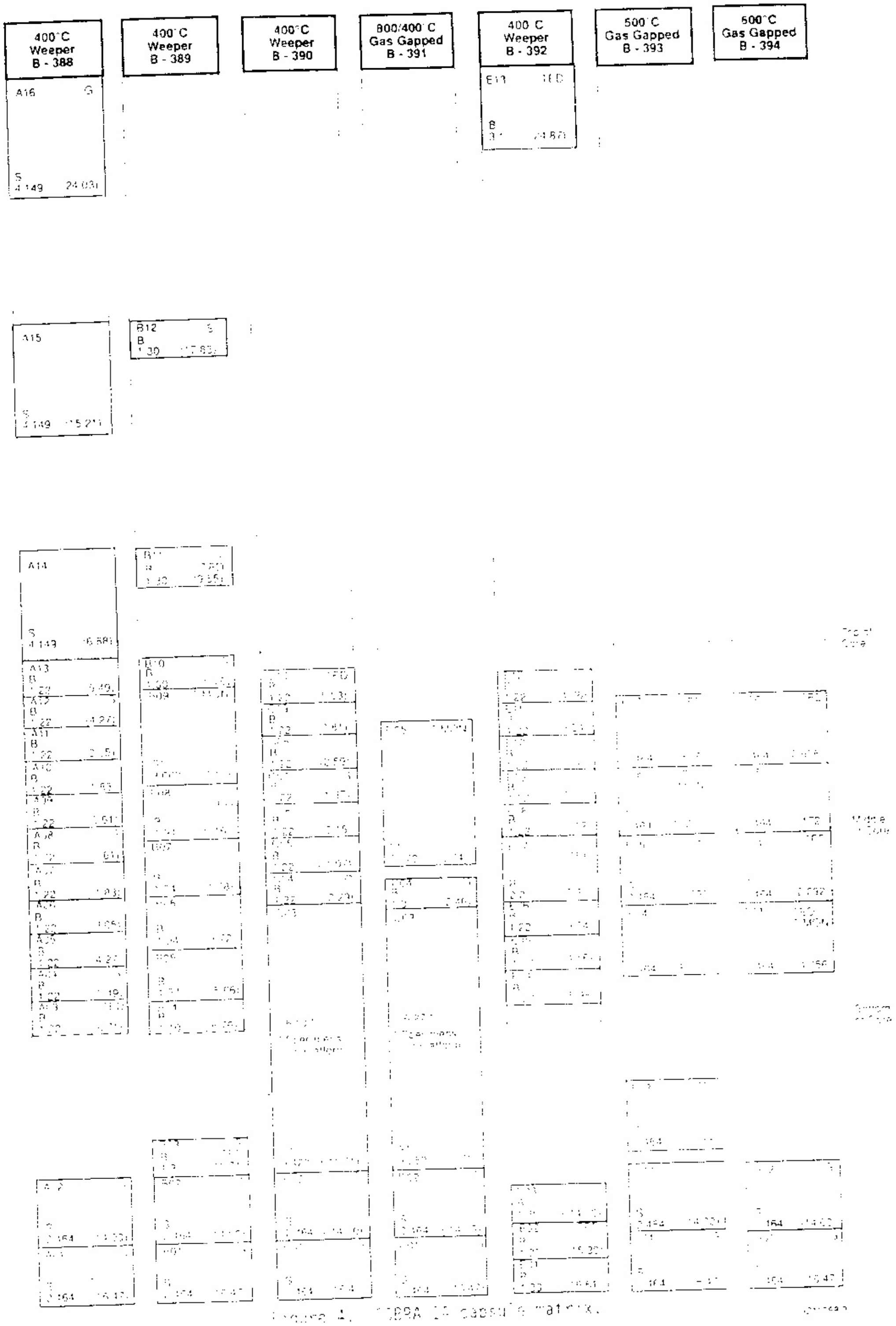

Figure 1. COBRA 1A capsule matrix.

Table 1. COBRA 1A Specimen Matrix

Subcapsule or Basket[1]	Specimen Type[2]	Alloy[3]	Number of Specimens[4]	Program[5]
D03-S	D	Be (100% dense)	18	US-E
D03-S	D	Be (80% dense)	18	US-E
D03-S	B	Be - SW	150	J/US-E,P
D03-S	B	Be - BW	75	J/US-E,P
D03-S	B_2	Be - BW	7	J/US-E,P
D03-S	B	Be - BW	7	J/US-E,P
E11-B	B (TZM/He)	Be - BW	>100	J
F07-S	B (TZM/He)	Be - BW	>100	J
G06-S	B (TZM/He)	Be - BW	>100	J
D03-S	B	Be - NGK	150	J/US-E,P
E06-B	B (TZM/He)	Be - NGK	>100	J
F04-S	B (TZM/He)	Be - NGK	>100	J
G03-S	B (TZM/He)	Be - NGK	>100	J
C01-S	F	Cu	4	US-P
C02-S	F	Cu	4	US-P
D01-S	F	Cu	4	US-P
D02-S	F	Cu	4	US-P
F01-S	F	Cu	1	US-P
G01-S	F	Cu	4	US-P
A01-S	F	CuAl25	4	US-P
A02-S	F	CuAl25	4	US-P
B01-S	F	CuAl25	4	US-P
B02-S	F	CuAl25	4	US-P
F02-S	F	CuAl25	4	US-P
G02-S	F	CuAl25	4	US-P
F06-S	TN	CuAl25, $CuAl_2O_3$	12	J/US-P
F03-S	TN	CuAl25, $CuAl_2O_3$	12	J/US-P
F08-S	TN(SS)	CuAl25, $CuAl_2O_3$	12	J/US-P
E03-B	TN(SS)	CuAl25, $CuAl_2O_3$	12	J/US-P
B03-B	TEM(S)	Cu alloys	[illegible]	J/US-P,O
F08-B	TEM(S)	Cu alloys	[illegible]	J/US-P,O
F03-S	TEM(S)	Cu alloys	[illegible]	J/US-P,O
F06-S	TEM(S)	Cu alloys	[illegible]	J/US-P,O
A03-B	TEM(W)	Fe alloys (F-M)	[illegible]	US-P
A13-B	TEM(W)	Fe alloys (F-M)	[illegible]	US-P
E09-B	TEM(W)	Fe-Cr-X	[illegible]	US-P
F02-B	TEM(W)	Fe-Cr-X	[illegible]	US-P
E09-B	TEM(W)	Fe alloy (2¼Cr-1Mo)	[illegible]	US-P
E13-B	SEM	Fe alloys	[illegible]	US-E
F13-B	D	Fe alloys	[illegible]	US-E
E05-B	TEM(S)	Fe alloys	[illegible]	[illegible]
F04-S	TEM(S)	Fe alloys	[illegible]	[illegible]
G03-S	TEM(S)	Fe alloys	[illegible]	[illegible]
C10-B	TEM(W)	Fe alloys	[illegible]	[illegible]
F05-S	TEM(W)	Fe alloys	[illegible]	[illegible]
G04-S	TEM(W)	Fe alloys	[illegible]	[illegible]
E05-S	TEM(S)	FeCrNiP	[illegible]	[illegible]
F04-S	TEM(S)	FeCrNiP	[illegible]	[illegible]
G03-S	TEM(S)	FeCrNiP	[illegible]	[illegible]
E07-B	TEM(S)	FeCrNiTi-B,C	[illegible]	[illegible]
F05-S	TEM(S)	FeCrNiTi-B,C	[illegible]	[illegible]
G04-S	TEM(S)	FeCrNiTi-B,C	[illegible]	[illegible]

Continued on next page...

Table 1. COBRA 1A Specimen Matrix

Subcapsule or Basket[1]	Specimen Type[2]	Alloy[3]	Number of Specimens[4]	Program[5]
Continued from previous page...				
A13-B	TEM(W)	High Mn γ	1	US-O
C08-B	T(SS-3)	High Mn γ	8	US-O
B06-B	T(SS-3)	High Mn γ	4	US-O
C09-B	T(SS-3)	High Mn γ	9	US-O
B08-B	T(SS-3)	High Mn γ	5	US-O
B04-B	T(SS-3)	High Mn γ	8	US-O
B05-B	T(SS-3)	High Mn γ	6	US-O
A12-B	T(SS-3)	Russian high Mn γ	5	US-O
A05-B	CT	HT9, RAF	3	US-P
A06-B	CT	HT9, RAF	9	US-P
A07-B	CT	HT9, RAF	8	US-P
A09-B	CT	HT9, RAF	9	US-P
A10-B	CT	HT9, RAF	8	US-P
A11-B	CT	HT9, RAF	3	US-P
A03-B	T(SS-3)	HT9, RAF	16	US-P
A13-B	T(SS-3)	HT9, RAF	16	US-P
B08-B	T(SS-3)	Fe alloys (9-12 Cr F/M)	4	US-O
B08-B	T(SS-3)	RAF	4	US-O
A04-B	T(SS-3)	RAF	5	US-O
A08-B	T(SS-3)	RAF	5	US-O
B06-B	T(SS-3)	RAF	2	US-O
B07-B	T(SS-3)	RAF	6	US-O
C04-B	T(SS-3)	RAF	4	US-O
C05-B	T(SS-3)	RAF	8	US-O
C06-B	T(SS-3)	RAF	8	US-O
C07-B	T(SS-3)	RAF	4	US-O
C06-B	1/3 C_v	HT9	12	US-P
C07-B	1/3 C_v	RAF	12	US-P
C08-B	1/3 C_v	RAF	4	US-P
C09-B	1/3 C_v	RAF	12	US-P
C10-B	1/3 C_v	Fe alloys (9-12 Cr F/M)	12	US-O
A04-B	1/3 C_v	RAF	12	US-O
A08-B	1/3 C_v	RAF	12	US-O
A12-B	1/3 C_v	RAF	12	US-O
B04-B	1/3 C_v	RAF	5	US-O
B05-B	1/3 C_v	RAF	6	US-O
B06-B	1/3 C_v	RAF	5	US-O
B07-B	1/3 C_v	RAF	5	US-O
C04-B	1/3 C_v	RAF	12	US-O
C05-B	1/3 C_v	RAF	12	US-O
G03-S	TN	RAF	4	J
G06-S	TN	RAF	11	J
E10-B	TN	RAF	11	J
F04-S	TN	RAF	4	J
F07-S	TN	RAF	11	J
E06-B	TN	RAF	1	J
Continued on next page...				

Table 1. COBRA 1A Specimen Matrix

Subcapsule or Basket[1]	Specimen Type[2]	Alloy[3]	Number of Specimens[4]	Program[5]
Continued from previous page...				
F04-S	TEM(N)	PAF, JPCA, J316	[illegible]	[illegible]
F06-B	TEM(N)	PAF, JPCA, J316	[illegible]	[illegible]
E08-B	T(SS-3)	JPCA, J316	15	[illegible]
F06-S	T(SS-3)	JPCA, J316	15	[illegible]
E06-S	TN	JPCA, J316	10	[illegible]
F07-S	TN	JPCA, J316	12	[illegible]
E05-B	TN(SS)	316 var	28	J
F04-S	TN(SS)	316 var	23	J
E03-S	TN(SS)	316 var	12	J
F10-B	T(SS-3)	316	[illegible]	US-D
F02-B	1/3 C[illegible]	HT9	3	J/US-P
F03-B	1/3 C[illegible]	HT9	12	J/US-P
F09-B	1/3 C[illegible]	HT9	[illegible]	J/US-P
E11-B	1/3 C[illegible]	HT9	10	J/US-P
F01-B	1/3 C[illegible]	JFMS	12	J/US-P
F04-B	1/3 C[illegible]	JFMS	12	J/US-P
E01-B	1.5 C[illegible]	JFMS	10	J/US-P
F03-B	1.5 C[illegible]	HT9	11	J/US-P
E04-B	1.5 C[illegible]	JFMS	10	J/US-P
E12-B	1.5 C[illegible]	HT9	12	J/US-P
F06-B	TN	HT9	5	[illegible]
F04-S	TN	HT9	[illegible]	[illegible]
E03-S	TN	HT9	[illegible]	[illegible]
E06-B	TN	JFMS	[illegible]	[illegible]
F04-S	TN	JFMS	[illegible]	[illegible]
F07-S	TN	JFMS	[illegible]	[illegible]
E06-S	TN	JFMS	[illegible]	[illegible]
F03-S	TN	JFMS	[illegible]	[illegible]
[illegible]14-S		[illegible]	[illegible]	[illegible]
[illegible]15-S		[illegible]	[illegible]	[illegible]
[illegible]16-S		[illegible]	[illegible]	[illegible]
[illegible]05-B	TEM(SS)	[illegible]	[illegible]	[illegible]
[illegible]04-S	TEM(SS)	[illegible]	[illegible]	[illegible]
[illegible]	TEM(SS)	[illegible]	[illegible]	[illegible]
[illegible]05-B	TN(SS)	[illegible]	[illegible]	[illegible]
[illegible]04-S	TN(SS)	[illegible]	[illegible]	[illegible]
[illegible]	[illegible]	[illegible]	[illegible]	[illegible]
[illegible]		[illegible]	[illegible]	[illegible]
[illegible]		[illegible]	[illegible]	[illegible]
[illegible]		[illegible]	[illegible]	[illegible]
[illegible]05-S		[illegible]	[illegible]	[illegible]
[illegible]		[illegible]	[illegible]	[illegible]
[illegible]15-[illegible]		[illegible]	[illegible]	[illegible]
[illegible]		[illegible]	[illegible]	[illegible]
[illegible]10-B	TEM(SS)	[illegible] alloys	[illegible]	[illegible]
[illegible]07-S	TEM(SS)	[illegible] alloys	[illegible]	[illegible]
[illegible]06-S	TEM(SS)	[illegible] alloys	[illegible]	[illegible]
[illegible]10-B	TEM(SS)	[illegible] alloys	[illegible]	[illegible]
[illegible]	TEM(SS)	[illegible] alloys	[illegible]	[illegible]
[illegible]06-[illegible]	TEM(SS)	[illegible] alloys	[illegible]	[illegible]
Continued on next page...				

Table 1. COBRA 1A Specimen Matrix

Subcapsule or Basket[1]	Specimen Type[2]	Alloy[3]	Number of, specimens	Program[5]
Continued from previous page...				
E11-B	TEM(W)	TiNi alloys		J
F07-S	TEM(W)	TiNi alloys		J
G06-S	TEM(W)	TiNi alloys	1	J
E05-B	TN	TiNi alloys	12	J
E11-B	TN	TiNi alloys	12	J
F04-S	TN	TiNi alloys	12	J
F01-S	TN	TiNi alloys	12	J
G03-S	TN	TiNi alloys	12	J
G06-S	TN	TiNi alloys	12	J
B09-S*	CT	V alloys	12	US-A
B05-B	1/3 C_v,SS-3,TEM (TZM/Li)	V alloys	1	US-A
B06-B	1/3 C_v,SS-3,TEM (TZM/Li)	V alloys	1	US-A
B07-B	1/3 C_v,SS-3,TEM (TZM/Li)	V alloys	1	US-A
B08-B	SS-3,TEM (TZM/Li)	V alloys	1	US-A
E13-B	SAM. SP (TZM/Li)	V alloys	1	US-I
E05-B	TEM(S)	V alloys	1	J
F04-S	TEM(S)	V alloys	1	J
G03-S	TEM(S)	V alloys	1	J
E07-B	TN,TEM (TZM/Li)	V alloys	1	J
F05-S	TN,TEM (TZM/Li)	V alloys	1	J
G04-S	TN,TEM (TZM/Li)	V alloys	1	J

1. "-B" and "-S" indicate that the specified segment within the capsule is either a basket **(weeper)** or a subcapsule **(sealed)**, respectively. A superscripted "*" indicates that the **subcapsule** is helium-filled TZM.

2.

1/3 C_v	1/3 size charpy specimen (J in parenthesis indicates the Japanese 1/3 **size** geometry)
1.5 C_v	1.5 mm charpy impact specimen
B_1, B_3, B_5	**ball** specimens **measuring 1.** 3, and 5 mm in **diameter** respectively
BB	bend bar **specimen**
CT	compact **tension specimen**
D	**~0.4"** diameter **disks**
f	fiber specimen
F	fatigue specimen
SAM	scanning Auger microscopy specimen
SP	**small** punch specimen
T(SS-3)	**SS-3** tensile specimen
TEM(S)	sealed TEM **packet**
TEM(W)	**weeper** TEM **packet**
TN	S-1 tensile specimen
(SS)	specimens in helium filled. sealed **stainless** steel container
(TZM/He)	specimens in helium-filled, **sealed** TZM container
(TZM/Li)	specimens in lithium-filled, sealed TZM container

3.

RAF	reduced activation ferritic
Be - NGK	Be made by NGK
Be - BW	**Be made** by Brush Wellman

4. **Refers** to **one** of the following, depending on the entry type:
   number of specimens. or
   number of **TEM packets, or**
   number of TZM containers

5.

J	Japanese	US-L	LANL
US-A	ANL-E	US-O	ORNL
US-E	EG&G	US-P	PNL
US-I	University of **Iowa at Ames**		

Table 2. Specimen **Geometries** in COBRA 1A

SPECIMEN TYPE	DIMENSIONS mm (in)	MATERIAL TYPE	AVERAGE MASS (gms)
Fatigue	6 OD x 50 l (0.24 OD x 1.97 l)	Cu alloys	8.58
TEM disks	3 OD x .25 t (0.118 OD x 0.010 t)	Fe alloys Cu V alloys	0.012 0.013 0.008
	3 OD x 1 t (0.118 OD x 0.04 t)	SiC and C Ti-50Al	0.005 0.006
	3 OD x 0.08 t (0.118 OD x 0.003 t)	Cu	0.045
SS-3 tensiles	25.4 l x 4.95 w x 0.76 t [7.6 gl x 1.5 gw] (1 l x 0.195 w x 0.03 t [0.3 gl x 0.06 gw])	Fe alloys V alloys	0.48 0.3
S-1 tensiles	16 l x 4 w x 0.25 t [5 gl x 1.2 gw] (0.63 l x 0.157 w x 0.01 t [0.2 gl x 0.047 gw])	Fe alloys V alloys Cu Ti 50Al Ti-Ni	0.08 0.06 0.09 0.04 0.06
1/3 size Charpy - PNL	23.6 x 3.33 x 3.33 (0.930 x 0.131 x 0.131)	Fe alloys	2.08
1/3 size Charpy - ORNL	25.4 x 3.33 x 3.33 (1 x 0.131 x 0.131)	Fe alloys V alloys	2.24 1.65
1/3 size Charpy - J	23 x 3.3 x 3.3 (0.905 x 0.13 x 0.13)	Fe alloys	2.00
1.5 mm Charpy	20 x 1.5 x 1.5 (0.787 x 0.059 x 0.059)	Fe alloys	0.32
Compact tension (CT)	16 OD x 2.54 t (0.63 OD x 0.1 t)	Fe alloys	3.5
	16 OD x 3.81 t (0.63 OD x 0.15 t)	V alloys	3.92
Ceramic disks	12.7 OD x 2.56 t (0.501 OD x 0.101 t) 10 OD x 0.91 t (0.393 OD x 0.036 t) 10 OD x 0.99 t (0.393 OD x 0.039 t) 10 OD x 0.99 t (0.393 OD x 0.039 t) 10.4 OD x 0.76 t (0.41 OD x 0.030 t) 12.39 OD x 1.34 t (0.488 OD x 0.053 t) 12.7 OD x 9.5 t (0.5 OD x 0.374 t) 7.75 OD x 4 t (0.305 OD x 0.157 t) 12.7 OD x 1.02 t (0.5 OD x 0.040 t)	MgAl O Al O Sc O ZrO [illegible] O Si N SiO SiO AlN	1.145 0.284 0.292 0.427 0.293 0.187 2.79 0.436 0.421
Disk	7.62 OD x 20.3 l (0.3 OD x 0.8 l) 7.62 OD x 6.35 t (0.3 OD x 0.25 t) 10.2 OD x 1.85 t (0.403 OD x 0.073 t) 10.13 OD x 3 t (0.399 OD x 0.118 t) 10.16 OD x 1.27 (0.4 OD x 0.05 t) 10.0 OD x 1.28 (0.39 OD x 0.05) 10.2 OD x 1.02 t (0.402 OD x 0.04 t) 10.2 OD x 3.17 t (0.402 OD x 0.125 t)	Be Be SiC SiC SiC SiC SiC SiC SiC SiC SiC SiC	1.55 0.49 0.37 0.63 0.21 0.32 0.20 0.33
Balls	1 OD (0.04 OD) 3 OD (0.12 OD) 5 OD (0.2 OD)	Be Be Fe	0.001 0.03 0.14
Bend bars	3.175 x 6.35 x 38.1 (0.125 x 0.25 x 1.5) 3.27 x 1.68 x 38.1 (0.129 x 0.066 x 1.5) 3.05 x 5.91 x 36.32 (0.120 x 0.233 x 1.43) 3.7 x 1.9 x 25.4 (0.147 x 0.075 x 1) 1 x 5 x 40 (0.04 x 0.2 x 1.57) 1.7 x 4 x 25 (0.07 x 0.16 x .98) 1.9 x 3.7 x 25 (0.075 x 0.147 x 1) 1.7 x 4 x 25 (0.066 x 0.16 x 0.98)	SiC SiC SiC SiC SiC SiC SiC SiC C C C C C C C C	2.17 0.51 1.715 0.445 0.342 0.33 0.383 0.335
Continued on next page...			

Table 7. Specimen Geometries in COBRA 1A

SPECIMEN TYPE	DIMENSIONS mm (in)	MATERIAL TYPE	AVERAGE MASS (gms)
Continued from previous page...			
Fiber tubes	7.54 OD x 38.1 (0.100 OD x 1.5) 3.175 OD x 31.75 (0.125 OD x 1.25) 3.175 OD x 20.3 (0.125 OD x 0.8)	SiC/SiC SiC/SiC Carbon	0.50 0.38 0.25
Temperature monitors	0.32 x 1.6 x 25.4 (0.0125 x 0.0625 x 1)	SiC	0.41
Scanning auger microscopy (SAM) specimens	16.5 l x 1.9 t x 3.17 (0.651 x 0.075 t x 0.125)	Fe alloys V alloys	0.7 0.57
Small punch (SP) specimens	8.05 OD x 0.5 t (0.317 OD x 0.07 t)	Fe alloys V alloys	0.19 0.14
TEM packets - weepers	3.65 OD x 77.3 x 0.18 t (0.144 OD x 0.879 x 0.007 t)	316	0.35 (empty)
TEM packets - sealed	3.65 OD x 72.3 x 0.18 t (0.144 OD x 0.88 x 0.007 t)	316	0.41 (empty)
Sealed tubes	9.4 OD x 20.3 x 0.38 wall (0.37 OD x 0.80 x 0.015 wall)	316	2.56 (empty)
TZM containers	9.53 OD x 57 l x 0.635 wall (0.375 OD x 2.05 l x 0.025 wall)	TZM	10.3 (with lithium)
	9.53 OD x 25.4 l x 0.635 wall (0.375 OD x 1 l x 0.025 wall)	TZM	5.4 (with lithium)
	9.53 OD x 44.45 l x 0.635 wall (0.375 OD x 1.75 l x 0.025 wall)	TZM	8.9 (with lithium)
	3.53 OD x 73.7 l x 0.635 wall (0.375 OD x 7.9 l x 0.025 wall)	TZM	14.3 (with lithium)

FABRICATION AND OPERATION OF HFIR-MFE RB* SPECTRALLY TAILORED IRRADIATION CAPSULES - A. W. Longest. J. E. Pawel, D. W. Heatherly, R. G. Sitterson, and R. L. Wallace (Oak Ridge National Laboratory).

OBJECTIVE

The objective of this work is to fabricate and operate irradiation capsules for irradiating magnetic fusion energy (MFE) candidate first-wall materials in the High Flux Isotope Reactor (HFIR) removable beryllium (RB*) positions. Japanese and U.S. MFE specimens were transferred to RB* positions following irradiation to 7.5 dpa at temperatures of 60, 200, 330, and 400°C in Oak Ridge Research Reactor (ORR) experiments ORR-MFE-6J and -7J.

SUMMARY

Fabrication and operation of four HFIR-MFE RB* capsules (60, 200. 330, and 400°C) to accommodate MFE specimens previously irradiated in spectrally tailored experiments in the ORR are proceeding satisfactorily. With the exception of the 60°C capsule, where the test specimens were in direct contact with the reactor cooling water, specimen temperatures (monitored by 21 thermocouples) are controlled by varying the thermal conductance of a thin gas gap region between the specimen holder outer sleeve and containment tube.

Irradiation of the 60 and 330°C capsules, which started on July 17, 1990, was completed on November 14, 1992, after 24 cycles of irradiation to an incremental damage level of approximately 10.9 displacements per atom (dpa). Assembly of the follow-up 200 and 400°C capsules was completed in November 1992, and their planned 20-cycle irradiation to approximately 9.1 incremental dpa was started on November 21, 1992. As of February 11, 1993, the 200 and 400°C capsules had successfully completed three cycles of irradiation to approximately 1.4 incremental dpa.

PROGRESS AND STATUS

Introduction

A series of spectrally tailored irradiation capsules are being fabricated and operated as part of the U.S./Japan collaborative program for testing MFE candidate first-wall materials in mixed-spectrum fission reactors. The test specimens are being irradiated in the RB* facility[1] of the HFIR.

Four HFIR-MFE RB* capsules were designed to accommodate Japanese and U.S.MFE specimens previously irradiated to 7.5 dpa at temperatures of 60, 200, 330, and 400°C in the ORR in spectrally tailored experiments ORR-MFE-6J and -7J. Details of these ORR experiments, including descriptions of the test matrix, mechanical property specimens, and techniques of spectral tailoring. have been reported elsewhere.[2,3] Hafnium liners are being used in the HFIR-MFE RB* experiments to tailor the neutron spectrum to closely match the helium production-to-atom displacement ratio (14 appm/dpa) expected in a fusion reactor first wall.

The HFIR-MFE RB capsules are being irradiated in pairs (first the 60 and 330°C capsules, then the 200 and 400°C capsules) to total damage levels on the re-encapsulated specimens of approximately 18.4 (24 HFIR cycles) and 16.6 dpa (20 HFIR cycles), respectively. Previously[4], the target exposure level was 17.5 total dpa on the re-encapsulated specimens (22 HFIR cycles) for all four capsules;

however. the 60 and 330°C irradiations were extended for two additional cycles until the 200 and 400°C capsules were ready to replace them.

60°C Capsule

The 60°C capsule, designated HFIR-MFE-60J-1, was an uninstrumented capsule with the test specimens in contact with the reactor cooling water. Capsule design, assembly, and details of the specimen loading were described previously.[1]

Irradiation of this capsule was started on July 17, 1990, and was completed on November 14, 1992, after 24 cycles of irradiation to a total damage level on the re-encapsulated specimens of approximately 18.4 dpa. **A** cycle-by-cycle summary of the irradiation history of the 60J-1 capsule **is** given in Table 1. Specimen operating temperatures in this capsule were predicted to be within 10°C **of** 60°C.

330°C Capsule

The **330°C** capsule. designated HFIR-MFE-330J-1, was an instrumented and singly contained capsule where the specimen temperatures **were** monitored by 21 thermocouples and controlled by adjusting the thermal conductance of a thin **gas** gap region between the specimen holder outer sleeve and containment tube. This capsule **was** cooled with 49°C reactor cooling water flowing downward over the containment tube surface. Capsule design, assembly, and details of the specimen loading were described previously.[6,7]

irradiation of this capsule was started on July 17, 1990, and was completed on November 14, 1992, after 24 cycles of irradiation to a total damage level on the re-encapsulated specimens of approximately 18.4 dpa. **A** cycle-by-cycle summary of the irradiation history ***of*** the 330J-1 capsule is given in Table 1.

Typical thermal operating data for the 330J-1 experiment were presented in detail previously! During this report period, measured temperatures in the aluminum alloy specimen holder continued to indicate specimen operating temperatures within about 25°C of 330°C. which satisfies the temperature criterion for these experiments.

200 and 400°C Capsules

The 200 and 400°C capsule designs are basically the same as that of the ***330°C*** capsule. The main differences in the three capsule designs are associated with (1) the number and spacing of the specimen holder slots and holes to accommodate differences in the numbers of specimens of the various types, (2) the width of the temperature control gas gap region between the specimen holder outer sleeve and containment tube to obtain the desired specimen operating temperatures, and ***(3)*** the instrumented test piece included in the aluminum plug and holder above the test specimen holder to obtain extra information.

Horizontal and vertical sections through the 200 and 400°C capsules, designated HFIR-MFE-200J-1 and -400J-1, are shown in Figures 1 through **4.** In addition to the main test specimen loadings, a simulated packet of transmission electron microscopy (TEM) specimens in the 200°C capsule and a simulated hourglass fatigue specimen in the 400°C capsule are located in the aluminum plug and

Table 1. IRRADIATION HISTORY OF US/JAPAN SPECTRAL TAILORED CAPSULES HFIR-MFE-60J-1, -330J-1,- 200J-1, AND -400J-1

HFIR OPERATION				60J-1,330J-1		200.-1.400.-1	
				INCREMENTAL		INCREMENTAL	
CYCLE NO.	START DATE	END DATE	MWd/ Cycle	MWd	dpa*	MWd	dpa*
289	07-17-90	09-07-90	1879	1879	0 46		
290	09-19-90	10-11-90	1852	3731	0 91		
291	10-17.90	11-13-90	1838	5569	1 36		
292	11-25-90	12-10-90	1847	7416	1 82		
293	12-27-90	01-23-91	1965	9381	2 30		
294	02-01-91	02-25-91	1906	11287	2 77		
295	03-01-91	03-24-91	1908	13195	3 23		
296	04-06-91	04-28-91	1874	15069	3 69		
297	05-19-91	06-15-91	1845	16914	4 14		
298	06-20-91	07-11-91	1747	18661	4 57		
299	07-25-91	08-15-91	1741	20402	5 00		
300	08-28-91	09-17-91	1724	22126	5 47		
301	09-27-91	10-19-91	1851	23977	5 87		
302	10-27-91	11-21-91	1829	25606	6 32		
303	12-01-91	12-22-91	1821	27627	6 77		
304	12-31-91	01-24-92	1826	29453	7.22		
305	01-30-92	02-27-92	1876	31329	7 68		
306	03-31-92	04-27-92	1845	33174	8.13		
307	05-01-92	05-28-92	1842	35016	8.58		
308	06-02-92	06-30-92	1938	36954	9.05		
309	07-03-92	08-01-92	1949	38903	9 53		
310	08-27-92	09-18-92	1849	40752	9.98		
311	09-25-92	10-12-92	1856	42608	10.44		
	10-22-92	11-14-92	1842	44450	10.89	BEGIN CYCLE 313	
	11-21-92	12-15-92	1850	REMOVED EOC 312		1850	0.45
	12-20-92	01-12-93	1866			3716	0.91
	01-19 93	02-11-93	1861			5577	1.37
316							
318							
319							
320							

* DPA levels based on achieving 0.000245 dpa/MWd.

ORNL-DWG-89-7850

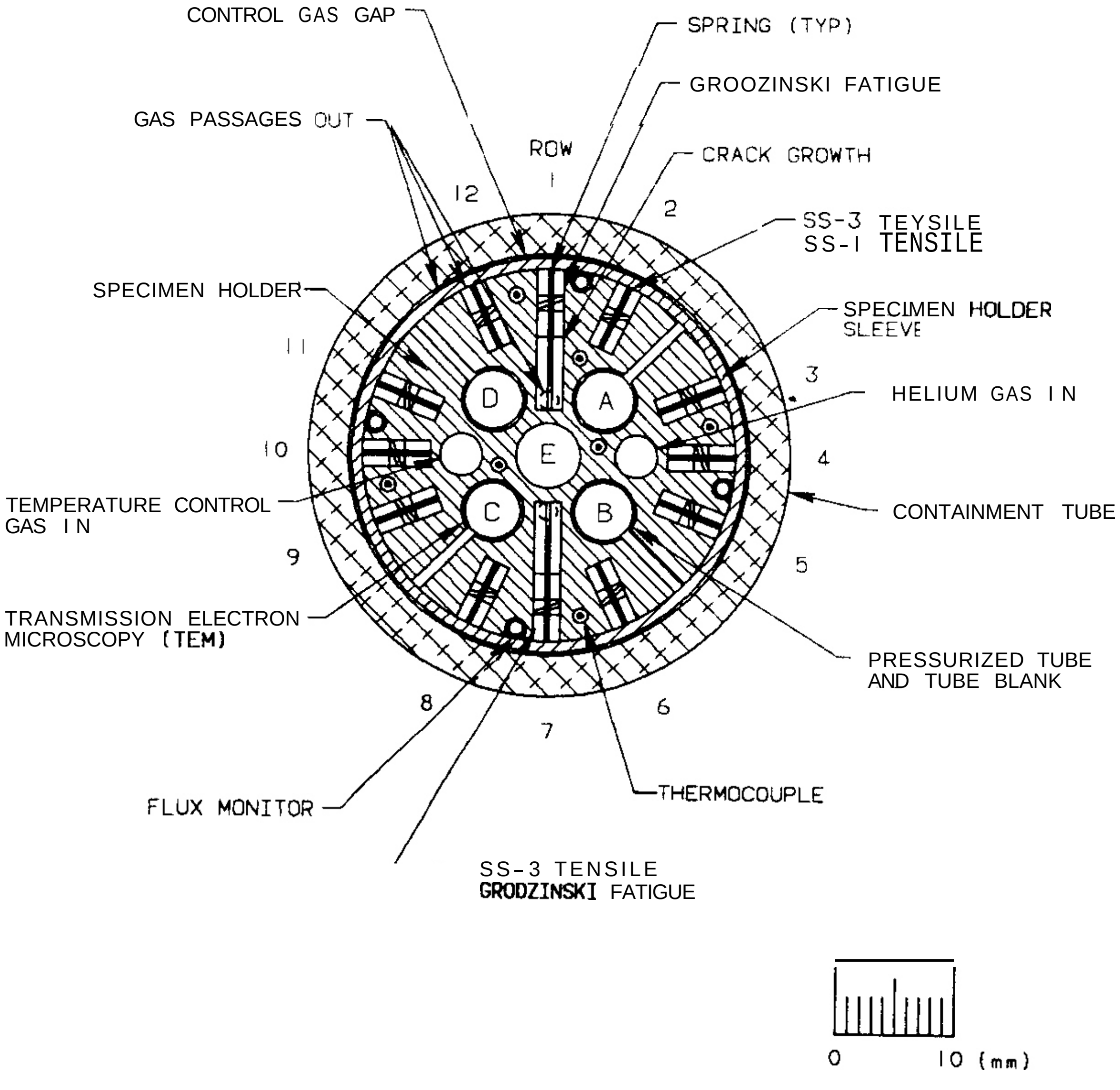

Fig. 1. Horizontal section through the HFIR-MFE-200J-1 capsule.

ORNL-DWG-89-7852

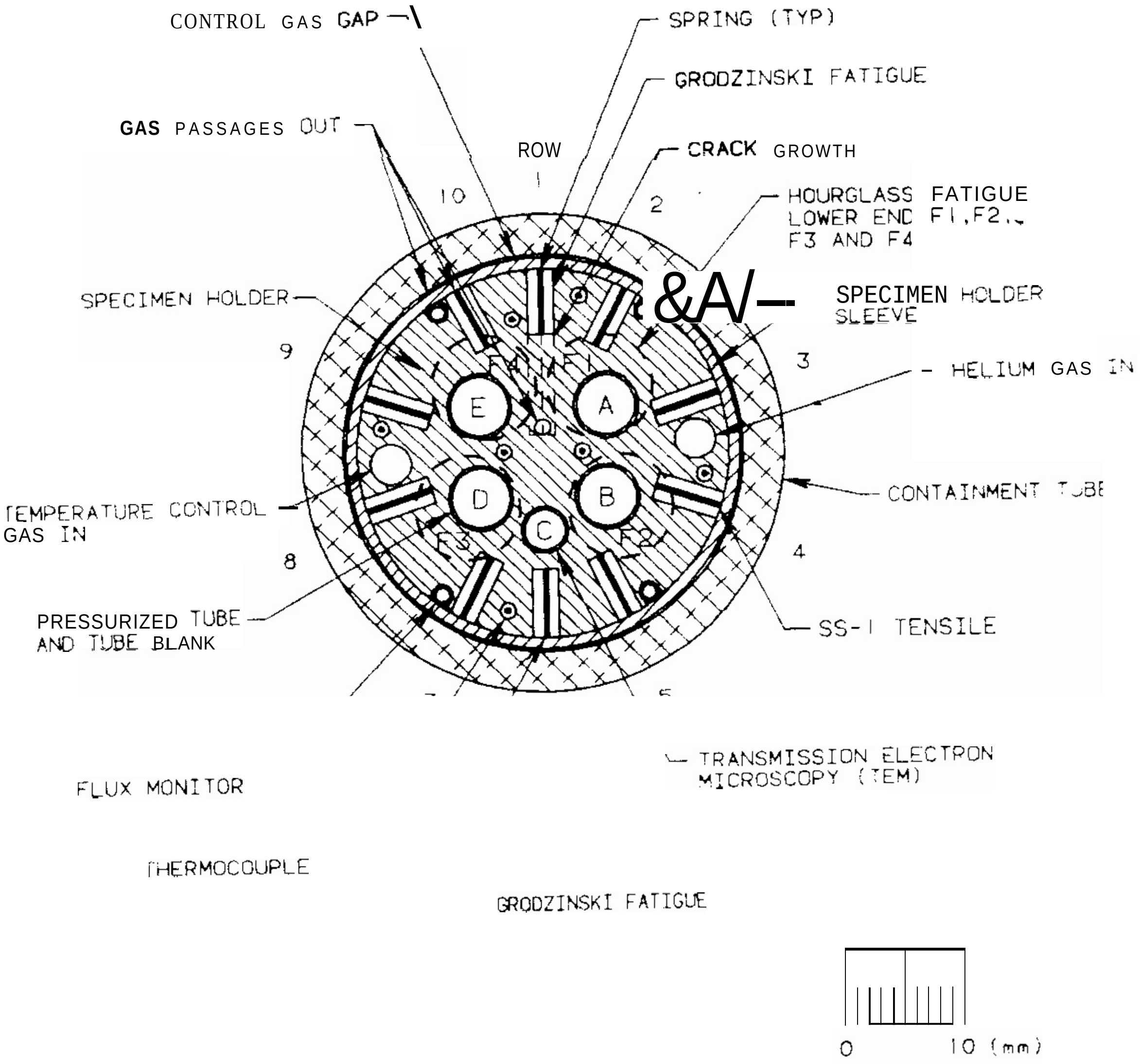

Fig. 2. Horizontal section through the HFIR-MFE-400J-1 capsule.

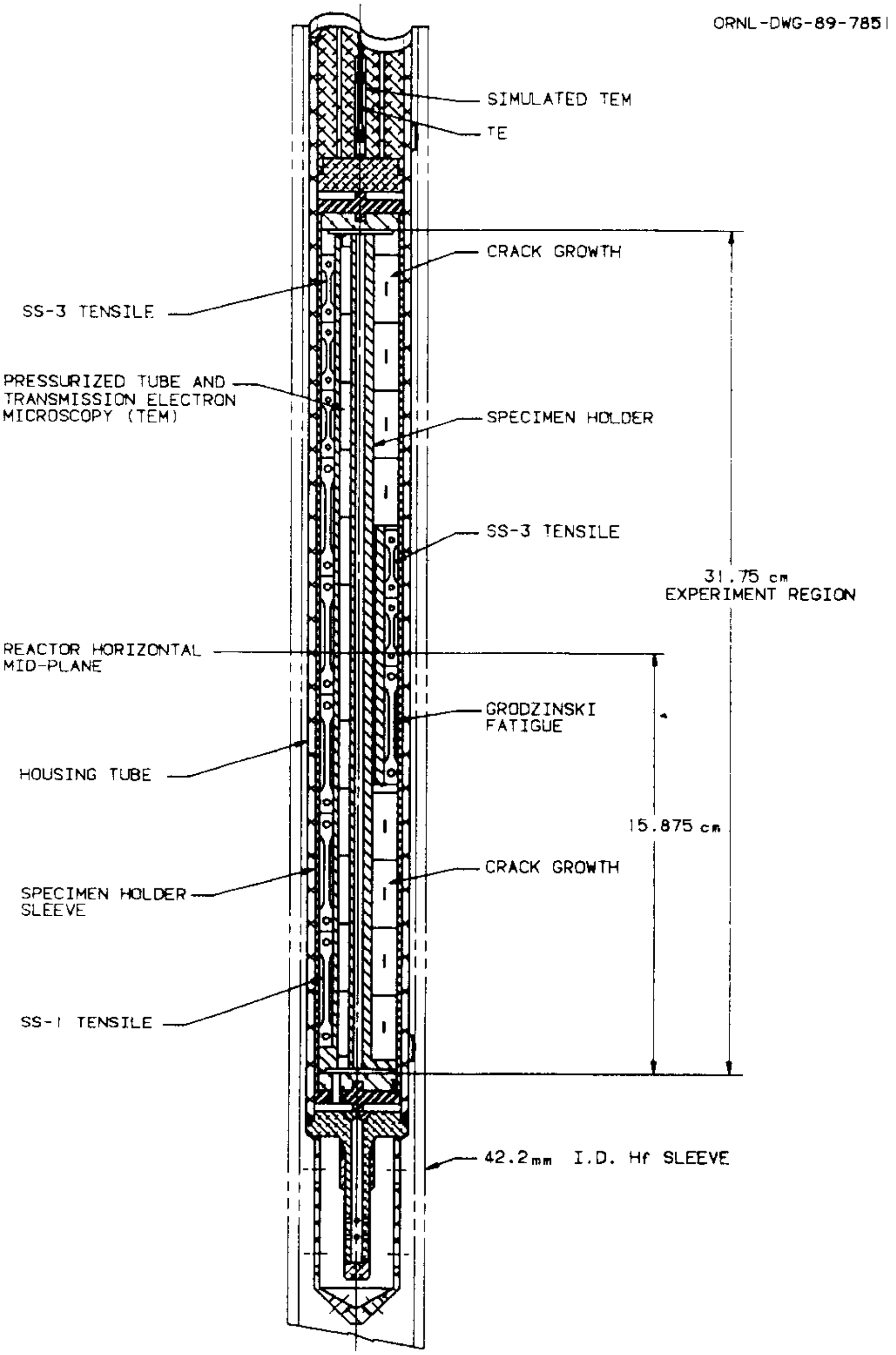

Fig. 3. Vertical section through the HFIR-MFE-200J-1 capsule.

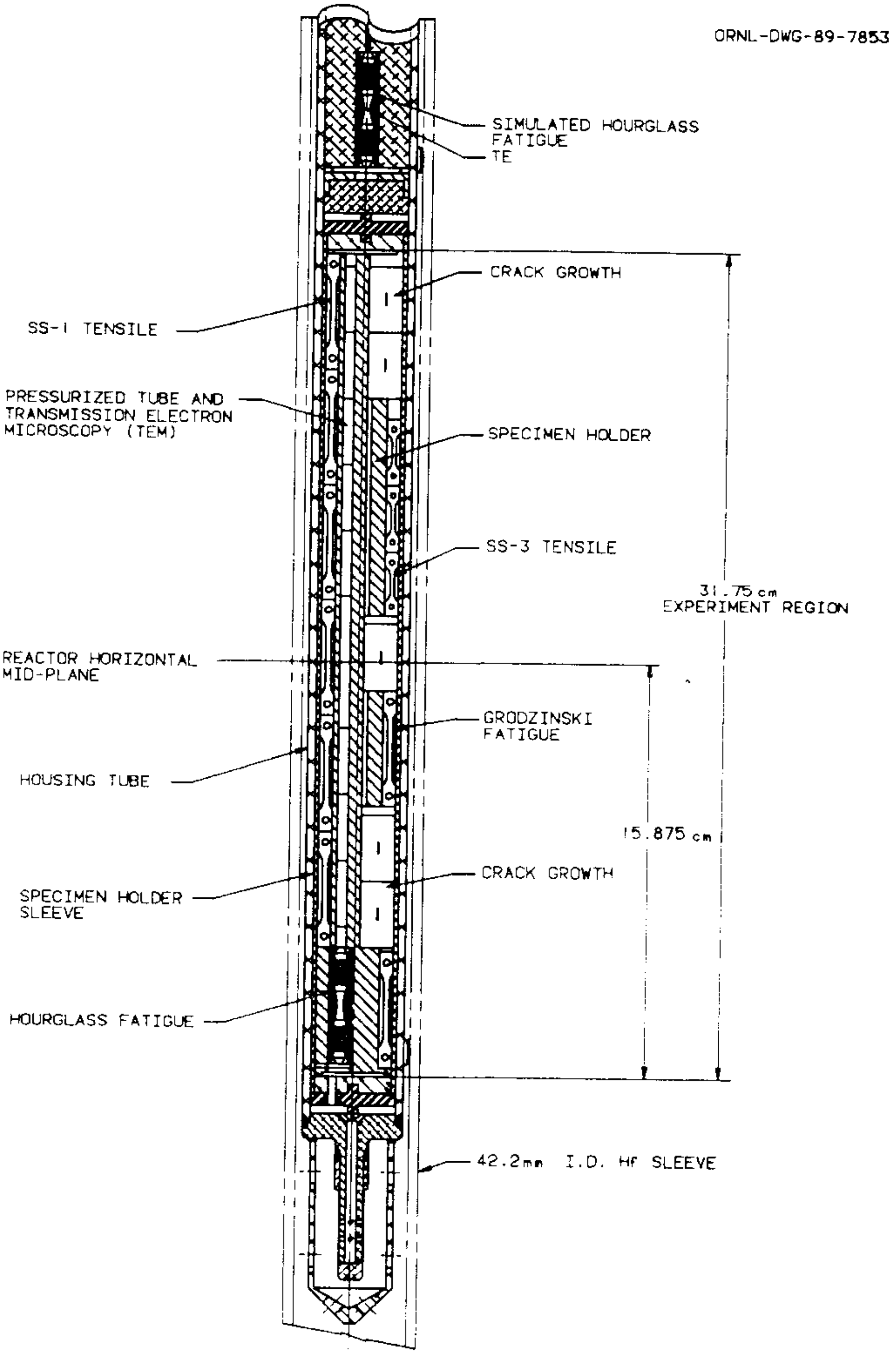

Fig. 4. Vertical section through the HFIR-MFE-400J-1 capsule.

holder above the test specimen holder and instrumented with three thermocouples to obtain temperature rise data for these respective specimen-specimen holder configurations.

Assembly of the 200 and 400°C capsules was completed this report period as planned, after having been delayed by approximately two months because of the aluminum welding difficulties described in the last report". After partial assembly of the capsules and loading of non-radioactive test specimens on the bench, the radioactive test specimens were successfully loaded in the hot cell and capsule assembly completed in about two weeks for each capsule. Special fixtures developed for hot cell loading of radioactive specimens into the 330°C capsule were again used for these capsules.

Specimen loading lists showing specimen identification numbers as a function of position in the capsule are given in Tables 2 and 3 for the 200 and 400°C capsules, respectively. Position is given by row number or hole designation (see Figs. 1 and 2) and level number. Level numbers in increasing order indicate the stacking order from top to bottom of the specimen holder. Detailed specimen information is given in Table 4 for the various types of specimens, respectively, loaded into these capsules. The individual specimens listed in Table 4 are categorized by type of specimen. source of material, and alloy type. Alloy conditions include solution annealed (SA) and cold worked (CW). Specimens denoted by an asterisk were re-encapsulated into these experiments and have already received 7.5 dpa in the ORR-MFE-6J and -7J experiments. The transmission electron microscopy (TEM) disks in each new (previously unirradiated) TEM holder tube are also listed. Several specimen materials in these capsules were not in the 60 and 330°C capsules. These new specimen materials include vanadium and copper alloys.

Irradiation of the 200 and 400°C capsules began on November 21, 1992, at the start of HFIR cycle 313. As of February 11, 1993, these capsules had successfully completed three cycles (1.37 dpa) of their planned 20-cycle (9.1 dpa) irradiation to a total damage level of approximately 16.6 dpa on the re-encapsulated specimens. A cycle-by-cycle summary of their irradiation history through HFIR cycle 315 is given in Table 1. Both capsules are operating as designed. Measured temperatures from the 21 thermocouples in the aluminum alloy specimen holder in each capsule indicate the specimen operating temperatures are within about 25°C of 200 and 400°C. respectively. which satisfies the temperature criterion for these experiments.

HFIR-MFE RB* Facilities

Facility preparations required for operation of two instrumented HFIR-MFE RB* capsules (200 and 400°C capsules) simultaneously were completed during the report period. These preparations included upgrade and final checkout of Materials Irradiation Facility No. 4 (MIF-4). connection of the instrumented 400°C capsule to MIF-4, disconnection of the 330°C capsule from MIF-3, and connection of the 200°C capsule to MIF-3.

FUTURE WORK

Design. preparation of fabrication drawings, procurement of parts. and assembly of a capsule for re-encapsulating specimens from the above capsules into a dual-temperature capsule (probably 200 and 400°C) is planned for FY 1994.

Table 2. HFIR-MFE-200J-1 Loading List

	Row 1		Row 2	Row 3	Row 4	Row 5	Row 6	Row 7		Row 8	Row 9	Row 10	Row 11	Row 12	Hole A	Hole B	Hole C	Hole D	Hole E
Level 1	H01 H02	A08 A06	E3 X3	T1 X1	A201 A203	W3 C2	W2 E2	PITCH		B201 B103	D402 D301	A104 H03	A301 D305	F1 T3	*spacer (.218")*	*spacer (.218")*	*spacer (.550")*	*spacer (.940")*	*spacer (.500")*
Level 2	B203 B204	C201 C104	E2 C3	W1 C1	EL-48 GFA-47	A101 A202	D401 A302	PITCH		A303 D501	PAN PAN	D502 A304	PITCH PAN	A102 A204	C3C0	PS09	J8	J18	4
Level 3	B102 C203	B401 B403	L01 A07	L03 L02	DL-52 DL-53	DL-45 GFD-50	C103 B202	A05		PITCH PITCH	GFC-44 E13-07	A103 D302	B3-07 CL-54	E4-07 B7-07	S2A7	C1A6	F	2	3
Level 4	TU-21 EK-46		GFD-48 DL-48	FL-43 E12-07	B13-07 GFB-44	EL-49 E10-07	GFC-46 IL-9	A01		GFA-49 FL-44	X2 EC-06	EL-53 B11-07	CL-53 B10-07	EL-50 CL-49	C3B1	3S05	E	PS14-2	J19
Level 5	HV-03 EL-03		HL-9 GFA-48	GFB-49 GFA-45	B1-07 E8-07	EL-52 E2-07	GFB-47 FL-46	W2		CL-48 EL-55	E11-07 B2-07	GFB-48 CL-47	FL-50 EL-51	B6-07 FL-51	FA59	C4A9	J7	CB2	*Al rod (9.43")*
Level 6	GFA-44 DL-47		E14-07 FL-55	KL-8 B5-07	TR-23 HV-07	GFD-49 FL-40	IL-8 E9-07	W1		E6-07 DL-6	GFB-46 E5-07	CL-52 DL-50	HL-8 EL-54	E1-07 FL-53	FA48	PS00	J12	3C12-2	*spacer (.500")*
Level 7	CGD-1 CGD-2		KL-9 FL-52	CL-51 CLW-18	EL-00 EK-41	TR-24 TW-16	B9-07 E3-07	L02		GFB-45 GFC-49	B12-07 GFA-46	49 15	B209 B109	MH-06 EC-08	3S10	FA62	J10	CC2	
Level 8	TL-29 TL-30	SB-37 SB-38	MH-07 EC-21	60 45	TZ-23 HV-04	47 47	EC-09 AE-37	L01		AE-35 FK-42	HV-08 EK-13		MH-05 MH-06	TL-21 TP-21	C2A6	S3A5	J6	S1A5-2	
Level 9	SD-37 SD-38	TL-7 TL-8						C106 C206	B104 C205						PS02	3S02	J9	3S13-2	
Level 10	42 43	50 41						DL-49 DL-46							PS05	3C09	J11	CA2	
Level 11								TP-22 TU-23							SA30	3S00	1	SA28-2	
Level 12								TX-16 TF-18							C1B3	C1C8	J16	FA2	
Level 13								AE-32 AF-34							SA21	C4C0	J17	3C05	
Level 14								C102 C202	B402 C205						*spacer (.218")*	*spacer (.218")*	*spacer (.550")*	C3B2	
Level 15								B404 C101	C204 B103									*spacer (1.1")*	
Level 16								12 16	UW UW									*spacer (4.093")*	

Table 3. HFIR-MFE-400J-1 Loading List

	Row 1	Row 2	Row 3	Row 4	Row 5	Row 6	Row 7	Row 8	Row 9	Row 10	Hole A	Hole B	Hole C	Hole D	Hole E	Hole R
Level 1	PITCH	GFB-23 DL-28	X6 C7	L06 H05	GFB-21 GFA-24	C8 X5	A09 A10	H06 L07	PITCH PITCH	L08 A11	*spacer (0.3")*	*spacer (0.3")*	*spacer (1.25")*	*spacer (0.3")*	CC2	*spacer (1.25")*
Level 2	PITCH	GFB-24 CLW-10	F4 T4	CL-27 CL-29	DL-30 GFC-19	F5 F6	EL-19 DL-25	GFB-19 DL-22	PITCH PAN	H04 D404	FA32	C3B4	*spacer (1.25")*	FA01	3S11-2	*spacer (1.25")*
Level 3	A07	EL-20 FL-12	X4 C6	GFA-20 GFD-23	IL-3 EL-17	T5 T6	HL-3 FL-4	DL-24 FL-5	PAN PAN	A305 A208	C1A7	C2A4	*spacer (1")*	PS07	CB2	7
Level 4	A08	GFB-22 FL-11	TL-10 TL-9	CL-28 FL-7	CL-25 ML-3	B406 W6	DL-27 CL-23	FL-9 FL-8	TI-32 SB-40	A108 D503	C3A6	S1A0	J11	C4B6	C3C6	8
Level 5	L06	DL-23 DL-29	B405 B207	CL-24 KL-4	CLW-9 GFD-24	SD-40 TI-31	GFA-19 GFC-17	CL-30 EL-18	B205 C109	D306 D504	SA31	FA12	E	C2C7	C4C3	6
Level 6	L07	GFA-23 GFB-20	B105 B107	CL-22 CL-26	IL-4 GFC-18	C207 C208	DL-26 GFA-21	ML-4 GFA-22	C209 B408	D403 D304	3C04	01	F	C1C0	PS04	5
Level 7	W5 W4		B106 C108			A308 A105			A307 A106		C3A2	SA32	J8	SA03	C4A2	J20
Level 8	SB-39 SD-39		B108 C110			A306 A206			A107 A205		S2A4	C5A2	J10	C4B4	C4B0	J21
Level 9	C107 C210		B208 B407			A207 D303			41 49		3C07	C4B2	J12	3S07	C5B0	J22
Level 10	CGB-3 CGB-4		43 47			B206 47W					S2A0	C3C4	*spacer (0.5")*	S1A1	SA37	J23
Level 11	KL-3 HL-4										SA58	FA05	*spacer (2.69")*	SA53	FA10	*spacer (2.69")*
Level 12	W3										SXAX2	PS11-2		3C10-2	3S04	
Level 13	W4										A02 L01 W2 A01 W1 PITCH PITCH	FE-31		FE-18	FA2	
Level 14	C112 B410 B210 B110														CA2	
Level 15	FL-10 GFD-18														SA2	
Level 16															FE-19	

REFERENCES

1. K. R. Thoms et al., "HFIR Irradiation Facilities Improvements--Completion of the HIFI Project," *J. Nucl. Mater.*, 155-157 (1988) 1340-45.

2. J. L. Scott et al., pp. 12-20 in ADIP Semiann. Prog. Rep., March 31, 1985, DOE/ER-0045/14, U.S. DOE, Office of Fusion Energy.

3. J. L. Scott et al., Second Annual Prog. Rep. on United States-Japan Collaborative Testing in the High Flux Isotope Reactor and the Oak Ridge Research Reactor, Sept. 30, 1985, ORNL/TM-10102.

4. A. W. Longest et al., "Fabrication and Operation of HFIR-MFE RB* Spectrally Tailored Irradiation Capsules," in Fusion Reactor Materials Semiann. Prog. Rep., March 31, 1992, DOE/ER-0313/12, U.S. DOE, Office of Fusion Energy.

5. A. W. Longest et al., "Design and Fabrication of HFIR-MFE RB* Spectrally Tailored Irradiation Capsules," in Fusion Reactor Materials Semiann. Prog. Rep., March 31, 1988, DOE/ER-0313/4, U.S. DOE, Office of Fusion Energy.

6. A. W. Longest et al., "Design and Fabrication of HFIR-MFE RB* Spectrally Tailored Irradiation Capsules," in Fusion Reactor Materials Semiann. Prog. Rep., Sept. 30, 1987, DOE/ER-0313/3, U.S. DOE, Office of Fusion Energy.

7. A. W. Longest et al., "Design and Fabrication of HFIR-MFE RB* Spectrally Tailored Irradiation Capsules," in Fusion Reactor Materials Semiann. Prog. Rep., Sept. 30, 1988, DOE/ER-0313/5, U.S. DOE, Office of Fusion Energy.

8. A. W. Longest et al., "Fabrication and Operation of HFIR-MFE RB* Spectrally Tailored Irradiation Capsules," in Fusion Reactor Materials Semiann. Prog. Rep., Sept. 30, 1991, DOE/ER-0313/11, U.S. DOE, Office of Fusion Energy.

9. A. W. Longest et al., "Fabrication and Operation of HFIR-MFE RB* Spectrally Tailored Irradiation Capsules," in Fusion Reactor Materials Semiann. Prog. Rep., Sept. 30, 1992, DOE/ER-0313/13, U.S. DOE, Office of Fusion Energy.

Table 4. Detailed specimen information for HFIR-MFE-200J-1 and -400J-1 capsules

	SS-3 Tensile Specimens (1 in. long)		
Program	Alloy (Condition)	200J-1 Specimens	400J-1 Specimens
US/ORNL*	PCA (25%CW)	EK-41*	-
"	PCA (25%CW)	EK-42*	-
"	PCA (25%CW)	EK-43*	-
"	PCA (25%CW)	EK-46*	-
"	316 (20%CW)	AE-32*	-
"	316 (20%CW)	AE-34*	-
"	316 (20%CW)	AE-35*	-
"	316 (20%CW)	AE-37*	-
"	PCA (25%CW)	EC-06*	-
"	PCA (25%CW)	EC-08*	-
"	PCA (25%CW)	EC-09*	-
"	PCA (25%CW)	EC-21*	-
"	PCA (B3)	EL-00*	-
"	PCA (B3)	EL-03*	-
"	PC-20 (25%CW)	HV-03*	-
"	PCA-20 (25%CW)	HV-04*	-
"	PCA-20 (25%CW)	HV-07*	-
"	PCA-20 (25%CW)	HV-08*	-
"	PCMA-6 (20%CW)	MH-05*	-
"	PCMA-6 (20%CW)	MH-06*	-
"	PCMA-6 (20%CW)	MH-07*	-
"	PCMA-6 (20%CW)	MH-08*	-
US/PNL*	VO-2262 (a)	TE-18*	-
"	VO-2267 (b)	TL-21*	-
"	VO-2266 (b)	TP-21*	-
"	VO-2266 (b)	TP-22*	-
US/PNL*	VO-2268 (b)	TR-23*	-
"	VO-2268 (b)	TR-24*	-
"	VO-2269 (b)	TU-23*	-
"	VO-2269 (b)	TU-24*	-
"	VO-2754 (c)	TW-16*	-
"	VO-2755 (c)	TX-16*	-
"	UC-19 (a)	TZ-23*	-
JAERI	F82H (base metal)	B101	B105
"	F82H (base metal)	B102	B106
"	F82H (base metal)	B103	B107
"	F82H (base metal)	B104	B108
"	F82H (base metal)	B109	B110
"	F82H (TIG weld joint)	B201	B205
"	F82H (TIG weld joint)	B202	B206
"	F82H (TIG weld joint)	B203	B207
"	F82H (TIG weld joint)	B204	B208
"	F82H (TIG weld joint)	B209	B210
"	F82H (laser weld joint)	B401	B405
"	F82H (laser weld joint)	B402	B406
"	F82H (laser weld joint)	B403	B407
"	F82H (laser weld joint)	B404	B408
"	F82H (laser weld joint)	-	B410
"	JPCA (SA)	C101	C107
"	JPCA (SA)	C102	C108
"	JPCA (SA)	C103	C109
"	JPCA (SA)	C104	C110

Table 4. Continued

SS-3 Tensile Specimens (1 in. long)

Program	Alloy (Condition)	200J-1 Specimens	400J-1 Specimens
JAERI	JPCA (SA)	C105	C112
"	JPCA (SA)	C106	-
"	JPCA (CW)	C201	C207
"	JPCA (CW)	C202	C208
"	JPCA (CW)	C203	C209
"	JPCA (CW)	C204	C210
"	JPCA (CW)	C205	-
"	JPCA (CW)	C206	
US/ORNL	9Cr-1MoVNb	TL-7	TL-9
"	9Cr-1MoVNb	TL-8	TL-10
"	9Cr-1MoVNb-2Ni	TL-29	TL-31
"	9Cr-1MoVNb-2Ni	TL-30	TL-32
"	12Cr-1MoVW	SB-37	SB-39
"	12Cr-1MoVW	SB-38	SB-40
"	12Cr-1MoVW-2Ni	SD-37	SD-39
"	12Cr-1MoVW-2Ni	SD-38	SD-40
US/ORNL	Glidcop Al25+B (as wrought)	W1	W4
"	Glidcop Al25+B (as wrought)	W2	W5
"	Glidcop Al25+B (as wrought)	W3	W6
"	Glidcop Al25+B (cold rolled)	C1	C6
"	Glidcop Al25+B (cold rolled)	C2	C7
"	Glidcop Al25+B (cold rolled)	C3	C8
"	Glidcop Al25 (cold rolled)	X1	X4
"	Glidcop Al25 (cold rolled)	X2	X5
"	Glidcop Al25 (cold rolled)	X3	X6
"	MAGT 0.2 (cold rolled)	T1	T4

SS-3 Tensile Specimens (1 in. long)

Program	Alloy (Condition)	200J-1 Specimens	400J-1 Specimens
US/ORNL	MAGT 0.2 (cold rolled)	T2	T5
"	MAGT 0.2 (cold rolled)	T3	T6
"	Glidcop Al15+B (as extruded, brazed)	F1	F4
"	Glidcop Al15+B (as extruded, brazed)	F2	F5
"	Glidcop Al15+B (as extruded, brazed)	F3	F6
"	MER Cu-Al$_2$O$_3$-graphite (pitch P120)	blank	blank
"	MER Cu-Al$_2$O$_3$-graphite (pitch P120)	blank	blank
"	MER Cu-Al$_2$O$_3$-graphite (pitch P120)	blank	blank
"	MER Cu-Al$_2$O$_3$-graphite (pan IM9)	notched	notched
"	MER Cu-Al$_2$O$_3$-graphite (pan IM9)	notched	notched
"	MER Cu-Al$_2$O$_3$-graphite (pan IM9)	notched	notched
US/ANL	V-10Ti	BL-12	-
"	V-20Ti	BL-15	
"	V-15Cr-5Ti	BL-41	BL-41
"	V-3Ti-0.5Si	BL-42	-
"	V-10Cr-5Ti	BL-43	BL-43
"	V-3Ti-1Si	BL-45	-
"	V-5Ti	BL-46	-
"	V-5Cr-5Ti	BL-47	BL-47
"	V-5Cr-5Ti	BL-47	-
"	V-5Cr-5Ti (TIG weld zone)	BL-47W	BL-47W
"	V-5Cr-5Ti (TIG weld zone)	BL-47W	-
"	V-7Cr-5Ti	BL-49	BL-49
"	V-1Ti	BL-50	-
"	V-3Ti-0.1C	BL-60	-

Condition codes
a 900°C/20 h/WQ + 950°C/20 min/WQ + 650°C/2 h/AC
b 1000°C/20 h AC + 1100°C/10 min AC + 700°C/2 h/AC
c 1000°C/20 h AC + 1100°C/5 min/AC + 650°C/2 h AC
B3 solution annealed for 1 h at 1100°C, aged 8 h at 800°C + 25% CW

Table 4. Continued

	SS-1 Tensile Specimens (1.75 in. long)		
Program	Alloy (Condition)	200J-1 Specimens	400J-1 Specimens
JAERI*	JPCA (SA)	CL-47*	CL-22*
"	JPCA (SA)	CL-48*	CL-23*
"	JPCA (SA)	CL-49*	CL-24*
"	JPCA (SA)	CL-51*	CL-25*
"	JPCA (SA)	CL-52*	CL-26*
"	JPCA (SA)	CL-53*	CL-27*
"	JPCA (SA)	CL-54*	CL-28*
"	JPCA (SA)	-	CL-29*
"	JPCA (SA)	-	CL-30*
"	JPCA (15%CW)	DL-6*	DL-22*
"	JPCA (15%CW)	DL-45*	DL-23*
"	JPCA (15%CW)	DL-46*	DL-24*
"	JPCA (15%CW)	DL-47*	DL-25*
"	JPCA (15%CW)	DL-48*	DL-26*
"	JPCA (15%CW)	DL-49*	DL-27*
"	JPCA (15%CW)	DL-50*	DL-28*
"	JPCA (15%CW)	DL-52*	DL-29*
"	JPCA (15%CW)	DL-53*	DL-30*
"	316SS (SA)	EL-48*	EL-17*
"	316SS (SA)	EL-49*	EL-18*
"	316SS (SA)	EL-50*	EL-19*
"	316SS (SA)	EL-51*	EL-20*
"	316SS (SA)	EL-52*	-
"	316SS (SA)	EL-53*	-
"	316SS (SA)	EL-54*	-

	SS-1 Tensile Specimens (1.75 in. long)		
Program	Alloy (Condition)	200J-1 Specimens	400J-1 Specimens
JAERI*	316SS (SA)	EL-55*	-
"	J316 (20%CW)	FL-40*	FL-4*
"	J316 (20%CW)	FL-43*	FL-5*
"	J316 (20%CW)	FL-44*	FL-7*
"	J316 (20%CW)	FL-46*	FL-8*
"	J316 (20%CW)	FL-50*	FL-9*
"	J316 (20%CW)	FL-51*	FL-10*
"	J316 (20%CW)	FL-52*	FL-11*
"	J316 (20%CW)	FL-53*	FL-12*
"	J316 (20%CW)	FL-55*	-
"	J316 (SAR)	HL-8*	HL-3*
"	J316 (SAR)	HL-9*	HL-4*
"	dual phase K (SA)	IL-8*	IL-3*
"	dual phase K (SA)	IL-9*	IL-4*
"	all martensite (heat treated)	-	ML-3*
"	all martensite (heat treated)	-	ML-4*
"	JPCA (SA, electron beam weld joint)	KL-8*	KL-3*
"	JPCA (SA, electron beam weld joint)	KL-9*	KL-4*
"	JPCA (SA, TIG weld metal)	CLW-18*	CLW-9*
"	JPCA (SA, TIG weld metal)	-	CLW-10*
US/ORNL*	B1 (SA)	B1-07*	-
"	B2 (SA)	B2-07*	-
"	B3 (SA)	B3-07*	-
"	B5 (SA)	B5-07*	-
"	B6 (SA)	B6-07*	-

Table 4. Continued

SS-1 Tensile Specimens (1.75 in. long)			
Program	Alloy (Condition)	2003-1 Specimens	4003-1 Specimens
US/ORNL*	B7 (SA)	B7-07*	-
-	B9 (SA)	B9-07*	-
-	B10 (SA)	B10-07*	-
-	B11 (SA)	B11-07*	-
-	B12 (SA)	B12-07*	
-	B13 (SA)	B13-07*	
-	E 1 (SA)	E1-07*	
-	E 2 (SA)	E2-07*	-
-	E 3 (SA)	E3-07*	-
-	E 4 (SA)	E4-07*	
-	E 5 (SA)	E5-07*	-
	E 6 (SA)	E6-07	
-	E 8 (SA)	E8-07*	
-	E 9 (SA)	E9-07*	
-	E 10 (SA)	E10-07*	
-	E 11 (SA)	E11-07*	-
-	E 12 (SA)	E12-07*	-
	E 13 (SA)	E13-07*	-
-	E 14 (SA)	E14-07*	
JAERI	AF3	A101	A105
-	AF3	A102	A106
-	AF3	A103	A107
-	AF3	A104	A108
-	AF5	A201	A205
JAERI	AF5	A202	A206
-	AF5	A203	A207
-	AF5	A204	A208
-	AF7	A301	A305
-	AF7	A302	A306
-	AF7	A303	A307
-	AF7	A304	A308
-	316-M5	D301	D303
-	316-M5	D302	D304
-	316-M5	D305	D306
-	316-M7	D401	D403
-	316-M7	D402	D404
-	316-M10	D501	D503
-	316-M10	D502	D504
US/ORNL	Copper, MRC Marz grade (as wrought)	A06	A09
-	Copper, MRC Marz grade (as wrought)	A07	A10
-	Copper, MRC Marz grade (as wrought)	A08	A11
	Glidcop Al25 (as wrought)	H01	H04
	Glidcop Al25 (as wrought)	H02	H05
-	Glidcop Al25 (as wrought)	H03	H06
-	Glidcop Al25+B (wrought sheet)	L01	L06
-	Glidcop Al25+B (wrought sheet)	L02	L07
-	Glidcop Al25+B (wrought sheet)	L03	L08

Condition code: SAR = strained, aged, and recrystallized

Table 4. Continued

Program	Alloy (Condition)	200J-1 Specimen I.D. (Stress, MPa)	400J-1 Specimen I.D. (Stress, MPa)
Pressurized Tube and Tube Blank Specimens (1 in. or 0.25 in. long)			
US/ORNL*	PCA (20%CW)	FA2 (0)*	FA2 (0)*
"	PCA (20%CW)	FA59 (50)*	FA01 (50)*
"	PCA (20%CW)	FA48 (100)*	FA32 (100)*
"	PCA (20%CW)	FA62 (200)*	FA10 (200)*
"	PCA (20%CW)	-	FA05 (300)*
"	PCA (20%CW)	-	FA12 (400)*
"	HT-9 (tempered martensite)	SA28-2 (0)*	SA2 (0)*
"	HT-9 (tempered martensite)	SA21 (200)*	SA58 (50)*
"	HT-9 (tempered martensite)	SA30 (400)*	SA37 (100)*
"	HT-9 (tempered martensite)	-	SA32 (200)*
"	HT-9 (tempered martensite)	-	SA53 (300)*
"	HT-9 (tempered martensite)	-	SA03 (400)*
"	HT-9 (tempered martensite)	-	SA31 (400)*
"	1B (SA)	CA2 (0)*	CA2 (0)*
"	1B (SA)	C1A6 (5)*	C5A2 (5)*
"	1B (SA)	C2A6 (10)*	C3A6 (10)*
"	1B (SA)	C4A9 (30)	C4A2 (20)
"	1B (SA)	-	C2A4 (30)*
"	1B (SA)	-	C3A2 (40)*
"	1B (SA)	-	C1A7 (40)*
"	2B (SA)	CB2 (0)*	CB2 (0)*
"	2B (SA)	C3B2 (5)*	C4B4 (5)*
"	2B (SA)	C1B3 (10)*	C3B4 (10)*
"	2B (SA)	C3B1 (30)*	C4B2 (20)*
"	2B (SA)	-	C4B0 (30)*
"	2B (SA)	-	C5B0 (30)*

Program	Alloy (Condition)	200J-1 Specimen I.D. (Stress, MPa)	400J-1 Specimen I.D. (Stress, MPa)
Pressurized Tube and Tube Blank Specimens (1 in. or 0.25 in. long)			
US/ORNL*	2B (SA)	-	C4B6 (40)*
"	3B (SA)	CC2 (0)*	CC2 (0)*
"	3B (SA)	C4C0 (20)*	C1C0 (10)*
"	3B (SA)	C1C8 (50)*	C3C4 (20)*
"	3B (SA)	C3C0 (100)*	C3C6 (50)*
"	3B (SA)	-	C2C7 (50)*
"	3B (SA)	-	C4C3 (100)*
"	SA (SA)	S1A5-2 (0)*	SXAX-2 (0)*
"	SA (SA)	S3A5 (20)*	S1A0 (10)*
"	SA (SA)	S2A7 (80)*	01 (20)*
"	SA (SA)	-	S2A4 (50)*
"	SA (SA)	-	S2A0 (80)*
"	SA (SA)	-	S1A1 (100)*
JAERI*	J316 (SA)	3S13-2 (0)*	3S11-2 (0)*
"	J316 (SA)	3S00 (80)*	3S04 (100)*
"	J316 (SA)	3S02 (100)*	3S07 (120)*
"	J316 (SA)	3S05 (130)*	-
"	J316 (SA)	3S10 (150)*	-
"	J316 (20%CW)	3C12-2 (0)*	3C10-2 (0)*
"	J316 (20%CW)	3C05 (200)*	3C04 (200)*
"	J316 (20%CW)	3C09 (300)*	3C07 (400)*
"	JPCA (SA)	PS14-2 (0)*	PS11-2 (0)*
"	JPCA (SA)	PS00 (100)*	PS04 (100)*
"	JPCA (SA)	PS02 (130)*	PS07 (150)*
"	JPCA (SA)	PS05 (160)*	-
"	JPCA (SA)	PS09 (180)*	-

Table 4. Continued

Grodzinski Fatigue Specimens (1.75 in. long)			
Program	Alloy (Condition)	200J-1 Specimen I.D.	400J-1 Specimen I.D.
JAERI*	JPCA (SA)	GFA-44*	GFA-19*
"	JPCA (SA)	GFA-45*	GFA-20*
"	JPCA (SA)	GFA-46*	GFA-21*
"	JPCA (SA)	GFA-47*	GFA-22*
"	JPCA (SA)	GFA-48*	GFA-23*
"	JPCA (SA)	GFA-49*	GFA-24*
"	JPCA (15% CW)	GFB-44*	GFB-19*
"	JPCA (15% CW)	GFB-45*	GFB-20*
"	JPCA (15% CW)	GFB-46*	GFB-21*
"	JPCA (15% CW)	GFB-47*	GFB-22*
"	JPCA (15% CW)	GFB-48*	GFB-23*
"	JPCA (15% CW)	GFB-49*	GFB-24*
"	J316 (SA)	GFC-44*	GFC-17*
"	J316 (SA)	GFC-48*	GFC-18*
"	J316 (SA)	GFC-49*	GFC-19*
"	J316 (20% CW)	GFD-48*	GFD-18*
"	J316 (20% CW)	GFD-49*	GFD-23*
"	J316 (20% CW)	GFD-50*	GFD-24*

Hourglass Fatigue Specimens (1.78 in. long)			
Program	Alloy (Condition)	200J-1 Specimen I.D.	400J-1 Specimen I.D.
JAERI*	JPCA (15% CW)	-	FE-18*
"	JPCA (15% CW)	-	FE-19*
"	JPCA (15% CW)	-	FE-31*

Crack Growth Specimens (1 in. long)			
Program	Alloy (Condition)	200J-1 Specimen I.D.	400J-1 Specimen I.D.
JAERI*	JPCA (15% CW)	CGD-1*	CGB-3*
"	JPCA (15% CW)	CGD-2*	CGB-4*

able 4. Continued

	TEM Disks		
Program	Alloy (Condition)	2003-1 Specimens (#1)	4003-1 Specimens (#5)
US/ORNL	Copper (JMC Puratronic, cold rolled)	P1	P3
"	Copper (JMC Puratronic, cold rolled)	P2	P4
"	Copper (JMC Puratronic, rexl'd 400°C, 1h)	K1	K3
"	Copper (JMC Puratronic, rexl'd 400°C, 1h)	K2	K4
"	Copper (JMC Puratronic, oxygenated 950°C)	K9	K10
"	Copper (A.D. Mackay, cold rolled)	M1	M3
"	Copper (A.D. Mackay, cold rolled)	M2	M4
"	Glidcop Al15+B (FED, wrought sheet)	F1	F3
"	Glidcop Al15+B (FED, wrought sheet)	F2	F4
"	Glidcop Al15+B (Sandia, wrought sheet)	S1	S3
"	Glidcop Al15+B (Sandia, wrought sheet)	S2	S4
"	Glidcop Al15+B(SCM Metals, wrought sheet)	G1	G3
"	Glidcop Al15+B(SCM Metals, wrought sheet)	G2	G4
"	Glidcop Al15+B(PNL VO,solution annealed)	H11	H13
"	Glidcop Al15+B(PNL VO,solution annealed)	H12	H14
"	Glidcop AL20 (PNL, 20% cold rolled)	D1	D3
"	Glidcop Al20 (PNL, 20% cold rolled)	D2	D4
"	Glidcop Al25+B (as wrought)	W1	W3
"	Glidcop Al25+B (as wrought)	W2	W4
"	Glidcop Al25+B (80% CW)	C1	C3
"	Glidcop Al25+B (80% CW)	C2	C4
"	MAGT 0.05 (Technology 2)	V1	V3
"	MAGT 0.05 (Technology 2)	V2	V4
"	MAGT 0.2 (Technology 1)	T1	T3
"	MAGT 0.2 (Technology 1)	T2	T4
"	MAGT 0.2 (Technology 2)	Z1	Z3
"	MAGT 0.2 (Technology 2)	Z2	Z4
"	Glidcop Al15+B (as extruded+brazed)	F11	F13
"	Glidcop Al15+B (as extruded+brazed)	F12	F14
"	Copper (Risϕ OFHC, annealed 550°C, 2h)	Cu-Risϕ	Cu-Risϕ

	TEM Disks		
Program	Alloy (Condition)	2003-3 Specimens (#1)	4003-3 Specimens (#5)
US/ORNL	Copper (Risϕ OFHC, annealed 550°C, 2h)	Cu-Risϕ	Cu-Risϕ
"	Cu-1.0%Ni (rexl'd 800°C, 4h)	Cu-1.0%Ni	Cu-1.0%Ni
"	Cu-1.0%Ni (rexl'd 800°C, 4h)	Cu-1.0%Ni	Cu-1.0%Ni
	Cu-2.0%Ni (rexl'd 800°C, 4h)	Cu-2.0%Ni	Cu-2.0%Ni
"	Cu-2.0%Ni (rexl'd 800°C, 4h)	Cu-2.0%Ni	Cu-2.0%Ni
"	Cu-5.0%Ni (rexl'd 800°C, 4h)	Cu-5.0%Ni	Cu-5.0%Ni
"	Cu-5.0%Ni (rexl'd 800°C, 4h)	Cu-5.0%Ni	Cu-5.0%Ni
"	Cu-10%Ni (rexl'd 800°C, 4h)	Cu-10.0%Ni	Cu-10.0%Ni
"	Cu-10%Ni (rexl'd 800°C, 4h)	Cu-10.0%Ni	Cu-10.0%Ni
"	Cu-0.5%Be (rexl'd 800°C, 4h)	Cu-0.5%Be	Cu-0.5%Be
"	Cu-0.5%Be (rexl'd 800°C, 4h)	Cu-0.5%Be	Cu-0.5%Be
"	Glidcop Al25+B (Risϕ 80% CW)	Cu-0.25%Al+	Cu-0.25%Al+
"	Glidcop Al25+B (Risϕ 80% CW)	Cu-0.25%Al+	Cu-0.25%Al+
"	Glidcop Al25 (PNL RH, 50% CW)	X1	X3
	Glidcop Al25 (PNL RH, 50% CW)	X2	X4
"	Cu-0.17%Ni (rexl'd 800°C, 4h)	E5	E7
"	Cu-0.17%Ni (rexl'd 800°C, 4h)	E6	E8
	Copper (MRC Marz, as wrought)	A02	A07
"	Copper (MRC Marz, as wrought)	A03	A12
"	Glidcop Al15+B (B/G wrought sheet)	L01	L04
"	Glidcop Al15+B (B/G wrought sheet)	L02	L06
"	Glidcop Al25 (Risϕ/PNL, as wrought)	H01	H05
"	Glidcop Al25 (Risϕ/PNL, as wrought)	H02	H06
"	MER Cu-Al$_2$O$_3$-graphite (Pitch P120)	pitch	pitch
"	MER Cu-Al$_2$O$_3$-graphite (Pitch P120)	pitch	pitch
	MER Cu-Al$_2$O$_3$-graphite (Pan IM9)	pan	pan
"	MER Cu-Al$_2$O$_3$-graphite (Pan IM9)	pan	pan

Table 4. Continued

		TEM Disks	
Program	Alloy (Condition)	200J-1 Specimens (#2)	400J-1 Specimens (#6)
US/ANL	V	BL51	BL51
"	V	BL51	BL51
"	V	BL20	BL20
"	V	BL20	-
"	V-1Ti	BL50	BL50
"	V-1Ti	BL50	-
"	V-15Cr-5Ti	BL24	BL24
"	V-15Cr-5Ti	BL24	BL24
"	V-15Cr-5Ti	BL41	BL41
"	V-15Cr-5Ti	BL41	BL41
"	V-15Ti-7.5Cr	BL10	BL10
"	V-10Cr-5Ti	BL43	BL43
"	V-10Cr-5Ti	BL43	BL43
"	V-3Ti-0.5Si	BL42	BL42
"	V-3Ti-0.5Si	BL42	BL42
"	V-3Ti-1Si	BL45	BL45
"	V-3Ti-1Si	BL45	BL45
"	V-3Ti-0.25Si	BL27	BL27
"	V-3Ti-0.25Si	BL27	BL27
"	V-10Cr-10Ti	BL44	-
"	V-10Cr-10Ti	BL44	-
"	V-5Cr-5Ti	BL47	BL47
"	V-5Cr-5Ti	BL47	BL47
"	V-5Ti	BL46	BL46
"	V-5Ti	BL46	BL46
"	V-10Ti	BL12	BL12
US/ANL	V-10Ti	BL12	-
"	V-20Ti	BL15	BL15
"	V-20Ti	BL15	BL15
"	V-20Ti	BL18	BL18
"	V-20Ti	BL18	BL18
"	V-15Ti	BL13	BL13
"	V-15Ti	BL13	BL13
"	V-12Cr-5Ti	BL40	BL40
"	V-12Cr-5Ti	BL40	BL40
"	V-7Cr-5Ti	BL49	BL49
"	V-7Cr-5Ti	BL49	BL49
"	V-15Cr-0.3Ti	BL25	BL25
"	V-15Cr-0.3Ti	BL25	-
"	V-15Cr-1Ti	BL26	BL26
"	V-15Cr-1Ti	BL26	BL26
"	V-15Cr-5Ti	BL21	BL21
"	V-15Cr-5Ti	BL21	BL21
"	V-15Cr-5Ti	BL22	BL22
"	V-15Cr-5Ti	BL22	BL22
"	V-15Cr-5Ti	BL23	BL23
"	V-15Cr-5Ti	BL23	BL23
"	V-10Cr	BL4	BL4
"	V-10Cr	BL4	BL4
"	V-15Cr	BL5	BL5
"	V-15Cr	BL5	BL5

Table 4. Continued

TEM Disks			
Program	Alloy (Condition)	200J-1 Specimens (#3)	400J-1 Specimens (#7)
US/PRC	316L (SA)	R2-01	R2-06
	316L (SA)	R2-02	R2-07
	316L (SA)	R2-03	R2-08
	316L (SA)	R2-04	R2-09
	316L (SA)	R2-05	R2-10
	316L (CW)	R3-01	R3-06
	316L (CW)	R3-02	R3-07
	316L (CW)	R3-03	R3-08
	316L (CW)	R3-04	R3-09
	316L (CW)	R3-05	R3-10
"	316Ti (SA)	R4-01	R4-06
"	316Ti (SA)	R4-02	R4-07
"	316Ti (SA)	R4-03	R4-08
"	316Ti (SA)	R4-04	R4-09
"	316Ti (SA)	R4-05	R4-10
"	316Ti (CW)	R5-01	R5-06
"	316Ti (CW)	R5-02	R5-07
"	316Ti (CW)	R5-03	R5-08
"	316Ti (CW)	R5-04	R5-09
"	316Ti (CW)	R5-05	R5-10

TEM Disks			
Program	Alloy (Condition)	200J-1 Specimens (#4)	400J-1 Specimens (#8)
US/ORNL	9Cr-1MoVNb	TL-80	TL-37
"	9Cr-1MoVNb	TL-88	TL-77
"	9Cr-1MoVNb-2Ni	TM-74	TM-43
"	9Cr-1MoVNb-2Ni	TM-82	TM-53
"	12Cr-1MoVW	SS-57	SS-16
"	12Cr-1MoVW	SS-96	SS-28
"	12Cr-1MoVW-1Ni	ST-24	ST-63
"	12Cr-1MoVW-1Ni	ST-53	ST-83
"	12Cr-1MoVW-2Ni	SU-23	SU-43
"	12Cr-1MoVW-2Ni	SU-94	SU-63
"	12Cr-1MoVW-2Ni adjusted	SV-33	SV-74
"	12Cr-1MoVW-2Ni adjusted	SV-93	SV-94

Table 4. Continued

Program	Alloy (Condition)	200J-1 Specimen I.D.	400J-1 Specimen I.D.
	Thermal Conductivity Cylinder Specimens (.24 in. dia. × .24 in. thick)		
US/ORNL	Copper, MRC Marz grade (as wrought)	-	A01
"	Copper, MRC Marz grade (as wrought)	-	A02
"	MER Cu-Al$_2$O$_3$-graphite (pitch P120)	-	blank
"	MER Cu-Al$_2$O$_3$-graphite (pitch P120)	-	blank
"	Glidcop Al15+B (wrought sheet)	-	blank
"	Glidcop Al25+B (as wrought)	-	L01
"	Glidcop Al25+B (as wrought)	-	W1
		-	W2

Program	Alloy (Condition)	200J-1 Specimen I.D.	400J-1 Specimen I.D.
	[illegible] Disk Specimens (0.36 in. dia. × 0.075 in. thick)		
US/ORNL	Copper, MRC Marz grade (as wrought)	A01	A07
"	Copper, MRC Marz grade (as wrought)	A05	A08
"	MER Cu-Al$_2$O$_3$-graphite (pitch P120)	blank	blank
"	MER Cu-Al$_2$O$_3$-graphite (pitch P120)	blank	blank
"	Glidcop Al15+B (wrought sheet)	L01	L06
"	Glidcop Al15+B (wrought sheet)	L02	L07
"	Glidcop Al25+B (as wrought)	W1	W3
"	Glidcop Al25+B (as wrought)	W2	W4

Program	Length of Holder, inches	200J-1 Specimen I.D.	400J-1 Specimen I.D.
	TEM Specimen Holders		
[illegible]	[illegible]	J6* (70)	J8* (73)
"	1	J7* (70)	J10* (75)
"	1	J8* (70)	J11* (78)
"	1	J9* (70)	J12* (76)
"	1	J10* (70)	-
"	1	J11* (82)	-
US/ORNL*	0.65	E* (38)	
	0.65	F* (38)	-
	0.75	-	* (52)
"	0.75	-	* (52)
JAERI	1	16 (44)	0 (55)
"	1	17 (44)	1 (56)
"	1	18 (69)	22 (56)
"	1	19 (69)	J23 (54)
	1	(58)	5 (58)
	0.5	[illegible]	[illegible]

Table 4. Continued

	TEM Disks		
Program	Alloy (Condition)	200J-1 Specimens (#J16)	400J-1 Specimens (#J20)
JAERI	Duplex AF3	A1-01	A1-06
"	Duplex AF3	A1-02	A1-07
"	Duplex AF5	A2-01	A2-06
"	Duplex AF5	A2-02	A2-07
"	Duplex AF7	A3-01	A3-06
"	Duplex AF7	A3-02	A3-07
"	F82H	B1-01	B1-21
"	F82H	B1-02	B1-22
"	F82H (laser weld joint)	B2-01	B2-06
"	F82H (laser weld joint)	B2-02	B2-07
"	HT-9	B3-01	B3-21
"	HT-9	B3-02	B3-22
"	JPCA (SA)	C1-01	C1-21
"	JPCA (SA)	C1-02	C1-22
"	JPCA (CW)	C2-01	C2-22
"	JPCA (CW)	C2-02	C2-23
"	JPCA K	-	C3-01
"	JPCA K	-	C3-02
"	JPCA C	-	C4-01
"	JPCA C	-	C4-02
"	316F (SA)	D1-01	D1-21

	TEM Disks		
Program	Alloy (Condition)	200J-1 Specimens (#J16)	400J-1 Specimens (#J20)
JAERI	316F (SA)	D1-02	D1-22
"	316F (CW)	D2-01	D2-22
"	316F (CW)	D2-02	D2-23
	316 M5	D3-01	D3-05
	316 M5	D3-02	D3-06
	316 M7	D4-01	D4-06
	316 M7	D4-03	D4-07
	316 M10	D5-02	D5-06
	316 M10	D5-03	D5-07
	JHD (SA)	-	F1-01
	JHD (SA)		F1-02
	JHD (CW)	-	F2-01
	JHD (CW)	-	F2-02
	JHF (SA)		F3-01
	JHF (SA)		F3-02
	JHF (CW)	-	F4-01
	JHF (CW)	-	F4-02
	JHG (SA)	-	F5-01
	JHG (SA)	-	F5-02
	JHG (CW)	-	F6-01
	JHG (CW)	-	F6-02
	JHH (CW)		

Table 4. Continued

TEM Disks			
Program	Alloy (Condition)	200 μm Specimens (#J16)	400 μm Specimens (#J22)
JAERI	[illegible] (CW)		[illegible]
	Ni [illegible]		[illegible]
	[illegible]		[illegible]
"	[illegible]		[illegible]
	[illegible]	E540	[illegible]
"	[illegible]	E580	[illegible]
"	[illegible]	[illegible]	[illegible]
	[illegible]	[illegible]	[illegible]
	[illegible]	[illegible]	[illegible]
	[illegible]	[illegible]	[illegible]
"	[illegible]	[illegible]	[illegible]
	[illegible]	[illegible]	[illegible]
	[illegible]	ARZ6	
"	[illegible]	A86M	
"	[illegible]	AKY[illegible]	
	[illegible]	AMY[illegible]	
	[illegible]	[illegible]	
	[illegible]	A7[illegible]R	
	[illegible]	[illegible]	
"	[illegible]	A86M	
	[illegible]	AZZA	
	[illegible]	A90K	

TEM Disks			
Program	Alloy (Condition)	200 μm Specimens (#J17)	400 μm Specimens (#J21)
JAERI	Fe-15Cr-16Ni	B1B3	B2B1
"	Fe-15Cr-16Ni	B1B2	B2B2
"	Fe-15Cr-16Ni-0.25Ti-0.05C-100appmB	G1G0	G1G3
"	Fe-15Cr-16Ni-0.25Ti-0.05C-1000appmB	G1G1	G1G4
	Fe-15Cr-16Ni-0.25Ti-0.05C-500appmB	H1H7	H1HA
	Fe-15Cr-16Ni-0.25Ti-0.05C-500appmB	H1H8	H1HD
"	Fe-15Cr-16Ni-0.25Ti-0.05C-2500appmB	K1K0	K1K3
	Fe-15Cr-16Ni-0.25Ti-0.05C-2500appmB	K1K1	K1K4
"	Fe-15Cr-16Ni-500appmB	L1L7	L1LA
	Fe-15Cr-16Ni-500appmB	L1L8	L1LB
	Fe-15Cr-16Ni-0.25Ti-500appmB	M1M7	M1MA
"	Fe-15Cr-16Ni-0.25Ti-500appmB	M1M8	M1MB
	Fe-15Cr-16Ni-0.25Ti	H101	H103
"	Fe-15Cr-16Ni-0.25Ti	H102	H104
"	Fe-15Cr-16Ni-0.25Ti-0.05C	H201	H203
"	Fe-15Cr-16Ni-0.25Ti-0.05C	H202	H204
"	Fe-15Cr-20Ni	H301	H304
"	Fe-15Cr-20Ni	H302	H305
"	316 S1 (SA)	H401	H404
"	316 S1 (SA)	H402	H405
"	316 S1 (CW)	H501	H504
"	316 S1 (CW)	H502	H505
"	316 S2 (SA)	H601	H604
"	316 S2 (SA)	H602	H605
"	316 S2 (CW)	H701	H704
"	316 S2 (CW)	H702	H705
"	Fe-16Cr-17Ni	Y000	Y006

Table 4. Continued

Program	TEM Disks		
	Alloy (Condition)	200J-1 Specimens (#J17)	400J-1 Specimens (#J21)
JAERI	Fe-16Cr-17Ni	Y001	Y007
	Fe-16Cr-17Ni-0.1P	Y002	Y008
	Fe-16Cr-17Ni-0.1P	Y003	Y009
.	Fe-16Cr-17Ni-0.25Ti-0.1P	Y004	Y100
.	Fe-16Cr-17Ni-0.25Ti-0.1P	Y005	Y101
.	JPCA2	A0AL	A0AS
.	JPCA2	A0AM	A0AT
.	Fe-16Cr-14Ni	A10F	A11F
.	Fe-16Cr-14Ni	A20F	A21F
.	Fe-18Cr-14Ni-2.5Mo	A30F	A31F
.	Fe-18Cr-14Ni-2.5Mo	A40F	A41F
.	Fe-18Cr-14Ni-2.5Mo-0.3Zr	A50F	A51F
.	Fe-18Cr-14Ni-2.5Mo-0.3Zr	A60F	A61F
.	Fe-18Cr-14Ni-2.5Mo-0.3Ti	A70F	A71F
.	Fe-18Cr-14Ni-2.5Mo-0.3Ti	A80F	A81F
.	Fe-18Cr-14Ni-2.5Mo-0.3Nb	A90F	A91F
.	Fe-18Cr-14Ni-2.5Mo-0.3Nb	A01F	A02F
.	V-5Cr	-	ARZ7
.	V-0.5Y	-	A80R
.	V	-	AKY6
.	V-5Ti	-	AMY4
.	V-2Y	-	A01M
.	V-1Zr	-	A70M
.	V-2Si	-	A40R
.	V-2Al	-	A50R
.	V-5Ti-1Y	-	AZZB
.	SiC (ß)	-	E2-01
.	SiC (ß)	-	E2-02
.	SiC (ß)	-	E2-03

Program	TEM Disks		
	Alloy (Condition)	200J-1 Specimens (#J18)	400J-1 Specimens (#J22)
JAERI	Duplex AF3	A1-03	A1-08
.	Duplex AF3	A1-04	A1-09
	Duplex AF3	A1-05	A1-10
	Duplex AF5	A2-03	A2-08
	Duplex AF5	A2-04	A2-09
	Duplex AF5	A2-05	A2-10
	Duplex AF7	A3-03	A3-08
	Duplex AF7	A3-04	A3-09
	Duplex AF7	A3-05	A3-10
	F82H	B1-03	B1-23
	F82H	B1-04	B1-24
	F82H	B1-05	B1-25
	F82H	B1-06	B1-26
	F82H	B1-07	B1-27
.	F82H	B1-08	B1-28
.	F82H	B1-09	B1-29
.	F82H	B1-10	B1-30
.	F82H	B1-11	B1-31
.	F82H	B1-12	B1-32
.	F82H	B1-13	B1-33
.	F82H	B1-14	B1-34
.	F82H	B1-15	B1-35
.	F82H	B1-16	B1-36

Table 4. Continued

	TEM Disks		
Program	Alloy (Condition)	200°C Specimens (#J18)	400°C Specimens (#J22)
JAERI	F82H	B1-17	B1-27
"	F82H	B1-18	[illegible]
"	F82H	B1-19	[illegible]
"	F82H	B1-20	[illegible]
"	F82H (laser weld joint)		B2-08
"	F82H (laser weld joint)	-	B2-09
"	F82H (laser weld joint)		B2-10
"	[illegible]	B3-03	B3-23
	[illegible]	B3-04	B3-24
"	[illegible]	B3-05	[illegible]
"	[illegible]	[illegible]	[illegible]
	[illegible]	B3-07	B3-27
	[illegible]	B3-08	B3-28
	[illegible]	B3-09	[illegible]
	[illegible]	B3-10	B3-30
	[illegible]	B3-11	B3-31
	[illegible]	B3-12	B3-32
"	[illegible]	B3-13	B3-33
	[illegible]	B3-14	B3-34
	[illegible]	B3-15	B3-35
	[illegible]	B3-16	B3-36
	[illegible]	B3-17	B3-37
	[illegible]	B3-18	B3-38
	[illegible]	B3-19	[illegible]
	[illegible]	B3-20	[illegible]

	TEM Disks		
Program	Alloy (Condition)	200°C Specimen (#J18)	400°C Specimens (#J22)
JAERI	JPCA (SA)	C1-03	C1-23
	JPCA (SA)	C1-04	C1-24
"	JPCA (SA)	[illegible]	[illegible]
	JPCA (SA)	C1-06	C1-26
	JPCA (SA)	[illegible]	C1-27
	JPCA (SA)	C1-08	C1-28
	JPCA (SA)	C1-09	C1-29
"	JPCA (SA)	C1-10	C1-30
	JPCA (SA)	C1-11	
	JPCA (SA)	[illegible]	
"	JPCA (SA)	[illegible]	
	JPCA (SA)	C1-14	
"	JPCA (SA)	[illegible]	
	JPCA (SA)	C1-16	
"	JPCA (SA)	C1-17	
	[illegible]	C1-18	
	[illegible]	[illegible]	
	JPCA (SA)	[illegible]	
	[illegible]	H303	
"	316 SS (SA)	H603	
	316 SS (CW)	H703	
"	[illegible]	A0AR	
"	316 SS (SA)	H403	
"	[illegible] (CW)	H503	

Table 4. Continued

TEM Disks			
Program	Alloy (Condition)	200J-1 Specimens (#J19)	400J-1 Specimens (#J23)
JAERI	F82H (laser weld joint)	B2-03	-
"	F82H (laser weld joint)	B2-04	-
"	F82H (laser weld joint)	B2-05	-
"	JPCA (CW)	C2-03	C2-24
"	JPCA (CW)	C2-04	C2-25
"	JPCA (CW)	C2-05	C2-26
"	JPCA (CW)	C2-06	C2-27
"	JPCA (CW)	C2-07	C2-28
"	JPCA (CW)	C2-08	C2-29
"	JPCA (CW)	C2-09	C2-30
"	JPCA (CW)	C2-10	C2-31
"	JPCA (CW)	C2-11	-
"	JPCA (CW)	C2-12	-
"	JPCA (CW)	C2-13	-
"	JPCA (CW)	C2-14	-
"	JPCA (CW)	C2-15	-
"	JPCA (CW)	C2-16	-
"	JPCA (CW)	C2-17	-
"	JPCA (CW)	C2-18	-
"	JPCA (CW)	C2-19	-
"	JPCA (CW)	C2-21	-
"	JPCA K	-	C3-03
"	JPCA C	-	C4-03
"	316F (SA)	D1-03	D1-23
"	316F (SA)	D1-04	D1-24
"	316F (SA)	D1-05	D1-25
"	316F (SA)	D1-06	D1-26
"	316F (SA)	D1-07	D1-27
"	316F (SA)	D1-08	D1-28
JAERI	316F (SA)	D1-09	D1-29
"	316F (SA)	D1-10	D1-30
"	316F (SA)	D1-11	-
"	316F (SA)	D1-12	-
"	316F (SA)	D1-13	-
"	316F (SA)	D1-14	-
"	316F (SA)	D1-15	-
"	316F (SA)	D1-16	-
"	316F (SA)	D1-17	-
"	316F (SA)	D1-18	-
"	316F (SA)	D1-19	-
"	316F (SA)	D1-20	-
"	316F (CW)	D2-03	D2-24
"	316F (CW)	D2-04	D2-25
"	316F (CW)	D2-05	D2-26
"	316F (CW)	D2-06	D2-27
"	316F (CW)	D2-07	D2-28
"	316F (CW)	D2-08	D2-29
"	316F (CW)	D2-09	D2-30
"	316F (CW)	D2-10	D2-32
"	316F (CW)	D2-11	-
"	316F (CW)	D2-12	-
"	316F (CW)	D2-13	-
"	316F (CW)	D2-14	-
"	316F (CW)	D2-15	-
"	316F (CW)	D2-16	-
"	316F (CW)	D2-17	-
"	316F (CW)	D2-18	-
"	316F (CW)	D2-19	-

Table 4. Continued

TEM Disks			
Program	Alloy (Condition)	200J-1 Specimens (#J19)	400J-1 Specimens (#J23)
JAERI	316F (CW)	D2-20	-
"	316 M5	D3-03	D3-07
"	316 M5	D3-04	D3-08
"	316 M5	-	D3-10
"	316 M7	D4-04	D4-08
"	316 M7	D4-05	D4-09
"	316 M7	-	D4-10
"	316 M10	D5-04	D5-08
"	316 M10	D5-05	D5-09
"	316 M10	-	D5-10
"	Fe-15Cr-16Ni	B2B0	B2B3
"	Fe-15Cr-16Ni-0.25Ti-0.05C-100appmB	G1G2	G1G5
"	Fe-15Cr-16Ni-0.25Ti-0.05C-500appmB	H1H9	H1HB
"	Fe-15Cr-16Ni-0.25Ti-0.05C-2500appmB	K1K2	K1K5
"	Fe-15Cr-16Ni-500appmB	L1L9	L1LD
"	Fe-15Cr-16Ni-0.25Ti-500appmB	M1M9	M1MD
"	JPCA2		A0AV
"	Fe-15Cr-20Ni		H306
"	316 S1 (SA)		H406
"	316 S1 (CW)		H506
"	316 S2 (SA)		H606
"	316 S2 (CW)	-	H706
"	JHD (SA)	-	F1-03
"	JHD (CW)	-	F2-03
"	JHF (SA)		F3-03
"	JHF (CW)		F4-03
"	JHG (SA)		F5-03
"	JHG (CW)		F6-03
"	JHH (CW)		F7-03

STATUS OF U.S./JAPAN COLLABORATIVE PROGRAM PHASE II HFIR TARGET CAPSULES

- J. E. Pawel and R. L. Senn (Oak Ridge National Laboratory) and K. Shiba (Japan Atomic Energy Research Institute)

OBJECTIVE

The objective of this program is to determine the response of various U.S. and Japanese austenitic and ferritic stainless steels with different pretreatments and alloy compositions to the combined effects of displacement damage and helium generation at temperatures in the range of 300 to 600°C and **doses** of 18 to 70 dpa.

SUMMARY

A complete description and details of the design, construction, and instellation **of** capsules JP9 through JP16 have been previously reported.[1,2,3] The capsules were installed in the High Flux Isotope Reactor (HFIR) target July 20, 1990 for irradiation beginning with HFIR fuel cycle 289. The capsules were removed and stored in the reactor pool during HFIR cycle 293 (12/27/90 - 1/23/91) to provide room for required isotope production. They were reinstalled for HFIR cycle 294 for continued irradiation. Of these eight target capsules, JP10, 11, 13, and **16** completed their scheduled number of cycles (11) and were removed from the reactor in September 1991. In addition, JP14 was removed from the reactor at the end of cycle **310** (9/18/92) after 21 **cycles.**

Three new capsules in **this** series. JP20, 21, and 22. **have** been designed. These capsules were added to the program in order to complete the experimental matrix included in the JP9 through JP16 capsules. The new capsules will contain transmission electron microscope (TEM) disks and **SS-3** flat tensile specimens at 300-600°C and will achieve doses of 8, 18 and 35 dpa. respectively. The preliminary experiment matrix is described in detail in a previous report.[4]

PROGRESS AND STATUS

Capsules JP9 through JP16

The as-built specimen matrix for the JP9 through JP16 series capsules can be found in a previous report.' These capsules contain primarily transmission electron microscopy **disks** (TEM) and *SS-3* tensile specimens. **A** wide variety of alloys and thermomechanical conditions are included. Msny of the TEM disks were made from isotopically tailored alloys to produce a range of He/dpa ratios (<0.1, 10, 20, 70). Details of the irradiation history of these capsules are shown in Table 1.

Many of the specimens from the JP10, 11, 13, and **16** capsules have been tested in the Irradiated Materials Examination and Testing Facility hot cells. Of 104 **SS-3** tensile specimens removed from these four capsules. 52 have been tested during this reporting period. Reduction-in-area measurements are currently underway on the broken halves. Analyses of these data are in progress and are expected to be reported in September 1993. The alloys tested include JPCA and type **316 (316F)** stainless steels in solution annealed, cold worked, and welded conditions.

Density measurements have been taken on specimens removed from the JP10 Position 6 TEM tube and the JP16 Position 6 TEM tube using the ORNL precision densitometer. The JP11 and JP13 Position 6 tubes have already been opened and are scheduled for sorting and densitometry during the

Table I. Irradiation history of the US/Japan Phase II HFIR Target Capsules.

HFIR OPERATION				JP-10,-11,-13,-16		JP-14		JP-9,-12,-15	
				11 CYCLE IRR.		21 CYCLE IRR.		37 CYCLE IRR.	
VCU NO	START DATE	END DATE	IWd/ Cycle	MWd	dpa*	MWd	dpa*	MWd	dpa*
289	07-20-90	09-07-90	1879	1879	1.64	1879	1.64	1879	1.64
290	09-19-90	10-11-90	1852	3731	3 26	3731	3 26	3731	3 26
291	10-17-90	11-13-YO	1838	5569	4.86	5569	4.86	5569	4 86
292	11-25-90	12-10-90	1847	7416	6.47	7416	6.47	7416	6 47
293	12-27-90	01-23-91	1965	CAPSULES OUT OF REACTOR FOR THIS CYCLE **					
294	02-01-91	02-25-91	1906	9322	8 14	9322	8 14	9322	8.14
295	03-01-91	03-24-91	1908	11230	9.80	11230	9.80	11230	9.80
296	04-05-91	04.28-91	1874	13104	11.44	13104	11.44	13104	11.44
297	05-19-91	06-15-91	1845	14949	13.05	14949	13.05	14949	13.05
298	06-20-91	07-11-91	1747	16696	14.58	16696	14.58	16696	14.58
299	07-25-91	08-15-91	1741	18437	16.10	18437	16.10	18437	16.10
300	08-28-91	09-17-91	1724	20161	17.60	20161	17.60	20161	17.60
301	09-27-91	10-19-91	1851	REMOVED EOC 300		22012	19.22	22012	19.22
302	10-27-91	11-21-91	1829			23841	20.81	23841	20.81
303	12-01-91	12-22-91	1821			25662	22.40	25662	22.40
304	12-31-91	01-24-92	1826			27488	24.00	27488	24 00
305	01-30-92	02-27-92	1876			29364	25.63	29364	25 63
305	03-31-92	04-27-92	1845			31209	27.25	31209	17.25
307	05-01-92	05-28-92	1842			33051	28.85	33051	28.85
308	06-02-92	06-30-92	1938			34989	30.55	34989	30.55
305	01-03-92	08-01-92	1949			36938	32.25	36938	32.25
31C	08-27-92	09-18-92	1849			38787	33.86	38787	33.86
311	09-25-92	10-12-92	1856			REMOVED EOC 310		40643	35.48
312	10-22-92	11-14-92	1842					42485	37 09
313	11-21-92	12-15-92	1850					44335	38.70
314	12-20-92	01-12-93	1866					46201	40.33
31t	01-19-93	02-10-93	1861					48062	41.95
31E	02-18-93	04-03-93	1807					49869	43.54
317									
31E									
319									
32C									

---

* **DPA levels based** on achieving 0 000873 *dpa/MWd*

** **Correction** from **previous** issues of **this document** The **experiments were** out of **reactor** for **cycle** 293 **rather** *than* 292 This slightly **reduces the** previously **reported** MWd **and** dpa **values**

next reporting period. These four tubes contain isotopically tailored alloys from both the ORNL and JAERI programs as well as other candidate fusion alloys. This experiment addresses the long-standing questions on the role of helium in microstructural evolution and will explore the high fluence swelling behavior of the most swelling-resistant materials currently available.

Capsule JP14 is scheduled to be disassembled in May 1993. This capsule, which achieved 34 dpa, contains SS-3 tensile specimens and TEM disks of many of the alloys included in the JP10, 11, 13 and 16 set of capsules, which achieved 18 dpa.

Capsules JP20 through 22

Three new capsules, JP20, 21, and 22, have been designed to complete the original experiment matrix of the JP9 through JP16 series capsules. It is planned to irradiate the three capsules in inner target positions for 5, 11, and 22 cycles, respectively, to achieve peak doses of approximately 8, 18, and 35 dpa. Specimen temperatures in each capsule will be 300, 400, 500, or 600°C.

PRESENT STATUS

Installation of JP20, 21, and 22 in the HFIR is currently scheduled for August 1993.

REFERENCES

1. R. L. Senn, "Status of U.S./Japan Collaborative Program Phase II HFIR Target Capsules," pp. 8-20 in Fusion Reactor Materials Semiann. Prog. Rep. Sept. 30, 1987, DOE/ER-0313/3, U.S. DOE Office of Fusion Energy.

2. R. L. Senn, "Status of U.S./Japan Collaborative Program Phase II HFIR Target Capsules," pp. 7-9 in Fusion Reactor Materials Semiann. Prog. Rep., March 31, 1988, DOE/ER-0313/4, U.S. DOE Office of Fusion Energy.

3. R. L. Senn, "Status of U.S./Japan Collaborative Program Phase II HFIR Target Capsules," pp. 6-13 in Fusion Reactor Materials Semiann. Prog. Rep., Sept. 30, 1988, DOE/ER-0313/5, U. S. DOE Office of Fusion Energy.

4. J. E. Pawel and R. L. Senn, "Status of U.S./Japan Collaborative Program Phase II HFIR Target Capsules," pp. 15-23 in Fusion Reactor Materials Semiann. Prog. Rep., March 31, 1992, DOE/ER-0313/12, U. S. DOE Office of Fusion Energy.

2.0 DOSIMETRY, DAMAGE PARAMETERS, AND ACTIVATION CALCULATIONS

HELIUM MEASUREMENTS FOR THE MOTA 1G DISCHARGE OF THE ^{59}Ni ISOTOPIC TAILORING EXPERIMENT - F. A. Garner (Pacific Northwest Laboratory)[*] and G. M. Oliver (Rockwell International)

OBJECTIVE

The objective of this effort is to determine the role of helium on radiation-induced microstructural evolution and associated changes in mechanical properties of model Fe-Cr-Ni alloys.

SUMMARY

The final measurements of helium generation in specimens used in the ^{59}Ni isotopic tailoring experiment have been completed. The results show that the target generation rates were sustained throughout the experimental series. It was also demonstrated that helium generation rates grow continuously in undoped specimens, reaching levels substantially larger than usually quoted in most other studies

PROGRESS AND STATUS

Introduction

In a previous report it was shown that the ^{59}Ni isotopic tailoring experiment conducted in FFTF was very successful in showing that the role of the helium generation rate on neutron-induced property changes was of second order importance compared to the action of other variables examined in the experiment (1). such a conclusion, of course, depends on demonstrating that the target generation rates were indeed maintained throughout the experiment. In an earlier report the helium/dpa rater for specimens from MOTA 1D, 1E, and 1F were presented (2). This report presents the measurements for the final discharge from MOTA 1G and also makes an assessment of the entire experiment. The helium measurement techniques have heen described earlier (2). For each specimen. two separate measurements were made, each on a one-quarter section of the rpecimen.

The damage levels and temperatures explored in this experiment are presented in Fig. I. The new measurements correspond to the right hand column of final Irradiation sequences of Fig. 1. The level 8 low dose series at 465°C in MOTA 1G was not measured. however, since all specimens were sent to Japan for microscopy examination by Professor H. Kawanishi of the University of Tokyo.

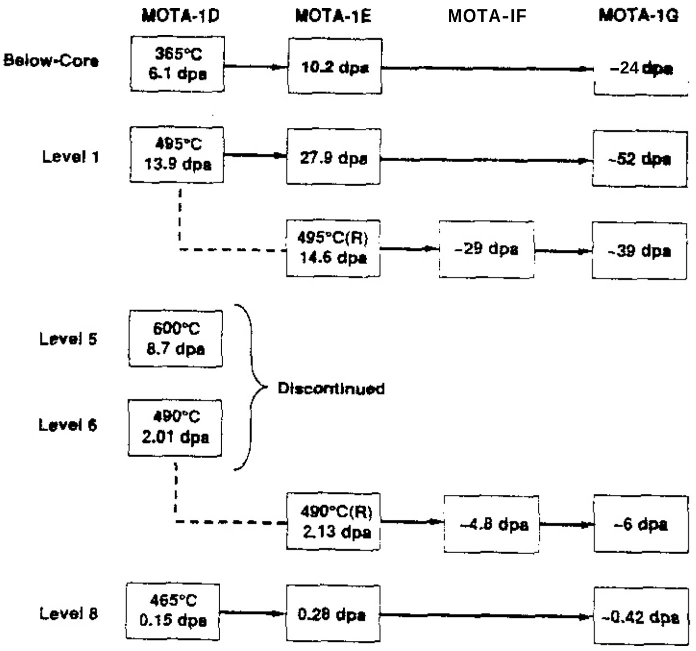

Fig. 1. Schematic representation of irradiation sequences for the ^{59}Ni isotopic tailoring experiment. "495°C(R)" and "490°C(4)" refer to the replacement sequences substituted for tne original compromised sequences at 495 and 490°C. Damage levels shown represent the cumulative totals.

Results

Table 1 presents a compilation of the helium measurements. In one case (Fe-15Cr-25Ni without ^{59}Ni at 495°C and 52 dpa) a specimen was not available but the helium generation rate can be calculated at 25/45 of the generation rate in the Fe-15Cr-45Ni specimen. Two separate Fe-15Cr-45Ni specimens at this set of irradiation conditions were examined to check on the reproducibility of the helium generation rate from specimen to specimen. The repoducibility appears to be Quite good. yielding 62.6±<0.1 and 63.1±0.3 appm for the two specimens.

---

[*] Pacific Northwest Laboratory is operated for the U.S. Department of Energy by Battelle Memorial Institute under Contract DE-AC06-76RLO 1830.

Table 1
Helium Concentrations in TEM Samples from MOTA 1G

Temperature, °C	Specimen	Material	Dopant	Mass^{a} (mg)	Measured ^{4}He (10^{15} atoms)	Helium Concentration (appm) Measured^{b}	Helium Concentration (appm) Average^{c}	Helium/dpa Ratio (appm/dpa)
490	ZXNK-A	Fe-15Cr-25Ni		1.882	0.006253	3.085	3.11	0.52
	B			3.155	0.1067	3.130	±0.03	
490	Z3NK-A	Fe-15Cr-25Ni	^{59}Ni	3.198	3.255	94.56	94.1	15.58
	B			3.030	3.057	93.68	±0.6	
490	Z7NK-A	Fe-15Cr-25Ni	P	2.908	0.1004	3.206	3.19	0.53
	B			2.400	0.08187	3.167	±0.03	
490	Z4NK-A	Fe-15Cr-25Ni	P ^{59}Ni	2.045	1.941	88.13	89.0	14.83
	B			2.000	1.935	89.83	±1.2	
490	Z1NK-A	Fe-15Cr-45Ni		2.035	0.1135	5.227	5.26	0.88
	B			2.783	0.1560	5.292	±0.05	
490	Z5NK-A	Fe-15Cr-45Ni	^{59}Ni	1.930	1.945	94.45	94.6	15.77
	B			2.349	2.375	94.75	±0.2	
495(R)	ZXNL-A	Fe-Cr-25Ni	-	2.271	0.6493	25.55	25.3	0.67
	B			2.059	0.5781	26.07	±0.3	
495(R)	Z3NL-A	Fe-Cr-25Ni	^{59}Ni	2.697	4.598	158.3	158	4.05
	B			3.109	5.281	157.7	±<1	
495(R)	Z1NL-A	Fe-Cr-45Ni		2.257	1.055	43.81	45.1	1.16
	B			2.388	1.182	46.39	±1.8	
495(R)	Z5NL-A	Fe-Cr-45Ni	^{59}Ni	2.240	4.283	179.2	180	4.62
	B			2.623	5.051	180.5	±1	
365	ZXLO-A	Fe-15Cr-25Ni		1.989	0.5026	23.46	23.3	0.27
	B			2.452	0.6099	23.10	±0.3	
365	Z3LO-A	Fe-15Cr-25Ni	^{59}Ni	2.951	9.585	301.6	300	12.5
	B			2.713	8.734	298.9	±2	
365	Z7LO-A	Fe-15Cr-25Ni	P	2.514	0.6220	22.97	23.0	0.96
	B			2.223	0.5499	22.97	±<0.1	
365	Z4LO-A	Fe-15Cr-25Ni	P ^{59}Ni	1.617	4.853	278.7	280	11.67
	B			1.920	5.812	281.1	±2	
365	Z1LN-A	Fe-15Cr-45Ni	-	2.201	0.9327	41.84	41.6	1.73
	B			2.803	1.234	41.26	±0.4	
365	Z5LN-A	Fe-15Cr-45Ni	^{59}Ni	2.040	6.961	316.8	317	13.2
	B			2.305	7.370	317.0	±<1	
495*	Z1MB-A	Fe-15Cr-45Ni	-	2.111	1.422	62.55	62.6	1.20*
	B			2.223	1.499	62.61	±<0.1	
495	Z2MB-A	Fe-15Cr-25Ni	^{59}Ni	2.695	5.[illegible]80	219.1	220	5.23
	B			2.414	5.120	220.0	±1	
495	Z1ML-A	Fe-15Cr-45Ni	-	2.546	1.709	62.91	63.1	1.21
	B			2.996	2.026	63.38	±0.3	
495	Z5MB-A	Fe-15Ni-45Ni	^{59}Ni	2.550	6.749	248.0	249	4.79
	B			2.675	7.119	249.1	±1	

[illegible] mg [illegible] r of atoms in the specimen.

[illegible]

Table 2
Helium Generation Rates Determined in Fe-15Cr-25Ni
[illegible] Rate [illegible] (dpa)

Temperature (°C)	MOTA 1D		MOTA 1E		MOTA 1F		MOTA 1G	
	Undoped	Doped	Undoped	Doped	Undoped	Doped	Undoped	Doped
365	0.30	13.9	0.59$^{(a)}$ (0.25)$^{(b)}$	16.0$^{(a)}$ ([illegible])	No Discharge		0.27 (0.18)	12.5 ([illegible])
495	0.35	1.69	0.47$^{(a)}$ (0.59)	[illegible] (4.73)	No Discharge		0.67$^{(a)}$ (0.90)	5.23 ([illegible])
495(R)$^{(c)}$			0.44	4.01	0.6[illegible]$^{(a)}$ (0.70)	4.08$^{(a)}$ (3.45)	0.67 (0.96)	4.05 (3.96)
600	0.40	4.4						
490	0.28	19.8						
490(R)$^{(d)}$			0.21	10.1	0.34$^{(a)}$ (0.46)	13.7$^{(a)}$ (17.2)	0.52 (1.24)	15.7 (23.7)
465	0.14	61.3	0.26$^{(a)}$ (0.40)	52.1$^{(a)}$ (73.1)	No Discharge		Not Measured	

(a) He/dpa level given is the average for a two-cycle irradiation sequence.
(b) Helium/dpa levels in parentheses represent average values calculated for the second MOTA cycle only.
(c) R denotes replacement series.
(d) Calculated by dividing the 45Ni result by 1.8.

Fig. 2 shows the average helium generation rates over the entire experiment for both the doped and undoped specimens. Fig. 2a shows that at 600 and 495°C [both the original and repeat isothermal sequences], the helium/dpa ratios are *close to* the original target of 5.0 although the ratio falls slowly as more ^{59}Ni is burnt out than is formed from ^{58}Ni. In the below-core (365°C) and level 6 (490°C) sequences the ^{59}Ni burn-out reaction rate is comparable in magnitude to the rate of formation of ^{4}He from ^{59}Ni. The net generation rates are thus more sensitive to the accumulated exposure and the details of surrounding experiments in this softer spectral environment, producing both increases and decreases in the net generation rate. The helium generation rates are much higher in these two levels, but exceed somewhat the 10 appm/dpa target level throughout the experiment. Not shown in Fig. 2a is the very low fluence experiment in level 8 at 465°C, which reached 54.3 appm/dpa at 0 to 14 dpa and 62.1 appm/dpa at 0.26 dpa. This is close to the target *level* of ~50. As mentioned earlier, measurements were not made at the final 0.42 dpa level of this irradiation sequence.

Fig. 2b demonstrates that in the non-doped alloys, it is the burn-in of ^{59}Ni from ^{58}Ni that dominates the helium generation rate. Thus, the average helium/dpa ratio increases throughout the experiment, with the rate of increase increasing as the neutron spectra become softer, and the dpa rate decreases with increasing distance from the core boundary. The competition between burn-out and burn-in of ^{59}Ni is discussed in more detail elsewhere (3).

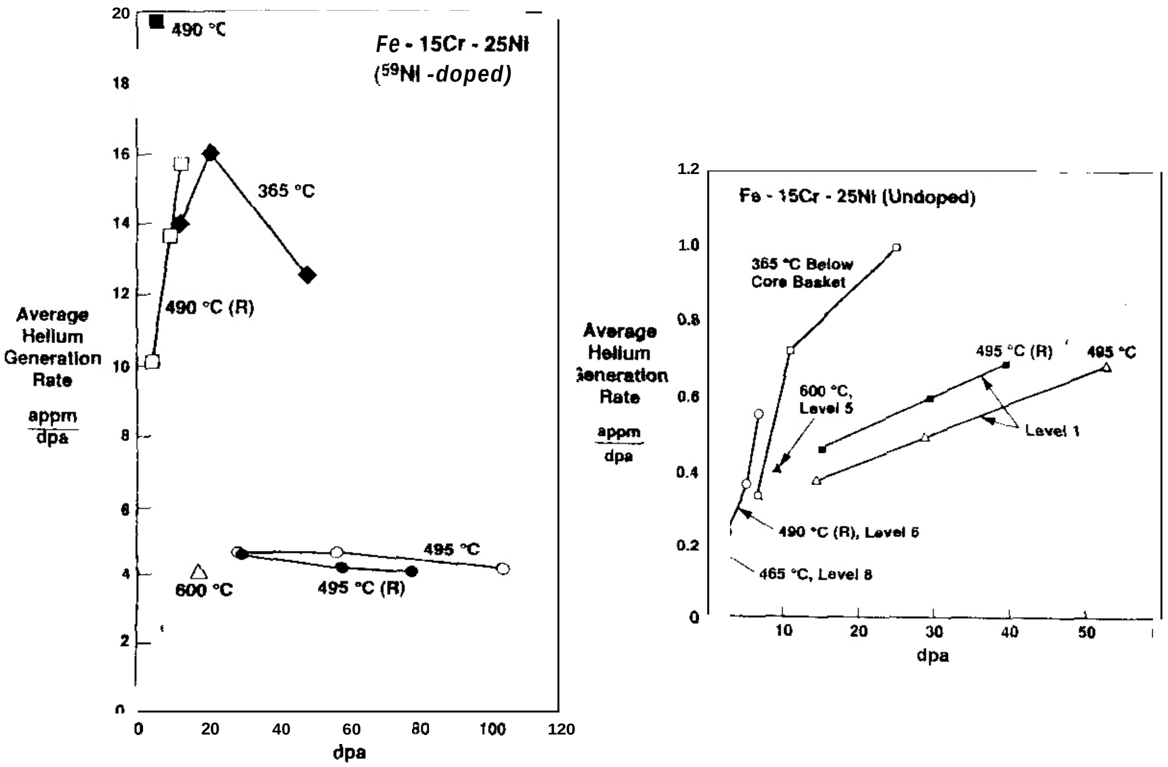

Fig. 2. Helium generation rates measured from the ^{59}Ni Isotopic Tailoring Experiment averaged over the full duration of the various discharges of the experiment, left) doped specimens and right) undoped specimens.

Discussion

It thus appears that the conclusions drawn earlier, concerning the second order role of helium on microstructural evolution, are correct. It is possible at this time, however, to also assess the performance of this experiment with respect to several criteria used to design the experiment. These are listed below:

1) Criterion #1: The helium generation rate should not vary significantly with nickel content in the doped alloys, and thus should allow a clean separation between the effects of helium and

nickel. Nickel is the major source of helium in the undoped alloys. Thus both 25Ni and 45Ni alloys were doped with 0.4% of ^{59}Ni.

The success of this goal can be tested using the MOTA 1G data for the 490, 365 and 495(R) sequences. Calculating the ratio of the helium in the two alloys generated only from ^{59}Ni $[(C_{25Ni,59} - C_{25Ni})/(C_{45Ni,59} - C_{45Ni})]$, we find that the ratios are 0.982, 1.024, and 1.005 for the 490, 495(R) and 365 sequences, respectively. If we assume that we can calculate C_{25N} from 25/45 of C_{45Ni} then the ratio of the doped helium generation rates for the 495°C sequence is 0.995. Thus, for the four irradiation series, the ratio of helium generation rates in the two alloys is 1.00 ±0.02, and the experiment may be judged a success based on this criterion.

2) The undoped specimens should exhibit helium generation rates that depend only on nickel level. Thus the 25Ni and 25Ni+0.04P alloys should exhibit identical generation rates and the 45Ni alloys should have 1.8 times more helium than the 25Ni alloys.

Referring to Table 1, we can calculate C_{45Ni}/C_{25N} ratios of 1.69, 1.71, and 1.79 for the 490, 495 and 365°C sequences, respectively. The small differences from the expected ratio of 1.8 probably reflect the fact that each alloy occupies a separate but nearby packet, and the three packets do not all experience exactly the same neutron environment.

The helium generation rates in the phosphorous-containing alloys were determined only for the 490°C and 365°C. The ratio of generation rates (C_{25Ni+P}/C_{25Ni}) for the undoped alloys were 1.03 and 0.99 respectively. For the doped alloys the ratio was 0.95 at 490°C and 0.93 at 365°C. Thus, the separate effects of helium generation rates and phosphorous could be successfully examined in this experiment.

CONCLUSIONS

It appears that the ^{59}Ni isotopic tailoring concept can be successfully used to study the separate and synergistic effects of helium and other important variables in Fe-Cr-Ni alloys. The helium generation rates in undoped alloys increase continually during irradiation, reaching values consistently larger than normally quoted for fast reactor irradiation.

FUTURE WORK

Only a small amount of microscopy examination is required to complete this experiment

References

1. F. A. Garner, M. L. Hamilton, L. R. Greenwood, J. F. Stubbins, and B. M. Oliver in Effects of Radiation on Materials: 16th International Symposium, ASTM STP 1175, A. S. Kumar, D. S. Gelles, R. K. Nanstad and E. A. Little, Eds., American Society for Testing and Materials, 1993, in press.

2. M. L. Hamilton, F. A. Garner, and B. M. Oliver, in Fusion Reactor Semiannual Progress Report DOE/ER-0313/9 (1991) pp. 61-68.

3. L. R. Greenwood, F. A. Garner, and B. M. Oliver, J. Nucl. Mater. 191-194(1992)1051-1055.

NEUTRON DOSIMETRY FOR THE MOTA-IG EXPERIMENT IN FFTF - L.R. Greenwood' and L.S. Kellogg (Pacific Northwest Laboratory)

OBJECTIVE

To provide dosimetry and damage analysis for fusion materials irradiation experiments

SUMMARY

Neutron fluence and spectral measurements and radiation damage calculations are reported for the MOTA-IG experiment in the fait Flux Test Facility (FFTF). The irradiation was conducted from January 4, 1990, to March 19, 1991, for a total exposure of 299.7 EFPD. The maximum fluence was 15.8 x 10^{22} n/cm^2, 10.0 x 10^{22} above 0.1 MeV producing 43.0 dpa in Iron. Neutron fluence and radiation damage maps are presented for the entire MOTA assembly based on the analysis of ten neutron spectral measurements and seven additional flux gradient measurements.

PROGRESS AND STATUS

Neutron dosimetry far the Materials Open lest Assembly (MOTA)-1G experiment in the Fast Flux lest Facility (FFTF) at Hanford provided comprehensive measurements Over the entire assembly with a total of seventeen capsules positioned at different axial locations in the assembly spanning a distance of -66 to + 122 cm. This irradiation occurred simultaneously with the MOTA-2A experiment reported previously.[1] Each stainless steel capsule measured about 2.1 cm long by 0.48 cm o.d. and contained dosimetry wires for either spectral or gradient measurements. The ten spectral capsules contained small wires of Fe, Ti, Ni, Cu, 0.1% Co-Al alloy, 0.825% ^{235}U in V, 0.936% ^{239}Pu in MgO, and 0.42% ^{237}Np in MgO whereas the twenty gradient capsules contained Fe and 0.1% Co-Al alloy wires. The Co, U, Pu, and Np materials wcre separately encapsulated in vanadium. In addition, small amounts of Be, B, and LiF were included in some of the spectral capsules for helium analyses and three of the spectral sets contained small Nb wires. Altogether, there were a total of 95 radiometric monitor wires and 18 helium monitors.

Following irradiation, each dosimetry capsule was opened in a hot cell and rich individual monitor was identified and mounted for gamma analysis. The measured activities were then converted to saturated activities by correcting for the sample weight, atomic weight, isotopic abundance, gamma absorption, reactor power history, and fission yield, as needed. Neutron self-shielding effects were not significant since the Co, U, and Pu were dilute alloys and the FFTF neutron spectrum has Few neutrons at lower neutron energies. For the U, Pu, and Np fission monitors, the gamma measurements detccted four fission products, namely, ^{95}Zr, ^{103}Ru, ^{137}Cs, and ^{144}Ce. The standard deviation from the mean fission rate was generally less than 56 except for the Np reactions at out-of-core locations, as discussed below.

Neutron burnup effects were found to be quite significant for the fission monitors and a small correction was necessary for the ^{59}Co(n,γ) and fission reactions. In the case of ^{59}Co this correction can be applied using an iterative procedure since the reaction itself is the sole source of the burnup, as described previously. In the case of the ^{59}Co(n,γ) reaction, the burnup effect varied from 0.4% at midplane to 2.6% in the below-core basket. Burnup effects for the fission monitors were very similar to those determined for the MOTA-2A experiment. In most cases, the burnup corrections far the fission monitors were about 20% at midplane and decreased away from core center. For ^{237}Np, there appears to be a significant effect from the lower energy neutrons at the out-of-core positions due to inbreeding of ^{235}U and eventually ^{239}Pu, as evidenced by the large scatter in the four measured fission products. Hence, the Np data was discarded at the out-of-core positions and was not used in the spectral analyses.

The corrected reaction rates are listed in Tables 1-3. All values are normalized to 291 MW operation and the values have an estimated absolute uncertainty of about 5%, although there is an additional uncertainty of about 5% for the fission reactions due to problems in determining the burnup rates. These rates appear to bc in reasonable agreement with previous measurements[1,2,3,4] except for the fission reactions. Neither of the earlier experiments (MOTA-1A/1B and 1E) made any attempt to determine neutron burnup corrections for the fission reactions. Hence, values measured for MOTA-1F, 2A and 1G are about 20-30% higher than the earlier measurements, when allowances are made for differences in reactor power (400 MW rather than 291 MW) and other core changes.

'Pacific Northwest Laboratory is operated for the U.S. Department of Energy by Battelle Memorial Institute under Contract DE-AC06-76RLO 1830.

Table 1 - Activation Measurements in MOTA-1G (atoms/atom-s)

Sample/ Level-Pin	Ht,cm.	$^{54}Fe(n,p)^{54}Mn$ (xE-11)	$^{58}Fe(n,\gamma)^{59}Fe$ (xE-11)	$^{59}Co(n,\gamma)^{60}Co$ (xE-10)
M1 BC-FB	-66.3	0.14	3.65	18.81
M81 BC-FB	-58.4	0.32	4.01	18.52
M3 1-FB	-39.2	1.00	4.05	11.71
M82 1-FT	-35.8	2.29	3.21	3.95
M7 2-FTP	-21.9	3.09	3.46	2.22
M10 3-C	-6.3	3.30	3.99	2.01
X35 3-DMP	-2.1	3.55	3.62	2.56
M4 3-BM	-1.7	3.33	4.15	2.18
X36 3-FMP	-1.1	3.81	3.92	2.32
M11 3-F	2.1	3.17	3.56	1.92
M83 4-FMP	18.9	2.53	3.73	1.97
M80 5-FB	40.5	1.63	2.36	2.63
M5 5-FT	50.7	0.77	2.62	4.46
M6 6-FB	74.3	0.068	1.55	7.05
M79 6-FT	79.3	0.044	1.32	6.68
X37 8-FB	109.4	0.0045	0.53	2.86
M78 8-FT	122.3	0.0019	0.37	2.23

Table 2 - Activation Measurements in MOTA-1G (atoms/atom-s)

Sample/ Level-Pin	Ht,cm.	$^{46}Ti(n,p)^{46}Sc$ (xE-12)	$^{58}Ni(n,p)^{58}Co$ (xE-11)	$^{60}Ni(n,p)^{60}Co$ (xE-13)	$^{58}Ni(n,x)^{57}Co$ (xE-14)	$^{63}Cu(n,\alpha)^{60}Co$ (xE-13)
M1 BC-FB	-66.32	0.154	0.188	0.335	0.401	0.073
M3 1-FB	39.22	1.21	1.33	2.29	2.65	0.54
M10 3-C	6.30	4.00	4.61	7.86	8.94	1.95
X35 3-DM	2.12	3.62	4.58	7.76	8.84	1.91
M4 3-BM	1.66	3.95	4.51	7.50	8.63	1.86
X36 3-FM	1.10	2.90	4.36	7.44	8.62	1.88
M11 3-F	2.13	3.90	4.42	7.32	8.68	1.86
M5 5-FT	50.72	0.98	1.09	1.77	2.08	0.42
M6 6-FB	74.26	0.079	0.104	0.160	0.209	0.035

Table 3 - Fission Reaction Measurements in MOTA-1G (fission/atom-s)

Sample/ Level-Pin	Ht,cm.	$^{237}Np(n,f)$ (xE-9)	$^{238}U(n,f)$ (xE-9)	$^{239}Pu(n,f)$ (xE-9)
M1 BC-FB	66.32	0.89	6.67	7.05
M3 1-FB	39.22	1.86	7.12	6.67
M10 3-C	6.30	2.04	9.42	
X35 3-DM	2.12	2.15	7.97	7.64
M4 3-BM	1.65	2.21	8.44	8.65
X36 3-FM	1.10	1.95	8.12	7.92
M11 3-F	2.13	1.83	7.85	
M5 5-FT	50.72	0.64	4.47	4.28
M6 6-FB	74.26	0.129	2.76	2.65
X37 8-FB	109.37	0.015	0.397	0.973

Table 4 - Neutron Fluence and Displacement Damage for MOTA-2A

Capsule-Position	Ht,cm	Total Fluence xE+22 n/cm^2	Fast Fluence (>0.1 MeV) xE+22 n/cm^2	Iron dpa	Ratio dpa/Fluence [illegible]
M1 BC-FB	66.32	3.74	1.37	5.35	3.9
M3 1-FB	39.22	7.48	4.10	16.8	4.1
M10 3-C	6.30	12.42	8.03	35.8	4.5
X35 3-DM	2.12	11.39	7.58	35.3	4.7
M4 3-BM	1.66	12.51	8.25	37.0	4.5
X36 3-FM	1.10	11.52	7.33	34.1	4.7
M11 3-F	2.13	11.61	7.49	33.1	4.4
M5 5-FT	50.72	4.87	2.73	11.5	4.2
M6 6-FB	74.26	1.63	0.700	2.68	3.8
X37 8-FB	109.37	0.43	0.123	0.48	3.9

The measured activities were used as input to the STAY'SL computer code^{5} to adjust the calculated neutron spectra determined for cycle 9A^{4}. STAY'SL performs a generalized least-squares adjustment of all measured and calculated values including the measured activities, calculated spectra, and neutron cross sections. Neutron cross sections and their uncertainties were generally taken from ENDF/B-V, although new data were available from ENDF/B-VI for the ^{46}Ti(n,p) and ^{53}Cu(n,α) reactions. The adjusted neutron fluence values are listed in Table 4. The neutron spectral adjustments for the ten spectral positions are illustrated in Figure 1 which shows neutron spectra results at midplane, the edge of the core, and for the below-core basket. In comparisons with the calculated spectra, the agreement is reasonable (20-30%) for in-core positions. However, at out-of-core positions, the disagreement becomes progressively worse, as seen in earlier experiments.^{1} At level 8 (+109 cm), the measured flux is about twice the calculated flux.

Damage calculations were performed at all spectral positions using the SPECTER computer code.^{6} Dpa rates for iron are shown in Table 4 as well as the ratio of dpa per 10^{22} n/cm^{2} fast flux above 0.1 MeV. Damage parameters for 40 other elements and several compounds have been calculated and will be made available on request.

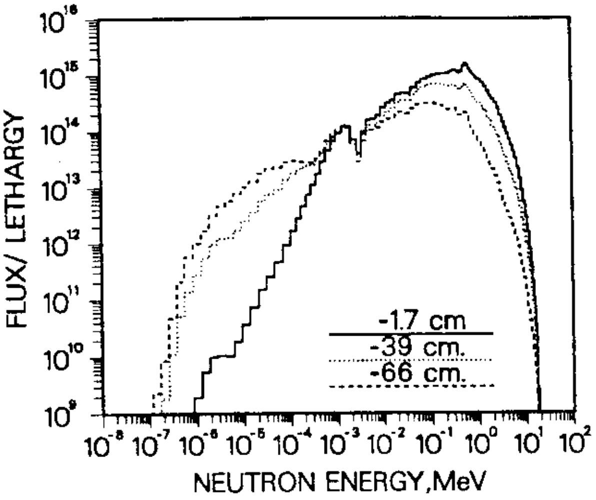

Fig. 1. Adjusted neutron flux spectra are shown at three axial locations in the MOTA-1G assembly. The solid line is at -1 cm, the dotted line is at -39 cm, and the dashed line is at -66 cm. Note the drop in fast flux and increase in low-energy flux at out-of-core locations.

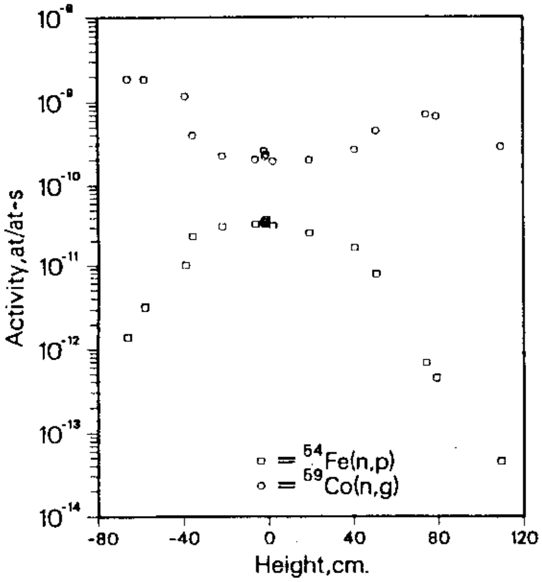

Fig. 2. Activity values are shown for the ^{54}Fe(n,p) ^{54}Mn and ^{58}Co(n,γ)^{60}Co reactions as a function of axial location in the MOTA-1G assembly. Some of the scatter is due to radial flux gradients.

The flux and damage values at gradient positions were calculated from the activity gradient data in Table 1, which are shown in Figure 2. Note that the ^{58}Fe and ^{59}Co(n,γ) reactions peak outside the core since they are sensitive to the lower-energy neutrons. The unusual behavior of the Co reaction is due to resonance effects. Fast fluence and dpa gradients from Table 4 are plotted in Figure 3. The apparent scatter in the data is caused by the radial flux gradients, as discussed below.

Close examination of the activity data indicates the presence of radial flux and spectral gradients. The letters A to F under the position column in Table 4 indicates the radial position at the height indicated. The MOTA basket has six radial positions (A to F); hence, for example, A and D are the furthest apart while A and B or F are adjacent. The maximum radial flux differences are on the order of 10%; however, we also see clear indications of spectral differences in the ratio of the fast flux to the ^{54}Fe(n,p) activity rate. Such differences are complex and we are now studying these effects to construct a more complete flux and damage map of the entire MOTA assembly.

FUTURE WORK

We plan to construct more detailed flux and damage maps for the entire MOTA-1G assembly. Damage parameters will also be provided for a variety of elements and alloys on request. Data from the MOTA-1G and -2A irradiations is being used to help reanalyze previous data from MOTA-1A through 1E, especially to include burnup effects for the fission monitors. We have received the dosimetry capsules from the MOTA-2B irradiation and plans are being made for their analysis. Dosimetry work is in progress for a variety of US/Japanese experiments in the High

Flux Isotopes Reactor at Oak Ridge National Laboratory.

REFERENCES

1. L. R. Greenwood and L. S. Kellogg, Neutron Dosimetry for the MOTA-2A Experiment in FFTF, Fusion Reactor Materials Semiannual Progress Report, DOE/ER-0313/12, pp.49-53, March 1992.

2. L. R. Greenwood and L. S. Kellogg, Neutron Dosimetry for the MOTA-1F Experiment in FFTF, Fusion Reactor Materials Semiannual Progress Report, DOE/ER-0313/9, pp. 31-36, 1990.

3. L. S. Kellogg, W. M. Mc Elroy, and W. Y. Matsumoto, FERRET-SAND II Physics-Dosimetry Analysis for the FTR MOTA-1E Experiments, PNL-NDC Report, December 1989.

4. R. L. Simons, Analysis of Damage Exposure Rates in the MOTA of the FFTF, Damage Analysis and Fundamental Studies Quarterly Progress Report, DOE/ER-0046/21, pp. 10-14, May 1985.

5. F. G. Perey, Least Squares Dosimetry Unfolding: The Program STAY'SL, ORNL/TM-6062, 1977.

6. L. R. Greenwood and R. K. Smither, SPECTER: Neutron Damage Calculations for Materials Irradiations, ANL/FPP-TM-197, January 1985.

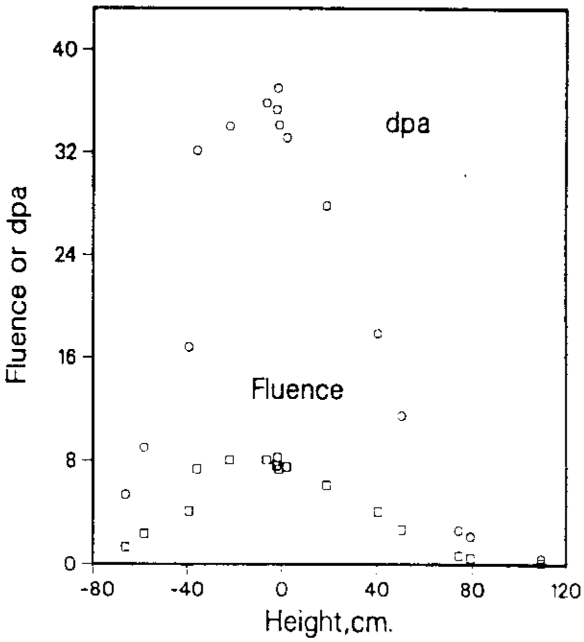

Fig. 3. Fast fluence (x10^{22} n/cm^2, >0.1 MeV) and dpa in iron are shown as a function of axial location in the MOTA-1G assembly. The apparent scatter is indicative of the radial gradients.

PUBLICATIONS

1. L. R. Greenwood, F. A. Garner, and H. L. Heinisch, The Impact of Spectral Effects in Fast Reactors on Data Analysis and Development of Fission-Fusion Correlations, Jou. Nucl. Mater. 191-194, pp. 1096-1100 (1992).

2. L. R. Greenwood, F. A. Garner, and B. M. Oliver, Helium Generation Rates in Isotopically Tailored Fe-Cr-Ni Alloys Irradiated in FFTF/MOTA, Jou. Nucl. Mater. 191-194, pp. 1051 1055 (1992).

3. T. B. O'Hearn, A. S. Kumar, and L. R. Greenwood, Comparison of Measured and Calculated Transmutation in Copper at Spallation Neutron Sources, Jou. Nucl. Mater. 191-194, pp. 1383-1386 (1992)

MEASUREMENT OF HELIUM GLNERATLD IN V-B ALLOYS IRRADIATED IN FFTF/MOTA

F. A. Garner (Pacific Northwest Laboratory[a]), E. M. Oliver (Rockwell International Corporation). and N. Sekimura (University of Tokyo)

OBJECTIVE

The objective of this **effort** is tn determine the role **helium** plays in the microstructural evolution **of** vanadium base alloys.

SUMMARY

V-B **and** V-5Cr-B alloys have been irradiated in FFTF to **assess** the impact of helium generation rate on microstructural evolution of vanadium-base alloys. Using this method it is somewhat difficult to separate the various effects of the original boron as **well** as the lithium and helium products of the ^{10}B (n, α) reaction. Past-irradiation measurements of helium concentrations have been completed **for** two sets of V-B alloys. one irradiated in-core **and** one below core. **It** appears that the boron doping technique **used** to produce the various alloys was reasonably successful in reaching the desired helium/dpa variations.

PROGRESS AND STATUS

Introduction

Swelling in FFTF-MOTA of V-B and V-5Cr-B alloys. where nominal baron **levels** of 0.100,500,2500 **and** 10000 appm **were used. was** reported previously[1]. Note that the boron Content **increases** a factor of five between each doped alloy. In that report the swelling data **were** plotted against **nominal** boron content, but the boron **levels were** not measured directly after the production of the alloys. The actual helium generation rates in these alloys will **be** a function not only of the local neutron spectra but also the actual **level** of boron dopant in each alloy. At low dopant levels there is some uncertainty of the actual concentrations attained. **Therefore** it was decided to measure the helium **concentrations** at Rockwell International Corporation using **well**-defined procedures[2,3]

Note in Table 1 that **four** irradiation Conditions **were** employed for **each** of the V-B **and** V-5Cr-B alloy **series.** Three of the four conditions **were** nominally similar in-core positions **with** no **large** variations neutron **spectra** expected. Therefore. it **was** decided that measurements **would be** performed **for one** representative in-core condition (600°C. 7.8X10^{22} n/cm^{2} E>0.1 **MeV)** and the below-core position. The latter was expected to have **a** much higher helium/dpa ratio than the in-core condition **since** the ^{10}B (n, α) **cross** section **increases at lower** neutron energies. Only the V-B alloys **were** measured for economy. **it was assumed** that their response would be typical of the V-5Cr-B alloys.

Table 1. Irradiation Conditions

Temperature °C	Neutron Fluence n cm^{-2} (E>0.1 MeV)	Displacement level. dpa*
600**	7.8 x 10^{22}	42.1
520	7.7 x 10^{22}	41.6
427	8.6 x 10^{22}	**46.4**
411**	2.9 x 10^{22}	15.1

*dpa defined far pure **vanadium**[illegible]
Helium **concentrations measured for V-B **alloys** only.

Results and Discussion

Table 2 presents the **results** of helium measurements **for** V-B **alloys** at 600°C **and** 411°C. **As** anticipated, the below-core irradiation at 411°C produced more helium/dpa than the in-core irradiation at 600°C. The "ratio" shown in Table 2 represents the calculated variations in helium production from boron for each factor of five in boron Content. **It appears** that the V-1%B **alloy** may have somewhat less than **a** factor. of 5.0 **increase** in baron compared to the 2.500 appm boron alloy. The larger deviations in this ratio at 600°C are thought to reflect the greater scatter or measurement error at lower **helium** generation rates. Altogether, it **appears** that the boron **doping technique employed** to **produce** there **alloys** was successful

---

[a] Pacific Northwest Laboratory **is** operated **far** the U.S. Department of Energy **by** Battelle **Memorial** Institute **under** Contract De-AC06-76RLO 1830.

Table 2. Helium Measurements on Pure Vanadium - Boron Alloys

600°C, 7.8 × 10[illegible] (in core) Specimen Identity	appm, Boron	appm He	Ratio*
MH25	0	1.21 ± 0.01	--
MHBA	100	5.54 ± 0.32	--
MK22	500	22.7 ± 0.6	4.95
MKBA**	2,500	82.6 ± 4.7	3.79
ML1A	10,000	368 ± [illegible]	4.51
411°C, 2.87 × 10[illegible] (below-core) Specimen Identity	**appm, Boron**	**appm He**	**Ratio***
MH00	0	1.07 ± 0.02	
MHA0	100	7.64 ± 0.03	--
MKC0	500	34.9 ± 1.2	5.145
MKA0	2,500	165 ± 8	4.852
ML01	10,000	754 ± 1	4.598

*Ratio = [illegible], when V_1 is the helium generated by vanadium in the absence of boron.

** Average of four separate and independent determinations to assess variability of boron in any given specimen. All other measurements involved only two separate determinations.

It is important to note that for every atom of helium generated there will be a [illegible] atom of lithium. Lithium is known to affect swelling strongly in stainless steels. [illegible] effect of the boron atoms must also be considered in interpretation of the swelling data.

Future Work

Microscopy examination of the various V-B and V-Ti-B alloys will [illegible]

References

1. [illegible] Sekimura and F. A. Garner, [illegible] Reactor Materials [illegible]
(1983) 225-231.

2. H. Farrar, IV, and B. M. Oliver, Journal of Vacuum Science Technology, A4 [illegible]

3. B. M. Oliver, [illegible] and H. Farrar, IV, [illegible]

4. [illegible]

5. [illegible] J. Nucl. Mater. [illegible]

6. [illegible] A. Garner and [illegible] Materials [illegible]

NEW ACTIVATION CROSS SECTION DATA -- F. M. Mann and O. E. **Lessor, Westinghouse** Hanford Company

OBJECTIVE

The objective of this **work** is to provide nuclear data for the fusion materials community. with an emphasis on the development of low-activation materials.

SUMMARY

New nuclear **cross** section libraries (**known** as USACT92) have been created for activation calculations. A point-wire file **was** created from merging the **previous** version of the activation library. the U.S. Nuclear Data Library (ENDF/B-VI), and the European Activation File (EAF-2). 175 ana 99 multi-group versions **were** also created. All **the** data **are** available **at** the National Energy Research Supercomputer Center.

PROGRESS AND STATUS

Introduction

Nuclear activation cross sections **are** needed to calculate the transmutation of **Isotopes.** The **last** ret of activation **cross** sections for the REAC transmutation code system (ref. 1) was created **in** December. 1990 and was bared mainly **on** ENDF/B-V **(ref.** *2)* and THRESH **(ref.** 3) calculations. The **new** ret covering **about** 625 target isotopes is based **upon** ENDF/B-VI (ref. 4) and European efforts (ref. 5). Point-wise as well as 99 and 175 group **cross** sections **were** created along with libraries suitable for HEAC calculations. The new set of libraries **are** denoted USACT92.

Target isotopes included in this library **are** all stable isotopes and isotopes having half-lives **greater** than ~1 day. The energy range covered is 10^{-5}eV to $40.\mathrm{x}10^{6}$eV, except for the (n,g) reaction where the upper limit is $20.\mathrm{x}10^{6}$eV All energetically allowed reactions below 20 MeV are Included. Cross sections to the production of isomeric. states (that is, states with a half-life greater than ~0.001 s) are also included

Point-wise Cross Sections

The general approach in creating the **new** set of point-wise files was to merge ENDF/B-VI evaluations with European files and the old REAC point-wise **cross** sections. The steps were

1) Correct the old REAC files,
2) Convert the European **files** to the required format.
3) Convert the resonance parameters of ENDF/B-VI into point-wise values, and
4) Merge the files.

The mort **recent** REAC point-wise **cross** Section files **were** retrieved from the Common File System (CFS) at the National Energy Research Supercomputer Center (NERSC). The reaction number (mt) was corrected on the (n,n*) reactions (mt = 4 -> 304) as needed. There reactions **were** then manually moved to the proper **location** so that the **mt numbers were in** numerical **order.** The FORTRAN program **CONVH** had previously been used to put the headings of these files into **a** new format.

The Energie Centrum Nederland (ECN) has the responsibility for creating activation **filer** for the European effort. The ECN files were converted from upper case to lower **care** to make them consistent with the old REAC **cross** section files before the two sets were merged. The order of the sections also needed to **be** changed in some of the ECN files far consistency. The reactions producing isomeric states (Ex. n,g*) **were** moved from immediately following the corresponding ground-state reactions to the position in which the mt **numbers were** in numerical order. A FORTRAN program ORDRMT was written tc do this re-"roering of ECN files.

4 FORTRAN program CHGCRS was written to merge the two sets of filer. This program read one mt **section** at **a** time from each of two **files.** If an mt section was missing from one file. the mt section from the other file was used without change. **if** the section was present in each file. the data from the primary file was **kept in** the common energy range **and** the Other data was normalized to the primary file data. Each time one mt section was **written** to the newly created file **a** new **one would he read** in far **processing** until **all** sections had been merged and Written to the new file.

In **general** the ECN files **were** treated as the primary and the old REAC files as the secondary filer for the merging; however the source for **each** isotope was checked individually before **merging.** For each isotope, **if** the old REAC **source** far a **given** mt section was known to be more correct or up to date, the corresponding mt section in ECN was deleted before merging.

There **were some** ECN filer for which no USA file existed. There filer were **run** through the FORTRAN program ADDSEQ2 to add a sequence number to each line. The **filer were** then processed with CONVH which read each of the section headings and rewrote them in the same format used in the USA files. The merged files **were** also processed with CONVH to correct the section headings from ECN files and make all section headings consistent.

The NJOY nuclear data processing code system (ref. 6) was used to convert those ENDF/B-VI evaluations having resolved or unresolved parameter descriptions into an evaluation having only a smooth description. Only the (n,gamma) reaction is affected.

The merging of ENDF/B-VI files and ECN files was done as explained above except that the ENDF/B-VI files were used as the primary files.

Appendix C contains a list of all the isotopes in the new Activation Cross Section Library and the number of reactions for each isotope.

The format for the point-wise cross sections is that of ENDF/B-VI file 3 (ref. 7) with the exception of two (2) added header cards at the beginning of each reaction and a modification of the mt numbers for reactions leading to isomeric products. The format of the two header cards is:

```
  Card 1:    columns  1-20: Reaction
        :    columns 27-34: Date
        :    columns 38-40: Version Number
        :    columns 47-66: Person Updating File
        :    columns 67-70: Mat Number
        :    columns 71-72: Mf Number
        :    columns 73-75: Mt Number
        :    columns 76-80: Sequence Number
  Card 2:    columns  1-40: Source of Data below 20 Mev
        :    columns 41-66: Source of Data above 20 Mev (if different from below 20 Mev)
        :    columns 67-70:  Mat Number
        :    columns 71-72:  Mf Number
        :    columns 73-75:  Mt Number
        :    columns 76-80:  Sequence Number
```

The reaction number mt is modified for reactions leading to an isomeric state to

mt (isomeric) = mt (ground state) + (n * 300),

where n denotes the nth isomeric state. Thus the mt number for the (n,np) reaction leading to the first isomeric state is 328 (=28+(1*300)). Note that n must be 1 or 2.

Group-wise Cross Sections

The multigroup cross sections were calculated by the MULTAV code from point-wise cross sections described above. MULTAV is a FORTRAN code which reads ENDF/B file 3 formatted cross sections and a user-supplied weighing function. MULTAV then calculates the group-averaged value either analytically or using adaptive Romberg integration. Calculations were made for 99 group and 175 group structures. The energy structure is displayed in Appendix A for the 99 group structure and in Appendix B for the 175 group structure. The flux used for group weighting is that used in the vitamin-E group constant set (ref. 8) as implemented in the NJOY processing code.

The 99 group structure is a group structure now in use [illegible] analyses with the thermal structure used [illegible] informally adopted as a standard for fusion [illegible]. Similarly, the choice of the vitamin-E weighting flux [illegible] a natural one given the fusion experience.

The format for group-wise cross sections is the same as the format for point-wise [illegible] interpolation law 2 (linear-linear interpolation) [illegible] for each group, [illegible] bound is used with the value for that group [illegible] repeated for each energy [illegible].

REAC Cross Sections

The FORTRAN code MULREAC was used to convert the above multigroup format into the [illegible] version of the REAC cross sections. The FORTRAN code BINLIB (ref. 9) then was used to create the binary version of the REAC cross section library.

Location of Files

All of the files are located on CFS at NERSC. Table 1 shows the location of the files used and those generated.

Table I
Location of Files

FILE NAME	PURPOSE	CFS LOCATION
addseq2.x	code to add sequence numbers	/001635/usact90/prog
binlib3.x	code to convert into binary REAC format	/001635/reac3.93
chgcrs.x	code to merge files	/001635/usact90/prog
convh.x	code to correct headings	/001635/usact90/prog
cross.99	99 group cross sections	/001635/reac3.93
cross.175	175 group cross sections	/001635/reac3.93
fluxwgt.vitaj	flux weighing file	/001665/multav/9-91
inpmer	input data for chgcrs	/001635/usact90/prog
inpseq	input data for addseq2	/001635/usact90/prog
'Isotope'	old REAC cross section files	/001665/usact6.0/'element'
'ISOTOPE'	ECN cross section files	/001665/ecn/ecnact
mudata	99 group structure	/001665/multav/9-91
mudatao	175 group structure	/001665/multav/9-91
mulact2.x	code to convert from multigroup to REAC format	/001665/mulact2
multav.x	code to convert from point-wise to multigroup format	/001665/multav
ordrmt.x	code to order mt numbers	/001665/ecn
'isotope'	point-wise cross sections	/001665/usaecn/'element'

Notes:
1) 'element' refers to the 2 letter chemical symbol for the element
2) 'isotope' or 'ISOTOPE' refer to 6 character string containing the 2 letter chemical symbol plus the (up to 3 digit) mass number plus the iosomeric flag (blank, m, or n)

Summary

A new point-wise activation cross Section set has been created from ENDF/B-VI and ECN activation files. Furthermore, new group-wise cross Sections using bath the Hanford 99 group structure and the International 175 group Vitamin-J structure has been created.

References

1. F. M. Mann, REAC*2: Users Manual and Code Description, WHC-EP-0282. Westinghouse Hanford Company. Richland. Wa, December. 1989.

2 R. Kinsey (compiler), ENDF/B Summary Documentation. BNL-NCS 17541 (ENDF-201). 3 d Edition (ENDF/B-V), Brookhaven National Laboratory, Upton, NY. July, 1979.

3. S. Pearlstein, Journal of Nuclear Energy, 27 (1973) ai.

4. P. F. Rose (compiler). ENDF/B-VI Summary Documentation. BNL-NCS-17541 (ENDF-201 , 4th Edition (ENDF/B-VI), Brookhaven National Laboratory, Upton, NY. October. 1991.

5. J. Kopecky, H. A. J. van der Kamp, H. Gruppelaar. and Nierop, The European Activation File EAF-2 with Neutron Activation and Transmutation Cross Sections, ECN-C-91-073. Netherlands Energy Research Foundation ECN, Petten, the Netherlands, July, 1991.

6. R. E. MacFarlane, D. W. Muir, and R. M. Boicourt, The NJOY Nuclear Data Processing System. Volume I: User's Manual, LA-9303-M, Los Alamos National Laboratory. Los Alamos. NM. May. 1982.

7. P. F. Rose and C. L. Dunford (editors), Data Formats and Procedures for the Evaluated Nuclear Data File ENDF-6. BNL-NCS 44945, Brookhaven National Laboratory. Upton. NY. October. 1991

8. C. R. Weisbin, R. W. Roussin, J. J. Wagschal. J.E. White, and R.Q. Wright. vitamin-E: An ENDF/B-V Multigroup Cross Section Library for LMFBR Care and Shield, Dosimetry. and Fusion Blanket Technology, ORNL-5505. Oak Ridge National Laboratory. Oak Ridge, TN, February. 1979.

FUTURE WORK

future work includes finishing documentation on this cross section Set. and an the decay set produced last year. Documentation will also be produced far the latest version (REAC3.93) of the REAC activation and transmutation code system.

Appendix A
99 Group Energy Structure

```
1.0000e-5 5.0000e-3 1.0000e-2 1.5000e-2 2.0000e-2 2.5000e-2
3.0000e-2 3.5000e-2 4.2000e-2 5.0000e-2 5.8000e-2 6.7000e-2
8.0000e-2 1.0000e-1 1.4000e-1 1.8000e-1 2.2000e-1 2.5000e-1
2.8000e-1 3.0000e-1 3.2000e-1 3.5000e-1 4.0000e-1 5.0000e-1
6.2500e-1 7.8000e-1 8.5000e-1 9.1000e-1 9.5000e-1 9.7200e-1
9.9600e-1 1.02000e0 1.04500e0 1.07100e0 1.09700e0 1.12300e0
1.15000e0 1.30000e0 1.50000e0 2.20000e0 2.60000e0 3.30000e0
4.00000e0 5.04348e0 8.31529e0 1.37096e1 2.26033e1 3.72665e1
6.14421e1 1.01301e2 1.67017e2 2.75365e2 4.53999e2 7.48518e2
1.23410e3 2.03468e3 2.40378e3 2.83954e3 3.35463e3 5.53084e3
9.11882e3 1.50344e4 1.98925e4 2.55424e4 4.08677e4 6.73795e4
1.11090e5 1.83156e5 3.01974e5 3.87742e5 4.97871e5 6.39279e5
8.20850e5 1.10803e6 1.35335e6 1.73774e6 2.23130e6 2.86505e6
3.67879e6 4.96585e6 6.06531e6 7.40818e6 8.60708e6 1.00000e7
1.16183e7 1.34986e7 1.49182e7 1.64872e7 1.82211e7 2.00000e7
2.25000e7 2.50000e7 2.75000e7 3.00000e7 3.25000e7 3.50000e7
3.75000e7 4.00000e7 4.50000e7 5.00000e7
```

Appendix B
175 Group Energy Structure

```
1.000e-5   1.000e-1   4.140e-1   5.316e-1   6.826e-1   8.764e-1
1.1254e0   1.4450e0   1.8554e0   2.3824e0   3.0590e0   3.9279e0
5.0435e0   6.4760e0   8.3153e0   1.0677e1   1.3710e1   1.7603e1
2.2603e1   2.9023e1   3.7267e1   4.7851e1   6.1442e1   7.8893e1
1.0130e2   1.3007e2   1.6702e2   2.1445e2   2.7536e2   3.5358e2
4.5400e2   5.8295e2   7.4852e2   9.6112e2   1.2341e3   1.5846e3
2.0347e3   2.2487e3   2.4852e3   2.6126e3   2.7465e3   3.0354e3
3.3546e3   3.7074e3   4.3074e3   5.5308e3   7.1017e3   9.1188e3
1.0595e4   1.1709e4   1.5034e4   1.9305e4   2.1875e4   2.3579e4
2.4176e4   2.4788e4   2.6058e4   2.7000e4   2.8500e4   3.1828e4
3.4307e4   4.0868e4   4.6309e4   5.2475e4   5.6562e4   6.7379e4
7.2000e4   7.9500e4   8.2500e4   8.6517e4   9.8037e4   1.1109e5
1.1679e5   1.2277e5   1.2907e5   1.3569e5   1.4264e5   1.4996e5
1.5764e5   1.6573e5   1.7422e5   1.8316e5   1.9255e5   2.0242e5
2.1280e5   2.2371e5   2.3518e5   2.4724e5   2.7324e5   2.8725e5
2.9452e5   2.9720e5   2.9850e5   3.0197e5   3.3373e5   3.6883e5
3.8774e5   4.0762e5   4.5049e5   4.9787e5   5.2340e5   5.5023e5
5.7844e5   6.0810e5   6.3928e5   6.7206e5   7.0651e5   7.4274e5
7.8082e5   8.2085e5   8.6294e5   9.0718e5   9.6164e5   1.0026e6
1.1080e6   1.1648e6   1.2246e6   1.2873e6   1.3534e6   1.4227e6
1.4957e6   1.5724e6   1.6530e6   1.7377e6   1.8268e6   1.9205e6
2.0190e6   2.1225e6   2.2313e6   2.3069e6   2.3457e6   2.3653e6
2.3852e6   2.4660e6   2.5924e6   2.7253e6   2.8650e6   3.0119e6
3.1664e6   3.3287e6   3.6788e6   4.0657e6   4.4933e6   4.7237e6
4.9659e6   5.2205e6   5.4881e6   5.7695e6   6.0653e6   6.3763e6
6.5924e6   6.7032e6   7.0469e6   7.4082e6   7.7880e6   8.1873e6
8.6071e6   9.0484e6   9.5123e6   1.0000e7   1.0513e7   1.1052e7
1.1618e7   1.2214e7   1.2480e7   1.2523e7   1.3499e7   1.3840e7
1.4191e7   1.4550e7   1.4918e7   1.5683e7   1.6487e7   1.6905e7
1.7333e7   1.9640e7
```

List of Isotopes in Activation Cross Section Library

Number	Isotope	Initial Record	Number of Reaction,
1	h 1	1	2
2	h 2	3	3
	h 3	6	2
4	he 3	8	6
5	li 6	14	9
6	li 7	23	8
7	be 9	31	19
8	be I0	50	15
9	b 10	65	22
10	h 11	87	19
11	c 12	106	17
12	c 13	123	19
13	c 14	142	18
14	n 14	!60	13
15	n 15	179	19
16	o 16	!?5	20
17	o I?	218	20
18	o 18	238	19
19	f 19	257	20
20	ne 20	277	20
21	ne 21	297	20
22	ne 22	317	19
23	na 22	336	20
24	na 23	356	20
25	mg 24	376	21
26	mg 25	397	22
27	mg 26	419	21
28	al 26	440	23
29	al 27	463	22
30	si 28	405	22
31	si 29	507	21
32	si 30	528	20
33	si 31	548	17
34	si 32	555	20
35	p 31	585	20
36	p 32	605	16
37	p 33	621	16
3	s 32	637	20
39	, 33	657	io
40	s 34	677	20
41	s 35	697	15
42	s 36	712	20
43	cl 35	73?	21
44	cl 36	753	21
45	cl 37	774	2:
46	ar 36	795	22
47	ar 37	817	15
48	ar 38	832	21
49	ar 39	853	22
50	ar 40	875	22
51	ar 41	897	20
12	ar 42	917	20
53	k 39	937	22
54	k 40	919	22
55	k 41	981	22
16	k 42	1003	20
17	ca 40	1023	22
58	ca 41	1045	21
59	ca 42	1065	20
60	ca 43	1086	20
61	ca 44	1106	20
62	ca 45	1126	20
63	ca 46	1146	20
64	ca 47	1166	15
65	ca 48	1181	19
66	sc 44	1200	18
67	sc 45	1218	22

List of Isotopes in Activation Cross Section Library

Number	Isotope	nitial Record	Number of Reactions
68	sc 46	1240	18
69	sc 47	1258	19
70	sc 48	1277	18
71	ti 44	1295	23
72	ti 45	1318	24
73	ti 46	1342	25
74	ti 47	1367	24
75	ti 48	1391	21
76	ti 49	1412	20
77	ti 50	1432	21
78	v 48	1453	19
79	v 49	1472	23
80	v 50	1495	16
81	v 51	1511	16
82	cr 50	1527	20
83	cr 51	1547	15
84	cr 52	1562	20
85	cr 53	1582	20
86	cr 54	1602	20
87	mn 52	1622	16
88	mn 53	1638	21
89	mn 54	1659	21
90	mn 55	1680	20
91	fe 54	1703	25
92	fe 55	1728	21
93	fe 56	1749	24
94	fe 57	1773	20
95	fe 58	1793	21
96	fe 59	1814	22
97	fe 60	1836	21
98	co 56	1857	16
99	co 57	1873	21
100	co 58	1894	20
101	co 59	1914	23
102	co 60	1937	23
103	ni 56	1960	20
104	ni 57	1980	16
105	ni 58	1996	21
106	ni 59	2017	22
107	ni 60	2039	23
108	ni 61	2062	23
109	ni 62	2085	23
110	ni 63	2108	23
111	ni 64	2131	22
112	ni 65	2153	[illegible]
113	cu 63	2170	23
114	cu 64	2193	20
115	cu 65	2213	22
116	cu 67	2235	[illegible]
117	zn 64	2252	20
118	zn 65	2272	20
119	zn 66	2292	20
120	zn 67	2312	20
121	zn 68	2332	22
122	zn 70	2354	24
123	zn 72	2378	20
124	ga 67	2398	17
125	ga 69	2415	22
126	ga 71	2437	26
127	ge 68	2463	20
128	ge 69	2483	17
129	ge 70	2500	21
130	ge 71	2521	19
131	ge 72	2540	23
132	ge 73	2563	22
133	ge 74	2585	25
134	ge 76	2610	24
135	as 71	2634	17

List of Isotopes in Activation Cross Section Library

Number	Isotope	Initial Record	Number of Reactions
136	as 72	2651	17
137	as 73	2668	19
138	as 74	2687	20
139	as 75	2707	24
140	as 76	2731	22
141	as 77	2753	21
142	se 72	2774	17
143	se 73	2791	18
144	se 74	2809	22
145	se 75	2831	18
146	se 76	2549	24
147	se 77	7873	23
148	se 78	2896	25
149	se 79	2921	24
150	se 80	2945	25
151	se 82	2970	24
152	br 77	2994	20
153	br 79	3014	26
154	br 81	3040	26
155	br 82	3066	23
156	kr 78	3089	26
157	kr 79	3115	73
158	kr 80	3138	29
159	kr 81	3157	28
160	kr 82	3195	29
161	kr 83	3224	27
162	kr 84	3251	28
163	kr 85	3279	27
164	kr 86	3306	25
165	rb 83	3331	27
166	rb 84	3358	23
167	rb 85	3381	29
168	rb 86	3410	27
169	rb 87	3437	25
170	sr 82	3462	21
171	sr 83	3483	24
172	sr 84	3507	29
173	sr 85	3536	20
174	sr 86	3555	28
175	sr 87	3584	27
176	sr 88	3611	25
177	sr 89	3636	23
178	sr 90	3659	21
179	y 87	3680	25
180	y 88	3705	28
181	y 89	3733	27
182	y 90	3760	25
183	y 91	3785	23
184	zr 88	3808	23
185	zr 89	3831	21
186	zr 90	3852	27
187	zr 91	3879	28
188	zr 92	3307	26
189	zr 93	3933	24
190	zr 94	3357	23
191	zr 95	3980	21
192	zr 96	4001	23
193	nb 91	4024	31
194	nb 91m	4055	31
195	nb 92	4086	31
196	nb 92m	4117	31
197	nb 93	4148	31
198	nb 93m	4179	31
199	nb 94	4210	28
200	nb 95	4238	25
201	nb 95m	4263	25
202	mo 92	4288	31
203	mo 93	4319	32

List of Isotopes in Activation Cross Section Library

Number	Isotope	Initial Record	Number of Reactions
204	mo 94	4351	28
205	mo 95	4379	27
206	mo 96	4406	25
207	mo 97	4431	24
208	mo 98	4455	24
209	mo 99	4479	25
210	mo100	4504	26
211	tc 95	4530	28
212	tc 95m	4558	28
213	tc 96	4586	27
214	tc 97	4613	27
215	tc 97m	4640	27
216	tc 98	4667	27
217	tc 99	4694	25
218	ru 96	4719	28
219	ru 97	4747	25
220	ru 98	4772	25
221	ru 99	4797	24
222	ru100	4821	23
223	ru101	4844	22
224	ru102	4866	22
225	ru103	4888	21
226	ru104	4909	22
227	ru105	4931	20
228	ru106	4951	19
229	rh 99	4970	25
230	rh101	4995	22
231	rh101m	5017	22
232	rh102	5039	23
233	rh102m	5062	23
234	rh103	5085	26
235	rh105	5111	24
236	pd100	5135	23
237	pd101	5158	24
238	pd102	5182	26
239	pd103	5208	24
240	pd104	5232	27
	pd105	5259	26
	pd106	5285	27
	pd107	5312	26
	pd108	5338	26
	pd109	5364	22
	pd110	5386	26
	ag105	5412	26
	ag106	5438	26
	ag107	5464	30
	ag108	5494	30
251	ag109	5524	31
252	ag110	5555	25
253	ag111	5580	27
254	cd106	5607	26
255	cd108	5633	27
256	cd109	5660	25
257	cd110	5685	30
258	cd111	5715	29
259	cd112	5744	30
260	cd113	5774	28
261	cd113m	5802	28
262	cd114	5830	28
263	cd115	5858	26
264	cd115m	5884	26
265	cd116	5910	28
266	in111	5938	26
267	in113	5964	31
268	in114	5995	26
269	in115	6021	29
270	in112	6050	29

List of **Isotopes** in Activation Cross Section Library

Number	Isotope	Initial Record	Number of Reactions
271	sn113	6079	26
272	sn114	6105	30
273	sn115	6135	23
274	sn116	6164	31
275	in117	6195	31
276	sn117m	5226	31
277	sn118	6257	33
278	sn119	6230	33
279	sn119m	6323	33
280	sn120	6356	33
281	sn121	6383	31
282	sn121m	6420	31
283	sn122	6451	32
284	sn123	6483	31
285	sn124	6514	30
286	sn125	6544	29
287	sn126	6573	27
288	sb119	6600	27
289	sb120	6527	28
290	sb121	6655	31
291	sb122	6686	27
232	sb123	6713	31
233	sb124	6744	29
294	sb125	6773	30
295	sb126	6803	30
296	sb127	6833	26
237	te118	6859	23
298	te119	6882	24
299	te119m	6906	24
300	te120	6930	26
301	te121	6956	25
302	te121m	6981	25
303	te122	7006	28
304	te123	7034	27
305	te123m	7061	2'
306	te124	7088	29
307	te125	7117	29
308	te125m	7146	30
309	te126	7176	30
310	te127	7206	23
311	te127m	7235	29
312	te128	7264	29
313	te129	7293	29
314	te129m	7322	23
315	te130	7351	30
316	te131	7381	28
317	te132	7409	28
318	i 124	7437	25
319	i 125	7462	23
320	i 126	7485	23
321	i 127	7508	28
322	i 128	7536	24
323	i 129	7560	28
324	i 130	7588	27
325	i 131	7615	27
326	re124	7642	23
327	xe125	7665	21
328	xe126	7686	24
329	xe127	7710	22
330	xe128	7732	24
331	xe129	7756	24
332	xe129m	7780	24
333	re130	7804	26
334	xe131	7830	26
335	xe131m	7856	26
336	xe132	7882	28
337	re133	7910	28

List of Isotopes in Activation Cross Section Library

Number	Isotope	Initial Record	Number of Reactions
338	xe133m		
339	xe134		
340	xe136	7995	26
341	cs129	8021	20
342	cs131	8041	21
343	cs132	8062	21
344	cs133	8083	29
345	cs134	8112	29
346	cs135	8141	32
347	cs136	8173	30
348	cs137	8203	30
349	ba128	8233	19
350	ba129	8252	21
351	ba130	8273	25
352	ba131	8298	22
353	ba132	8320	25
354	ba133	8345	24
355	ba133m	8369	24
356	ba134	8393	26
357	ba135	8419	29
358	ba135m	8448	29
359	ba136	8477	31
360	ba137	8508	31
361	ba138	8539	29
362	ba139	8568	22
363	ba140	8590	21
364	la137	8611	30
365	la138	8641	30
366	la139	8671	27
367	la140	8698	23
368	la141	8721	18
369	ce136	8739	26
370	ce137	8765	24
371	ce138	8789	28
372	ce139	8817	23
373	ce140	8840	24
374	ce141	8864	21
375	ce142	8885	20
376	ce143	8905	19
377	pr141	8924	23
378	pr142	8947	22
379	pr143	8969	21
380	nd140	8990	22
381	nd141	9012	22
382	nd142	9034	25
383	nd143	9059	23
384	nd144	9082	23
385	nd145	9105	24
386	nd146	9129	21
387	nd147	9150	20
388	nd148	9170	23
389	nd149	9193	19
390	nd150	9212	22
391	pm143	9234	20
392	pm144	9254	22
393	pm145	9276	23
394	pm146	9299	22
395	pm147	9321	23
396	pm148	9344	19
397	pm148m	9363	22
398	pm149	9385	21
399	pm150	9406	19
400	pm151	9425	21
401	sm144	9446	24
402	sm145	9470	22
403	sm146	9492	20
404	sm147	9512	20

List of Isotopes in Activation Cross Section Library

Number	Isotope	Initial Record	Number of Reactions
405	sm148	9532	21
406	sm149	9553	22
407	sa150	9575	22
'08	sm151	9597	21
409	sm152	9618	22
410	sm153	9640	23
411	sm154	9653	24
412	eu145	9687	19
413	eu146	9706	19
414	eu147	9725	17
415	eu148	9742	18
416	eu149	9760	22
417	eu150	9782	22
418	eu150m	9804	22
419	eu151	9826	27
420	eu152	9853	23
421	eu152m	9876	23
322	eu153	9899	27
423	eu154	9926	25
424	eu155	9951	24
425	eu156	9975	23
426	eu157	9998	2
427	gd146	10000	18
428	gd147	10018	20
429	gd148	10038	20
330	gd149	10058	18
431	gd150	10076	21
432	gd151	10097	22
433	gd152	10119	24
434	gd153	10143	22
435	gd154	10165	25
436	gd155	10190	24
437	gd156	10214	22
438	gd157	10236	21
439	gd158	10257	20
440	gd159	10277	17
441	gd160	10294	20
442	tb153	10314	22
443	tb154	10336	22
344	tb155	10358	22
445	tb156	10380	23
446	tb156m	10403	23
447	tb157	10426	25
448	tb158	10451	24
449	tb159	10475	21
450	tb160	10496	20
451	tb161	10515	17
452	dy154	10533	25
453	dy155	13558	23
354	dy156	10581	23
455	dy157	10604	23
456	dy158	10627	25
457	dy159	10652	21
458	dy160	10673	22
459	dy161	10695	21
460	dy162	30736	20
451	dy163	10736	20
462	dy164	10756	21
463	dy165	10777	18
464	dy166	10795	18
455	ho163	10813	24
466	ho165	10837	24
467	ho166	10861	24
358	ho166m	10885	24
469	er162	10909	26
470	er164	10935	26
471	er165	10961	22

List of Isotopes in Activation Cross Section Library

	Isotope	Initial Record	Number of Reactions
	er166	10983	26
	er167	11009	25
	er168	11034	24
	er169	11058	20
	er170	11078	21
	er171	11099	19
478	er172	11118	19
479	tm165	11137	22
480	tm166	11159	21
481	tm167	11180	21
482	tm168	11201	21
483	tm169	11222	24
484	tm170	11246	19
485	tm171	11265	18
486	tm172	11283	18
487	yb166	11301	19
488	yb168	11320	18
489	yb169	11338	19
490	yb170	11357	19
491	yb171	11376	19
492	yb172	11395	17
493	yb173	11412	17
494	yb174	11429	17
495	yb175	11446	17
496	yb176	11463	18
497	lu169	11481	20
498	lu170	11501	21
499	lu171	11522	22
500	lu172	11544	21
501	lu173	11565	19
502	lu174	11584	19
503	lu174m	11603	19
504	lu175	11622	23
505	lu176	11645	24
506	lu177	11669	22
507	lu177m	11691	22
508	hf174	11713	24
509	hf175	11737	20
510	hf176	11757	24
511	hf177	11781	28
	hf178	11809	33
	hf178m	11842	31
	hf179	11873	35
	hf179m	11908	34
	hf180	11942	31
	hf180m	11973	30
	hf181	12003	22
	hf182	12025	20
	ta177	12045	21
	ta179	12066	31
	ta180	12097	37
	ta180m	12134	33
	ta181	12167	34
	ta182	12201	28
	ta183	12229	22
	w 178	12251	20
	w 180	12271	31
	w 181	12302	28
	w 182	12330	33
	w 183	12363	33
	w 184	12396	30
	w 185	12426	22
	w 186	12448	24
	w 187	12472	18
	w 188	12490	18
	re181	12508	21
538	re182	12529	21

List of Isotopes in Activation Cross Section Library

Number	Isotope	Initial Record	Number of Reactions
539	re183	12550	22
540	**rei84**	12572	24
541	re184m	12596	24
542	re185	12620	31
543	re186	12651	27
544	re186m	12678	27
545	re187	12705	26
546	re188	12731	20
547	re189	12751	18
548	os184	12763	25
549	os185	12794	22
550	os186	12816	26
551	os187	12842	25
552	os188	12867	26
553	os189	12893	26
554	os190	12919	26
555	os191	12945	23
556	**"Si92**	12968	25
557	os193	12993	20
558	os194	13013	20
559	ir188	13033	20
560	ir189	13053	20
561	ir190	13073	23
562	ir191	13096	32
563	ir192	13128	34
564	ir192m	13162	33
565	ir193	13195	32
566	ir193m	13227	32
567	ir194	13259	25
568	ir194m	13284	25
563	pt190	13309	23
570	pt191	13332	25
571	pt192	13357	33
572	pt193	13390	35
573	pt193m	13425	35
574	pt194	13460	34
575	pt195	13434	31
576	pt195m	13525	31
577	pt196	13556	29
578	pt197	13585	25
579	pt198	13610	27
580	nu194	13637	28
581	au195	13665	29
582	au196	13694	29
583	au197	13723	33
584	au198	13756	28
585	au198m	13784	28
586	au199	13812	25
587	hg194	13837	30
588	hg195	13867	28
589	hg195m	13895	28
590	hg196	13923	34
591	hg197	13957	30
592	hg198	13987	33
593	hg199	14020	30
594	hg200	14050	28
595	hg201	14078	25
596	hg202	14104	24
597	hg203	14123	20
598	hg204	14148	19
599	tl200	14167	25
600	tl201	14192	22
601	tl202	14214	20
502	tl203	14234	22
603	tl204	14256	18
604	tl205	14274	21
605	pb202	14295	24

List of Isotopes in Activation Cross Section Library

Number	Isotope	Initial Record	Number of Reactions
606	pb203	14319	21
607	pb204	14340	24
608	pb205	14364	23
609	pb206	14387	23
610	pb207	14410	24
611	pb208	14434	24
612	pb209	14458	23
613	pb210	14481	21
614	bi205	14502	24
615	bi206	14526	21
616	bi207	14547	23
617	bi208	14570	25
618	bi209	14595	27
619	bi210	14622	25
620	bi210m	14647	25
621	po206	14672	21
622	po207	14693	22
623	po208	14715	22
624	po209	14737	24
625	po210	14761	20

TRANSMUTATION OF TUNGSTEN IN FFTF. HFIR AND STARFIRE - F. A. Garner and L. R. Greenwood (Pacific Northwest Laboratory)

OBJECTIVE

The objective of this effort is to determine the role of transmutation on the interpretation of fission data and its extrapolation toward fusion goals.

SUMMARY

Tungsten has been used in a variety of low activation ferritic alloys and also in copper composite alloys. both currently being irradiated in various furion materials experiments. It has been proposed as an armor material also. Tungsten transmutes strongly to rhenium and then osmium, however. in a manner that is strongly dependent on neutron spectra. Thin adds significant complexity to the interpretation of data developed in one spectral environment but intended for application to another environment.

PROGRESS AND STATUS

Introduction

Tungsten is currently being used in a variety of fusion materials now under irradiation in the U.S. and Japanese materials programs. Examples are:

1) Tungsten-containing low activation ferritic alloys (PNL. ORNL. NRIM, Monbusho. irradiating in HFIR. EBR-II, FFTF. JOYO).
2) Comparative irradiations of alloys such a HT9 in HFIR. EBR-II and FFTF (PNL. ORNL).
3) Tungsten metal as an armor for plasma-facing components (MIT and PNL, irradiating in FFTF).
4) Cu-W composite alloys (ORNL and PNL. irradiating in FFTF. SM-2).

It has been recently recognized, however, that significant amounts of transmutation occur in tungsten. The spectral sensitivity of this transmutation will require that care be taken in the application to fusion environments of data generated in various fission reactor facilities. Differences in transmutation will also complicate the comparison of data from various fission reactors.

Tungsten has three isotopes which produce significant transmutation via (n,γ) reactions. The isotopes 184-W and 186-W have large reactions rates leading to Re. Much of the Re produced will. in tarn. transmute to Os, especially in HFIR. The isotopic 180-W produces 181-W (121 d) which decays to 181-Ta. During a long irradiation. 181-Ta will transmute to 182-Ta (114 d) which decays to 182-W. The isotopic 181-W may also transmute directly to 182-W. The net effect thus depends on the details of the irradiation; however. the abundance of 180-W is only 0.12%. so this reaction is not very Important. Burnup is also severe far 182-W and 183-W. In these cases. 182-W capturer to 183-W which in turn captures to 184-W. thus increasing the fraction of 184-W. which in turn transmutes to 185-Re and so on. It is also necessary ti include the decay of three Isotopes. namely, 181-W (121 d to 181-Ta); 182-Ta (114 d to 182-W); and 185-W (75 d to 185-Re). All of those will continue to decay after the Irradiation. leading to significant changes in composition after reactor shutdown.

A spreadsheet program was developed to include all of the above effects of burnup and decay. The (n,p) reactions on W all lead to products which eventually decay back to W. as do many of the (n,α) reaction channels. Small amounts (<1 appm) of Ta and Hf will he produced; however. these reactions are not well-known and have thus been neglected.

The reaction data were obtained from ENDF/B-V or VI and, in some cases, were estimated from known flux spectra and evaluated neutron cross sections. Calculations were performed for FFTF at the midplane and the middle of the MOTA below-core Canister (-66 cm). The HFIR calculations are for the PTP position at midplane with the reactor operating at 85 MW. The STARFIRE calculations are for the first wall position it a wall loading of 3.8 MW/m^2.

Some of the highest transmutation rates tan be significantly moderated by neutron self-shielding, especially in thick structures. In HFIR, the rater are so large that this is a moot point, however. Many of the Re and W isotopes will eventually burn up. thus having the same net long-term effect in changing composition. In FFTF, self-shielding is not so Important; however, some of the resonance region reactions will be moderated and this should be explored in more detail. The nearby presence of other strong neutron moderators (eg - Cd. Gd. 6. Li, etc.) would also reduce the transmutation rates of these isotopes.

---

[1] Pacific Northwest Laboratory is operated for the U. S Department of Energy by Battelle Memorial Institute under contract DE-AC06-76RLO 1833.

Results and discussion

Table 1 presents the results of these calculations as a function of full power days (FPD), total neutron fluence, and dpa (Fe). The results are also plotted in Figure 1-3. It is obvious, that the transmutation is strongest in FFTF in the below-core position (Figure 1). Unfortunately, much of ferritic data currently being generated in FFTF is being derived in this location. The strong spectral sensitivity of transmutation in tungsten will definitely complicate the comparison of data from below-core and in-core canisters.

In HFIR irradiations, the transmutation *is even stronger, but the primary transmutant atom shifts* from Re to Os, a development that further complicates comparison of data generated in the HFIR and FFTF reactors. In the STARFIRE spectrum, a large level of transmutation also occurs, but it takes approximately three full power years for the osmium to surpass rhenium in concentration.

There is little doubt that such large changes in composition during irradiation will affect the performance of tungsten. Tungsten-rhenium thermocouples (5, 11, 25% Re) are known to quickly decalibrate during irradiation [2], primarily due to radiation-induced precipitation of rhenium-rich chi phase. The role of transmutation-induced changes in rhenium level and the influence of osmium on phase stability have not yet been investigated, however.

References

1. R. K. Williams, F. W. Wiffen, J. Bentley, and J. O. Steigler, Met. Trans. 14A (1983) 655-666.
2. D. C. Thompson, N. C. Hoitink, and J. L. Jackson in Fast Flux Test Facility Quarterly Technical Report, July-August 1968, BNWL-917, pp. 4.31-4.35.

Table 1 Calculated Transmutation Products in Tungsten (Atomic percent)

	FFTF Midplane			FFTF Below Core			HFIR Midplane	STARFIRE
FPD*	244	488	933	244	488	933	365	365
Fluence** $x10^{23}$	1.0	2.1	3.4	0.30	0.61	1.02	0.36	0.58
dpa, Fe	30	60	100	4.4	9.7	14.5	27.0	12.0
Re	0.49	0.92	1.43	4.1	7.0	9.5	2.1 (5.1)***	2.1
Os	0.024	0.095	0.26	0.30	1.2	2.6	3.7	1.6
Ta	0.0009	0.0017	0.0027	0.007	0.014	0.020	0.048	[illegible]

*Full Power Days

**Total Fluence in FFTF, E>0.1 MeV fluence in HFIR.

***The Re eventually increases from 2.1 to 5.1% due to the decay of 185-W [illegible]

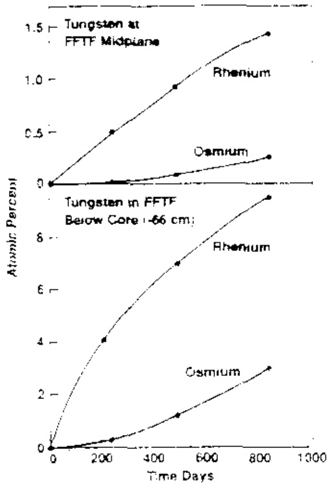

Fig. 1. Formation of Re and Os from W irradiated in FFTF at both the core midplane and the middle of the below-core basket of MOTA.

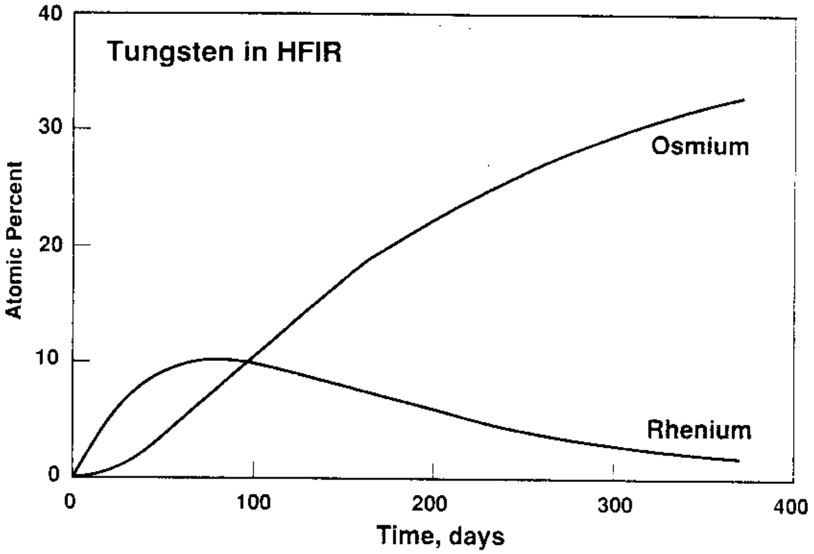

Fig. 2. Formation of Re and Os from irradiated in the PTP position of HFIR at 85 MW.

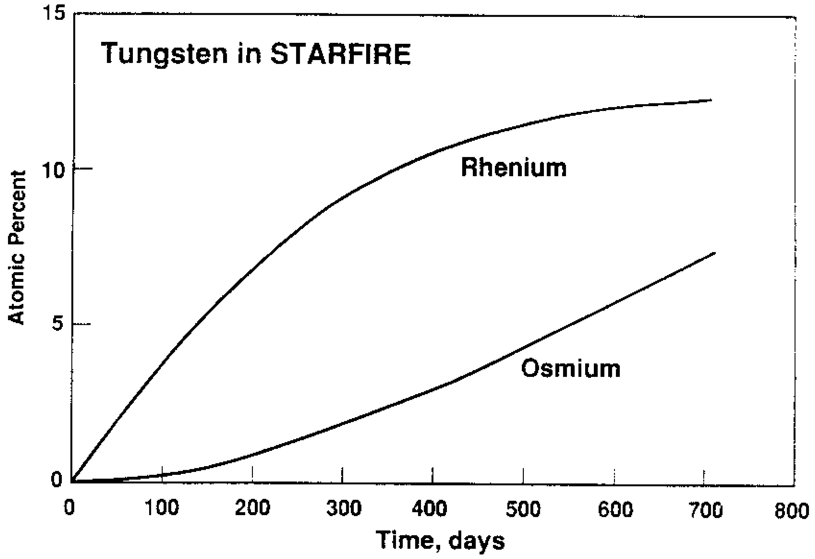

Fig. 3. Formation of Re and Os from W irradiated at the first wall position of STARFIRE at 3.8 MW/m^2.

SUMMARY OF IONIZING AND DISPLACIVE IRRADIATION FIELDS IN VARIOUS FACILITIES -- S.J. Zinkle (ORNL) AND L.R. Greenwood (PNL)

OBJECTIVE

The purpose of this report is to summarize the ionizing radiation and displacement damage fluxes present in representative materials irradiation facilities.

SUMMARY

Calculations have been performed to estimate the ionizing and displacive irradiation fields that will occur in ceramics during irradiation in accelerators and fission and fusion reactors. A useful measure of the relative strength of ionizing vs. displacive radiation is the ratio of the absorbed ionizing dose to the displacement damage dose, which in the case of ion irradiation is equal to the ratio of the electronic stopping power to the nuclear stopping power. In ceramics such as Al_2O_3, this ratio is about **20** at a fusion reactor first wall, and has a typical value of about 100 in a fusion reactor blanket region and in mixed spectrum reactors such as HFIR. Particle accelerator sources typically have much higher ionizing to displacive radiation ratios, ranging from about 2000 for 1 MeV protons to >10,000 for 1 MeV electrons.

INTRODUCTION

Considerable progress has been made over the past twenty years toward accurately characterizing the irradiation spectra in facilities used for materials science radiation effects studies [1-4]. Almost all of the emphasis in these spectral characterization studies has been devoted to analysis of the displacement damage component, in order to calculate standardized damage parameters such as displacements per atom (dpa) for various materials. There is a second major component of the irradiation spectrum, namely the ionizing radiation field, that has been largely ignored in irradiation spectrum tabulations. Ionizing radiation does not affect the radiation response of metals (other than to contribute to volumetric heating), because metals have a high concentration of electrons in their conduction band. The displacement damage effects associated with gamma rays in a nuclear reactor are generally negligible compared to neutron-induced displacements.

The response of insulators to ionizing radiation is considerably different from the case of metals. Due to high band gap energies, the concentration of valence electrons in the conduction band in polymers and ceramics is generally very low. Ionizing radiation can excite significant concentrations of these valence electrons into the conduction band. This produces very large changes in the electrical properties of the insulator during irradiation [5,6]. In some insulators such as the alkali halides, ionizing radiation can indirectly produce significant amounts of displacement damage from the decay of self-trapped excitons [7].

Several recent studies on ceramics indicate that the irradiation spectrum can have a pronounced effect on the radiation-induced changes in the microstructure or electrical properties [8,9]. In particular, irradiation spectra which produced a large amount of ionization relative to the amount of displacement damage were found to significantly enhance the amount of point defect diffusion (ionization-enhanced diffusion, IED) [8]. The ionization-rich radiation sources also produced an apparent acceleration in radiation-induced electrical degradation of Al_2O_3 [9]. These observations highlight the importance for fusion ceramics of a complete characterization of the ionizing radiation environment in addition to the primary knock-on atom (PKA) characterization. Calculations were performed in an attempt to assess the magnitude of the ionizing and displacive radiation components in ceramics for a wide range of irradiation sources.

RESULTS

Two parameters can be used to characterize the relative magnitudes of ionizing radiation and displacement damage for materials exposed to radiation. The most straightforward approach is to examine the ratio of the absorbed dose from gamma rays (which are primarily ionizing) to the absorbed dose from neutrons (which produce the displacement damage). However, this simple approach ignores the substantial amount of ionization that is produced via the PKAs generated by the neutrons. In addition, this ratio can only be applied to neutron irradiation facilities. A more appropriate measure of the ionizing and displacive radiation fields is the spectrum-averaged ratio of the electronic stopping power (S_e) to the nuclear stopping power (S_n). The spectrum-averaged nuclear stopping power (damage energy) contains only the fraction of deposited energy that induces displacement damage. The electronic stopping power includes ionization effects from both PKAs and gamma rays. In the following the spectrum averaged ratio of S_e/S_n will be referred to as the ionizing to displacive absorbed dose (IDAD) ratio:

$$\mathrm{IDAD} = \int \phi\ (E)\, S_e(E) \,/\, \int \phi\ (E)\, S_n(E) \qquad (1)$$

where the integration is carried out for both the neutron and gamma ray spectra

The IDAD ratio is a convenient parameter for comparing the relative strength of ionizing radiation in different irradiation facilities such as fission reactors and electron and ion accelerators. One shortcoming of this ratio (as with dpa calculations) is that it does not provide information of the spatial uniformity of the radiation fields. Just as displacement cascade effects have been shown to he an important factor associated with defect production in metals [10], spatially localized ionization "cascades" in the tracks of energetic incident or knock-on atoms may modify the resultant ionization effect. However, given the present lack of information on ionization effects as a whole, the IDAD ratio is a worthwhile first-order correlation parameter.

The TRIM-90 computer code [11] was used to calculate the energy deposited into ionizing and displacive events in Al_2O_3 for energetic ions ranging from 1 MeV protons to 4 MeV Zr^+ ions. The third possible component of deposited energy, phonons (heat) was generally found to be insignificant except for irradiation with massive ions with energies below 200 keV. A total of 3000 to 10000 ion trajectories were run for each condition. The calculations used an electron binding energy of 2 eV and a sublattice-averaged threshold displacement energy of 40 eV. Identical results were obtained when the TRIM calculations were repeated for the lightest and heaviest ions using the measured [12] Al and O sublattice displacement energies of 24 and 79 eV, respectively. The results of the calculations are summarized in Table 1. Due to the high stopping powers of the incident ions, the ionizing to displacive absorbed dose showed a strong depth dependence-the IDAD ratio decreased rapidly with increasing depth as the ions slowed down and approached values ≤ 1 at the depth where the ions came to rest [13]. The IDAD ratios given in Table 1 refer to values for the incident surface.

The corresponding IDAD ratio for 1.8 MeV electrons is given in Table 1 for comparative purposes. Published results [14] on the displacement damage (dpa) and ionizing dose (Gy) associated with 1.8 MeV electron irradiation of Al_2O_3 were converted to nuclear and electronic slopping powers using the conversion factor for Al_2O_3 of

$$\mathrm{IDAD} = 2.12 \times 10^{-9} * (\mathrm{Gy/DPA}) \qquad (2)$$

This conversion factor makes use of the Al_2O_3 atomic density of $1.17 \times 10^{29}/m^3$ ano assumes a sublattice-averaged threshold displacement energy of 40 eV. The extrapolated range for 1.8 MeV electrons given in

Table 1 was calculated using the well-known experimental results for **Al** [15] **and** correcting for the difference in density hetween Al_2O_3 and Al.

Table 1. Ioni ı and disp ve radiation fi . for Al_2O_3 in ous irradiation ırces

Irradiation Source	Ion Range	Gamma/ Neutron Absorbed Dose	Ionization/ Displacements Absorbed Dose	Damage Rate (dpa/s)	Ionizing Dose Rate (Gy/s)
1.8MeV electrons	2.1 mm	–	~10,000	–	–
20 MeV protons	**1.3** mm	–	3800♦	1.2 x 10^{-8}**	2.2 x 10^{4}**
10 MeV **protons**	0.39 mm	–	4400♦	1.8 x 10^{-8}**	3.8 x 10^{4}**
1 MeV protons	X.7 µm	–	1900	2.1 x 10^{-7}**	2.0 x 10^{5}**
28 MeV He^+ ions	0.21 mm	–	3400♦	1.2 x 10^{-7}**	2.0 x 10^{5}**
1 MeV He^+ ions	2.0 µm	–	820	3.8 x 10^{-6}**	1.5 x 10^{6}**
3 MeV C^+ ions	1.8 µm	–	280	**4.3** x 10^{-5}**	5.7 x 10^{6}**
2 MeV **Al+** ions	1.2 µn	–	33	4.1 x 10^{-4}**	6.3 x 10^{6}**
4 MeV Fe^+ ions	1.5 µm	–	15	1.4 x 10^{-3}**	1.0 x 10^{7}**
4 MeV Zr^+ **ions**	1.1 µm	–	3.9	4.0 x 10^{-3}**	7.5 x 10^{6}**
Mixed spectrum fission eactor (HFIR RB*)	--	23	107	3.2 x 10^{-7}	1.6 x 10^{4}
ast fission reactor FFTF MOTA)	--	1.0	4.4	3.8 x 10^{-6}	8000
usion Reactor					
- 1st wall	--	0.14	13	1.5 x 10^{-6}	9300
- magnet coils	--	0.7 to 210	40 to 330	<2 x 10^{-9}	<300
14 MeV neutrons (RTNS-II)	--	0.01	35	6.8 x 10^{-9}	110

'These calculations neglect displacements due to nuclear reactions, which can he significant lor light ion energies >10 MeV (see D. W. Muir and J. M. Bunch, in Radiation Effects and Tritium Technology for Fusion Reactors, p. II-517).

**Displacive and ionizing dose rates calculated lor a beam current of 1 µA/cm^2 of singly charged ions

The IDAD and gamma ray to neutron absorbed dose ratios for several neutron irradiation facilities are shown in Table 1. The ionizing and displacive absorbed doses in A1203 due to neutrons were calculated

using the SPECOMP code [16]. The energy deposited by gamma rays in the fission reactor facilities was obtained by subtracting the neutron absorbed dose from **the** measured volumetric heating rates. The gamma

ray absorbed dose was calculated for Fe, since volumetric heating has not been measured in materials such as Al_2O_3. Since the gamma ray mass absorption coefficients for I MeV gammas **are** nearly constant for elements with atomic weights between C and Ag [17], it was assumed that the gamma ray portion of the volumetric heating (absorbed dose) was equivalent for Fe and Al_2O_3. The volumetric heating rates in Fe for the HFIR **RB*** position (85 MW_{th} power) and FFTF MOTA facility are 16000 and 4500 Gy/s, respectively (16 and **4.5** w/g) [18].

Table 1 also summarizes the absorbed dose ratios for 14 MeV neutrons and for **2** positions in a fusion reactor, The absorbed dose ratios for positions near the superconducting magnet coils in a fusion reactor depend strongly on the choice of blanket and shielding materials, and also depend on exact location **due** to radiation streaming effects [19,20]. **As** shown in Table 1, calculated IDAD ratios in Al_2O_3 between 40 and **330** at the superconducting magnet **can** be obtained for different combinations of blanket and shielding materials [19].

DISCUSSION

The calculated ionizing radiation parameters for the neutron irradiation facilities need further study to evaluate their quantitative accuracy. For example, calculations by Dell and Goland [4] for Al_2O_3 irradiated in the **14** MeV neutron source RTNS-II give an IDAD ratio of 5.5 as opposed to the value of 35 calculated in the present work. Similar (although smaller in magnitude) discrepancies appear between Dell and Goland and the present **work** for mixed spectrum and fast reactor irradiation sources. In all **cases,** the Al_2O_3 displacement damage calculations from the two studies are in good agreement. The main source of the discrepancy lies in the calculations of the amount of ionizing radiation produced by neutrons. The values obtained by **Dell** and Goland are consistently smaller than the values calculated in the present study by a factor of **2** to 6, depending on the neutron spectrum. The source of this discrepancy is unknown at the present time. This highlights the need for better characterization of the ionizing radiation environments in irradiation facilities.

It is worth noting that even "pure" neutron sources such as RTNS-II are highly ionizing (IDAD ratio ~35). The high amount of ionization **is** due to the dense ionization associated **with** the high average PKA energy created by energetic neutrons. The fraction of absorbed dose associated with ionization increases rapidly with increasing neutron energy. For example, the IDAD ratio for Al_2O_3 in a fast fission reactor is only about 4.4. whereas the value **is -35** for 14 MeV neutrons

The IDAD values presented in this report are only valid for Al_2O_3. Significantly different results will be obtained for different ceramic materials such as SiC, and the appropriate values for polymers will be much different.

A range **of** irradiation facilities may be needed to obtain **data** appropriate for insulators to be used in different locations in a fusion reactor. According to the present calculations, the range of IDAD ratios relevant **for** Al_2O_3 **vary** between –15 for applications near the first wall to –100 for blanket applications. **Further** work is needed to determine the sensitivity of ceramic insulators to slight variations in the **IDAD** ratio. Scoping studies performed to date have shown that significant differences in the microstructural and electrical *property* evolution can be obtained when the IDAD ratio is varied by a factor of ten or more [8,9]. It remains to be seen if detectable differences will occur when the **IDAD** ratio is altered by a factor of **–2.**

REFERENCES

1. T.A. Gabriel, B.L. Bishop and F.W. Wiffen, Calculated Irradiation Response using Fission Reactor (HFIK. ORR, and EBR-II) Neutron Spectra, ORNL-TM-6361 (August 1979).

2. L.R. Greenwood, J. Nucl. Mater. 141-143 (1986) 654

3. D.G. Doran, Report of the LASREF Evaluation Committee, PNL-SA-18584 (July 1990).

4. G.F. Dell and A.N. Goland. J. Nucl. Mater. 102 (1981) 246.

5. V.A.J. van Lint et al., Mechanisms of Radiation Effects in Electronic Materials, Vol. 1 (Wiley and Sons. New York, 1980).

6. R.E. Stoller. R.H. Goulding and S.J. Zinkle, J. Nucl. Mater. 191-194 (1992) 602.

7. N. Itoh, K. Tanimura and Y. Nakai, Nucl Instr. Meth. B65 (1992) 21

8. S.J. Zinkle, Effect of Irradiation Spectrum on the Microstructural Evolution of Oxide Ceramics, this semiannual.

9. S.J. Zinkle and W. Kesternich, Electrical Conductivity of Ceramic Insulators during Extended Ion Irradiation. this semiannual.

10. S.J. Zinkle and B.N. Singh, J. Nucl. Mater. 199 (1993) 173

11. J.F. Ziegler, J.P. Biersak and U.L. Littmark, The Stopping and Range of Ions in Solids (Pergamon Press, New York, 1985).

12. P. Agnew, Phil. Mag. A 65 (1992) 355.

13. S.J. Zinkle, Fusion Reactor Materials Semiann. Prog. Report for period ending March 31, 1991, DOE/ER-0313/10.

14. S.J. Zinkle and E.R. Hodgson, J. Nucl. Mater. 191-194 (1992) 58.

15. R.D. Evans, The Atomic Nucleus (McGraw-Hill, New York, 1955) p. 625.

16. L.K. Greenwood. "Radiation Damage Calculations for Compound Materials", in Effects of Radiation on Materials, Vol. I, ASTM STP 1046, N.H. Packan, R.E. Stoller and A.S. Kumar, Eds. (ASTM, Philadelphia, 1990) p. 633.

17. J.K. Lamarsh, Introduction to Nuclear Engineering (Addison-Wesley, Reading, MA, 1977) p. 86

18. G.R. Hicks, B.H. Montgomery. K.R. Thoms and C.D. West, J. Nucl. Mater. 141-143 (1986) 1018.

19. M.E. Sawan and L.A. El-Guebaly, "Magnet Shielding Performance", ITER First Wall/Blanket/Shield Meeting, Argonne, IL, Feb. 19, 1993.

20. R.T. Santoro, J.S. Tang, R.G. Alsmiller, Jr., and J.M. Barnes. Nucl. Technol. 37 (1978) 65.

IMPROVEMENT OF DECAY AND CROSS-SECTION DATA LIBRARIES FOR ACTIVATION CALCULATIONS

-11. Attaya (Argonne National Laboratory).

OBJECTIVE

The objective of this work is to upgrade and improve the activation decay and cross-sections data libraries to provide accurate and more comprehensive estimates of fusion reactor activation.

SUMMARY

A new decay data library has been completed. The new library contains up-to-date decay information (half-lives. branching ratios, decay energies, γ's energies and intensities). Activation responses such as the air and water biological hazard potentials. the waste disposal rating. and the biological dose are also included in this library. Recently developed cross-section libraries have been acquired to be used together with the decay data library.

STATUS AND PROGRESS

Introduction

To enhance the safety of fusion reactors, materials' activation characteristics became an important factor in selecting the materials for use in fusion reactors. Therefore, the evaluation of the materials activation characteristics must be accurate and reliable. Decay and cross-section libraries are primary and essential inputs for activation calculations. Thus, the quality of these calculations depends on the quality of these libraries as well as the method of solution and the accurate modeling of the problem under consideration.

Activation Data Library

The activation data library contains information that is essential in constructing the decay and transmutation chains. This information includes the half-lives, the decay modes, and the branching ratios of the different decay modes. In addition. the decay energies of the emitted radiation are required to calculate the decay heat generation rate, and the γ's energies and intensities are required to calculate the biological dose.

We have utilized the computer data bases of the Isotope Project in Lawrence Berkeley *Laboratory* (which is reflected in the 'Table of Radioactive Isotopes') and of the National Nuclear Data Center at Brookhaven to generate an up-to-date activation data library. The genetic feedings (which are the branching ratios of a particular decay mode to different isomeric states) used in this library are from the Table *of* Isotopes[2].

Several activation responses *are* included in this library. These *are* the air and water maximum permissible concentrations[3] to calculate the inhalation and ingestion biological hazard potential, the waste disposal limits[4] to calculate the waste disposal rating. and the biological dose rates at 1 meter from a point source. The decay data library contains 2682 isotopes (521 isomers) compared to only 166 isotopes (26 isomers) in the old decay data library.

Activation Cross-Section Data Library

Several activation cross-section data libraries have been acquired to be used with the new decay data library. The most recent ones *are,* the new WAC-3 cross-section library and the European Activation File EAF-3[5]. The latter library has 10456 reactions' cross section data for 72Y isotopes. Both libraries were made available by F. Mann (Westinghouse Hanford Company).

Activation of Pure Elements

Figures 1 and 2 show the radioactivity of some elements that are important in the development of fusion reactor materials. These results have been calculated using the radioactivity code RACC[6]. The calculations are based on average neutron wall loading of 5 MW/m^2 and 5 years of continuous operation using the first wall neutron flux of the TPSS conceptual design[7]. Figures 3 and 4 show the air-BHP of these elements.

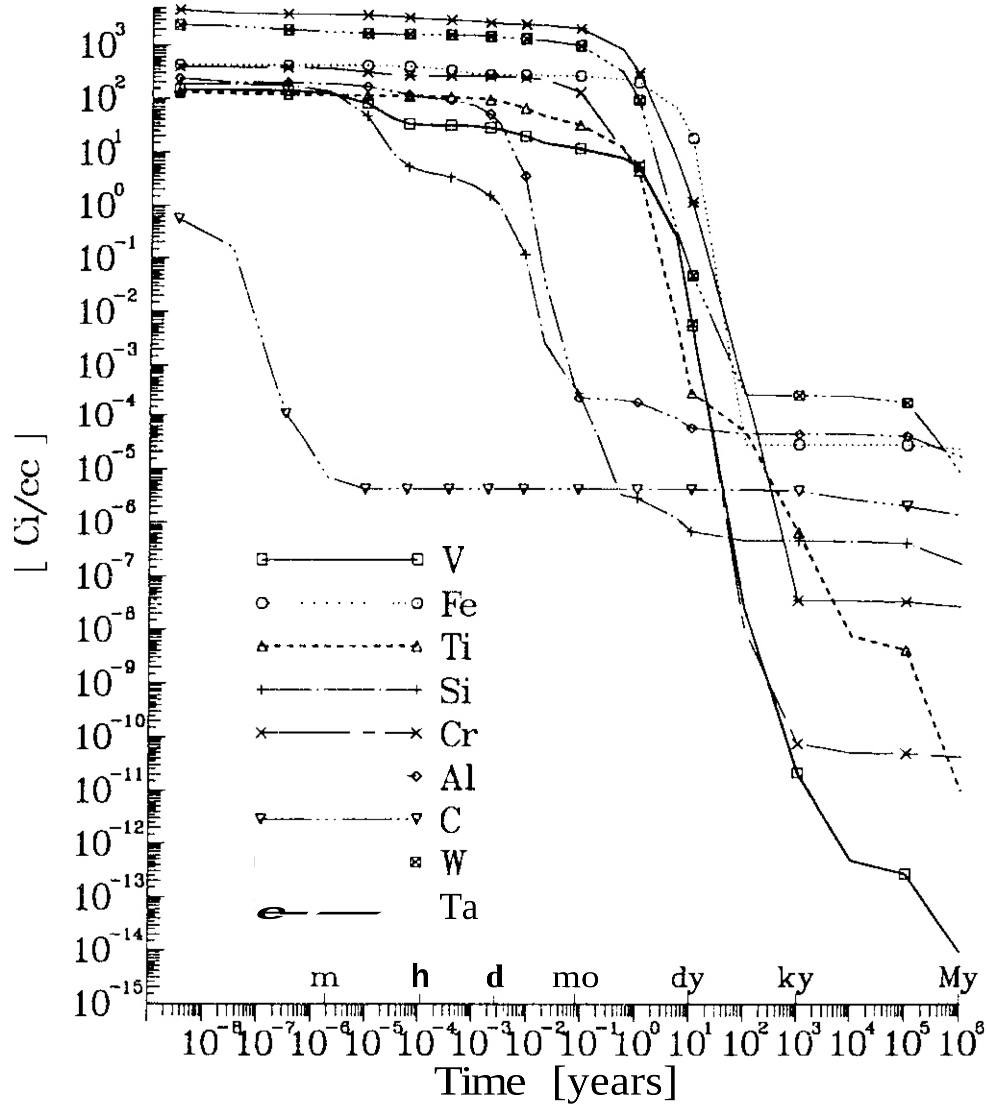

Fig. 1. Inducted activities in pure V, Fe, Ti, Si, Cr, Al, C, W, and Ta.

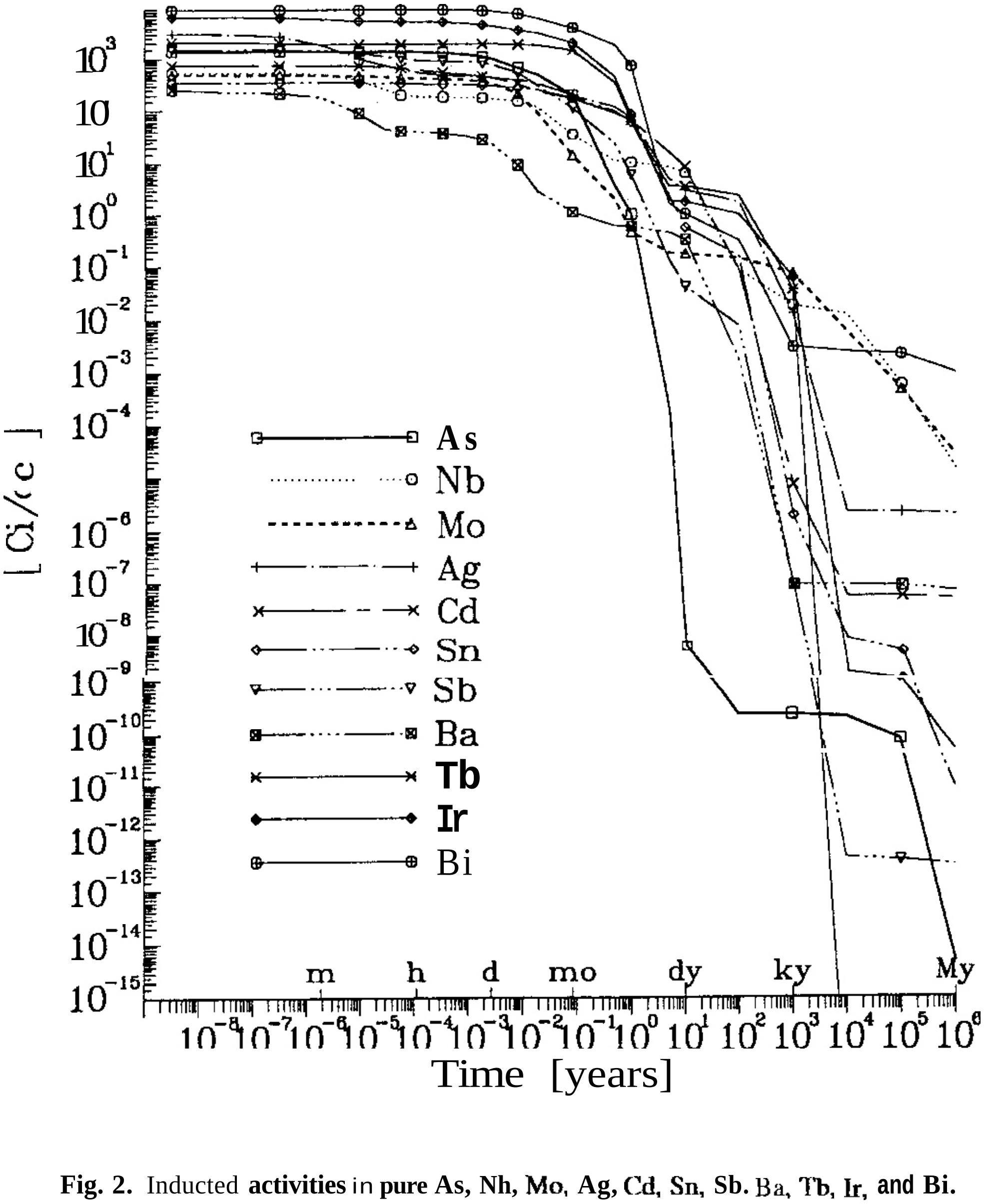

Fig. 2. Inducted activities in pure As, Nh, Mo, Ag, Cd, Sn, Sb. Ba, Tb, Ir, and Bi.

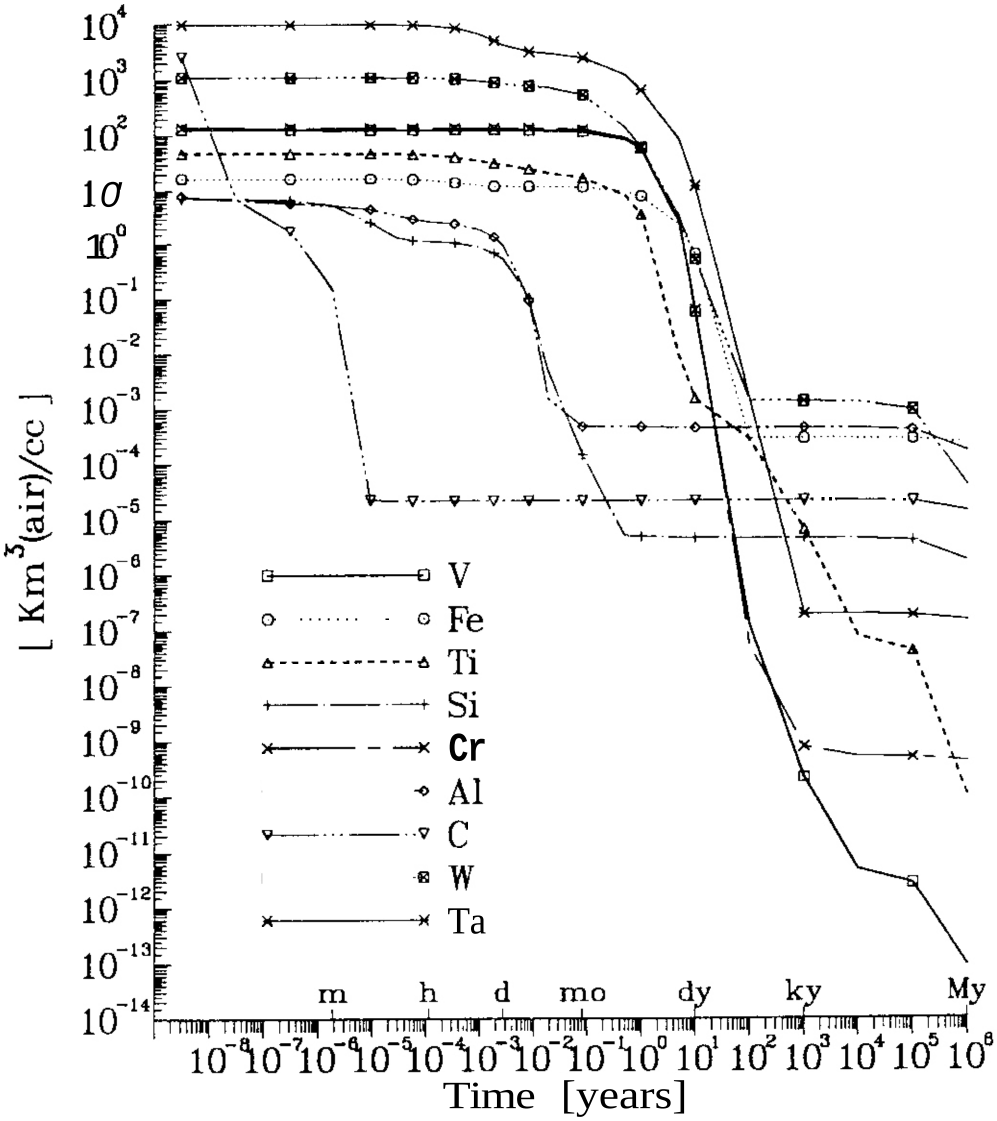

Fig. 3. Air biological hazard potential of V, Fe, Ti, Si, Cr, Al, C, W, and Ta.

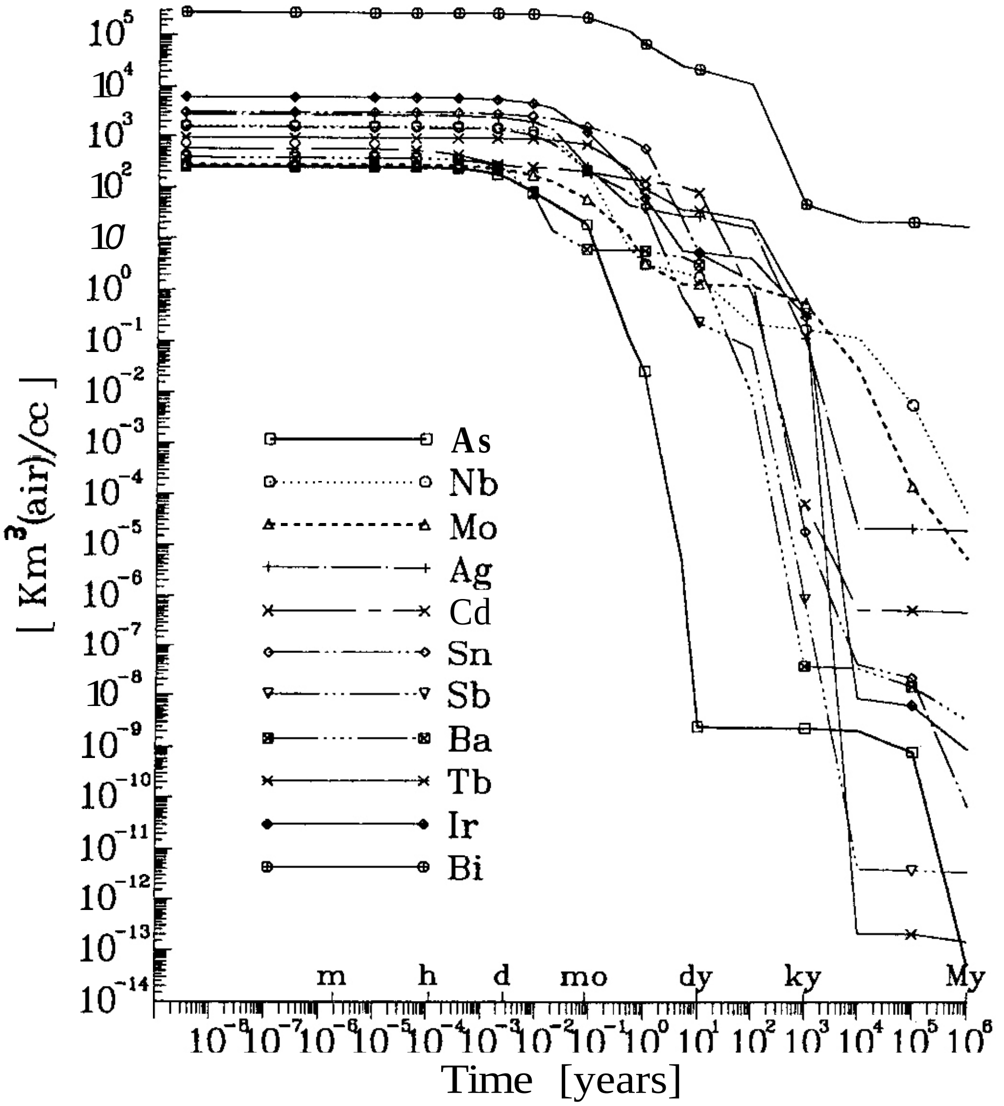

Fig. 4. Air biological hazard potential of **As, Nb.** Mo, **Ag. Cd,** Sn, **Sh. Ba, Tb, Ir, and** Bi.

FUTURE WORK

Available dosimetric experimental results will be used to verify the activation calculations.

REFERENCES

1. E. Browne and R. Firestone, "Table of Radioactive Isotopes," John Wiley and Sons, Inc., New York (1986).
2. C. M. Lederer and V. S. Shirley, Editors, "Table of Isotopes," Seventh Edition, Wiley-Interscience, New York (1978).
3. "Standards for Protection Against Radiation," Code of Federal Regulations, Title 10, Part 20.
4. "Licensing Requirements for Land Disposal of Radioactive Waste," Code of Federal Regulations, Title 10, Part 61.
5. F. Mann, private communications.
6. J. Jung, "Theory and Use of the Radioactivity Code RACC," ANL/FPP/TM-122, Argonne National Laboratory (1979).
7. D. Ehst et al., Argonne National Laboratory, ANL/FPP/86-1 (1987).

ACTIVATION ANALYSES FOR DIFFERENT STRUCTURAL ALLOYS CONSIDERED FOR ITER

H. Attaya and D. Smith (Argonne National Laboratory).

OBJECTIVE

The objective of this work is to evaluate the activation characteristics of different structural alloys that are being considered for ITER.

SUMMARY

Activation calculations have been made for the austenitic steel 316SS, the ferritic alloy HT-9, the titanium alloy Ti6Al4V, and the vanadium alloy V5Cr5Ti in a liquid metal (Na) design suggested recently for ITER. The calculations show that the vanadium alloy has the minimum short and long-term radioactivity and BHP. It also has the minimum decay heat all the time. The titanium alloy has less radioactivity than the austenitic and the ferritic alloys. However. the decay heat of this alloy could exceed that of the conventional alloys.

STATUS AND PROGRESS

Introduction

Several structural alloys have been considered for ITER. In addition to the austenitic, ferritic, and vanadium alloys. there is an interest in considering the titanium alloys. The interest in the titanium alloys is due to the fact that they are less radioactive than the conventional austenitic and ferritic alloys. In this work, using a recently suggested liquid metal design (Na) for ITER, different activation responses of these alloys *are* examined and compared.

Activation Calculations

Several liquid metal; Na, NaK, K, Pb, and Li have been envisaged for a liquid metal coolant design of ITER. The sodium coolant appears to have the minimum activation (for times > 1 day after shutdown). An optimized inboard design that protects the magnet consists of 0.5 cm FW, 65 cm shield (50% Na, 50% structure), and 35 cm vacuum vessel (62% structure. 38% water). Using this design. the radioactivity, the air-BHPs, and the decay heat generation rates in the inboard first wall are calculated for the four alloys using the radioactivity *code* RACC.[1] The calculations are based on 3 years of ITER operation with 1 MW/m^2 neutron wall loading.

The radioactivity of the four alloys after shutdown is shown in Fig. 1. It is clear in this figure that the long-term radioactivity of the vanadium alloy is several orders of magnitude less than the radioactivity of any other alloy. It is only in the period from *2* years to 20 years after shutdown, that the titanium alloys radioactivity *is* less than that of the vanadium. This is due to the fact that the radioactivity of the vanadium alloy is dominated by ^{49}V isotope, see Fig. 2, which is produced mainly by ^{50}V (n, 2n)^{49}V reaction. The titanium alloy's radioactivity, however, is much less than the radioactivity of the ferritic and the austenitic alloys. Figures 2 and 3 identify the dominant isotopes in the vanadium and the titanium alloys, respectively. The air biological hazard potentials of the four alloys are shown in Fig. **4.** Here, again, the short and the long-term vanadium's BHP is less than that of the other alloys. However. the period over which the titanium alloy's BHP is less than the vanadium alloy's BHP is longer and extends from just a few hours to 20 years. **This** ***is*** because the vanadium alloy's BHP is dominated by the isotope ^{49}V from the onset of the cooling period (80% at shutdown and ~100% at ~4 years).

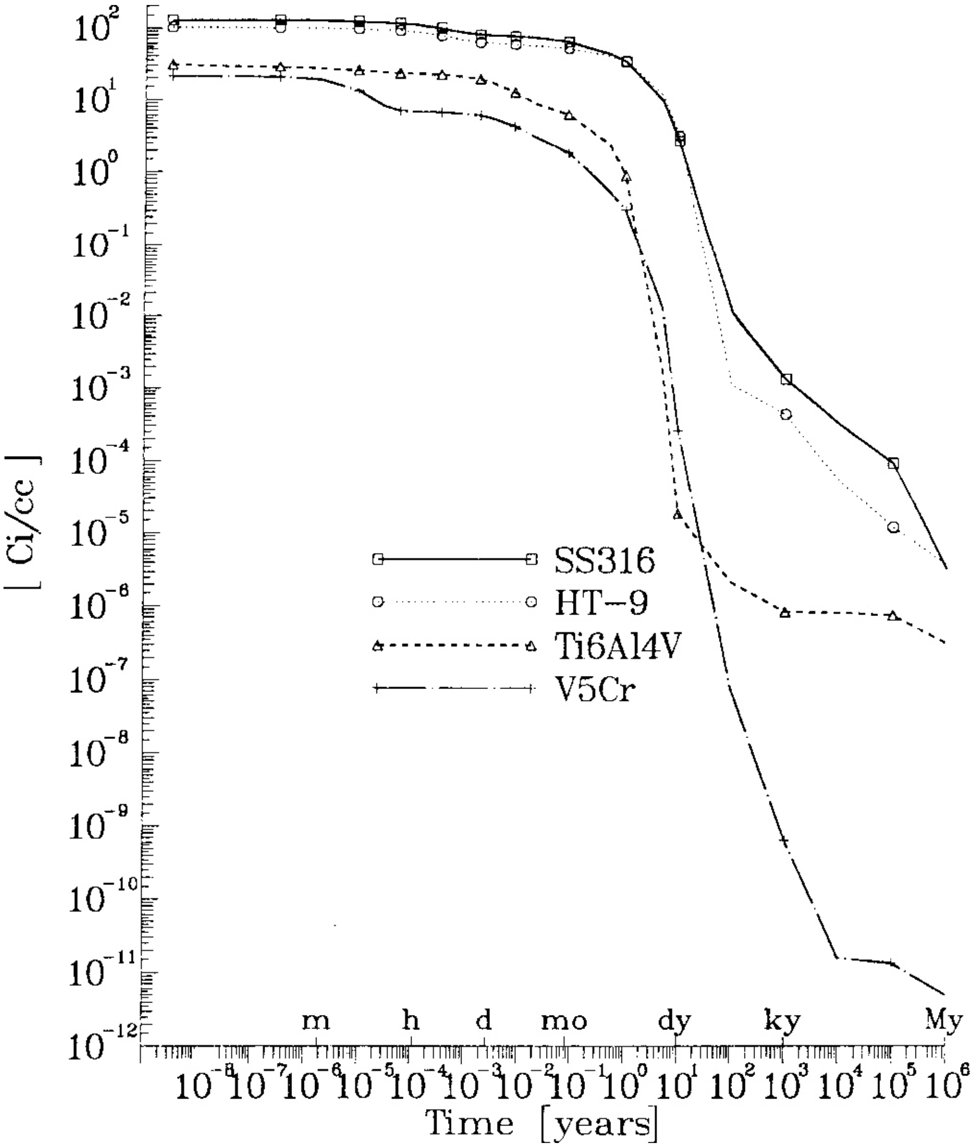

Fig. 1. The specific radioactivity in the first wall for the four alloys.

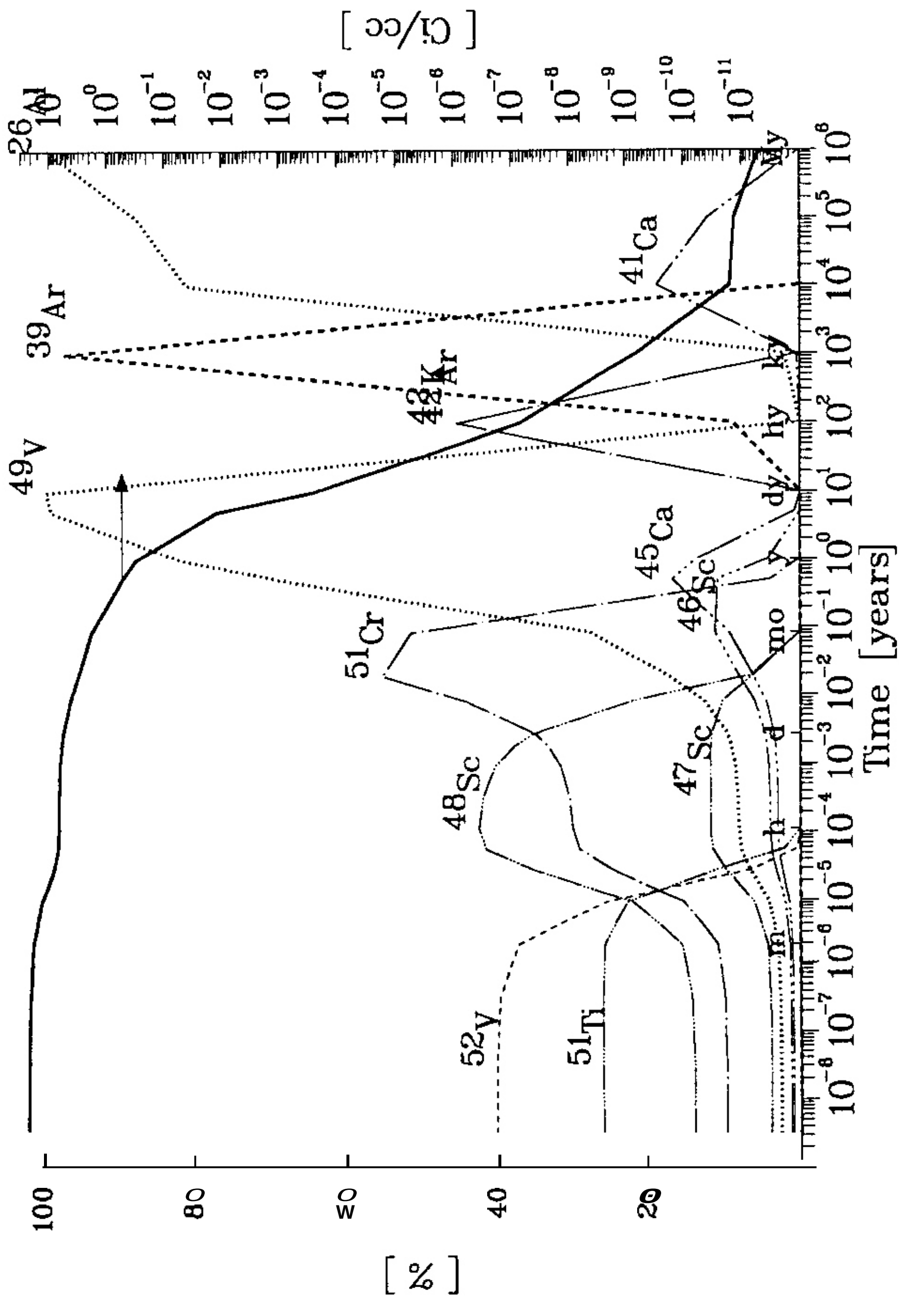

Fig. 2. The isotopic contributions to the radioactivity of the first wall vanadium alloy.

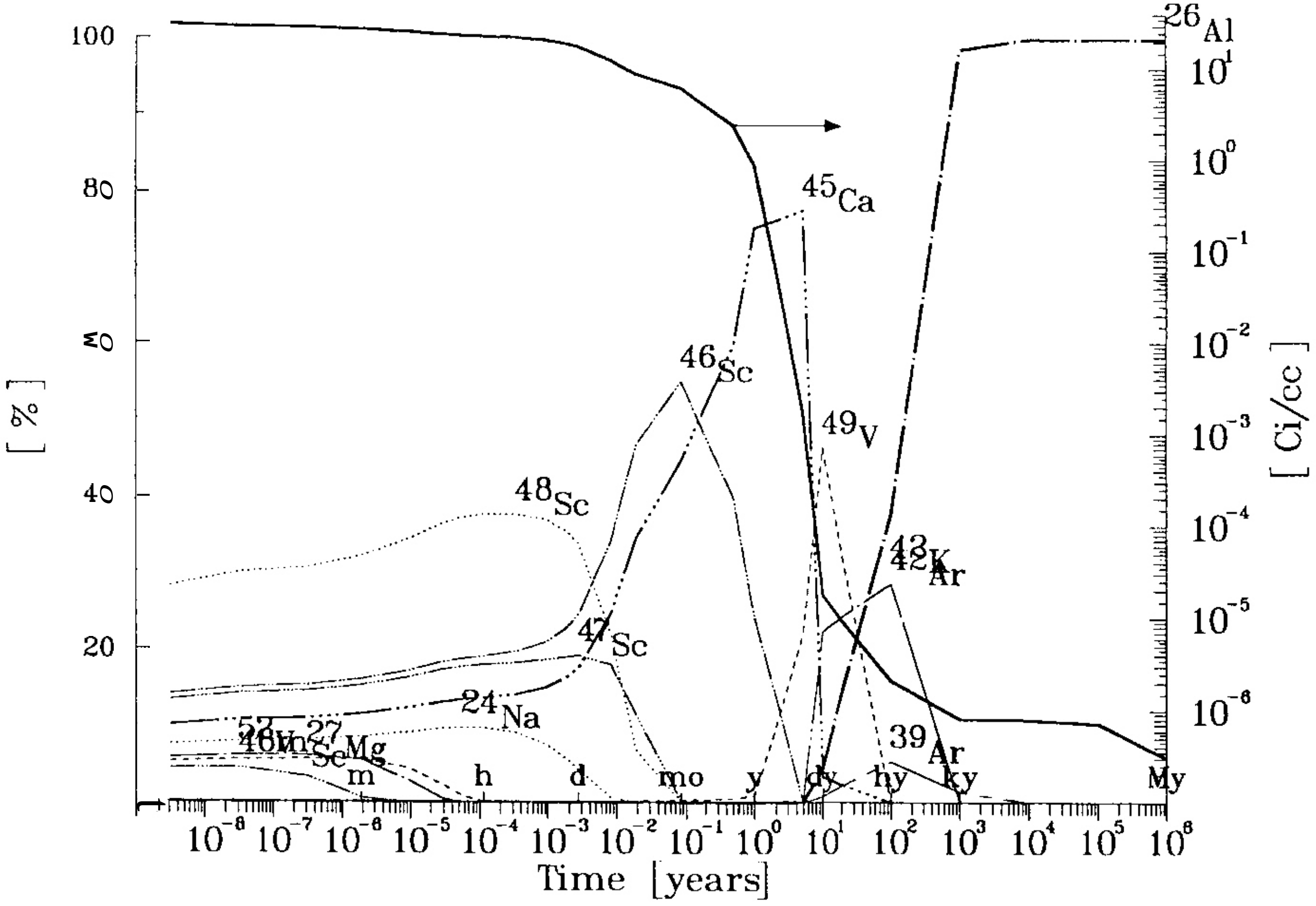

Fig. 3. The isotopic contributions to the radioactivity of the first wall titanium alloy.

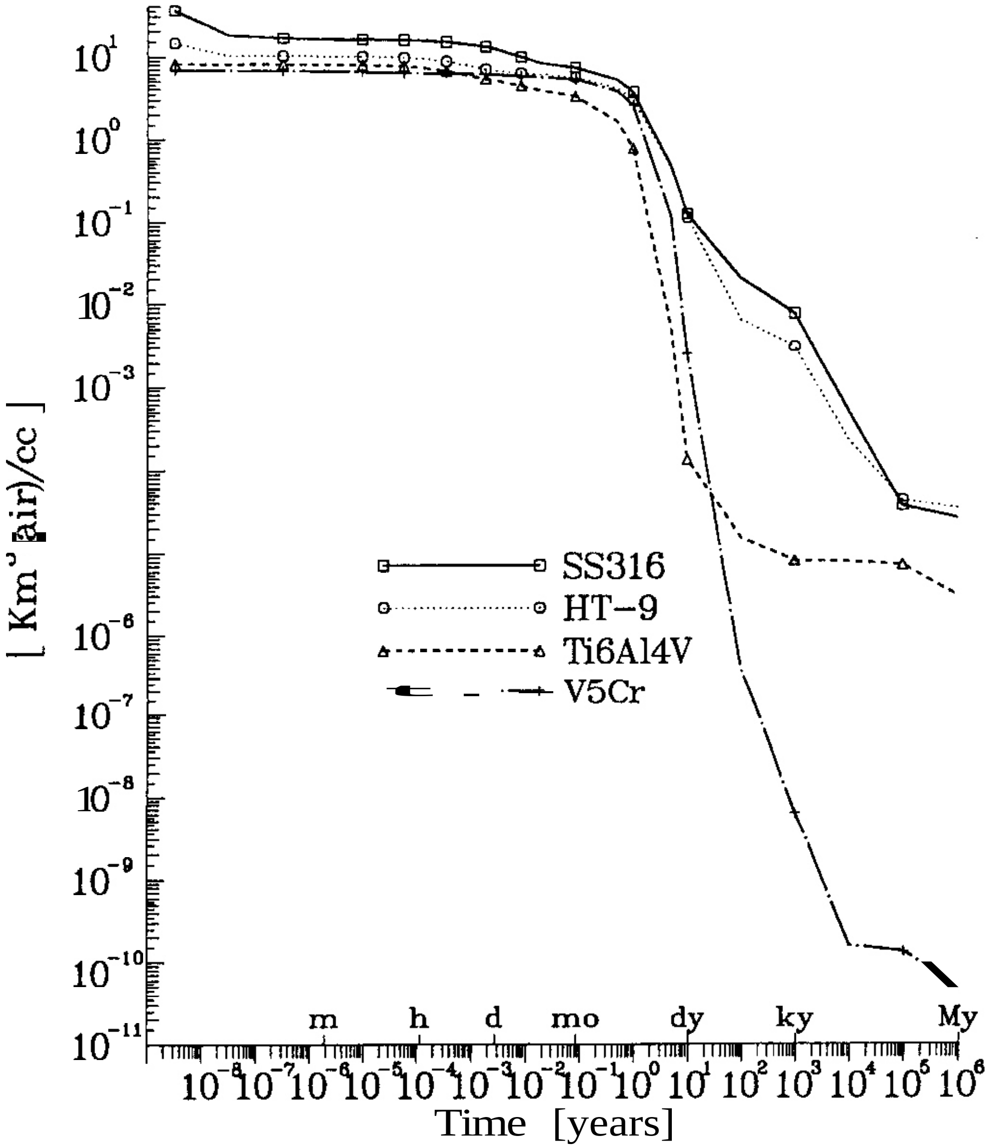

Fig. 4. The air-BPH of the first wall for the four **alloys**

The decay heat generation rates (DHGRs) of the four alloys are shown in Fig. 5. The vanadium alloy has the least DHGR all the times after shutdown. Only the ferritic alloy's DHGR comes close to that of the vanadium at about 1 day after shutdown. The DHGR of the titanium alloy is dominated by the isotopes ^{48}Sc ($T_{1/2}$ = 1.82 d, 3.35 MeV γ, .221 MeV β) and ^{46}Sc ($T_{1/2}$ = 83.83 d, 2.01 MeV γ, .121 MeV β). These strong γ ***and*** β emitters make the DHGR of the titanium alloy larger than the DHGR of HT9 in the period from 2 hours to ~1 month after shutdown. The DHGR of the titanium alloy even exceeds that of the 316SS alloy from 2 hours to about 1 week after shutdown.

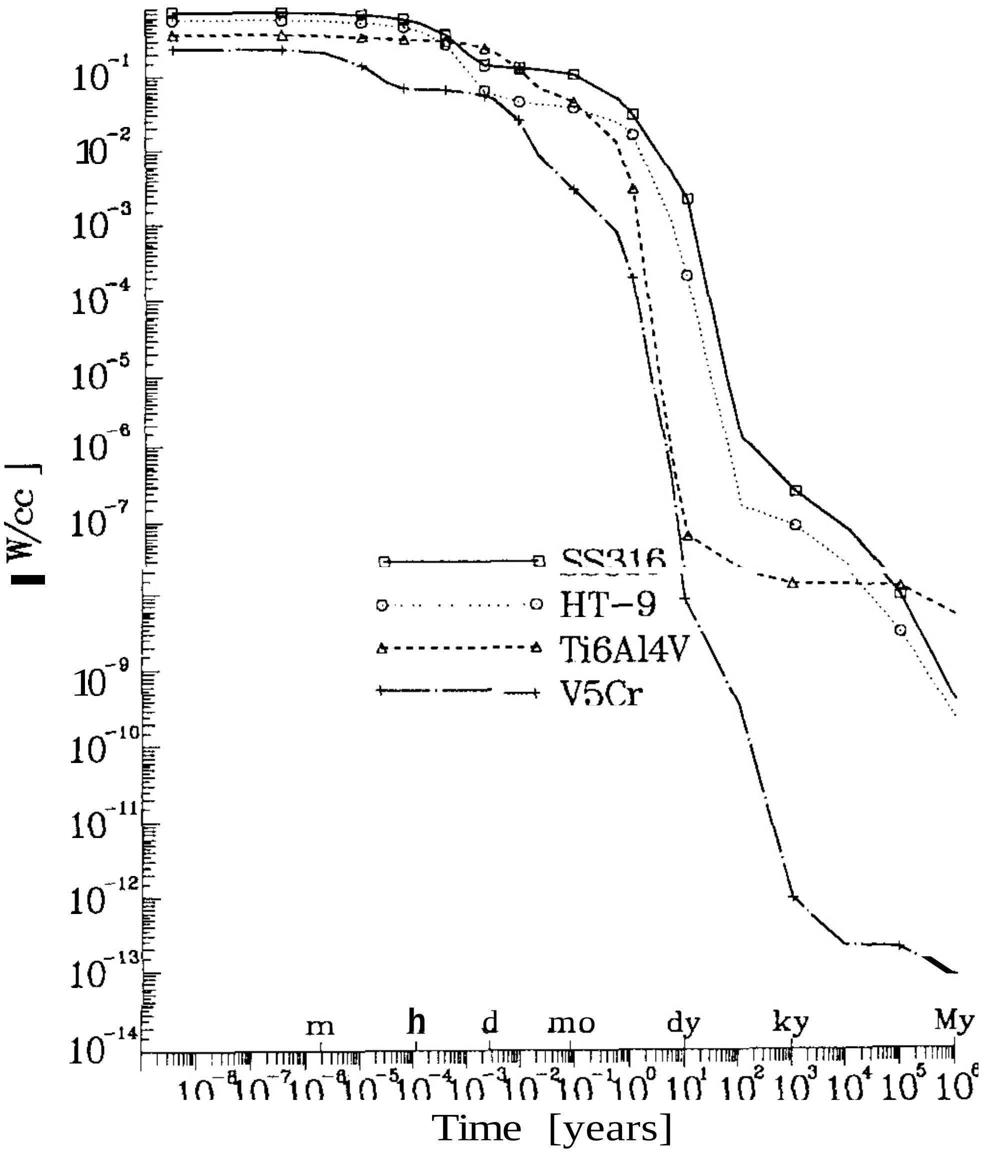

Fig. 5. The decay heat generation rates in the first wall for the four alloys.

REFERENCES

1. J. Jung, "Theory and Use of the Radioactivity Code RACC," ANL/FPP/TM-122, Argonne National Laboratory (1979).

3.0 MATERIALS ENGINEERING AND DESIGN REQUIREMENTS

No contributions.

4.0 FUNDAMENTAL MECHANICAL BEHAVIOR

MECHANICAL PROPERTIES ALONG INTERFACES OF BONDED STRUCTURES IN FUSION REACTORS - M. H. Hassan and G. L. Kulcinski (University of Wisconsin)

OBJECTIVE

The objective of this work is to be able to characterize unirradiated bonded structures used in fusion reactors based on differences in mechanical properties along interfaces due to fabrication techniques.

SUMMARY

Proper assessment **of** the mechanical properties along interfaces of bonded structures currently used in many fusion reactor designs is essential to compare the different fabrication techniques. A Mechanical Properties Microprobe (MPM) was used to measure hardness and Young's modulus along the interfaces of Be/Cu bonded structure. The MPM was able to distinguish different fabrication techniques by a direct measurement of the hardness, Young's modulus, and H/E^2 which reflects the ability of deformation of the interfacial region.

Introduction

Current proposals for high heat flux fusion components (such as divertor plates) include duplex thin walled structures. The structure may be subjected to high temperatures, high temperature gradients, thermal and irradiation creep, swelling, sputtering. and thermal expansion. A major point of concern for these bonded structures is the initial adhesion along the interfaces and the relevant mechanical properties. These properties, if properly assessed before irradiation, can help in screening the different fabrication techniques. This will ultimately reduce the time needed for irradiation testing by only considering joints that are compatible with the needed specifications.

For fusion material characterization programs, a Miniaturized Specimen Technology had to be developed to account for smaller irradiation volumes, lower post-irradiation testing doses to personnel, etc. **A** wide variety **of** tests have been developed for determining strength, ductility, **and** fracture-related **dam.**' Measurement of mechanical properties of interfacial zones is very complicated and usually requires the support **of** mathematical micromechanical models? Adhesion tests based on fracture mechanics principles are the most likely source **of** quantitative **data.** However. currently available adhesion tests are of restricted application and are too complex for most purposes?

Despite the difficulty **of** predicting the serviceability of a coating from its microhardness value. it is probably the mechanical property most often measured! Conventional microhardness has several characteristics that make it attractive for mechanical property characterization in small specimens? Primarily. the volume **of** material "sampled" during the test is small. Also, conventional microhardness data have been shown to be related to mechanical properties of the test material, such **as** ultimate tensile strength. largely by empirical means. It should be noted that conventional microhardness testers require direct imaging of the indentations to obtain hardness and large errors are introduced due to measurement of the diagonal lengths. especially when the indentations are small.[6]

Elastic properties along interfaces are very important for several reasons. First: modelling of bonded structure behavior is very complicated since some of the critical input parameters such **as** bond strength and interface compliance are not well known and the lab testing of these properties is believed to be even more critical than it would be for a simple structure? Second fabrication techniques, like brazing **or** plasma spray, do not **produce** sharp interfaces. and a certain degree of elemental mixing along the interfaces takes place. Elastic properties are known to dcpcnd on the composition, especially along interfaces where elemental mixing may be promotcd.[8] There are two extreme cases to consider for bonded structures. At the one extreme, a stress is applied transverse to the interface and the other, the load is applied parallel to the interface. It is imponant to remember that many bonded structures will dcform by a combination of the two cases.

Radiation damage in bonded structures is expected to induce certain changes in clastic propcnies. Swelling can reduce the elastic properties by up to 2% for every 1% swelling in AISI 316 Stainless Steel? Designers usually do not allow swelling 10 exceed 5-10%. Baed on this figure, we may expect a maximum of 10-20% reduction in Young's modulus by the end of the component lifetime. Detecting changes in Young's modulus from small material volumes along interfaces thus becomes a necessity to forecast the irradiation behavior of certain structures, especially intcrfaccs of bonded structures. Collisional mixing due to neutron irradiation may also causc elcmcntal mixing alnng interfaces of bonded structures. These changes need to be quantified and measured.

The Nanoindcnter

An automated system with the ability to evaluate the mechanical response of a sample with submicron spatial resolution has an extremely wide range of applications. A testing system must have certain characteristics to be considered a Mechanical Propcrtics Microprobc (MPM).''' It can measure the required propcrtics from volumes of material at least as small as one micron in diamctcr. Ideally. thc system could dctcrminc a constitutive equation for that volume of material; hence, it must measure both the elastic and plastic mechanical propcrtics. To do this reproducibly, the system must control or measure all the panmeters affecting such propcrtics. These paramctcrs include the swain, strain ratc, tcmpcraturc, stress, and the environment. Finally, the system must takc thcsc mcasurcmcnts with rcasonablc precision and with reasonablc invcstmcnt of time and effort

At the present time. only onc type of mechanical tcst can potentially satisfy all of thc above requircmcnts.[10] Properly instrumented and controlled, a (depth sensing) microindcntation tcst can accomplish many of *these* goals. During an indentation test, both elastic and plastic strains are generated. For many materials the swains from both **fields** arc of sufficient magnitude to bc mcasurcd. Thc lest can be scalcd down so that submicron volumcs of malerials arc samplcd. Microindcntation tcsts have bccn used to measure an extremely wide variety of material propcrties: yield strcngth, creep resistance, strcss relaxation, modulus, fracture toughness, and even fatigue tcsts. In addition, bccause the material bcing tested is close to a surface. cnvironmcntal effects can bc measured. With thc propcr combination of microindcntation test?. a nearly complctc constitutive equation of thc samplc's mechanical rcsponse can bc mappcd.

A schematic of a commercially available ultralow force indentation systcm, the Nanoindcnter. is shown in Figure 1.[6] A typical loading curve is shown in Figure 2. Thc **depth** plottcd represents thc total displacement of thc indenter relative to the initial position of thc surface. The displacement has compunents of both elastic and plastic dcformation.[11]

cross sectional measurement of mcchanical propcrtics alone intcrfaccs

There is a great need for the determination of hardness and elastic profiles along thc interface of bonded structurcs as well as to probc certain microstructures like thc intermetallic compounds formcd in some of the brazing joints. If the specimens are prepared in cross section. the Nanohardncss unit. with its high accuracy in the placement of indcnts, can be used to probe the mechanical propcrtics along interfaces. Regardless of the fact that thc measurement of hardness on cross sectioned samples was suggested early in the literature,[12] there has only been a substantial activity in this area in thc last few years as the use of coatings as well as composite materials has increascd.[13-16]

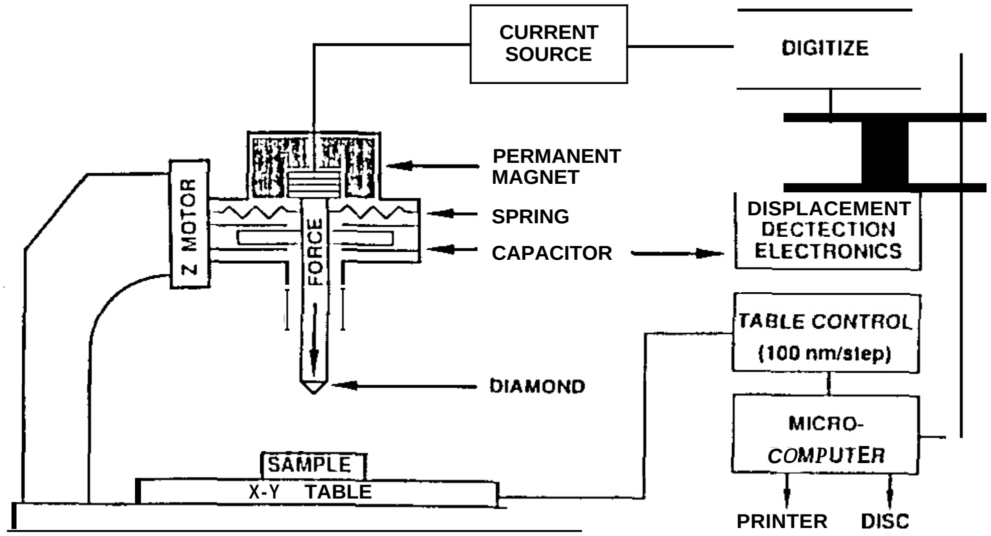

Fig. 1. Schematic diagram of the Nanoindenter.

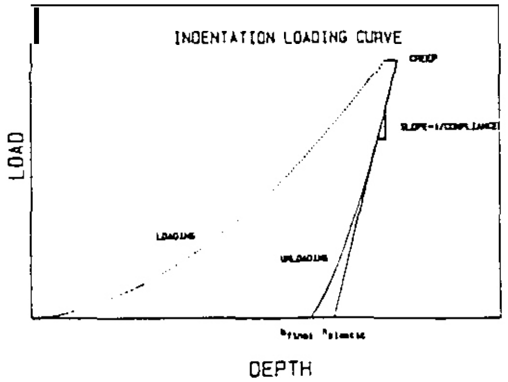

Fig. 2. Typical load-displacement curve obtained using the Nanoindenter showing the difference between the plastic and final depth?

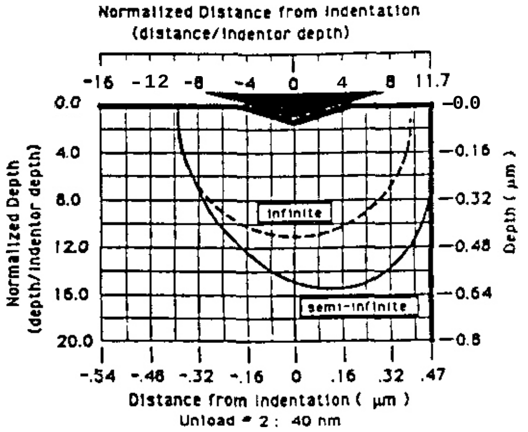

Fig. 3. Elastic plastic boundaries for indentations on infinite and semi-infinite media.[15]

A major point of concern for cross sectional measurements of mechanical properties, especially along interfaces, is how close successive indents can be to each other and how close an indent comes to a material discontinuity such as an edge or an interface without interference. Standard specifications for macroindentations require that the center spacing of pyramidal indentations be at least three indentation diagonals (3D).[17] The origin of this value seems to be lost in the early history of the development of hardness testing, and there appears to be no modern published reports of experimental investigation to support the value of 3.[17]

Samuels and Mulhearn[18] experimentally quantified these limits using Vickers-pyramid and Brinell-ball indentations for 7030 brass. Since the isostrain contours below the indenter are independent of indenter geometry away from the plastic imprint, their results apply also to the Berkovich pyramid of the Nanoindenter.[15] Figure 3 shows the elastic-plastic boundaries for an infinite and semi-infinire material. The indenter geometry is that of the Berkovich pyramid which has an imprint diagonal to depth ratio of 6.5. From the figure it is apparent that for the infinite medium the elastic plastic-boundary is spherical for infinite material.

The knowledge that is available on the plastic zone associated with the indentations permits an assessment to be made of what should be an acceptable spacing. As a starting point, it might be said that the elastic-plastic boundaries of adjoining indentations should not overlap.[17] This criterion would permit a center spacing of about 3 D for metals of moderately low yield stress, and 1 D for metals of moderately high yield stress. But these would be conservative values because hardness is not sensitive to small plastic strains even in materials which work-harden considerably. A more realistic criterion perhaps would be that the iso-strain boundaries for something approaching Tabor's equivalent strain should not overlap. To be on the safe side, one might require that the **5%** iso-strain boundaries should not overlap. By this criterion. the indentations could nearly touch one another without error, except perhaps in the very softest of materials. **As** a guide, it can be assumed that a serious error has not been introduced **if** the shape of the preexisting indentation has not been distorted noticeably by the new indentation. This criterion is particularly likely to be acceptable with microindenwtions in which there is so many other experimental uncertainties.[17]

The iso-strain contours are deformed significantly for indents close to the edge of a sample. From Figure 3[15] it is Seen that the elastic-plastic boundary for a semi-infinite sample is skewed such that the boundary contacts the edge of the sample **at a** distance/indenter depth ratio of 11.7. The minimum approach distance to an edge should therefore be 11.7 times the depth **of** the indent. While this would lead to the conclusion that he shallowest indents are the best, considerations of surface roughness must also be addressed. **A** tradeoff must be made between decreased volume averaging below the indenter and the inaccuracy due to surface imperfections.[19] Once more, Samuels suggested hat the standards are certainly excessively conservative for microindentation testing.[17]

Another point of concern for the cross-.sectional measurement of mechanical properties of bonded structures is the anisotropy **of** these properties.[20] For example, there is a typically crystallographic variation in Young's modulus. The reported values **of** elastic properties *are* usually average values taken from polycrystalline materials with a random orientations of he individual grains.[10] The question that is usually addressed is whether to average over the elastic constants (Voight averages) or over the elastic compliances (Reuss averages). The former is appropriak for a polycrystal in which the grains have the same State of **swain:** the latter for the case when they have the same stress.[21] If one is interested in probing the anisotropy along interfaces for bonded structures in fusion reactors, where the structures at the interfaces are subject to the same swain, the use **of** the Voight average is more suitable.

Mechanical properties alone the interfaces of Be/Cu structures

The Mechanical Propertics Microprobe (MPM) at the University of Wisconsin was used in measuring the mechanical properties along interfaces of Be/Cu structures fabricated at Sandia National Laboratory. Samples of two fabrication techniques were studied:

1. Beryllium hipped (Hot Isostatic Pressed) to Oxygen Free High Conductivity (OFHC) copper.
2. Beryllium brazed to OFHC using a silver based brazing alloy.

The samples were polished using 1 μm diamond paste. Hardness and Young's modulus were then measured using the Nanoindenter.

Be/Cu Brazed structure. Thirty two indentations were first made in two runs in Be and Cu bulks away from the interface to compare the **bulk** and interface values. Fifty indentations were then made starting from the Be side into the interfacial zone in two runs **(20** and 30 indentations respectively). The large number of indentations is needed to assess the variation along the interface and also to increase the

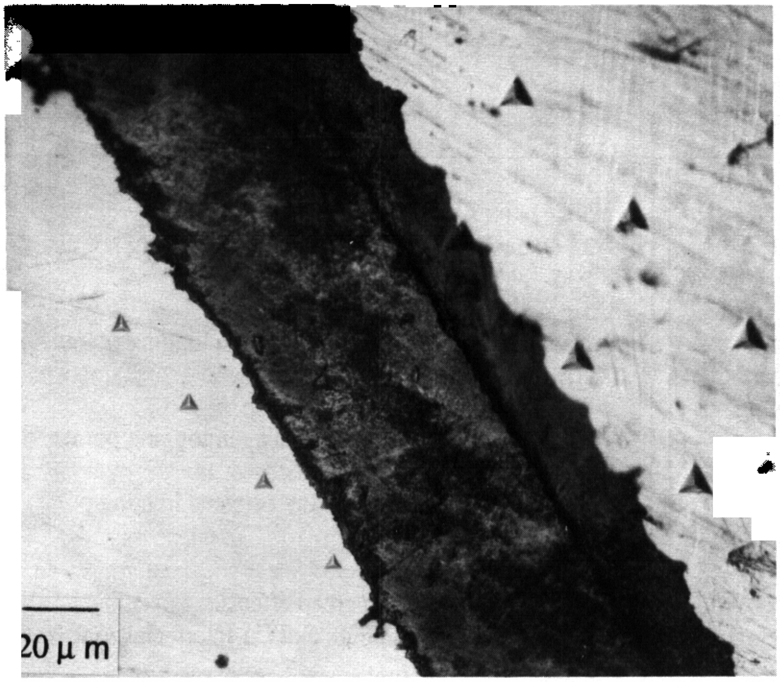

Fig. 4. Indentation run along the interfacial zone of a Be/Cu brazed joint

statistical certainty in the results. The high load range (0-120 mN) was used to obtain indentation depths of 500,750. and 1000 nm. The minimum spacings between indents were 53.34 µm for the two runs respectively (>30 times depth). The distance to the interface was approached at nearly 10 and 7 µm per indentation for the two runs respectively. As shown in Figure 4, indentations were made at an angle to the interface. so that a proper assessment of the properties along the interface could be made (notice that indentation size reflects the different hardness values). Forty indentations were then made starting from the interfacial zone into the Cu side in two runs (20 each) at indentation depths 500, 1000, and 1500 nm. Minimum spacing of indentations in this case was 51 µm. The interface was approached at nearly 12 and 10 µm per indentation for the two runs respectively. Table 1 represents the indentation segments for both the Be-Interfacial zone and Interfacial zone-Cu regions.

Be/Cu hipped structure. The same techniques were used for the other type of structure (the brazed type). Indentations were first made in the Be and Cu bulk regions away from the interface to compare the bulk and interface values. In this case, a separate run had to be done for the interface since its thickness varies from 400 to 450 µm.

Results

Figures 5.6. and 7 show the variation of hardness (H), Young's modulus (E), as well as the load over the compliance squared (i.e. H/E^2) for indentation depth 1000 nm for the brazed structure. Several points can be observed:

1. The jump in the mechanical properties between the Be side and the interfacial zone is quite obvious compared with the smooth transition along the interface between the copper and the interfacial zone.

Table 1. Indentation Test Configuration Used for Be, Cu Bulks and the Interfacial Zone.

Segment Number	Segment Type	Rate (nm/sec)	Depth Limit (Loading Segment) (nm)	Unloading (Unloading Segment) (% of final load)
1	Approach	10	...	...
2	Loading	5	500	...
3	Hold	25 data points; 1 sec delay between logging points		
4	Unloading	50%	...	80
5	Loading	5	750 (1000)**	...
6	Hold	25 data points; 1 sec delay between logging points		
7	Unloading	50%	...	80
8	Loading	5	1000 (1500)**	...
9	Hold	25 data points; 1 sec delay between logging points		
10	Unloading	50%	...	80
11	Hold	100* data points; 1 sec delay between logging points		
12	Unloading	300	...	100

*For copper, a 25 min. Hold period was performed to avoid creep effects.
**Values between parentheses represent depth limits for Cu bulk and Cu-Interfacial zone interface.

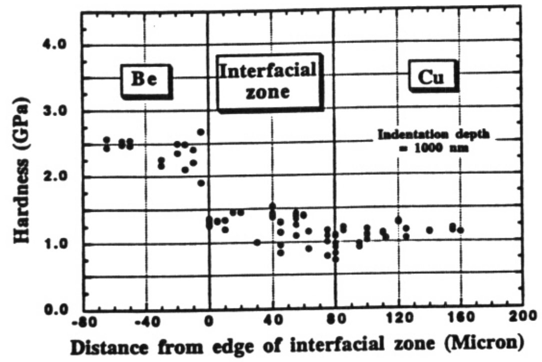

Fig. 5. Variation of hardness along interface of a Be/Cu brazed joint.

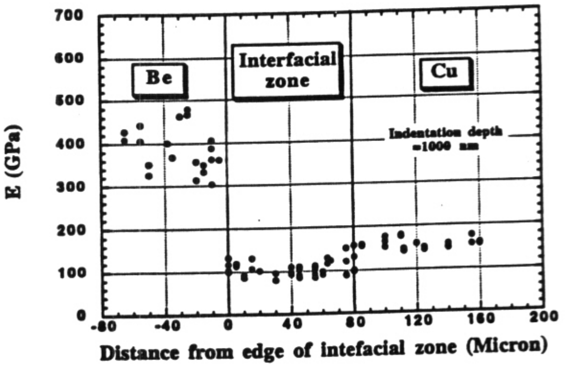

Fig. 6. Variation of E along interface of a Be/Cu brazed joint.

2. The lowest hardness value occurred at the edge of the interfacial zone with the copper side. As for the Young's modulus, the lowest value occurred in the interfacial zone which further widened the difference in Young's modulus values between the copper and the beryllium parts.

3. The largest values of hardness and Young's modulus occurred in the beryllium bulk.

4. Values of H/E^2 are considered to be a good representation of the resistance for plastic deformation as mentioned by Oliver.[22] Thus, the high values of H/E^2 in the interfacial zone, compared with the beryllium and copper bulk region, is a good indication of its ability to resist plastic deformation.

As for the hipped structure, several interesting points were observed. First, as shown in Figures 8 and 9, there are some microstructural islands in the interface between the filler metal and the Be side. These extend for about 100 μm as shown from the metallographic picture in Figure 10. The Nanoindenter successfully detected these changes in the microstructure that was reflected in discontinuities in the mechanical properties.

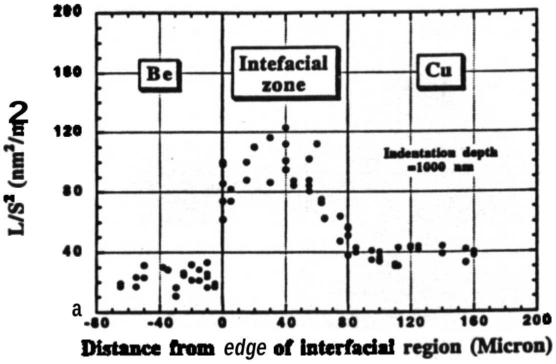

Fig. 7. Variation of L/S^2 along interface of a Be/Cu brazed joint

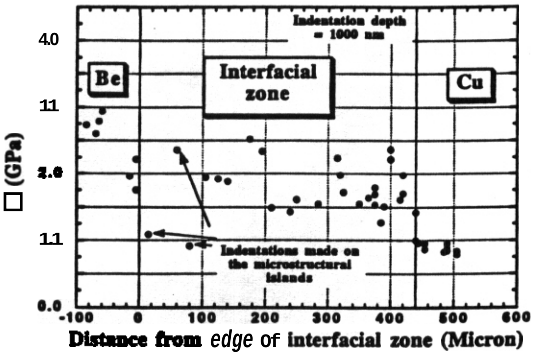

Fig. 8. Variation of hardness along interface of a Be/Cu hipped joint

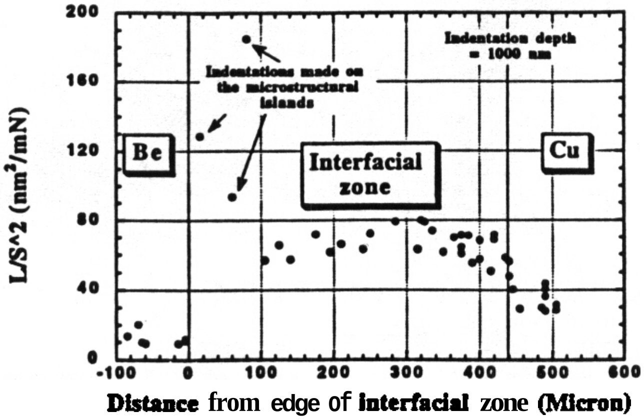

Fig. 9. Variation of L/S^2 along interface of a Be/Cu hipped pint

The following points can be observed in the hipped structure:

1. The discontinuity in the mechanical properties along the edge of the interfacial zone with beryllium still exists. It is even much more dramatic than in the hipped joint due to the existence of the microstructural islands.
2. The smooth transition along the edge of the interfacial zone with the copper still exists. However, a mismatch in hardness values can still be observed.
3. Away from the microstructural islands, Young's modulus values are slightly higher in the interfacial region for the brazed joint compared with the hipped joint. This bridges the large gap between the Young's modulus values of the Be and the Cu. The same trend is also observed for the hardness values. Also, the H/E^2 values of the interfacial zone in the brazed pint are lower than the hipped joint.

The microstructural islands are believed to be intermetallic formations due to interdiffusion between beryllium and copper. It is well known that in case of beryllium pining, as atoms in the base. metal migrate by diffusion into the other metal and vice versa, changes in the properties of the boundary layer between the two metals may occur. This can sometimes affect the joint strength by formation of brittle intermediate phases. In other cases, on the contrary, one can obtain, deliberately or not, higher qualities of the joint.[23] In this case, the strength of the joint no longer depends on the bond strength between the two metals. Instead it depends on the bond strength between either of these and the newly formed intermediate layer.[23]

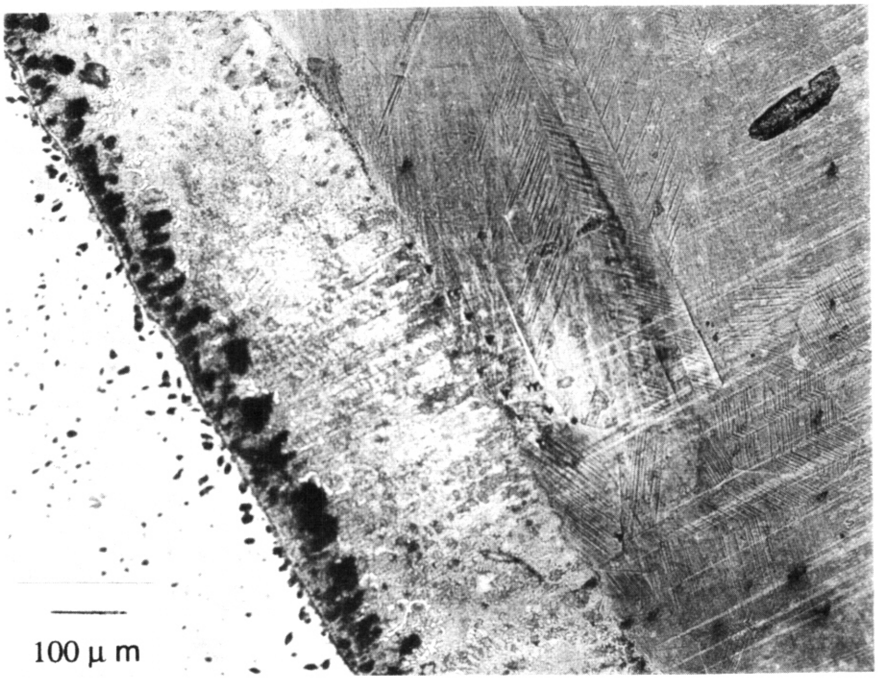

Fig. 10. Microstructure islands observed along the Be/interfacial region of the Be/Cu hipped joint.

Based on the above observations, it can be stated that the unirradiated brazed joint is more suitable than the unirradiated hipped joint due to (1) more uniform mechanical properties, (2) smoother transition of mechanical properties along the edge of the interfacial zone with the copper part, (3) less mismatch in mechanical properties between the interfacial zone and the beryllium bulk, and (4) high deformation ability of the interfacial zone (as shown in Figure 11).

FUTURE WORK

TEM samples from the hipped joint will be tested to verify the nature of the microstructural islands.

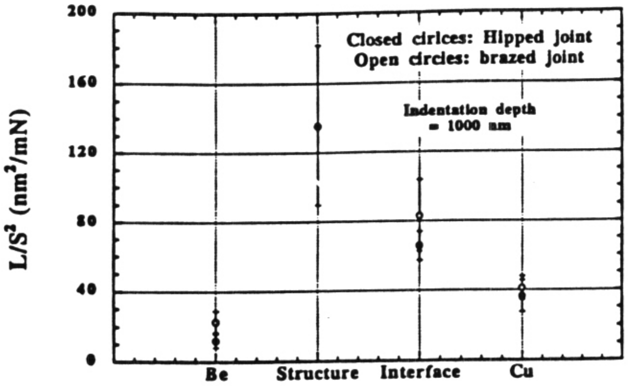

Fig. 11. Comparison of the ability of deformation for Be/Cu hipped and brazed joints.

ACKNOWLEDGEMENT

Financial support for this work has been provided by the University of Wisconsin and the U.S. Department of Energy.

REFERENCES

1. G.E. Lucas and G.R. Odette, Nucl. Eng. and Design/Fusion **2** (1985) 145.
2. A. Deruyttere and L. Froyen (eds.) in Proc. on Interfaces in Materials, Brussels (1988).
3. S. S. Chiang, et al., in Materials Science Research, Surfaces and Interfaces in Ceramic and Ceramic-Metal Systems (J. Pask and A. Evans, eds.) 14 (1980) 603.
4. G. A. Di Bari, in ASTM **947,** Testing of Metallic and Inorganic Coatings (W. B. Harding and G. A. Di Bari, eds.) (1986) 4.
5. G. E. Lucas, et al., ASTM 888 (1986) **112.**
6. M. F. Doerner and W. D. Nix, J. Mater. Res. 4 (1986) 601.
7. J. B. Whiltley, J. Nucl. Mat. *85* (1979) 40.
8. C. R. Barrett, et al., The Principles of Eneinnerine Materials, Prentice-Hall, Inc. (1973).
9. M. O. Marlowe and W. K. Appleby, Trans. Am. Nucl. Soc. **16** (1973) 95.
10. W. C. Oliver, MRS Bulletin, XI, (1986) 15.
11. W. D. Nix. Met. Tmns. **20A** (1989) **2217.**
12. K. L. Mittal, in ASTM 640, Adhesion Measurement of Thin Films, Thick Films, and Bulk Coatings (K. L. Mittal, ed.) (1976) 5.
13. R. P. Martukanitz, et al., in Proc. of the International Metallographic Society on Structural Science *14* (1987) 53.
14. A. David, et al.. Weldine Res. Suppl. 236s (1987).
15. L. L. Snead, DOE/ER-0313/10 (1991) **320.**
16. L. L. Snead and S. J. Zinkle. DOE/ER-0313/11 (1991) 316.
17. L. E. Samuels, in Microindentation Techniaues in Materials Science and Engineering, eds. Blau/Lawn, ASTM **STP** 889 (1984) 5.
18. L. E. Samuels and T. O. Mulhearn, J. of Mechanics and Phvsics of Solids *5* (1957) 125.
19. L. Snead, unpublished work (1992).
20. R. A. Dodd, private communications (1988).
21. J. P. Hirth and J. Lothe, Theorv of Dislocations, McGraw-Hill, New York (1968).
22. D. L. Joslin and W. C. Oliver, J. Mater. Res. *5* (1990) 123.
23. M. M. Schwartz (Ed.), Source Book on Brazing and Brazine Technology, American Society for Metals, Metals Park (1987).

GREEN'S FUNCTION METHODOLOGY FOR FRACTURE MECHANICS OF SiC-SiC COMPOSITE STRUCTURES[1]

A. El-Azab and N. M. Ghoniem, University of California, Los Angeles

OBJECTIVE

The purpose of this work is to develop new methods for the analysis of fracture processes in SiC-SiC wmposite structures under fusion conditions. Presently, no satisfactory method is available for determination of crack growth characteristics in real structures, where crack-crack interaction is important.

SUMMARY

A fundamental solution of plane elasticity in a finite domain is developed in this paper. A closed-form Green's function for the elastic field of an edge dislocation of arbitrary Burger's vector at an arbitrary point in an orthotropic finite elastic domain, that is free of traction, is presented. The method is based on the classical theory of potential fields, with an additional distribution of surface dislocations to satisfy the free traction boundary condition. A solution is first developed for a dislocation in a semi-infinite half-plane. The resulting field is composed of two parts: a singular contribution from the original dislocation, and a regular component associated with the surface distribution. The Schwarz-Christoffel transformation is then utilized to map the field quantities to a finite, polygonal domain. A closed form solution containing Jacohi elliptic functions is developed for rectangular domains, and applications of the method to problems of fracture and plasticity are emphasized.

PROGRESS AND STATUS

Introduction

The concept of a dislocation was first introduced by Weingarten [1], Timpe [2] and Volterra [3] as a mathematical device to deal with the possibility of solutions which satisfy the governing equations of the theory of elasticity, but possess the property of a multi-valued displacement field. For many years after its introduction, the mathematical device was termed a volterra dislocation [4]. On the other hand, the existence of crystal dislocations was found to be necessary for explaining the fact that most ductile materials yield and fail at stress levels that are at least three orders of magnitude smaller than the theoretical values predicted by atomic potential considerations alone [5-8]. The advent of analytical techniques in materials science proved, beyond doubt, the important role which crystal dislocations play in deformation, micromechanics of fracture, and other materials properties. The **materials** ***science*** applications of the theory of dislocations are extensively reviewed by Hirth and Lothe [9] and Nabarro [10]. A detailed work on the use of dislocation theory in modeling materials phenomena such as twining, grain boundaries [11, 12], interfacial energy and surface tension [13, 14] was conducted by Marcinkowski and Jagannadham. More recently, Amodeo and Ghoniem [15, 16] developed a dynamical method for the study of the micromechanics of plasticity in ductile materials. They termed their method ***Dislocation Dynamics*** , in which they solved for the simultaneous equations of motion of distributions of dislocations under a variety of applied stress conditions. In their work, however, they used elasticity solutions for dislocations in an infinite isotropic medium.

---

[1] This material is based upon work supported by the U.S. Department of Energy under award number DE-FG03-91-EM4114 at UCLA

Applications of dislocation theory to fracture mechanics, deals with dislocations in a continuum. The continuum theory of dislocations is reviewed by Hirth and Lothe [9], Nabarro [10], Mura [17, 18], and Lardner [19]. In fracture applications closed form solutions can be obtained by modeling cracks by continuous (or discrete) distributions of dislocations. However, the proper dislocation elastic fields (Green's function) in the crack domain must be available. Examples on application of dislocation theory to fracture mechanics are reported by A. N. Stroh [20], J. Qu and Q. Li [21], J. R. Willis [22], Delale and Erdogan [23], Lardner [24], Atkinson [25], and Vitek [26]. A review of dislocation models in fracture is given by Lardner [19], Vitek and Chell [27], Jagannadham and Marcinkowski [28] and Bilby and Eshelby [29], where dislocation Green's functions developed for infinite domains were used. In Ref. [28] extensive use of dislocation theory in modeling elastic and elastic-plastic fracture problems has been made.

In some cases dislocation fields are obtained for finite (circular, infinite strip of finite width) domains using the image dislocation method [9, 10]. Marcinkowski et al [30] argued that the image dislocation method is inadequate to obtain dislocational fields in finite domains since the resulting elastic fields do not vanish outside the domain ofsolution. They also introduced the method of surface dislocations to obtain dislocation fields in semi-infinite domains. The idea of the surface dislocation technique is based on the use of a correcting field, which yields the field in a finite domain if added to the infinite domain solution , with the boundary conditions satisfied. Marcinkowski et al [30, 31] used distributions of dislocations along a semi-infinite domain boundary to generate the additional correcting field. They developed analytical expressions for edge dislocations in isotropic half-planes. Their method proved to be exact and realistic in the sense that the dislocation fields identically vanish outside and on the domain boundaries. For rectangular domains, they used numerical methods to obtain the solution [32]. These approaches are based upon the classical theory of potential fields, and rely on solving an integral equation for the surface dislocation distribution. Other authors obtained the dislocational fields in half-space using the analytic continuation technique [33, 34]. In this method , additional correcting fields are determined so as to satisfy the free traction boundary condition on the domain boundary. However, Miller [33] and J. C. Lee [34] used two different methods to find the correcting fields, which yielded different expressions.

In applying dislocation theory to fracture mechanics or other materials science phenomena, the importance of development of an accurate solution to the governing equations of elasticity for a dislocation cannot be underestimated. It is from this prespective that we develop our present dislocation Green's function in a finite orthotropic domain. The problem formulation makes use of the classical theory of potential fields, with the surface dislocation technique to obtain the solution in a half-plane. The Schwarz-Christoffel transformation [35-37] is then utilized to obtain the solution in a finite (rectangular) domain. As will be shown here, only the elastic field of a dislocation in an infinite domain is a necessary ingredient in our present formulation.

Green's function for a dislocation in an infinite domain

For elastic anisotropic continua with material constants s_{mn} $(m, n = 1, 2, 6)$ Hooke's law is written as :

$$\begin{aligned} \epsilon_x &= s_{11}\sigma_x + s_{12}\sigma_y + s_{16}\sigma_{xy}, \\ \epsilon_y &= s_{12}\sigma_x + s_{22}\sigma_y + s_{26}\sigma_{xy}, \\ 2\epsilon_{xy} &= s_{16}\sigma_x + s_{26}\sigma_y + s_{66}\sigma_{xy} \end{aligned} \tag{1}$$

The stresses and complex displacement, $\mathcal{U}$, are written in terms of the complex potentials, $\phi_1(z_1)$ and $\phi_2(z_2)$ as follows [33, 34] :

$$\sigma_x = 2Re\left[\lambda_1^2\phi_1'(z_1) + \lambda_2^2\phi_2'(z_2)\right],$$

$$\begin{aligned}
\sigma_y &= 2Re\left[\phi_1'(z_1) + \phi_2'(z_2)\right], \\
\sigma_{xy} &= -2Re\left[\lambda_1\phi_1'(z_1) + \lambda_2\phi_2'(z_2)\right], \\
\mathcal{U} &= p(\lambda_1)\phi_1(z_1) + p(\lambda_2)\phi_2(z_2) + p(\bar{\lambda}_1)\bar{\phi}_1(\bar{z}_1) + p(\bar{\lambda}_2)\bar{\phi}_2(\bar{z}_2)
\end{aligned} \tag{2}$$

in which ***Re*** = *real* ***of*** and the overbar represents complex conjugation. The primed variables are derivatives with respect to z_1 or z_2. The constants λ_1 and λ_2 and their complex conjugates are the roots of the following characteristic equation [38]:

$$s_{11}\lambda^4 - 2s_{16}\lambda^3 + (2s_{12} + s_{66})\lambda^2 - 2s_{26}\lambda + s_{22} = 0 \tag{3}$$

and z_1 and z_2 are complex variables defined as :

$$\begin{aligned}
z_1 &= x + \lambda_1 y = (\gamma_1 z + \delta_1\bar{z})/2, \\
z_2 &= x + \lambda_2 y = (\gamma_2 z + \delta_2\bar{z})/2
\end{aligned} \tag{4}$$

where $z = x + iy, \gamma_j = 1 - i\lambda_j$ and $\delta_j = 1 + i\lambda_j, j = 1, 2$. The functions $\phi_1(z_1)$ and $\phi_2(z_2)$ are the complex potentials of the dislocation and are analytic within the body except at z_0. The polynomial $p(\lambda)$ is given by [38] :

$$p(\lambda) = \left(s_{12} - s_{16}\lambda + s_{11}\lambda^2\right) + \frac{i}{\lambda}\left(s_{22} - s_{26}\lambda + s_{12}\lambda^2\right) \tag{5}$$

The complex potentials at a point z (or ***alternatively*** $z_{1,2}$) due to a single dislocation at $z_o = x_o + iy_o$ in an infinite anisotropic plane are given by [33, 34] :

$$\begin{aligned}
\phi_{1s}(z_1) &= A_1 \log(z_1 - z_{1o}), \\
\phi_{2s}(z_2) &= A_2 \log(z_2 - z_{2o})
\end{aligned} \tag{6}$$

where z_{1o} and z_{2o} are related to z_o by the set of equations **(4).** The subscript s is added to indicate that the infinite domain potentials are **singular** at the location of the dislocation z_o. The complex constants $A_{1,2}$ are determined by the conditions that the deformation due to a single dislocation is ***not*** single-valued ***(dislocational),*** and the traction integral along any arbitrary contour surrounding the dislocation vanishes (*self-equilibrium*). The dislocational condition can be expressed **as** :

$$b = 2\pi i\left[p(\lambda_1)A_1 - p(\bar{\lambda}_1)\bar{A}_1 + p(\lambda_2)A_2 - p(\bar{\lambda}_2)\bar{A}_2\right] \tag{7}$$

where $b = |b|e^{i\theta}$ is the Burger's vector of the dislocation. The self-equilibrium condition yields the following equation :

$$\delta_1 A_1 - \bar{\gamma}_1\bar{A}_1 + \delta_2 A_2 - \bar{\gamma}_2\bar{A}_2 = 0 \tag{8}$$

By taking the complex conjugate of equations (7) and (8), two additional equations are obtained. The four equations can be solved for A_1, $\bar{A}_1, A_2$, and $\bar{A}_2$. El-Azab and Ghoniem [39] obtained a solution for A_1 and A_2 for the case of an ***orthotropic*** domain, where $s_{16} = s_{26} = 0$, which is written **as:**

$$\begin{aligned}
A_1 &= c_{11}Im(b) + ic_{12}Re(b), \\
A_2 &= c_{21}Im(b) + ic_{22}Re(b)
\end{aligned} \tag{9}$$

where c_{ij} are ***real*** constants which depend on the material constants s_{mn}. $Re(b)$ and $Im(b)$ are the real and imaginary parts of the Burger's vector, respectively.

Dislocation in a finite domain : General formulation

Consider an edge dislocation of arbitrary Burger's vector, $b = |b|e^{i\theta}$, which is located at z_o in the finite domain D^+ bounded by the contour L, as shown in Figure (1). ***The Green's function in an unbounded medium automatically satisfies the governing field equations. Any linear wmbination of the infinite domain Green's functions, which also satisfies specified boundary conditions for a finite domain, must be the Green's function in that finite domain.*** The solution, therefore, will be constructed as a linear combination of the singular, infinite domain solution, and an additional distribution of surface dislocations, such that the boundary is free of forces (*i.e.,* zero surface tractions).

Let $F(t)$ be a distribution function of surface dislocations, which is complex, and written as:

$$F(t) = f_1(t) + if_2(t) \tag{10}$$

where t is a complex variable describing the domain boundary L, and $f_1(t)$ and $f_2(t)$ are real functions of the complex variable t. Physically, $F(t)ds$ is defined as the Burger's vector of the surface dislocation in the interval ds, where $s = s(t)$ is the scaler distance along the domain boundary. The traction caused by the original dislocation and the surface distribution, evaluated at any arbitrary point along the boundary, must be equal to any prescribed boundary tractions. For the case of a free surface, this condition is written as :

$$X_d(t) + iY_d(t) + \oint_L [X_s(t_o,t) + iY_s(t_o,t)]\, ds_o = 0 \tag{11}$$

where $s_o = s(t_o)$ and X_d+iY_d is the residual complex traction at t on L due to the original dislocation at z_o inside D^+. $X_s(t_o,t)+iY_s(t_o,t)$ is the complex traction at t on L due to a surface dislocation of Burger's vector $F(t_o)$ at t_o on L. If the surface experiences any localized or distributed forces, $T(t)$, the right hand side of equation (11) is no longer zero, but rather $= T(t)$. Here, we consider only free surfaces. Equations (2), (6) and (9) will be used to determine $X_d + iY_d$ at any point t on L. The same equations will be used to determine $X_s(t_o,t)+iY_s(t_o,t)$ at t on L, with one difference, that is; $Re(b)$ and $Im(b)$ in equation (9) will be replaced by $f_1(t_o)$ and $f_2(t_o)$. This means that the complex quantities A_1 and A_2 are no longer constants when dealing with surface dislocations. Let these quantities be denoted by B_1 and B_2, and be written as :

$$\begin{aligned} B_1(t) &= c_{11}f_2(t) + ic_{12}f_1(t), \\ B_2(t) &= c_{21}f_2(t) + ic_{22}f_1(t) \end{aligned} \tag{12}$$

Equation(11) can now be rewritten in terms of $f_1(t)$ and $f_2(t)$, and can be utilized to determine these two functions. Once $f_1(t) + if_2(t)$ is determined the total stress field can be determined at any point in the domain D^+ by adding together the singular field and the additional field due to surface dislocations.

When a rectangular domain is considered, as shown in Figure (2), two mathematical difficulties arise:

1. the residual singular traction, $X_d + iY_d$, will have different expressions at t describes different sides of the rectangle, and
2. the contour L is not smooth.

Because of that, a suitable numerical method may be used to solve equations (11) and **(12)** for the complex function $f_1(t) + if_2(t)$. Such an approach was used by Jagannadham and Marcinkowski [32], to predict the **stress** field for an edge dislocation in an ***isotropic*** rectangular domain. Their solution yielded inaccurate results outside and close to the domain boundary, and they were able *to* satisfy the boundary conditions in an approximate point collocation fashion . The reader is advised to compare the present results with those of Ref [32]. From the mathematical point of view, there

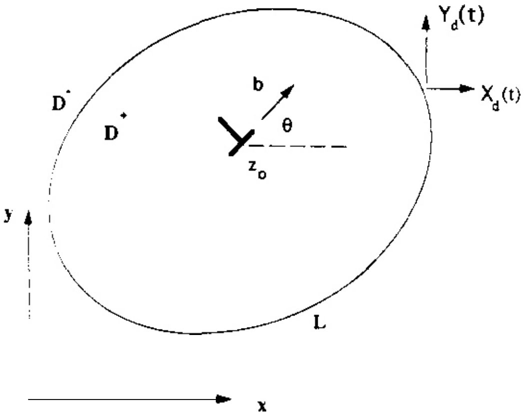

Figure 1: Arbitrary dislocation in a finite domain

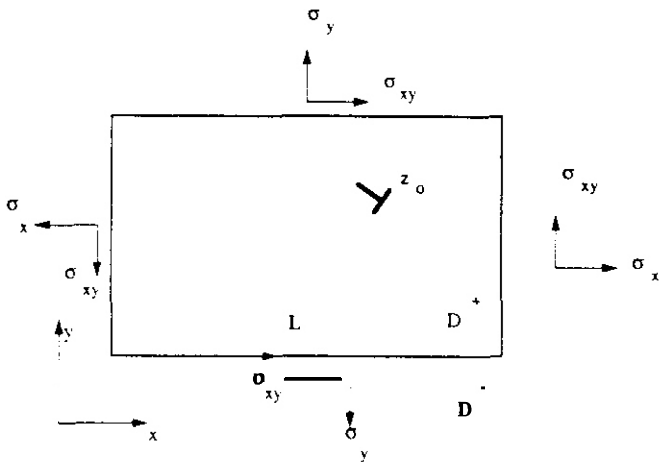

Figure 2: Variation of the residual surface traction for a dislocation in a rectangular domain

is an inherent difficulty associated with the problem of finding the elastic field of a dislocation in a polygonal domain. **As** can be noticed from the forms of the functions $\phi_1(z_1)$ and $\phi_2(z_2)$, the field is a cylinderical potential field. which **is** to be fit onto a geometrically incompatible polygonal boundary. However, the approach taken here is to obtain the solution in a semi-infinite domain and then use the Schwarz-Christoffel transformation to map the solution onto a polygon. This approach is illustrated in the next two sections.

Dislocation solution in an orthotropic semi-infinite domain

Distribution function of surface dislocations

Consider a dislocation of an arbitrary Burger's vector $b = |b|e^{i\theta}$ at the point $z_o = x_o + iy_o$, as shown in Figure **(3).** The domain of solution D^+ is the upper half-plane, $Im(z) \geq 0$, so that the contour L is taken to be the *x-axis* from $-\infty$ to $+\infty$. In this case the residual singular traction $X_d(t) + iY_d(t)$ is given by :

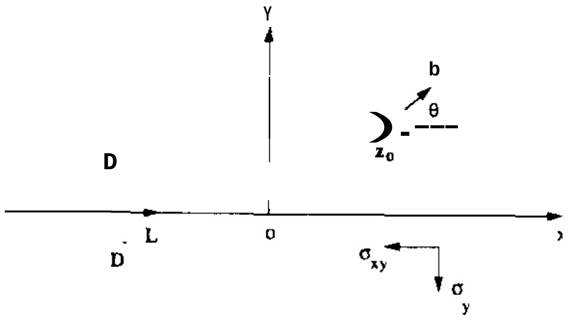

Figure 3: Dislocation in a semi-infinite domain

$$X_d(t) + iY_d(t) = \sigma_{xy}(z_o, x) + i\sigma_y(z_o, x) \tag{13}$$

similarly,

$$X_s(t_o, t) + iY_s(t_o, t) = \sigma_{xy}(x_o, x) + i\sigma_y(x_o, x) \tag{14}$$

so that equation (11) is rewritten as :

$$\sigma_{xy}(z_o, x) + i\sigma_y(z_o, x) + \int_{-\infty}^{+\infty} ((\sigma_{xy}(x_o, x) + i\sigma_y(x_o, x)))\, dx_o = 0 \tag{15}$$

Using equations (2), for stresses in terms of the complex potentials, expressions for $\sigma_{xy}(z_o, x)$ and $\sigma_y(z_o, x)$ are written as :

$$\begin{aligned} \sigma_{xy}(z_o, x) &= -2Re\left[\frac{\lambda_1 A_1}{x - z_{1o}} + \frac{\lambda_2 A_2}{x - z_{2o}}\right], \\ \sigma_y(z_o, x) &= 2Re\left[\frac{A_1}{x - z_{1o}} + \frac{A_2}{x - z_{2o}}\right] \end{aligned} \tag{16}$$

where $A_{1,2}$ are given by equations (9). Similar expressions can be written for $\sigma_{xy}(x_o, x)$ and $\sigma_y(x_o, x)$, by replacing A_1 and A_2 by B_1 and B_2 given by equations **(12).** The result is stated as follows :

$$\begin{aligned} \sigma_{xy}(x_o, x) &= -2Re\left[\frac{\lambda_1 B_1(x_o)}{x - x_o} + \frac{\lambda_2 B_2(x_o)}{x - x_o}\right] \\ \sigma_y(x_o, x) &= 2Re\left[\frac{B_1(x_o)}{x - x_o} + \frac{B_2(x_o)}{x - x_o}\right] \end{aligned} \tag{17}$$

If equation (12) is used in (17), the following simplified expressions for $\sigma_{xy}(x_o, x)$ and $\sigma_y(x_o, x)$ are obtained for the case of *orthotropic* domains :

$$\sigma_{xy}(x_o, x) = \frac{2(\beta_1 c_{12} + \beta_2 c_{22}) f_1(x_o)}{x - x_o} = \frac{a_1 f_1(x_o)}{x - x_o}$$

$$\sigma_y(x_o, x) = \frac{2(c_{11} + c_{21}) f_2(x_o)}{x - x_o} = \frac{a_2 f_2(x_o)}{x - x_o} \tag{18}$$

where σ_{xy} and σ_y in equations (16) and (18) are real quantities. β_1 and β_2 are the imaginary parts of the roots X1 and λ_2. Note that X1 and λ_2 are pure imaginary in the case of orthotropic materials (see Appendix B).

The integral Equation (15) can then be rewritten **as** :

$$\sigma_{xy}(z_o, x) + i\sigma_y(z_o, x) + \int_{-\infty}^{+\infty} \frac{a_1 f_1(x_o) + i a_2 f_2(x_o)}{x - x_o} dx_o = 0 \tag{19}$$

which is a singular integral equation with a Cauchy-type kernel. The integral part exists in the sense of its principal value. The integral equation (19) can be directly solved for $a_1 f_1(x) + i a_2 f_2(x)$. Alternatively, the real and imaginary parts of the integral equation can he separated to obtain two real integral equations for $f_1(x)$ and $f_2(x)$. Following Muskhelishvili's methods for the solution of singular integral equations [40, 41], and excluding mathematical details, the following two expressions are obtained for $f_1(x)$ and $f_2(x)$:

$$f_1(x) = \frac{-i}{\pi a_1}\left[\frac{\lambda_1 A_1}{x - z_{1o}} - \frac{\bar{\lambda}_1 \bar{A}_1}{x - \bar{z}_{1o}} + \frac{\lambda_2 A_2}{x - z_{2o}} - \frac{\bar{\lambda}_2 \bar{A}_2}{x - \bar{z}_{2o}}\right],$$

$$f_2(x) = \frac{i}{\pi a_2}\left[\frac{A_1}{x - z_{1o}} - \frac{\bar{A}_1}{x - \bar{z}_{1o}} + \frac{A_2}{x - z_{2o}} - \frac{\bar{A}_2}{x - \bar{z}_{2o}}\right] \tag{20}$$

where $f_1(x)$ and $f_2(x)$ are real quantities. The complex function $F(x) = f_1(x) + i f_2(x)$ must satisfy overall material compatibility condition, i.e., conservation of Burger's vector [30], which can bc examined using the following integral :

$$\int_{-\infty}^{x} F(x')dx' = b_s(x)$$

$$\begin{aligned} b_s(x) = - \quad & b\left(\frac{-i}{\pi a_1}\right)\left[\lambda_1 A_1 \log(x - z_{1o}) - \bar{\lambda}_1 \bar{A}_1 \log(x - \bar{z}_{1o})\right. \\ & \left. + \lambda_2 A_2 \log(x - z_{2o}) - \bar{\lambda}_2 \bar{A}_2 \log(x - \bar{z}_{2o})\right] \\ & + \left(\frac{-i}{\pi a}\right)\left[A_1 \log(x - z_{1o}) - A\,,\log(x - \bar{z}_{1o})\right. \\ & \left. + A_2 \log(x - z_{2o}) - \bar{A}_2 \log(x - \bar{z}_{2o})\right] \end{aligned} \tag{21}$$

It can be shown that $b_s(x) \rightarrow -b$ **as** $x \rightarrow$ +m.

The results are specialized for an orthotropic domain for which $s_{16} = s_{26} = 0$. To test the theory presented here, the properties of the Nicalon/CVD-SiC (fiber/matrix), which is an orthotropic material, are chosen. The elastic constants are evaluated using the rule of mixture for the fiber and matrix properties given in Ref. [43, 44]. The plane stress compliance constants are determined to be $s_{11} = \mathbf{3.125} \times 10^{-12}$, $s_{22} = \mathbf{3.503} \times 10^{-12}$, $s_{12} = -6.563 \times 10^{-13}$, and $s_{66} = \mathbf{9.31} \times 10^{-12}$ Pa^{-1}.

In presenting the results all distances are normalized to the magnitude of the burgers vector. Figure **(4)** shows a typical surface distribution **as** a function of the distance along the **free** surface, for a dislocation at $z_o = +i50$ with a purely real Burger's vector. It is obvious that $F(x) \rightarrow 0$ **as** x $\pm\infty$. The effect of varying the distance y_o from the free surface on $|F(x)|$ is shown in figure *(5)*. The distribution becomes sharper **as** y_o becomes smaller and localized at $x = 0$. It also broadens as

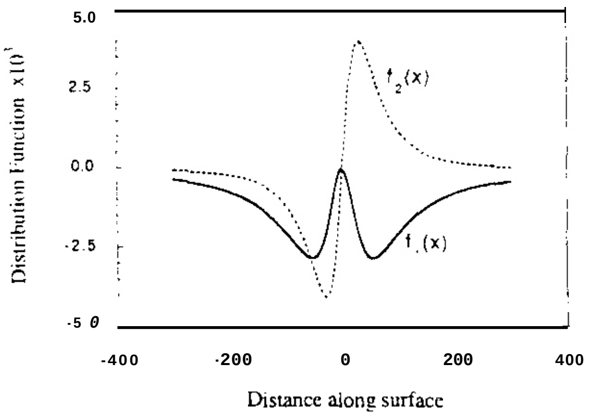

Figure 4: The surface distribution $(F(x) = f_1(x)+if_2(x))$ as a function of distance along the surface, $z_0 = +i50$. The Burger's vector is real

y_o becomes large. In fact, this is a fundamental difference between the surface dislocation technique and the image dislocation method for which the image dislocation represents an extremely localized distribution at the point $x = 0$. In figure (6), the integral surface Burger's vector $b_s(x)$, which is given by equation (21) is shown on an Argand diagram for different orientation of the Burger's vector of the lattice dislocation. x describes one curve as it varies from $-\infty$ to $+\infty$. $b_s(x)$ is given by the vector drawn from the point $(0,0)$ to any point on a curve. The results clearly indicate that the condition of material compatibility is satisfied. That is to say $b+\int_{-\infty}^{+\infty} F(x')dx' = 0$ [30]

Field Quantities in a semi-infinite domain

The complex potentials due to surface dislocations will be denoted by $\phi_{1r}(z_1)$ and $\phi_{2r}(z_2)$. These potentials will be evaluated as integrals over the distribution function of surface dislocation on $x-axis$, as follows :

$$\phi_{jr}(z_j) = \int_{-\infty}^{+\infty} B_j(x)\log(z_j - x)dx \tag{22}$$

where $j = 1,2$. Since the stresses are determined in terms of the derivatives of two complex potentials, it is convenient to develop an expression for $\phi'_{jr}(z_j)$, which is written as :

$$\phi'_{jr}(z_j) = \int_{-\infty}^{+\infty} \frac{B_j(x)}{z_j - x}dx \tag{23}$$

where, again, B_j is determined in terms of $f_1(x)$ and $f_2(x)$ using equations (12). Omitting mathematical details, expressions for $\phi'_{1r}(z_1)$ and $\phi'_{2r}(z_2)$ are obtained as follows :

$$\phi'_{1r}(z_1) = \left(\frac{2ic_{12}}{a_1}\right)\left[\frac{\bar{\lambda}_1\bar{A}_1}{z_1 - \bar{z}_{1o}} + \frac{\bar{\lambda}_2\bar{A}_2}{z_1 - \bar{z}_{2o}}\right] + \left(\frac{-2c_{11}}{a_2}\right)\left[\frac{\bar{A}_1}{z_1 - \bar{z}_{1o}} + \frac{\bar{A}_2}{z_1 - \bar{z}_{2o}}\right]$$

$$;(z_1 \in D^+),$$

$$= \left(\frac{2ic_{12}}{a_1}\right)\left[\frac{\lambda_1 A_1}{z_1 - z_{1o}} + \frac{\lambda_2 A_2}{z_1 - z_{2o}}\right] + \left(\frac{-2c_{11}}{a_2}\right)\left[\frac{A_1}{z_1 - z_{1o}} + \frac{A_2}{z_1 - z_{2o}}\right]$$

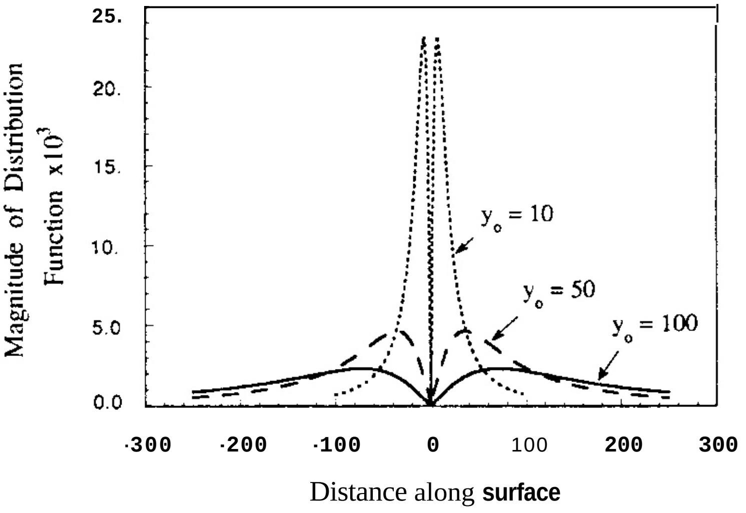

Figure 5: Magnitude of $F(x)$ as a function of distance along the surface for different positions of the dislocation $(z_0 = +iy_0)$. The Burger's vector is real

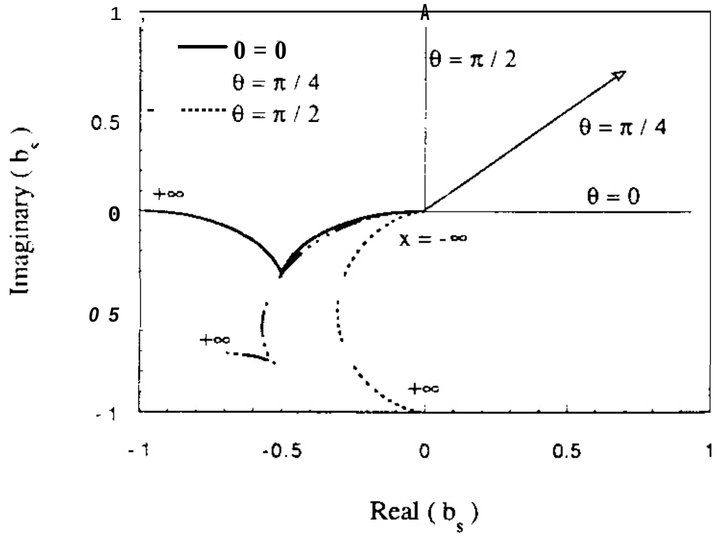

Figure 6: Argand diagram for b_s as given by (21) for three different orientations of the Burger's vector b. The curves represent $b_s(x)$, where x varies form $-\infty$ to +m. The arrows represent the Burger's vectors b of the lattice dislocation. As $x \to +\infty b_s \to -b$.

$$; (z_1 \in D^-) \tag{24}$$

$$\phi'_{2r}(z_2) = \left(\frac{2ic_{22}}{a_1}\right)\left[\frac{\bar{\lambda}_1\bar{A}_1}{z_2 - \bar{z}_{1o}} + \frac{\bar{\lambda}_2\bar{A}_2}{z_2 - \bar{z}_{2o}}\right] + \left(\frac{-2c_{21}}{a_2}\right)\left[\frac{\bar{A}_1}{z_2 - \bar{z}_{1o}} + \frac{\bar{A}_2}{z_2 - \bar{z}_{2o}}\right] \quad ; (z_2 \in D^+),$$

$$= \left(\frac{2ic_{22}}{a_1}\right)\left[\frac{\lambda_1 A_1}{z_2 - z_{1o}} + \frac{\lambda_2 A_2}{z_2 - z_{2o}}\right] + \left(\frac{-2c_{21}}{a_2}\right)\left[\frac{A_1}{z_2 - z_{1o}} + \frac{A_2}{z_2 - z_{2o}}\right] \quad ; (z_2 \in D^-) \tag{25}$$

The two derivatives $\phi'_{jr}(z_j), j = 1, 2$ are *regular* everywhere in the entire z_1 and z_2 (or z) planes, including boundary points because the poles lie outside the respective domains. The total field is now constructed as the superposition of *the singular and regular fields,* as follows:

$$\phi'_j(z_j) = \phi'_{js}(z_j) + \phi'_{jr}(z_j) \tag{26}$$

where $\phi'_{js}(z_j)$ are given by equations (6). The stress tensor components in the half-plane are given by equations (2), where derivatives of the complex potential functions are given by equations (26). With some laborious algebra, the derivatives of the total potentials given by **(26)** can be shown to be identically zero at any point in the lower half-plane $(Im(z) \leq 0)$. The stress tensor components, σ_x, σ_y and σ_{xy}, will therefore vanish outside the domain boundary.

Figures (7), (8) and (9) show equi-stress contours for different stress components for a dislocation in a semi-infinite domain. x and y refer to the real and imaginary axes of the complex z-plane, respectively. The stresses and distances are normalized to the shear modulus $G_{12} = 1/s_{66}$, of the material, and the magnitude of the Burger's vector, respectively. Only zero stress contours of the stress components σ_y and σ_{xy} intersect with the boundary (real-axis), which means that the stress field satisfies the free traction boundary condition. These results illustrate the usefulness of the powerful complex potential field theory, when contrasted with the method of image dislocations [9], analytic continuation techniques (33,34]and spectral expansion methods [42]. In the immediate neighborhood of the dislocation, the singular stress component (infinite domain field) dominates, which is clearly shown by the behavior of the contour lines close to the point z_o.

Green's function for a dislocation in a rectangular orthotropic domain

In this section the Schwarz-Christoffel transformation, which maps the upper half-plane onto a polygon, will be applied to the semi-infinite domain solution to obtain the solution in a rectangular domain. We will consider the case where the boundaries of the rectangular domain are free of tractions. If a set of surface tractions are subsequently applied, a convenient method can be used, and the total solution is obtained by superposition.

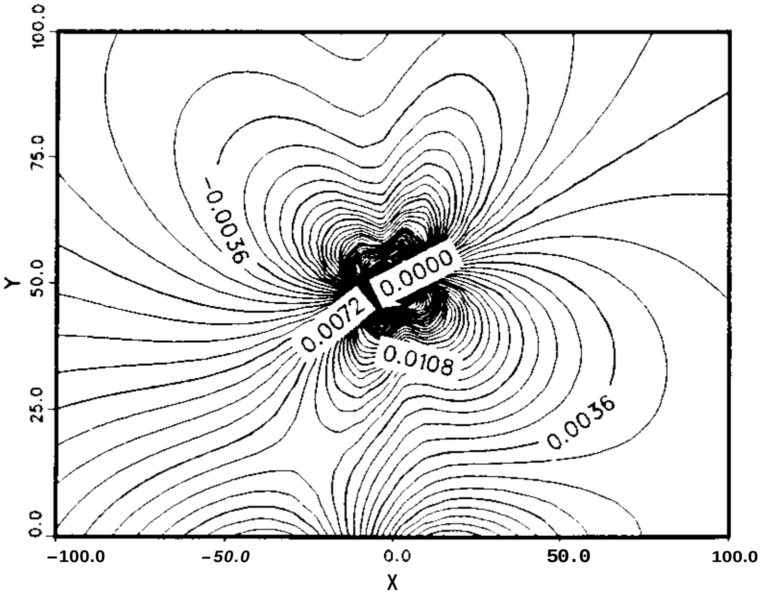

Figure 7: σ_x for **a** dislocation ($b = e^{i\pi/4}, z_0 = +50i$) in **a** semi-infinite domain. The free surface **is** the real axis.

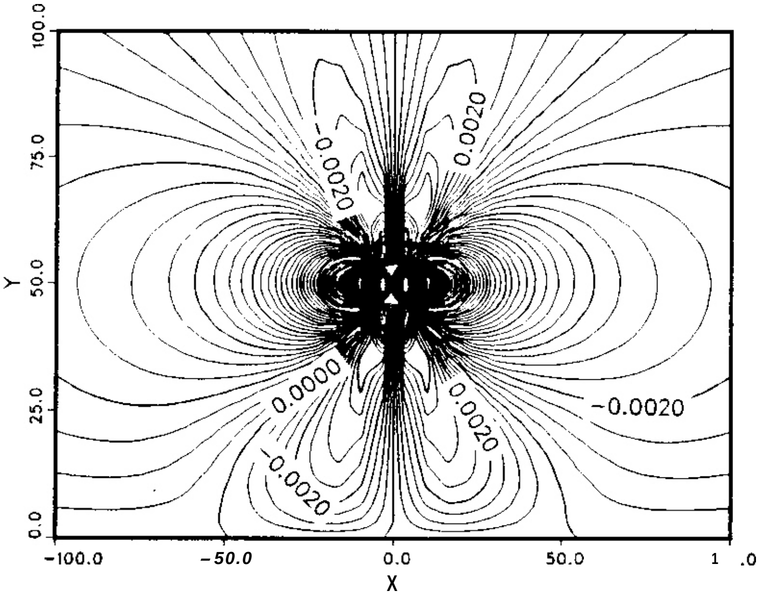

Figure 8: σ_{xy} for a dislocation ($b = e^{i\pi}, z_0 = +50i$) **in** a semi-infinite domain. Only zero stress contours intersect with the free surface (real axis)

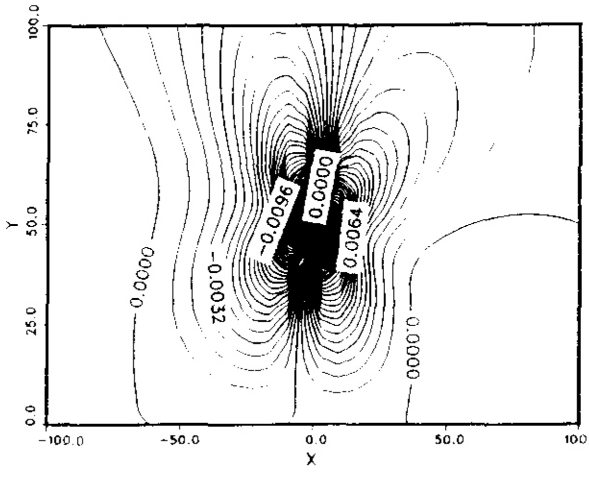

Figure 9: σ_y for a dislocation $(b = e^{i\pi/4}, z_0 = +50i)$ in a semi-infinite domain. Only zero stress **contours** intersect with the free surface (real axis).

The Schwarz-Christoffel transformation

The general form of the Schwarz-Christoffel transformation is written **as** [35-37] :

$$w = f(z) = C_1 \int_o^z \prod_{j=1}^{n} (z - a_j)^{\alpha_j - 1} dz + C_2 \tag{27}$$

This transformation maps the upper half of the r-plane onto a polygon on n vertices in the w-plane. $C_{1,2}$ are complex constants which adjust the size, orientation and location of the polygon. The points $a_j$on the $x - axis$ (z-plane) transform to the vertices of the polygon, and $\alpha_j\pi$ are the interior angles of the polygon. With this transformation, solutions in polygonal domains ($e.g.$ hexagons, pentagons, etc) can be obtained from the semi-infinite domain solution.

In the special case of a rectangle, $a, = \frac{1}{2}$, and n = 4. Equation (27) can be written as [36] :

$$\begin{aligned} w = f(z) &= \int_o^z \frac{d\xi}{\sqrt{(1-\xi^2)(1-k^2\xi^2)}} \\ &= F(z,k) \qquad ; o < k < 1 \end{aligned} \tag{28}$$

where $F(z,k)$ is the elliptic integral of the first kind [45, 46]. The integral **(28)** maps the upper half of the z-plane onto a rectangle in the w-plane for any k, Figure (IO). The vertices of the rectangle in the w-plane are $\pm K(k)$ and $\pm K(k) + iK(k')$; $k^2 + k'^2 = 1$, where $K(k)$ is a complete elliptic integral of the first kind, which is written **as** :

$$K(k) = \int_o^1 \frac{d\xi}{\sqrt{(1-\xi^2)(1-k^2\xi^2)}} \tag{29}$$

and $K(k')$ is the complementary complete elliptic integral of the first kind defined by **(29)** for k'. The vertices of the rectangle are mapped to the points ± 1 and $\pm 1/k$, on the $z - axis$ in the z-plane.

Let the actual rectangular domain which contains the dislocation be defined in the w^*-plane, where $w^* = u^* + iv^*$, as shown in Figure (10). Let the vertices of the rectangle be given by $\pm H_1$ and $\pm H_1 + iH_2$, which correspond to the four vertices in the w-plane. Consequently, it is necessary to establish a relationship between the w^*-plane and the w-plane before actually using equation **(28)** to

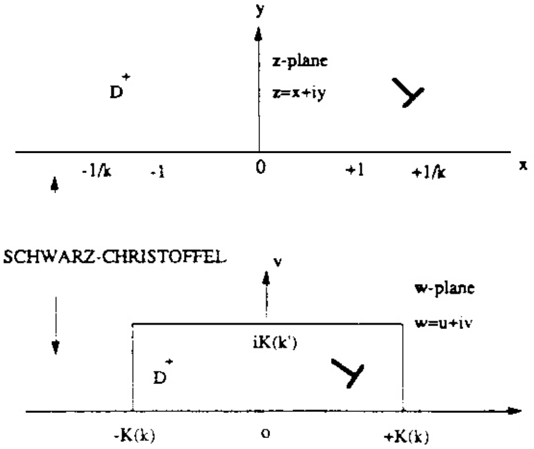

Figure 10: Schematic of the different complex planes and their interrelationships

perform the mapping. In fact the mapping process will be multi-step, from w^*-plane to the w-plane, and then to the z-plane. Let the w^* and the w (where $w = u + iv$) be related as follows :

$$
\begin{aligned}
u^* &= \frac{H_1}{K(k)}u, \\
v^* &= \frac{H_2}{K(k')}v, \\
w^* &= u^* + iv* = \frac{H_1}{K(k)}u + i\frac{H_2}{K(k')}v
\end{aligned}
\tag{30}
$$

If we arbitrarily choose $\frac{H_1}{K(k)} = \frac{H_2}{K(k')} = c$, *i.e.*, $w^* = cw$, then the transformation between the w^* and w-planes is linear, where the constant c will be determined once the parameter k is determined. The latter is found by solving the following transcendental equation :

$$\frac{H_2}{H_1} = \frac{K(k')}{K(k)} \tag{31}$$

where $k^2 + k'^2 = 1$

Field quantities in a rectangular domain

The fundamental stress combinations, Θ_z and Φ_z, in the z-plane are written as [38, 40] :

$$
\begin{aligned}
\Theta_z &= \sigma_y + \sigma_x, \\
\Phi_z &= \sigma_y - \sigma_x + 2i\sigma_{xy}
\end{aligned}
\tag{32}
$$

Under conformal transformation from the z-plane to the w-plane, the fundamental stress combinations transform according to the following relations :

$$
\begin{aligned}
\Theta_w &= \Theta_z, \\
\Phi_w &= \Phi_z e^{2i\psi}
\end{aligned}
\tag{33}
$$

It is clear that Θ_z is an invariant of the transformation, while Φ_z has the transformation Jacobian given by:

$$e^{2i\psi} = \left(\frac{dz}{dw}\right) / \left(\overline{\frac{dz}{dw}}\right) \tag{34}$$

The stress components in the w-plane are determined in terms of Θ_w and Φ_w as follows :

$$\begin{aligned}\sigma_u &= \frac{\Theta_w}{2} - \frac{1}{4}\left(\Phi_w + \bar{\Phi}_w\right), \\ \sigma_v &= \frac{\Theta_w}{2} + \frac{1}{4}\left(\Phi_w + \bar{\Phi}_w\right), \\ \sigma'''' &= -\frac{i}{4}\left(\Phi_w - \bar{\Phi}_w\right)\end{aligned} \tag{35}$$

Since the transformation between the w and w^* plane is linear with the constant c is real, the corresponding jacobian is unity and, in turn, the field quantities are identical in these two planes. The derivative $\frac{dz}{dw}$ is found from **(28)** as :

$$\frac{dz}{dw} = \sqrt{(1-z^2)(1-k^2z^2)} \tag{36}$$

The transformation works as follows: to determine the stress field at a point w^*, w is found using equation (30) **as** w $= w^*/c$ then the inverse of the relation (28) is used to find z. Once z is determined, equations **(32)** through (35) are used to completely determine the stress field in the w-plane (*i.e.*, in the w^*-plane). The inverse of the relation **(28)** is known as the **Jacobi** elliptic sane function, which is written as follows:

$$z = sn(w, k) \tag{37}$$

The form of the elliptic sine function, and the associated numerical accuracy of the computation are given in [39]. Note that the dislocation solution in the w-plane is recovered from the solution in the r-plane. Let the displacement vector in the $z-$ and w-planes be denoted by $\mathcal{U}_z$ and $\mathcal{U}_w$, respectively.The displacement vector transforms as :

$$\mathcal{U}_z = \mathcal{U}_w e^{i\psi} \tag{38}$$

The Burger's vectors must have the same relation. Let the burgers vector in the $z-$ and w-planes be denoted by b_z (at the point z_o) and b_w (at the point w_o), respectively. Therefore, the Burger's vector in the z-plane is given by :

$$b_z = b_w e^{i\psi} \tag{39}$$

where b_w is the prescribed one, and ψ is given by **(34)** evaluated at z_o.

Discussion **and** Conclusions

Representative results for the stress field in a rectangular orthotropic domain are shown in figures (11) through (16). u^* and v^* refer to the real and imaginary axes of the complex w^* plane, which is the actual domain of the dislocation. The stresses are normalized to the shear modulus G_{12}. In calculating the stress field a value of k^2 = 0.5 is chosen, for which $K(k) = K(k')$ = 1.85407467. ***It*** is important to note that the shear and normal stresses identically vanish on the domain boundary. **Also,** the stress field shows the proper singularity at the location of the dislocation (Fig. (16).

The solution presented here is general in the sense that it accounts for the domain orthotropy and geometry effects, which is an essential factor in boundary value problems of elasticity, as well **as** the arbitrariness in specifying the Burger's vector (magnitude and direction). The solution can be easily extended to domains of general anisotropy. With this solution, a large number of materials macro/micromechanics problems can be accurately treated in the sense that more realistic dislocational fields in domains of finite sizes (present work) can replace the infinite domain field. Among these problems are the following :

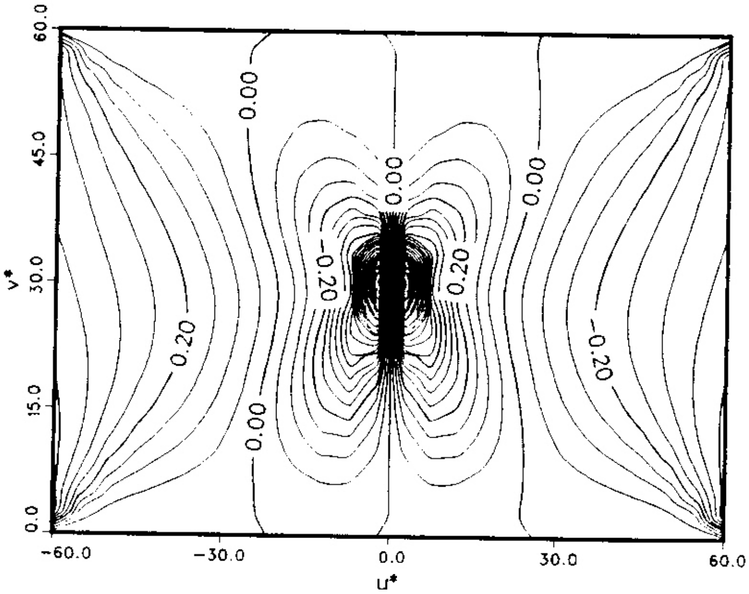

Figure 11: σ_{v^*} for a dislocation $(b = e^{i\pi/2}, w_0^* = +30i)$ in a rectangular domain. σ_{v^*} identically vanishes on the upper and lower sides of the rectangle.

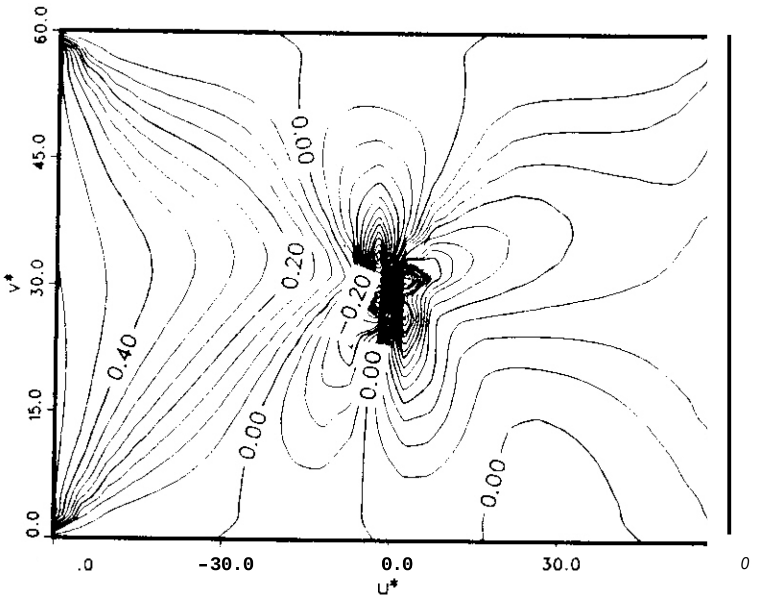

Figure 12: σ_{v^*} for a dislocation $(b = e^{i\pi/6}, w_0^* = +30i)$ in a rectangular domain. σ_{v^*} identically vanishes on the upper and lower sides of the rectangle.

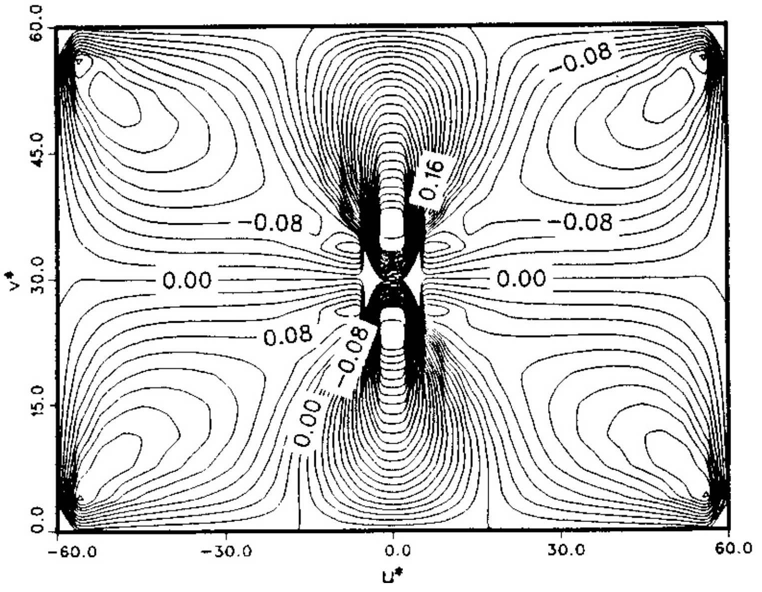

Figure **13:** $\sigma_{u^*v^*}$ for a dislocation $(b = e^{ix/2}, w_0^* = +30i)$ in a rectangular domain. $\sigma_{u^*v^*}$ identically vanishes on all sides of the rectangle.

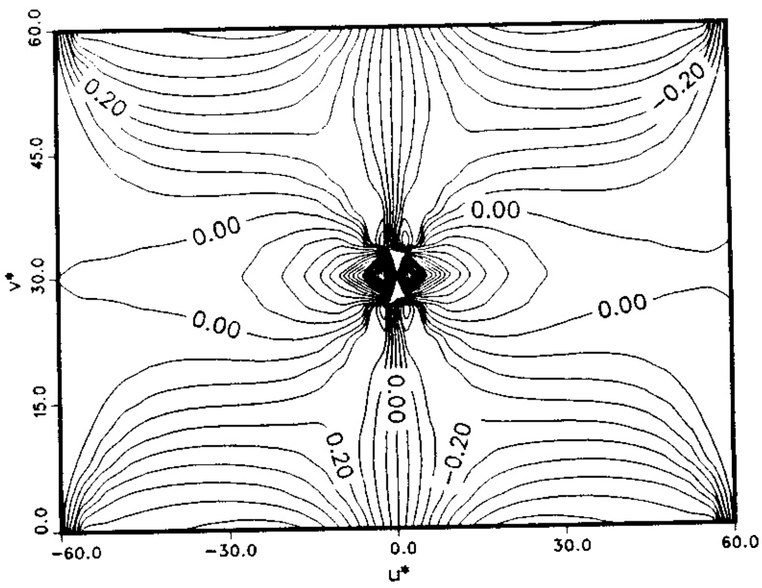

Figure 14: σ_{u^*} for a dislocation $(b = e^{ix/2}, w_0^* = +30i)$ in a rectangular domain. $\sigma_{u^*_{v^*}}$ identically vanishes on the right and left sides of the rectangle.

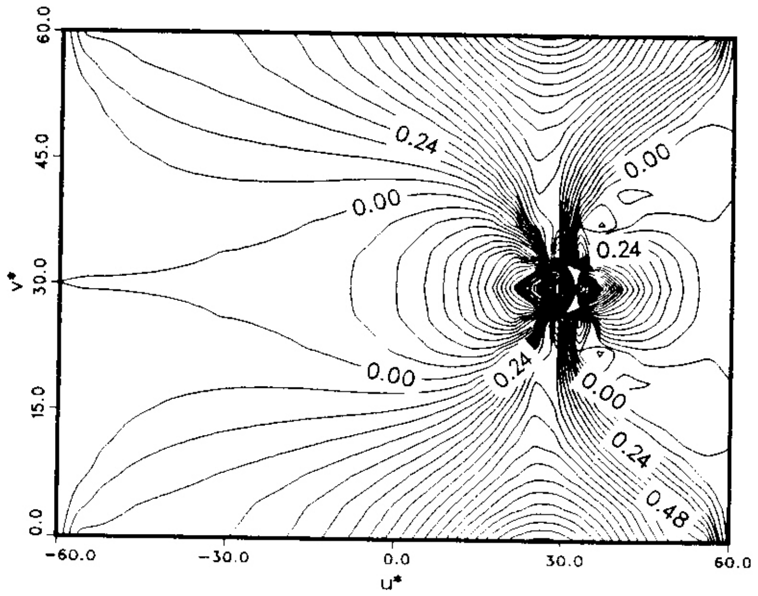

Figure 15: σ_{u^*} for a dislocation $(b = e^{i\pi/2}, w_0^* = 30+30i)$ in a rectangular domain. σ_{u^*} identically vanishes on the right. and left sides of the rectangle.

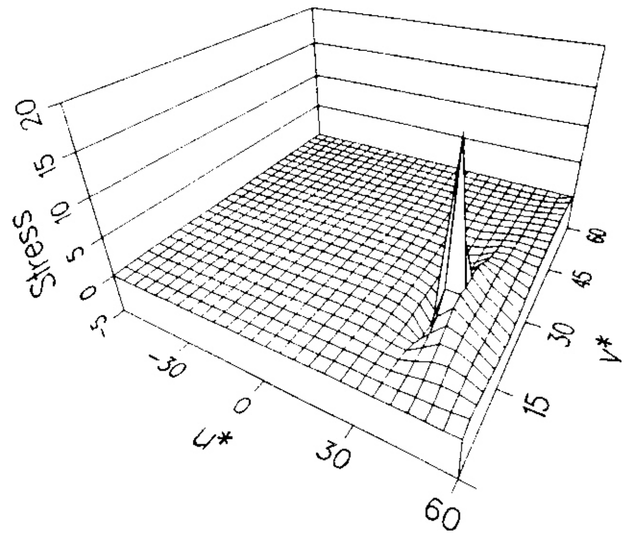

Figure **16:** σ_{u^*} for a dislocation $(b = e^{i\pi/2}, w_0^* = 40+30i)$ in a rectangular domain showing the singular behavior of the stress field at w_0.

1. Elastic and elastic-plastic fracture mechanics problems, where cracks of any size, shape and under generalized loading are modeled using distributions of dislocations, in finite size structural elements. Ref. [27] contains a list of the most important applications of dislocation theory in fracture. The reader is also advised to check the book written by Lardner [19] as well as Bilby and Eshelby's article [29].
2. Dislocation-crack interaction problems, such as the spread of plastic yield from crack tips [47], cleavage, dislocation emission and crack shielding under generalized loading conditions [48]
3. Problems of micromechanics of plasticity and viscoplasticity (dislocation creep), which involve detailed description of dislocation motion as well as dislocation-dislocation interactions in real crystals or in specimens of finite sizes [15, 16, 49].

A major outcome of the present work is that it demonstrates the weakness of the infinite domain dislocation solution in a large number of problems in which the range of interest for the dislocational field is comparable to the domain size. This is illustrated in figure (11), where the stress component σ_{v^*} changes between tensile and compressive on one side of the v^* axis, which is not a feature of the infinite domain solution. **Also,** a rotation of the burgers vector can dramatically change the features of the stress field for the same geometry. This is shown by comparing figures (11)and (12). Another important effect is the behavior of the stress field close the domain corners and edges (Figs. (13)to (15)).

It must be noted that the general method developed in this paper is also applicable for obtaining the Green's function for screw dislocations, and for dislocations of mixed-mode character in finite domains

FUTURE WORK

The method will he applied to solutions for the elastic stress field, crack opening displacement and stress intensity factors for cracks in Sic-Sic composites under mixed mode I/II loading conditions.

References

[1] G. Weingarten, *Atti Accademia Nazionale die Lincie* 10(1901)57-61.
[2] A. Timpe, *Zeitschrift fur Mathematik und Physik* 52(1905) 348-383.
[3] V. Volterra, *Annale Scientifiques de l' Ecole Normale Superieure*(Paris) 24(1907)401-517.
[4] A. E. H. Love, *A Treatise on the Mathematical Theory of Elasticity*, Cambridge University Press, Cambridge, (1927).
[5] Th. v. Karman and L. Föppl, *Enzyklopadie Der Mathematischen Wissenschaften Mechanak* 4(1913)695-770.
[6] L. Prandtl, *Zeitschrift* **fur** *Angewandte Mathematik und Mechanik* 8(1923)85-106.
[7] G. I. Taylor, *Transactions of the Faraday Society* 24(1928)121-125.
[8] **E.** Orowan, *Diplomarbeit,* T. H. S. Berlin (1929).
[9] J. P. Hirth and J. Lothe, *Theory of Dislocations*, Second Edition, John Wiley and Sons (1982).
[IO] F. R. N. Naharro, *Dislocations in Solids,* North-Holland Publishing Company, 1979.
[11] M. J. Marcinkowski *et al* , *Physica Status Solidi* (a) 17(1973) 423-433.
[12] M. J. Marcinkowski *et al* , *Physica Status Solidi* (a) 18 (1973) 361-375.
[13] K. Jagannadham and M. J. Marcinkowski, *Journal of Materials Science* 15 (1980) 563-574.
[14] K. Jagannadham and M. J. Marcinkowski, *Journal of Materials Science* **14** (1979) 1717-1732.
[15] R. J. Amodeo and N. M. Ghoniem, *Physical Review E,* 41(1990) 69586967.
[16] R. J. Amodeo and N. M. Ghoniem, *Physical Review B*, 41(1990) 6968-6976.

[17] T. Mura, in *Advances in Materials Research*, vol. 3, Editor: H. Herman, John Wiley and Sons (1968)1-108.

[18] T. Mura, *Micromechanics of Defects in solids*, Martinus Nijhoff Publishers (1987).

[19] R. W. Lardner, *Mathematical Theory of Dislocations and Fracture*, University of Toronto Press (1974).

[20] A. N. Stroh, *Philosophical Magazine* 3(1958)625-646.

[21] J. Qu and Q. Li, *Journal of Elasticity* 26(1991)169-195.

[22] J. R. Willis, *Journal of Mechanics and Physics of Solids* 19(1971)353-368.

[23] F. Delale and F. Erdogan, International Journal *of Fracture* 20(1982)251-265.

[24] R. W. Lardner, *International Journal of Fracture Mechanics* 4(1968)299-319.

[25] C. Atkinson, *International Journal of Fracture Mechanics* 2(1968)567-575.

[26] V. Vitek, *International Journal of Fracture* 13(1977)481-501.

[27] V. Vitek and G. G. Chell, in *Dislocation Modelling in Physical Systems*, Proceedings of International Conference, Gainesville, Florida, USA, June 22-27, 1986. Editor: M. F. Ashby, R. Boullough, C. S. Hartly, and J. P. Hirth (1986) 92-109.

[28] K. Jagannadham and M. J. Marcinkowski, *Unified Theory* of *Fracture*, Trans Tech Publications (1983).

[29] B. A. Bilby and J. D. Eshelby, in *Fracture, An Advanced Treatise*, Vol. 1, Editor : H. Liebowitz, Academic Press, New York and London (1968)99-182.

[30] K. Jagannadham and M. J. Marcinkowski, *Physica Status Solidi* (a) *50* (1978) 293-302.

[31] K. Jagannadham and M. J. Marcinkowski. *Journal of Materials* Science 14 (1979) 1052-1070.

[32] K. Jagannadham and M. J. Marcinkowski, *Materials* Science *and* Engineering *38* (1979) 259-270.

[33] G. R. Miller, *Journal of Applied Mechanics* 53 (1966) 368-389.

[34] J. C. Lee, *Engineering Fracture Mechanics* 37(1990) 209-219.

[35] L. Volkovyski, G. Lunts, and I. Aramanovich, *Problems in the Theory of Functions of a Complex Variable*, Mir Publishers, Moscow (1972).

[36] Zeev Nehari, *Conformal Mapping*, Dover Publications Inc, New York (1952).

[37] Ruel V. Churchill and James Ward Brown, *Complex Variables and Applications*, Fifth Edition, McGrow-Hill (1990).

[38] L. M. Milne-Thomson, *Plane Elastic Systems*, Springer Verlag (1968).

[39] A. El-Azab and N. M. Ghoneim, Green's *Function* for *the Elastic Field of an Edge Dislocation in a Finite Orthotropic Medium*, accepted for publication in Int. J. Fract. 1993.

[40] N. I. Muskhelishvili, Some *Basic Problems of the Mathematical Theory of Elasticity*, P. Noordhoff Ltd. (1963).

[41] N. I. Muskhelishvili. *Singular Integral Equations*, Moscow (1946).

[42] R. Solecki, in *Yamada Conference IX* on *Dislocations in Solids*, Editor : H. Suzuki, University of Tokyo Press (1985)25-28.

[43] J. A, Dicarlo and Gregory N. Morscher, in Failure *Mechanisms in High Temperature Composite Materials*, AD - Vol - 122, ASME (1991)15-22.

[44] T. D. Gulden, *Journal of the American Ceramic Society* 52(1969) 585-590.

[45] M. Abramowitz and I. A. Stegun, *Handbook* of *Mathematical Functions with Formulas, Graphs and Mathematical Tables*, Ninth Edition, Dover Publications Inc, New York (1972).

[46] Harold T. Davis, *Introduction to Nonlinear Differential and Integral Equations*, Dover Publications Inc, New York (1962).

[47] V. Vitek, *Journal Mechanics and Physics of Solids* 24(1975)67-76.

[48] I.-H. Lin and R. Thomson, *Acta Metallurgica* 34 (1986)187-206.

[49] E. H. Jordan and K. P. Walker, *Journal of Engineering Materials and Technology* ASME 114(1992)19-26.

5.0 RADIATION EFFECTS, MECHANISTIC STUDIES, THEORY AND MODELING

FACTORS WHICH CONTROL THE SWELLING OF Fe-Cr-Ni TERNARY AUSTENITIC ALLOYS - F. A. Garner and D. J. Edwards (Pacific Northwest Laboratory)[a].

OBJECTIVE

The objective of this effort is to determine the factors which control the response to irradiation of materials used in fusion environments.

SUMMARY

In agreement with limited earlier studies. a comprehensive irradiation experiment conducted in EBR-II demonstrates that while cold-working decreases swelling of Fe-15Cr-XNi (X=12-45 wt%) alloys at relatively low irradiation temperatures. It Increases swelling at higher temperatures. Aging of cold-worked specimens to produce polygonized dislocation networks tends to further increase swelling, especially at higher nickel (>25%) levels. Swelling at lower nickel levels also appears to be sensitive to details of the annealing treatment.

PROGRESS AND STATUS

Introduction

There is a very general perception. developed primarily from research an stainless steels, that cold-working a metal prior to irradiation always reducer swelling. exerting a monotonic but diminishing Influence with increasing cold-work level. It is also generally accepted that factors which promote void nucleation, such as high helium generation rates. can at least partially overcome the suppressive effect of cold-work an void nucleation.

In a recent review[1], however. it was shown that the role of starting dislocation density and dislocation arrangements, as well as their interactions with variables such as helium generation rate. are much more complex than previously assumed. In many cases. cold-working can actually increase swelling, especially in pure metals such as Ni and Al and also in simple ternary and quaternary austenitic alloys.[1]

instead of delaying swelling, Garner and coworkers have recently shown that cold-working often increases swelling of Fe-Cr-Ni model alloys, especially under conditions where void nucleation is relatively difficult, i.e., for relatively high nickel or phosphorus levels and at relatively high irradiation temperatures[2,3]. At lower nickel levels and temperatures, where Void nucleation is relatively easy, cold-working usually reduces swelling.

The current interest in cold-work's Influence On swelling arises rom the use of both annealed and cold-worked alloys in on-going isotopic tailoring[4] and spectral tailoring.'.'' experiments directed toward determining the separate and synergistic influence of helium on radiation-induced microstructural evolution in competition with 'various important material and environmental variables.

To aid in the understanding of such relationships, a series of Fe-Cr-Ni specimens irradiated in the EBR-II AA-14 experiment was examined. Seven Fe-15Cr-XNi alloys (X=12-45 wt%) were irradiated in the form of 3 mm microscopy dirks at 425°C to 31 dga and to 32 dpa at 500 and 600°C. Each alloy was irradiated side-by-ride in three conditions: annealed (975 C/10 min/WQ), 30% cold-worked, and 30% cold-worked and aged (650°C/10 hr/WQ) Measurements of density changes were made using an immersion density technique known to be accurate to ±0.16% change in density.

The swelling values calculated from measured density changes are presented in Figure 1. The fallowing features of these data should be noted.

1. The strong decrease of swelling with increasing nickel content usually observed in Fe-Cr-Ni austenitic alloys is preserved in this experiment in all three starting conditions, but with one important exception. Note that In eight of the nine sets of data, swelling decreases at the lowest nickel levels, producing a peak in swelling vs. nickel content.

2. The swelling at 31-32 dpa of annealed Fe-Cr-Ni steels at 425 and 500°C is relatively independent of temperature. but decreases significantly at 600°C, in agreement with earlier studies(7)

---

[a] Pacific Northwest Laboratory is operated far the U. S. Department of Energy by Battelle Memorial Institute under Contract DE-AC06-76RLO 1830

3. Swelling is decreased by cold-working at 425 and 500°C but at 600°C it is increased at higher nickel levels.

4. Under some conditions. cold-working followed by aging can also significantly increase swelling.

Discussion

The peak in swelling observed at 12-15% nickel is inconsistent with the behavior observed in earlier studies:", where swelling either increased monotonically with decreasing nickel content, or exhibited a plateau at low nickel levels and relatively low temperatures. It is felt that this difference may arise from the fact that the specimens in the earlier study were better annealed. 1030°C for 0.5 hr and air cooled, as opposed to the 975°C for 10 min and water quenched treatment used in the current study. One possible consequence of this difference is the fact that specimens appeared to be increasingly magnetic at lower nickel levels. as indicated by their interactions with the electron beam during microscopy examination. The cold-worked and aged specimen at 12% Ni did not exhibit magnetic behavior in the unirradiated condition, while the annealed and the cold-worked specimens were found to be very magnetic. Thus. there is an apparent correlation of magnetic behavior with the peaked swelling behavior observed at 425°C.

in the review mentioned earlier.[1] it was shown that the role of cold-work in increasing swelling arose from the establishment of stable dislocation networks at higher temperatures where networks are slow to develop from radiation alone. The influence of aging was thought to be in the development of polygonal cellular dislocation-networks, with relatively dislocation-free areas for void nucleation to occur within the cells. Preliminary results of microscopy examination confirm that this interpretation is valid for the Fe-Cr-Ni alloys irradiated in the AA-14 experiment.

Future Work

Microscopy analysis of starting dislocation microstructures will proceed

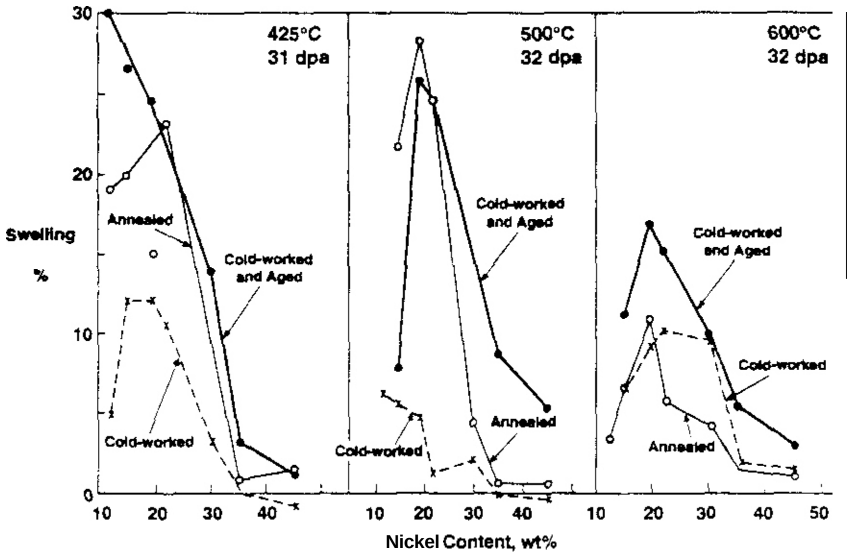

Fig 1. Swelling observed in Fe-15Cr-Ni alloys irradiated in EBR-II as part of the AA-14 experiment

REFERENCES

F A. Garner, "Evolution of Microstructure in Face Centered Cubic Metals during Irradiation: A Review," accepted for publication in J. *Nuc. Mater.*

2. F.A. Garner. M. Miyahara, J.W. Newkirk. and H. Kinoshita, *J. Nuc. Mater.*, 199 (1993) 132-142.

3 F.A. Garner and H.P. Brager. in Damage Analysis and Fundamental Studies Quarterly Progress Report. DOE/ER-0046/19 (1984) pp. 62-65.

4 M.L. Hamilton and F.A. Garner, *J. Nuc. Hater.*. 191-194 (1992) 1239-1243.

5 N. Sekimura. F.A. Garner and R.D. Griffin. J. *Nuc.* Mater., 191-194 (1992) 1234-1238.

6 M.L. Hamilton. A. Okada and F.A. Garner. *J. Nuc. Mater.*, 179-181 (1991) 558-561.

7 F A. Garner and A.S. Kumar. in Radiation-Induced Changes in Microstructure: 13th International Symposium (Part I), ASTM STP 955, F.A. Garner, N.H. Packan. and A.S. Kumar, ids.. American Society for Testing and Materials, Philadelphia PA. 1987, pp. 287-314.

THE INFLUENCE OF COLD WORK LEVFL ON SWELLING OF PURE COPPER *IRRADIATED* BY FAST NEUTRONS OK ELECTRONS - *F.* **A.** Garner (Pacific Northwest Laboratory[1]) and **B.N.** Singh (Risø National Laboratory).

OBJECTIVE

The objective of this effort is to determine the factors which influence the radiation **response** of copper high **heat** flux components in fusion reactors.

SUMMARY

Pure copper has been irradiated in **a** variety of starting conditions by either 1.0 MeV electrons or fait neutrons in FFTF-MOTA. Electron irradiation at 250 and 350°C produces a non-monotonic swelling behavior as **a** function of Cold work level. increasing Swelling at lower cold-work levels and decreasing swelling at higher cold-work **levels**. In FFTF at 365 and 430°C, **however,** 10% cold-work **reduces** Swelling initially. *with* little *additional* Influence at higher cold-work levels. Swelling at 520 and 600°C is less than 1% **at** 35.9 and 13.6 dpa, respectively, with little effect of cold work level.

PROGRESS AND STATUS

Introduction

Leffers. Singh, and Barlow showed that the swelling of pure copper (99.999%) during electron irradiation was sensitive to cold-work **level** at 250 and 350°C.[1] As **shown** in Figure 1, both the incubation period **and** steady-state swelling **rate were** functions of cold work level. In general, cold-working first increased swelling **at** there temperatures, but the swelling reached a peak and then declined With increasing cold work.[2]

It was not certain. however, that such behavior would be typical of that expected at the higher temperatures and **lower** displacement rates typical of neutron irradiation. Therefore. *specimens* that **were** archives of those employed in the electron study **were** irradiated in FFTF **NOTA-28** at 365, **423.** 520 and 600°C. The starting conditions used in the FFTF study **were** annealed (600°C for 2 hrs), 10, 25 and 50% cold-worked. and ***25%*** cold work followed by aging at 300°C for 2 hrs. The specimens **were** irradiated in the form of standard *3* mm microscopy dirks contained in sealed helium-filled **stainless** steel capsules. Density changes **were** measured using **an immersion** technique known to be accurate to ±0.16% swelling.

Results and Discussion

Figures 2a **and** 2b show the swelling **observed** in neutron-irradiated pure capper as **a** function of irradiation temperature and cold-work **level**. At 365 **and** 433°C and **47.3** and 16.9 dpa, respectively, swelling is initially reduced by 10% cold-working, With very little influence of cold-work observed at higher levels. Based on density measurements. there appears to be **a** mall amount of swelling at 570 and 600 C. but the Influence of cold-work level is small. The small peak at 520°C for 13% cold work may represent some measurement **error.** Microscopy is necessary to confirm that swelling and not transmutation is responsible for the observed small ***changes in*** density at 520 ***and*** 600°C. *Aging at* **300°C** for *2 hrs* appeared to have no significant effect on swelling of 25% cold-worked copper.

The different behavior with respect to cold-nark level observed in electron and neutron irradiations may **arise** from the differences in temperature and displacement rate **employed** in the two types of experiments. Another possible factor may be the strong **role** played by the two specimen surfaces on dislocation evolution in the very thin foils employed during electron Irradiation. Loss of dislocations to the surface will be large, and pre-existing cold-work induced dislocation networks **may** assist in the development and maintenance of **a** stable dislocation network during electron Irradiation. Stabilization of the dislocation *structure* against surface losses would then lead to **earlier** swelling at law cold-work levels. The absence of such surfaces during neutron irradiation would then simplify the role of cold-work an swelling, allowing it to exert its normally suppressive influence.

Future Work

Microscopy examination will proceed at the Risø National Laboratory.

REFERENCES

1. T. Leffers, B. N. Singh, and F. Barlow, Risø National Laboratory Report Risø-M-1937, May, 1977,
2. F. A. Garner et al, Fusion Reactor Materials Semiannual Progress Report DOE/ER-0313/10 (1991) pp. 186-191

---

[1] Pacific Northwest Laboratory is operated for the U.S. Department of Energy by Battelle Memorial Institute under Contract DE-AC06-76RLO 1830.

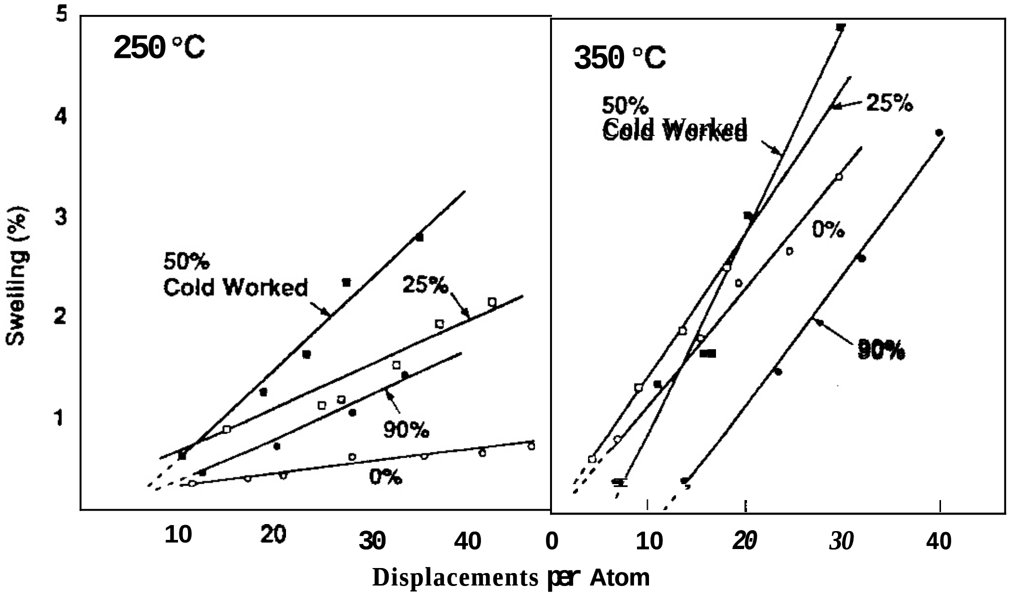

Fig. 1. Effect of cold-work level on electron-induced swelling of 99.999% cooper (1,2)

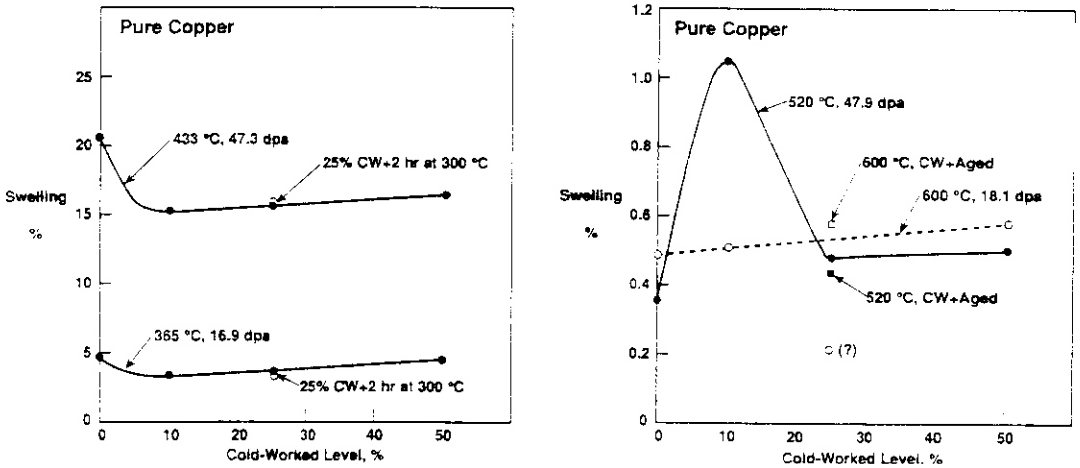

Fig. 2. Effect of cold-work level and aging on neutron-induced swelling of 99.999% copper in FFTF-MOTA

The influence of Details of Reactor History on Microstructural Development During Neutron Irradiation -

F. A. Garner, (Pacific Northwest Laboratory)[1], N. Sekimura, (Univ. of Tokyo), M. L. Grossbeck, [Oak Ridge National Laboratory). A. M. Ermi, [Westinghouse Hanford Company), J. W. Newkirk, (U. of MO-Rolla), H. Watanabe, (Kyushu University), and M. Kiritani, (Nagoya University)

OBJECTIVE

The objective of this effort is to determine the influence of irradiation temperature history on the neutron-induced evolution of microstructure in metals.

SUMMARY

Microstructurally-oriented irradiation experiments are shown in this paper to be strongly dependent on details of reactor history that frequently are not brought to the experimenter's attention. In some cases, these details can dominate the experiment so as to produce very misleading results. To aid in the design and interpretation of microstructurally-oriented experiments, a number of studies are reviewed to highlight history effects and then guidelines are presented to minimize the impact of reactor history in new experiments.

PROGRESS AND STATUS

Introduction

Materials scientists conducting experiments in nuclear reactors rely on information provided by reactor operators concerning the environment in which the experiment will be conducted. In addition to well known uncertainties associated with the determination of temperature and atomic displacement level in reactor experiments, small details of reactor operation that ensure safe, reliable operation of the reactor can often have large, unanticipated Consequences on microstructural evolution. In some cases these details can dominate the microstructural evolution and lead to misperceptions concerning the variables thought to be under study. Start-up and shut-down procedures are especially important in this respect.

The realization that previously neglected details of temperature history could exert a strong influence on microstructural evolution arose from the studies of Kiritani and coworkers, who predicted and then demonstrated that such details could dominate microstructurally-oriented experiments, especially on simple model materials.'" Using an in-core irradiation rig with active temperature control in the Japanese Materials Testing Reactor (JMTR), Kiritani showed that small increments of irradiation at lower-than-target temperatures during reactor start-up and shut-down often yielded microstructures that were completely different from those developed during totally isothermal irradiation. Two examples from Kiritani's studies are shown in figs. 1 and 2.

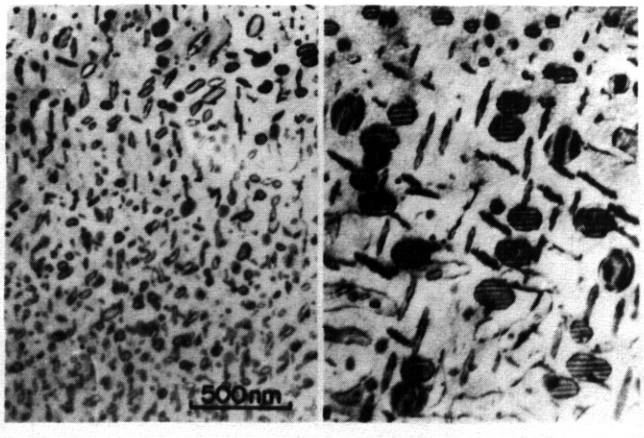

fig. 1. Ni-2at% Si. irradiated as thin foils at 400°C in JMTR. (a) Conventional control ($0.92 \times 10^{24} n/m^2$ E>1.0 MeV); (b) Improved control ($0.96 \times 10^{24} n/m^2$).[2]

---

[1] Pacific Northwest Laboratory is operated for the U.S. Department of Energy by Battelle Memorial Institute under Contract DE-AC06-76RLO 1830.

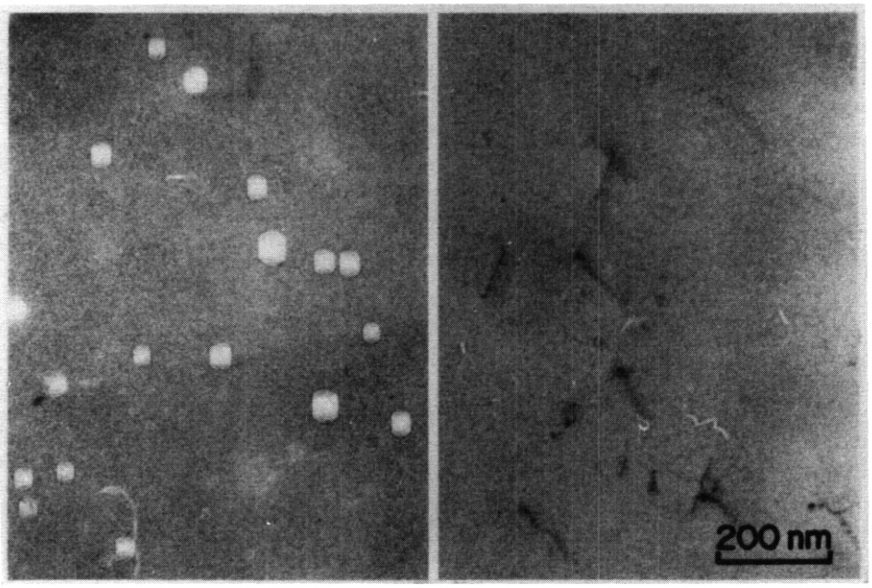

Fig. 2. Difference in void formation observed in bulk copper at 400°C. (a) Conventional control; (b) Improved control. Same dose levels as Fig. 2.

When the results of these studies were first presented in a joint Japan/U.S. Experimenters Workshop[1] as an argument that better temperature control during power ascent was required for the operation of the Materials Open Test Assembly (MOTA) in the Fast Flux Test Facility (FFTF), the U.S. side was initially very skeptical. Whereas the joint Japan/U.S. fusion materials program was very fundamentally oriented and focused strongly on low fluence microstructural response as a measure of neutron spectral recoil and transmutation effects, previous U.S. fast reactor studies had focused on macroscopic engineering property changes at high exposure. This latter approach tended to minimize the impact of small "off-normal" or transient irradiation segments.

Subsequent experience has shown, however, that Kiritani's concerns and predictions were valid. At the request of the Japanese side, the MOTA start-up procedure was modified within the limits of the MOTA design. Procedures were also chosen to minimize the impact of interim and shut-down history effects. As will be shown in this paper, however, the influence of lower-than-target irradiation temperatures still persists to some degree.

As the radiation damage community has become more sophisticated in its approach to design and interpretation of microstructurally-oriented experiments, it has become obvious that other routine and apparently inconsequential procedures during the irradiation can strongly influence the microstructural development. The experimenter is often unaware of these procedures. In some cases, the experiment itself can perturb the environment in ways that do not impact reactor operation and, therefore, do not come to the attention of the experimenter or the reactor operator. Frequently, it was the receipt of anomalous microstructural data that signaled that some facets of the irradiation environment were not as well known or as stable as originally assumed.

A series of recent examples from microstructural studies conducted in various reactors are presented in this paper, concentrating on the microstructural consequences observed in each. Guidelines are then presented to aid in minimizing the impact of temperature history and its associated uncertainties.

Impact of gamma heating

The temperature experienced in a given irradiation capsule is determined by the local coolant temperature, the gamma heating level and the thermal resistance between specimen and coolant, providing auxiliary heating or cooling is not involved. Gamma ray absorption heats materials in a manner analogous to the famous "greenhouse effect", depositing energy that crosses the capsule boundary easily as a photon but which, once converted to thermal energy, must overcome the thermal resistance of the experiment before reaching the coolant. To a first approximation the gamma heating is proportional to the reactor power

---

[1] Experimenters Workshop on FFTF/MOTA Utilization. No proceedings were issued. Workshop was held at the University of Tokyo, on August 24-26, 1987.

level, or more appropriately, to the local neutron flux. While gamma heating values are usually supplied by the reactor staff. there are most probably calculated values for an Idealized core loading and are easily perturbed by surrounding subassemblies or by the experiment itself. Many of the gamma rays arise not from fission events but from inelastic scattering events between neutrons and the coolant or solid materials in the experiment. In water-cooled reactors the major source of the gamma heating arises from neutron interactions with the water coolant. One usually knows the characteristics of the neutron spectra and fluxes better than those of the gamma ray Spectra and fluxes.

Three types of experiments can be categorized with respect to the confidence placed in their temperature history. The first of these involves those heated passively by the gamma flux and not monitored by thermocouples. Therefore, the temperatures are calculated. The second also involves passive heating but is monitored. and the third employs both active temperature measurement and control. the latter either by supplementary heating or cooling. In the first two categories the temperature will rise or fall as the local neutron and gamma fluxes change. While changes in power level will obviously cause changes in temperature, not-so-obvious changes can arise from the progressive movement of control rods, changes in surrounding experiments or fuel loading, or from the burnup of nearby fuel, which changer the power distribution within the core.

Actively controlled experiments can also suffer unwanted changes in temperature. especially those experiments that utilize changes in coolant conductivity. In general. actively heated experiments can be designed to have more flexibility than passively heated experiments in resisting changes in temperature.

Thus, for most reactor experiments the most important factors determining the irradiation temperature are the local gamma heating rate and its time-dependent history. For example, the temperature assignments reported far many early experiments conducted without thermocouples in the High flux Isotope Reactor (HFIR) were later found to be very low compared to their actual values. Because of this problem, Garner has shown that early comparisons of HFIR and fast reactor data are quite inconclusive with respect to the influence of helium an microstructural development. Whereas the original calculations far this water-moderated. highly thermalized neutron Spectrum yielded an estimate of 35 watts/gram for stainless steel. it was later determined experimentally that 54 watts per gram was a more correct value. A more recent thermal analysis indicates that the temperatures were from 70 to 125°C higher than originally calculated. The more accurate values have been used in HFIR temperature calculations since about 1981. The realization that the calculated gamma heating rate was too low arose from microstructural observations by Maziasz that the precipitate microstructures developed in 316 stainless steel during HFIR irradiation were characteristic of those at higher temperatures. especially those of the intermetallic phases

The very high gamma heating rates characteristic of HFIR and other highly thermalized water-moderated reactors leads to a very unforgiving irradiation environment. Small changes in thermal resistance during irradiation yield very large change: in temperature. Changes in gas gap width between the inner and outer capsules can arise from the temperature dependence of void swelling and irradiation creep. it high gamma heating rates, the resulting difference in temperature between the inner and outer capsule walls can be very large and therefore differential swelling can also be large. Even precipitate-related densification or dilation of the capsule walls can have a very large impact on the temperature. Swelling of the specimen Itself can also change the thermal resistance. As a consequence. the degree of data scatter is generally larger in experiments conducted in such reactors compared to those with lower gamma heating levels.

Changes in reactor operation beyond the boundaries of the reported experiment can also exert a large and sometimes unrealized Influence on both the neutron exposure and irradiation temperature. Such changes involve the sometimes strong Influence of neighboring experiments, changes in core loading patterns and changes in reflector materials over the course of long irradiation programs. Sometimes, the experimental program itself leads to significant changes in displacement rate and gamma heating. For example, the U.S. Breeder Reactor Materials Program in its buildup phase involved the progressive insertion of non-fueled Experiments in the Central region of EBR-II, displacing some of the power generation and the associated gamma heating toward the outer rows, thereby gradually lowering the temperature and neutron flux in each subcapsule. The total neutron exposures were measured and reported to the experimenters but the impact of the flux displacement on temperature changes took much longer to be realized. Thus the temperature assignments reported in many early papers had to be revised in later publications. As the irradiation program peaked and subassemblies were progressively removed, the gamma heating rate and neutron flux again Increased for the remaining experiments.

changes in irradiation temperature in a given irradiation experiment can arise not only from changes in gamma heating and thermal resistance but also from changer in coolant characteristics, often resulting from the experiment itself. Both gradual and abrupt decreases in temperature have been shown to have pronounced effects on neutron-induced microstructural evolution of stainless steels and thereby strongly enhance their void swelling and irradiation creep behavior. In this *group* of studies it was shown that a slowly failing temperature. after irradiation had initially proceeded at higher temperatures. was a very effective way to nucleate and grow the γ' (Ni_3Si) phase. formation of this sluggishly growing phase has been identified as a precursor to rapid swelling in 316 stainless steels.

The potential impact of both deliberate or unintentional changes in irradiation temperature depends not only on the steel being studied, as well as the magnitude and direction of the temperature change, but also on the accumulated exposure when the change was initiated. Sometimes the effect on microstructural evolution is small and sometimes it is very large.

Influence of details of reactor history

Even in highly thermalized reactors operating at lower power levels or in high flux fast reactors with inherently lower gamma heating rates, it is possible that substantial temperature history effects can develop in response to apparently inconsequential operations, often without the knowledge of the experimenter. The root cause of many of these situations is that most currently available reactors do not have as their primary responsibility the conduct of materials-related experiments. For instance, HFIR exists primarily to produce radioisotopes and the Fast Flux Test Facility (FFTF) operates primarily to test fast reactor fuel assemblies. Most materials experiments operate in a parasitic mode and their requirements cannot be used to dictate all aspects of operational procedure. Even more important, many reactor procedures are directed toward safety or economic considerations which cannot be relaxed to accommodate the **needs** of the **experimenter.**

For instance, reactor operators are often required to run reactivity feedback tests at a fraction of full power or to reduce the power level when off-normal conditions are detected. Reduction in power or termination of power can occur for a wide variety of reasons. For example, FFTF has experienced power interruptions as a result of minor operator errors, large brush fires in the vicinity and lightning strikes on the Pacific Northwest electrical distribution grid. HFIR has also experienced occasional shutdowns, especially during the electrical storm season.

An example of economic considerations having a strong impact on a microstructurally-oriented experiment was provided by Yoshida and co-workers, who compared the very different microstructures developed in irradiation of AISI 316 at 290°C in the Omega West Reactor and the 14 MeV Rotating Target Neutron Source (RTNS-II). The latter experiment was essentially a continuous irradiation with independent temperature control, but the Omega West Reactor was operated for a cost-effective single 8-hour shift each day, and a daily ascent to full power was required. This introduced repeated transients in atomic displacement rate and, more important, temperature. Whereas the spectral effects comparison of Heinisch on these same specimens was originally interpreted in terms of recoil spectra and the possible influence of displacement rate at higher temperatures, it appears that temperature history actually played the major role.

Even in reactors operated for long continuous periods, there are often unrecognized effects of temperature history. Kiritani, Yoshida and coworkers were the first researchers to spotlight the impact of temperature history during the early power-up stages and to clearly demonstrate experimentally the impact of such history on microstructural evolution. They showed that most of the microstructure observed in passively operated experiments to relatively low fluences was actually nucleated at lower temperatures during the power-up phase. When compared in the same irradiation sequence with the results of active temperature-controlled irradiations, the microstructures obtained in passive experiments were often found to be very different. One quote of Kiritani of significance to later sections of this paper is that "only several percent of exposure to neutrons at lower temperature was found to result in one hundred percent difference in the final defect structures in some cases, while it causes only a slight difference in others." Kiritani also demonstrated that most researchers report the bare minimum of information concerning the temperature history of their experiments, with the implicit but inadvertently incorrect assumption that a completely isothermal history was involved.

There are several ways to avoid or at least minimize the problems defined by Kiritani during the power ascent stage. One method is to employ electrical heating to bring the specimens to temperature prior to startup. This was the solution employed by Kiritani and coworkers in JMTR. In higher power reactors, however, designers are often reluctant to employ such heating, seeing it as unreliable, with the heating coils possibly degrading at higher displacement levels. An alternate approach is to ascend to power as quickly as possible. This latter method is often limited by safety and life extension considerations. For short-lived replaceable cores, such as employed in HFIR, life extension issues are not as important and therefore relatively rapid ascents are employed. As shown in Fig. 3, HFIR reached full power in ~85 minutes during an experiment designed to measure the gamma heating level. This corresponds to ~0.003 dpa, but on the average most power ascent were accomplished in ~40 minutes (0.0014 dpa). The start-up procedure in HFIR irradiations has recently been modified to use pure neon or argon as the control gas during an extended start-up in order to keep the temperature as close to the operating temperature as possible.

It is important to note, however, that HFIR undergoes core replacements approximately every twenty-two days to maintain efficient production of ^{252}Cf. (The high flux and power level in HFIR burn out the fuel in this short period). When unanticipated power outages during a core lifetime are added this means repeated descents and ascents in power during the lifetime of a high fluence experiment.

As the level of regulatory scrutiny and emphasis on safety and startup checks increases, however, the ascent to power times have tended to increase. During a six month period between March and September 1992 for instance, the fourteen ascent to power times ranged from 30 minutes to 3.6 hours. The longest period of delay in most cases involved a start up check at 10% power.

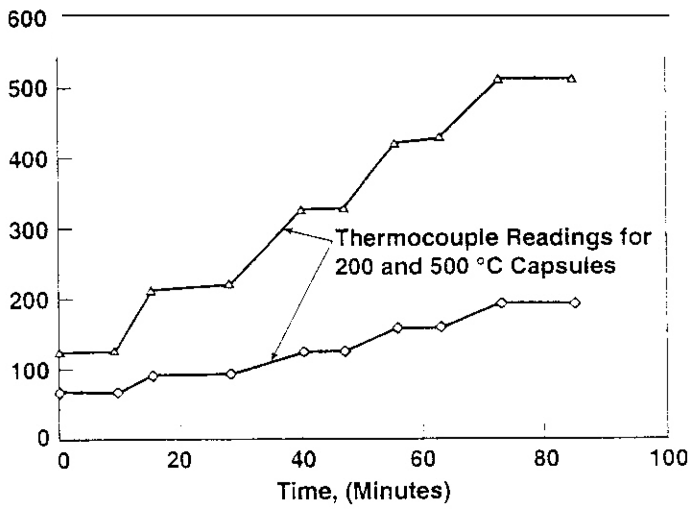

Fig. 3. Ascent to power history of the HFIR Target Nuclear Heating Experiment.

In larger cores, such as that of FFTF, the approach to power is typically on the order of 1-2 days. This is done to assess the impact of new core loadings on reactor reactivity and to minimize thermal shock of components as the temperature rises. In response to Kiritani's concerns, it was not possible to modify th power ascent procedure of FFTF but the operational procedure of the Materials Open Test Assembly (MOTA) wa modified, placing the temperature control system into operation at the earliest opportunity, instead of waiting until the reactor approaches full power. MOTA achieves temperature control to ±5°C by measuring the temperature of each canister and then modifying, if necessary, the thermal resistance by choosing varying mixtures of helium and argon cooling gases. Purging with 100% helium during reactor operation leads to the lowest possible temperature in each canister.

Since the initial studies of Kiritani, Yoshida and their coworkers in JMTR and ORR, it has come to the attention of the materials community that temperature history effects have occurred in other reactors, bot during irradiation and upon shutdown. A series of recently observed examples are given in the following sections.

Influence of FFTF shutdown procedures

Irradiations conducted using the MOTA in FFTF typically involve three one-hundred day irradiation sequences, separated by controlled shutdowns and interim zero-power periods for fuel rotation and other maintenance operations. These segments are typically designated as subcycles such as 10a, 10b and 10c, where Cycle 10 is the designation for a particular 300 day cycle.

There are a number of ways in which the MOTA temperatures and FFTF power can vary during an FFTF cycle shutdown. Various combinations that have occurred are as follows:

(1) Controlled reactor shutdown over a period of several hours; MOTA not helium purged.

(2) Controlled reactor shutdown over a period of several hours; MOTA helium purged before shutdown.

(3) Reactor scrammed by dropping the rods; MOTA not purged.

(4) Reactor scrammed by running the control rods into the core over a period of minutes; MOTA not purged.

(5) Reactor power and flow reduced to 75% during a reactivity feedback measurement test, followed by controlled reactor shutdown over a period of several hours; MOTA not purged.

Controlled shutdowns involve reducing the power level several percent at a time and then holding each new power level for 20-25 minutes. This produces an approximate ramp-down in power with "stairstep" reduction in temperature occurring in the MOTA canisters

The controlled shutdowns without helium purging of the MOTA, (1) and (5) above, are the preferred methods of shutdown. The procedures employed for MOTA operation now require this kind of shutdown. The controlled shutdown of the reactor is used to minimize thermally-induced stresses in piping, instrument trees and drive lines. Reactor scrams are permitted and sometimes required to demonstrate fail-safe behavior, but excessive numbers of reactor scrams can reduce the plant life and are thus normally reserved for safety considerations involving the termination or avoidance of off-normal behavior.

Purging the MOTA before a controlled shutdown, (2) above, was the policy on earlier MOTAs, and was used primarily to obtain end-of-cycle helium purge data. Although this is no longer considered to be desirable, this procedure was used as recently as Cycle 10c. Reactor scrams occasionally occur during cycles, but an FFTF cycle and MOTA irradiation sequence sometimes also end on a reactor scram, as was the case for MOTA-1G and MOTA-2A, both conducted in FFTF Cycle 11c.

Sekimura and Ishino recently noted that Fe-15Cr-16Ni and two Fe-15Cr-16Ni solute-modified alloys irradiated to ~30 dpa in MOTA-1F during FFTF Cycle 10 had developed many small dislocation loops at 520 and 600°C that were atypical of irradiation at such temperatures.[illegible] Based on the loop size, density, and independence of alloy composition, as shown in Fig. 4, Sekimura and Ishino deduced that these loops were formed at lower temperatures at the end of the irradiation.[illegible] Note that the density of the loops is larger for the specimens irradiated at 600°C than those irradiated at 520°C, a behavior which is also atypical of isothermal irradiation. Specimens irradiated at 420°C did not exhibit the anomalous loop behavior. As shown in Fig. 5, a comparable irradiation conducted in MOTA-2A did not exhibit the anomalous loop formation observed in MOTA-1F. In the first case MOTA-1F was purged with helium and then the reactor was reduced to ~5% power over a six hour period. In the second case MOTA was held in control and the reactor scrammed by running in the rods, dropping both the neutron flux and temperature in several minutes. A full description of the temperature history for both MOTAs is presented elsewhere.[illegible]

As shown in Fig. 6, similar anomalous loop formation was also observed in Fe-15Cr-25Ni-XP alloys irradiated in another subcapsule in MOTA-1F,[illegible] indicating that the observation of Sekimura and Ishino was not an exceptional case.

After helium purging of MOTA-IF, six hours was required for the power level to be reduced from 100 to 5%. This was equivalent to 3 effective full-power-hours of neutron irradiation, during which an additional 0.02 dpa was accumulated. In the "600°C" capsule, there was an immediate drop of ~110°C upon helium purging, followed by a much more gradual decline over the next six hours. In the "520°C" capsule, the initial drop was only ~50°C, followed by a less rapid decline. These different temperature drops account in part for the atypical behavior shown in Fig. 4, where more loops were formed at 600°C than at 520°C. Radiation-induced microstructural densities are known to increase at lower target irradiation temperatures, providing greater numbers of sinks for absorption of point defects produced during the shutdown period. Thus, the tendency toward nucleation of new dislocation loops decreases at lower target temperatures. Based on the two considerations of higher sink strength and lower temperature drop upon purging, it is not surprising that small loops were absent after irradiation at ~420°C by Sekimura and Ishino.[illegible] A similar observation was made in the Fe-15Cr-25Ni XP alloys irradiated at 420°C by Garner and coworkers.

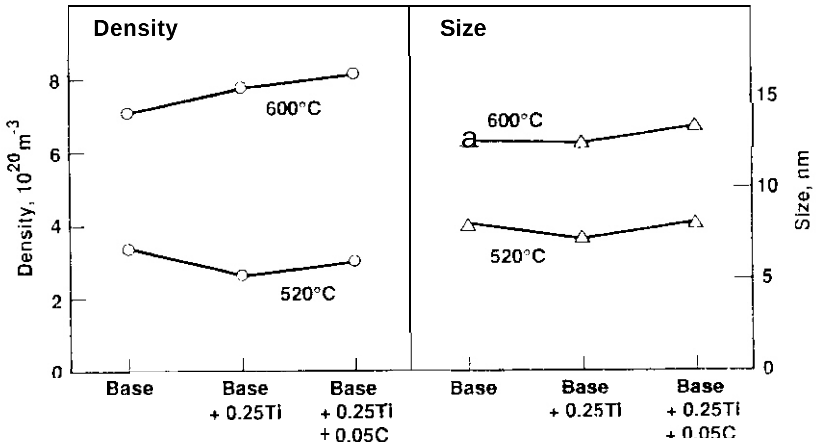

Fig. 4. Description of small dislocation loops observed in three Fe-15Cr-16Ni alloys irradiated in FFTF Cycle 10 in MOTA-1F.[illegible]

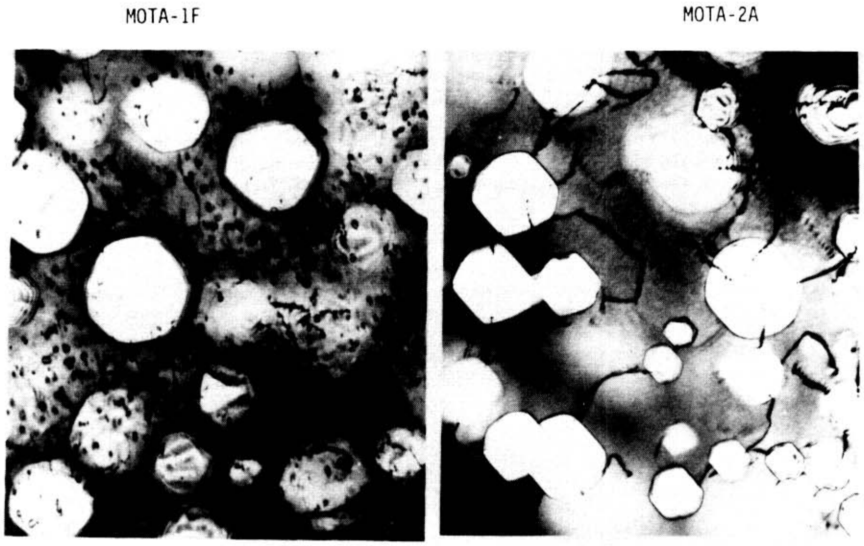
MOTA-1F

MOTA-2A

MOTA Helium Purged Before Slow Shutdown at 40.5 dpa

Reactor Scrammed at 36.1 dpa

Fig. 5. Small loops formed in Fe-15Cr-16Ni irradiated at 600°C in MOTA-1F, but not formed in MOTA-2A.[19]

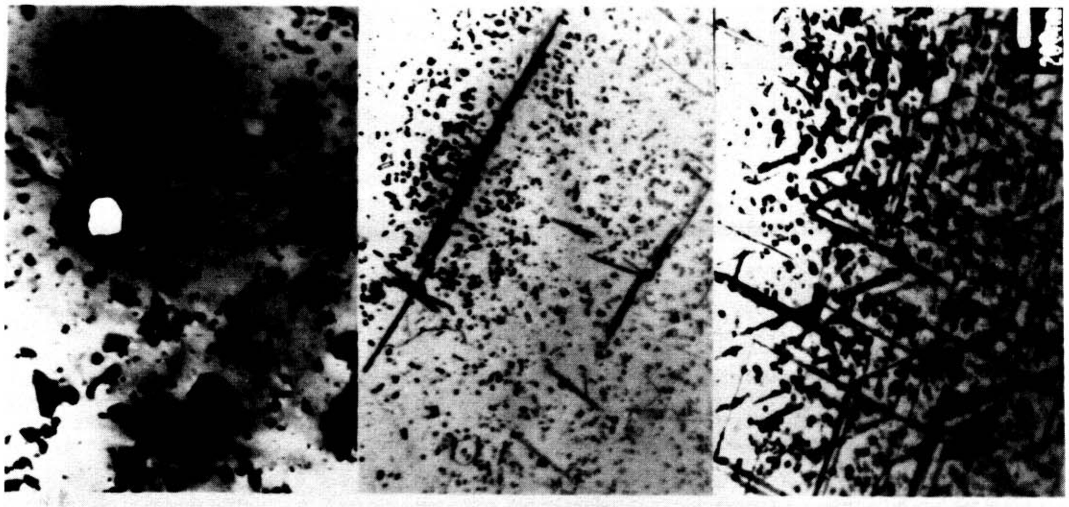
20% CW <0.005P

Annealed 0.013P

Annealed 0.10P

Fig. 6. Anomalous loop production observed in three Fe-15Cr-25Ni-XP alloys after irradiation at 600°C to 31.8 dpa in FFTF Cycle 10 using MOTA-1F. Increasing concentrations of phosphorus in solution increase both the precipitate and the loop production.[17]

Since helium purging was not involved at the end of Cycles 10A and 10B, it is expected that the influence of temperature history in the first two cycles would be small since the ~0.02 dpa irradiation during shutdown proceeded at temperatures closer to the target temperature. It is also anticipated that any accumulated lower temperature microstructure would quickly be dissolved at the beginning of the next reactor subcycle. This also implies that final shut-down procedures may be more important than start-up procedures or earlier shut-downs. It cannot be said for certain, however, that the intermittent nucleation of this atypical microstructure did not have any consequence on cavity evolution. Sekimura and Ishino noted that the short term accumulation of small loops during the three shutdown sequences of Cycle 10c may or may not have influenced the void swelling or precipitation very much, but the addition of small loops at the end of the last irradiation segment would strongly affect mechanical property measurements because of their associated hardening.

Even a controlled reactor scram does not guarantee that the shutdown procedure will not influence the microstructure, however. Fig. 7 shows the microstructure of 20% cold-worked Fe-17Cr-16Ni irradiated to 36 dpa at 600°C in MOTA-2A.[20] This sequence was terminated by a controlled scram. The temperature reached by the specimens following the scram was 325°C, the normal preheat temperature from which power ascent begins. The sodium temperature in FFTF is maintained at this temperature by a combination of coolant pump speed, resistive heating and baffle control on the dump heat exchangers. One day after the scram these parameters were adjusted to drop to the standby temperature of 210°C, at which MOTA resides for periods ranging from 2 to 29 days before being removed from FFTF.

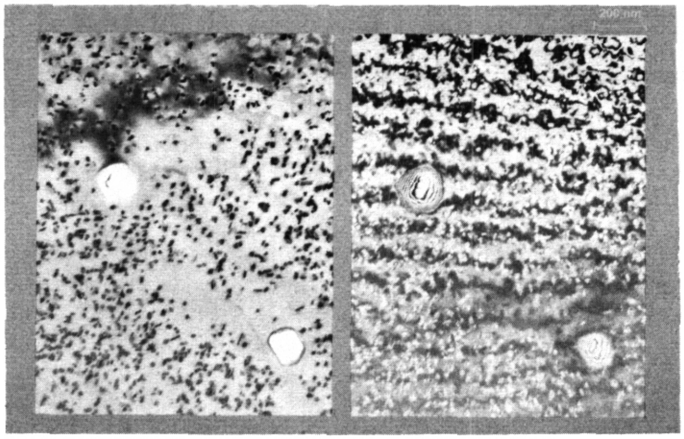

Fig. 7. Stacking fault tetrahedra observed to form in cold-worked Fe-17Cr-16Ni following irradiation at 600°C to 36 dpa in FFTF Cycle 11 using MOTA-2A, (a) bright field and (b) dark field images.[20]

During the 24-hour period at 325°C extensive formation of vacancy stacking fault tetrahedra developed in this pure quaternary alloy as shown in Fig. 7. These tetrahedra probably arise from a vacancy supersaturation resulting from the relatively quick drop in temperature. A greatly reduced and almost overlooked density of tetrahedra was observed in a companion specimen irradiated in the annealed condition.[20] The much larger swelling level (~20%) in the annealed steel provided extensive cavity sinks for the vacancies that otherwise would agglomerate and form tetrahedra. Note in Fig. 7 that the few voids observed in the cold-worked specimen appear to denude the adjacent regions of tetrahedra. As would be expected, alloys containing significant levels of solutes did not form tetrahedra.

Power setbacks in ORR

Comparative irradiation studies were recently conducted in the Experimental Breeder Reactor II (EBR-II) and the Oak Ridge Research (ORR) reactor to study the influence of helium/dpa ratio and displacement rate on the microstructural evolution of Fe-15Cr-XNi (X=10-45 wt%) and Fe-YCr-35Ni (Y=7.5, 15 and 22 wt%).[21-23] As shown in Fig. 8 there was an unprecedented refinement of the cavity microstructure in the ORR experiment which was conducted at nickel-dependent helium/dpa levels ranging from 27 to 58 appm/dpa. In EBR-II the levels were 0.66 to 1.2 appm/dpa. As shown in Fig. 9 one consequence of this refinement was a substantial difference in the radiation-induced hardening in the two irradiations.[23]

When compared to the much less responsive behavior with helium content observed in the ^{59}Ni isotope tailoring experiment conducted in FFTF/MOTA,[25-28] it was decided to review the operational history of the ORR experiment, which also has a low inlet temperature and a relatively high gamma heating rate. It was discovered in this review that there were indeed frequent and large reductions in power (designated as "setbacks") throughout the irradiation history in response to various routine or non-routine operating

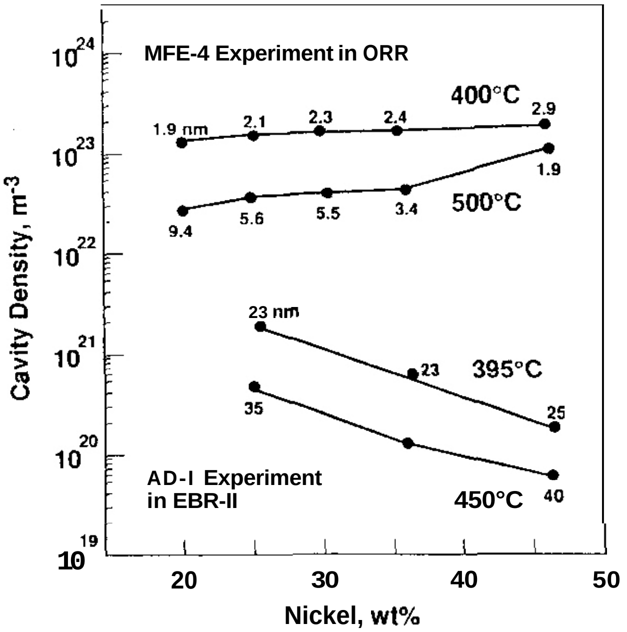

Fig. 8. Cavity densities observed in Fe-15Cr-XNi alloys irradiated in the AD-I experiment in EBR-II (9.5 to 11.3 dpa) and the MFE-4 experiment in ORR (12.5 to 14.3 dpa).[21] Mean cavity sizes in nm are shown next to each data paint.

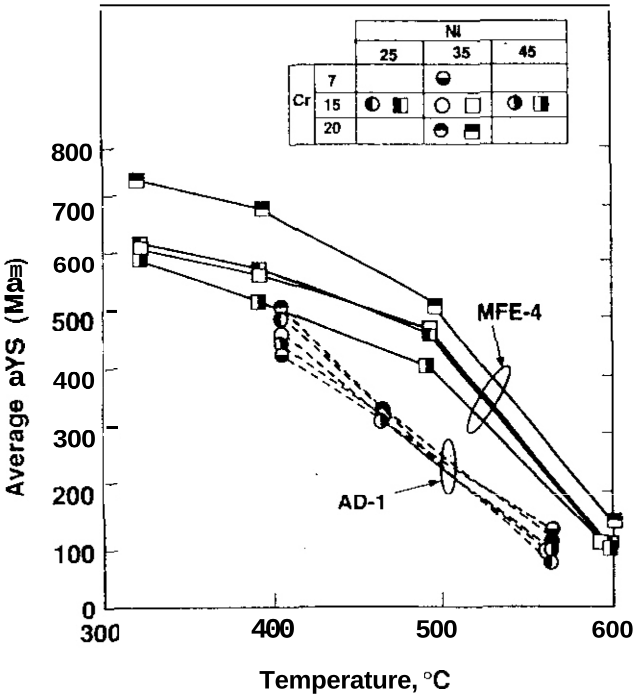

Fig. 9. Comparison of yield strength changes of Fe-YCr-XNi alloys observed in ORR and EBR-II as a function of irradiation temperature and nickel concentration in wt%.[23]

contingencies, examples of which are shown in Tables I and II. The 600°C Irradiation. for instance, was interrupted by 237 cutbacks in temperature during just one year of the three year experiment. Thus, 0.12 dpa of the 3.5 dpa accumulated that year was at temperature; well below 600°C. This is much larger than the levels shown by the separate studies of Kiritani. Sekimura. Garner and their coworkers to produce large densities of small loops

It is proposed that the frequent intermittent reductions in temperature caused periodic and profuse production of small dislocation loops, known to be efficient nucleation sites for helium bubbles[22] in this high He/dpa experiment. Once formed. these bubbles are sessile and remain after the loop disappears when the target temperature is re-established. By this mechanism the cavity microstructure is refined to an unprecedented extent, and the resultant cavity microstructure is completely atypical of that attained in isothermal irradiation.

Impact of operational choices

Results of extensive void swelling studies conducted on simple Fe-YCr-XNi ternary alloys in FFTF/MOTA employing the early MOTA vehicles are now being analyzed.[32] One unusual feature of these results is that more swelling is observed at 600°C than at 520°C. This is in conflict with the results of identical studies conducted in EBR-II.[31,32] In the EBR-II studies there was always a monotonic increase in the duration of the transient regime of swelling with increasing temperature, especially at higher nickel levels (≥25% Ni). There were also other striking differences in behavior observed between specimens irradiated in the two reactors.

Since there was ample precedent established for temperature history effects when this disparity was observed. the early MOTA temperature history was reviewed in detail It was found that several prolonged, unannounced helium purgings of MOTAs 1B and 1C had occurred. This example demonstrates haw the primary mission of a reactor is sometimes in conflict with the goals of minor experiments. The necessity to make such a choice arose because the various MOTAs also contained large numbers of gas-pressurized stress-rupture tubes designed to fail during irradiation, with each individual failure detected by the release and detection of a mixture of various isotopes of xenon and krypton tag gases.[33] A similar but slightly different system was also used to identify failure of individual fuel pins in FFTF. Since the major mission of FFTF was to conduct fuel pin evaluations, the identification of each detected fuel pin failure in the early stages of the FFTF program became the immediate and paramount objective of the reactor operations staff. To ensure that no competing gas tag signals occurred to interfere with easy identification of the

Table 1. Setbacks recorded in the 600°C capsule of the MFE-4 experiment in ORR during the first year

Temperature Reached (°C)	Number of Setbacks	Total dpa during setback
50-100	1	1.7
100-150	10	20.2
150-200	6	21.7
200-250	8	61.3
250-300	6	37.5
300-350	18	401.2
350-400	46	6237
400-450	77	3897
450-500	20	458
500-550	45	759
Total	237	11.894.6 = 0.12 dpa

Table 2. Setbacks recorded in the 330°C capsule of the MFE-4 experiment during a six month period

Temperature Reached (°C)	Number of Setbacks	Total dpa during setback (x10 dpa)
50-100		18.5
100-150		10.1
150-200	3	36.5
200-250	12	316.5
250-300	25	1506.
Total	50	1887.6 = 0.019 dpa

leaking fuel pin, the decision was made to purge the MOTA with helium for 2-3 days at a time, lowering the temperatures of all specimens substantially, and thereby discouraging the rupture of creep tubes in MOTA. Of course, this lowered the temperature of all specimens in the MOTA.

One of the most effective ways to nucleate voids in Fe-Cr-Ni austenitic alloys at high temperatures is to develop dislocation microstructures at the target temperature and then drop to lower temperatures where void nucleation is much easier. Radiation-induced segregation and helium diffusion also play roles in void nucleation and both of these increase with irradiation temperature. The net result is that a stable void population begins to develop sooner at a target temperature of 600°C following a strong temperature reduction than it does at 520°C.

Some operational procedures involving day-to-day maintenance of an individual experiment by reactor staff carry the risk of errors. One of the most significant examples involves the inadvertent substitution by reactor staff of argon for helium in the backup gas supply system for MOTA 1D. This led to a severe overtemperature event of about one hour duration that compromised the integrity of the experiment, especially that portion involving gas-pressurized creep tubes. For microstructurally-oriented experiments this excursion may have been overlooked or incorporated into the interpretation of the experiment. The influence of the overtemperature was overshadowed, however, by the joint decision of the experimenters and reactor staff to helium-purge the MOTA for the remainder of the reactor cycle. During this time all temperatures were at lower than target values. When the results of the compromised experiments were compared with isothermal repeat experiments conducted later, it was clearly the lower temperature portion of the irradiation that dictated the final microstructure and mechanical properties.

With increasingly stringent controls being applied to all reactors since the Three Mile Island and Chernobyl incidents, an ever-increasing number of reactivity feedback and periodic safety checks are being conducted at all reactors. Many of these tests involve power reductions that may influence the temperature of individual experiments. Such tests always have priority over the needs of individual experiments.

Recommendations for experimenters

1. Develop a greater sensitivity to potential history effects and communicate often with reactor staff to avoid unnecessary transient conditions.

2. Design all experiments to record temperature directly and use active temperature control if possible. Monitor the output of the thermocouples in detail.

3. Avoid irradiating during periods of off-normal reactor testing. Otherwise, design the experiment to be removed from the reactor for these periods.

4. Modify the temperature control of the experiment to minimize the effect of reduced power operation.

5. Develop contingency plans wrth reactor staff for foreseeable contingencies involving power variations and interruptions.

6. Design individual experiments such that temperature history is not the dominant variable, assessing other variables in side-by-side Irradiations.

Discussion and conclusions

As the radiation damage scientific community has become more aware of the many factors that Influence the evolution of radiation-induced microstructure. the impact of the details of temperature history has assumed a larger role, especially for experiments where relatively low levels of total exposure are used to Study the effects of neutron spectra or damage rate. There is also some concern that repeated transients in temperature over the lifetime of an Irradiation experiment will yield a microstructure at high fluence that. is atypical of that produced during completely isothermal operation. It should also be noted that many published theoretical explanations of the temperature dependence of nucleation of microstructural components do not in general include the influence of the kinds of temperature history discussed in this paper. Thus. the material parameters derived in these experiments, especially energies of formation, migration and binding of point defects. may have been strongly affected by the mall increments of irradiation at lower temperatures.

'While it appears that low temperature microstructure produced at low fluence levels will tend to dissolve at higher temperatures and higher fluences, several examples have been presented in this paper where significant microstructural alteration persisted. This was shown to be especially important when high rates of helium generation were involved.

The extensive high fluence data base on dimensional instabilities and mechanical properties that were generated in the reactors discussed in this paper is not necessarily invalidated by anomalies related to temperature history. When such data are applied in design situations similar to those in which the data were derived, the impact of unavoidable transients becomes in most cases a relatively minor facet of the irradiation environment, but one that is typical of the actual history of an irradiated material. When data are derived in one reactor environment, however. but then applied to another environment where the neutron spectra and reactor environment (displacement rate and temperature history) are significantly different, then allowance must be made to account for the impact of history-related phenomena.

FUTURE WORK

This effort is complete

ACKNOWLEDGMENTS

The participation of the U.S. participants was sponsored by the U.S. Department of Energy under three separate contracts. The participation of the Japanese participants was sponsored by the Japan/U.S. Collaboration between the U.S. Department of Energy and Monbusho, the Japanese Ministry of Education, Science and Culture. Pacific Northwest Laboratory is operated for the U.S. DOE by Battelle Memorial institute under Contract DE-AC06-76RLO 1830. Oak Ridge National Laboratory is operated for the U.S. DOE by Martin Marietta Energy Systems, Inc. under Contract De-AC05-84OR21400O.

REFERENCES

1. M. Kiritani, Journal of Nuclear Materials 160 (1988) 135-141.

2. M. Kiritani, T. Yoshiie, S. Kojima, !. Satoh and K. Hamada, Journal of Nuclear Materials 174 (1990) 327-351.

3. F. a. Garner, H. L. Heinisch, R. L. Simons and F. M. Mann, Radiation Effects and Defects in solids 113 (1990) 229-255.

4. F. A. Garner, Journal of Nuclear Materials 179-181 (1991) 111-117

5. P. J. Maziasz, "Effects of Helium Content on Microstructural Development in Type 3i6 Stainless Steel Under Neutron irradiation." ORNL-6121, Oak Ridge National Laboratory. November 1985.

5. F. A. Garner, W. V. Cummings, J. F. Gates and E. R. Gilbert. "Densification-Induced Strains in 20% Cold-Worked 316 Stainless Steel During Neutron Irradiation." HEDL-THE 78-79, Hanford Engineering Development Laboratory, June 1978.

7. R. J. Puigh. A. J. Lovell and F. A. Garner. Journal of Nuclear Materials 122-123 (1984) 242-245.

8 ?. W. Clark, A. S. Kumar and F. A. Garner. Journal of Nuclear Materials 155-157 (1988) 845-849.

3. F. A. Gamer. E. R. Gilbert. O. S. Gelles and J. P. foster. pp. 698-712 in Effects of Radiation on Materials: Tenth Conference ASTM STP 725. D. Kramer, H. R. Brager and J. S. Perrin. Eds., American Society for Testing and Materials, 1981.

10. W.J.S. Yang and F. A. Garner, pp. 186-206 in Effects of Radiation on Materials: Eleventh Conference, ASTM STP 782, H. R. Brager and J. S. Perrin, Eds., American Society for Testing and Materials, 1982.

11. D. L. Porter, E. L. Wood and F. A. Garner, pp. 551-569 in Effects of Radiation on Materials: 14th International Symposium (Vol. II), ASTM STP 1046, N. H. Packan, R. E. Stoller and A. S. Kumar. Eds., American Society for Testing and Materials, 1990.

12. N. Yoshida, Journal of Nuclear Materials 174 (1990) 270-228.

13. N. Yoshida, H. L. Heinisch, T. Muroga, K. Araki and M. Kiritani, Journal of Nuclear Materials 179-181 (1991) 1078-1082.

14. H. L. Heinisch, Journal of Nuclear Materials 155-157 (1988) 121-129.

15. N. Yoshida, Q. Xu, H. Watanabe, T. Muroga and M. Kiritani, Journal of Nuclear Materials 191-194 (1992)1114.

16. R. J. Puigh and R. E. Schenter, pp. 759-802 in Effects of Radiation on Materials: Twelfth International Symposium. ASTM STP 870, F. A. Garner and J. S. Perrin, Eds., American Society for Testing and Materials, 1985.

17. F. A. Garner, A. M. Ermi, N. Sekimura, and J. W. Newkirk, pp. 8-16 in Fusion Reactor Materials Semiannual Progress Report DOE/ER-0313/11 (1992).

18. N. Sekimura and S. Ishino, Journal of Nuclear Materials 179-181 (1991) 542-545.

19. N. Sekimura, K. Hamada and S. Ishino, in Effects of Radiation on Materials: 15th International Conference, ASTM STP 1175, Denver, CO, June 1992, American Society for Testing and Materials, in press.

20. H. Watanabe, T. Muroga and N. Yoshida, Proceedings of conference on Evolution of Microstructure in Metals During Irradiation, Sept. 29 - Oct. 2, 1992, Minnet, Ontario, Canada, (in press).

21. N. Sekimura, F. A. Garner and R. D. Griffin, Journal of Nuclear Materials 191-194 (1992) 1234.

22. N. Sekimura and F. A. Garner, Proceedings of conference on Evolution Metals During Irradiation, Sept. 29 - Oct. 2, 1992, Minnet, Ontario, Canada, (in press).

23. M. L. Hamilton, A. Okada and F. A. Garner, Journal of Nuclear Materials 179-181 (1991) 558-562.

24. M. L. Hamilton and F. A. Garner, Journal of Nuclear Materials 191-194 (1992) 1239-1243.

25. F. A. Garner, M. L. Hamilton, L. R. Greenwood, J. F. Stubbins and B. M. Oliver, in Effects of Radiation on Materials: 16th International Symposium, ASTM STP 1175, Denver, CO, American Society for Testing and Materials, (in press).

26. J. F. Stubbins and F. A. Garner, Journal of Nuclear Materials 179-181 (1991) 523-525.

27. H. Kawanishi, F. A. Garner and R. L. Simons, Journal of Nuclear Materials 179-181 (1991) 511-514.

28. J. F. Stubbins and F. A. Garner, Journal of Nuclear Materials 191-194 (1992) 1300.

29. E. A. Kenik, Journal of Nuclear Materials 85 86 (1979) 659-663.

30. F. A. Garner, "Factors Which Influence the Swelling of Neutron-Irradiated Fe-Cr-Ni Alloys", in this semiannual report.

31. F. A. Garner and H. R. Brager, pp. 197-201 in Effects of Radiation on Materials: Twelfth International Symposium, ASTM STP 870, F. A. Garner and J. S. Perrin, Eds., American Society for Testing and Materials, 1985.

32. F. A. Garner and A. S. Kumar, pp. 289-314 in Radiation Induced Changes in Microstructure: 13th International Symposium (Part I) ASTM STP 955, F. A. Garner, N. H. Packan and A. S. Kumar, Eds., American Society for Testing and Materials, 1987.

NEUTRON-INDUCED SWELLING OF PURE NICKEL AND NICKEL BINARY ALLOYS - F. A. Garner (Pacific Northwest Laboratory)'

OBJECTIVE

The objective of this effort is to provide insight on the factors which control the microstructural evolution of irradiated metals.

SUMMARY

The second and last phase of the EBR-II AA-14 experiment confirms many of the trends observed in Phase I of the experiment. Phase I reached 12 to 14 dpa for pure nickel and nickel-binary alloys at 425, 500 and 600°C. Phase II reached 31.1 to 31.8 dpa at the same temperatures.

Annealed nickel exhibits a strongly temperature-dependent tendency toward Saturation of void swelling. This tendency is reduced by cold-working and thus swelling is increased initially by cold-working, but this does not preclude attainment of saturation. Ni-5Al in the annealed condition Continues to swell in the 12-31 dpa interval, but swelling is suppressed somewhat by cold-working. Aging of the cold-worked material tends to restore the swelling to levels near that of the annealed alloy. The suppression in swelling observed in Ni-5Si and Ni-8Si at 12-14 dpa is preserved to -31 dpa.

PROGRESS AND STATUS

Introduction

In several earlier reports, the results of Phase I of the AA-14 fusion materials experiment in EBR-II were presented for pure nickel (99.999%), Ni-5Si, Ni-8Si and Ni-5Al, all in atomic percent'.'. In the first phase at 12-14 dpa, pure nickel tended to exhibit an eventual collapse in dislocation density that caused a saturation in swelling. As shown in Figure 1, the strong temperature dependence of swelling in annealed material at this dose level was not observed in cold-worked or cold-worked and aged specimens. Dislocation networks induced by cold-working resist the tendency toward collapse of the dislocation density. a process which is strongly dependent on temperature.

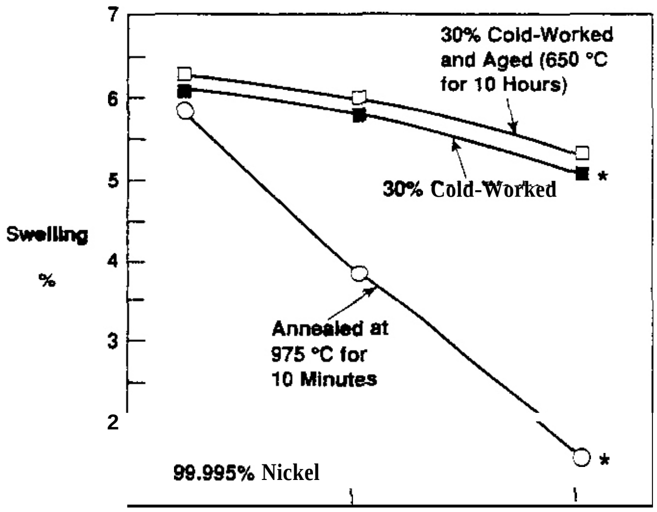

It was also shown that addition of 5 atomic percent of either silicon or aluminum caused substantial reductions in swelling, but increasing silicon from 5 to 8 atomic percent led to a reversal in swelling behavior. increasing it somewhat (Figures 2 and 3) Collapse of the dislocation population was not observed in any of the three binary alloys at any irradiation temperature'

The second and last phase of the AA-14 experiment reached 31.1 and 31.8 dpa in EBR-II and has now been examined using immersion

alloy. cold-worked

'Pacific Northwest Laboratory is operated for the U.S. Department of Energy by Battelle Memorial Institute under Contract DE-AC06-76RLO 1830.

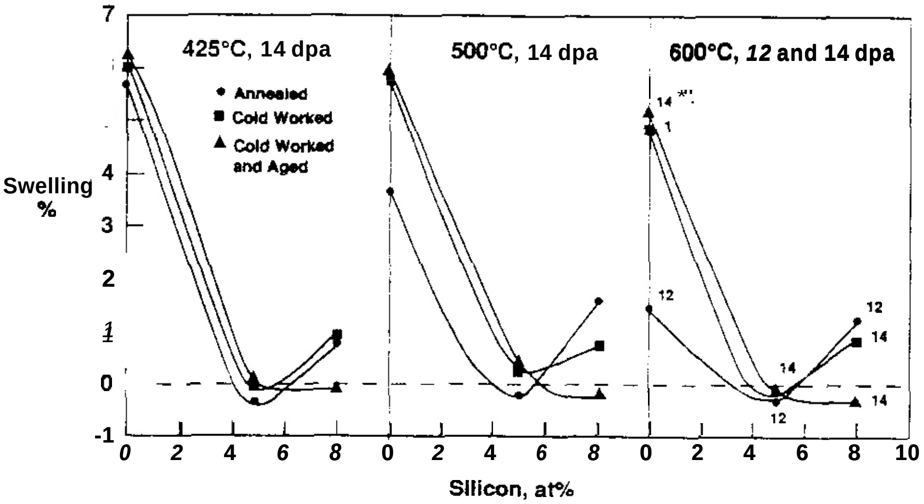

Fig. 2. The influence of aluminum, thermomechanical starting condition, and irradiation temperature on the swelling of nickel at 12 - 14 dpa in Phase I.

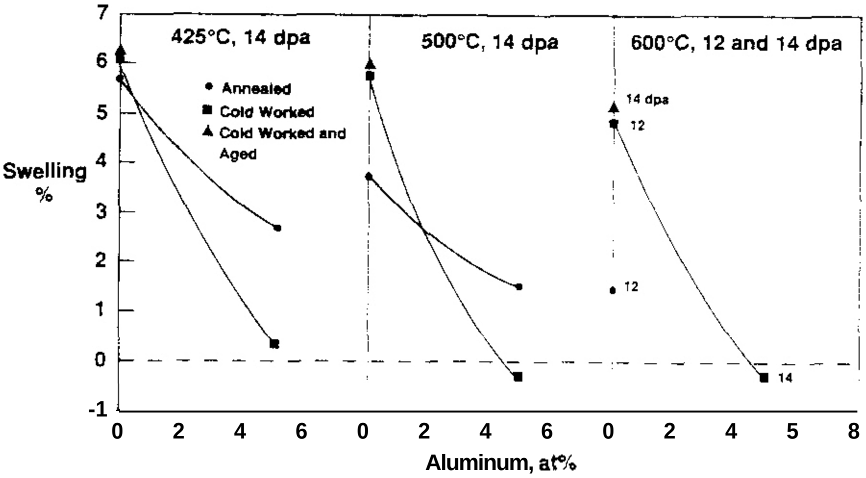

Fig. 3. The influence of silicon level, thermomechanical starting condition, and irradiation temperature on the swelling of Ni-Si alloys at 12-14 dpa in Phase I.

Experimental Details

The specimens were irradiated in the form of 3 mm diameter microscopy disks of ~0.25 mm thickness and were in contact with the reactor sodium coolant at temperatures of 425, 500 and 600°C in Phase I. During Phase I, however, the 500°C specimens were irradiated at 550°C. No changes in temperature occurred for the 425 and 600°C specimens. Post-irradiation changes in density were determined using an automated immersion density technique known to be accurate to ±0.16% swelling.

Results and Discussion

The density change data for both phase I and phase II are listed in Table 1. Figure 4 shows that the swelling of annealed nickel indeed appears to saturate at 600°C and that the tendency toward saturation is delayed by cold-working, especially at higher irradiation temperatures. At the lower irradiation temperatures there is almost no effect of cold-working, however.

Table 1. Swelling Observed in Phases I and II of the M.14 Experiment

ALLOY	TEMPERATURE °C	DOSE dpa	SWELLING % SA[1]	CW[1]	CWA[1]
Ni	425	14.0	5.70	6.01	6.20
Ni	425	31.1	7.48	9.14	—
Ni	500	14.0	3.73	5.68	5.83
Ni	500-550	31.8	6.30	---	----
Ni	600	12.0-14.0	1.39^{**}	4.76^{**}	5.00
Ni	600	31.8	2.24	7.43	---
Ni-5Al	425	14.0	2.88	0.21	---
Ni-5Al	425	31.1	6.92	----	5.63
Ni-5Al	500	14.0	1.46	-0.36	----
Ni-5Al	500-550	31.8	4.19	----	4.05
Ni-5Al	600	14.0	---	-0.39	---
Ni-5Al	600	31.8	0.86	—	0.30
Ni-5Si	425	14.0	-0.48	-0.11	0.06
Ni-5Si	425	31.1	-0.59	—	0.28
Ni-5Si	500	14.0	-0.41	0.12	0.10
Ni-5Si	500-550	31.8	-0.21	----	1.42
Ni-5Si	600	12.0-14.0	-0.22^{**}	----	-0.12
Ni-5Si	600	31	0.06	----	0.15
Ni-8Si	425	14.0	0.87	0.84	-0.06
Ni-8Si	425	31.1	—	----	-0.17
Ni-8Si	500	14.0	1.23	0.78	-0.12
Ni-8Si	500-550	31.8	—	----	0.52
Ni-8Si	600	12.0-14.0	1.13^{**}	0.90	-0.37

---

[1] SA, CW, CWA = solution annealed, cold worked, and cold worked and aged, respectively.

As shown in Figure 5, Ni-5Al swells less than pure nickel but continues to swell in the 12 to 31 dpa interval without hint of saturation. The behavior observed vs. temperature and dpa level in this rather limited experiment is consistent with the behavior observed in a more comprehensive experiment on Ni-Al alloys;. Whereas cold-working suppresses the swelling of Ni-5Al somewhat, aging at 650°C restores the swelling to levels close to those observed in annealed specimens.

The addition of 5% silicon to nickel is more effective in reducing swelling than is 5% aluminum, but unlike the effect of aluminum. the swelling suppression by silicon appears to be maintained in the 12-31 dpa interval at all three Irradiation temperatures. While the specimen matrix is rather sparce for Ni-8Si, it appears that swelling in general is larger than for Ni-5Si. This was the behavior observed in phase I, and it appears that swelling of Ni-8Si increases slowly with increasing neutron exposure in the 12-31 dpa interval

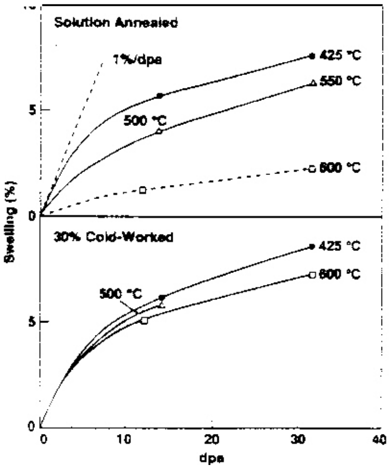

Fig. 4. Influence of displacement level. temperature and cold-work on the tendency toward saturation in pure nickel

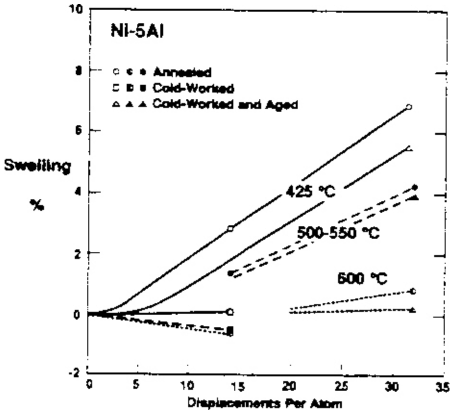

Fig. 5. Swelling of Ni-5Al in phases I and II

Expected Achievements In the *Next* Reporting Period

The microstructural origins of the observed changes in density will be examined in a joint study with S Ohnuki of Hokkaido University.

REFERENCES

1. J. F. Stubbinr and F. A. Garner, "Swelling and Microstructure of High Purity Nickel Irradiated with Fast Neutrons in EBR-II", J. Nucl. Mater. 191-194(1992) 1295-1299.

2. H. Takahashi and F. A. Garner. 'Microstructural Evolution of Neutron Irradiated Ni Si and Ni-Al Alloys", J. Nucl. Mater. 195(1992) 1-10.

3. M. A. Mitchell and F. A. Garner. "Neutron-Induced Swelling of Binary Ni-Al Alloys", J. Nucl. Mater 187(1992) 102-108.

DEFECT PRODUCTION IN IRRADIATED METALS - H. L. Heinisch (Pacific Northwest Laboratory[a])

OBJECTIVE

The objective of this work is to determine the spectral dependence of defect production and microstructure evolution under neutron irradiation,

SUMMARY

Our knowledge of the processes involved in creating defects during cascade-producing irradiations is reviewed. Molecular dynamics simulations within the past few years have led to an understanding of the creation and survival of point defects in the critical first picoseconds of the cascade process. through the quenching of the thermal spike. The concept that "freely migrating defects" arise only from isolated Frenkel pairs produced in a cascade is critically discussed.

PROGRESS AND STATUS

Introduction

Any models or theories that describe the effects of radiation damage on a material should have as their basis a quantitative description of the production of the defects that cause microstructural changes. When a single radiation event occurs, a distribution of single point defects and clusters of point defects is produced in the local region where the displacement energy was deposited. This distribution evolves with time and can interact in various ways with the existing microstructure or with defects produced elsewhere in the material. In general, two types of defects are produced: relatively mobile defect? and relatively immobile defects. The mobile defects are single point defects and small clusters. They can interact among themselves, annihilating or clustering, interact with immobile clusters formed in the same event, or migrate throughout the material until they interact with the existing microstructure or defects from other events. The immobile clusters can collapse to dislocation loops. becoming part of the dislocation structure of the material. Immobile clusters are sinks for mobile defects, or, depending on the temperature, they can contribute to the mobile defect population through thermal decomposition. Evidence also exists that small, glissile self-interstitial loops can form under damage conditions. gliding in one dimension'.

The production rate of the mobile or "freely migrating defects" is not a directly measurable quantity. It must be inferred from measurements of the observable effects produced by the freely migrating defects. as interpreted through some model that relates defect production to changes in observable properties. Thus, one must have a clear idea of the processes and mechanisms involved in order to extract the correct quantitative information from the analysis of the experiments. In particular, it is necessary to start with the correct definition of "freely migrating defects" as a function of the irradiation parameters (time, temperature, flux and material properties). It is helpful to review the defect production process.

---

[a] Pacific Northwest Laboratory is operated for the U.S. Department of Energy by Battelle Memorial Institute under Contract DE-AC06-76RLO 1830.

Defect Production

In the first step, the irradiating particles impart their energy to the atoms of the material. The response of the material to irradiating particles can be described in terms of a primary recoil atom spectrum, as long as the primary recoils are sufficiently separated in space or time from each other (an exception, for example, is when heavy ions deposit energy with much higher density than can be achieved by recoil atoms of the material—-in essence. the cascades originate simultaneously from nearly adjacent lattice sites and overlap). Damage by neutrons and many ions (especially self-ions) can be addressed in terms of energetic recoil atoms.

The dissipation of recoil energy occurs in four definable phases relevant to the production and disposition of lattice defects: the collisional phase, the thermal spike phase, the quenching phase and the annealing phase.

Collisional Phase

In the collisional phase a primary recoil atom initiates a cascade of displacive collisions that continues until no atom contains enough energy to create further displacements. The creation of displaced atoms at this stage is conceptually similar to the Kinchin-Pease[2] model for the creation of displaced atoms that forms the basis for calculations of "displacements per atom" (dpa), a commonly used exposure parameter. The "modified Kinchin-Pais? expression of Norgett. Robinson and Torrens' is the recognized standard for dpa calculations. viz.

$$n(T) = 0.8T/2E_d \,.$$

where T is the recoil damage energy. E,, is the displacement energy and the factor 0.8 is the "displacement efficiency factor," (the displacement efficiency factor is a correction to the original hard-sphere scattering model assumed by Kinchin and Pease that accounts for somewhat fewer displacements obtained when using more realistic scattering potentials[4]. It is descriptive of the collisional phase and does not include any information on subsequent behavior of displaced atoms, such as recombination. This should not be confused or combined with other defect production efficiency factors.) A ballistic effect that occurs during the collisional phase is the replacement collision sequence (RCS), which can result in extended vacancy-self-interstitial atom separations. Molecular dynamics (MD) simulations of energetic collision cascades[5] show that the collisional phase lasts up to a few times IO'' s, depending on the recoil energy.

Thermal Spike Phase

During the collisional phase, the thermal spike phase is also beginning. as the energy in the cascade is shared among many atoms through lower energy collisions in a localized region of high energy density. Molecular dynamics simulations show that, at recoil energies above a few keV. a molten zone is created that exhibits liquid-like properties". Outside the molten zone are displaced atoms, mostly at the end of RCSs. The RCSs propagate supersonically and, therefore. are at the periphery of the cascade region before the molten zone fully develops, which takes about 1 ps[7]. During the thermal spike phase, the identity of defects within the molten zone is largely lost, but the defects outside the molten zone (mostly displaced atoms at the ends of RCSs) retain their identity. The displaced atoms become self-interstitial atoms (SIA). Molecular dynamics simulations indicate that elastic interactions lead to clustering of SIAs outside the molten zone[8].

Quenching Phase

The quenching phase begins as the spike energy is dissipated to the rest of the material. During this time the molten zone returns to a condensed state containing a distribution of vacancies within it. MD simulations have even shown the formation of small vacancy loops during quenching'. The thermal spike forms and is quenched within a few picoseconds. depending on the cascade energy and energy transport properties of the material. In general, after quenching, the vacancy-type defects tend to occupy the center of the defect configuration and are somewhat more closely spaced than the surrounding interstitial-type defects.

Annealing Phase

After the quenching phase, further rearrangement and interaction of the remaining defects take place by normal, thermally-activated diffusion of mobile defects (single point defects, small clusters, and, depending on the temperature, mobile defects resulting from dissolution of clusters). During this annealing phase, some of the mobile defects escape annihilation or clustering within the cascade region. becoming the "freely migrating defects" that can migrate away from the cascade region and interact with other elements of the microstructure.

Computer simulations of the annealing phase in Cu cascades (allowing no cluster dissolution) showed that at least 10% of the SIAs remaining after the quenching phase escaped the cascade region''', even when the simulation was performed using extreme clustering of SIAs during the quenching phase. The SIAs escape because they tend to lie at the periphery of the cascade defect distribution. A smaller fraction of vacancies escape because their relatively closer proximity near the center of the cascade defect distribution leads to greater probability of clustering among themselves.

Cascade Energy Dependence

The creation and disposition of defects during all the phases of cascade development depend on the cascade energy. material parameters and the temperature. At any energy, the initial arrangement of defects produced (during the collisional phase) is determined largely by ballistic processes such as RCSs. The self-interstitial atoms tend to be at the periphery of the cascade defect distribution at all energies, and some fraction of the mobile SIAs will always tend to escape. At very low energies, up to several hundred eV, where only a few defects pairs are produced, most of the surviving defects will be free to migrate from the cascade site. With increasing cascade energy. the surface-to-volume ratio of the defect distribution decreases, and a decreasing fraction of SIAs will escape rather than cluster or annihilate, tending toward a constant value at the threshold energy for formation of subcascades.

A minimum cascade energy is required for formation of a thermal spike. They do not form in cascades with energies less than about 1 kev in Cu (reduced energy 0.003)[9]. When a spike occurs, SIAs within the molten zone disappear, and during quenching, vacancies are formed, equal in number to the displaced atoms remaining outside the molten zone. With increasing energy the molten zones become larger, so they quench more slowly. Thus, vacancy clustering is more likely in higher energy cascades because the vacancies have a longer time to interact. However, even the largest molten zones quench within a few tens of lattice vibrations, so formation of large clusters or collapse to loops is not assured. The maximum melt zone size is achieved at energies where subcascades form.

Material Properties

The physical properties of a material can affect the amount and type of defect production in cascades Molecular dynamics simulations comparing cascades in Cu and Ni, which have significantly different melting points'', have shown that the slower quenching in Cu leads to greater clustering of vacancies and greater chances for collapse to loops than in Ni. Contributions of electron-phonon coupling, which do not appear to be significant in Cu, may be important in other materials[9].

Effects of Temperature

Higher temperatures may result in somewhat shorter RCSs during the collisional phase and in somewhat larger molten zones during the thermal spike phase. Since only the SIAs outside the molten zone survive, the net result could be a decrease in total defect production at higher temperatures. Higher temperatures also mean slower quenching, which increases the opportunities for clustering of vacancies. At temperatures where vacancy clusters are thermally unstable, (small) vacancy clusters will not readily form during the quenching and annealing stages. Instead, mobile vacancies will diffuse from the center of the cascade. Some will annihilate at the surrounding interstitial clusters. and some will escape the cascade. Results of a simple diffusion model[12] show that a significant fraction of vacancies can escape from a cascade in this way.

Freely Migrating Defects

In a letter to the editor of the Journal of Nuclear Materials Naundorf suggests that the origin of freely migrating defects in ion and neutron irradiated metals is free single Frenkel pairs produced by "low recoil energies transferred by the primary collisions."[13] As evidence for this assertion, a simple calculation was performed in which the number of single Frenkel pairs produced was found to be consistent with the very low efficiencies of free defect production extracted from diffusion experiments[14-17]. The calculation was performed using a Kinchin-Pease displacement model including an exponential distribution of separations between primary collisions. It was assumed that a free Frenkel pair was produced if the energy transfer to the atoms was less than *2.5* times the displacement energy (to create just one Frenkel pair) and if the distance between two consecutive collisions was larger than the spontaneous recombination volume (so the Frenkel pairs would neither recombine nor cluster). Calculations were made for the same systems on which diffusion experiments have been performed, and the calculated fractions of freely migrating defects were compared with the experimental values, showing the same trend as the experiments.

The calculations are essentially an analytical approximation describing the collisional phase of a cascade. The actual spatial distribution of the collisions is not represented. The thermal spike. quenching and annealing phases are completely ignored. The four-phase description of defect production in cascades outlined above is well-supported by hundreds of MD cascade simulations, as well as binary collision studies and annealing simulations. It is clear that Naundorf's calculation is not relevant to the production of defects in cascades.

The diffusion experiments to which the Naundorf calculations are compared are good experiments carefully performed, Unfortunately, the interpretation of their results has not been done in light of our knowledge of defect production in cascades. It would be interesting to reinterpret the results of these valuable experiments using a more physically-based description of the defect production.

REFERENCES

1. H. Trinkaus, B.N. Singh and A.J.E. Foreman, Phil. Mag., in press

2. G.H. Kinchin and R.S. Paise. Rep. Prog. Phys., 18 (1955) 1

3. M.J. Norgett, M.T. Rohinson and I.M. Torrens. Nucl. Eng. Design 33 (1975) 50

4. M.T. Rohinson, Proc. Int. Conf. on Irradiation-induced Voids in Metals, Albany, N.Y., June 9-11, 1971 397.

5. H.L. Heinisch and B.N. Singh, J. Nucl. Mater. 191-194 (1992) 1083.

6. T. Diaz de la Rubia, R. S. Averhack, R. Benedek and W. E. King, Phys. Rev. Lett. 59 (1987) 1930

7. R. S. Averhack. T. Diaz de la Rubia and R. Benedek, Nucl. Inst. Meth. B33 (1988) 693.

8. T. Dinz de la Rubia and M.W. Guinan, Mat. Sci. Forum 97-99 (1992) 23.

9. T. Diaz de la Rubia and W.J. Phythian, J. Nucl. Mater. 191-194 (1992) 108.

10. H.L. Hcinisch, J. Nucl. Mater. 117 (1983) 46.

11. T. Diaz de la Rubia, R. S. Avcrhack, H. Hsieh and R. Benedek, J. Mater. Res. 4 (1989) 579.

12. B.N. Singh and A.J.E. Foreman, J. Nucl. Mater. in press.

13. V. Naundorf, I. Nucl. Mater. 182 (1991) 254.

14. L.E. Rchn and P. Okamoto, Mat. Sci. Forum 15-18 (1987) 985.

15. A. Mueller, V. Naundorf and M-P. Macht, I. Appl. Phys. 64 (1988) 3445.

16. R.A. Erck and L.E. Rehn, I. Nucl. Mater. 16X (1989) 208.

17. M-P. Macht, R. Willecke and V. Naundorf, Nucl. Instr. and Mcth. B43 (1989) 507.

MOLECULAR DYNAMICS CALCULATIONS OF DEFECT ENERGETICS IN β-SiC* -- Hanchen Huang, Anter El-Azab, **and** Nasr Ghoniem (Mechanical, Aerospace and Nuclear Engineering Department, University of California. **Los** Angeles, CA 90024-1597, USA)

OBJECTIVE

The objective of the present work is to establish a data base for defect formation and migration energies in SiC. Experimental and theoretical studies of microstructure evolution will rely on this data base.

SUMMARY

The Molecular Dynamics (MD) method is used to calculate defect energetics in β- silicon carbide. Many-body interaction effects in this covalent material are accounted for by using a hybrid of two-body and three-body potentials. Calculated bulk properties of β-SiC based on this potential are in agreement with experimental data to within 17%. A micro-crystal is constructed to represent the computational cell and external forces are applied to *the* micro-crystal so that it behaves as a part of an infinite medium. The potential energy for the unperturbed computational cell is fist calculated. The cell is then set at a defect configuration and relaxed, and the potential energy of the relaxed cell is calculated. The difference between the potential energy of the unperturbed cell and that of the defect-containing cell is used to calculate the formation and binding energies of point defects, defect clusters and helium-vacancy clusters in SiC.

PPROGRESS **AND** STATUS

Introduction

Defect energetics in covalent materials have not yet been studied by the Molecular Dynamics (MD) simulation technique. Several approximate calculations were performed for vacancy formation

---

* **Work** supported by the Office of Fusion Energy, US DOE under grant DE-FG03-91ER54115

energies[1-6] in germanium, diamond, silicon, and silicon-carbide. These studies can be classified into two categories. The first one[1,2,3] employed a Morse-type potential and made several approximations about the relaxation of atoms neighboring a vacancy. The shortcomings of this approach are: (1) it does not fully relax the defected lattice, and (2) it does not consider surface distortion associated with forming a vacancy. The second approach[4,5,6] considered the electronic structure of a defected lattice and omitted lattice relaxation. Since a defected lattice does relax, this approach shouldn't be able to give reasonable results. Surprisingly, results of both approaches are in good agreement with experimental data.

In our numerical simulations, an empirically-calibrated potential function for Si and SiC[8] is used. Many-body effects are taken into account by employing a phenomenological three-body potential. The bulk and cluster properties calculated using this potential function agree with experimental data to within 17%. An important process to consider is surface distortion of the crystal when a vacancy or a vacancy cluster is formed. When an atom is put on a surface of a crystal. some bonds will be formed. Meanwhile, there will also be surface distortion. This process is demonstrated in figures (1) and (2).

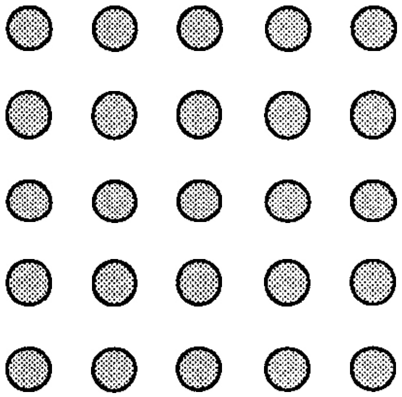

Fig 1. Crystal configuration before surface distortion

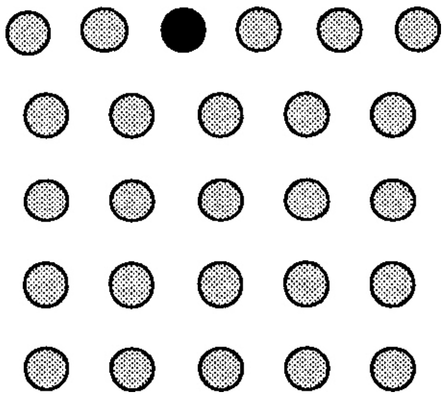

Fig 2. Crystal configuration after surface distortion

MD Simulation

The Molecular Dynamics simulation method is well established. Several numerical algorithms have been used to solve Newtonian mechanics equations. Calibrating interatomic potential functions and constructing a representative computational cell are generally the two main considerations when the technique is applied to a class of problems.

Newtonian Mechanics

According to Newtonian mechanics, a particle of given initial position and velocity can be tracked if the potential or force acting on it is known. In solid crystal, an empirical potential form describing interactions of lattice atoms is required for solution of the equations of motion. Theoretically speaking. one can track all lattice atoms in a solid crystal. In practice, however, this is not feasible and a cutoff distance for atom interactions is always used. The coupled equations of motion for an atom i are given by:

$$\frac{d\vec{r}_i}{dt}=\vec{v}_i$$

$$\frac{d\vec{v}_i}{dt}=\frac{\vec{F}_i(\vec{r}_1,\vec{r}_2,\ldots\ldots,\vec{r}_n)}{m_i} \qquad i=1,2,\ldots\ldots,n \tag{1}$$

with $\vec{r}_i(0)$ and $\vec{v}_i(0)$ given.

For a conservative force, $F_i(\vec{r}_1,\vec{r}_2,\ldots\ldots,\vec{r}_n)=-\vec{\nabla}\Phi_i(\vec{r}_1,\vec{r}_2,\ldots\ldots,\vec{r}_n)$. For boundary atoms, additional forces, $\mu\frac{d\vec{r}_i}{dt}$, will also be included. Here, $\vec{r}_i$ and $\vec{v}_i$ are space and velocity coordinate vectors of the i-th atom, and $\Phi_i(\vec{r}_1,\vec{r}_2,\ldots\ldots,\vec{r}_n)$ is the potential energy of the i-th particle

Interatomic Potentials in Silicon Carbide

Two-body potentials have been widely used for metals[9]. When one considers a covalent material (e.g. SiC) short range interactions become imponant. A many-body potential appropriate for this purpose has been developed by Born and Opperheimer{7}, and the potential is given in the form:

$$\Phi_i(\vec{r}_1,\vec{r}_2,\ldots\ldots,\vec{r}_n)=\frac{1}{2!}\sum_{i\neq j}V^{(2)}(\vec{r}_{ij})+\frac{1}{3!}\sum_{j\neq i}\sum_{k\neq j\neq i}V^{(3)}(\vec{r}_{ij},\vec{r}_{ik},\vec{r}_{jk})$$

$$+\ldots\ldots+\frac{1}{n!}\sum_{i\neq}\ldots\sum_{\neq n}V^{(n)}(\vec{r}_{ij},\ldots,\vec{r}_{in},\ldots) \tag{2}$$

To make this many-body potential usable in practice, Pearson et al[8] truncated the expansion up to the three-body level. For SiC, they combined Lennard-Jones two-body potential[9] and Axilrod-Teller three body potential[10] in the form:

$$V^{(2)}(\bar{r}_{ij}) = \frac{\varepsilon}{m-n}\left[n\left(\frac{R_o}{r_{ij}}\right)^m - m\left(\frac{R_o}{r_{ij}}\right)^n\right] \tag{3}$$

$$V^{(3)}(\bar{\bar{r}}_{ij},\bar{\bar{r}}_{ik},\bar{\bar{r}}_{jk}) = Z\left[\frac{1+3\cos\theta_{ij}\cos\theta_{ik}\cos\theta_{jk}}{\left(r_{ij}r_{ik}r_{jk}\right)^3}\right] \tag{4}$$

Where the energy parameters (ε, Z) and the two-body structure parameters (m, n, R_O) were determined to give the best fit to experimental data for bulk solid and atomic clusters (e.g. bonding energies and bond length). For SiC, Pearson et al give[8]:

(m. n) value: (12, 6)

ε value(eV): (Si-Si)=2.817, (Si-C)=3.895, (C-C)=5.437

R_O value(Å): (Si-Si)=2.2951, (Si-C)=1.7400, (C-C)=1.4806

Z value(eV/Å):(Si-Si-Si)=3484.0, (Si-Si-C)=698.2, (Si-C-C)=261.8, (C-C-C)=167.3

Interatomic Potentials in He-C and He-Si Systems

Interaction between closed shell atoms is dominated by Van der Waals mechanism. Using a perturbation method, Slater et al[11] calculated the interatomic potential between two helium atoms. Their calculated result of polarizability is close to that measured experimentally, and their potential function is given by:

$$V_{He-He} - \frac{0.91}{r^6}eV \tag{5}$$

It is also shown by Slater et al[11] that the potential is proportional to $\alpha_1^{3/4}\alpha_2^{3/4}$, where a denotes the polarizability, while the subscripts represent interacting particles. The polarizability data for silicon or carbon atoms is not available. Since the electronic structure of carbon is intermediate between helium and neon, while that of silicon is intermediate between neon and argon, as a first order approximation, the polarizability of carbon is taken as an average for that for helium and neon. Likewise, the polarizability of silicon is taken as an average for that for neon and argon. The polarizabilities for silicon and carbon can therefore be written as:

$$\alpha_{Si} \approx \frac{1}{2}(\alpha_{Ne} + \alpha_{Ar}) \tag{6}$$

$$\alpha_C \approx \frac{1}{2}(\alpha_{He} + \alpha_{Ne}) \tag{7}$$

According to Slater et al[11], α_{He}, α_{Ne}, and α_{Ar} are $0.39\text{x}10^{-24}$ cm^{-3}, $1.65\text{x}10^{-24}$ cm^{-3}, and 2.50x 10^{-24} cm^{-3}, respectively. Interatomic potentials between helium and carbon and that between helium and silicon can then be derived from the helium-helium interatomic potential. They can be expressed as:

$$V_{He-C} = \left(\frac{\alpha_C}{\alpha_{He}}\right)^{3/4} V_{He-He} \tag{8}$$

$$V_{He-Si} = \left(\frac{\alpha_{Si}}{\alpha_{He}}\right)^{3/4} V_{He-He} \tag{9}$$

Using Lennard-Jones potential to account for the intrinsic repulsive interaction, we can write the total interatomic potential between helium **and** carbon or that between helium **and** silicon **as:**

$$V = \frac{\varepsilon}{6}\left(6\frac{r_0^{12}}{r^{12}} - 12\frac{r_0^6}{r^6}\right) \tag{10}$$

Where r_0 is equilibrium interatomic distance, which is approximated as the sum of atomic radius of the interacting atoms. When bonds are formed, the atomic radii of helium, carbon, and silicon are 0.93 Å, 0.77 Å, and 1.11 Å, respectively[12]. On this basis, ε is calculated to be $2.07\text{x}10^{-2}$ eV and $2.46\text{x}10^{-2}$ eV for helium-silicon and helium-carbon interaction, respectively.

Construction of a Computational Cell

A computational cell is surrounded by boundary atoms, whose thickness is larger than effective range of interactions in the crystal. The boundary consists of a hybrid of fixed and flexible atoms. Due to the cutoff of interatomic interactions, a net force on an atom in a perfect crystal is not zero. External forces are applied to the lattice atoms to balance these forces. A vacancy is created by moving an inner lattice atom to the surface of the crystal. A vacancy cluster is created by moving several neighboring atoms to surfaces of the crystal. These atoms are located far away from each other on surfaces, *so* that mutal interactions do not take place. An antisite defect is formed by replacing a silicon (or carbon) atom by a carbon (or silicon) atom. A cavity consisting of a vacancy and a helium atom is formed by: (1) creating a vacancy, and (2) filling the vacancy by a helium atom. In each case, the defected lattice is relaxed to its equilibrium state.

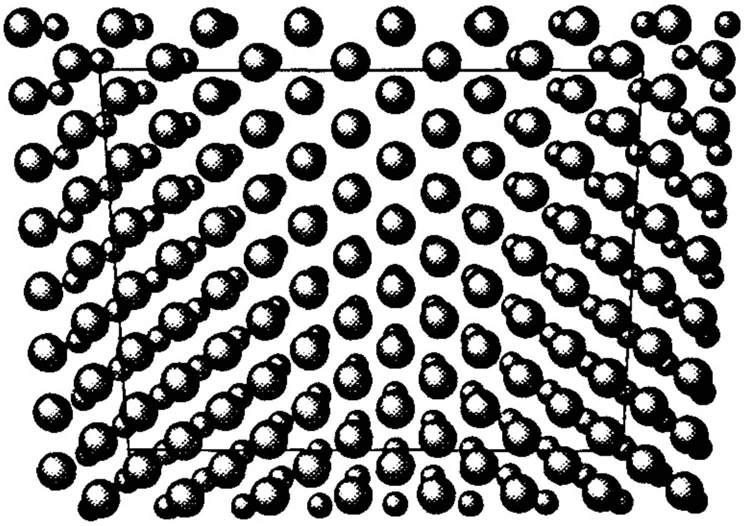

Fig **3.** View of the computational cell from (100) direction. The larger spheres represent silicon atoms, while the smaller ones represent carbon atoms. Boundary atoms and inner atoms are separated by solid lines.

A computer code for solving these coupled equations was developed at UCLA[13]. The standard Leapfrog numerical method was used in solving the coupled differential equations. In **the** simulation process, a velocity component is quenched to zero whenever it is in the opposite direction to the corresponding acceleration component. Figure **(3)** shows a typical computational cell for SiC.

Defect Energetics

A self-diffusion process is controlled by its activation energy. If vacancy diffusion is the **operating** mechanism, the activation energy **can be** divided into: **(1)** vacancy formation energy. and (2) atom migration energy.

Defect Formation Energies

The vacancy formation energy consists of several parts. In covalent materials. several **bonds** are broken when **an** atom is moved away from its lattice position. The potential energy of the crystal increases by ΔE. Relaxation of surrounding atoms decreases the potential energy of the cell by E'_{rel}.

The relaxation of lattice **atoms** surrounding a silicon single vacancy is shown in figure **(4).** Relaxation of nearest neighbors to a silicon vacancy and and those to a carbon vacancy **are** compared in figure (5)

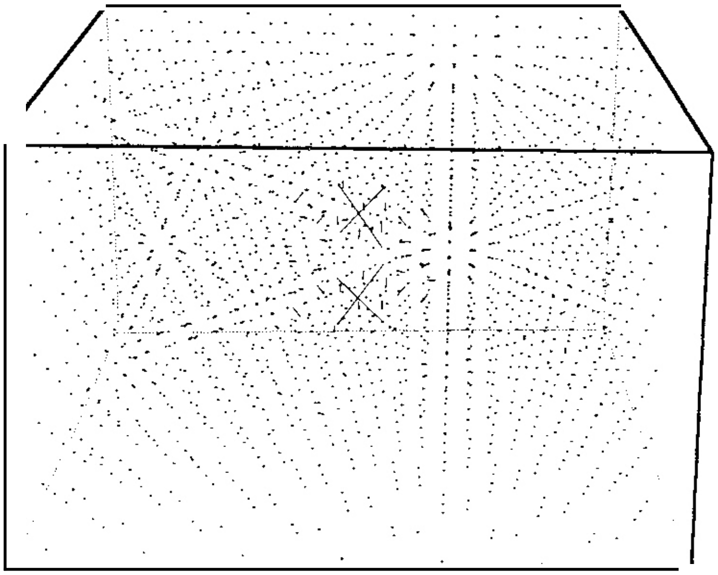

Fig **4.** Relaxation of lattice atoms around a silicon vacancy. Length of the lines corresponds to magnitude of the relaxation.

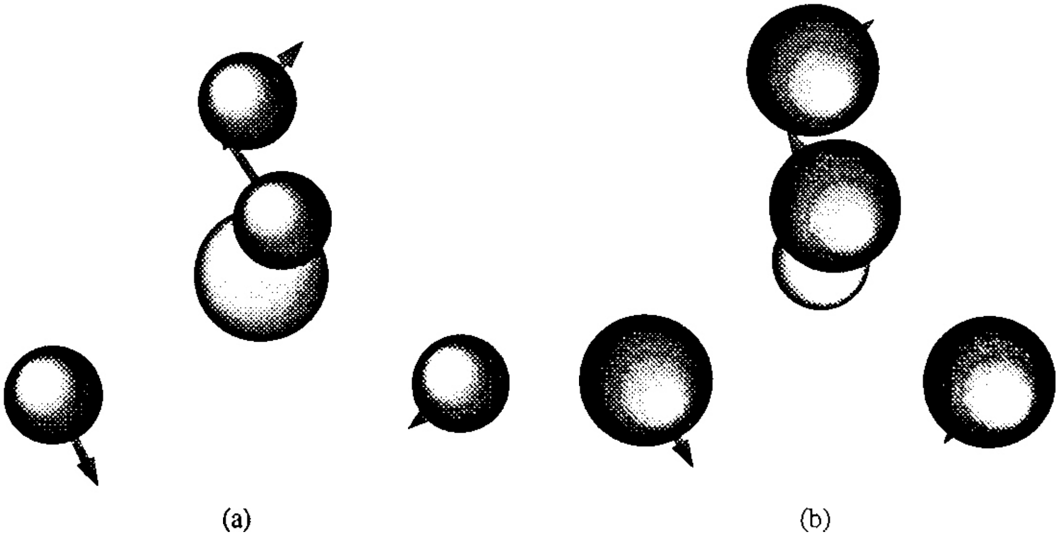

(a) (b)

Fig 5. Relaxation of the nearest neighbors: (a) around a silicon vacancy, (b) around a carbon vacancy. The larger spheres are silicon **atoms** and the smaller ones are carbon atoms.

When an atom is placed on a surface of the crystal, half of the bond energy, $\frac{1}{2}\beta D$, is restored. Meanwhile, distortion of the surface near this atom increases the potential energy of the cell by $\frac{1}{2}E_{rel}$. The formation energy of a single vacancy is therefore given by:

$$E_v^f(1) = AE - E'_{rel} - \frac{1}{2}\beta D + \frac{1}{2}E_{rel} \tag{11}$$

Similarly, the formation energy of a vacancy cluster is given by:

$$E_v^f(n) = AE - E_{rel} - \sum_{i=1}^{n}\left(\frac{1}{2}\beta D - \frac{1}{2}E_{rel}\right) \tag{12}$$

When a lattice atom (say Si in SiC) is replaced by an atom of the other type (say C), potential energy of the crystal increases by AE. Relaxation of the surrounding atoms decreases the potential energy of the crystal by E'_{rel}. Formation energy of an antisite defect is given by:

$$E_s^f = \Delta E - E'_{rel} \tag{13}$$

Where β is coordination number of the crystal, D is bonding energy, βD equals AE in forming a single vacancy, E, is the relaxation energy of lattice atoms surrounding a single vacancy, and E'_{rel} is the relaxation energy of lattice atoms surrounding the given defect. The formation energy of a gas tilled vacancy is calculated in the same way as for a single vacancy. The only difference is that a helium atom is placed at the vacant lattice point before the crystal is relaxed.

Binding energies of a vacancy in a vacancy cluster of n vacancies *can* be calculated by:

$$E_v^b = E_v^f(n) - E_v^f(n-1) \tag{14}$$

Where the cluster of (n-1) vacancies has one less vacancy (Si or C depending on which vacancy type is being considered) than the cluster of n vacancies.

Defect Migration Energies

Self-atom migration energy can be deduced from thermal diffusion data if the atom migrates through vacancies. The migration energy is the difference between the thermal activation energy and the vacancy formation energy. For SiC, the thermal diffusion data has been documented by Ghoshtagore et al[14], Hong et al[15,16] and Hon et al[17,18]. Experimental data and theoretical simulation results will be combined to give the defect migration energies. The thermal diffusion data for β-SiC, given by

Hon et al[17,18], are listed in table 1. For comparison, thermal diffusion data for a-Sic, given by Hong et al[15,16], are appended to table 1.

A vacancy diffusion mechanism is strongly suggested by the experimental data{14-18]. It is found that acceptor dopants always occupy Si-sites[19,20]. Hong et al[15,16] found that n-doping increases Si diffusivity and decreases C diffusivity. These results imply that Si atom diffuses through Si vacancies while C atom diffuses through C vacancies. Based on these experimental evidences, we can divide the measured activation energy of Si into two parts. The first is the formation energy of the Si vacancy, and the second is the migration energy of the Si atom. Similar arguments apply to C.

TABLE 1: Diffusion Data for Point Defects in SiC

Sample	Diffusion Atom	T-Range(K)	D_0(cm^2/s)	Q(eV)	Ref
β-SiC	C	2128-2384	2.6×10^8	8.7	15
	Si	2283-2547	8.4×10^7	9.5	16
α-SiC	C	2123-2453	8.6×10^5	7.4	13
	Si	2273-2563	5.9×10^2	7.2	14

Results and Conclusions

The energy increase due to atom displacement, $\Delta E\text{-}E'_{rel}$ is first calculated. Then, energy changes due to surface restoration and surface distortion arc derived from bond energies and the energy of relaxation around a vacancy, respectively. With this procedure, the formation energies of several types of defects are deduced. Binding energies of vacancy clusters, antisite defects, and gas filled vacancies are also calculated. Migration energies of single vacancies are obtained by combining the theoretical vacancy formation energies and the experimental thermal activation energies. The **results** are shown in table 2. From these calculated results, several salient conclusions can be drawn:

TABLE 2: Calculated Results for Defect Energetics in β-SiC

Defect Sample	ΔE-E'rel (eV)	Surface Restoration (eV)	Surface Distortion (eV)	Formation Energy (eV	Binding Energy (eV	Migration Energy (eV
He-filled Si	6.57	5.64	2.30	3.23	-0.11	——
He-filled C	9.88	5.35	0.30	4.83	-0.23	——
Antisite-Si	-3.75	N/A	N/A	-3.75	N/A	——
Antisite-C	6.18	N/A	N/A	6.18	N/A	——
Si-vacancy	6.68	5.64	2.30	3.34	N/A	2.52
C-vacancy	10.11	5.35	0.30	5.06	N/A	6.16
SiC-divacancy	16.28	10.99	2.60	7.89	-0.51	——
Si$_2$C-trivacancy	23.99	16.63	4.90	12.26	+1.03 for Si	——
SiC$_2$-trivacancy	25.99	16.34	2.90	12.55	-0.40 for C	——
Si$_3$C-tetravacancy	31.58	22.27	7.20	16.51	+0.91 for S	——
SiC$_3$-tetravacancy	35.82	21.69	3.20	17.33	-0.28 for C	——
Si$_2$C$_2$-tetravacancy	35.02	21.98	5.20	18.24	+2.35 for Si +0.92 for C	——

(1) The surface distortion energy is found to have an important contribution to defect energetics calculation.

(2) A silicon atom can be spontaneously replaced by a carbon atom from the energy point of view. This means that more carbon atoms may be present in non-stoichiometric cases.

(3) Atoms surrounding a silicon vacancy undergo substantial relaxation while atoms surrounding a carbon vacancy do not relax as much. This is due to the size asymmetry of silicon and carbon atoms

(4) A divacancy is thermodynamically stable against single vacancies. A divacancy is always composed of one silicon vacancy and one carbon vacancy because the nearest neighbors are always of different types.

(5) Vacancy clusters of up to 4 vacancies prefer absorbing a carbon vacancy to a silicon vacancy in forming larger vacancy clusters.

(6) Helium-filled vacancies are more stable as compared to unoccupied vacancies. The effect of helium in stabilizing vacancies is therefore important.

FUTURE WORK

Defect energetics established in this work will be included in a comprehensive microstructure evolution model of SiC under neutron irradiation.

ACKNOWLEDGMENT

Special thanks are directed to Mr. Ed Aguilar for his assistance in typing the manuscript. Support of the Office of Fusion Energy, through the DOE-grant DE-FG03-91ER54115 with UCLA, is greatly acknowledged.

REFERENCES

1 R. Swalin, J. Phys. Chem. Solids 18(1960)290

2 A. Scholz, Phys. Status Solidi 3(1063)43

3 A. Scholz and A. Seeger, Phys. Status Solidi 3(1963)1480

4 C. Hwang and L. Watt, Phys. Rev. 171(1965)958

5 K. Bennemann, Phys. Rev. 137A(1965)1497

6 J. Bernholc, S. Kajhara, C. Wang. and A. Antonelli, Mater. Sci. Engr. B11(1992)265

7 J. Lennard-Jones, Interatomic Forces, Special Publication No. VIII, Indian Association for the Cultivation of Science,Calcutta, India, 1939

8 E. Perason, T. Takai, T. Halicioglu and W. Tiller, J. Crystal growth 70(1984)33

9 G. Maitland et al, Intermolecular Forces, Oxford, 1981, Appendix 1.

10 B. Axilrod and E. Teller, J. Chem. Phys. 54(1971)2129

11 J. Slater and J. Kirwood, Phys. Rev. 37(1931)690

12 Table of Periodic Properties of the Elements, Sargent-Welch Scientific Company, USA, 1992

13 P. Chou and N. Ghoniem, Phys. Rev. B43(1991)2490

14 R. Ghoshtagore and R. Coble, Phys. Rev. 143(1966)623

15 J. Hong and R. Davis, J. Am. Ceram. Soc. 63(1980)546

16 J. Hong, R. Davis and D. Newbury, J. Mater. Sci. 16(1981)2485

17 M. Hon and R. Davis, J. Mater. Sci. 14(1979)2411

18 M. Hon and R. Davis, J. Mater. Sci. 15(1980)2073

19 W. Choyke and L. Patrick, Phys. Rev. B2(1970)4959

20 Y. Vodakov and E. Mokhov, Silicon Carbide-1973, ed by R. Marshall, J. Faust Jr, and C. Ryan, University of Southern California Press, 1974, p508

6.0 DEVELOPMENT OF STRUCTURAL ALLOYS

6.1 Ferritic Stainless Steels

EFFECTS OF HYDROGEN AND LOADING MODE ON THE FRACTURE TOUGHNESS OF A REDUCED ACTIVATION FERRITIC STAINLESS STEEL

H. Li (Washington State University), R. H. Jones (Pacific Northwest Laboratory), J. P. Hirth (Washington State University), and D. S. Gelles (Pacific Northwest Laboratory)

OBJECTIVE

The purpose of this effort is to investigate the effects of hydrogen and loading mode on the fracture toughness of a reduced activation ferritic stainless steel (F-82H).

SUMMARY

The full spectrum of fracture toughness (J integrals), including pure mode I, different mixed mode I/III and pure mode III, will be examined for a ferritic/martensitic stainless steel with 0.1C-8Cr-2W-0.2V-0.04Ta-Fe (by wt%), designated as F-82H. The J integrals of pure mode I (J_{Ic}) and mixed mode I/III (J_{mixed}) are determined with single specimen method using standard compact tension specimens and modified compact tension specimens, respectively. The pure mode III integral is measured with multiple specimen method using "triple-pantleg" specimens. Effects of hydrogen on the J integrals of pure mode I and mixed mode I/III are also going to be studied. 9 ppm H (about 500 appm) is pre-charged into specimens cathodically. The details of experimental procedure were described in this report. The preliminary results showed that addition of mode III stress (shear stress) to mode I loading had a significant negative effect on the fracture toughness of F-82H. The complete results, analysis and conclusion will be reported in next report. The results would be important to fusion reactor design.

PROGRESS AND STATUS

Introduction

Since the late 1970s, ferritic/martensitic Cr-Mo steels have been considered alternate candidate structural materials to austenitic stainless steels for first wall and blanket structure applications. Irradiation studies (1,2) in fast reactors showed these steels are superior to austenitic steels in several aspects, such as swelling resistance, higher thermal conductivity and lower thermal expansion, and compatibility with potential breeder and coolant materials. Investigation indicates that ferritic steels are corroded by liquid lithium and Pb-Li eutectic at the rates of 5 to 10 times slower than austenitic stainless steels. By replacement of molybdenum in conventional Cr-Mo steels with vanadium and/or tungsten, reduced-activation ferritic steels have been developed since the mid 1980s. Among them martensitic steels with 7-9% Cr have been favored over 12% Cr steels, because it is difficult to eliminate δ-ferrite in a 12% Cr steel without increasing carbon or manganese for austenite stabilization. Delta-ferrite can lower toughness, and manganese promotes chi-phase precipitation during irradiation, which can cause embrittlement. As a potential material used as first wall or blanket, fracture toughness is an important mechanical property. However, there is little fracture toughness data, especially J integral, on either unirradiated or irradiated conditions. Critical values of J integral can be used as an engineering estimate of fracture toughness near the initiation of slow stable crack growth of a pre-existing crack in metallic materials.

Traditionally, mode I fracture has been used to study elastic-plastic fracture mechanics. However, in recent years, mixed mode fracture has become the focus of many studies because many observed failures include shear components (3-11). Fracture characteristics have been found to differ, depending on microstructure, strength, and toughness level of materials. In low toughness high-strength alloys, such as 0.29C, 0.83Cu steel and 1.25C bainitic steels (9-11), mode III additions to mode I loading had little or no effect on the overall value of J_{Ic}, the mode I component J integral for mixed mode crack initiation, and tended to increase J_{c}, the total J integral for mixed mode crack initiation. In the tougher materials, such as 3.5NiCrMoV steel, A710A and a high purity rotor steel (HPRS) (3-11), which failed primarily by a microvoid nucleation and growth mechanism, mode III additions lowered the J_{c} values considerably from their pure mode I values. The J_{c} values passed through a minimum at a position between pure mode I and pure mode III on a plot of J_{c} vs crack inclination angle. It was also found that introducing hydrogen to a tough material, such as HPRS, further lowered the total J integral (see Figure 1) even though hydrogen showed little effect on the elongation of tension specimen.

Pacific Northwest Laboratory is operated for the U.S. Department of Energy by Battelle Memorial Institute under Contract DE-AC06-76RLO 1830.

A **steel** with 0.1C-8Cr-2W-0.2V-0.04Ta (designated as F-82H) has been developed as **a** reduced activation ferritic/martensitic **steel** by **Japanese** Scientists. F-82H **has** been **considered** as one of the candidates far first wall material of **a** fusion **reactor.** Preliminary J Integral data (12) obtained from **three** point **bending** specimens showed that F-82H is a very tough steel. It is possible that introduction of mode III component to pure **made I** loading would **also lower** the total J integral of F-82H as in the **case** of **HPRS.** Furthermore, **it** is well **known** that the next generation of fusion reactors will **produce** hydrogen during operation. Hence, **investigation** of combined effects of mixed mode **loading and** hydrogen on fracture toughness of F-82H **is** critical far the steel to **be used as** first wall material

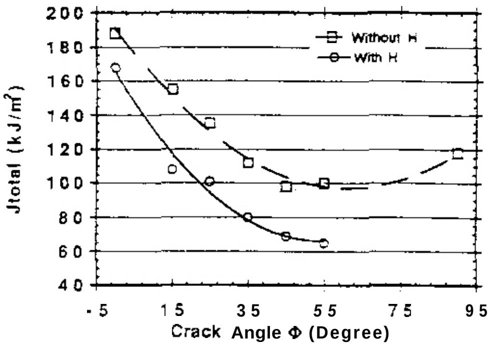

Fig. I. A plot of critical total J integral vs crack inclination **angle** Φ showing J_{total} of HPRS **parsing a minimum between** made I and mode III loading and being **'lowered** further by hydrogen. Φ = 0 deg. and Φ = 90 deg. represent pure **mode** I (J_{Ic}) and ***mode*** III (J_{IIIc}), respectively (Ref. *8)*

Material and Experimental Methods

i. Material

F-82H plate used in this Study **was** supplied by Nippon **Kokan** steel Company (NKK) in Japan. The chemical composition of the plate is in **Table** 1. Specimens ***used* in** this study **were heat-treated** with the **procedure** of 1000°C/20 hours/air cooling, 1100°C/7 minutes/air **cooling, and** 700°C/2 hours/air cooling. The microstructure was **tempered** martensite. **average** intersection **distance** of grains was 25 μm **(ASTM** #7.5).

Table 1 Chemical Composition of F-82H (Heat No. 8033), Wt Pct

C	Cr	W	V	Ta	Mo	P	S	Si	Mn	Cu	Ni	Ti	Nb	SoLAl	B	T.N	T.O	Fe
0.096	7.71	2.1	0.18	0.04	<0.01	0.003	0.003	0.10	0.15	0.01	<0.1	0.008	<0.005	0.005	0.0004	0.0043	0.0028	bal

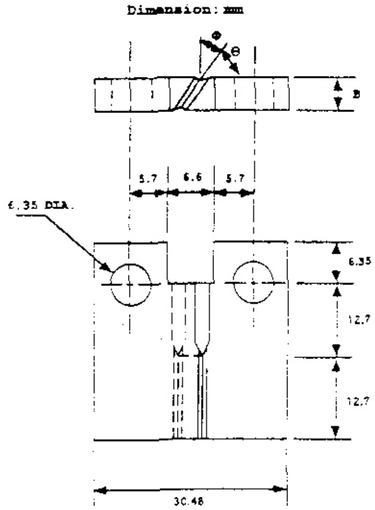

Fig. 2. Modified compact tension specimen geometry used in Mode I and combined

2. Experimental Methods

i. Tests with Modified Compact Tension Specimens

The geometry of modified compact tension specimens to be used for mixed-mode I/III testing is schematically shown in Figure 2. The magnitude of mode III components can be varied by changing the crack slant angle Φ. 0 degree represents the pure mode I loading, the geometry of the 0 degree specimen becomes the standard compact tension specimen as specified in ASTM standard E813-89. As the crack inclination angle (Φ) increases, the contribution of mode III component increases. The crack inclination angles to be used in this study were 0, 10, 20, 30, 45, 55 dgr.. Side grooves of 20% reduction of total thickness were incorporated in all compact specimens. These side grooves can increase the triaxiality at the edges of the growing crack and constrain the advancing crack in the original crack plane. The calculation of J integral in mixed-mode I/III involves the measurements of both vertical displacement (δ_v) and horizontal displacement (δ_h) of load points. Knife edges were secured to the front face of the specimen. A standard clip COD (Crack Opening Distance) gage was positioned on the knife edges. The load line δ s were calculated from front face δ s with the method proposed by Saxena and Hudak, Jr. (13). The horizontal displacements were small when compared with vertical displacements. It was found that the δ_h increased with δ_v in a linear mode (3,5). Hence, δ_hs were calculated approximately from δ_vs with a relationship of $\delta_h = \alpha \times \delta_v$, where $\alpha = \delta_h(\max)/\delta_v(\max)$.

An electric discharge machine (EDM) was used to make a cut with small radius (radius = 0.051 mm) approximately 1.3 mm long as a substitute of pre-fatigued-crack. The pre-fatigue-crack tended to grow out of original crack plane in mixed-mode specimens while the fine EDM cut was found identical to a pre-fatigued-crack (6). The EDM cuts were made after final heat-treatment and specimens with cuts were heated to about 100°C for 24 hours in a vacuum oven (10^{-} Pa) to outgas possible hydrogen introduced by EDM cutting (14). The single specimen technique was used in this study. Crack length and crack extension were calculated from compliances following the procedure described in E813-89 and Ref. 13.

ii. Tests with "Triple-Pantleg" Specimens

Specimen geometry for pure mode III J integral were depicted in Figure 3, which looks like "triple-pantleg" (5). Side grooves of 40% reduction of the total thickness were made in order to guarantee crack propagation before general yielding in the cantilever beam arms of the specimen. The Outer two legs of the specimen were bolted to a U-shaped base through the 6.36 mm holes. Load was applied to the central leg in a direction normal to the plane of the drawing. The Incorporation of two cracks in the specimen leads to a symmetric loading arrangement minimizing the out-of-plane bending (6). Two 1.3 mm EDM cuts were also made as the substitutes of fatigue cracks. Indirect crack length monitoring techniques such as the electrical potential drop method or unloading compliance are affected by the contact of the asperities on the two specimen surfaces during pure Mode III deformation. Hence, a multiple specimen technique was adapted and the crack lengths were measured after breaking open the specimens.

iii. Charging of Hydrogen

Hydrogen was introduced by cathodic charging at a current density of 80 A/m^2 in a solution of 1N H_2SO_4 with 200 mg/L of As_2O_3 added to the solution as a hydrogen recombination poison. All specimens were ground to 600-grit before cathodic charging. Samples were nickel-plated immediately following hydrogen charging. The goal hydrogen content was 9 ppm. The length of charging time to achieve 9 ppm H was determined experimentally by charging several small samples of 5x5x2.5 mm^3 for different lengths of time and measuring total hydrogen quantitatively with LECO Hydrogen Determinator (Model RH-1SP) using inert gas fusion technique. The time needed to charge real specimens was calculated by the means of diffusion equations described in Ref. 15. Effects of hydrogen on fracture toughness were only carried out on pure mode I and mixed I/III specimens with 0, 15, 25, 35, 45, and 55 deg.

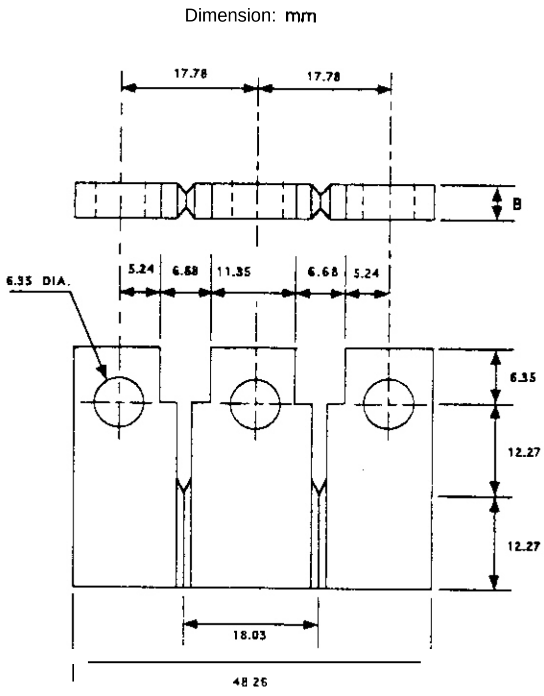

fig. 3. "Triple-Pantlet" specimen geometry used in mode III testing.

DATA ANALYSIS

1. Mode I and Mixed Mode I/III J Integral

The mode I J integral was calculated from the area under the load-displacement curve by means of Eq. [1](16)

$$J = \frac{2}{B\, b_0} \int_0^{\delta} P\, dV \qquad [1]$$

where: B = specimen thickness.

b_0 = the initial uncracked ligament, $W - a_0$,

W = specimen width,

a_0 = the original crack length.

The physical crack length a_p was calculated using the unloading compliance technique outlined in ASTM standard E813-89 and Ref. 13. The mode I and mode III components of mixed mode J, designated as J_i and J_{iii} respectively were calculated by the procedure proposed by Hirth et al (6). The resolved Mode I and Mode III loads and displacements were first calculated in the way as shown schematically in figure 4 and then used to calculate J_i and J_{iii}, by means of Eq. [1]. The subscripts i and iii are used to emphasize that these are not standard values. However, in the case of Φ = 0 deg. J_{ic} becomes the plain strain mode I value of J_{Ic}. Equations [2a] and [2b] show the calculations of J_i and J_{iii}, respectively.

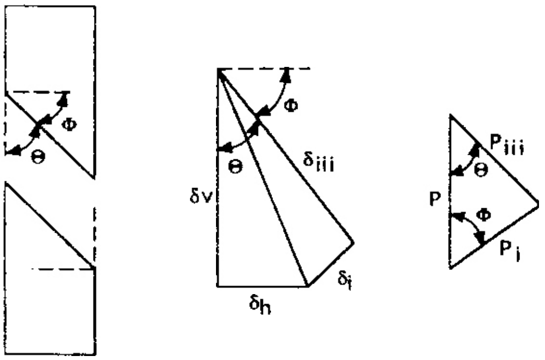

$$P_i = P \cos \Phi$$

$$P_{iii} = P \sin \Phi$$

Fig. 4. Resolution of applied load and measured displacements into mode I and mode III components.

$$J_i = \frac{2}{} \int P_i \, d V$$

$$J_{iii} = \frac{2}{B_{net} \, b_0} \int_0^{\delta_{iii}} P_{iii} \, d V_{iii} \qquad [2b]$$

Here. B_{net} is the net **crack** front width excluding the 10% side **grooves** on each ride. Eq. [3] gives B_{net} in terms of the overall specimen thickness B.

$$B_{net} = \frac{0.8 \, B}{\cos \Phi} \qquad [3]$$

The standard ASTM E813 has two versions, E813-81 and E813-89. There are some differences between the two versions regarding construction of J-Δa curves and determination of critical J values. Because previous studies of mixed mode I/III J integral were guided by E813-81, critical J values will be calculated with the two versions in this study so that a comparison could be made.

In ASTM E813-81, a J vs Δa curve, also referred to as a J-R curve is first generated. Figure 5 shows a typical J-Δa curve with blunting line and two exclusion lines. In the case of pure Mode I J integral, the slope of the blunting line is $J_I/\Delta a = 2\sigma_f$, where $\sigma_f = (\sigma_y + \sigma_{uts})/2$. The exclusion lines parallel to the blunting line are constructed at crack growth increments of 0.15 and 1.5 mm. The J-Δa data between the two exclusion lines are used for the best line fitting. The intersection points between the best straight line and the blunting line and the two exclusion lines define the values of J_{IC} and J_{Iexc}, respectively. The mixed mode data are analyzed similarly. The blunting line slope m_i of mode I component is calculated as $J_i/\Delta a = 2\sigma_f$ same as pure mode I. The blunting line slope m_{iii} of mode III component is given by $J_{iii}/\Delta a = 2\tau_f$, where $\tau_f = (\sigma_y + \sigma_{uts})/4$. The total mixed mode blunting line slope in terms of m_i and m_{iii} is given by Eq. [4].

$$m_{i/iii} = \frac{m_i \cos \Phi + m_{iii} \sin \Phi}{\sin \Phi + \cos \Phi} \qquad [4]$$

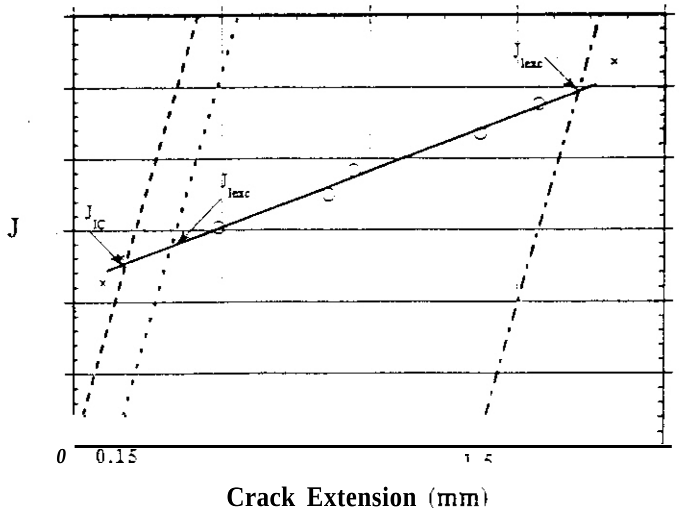

Fig. 5. **Mode** I J-R curve **and** determination of J., and J_{Iexc}.

This **mixed** made blunting line can not **be** used to evaluate the values of J_{ic} **and** J_{iic} separately, because the initiation values of Δa and Δa_i, might **be** different. which would not be sensible for a real crack. Hence, J. (total J) vs Aa is plotted first. Mixed **mode** blunting line **and** exclusion lines in this plot are **used** to evaluate J_c and J_{exc} **and** corresponding values of Δa_c and Aa_{exc}. Vertical lines corresponding to the Δa_c **and** Δa_{exc} are drawn in the J -R **and** J_{iii}-R plots. which act as blunting **and** exclusion liner, respectively. The intersections of there vertical lines with J-Δa curves define the respective **mode** I and **mode** III component J initiation **and** exclusion **values.** This procedure is illustrated schematically in Figure 6. The same procedure is also utilized to modify RSTM E813-89. **Due** to the large amount of calculation. a computer program was written with QBasic to calculate the compliances, crack length. J integrals, best J-Δa data curve fitting and critical J valuer.

11. Mode III J Integral

Due to two cracks in the "triple-pantleg" specimen, Eq. [1] is divided by a factor of 2, hence J_{III} was calculated by Eq. [6].

$$J_{III} = \frac{1}{B_{net}} \int P_{III}\, d V_{III}$$

Here, B_{net} = 0.60B due to the 20% ride grooves on each side. The procedure to determine critical J valuer is the same as that described in the last section. The slope of the blunting line is $J_{III}/\Delta a = 2\tau_f l$, where $\tau_f = (\sigma_y + \sigma_{uts})/4$.

Preliminary Results

Preliminary tests with 10 and 30 deg. modified compact tension specimens showed that the addition of mode III loading (shear stress) to mode I loading had a significant negative effect on fracture toughness of F-82H steel. These preliminary results appear to be similar to those observed for the HPRS as shown in Figure 1. The complete results, analysis and conclusion will be reported in the next Semiannual Report.

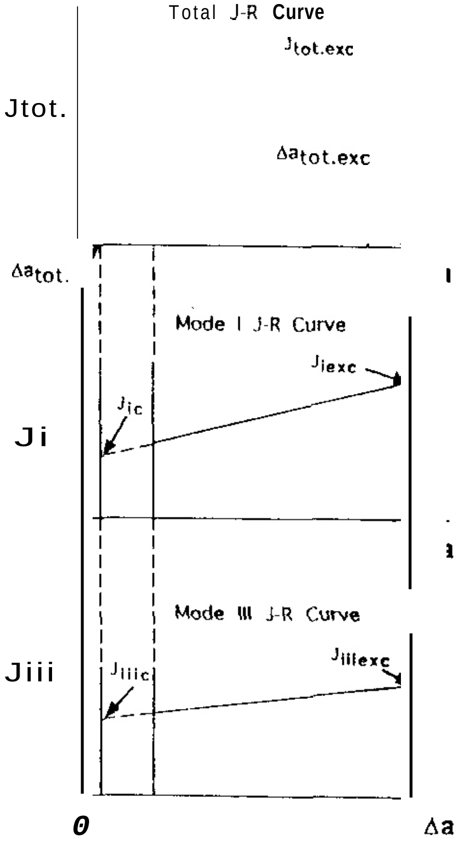

Fig. 6. Evaluation of J_{tot}, J, and J_{iii} initiation and exclusion values from respective J-R curves.

References

1. David S. Gelles, "Effects of Irradiation an Low Activation ferritic Alloys: A Review," Reduced Activation Materials for Fusion Reactors. R. L. Klueh, D. S. Gelles, M. Okada. and N. H. Packan, Eds., American Society far Testing and Materials, Philadelphia, 1990, pp. 113-129.

2. R. L. Klueh. K. Ehrlich, Kernforschungszentrum Karlsruhe, and F. Abe, "Ferritic/Martensitic Steels: Promises and Problems", Fusion Reactor Materials Semiannual Progress Report For The Period Ending March 31, 1992, pp. 131-141.

3. M. T. Miglin, I.-H. Lin, J. P. Hirth, and A. R. Rosenfield, Fracture Mechanics: 14th Symp. --Vol. II: Testing and Applications. ASTM STP 791, J .C. Lewis and G. Sines, Eds., ASTM. Philadelphia, PA, 1983, pp. II-353-II-369.

4. M. T. Miglin, J. P. Hirth and A. R. Rosenfield, Res Mechanica, 11 (1984), pp. 85-95.

5. J. G. Schroth, J. P. Hirth. R .G. Hoagland, and A. R. Rosenfield. Met. Trans. A. 18A (1987), pp. 1061-1072.

6. M. Manoharan. J. P. Hirth, and A. R. Rosenfield, J. of Testing and Evaluation, JTEVA, 18 (1990), No.2, pp. 106-114.

7. S. Raghavachary, A. R. Rosenfield, and J. P. Hirth, Met. Trans. A, 21A (1990). pp. 2539-45.

8. J. A. Gordon. J. P. Hirth. A. M. Kumar, and N. R. Moody, Jr., Met. Trans. A, 23A (1991), pp. 1013-1020.

9. M. Manoharan, S. Raghavachary, J. P. Hirth, and A. R. Rosenfield. J. of Eng. Materials and Technology, 111 (1989), October, pp. 440-442.

10. A. M. Kumar and J. P. Hirth, Scripta METALLURGICA. et MATERIALIA, 25 (1991), pp. 985-90

11. M. Manoharan, Scripta METALLURGICA. et MATERIALIA. 26 (1992), pp. 1187 - 1192.

12. Yoshiro Kuriki, Akihide Yoshitake, and Manabu Tamura, "Fracture Toughness Test Results of Low Activation Ferritic Steel far First Wall Material (F-82H)", NKK Steel Research Center, Japan, April, 1989

13. Ashok Saxena and S. J. Hudak, Jr. Int. Journ. of Fracture, 14 (1978), pp. 453-468.

!4. T. Foecke, P. G. Harsh. N. R. Moody, and W. W. Gerberich, Scripta METALLURGICA. et. MATERIALIA, 28 (1993), pp. 77-80.

15. P. G. Shewmon, Diffusion in Solids. Chapter 1, McGraw-Hill Book Company, 1963.

16. J. R. Rice, P. C. Paris, and J. G. Merkle. ASTM STP 536, ASTM, Philadelphia, PA, 1973. pp. 231-235.

IRRADIATION CREEP AND SWELLING OF THE FUSION HEATS OF HT9 AND 9Cr-1Mo TO 208 OPA AT ~400°C.

F.A. Garner (Pacific Northwest Laboratory'), M.K. Toloczko (University of California at Santa Barbara) and C.R. Eiholrer (Westinghouse Hanford Company)

OBJECTIVE

The objective of this effort is to determine the factors which control the response of structural alloys to radiation and applied Stress.

SUMMARY

The irradiation creep behavior of the fusion heats of HT9 and 9Cr-1Mo at ~400°C has been measured to exposures as large as 208 dpa. HT9 is somewhat nonlinear in its response to hoop stress level in the range 0-200 MPa, but 9Cr-1Mo exhibits only slightly greater than linear behavior with stress level. The strain data of both alloys appear to include some contributions from precipitate-related density changes. Swelling may have occurred in 9Cr-1Mo.

PROGRESS AND STATUS

Introduction

Helium pressurized creep tuber constructed from the fusion heats of the ferritic martensitic alloys HT9 and 9Cr-1Mo (fusion heats 9607R2 and 30176) have completed their irradiation in FFTF at a nominal temperature of ~400°C. The composition and heat treatment of these alloys is listed in Table 1. There 2.24 cm long tubes were periodically discharged from reactor and measurements made of their diameter prior to reinsertion into reactor. (1) The tubes were inserted in all MOTA vehicles from MOTA-1B through MOTA-1G and then continued into MOTA-28. Both alloys were irradiated at hoop stress levels of 0, 60, 100, and 140 MPa, and HT9 was also irradiated at 200 MPa. Irradiation temperatures varied somewhat from one MOTA to the next. but during any one irradiation interval. the temperature was actively controlled within ±5°C of the nominal temperature. Table 2 presents the detailed temperature history of these tubes. There tuber reached exposure dpa levels as large as 208 dpa. The strains of these tubes were last reported at ~150 dpa. *(2)*

Table 1 Composition of Alloys in Weight Percent

	C	Si	Mn	P	S	Cr	Mo	Ni	V	W	N	Al	Ti
HT9	0.20	0.17	0.57	0.016	0.003	12.1	1 04	0.51	0.28	0.45	0 027	0.006	0.001
9Cr-1Mo	0 08	0.11	0.37	0 010	0.003	8.61	0.89	0.09	0.21	< 0.01	0.055	0.007	0.004

Table 2 Irradiation History of Pressurized Tubes

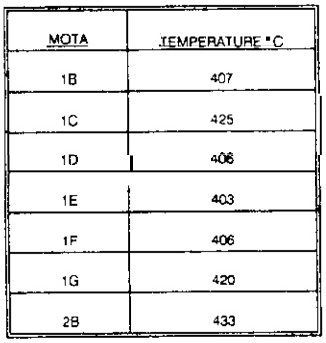

MOTA	TEMPERATURE °C
1B	407
1C	425
1D	406
1E	403
1F	406
1G	420
2B	433

Results and Discussion

Figure 1 presents the total diametral strain and midwall creep strain far HT9, and Figure 2 presents the strains for 9Cr-1Mo. The midwall creep strain is calculated assuming that the strain at zero stress is isotropic and unaffected by stress. Since the strain at zero stress saturates with increasing exposure. it is possible that it arises from precipitation-related changes in density rather than void swelling. In this case. the strain may not be isotropically distributed, however

The strains observed in 9Cr-1Mo exhibit more complexity, especially at higher fluence. Since such complexity was not observed in HT9, it is assumed that the Origin of the complexity is related to a material difference from HT9, rather than some artifact of reactor history. Note that the strain at zero stress for 9Cr-1Mo is larger than that of HT9 with less tendency toward saturation. and therefore may include some contribution from void swelling.

'Pacific Northwest Laboratory is operated for the U.S. Department of Energy by Battelle Memorial Institute under Contract DE-AC06-76RLO 1830.

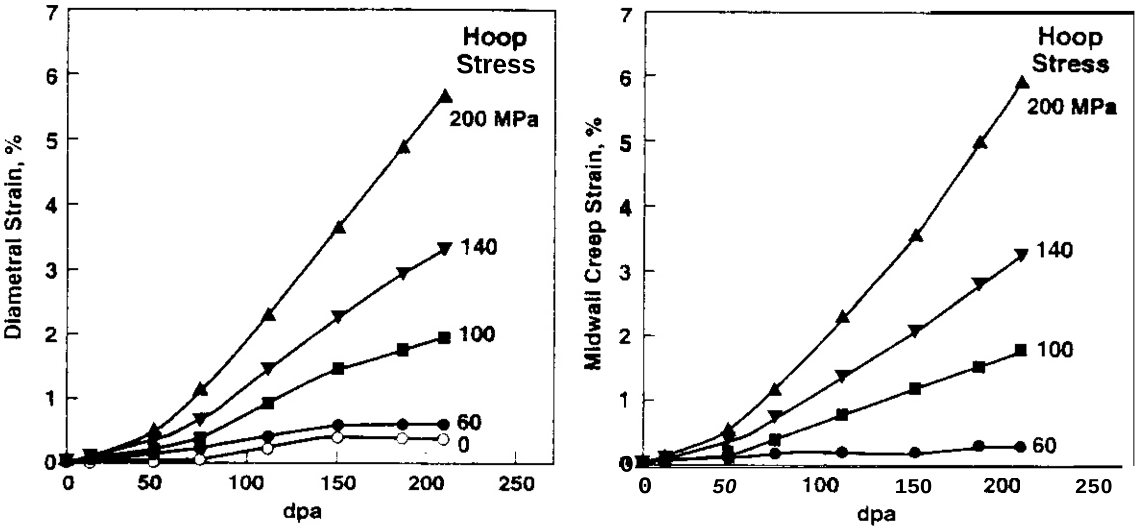

Fig. 1. Total diametral strains and midwall creep strains for HT9

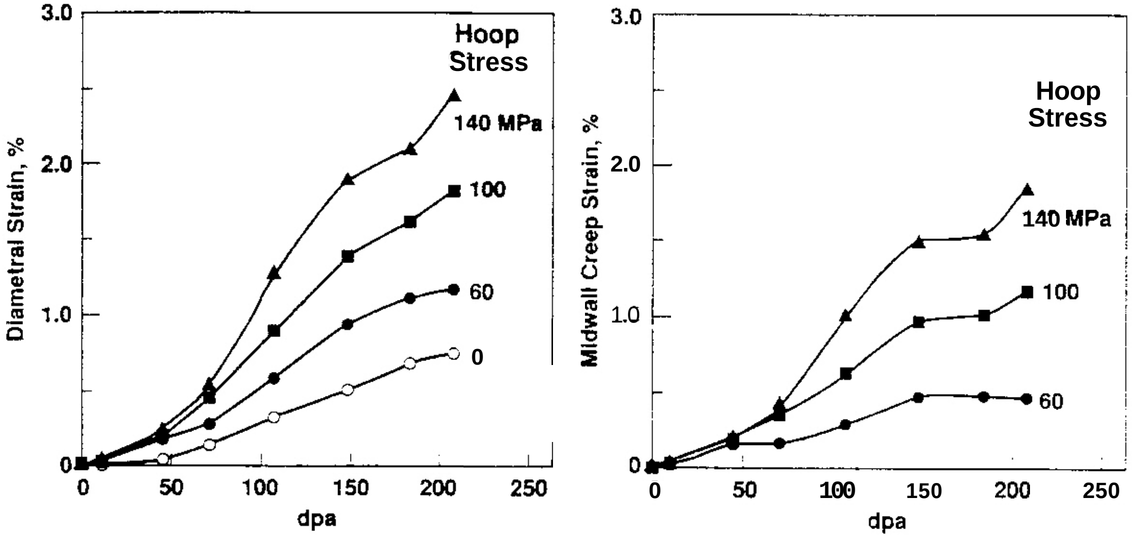

Fig. 2. Total dimetral strains and midwall creep strains for 9Cr-1Mo.

When the midwall creep strains are normalized to their respective hoop stresses, it is obvious that the response of HT9 to stress is characterized by a stress exponent somewhat greater than 1.0 (as shown in Figure 3). The behavior of 9Cr-1Mo is only slightly greater than 1.0 to doses of ≤150 dpa. Above 150 the complexity of response mentioned earlier dominates the normalized creep behavior of 9Cr-1Mo, as shown in Figure 4.

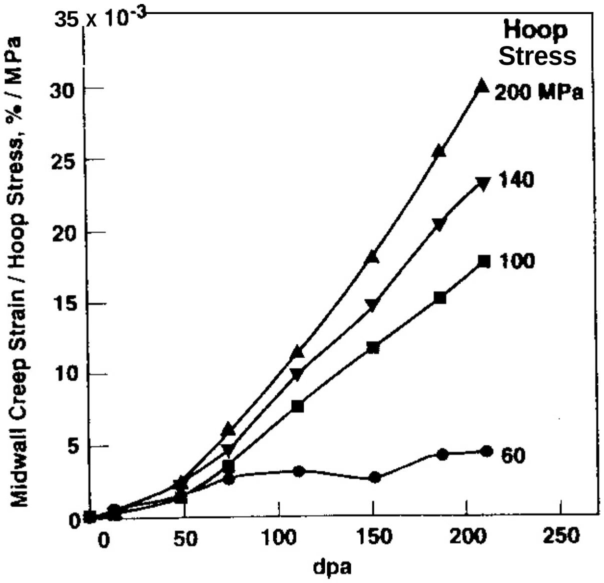

Fig. 3. Stress-normalized midwall creep strains for HT9

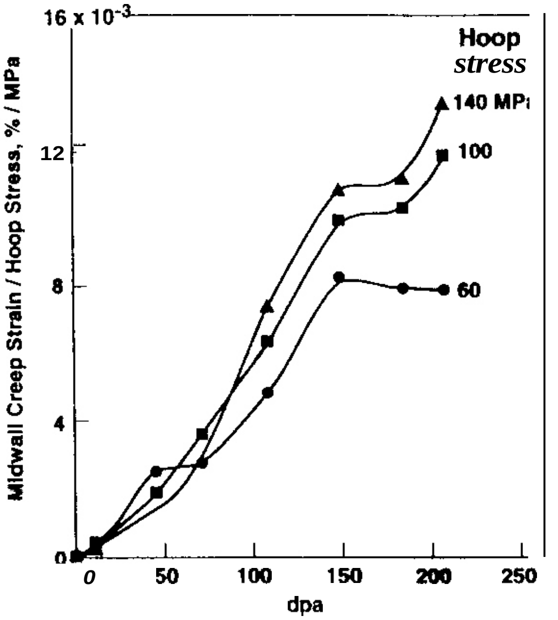

Fig. 4. Stress-normalized midwall creep strains for 9Cr-1Mo.

Expected Achievements in the Next Reporting Period

The pressurized tubes will be cut to produce open tubes and the density of these will be measured. Microscopy examination will also proceed

REFERENCE

1. E.R. Gilbert and B.A. Chin, in Effects of Radiation On Materials: Tenth Conference, ASTM STP 725, 1981, pp. 665-679.

2. F.A. Garner and R.J. Puigh, J. Nucl. Mater., 199-181 (1991) 577-580.

EFFECT OF VANADIUM AND TITANIUM ON MECHANICAL PROPERTIES OF LOW-CHROMIUM. REDUCED-ACTIVATION FERRITIC STEELS -- K. L. Klueh and D. J. Alexander

OBJECTIVE

The goal of this study is the development of a low-chromium reduced-activation ferritic steel

SUMMARY

Tensile and Charpy **impact tests** were made on three normalized-and-tempered 2 1/4Cr-2WV (0.1% C) steels with 0.1, 0.25, and 0.5% V (all concentrations are in weight percent). Increasing vanadium from 0.1 to 0.25% increased the yield stress up to twenty percent. A higher ductile-brittle transition temperature (DBTT) accompanied the higher strength of the 0.25% V steel when both were tempered at 700°C. Tempering at *750°C* gave similar DBTTs. Increasing vanadium from 0.25 to 0.5% caused a slight increase in strength with **a** large decrease in toughness. Thus, a balance between strength and impact toughness is achieved with an intermediate vanadium concentration. Addition of 0.02% Ti to 2 1/4Cr-0.25V, 2 1/4Cr-2W, and 2 1/4Cr-2W-0.25V (0.1% C) steels caused a yield stress decrease of 10 to 30%, which was attributed to the effect of titanium on the MC precipitate distribution. The strength loss was accompanied by an increase in impact toughness, which may also have been affected by a decrease in prior austenite grain **size.** Furthermore, there was little difference in the DBTT of the Ti-modified steels tempered at 700 or 750°C. If it were possible to use a Ti-modified steel tempered at 700°C, this might offset the strength advantage of steels without titanium, which have to be tempered at the higher temperature.

PROGRESS AND STATUS

Introduction

Much of the effort to develop reduced-activation ferritic steels has been concentrated on Cr-W-V steels with 8-10% Cr [1-3]. Low-chromium steels have advantages as structural materials [1], and preliminary work indicated that these steels can have strengths as good **or** better than the higher chromium steels [4]. The strength of a 2.25Cr-2W-0.25V-0.1C (2 1/4Cr-2WV) steel (all concentrations are in wt. %) exceeded that for 9Cr-2W-0.25V-0.07Ta-0.1C (9Cr-2WVTa) steel, the strongest 9Cr reduced-activation steel tested. However. the Charpy impact toughness of the 2 1/4Cr-2WV steel was inferior to that of the 9Cr-2WVTa. Because toughness decreases during neutron irradiation, it would be necessary to improve this property for a low-chromium steel before it could be considered for fusion applications.

Reduced-activation steels cannot contain molybdenum and niobium, two alloying elements in conventional steels of interest for fusion (2 1/4Cr-1Mo, 9Cr-1MoVNb, and 12Cr-1MoVW). Tungsten is considered a replacement for molybdenum, and titanium and tantalum have been considered possible replacements for niobium [1]. **A** series of low-chromium steels was examined previously [4-6]. These included: 2 1/4CrV, 2 1/4Cr-1WV, 2 1/4Cr-2W, and 2 1/4Cr-2WV steels, where the vanadium concentration was constant at 0.25% and all steels contained 0.1% C.

Work is in progress to develop reduced-activation low-Cr steels. **As** part of that work compositional variations were **examined** in an effort to obtain an optimum composition. In this report. 2.25Cr steels are examined to determine the effect of vanadium on strength and impact toughness. Another series of steels were examined to determine how small amounts of titanium affect properties. Impact toughness was evaluated from the ductile-brittle transition temperature (DBTT) and upper shelf energy (USE) in a Charpy test

Experimental Procedure

Experimental alloys were obtained in the form of 600-g vacuum arc-melted button heats. As starting stock for the present studies, material from the original four low-chromium heats were used [4]. These were electroslag-remelted heats prepared by Combustion Engineering, Inc. (CE), Chattanooga, Tennessee. In addition to nominal compositions of Cr, W, and V, concentrations of elements normally found in steels, such as Mn, P, Si, etc., were adjusted to levels typical of commercial practice. Details on chemical composition, microstructure, and mechanical properties of the original heats have been published [4-6].

For the steels with varying vanadium content, heats containing 0.1, 0.25, and 0.5%V were obtained by adding vanadium to the 2 1/4Cr-2W heat from CE. The 0.02% Ti additions were made to the 2 1/4CrV, 2 1/4Cr-2WV (both with 0.25% V), and 2 1/4Cr-2W heats to obtain 2 1/4CrVTi, 2 1/4Cr-2WTi, and 2 1/4Cr-2WVTi, respectively. The original CE heats contained 0.1%C. Alloys were cast into ingots with a rectangular cross section of 12.7 mm by 25.4 mm and 152 mm in length. The ingots were hot rolled at 700°C to approximately 6.4 mm. Half of this plate was cold rolled to 0.76-mm-thick sheet, with an intermediate 700°C anneal. Chemical compositions are given in Table 1.

Tensile specimens with a reduced gage section of 20.3-mm long by 1.52-mm wide by 0.76-mm thick were machined from the 0.76-mm sheet with gage lengths parallel to the rolling direction. One-third size Charpy specimens measuring 3.3 by 3.3 by 25.4 mm with a 0.51-mm-deep 30° V-notch and a 0.05- to 0.08-mm-root radius were machined from the 6.4-mm plate. Specimens were taken along the rolling direction with the notch running transverse to the rolling direction (L-T orientation).

Specimens were tested in the normalized-and-tempered condition. Normalizing of all but the 2 1/4Cr-2W steel involved austenitizing 0.5 h at 1050°C in a helium atmosphere and then rapidly cooling in flowing helium. The 2 1/4Cr-2W was austenitized 0.5 h at 900°C. Two tempering conditions were tested: 1 h at 700°C and 1 h at 750°C. Heat treatments were carried out on machined tensile specimens, and the 6.4-mm plate was heat treated before the Charpy specimens were machined from it.

Tensile tests were made in vacuum from room temperature to 600°C on a 44-kN-capacity Instron universal testing machine at a nominal strain rate of 4.2×10^{-4}/s. Charpy tests were carried out in a pendulum-type impact machine specially modified to accommodate subsize specimens. Details on the test machine and test procedure have been published [7].

Results and Discussion

This report will concentrate on the effect of the alloying additions on mechanical properties. Microstructures will be described only briefly and will be presented in more detail in a future report.

Vanadium variations

Increasing vanadium concentration had two effects on the tempered bainitic microstructure of the steels with 0.1, 0.25, and 0.5%V. First, prior austenite grain size decreased with increasing vanadium concentration. ASTM grain size numbers were estimated at 3, 4, and 5 for the steels with 0.1, 0.25, and 0.5% V, respectively. The second effect involved the fine precipitates that formed in the steels. With increasing vanadium, the number density of fine precipitates increased and the size decreased. The greatest change occurred between 0.1 and 0.25% V, with less change between 0.25 and 0.5% V. These fine precipitates were mainly V_4C_3, but the steels also contained coarser M_3C and M_7C_3 precipitates [5].

Tensile data plotted as a function of test temperature are shown in Figs. 1 and 2. The relative behavior is similar for specimens tempered at either 700 or 750°C, although there is a decrease in strength with increasing tempering temperature. Yield stress [Fig. 1(a)] and ultimate tensile strength [Fig. 1(b)] increase with increasing vanadium concentration. The greatest strength difference occurred between 0.1 and 0.25% V, with much less change between 0.25 and 0.5% V. This observation is probably associated with the observation that a larger change in precipitate number density occurred between the 0.1 and 0.25% V steels than the change between 0.25 and 0.5% V. The 0.25 and 0.5% V steels are considerably stronger than the 0.1% V steel, again a reflection of the microstructure.

Total elongation [Fig. 2(a)] and uniform elongation [Fig. 2(b)] behavior is essentially inverse to the yield Stress behavior, in that the strongest steel has the lowest elongation and vice versa. There is much less difference between the behavior after tempering at 700 and 750°C than there was for the yield stress and ultimate tensile strength. The ductility data show more scatter than the strength data. No explanation is available for the large drop in total elongation for the 0.1% V steel tempered at 750°C and tested at 600°C [Fig. 2(a)]. The relative behavior of the uniform elongation [Fig. 2(b)] with test temperature was similar to the total elongation.

Charpy impact behavior is affected by vanadium composition (Fig. 3). For a given tempering temperature. the DBTT increased with increasing vanadium [Fig 3(a)]. Relatively low values were obtained for the 0.1% V steel for both tempering conditions, as was true for the 0.25% V steel tempered at 750°C. The steel with 0.5% V had a negative DBTT only after the 750°C temper, and then the value was less than half that of the other two steels tempered at this temperature.
As opposed to the large effect of vanadium on DBTT, only a minimal effect was observed for the USE, with essentially no difference for the three steels after the 750°C temper [Fig 3(b)]. After the 700°C anneal, a small decrease occurred between the steel with 0.1 and 0.25% V, with little difference between the 0.25% and 0.5% V steels.

The observations on the DBTT reflect the strength differences of the three steels. Observations on USE are probably a consequence of the ductile fracture process, which must be similar for the three steels. Fracture on the upper shelf is generally determined by the nucleation of voids at precipitate or inclusion particles, and a similar USE implies that similar microstructural features nucleate the fracture in the three steels.

These results indicate that for an optimization of the strength and impact toughness of a 2.25% Cr steel with 2% W, vanadium should be limited to about 0.25%. Increasing the vanadium concentration from 0.25 to 0.5%;results in only a minimal increase in strength at the cost of substantially raising the DBTT.

Titanium additions

The *0.02%* Ti additions were made in 2 1/4Cr-0.25V (2 1/4CrV), 2 1/4Cr-2W, and 2 1/4Cr-2W-0.25V (2 1/4Cr-2WV) steels, which were previously tested and examined [4-6]. The microstructures of *the* test specimens were tempered bainite. Addition of titanium caused a decrease in the prior austenite grain size of the two steels with vanadium, and a decrease in the number density of precipitates relative to all three steels without titanium. Estimated ASTM grain size numbers changed from approximately 4 to 7 for the 2 1/4 CrV and 2 1/4 CrVTi, from 4 to 8 for 2 1/4Cr-2WV and 2 1/4Cr-2WVTi; a grain size number of 10 was estimated for both 2 1/4Cr-2W and 2 1/4Cr-2WTi.

Steels with vanadium and no titanium contained a fine distribution of vanadium-rich MC (V_4C_3) in addition to M_3C and M_7C_3; the *2* 1/4Cr-2W also contained some $M_{23}C_6$ [5]. Although TEM analysis has not been completed on the steels with titanium, they are expected to contain some MC rich in titanium, in addition to vanadium-rich MC, along with the other carbides observed in the steels without titanium.

It is suggested that that all of the titanium-rich MC dissolved during the austenitization treatment. This would limit the grain growth and result in a smaller prior austenite grain size. The reduction in the number density of precipitates of the steels containing titanium could be caused by undissolved titanium-rich carbides acting as nuclei for the vanadium-rich MC that formed during tempering. The limited number of these pre-existing nuclei reduced the number of precipitates that formed.

Addition of 0.02% Ti to the Cr-W-V steels affected the tensile behavior (Figs. 4-7). It caused a marked decrease in the yield stress and ultimate tensile strength of all three steels, as shown in Figs. 4 and 6 for the steels tempered at 700 and 750°C. respectively. The magnitude of the yield strength decrease [Figs. 4(a) and 6(a)] depended on the strength of the steel without the titanium. The 2 1/4Cr-2WV steel was the strongest steel, and it showed the largest decrease. Smaller changes occurred for the other two steels. These observations reflect the observations on the reduction in the precipitate number density caused by the titanium. Ultimate tensile strength behavior [Figs. 4(b) and 6(b)] was similar to the yield stress behavior.

A slight increase in total and uniform elongation (Figs. 5 and 7) accompanied the strength decrease caused by the titanium addition, although there was considerable scatter in the data. Ductility increased with decreasing strength, and the steels tempered at 750°C had a higher ductility than those tempered at 700°C.

Titanium had a large effect on the DBTT of the steels that contained vanadium--the 2 1/4CrV and 2 1/4Cr-2WV steels [Fig. 8(a)]. It had relatively little effect on the 2 1/4Cr-2W steel, which had the lowest DBTT prior to the titanium addition. These observations must be attributed to the change in grain size, in addition to the reduction in strength caused by the titanium addition. The addition of titanium to 2 1/4Cr-2W did not cause a large change in prior austenite grain size, and thus did not cause a noticeable change in DBTT. There was no effect on the prior austenite grain size of the 2 1/4Cr-2W because it was austenitized at 900°C without titanium and at 1050°C when titanium was present. A higher austenitizing temperature was used for the 2 1/4CrV, 2 1/4Cr-2WV, and the steels with titanium in order to ensure the dissolution of the V-rich and Ti-rich carbides.

Note that whereas there is no effect of tempering temperature on the 2 1/4CrV, there is a significant difference for the 2 1/4Cr-2WV. The change for this latter steel probably reflects the reduction of the dispersion strengthening effect because of the larger precipitate particles formed by tempering at 750°C. (The higher number density of samaller precipitate particles in the 2 1/4Cr-2WV makes this steel much stronger than the 2 1/4CrV, which contains a lower density of larger particles.) When titanium is added to this steel, the difference in DBTT for the 700 and 750°C tempering temperatures, is reduced significantly.

There was relatively little difference in the USE of the steels with and without titanium, regardless of the tempering temperature [Fig. 8(b)]. In fact, there was little difference between the different steels. Only the 2 1/4Cr-2WV steel showed some variation, but it was relatively minor compared to the differences noted for the DBTT. Again, this must reflect a similarity in the ductile fracture behavior of these steels, as suggested above for the steels with different vanadium compositions.

These results indicate that titanium might be used to improve impact toughness. Such improvement is desirable, since the DBTT is increased by irradiation. However, this improvement comes at the expense of strength. The effect on strength may be alleviated somewhat by austenitizing at a higher temperature than the 1050°C used in this experiment. This would cause more titanium carbide to dissolve, although it would also increase the prior austenite grain size. Therefore, the best austenitization temperature would have to be determined, because if the temperature was too high, the large prior austenite grain size would negate the positive effect of titanium.

SUMMARY AND CONCLUSION

As part of the effort to develop low-chromium, reduced-activation ferritic steels for fusion reactors, a series of 2 1/4Cr steels was tested to determine the effect of vanadium and titanium on tensile and Charpy impact properties. The steels were tested after normalizing and tempering at 700 and 750°C. The first part of the study examined the effect of adding 0.1, 0.25, and 0.5% V to a 2 1/4Cr-2W steel. Increasing the vanadium from 0.1 to 0.25% caused a large strength increase. Little further increase occurring when vanadium was increased from 0.25 to 0.5%. The DBTT in the Charpy impact tests increased with vanadium, with the largest increase for steels tempered at 700°C; the DBTT of the 0.5% V steel was above room temperature. After tempering at 750°C, there was less difference between the steels with 0.1 and 0.25% V with a greater difference between the 0.25 and 0.5% V steels. Based on these observations, it was concluded that for optimum strength and impact toughness, a 2 1/4Cr-2WV steel should contain about 0.25% V. A 0.02% Ti addition to 2 1/4CrV, 2 1/4Cr-2W, and 2 1/4Cr-2WV steels caused a strength decrease, but it improved the Charpy impact behavior. An improved DBTT would be desirable, since the DBTT increases during irradiation. It may be possible to maintain the improved DBTT and improve the strength by increasing the austenitizing temperature.

REFERENCES

[1] R. L. Klueli and E. E. Blown, Nucl. Eng. Design/Fusion, **2** (1985) 383.

[2] M. Tamura, H. Hayakawa, M. Tanimura, A Hishinuma, and T. Kondo, J. Nucl. Mater., 141-143 (1986) 1067.

[3] D. Dulieu, K. W. Tupholme, and G. J. Butterworth, J. Nucl. Mater.. 141-143 (1086) 1097.

[4] R. L. Klueh. Met. Trans. **20A** (1989) p. 463.

[5] R. L. Klueh and P. J. Maziasz, Met. Trans. **20A** (1989) 371.

[6] R. L. Kluch and W. R. Corwin, J. Materials Eng. 11 (1989) 169.

[7] D. J. Alexander, R. K. Nanstad, W. R. Corwin, and 1. T. Hutton, Applications of Automation Technology to Fatigue and Fracture Testing, ASTM STP 1092, A. A. Braun, N. E. Ashbaugh, and F. M. Smith, Eds. (American Society for Testing and Materials, Philadelphia, 1990) p. 83

Element	2 1/4Cr-2W with			2 1/4 CrVTi	2 1/4Cr-2WTi	2 1/4Cr-2WVTi
	0.1V	0.25V	0.5V			
C	0.097	0.10	0.099	0.10	0.10	0.11
Mn	0.35	0.35	0.36	0.37	0.35	0.39
P	0.016	0.016	0.016	0.016	0.017	0.018
S	0.006	0.006	0.006	0.007	0.003	0.003
Si	0.12	0.12	0.12	0.14	0.15	0.16
Ni	0.01	0.01	<0.1	0.01	0.01	0.01
Cr	2.40	2.40	2.45	2.37	2.47	2.44
Mo	<.01	<.01	<.01	<.01	<.01	<.01
V	0.10	0.25	0.49	0.25	0.009	0.23
Cb	<.01	<.01	<.01	<.01	<.01	<.01
Ti	<.01	<.01	<.01	0.024	0.024	0.020
Co	0.008	0.008	0.008	0.007	0.009	0.009
Cu	0.03	0.03	0.03	0.03	0.03	0.03
Al	0.009	0.009	0.009	0.005	0.013	0.013
B	0.001	0.001	0.001	<.001	0.002	0.002
W	2.10	2.11	2.08	0.01	1.90	1.90
As	0.024	0.025	0.026			
Sn	0.002	0.002	0.002			
Zr	<.001	<.001	0.013			

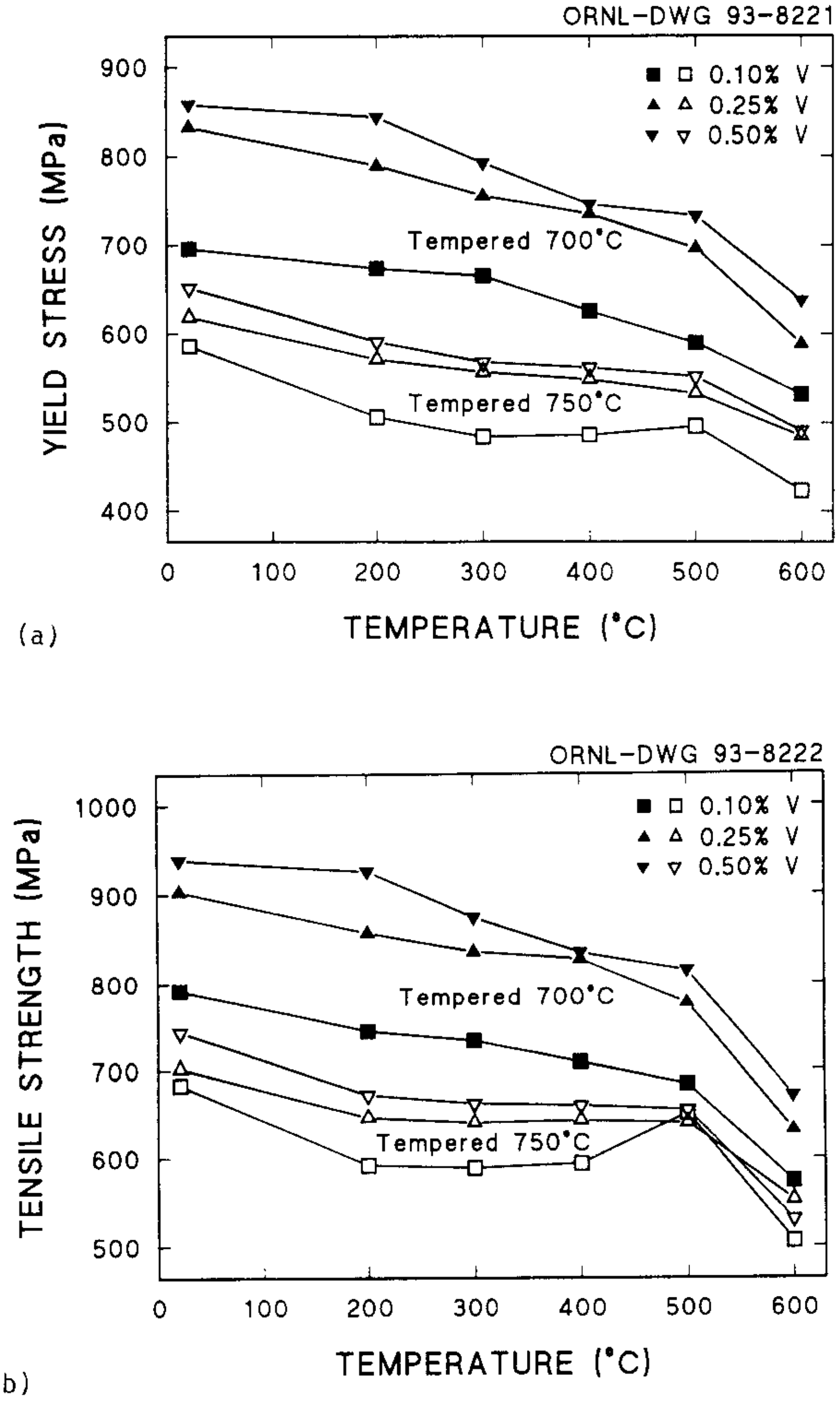

Fig. 1. a) Yield stress and (b) ultimate tensile strength as a function of test temperature of the steels with varying vanadium concentration.

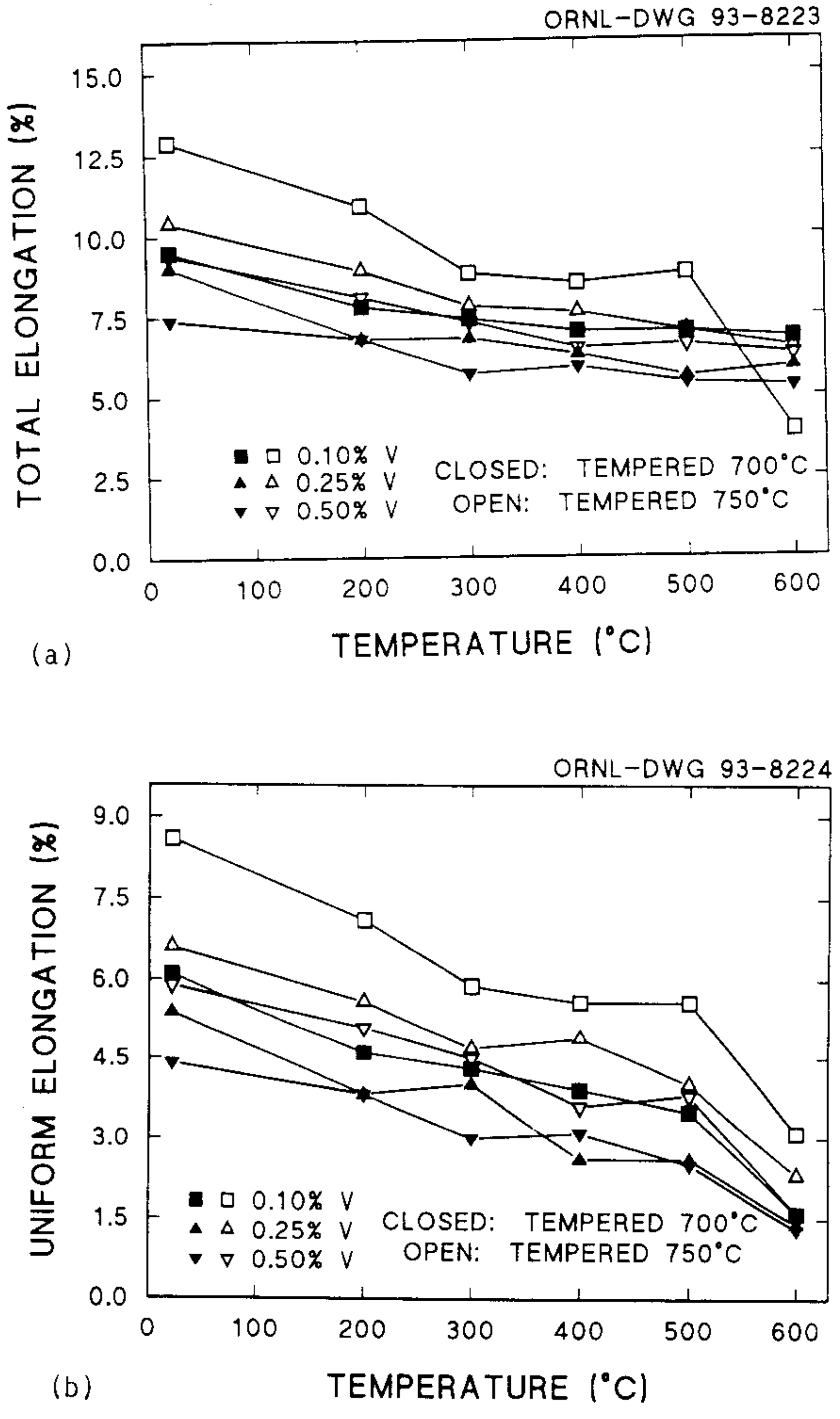

Fig. 2. (a) Total and (b) uniform elongation as a function of test temperature of the steels with varying vanadium concentration.

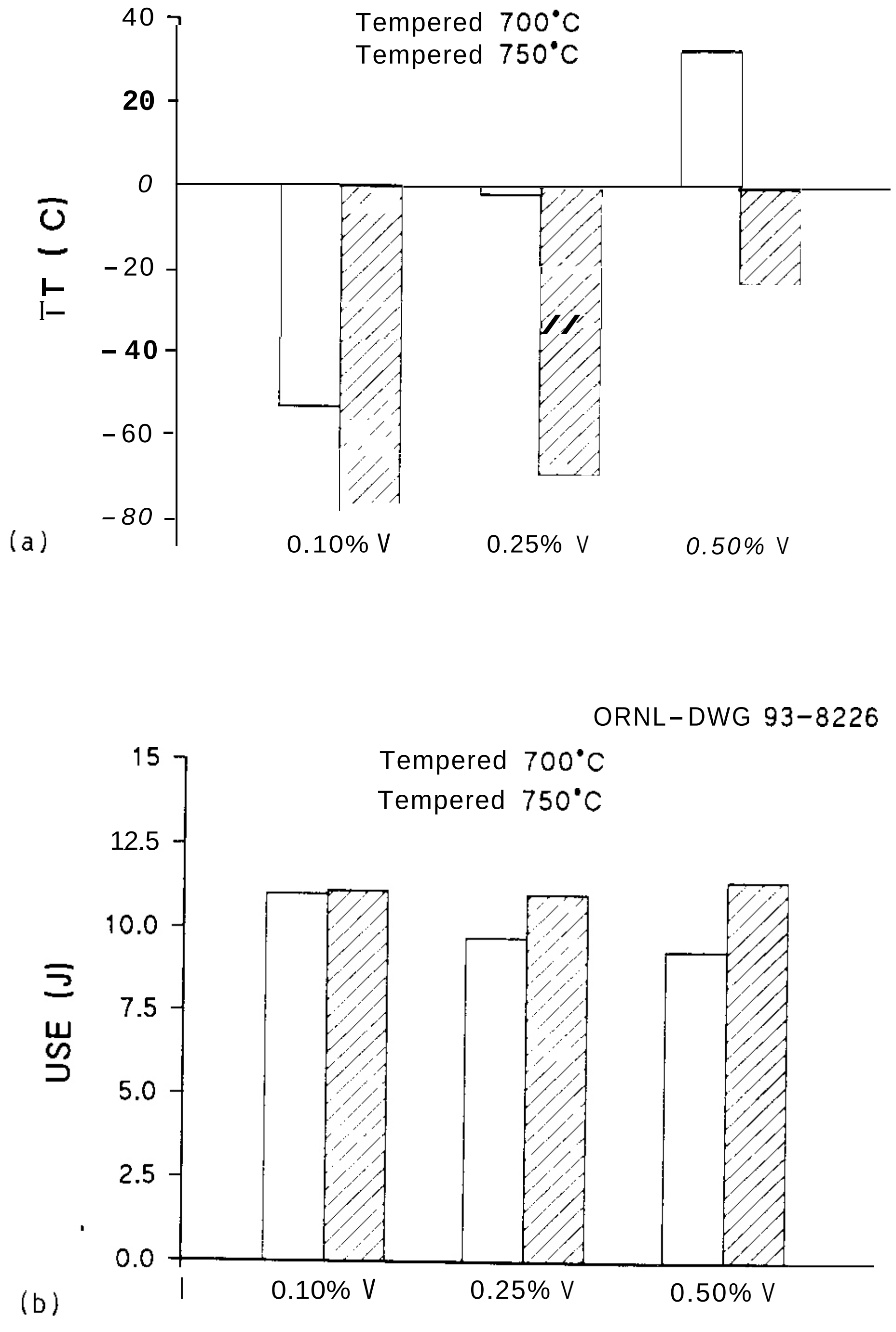

Fig. 3. (a) Ductile-brittle transition temperature and (b) upper shelf energy for the three steels with varying vanadium concentration.

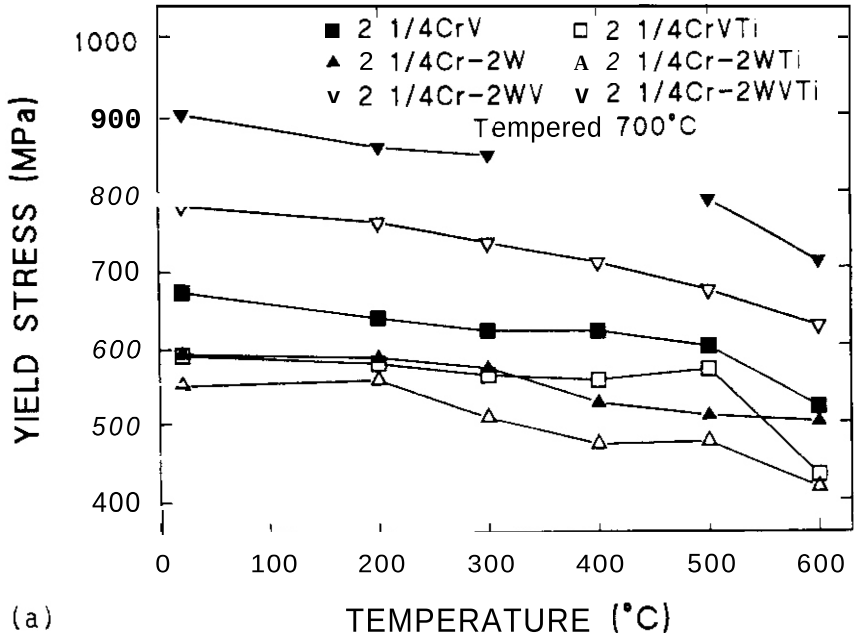

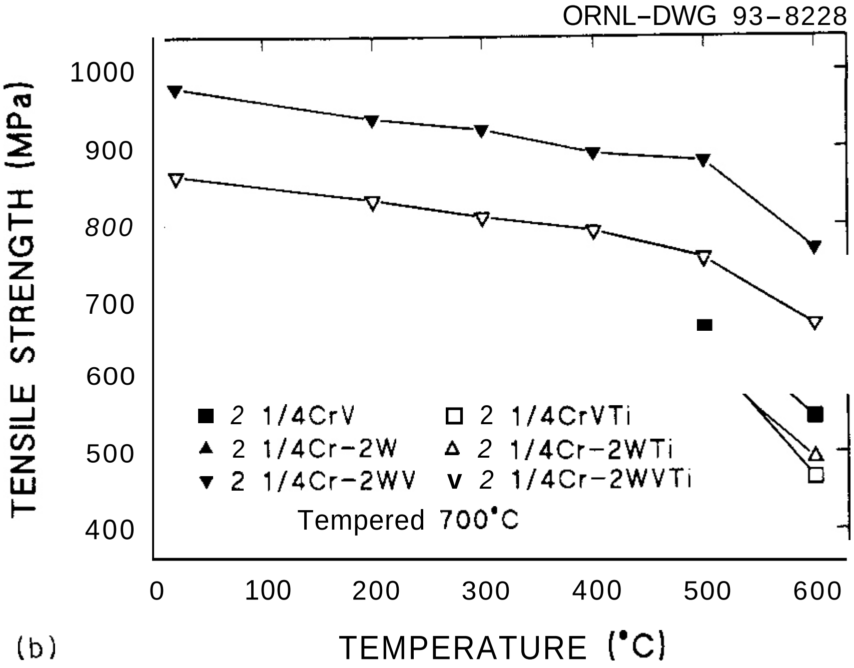

Fig. 4. (a) Yield stress and (b) ultimate tensile strength as a function of test temperature of the 2 1/4CrV, 2 1/4Cr-2W, and 2 1/4Cr-2WV steels with and without an addition of 0.02% Ti after normalizing and then tempering 1 h at 700°C.

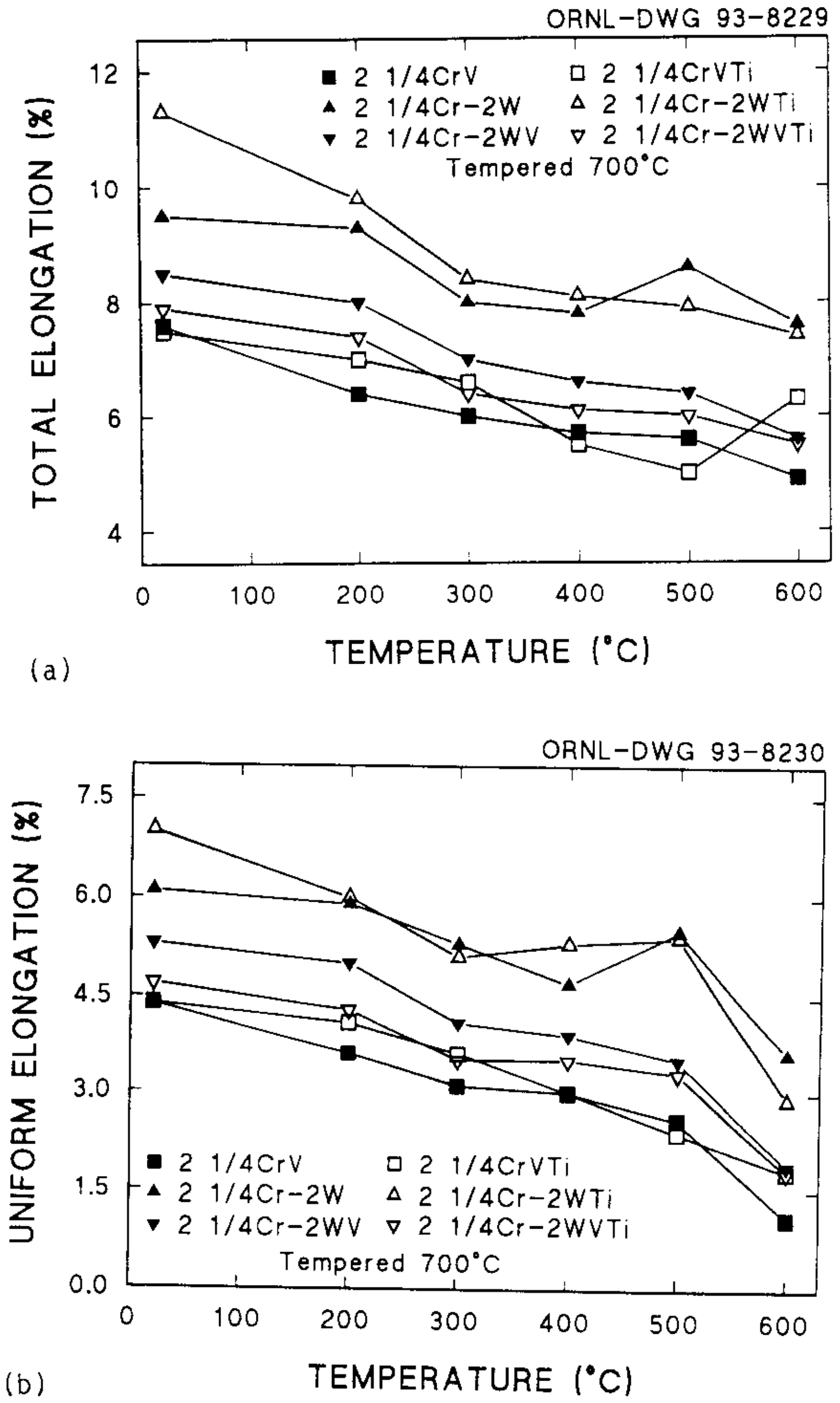

Fig. 5. (a) Total and (b) uniform elongation as a function of test temperature of the 2 1/4CrV, 2 1/4Cr-2W, and 2 1/4Cr-2WV steels with and without an addition of 0.02% Ti after normalizing and then tempering 1 h at 700°C.

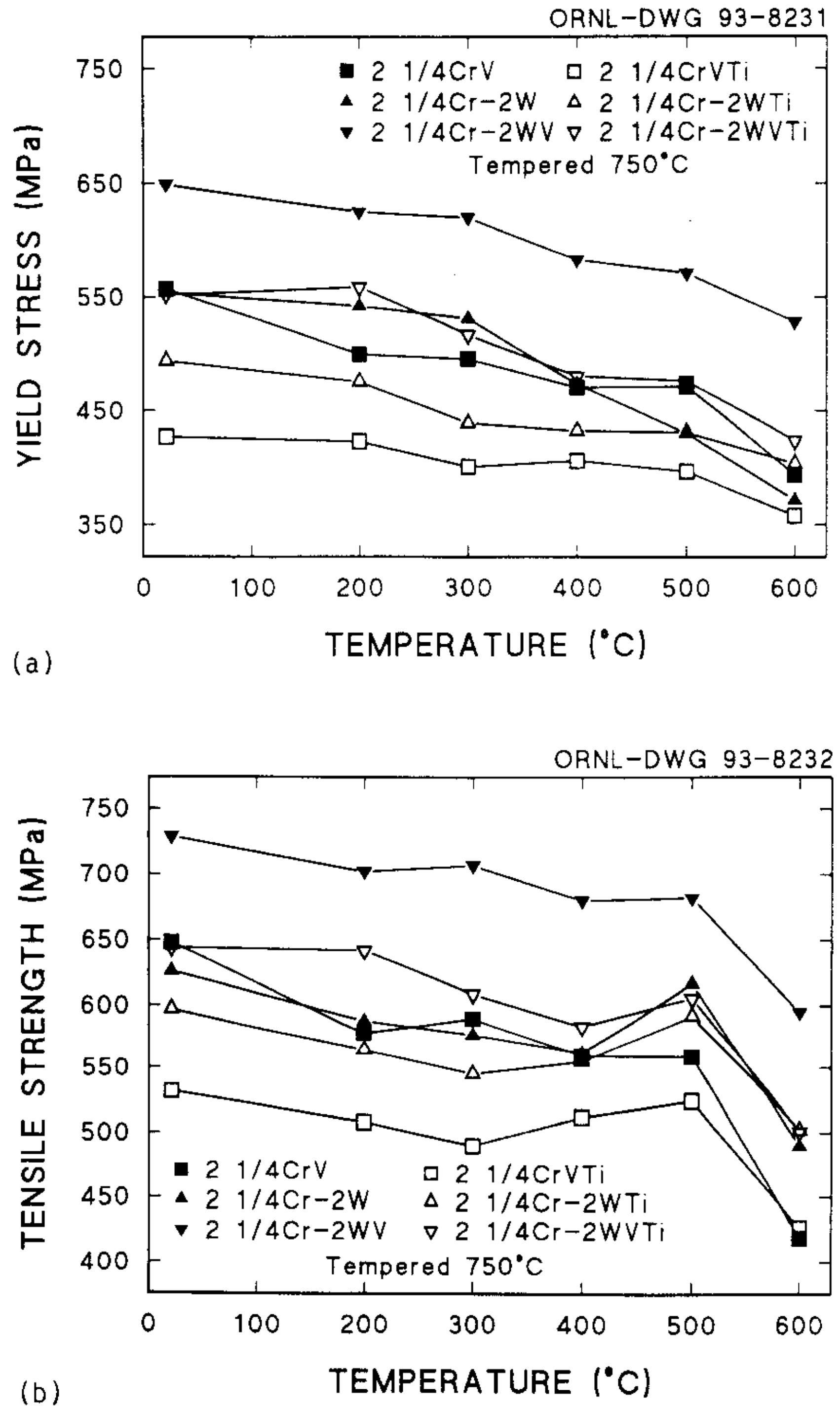

Fig. 6 (a) Yield stress and (b) ultimate tensile strength as a function of test temperature of the 2 1/4CrV, 2 1/4Cr-2W, and 2 1/4Cr-2WV steels with and without an addition of 0.02% Ti after normalizing and then tempering 1 h at 750°C.

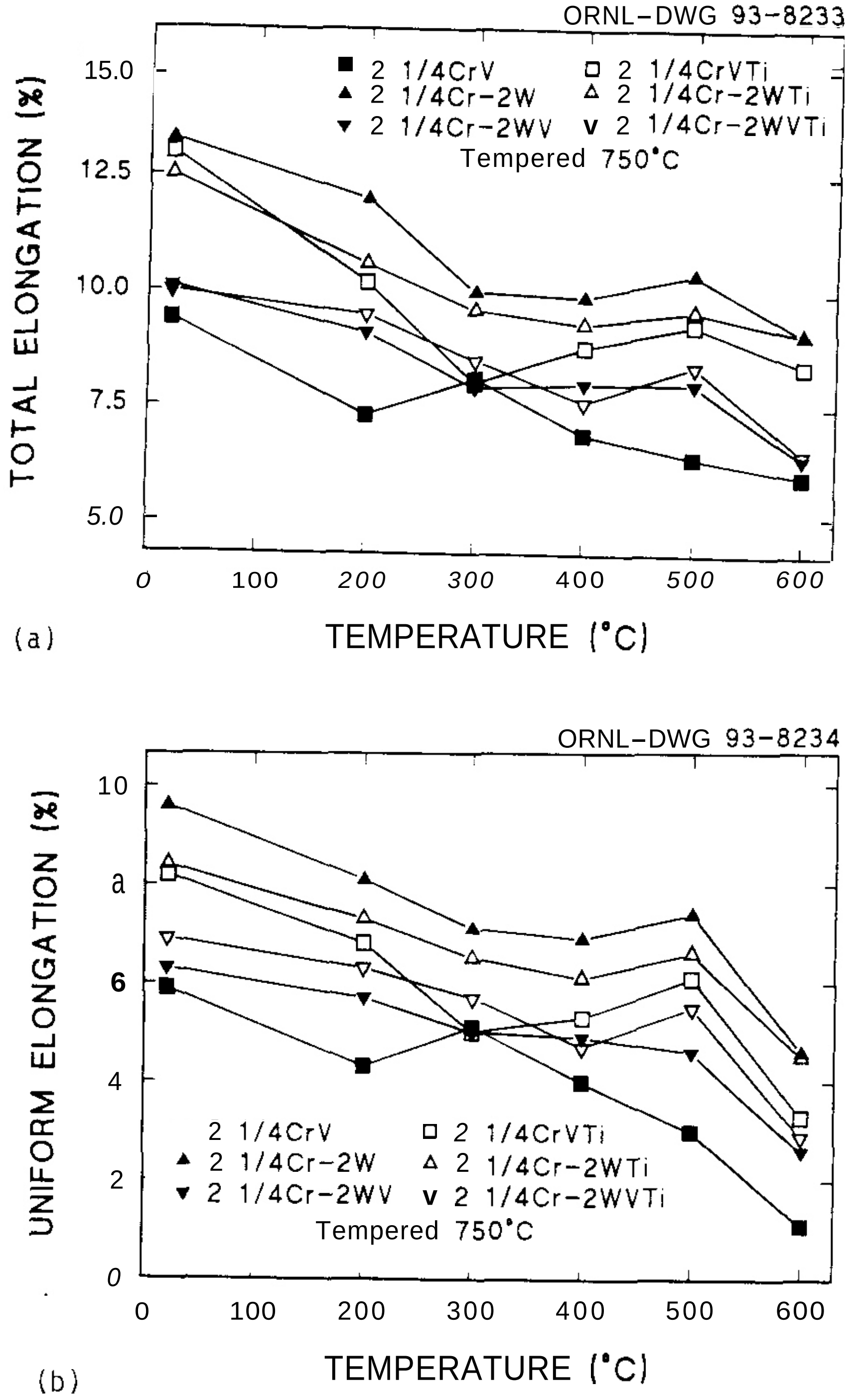

Fig. 7. (a) Total and (b) uniform elongation as a function of test temperature of the 2 1/4CrV, 2 1/4Cr-2W, and 2 1/4Cr-2WV steels with and without an addition of 0.02% Ti after normalizing and then tempering 1 h at 750°C.

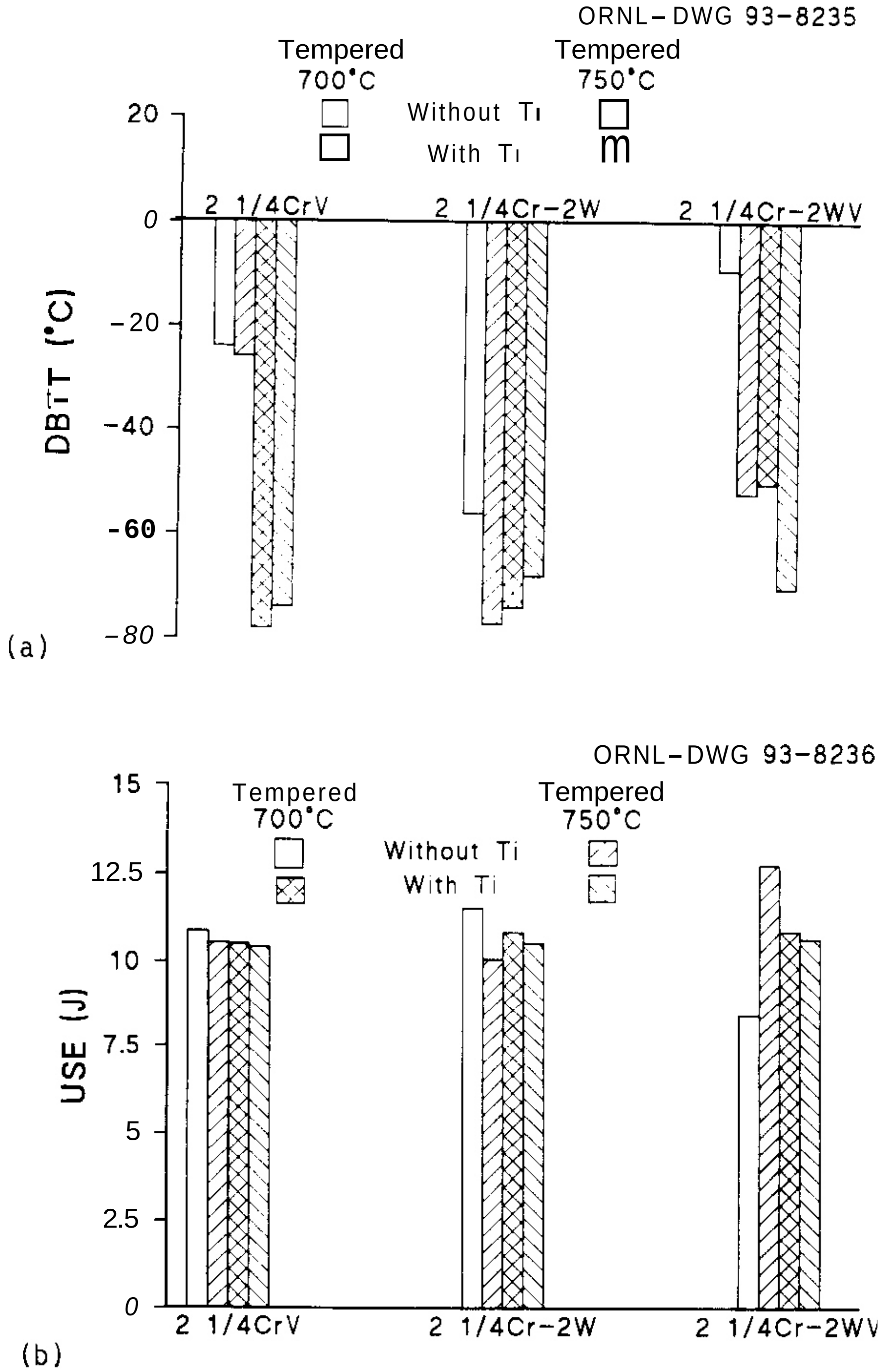

Fig. 8. (a) Ductile-brittle transition temperature and (b) upper shelf energy of the 2 1/4CrV, 2 1/4Cr-2W, and 2 1/4Cr-2WV steels with and without an addition of 0.02% Ti after normalizing and then tempering 1 h at 700°C and 1 h at 750°C.

6.2 Austenitic Stainless Steels

STRESS-MODIFIED WELDING PROCESS FOR HELIUM-BEARING TYFE 316 STAINLESS STEELS - C. A. Wang and B. A. Chin (Auburn University), and M. L. Grossbeck (Oak Ridge National Laboratory)

OBJECTIVE

The objective of this work is to evaluate the new technique for the welding of helium-bearing materials.

SUMMARY

Experiments have shown that Type 316 stainless steel is susceptible to heat-affected-zone (HAZ) cracking upon cooling when welded using the gas tungsten arc (GTA) process under lateral constraint. The cracking has been hypothesized to be caused by stress-assisted helium bubble growth and rupture at grain boundaries. This study utilized an experiniental welding setup which enabled different compressive stresses to be applied to the plates during welding. Autogenous GTA welds were produced in Type 316 stainless steel doped with 256 appm helium. The application of a compressive stress, 55 MPa, during welding suppressed the previously observed catastrophic cracking. Detailed examinations conducted after welding showed a dramatic change in helium bubble morphology. Grain boundary bubble growth along directions parallel to the weld was suppressed. The results suggest that stress-modified welding techniques may be used to suppress or eliminate helium-induced cracking during joining of irradiated materials.

PROGRESS AND STATUS

Introduction

Large amounts of helium will be generated within many materials from transmutation reactions as a consequence of neutron bombardment of structural components in a fusion reactor[1-3]. Due to its inert nature and extremely low solubility in metals, helium will diffuse and agglomerate to form bubbles after being trapped at point defect aggregates, dislocations, and grain boundaries. Such bubbles have been shown to degrade materials properties [3-12]. Investigations have **also** shown that helium bubbles grow rapidly along grain boundaries that are subjected to a tensile stress at high temperature [9-15]. Both high stress and high temperature are typically encountered following conventional gas tungsten arc (GTA) welding upon cooling. Shrinkage-induced tensile stresses are produced due to the volume contraction of the weld upon solidification and subsequent thermal contraction during cooling. Intergranular heat-affected-zone (HAZ) cracking following GTA welding with lateral constraint was observed by Lin et al. in Type 316 stainless steel with helium concentrations greater than 2.5 appm [9-12]. HAZ cracking was found to occur at the grain boundaries parallel to the welding direction, approximately 2 to 3 grain diameters (grain size was about 70 μm) from the fusion boundary. Centerline interdendritic fractures in the fusion zone have also been observed in GTA welds of Type 316 stainless steels containing more than 100 appm helium. These severe failures are attributed to the growth of helium bubbles at both HAZ grain boundaries and weld dendrite boundaries.

The objective of the present study was to investigate techniques which might be used to eliminate heat-affected-zone cracking in helium-containing steels subjected to GTA welding. These techniques need to be identified to enable repair and maintenance of the first wall of a fusion reactor. This work investigated the weldability of helium-bearing austenitic Type 316 stainless steel under controlled stress conditions during welding. Modification of the stress field was accomplished by the application of a compressive stress perpendicular to the weld direction during welding.

Experimental Procedure

The material investigated in this study was 0.76 mm thick austenitic Type 316 stainless steel sheet. Following a solution anneal at 1050°C for one hour, the average grain size was about 70 μm. Helium was implanted into the steel using tritium doping and decay'. The steel was exposed to tritium gas at 125 MPa at 300°C for 30 days. The dissolved tritium was then allowed to decay to helium at -40°C for six months. The excess tritium was then pumped off under a vacuum (10^{-3} Pa) at 400°C to prevent further helium generation. This doping process introduced 256 appm helium into the steel. The pump-off treatment resulted in the formation of stable helium bubbles about $4.5 \times 10^{20}/m^3$ in density and approximately 1.7 nm in diameter in the matrix while a density of $8.8 \times 10^{14}/m^2$ and 2.0 nm diameter bubbles were observed on the grain boundaries.

Autogenous single pass GTA welds were produced under laterally constrained conditions. The edges of the plates parallel to the weld direction were securely fastened to the welding stage to simulate the restraints encountered in practical weld repair and maintenance of structural components. Welding was performed at 10 V-dc. 24 A at a torch travel speed of *3.6* mm/s under a protective argon atmosphere. The resulting heat input was 66.7 J/mm, which produced a full penetration weld approximately 3 mm wide.

A theoretical model has been proposed by Lin et al. to describe the helium bubble growth during GTA welding of helium containing materials [9-12]. The model indicates that the growth of grain boundary helium bubbles should be significantly altered by a change in the stress state during cooling of the weld. To investigate this hypothesis, a weld plate fixture system was constructed to apply a controlled compressive stress (55 MPa, i.e., 25% of the yield stress) perpendicular to the weld path (Figure 1).

The compressive stress is produced by applying a constant compressive strain perpendicular to the weld direction from the edges of weld plates. Both optical microscopy and scanning electron microscopy (SEM) were used to examine the integrity of the weld and the surrounding heat-affected zone. Transmission electron microscope (TEM) specimens were prepared from the fusion zone/heat-affected-zone interface for both standard (control welds) and stress-modified welds for further examination.

Results and Discussion

According to the proposed model, most of the grain boundary helium bubble growth which occurs during welding is stress-assisted [9-12]. The growth of grain boundary bubbles in the HAZ can be divided into three regimes. In regime I. the heat-up regime before the material reaches its melting temperature, compressive stresses are introduced normal to the welding direction due to thermal expansion of the plates. Although grain boundary helium bubbles can grow by thermal vacancy absorption in this regime, the compressive stress tends to retard the bubble growth. Consequently, it was assumed that there is no bubble growth in this heat-up

'The tritium doping was performed at Sandia National Laboratory, Livermore. CA.

ORNL-DWG **93-1654**

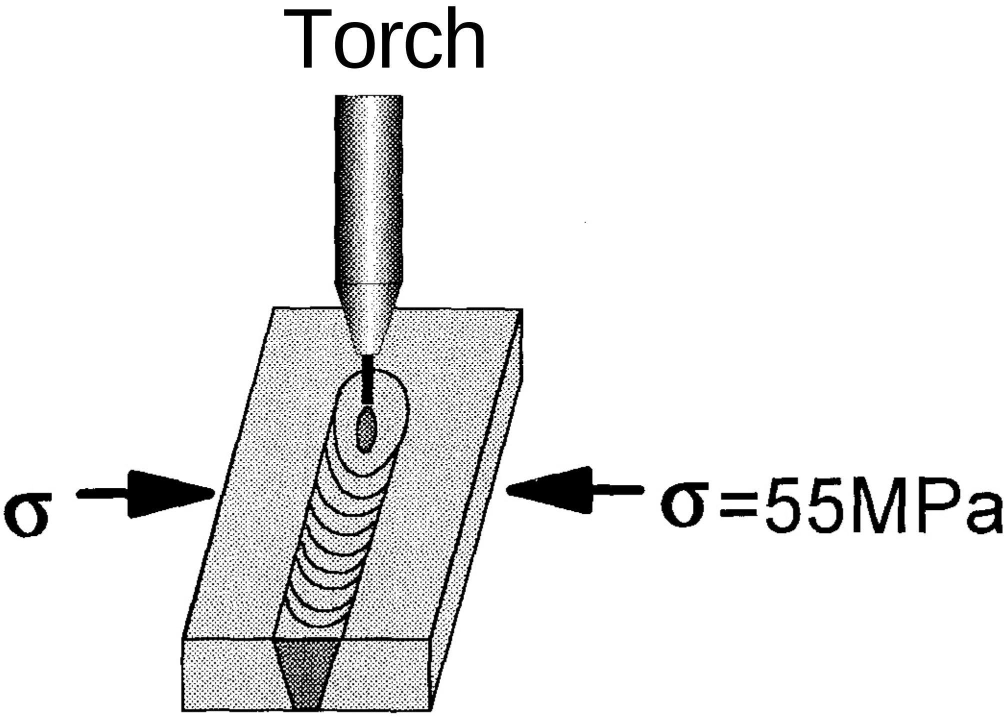

FIG. 1--Schematic of applied compressive stress during welding.

period. In regime II, where the torch passes through, the material reaches the melting temperature and a stress-free state is obtained in the melted region. Therefore, the stress is assumed to be zero in areas adjacent to the melted region. The bubbles grow mainly by vacancy absorption during this stage due to the high vacancy concentration and diffusivity at that temperature. The grain boundary bubble growth in this regime is derived based on the theory of helium bubble growth in the matrix by vacancy absorption presented by Greenwood and Speight [16]. The final bubble radius, R, was expressed by Lin et al [9,10,12] as

$$R^3 - R_i^3 = 3\delta_{gb}\Omega D_{gb}C_v\Delta t/2 \qquad (1)$$

where

R = bubble radius, m,
R_i = bubble radius at regime I, m,
δ_{gb} = grain boundary thickness, m,
Ω = atomic volume, m^3,
D_{gb} = grain boundary vacancy diffusivity, m^2/s,
C_v = equilibrium vacancy concentration, m^{-3}, and
Δt = elapsed time in regime II, s.

Finally, in regime III, the stress state becomes tensile at grain boundaries parallel to the welding direction due to weld solidification and cooling. Stress-assisted bubble growth dominates, and most of the grain boundary bubble growth during welding occurs in this regime. The bubble growth at grain boundaries in this regime can be expressed by the following equation, which is based on Hull and Rimmer's models [17,18]:

$$\Delta R = 2\pi \delta_{gb} \Omega D_{gb}(t) \sigma(t) \Delta t / \{R(t)^2 k T(t) \log(a/R(t)-0.75)\} \qquad (2)$$

where

k = Boltzmann's constant, J/K,
a = average bubble spacing, m,
ΔR = amount of bubble growth, m,
$T(t)$ = temperature at time t, K,
$\sigma(t)$ = thermal stress at time t, Pa,
$R(t)$ = bubble radius at time t, m, and
$D_{gb}(t)$ = grain boundary vacancy diffusivity at time t, m^2/s.

It should be emphasized that this model is not meant to predict the resulting stress state of the weld but rather to give physical insight into what may be occurring during the weld process.

Results of grain boundary bubble growth calculations for the final stage are shown in Figure 2. In this study, grain boundary thickness is assumed to be 8 Å. The average bubble spacing on grain boundaries was assumed to be 1 μm from examination of the **HAZ** fracture surfaces which were decorated with uniformly distributed dimples about 1 μm in diameter. The initial bubble radius at regime III, i.e., final radius at regime II, was 0.049 μm after calculations according to equation (1).

In the standard weld, curve **A,** *HAZ* cracking occurs approximately 2 seconds after the onset of Regime III, where bubbles reach 1 μm. This is consistent with the results of video-taping during welding, which showed cracks that initiate 1 to 2.2 seconds after passage of the weld pool. When a compressive stress is applied during welding, bubble growth is retarded, and bubble size may never reach the critical size which leads to cracking (curves B, *C* and D). Bubble growth was also retarded when the bubble surface tension is greater than thermal tensile stresses (where $\delta(t)$ became negative in equation (2), i.e., in compressive state), **as** indicated at the beginning region of Figure 2.

Figure *3* shows the results of macroscopic examination of weld integrity. Continuous through-thickness heat-affected zone cracking was observed in standard welds of Type 316 stainless steel containing *256* appm helium. Further examination also revealed that the crack was completely intergranular. The crack ran parallel to the welding direction and was within 2 to 3 grain diameters of the fusion zone/heat-affected-zone interface. Helium bubbles had migrated and grown rapidly at grain boundaries under the combined actions of high temperature and internal tensile stress, which occurred during the welding process. Grain boundary strength decreases as the grain boundary helium bubbles grow and the area fraction of bubbles increases. Rupture occurs as the cohesive strength of the grain boundaries, reduced by the growing bubbles. can no longer bear the shrinkage-induced internal tensile stress during cooling.

Results from stress-modified GTA welds reveal no visible cracks in the heat-affected zone, as shown in Figure 3b. A compressive stress of *55* MPa, about 25% of the room temperature yield stress of Type 316 stainless steel, was applied in these experiments, as measured by strain gauges attached to the weld plates. This result is consistent with the conclusion from Lin's study that high temperature alone is not sufficient to cause significant grain boundary helium bubble growth and HAZ Cracking. The combination of both high temperature and high tensile shrinkage stress are required for intergranular HAZ cracking [9-12].

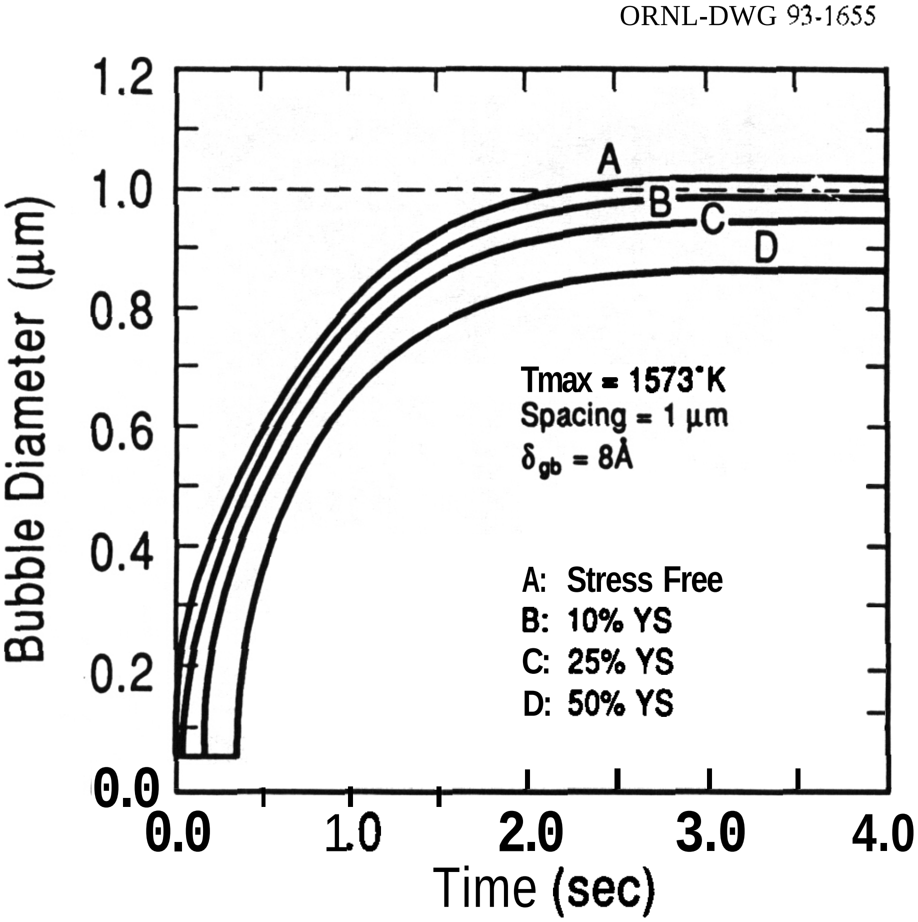

FIG. 2--The predicted grain boundary bubble size in Regime IIL In a standard weld without external applied stress, curve A, bubbles reach critical size, dotted line, at about 2 seconds after the onset of Regime III, while bubble growth is retarded by the application of a compressive stress (indicated as a percentage of the yield strength) during welding, curves B, C and D.

Further examinations on TEM disks, prepared from the fusion zoneheat-affected-zone boundary, were conducted using scanning electron microscopy following jet thinning. The results are shown in Figures 4 for both standard and stress-modified welds. Welding directions are indicated by the large arrows. In the standard GTA weld, as shown in Figure 4a, severe perforation and cracking are observed with crack tending to align parallel to the welding direction. On the other hand, parallel cracking associated with grain boundary helium bubble growth has been effectively suppressed by the application of a compressive stress in the stress-modified GTA welding process, as shown in Figure 4b. In addition, the bubble growth has been altered such that larger bubbles grow,predominantly along grain boundaries perpendicular to the weld direction, whereas previously they occurred principally on grain boundaries parallel to the weld. It should be pointed out that jet polishing during TEM specimen preparation attacks the grain boundaries and enlarges grain boundary holes. Therefore, the grain boundary bubble sizes indicated in Figures 4 are exaggerated as compared to the as-welded material. Figure 4c and 4d are magnified views of the circled areas in Figure 4a and 4b respectively. Results of TEM examinations are not available at this time, and will be presented in the future.

ORNL-DWG 93-1656

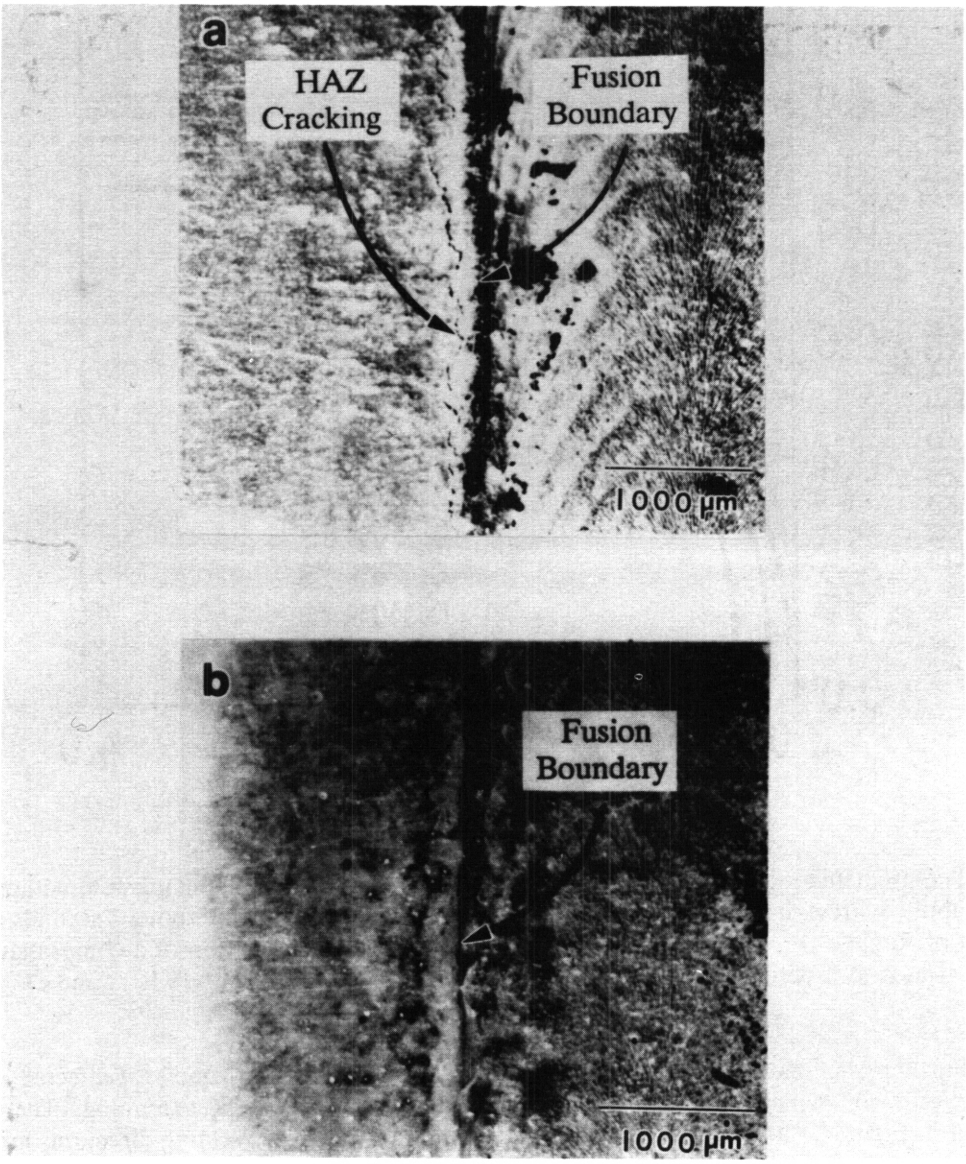

FIG. 3--Comparison of as-welded heat-affected zones in Type 316 stainless steel containing 256 appm helium: (a) continuous through-thickness intergranular HAZ cracking in standard weld; (b) no visible HAZ cracking in stress-modified weld.

During weld solidification and cooling, the principal shrinkage-induced internal tensile stress is perpendicular to the welding direction. The stress level is enhanced by the lateral constraints as in the repair welding of structural components. This stress causes the helium bubbles to grow rapidly at the grain boundaries at high temperatures, preferentially along grain boundaries aligned perpendicular to the stress (parallel to the weld). Since the shrinkage-induced tensile stress is altered by applying an initial compressive stress perpendicular to the welding

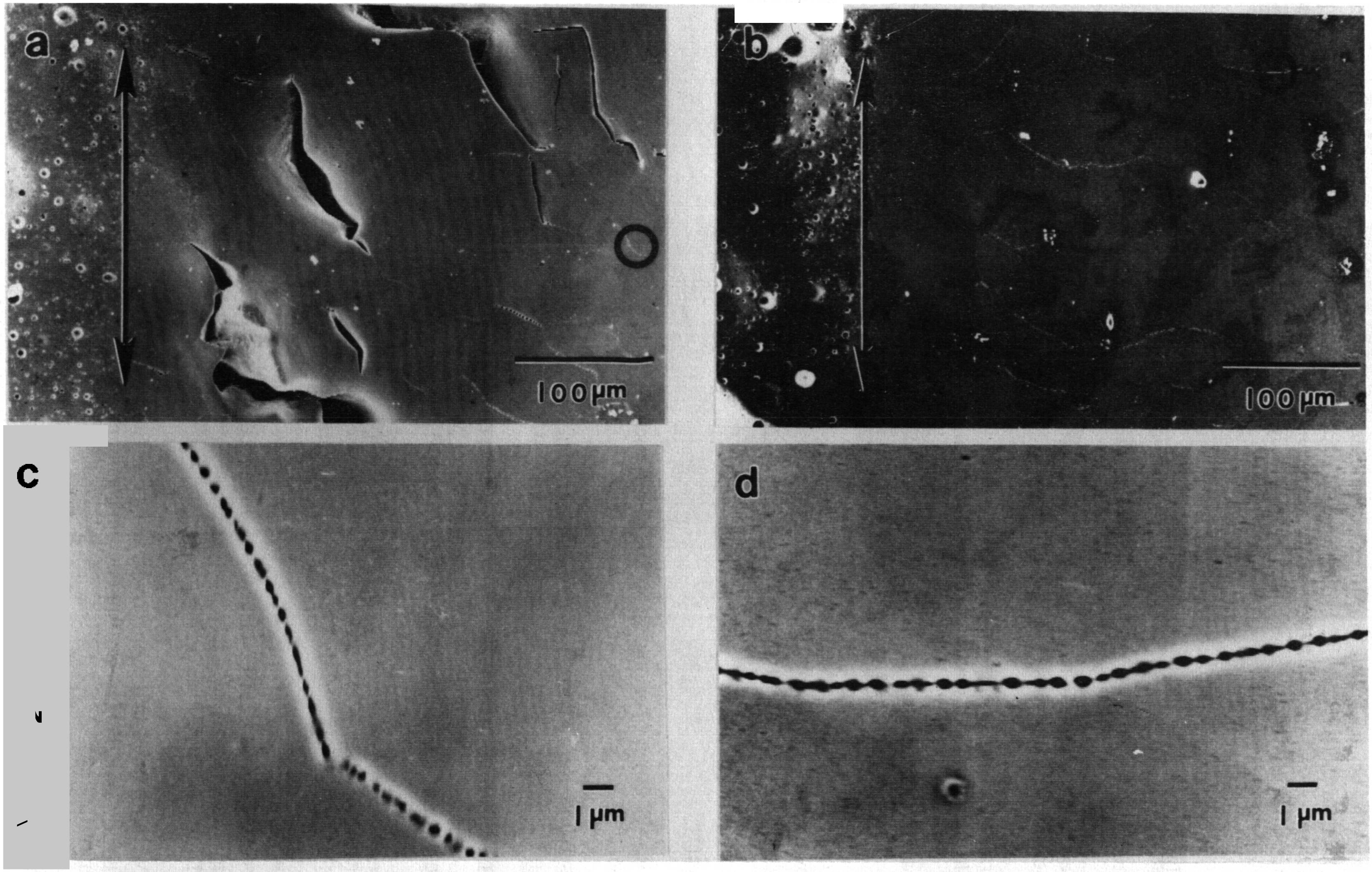

FIG. 4--SEM photographs of the jet-polished TEM discs from (a) standard GTA weld; (b) stress-modified GTA weld. Arrows indicate the welding direction. Note that the applied compressive stress in 3b effectively suppressed grain boundary cracking associated with bubble growth and favored bubble growth on grain boundaries perpendicular to the weld. (c) and (d) are magnified views of the circled areas in (a) and (b) respectively.

direction, the helium bubble growth process is retarded along grain boundaries parallel to the weld; therefore, HAZ cracking is less likely to occur. However, a small number of helium bubbles still grow preferentially along the direction perpendicular to the weld. This may be due to the internal tensile stresses generated by bulk body constraint of the steel along the weld direction during cooling.

Conclusions

The following conclusions can be drawn from this study:

1. Severe intergranular heat-affected-zone cracking during welding of helium-bearing Type 316 stainless steel is caused by the grain boundary helium bubble growth.

2. Grain boundary helium bubble growth is enhanced by the combined action of high temperature and shrinkage-induced tensile stress generated during the welding process.

3. Sound autogenous GTA welds can be produced in helium-bearing Type 316 stainless steel by the application of a compressive stress to alter grain boundary bubble growth kinetics.

The results of this study suggest that the stress-modified welding process can effectively suppress the helium bubble growth and may be applied to eliminate the severe HAZ cracking which occurs during GTA repair welding of irradiated materials.

References

1. R. W. Conn, "Tokamak Reactors and Structural Materials", Journal of Nuclear Materials, 85&86(1979)9-16.

2. E. E. Bloom, "Mechanical Properties of Materials in Fusion Reactor First-Wall and Blanket Systems", Journal of Nuclear Materials, 85&86(1979)795-804.

3. M. M. Hall, Jr., A. G. Hins, J. R. Summers,and D. E. Walker, "Fusion Welding of Irradiated AISI 304L Stainless Steel Tubing", Weldment:Physical Metallurgy and Failure Phenomena, Proceedings of the Fifth Bolton Landing Conference, August 1978, pp. 365-378.

4. J. P. Maloney, D. Baker, W. A. Day, W. G. Fraser, H.R. Huxford, K. E. Kehr, W. R. Kennedy, J. B. McClain, D. H. McKenney, C. A. Meyer, R. F. Mittelberg and J. E. Walls , "Repair of a Nuclear Reactor Vessel", DP-1199, E. I. du Pont de Nemours & Co., Savannah River Laboratory, Aiken, SC, June 1969.

5. S. D. Atkin, "Weld Bend Tests on Irradiated, 20% Cold-Work 316 Stainless Steel", Fusion Reactor Materials, ADIP Semiannual Progress Report, Sept. 30, 1981, DOE/ER-0045/7, pp. 110-117, U.S. DOE, Office of Fusion Energy.

6. W. K. Kanne, C. L. Angerman and B. J. Eberhard, "Weldability of Tritium-Charged 304L Stainless Steel", DP-1740, E. I. du Pont de Nemours & Co., Savannah River Laboratory, Aiken, SC, February 1987.

7. W. R. Kanne, "Helium Embrittlement Cracking During Patch Welding in Savannah River C reactor," DPMS-8940, E. I. Dupont Co., Savannah River Laboratory, Aiken, SC, 1989.

8. **A.** K. Birchenall, "Helium Induced Weld Cracking in Irradiated 304 Stainless Steel," DPMS-8941, E. I. Dupont Co., Savannah River Laboratory, Aiken, SC, 1989.

9. H. T. Lin, M. L. Grossbeck and B. A. Chin, "Cavity Microstructure and Kinetics During Gas Tungsten Arc Welding of Helium Containing Stainless Steel," Metallurgical Transactions **A,** V21A, September 1990, pp.2585-2596.

10. H. T. Lin, Ph.D. Dissertation, Auburn University, 1989

11. H. T. Lin, S. H. Goods, M. L. Grossbeck. and B. A. Chin, "Helium-Induced Degradation in the Weldability of an Austenitic Stainless Steel", Effect of Radiation on Materials, 14th International Symposium, Volume I, ASTM STP 1064, N. H. Packan, R. E. Stoller, and A. S. Kumar, Eds., American Society for Testing and Materials, Philadelphia, 1989, pp. 301-314.

12. H. T. Lin, "Simulation of the Welding of Irradiated Materials", ORNL/TM-11158, Oak Ridge National Laboratory, Oak Ridge, TN, 1989.

13. D. Hull and D. E. Rimmer, "The Growth of Grain-Boundary Voids Under Stress," Philosophical Magazine, 4(1959)673-687.

14. M. V. Speight and J. E. Harris, "The Kinetics of Stress-Induced Growth of Grain-Boundary Voids," Metal Science Journal, Vol.1, 1967, **pp.83-85.**

15. H. Trinkaus, "Stress Induced Drift Diffusion **in** Grain Boundaries - Application to Creep and to the Growth of Grain boundary Voids." Berichte der Bundes Gesellschaft fur Physikalische Chemie, 82(1978)249-253.

16. G. W. Greenwood and M. V. Speight, "An Analysis of the Diffusion of Fissile Gas Bubbles and its Effect on the Behaviour of Reactor Fuels," Journal of Nuclear Materials, 10(1963)140-144.

17. D. Hull and D. E. Rimmer, "The Growth of Grain-Boundary Voids Under Stress," Philosophical Magazine, 4(1959)673-687.

18. J. Weertman, "Hull-Rimmer Grain Boundary Void Growth Theory - **A** Correction," Scripta Metallurgica, **Vol. 7, 1973,** pp. 1129-1130.

RELATIONSHIP BETWEEN SWELLING AND IRRADIATION CREEP IN COLD WORKED PCA STAINLESS STEEL TO 178 DPA AT ~400°C

M. B. Toloczko (University of California at Santa Barbara) and F. A. Garner (Pacific Northwest Laboratory[*]).

OBJECTIVE

The objective of this effort is to determine the factors which control the response of structural alloys to radiation and applied stress.

SUMMARY

At 178 dpa and ~400°C, the irradiation creep behavior of 20% cold-worked PCA has become dominated by the creep disappearance phenomenon. The total diametral deformation rate has reached the limiting value of 0.33%/dpa at the three highest stress levels. The stress-enhancement of swelling tends to camouflage the onset of creep disappearance, however.

PROGRESS AND STATUS

Introduction

Helium pressurized tubes constructed from the fusion heat K280 of the austenitic Prime Candidate Alloy (PCA) in the 20% cold worked condition have completed their irradiation in FFTF/MOTA at a nominal temperature of ~400°C. These 2.24 cm long tubes were periodically discharged from reactor and measurements made of their diameter prior to reinsertion into reactor. There tubes were inserted in all MOTA vehicles from MOTA-1A through MOTA-1G and then continued into MOTA-2B. The tubes were pressurized to hoop stress levels of 0, 30, 50, 100, 140 and 200 MPa. Irradiation temperatures varied somewhat from one MOTA to the next, but during any one irradiation interval, the temperature was actively controlled within ±5 of the nominal temperature. Table I presents the detailed temperature history of these tubes, which reached dpa levels as large as ~178 dpa. The strains of these tubes were last reported for MOTA-1F at ~119 dpa.[1]

Table 1 Irradiation History of Pressurized Tubes

MOTA	Temperature, °C
1A	405
1B	401
1C	396
1D	386
1E	384
1F	386
1G	390
2B	433

Results and Discussion

Figure 1 shows the total diametral strains measured in each of the tubes, reaching levels as large as 26% ΔD/D without failure. Note that the tubes at the three highest stress levels have developed the 0.33%/dpa maximum diametral deformation rate often observed in pressurized tubes at sufficiently high enough neutron exposures.[1-3] Thus, the creep rate becomes unresponsive to significant increases in stress level. Even though a volumetric swelling level of ~21% was attained in the absence of stress, the stress-free swelling rate at 0.46%/dpa is still far from its maximum possible rate of ~1%/dpa, as shown in Figure 2. Since stress normally accelerates the onset of swelling, it is expected that the stress-affected swelling rates are probably larger.

---

[*] Pacific Northwest Laboratory is operated for the U.S. Department of Energy by Battelle Memorial Institute under Contract DE-AC06-76RLO 1830.

If we assume, however, that stress does not affect swelling, we can calculate the creep coefficient associated with the $B_o + DS$ creep model, where B_o is the creep compliance and D is the creep-swelling coupling coefficient, relating the creep rate $\dot{\epsilon}/\sigma$ to the swelling rate S. Table 2 shows that for each tube, $B_o \sim 2 \times 10^{-6}$ MPa^{-1} dpa^{-1} and $D \sim 0.6 \times 10^{-2}$ MPa^{-1}, in agreement with the results of earlier studies.[5-7] The attainment of the ~0.33%/dpa diametral deformation rate signals, however, that stress enhancement of swelling has Indeed occurred, and the creep disappearance phenomenon is dominating the experiment.[3]

Table 2. Creep coefficients derived over the interval of **0 to 178 dpa**, assuming that stress ***does* not** affect swelling.

Stress Level MPa	D MPa^{-1}	B_o MPa^{-1} dpa^{-1}
30	0.58×10^{-2}	1.7×10^{-6}
60	0.53×10^{-2}	2.0×10^{-6}
100	0.57×10^{-2}	2.2×10^{-6}
140	0.54×10^{-2}	2.3×10^{-6}
200	0.57×10^{-2}	2.3×10^{-6}

be made, providing that the analysis proceeds at a dpa level where the creep disappearance phenomenon has not yet become totally dominant. This appears to be the case at the end of MOTA-1G at ~153 dpa. Assuming that the creep strain must be linearly proportional to stress, an estimate of the stress-affected swelling can be calculated, as shown in Figure 3. This estimate implies that the swelling at 200 MPa and *178* dpa may be twice as large as that at zero stress.

Such large swelling levels will also cause a decrease in the gas pressure and thereby the stress level in the tube wall, but the correction to the midwall creep strains are not very large, as shown in Figure 4. The creep coefficients derived from both the stress-insensitive and stress-affected swelling assumptions are shown in Figure 5. It is clear that the Influence of stress on swelling camouflages the onset of the creep disappearance phenomenon. These calculations are based on the entire data set, however. Thus, the values shown in Figure 5 are average coefficients taken over the entire period where the creep disappearance phenomenon evolves from a minimal to a near-dominant influence.

If we calculate D_N, the creep-swelling coefficient for each of the last three irradiation segments, using the average creep and swelling rates for each segment, the decrease in the D coefficient becomes more pronounced as the swelling rate increases and the creep disappearance phenomenon also increases. The progressive influence of this process is clearly shown in figure 6.

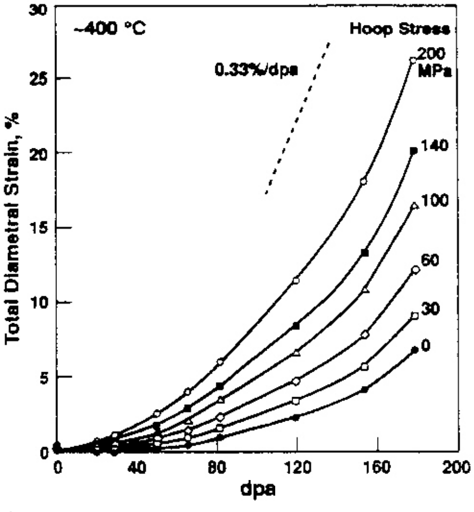

Fig. 1 Total diametral strains observed in PCA tubes at ~400 C and 0 to 178 dpa

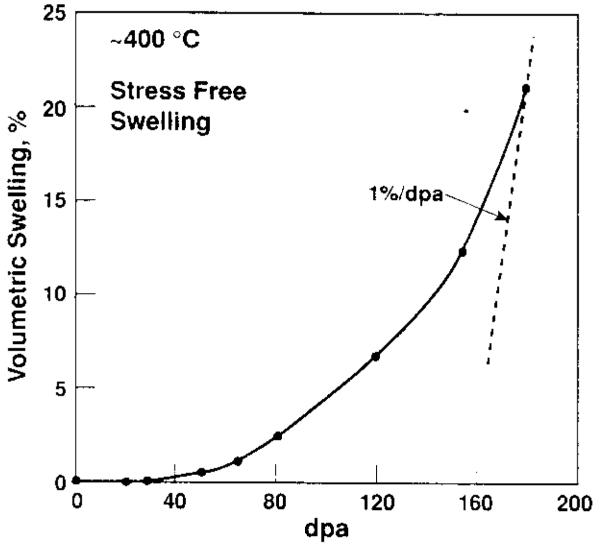

Fig. 2 Stress-free volumetric swelling, reaching a swelling rate of 0.46%/dpa at 178 dpa.

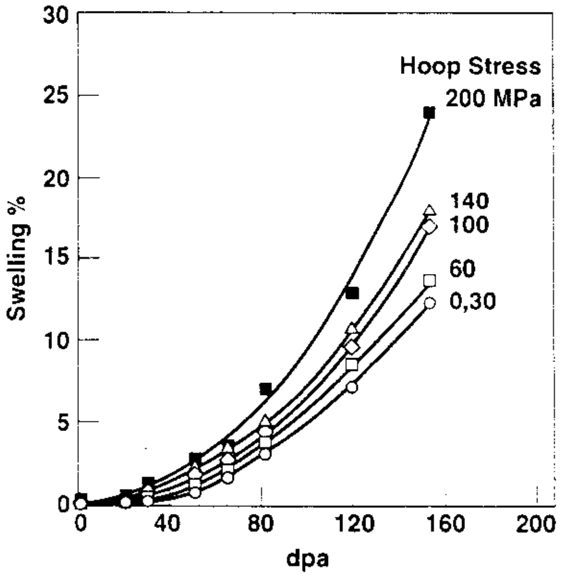

Fig. 3 Calculated estimate of stress-affected swelling behavior using data to 150 dpa, assuming that creep strains must be proportional to stress.

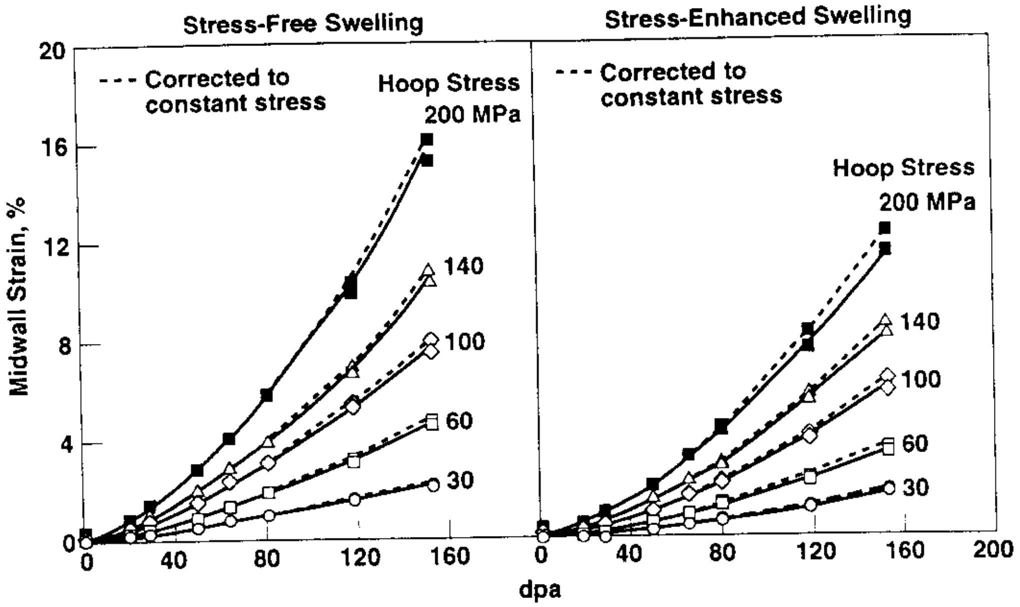

Fig. 4 Midwall creep strains calculated for both the stress-insensitive and stress-affected swelling cases. Large levels of swelling also decrease the stress level in the tube wall and a correction to constant stress must be made.

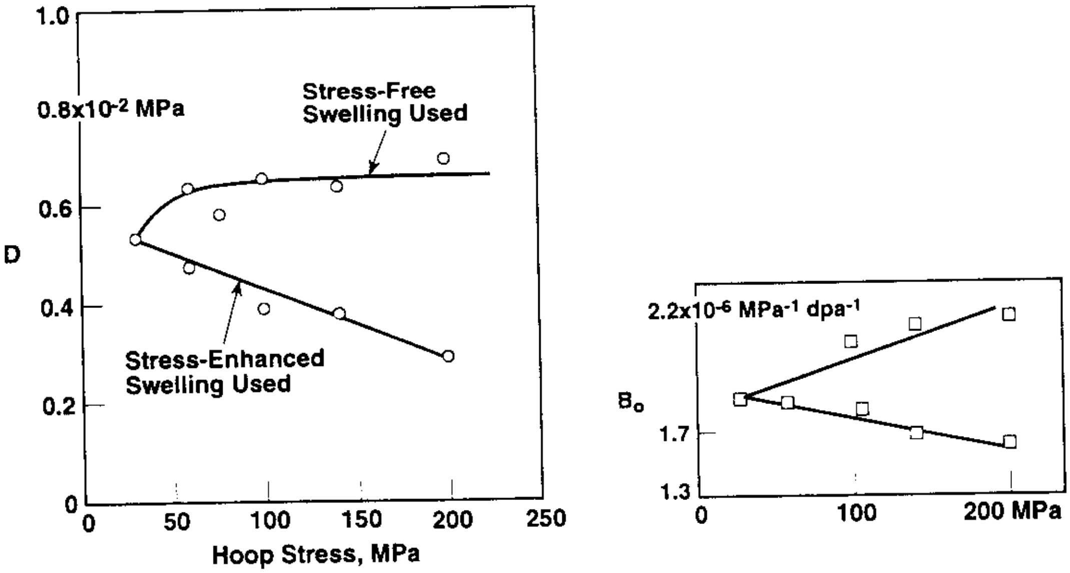

Fig. 5 Average creep coefficients derived from the full irradiation sequence.

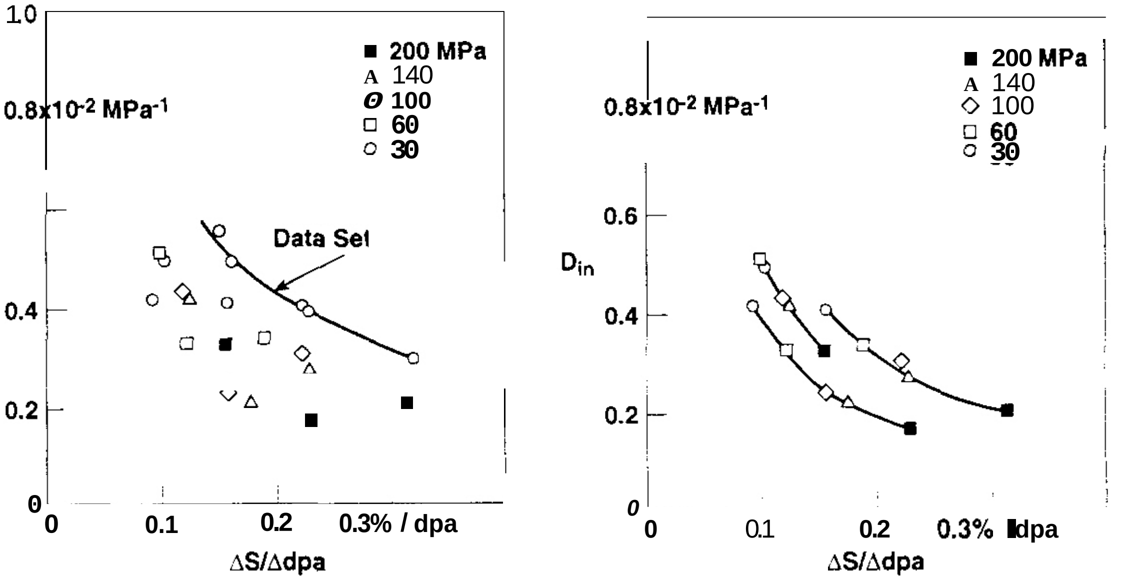

Fig. 6 a) Comparison of creep-swelling coupling coefficient derived from the full irradiation sequence with the incremental coefficients derived for each of the last three irradiation segments in MOTAs 1F, 1G, and 2B; b) Each curve corresponds to a different fluence increment. Note that data are plotted against the average stress-free swelling rate for the individual irradiation segment, and the final stress-free swelling rate for the full irradiation sequence. The actual stress-affected average swelling rates will be significantly larger

Future Work

This effort will continue, with primary emphasis on determining the true stress-affected swelling behavior. This will be done by sectioning the tubes and measuring the actual density changes. The creep analysis will then be updated.

REFERENCES

1. E. R. Gilbert and B. A. Chin, in Effects of Radiation on Materials: Tenth Conference, ASTM STP 725, 1981, pp. 665-679.
2. M. B. Toloczko, F. A. Garner, and C. R. Eiholrer, J. Nucl. Mater. 191-194 (1992) 803-807.
3. D. L. Porter and F. A. Garner, J. Nucl. Mater. 159 (1488) 114-121.
4. F. A. Gamer and M. B. Toloczko, in: Fusion Reactor Materials Semiannual Progress Report DOE/ER-0313/12 (1992) pp. 145-147.
5. F. A. Garner, M. B. Toloczko and R. J. Puigh, ibid., pp. 148-162.
6. F. A. Garner and D. L. Porter, J. Nucl. Mater. 155-157 (1988) 1006-1013.
7. D. L. Porter, G. D. Hudman, and F. A. Garner, J. Nucl. Mater. 179-181 (1991) 581-584.
8. C. H. Woo and F. A. Garner, J. Nucl. Mater. 191-194 (1992) 1309-1312.
9. C. H. Woo, F. A. Garner, and R. A. Holt, in: Effects of Radiation on Materials, 16th International Symposium, ASTM STP 1175, 1993 (in press)

Density Changes Observed in Pure Molybdenum and Mo-41Re After Irradiation in FFTF/MOTA - F. A. Garner and L. R. Greenwood, (Pacific Northwest Laboratory)[a]

OBJECTIVE

The objective of this effort is to provide data on the performance during irradiation of candidate materials for fusion reactor application.

SUMMARY

Pure molybdenum and Mo-41wt% Re, in both the 20% cold-worked and aged and the annealed and aged conditions, were irradiated in FFTF/MOTA to exposures as high as 111 dpa. Pure molybdenum appears to approach a saturation swelling level that is independent of the starting state. Cold-worked and aged molybdenum initially swells at a higher rate than that of solution-annealed and aged molybdenum and overshoots the saturation level at lower irradiation temperatures. This requires that part of the accumulated swelling be removed to approach saturation, probably by void shrinkage. The alloy Mo-41Re exhibits a more complex behavior with the annealed and aged condition initially swelling faster, but eventually the density change of both conditions begins to turn downward and tends toward densification. The role of solid transmutation to Tc, Re, and Os is thought to be very important in the irradiation behavior of these two metals. Calculations of transmutant generation are provided for FFTF, HFIR and STARFIRE spectra.

PROGRESS AND STATUS

Introduction

Molybdenum and molybdenum-rhenium alloys are being considered as possible candidates for fusion reactor application:[1-2] Pure molybdenum and Mo-41wt% Re were irradiated in MOTA-1B, 1C, 1D, and 1E at five target temperatures between 420 and 722°C, with peak exposures on the order of 60 dpa (Steel) at most temperatures and -100 dpa at 420°C.[3] The specimens were in the form of 3 mm diameter microscopy disks. Both materials were irradiated in two starting conditions: solution annealed for 1 hr at 760°C followed by aging at 320°C for 2 hrs, and 20% cold worked followed by the same aging treatment. Irradiation proceeded in weeper packets so that the specimens were in contact with the sodium coolant of the reactor.

Although the irradiation in MOTA proceeded largely under active temperature control (±5°C) in MOTA's 1B, 1C, and 1E. there was a short (-50 minutes) temperature excursion in MOTA-1D during FFTF cycle 7. referred to as an overtemperature event. This event compromised the integrity of many of the pressurized tube experiments in MOTA 1D. Therefore, a decision was made to run the MOTA in the helium-purged mode for the remainder of FFTF cycles 7 and 8 while a series of reactivity feedback tests were conducted. The majority of the MOTA canisters thereafter operated at variable but lower-than-target temperatures until the end of FFTF cycle 8. Isothermal irradiation was reestablished in MOTA 1E. but only the 420°C specimens were included in that irradiation segment. A summary of the target conditions for these specimens is shown in Table 1

Results

Density measurements were performed using an immersion technique whose accuracy has been established to be ±0.15% swelling. The displacement levels quoted are those for stainless steel. Detailed calculations for molybdenum have not yet been run, but should be on the order of -80% of those of steel. No guidance is available to calculate dpa levels for Mo-41Re.

The density change data are presented in Table 2 and represent the average values for two identical specimens. Figure 1 shows that the cold-worked and aged condition of pure molybdenum swelled -1% or more at 420°C during the first irradiation segment and then declined thereafter. The annealed and aged condition appeared to densify, although the reasons for such densification are hard to identify. In the annealed and aged state at 420°C, Mo-41Re appears to swell initially and then decline in swelling. The cold-worked and aged condition appears to be swelling between 53 and 100 dpa.

Figure 2 shows that the cold-worked and aged condition of pure molybdenum always swells at a faster rate initially than the annealed and aged condition. but the swelling of the two conditions appears to be converging by the end of MOTA-1D. This convergence requires that the cold-worked and aged specimen must decline in swelling at the 471 and 596°C target temperatures. Note also in Figure 2 that three of the four specimen groups are converging to the same level (- 2%).

Figure 3 shows that at three of four irradiation temperatures. the annealed and aged condition of Mo-41Re swelled more than the cold-worked and aged condition. in agreement with the behavior observed at 420°C in

---

[a] Pacific Northwest Laboratory is operated for the U.S. Department of Energy by Battelle Memorial Institute under Contract DE-AC06-76RLO 1830.

Figure 1. The most surprising aspect of the data in Figure 3, however, is that the initial swelling appears to be fallowed by a decline in swelling. in several cases reaching a net densification.

Table 1
Irradiation Conditions for Molybdenum and Mo-41Re Specimens Examined in This Study

		MOTA-1B		MOTA-1C		MOTA-1D		MOTA-1E		
Packet	Contents[a]	Temperature, °C	dpa[b]	Temperature, °C	dpa	Temperature, °C	dpa	Temperature, °C	dpa	Total dpa
MAEZ	A	431	15.0	--	--	--	--	--	--	15.0
NAEZ	A	431	15.0	420	35.3	--	--	--	--	50.3
N6EZ	B	431	14.1	420	33.1		--	--	--	47.2
M6EZ	B	431	14.5	420	33.9	404	24.5	414	32.8	105.7
PAEZ	A	431	15.0	420	35.3	404	25.5	414	35.0	110.8
MAE1	A	471	11.4	--	--	--	--	--	--	11.4
NAE1	A	471	11.4	470	26.8	--	--	--	--	38.2
N6E1	B	471	9.6	470	22.6	--	--	--	--	32.2
P6E1	B	471	8.7	470	20.3	470	14.7	--	--	43.7
PAE1	A	471	11.4	470	26.8	470	19.4	--	--	57.6
MAE7	A	569	11.5	--	--	--	--	--	--	11.5
NAE7	A	569	11.5	550	27.0	--	--	--	--	38.5
N6E7	B	569	12.2	550	28.6	--	--	--	--	40.8
PAE7	A	569	11.5	550	27.0	549	19.6	--	--	58.1
RAE7	A	569	11.5	550	27.0	549	19.6	--	--	58.1
MAE5	A	645	11.5	--	--	--	--	--	--	11.5
NAE5	A	645	11.5	652	27.0	--	--	--	--	38.5
N6E5	B	645	12.2	652	28.6	--	--	--	--	40.8
R6E5	B	645	12.7	652	30.8	650	22.3	--	--	65.8
PAE5	A	645	11.5	652	27.0	650	19.6	--	--	58.1
MAE6	A	722	11.5	--	--	--	--	--	--	11.5
NAE6	A	722	11.5	730	27.0	--	--	--	--	38.5
N6E6	B	722	12.2	730	28.6		--	--	-	40.8
M6E6	B	722	12.2	730	28.6	730	20.7	--	--	61.5
PAE6	A	722	11.5	730	27.0	730	19.6	--	--	58.1

(a) Group A contains cold-worked and aged Mo only. Group B contains Mo-41Re (both annealed and aged as well as cold-worked and aged) and annealed and aged Mo.
(b) dpa values calculated for stainless steel.

	Annealed and Aqed			Cold-Worked and Aged	
Temperature°C	Dose dpa	-Δρ/ρ	Temperature°C	Dose dpa	-Δρ/ρ
420	47.2	-0.45	420	15.0	0.96
420	105.1	0.36	420	50.3	0.28
			420	110.8	0.0
471	32.2	1.19	471	11.4	1.10
471	43.7	1.8	471	38.2	3.41
			411	57.6	1.68
569	40.8	1.18	563	11.5	1.93
569	63.9	3 10	569	38.5	1.12
			569	58.I	3.02
645	40.8		645	11.5	1.57
645	65.8		645	38.5	I.e9
			645	58.1	1.83
730	40.8		73	11.5	1.56
730			730	38.5	I 9R
			730	5e.i	i91

Table 2b
Density Changes (-Δρ/ρ₀) Measured in Irradiated Mo-41Re

		Density Change, %	
Temperature°C	Dose dpa	Annealed and Aged	Cold-Worked and Aged
420	47.2	0.33	-0.08
420	105.7	0.11	0.28
471	32.2	2.26	0.06
471	43.7	-0.28	-0.25
569	40.8	0.72	1.14
569	63.9	0.52	0.12
645	40.8	0.66	0.04
645	65.8	1.41	0.15
730	40.8	1.45	0.47
730	61.5	-0.07	-0.49

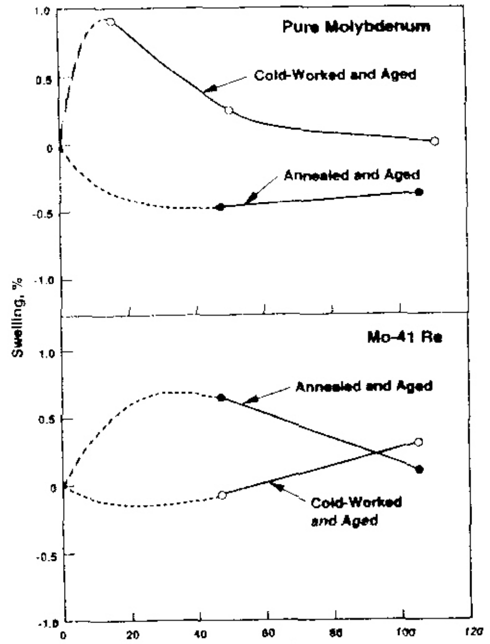

Fig. 1. Swelling ($-\Delta\rho/\rho_0$) of pure Mo and Mo-41Re after irradiation in FFTF/MOTA at a target temperature of 420°C.

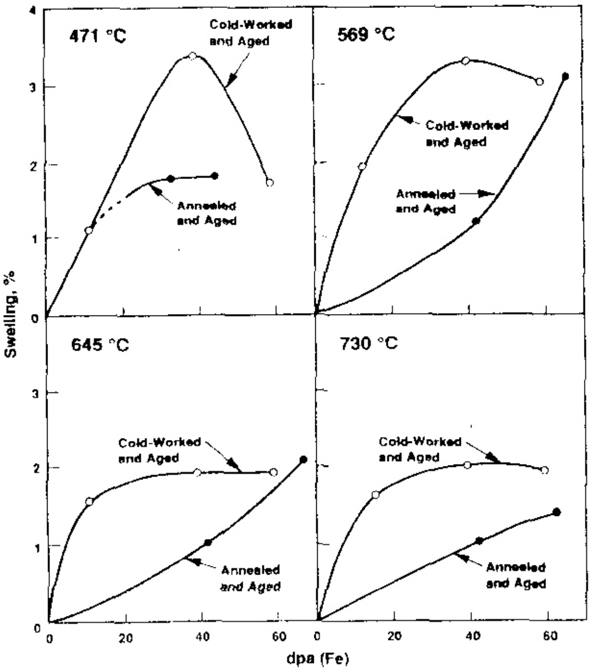

Fig. 2. Swelling ($-\Delta\rho/\rho_0$) of pure Mo at target temperatures between 471 and 730°C.

Discussion

From density change measurements alone, it is impossible to determine for Mo-41Re whether the *observed changes are due solely or in part to* lattice parameter changes accompanying precipitation. Chi-phase precipitates are known to develop in ion-irradiated Mo Re alloys, even though ?he equilibrium phase diagram would not *predict the formation of this* phase.[?] The densification of annealed and aged pure molybdenum at 420°C is also difficult to explain. Since technicium formation by transmutation was invoked previously to explain void shrinkage in molybdenum, calculations wire performed to assess the level of solid transmutants produced in these two alloys. Since the alloys are also being irradiated in thermal reactors in other laboratories. calculations were performed both for FFTF and HFIR to assess the range of possible transmutation in those materials. The STARFIRE spectrum was used to assess the transmutation produced in a typical fusion spectrum.

Calculation of Transmutation Products

The calculations required several steps Including the determination of the principal nuclear reactions and subsequent decays. extraction oi nuclear cross sections iron ENDF/B-V or VI, addition of there new cross sections to existing PNL libraries, spectral averaging of each cross section using the STAY'SL computer code, and numerical calculations for different irradiation times. In most cases, the accuracy is estimated at 10 to 20% due both to uncertainties in the adjusted neutron spectra and in the evaluated neutron activation cross sections. In the majority of cases, second-order transmutation of the primary reaction products into secondary products was neglected. This is generally a good assumption, unless either the primary transmutation is quite high (above 1%) and/or the product has a very high transmutation rate.

The results are listed in Table 3. Results for FFTF are given at 30, 60, and 100 dpa (iron) at midplane, corresponding to full-power-day irradiations of 244, 488, and 813 FPD at 291 MW; total neutron fluences are 1.02, 2.04 and 3.40 x 10^{23} n/cm^2. Calculations are also provided for the midplane of the FFTF below-core canister (-66.3 cm) for the same irradiation times, corresponding to Fe dpa values of 4.4, 8.7, and 14.5 and total fluences of 0.30, 0.61, and 1.02 x 10^{23} n/cm^2, *respectively*. These FFTF conditions correspond to the new core configuration used for fusion experiments, such as MOTA-1F, 1G, 2A, and 2B.

Calculations for HFIR are shown at midplane of *the Peripheral Target Position (PTP)* for 1 full power year at 85 MW, corresponding to 27 dpa in iron and a fast fluence of 3.6 x 10^{22} n/cm^2. This reflects HFIR operating conditions employed since the reactor was restarted in 1990.

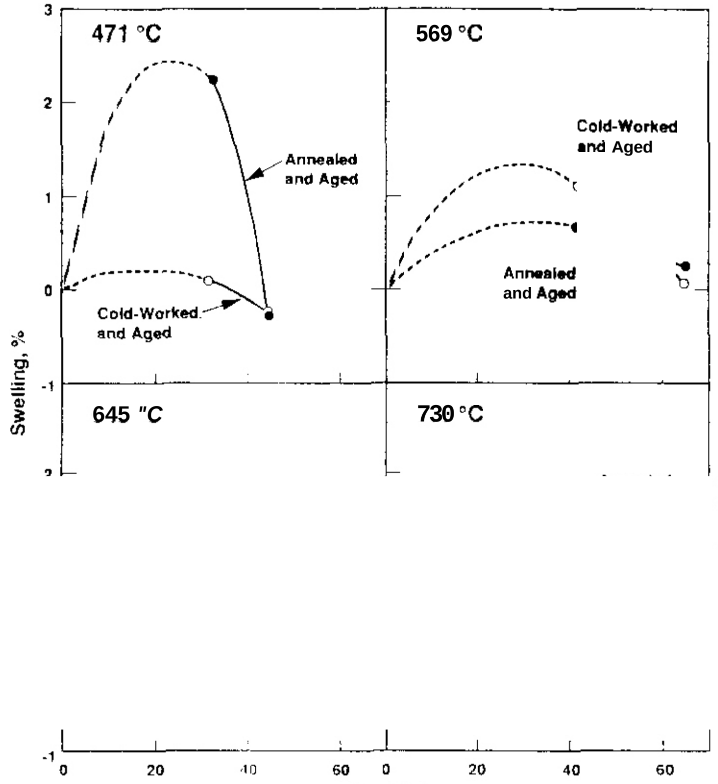

Fig. 3. Swelling ($-\Delta\rho/\rho_0$) of Mo-41Re at temperatures between 471 and 730°C.

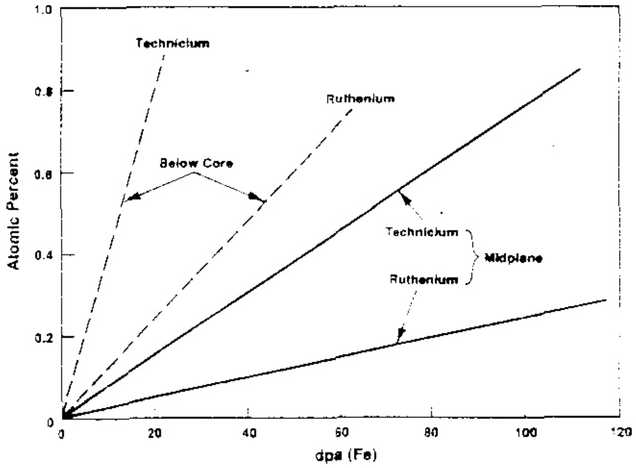

Fig. 4. Predictions of technicium and ruthenium formation in pure molybdenum during irradiation in FFTF.

The principal transmutation reactions for Mo are the (n,γ) capture reactions on Mo-98 to Mo-99 (2.7 d) to 99-Tc (200,000 y) and on Mo-100 to Mo-101 (15 m) to Ru-101. Capture reactions an the other isotopes lead to other stable Mo isotopes. Weaker reactions considered include (n,p) and (n,α). Many of the (n,p) reactions produce short-lived products 'which decay back to other Mo isotopes. However, the nuclear reactions Mo-94 (n,p) Nb-94 (20,000 y) and Mo-92 (n,p) Nb-92 (10 d) 'which decays to Zr-92 must be Considered. The (n,α) reactions to Zr were included for all of the Mo isotopes except that Mo-92 produces Zr-89 13.3 d) which decays to 1-89. and Mo-98 and Mo-100 have products which decay back to other Mo isotopes. Hence, nine reactions were used in the transmutation calculations. Some of these transmutation products may be further transmuted; in general this is not important except for isotopes that have significant capture gamma cross sections. For Mo, the only significant second order transmutation is Tc-99, which in turn will partially transmute to Ru-100 in HFIR.

Both Re-185 and Re-187 have large (n,γ) reaction rates leading to significant transmutation in both HFIR and FFTF. Both reactions lead to Os where further reactions lead only to other stable Os isotopes. All of the (n,p) reactions lead to short-lived tungsten isotopes which decay back to Re. The (n,α) reactions produce small amounts of W-182 and W-184.

Figure 4 shows that the technicium and ruthenium levels generated in FFTF are not negligible, especially for below core irradiation. Whether concentrations of this magnitude can account for the densification of molybdenum observed at 420°C has not yet been established. Table 3 indicates that the transmutation rate will be higher in HFIR, especially for ruthenium. Figure 5 shows that rhenium will transmute to osmium very strongly in FFTF with the rate increasing sharply below and near the edges of the core. In HFIR, however, rhenium will be almost completely transmuted to osmium at a moderate dpa level, as shown in Figure 5.

Table 3
Transmutation in FFTF and HFIR
(Values are listed in at%, unless noted as appm)

	FFTF Midplane			FFTF Below Core			HFIR Midplane*
Transmutant	244	488	833	244	488	833	365 FPD
Fluence,** × 10^{23} dpa, Fe	1.0 30	2.1 60	3.4 100	0.30 4.4	0.61 8.7	1.02 14.5	3.6 27.0
Molybdenum:							
Tc-99	0.24	0.45	0.76	0.17	0.35	0.62	0.49
Ru	0.07	0.14	0.24	0.05	0.10	0.17	0.64
Nb-94 appm:	0.02	0.04	0.07	0.001	0.002	0.003	0.11
Zr appm:	2.0	4.0	6.8	0.08	0.16	0.27	9.1
Rhenium:							
Os	10.1	19.2	29.9	17.7	32.1	47.3	99.5+
W appm:	0.4	0.8	1.4	0.02	0.04	0.08	0.33

* Self-shielding has not been incorporated in these calculations.

** Exposures for FFTF are total fluences, but fluence for HFIR is based on E>0.1 MeV

† Initial rate for transmuting Re to Os in HFIR is 2.1% per day.

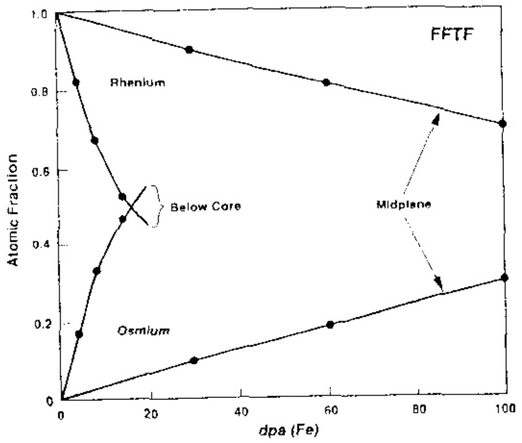

Fig. 5. Prediction of osmium formation in rhenium during irradiation in FFTF.

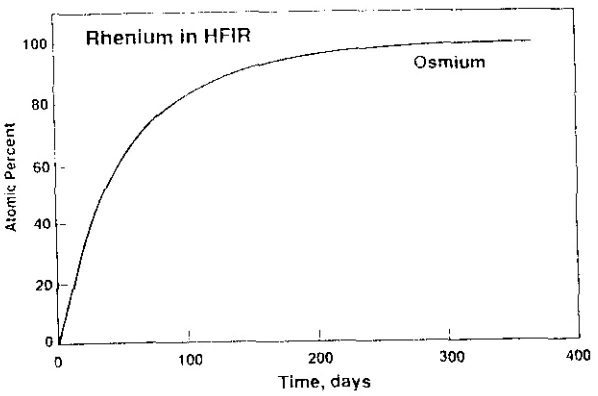

Fig. 6. Prediction of osmium formation in rhenium during irradiation in HFIR.

It is safe to say that the Mo-41Re specimens irradiated in FFTF are now Mo-Re-Os-Tc-Re alloys of varying composition, depending on their location in the FFTF core and the total exposure. Microscopy and EDX analysis are necessary to determine the composition of these alloys and the role of transmutation and precipitation in determining the density changes induced by radiation. It is also suspected that large levels of osmium may change the formation rate of chi phase.

Recent Russian studies showed that Mo-Re alloys irradiated in SM-2 (similar to HFIR in spectrum) lost 20 to 30% of their electrical conductivity and much of their fracture resistance at relatively low exposures (~5 x $10^{[illegible]}$ n cm^{-2}). Based on the preceding calculations, osmium formation was probably the major cause of the conductivity degradation, but the loss of fracture resistance may be due to both precipitation and osmium formation.

It appears that transmutation will also be important in fusion spectra at levels intermediate to that in FFTF and HFIR. This is demonstrated in Figures 7 and 8 for the STARFIRE spectra.

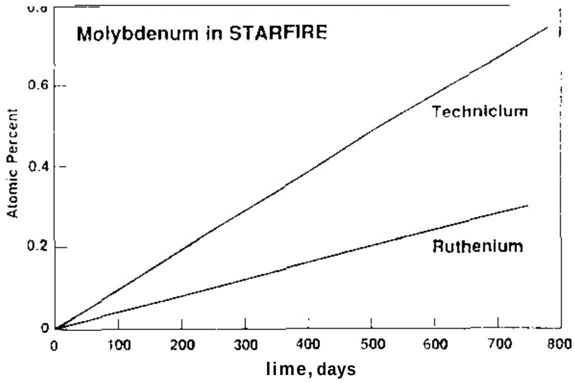

Fig. 7. Prediction of transmutation in pure molybdenum in STARFIRE.

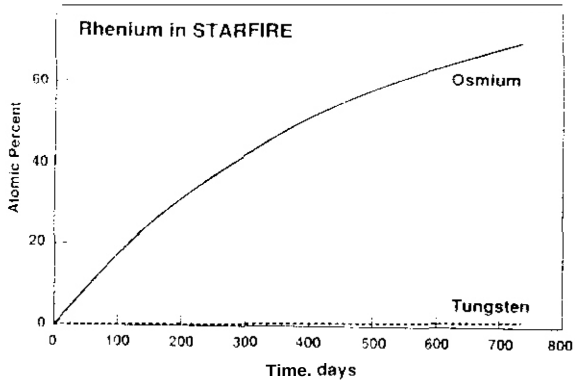

Fig. 8. Prediction of transmutation in pure rhenium in STARFIRE.

FUTURE WORK

These specimens will be made available to Japanese or NORCUS-sponsored U.S. scientists for microscopy examination.

REFERENCES

1. S. A. Fabritsiev et al., J. Nucl. Mater., 191-194 (1992) 426-429.

2. I. V. Gorynin et al., J. Nucl. Mater., 191-194 (1992) 421-425.

3. F. A. Garner, "FFTF/MOTA Irradiation of Refractory Alloys Under Consideration as Plasma Facing Components." Fusion Reactor Materials Semiannual Progress Report, DOE/ER-0313/9 (1991), pp. 169-171.

4. R. A. Erck and L. E. Rehn, Phil. Mag. A, 62, (1990) 29-51.

5. R. A. Erck and L. E. Rehn, J. Nucl. Mater., 168 (1989) 208-219.

6. R. A. Erck, C. M. Wayman, and L. E. Rehn, in Radiation-Induced Changes in Microstructure: 13th International Symposium (Part I), ASTM STP 955. F. A. Garner, N. H. Packan and A. S. Kumar, Eds., American Society for Testing and Materials, Philadelphia, 1987. pp. 721-729.

7. J. H. Evans, J. Nucl. Mater., 88 (1980) 31-41.

Irradiation Creep of Russian Federation Pressurized Tubes in MOTA-2B - F. A. Garner, (Pacific Northwest Laboratory)[a], C. R. Eiholzer, (Westinghouse Hanford Company), E. V. Demina and [illegible] I. Ivanov, (Baikov Institute)

OBJECTIVE

The objective of this effort is to provide irradiation creep data on a reduced activation austenitic alloy supplied by the Baikov Institute.

SUMMARY

Irradiation has been completed in MOTA-2B for creep tubes constructed from a candidate reduced activation austenitic alloy supplied by the Baikov Institute in Moscow. The total strains are strongly dependent on irradiation temperature in the range 425-600°C, but are not completely linear with stress level

PROGRESS AND STATUS

Introduction

In a previous report[1] the first details of a joint US/RF (Russian federation) irradiation study were presented. This effort involved the irradiation of two groups of reduced activation austenitic alloys in FFTF using the MOTA-2B irradiation vehicle. One of these material groups was supplied by the Baikov Institute as tubing in the annealed condition for fabrication into pressurized creep tubes. Table 1 provides the composition of these tubes. The tubing dimensions are 4.57 mm (0.180 in) OD and 0.2 mm (0.008 in) wall thickness. End caps for these tubes were of standard WHC design and were fabricated from the U.S. D9 variant of AISI 316 stainless steel, the composition of which is provided in Table 2.

Table 1.
Chemical Composition of Austenitic Steel 10Kh12G20V, Heat 394, Tubing

Element	Fe	Cr	Mn	W	Si	C	P	S
wt%	Bal.	13.0	19.0	1.0	0.32	0.09	0.024	0.012

Table 2.
Nominal Chemical Composition of D9, (Heat 2966) Rod Used for End Caps

Element	Fe	Ni	Cr	Mn	Mo	Si	Ti	Nb
wt%	Bal.	15.64	14.03	2.19	1.45	1.05	0.25	0.02

Element	C	V	Al	P	Ta	Co	S	N
wt%	0.046	0.04	0.04	0.012	0.01	0.03	0.001	0.009

Experimental Details

The components were ultrasonically cleaned in acetone for 5 min. and then in alcohol for 5 min. The components were air dried. The cleaned components were handled with white gloves.

A laser engraver was used to put ID numbers on set of top and bottom end caps. The ID code consists of two characteristic letters followed by a two number sequence starting with 00. The characteristic letters for the Russian Federation pressurized tubes are FG. Identification codes used were FG00 through FG35.

The end caps were electron beam welded to the gage sections. Before welding the test specimens, qualification welds were made to determine if the welding parameters were correct for the material. The qualification procedure consisted of making six welds which had the same joint and materials that would be welded on the test specimens. The qualification welds were leak checked and then metallographically examined for penetration. The required penetration is 85% of the wall thickness. All production welds were made to this procedure.

---

[a] Pacific Northwest Laboratory is operated for the U.S. Department of Energy by Battelle Memorial Institute under Contract DE-AC06-76RLO 1830.

The electron beam production welds were inspected before the specimens were accepted for further fabrication steps. A visual inspection was then made on all the production welds. All the welds passed the inspection. Two production specimens from each production lot were sacrificed to determine if the weld penetration for the lot was correct. These specimens had the beginning or ending lot production welds made on them. The welds were then metallographically examined. The tubes were electron beam welded in two lots. The sacrificial specimens from each lot showed the correct penetration. Both lots of specimens were accepted for further fabrication steps.

The desired hoop stresses and corresponding fill pressures were determined before the specimens were filled with gas. The desired hoop stresses were based on the ultimate tensile strength of the material, creep behavior of similar material, and the irradiation history of the material. The tensile data provided by the Baikov Institute showed that the material behaved similarly to solution annealed 316 stainless steel. The final desired hoop stresses were based on the limited creep data on solution annealed 316 SS. The test matrix is given in Table 3.

Table 3.
Test Matrix for Pressurized Tubes

	Stress (MPa)				
Temperature (°C)	0	30	60	100	140

The FILPRES computer program was used to determine the gas fill pressures. This program uses elastic stress-strain relationships for cylindrical tubes to calculate fill pressures for the specimens to achieve the desired stress at temperature. The code also incorporates the effects of wall thickness, material type, fill gas, test temperature, and desired hoop stress. The fill pressures were based on the thick wall equation for hoop stress, austenitic materials, helium fill gas, helium compressibility equations, and the matrix given in Table 3. Table 4 presents the fill pressures that were selected.

The pressurized tubes were filled with ultra-pure helium in a laser weld chamber. The specimens were put in a pressure vessel that has a quartz port on its top. After filling, a closure weld was performed with a laser pulse through the quartz port.

The laser welding parameters were qualified before the production welds were performed on the test specimens. The qualification procedure consisted of making six laser welds. Three of the qualification welds were leak checked and then metallographically examined for full hole closure. All production laser welds were made to the qualifying procedure.

The production laser closure welds were inspected and helium leak tested before the pressurized tubes were accepted for testing. First, the laser closure welds were visually inspected, then the welds were helium leak checked. The leak check has a sensitivity of 2 × 10 [illegible] atm-cm [illegible]/s. All specimens passed both the inspection and leak test.

The diameters of the pressurized tubes were measured using a non-contacting laser system. The laser system takes five equidistant diameter measurements along the gage section of the specimen. The third measurement is taken at the center of the specimen. The distance between measurements was 26.7 mm (1.05 in.). The accuracy of the measurements is ± 0.001 mm (0.00004 in.). The average of the three middle measurements determines the average diameter. If the middle three measurements are not within 0.00127 mm (50 μin.), then the specimen is remeasured. When repeat measurements are required, the specimen is measured two more times. When three measurements were taken, all data were averaged to determine the average diameter value. Diametrical measurements were taken before and after pressurizing. Table 4 gives the pre- and post-filled measurements taken on the pressurized tubes.

All the specimens made were used for in-reactor testing, thermal control, weld check, or archive. Table 4 presents the specimen usage. The fifteen in-reactor test specimens were put into MOTA-2B in FFTF cycle 12. All the in-reactor test specimens with the same test temperatures were put in the same MOTA canister. Table 5 gives the canister and basket numbers for each specimen group.

Table 4.
Summary of Fabrication Data

ID	Hoop Stress (MPa)	erl Temp °C)	Fill Pressure (psig)	Average Pre-fill Diameter (in.)	Average Post-fill Diameter (in.)	Specimen Usage
FG00	NA	NA	NA	NA	NA	Check EB weld lot
FG01	NA	tin	NA	NA	NA	Check EB weld lot
FG02	0	420	9.7'	.18004	.18005	Reactor
FG03	0	420	9.7*	.18019	.18027	Thermal
FG04	30	420	181	.18060	.18061	Reactor
FG05	30	420	182	,18014	.18021	Thermal
FG06	60	420	369	.17991	.17994	Reactor
FG07	60	420	369	.18017	.18025	Thermal
FG08	100	420	620	.17961	.17965	Reactor
FG09	100	420	620	.18022	.18034	Thermal
FG10	140	420	873	.18034	.18038	Reactor
FG11	140	420	813	.18038	,18050	Thermal
FG12	0	320	8.6*	,18022	.18023	Reactor
FG13	0	520	8.6*	.18007	.18014	Thermal
FG14	30	320	158	.18030	.18031	Reactor
FG15	30	520	158	.18003	.18010	Thermal
FG16	60	520	323	.18020	.18019	Reactor
FG17	60	520	323	.17998	.18007	Thermal
FG18	100	520	544	.18013	.18015	Reactor
FG19	100	520	514	.17987	.17998	Thermal
FG20	140	520	766	.18014	.18020	Reactor
FG21	140	520	767	.18004	.18012	Thermal
FG22	0	600	7.8*	.17996	.17997	Reactor
FG23	0	600	7.8*	,18034	.18043	Thermal
FG24	NA	NA	NA	NA	NA	Check EB weld lot
FG25	NA	NA	NA	NA	NA	Check EB weld lot
FG26	30	600	143	.17994	.17996	Reactor
FG27	30	600	143	.17986	.17996	Thermal
FG28	60	600	294	.18002	.18004	Reactor
FG29	60	600	294	.18020	.18033	Thermal
FG30	100	600	496	.18023	,18025	Reactor
FG31	100	600	497	18030	.18045	Thermal
FG32	140	600	699	.17969	.17974	Reactor
FG33	140	600	699	.18040	.18059	Thermal
FG34	NA	NA	NA	.18005	NA	Archive
FG35	NA	NA	NA	.18023	NA	Archive

*These are psia values. Low or negative pressures can only be acheived using psia gage.

Table 5
Location of **Pressurized** Tubes in MOTA-ZR

Pressurized Tube Test Temperature (C)	MOTA-2B Canister No. Basket
420	4B-2
520	2F-3
600	4F-4

NOTE: The specimens designated for 420°C were placed in a 425°C canister. The hoop stress should not differ significantly for the 5°C difference

The tubes were maintained close to their target temperatures throughout the irradiation sequence, as shown in Table 6, reaching fluences between 5.3 and 5.8 x 10^{22} n/cm^2 (E> 0.111 MeV). After discharge from MOTA-2B, the diameters of the tubes were again measured. All specimens were observed to be in good shape with no obvious failures.

Table 6.
Average Test Temperatures

Canister	Canister Type	Target Test Temp. (°C)	Maximum Test Temp. (°C)	Average Test Temp. (°C)	Time at Average Test Temp. (Days)
2F	Gas-Gapped	520	533	519	200.4
4B	Weeper	425	434	428	199.3
4F	Gas-Gapped	600	614	599	200.3

Results and Discussion

Table 7 presents the average diametral strains measured for the fifteen irradiated tubes. The amount of diametral strain ΔD/D was determined by

$$\frac{\Delta D}{D}(\%) = 100[(D_m - D_p)/D_p]$$

where D_m is the current diameter and D_p is the post-filled diameter.

Table 7.
MOTA-2B In-Reactor Creep Data

Specimen ID	Hoop Stress (MPa)	Average Test Temp. (C)	Basket	MOTA-2B Fluence 10^{22}n/cm^2 E>0.111 MeV	Average Postfilled Diameter (mm)	Average Final Diameter (mm)	Total Diametral Strain (%)	Creep Strain*, %	Stress Normalized Creep Strain* %/MPa
FG02	0	428	4B-2	5.3	4.57327	4.57683	0.08	--	--
FG04	30				4.58749	4.59638	0.19	0.11	3.7×10^{-3}
FG06	60				4.57348	4.58368	0.29	0.21	3.5×10^{-3}
FG08	100				4.55311	4.57733	0.31	0.23	2.3×10^{-3}
FG10	140				4.58165	4.59638	0.32	0.24	1.7×10^{-3}
FG12	0	519	ZF-3	5.8	4.57784	4.59486	0.37	--	--
FG14	30				4.57962	4.59943	0.43	0.06	2.0×10^{-3}
FG16	60				4.57683	4.60299	0.57	0.20	3.3×10^{-3}
FG18	100				4.57581	4.61416	0.84	0.47	4.7×10^{-3}
FG20	140				4.57708	4.63220	1.20	0.83	5.9×10^{-3}
FG22	0	599	4F-4	5.4	4.57124	4.57810	0.15	--	--
FG26	30				4.57098	4.59435	0.51	0.36	1.2×10^{-2}
FG28	60				4.57302	4.63626	1.38	1.23	2.1×10^{-2}
FG30	100				4.57835	4.68935	2.42	2.27	2.3×10^{-2}
FG32	140				4.56540	4.70103	2.97	2.82	2.0×10^{-2}

*Calculated values assume that stress does not influence swelling and that no phase-related strains occur. These assumptions are probably not completely valid.

Figure 3 shows that the total strain is strongly dependent on both irradiation temperature and stress level, but is not completely linear with stress at any temperature. Such behavior implies that, in addition to irradiation creep, phase-related density changes and stress enhanced swelling are probably involved. The various contributions to the total strain cannot be determined without performing microscopy and density change measurements.

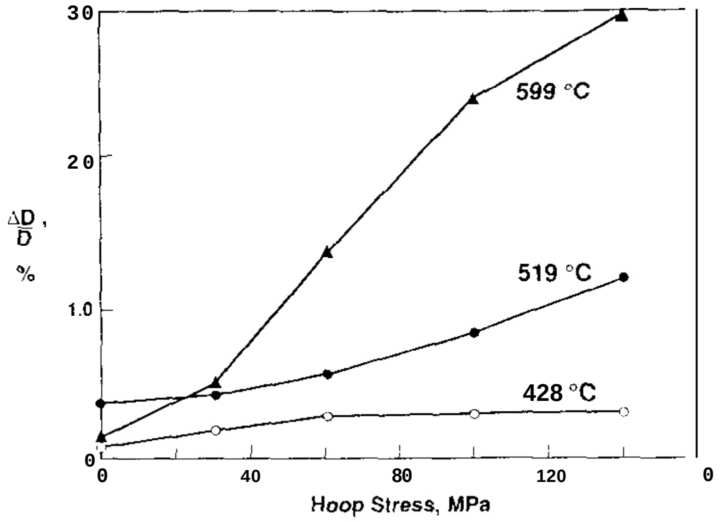

Figure 1. Diameter changes observed in pressurized tubes after irradiation in MOTA-2B.

FUTURE WORK

These tubes will be *examined by a* Russian Federation assignee at Oak Ridge National Laboratory. Since the MOTA irradiation will not be continued, these tubes may be sacrificed for density measurements. Thermal control studies have not been initiated and may be abandoned.

REFERENCES

1. F. A. Garner, M. L. Hamilton, C. R. Eiholzer, R. L. Klueh, H. Takahashi, S. Ohnuki, K. Miyahara, P. Schiller, and L. I. Ivanov, in Fusion Reactor Materials Semiannual Progress Report DOE/ER-0313/10 (1991) pp. 109-112.

Density Measurements Performed on Ispra Second Generation AMCR Alloys Irradiated in MOTA-2A - F. A. Garner, (Pacific Northwest Laboratory)[a], P. Schiller, (Ispra Establishment), and H. Takahashi, (Hokkaido University)

OBJECTIVE

The objective of this effort is to provide information on the radiation response of reduced activation alloys considered for fusion application.

SUMMARY

Density change measurements have been completed on the Ispra second generation AMCR alloys irradiated in MOTA-2A. The various compositional modifications induce a wide variation of swelling behavior in the range 423-600°C at 32-36 dpa.

PROGRESS AND STATUS

Introduction

In the early FFTF irradiation studies on commercial Fe-Cr-Mn alloys it was shown that the AMCR alloy supplied by Creusot-Marrel (Fe-10Cr-18Mn-0.7Ni-0.6Si-0.06N-0.2C) exhibited somewhat better performance than the other alloys investigated.[1] Researchers at the Ispra Establishment have developed a series of lower activation variations on this steel[2] which was inserted for irradiation in MOTA-2A during FFTF cycle 11 and 12 at 420, 520, and 600°C. (See Table 1 for the composition of these steels). Cycle 11 has been completed and density measurements performed.

Table 1
Composition (wt%) of ISPRA Second Generation AMCR Alloys

Alloy	Cr	Mn	Ni	Mo	C	N	Si	S	P	Cu	Al	Nb	V	W	Ta	Pb	Co	B
ISPRA-A	12.5	10.5	2	<0.1	0.10	<0.05	0.5	<0.01	<0.02	<0.1	<0.05	<0.001	0.75	1.4	<0.005	<0.001	<0.1	<0.005
ISPRA-B	12.5	10.5	<0.25	<0.1	0.30	<0.05	0.5	<0.01	<0.02	<0.1	<0.05	<0.001	0.75	1.4	<0.005	<0.001	<0.1	<0.005
ISPRA-C	12.5	17.5	2	<0.1	0.10	<0.05	0.5	<0.01	<0.02	<0.1	<0.05	<0.001	<0.1	2.0	<0.005	<0.001	<0.1	<0.005
ISPRA-D	10.0	17.5	<0.25	<0.1	0.30	<0.05	0.5	<0.01	<0.02	<0.1	<0.05	<0.001	<0.1	2.0	<0.005	<0.001	<0.1	<0.005
ISPRA-E	17.0	10.5	2	<0.1	0.10	<0.05	0.5	<0.01	<0.02	<0.1	<0.05	<0.001	0.75	2.0	<0.005	<0.001	<0.1	<0.005

Results

Table 2 presents the results of the density measurements, and demonstrates that a large variation in swelling behavior occurs. Note that the AMCR steel used in the previous US studies was also included in MOTA 2A and 2B for comparison with the behavior of the new Ispra alloys.

---

[a] Pacific Northwest Laboratory is operated for the U.S. Department of Energy by Battelle Memorial Institute under Contract DE-AC06-76RLO 1830.

	Original Density (g cm^{-3})	423°C 35.1 dpa**	520°C 36.3 dpa**	600°C 32.3 dpa**
ISPRA-A	7.94758	0.96	1.23/0.28	-0.15
ISPRA-a	7.94955	0.30	0.07	0.99
ISPRA-C	7.98265	1.49	3.97	1.96
ISPRA-D	7.97152	0.28	0.58	-0.72
ISPRA-E	7.85483	**0.52**	4.08	0.58
AMCR	7.85452	0.96	0.71	1.19

FUTURE WORK

The specimens from MOTA-2A have **been** snipped to Hokkaido University for microscopy examination. A second discharge of this experiment from MOTA-28 **has** been completed and density measurements will be **measured.**

REFERENCES

1. F. A. **Garner** and J. M. McCarthy in "Reduced Activation Material, far Fusion Reactors." ASTM STP 1047, **American** Society for Testing and Materials. Philadelphia (1990) pp. 19-29.

2. G. Piatti, D. Boerman and J. Heritier, Fusion Technology 1988, **Proceedings** of 15th Symposium an Fusion Technology (1989). pp. 983-990.

THERMAL STABILITY OF MANGANESE-STABILIZED STAINLESS STEELS -- R. L. Klueh and E. A. Kenik

OBJECTIVE

Induced radioactivity in the first-wall and blanket-structure materials of fusion reactors will *make* these components highly radioactive after their service lifetime, leading to difficult radioactive waste-management problems. One way to minimize the disposal problem is to use structural materials in which radioactive isotopes induced by irradiation decay quickly to levels that allow simplified disposal techniques. We have assessed the feasibility of developing such austenitic stainless steels.

SUMMARY

Previous work on a series of experimental high-manganese reduced-activation austenitic stainless steels demonstrated that they had improved tensile properties relative to type 316 stainless steel in both the annealed and 20% cold-worked conditions. Steels were tested with an Fe-20Mn-12Cr-0.25C (in weight percent) base composition, to which various combinations of Ti, W, V, P, and B were added. Tensile tests have now been completed on these steels after thermal aging at 600°C. Thermal stability varied with composition, but the alloys were as stable or more stable than type 316 stainless steel. The strength of the annealed steels increased slightly after aging to 5000 h, while a strength decrease occurred for the cold worked steel. In both conditions, a steel containing a combination of all the alloying elements was most stable and had the best strength after thermal aging 5000 h at 600°C. Despite having much higher strength than 316 stainless steel after aging, the ductility of the strongest experimental alloy was still as good as that of 316 stainless steel.

PROGRESS AND STATUS

Introduction

Conventional structural alloys used for components of a fusion reactor will become highly radioactive during the service lifetime, making the disposal of the components a difficult nuclear waste problem. This has led to a proposal to develop reduced-activation alloys [1]. Such alloys would contain only elements in which the induced radioactivity would decay much more rapidly than in conventional alloys. Common alloying elements that must be eliminated from reduced-activation alloys include Ni, Mo, Cu, Nb, and N.

Nickel-stabilized austenitic stainless steels have long been considered potential structural alloys for fusion reactors. Therefore, a reduced-activation austenitic stainless steel substitute was sought. There have been several programs to develop such a steel [2-6], including a program at Oak Ridge National Laboratory (ORNL) [4,8,9].

The ORNL program sought to develop reduced-activation or fast induced-radioactivity decay (FIRD) austenitic stainless steels using manganese as a replacement for nickel. It was recognized that this could prove difficult, because manganese is not as strong an austenite stabilizer as nickel and because the metallurgical effects of nickel and manganese in the alloy may not otherwise be equivalent [4]. The first step was the determination of a "modified Schaeffler diagram" for high-manganese alloys [8]. This diagram differed significantly from the standard Schaeffler diagram determined for high-nickel steels with small amounts of manganese. The modified diagram was used to pick a composition range where stable austenite, high-manganese Fe-Mn-Cr-C alloys should be obtained.

Based on the original work [8], a nominal Fe-20Mn-12Cr-0.25C steel was chosen as a base composition. This composition was then alloyed for strength and irradiation resistance by adding various combinations of Ti, W, V, P, and B. Seven Fe-Cr-Mn-C steels with various combinations of Ti, W, V, B, and P were examined and shown to have strength and ductility as good or better than type 316 stainless steel [9].

After the program began, the high-manganese steels were concluded to pose potential safety problems in a fusion reactor first wall, and they no longer have a high *priority in the* U. S. *fusion* program. Although the development program has been discontinued, knowledge obtained in the program could be of interest for the fusion program in the future and for other applications. For the record, therefore, we intend to publish the information obtained. In this paper, microstructural observations and tensile property determinations were made on the seven solute-modified alloys after thermally aging for 5000 h at 600°C.

Experimental Procedure

Seven experimental alloys, including the base composition. were obtained in the form of 600-g vacuum arc-melted button heats. Table 1 lists alloy compositions and designations. By making elemental additions to the base composition (designated MnCrC), alloys were obtained with titanium (MnCrCTi), tungsten (MnCrCW), a combination of titanium and tungsten (MnCrCTiW), and combinations of these elements with V, B, and P (MnCrCTiBP, MnCrCTiVBP, and MnCrCTiWVBP). Nominal levels of Ti, W, V, B, and P of 0.1, 1, 0.1. 0.005, and 0.03 weight percent, respectively, were sought. Actual compositions are given in Table 1

Alloys were cast into ingots with a rectangular cross section of 12.7 mm by 25.4 mm and 152 mm in length. The ingots were hot rolled at 1050°C to a thickness of approximately 6.4 mm. After homogenizing for 5 h at 1200°C, the steel was cold rolled in five stages to 0.76-mm-thick sheet. Between each stage, the steel was annealed 1 h at 1150°C. The sheet was finished in the 20% cold-worked condition.

Tensile specimens with gage lengths parallel to the rolling direction and a reduced gage section 20.3-mm long by 1.52-mm wide by 0.76-mm thick were thermally aged. They were aged for 500, 1000, 2500, and 5000 h at 600°C in the 20% cold-worked condition and after a solution anneal of 1 h at 1050°C. Tests were at 600°C in vacuum on a 120-kN-capacity Instron universal testing machine at a crosshead speed of 8.5 mm/s (a nominal strain rate of 4.2×10^{-4}/s).

Microstructures were examined by optical and transmission electron microscopy. Analytical electron microscopy was performed on foils and on carbon extraction replicas in Philips EM 400T/FEG and CM30 microscopes equipped with EDAX 9100/70 or 9900 energy dispersive x-ray analyzers, respectively. Some information on the composition of precipitates observed after aging 5000 h at 600°C was previously published [10]

RESULTS AND DISCUSSION

Microstructures

The microstructures of the unaged steels were previously presented [9]. Addition of the alloying elements to the MnCrC base composition affected the grain size and the amount of precipitate present. All of the steels with titanium had an estimated ASTM grain size number 8, compared to 3 for MnCrC and 4 for MnCrCW. The annealed 316SS had ASTM grain size 4 [9].

After the 1050°C anneal, no precipitate was detected in MnCrC and MnCrCW--the steels without titanium [9]. Steels with titanium contained MC precipitates after annealing at 1050°C [9]. The MnCrCTiVBP and MnCrCTiWVBP also contained $M_{23}C_6$. Most of the MC occurred in the matrix, although some grain boundary MC was detected in the MnCrCTiBP, MnCrCTiVBP, and

Table 1. Fe-Cr-Mn Alloys Tested

Alloy Designation	Composition wt%							
	Cr	Mn	C	Ti	W	V	P	B
MnCrC	11.83	20.51	0.24			0.01	0.003	
MnCrCTi	11.73	20.50	0.25	0.11	0.09	0.01	0.003	
MnCrCW	11.80	20.46	0.23		0.83	0.01	0.004	
MnCrCTiW	11.71	21.13	0.25	0.12	0.77	0.01	0.003	
MnCrCTiBP	11.85	20.50	0.24	0.10		0.01	0.034	0.005
MnCrCTiVBP	11.84	20.82	0.22	0.10		0.10	0.033	0.005
MnCrCTiWVBP	11.70	20.39	0.25	0.10	1.08	0.10	0.027	0.005

Balance iron

MnCrCTiWVBP. Grain houndary precipitates in the latter two steels were mainly $M_{23}C_6$. The cold-worked steels also contained precipitates that remained froin intermediate anneals at 1150°C during deformation [9].

Thermal aging resulted in more precipitate formation. Optical microscopy (Fig 1) indicated that precipitation in the solution-annealed steels occurred primarily on grain boundaries Fig. 1(a)]. For the cold-worked steels, considerable precipitation appeared to occur in the matrix on slip hands, although grain boundary precipitation was also observed [Fig. 1(b)].

Specimens aged 5000 h were examined by elecuon microscopy. Solution-annealed steels were characterized by extensive grain boundary precipitation, as seen in Fig. 2 for the replica from MnCrCW. Little matrix precipitation occurred in steels without titanium. Although the grain boundary precipitate for this steel was $M_{23}C_6$, steels with titanium also contained coarse TiC, which may not have completely dissolved during the anneal at 1050°C. Figure 3 shows grain boundary and matrix precipitation in MnCrCTi; mauix precipitation was primarily MC. When vanadium was added (MnCrCTiVBP), there was a slight increase in MC precipitate (Fig. 4), compared to alloys without vanadium. The most intergranular precipitation was ohserved for MnCrCTiWVBP, which. as discussed below, was the strongest steel and showed the greatest resistance to thermal aging

Matrix precipitation was often observed to lie in parallel straight lines (Fig. 4). This was also observed after the 1050°C anneal before aging and was attributed to grain boundary migration during annealing [9]. Examination of micrographs of the aged steel indicates that lines of precipitate within a given grain often cross and are at angles to the grain boundaries, suggesting that precipitation may be occurring on preferential crystallographic planes.

Some $M_{23}C_6$ was found in the matrix after aging, and it often appeared to contain large amounts of titanium (up to 10%) [10]. However, on closer examination it was found that this $M_{23}C_6$ had formed on Ti-rich MC particles, resulting in a Ti-rich core with an outer shell that contained little titanium [Fig. 5(a)]. It was concluded that pre-existing TiC particles (those not completely dissolved during the solution anneal) served as heterogeneous nucleation sites for the $M_{23}C_6$ [10]. Another example of this phenomenon is seen in Fig. 5(b). Here, a coating of $M_{23}C_6$ has formed on the TiC and then smaller $M_{23}C_6$ particles nucleated on, or near to, or grew out of this precipitate. From an examination of the replica, it is not clear whether the precipitates are attached to the $M_{23}C_6$ that coats the TiC. Examination of foil specimens of the annealed material indicated that TiC particles often are surrounded hy dislocations, and the $M_{23}C_6$ particles could have nucleated on them, in addition to coating the TiC panicles.

Cold-worked specimens showed extensive precipitation in hoth the grain boundaries and matrix, as shown for the MnCrCTiVBP in Fig. 6. Much of the matrix precipitate appeared to be aligned along crystallographic planes, as seen in the optical microstructures (Fig 1). Just as for the annealed steels, precipitates consisted of $M_{23}C_6$ and MC, the latter appearing in the steels that contained titanium. No Laves phase was found in either the annealed or cold-worked steels after thermal aging.

Tensile behavior

Figures 6 through 9 show the tensile behavior of the unaged and aged solution-annealed (Figs. 6 and 7) and cold-worked (Figs. 8 and 9) steels. Yield stress and total elongation data are shown for the seven different steels as a function of aging time, along with data for type 316 stainless steel (316 SS), which was tested in the same condition as the high-manganese steels.

The yield stress of all the solution-annealed steels was higher after aging 5000 h than in the unaged condition Fig. 6(a)]. All of the steels were stronger than type 316 SS. The manganese steels fell into two categories: those with and those without titanium. Those with titanium were considerably stronger than those without, which included the base composition and the composition with just tungsten added. These latter two steels were only slightly stronger than 316 SS. The five steels with titanium were considerably stronger.

Although tungsten hy itself had little effect on the yield stress of the solution-annealed base composition, tungsten in combination with the other alloying elements was effective in strengthening the steels. The MnCrCTiWVBP steel, which contains tungsten in combination with all the other

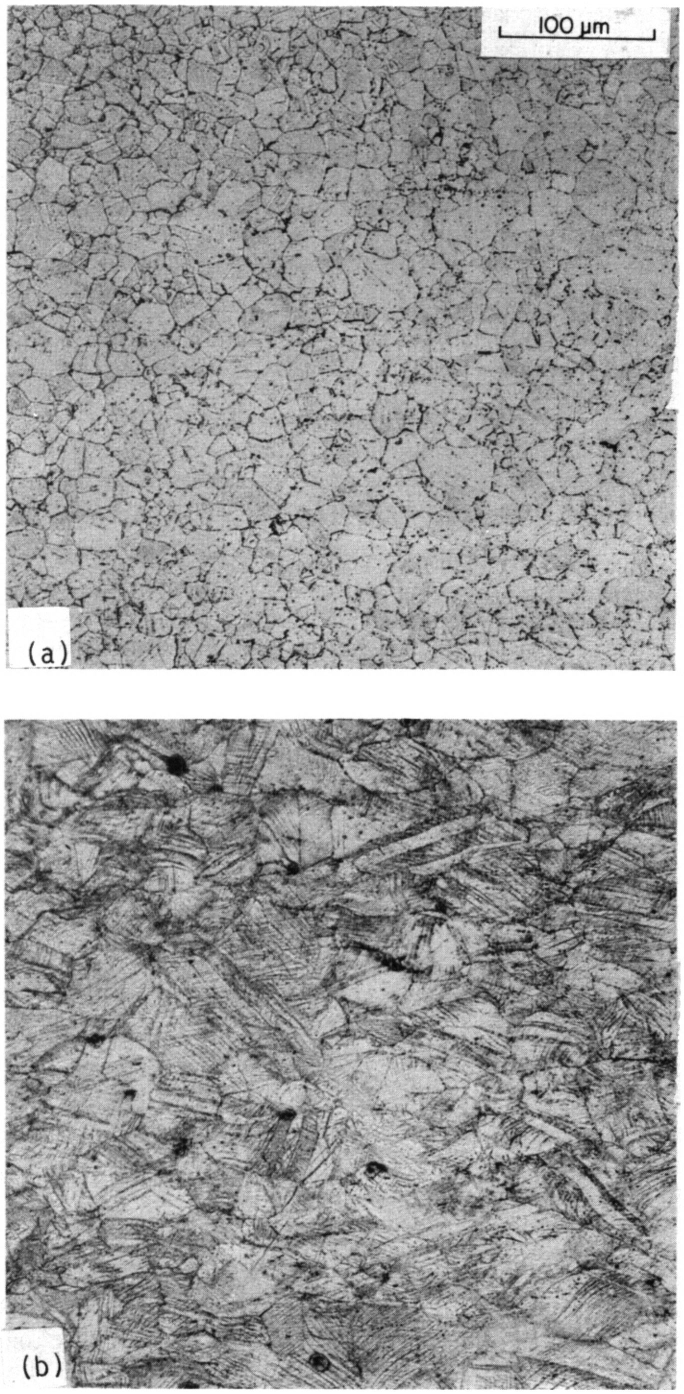

Fig. 1. Optical microstructure of the MnCrCTi alloy in the (a) annealed and (b) cold-worked conditions after thermally aging 5000 h at 600°C.

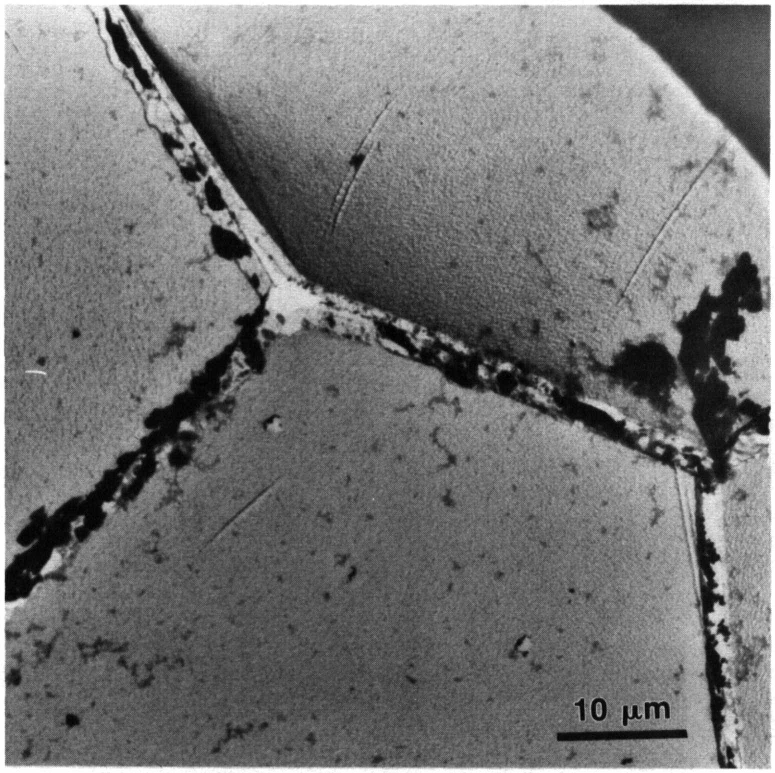

Fig. 2. Extraction replica of the annealed MnCrCW alloy after thermally aging 5000 h at 600°C.

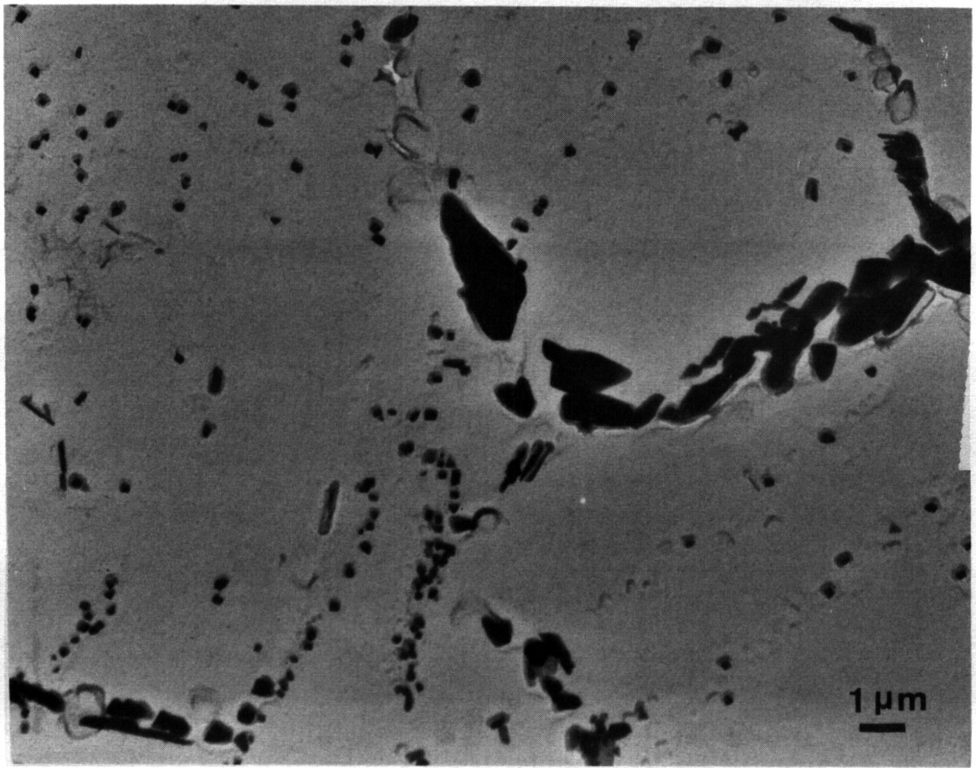

Fig. 3. Extraction replica of the annealed MnCrCTi alloy after thermally aging 5000 h at 600°C.

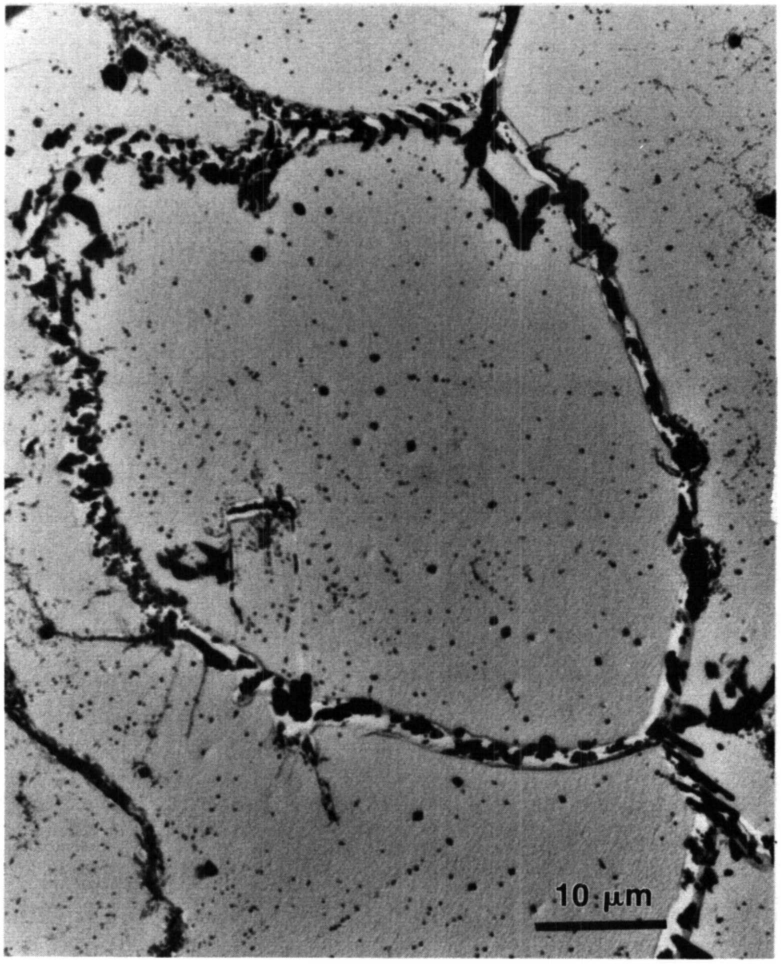

Fig. 4. Extraction replica of the annealed MnCrCTiVBP alloy after thermally aging 5000 h at 600°C.

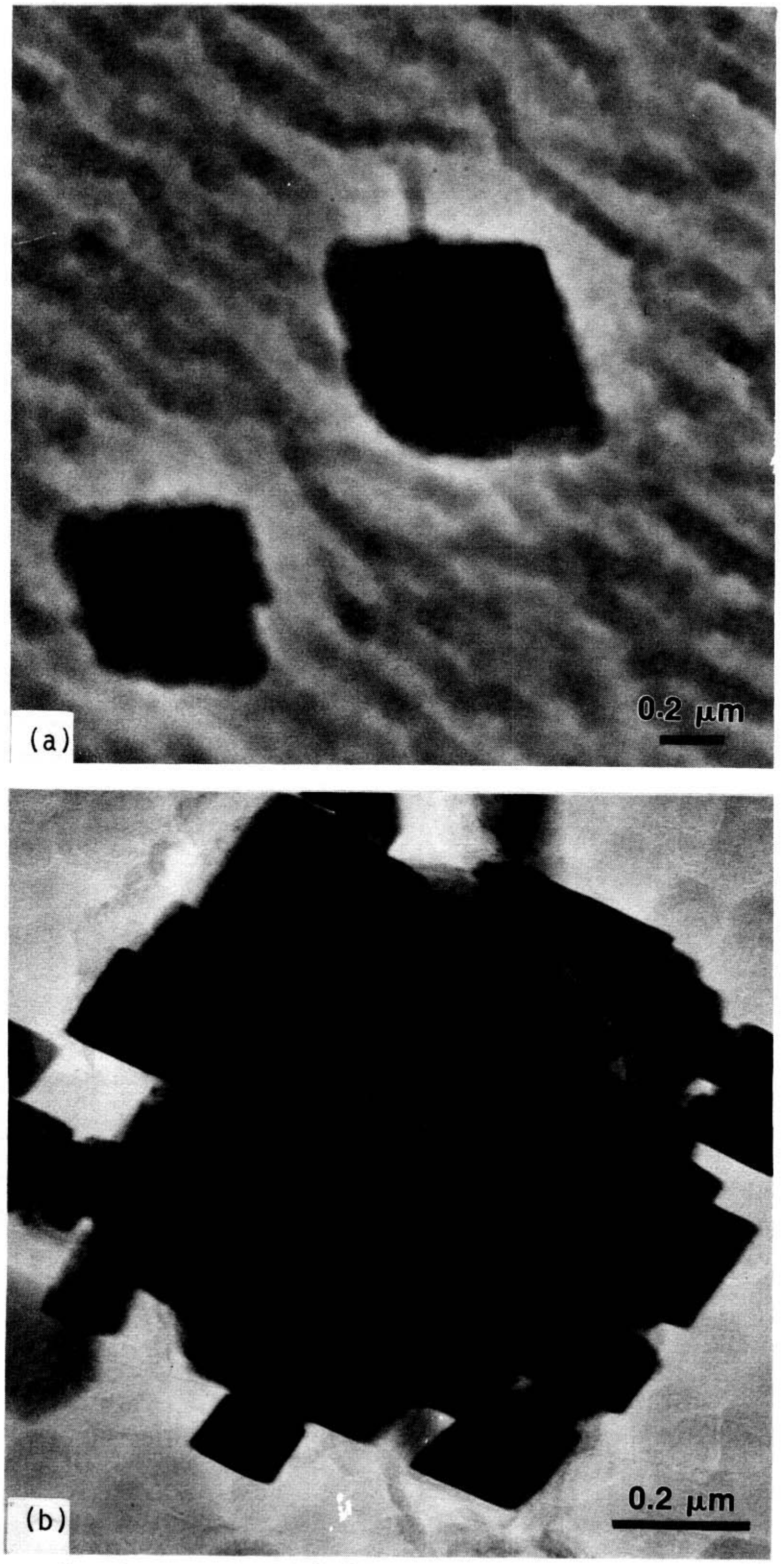

Fig. 5. Extraction replicas from annealed MnCrCTiVBP alloy after thermally aging 5000 h at 600°C. (a) $M_{23}C_6$ precipitate coating on a TiC particle, and (b) a coated particle surrounded by other $M_{23}C_6$ precipitate particles.

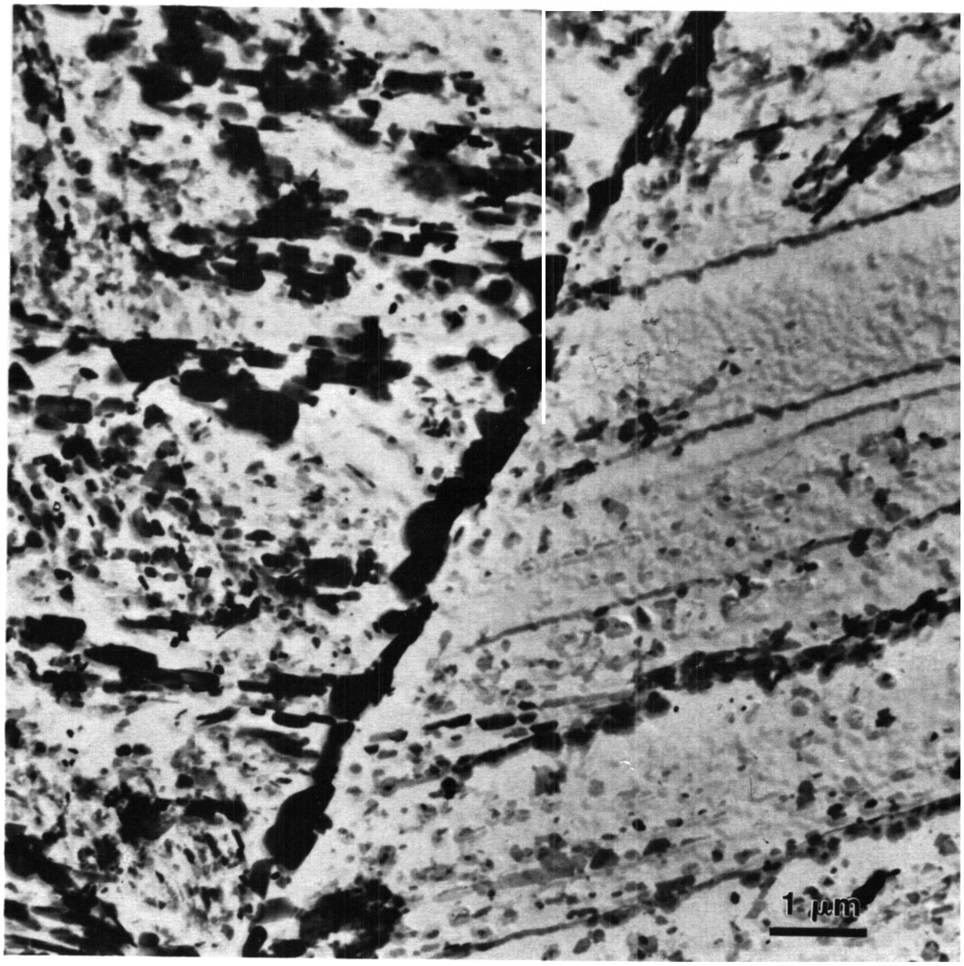

Fig. 6. Extraction replica of the cold-worked MnCrCTiVBP alloy after thermally aging 5000 h at 600°C

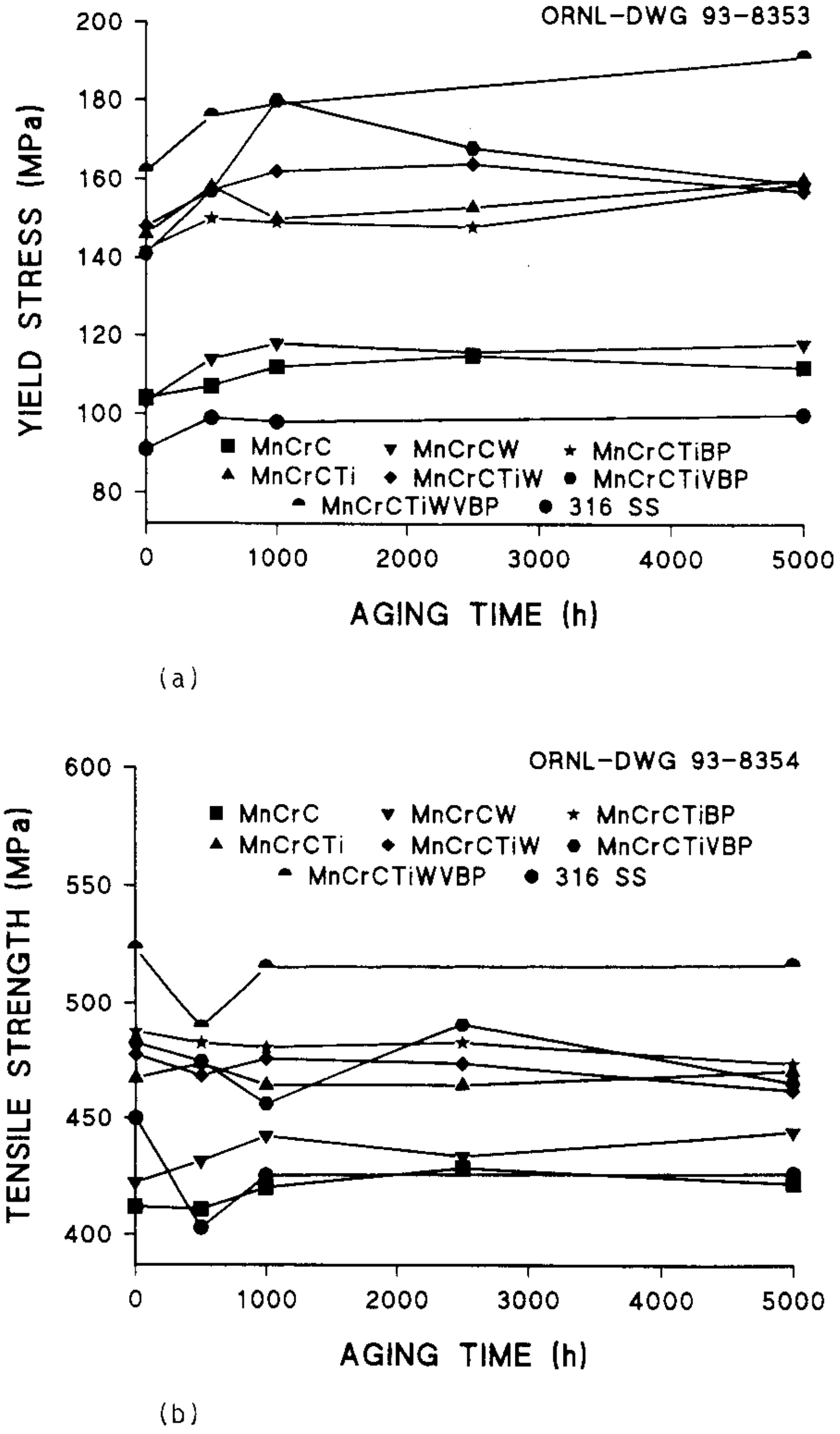

Fig. 7. (a) Yield stress and (b) ultimate tensile strength as a function of aging time for annealed high-manganese steels and type 316 stainless steel.

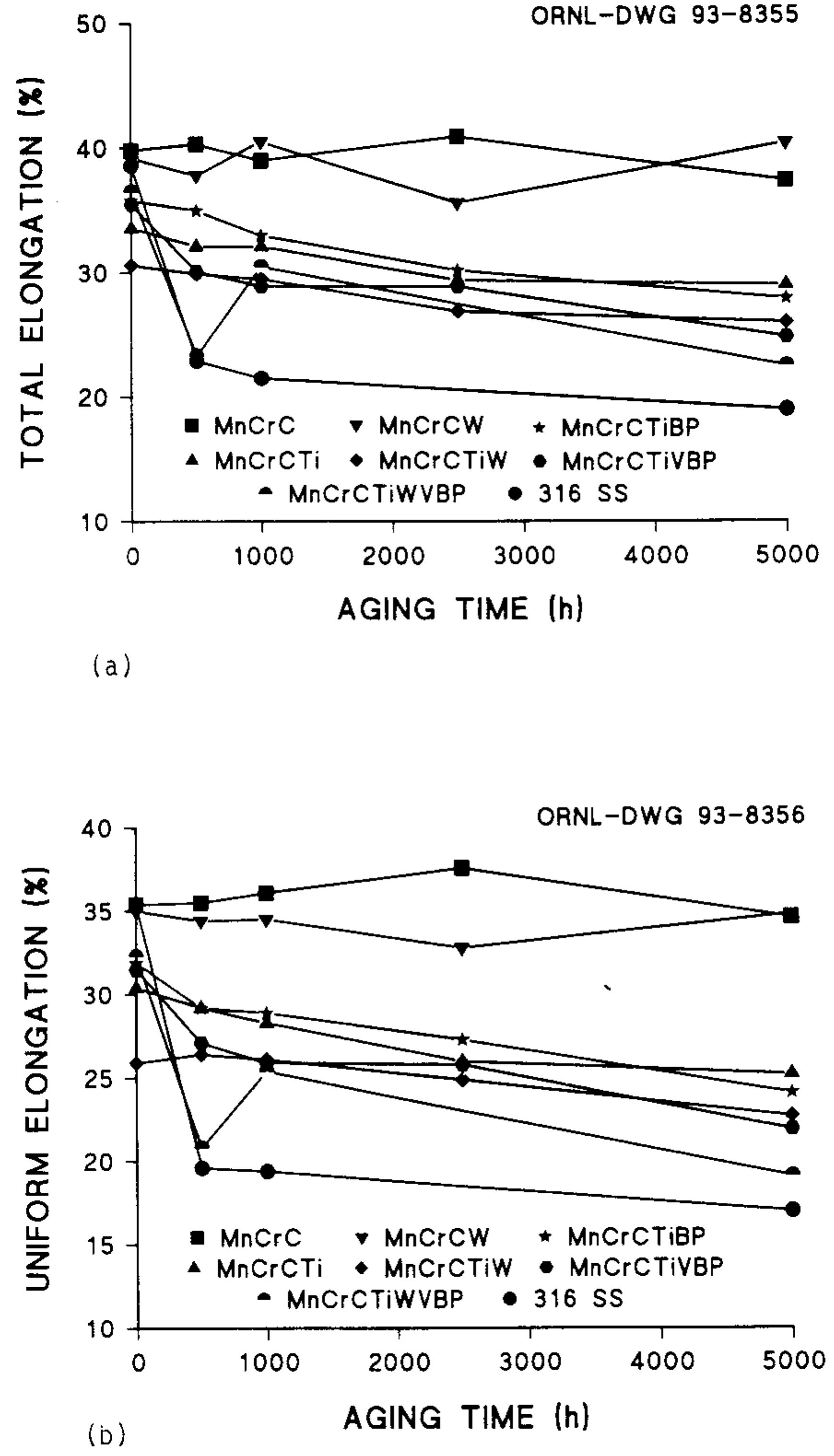

Fig. 8. (a) Total elongation and (b) uniform elongation as a function of aging time for annealed high-manganese steels and type 316 stainless steel.

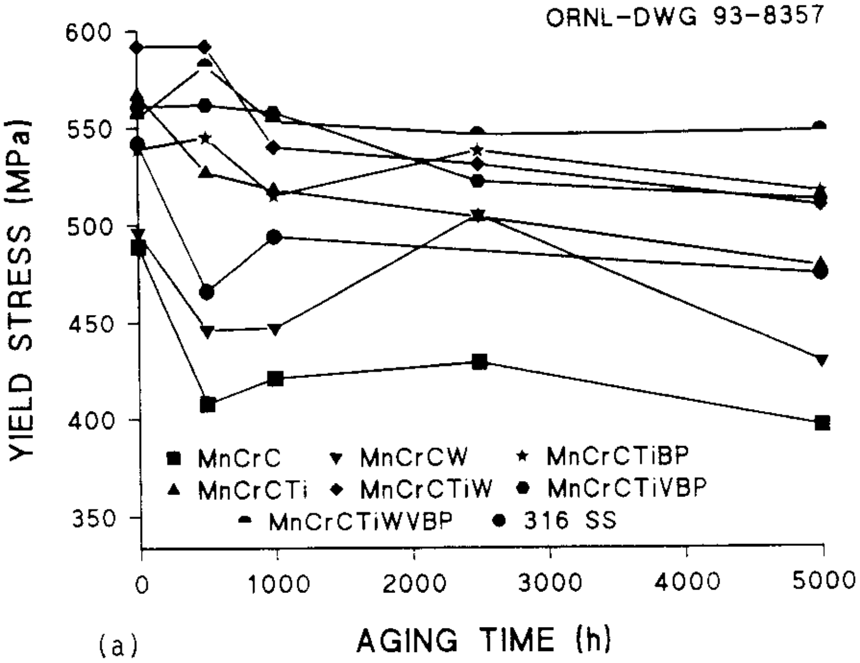

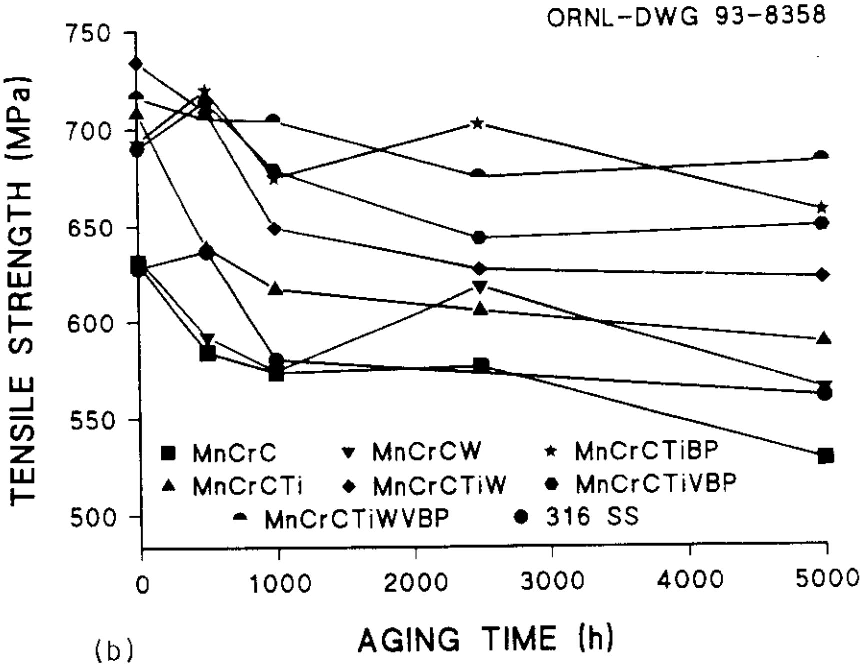

Fig. 9. (a) Yield stress and (b) ultimate tensile strength as a function of aging time for cold-worked high-manganese steels and type 316 stainless steel.

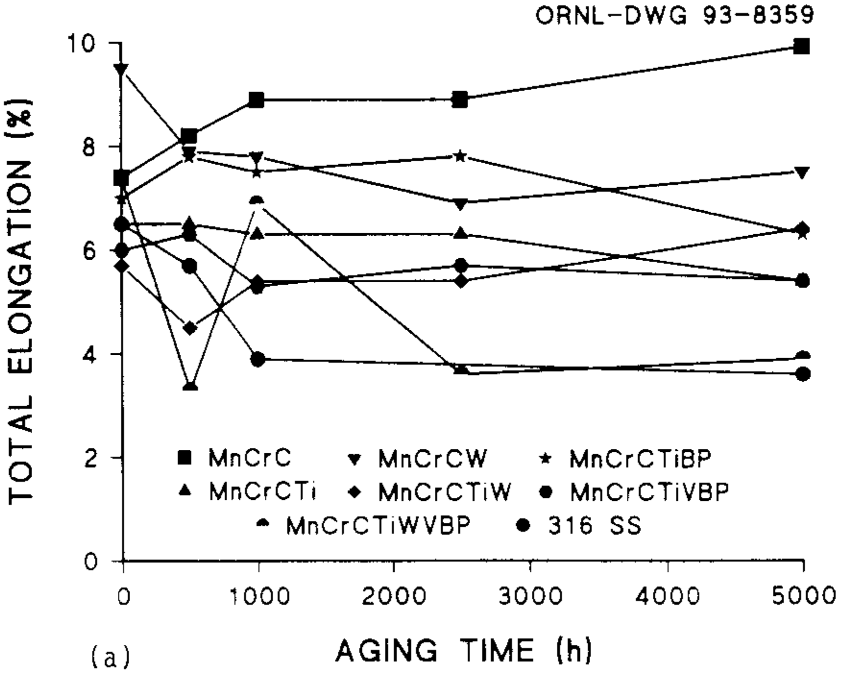

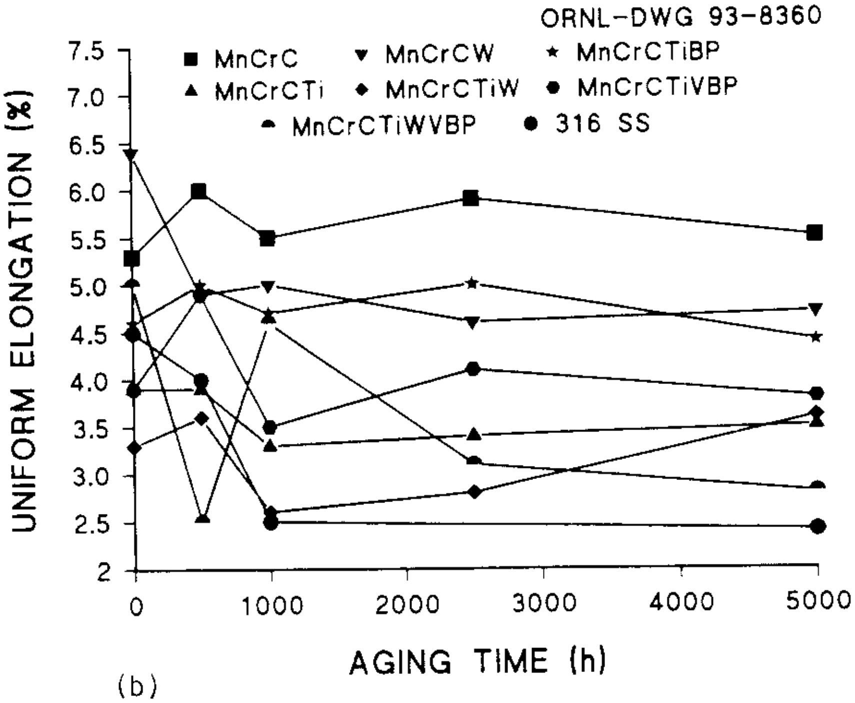

Fig. 10. (a) Total elongation and (b) uniform elongation as a function of aging time for cold-worked high-manganese steels and type 316 stainless steel.

selected elements, is the strongest alloy in the unaged condition and after aging 5000 h at 600°C. After the 5000 h age, this steel is substantially stronger than the other four titanium-containing steels, which have similar strengths.

Ultimate tensile strength behavior of the solution annealed steels was relatively similar to that for the yield stress [Fig. 6(b)], although it did not show the kind of strength increase observed for yield stress. In **most** cases, there was little change in strength between the annealed steel and the one aged 5000 h. The differences between the manganese steels and the 316 SS were also not as large as they were for the yield stress.

The ductility of the solution-annealed steels, as measured by uniform [Fig. 7(a)] and total [Fig. 7(b)] elongation, indicated that the strongest manganese steels had the lowest ductility in both the unaged and aged conditions. Relative trends in uniform and total elongation were similar. The MnCrCTiWVBP, which was the strongest high-manganese steel, had the lowest ductility, while the MnCrC and MnCrCW, the weakest of these steels, had the highest ductility. The ductilities of the other five high-manganese steels fell between those extremes, similar to the observations on the yield stress. However, the ductilities of all the manganese-stabilized steels exceeded that for 316 SS, even though the 316 SS was the weakest steel.

Thermal aging of the cold-worked steels to 5000 h caused a decrease in the yield stress [Fig. 8(a)] and ultimate tensile stress [Fig. 8(b)] of all steels. Steels without titanium were again the weakest, and in this condition were weaker than 316 SS. The other live high-manganese steels were stronger than the 116 SS. Although the MnCrCTiW steel was the strongest cold-worked steel in the unaged condition, the MnCrCTiWVBP was strongest after the *5000* h age, just as it was in the solution-annealed condition. The reason for this was that the MnCrCTiWVBP showed little strength decrease after SOW h at 600°C.

Total [Fig. 9(a)] and uniform [Fig. 9(b)] elongations of the cold-worked steels reflected the strength behavior, with the strongest steels having the lowest ductility and vice versa. The MnCrCTiWVBP steel had the lowest ductility of the manganese-stabilized steels alter the 5000 h age. However, the ductility was comparable to that **of** 316 SS, even though the 316 SS had a substantially lower strength.

The results indicate that the high-manganese steels are quite resistant to thermal aging at 600°C. This **is** especially true for the MnCrCTiWVBP in both the annealed and cold-worked condition.

SUMMARY AND CONCLUSIONS

Thermal aging studies were conducted on a series of experimental, high-manganese austenitic stainless steels. An Fe-20Mn-12Cr-0.25C base composition was used, to which various combinations of titanium, tungsten, vanadium, boron, and phosphorus were added for improved strength. Aging was **at** 600°C to 5000 h on the steels in the solution-annealed and 20% cold-worked conditions. Results were compared with type 316 SS.

The yield stress of all the high-manganese steels in the solution-annealed condition increased with thermal aging, and the strength of the steels before and after aging exceeded that for 116 SS. Despite the greater strength, the total elongation of the manganese steels also exceeded that for 316 SS. Cold-worked steels showed a decrease with aging time at 600°C. All but two of the experimental cold-worked steels had yield **stresses** that exceeded that for 316 SS. The ductility of all of the cold-worked high-manganese steels was as **good** or better than that for 316 SS.

In both the solution-annealed and cold-worked conditions, an Fe-20Mn-12Cr-0.25C-1W-0.03P-0.005B steel was most stable. It showed the most increase in strength in the solution-annealed condition and the smallest loss of strength in the cold-worked condition. The maintenance of strength was accompanied by excellent ductility.

REFERENCES

1. R. W. Conn et al., Panel Report on Low Activation Materials for Fusion Applications, UCLA Report PPG 728, University of California at Los Angeles, June 1983.
2. E. Ruedl, D. Rickerby, and T. Sasaki, Fusion Technology, Vol. 2, p. 1029, Pergamon Press, London, 1984.
3. E. Ruedl and T. Sasaki, Journal of Nuclear Materials, Vol. 122 & 123, 1984, pp. 794-798.
4. R. L. Klueh and E. E. Bloom, Optimizing Materials for Nuclear Applications, F. A. Garner, D. S. Gelles, and F. W. Wiffen, Eds., The Metallurgical Society, Inc., Warrendale, Pennsylvania, 1985, pp. 73-85.
5. H. R. Brager, F. A. Garner, D. S. Gelles, and M. L. Hamilton, Journal of Nuclear Materials, Vol 133 & 134, 1985, pp. 907-911.
6. A. H. Bott, F. B. Pickering, and G. I. Butterworth, Journal of Nuclear Materials, Vol. 141-143, 1986, pp. 1088-1096.
7. M. Tamura, H. Hayakawa, M. Tanimura, A. Hishinuma, and T. Kondo, Journal of Nuclear Materials, Vol. 141-143, 1986, pp. 1067-1073.
8. R. L. Klueh, P. J. Maziasz, and E. A. Lee, Mater. Sci. Eng., Vol. 102, pp. 115-124.
9. R. L. Klueh and P. J. Maziasz, Mater. Sci. Eng., vol. A127 (1990) pp. 17-11
10. E. A. Kenik, P. J. Maziasz, and R. L. Klueh, Proceedings of the 47th Annual Meeting of the Electron Microscopy Society of America, Ed., G. W. Bailey (San Francisco, 1989) pp. 284-285.

COMPARISON OF MICROSTRUCTURAL EVOLUTION IN REACTOR-IRRADIATED AUSTENITIC STAINLESS STEELS WITH AND WITHOUT SPECTRALLY TAILORING

-- S. Jitsukawa, T. Sawai, ti. Shiba. S. Hamada and A. Hishinurna (Japan Atomic Energy Research Institute)

OBJECTIVE

The objective of this work is to evaluate the microstructural data so far obtained through the US-Japan collaborative program using HFIR and OUR and examine the effect of spactrally tailoring conducted in ORU experiment by comparing the microstructural evolution in the same set of austenitic stainless steels irradiated in HFIR and ORR.

SUMMARY

The effects of Heidpa ratio on swelling behavior were examined on three austenitic stainless steels. Materials were solution-annealed JPCA and two low carbon containing alloys (C and K) modified with titanium and niobium. These steels were neutron-irradiated in ORR and HFIR with and without spectrally tailoring. respectively Achieved damage level was 7.4 dpa in ORR irradiation with average He/dpa of about 21 appmidpa. In case of HFIR irradiation, they were 33 dpa and 76 appm/dpa, respectively. Alloy to alloy variation and temperature dependence of swelling behavior are far more distinctively detected in ORR irradiation than in HFIR irradiation. in spite of the lower damage level of ORR irradiation. In the case of ORR-irradiation. JPCA exhihited small swelling values of <0.01 and 0.03 % at 603 and 673 K, respectively, while a low carbon alloy K showed relatively larger swelling; 0.2 % at 603 K and 0.6 % at 673 K. Swelling of JPCA and K irradiated in HFIR were almost same values of 0.2 % at temperatures of 573 and 673 K. Number densities of cavities in HFIR-irradiated alloys were larger than those observed in ORR by one lo two orders. On the other hand, number densities and sizes of dislocation loops produced by ORR irradiation were two to five times as large as those by HFIR irradiation. These facts suggest that in ORR condition with closer He/dpa to that of fusion. mutual annihilation rate of point defects was reduced and then bias driven cavity growth might he enhanced compared with HFIR condition.

PROGRESS AND STATUS

1. Introduction

Materials for the first wall of blanket structures of a fusion reactor will be exposed to high-energy fusion neutrons with 14 MeV peak. Main damages induced in materials irradiated by the fusion neutrons, consist of displacement damage and generation of transmutans. To evaluate the irradiation effects of fusion neutrons on material behavior. fission reactors have been often used, because we have no high energy neutron sources for irradiation experiments. However, there are big differences between fusion and fission neutron damages in terms of primary knock-on energies and gaseous and solid transmutants by transmutation reactions that strongly depend on neutron energy. Among such differences, the ratio of He in appm and displacement damage production rates (He/dpa ratio) has been demonstrated to affect strongly the microstructural evolution in austenitic alloys and then it has been considered as the most important factor for evaluating the differences[1].

For evaluation of the He/dpa effects on fusion materials, a spectrally tailored irradiation in the *Oak* Ridge Research Reactor (ORR) by the U.S.-Japan Collaborative Experiment on Fusion Materials was planned and has been conducted to accomplish typical He/dpa ratio of fusion neutron environment for austenitic alloys[2]. This study is a continuation of the previous ORR works[3,4] and to understand the the effects **of** He/dpa ratio on microstructural development including the compositional effects, three kinds of austenitic steels were irradiated by spectrally tailored ORR capsules and discussed compared with the results by irradiated in the High **Flux** Isotope Reactor (HFIR) producing larger amount of He.

2. Experimental procedure

Specimens used were Japanese Prime Candidate Alloy (JPCA), a titanium and niobium modified low-carbon alloy (K alloy) and a titanium -modified low-carbon alloy (C alloy) in solution annealed condition. Nominal chemical compositions of alloys are shown in table 1. Transmission electron microscope (TEM) specimens of those were irradiated in the ORR-MFE-7J capsule at temperatures of 603 and 673 K with **fluxes** of approximately 2×10^{18} n/m^2s for both thermal and fast (E > 0.1 MeV) neutrons to a damage level of 7.4 dpa with a He concentration of about 155 appm (for JPCA)[5] and JPCA and K were irradiated in HFIR target capsules with fluxes of $1.4\times10^{19} n/m^2s$ of fast and 2.8×10^{19} n/m^2s of thermal to a damage level of 33 dpa with He concentration *of* about 2500 appm[6]. After the irradiation. specimens were perforated in a Tenupol twin jet electro-polishing unit for transmission electron microscopy. A JEM-2000FX TEM operated at 200 keV was used for microstruclural observation at the areas with thickness of ranging from 100 to 200 nm. Foil thickness was evaluated by improved contamination spot separation (CSS) method [7,8] for ORR data. *Some* of the HFJR data already published [6,9], where CSS error lead to overestimation of thickness and. therefore. underestimation of volume concentration of microstructural features. were up-dated. Detailed experimental procedure are shown elsewhere[6,8].

Table 1 Chemical compositions of used materials

	C	Si	Mn	P	S	Ni	Cr	Mo	Nb	Ti	B	N
JPCA	0.06	*0.50*	1.77	0.027	0.005	15.6	14.2	2.3	–	0.24	.0031	.0039
C	0.02	0.51	1.56	0.017	0.007	15.6	15.4	2.4	0.08	0.25	–	.0018
K	0.02	0.48	1.46	0.015	0.005	17.6	18.0	2.6	–	0.29	–	.004

3. Results

Microstructure of JPCA, K and C alloys irradiated in a spectrally tailored MFE-7J capsule of the ORR. and those of JPCA and K alloy irradiated in the JP-1 and 3 capsules of the HFIR are shown in Fig. 1. Cavities formed by HFIR irradiation were finer than those produced during ORR irradiation.

Figurer 2 (a) to (c) show cavity microstructural components in alloys irradiated in ORR at 603 and 673 K and irradiated in HFIR at 573 and 673 K. Average cavity diameters (d_c) were about 6 nm for K and C alloys ORR-irradiated at 603 and 673 K. The values were greater than that of JPCA irradiated in the ORR, and also of JPCA and K alloy irradiated in HFIR. Average cavity diameter of *3.5* nm formed during HFIK irradiation were almost constant for both JPCA and K alloy at temperatures of 573 and 673 K. It should be noted that the average cavity diameter is usually affected by tiny but many bubbles and that the difference of bias-driven voids growth would be much more than the difference of average cavity size. The ratio of d_c at lower and higher irradiation temperatures was highest in ORR-irradiated JPCA than other materials or irradiation conditions.

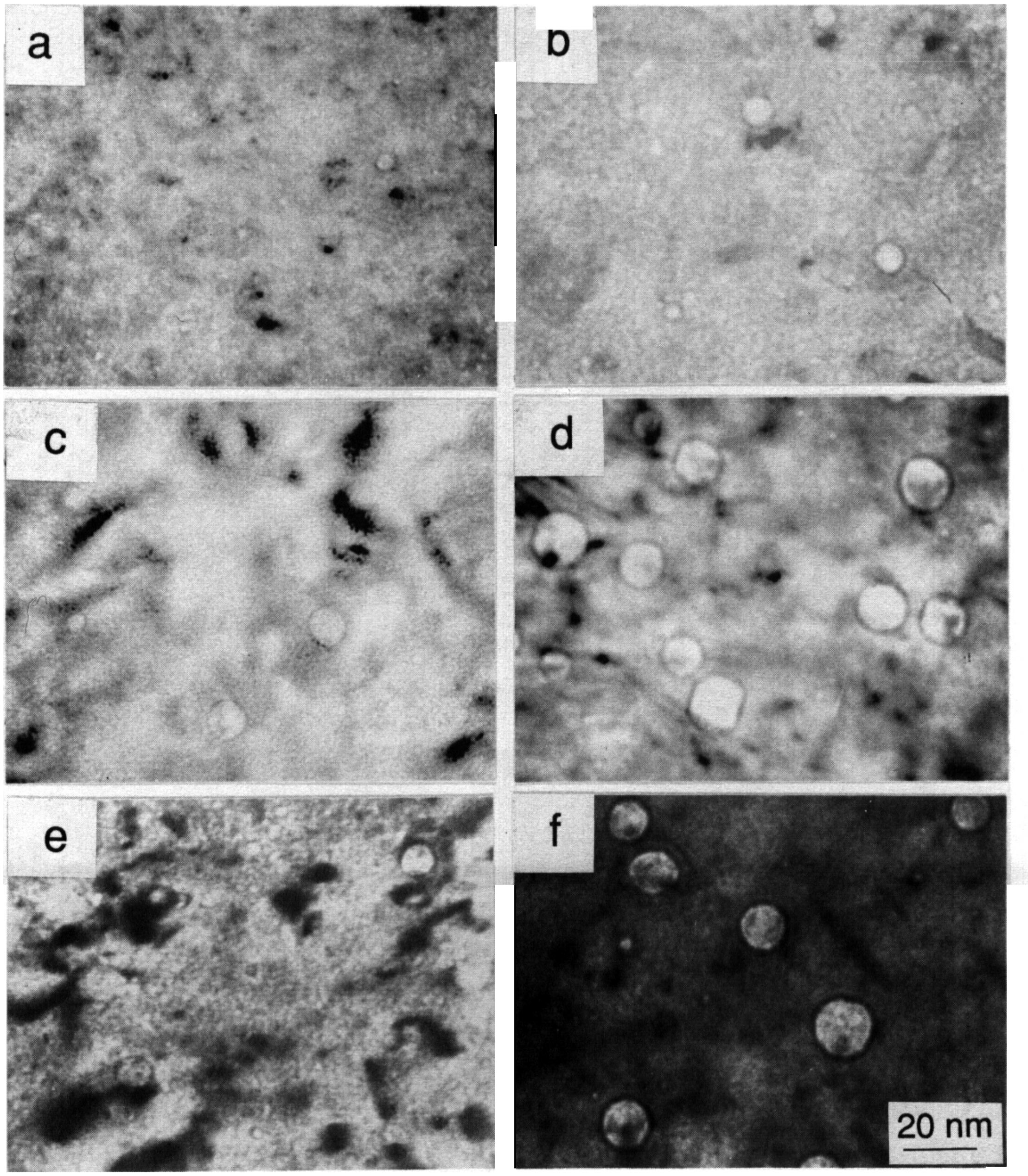

Fig. 1 Microstructure of ORR-irradiated JPCA(a, b), K(c, d) C(e,f) alloys and HFIR-irradiated JPCA(g,h), K(i,j) alloys. Irradiation temperature are 603K for a, c, e, 673K for b, d, f, h, j and 573K for g,i.

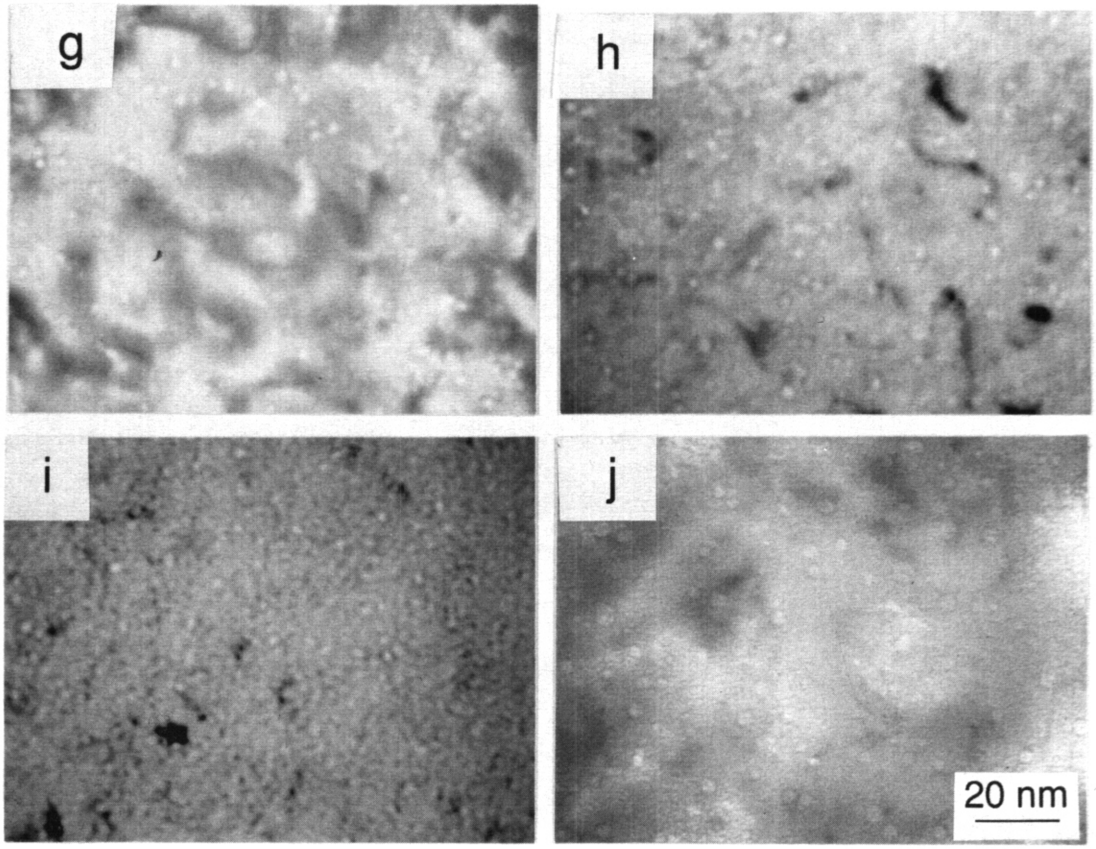

Fig. 1 (continued)

Number densities of cavities (N_c) in the alloys irradiated in the HFIR were one to two orders higher than those produced by ORR irradiation. In ORR, JPCA exhibited higher N_c value of $4x10^{22}/ m^3$ at a lower temperature of 603 K compared with other alloys. At high temperature 673K, however, the values were of about $1x10^{22}/m^3$ for all the alloys. On the other hand, HFIR irradiated JPCA and K alloy showed almost same N_c of $4x10^{23}/m^3$ at 573 K, and also same N_c of $2x10^{23}/m^3$ for both alloys at 673 K. Marked difference in N_c between both alloys was only observed in ORR irradiation at lower temperature 603 K.

Swelling for ORR irradiated K and C alloys were relatively large at higher temperature 673K. K alloy exhibited swelling value of 0.7 % at temperatures of 673 K while JPCA exhibited much smaller values (<0.04%). HFIR irradiation caused almost constant swelling of about 0.2% for both JPCA and K alloy at 573 K. At higher temperature, swelling shows slight increase for K alloy and effectively no change for JPCA. Temperature dependence and alloy to alloy variations of swelling were larger for ORR irradiated specimens.

Figures 2 (d) and (*e*)show average diameters (D_l) and number densities (N_l) of dislocation loops. Both D_l and N_l of ORR irradiated JPCA, K and C alloys tended to be larger than those of HFIR irradiated JPCA. Line dislocations were merely observed in these specimens. Microstructural parameters for precipitates were not quantitatively analyzed yet, however MC precipitations were observed for all the specimens examined. MC precipitates formed during irradiation in K and C alloys were rather coarser than those in JPCA after irradiation in the ORR.

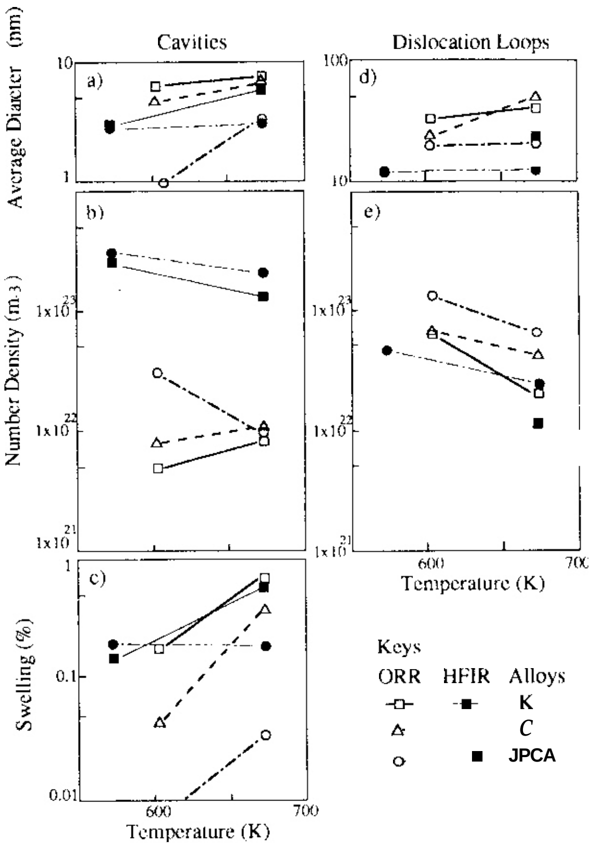

Fig.2 Microstructural data of cavities (a,b and c) and dislocation loops (d and e) in ORR- and HFIR irradiated JPCA, K and C alloys.

4. Discussion

4.1. Effect of He/dpa on microstructural evolution

Number densities of cavities found in ORR irradiated alloys were smaller than those by HFIR irradiation one to two order. On the other hand, number density of loops in ORR irradiated JPCA was five to ten times larger than that formed during irradiation in the HFIR. Displacement damage level of 7.4 dpa by the ORR was about one fourth of that produced by the HFIR. Both N_c and N_l are reported to Saturate with dose up to about 10 dpa at temperatures 673 K or below during EBR-II[10] and HFIR[11] irradiations producing lower and higher He levels comparing with levels by ORR spectrally tailored irradiation at a damage level of 1.4 dpa in the alloys. Therefore, it seems unlikely that the differences in number densities resulted from smaller damage level by the ORR.

Irradiation by HFIR producing higher levels of He formed cavities with much larger number density. Larger cavity number density is thought to increase mutual recombination of radiation produced vacancies and interstitials at cavity surfaces, and reduce point defect fluxes to dislocations[12]. This leads to reduce **excess** vacancy concentration which resulted from dislocation bias for interstitials, and retards bias-driven cavity growth. Sink strength of cavities and dislocation loops for vacancies are calculated using equations,

$$S_l = 2\pi\rho_d/\ln((2\rho_d)^{-1/2}/4b), \quad \text{and} \qquad (1)$$

$$S_c = 2\pi d_c N_c (1+(S_c+S_l)^{1/2} d_c/2), \qquad (2)$$

where these equations, S_l and S_c are sink strengths of loops and cavities: ρ_d and b are dislocation density (=$\pi D_l N_l$) and Burgers vector of dislocation. Because more than half population of dislocation loops were faulted loops, b was chosen to he Burgers vector of Frank loop. Bias factor of dislocation loops for interstitials only slightly affects sink strengths (less than about 10 %), therefore only S_c and S_l for vacancies were calculated. Calculation was carried out using microstructural data given in Fig. 2. Estimated partitioning of radiation induced point defects between dislocation loops and cavities at 673 K are shown in Fig. 3. Sink strength of precipitates and grain boundaries were also calculated. however the values were negligibly small: smaller by one to two order than S_l and S_c. Figure 3 shows that dislocation is the main sink in ORR irradiation for both JPCA and K alloys. while cavity component become larger than dislocation component in HFIR irradiation for both alloys. Cavity component would he still larger in case of HFIR irradiation if tiny bubbles under TEM resolution are considered. Difference of dislocation sink strength between JPCA and K in ORR irradiation can be attributed to the difference of their swelling resistance, or suppression of loop growth by MC precipitate was more successful in JPCA than K[13]. On the ther hand, suppression of loop growth by tiny hut many bubbles is equally dominant in HFIR irradiation for both alloys and thus slight difference of dislocation sink strength between hoth alloys is resulted. These suggest that bias-driven cavity growth was suppressed by stronger cavity sink strength during irradiation in the HFIR, while dislocation loops acted as a major sink producing excess vacancies caused by bias for interstitials. This also agrees the result that d_ls in OKR irradiated alloys were larger than those in HFIR inadiated alloys

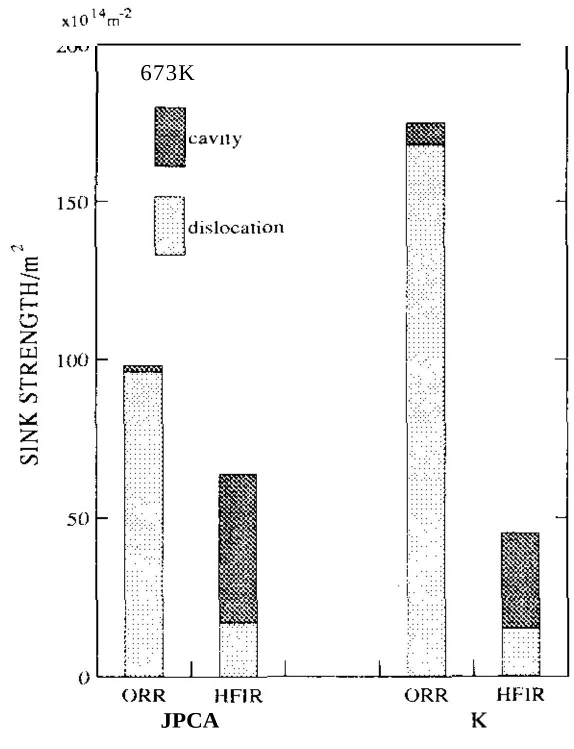

Fig. 3 Comparison of cavity and dislocation sink strength in HFIR- or ORR-irradiated JPCA and K alloy.

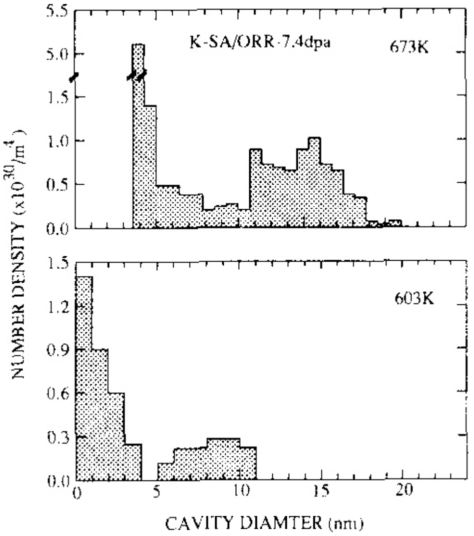

Fig. 4 Cavity size distribution in K alloy irradiated in ORR at 603K and 673K.

Bimodal cavity size distribution shown in Fig. 4(a) indicates that bias-driven cavity growth (BDG) occurred in K alloy during ORR irradiation at 673 K. Cavity size distribution even a low temperature of *603* K (Fig. 4(b)) is rather wide, and this may indicate BDG mechanism operated during irradiation[14,15]. On the other hand, cavities in HFlR irradiated K alloy to **33** dpa were reported to he equilibrium bubbles; bimodal size distributions were observed in K alloy and JPCA only at 773 and 873 K. These facts may indicate that spectrally tailored irradiation in the ORR extended temperature regime of BDG to lower temperatures comparing with irradiation in the HFIR.

4.2. Alloy dependence of swelling by irradiation in the ORK

It has been indicated in many researches that MC precipitation during irradiation is effective to suppress swelling in titanium (Ti) and niobium (Nb) containing austenitic steels[16,17,18]. Swelling values of two low carbon alloys (K and C alloys) by irradiation in the ORR were much larger than that found in JPCA. JPCA containing larger amount of carbon should have higher tendency of MC forming during irradiation; finer but smaller total volume of MC were observed in JPCA comparing with MC in K and C alloys after irradiation at 673 K. It has been reported that MC in HFIR and He-ion irradiated austenitic alloys suppressed cavity migration to retard cavity coalescence and reduced swelling[19.201. If the MC effects for swelling supression were mainly preventing the cavity coalescence , this mechanism would he more eff'ective in HFlR irradiation where higher number density of caivies were formed. The fact that alloy dependence of swelling was large for ORR inadiation than for HFIR irrddialion suggests MC precipitations and alloying elements (Ti, Nb and C) might reduce dislocation bias and point defect migration to enhance mutual annihilation.

5. Conclusions

1. Swelling in ORR irradiated two low C alloys were much larger than those found in JPCA and HFlR irradiated JPCA and low C alloy.
2. ORR irradiation exhibited larger alloy dependence of swelling comparing with HFIR irradiation.
3. Number density of cavities in ORR irradiated alloys were smaller than those in HFIR irradiated same alloys by one to two order.
4. Calculations of sink strengths revealed that fraction of radiation induced point defects absorbed by dislocations (mostly, dislocation **loops)** was larger during ORR spectrally tailored irradiation comparing with HFIR irradiation.
5. MC precipitations and alloying elements might reduce dislocation bias and point defect migration to suppress swelling during ORR spectrally tailored irradiation by enhancing mutual annihilation of radiation induced point defects.

REFERENCES

[1] R. E. Stoller, P. J. Maziasz, A. F. Rowcliffe and M. P. Tanaka, J. Nucl. Mater. 155-157(1988)1328.

[2] J. L. Scott, L. K. Mansur, M. L. Grossbeck, E. H. Lee, K. Farrell, L. L. Horton, **A.** F. Rowcliffe and M. P. Tanaka, "DESCRIPTION OF THE U.S./JAPAN SPECTRAL TAILORING EXPERIMENT IN ORR," p.12 in ADIP Semiannu. Prog. Reo., Mar. 31, 1985, DOE/ER-ER0045/14, U.S. DOE, Office of Fusion Energy.

[3] T. Sawai , P. J. Maziasz, and **A.** Hishinuma, J. Nucl. Mater. 179-181(1991)519.

[4] T. Sawai, P. J. Maziarz. H. Kanazaswa and A. Hishinuma. J. Nucl. Mater. 191-194(1992) p.712

[5] L. R. Greenwood, "NEUTRON DOSIMETRY AND DAMAGE CALCULATIONS FOR THE ORR-MFE 7J EXPERIMENT," p.23 in FRM Semiannu. Proe. Rep., Mar. 31, 1989, DOE/ER-

0313/6, USDOE, Office of Fusion Energy.

[6] M. P. Tanaka, P. J. Maziasz, A. Hishinuma and S. Hamada, J. Nucl. Mater. 141-143(1986) 943.

[7] T. Sawai and M. Suzuki, Script. Met. 24(1990)2047.

[8] T. Sawai. M. Suzuki, P. J. Maziasz and A. Hishinuma, J. Nucl. Mater. 187(1992)146.

[9] M. P. Tanaka, S. Hamada, A. Hishinuma and P. J. Maziasz. J. Nucl. Mater. 155-157(1988) p.801.

[10] H. R. Brager and J. L. Straalsund, J. Nucl. Mater. 46(1973)p.134

[11] P. J. Maziasz, "Effects of Helium Content on Microstructural Development in Type 316 Stainless Steel Under Neutron Irradiation," ORNL-6121, ORNL.

[12] R. E. Stoller and G. R. Odette, "The Effect of Helium on Swelling in Stainless Steel: Influence of Cavity Density and Morphology," p.275 in Effect of Radiation on Materials: 11th Conf., ASTM STP 782, ed., H. R. Brager and J. S. Perrin, American Society for Testing Materials, Philadelphia. 1982.

[13] S. Jitsukawa, to be published.

[14] A. Hishinuma and L. K. Mansur, J. Nucl. Mater. 118(1983)91

[15] L. K. Mansur, E. H. Lee, P. J. Maziasz and A. F. Rowcliffe, J. Nucl. Mater. 141-143(1986)633.

[16] M. J. Makin, J. Nucl. Mater. 107(1982)133.

[17] T. M. Williams, J. M. Titchmarch and D. R. Arkell, J. Nucl. Mater. 107(1982)222.

[18] A. F. Rowcliffe, G. J. C. Carpenter. H. E Merrick and R. B. Nicholson, "An Electron Microscope Investigation of High-Temperature Embrittlenient of Irradiated Stainless Steel," p.161, in The Effects of Radiation on Structural Metals: ASTM STP 426, American Society for Testing Materials, Philadelphia. 1967.

[19] P. J. Maziasz. pp.477 in Phase Stability During Irradiation, TMS-AIME. The Metallurgical Society of AIME. New York. 1981.

[20] S. Jitsukawa. K. Hojo and A. Hishinuma, J. Nucl. Mater. 179-181(1991)538.

MICROSTRUCTURES OF A WELDED JOINT USING AN IRRADIATED WRAPPER TUBE–

S. Hamada, K. Watanabe, A. Hishinuma, I. Takabashi and T. Kikuchi (Japan Atomic Energy Research Institute)

OBJECTIVE

The objective of this work is to clarify the effect of the helium bubbles evolution on the fracture mechanism in welded joints using an irradiated wrapper tube.

SUMMARY

The behavior of helium in welded joint fabricated using tungsten inert gas (TIG) welding process for a type 316 stainless steel wrapper tube irradiated in a fast reactor was investigated. The wrapper tube was irradiated to $(1.5 - 4.2) \times 10^{26}$ n/m^2 (helium level of 3 to 9 appm) at 395 - 410°C. All welded joints fractured in the heat-affected zone (HAZ). The microstructures of each portion of the base metal. the HAZ and the fusion zone in a welded joint were examined through a transmission electron microscope. Small helium bubbles were observed in number density of 2×10^{20} m^{-3} in the matrix and rarely found on the grain boundaries of the base metal. In the HAZ, small and large helium bubbles mixed and lined up along the grain boundaries. In particular, some of them elongated along the grain boundary. In the matrix of the fusion zone, delta-ferrite phases and unresolved carbides were scattered. Large cavities were attached to these precipitates and also occurred along grain boundaries. These results suggest that the failure in the HAZ of welded joints is attributed to the preferential growth and coalescence of helium bubbles in the grain boundaries of the HAZ caused by weld heat input and stress during welding.

PROGRESS AND STATUS

Introduction

The reactor components, such as the reactor vessel and interiors of fission reactors and the fust wall and blanket structures in fusion reactors, are exposed to the severe environment of displacement damage and helium produced by nuclear transmutation reactions with energetic neutrons. The long term exposure of materials under such environments will gradually deteriorate their mechanical properties and corrosion resistance, which play a decisive role in the life time of components of nuclear reactors. The repair and replacement of some pans of degraded reactor components will therefore eventually be required. Such repair will require the use of conventional welding techniques. Neutron irradiated steels contain entrapped helium, which forms bubbles at elevated temperatures. Helium bubbles grow and coalesce rapidly along grain boundaries under tensile stresses[1-4], which weaken the grain boundaries. This situation is typically found in welding processes which produce both internal stress and elevated temperature.

In order to simulate this situation. tungsten inert gas (TIG) welding has been performed for type 316 stainless steel contained helium using tritium doping and decay[5-8]. The heliumdoped materials containing levels greater than 2.5 appm induced intergranular cracking in the HAZs during welding[5-7]. Helium introduced through this method tends to precipitate preferentially to form helium bubbles on grain boundaries before welding. In this study. it was tried to evaluate helium effects on the fusion welding using neutron irradiated stainless steel instead of helium-doped materials.

Experimental Procedure

The material employed in this study was 10% cold worked type 316 stainless steel. which was used as a wrapper tube with 1.9 mm in thickness in the MK-I core of the JOYO fast breeder reactor of Power Reactor and Nuclear Fuel development corporation in Japan. the chemical composition of this alloy is shown in

Table 1. The wrapper tube was irradiated to a fluence of 1.5 - 4.2 x 10^{26} n/m^2 (helium level of 3-9 appm) in the temperature range of 395 - 410°C. Rectangular sheets 70 mm long and 40 mm wide were cut out of each of the faces of the hexagonal wrapper tube following irradiation.

Table 1. Chemical Composition used in the Present Experiment (wt %).

C	Si	Mn	P	S	Ni	Cr	Mo	Co	B	N	Al	As	Cu	Nb+Ta	V
0.05	0.48	1.72	0.024	0.006	13.60	16.80	2.18	0.31	0.0001	0.0254	0.0100	0.0040	0.2500	0.0040	0.0037

Butt-joint welds with full penetration were made using the single path Tungsten Inert Gas (TIG) welding process at 12 V-ac, 25A at a travel speed of 3.6 mm/s. During welding, filler wire was automatically supplied. Welding for an unirradiated wrapper tube also was performed under similar conditions as an irradiated wrapper tube. After welding, grinding of the portion of convex bead was made by a grinder wheel. A sheet of 30 mm x 20 mm including a bead in the middle portion was cut from a rectangular sheet described above. The 5 mm square sheets for transmission electron microscope (TEM) were cut from each location corresponding to HAZ, fusion zone and base metal in the sheet of 30 mm x 20 mm as shown in Fig. 1. Subsequently these were thinned from 1.9 mm to 0.2 mm thick by mechanical polishing with emery papers. The discs were manufactured to about 3 mm in diameter by cutting the corners of 5 mm square sheets with a nipper. Samples were subsequently electropolished to perforation in a Struers Tenupol twin jet using a 5% perchloric acid ($HC1O_4$) and 95% acetic acid (CH_3COOH) electrolyte at 15°C using 150 mA and 70V- dc. The polishing tasks for TEM discs were performed in a glove box. Thin foils were examined using H800 TEM operated at 200 kV.

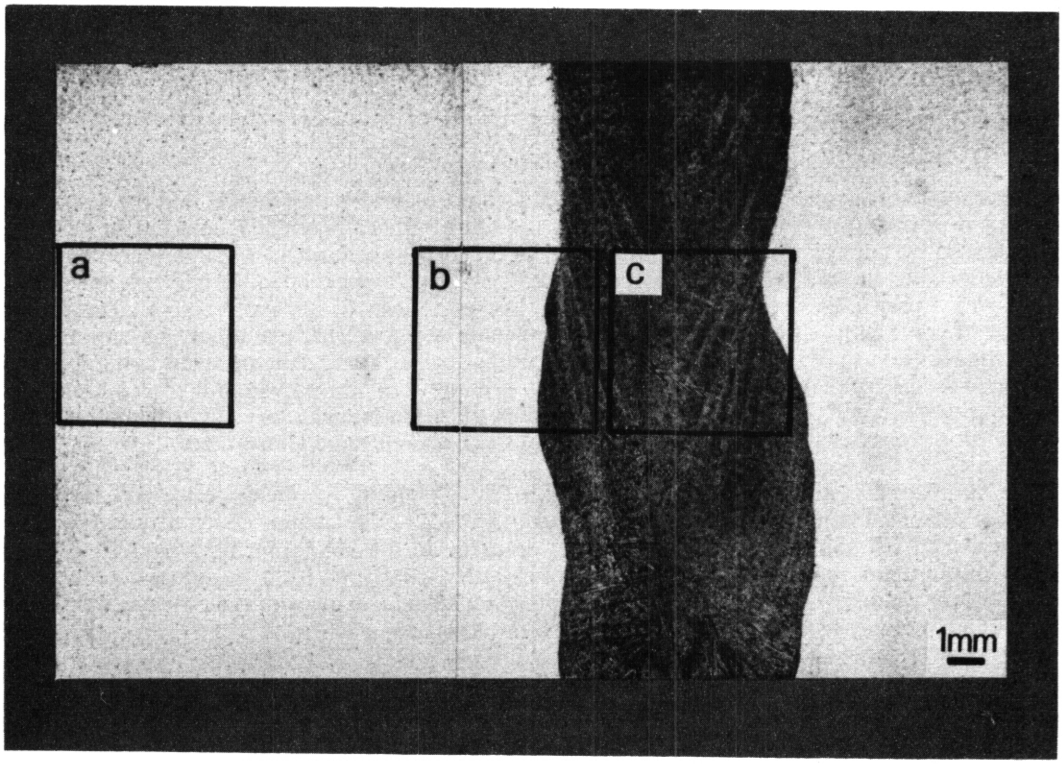

Fig. 1. Micrograph of a TIG welded joint and areas cut from it for TEM samples: (a) base metal; (b) heat-affected zone and (c) fusion zone.

Results

No cracks were found in **the** fusion zone and the HAZ of as-welded joints. Tensile tests for **base** metals and welded joints of **both** un- and irradiated materials were carried out at room **temperature,** 400, 500, and 600°C. Figure **2** shows **the** location of fractures. All irradiated welded joints **fractured** in the fusion zone, while ones fractured in the HAZ of each tensile test temperature. The failure position was adjacent to the fusion line. Figure 3 shows an optical micrograph at high magnification of the fractures portion on the HAZ of a sample tensile-tested at 500°C. Many intergranular cracks occurred in the HAZ. They were often found to be located **on** the grain boundaries parallel to an applied stress. There were no cracks **in** the fusion zone.

Figure **4** shows **microstructures of the base** metal in a welded joint. Small helium bubbles were uniformly **scattered in density of 2×10^{20} m^{-3} in** a **matrix.** The size distribution of helium bubbles was a relatively narrow range of 3 to 15 nm diameter. **The** average diameter of them was about 8 nm. A few small helium bubbles also were sometimes found ***on*** the **grain** boundaries. **Furthermore,** dislocation loops in **the** range of 10 - 100 nm in diameter were observed in density of 3.3×10^{21} m^{-3}. Helium bubble evolution between the base metal and the HAZ indicated a big difference. Figure ***5*** shows microstructures found in the HAZ. Helium bubbles in the HAZ were greater than those **in** the base metal **as** a whole. Helium bubbles of 10 to 70 nm diameter slightly un-uniformly distributed in the matrix. that is, most of them attached on dislocation lines and/or at the adjacency of dislocation lines, which **has** grown from dislocation loops **as** seen in the matrix of the base metal (Fig. 5a). In the **grain** boundaries, small (several tens nm) and large (100 - **400nm)** helium bubbles mixed and lined up along the **grain** boundaries (Fig. 5b). Some of them elongated along a **grain boundary** and a typical example is shown in Fig. 5c. The maximum size of elongated helium bubbles observed in this experiment was about 600 nm. High heat input through only a single pass in welding may not produce such big elongated helium bubbles on a grain boundary. The effect of **stress** including compression and tensile in addition to the thermal effect may enhance the formation of elongated helium bubbles. Dislocation network, developed from dislocation loops subjected to heat input in welding. No dislocation loops were found in the matrix of the HAZ ***at*** a distance of 1 mm from the fusion line (Fig. 5d).

Delta-ferrite phases of several microns, unresolved carbides (200-300 nm diameter) were scattered in a matrix of the fusion zone. The huge cavities attached to delta-ferrite phases and unresolved carbides **(Fig.** 6a) **are** penetration holes formed at the position of each initial helium bubble during electro-polishing. The sizes of initial helium bubbles presented in the fusion zone would be smaller **than** those of holes observed after electro-polishing. A fairly high density of dislocation network induced during cooling process after fusion was observed in the matrix. Hugh holes **as** described above were also found on the grain boundaries **as** shown in Fig. 6b.

Discussion

The optical **micrographs** shown in **Fig.** 3 **reveal** intergranular failure of **the** HAZ only in welded joints of an irradiated wrapper tube. In order to understand the mechanism of **fracture.** in the HAZ, it is important **to** know **the** behavior of helium bubbles **in the grain boundaries an**d their effect on the strength of grain **boundaries.**

Two main **factors are** considered to influence **the** behavior of helium bubbles: **one** is temperature through weld heat input, the other is thermal **stress** induced during welding. The temperature of the position of a TEM disc cut from the HAZ for TEM observation was evaluated by calculation. Figure **7** shows the temperature profile **as** a function of a distance from the fusion line in **the** HAZ of type **316** stainless **steel** measured and calculated by Lin[7]. His data was available to the present study **because** of similar welding conditions and materials. The data suggest the temperature of the position of the observed HAZ to be about 1100°C. Such elevated temperature promotes the growth and coalescence of helium bubbles in the grain **boundaries.** The temperature. therefore, of the failure position in the HAZ (a distance of 0.1 to 0.5 mm from a fusion line) was estimated to be in the range of temperature of 1200 to 1300°C. This temperature range will provide more rapid growth and coalescence of helium bubbles in the **grain** boundaries. Above such temperatures, migration of helium atoms to free ***surfaces*** will suppress the growth and coalescence of helium bubbles in the boundaries, although **this** is **necessary** to clarify in the future.

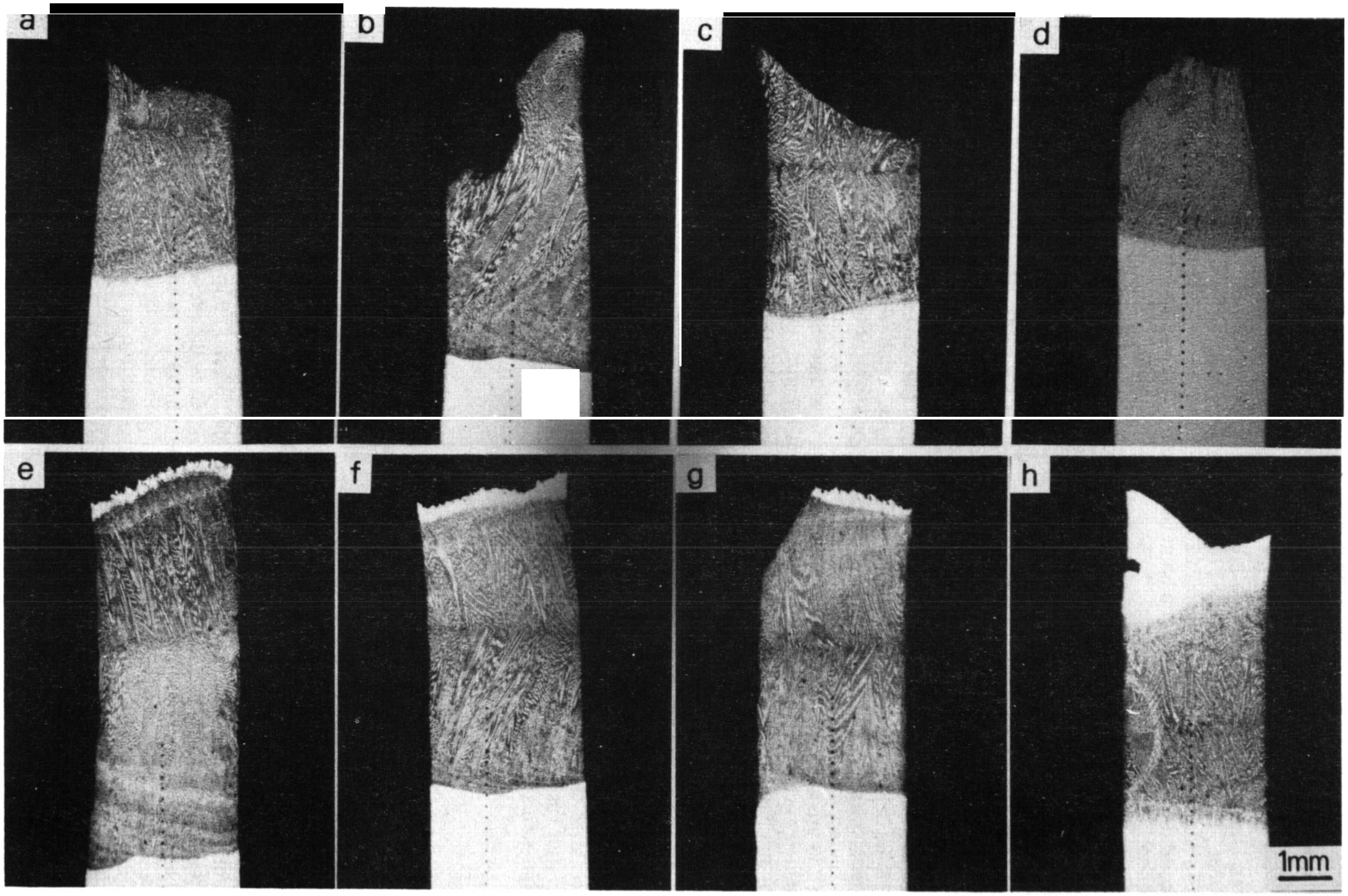

Fig. 2. Optical metallographies of samples fractured during tensile testing under each temperature: (a) and (e) room temperature; (b) and (f) 400°C; (c) and (g) 500°C; (d) and (h) 600°C. Upper and lower row show un- and irradiated welded joints, respectively.

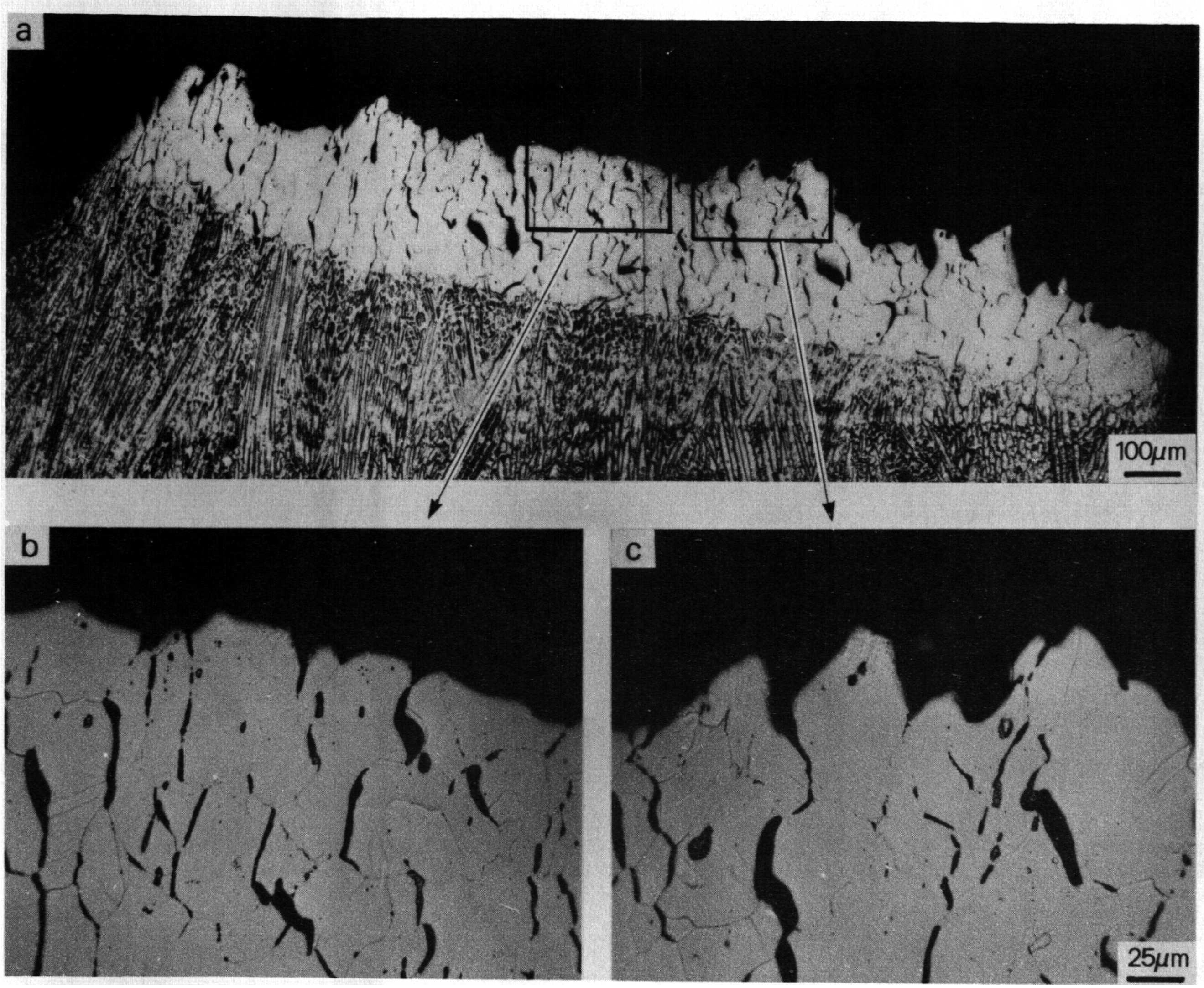

Fig. 3. Micrographs of intergranular cracks observed in the heat-affected zone fractured during tensile testing at 500°C: (a) (b) and (c) high magnification.

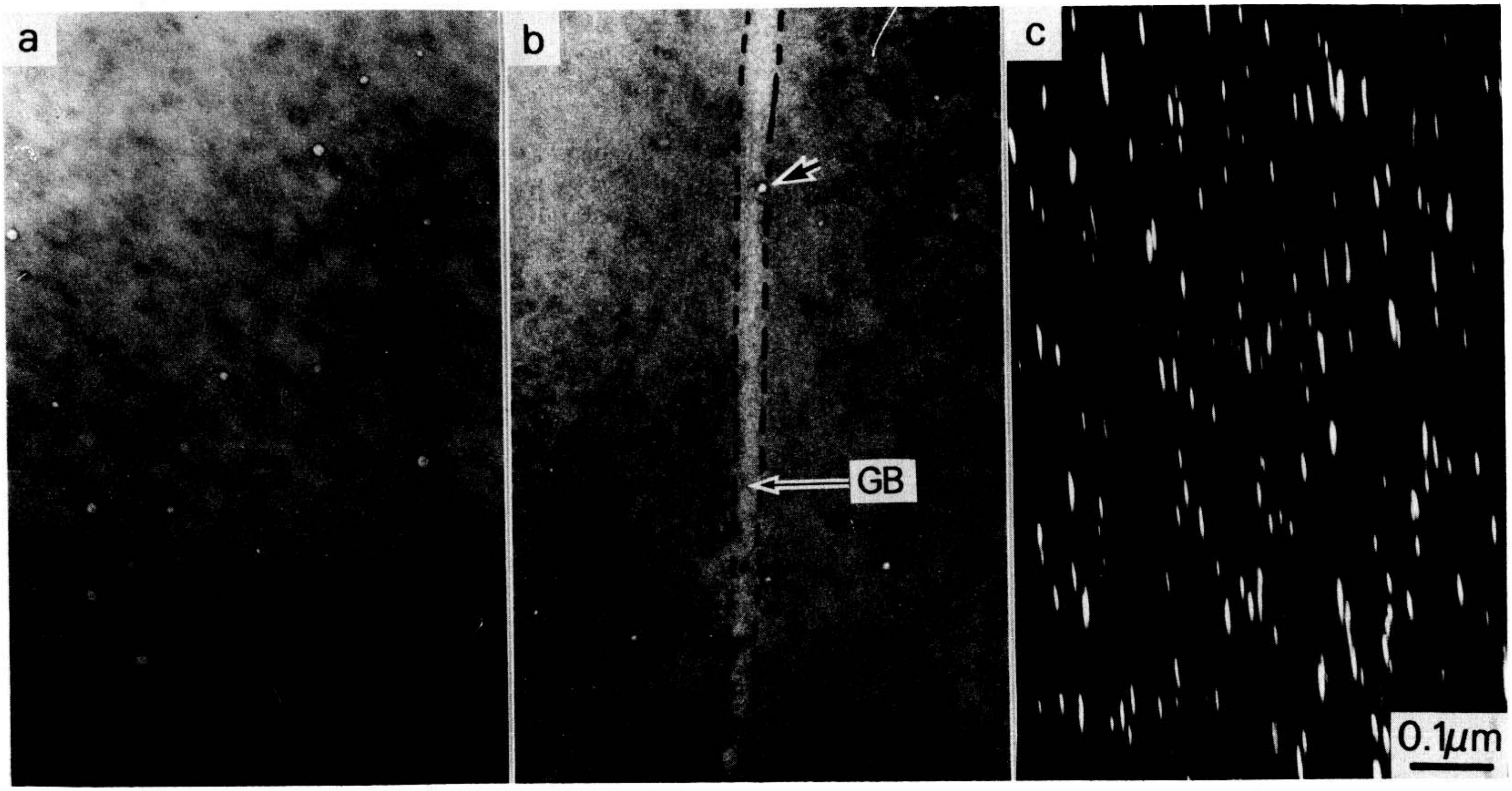

Fig. 4. Microstructures observed in a base metal: (a) helium bubbles in a matrix; (b) helium bubbles in a grain boundary; and (c) dislocation loops (dark field).

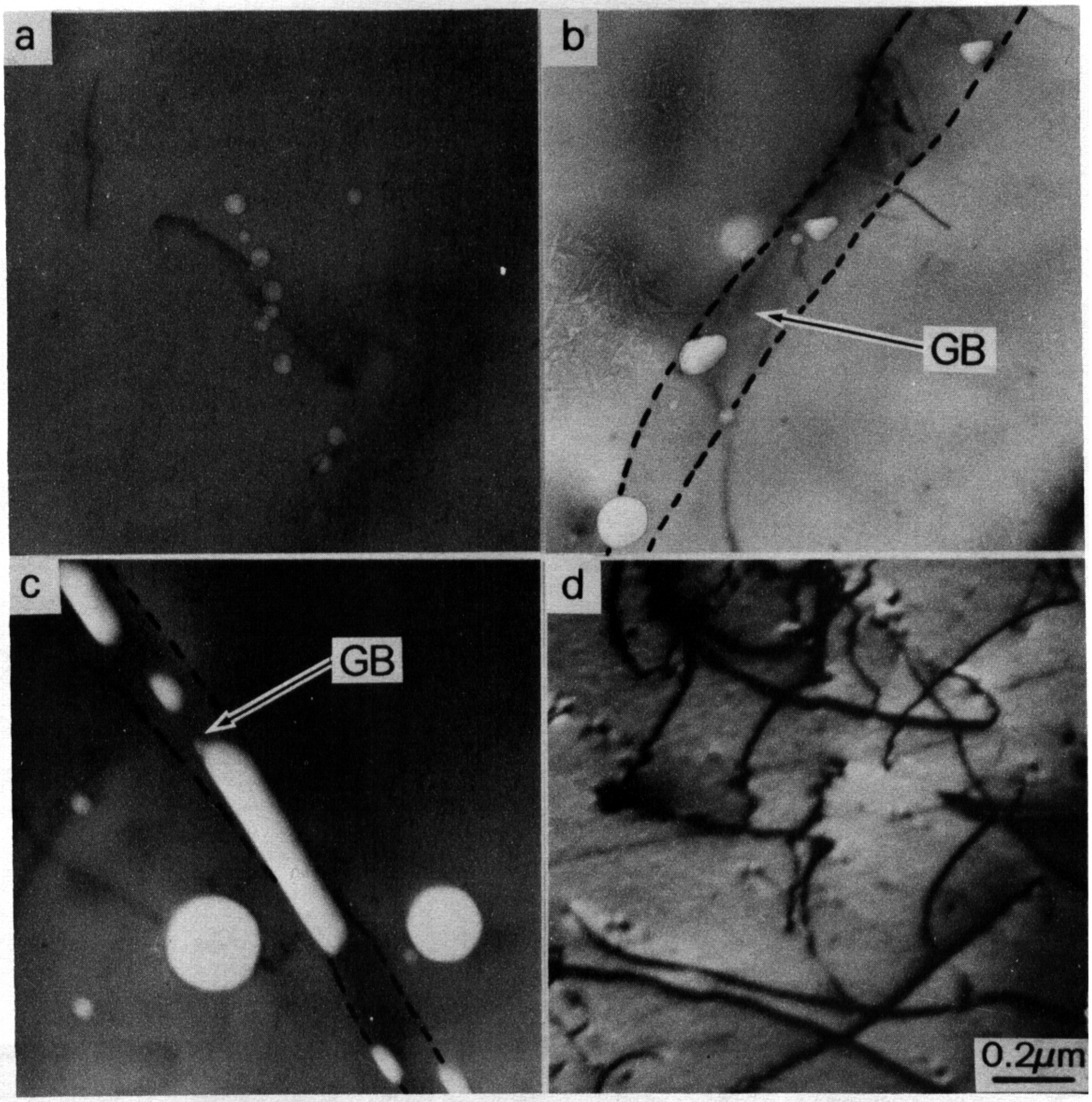

Fig. 5. Microstructures observed in the heat-affected zone: (a) helium bubbles in a matrix; (b) big helium bubbles in a grain boundary; (c) elongated helium bubbles in a grain boundary.

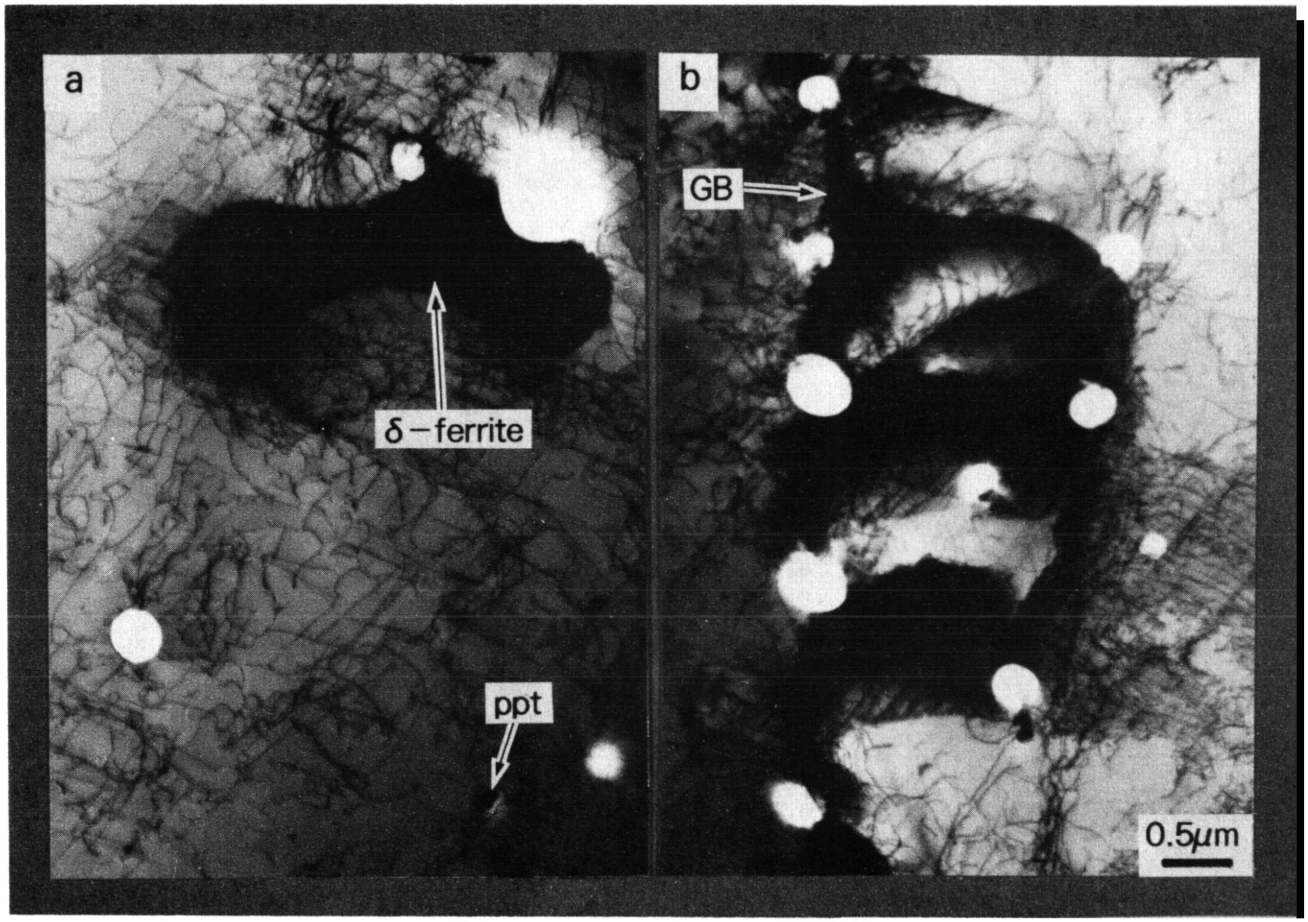

Fig. 6. Microstructures found in the fusion zone: (a) cavities attached to a delta-ferrite phase and an undissolved carbide; (b) cavities precipitated in the grain boundaries.

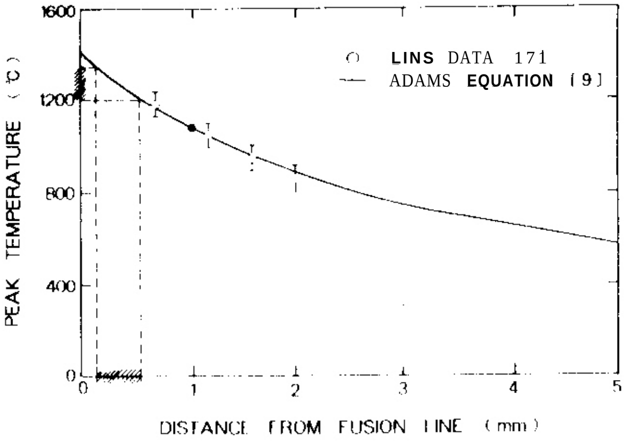

Fig. 7. Temperature-position profile in the heat-affected zone as a function of a distance from the fusion line of type 316 stainless steel. A filled circle means the position of the HAZ observed in this study. Two shaded areas show the fractured position and the corresponding temperature.

Secondly, helium bubbles have been observed to grow and coalesce rapidly along grain boundaries subjected to a tensile stress[1-4,8]. Under the fully constrained conditions of butt-TIG welding, restrained stresses of compression and tension take place during welding and they remain in a welded joint after welding. In particular, considerably large tensile stress remains in a central region including **HAZ** and fusion zone under the constrained condition of welding after cooling. The un-constrained condition decreases the tensile stress in a central region and spreads the lower tensile stress to a normal direction to a welding bead direction. Tensile stress is evaluated to be somewhat uniform in entire HAZ[10]. The effect of tensile stress on growth and coalescence of helium bubbles in the grain boundaries **does** not depend on the positions in the HAZ in this study.

Simultaneous effects of both elevated temperatures and stress may enhance the growth and coalescence **of** helium bubbles in the grain boundaries. In particular, the temperature effect would be larger than the stress effect on the behavior of helium bubbles in the grain boundaries. **As** a result, intergranular fracture occurs in the region of the HAZ adjacent to the fusion line, in which the largest effect on growth and coalescence of helium bubbles in the grain boundaries would develop.

SUMMARY AND CONCLUSION

The behavior of helium bubbles in welded joints fabricated using a TIG welding process for a type **316** stainless steel wrapper tube actually employed in the fast reactor JOYO was investigated. The wrapper tube was irradiated to **(1.5 - 4.2)** x 10^{26} n/m^2 at 395-410°C. Most of the welded joints fractured intergranularly in the heat-affected zone adjacent to the fusion line. The cause is attributed to the growth and coalescence of helium bubbles due to elevated temperature and tensile stress induced by the welding heat input in this region.

FUTURE WORK

The examination of weldability for a wrapper tube irradiated to higher damage levels will be performed in the future.

REFERENCES

1. D. Hull and D. E. Rimmer, Philo. Mag. 4 (1959) 673.
2. M. V. Speight and I. E. Harris, Metal Sci. J. 1 (1967) 83.
3. H. Trinkaus. Ber. Bunsenges. Phys. Chem. 82 (1978) 249.
4. H. Ullmaier, Nucl. Fusion, 24 (1984) 1039.
5. H. T. Lin, M. L. Grossbeck, and B. A. Chin, Metall. Trans. A21 (1990) 2585.
6. H. T. Lin, S. H. Goods, M. L. Grossbeck, and B. A. Chin, Effects of Irradiation on Materials: Fourteenth Conference, Vol. I, ASTM-STP 1064, N. H. Packan, R. E. Stoller, and A. S. Kummer, Eds., American Society for Testing Materials, Philadelphia, 1989. p. 301.
7. H. T. Lin, Simulation of the Welding of Irradiated Materials, ORNL/TM-11158, *Oak* Ridge National Laboratory, 1989.
8. C. A. Wang, H. T. Lin, M. L. Grossbeck, and B. A. Chin, J. Nucl. Mater. 191-194 (1992) 696.
9. C. M. Adams, Jr., Weld. J. 37 (1958) 210.
10. K. Satoh, Y. Mukai and M. Toyoda, Welding Engineering, Rikohgakusha, 1985, Tokyo (in Japanese).

DOSE DEPENDENCE OF THE MICROSTRUCTURAL EVOLUTION IN NEUTRON-IRRADIATED AUSTENITIC STAINLESS STEEL --

S.J. Zinkle, P.J. Maziasz and R.E. Stoller (*Oak* Ridge National Laboratory)

OBJECTIVE

The objective of this work is to examine the duration of the microstructural transient regime in neutron irradiated austenitic stainless steels

SUMMARY

Microstructural **data** on the evolution of the dislocation loop, cavity, and precipitate populations in neutron-irradiated austenitic stainless **steels** are reviewed in order to estimate the displacement damage levels needed to achieve the "steady state" condition. The microstructural data **can** be conveniently divided into two temperature regimes. In the low temperature regime (below about 300°C) the microstructure of austenitic stainless steels is dominated by "black **spot**" defect clusters and faulted interstitial dislocation loops. The dose needed to approach saturation of the loop and defect cluster densities is generally on the order of 1 displacement per atom (dpa) in this regime. In the high temperature regime (–300 to 700°C), cavities, precipitates, **loops** and network dislocations are all produced during irradiation; doses in excess of 10 dpa are generally required to approach a "steady state" microstructural condition. Due to complex interactions between the various microstructural components that form during irradiation, a secondary transient regime is typically observed in commercial stainless steels during irradiation at elevated temperatures. This slowly evolving secondary transient may extend to damage levels in excess of 50 dpa in typical 300-series stainless steels, and to >100 dpa in radiation-resistant developmental **steels.** The detailed evolution of any given microstructural component in the high-temperature regime is sensitive to slight variations in numerous experimental variables, including heat-to-heat composition changes **and** neutron spectrum.

1. Introduction

Austenitic stainless steels have been the subject of numerous investigations on radiation effects. Most **of** these studies have been driven **by** technological applications, ranging from light water and fast breeder fission reactors to fusion reactor first-wall structures. It is well established that the microstructural response of austenitic stainless steels to neutron irradiation is sensitive to heat-to-heat compositional variations (e.g., N-lot vs DO heats of type 316 stainless steel in the US breeder reactor program) [1-3]. **This** inherent sensitivity to slight compositional changes has made it difficult to systematically sort out "generic" effects associated with irradiation spectrum, damage rate, or He/dpa variations, since many studies were performed using different heats of otherwise similar material.

There are three major categories of transient behavior that can be identified in irradiated metals: Point defect (vacancy and interstitial) supersaturation; microscopic nucleation of defect aggregates such **as** dislocation loops, voids and precipitates; and macroscopic changes such as void swelling and mechanical property transients. Previous reviews of neutron irradiation effects in austenitic stainless steel have concentrated on the cavity swelling and precipitate evolution associated with high-dose (>10 dpa) neutron irradiation [2-9]. The transient behavior of point defects is addressed in a companion paper in these proceedings [10], and reviews on the transient swelling [5,11] and mechanical property [12] behavior **of** neutron-irradiated stainless steel are also available. The focus of the present paper is to critically review the microstructural response of stainless steel to neutron irradiation at low to moderate doses, where the microstructure evolves rapidly. The bulk of the analysis will be restricted to relatively simple Fe-Cr-Ni ternary austenitic alloys or ***300*** series stainless steels in order to establish the intrinsic behavior of "pure" austenitic stainless **steels** to neutron irradiation. Unfortunately, the lack of low-fluence data on a standardized heat *of* steel makes it difficult to rigorously define the extent of the transient regime **for** microstructural evolution. This paper incorporates **data from** a range of steel compositions, and therefore is only strictly relevant for examining qualitative rather than quantitative trends. Three microstructural categories will be examined: (1) dislocation Imps and network dislocations, (2) cavities, and (3) precipitates.

The specific goals of this review are to establish the temperature dependence of the "steady slate" microsuuctural components, to determine the neutron darnage level required to attain these "steady-slaw" densities, and to examine the influence of controlled solute additions on the duration of transient regimes prior to "steady-slate". It should he recognized that the individual microstructural components listed above interact with each other as they evolve. Thus, although a given microstructural component (e.g., dislocation loop density) may approach an apparent "saturation" density at low fluence, its value may be subsequently affected by changes in another component of the microstructure [11]. Hence, it will be seen that the term "steady state" is in general only an approximation **for** the overall microstructural response of austenitic steels irradiated to high fluences.

Table 1 lists the alloy compositional ranges for several different austenitic stainless steels that have been the subject of *numerous* published *radiation* effects studies. These steels can **he** categorized as either conventional low-carbon steels (AISI 304 and 316) or Ti- or Nb-stabilized sleels (DIN 1.4970, FV548, D9I, and PCA). Macroscopic swelling due to void formation and growth can have profound implications on the allowable operating lifetime of austenitic steel components irradiated **at** temperatures ≥400°C. The dose-dependent behavior **of** macroscopic swelling includes an initial low-swelling transient regime followed by a linear high swelling rate regime. Therefore, the philosophy of most materials programs engaged in developing swelling-resistant structural alloys has been to manipulate metallurgical variables such as thennomechanical condition and alloy composition to extend the low-swelling transient regime to the highest doses possible [3]. Alloy modifications with specific solute additions. like titanium, have generally been quite successful in improving void swelling resistance for fast breeder reactor applications [13-18]. The **best** swelling-resistant steels invoke additional microstructural refinements that produce finely dispersed *precipitates and dislocations* which can remain stable up to high damage levels. These radiation-resistant microstructures are not permanent or true "steady-state" microstructures. however, and they eventually become unstable at some higher dose.

able 1. Chemical comp

	Cr	Ni	Mn	Si	C	Mo	Ti
AISI 304	18-20	8-12	<2.0	<1.0	<0.08	–	–
AISI 316	16-18	10-14	<2.0	<1.0	<0.08	2-3	–
FV548[a]	16-17	11-12	0.75-1.25	<0.6	0.06-0.09	1-1.75	<0.05
DIN 1.4970[b]	15	15	1.5	0.4	0.1	1.2	0.5
	14	16.2	1.8	0.4	0.05	2.3	0.24
	13.5	15.5	2	0.4	0.04	1.8-2.2	0.25

[a] Nb-stabilized steel, also contains <1.05 Nb and 0.001-0.003B

[b] Ti-stabilized steel, also contains 0.005 B

[c] U.s. Fusion material Program's Prime Candidate Alloy, also contains 0.01 P

[d] Alloy developed for U.S. Breeder Reactor Program, also conlains 0.05 V, 0.004-0.006 B, 0.025-0.04 P

2. Classification of Temperature Regimes

As shown in Fig. 1, the microstructural data obtained on neutron-irradiated austenitic stainless steels at temperatures above 50°C can be conveniently classified into three broad temperature regimes. This temperature classification **parallels** the conventions established from numerous isochronal annealing studies **performed** on pure metals [19,20]. The "low-temperature" regime extends from the onset of vacancy motion (annealing Stage III) **up** to temperatures where vacancy clusters created in the displacement cascade become thermally unstable (annealing Stage V). For neutron irradiated austenitic stainless steel, this low temperature regime covers the temperature range from abut 50°C to about 300°C [21]. It should be recognized that since the mobility and thermal stability of defects depends on the length of observation (i.e. irradiation time), the actual temperatures associated with observable monovacancy migration and vacancy cluster evaporation for a given damage dose will he somewhat dependent on the irradiation time and hence damage rate. The temperature range between vacancy migration (Stage Ill) and vacancy cluster evaporation (Stage V) for ion-irradiation conditions, which are typically performed at high damage rates, would therefore lie at correspondingly higher temperatures relative to neutron irradiation conditions.

ORNL-DWG 92M-15838

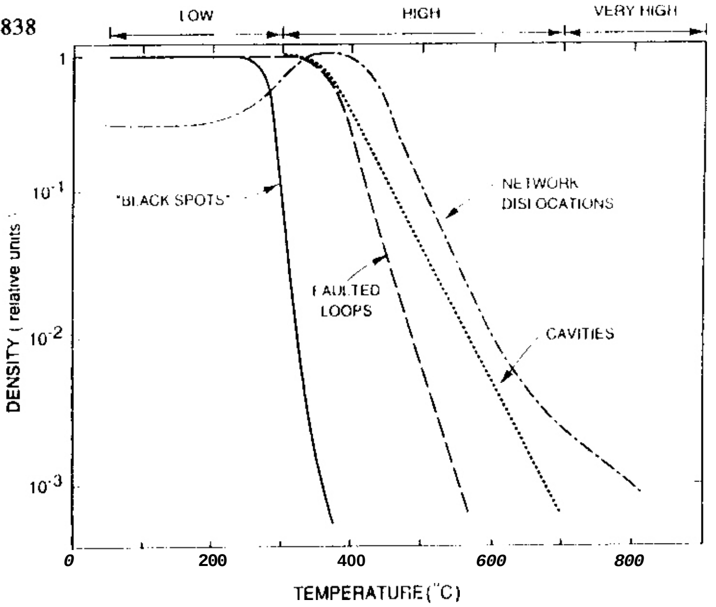

Fig. 1. Temperature dependence of the experimentally observed "saturation" densities of the various microstructural components in neutron-irradiated austenitic stainless **steel** (see Sections **3-5** for derails). The microstructural data can be grouped into "low temperature", "high temperature" and "very high temperature" regimes.

The typical microstructural features observed in the "low-temperature" regime are small defect clusters ("black spots"), faulted dislocation loops, and network dislocations [6,22]. The observable densities of "black spots", faulted loops and network dislocations are nearly independent of irradiation temperature in the low-temperature regime (Fig. 1); as described later, the "black spot" density begins to decrease at temperatures above abut 250°C and there are indications [22] that the network dislocation density may simultaneously increase slightly. Radiation-produced cavities and precipitates are generally not observed in the low-temperature regime. The degree of radiation-induced **solute** segregation (RIS) is minimal due to the limited point defect mobility and the high sink strengths associated with the high density of small defect clusters that are **formed** at low doses. The microstructure is relatively insensitive to variations in the damage rate or He/dpa ratio in this temperature regime, and reaches a "saturation" level at relatively low **doses.**

The "high-temperature" regime extends from the onset of thermally-induced vacancy emission from vacancy clusters (annealing Stage V) up to temperatures at which interstitial clusters become thermally unstable. For typical neutron irradiation conditions, this regime covers the temperature range from about 300°C to about 700°C. The microstructural evolution during irradiation in the high temperature regime is complex, and consists **of** cavities (helium **bubbles** and/or voids), dislocation **loops** and network dislocations, and various types of precipitates [6,9]. The "saturation" densities of helium bubbles, voids, dislocation loops, and network dislocations all decrease with increasing temperature in this regime (Fig. **1**). There is some evidence [22] that the network dislocation density may reach **a** local maximum at a temperature near 350°C, but additional high-dose studies are needed to confirm this possibility. High doses (> 10 dpa) are often required to reach a "steady-state" defect microstructure in the high temperature regime. due to extensive interactions between the individual microstructural components. The density of small "black-spot" defect clusters is negligible in this temperature regime. Radiation-induced solute segregation effects can **be** very significant in the "high-temperature" regime. The specific details of the microstructural evolution are sensitive to numerous parameters including damage rate, alloy composition, and He/dpa ratio.

In the "very high-temperature" regime. which corresponds to temperatures above about 700°C, all radiation-induced defect clusters except gas-pressurized bubbles are thermally unstable. Hence, the microstructure in this temperature regime is essentially identical to that found in unirradiated steels aged at the same temperature. There are no significant concentrations of dislocation loops or radiation-produced voids, and the precipitate and network dislocation behavior is equivalent to that observed thermally. Helium bubble formation can still occur in this temperature regime, but its behavior is determined primarily by the thermal equilibrium vacancy concentration and He concentration.

3. Dislocation Loops and Network Dislocations

3.1 Dislocation Loops

Figure *2* presents the temperature dependence of the faulted dislocation loop density that is formed during high-dose neutron irradiation of Type **316** austenitic stainless steel [22-31]. Essentially all of the

ORNL-DWG **92M-13829**

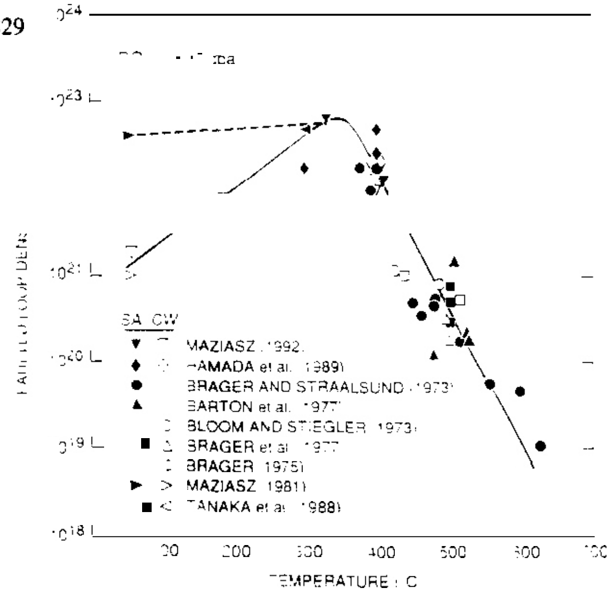

Fig. **2.** Effect of irradiation temperature on the faulted dislocation loop density in neutron-irradiated austenitic stainless steel [22-31].

faulted loops formed during neutron irradiation in austenitic steels that are larger than 10 nm in diameter have been identifed as interstitial in nature, lying on {111} planes with Burgers vectors of the type $h = a_0/3<111>$ [23,32-34]. A fairly sharp transition in the loop density occurs between the "low temperature" and the "high temperature" regime. The loop density decreases rapidly with increasing temperature above 350 °C, and for damage levels >5 to 10 dpa there is no significant difference between solution annealed (SA) and 20% cold-worked (CW) material. There can be a substantial difference between the dislocation evolution in SA and CW steels at low doses (<10 dpa) in the "high temperature" regime, but there is little systematic data to quantify this behavior.

The dislocation loop and "black spot" defect cluster densities are very high at low temperatures (<300°C), which causes a high sink strength for point defects. Furthermore, the low point defect mobilities at these temperatures can extend the transient period for the evolution of the loops and network dislocations before reaching a "steady state" microstructure. The available data suggest that the observable faulted loop density in the low-temperature regime is lower for cold-worked alloys than for solution annealed material for damage levels up to about 10 dpa (Fig. 2). Since the development of observable faulted loops in cold-worked alloys first requires a significant reduction of the initially high network dislocation density to take place, it is possible that the cold-worked material does not reach its "steady-state" loop density even after 10 dpa at these temperatures. A systematic study of the same heat of solution annealed and cold-worked steel irradiated over a wide range of doses in this low-temperature regime is needed to evaluate this possibility.

Figure 3 shows a typical microstructure produced in austenitic stainless steel by neutron irradiation in the Low-temperature regime [35]. The dominant microstructural feature is a high density of small "black spot" defect clusters. The average size of the small defect clusters is about 2 nm [22,28,34-36]. Numerous studies performed on Fe-Cr-Ni alloys and pure facecentered cubic (FCC) metals indicate that much of the "black spot" cluster density is created directly in the displacement cascade during the cascade quench [33,36,37]. The total density of the small defect clusters in austenitic steel is comparable to the densities observed in pure FCC metals of similar mass, such as Ni or Cu. However, it is interesting to note that the fraction of defect clusters that are resolvable as stacking fault tetrahedra in stainless steel is <1% [34-36], which is much less than the corresponding fraction of 25 to 50% observed in Ni or Cu following irradiation at comparable conditions [38]. This suggests that the solutes in stainless steel somehow modify the cascade quench behavior and inhibit SIT formation in the displacement cascade.

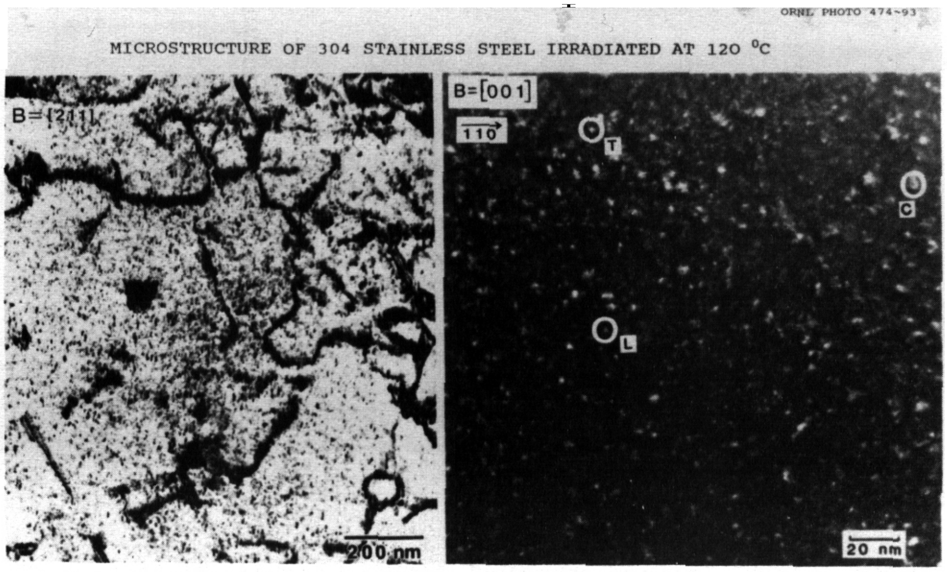

Fig. 3. Microstructure of 304L stainless steel after fission neutron irradiation at 120 °C to ~4.5 dpa [35].

Due to a lack of neutron irradiation studies on stainless steel in the low temperature regime, the dose dependence of the small defect clusters, network dislocations and faulted dislocation loops is not well established. The available data [22,28,34,36] suggest that the "saturation" density of black spot damage may be greater than $10^{24}/m^3$, and that this density is attained after doses of about 0.1 dpa. Mechanical property measurements made on *Type* 304 and 316 stainless steel following fission neutron irradiation at temperatures less than 100°C also suggest that defect cluster saturation occurs at damage levels <0.1 dpa [39]. The dose dependence for the accumulation of defect clusters during neutron irradiation at low temperatures is apparently sublinear from 0.002 to 0.03 dpa [36], which is an indication of interaction between displacement cascades and surrounding defect clusters even at these low doses. The density of resolvable faulted loops increases with increasing temperature between 50 and 300°C [22]. Although conventional theoretical models predict that the as cold-worked network dislocation structure should be relatively stable at low temperatures [11], some experimental results suggest that significant dislocation recovery can occur at low doses for irradiation temperatures below 300°C [22]. Additional data in this temperature regime on both solution annealed and cold worked material are needed in *order* to better define the "inherent" material response.

In the high-temperature regime (300 to 700°C), faulted (Frank) interstitial loops are formed at low dose and approach a maximum density after a damage level of a few dpa. Figure 4 shows a typical example of the dose dependence of the faulted loop density for solution annealed stainless steel irradiated at temperatures near 400°C [22,23,30,31,40-44]. The loop density reaches an apparent saturation level after about 3 dpa, and this density is then maintained up to much higher doses. The loop densities in simple austenitic steels are similar for both mixed-spectrum and fast reactor fission-neutron irradiations. The exact saturation values attained during irradiation depend on experimental conditions such as alloy composition and dose rate [40]. The sensitivity of the loop density to experimental conditions increases with increasing irradiation temperature [9].

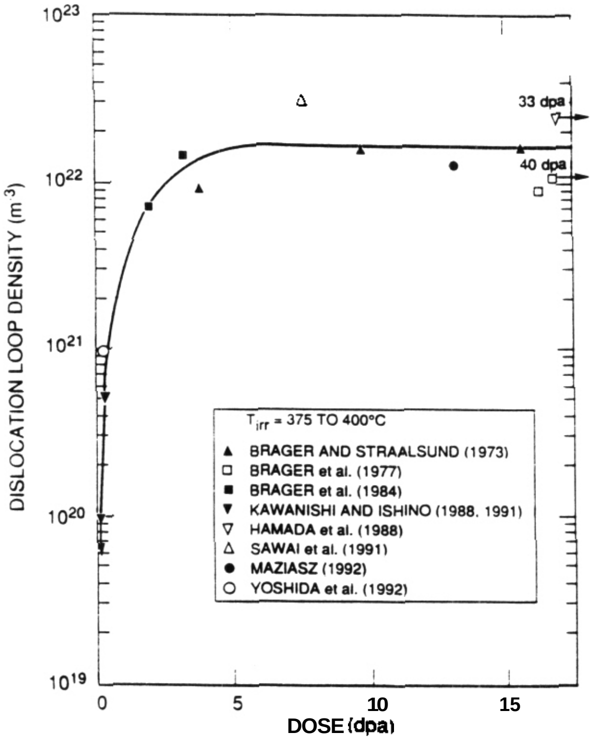

ORNL-DWG 92M-13863R

Fig. 4. Evolution of the faulted dislocation loop density in austenitic stainless steel irradiated with fission neutrons at 375 to 400 °C [22,23,30,31,40-44]

At higher irradiation temperatures (≥450°C), the loop dcnsity has been observed to reach a maximum value after low doses, and then begins to decrease with increasing fluence [6,30,31,45]. Frank **loops** which have grown beyond a diameter of SO to 100nm tend to unfault lo form the lower-energy perfect **loop** configuration with $b = a_0/2\langle 110\rangle$ Burgers vectors. The unfaulting reaclion is usually triggered **by** physical impingement of adjoining Frank loops **as** a result of loop growth [31,33]. While Frank **loops are** sessile, the perfect loops formed by the unfaulting process are glissile and can glide *to* interact and form network dislocations. The maximum in the faulted **loop** density at moderate doses during elevated temperature *neutron* irradiation may ***he** attributed* to a sink competition *effect* due to interaction between different radiation-produced microstructural components. Radiation-produced precipitation, along with the dislocation network created by the growth and unfaulting of dislocation loops generated earlier in the irradiation, produces new point defect sinks in the lattice that compete with the loops for the available interstitials. Hence, once the initial population ***of*** loops grows to a size where significant overlapping and associated unfaulting occurs, a new population of loops cannot be nucleated in sufficient density ***to*** replace them. Additional mechanisms may also contribute. For example, radiation induced solute segregation (RIS) could modify the chemical composition of the matrix in a manner that inhibited the formalion of new **loops** (see Section *5).*

3.2 Total Dislocation Density

The total dislocation density (loop **plus** network) observed in solution-annealed (SA) type 316 stainless steels after irradiation to high damage levels is plotted in Fig. 5 as a function of irradiation temperature [22,45]. At temperatures below about 400°C, the total dislocation density is dominated by faulted loops [22,23,27,45]. **As** the irradiation temperaturc increases above about 350°C, the total dislocation density decreases rapidly with increasing temperature and the relative contribution from faulted loops becomes progressively smaller. The total dislocation dcnsity is dominated by the network dislocation component at irradiation temperatures above about 500°C [22,23,27,45,46]. The tcmperature-dependent transition from a loop-dominalcd dislocation microstructure **lo** a network-dominated dislocation microstructure depends synergistically upon several parameters, including alloy composition , irradiation spectrum and dose. Due to the decrease in the faulted loop density with increasing dose at elevated temperatures, the transition temperature hetween a loop-dominant arid a network-dominant microstructure shifts to lower temperatures **as** the dose increases.

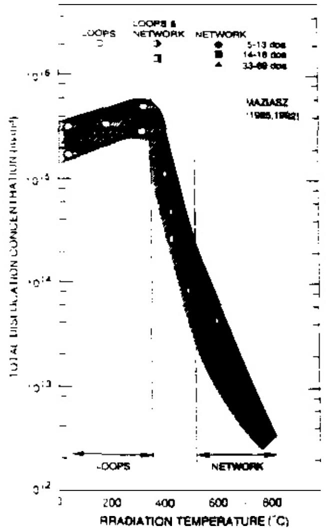

ORNL-DWG 92M-15862

Fig. **5**. Temperature dcpcndence of the total dislocation density in solution annealed 316 stainless steel irradiated in the HFIR mixed spectrum and EBR-II fast fission reactors [22,45]. The Figure also includes recent unpublished data **by** Maziasz on specimens irradiated to **34** dpa at 300 to 600°C in HFIR.

figure 6 shows the **dose** dependence of **the** total dislocation density observed in stainless steel irradiated at about 400°C [22,23,40-42]. The damage level needed for the total dislocation density to approach a "steady-state" value **is** 10 dpa or more, which is significantly higher than the dose needed **to** achieve the "steady **state"** loop density at that temperature (Fig. **4).** This difference in doses to achieve the two different "steady-stile" conditions is due to the fact that the total dislocation densitydepends on the product of *the* loop density and the loop size along with the network dislocation density. The network dislocation density in turn depends on loop growth and unfaulting to achieve its "steady-state" value. Therefore, significant growth **of** dislocation loops must occur after loop nucleation saturates in order for the tool dislocation density **to** achieve its "steady-slate" value.

ORNL-DWG **92M-13862**

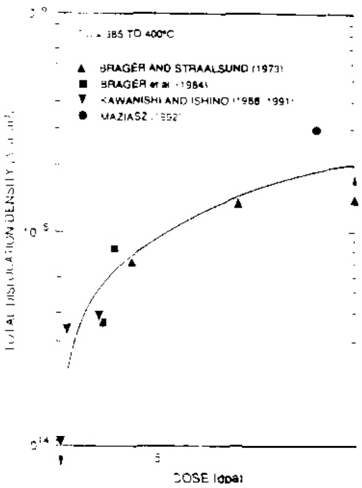

Fig. 6. Effect of neutron irradiation on the total dislocation density in solution annealed austenitic stainless steel irradiated near 400 ^{o}C [22,23,40-42].

Figure 7 summarizes the evolution of the total dislocation density in **SA** 316 stainless steel irradiated at three different temperatures within the "high-temperature" regime [23,31,40-42,45]. **An** initial transient associated with the rapid buildup **of** dislocation density is completed within about 10 dpa at all temperatures. **A** secondary microstructural transient subsequently occurs in specimens irradiated at the higher tempenlure end of **this** regime. The total dislocation density can either increase or decrease slightly in this secondary transient regime, depending on temperature and steel heat chemistry. This is a reflection of the dynamic balance between the process **of** loop nucleation, growth, and unfaulting to create network dislocations, and the process of radiation-assisted recovery to remove network dislocations. The particular total dislocation density achieved depends on the details of the other microstructural components created **during** irradiation (in particular precipitates and cavities), and hence is very sensitive to alloy composition and neutron spectrum [45].

Irradiation of cold-worked stainless steel causes **the** network dislocation density to initially decrease rapidly below its preirradiation value. Figure 8 shows an example **of** the evolution of the loop and network components of the total dislocation density obtained from a recent spectrally-tailored irradiation experiment on 20%CW PCA **stainless** steel conducted at fusion-relevant damage rates and He/dpa levels [22]. The network dislocation density decreased by one order **of** magnitude after irradiation to 7.4 dpa at 330 and 400°C, then increased with further irradiation due to the formation of additional network dislocations from **loops** that had grown and unfaulted. The corresponding changes in the total dislocation density were less dramatic than the changes in network component done. The lack of data at doses less than 7 dpa under similar, fusion-relevant irradialion conditions raises an important question, namely - how rapidly **does** such

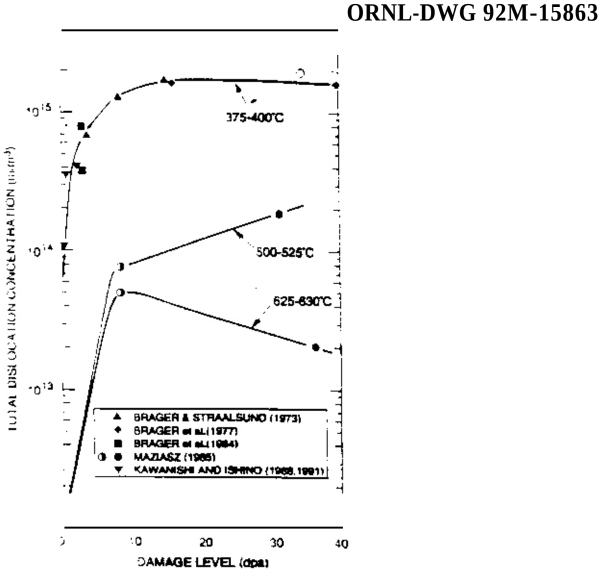

Fig. 7. Evolution of the total dislocation density in neutron irradiated solution annealed austenitic stainless steel [23,31,40-42,45]. The filled symbols denote loop-dominant dislocation microstructures, whereas the half-filled symbols refer to microstructures containing comparable dislocation line densities from loops and network dislocations

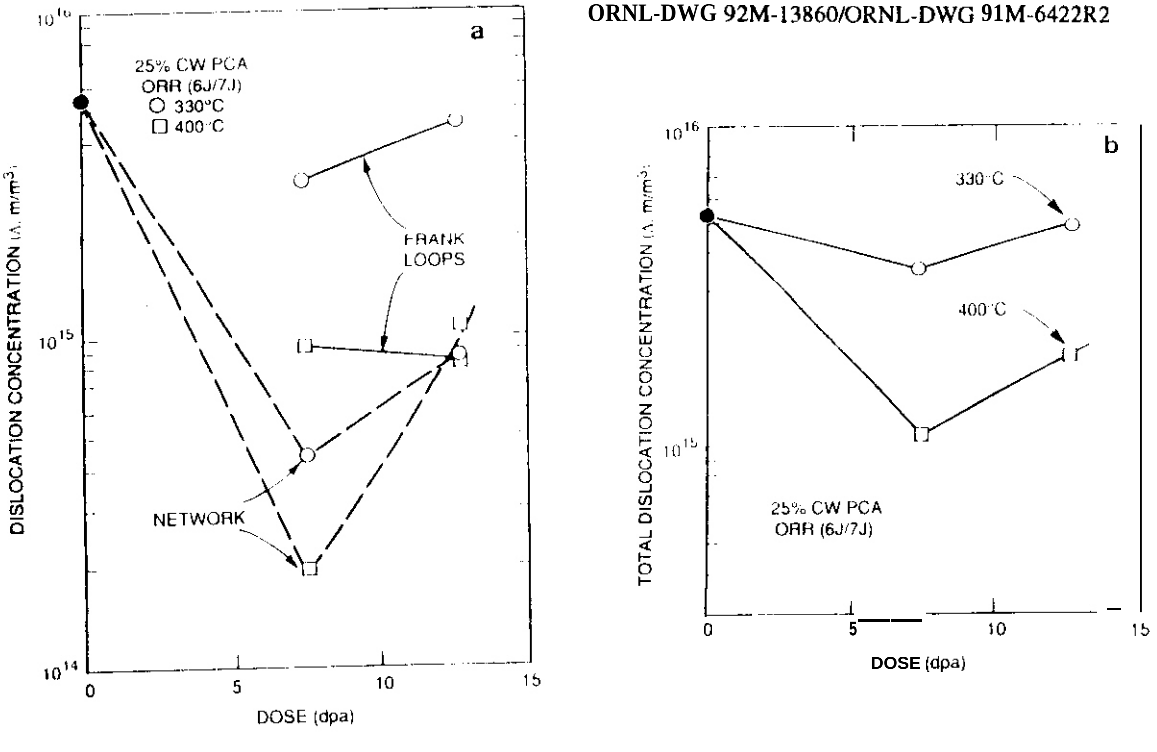

Fig. 8. Effect of ORR fission neutron irradiation at 330 and 400°C on the evolution of the a) network dislocation and faulted loop density and b) total dislocation density in cold worked PCA austenitic steel [22].

network dislocation recovery occur during the initial stages of the irradiation'? It is possible that the combination of a rapid recovery of the cold-worked dislocation density during irradiation and the delayed nucleation of faulted loops in cold-worked material could create a low-dose regime where both the dislocation network and the loop densities are low? Such dislocation behavior could produce a transient radiation-induced softening in cold-worked steel prior to the radiation-induced hardening traditionally seen at higher doses. The possibility of unanticipated transient softening in cold-worked steel would be of obvious importance for fusion structural engineering designs. Further studies are needed at damage levels between 0.1 and 10 dpa to clearly establish the microstructural evolution in cold-worked austenitic stainless steels.

Irradiation of cold-worked type 316 stainless steel in the HFIR mixed-spectrum reactor at elevated temperatures [45] resulted in a slower recovery of the network dislocation density than was observed in the spectrally-tailored OKR irradiations of cold-worked PCA stainless steel at temperatures ≤400°C [22] (only a factor of three decrease after 8 dpa at 425450°C). Unfortunately, there are too many experimental differences between these two studies (damage rate, irradiation temperature, PCA vs. 316SS, He/dpa ratio) to draw any firm conclusions regarding the controlling mechanism for the kinetics of the recovery of the CW network dislocation structure. The physical mechanisms responsible for the evolution of the dislocation microstructure in both simple and complex alloys must be better understood before engineering designs for fusion reactors can be finalized.

Figure 9 compares the evolution of *the* total dislocation density of SA and *25%* CW stainless steels irradiated near 400°C [22,23,40-42]. The total dislocation densities of both SA and 25% CW materials approach a common value of 1 to 2 x $10^{15}/m^2$ after a damage level of about 5 dpa. Similar conclusions regarding the common saturation value of the total dislocation density have also been obtained from TEM observations of SA and 20%CW 316 irradiated in a fast reactor [31]. A common dislocation saturation density in SA and 20%CW steels has also been inferred from analyses of tensile data [47,48] obtained at temperatures above 300°C, although the dose required to reach saturation of mechanical properties was often greater than 20 dpa [48]. On the other hand, recent tensile results on SA and CW stainless steel irradiated at 250°C (i.e., near the upper limit of the "low-temperature" regime) showed that the SA and CW materials saturated at different strength levels [49]. Once again, more experimental studies are needed to complete our understanding of the microstructural evolution at low temperatures.

Figure 10 summarizes the temperature dependence of the various individual microstructural components that make up the total dislocation concentration in PCA steel irradiated to 7.4 dpa at a fusion-relevant damage rate and He/dpa ratio [22]. The irradiated network dislocation density is approximately one-tenth of the preirradiated 25% cold-worked value even for an irradiation temperature as low as 60°C. The total dislocation density in the "low temperature" regime is dominated by the dislocation line-length contribution from "black spot" defect clusters, whose size and density are nearly independent of irradiation temperature up to 20°C. The resolvable Frank loop concentration increases with increasing irradiation temperature in the "low-temperature" regime. This causes the Frank loops to dominate the total dislocation density at irradiation temperatures near 300°C, which corresponds to the transition from the "low-temperature" to &< "high-temperature" regime. The rapid decrease of the Frank loop density at temperatures above 300°C eventually leads to a transition from a loop-dominant to a network-dominant dislocation structure at temperatures above 400°C for a damage level of 13 dpa [22]. The large amount of dislocation network recovery at low temperatures, and the temperature dependence of the network dislocation density may both be related tom extended point defect transient which was invoked to explain the high levels of *creep* at 60°C in pressurized-tube specimens of 25% CW PCA steel irradiated in this experiment [50].

4. Cavity Evolution

Pronounced cavity (He bubble and void) formation generally occurs in steels irradiated in the "high-temperature" regime (300 to 700°C). Figure 11 summarizes the temperature-dependent cavity densities

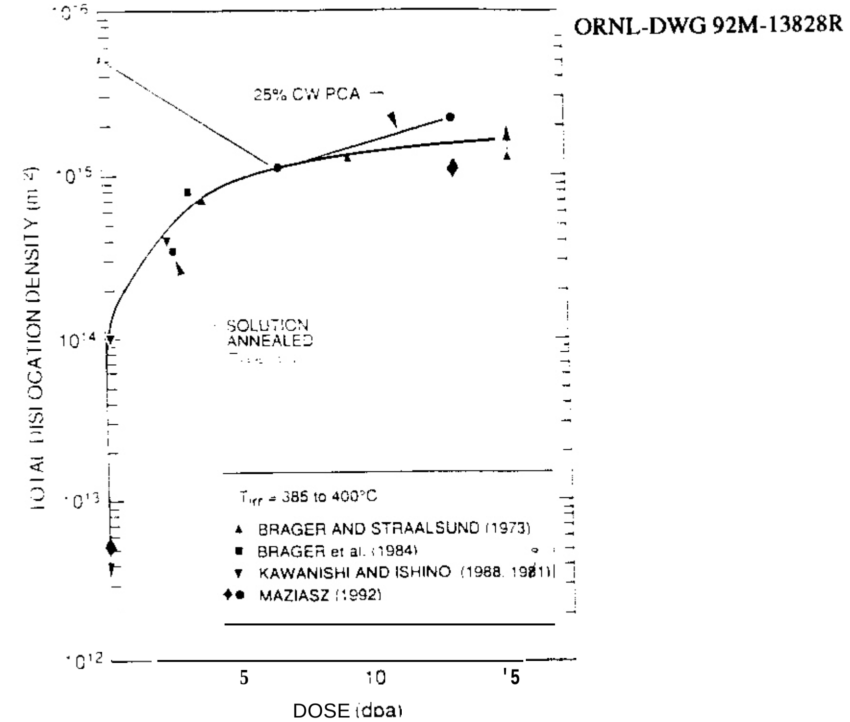

Fig. 9. Comparison of the total dislocation density in solution annealed 316 and cold worked PCA austenitic steel after fission neutron irradiation near 400°C [22,23,40-42].

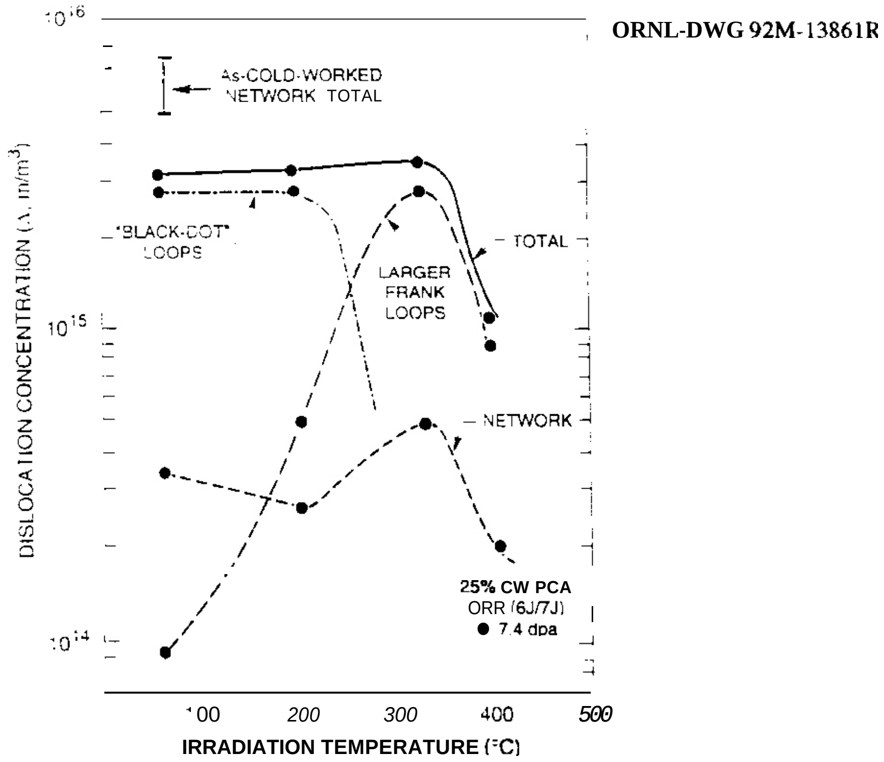

Fig. 10. Effect of irradiation temperature on the various components of the total dislocation density in neutron-irradiated cold worked PCA austenitic steel [22].

observed in neutron-irradiated stainless steel [22,23,30,35,45,51,52]. A bimodal distribution of cavities, consisting of voids and small helium bubbles, is often observed at temperatures between 400 and 650°C. The precise temperature range where helium bubbles and voids coexist is strongly dependent on the experimental conditions such as He/dpa ratio, damage rate and alloy composition. The bubble and void density both decrease rapidly with increasing temperature for irradiations above 400°C. Void formation has been observed in neutron-irradiated austenitic steel at temperatures as low as 325°C [53] and as high as 730°C [6,23,51]. The regime where significant void swelling occurs ranges from about 370 to 700°C. At low temperatures (<300°C), the high sink density associated with thermally stable defect clusters Figs 1 and 2) increases the recombination of point defects at sinks, which suppresses the vacancy supersaturation and thereby inhibits cavity nucleation and growth. At high temperatures, thermal vacancy emission from cavity embryos limits the nucleation of voids, and low sink densities cause an increase in the matrix recombination of point defects.

The "saturation" void density and post-transient swelling rate of austenitic steels in the temperature range of 400 to 650°C is relatively insensitive to irradiation spectrum and cold work level [2,51,54-56]. The primary effect of cold-work is to cause an extension of the low-swelling transient regime by delaying void nucleation. Cold-work generally suppresses the cavity density observed during the low-swelling transient in steels irradiated in fast reactors (low He/dpa ratio), whereas it generally causes an increase in *the* cavity density in alloys irradiated in mixed spectrum reactors (high He/dpa ratio). The higher dislocation density in cold-worked material can enhance helium bubble formation by providing heterogeneous nucleation sites as well as fast paths for helium diffusion. As discussed later, solutes such as titanium, silicon or phosphorus can stabilize the dislocation structure against radiation-induced recovery, and will thereby affect bubble and void nucleation.

Helium bubble formation has routinely been observed after mixed-spectrum (high He/dpa ratio) neutron irradiation at temperatures from 300°C to greater than 850°C [6,22,23,30]. There has been at least one reported observation of small He bubbles after irradiation at a temperature as low as 120°C [35]. Since vacancies in austenitic steels are mobile at temperatures above about 50°C [21], the formation of observable He bubbles is possible in the "low temperature" regime (50 to 300°C). However, the high sink densities associated with the thermally stable "black-spot" defect clusters created in the displacement cascade suppress the vacancy supersaturation and thereby inhibit bubble nucleation and growth. In addition, most of *the* vacancies that survive the displacement cascade quench will be contained in sessile vacancy clusters which are thermally stable up to about 300°C. Hence, only a small fraction of the surviving vacancies are capable of free migration to form He bubbles in this temperature regime.

The He bubble density is typically an order of magnitude higher than the void density at a given irradiation temperature (Fig. 11). The precise bubble density for any given case depends strongly on the details of the irradiation conditions (He/dpa ratio and total dose) as well as metallurgical factors, and tends to be highest when no voids form. The He bubble density observed after irradiation in a mixed-spectrum reactor at low temperatures (≤400°C) is typically in excess of $10^{23}/m^3$ [22,30,57]. These very high bubble densities are nearly comparable to the "black-spot" defect cluster saturation densities obtained after irradiation at lower temperatures (Section 3). At the intermediate helium generation rates characteristic of DT-fusion reactors (10-20 appm He/dpa), helium has recently been shown to lead to "unprecedented" high cavity densities in isotopic tailored steel specimens irradiated in a fast reactor [58]. However, it should be noted that these high cavity densities are comparable to those that have been commonly observed in numerous mixed-spectrum (high He/dpa) reactor irradiations [6,8,9,11,22,30].

As shown in Fig. 12, the void density in simple austenitic steels like SA type 316 or an Fe-Cr-Ni ternary alloy can reach a saturation value at doses of less than 0.5 dpa during irradiation near 400°C [23,41,42,45,59-61]. There is some evidence that higher doses of 15 to 20 dpa are required to achieve the saturation void density at higher temperatures [6], but further work is needed to clarify this issue. At

ORNL-DWG 92M-13830 R

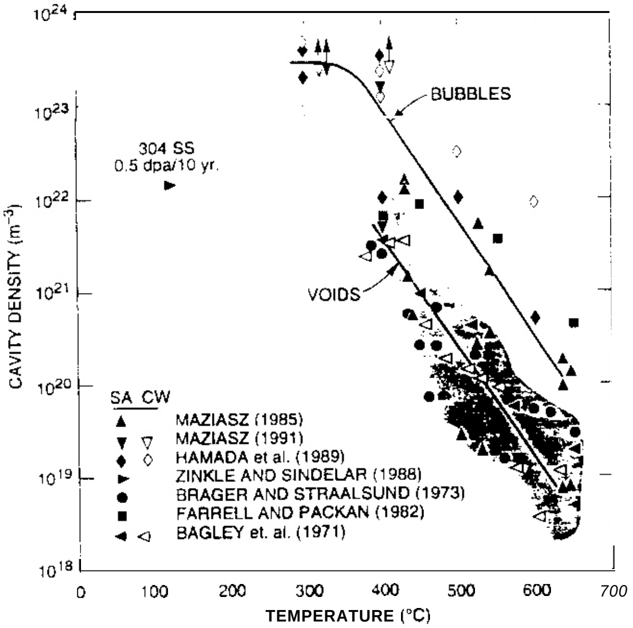

Fig. 11. Effect of neutron irradiation temperature on the cavity density observed in austenitic stainless steel [22,23,30,35,45,51, 52].

ORNL-DWG 92M-13858R2

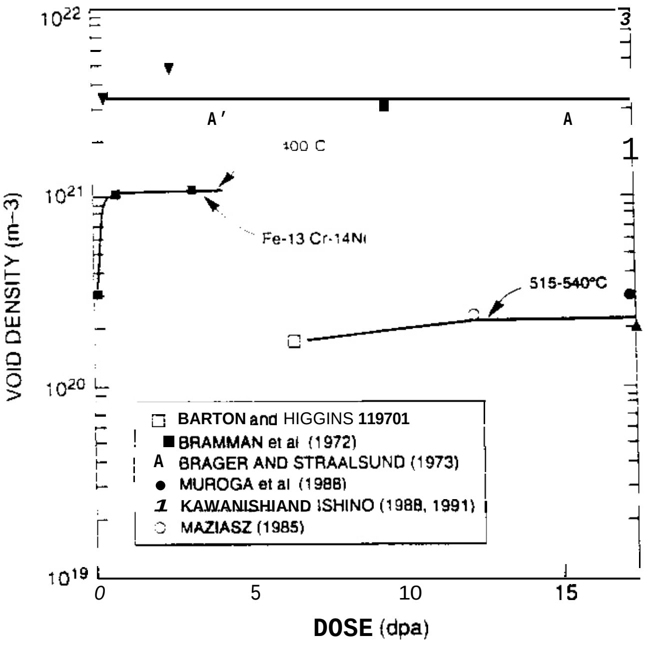

Fig. 12. Dose dependence of the void density in neutron-irradiated solution annealed austenitic steel [23,41,42,45,59-61].

temperatures of 500-650°C, void formation in SA 316 and other steels usually requires higher doses to saturate than for simple ternary alloys, largely because void formation is coupled to **RIS** and the formation of microstructural features such as Frank loops and precipilates (see Section 5). While there is good evidence for the "saturation" void density remaining constant to about 70 **dpa** in **SA** 316 irradiated in fast reactors at 450-550°C, there is also some data suggesting that void densities can decline somewhat with hence at 30-70 dpa at 600 to 670°C [45]. **Void** coalescence due to growth **and** impingement could cause such an effect [62]. In high-swelling ternary alloys, the void density has been observed to decline slightly during fast reactor irradiation at doses > 10 dpa for irndiation temperatures as low as 510°C [63].

Ilie addition of certain solutes such as C, P, Si, or Ti can extend the transient regime for cavity nucleation in austenitic steels by a considerable amount, particularly in cold-worked alloys [1,3,9,13,41,61,64-69]. The magnitude of the solute influence on enhancing or inhibiting void swelling depends on the solute concentration, with the strongest influence typically occurring at intermediate concentrations on the order of 0.1 wt.% [65,66]. Figure 13 shows the effect of titanium additions on the cavity density in two austenitic stcels irradiated near 400°C in either a last (JOYO) or a mixed-spectrum (HFIR) reactor [61,64]. In the Fe-Cr-Ni ternary irradiated in a fast reactor (low He/dpa ratio), the addition of 0.12 wt.% Ti increased die transient void nucleation regime from about 0.5 dpa to 3 dpa or higher. The addition of 0.23 wt.% Ti to 20% CW 316 slainless steel caused extensive refinement of the He bubbles produced during irradiation in a mixed-spectrum reactor (high He/dpa ratio). The density of observable **bubbles** had not yet reached saturation after 13 dpa, **aid** none of the **buhbles** had converted to voids. Similar dose-dependent behavior for the bubble evolution has also been ohscrved in 25% CW Ti-modified PCA steel irradiated in spectrally-tailored experiments ut 400°C to 7.4 and 13 dpa [70]. The detectable bubble concentration in Uiat case increased by aboul a factor of ten to reach >2.5 x $10^{23}/m^3$ at 13 dpa wilhout evidence of saturation. Alloying elements like titanium and phosphorus can have indirect effects on void fonnation **arid** growth when they are in solid-solution, **and** can also directly affect helium hubhle nucleation in steels by causing the formation of line MC or M_2P precipitates.

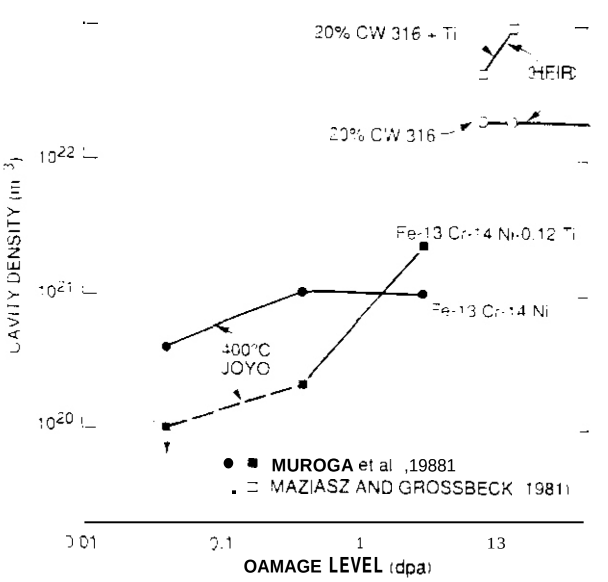

Fig. 13. Effect of Ti additions on extending the transient regime for cavity nucleation in austcnitic stainless steels irradiated in a fast neutron [61] **aid** mixed spectrum [64] fission reactor.

The transition in the macroscopic void swelling behavior from a low-swelling regime to a linear high-swelling regime is directly related to the microscopic void nucleation. However, the duration of the low-swelling transient regime is typically much greater than the dose required for the "steady-stale" cavity density to evolve. Whereas the cavity density in an alloy such as Type 316 steel typically reaches its "saturation" level within a few dpa, the swelling transient can extend to doses in excess of 10 dpa. The difference in the duration of the cavity nucleation and void swelling transients is due to the dose needed to convert gas-stabilized bubbles to bias-driven voids [71,72]. Cavities below a certain critical size are unstable because they emit vacancies faster than they absorb vacancies: such cavities require an internal gas pressure to exist, and therefore only grow as bubbles driven by gas absorption (and at high densities, coalescence). When a cavity reaches a critical size, vacancy absorption overcomes emission and the cavity can grow without further need of additional gas absorption. The macroscopic void swelling transient is largely determined by the time required for the bubbles to reach the critical size and convert to voids. Since cavity nucleation necessarily precedes the conversion of bubbles to voids, the cavity nucleation transient regime is always somewhat shorter than the void swelling transient.

Figure 14 summarizes the dose-dependent void swelling behavior of several different types of austenitic stainless steels [3,4]. In high-purity ternary alloys, the swelling transient may last only a few dpa, whereas in fast-breeder reactor irradiated SA 316 that period is about 30 dpa, and in 20% CW 316 can be about 50 dpa. Studies in which the transient regime for macroscopic swelling during neutron irradiation of advanced austenitic steels extends to damage levels of 70 dpa or more correlate with similar extensions of the "incubation" dose for microscopic void formation [8,69,73-76]. Such prolonged transients in advanced steels are always related to delayed void formation (bubble to void conversion) as opposed to delayed void growth.

ORNL-DWG 83-11074

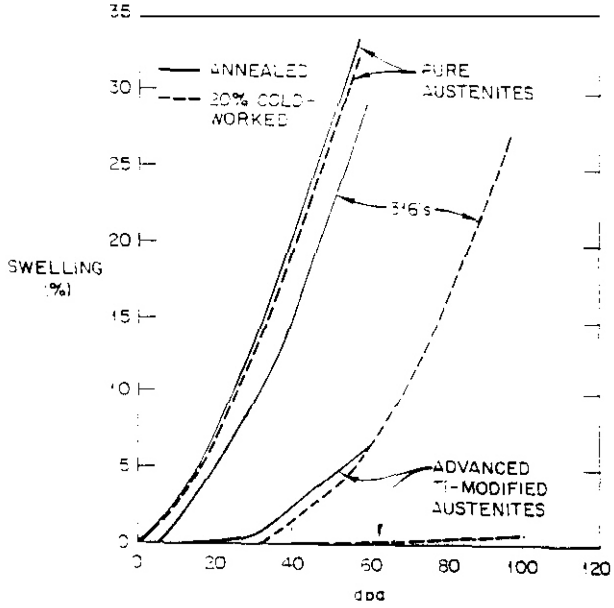

Fig. 14. Trend lines for swelling of austenitic steels irradiated in the EBR-II fast reactor at temperatures of 500 to 650°C [3,4].

Only small dimensional changes can be tolerated in most reactor structural components. Post-transient swelling rates in austenitic steels are typically from 0.4% to 1% per dpa for irradiation temperatures between 400 and 600°C [56,67,77]. Therefore, the most realistic engineering goal for changing materials behavior in an irradiation environment is to extend the low-swelling transient period. The scientific approach to development of swelling-resistant alloys has been to control microstructural development during irradiation in order to delay void formation as long as possible. Several factors can influence the duration of the void swelling "incubation" period. One major factor is the amount of gas available to promote bubble formation and growth. Reaching the critical cavity size for void formation is equivalent to the bubble obtaining a critical number of gas atoms [71,72]. Both residual gases (O) and gases generated by transmutation reactions (H, He) can play a role. The simplest effect of adding some of the solutes commonly found in steels (C, Si, Ti are all potent deoxidizers) is to react with residual oxygen and remove it from the alloy system [78], so that void nucleation now must depend on the transmutation-generated gas buildup during irradiation to stabilize bubble nuclei. In commercial steels. residual gases can play a significant role in the low-dose cavity behavior, whereas at higher doses transmutant gases increasingly influence bubble formation, growth. and conversion to voids. Helium has generally been shown to be the most important gaseous transmutant [71]. The dose to obtain the critical number of gas atoms to induce conversion of bubbles to voids for a fixed bubble density is inversely proportional to the helium generation rate. In addition. helium has a strong direct influence on the evolution of bubble density, with many experimental observations supporting a roughly square-root dependence of the bubble density on the helium generation rate [79]. This ha.. been shown to lead to void swelling behavior which is not a simple, monotonic function of the helium generation rate [8,80].

5. Precipitation and Solute Segregation

Several different precipitate phases normally form in type 316 austenitic sleek during thermal aging at 550 to 900°C in the absence of irradiation [6,15,81-83]. These phases include carbides such as $M_{23}C_6$ and M_6C (and MC if Ti or Nh are present) and intermetallic phases such as Laves, sigma and chi. If type 316 steel is appropriately modified, phosphides (M_2P or M_3P) or G-phase ($M_6Ni_{16}Si_7$) silicides can also precipitate during aging. The main feature of neutron irradiation is to introduce new or composition-modified phases which arc not ohserved during thermal aging. Radiation-induced solute-segregation and radiation-affected precipitation in austenitic steels are complex topics that have been the subject of numerous conferences and review articles [6,7,9,15,81-83]. For this paper, we will merely present a brief overview of the salient features of precipitation that enable us to discuss the overall microstructural evolution. l'hc reader will find more detailed information on precipitation behavior in neutron-irradiated steels in the papers cited ahove.

Figure 15 shows the experimental dose and temperalure regimes in which precipitation has been observed in SA type 316 austenitic steel following fast reactor irradiation 161. The detailed phase evolution in austenitic steel is sensitive to several factors, including metallurgical variables such as alloy composition and irradiation parameters such as spectral or damage-rate effects [7]. Despite such differences, precipitation generally occurs only in the temperature range of about 300 to 800°C for both mixed-spectrum and fast reactor irradiations [6,7]. Significant amounts of prccipitation typically does not begin to occur until doses on the order of 1 to 10 dpa. In some cases, the formation of certain phases peculiar to the irradialion environment (silicides like γ'-Ni_3Si or G-phase) can be delayed until doses in excess of SO dpa are achieved [6,7]. In other cases, *some* radiation-induced phases (fine γ' or M_2P/M_3P phosphide needles) form in the high-temperature regime after only a few dpa and then dissolve at higher doses of 20 to 40 dpa. It is therefore difficult to categorize transient and "steady-state" regimes for radiation-prcduced precipitation. Indeed, the concept of a "steady-state" precipitate microstructure may not he appropriate until doses in excess of 50 dpa. The extended transient associated with the formation of radiation-produced precipitation can have a profound impact on the other microstructural components, such as Frank loop formation atid the total dislocation density.

The formation of precipitates in steels is controlled by solute segregation, which can be substantially modified during irradiation as a result of preferential solute-defect coupling [6,7,9]. Therefore, RIS and the associated precipitation are sensitive to anything Uiat modifies point-defect behavior [84-87]. Solute segregation creates spatially localized variations in *the* alloy composition: initially RIS effects occur

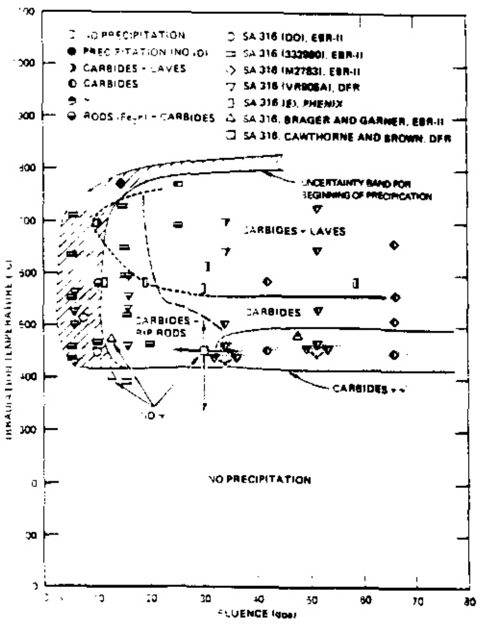

Fig. **15.** Temperature and dose regimes where precipitation is observed in solution annealed Type **316** stainless steel irradiated in fast neutron fission reactors [6].

only at sinks such as Frank **loops** and voids, but at high doses RIS eventually also affects the matrix between the various microstructural features [88-90]. This creates the possibility of triggering precipitation of phases in these segregated volumes that would not normally be seen during aging in alloys of the original bulk composition.

The general effect of FUS in austenitic alloys is to cause the buildup of undersized solutes such as Ni, Si, and to a lesser extent, P at sinks, mainly by the interstitial drag mechanism. Since the interstitial-solute complexes are generally highly mobile, this segregation mechanism usually dominates at lower temperatures and doses. **RIS** typically also causes depletion of oversized (fast-diffusing) substitutional elements like Cr and Mo at sinks during irradiation, mainly due to the inverse-Kirkendall vacancy diffusion mechanism. These effects are usually more prominent at higher temperatures and doses due to the relatively sluggish vacancy diffusivities. Nickel is a slow-diffusing solute in steel, so it is enriched at sinks via both the inverse-Kirkendall mechanism and the interstitial drag mechanism. The buildup of Ni at sinks is a characteristic feature of **RIS** over a wide range of dose and temperature. Conversely, while silicon is enriched at sinks via the interstitial drag mechanism, it is a fast-diffusing substitutional solute and can be depleted via the inverse-Kirkendall mechanism. Figure **16** shows an example of the net effects of ELS described above (Si and Ni enrichment, Cr depletion) that occurred at a large Frank loop in neutron-irradiated austenitic steel [88]. Manganese is an example of an alloying element whose RIS behavior depends on alloy composition. In type **316** steel with a small amount of Mn (2 wt %). little effect of RIS is found, whereas in a Mn-stabilized steel (Russian EP-838, 13.5 wt %), Mn was depleted at sinks instead of Cr due to its faster substitutional diffusivity [88]. While it is simple to say that *RIS* is the dominant mechanism affecting radiation-produced precipitation, it can be seen that the detailed RIS behavior of the various solute elements in each particular heat of steel is complicated.

The precipitates that form in austenitic steels during irradiation can be classified into three general groups, as **outlined** in Table 2 [9,83]. The first precipitate category includes radiation-enhanced and -retarded thermal phases. These precipitates are normally found to have the same phase composition after thermal

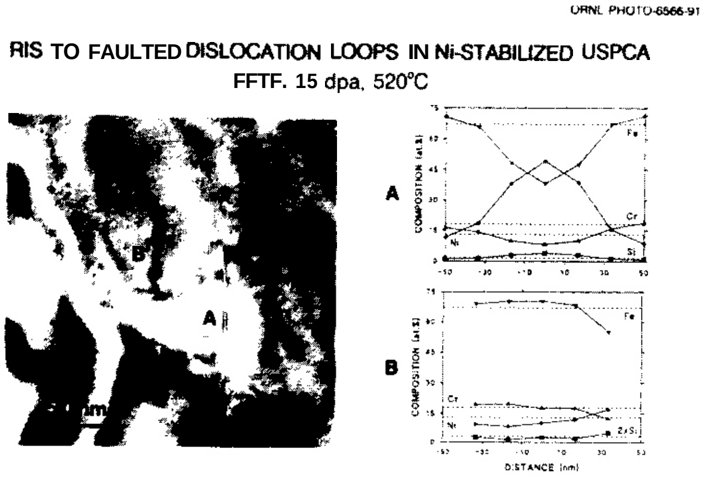

Fig. 16. (a) Nearly edge-on dislocation loops (A,B) in solution annealed **PCA steel** irradiated in the FFTF fast fission reactor to 15 dpa at 520°C. (b) **RIS** profiles at loop **A,** which has **a** diameter of ~100 nm. (c) RIS profiles at **loop** B, which has a diameter of –50 nm. Dashed lines indicate the composition levels in the unperturbed matrix [88].

aging or neutron irradiation, but their relative abundances are different in the two environments. Radiation-enhanced precipitation refers to an enhancement in the kinetics or nucleation level of a thermal precipitate **phase,** or *to* the formation of the phase **at** a lower temperature during reactor irradiation compared to thermal aging of the same steel. Conversely, radiation-retarded precipitation refers to phase formation which is less abundant or shifted *to* higher temperatures in the presence of irradiation. Radiation-enhanced and -retarded **phases** are thermally stable and do not disappear or change chemical composition during postirradiation annealing at the irradiation temperature [91]. The particular thermal phases enhanced or retarded during irradiation depend on the level of RIS during irradiation. When RIS is at a high level (e.g., **SA** 316, fast-reactor irradiation), M_6C and Laves formation is enhanced during irradiation, while $M_{23}C_6$ (and in Ti-modified steels, MC) formation is retarded during irradiation. At a lower level of **RIS** (e.g., CW 316, mixed-spectrum reactor irradiation) a phase like $M_{23}C_6$ that was retarded in the previous case *can* now **be** enhanced during irradiation. Another group of precipitates are the irradiation-modified thermal **phases,** such **as** M_6C and Laves. These phases have the same crystal structure (and often same morphology) **as** the corresponding **phases** formed during aging, hut their phase composition is different during irradiation. Generally the compositional differences reflect the effects of **RIS** (more Ni and Si, **less Cr** and Mo) balanced against the inherent compositional flexibility of the thermal phase. The third **group** of precipitates are radiation-induced phases. Such **phases** are unique to the irradiation environment, and would not form in that particular heat of steel during aging at any temperature. **These** phases **are** thermally unstahle and dissolve during postirradiation annealing **at** the irradiation temperature [91]. The formation of radiation-induced precipitates is caused by **RIS** creating a localized compositional modification around a sink that is sufficient *to* induce precipitation of a new phase.

Radiation-enhanced -retarded phases	Radiation-modified phases	Radiation-induced phases
M_6C, Laves, $M_{23}C_6$, MC, σ, χ	M_6C, Laves, M_2P	$M_6Ni_{16}Si_7$ (G), Ni_3Si (γ'), MP, M_2P, M_3P

Figure 17 shows the fluence-dependent nickel content of Laves precipitates in **SA** and 20%CW **type** 316 steel irradiated **at** 500 to 550°C in fast and mixed-spectrum reactors [9,45,92,93]. Similar fluence-dependent compositional changes have been observed for other precipitates, such **as** the radiation-enhanced MC phase [94]. During thermal aging, the Ni content of the Laves phase is characteristically low (5 to 8 wt %) in both **SA** and 20%CW material. The nickel content of radiation-produced Laves is directly related to the degree **of** compositional modification caused by RIS. When RIS is intense (e.g., when voids are forming easily during irradiation, **SA** 316 in HFIR or 20%CW 316 in EBR-II), the Ni-content of the Laves phase increases significantly with dose, and does not appear to have stabilized even after doses in excess of 50 dpa (Fig. 17a and 17b). Conversely. when RIS **is** low or suppressed (e.g., when a high density of bubbles form and do not convert to voids, 20%CW 316 in HFIR), the Laves Ni-content remains low and does not change during extended irradiation (Fig. 17b). When type 316 stainless steel is aged to produce thermal precipitation **prior** to irradiation, these precipitates consistently dissolve rapidly before the **appropriate** radiation-produced **phases** form [OS]. The detailed behavior of radiation-produced precipitation in steels is very sensitive to irradiation parameters (temperature, He/dpa ratio. damage rate) and metallurgical variables (heat-to-heat compositional variations, pretreatment).

ORNL-DWG 83-15910/ORNL-DWG 82-13222

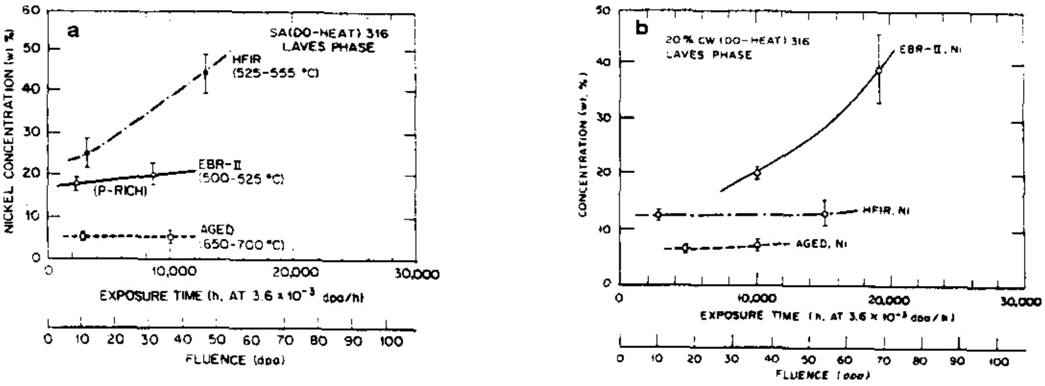

Fig. 17. Energy dispersive x-ray spectroscopy measurements of the Ni concentntion of individual Laves phase particles on extraction replicas from a) **SA** 316 and b) CW **316** after thermal aging or neutron irradiation in a fast neutron (EBR-II) or mixed spectrum (HFIR) fission reactor [45].

The presence of radiation-modified or -induced phases during irradiation at temperatures of 450 to 600°C is generally a sign of poor radiation resistance. These precipitates are indicators that significant solute segregation has taken place during the irradiation, which implies that a high level of solute-coupled point defect fluxes were present. Since high point defect fluxes generally accelerate deleterious radiation-induced processes such as void swelling, the presence of high levels of RIS (directly visible in the form of radiation-induced or modified precipitates) is an indication of a microstructure with poor radiation stability. Conversely, the presence of thermally stable precipitates (radiation-enhanced or -retarded) is an indicator of **a** radiation-resistant microstructure. As discussed below, the fine radiation-induced M_2P precipitates in phosphorus-modified steels are a notable exception to this general rule.

Precipitates can directly affect partitioning of defect fluxes when the matrix-precipitate interfaces act **as** sinks for point defects. Relatively high precipitate densities are required for such precipitate sink-strength effects to be significant in irradiated materials. Due to their small size and high density, the radiation-induced M_2P precipitates that form in phosphorus-modified steels effectively disperse He atoms and promote point defect recombination. Since the M_2P precipitates are resistant to coarsening up to high doses [96], this produces a swelling-resistant microstructure. The γ' radiation-induced precipitates also initially act to suppress void swelling due to their high density (high sink strength). However, γ' coarsens rapidly during irradiation at temperatures $\geq$500°C [96]. This reduces the γ' sink strength to a level where it is not effective in dispersing He atoms or promoting point defect recombination, producing poor swelling resistance. Most of the radiation-induced and -modified phases in austenitic steels (Table **2**) have undersized volumetric misfit strains relative to the lattice. Such misfit-strain effects lead to **a** further enhancement of void swelling because interstitials will be preferentially attracted to the precipitate-matrix interface, creating a precipitate-**based** interstitial **bias** component that complements the more familiar dislocation bias. Another way in which certain precipitates directly enhance void formation and growth is when coarse precipitate particles are attached to voids of comparable size [92,96]. Generally, such behavior is observed for radiation-induced or modified G, Laves and M_6C phases [92,96,97], which is an indication of strongly coupled RIS and vacancy fluxes. Since RIS is normally strong **to** large voids, it is logical that the formation of phases that require RIS would occur at void sites. Moreover, the formation and growth of such RIS-compatable precipitates at voids then directly enhances void growth by mechanisms that involve the precipitate as a vacancy collector for the void [92,96,98].

Precipitate formation is just one of the microstructural factors that contribute to the extension of the low-swelling transient regime in type 316 steel relative to simple ternary alloys. However, precipitation **is** the dominant microstructural feature responsible for extension of the low-swelling transient to doses in excess of 80 dpa in swelling-resistant advanced steels. In this case, the combination of alloy compositional modification (Ti, C, Si, P additions) and pretreatment condition (20-25% CW) causes fine precipitation of radiation-enhanced thermal phases (MC and/or FeTiP needles) instead of the radiation-affected RIS-compatable phases generally associated with voids. These special carbides and phosphides contain titanium (and Mo, **V** and Nb in some cases), and generally contain little or no nickel and silicon. By contrast, the radiation-induced or -modified phases (G, γ', M_6C and Laves) have nickel and silicon as their main constituents.

The fine stable thermal phases that form in advanced **steels** during irradiation at 400 to 600°C impart void formation resistance through several mechanisms, which include: (a) interfacial helium trapping, often resulting in finer and more profuse helium bubble nucleation **than** would occur without the precipitates [96,99,100], (b) increased **sink** strength, which promotes point defect recombination at the precipitate/matrix interface [96], and (c) precipitate pinning of dislocations to hinder climb associated with excess interstitial absorption [96]. Such void-resistant microstructures establish themselves quickly during irradiation and then remain relatively unchanged for long periods of time [9,69,73-76,93]. However, they represent a transient rather than a "steady state" microstructure during irradiation. Indeed, as voids finally begin to form at higher doses, the fine thermal precipitates begin to dissolve [69,73-76,94,101]. This eventually produces a transition from the low-swelling to the high-swelling rate regime. **A** key point is that very dramatic changes occur in the microstructure before macroscopic swelling changes are observed. Fast reactor irradiation **data** from **both** the French 20-25% CW 15-15Ti steel modified with B+P and the Japanese PNC316 steel modified with Ti+P+B indicate that the extension of the low-swelling transient to beyond E0 dpa depends on the existence of fine dispersions of MC or FeTiP precipitates and their resistance to dissolution [69,73-76]. The French data in particular indicates that such microstructures may be stable to more than 1.50dpa [75].

6. Discussion

There is no simple relation that connects the neutron displacement damage level directly to the establishment of a "steady-state" or saturation microstructure in austenitic stainless steel. Although the concept of **a** "steady-slate" microstructure may be viable in the low-temperature irradiation regime, that concept **loses** meaning for many of the microsuuctural components in certain types of austenitic steels at higher irradiation temperatures. The duration of the macroscopic low-swelling transient regime is the result of a complex microstructural evolution, which in turn depends (synergistically) **on** many other irradiation parameters and metallurgical variables, not just dose.

Io the "**low** temperature" regime (<300°C), the high sink density associated wilh thermally stable vacancy clusters produced in the displacement cascades suppresses the concentration of freely-migrating point-defects and inhibits their long-rmge migration. Hence, die length of the microstructural transient at these temperatures is largely controlled by the dose needed to induce significant physical cascade overlap (i.e., - 0.1 dpa). However, despite the high density of sinks, the low point defect mobilities associated with this temperature regime can lead to extended transients in the point defect concentrations [10,50]. For irradiation temperatures below about 150°C, the time required for the point defect concentrations to reach steady state can exceed the duration of typical reactor irradiation experiments. For example, the calculated point defect transient lasts about six years at 100°C [50]. The interstitial concentrations would he much higher and the corresponding vacancy concentration much lower than their steady slate values during this transient. Since microstructural evolution is generally driven by the difference in the point defect fluxes, the **use** of theoretical models which assume steady slate point defect concentrations can lead to significant errors in predicting microstructural evolution at low temperatures. The significant dislocation recovery shown at **low** temperatures in Fig. 10 and the surprisingly **large** amount **of** creep observed **in** Steel irradiated at <150°C 1501 **are** examples **of** the potential impact of the extended point defect transient. Hence, the relationship between point-defect behavior and microstructural evolution is complex, even at low irradiation temperatures.

The evolution of the dislocation loop and cavity densities in simple Fe-Cr-Ni ternaries during irradiation in the "high-temperature" regime **(300** to 700°C) can be described **by** a rclatively rapid initial microstructural transient that is completed within damage levels of about 0.5 to 5 dpa. This initial transient **is** subsequently followed by a secondary microstructural transient **that can** extend to doses in excess of 50 dpa, due to interaction between the various microstructural components. The initial microstructural transient regime for the total dislocation density **(loops** plus network) generally requires doses in excess ***of*** **10** dpa and is controlled primarily **by** the process of loop growth and unfaulting. Since solute segregation to dislocation loops can be pronounced (Fig. 16) [88], the duration of the transient regime for the total dislocation density may be influenced by RIS. The evolution of bubbles and voids in the high-temperature regime is controlled by RIS-modified accumulation of helium atoms and vacancies. Microcompositional studies [102,103] have found that substantial RIS ***of*** nickel is dctectahle around tiny helium bubbles and small voids. Other studies have shown thick **(20-40** nm) RIS zones around larger voids [6,9], so that RIS is involved in all stages of void evolution. Under certain conditions at 400 to 550°C, the initially homogeneous austenite matrix can break up into a heterogeneous mixture of austenite (the Ni-rich regions around sinks) and a-ferrite at doses in excess of 30 dpa [7,90,104,105]. This may represent the true "steady state" microstructure during irradiation (and corresponds with swelling saturation), but is technologically uninteresting since it only occurs after a Large amount of void swelling and is a highly embrittled mechanical condition.

Clearly the most difficult phenomena to classify in terms of a "steady state" microstructure is radiation-produced precipitation. In most steels, the precipitate behavior falls somewhere between the extremes of highly RIS-affected phase formation and radiation-enhanced thermal phase formation with relatively weak RIS effects. Because both of these precipitate classes require sustained solute segregation and point defect fluxes to form and remain stable, this component of the evolving microstructure usually lags behind the others during irradiation. Since the stability of fine radiation-induced precipitates is dependent on the same mechanisms that caused them to form, subtle changes in the global microstructure. point defect fluxes, or RIS generally affects *the* precipitate structure more than the void or dislocation network structures. The transient for precipitate formation in relatively simple alloys like type 316 is generally greater than 10 dpa.

In advanced swelling-resistant steels, fine dispersions of thermal phases that are not compatible with RIS (e.g., MC) develop rapidly during irradiation and remain stable up to high doses (>50 dpa). This dense precipitate microstructure promotes uniform dispersal of helium atoms and forces virtually all of the freely migrating defects to recombine at sinks, which depresses the vacancy supersaturation and thereby inhibits cavity nucleation. The finely dispersed sinks also dilute KIS to the point that it is not significant. The extended period during which this nearly-thermal microstructure exists is not a true "steady state", because when point defect concentrations eventually move toward "steady state" values and KIS begins to develop, the "thermal" precipitates dissolve and the microstructure enters a new transient that evolves toward a strongly radiation-affected microstructure of voids, dislocations and radiation-modified or -induced precipitates.

The complexities in the microstructural evolution of austenitic steels in the transient regime may be contrasted with the relatively straightforward behavior of pure metals [38]. The irradiation dose needed for void and dislocation loop nucleation to be completed in Ni during neutron irradiation at elevated temperature is only about 1 dpa, and compared to austenitic steel the length of the transient is relatively insensitive to neutron spectrum differences. This comparison highlights the importance of solutes and precipitates on the extension of the transient regime. The situation for steel becomes increasingly complex as additional solutes are added to the base ternary composition. The strong synergistic effects between the various alloying elements, and interactions between the various components of the microstructure cause an extension of the microstructural transients and the macroscopic low-swelling regime to very high doses in technologically relevant steels. Mechanistically, macroscopic low swelling behavior is only possible when the microstructure inhibits the normally efficient biased partitioning of vacancies and interstitials to sinks and instead promotes point defect recombination during irradiation.

7. Conclusions

The damage level needed to achieve a "steady state" microstructural condition in neutron-irradiated austenitic stainless steel varies from less than 0.1 dpa to greater than 50 dpa, depending on the irradiation conditions and the specific microstructural component being investigated. The evolution of most of the microstructural components can be characterized by a relatively rapid initial transient regime lasting for a damage level of about 1 dpa, followed by a slowly evolving secondary transient regime. Due to interactions between the various microstructural components which evolve at different rates, the overall microstructure typically remains in this secondary transient regime up to very high damage levels (>50 dpa). In some (but not all) cases, steady state approximations may be invoked for the purposes of irradiation effects modeling in this secondary transient regime.

Despite the hundreds of neutron irradiation studies performed on austenitic stainless steels over the **past** 25 years, it is apparent that further irradiation experiments **are** needed due to a lack of systematic data at low temperatures (<350°C) and low doses (<10 dpa). Data **are** needed on both complex and simple model alloys to further our understanding of the microstructural evolution. For fusion reactor applications, single-variable experiments at fusion-relevant He/dpa ratios (utilizing spectral tailoring or isotopic tailoring techniques) are needed to investigate the important experimental panmeters and controlling mechanisms associated with the transient regime.

Acknowledgments

This work was sponsored by the Office of Fusion Energy and the Office of Basic Energy Sciences, U.S. Department of Energy, under contract DE-AC05-84OR21400 with **Martin** Marietta Energy Systems, Inc.

References

[1] P.J. Maziasz and D.N. Braski, J. Nucl. Mater. 122&123 (1984) 311.
[2] H.R. Brager and F.A. Garner, J. Nucl. Mater. 108&109 (1982) 347.
[3] P.J. Maziasz, J. Nucl. Mater. 122&123 (1984) 472.
[4] H.R. Brager and F.A. Garner, J. Nucl. Mater. 117 (1983) 159.
[5] F.A. Gamer and H.R. Brager, in Effects of Radiation on Materials, **Vol.** I, ASTM STP 870, Eds. F.A. Garner and J.S. Pemn (ASTM, Philadelphia, 1985) p. 187.
[6] P.J. Maziasz and C.J. McHargue, Intern. Mater. Kev. 32 (1987) 190.
[7] P.J. Maziasz, J. Nucl. Mater. 169 (1989) 95.
[8] R.E. Stoller, J. Nucl. Mater. 174 (1990) 289.
[9] **P.J.** Maziasz. J. Nucl. Mater. 205 (1993), in press.
[10] L.K. Mansur, J. Nucl. Mater., in press.
[11] R.E. Stollcr and G.R. Odette, in Radiation-Induced Changes in Microstructure (Pan I), **ASTM** STP 955, Eds. **F.A.** Garner, N.H. Packan and A.S. Kumar (ASTM, Philadelphia, 1987) **p.** 371.
[12] G.E. Lucas. J. Nucl. Mater.. in press.
[13] **J.I.** Bramman, K.Q. Bagley, C. Cawthorne, E.J. Fulton and W.D.J. Sinclair, in Voids Formed by Irradiation of Reactor Materials, Eds. S.F. Pugh, M.H. Loretto and D.I.K. Noms (BNES, 1971) **p.** 27.
[14] H.J. Bergmann. W. Dietz and D. Haas, J.Nucl. Mater. 65 (1974) 210.
[15] D.R. Harries, in Mechanical Behaviour and Nuclear Applications **of** Stainless Steel at Elevated Temperatures (The Merals Society, London, 1982) **p.** 1.
[16] B.A. Chin, R.J. Neuhold and J.L. Straalsund, Nucl. Tech. 57 (1982) 426.
[17] **J.L.** Seran et al., in Effects of Radiation on Materials, Vol. I, ASTM STP 870, Eds. F.A. Gamer and J.S. Perrin (ASTM, Philadelphia, 1985) p. 233.
[18] **P.J.** Maziasz and T.K. Roche, J. Nucl. Mater. 103&104 (1981) 797.
[19] J.W. Corbett, Electron Radiation Damage in Semiconductors and Metals, Solid State Physics Suppl. 7 (Academic **Press,** New York, 1966).
[20] W. Schilling, P. Ehrhart and K. Sonnenberg, in Fundamental Aspects of Radiation Damage in Metals, Vol. 1, Eds. M.T. Robinson and **F.W.** Young, Jr., CONF-751006-P1, (NTIS. Springfield, VA, 1975) **p.** 470.
[21] C. Dimitrov, **A.** Benkaddour, **O.** Dimitrov, C. Corbel and P. Moser, Mater. Sci. Forum 15-18 (1987) 1275.
[22] P.J. Maziasz, J. Nucl. Mater. 191-194 (1992) 701.
[23] H.R. Brager and **J.L.** Straalsund. J. Nucl. Mater. 46 (1973) 134.

[24] E.E. Bloom and J.O. Stiegler, in Effects of Radiation on Substructure and Mechanical Properties of Metals and Alloys, ASTM SIP 529 (ASTM, Philadelphia, 1973) p. 360.

[25] H.R. Brager, J. Nucl. Mater. 57 (1975) 103.

[26] H.R. Brager, F.A. Garner and G.L. Guthrie, J. Nucl. Mater. 66 (1977) 301.

[27] P.J. Barton, B.L. Eyre and D.A. Stow, J. Nucl. Mater. 67 (1977) 181.

[28] P.J. Maziasz, Trans. ANS 39 (1981) 433.

[29] M.P. Tanaka, S. Hamada, A. Hishinuma, and P.J. Maziasz, J. Nucl. Mater. 155-157 (1988) 801.

[30] S. Hamada, M. Suzuki, P.J. Maziasz, A. Hishinuma and M.P. Tanaka, in Effects of Radiation on Materials, ASTM STP 1046, Vol. I, Eds. N.H. Packan, R.E. Stoller and A.S. Kumar (ASTM, Philadelphia, 1989) p. 172.

[31] H.R. Brager, F.A. Gamer, E.R. Gilbert, J.E. Flinn and W.G. Wolfer, in Radiation Effects in Breeder Reactor Structural Materials, Eds. M.L. Bleiherg and J.W. Bennett (TMS-AIME, New York 1977) p. 727.

[32] H.R. Brager, E.R. Gilbert and J.L. Straalsund, Rad. Effects 21 (1974) 37.

[33] B.L. Eyre, in Fundamental Aspects of Radiation Damage in Metals, Vol. 2, Eds. M.T. Robinson and F.W. Young, Jr. CONF-751006-P2 (NTIS, Springfield, VA, 1975) p. 729.

[34] T. Muroga, Y. Miyamoto, H. Watanabe and N. Yoshida, J. Nucl. Mater. 155-157 (1988) 810.

[35] S.J. Zinkle and K.L. Sindelar, J. Nucl. Mater. 155-157 (1988) 1196.

[36] N. Yoshida, J. Nucl. Mater. 174 (1990) 220.

[37] T.M. Robinson and M.L. Jenkins, Phil. Mag. A 34 (1981) 999.

[38] B.N. Singh and S.J. Zinklc, in press, J. Nucl. Mater.

[39] H.R. Higgy and F.H. Hammad, J. Nucl. Mater. 55 (1975) 177.

[40] H.R. Brager, L.D. Blackburn and D.L. Greenslade, J. Nucl. Mater. 122&123 (1984) 332.

[41] H. Kawanishi and S. Ishino, J. Nucl. Mater. 155-157 (1988) 806.

[42] H. Kawanishi and S. Ishino, J. Nucl. Mater. 179-181 (1991) 534.

[43] T. Sawai. P.J. Maziasz and A. Hishinuma. J. Nucl. Matcr. 179-181 (1991) 519.

[44] N. Yoshida, Q. Xu, H. Watannhc, T. Muroga and M. Kiritani, J. Nucl. Mater. 191-194 (1992) 1114.

[45] P.J. Maziasz. Effects of He Content on Microstructural Development in Type 316 Stainless Steel under Neutron Irradiation, ORNL-6121 (Oak Ridge, TN, 1985).

[46] J.I. Bramman, C. Brown, C. Cawthorne, E.J. Fulton and G.A.B. Linckar, in The Physics of Irradiation Produced Voids, UKAEA Report AERE-R7934, Ed. R.S. Nelson (Harwell, UK. 1975) p. 71.

[47] G.D. Johnson, F.A. Gamcr. H.R. Bragcr and R.L. Fish, in Effects of Radiation on Materials, ASTM STP 725, Eds. D. Kramer, H.R. Brager and J.S. Perrin (ASIM, Philadelphia, 1981) p. 393.; F.A. Garner, M.L. Hamilton, N.F. Panayotou and G.D. Johnson, J. Nucl. Mater. 103&104 (1981) 803.

[48] M.L. Grossheck, K. Ehrlich aid C. Wassilew, I. Nucl. Matcr. 174 (1990) 264.

[49] J.D. Elen and P. Fenici, J. Nucl. Mater. 191-194 (1992) 766.

[50] R.E. Stoller, M.L. Grossbeck and L.K. Mansur, in Effects of Radiation on Materials, ASTM STP 1125, Eds. R.E. Stoller, A.S. Kumar aiid D.S. Gelles (ASTM, Philadelphia, 1992) p. 517.

[51] K.Q. Bagley, J.I. Bramman and C. Cawthorne, in Voids Formed by Irradiation of Reactor Materials, Eds. S.F. Pugh, M.H. Loretto and D.I.R. Norris (BNES, 1971) p. 1.

[52] K. Farrell and N.H. Packan, in Effects of Radiation on Materials, ASTM STP 782, Eds. H.R. Brager and J.S. Perrin (ASTM, Philadelphia 1982) p. 953.

[53] C. Brown, J.K. Butler and E.J. Fulton, in Irradiation Bchavior of Metallic Materials for Fast Reactor Core Components, Eds. J. Poirier and J.M. DuPouy (CEA, Gif-Sur-Yvette. France, 1979) p. 129.

[54] W.K. Appleby and U.E. Wolff, in Effects of Radiation on Substructure and Mechanical Properties of Metals and Alloys, ASTM STP 529 (ASTM. Philadelphia, 1973) p. 122.

[55] H.R. Brager and F.A. Gamer, J. Nucl. Mater. 103&104 (1981) 993.

[56] F.A. Gamer, J. Nucl. Mater. 122&123 (1984) 459.

[57] F.A. Garner, J. Nucl. Mater. 174 (1990) 229.

[58] N. Sekimura, F.A. Garner and R.D. Griffin, J. Nucl. Mater. 191-194 (1992) 1234.

[59] P.J. Barton and P.R.B Higgins. in Irradiation Effects on Structural Alloys for Nuclear Reactor Applications, ASTM STP 484 (ASTM, Philadelphia. 1970) p. 362.

[60] J.I. Bramman. K.Q. Bagley, C. Cawthorne and J.E. Fulton, in Radiation-Induced Voids in Metals, Eds. J.W. Corhett and L.C. Ianniello. COW-710601 (NTIS. Spring field, VA, 1972) p. 125.

[61] T. Muroga, K. Araki, Y. Miyamoto and N. Yoshida, J. Nucl. Mater. 155-157 (1988) 1118.

[62] L.K. Mansur. Nucl. Tech. 40 (1978) 5.

[63] T. Muroga, F.A. Gamer and S. Ohnuki. J. Nucl. Mater. 179-181 (1991) 546.

[64] P.J. Maziasz and M.L. Grossbeck, in Alloy Development for Irradiation Performance Semiann. Progress Report. DOE/ER-0045/7 (Sept. 1981) p. 28.

[65] F.A. Gamer and A.S. Kumar, in Radialion-Induced Changes in Microstructure (Part I), ASTM STP 955, Eds. F.A. Gamer, N.H. Packan and A.S. Kumar, (ASTM, Philadelphia, 1987) p. 289.

[66] N. Sekimura, F.A. Gamer and J.W. Newkirk, J. Nucl. Mater. 191-194 (1992) 1244.

[67] F.A. Gamer and H.R. Brager, J. Nucl. Mater. 155-157 (1988) 833.

[68] E.H. Lee and N.H. Packan. in Effects of Radiation on Materials, Vol. I, ASTM STP 1046, Eds. N.H. Packan, R.E. Stoller and A.S. Kumar (ASTM, Philadelphia, 1989) p. 133.

[69] M. Itoh, S. Onose arid S. Yuhara, in Radiation-Induced Changes in Microstructure (Part I), ASTM STP 955, Eds. F.A. Gamer. N.H. Packan and A.S. Kumar (ASTM, Philadelphia, 1987) p. 114.

[70] P.J. Maziasz, in Fusion Reactor Materials Scmiann. Progress Report, DOE/ER-03 13/10, (July 1991) p. 99.

[71] R.E. Stoller and G.K. Odette, in Radiation-Induced Changes in Microstructure (Part I), Eds. F.A. Garner, N.H. Packan and A.S. Kumar, ASTM STP 955 (ASTM, Philadelphia, 1987) p. 358.

[72] L.K. Mansur and W.A. Coghlan, J. Nucl. Mater. 119 (1983) 1.

[73] P. Duhuisson, A. Maillard. C. Delalande, D. Gilbon and J.L. Seran, in Effects of Radiation on Materials. ASTM STP 1125. Eds. R.E. Stoller, A.S. Kumar and D.S. Gelles (ASTM, Philadelphia, PA, 1992) p. 995.

[74] J.L. Seran, el al., ihid, p. 1209.

[75] A. Maillard, H. Touron, J.L. Seran arid A. Chalony, in Effects of Radialion on Materials, ASTM STP 1175, eds. A.S. Kumar, D.S. Gelles and R.K. Nanstad (ASTM, Philadelphia, PA, 1993) in press.

[76] I. Shihahara, Sukai, S. Onose, and S. Shikakura, "Irradiation Performance of Modified 316 Stainless Steel for Moniuo Fuel." J. Nucl. Mater. in press.

[77] R.E. Stoller, in Fusion Reactor Materials Semiann. Progress Report, DOE/ER-0313/1 (1987) p. 171.

[78] S.J. Zinkle and E.H. Lee. Met. Trans. A 21 (1990) 1037.

[79] G.R. Odette, P.J. Maziasz and J.A. Spitznagel. J. Nucl. Mater. 103&104 (1981) 1289.

[80] R.E. Stoller and G.R. Odette, in Effects of Radialion on Materials, ASTM STP 782, Eds. H.R. Brager and J.S. Pemn (ASTM, Philadelphia, 1982) p. 275.

[81] T.M. Williams, in Effects of Radiation of Materials, ASTM STP 782, Eds. H.R. Brager and J.S. Perrin (ASTM, Philadelphia, 1982) p. 166.

[82] W.J.S. Yang, in Radiation-Induced Changes in Microstructure, ASTM STP 955, Eds. F.A. Garner, N.H. Packan and A.S. Kumar (ASTM. Philadelphia, 1887) p. 628.

[83] E.H. Lee, P.J. Maziasz and A.F. Rowcliffe, in Phase Stability During Irradiation, Eds. J.R. Holland, L.K. Mansur and D.I. Potter (TMS-AIME, Warrendale, PA, 1981) p. 191.

[84] P.R. Okamoto and H. Wiedersich. J. Nucl. Mater. 53 (1974) 336.

[85] R.A. Johnson and N.Q. Lam, Phys. Rev. B, 13 (1976) 4364.

[86] R.A. Johnson and N.Q. Lam, J. Nucl. Mater. 69&70 (1978) 424.

[87] H. Weidersich, P.R. Okamoto and N.Q. Lam, J. Nucl. Mater. 83 (1979) 98.

[88] E.A. Kenik and K. Hojou, J. Nucl. Mater. 191-194 (1992) 1331.

[89] E.A. Kenik, J. Nucl. Mater. 187 (1992) 239.

[90] D.L. Porter and E.L. Wood. J. Nucl. Mater. 83 (1979) 90.

[91] P. Wilkes, J. Nucl. Mater. 83 (1979) 166.

[92] D.F. Pedraza and P.J. Maziasz, in Radiation-Induced Changes in Microstructure (Part I), ASTM STP 955, Eds. F.A. Garner, N.H. Packan and A.S. Kumar (ASTM, Philadelphia, 1987) p. 161.

[93] P.J. Maziasz, in Proc. Symp. MiCon 86: Optimization of Processing, Properties and Service Performance Through Microstructural Control, ASTM STP 979, Eds. B.L. Bramfitt, R.C. Benn, C.R. Brinkman and G.F. Vander Voort (ASTM, Philadelphia, PA, 1988) p. 116.

[94] M. Suzuki, S. Hamada, P.J. Maziasz, S. Jitsukawa and A. Hishinuma, J. Nucl. Mater. 191-194 (1992) 1351.

[95] D.L. Porter, J. Nucl. Mater. 92 (1980) 155.

[96] E.H. Lee and L.K. Mansur, Met. Trans A 23 (1992) 1977.

[97] A.S. Bakai, et al., J. Nucl. Mater. 185 (1991) 260.

[98] L.K. Mansur, Phil. Mag. A 44 (1981) X67.

[99] P.J. Maziasz, Scripta Met. 14 (1980) 1251.

[100] W. Kesternich, Rad. Eff. 78 (1983) 261.

[101] E.H. Lee, N.H. Packan and L.K. Mansur, I. Nucl. Mater. 117 (1983) 123.

[102] C.M. Shepherd and S.M. Murphy, J. Nucl. Mater. 172 (1990) 143.

[103] C.M. Shepherd, J. Nucl. Mater. 175 (1990) 170.

[104] D.L. Porter, J. Nucl. Mater. 79 (1979) 787.

[105] H.R. Brager and F.A. Garner, in Phase Stability During Irradiation, Eds. J.R. Holland, L.K. Mansur and D.I. Potter (TMS-AIME, Warrendale, PA, 1981) p. 219

FRACTURE TOUGHNESS OF IRRADIATED CANDIDATE MATERIALS FOR ITER FIRST WALL/BLANKET STRUCTURES: PRELIMINARY RESULTS - D. J. Alexander, J. E. Pawel, M. L. Grossbeck, and A. F. Rowcliffe (Oak Ridge National Laboratory)

OBJECTIVE

The purpose of this work is to determine the effect of irradiation at low temperatures (less than 300°C) to damage levels of about 3 dpa on the mechanical properties, in particular the fracture toughness, of candidate materials for the International Thermonuclear Experimental Reactor (ITER) first wall/blanket structures.

SUMMARY

Candidate materials for first wall/blanket structures in ITER have been irradiated to damage levels of about 3 dpa at temperatures of either 60 or 250°C. Preliminary results have been obtained for several of these materials irradiated at 60°C. The results show that irradiation at this temperature reduces the fracture toughness of austenitic stainless steels. but the toughness remains quite high. The unloading compliance technique developed for the subsize disk compact specimens works quite well, particularly for materials with lower roughness. Specimens of materials with very high toughness deform excessively, and this results in experimental difficulties.

PROGRESS AND STATUS

Introduction

Work is under way at Oak Ridge National Laboratory (ORNL) to evaluate the fracture toughness of candidate materials for first wall/blanket structure applications in the ITER. A variety of austenitic stainless steels are being examined, as well as several additional materials. These materials have been irradiated in the High Flux Isotope Reactor (HFIR) at ORNL. To date, three capsules have been designed, fabricated, and irradiated to dose levels of approximately 3 dpa. These capsules were designed for irradiation temperatures of either 60 to 125°C (capsules HFIR-JP-18 and -19) or 250 to 300°C (HFIR-JP-17) [1-3]. All of the capsules have been successfully irradiated in HFIR, and two of the capsules (JP-18 and -19) have been disassembled. Work has begun on testing the fracture toughness specimens from these capsules, and some preliminary results are reported here.

Experimental Procedure

Several variants of type 316 austenitic stainless steel are being considered for structural applications in ITER. These include American and Japanese type 316 steels (designated US316 and J316, respectively), a European type 316L steel (EC316L), and the JPCA alloy. Some ferritic steels were also included in this experiment, including HT-9 and F82H. Specimens were fabricated from material in several different conditions, including annealed or cold worked, as well as weldments.

In order to utilize the HFIR target region for the irradiations, the specimen size was severely limited. Therefore, a small disk compact specimen 12.5 mm in diameter was selected for the fracture toughness experiments. Techniques were developed for generating the J-integral-resistance (J-R) curve using either unloading compliance (UC) or dc-potential drop (PD) to monitor crack extension [4,5]. Initial trials showed that either method could be used to develop useful fracture toughness data from these small specimens [4-6]. As a result of the success of the laboratory trials, it was decided to use the unloading compliance technique for testing the irradiated specimens.

The disk compact specimens [designated DC(T)] were 12.5 mm in diameter by 4.63 mm thick. All specimens were fabricated from the middle of the thickness of the parent plates of material, with the notch oriented so that crack growth would occur parallel to the rolling direction (T-L orientation). The specimens were fatigue precracked at room temperature and side grooved 10% of their thickness on each side, prior to irradiation. Filler pieces were inserted in the loading holes and in the notches to reduce disturbances in the flow of cooling water over the specimens in the capsule and to improve the uniformity of heat transfer across the specimens.

Capsules JP-18 and 19 completed their irradiation in October 1991 [3], and have been disassembled. Capsule JP-17 completed its irradiation in February 1992 [3] and is awaiting disassembly. After the disassembly, the inserts in the individual specimens were pushed out of the loading holes using an arbor press and punch. The filler in the notch was removed with the aid of a hammer and a thinned screwdriver blade.

Tests were conducted in general accordance with American Society for Testing and Materials standards E 813-89, Standard Test Method for J_{Ic}, A Measure of Fracture Toughness, and E 1152-87, Standard Test Method for Determining J-R Curves. The specimens were tested with a computer-controlled testing and data acquisition system [7]. Tests in the laboratory used an 89-kN capacity servohydraulic test machine. In the hot cell, a 445-kN servohydraulic testing machine with an ultraprecision 22-kN load cell was used. All tests were run in strain control. The displacements were measured with an "outboard" clip gage that seated in grooves machined on the outer edge of the specimen along the load line [4,5]. This arrangement provided very good load-displacement and UC results. Test temperatures were maintained within ±2°C of the desired temperature with a split-box furnace that enclosed the specimen and the grips during the test. Temperature was monitored throughout the testing with a thermocouple that was held in contact with the specimen by a spring-loaded clip. Since tensile tests for materials irradiated under these conditions have not yet been conducted, estimated values of the yield and ultimate tensile strengths and Young's moduli were used in the calculations for the J-R curves. These estimated values are given in Table 1.

After testing, the specimens were heat tinted by placing them on a hot plate and heating them until a noticeable color change had occurred. The specimens were cooled in liquid nitrogen and then broken open. The initial and final crack lengths for the unirradiated specimens were measured with the use of an optical measuring microscope. For the irradiated specimens, photographs of the fracture surfaces were fastened to a digitizing tablet to measure the crack lengths.

Results and Discussion

Six different materials were tested in the laboratory to establish baseline fracture toughness properties for the unirradiated materials. These include EC316L annealed, JPCA annealed, JPCA cold worked (15%), J316 annealed, US316 cold worked, and HT-9. The EC316L and JPCA annealed material was tested at 22, 100, and 200°C; the remaining tests were conducted at 22°C. EC316L and JPCA annealed irradiated specimens were tested in the hot cell at 25, 100, and 200°C.

Materials with very high toughness and low yield strength, such as the annealed austenitic stainless steels, proved to be more difficult to test than material with lower toughness such at HT-9. The soft, tough materials showed enormous crack-tip blunting before stable crack growth began. This resulted

Table 1. Estimated tensile properties

Alloy	Condition	Temperature (°C)	Strength (MPa) Yield	Strength (MPa) Ultimate tensile	Young's modulus (GPa)
EC316L annealed	Unirradiated	22	275	582	193
		100	225	504	186
		200	186	441	179
EC316L annealed	Irradiated	22	425	650	193
		100	375	600	186
		200	325	550	179
JPCA annealed	Unirradiated	22	250	580	193
		100	230	520	186
		200	210	460	179
JPCA annealed	Irradiated	22	410	630	193
		100	390	570	186
		200	370	510	179
JPCA cold worked	Unirradiated	22	671	710	193
US316 cold worked	Unirradiated	22	725	785	193
J316 annealed	Unirradiated	22	295	570	193
HT-9	Unirradiated	22	650	800	207

in gross changes in the specimen geometry (see Fig. 1), and so the crack length predictions were not very accurate. The J-R curve is much steeper than the calculated blunting line. In these cases, the data were used to calculate a blunting line. A straight line was fit by eye through the initial portion of the data points, and a second line was drawn parallel to the first but offset by an amount corresponding to a crack extension of 0.2 mm (see Fig. 2). The candidate toughness value J_Q was then determined from the intersection of the data with this offset line. Materials with lower toughness, such as the cold-worked austenitic stainless steels, behaved in a much more conventional manner. For these materials, the data followed the calculated blunting line quite closely, so no additional construction was required. These specimens also showed very good agreement between the measured and predicted final crack lengths.

The results of the testing are given in Table 2 and the various J-R curves are shown in Figs. 3 to 7. These curves show that the toughness of the austenitic steels is very high. In most cases, the toughness decreases slightly as the temperature increases, but remains very high. The **EC316L** annealed steel shows a slight decrease in toughness after irradiation. The **JPCA** annealed material responds much more to irradiation, with a much greater decrease in toughness than the **EC316L** steel showed. Even in this case, the toughness is still quite high, as Table 2 shows. The other materials also have high toughness values, with the exception of the cold-worked **US316** steel. This material has by far the lowest toughness of all the materials tested.

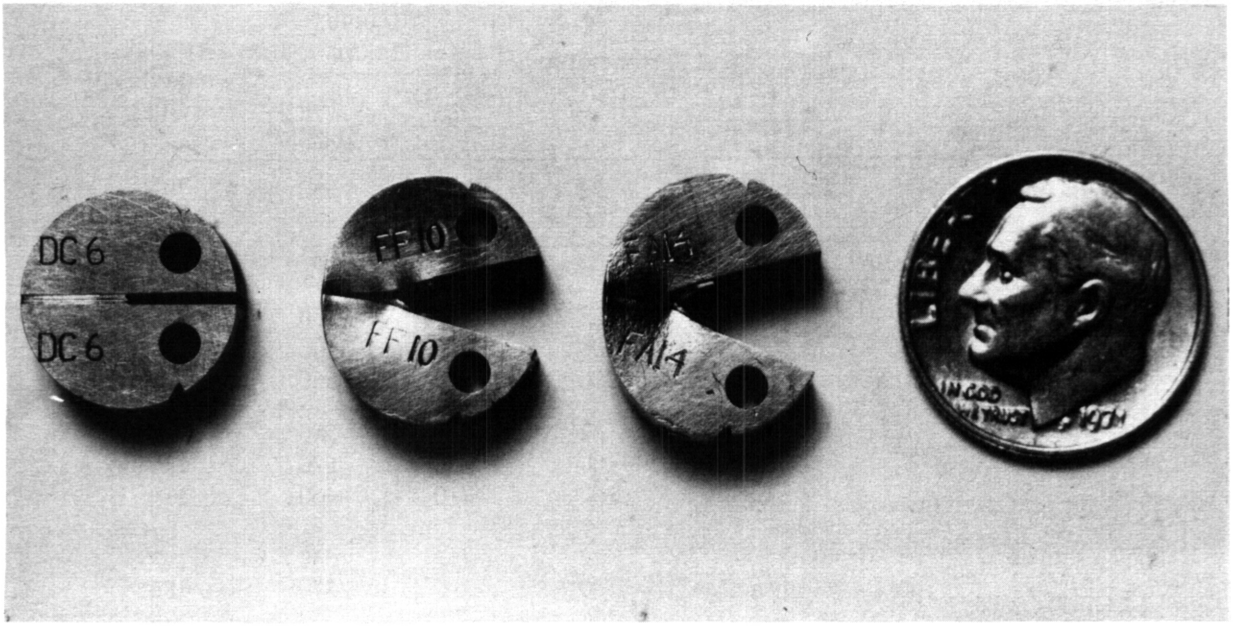

Fig. 1. An example of the gross changes in geometry that resulted when testing the annealed austenitic stainless steel specimens.

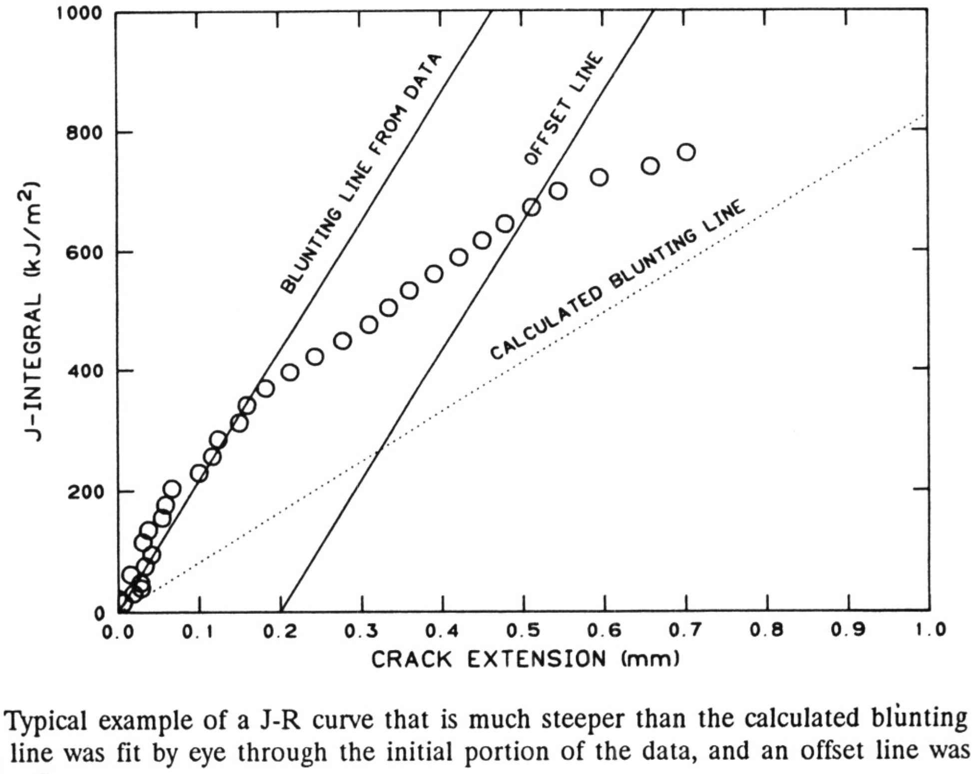

Fig. 2. Typical example of a J-R curve that is much steeper than the calculated blunting line. A straight line was fit by eye through the initial portion of the data, and an offset line was used to determine J_Q.

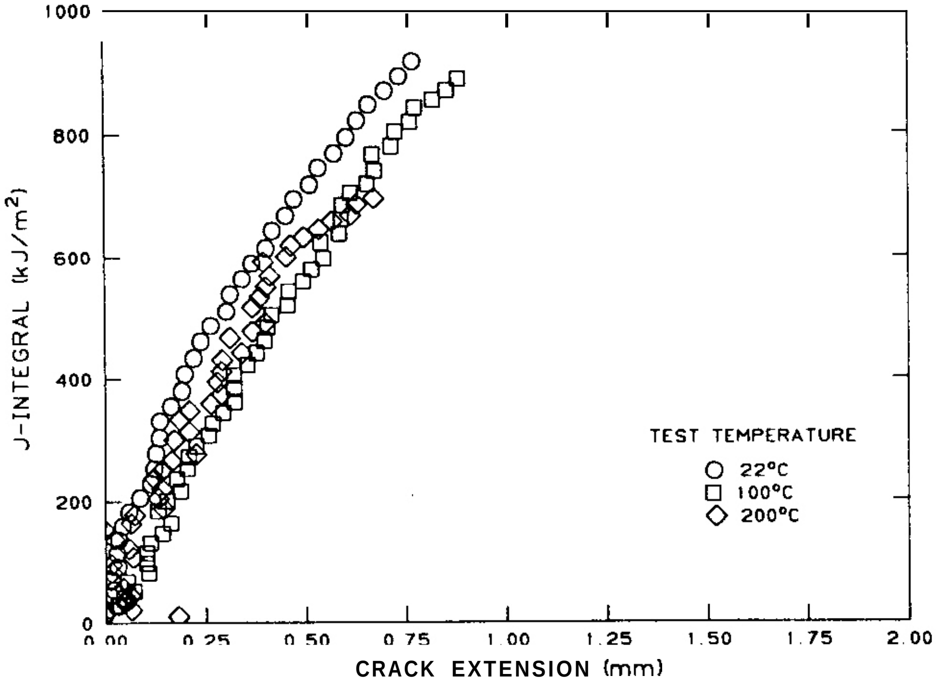

Fig. 3. J-R curves for unirradiated EC316L steel.

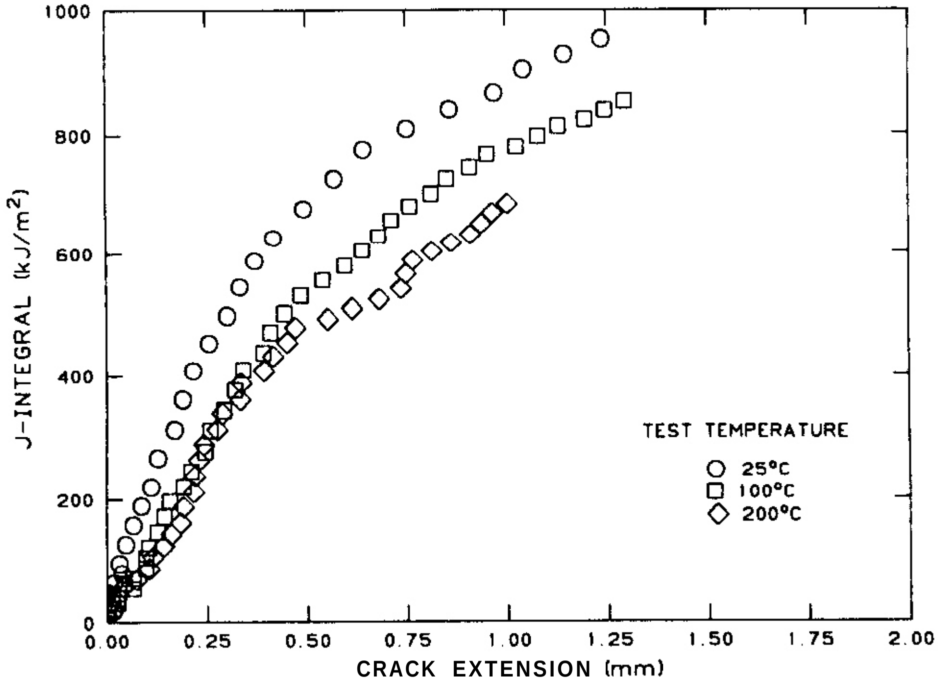

Fig. 4. J-R curves lor EC316L steel irradiated to 3 dpa at 60 to 125°C.

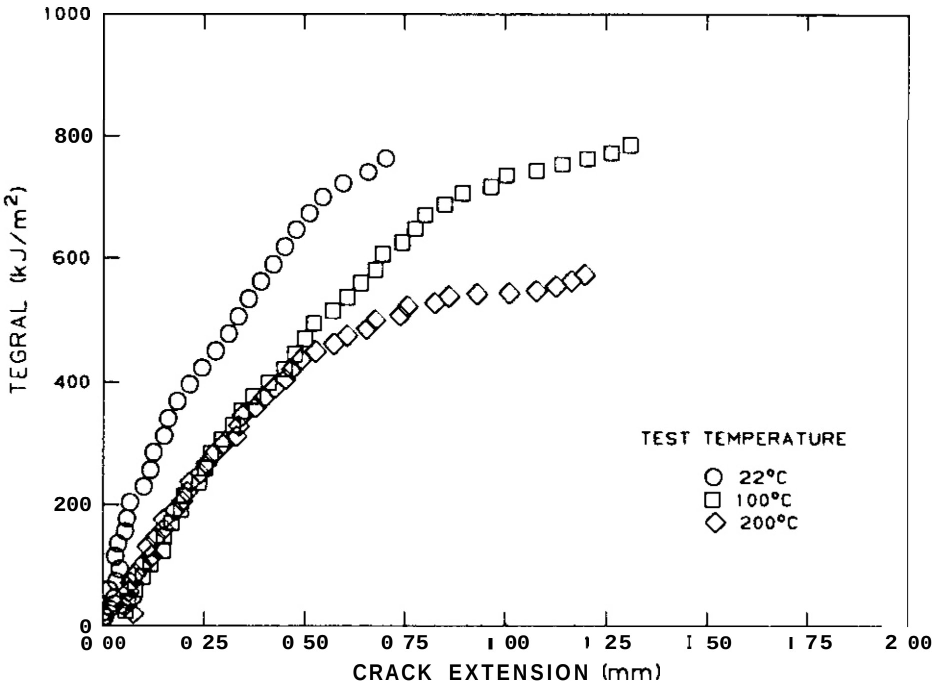

Fig. 5. J-R curves for unirradiated JPCA annealed steel.

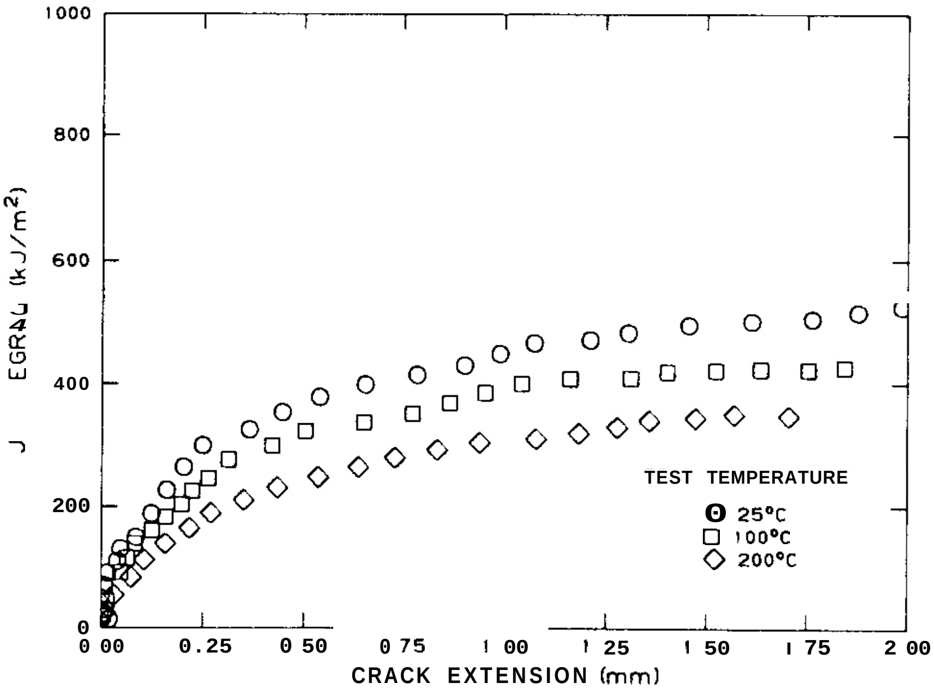

Fig. 6. J-R curves for irradiated JPC'A annealed steel irradiated to 3 dpa at 60 to 125°C

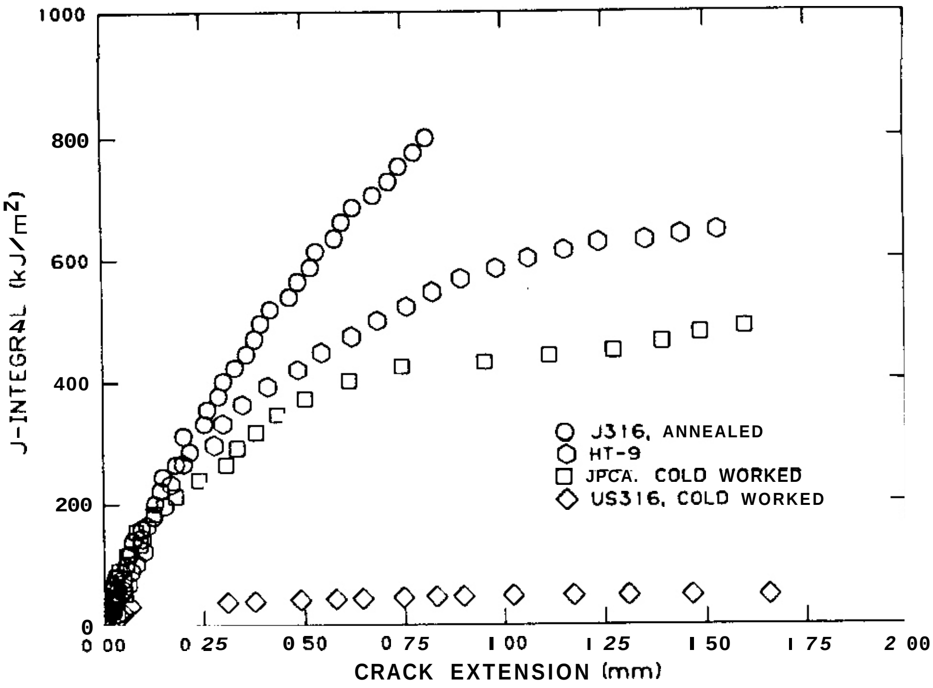

Fig. 7. J-R curves for the remaining unirradiated materials

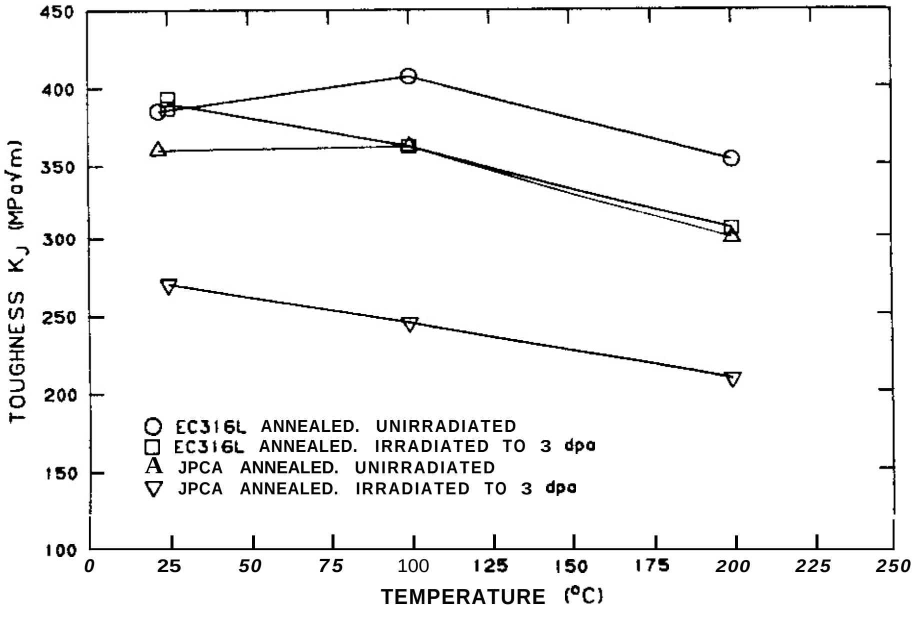

Fig. 8. Fracture toughness values for EC316L and JPCA annealed steels as a function of temperature, showing the effects of irradiation and test temperature.

Table 2. Fracture toughness values

Material	Condition	Specimen	Temperature (°C)	J_Q (kJ/m^2)	K_J (MPa$\sqrt{m}$)
EC316L annealed	Unirradiated	FA14	22	769	385
		FA22	100	889	407
		FA5	200	696	353
EC316L annealed	Irradiated	FA16	25	775	387
		FA3	25	802	393
		FA6	100	703	362
		FA17	200	521	306
JPCA annealed	Unirradiated	FF10	25	572	360
		FF13	100	705	362
		FF20	200	499	299
JPCA annealed	Irradiated	FF5	22	379	270
		FF16	100	323	245
		FF2	200	242	20s
J316 annealed	Unirradiated	FC8	22	798	393
JPCA cold worked	Unirradiated	FE6	22	356	262
US316 cold worked	Unirradiated	FL13	22	37	85
HT-9	Unirradiated	FH11	22	447	304

The effects of test temperature and irradiation are summarized in Fig. 8 for the EC316L annealed and JPCA annealed materials irradiated at 60 to 125°C. The EC316L material has a higher toughness than the JPCA material. Both show a tendency for lower toughness as the test temperature is increased. The JPCA alloy shows a much greater decrease in toughness following irradiation than the EC316L material. However, even in the worst case, the toughness is still quite high.

CONCLUSIONS

Useful fracture toughness data can be generated using the unloading compliance technique and the small disk compact specimens. Specimens of several austenitic stainless steels have been irradiated in HFIR to about 3 dpa at 60 to 125°C. Preliminary results have shown that the toughness of the annealed EC316L and JPCA austenitic stainless steels is quite high. The JPCA alloy shows a greater response to irradiation, with a more significant decrease in the toughness after irradiation. The effect of irradiation is most noticeable at higher test temperatures (200°C). However, even in this case the toughness is still high.

FUTURE WORK

Additional specimens will be tested in both the irradiated and unirradiated conditions. The third capsule (JP-17) that was irradiated at higher temperature (250 to 300°C) will be disassembled, and these specimens will be tested as well. Tensile tests will be conducted to provide actual values for the yield and ultimate tensile strengths after irradiation. These values will be used to revise the fracture toughness analyses of all of the fracture toughness tests.

ACKNOWLEDGMENTS

The fracture toughness testing was performed by R. L. Swain. We would like to thank F. M. Haggag and R. L. Klueh for their helpful reviews of the manuscript, which was prepared by J. L. Bishop.

REFERENCES

1. A. W. Longest, D. W. Heatherly, K. R. Thorns, and J. E. Corum. "Design and Fabrication of HFIR-MFE-JP Target Irradiation Capsulcs," *Fusion Reactor Materials Semiannual Progress Report for Period Ending March 31, 1991,* DOE/ER-0313/10, 1991, p. 3.

2. A. W. Longest, D. W. Heatherly, J. E. Wolfe, K. R. Thorns, and J. E. Corum, "Fabrication and Irradiation of HFIR-MFE-JP-17, -18, and -19 Target Irradiation Capsulcs," *Fusion Reactor Materials Semiannual Progress Reporr for Period Ending September 30, 1991*, DOE/ER-0313/11, 1992, p. 30.

3. A. W. Longest, D. W. Heatherly, K. R. Thorns, and J. E. Corum, "Fabrication and Irradiation of HFIR-MFE-JP-17, -18, and -19 Target Irradiation Capsules," *Fusion Reactor Materials Semiannual Progress Report for Period Ending March 31, 1992,* DOE/ER-0313/12, 1992, p. 24.

4. D. J. Alexander, "Fracture Toughness Measurements with Subsize Disk Compact Specimens, *Fusion Reactor Materials Semiannual Progress Report for Period Ending March 31, 1992,* DOE/ER-0313/12, 1992, p. 35.

5. D. J. Alexander, "Fracture Toughness Measurements with Subsize Disk Compact Specimens," in ASTM Symposium on Small Specimen Test Techniques and Their Application to Nuclear Reactor Vessel Thermal Annealing and Plant Life Extension," to be published by American Society for Testing and Materials, Philadelphia, 1993.

6. C. Elliot, M. Enmark, G. E. Lucas, and G. R. Odette, "Development of Disc Compact Specimens and Test Techniques for HFIR Irradiations," *Fusion Reactor Materials Semiannual Progress Report for Period Ending Septenıber 30, 1990,* DOE/ER-0313/9, 1991, p. 7.

7. R. K. Nanstad, D. J. Alexander, R. L Swain, J. T. Hutton, and D. L. Thomas, "A Computer-Controlled Automated Test System for Fatigue and Fracture Testing," in *Applications of Automation Technology to Fatigue and Fracture Testing, ASTM STP 1092,* A. A. Braun, N. E. Ashbaugh, and F. M. Smith, eds., American Society for Testing and Materials, Philadelphia, 1990, p. 7.

6.3 Refractory Metal Alloys

Density Changes Induced by Neutron Irradiation in Dynamically Compacted Tungsten and PCA - F. A. Garner (Pacific Northwest Laboratory)[1] and J. Megusar, (Massachusetts Institute of Technology)

OBJECTIVE

The objective of this effort is to determine the potential of rapid solidification and dynamic compaction as tools for improving the performance of candidate fusion materials.

SUMMARY

Dynamically compacted tungsten with a starting density of 95.3% of the theoretical value densified 2 to 3% when irradiated in FFTF/MOTA-2A at three temperatures between 423 and 600°C and displacement levels corresponding to 32 to 36 dpa in stainless steel. Rapidly solidified and dynamically compacted PCA with high levels of titanium and carbon were also irradiated at these conditions. The density changes were small enough to determine that significant swelling had not occurred but, microscopy is necessary to determine whether void growth occurred in addition to precipitate-related strains

PROGRESS AND STATUS

Introduction

Rapid solidification and dynamic compaction have been proposed as methods to produce alloys for use in fusion environments.[1] One such material, a titanium-modified austenitic Stainless steel designated PCA, was irradiated earlier in EBR-II to 15 dpa in the range 395 to 550°C. A total absence of swelling was observed in this alloy. although some swelling was observed in fully annealed specimens that were also irradiated.[2]

Both the as-produced and fully annealed material were also irradiated in MOTA-2A and MOTA-2B at 423, 520 and 600°C. Density measurements have now been performed on the MOTA-2A specimens. Dynamically compacted tungsten was also included in the same packets. This material might serve as an armor material for the first wall or divertor.

Experimental Procedure

The titanium-modified austenitic stainless steel (PCA) was provided by the Oak Ridge National Laboratory with the following composition (in wt%): 16.59 nickel: 14.27 chromium: 1.96 molybdenum: 0.32 titanium: 1.62 manganese; 0.53 silicon: 0.046 carbon; 0.008 nitrogen: 0.04 cobalt: 0.014 phosphorus; 0.002 sulfur: and balance iron. Additional carbon and titanium were added in a remelt followed by rapid solidification and dynamic compaction. This material contained approximately triple the nominal amounts of carbon and titanium (that is. 0.17 wt% carbon and 0.92 wt% titanium) originally in PCA. Rapid solidification was performed in a roller quenching apparatus, with an estimated cooling rate of 10^{-} K/s.

Dynamic compaction was performed at the Institut Cerac, Ecublens, Switzerland. Rapidly solidified foils were cut into pieces with a length to thickness ratio of 30 to 1 or less and were compacted with the gun speed at 1200 m/s. The diameter of the compacted material was 5 cm, and the height was 1 cm. Compaction was achieved With a shock wave that was produced by impact of the projectile on the powder. Calculations showed the following relation between the shock speed. particle velocity, and the internal energy. Steel powder of ~50% loose density and compacted to a shock pressure of 5 GPa gave a shock velocity of 1600 m/s, a particle velocity of 800 m/s, and an internal energy change of 3 x 10^{5} J/kg. This energy change corresponds to a temperature rise of 600 K. and if the energy is considered to be deposited predominantly at the powder particle surface. the value of 2 x 10^{7} J/m^2 for energy density is deduced

Some of this material was subsequently annealed 8 h at 650°C, resulting in a homogeneous precipitation of coherent TiC precipitates approximately 5 nm in size. Some recovery of dislocation structure probably took place during annealing, as evidenced by a large drop in the knoop microhardness. Both the as-produced and annealed conditions were irradiated in MOTA-2A and MOTA-2B along with dynamically compacted tungsten. The latter was produced at Lawrence Livermore National Laboratory. Density changes were determined by an immersion density technique determined to be accurate to ± 0.15% swelling.

Results

Table I presents the density change data for the specimens discharged from MOTA-2A. It is obvious that the dynamically compacted tungsten is densifying on the order of 2 to 3%. The preirradiation density of 18.4 g cm^{-3} is 95.3% of the textbook value of 19.3 g cm^{-3}. Therefore. during irradiation the compacted tungsten is

---

[1] Pacific Northwest Laboratory is operated for the U.S. Department of Energy by Battelle Memorial Institute under Contract DE-AC06-76RLO 1830.

approaching, but has not yet reached, the theoretical density. Some portion of the densification may also result from transmutation of tungsten to rhenium and osmium.[4]

The density changes for PCA in both starting conditions are small enough to preclude drawing conclusions concerning the onset of swelling. Both positive and negative changes were observed, indicating that precipitation-related chages in lattice parameter are occuring.

Table 1
Swelling in Percent from Dynamically Compacted Specimens in MOTA-2A*

	Pre-Irradiation Density	423°C, 36.1 dpa	520°C, 36.3 dpa	600°C, 32.3 dpa
W**	18.4098	-2.23	-2.05/-3.19	-2.07
PCA	7.8677	-0.29	-0.28	-0.04
PCA-Annealed	7.9083	+0.51	+0.37	-0.13/-1.04

*Unless two values are given, the swelling is the average of two separate specimens which agreed within ± 0.2%.

**dpa for W is less than that of steel, but has not yet been calculated.

FUTURE WORK

Density changes will be determined for the second discharge of the experiment (MOTA 2B). Microscopy and EDX analyses will also be performed.

REFERENCES

1. N. J. Grant, O. K. Harling, G. Kohse, J. Megusar, and T. Lee, J. Nucl. Mater. 141-143 (1986) 427.

2. D. Imeson et al., three sucessive papers in J. Nucl. Mater. 122 & 123 (1984) 266-271; 272-277; 278-283.

3. J. Megusar, in Effects of Radiation on Materials: 14th International Symposium, Volume 1, ASTM STP 1046, N. H. Packan R. E. Stoller, and A. S. Kumar, Eds., American Society for Testing and Materials, Philadelphia, 1989, pp. 185-192.

4. F. A. Garner and L. R. Greenwood, in this Semiannual Report.

Density Changes Observed in Nb-1Zr After Irradiation in FFTF-MOTA - F.A. **Garner** (Pacific Northwest Laboratory~).

OBJECTIVE

The objective of this effort is to provide **data** on the irradiation **behavior** of Nb-1Zr, an alloy proposed for potential application to ITER **and** possibly other **long-range** fusion goals.

SUMMARY

Nb-1Zr has **been** proposed far potential application to ITER. **Whereas** previous irradiation studies **on** Nb-1Zr **were focused on** the annealed condition, this **study** involved **a** comparative irradiation of both the annealed **and** aged. and the cold-worked **and** aged conditions. Based **on** measurements of **density** change. the cold-worked and aged condition appears to first undergo a phase-related dilation prior to the onset of void swelling, **while** the annealed condition densifies prior to **swelling** and in **some cases** does not **swell** at all.

PROGRESS **AND** STATUS

Introduction

The **commercial** alloy *Nb-1Zr* is currently being considered **ai** a candidate *for* high *heat flux* ***service*** in the ITER divertor. This **alloy was** therefore irradiated in **MOTA** 1B, 1C. 1D, and 1E at five target temperatures **between** 420 and 722°C, with peak exposures on the **order** of 60 dpa (steel) at most temperatures and to ~100 dpa **at** 420 C.(1) Most **previous** studies **focused** only on the annealed condition.(2-4)

The specimens were in the form of 3 mm diameter **microscopy** disks in two starting conditions. The **first** condition **was** solution annealed for 1 hr at 760°C **and** then aged for 2 hrs. **at** 320°C. The second was 20% cold-'worked following the 760°C, 1 hr annealing, **and** then aged at 320°C for 2 hrs. Irradiation proceeded in weeper packets, and thus the specimens **were** in contact with the sodium coolant. of the reactor Table 1 lists the irradiation conditions.

Table 1
Irradiation Conditions far Nb-1Zr **Specimens** Examined in This Study

		MOTA-1B		MOTA-1C		MOTA-1D		MOTA-1E		
Packet	Contents[a]	Temperature, °C	dpa[b]	Temperature, °C	dpa	Temperature, °C	dpa	Temperature, °C	dpa	Total dpa
MAEZ	A	431	15.0	--	--	--	--	--	--	15.0
NAEZ	A	431	15.0	420	35.3	--	--	--	--	50.3
N6EZ	B	431	14.1	420	33.1	--	--	--	--	47.2
M6EZ	B	431	14.5	420	33.9	404	24.5	414	32.8	105.7
PAEZ	A	431	15.0	420	35.3	404	25.5	414	35.0	110.8
MAE1	A	471	11.4	--	--	--	--	--	--	11.4
NAE1	A	471	11.4	470	26.8	--	--	--	--	38.2
N6E1	B	471	9.6	470	22.6	--	--	--	--	32.2
P6E1	B	471	8.7	470	20.3	470	14.7	--	--	43.7
PAE1	A	471	11.4	470	26.8	470	19.4	--	--	57.6
MAE7	A	569	11.5	--	--	--	--	--	--	11.5
NAE7	A	569	11.5	550	27.0	--	--	--	--	38.5
N6E7	B	569	12.2	550	28.6	--	--	--	--	40.8
PAE7	A	569	11.5	550	27.0	549	19.6	--	--	58.1
RAE7	A	569	11.5	550	27.0	549	19.6	--	--	58.1
MAE5	A	645	11.5	--	--	--	--	--	--	11.5
NAE5	A	645	11.5	652	27.0	--	--	--	--	38.5
N6E5	B	645	12.2	652	28.6	--	--	--	--	40.8
R6E5	B	645	12.7	652	30.8	650	22.3	--	--	65.8
PAE5	A	645	11.5	652	27.0	650	19.6	--	--	58.1
MAE6	A	722	11.5	--	--	--	--	--	--	11.5
NAE6	A	722	11.5	730	27.0	--	--	--	--	38.5
N6E6	B	722	12.2	730	28.6	--	--	--	--	40.8
M6E6	B	722	12.2	730	28.6	730	20.7	--	--	61.5
PAE6	A	722	11.5	730	27.0	730	19.6	--	--	58.1

(a) **Group** A **contains cold**-worked **and** aged specimens only. Group B contains **annealed** and aged specimens.
(b) dpa valuer **calculated for** stainless steel in **early** FFTF **core** configurations.

'Pacific Northwest **Laboratory** is **operated** for the U.S. Department of Energy by Battelle Memorial Institute under Contract DE-AC06-76RLO 1830.

Although irradiation in MOTA proceeded largely under active temperature control (±5 C) in MOTA's 1A, 1C and 1E, there was a short (-50 minutes) temperature excursion in MOTA 1D during FFTF cycle 7, referred to as an over-temperature event. The event compromised the integrity of many of the other experiments in MOTA 1D. Therefore, a programmatic decision was made to run MOTA 1D in the helium-purged mode for the remainder of FFTF cycles 7 and 8 while a series of reactor feedback tests were conducted. The majority of the MOTA canisters therefore operated at variable but lower than target temperatures until the end of FFTF cycle 8. Isothermal irradiation was reestablished in MOTA 1E, but only the 420°C specimens were included in that irradiation segment.

Density measurements were performed using an immersion density technique whose accuracy has been established to be ±0.15% swelling. The displacement levels (NRT) quoted are those calculated for stainless steel. Detailed calculations for Nb-1Zr have not yet been performed but should be on the order of 114% of those of steel.(5)

Results and Discussion

Figure 1 presents the results of density measurements performed on the Nb-1Zr specimens. It is obvious that some phase-related dilation of the alloy matrix probably occurs in the cold-worked alloy early in the irradiation, producing a density decrease of 0.5±0.1%. This conclusion is drawn from the relative temperature independence of the density change. This change may actually include contributions from void swelling, however, a possibility that will be examined by microscopy. The swelling behavior thereafter appears to be rather complex, both with irradiation temperature and increasing neutron exposure. In general, however, there is a tendency at the higher temperatures for swelling to continue. There are indications of shrinkage at 420 and 569 C.

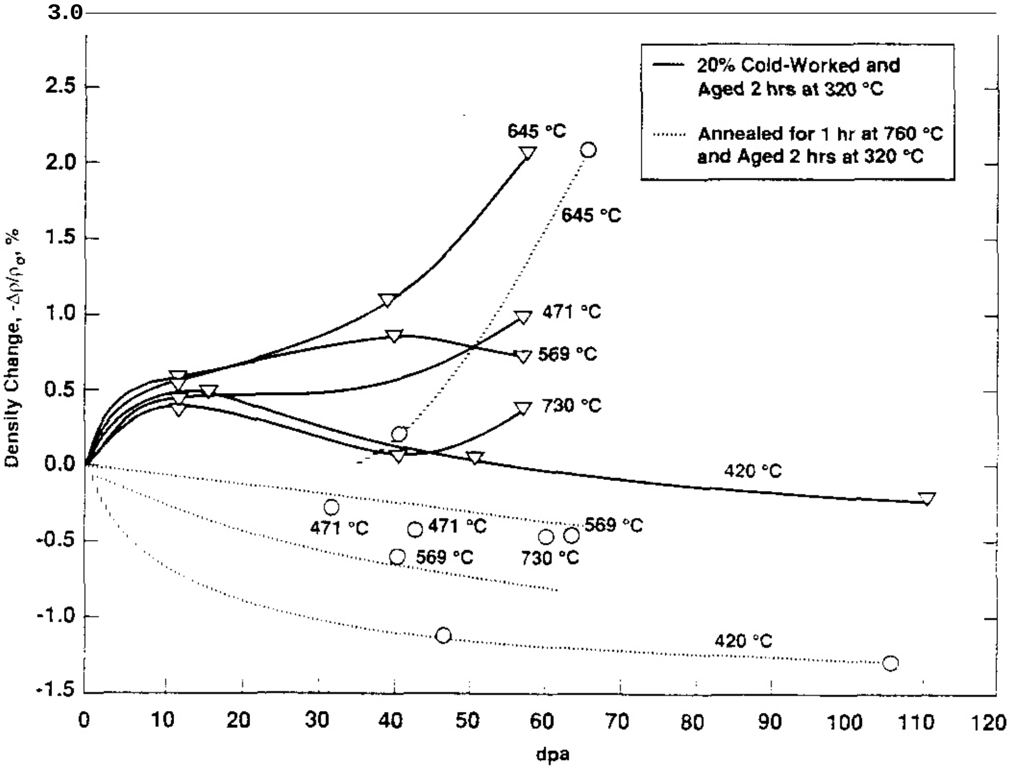

Fig. 1. Density changes observed in Nb-1Zr after irradiation in FFTF-MOTA.

The annealed and aged condition, with one exception, appears to densify, probably as a result of some precipitation reaction. The exception is significant in that the behavior at 645°C parallels that of the cold-worked and aged condition at this temperature, with the offset between the behavior of the two conditions consistent with their respective differences in phase-related density changes.

Of particular interest is the parallel behavior of both starting conditions observed at 420°C, leading to densification. It is obvious that two or more processes are competing to produce the observed changes in density and that the starting state affects at least one of there processes. It is surmised tha: the primary difference between the two starting states resides in the distribution of grain sizes. In companion studies conducted an molybdenum in this same irradiation series, small grain sizes produced by an identical heat treatment have been found to cause earlier and, therefore, larger swelling. similar to that observed in Nb-1Zr. (6)

FUTURE WORK

These specimens will be examined by microscopy in a collaboration with H. Watanabe of Kyushu University

References

1. F. A. Garner. "FFTF/MOTA Irradiation of Refractory Alloys Under Consideration as Plasma Facing Components." in fusion *Reactor Materials Semiannual Progress Report.* DOE/ER-0313-9 (1990) pp. 169-171.

2. R. W. Powell, D. T. Peterson. M. K. Zimmershied. and J. F. Bates, *J. Nucl. Mater.*. 103&104 (1981) 969-974.

3. D. S. Gellei, *J. Nucl. Mater.*. 122&123 (1984) 207-213.

4. H. Jang and J. Moteff. in Proc. Conf. on *Radiation Effects and Tritium Technology for Fusion Reactors.* Vol. I. *CONF-750989 (1975) pp. I-106* to I-121.

5. F. A. Garner and L. R. Greenwood. Fusion Reactor Materials Semiannual Progress Report. DOE/ER-0313/12 (1992) pp. 54-58.

6. F. A. Garner and L. R. Greenwood. "Density Changes *Observed in Pure Molybdenum* and *Mo-41Re* After Irradiation in FFTF-MOTA", in this semiannual report.

ASSESSMENT OF NIOBIUM-BASE ALLOYS FOR STRUCTURAL APPLICATIONS IN THE ITER DIVERTOR* — I. M. Purdy (Argonne National Laboratory)

OBJECTIVE

Niobium-base alloys are under consideration as candidate materials for the divertor structure of the International Thermonuclear Experimental Reactor (ITER). Criteria for suitability of the alloys include resistance. to aqueous corrosion, erosion/corrosion, fatigue, stress corrosion cracking, hydrogen embrittlement, and radiation-induced embrittlement. Because high thermal fluxes are predicted, thermal conductivity, thermal expansion, and heat capacity are important properties. Corrosion resistance, mechanical properties, and physical characteristics are being investigated to identify the most promising Nb-base alloys.

SUMMARY

The corrosion and embrittlement of pure Nb, Nb-1Zr, Nb-5Mo-1Zr, and Nb-5V-1.25Zr (alloy elements in wt.%) were evaluated in high-purity (HP) deoxygenated water at 300°C for up to 120 days. One heat of the Nb-5V-1.25Zr alloy ("O" lot) exhibited both a modest corrosion rate and good resistance to embrittlement relative to other Nb-base alloys. At present, Nb-5V-1.25Zr is the most promising Nb-base alloy on the basis of both corrosion and embrittlement characteristics in HP deoxygenated water at 300°C.

PROGRESS AND STATUS

In previous work,[1-3] the corrosion behavior of Nb-base alloys (Nb-2.5V, Nb-2.5Ta, Nb-2.5W, Nb-2.5Zr, Nb-2.5Hf, Nb-2.5Mo, Nb-2.5Fe, and several ternary alloys, namely, Nb–2.5Ti–2.5Ta, Nb–2.5Mo–2.5Ti, and Nb–2.5Mo–2.5Hf) was investigated in HP deoxygenated water at 300°C. Although the weight–gain corrosion rates were not excessive and only a fraction (<20%) of the hydrogen that was liberated by the overall corrosion reaction was absorbed by the alloys, most of the alloys were deemed to be brittle, i.e., fracture occurred during a 90° bend test. Microstructural characteristics of the corrosion–product layers were examined by optical and scanning electron microscopy (SEM).[2] These evaluations revealed numerous cracks and spalling of the oxide layers, which is characteristic of nonprotective film formation. Some crack surfaces in the alloys were covered by corrosion product, indicating that the cracks formed during exposure to high–temperature water. The results suggest that Nb alloys with higher concentrations of alloying elements (namely, V, Mo, and Zr) are required to improve the protective nature of the corrosion–product layers and to decrease hydrogen uptake and embrittlement. During this reporting period, pure Nb, Nb-1Zr, Nb-5Mo-1Zr, and Nb-5V-1.25Zr were exposed to HP deoxygenated water at 300°C for up to 120 days. The corrosion behavior and degree of embrittlement of these alloys has been assessed and compared with earlier results.

Experimental Procedures

Thin sheets of pure Nb and Nb-base alloys were sheared to approximate dimensions of 8 x 20 mm. The Nb-5V-1.25Zr alloy. formerly designated "Ch 753" by Haynes, was obtained from two different lots; hence the "N" and "O" designations in Table 1. Thickness of the Nb and "O" lot sheet was 0.5 mm; that of the other materials was 0.8 mm. The materials designated "O" and "N" differ mainly in the impurity content; the levels in the "N" material are higher by a factor of ≈2.

---

[*] Work supported by the U.S. Department of Energy. under Contract W-31-109-Eng-38

Table 1. Composition of niobium and niobium-base alloys

Alloy[a]	wt.%			ppm							
	Mo	V	Zr	O	N	C	H	Si	Al	Fe	Cr
Nb	0.01	<0.01	<0.01	5700	1700	130	2.9	<100	50	<50	<20
Nb-1Zr	<0.01	<0.01	0.82	153	57	70	4.0	<100	65	<50	<20
Nb-5Mo-1Zr	4.86	<0.01	0.81	186	56	70	8.5	<100	70	<50	<20
Nb-5V-1.25Zr (N)	<0.01	5.76	1.11	720	75	300	10.3	150	155	100	150
Nb-5V-1.25Zr (O)	<0.01	5.69	0.84	310	95	130	4.1	260	65	35	25

[a] Concentrations of HI. W, Ta. and Ti are 1100 ppm; Mn, Cu. and Ni 150 ppm; and Mg 15 ppm.

The surface area of each specimen was determined by an image analysis technique, using Image™ software.[4] The specimens were annealed in vacuo at 1000°C for 2 h. Prior to testing, the samples were cleaned with methanol and dried. Corrosion exposures were conducted in a refreshed autoclave system at 300°C (± 2°C) and 1400 psi. Water flow rate through the system was ≈0.07 $cm^3 \cdot s^{-1}$. The dissolved-oxygen concentration of the inlet water was maintained at <12 ppb and was monitored with an Orbisphere oxygen meter. The 120-day immersion test was interrupted at approximately 30, 60, and 90 days for removal of specimens. Weight changes of the specimens were determined to ± 0.001 mg with a Mettler microbalance. A mechanical-bend test was used to screen the samples for ductility in order to evaluate embrittlement.

Results and Analysis

The weight-change data from the tests are shown in Table 2. Nearly all of the alloys showed consistent weight gains, although the pure Nb specimen lost weight during the last 30-day exposure. Corrosion rates of the alloys followed power-law kinetics, as shown in Fig. 1. The weight-gain vs. time data for Nb-Zr, Nb-5Mo-1Zr, and Nb-5V-1.25Zr alloys exhibit $t^{0.68}$, $t^{0.58}$, and $\approx t^{0.35}$ kinetics, respectively. Corrosion behavior of the two heats of the Nb-5V-1.25Zr alloy was quite similar and showed significantly slower weight gain than did the other materials.

Table 2. Weight change per unit area ($g \cdot m^{-2}$) with exposure time

Time (h)	Nb	Nb-1Zr	Nb-5Mo-1Zr	Nb-5V-1.25Zr (N)	Nb-5V-1.25Zr (O)
76X	11.74	15.83	3.865	2.928	2.290
1564	36.15	25.97	6.691	3.869	3.435
2287	39.66	33.38	1.594	4.552	3.257
3052	31.24	40.46	8.639	4.588	3.981

Ductility after each exposure period was assessed by a simplified bend test on a scale of 1 to 6, as devised by Hull et al.[1] Material response when the specimens were bent at ambient temperature was categorized according to the fracture index (FI) explained in Table 3.

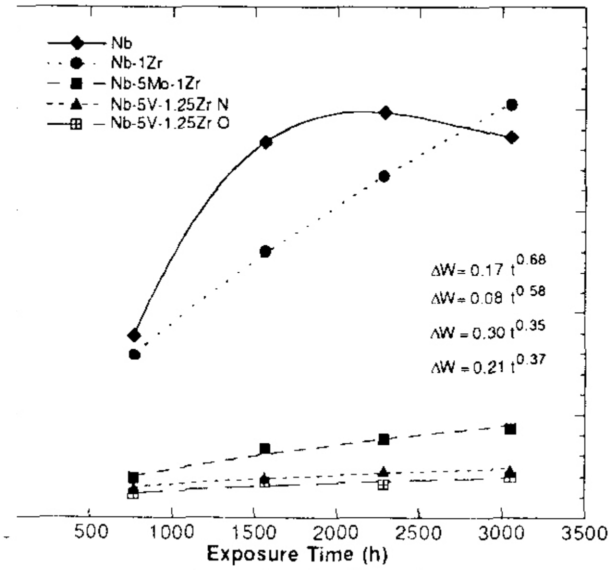

Figure 1. Weight gain vs. time for Nb and Nb-base alloys exposed to HP deoxygenated water at 300°C

Although both heats of the Nb-5V-1.25Zr alloy showed very similar corrosion behavior, the "N" lot became progressively more brittle with increasing exposure time compared with the other metals that were tested, including pure Nb (Table 3). In terms of ductility evaluated by this test, Nb-5V-1.25Zr ("O" lot) showed the least embrittlement. During the bend tests, it was observed that the oxide scale readily flaked from the bend region of the Nb and Nb-1Zr specimens.

Table 3. Fracture susceptibility of Nb and Nb-alloy specimens versus exposure time

Metal	Fracture Index[a] after Exposure (days)			
	30	60	90	120
Nb	2	3	4	5
Nb-1Zr	2	2	3	3
Nb-5Mo-1Zr	3	4	4	5
Nb-5V-1.25Zr (O)	2	2	2	2
Nb-5V-1.25Zr (N)	2	4	5	5

[a] Fracture susceptibility was categorized according to the following fracture index (FI): an FI of 6 indicates breakage before bending began; an FI of 5 denotes fracture at a 90° bend; an FI of 4, fracture occurs after a 180° bend; an FI of 3, the specimen fractures only after unbending of a fold; an FI of 2, no fracture even on unbending of a fold: and an FI of 1, no fracture or surface cracking of the oxide scale that formed during exposure.

The corrosion and embrittlement characteristics of the ternary alloys determined from this and a previous experiment[1] after 120 days at 300°C are shown in Figs. 2 and 3. The corrosion weight gains for the Nb–5Mo–1Zr and Nb–2.5Ti–2.5Ta alloy from the previous experiment[1] are similar, namely, ≈8–10 $g \cdot m^{-2}$, whereas the values for the other alloys are lower by a factor of **2.** However, the fracture index of one heat (lot "O") of the Nb–5V–2.5Zr alloy (Fig. 3) indicates less embrittlement, **as** determined from room-temperature bend tests, than any of the Nb–base alloys evaluated **thus** far. Metallographic and SEM analyses and hardness profiles will be obtained to rationalize differences in the embrittlement characteristics of the two heats of the Nb–5V–2.5Zr alloy.

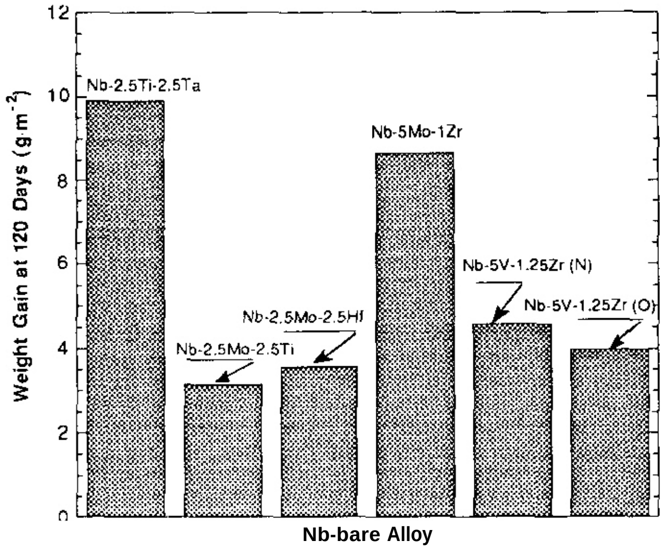

Figure 2. Weight gains for Nb–base alloys after **exposure** *to HP deoxygenated* **water** *for 120* **days** *at 300°C*

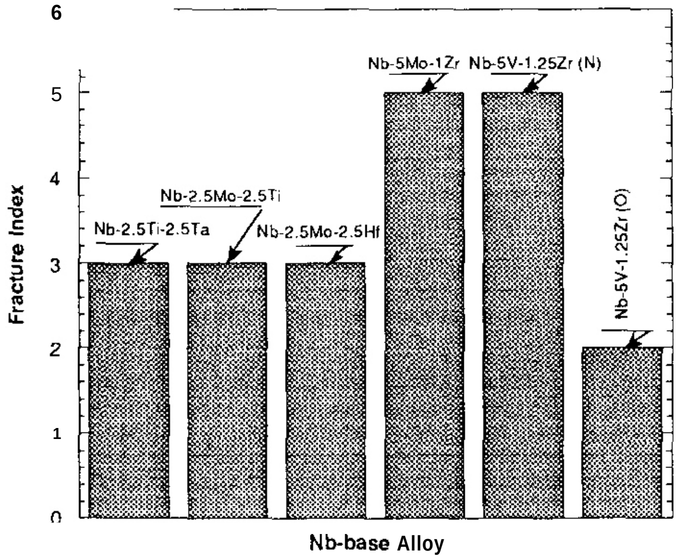

Figure 3. Fracture index for Nb–base alloys after **exposure** **to** *HP deoxygenated water for 120 days at 300°C*

CONCLUSIONS

Experience has shown that alloys with high W (≈10 wt.%) and Mo (≈5 wt.%) contents are difficult to fabricate and weld, and that a high Ta content reduces the irradiation resistance of the material.^{3} Our results have shown that (a) V additions lower the corrosion rate and (b) Hf and Zr additions lower both the H concentrations and the percentage of corrosion-product H that is absorbed by Nb–base alloys^3 (compared to Nb–V alloys). Further. Nb–5V-1.25Zr shows the greatest promise in terms of resistance to both corrosion and embrittlement for ITER divertor applications.

FUTURE WORK

The next series of corrosion tests on two heats of the Nb-5V-1.25Zr alloy will be conducted at a somewhat lower temperature to determine the temperature dependence of the corrosion rate and the degree of embrittlement. A detailed microstructural evaluation of the corrosion films on specimens from the present test will be conducted to quantify differences in the embrittlement characteristics of the two lots of the alloy.

REFERENCES

1. A. B. Hull, B. A. Loomis, and L. J. Nowicki. *Preliminary Assessment of Aqueous Corrosion of Niobium Alloys for Structural Applications in the ITER Divertor*, Fusion Reactor Materials Semiannual Report for Period Ending March 31, 1991, DOE/ER-0313/10, Oak Ridge National Laboratory, p. 248.

2. J. A. Todd and I. M. Purdy, *Preliminary Assessment of Candidate Niobium Alloys for the Divertor Structures*, Fusion Reactor Materials Semiannual Report for Period Ending Sept 30, 1992, DOE/ER-0313/13, Oak Ridge National Laboratory, p. 203.

3. D. T. Peterson, A. B. Hull, and B. A. Loomis, *Hydrogen Embrittlement of Niobium-Base Alloys for Application in the ITER Divertor*, Fusion Reactor Materials Semiannual Report for Period Ending Sept 30, 1992, DOE/ER-0313/13, Oak Ridge National Laboratory, p. 182.

4. W. Rasband, *Image, Public Domain Program for the Macintosh Computer*, distributed by Twilight Clone BBS, Silver Spring, MD, 1990

MICROSTRUCTURAL EVOLUTION INDUCED BY BORON TRANSMUTATION IN NEUTRON-IRRADIATED VANADIUM-BASE ALLOYS* — H. M Chung (Argonne National Laboratory).

OBJECTIVE

The objective of this work is to characterize the microstructural evolution induced by transmutation of ^{10}B in neutron-irradiated vanadium-base alloys, and thereby to provide a better understanding of the boron-doping technique that is used to simulate the effect of helium generation under fusion reactor conditions.

SUMMARY

Microstructural evolution associated with transmutation of ^{10}B to helium and lithium has been characterized to provide a better understanding of the boron-doping technique, a technique frequently used to simulate the effect of helium generation under fusion reactor conditions. Transmission electron microscopy (EM) was used to examine specimens of V-20Ti alloy after irradiation at 600°C to ≈44-80 dpa in the Fast Flux Test Facility (FFTF). In the earlier stage of irradiation to low fluence, concentric shells of He-damage and Li-damage zones are produced around a V_3B_2 precipitate or a ^{10}B-rich cluster. On further irradiation, helium atoms diffuse away from the damage shell either to be dissolved in the matrix or to form microcavities, leaving a shell rich in Li, defect clusters, and dislocations. Oxygen atoms in solid solution migrate toward the Li-rich shells, and γ-LiV_2O_5 shells precipitate subsequently. In view of this behavior, neither boron nor Li produced from the transmutation is likely to result in a detrimental weakening of grain boundaries.

INTRODUCTION

Vanadium-base alloys are considered promising candidate structural materials for a fusion reactor first wall because they offer the important advantages of inherently low irradiation-induced activity. good mechanical properties. good compatibility with lithium, high thermal conductivity, and good resistance to irradiation damage. One of the properties of the vanadium-base alloys that is not well understood yet is the effect of simultaneous generation of helium and neutron damage under conditions relevant to fusion-reactor operation (i.e., at a ratio ≈5 appm He/dpa).[1-15] Several methods have been utilized in the past to simulate the effect of helium generation in neutron-irradiated vanadium-base alloys, i.e., the "tritium-trick" technique,[1-5] cyclotron-injection of helium,[6-9,12] boron-doping technique,[10-13] and dynamic helium charging experiment.[14-15]

The ^{10}B-doping method is a convenient technique in that it requires a relatively simple procedure to prepare specimens. Furthermore, based on results of tensile tests reported in the literature,[12] no detrimental side effect seems to be associated with this technique in contrast to the "tritium-trick" method in which a damaging effect of charged hydrogen (tritium) or the unrealistically high initial helium content is suspected to weaken grain boundaries in some alloys. The boron-doping technique utilizes the large thermal-neutron cross section (≈3840 barn) of the $^{10}B(n,\alpha)^7Li$ reaction. By adjusting the level of doped ^{10}B, the method can be tailored to suit the characteristic neutron spectrum of a fission reactor. However, to assess the viability of the technique and to understand the effect of the Li by-product on swelling and mechanical properties, it is necessary to understand the behavior of B and Li during irradiation. For this

---

* Work supported by the Office of Fusion Energy. U.S. Department of Energy. under Contract W-31-109-Eng-38.

purpose, microstructural evolution associated with transmutation of ^{10}B has been characterized in specimens of a vanadium-base alloy that were irradiated to high fluence in the Fast Flux Test Facility (FFTF).

MATERIALS AND PROCEDURES

TEM examination was conducted on disk specimens from a V-20Ti alloy irradiated in the FFTF. The chemical composition of the alloy is given in Table 1. The content of boron, apparently dissolved in the alloy as an impurity, was not known prior to irradiation. The disks were irradiated at 600°C to neutron fluences (E > 0.1 MeV) of 7.8x 10^{22} n·cm^{-2} (≈44 dpa) and 1.33 x 10^{23} n·cm^{-2} (≈80 dpa). They were sealed in Li^7-filled TZM capsules during irradiation to prevent contamination with O, N, and C impurities dissolved in the sodium coolant of the FFTF. The irradiated specimens were jet-thinned for TEM in a solution of 15% sulfuric acid-72% methanol-13% butyl cellosolve maintained at -5°C. TEM was conducted with a JEOL 100CX-II scanning transmission electron microscope operating at 100 keV.

Table 1. Composition of V-18Ti alloy irradiated in the FFTF and analyzed to characterize boron-transmutation-induced microstructural evolution

Alloy ID	Nominal Composition (wt.%)	Impurity Concentration (wppm) O	N	C	Si
BL-15	V 17.7Ti	830	[illegible]	380	480

RESULTS AND DISCUSSION

The irradiated V-20Ti alloy specimens exhibited a hitherto unknown peculiar microstructural feature. As an example, characteristic TEM microstructures observed in specimens irradiated to ≈44 and ≈80 dpa are shown in bright- and dark-field morphology, respectively, in Figs. 1A and 1B. Both micrographs show characteristic circular shells in dark contrast. The morphology of the shells in Fig. 1A is strikingly similar to those of the cylindrical damage shells reported by Rau and Ladd[16] for neutron-irradiated unalloyed vanadium doped with <10 wppm boron. In that study, the specimens were irradiated at ≈70°C to a relatively low fast-neutron fluence of 5.4 x 10^{19} n·cm^{-2} (E > 1 MeV) and a thermal-neutron fluence of 3.5 x 10^{20} n·cm^{-2} in the Oak Ridge Reactor (ORR). Two concentric shells, surrounding rod-like precipitates of V_3B_2, were produced by recoil Li and He atoms during transmutation of ^{10}B. On further annealing of the irradiated specimens at ≥650°C, the defect clusters that made up the damage shells were removed and replaced by dislocation tangles. At the same time, blocky precipitates ≈100 nm in size emerged in the inner Li-damage shells. Although they were not positively identified, the blocky precipitates were believed to be an Li-rich vanadium compound.

In the study of Kawanishi et al.,[13] V-20Ti specimens doped with 120 wppm ^{10}B were examined after irradiation at 520°C to 42 dpa in FFTF. Halo images due to high-density microcavities ≈50-200 nm in size were observed roughly within the range of recoil Li (i.e., ≈1200 nm) from V_3B_2 particles. Infrequently, unidentified particles believed to be lithium precipitates were observed in the vicinity of the halo. Such particles were absent in specimens irradiated at 365 and 406°C. However, in the absence of a dark-field image produced from a reciprocal lattice spot of the particles, the nature of such precipitates is not clear. For instance, the precipitates could be confused with Ti_5Si_3 particles that are commonly observed in irradiated vanadium alloys containing Ti.[17,18]

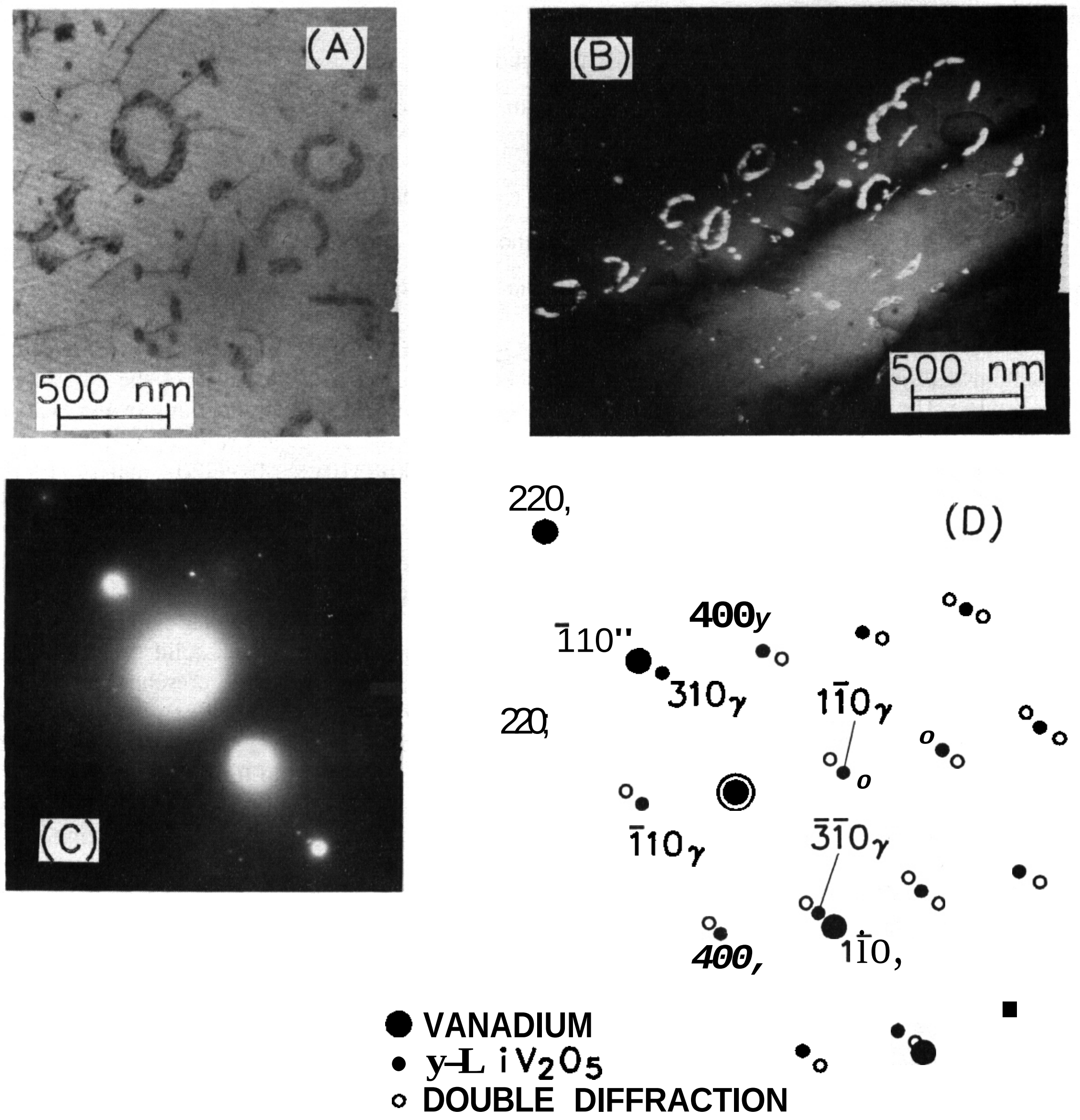

Figure 1. Shell-shaped γ-LiV_2O_5 precipitates observed in V-20Ti specimens after irradiation at 600°C (A) to ≈44 dpa (bright-field) and (B) to ≈80 dpa (dark-field); (C) SAD pattern of (B) and (D) indexed pattern of (C) showing refections from γ-LiV_2O_5 and double-diffraction spots

The shell-shaped and nearby globular features observed in Figs. 1A and 1B indicate a secondary precipitation that occurred in association with the damage zones reported by Rau and Ladd.[16] To identify positively the nature of the precipitates. SAD and dark-field-imaging analyses were. conducted. The result showed that the precipitates are γ-LiV_2O_5 phase. Examples of observed and indexed SAD patterns are. given, respectively, in Figs. 1C and 1D. The dark-field image of Fig. 1B was produced from the (400) reflection of γ-LiV_2O_5 in Fig. 1D.

Stoichiometry and crystallographic structures of $Li_xV_2O_5$ phases have been reported by Hagenmuller et al.[19] as:

α-$Li_xV_2O_5$, $0 < x \leq 0.13$, orthorhombic
(a = 1.1460 nm, b = 0.3554 nm, c = 0.4368 nm)
β-$Li_xV_2O_5$, $0.22 \leq x \leq 0.62$, monoclinic
(a = 1.003 nm, b = 0.360 nm, c = 1.538 nm, b = 110°40')
γ-$Li_xV_2O_5$, $0.88 \leq x \leq 1$, orthorhombic
(a = 0.9702 nm, b = 0.3607 nm, c = 1.0664 nm)

Lattice spacings of the α-$Li_xV_2O_5$ and γ-$Li_xV_2O_5$ phases calculated on the basis of these structures are tabulated in Table 2. The SAD patterns could be indexed only on the basis of the structure of γ-$Li_xV_2O_5$. The measured lattice spacings of the (110), (310), and (400) reflections in Fig. 1D are, respectively, 0.337, 0.242, and 0.243 nm, which agree well with the calculated values given in Table 2. Interplanar angles measured for $(1\bar{1}0)/(400)$, $(\bar{1}10)/(310)$, $(400)/(310)$, $(\bar{1}10)/(220)$, and $(1\bar{1}0)/510)$ reflections were, respectively, 69.6, 68.5, 42.2, 41.0, and 41.5°. These values also agree well with the respective calculated values, i.e., 69.66, 68.59, 42.23, 40.82, and 41.37°.

Based on the result of present study and information reported by Rau and Ladd,[16] the behavior of B and Li can be summarized by the schematic illustration in Fig. 2. According to the phase diagram reported in the literature,[20] there is no solubility between vanadium and lithium in the solid or liquid state. Therefore, virtually all Li atoms produced from the transmutation are expected to present themselves in $Li_xV_2O_5$ precipitates. Consequently, grain-boundary segregation of Li is not likely to occur. The precipitation of the Li-rich compound could be strongly influenced by the O level in the alloy, as well as by irradiation temperature, because a sufficient number of O atoms are needed to form the $Li_xV_2O_5$ phase. Solubility of B in vanadium-base alloys is also very low, although the solubility limit is not well known yet and values as low as 10 wppm[16] and as high as 140 wppm[13] have been mentioned for the temperature range of present interest. Boron atoms seem to be distributed more or less uniformly either in solid solution or in small V_3B_2 precipitates, and no evidence of grain-boundary segregation of B has been reported. This behavior of Li and B, therefore, seems to strongly support the viability of the ^{10}B-doping technique.

CONCLUSIONS

1. Microstructural evolution associated with transmutation of ^{10}B to helium and lithium has been characterized to provide a better understanding of the boron-doping technique, a technique frequently used to simulate the effect of helium generation under fusion reactor conditions. In the earlier stage of irradiation to low fluence, concentric shells of He-damage and Li-damage zones are produced around a V_3B_2 precipitate or a ^{10}B-rich cluster. On further irradiation, helium atoms diffuse away from the damage shell either to be dissolved in the matrix or to form microcavities, leaving a shell rich in Li, defect clusters, and dislocations. Oxygen atoms in solid solution migrate toward the Li-rich shells, and γ-LiV_2O_5 shells precipitate subsequently.

2. Grain-boundary segregation of B or Li is not expected to occur either during fabrication or irradiation. This behavior of Li and B, therefore, strongly supports the viability of the ^{10}B-doping technique.

Table 2. Calculated reciprocal lattice spacing (in unit of 0.1 nm) of α-$Li_xV_2O_5$[a] and γ-$Li_xV_2O_5$[b]

(hkl)	α-Li_xV_2O5	γ-$Li_xV_2O_5$	(hkl)	α-$Li_xV_2O_5$	γ-$Li_xV_2O_5$
100	11.46	9.70	130	1.18	1.19
010	3.55	3.61	103	1.44	3.33
001	4.37	10.66	013	1.35	2.53
110	3.39	3.38	311	2.24	2.34
011	2.76	3.41	113	1.34	2.45
101	4.08	7.17	131	1.14	1.18
200	5.73	4.85	222	1.34	1.61
020	1.78	1.80	320	1.61	1.57
002	2.18	5.33	302	1.90	2.76
201	3.47	4.41	203	1.41	2.86
021	1.65	1.78	230	1.16	1.17
120	1.76	1.77	032	1.04	1.17
102	2.14	4.67	023	1.71	1.61
012	1.86	2.98	321	1.51	1.56
210	3.02	2.89	312	1.67	2.19
220	1.70	1.69	231	1.12	1.16
022	1.38	1.71	213	1.31	2.24
202	2.04	3.59	123	1.12	1.59
111	2.68	3.22	132	1.04	1.16
112	1.83	2.85	322	1.30	1.51
121	1.63	1.75	232	1.02	1.14
211	2.48	2.79	223	1.10	1.53
221	1.58	1.67	400	2.87	2.42
212	1.77	2.54	040	0.89	0.90
211	1.37	1.68	004	1.09	2.66
300	3.82	3.23	401	2.40	2.36
030	1.18	1.20	410	2.23	2.01
003	1.45	3.55	140	0.88	0.89
301	2.87	3.09	104	1.09	2.57
031	1.14	1.19	014	1.04	2.14
310	2.60	2.40	041	0.87	0.90

[a] Orthorhombic, a = 1.1460 nm, b = 0.3554 nm, and c = 0.4368 nm, $0 < x \leq 0.13$.

[b] Orthorhombic, a = 0.9702 nm, h = 0.3607 nm, and c = 1.0664 nm, $0.88 \leq x \leq 1$.

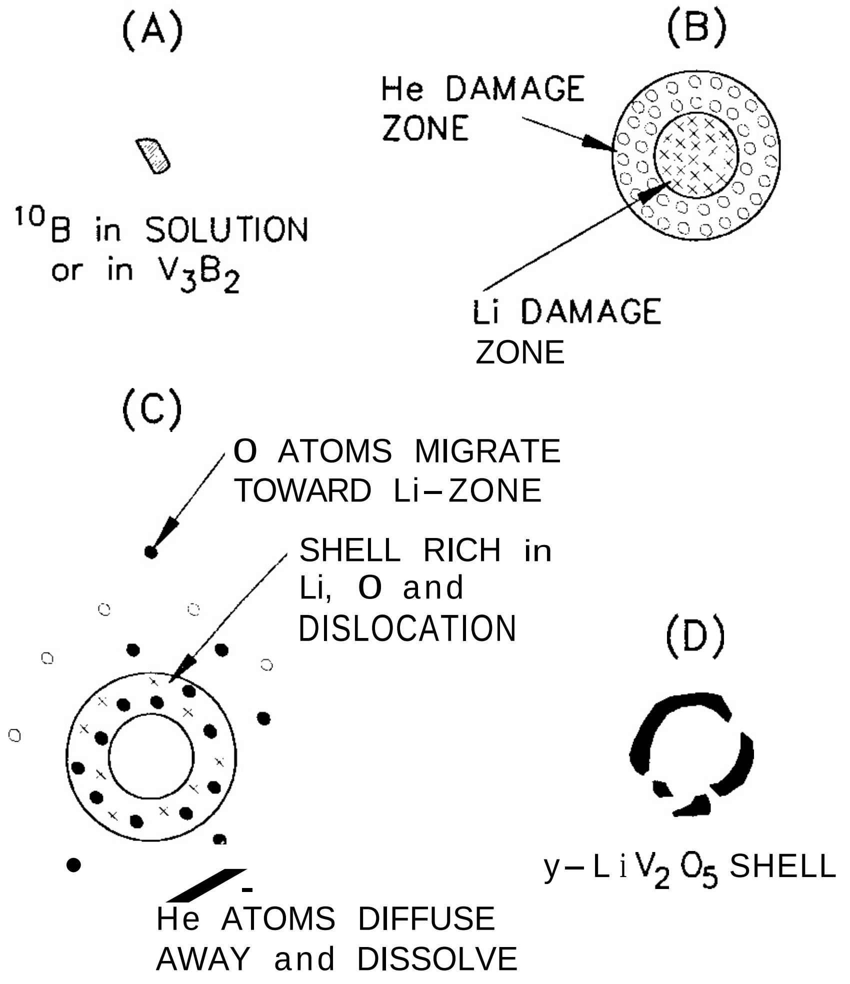

Figure 2. *Schematic illustration of microstructural evolution associated with transmutation of ^{10}B in neutron-irradiated vanadium-base alloys*

FUTURE WORK

Behavior of Li produced from transmutation of ^{10}B will be examined in similar specimens irradiated at 420 and 520°C.

REFERENCES

1. D. N. Braski, in Influence of Radiation on Material Properties, ASTM-STP 956 (1986) *pp*. 271-290.
2. D. N. Braski, J. Nucl. Mater. 141-143 (1986) 1125.
3. D. N. Braski, in Reduced Activation Materials for Fusion Reactors, ASTM-STP 1047 (1988) **pp.** 161-178.
4. H. Matsui, M. Tanaka, M. Yamamoto, and M. Tada, J. Nucl. Mater. 191-194 (1992) 919

5. M. Satou, K. Abc, and H. Matsui, J. Nucl. Mater. 191-194 (1992) 938.
6. W. van Witzenburg, A. Mastcnbroek. and J. D. Ellen. J. Nucl. Mater. 103-104 (1981) 1187.
7. M. P. Tanaka, E. E. Bloom, and J. A. Horak, J. Nucl. Mater. 114 (1981) 895.
8. M. L. Grossbcck and J. A. Horak, in Influence of Radiation on Material Proncnies, ASTM-STP 956 (1986) 291.
9. J. M. Vitek, D. N. Braski, and J. A. Horak. J. Nucl. Mater. 141-143 (1986) 982.
10. L. L. Horton and K. Farrell, J. Nucl. Mater. 122-123 (1984) 687.
11. H. Kawanishi and S. Ishino. in Reduced Activation Materials for Fusion Reactors, ASTM-STP 1047 (1988) pp. 179-189.
12. W. van Witzenburg and E. de Vries, in Effects of Radiation on Materials. ASTM-STP 1125 (1990).
13. H. Kawanishi, Y. Arai, and S. Ishino, J. Nucl. Mater. 191-194 (1992) 933.
14. D. L. Smith, H. Matsui, L. R. Greenwood, and B. A. Loomis, J. Nucl. Mater. 155-157 (1988) 1359.
15. D. L. Smith, B. A. Loomis, H. Matsui, M. L. Hamilton, K. L. Pearce, J. P. Kopasz, C. E. Johnson, R. G. Clemmer, and L. R. Greenwood, in Fusion Reactor Materials. Semiannual. Prog. Rep. DOE/ER-0313/10, *Oak* Ridge National Laboratory, Oak Ridge, TN (1991) 159.
16. R. C. Rau and R. L. Ladd, J. Applied. Phys. 40 (1969) 2899.
17. H. M. Chung and D. L. Smith, J. Nucl. Mater. 191-194 (1992) 942
18. H. M. Chung, B. A. Loomis, and D. L. Smith, in Effects of Radiation on Materials: 16th International Symposium, ASTM STP 1175, A. S. Kumar, D. S. Gelles. R. K. Nansod, and T. A. Little, eds., American Society for Testing and Materials, Philadelphia, 1993.
19. P. Hagenmuller, J. Galy, M. Pouchard, and A. Casalot, Mat. Res. Bulletin 1 (1966) 45
20. T. B. Massalski, J. L. Murray, L. H. Bennett, and H. Baker (Eds.), Binary Alloy Phase Diagrams, American Society for Metals. Metals Park, OH, 1986.

STATUS OF THE DYNAMIC HELIUM CHARGING EXPERIMENT (DHCE)* -- H. Tsai, H. M. Chung, B. A. Loomis, D. L. Smith (Argonne National Laboratory), H. Matsui (Tohoku University), M. L. Hamilton, L. R. Greenwood, and R. Ermi (Pacific Northwest Laboratory)

OBJECTIVE

The objective of this experiment is to investigate the effects of concurrent helium production and fast-neutron irradiation on the physical and mechanical properties of vanadium-base alloys. To isolate the helium effects, sibling samples were irradiated under comparable fast-neutron conditions but without helium production.

SUMMARY

Irradiation of the seven DHCE capsules was completed in the Materials Open Test Assembly (MOTA)-2B at the end of Cycle 12B in the Fast Flux Test Facility (FFTF). The accrued exposure was 203.3 effective full–power days (EFPDs), vis-a-vis the target exposure of 300 EFPDs. Peak damage in the samples was ∼29 displacement per atom (dpa). All seven capsules have been discharged from the FFTF and are being shipped to Argonne National Laboratory (ANL). where the samples will be retrieved from the capsules and distributed to the experimenters, including Monbusho of Japan, for examination and testing. A substantial effort is underway at ANL to retrieve the samples from the highly tritiated capsules.

PROGRESS AND STATUS

Introduction

Helium generation by (n,a) reactions in vanadium-based structural materials in fusion reactors may affect the physical and mechanical properties of the materials. To study these effects, it is important that the prototypical rates of helium generation be achieved in specimens during irradiation testing. Because of the fission neutron spectrum in the FFTF, the rate of helium production in vanadium is normally low (about 0.02 appm/dpa). The production rate in fusion reactors, on the other hand, is much higher (≈5 appm/dpa), due to the higher–energy 14–MeV fusion neutrons. The objective of the DHCE in the FFTF is to enhance helium production by in-situ decay of tritium, which is generated in the capsule lithium bond and subsequently diffuses into the vanadium-alloy samples. Detailed descriptions of the DHCE capsules can be found in Refs. 1 and 2.

Test Matrix

Seven capsules containing a large number of tensile samples and transmission electron microscope (TEM) disks were built and irradiated. The test matrix is shown in Table 1. A detailed listing of specimens is provided in Ref. 1. To ensure that helium generation starts immediately after the reactor startup, each capsule was precharged with a controlled amount of tritium contained in a tritiated vanadium foil. The ^{6}Li content in the lithium bond in each capsule was adjusted to maintain a near-constant rate of tritium influx into the samples during the irradiation.

---

*Work supported by the Office of Fusion Energy. U.S. Department of Energy, under Contract W-31-109-Eng-38.

Irradiation History

The DHCE was designed for a cumulative exposure of 300 EFPDs, in three 100-EFPD cycles. However, because of the halt of FFTF operation, the irradiation was terminated after two cycles, 12A and 12B, for a total exposure of 203.3 EFPDs. Two of the capsules, 4D1 and 4D2, located at Level **4** in the FFTF/MOTA, attained an estimated peak fluence of ≈5.3 x 10^{22} n/cm^2 and a damage of ≈29 dpa in vanadium. The other five **capsules** (5C1, 5C2, 5D1, 5E1, and 5E2) were located in Level 5 and attained estimated fluence and damage of –2.9 x 10^{22} n/cm^2 and =15 dpa, respectively.

Table 1. MOTA-2B DHCE test matrix

capsule	Irradiation Temperature (°C)	Initial Tritium (Ci)	^{6}Li^a Fraction (%)	Total Number of Specimens^b Japan TS(S)	Japan D3	U.S. SS3	U.S. TEM	Total Specimen Mass (g)^c
4D1	425	99	5.0	24	94	8	45	5.86
4D2	425	70	4.5	16	96	8	44	5.38
5E2	425	26	1.0	16	100	8	42	5.38
5D1	500	74	6.5	23	94	8	42	5.77
5E1	500	57	1.0	24	102	8	43	5.82
5C1	600	16	8.0	24	93	8	45	5.82
5C2	600	18	8.0	24	108	8	45	5.95

[a] Atomic ratio of ^{6}Li to total lithium.
[b] TS(S) and SS3 are tensile **specimens:** D3 and TEM are TEM **disks**
[c] Does not include tritiated vanadium foil.

Because of the uncertainties in the FFTF schedule, the DHCE capsules were not immediately discharged after Cycle 12B (March 1992). In the interim holding period, additional helium was generated in the samples due to the continued tritium diffusion and decay. As a result, the actual He/dpa ratios **will be** greater than those for the end-of-irradiation conditions listed in Table 2. The difference, however, is expected to be limited because of **a** lower distribution coefficient of tritium at the holding temperature (–200°C). A lower tritium concentration in vanadium at 200°C results in a lower helium production rate than at the higher test temperatures. The actual He/dpa ratios in the samples will be determined with helium assays when the samples are retrieved from the capsules.

Status

All seven DHCE capsules have been successfully removed from the MOTA-2B vehicle. The capsules are being shipped from Pacific Northwest Laboratory (PNL) to ANL for disassembly. To date, a shipment **of** three capsules has been completed. At ANL, the capsules will be opened to retrieve the samples for postirradiation examination and testing. The Monbusho samples in the capsules will be cleaned and returned to Japan.

Considerable design and engineering effort is being applied toward the disassembly of the DHCE capsules. The principal challenge **is** to safely retrieve and dispose of the tritium in the capsules. To ensure

Table 2. Preliminary calculated conditions for DHCE irradiation (203.3EFPDs)

Capsule	Irradiation Temp. (°C)	Plenum Vol. (mL)	Fast Fluence (10^{22} n/cm^2)	Damage (dpa)	He(appm)/dpa[a] End of Irr. (3/92)
4D1	425	2.85	5.3	29	3.8–23.2
4D2	425	2.93	5.3	29	2.8-17.4
5E2	425	3.11	2.9	15	2.1-12.5
5D1	500	2.53	2.9	15	4.4-29.0
5E1	500	2.49	2.9	15	3.1–20.2
5C1	600	2.77	2.9	15	1.1–6.7
5C2	600	2.47	2.9	15	1.1–6.8

[a] The first numbers assume Ka, the equilibrium ratio of tritium in vanadium alloy to that in the lithium bond. to be 0.073. The second numbers assume Ka to be 0.73. The two numbers cover the estimated possible range.

compliance with regulations. all of the high-risk operations will be completed remotely in enclosed systems inside the hot cells. In an enclosed chamber, the capsule plenum will be punctured to trap the cover gas, which may contain tritium. The lithium in the capsule will be dissolved with liquid ammonia in a second enclosed chamber. The released gaseous ammonia will be condensed in cold traps maintained at liquid nitrogen temperature, and the released tritium will be collected in chemical getters. After retrieval, the samples will be annealed at 400°C in high vacuum for ≈1 h to remove the residual tritium in the materials.

It is expected that the disassembly of DHCE capsules will commence in the summer of 1993.

REFERENCES

1. D. L. Smith et al., "Status of the Dynamic Helium Charging Experiment (DHCE) in FFTF/MOTA," Fusion Reactor Materials Semiannual Progress Report DOE/ER-0313/10, March 31, 1991, pp. 159-163.
2. L. R. Greenwood, "Revised Calculations for the Dynamic Helium Charging Experiment in FFTF/MOTA 2B," Fusion Reactor Materials Semiannual Progress Report DOE/ER-0313/10, March 31, 1991, pp. 156-158.

THERMAL CREEP BEHAVIOR OF V-5Cr-5Ti AND V-10Cr-5Ti ALLOYS[*] -- H. M Chung, B. A. Loomis, L. J. Nowicki, and D. L. Smith (Argonne National Laboratory)

OBJECTIVE

The objective of this work is to determine the thermal creep behavior of several promising V-Cr-Ti alloys, and thereby identify an alloy that exhibits an optimal combination of creep strength, tensile properties, fracture toughness, corrosion resistance, fabricability, and weldability for use as a structural material in a magnetic fusion reactor.

SUMMARY

The thermal creep rates and stress-rupture life of V-5Cr-5Ti and V-10Cr-5Ti alloys were determined at 600°C and the impurity composition and microstructural characteristics of creep-tested specimens were analyzed and correlated with the measured creep properties. The results of these tests show that V-5Cr-5Ti, which contains impurity compositions typical of a commercial vanadium-base alloy, exhibits creep strength substantially superior to that of V-20Ti, HT-9, or Type 316 stainless steel. The V-10Cr-5Ti alloy exhibits creep strength somewhat higher than that of V-5Cr-5Ti.

INTRODUCTION

Vanadium-base alloys are considered promising candidate structural materials for a fusion reactor first wall because they offer the important advantages of inherently low irradiation-induced activity, good mechanical properties, good compatibility with lithium, high thermal conductivity, and good resistance to irradiation damage. As part of a program to screen candidate alloys and develop an optimal alloy, extensive investigations have been conducted on the swelling behavior, tensile properties, impact toughness. and microstructural evolution of V, V-Ti, V-Cr, V-Cr-Ti, and V-Ti-Si alloys after irradiation by fast neutrons at 420, 520, and 600°C. From these investigations, V-Cr-Ti alloys containing 5-7 wt.% Cr. 3-5 at.% Ti, 500-1000 wt. ppm Si. and <1000 wt. ppm O+N+C were identified as desirable alloys that exhibit superior resistance to swelling, embrittlement, and hydrogen-induced effects during irradiation in lithium.[1-4] As a result, recent attention has focused primarily on the ternary alloys V-5Cr-5Ti, V-5Cr-3Ti, and V-7Cr-5Ti. For these alloys, however, no data base has been reported on thermal or irradiation creep, and a favorable creep behavior commensurate with the superior resistance of the alloys to swelling and embrittlement has not been demonstrated. In the work reported here, the thermal creep behavior of a V-5Cr-5Ti alloy was investigated at 600°C. The creep of V-10Cr-5Ti was also investigated to provide information on the effect of increased Cr content. Preliminary results of the creep tests have been described in a previous report.[5]

MATERIALS AND PROCEDURES

Details of experimental procedures have been reported elsewhere.[5] The chemical composition of the two alloys is given in Table 1. The 0.635-mm-thick tensile specimens were recrystallized prior to the creep test by annealing at 1125°C for 1 h in a vacuum of 2 x 10-5 Pa. The creep tests were conducted in an ion-pumped system in which vacuum was typically maintained at 2 x 10^{-6} Pa during testing at 600°C. The specimen was wrapped with a Ti or Ta foil to reduce contamination with impurities during testing. The elongation of a specimen was determined with a linear variable differential transformer (LVDT) with digitized output. The concentration of interstitial impurities (i.e., O, N, and C) and hardness (V' ') of

---

[*] Work supported by the Office of Fusion Energy. U.S. Department of Energy. under Contract W-31-109-Eng-38.

specimens were measured after testing. The phase and dislocation structures of the specimens were examined by transmission electron microscopy (TEM) before and after the creep test. In addition to the normal constant-load stress-to-rupture tests, applied stress was increased stepwise in some tests to measure a set of steady-state (minimum) creep rates corresponding to each stress level. An example of this kind of testing is shown in Fig. 1.

Table 1. Chemical composition of V-5Cr-5Ti and V-10Cr-5Ti alloys[a]

		Composition (wt.% or wt. ppm)					
Material	ANL ID	Cr	Ti	Si	O	C	N
V-5Cr-5Ti	BL-47	4.1 %	4.3 %	870	350	200	220
V-10Cr-5Ti	BL-43	9.2 %	4.9 %	340	230	100	31

[a] Annealed at 1125°C for 1 h.

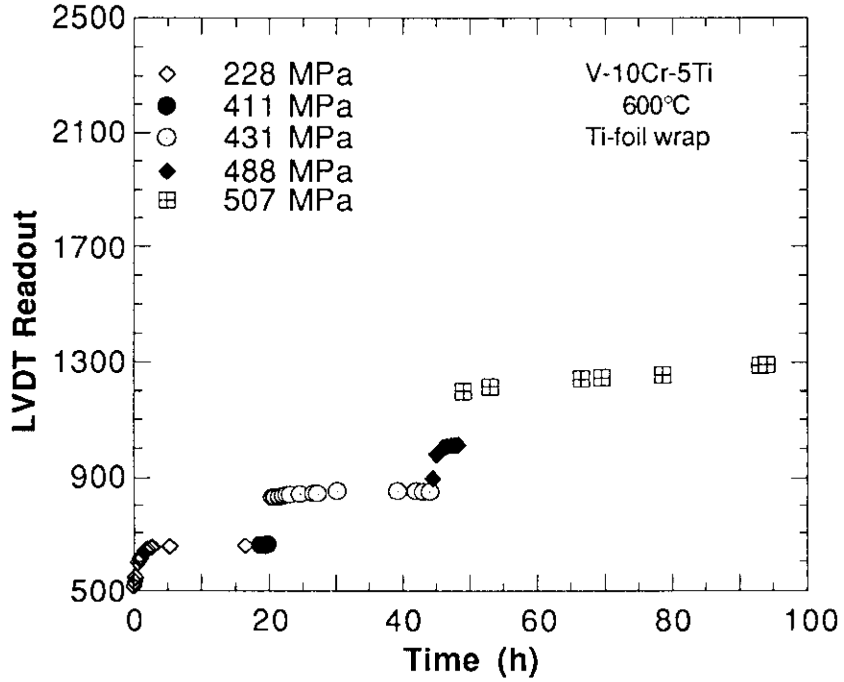

Figure 1. Elongation (LVDT readout) vs. time for V-10Cr-5Ti under stepwise increase in loading at 600°C, used to measure steady-state creep rates

RESULTS AND DISCUSSION

Stress-Rupture Life and Creep Rate

The stress-to-rupture time of V-5Cr-5Ti and V-10Cr-5Ti is given in Fig. 2. The figure shows that the creep strength of the V-10Cr-5Ti alloy is significantly higher (≈100 MPa) than that of V-5Cr-5Ti. This finding is consistent with the higher ultimate tensile strength (UTS) of V-10Cr-5Ti, i.e., ≈512 vs.

≈434 MPa.[6] At 600°C, the stress-to-rupture time of the two alloys is extremely sensitive to applied stress. For example, an increase in rupture time of more than two orders of magnitude was observed for V-5Cr-5Ti when applied stress was decreased only ≈5%. In previous investigations of creep properties of V-13Cr-3Ti, V-15Cr-3Ti, V-15Cr-5Ti, and Vanstar alloys at ≥650°C, a similar trend was observed.[7-9] **Because** of the high creep strength, determination of stress-rupture life of V-5Cr-5Ti at 600°C for stress ≤350 MPa **is** estimated to take impractically long test times (23 years).

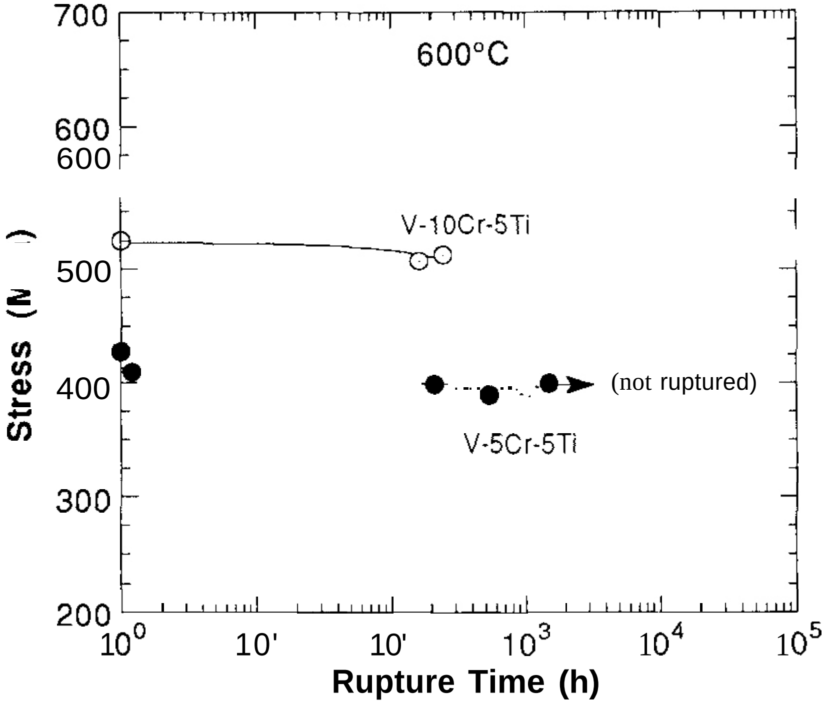

Figure 2. Stress-to-rupture time for V-10Cr-5Ti and V-5Cr-5Ti at 600°C

In Fig. 3, steady-state (minimum) creep rates of V-5Cr-5Ti and V-10Cr-5Ti alloys are shown as a function of applied stress. In the stress range between ≈300 and ≈420 MPa, the steady-state creep rate of V-5Cr-5Ti at *600°C* was between $\approx 10^{-3}$ and 5×10^{-2} %/h; for a comparable stress level, the creep rate of V-10Cr-5Ti was =7-8 times lower.

In Fig. 4, the creep strengths of V-15Cr-5Ti, V-10Cr-5Ti, and V-5Cr-5Ti are given. Although data for V-*15Cr-5Ti* were obtained at temperatures higher than 600°C,[9] the creep strengths can be compared from a plot of the Larsen-Miller parameter, which is defined by the equation

$$P = T(20 + \log t), \tag{1}$$

where creep temperature T is in K and rupture time t is in hours. The V-15Cr-5Ti specimens tested by Bajaji and Gold[9] contained 200-1400 wppm O, 500 wppm N, and 170 wppm C. By comparison, the impurity content measured in the creep-tested specimens of V-10Cr-5Ti and V-5Cr-5Ti in the present investigation were significantly lower; i.e., O, 370-770 wppm, N, 99-200 wppm, and C, 252-270 wppm (see Table *2)*. Within the uncertainties associated with the variations in impurity content, the results indicate that the creep strengths of V-15Cr-5Ti and V-10Cr-5Ti are similar, The UTS of the present V-10Cr-5Ti (541 MPa) and that of a V-15Cr-5Ti alloy containing 400 wppm O, 490 wppm N, and 280 wppm C was found to be similar (555 MPa). Therefore, it is not surprising that the creep strengths of the V-10Cr-5Ti and V-15Cr-5Ti shown in Fig. 3 are similar.

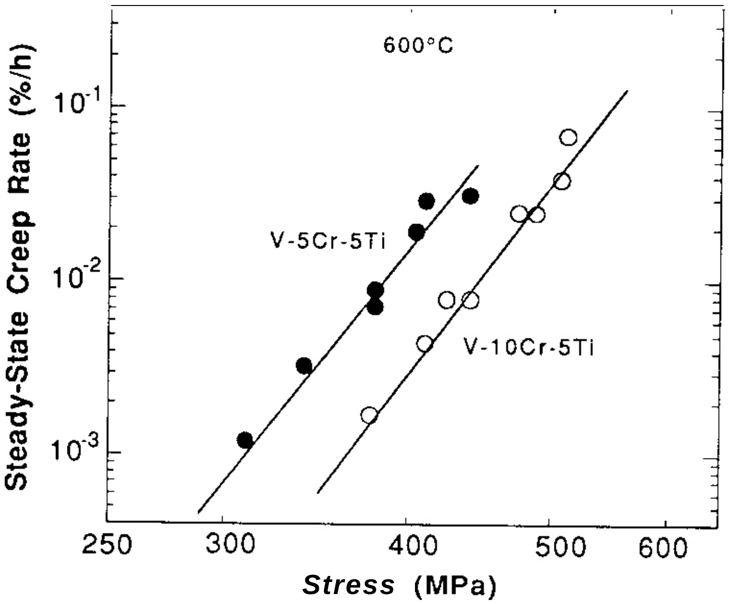

Figure 3. Steady-state **creep** *rate* **vs.** *stressfur V-10Cr-5Ti and V-5Cr-5Ti ar 600%*

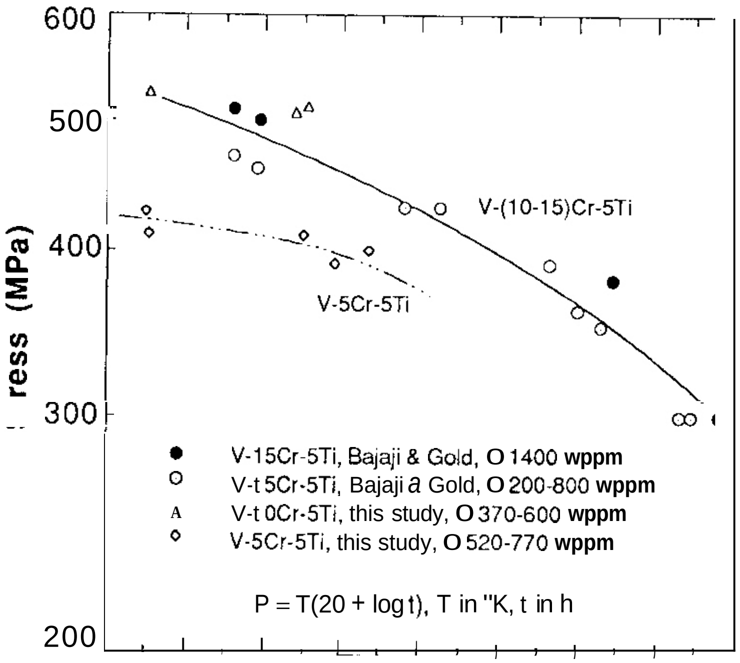

Table 2. Impurity content of creep specimens from V-5Cr-5Ti[a] and V-10Cr-5Ti[b] after testing at 600°C

			Time to	Composition (wt. ppm)			
Material	Specimen ID	Stress (MPa)	Rupture (h)	Wrap	O	C	N
V-5Cr-5Ti	BL-47A	420	1	none	560	252	160
V-5Cr-5Ti	BL-47C	408	1.1	Ta	520	261	200
V-5Cr-5Ti	BL-47E	387	541	Ta	770	-	200
V-5Cr-5Ti	BL-47F	410	213	Ta	520	270	190
V-10Cr-5Ti	BL-43A	512	243	none	600	–	120
V-10Cr-5Ti	BL-43B	507	162	Ti	370	-	99

[a] Ultimate tensile strength -434 MPa, hardness VHN ≈171

[b] Ultimate tensile strength ≈512 MPa, hardness VHN –192

Impurity Content and Microstructure

The creep of unalloyed vanadium is known to be sensitive to impurities (in particular dissolved O), although the creep of V-15Cr-5Ti, V-20Ti, and Vanstar-7 (V-9Cr-3Fe-1.3Zr-0.05C) appears to be less sensitive to O contamination (see Fig. 4).[7-9] In view of this, it was considered necessary to characterize the specimen impurity content, hardness. phase distribution, and other undesirable microstructural changes associated with the creep test to qualify the data obtained in this study.

The results obtained from analysis for O, N, and C concentrations are summarized in Table 2. Compared with the impurity content of the as-annealed specimens before the test (Table 1), N content in V-5Cr-5Ti decreased to some extent (from 220 to 160-190 wppm) and C content increased modestly (from 200 to 250-270 wppm). Nitrogen content in V-10Cr-5Ti increased from 31 to ≈100 wppm. However, the O content of both alloys increased significantly after testing (from 230-350 wppm to 370-770 wppm). The increase in O content was more pronounced in specimens tested without a wrap or with a Ta-foil wrap. For a specimen with a Ti wrap, the increase in O content was minimal (e.g., from 230 to 370 wppm). The more pronounced O contamination in the Ta-wrapped specimens is probably associated with the volatility of tantalum oxide. Because of the smaller contamination when Ti foil was used, all subsequent tests are being conducted with a Ti wrap. Despite the increase in O and C. the impurity content of the two alloys is still comparable to that typical of a commercial vanadium-base alloy.

To detect any undesirable phase structure that might have been produced during testing, TEM specimens excised from near the gage section were examined. The results are. shown in Fig. 5. A comparison of Figs. 5A and 5B shows that the phase structure of V-5Cr-5Ti did not change appreciably during testing at 600°C for 541 h. That is, the size and distribution of the Ti(O,N,C) precipitates. normally observed in these alloys after fabrication? were similar before and after testing, and no new types of precipitates were produced.

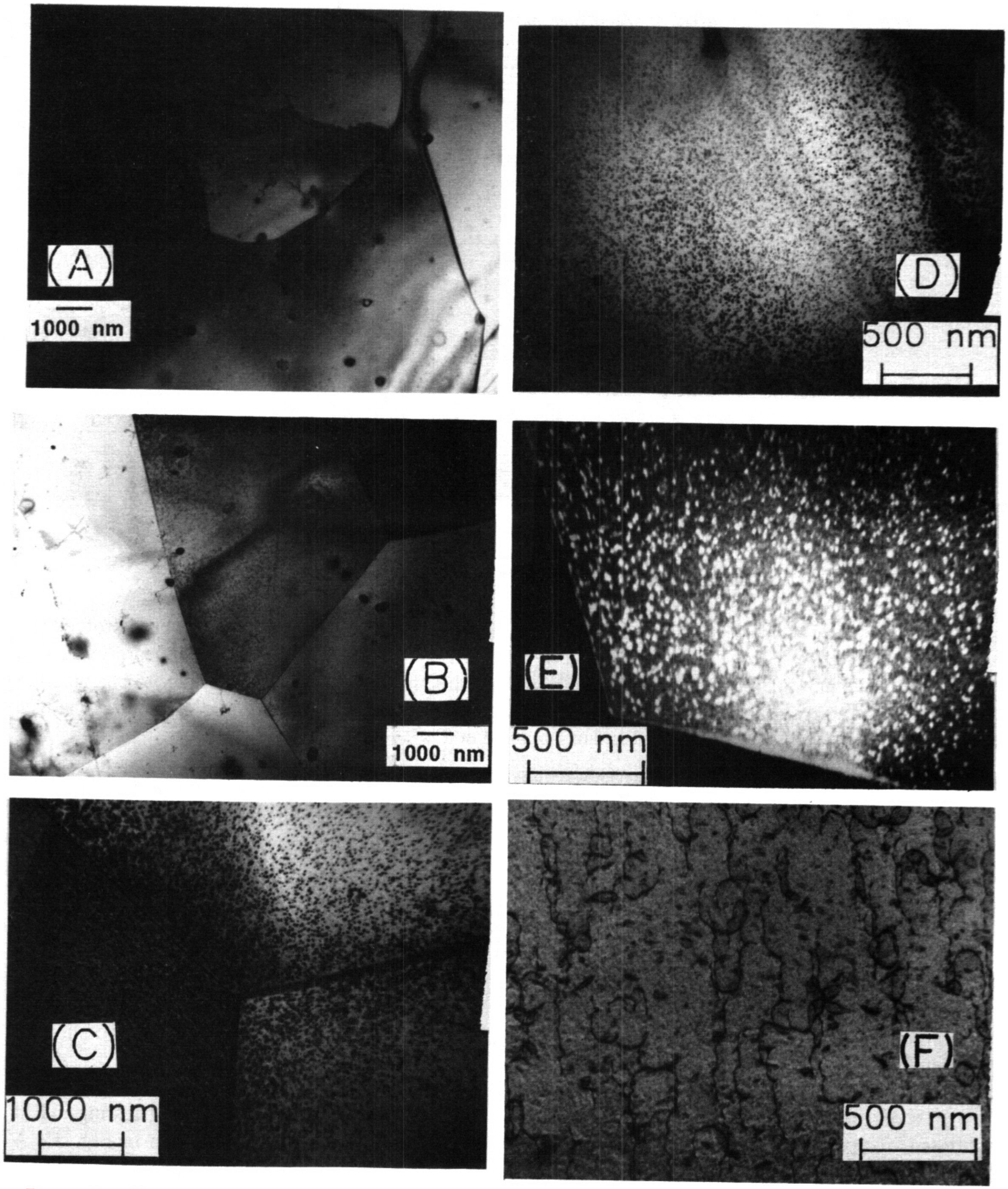

Figure 5. Phase structure of V-5Cr-5Ti (A) before and (B) after creep test at 600°C for 541 h; (C) dislocation loops in the specimen shown in (B), and (D) in V-10Cr-5Ti after test at 600°C for 216 h; (E) dark-field image of loop distribution of (C); and (F) bright-field image of dislocations and dislocation loops of (C)

However, dislocation loops were observed in high density in creep-tested specimens of both V-5Cr-5Ti and V-10Cr-5Ti (Figs. 5C and 5D, respectively). From bright-field imaging alone, the dislocation loops (≤100 nm in size) can be mistakenly confused with small precipitates. However, results of selected-area diffraction and dark-field imaging showed that they are indeed dislocation loops. Line dislocations were also observed frequently in conjunction with loops (Fig. 5E). A major difference in the microstructural aspect of creep-tested V-5Cr-5Ti and V-10Cr-5Ti specimens was the distribution of dislocation loops. In V-10Cr-5Ti, loop distribution was more or less uniform within a grain. In contrast, size and density of the loops were higher near a grain boundary in V-5Cr-5Ti. This can be seen by comparing the two bright-field images of Figs. 5C and 5D. The dark-field image shown in Fig. 5F reveals more clearly a dense loop distribution of V-5Cr-5Ti in the vicinity of a grain boundary.

Hardness profiles were measured across the specimen thickness (nominal thickness 0.635 mm) after the creep test. An example of typical hardness profiles is given in Fig. 6, which was determined for a V-10Cr-5Ti specimen that ruptured after 162 h. Except for narrow regions ≤0.01 mm underneath the free surfaces, a more or less uniform hardness of ≈205 VHN was observed, a slight increase from the original hardness of ≈192 VHN. The hardness increase is attributed not only to the effect of the increase in O content (i.e., from 230 to 370 wppm) but also to the effect of the high-density dislocation loops.

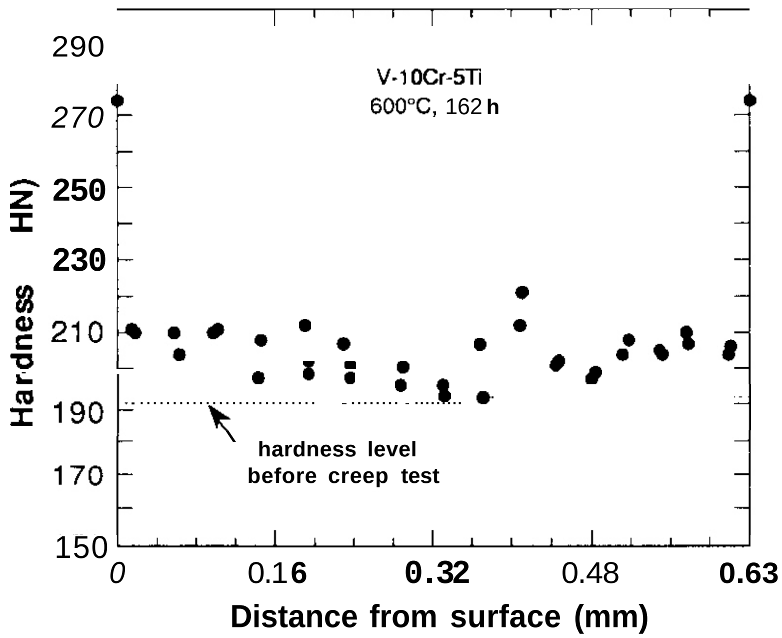

Figure 6. Vickers hardness profile across wall rhickness of V-10Cr-5Ti after creep test ar 600°C for 162 h

In summary, no unusual features were observed that indicate an unacceptable effect of the environment of the creep test at 600°C. Impurity content and phase structure of the test specimens were similar to those of typical commercial alloys.

Comparison with Other Materials

In Fig. 7, the creep property of V-5Cr-5Ti and ferritic and austenitic steels is shown in Larsen-Miller plots. From the figure, it is obvious that the creep strength of the alloy is substantially superior to that of

HT-9, Type 316 stainless steel, and V-20Ti. In particular, this difference in creep strength is more pronounced when hen-Miller parameters are higher, i.e., at higher temperatures or longer times.

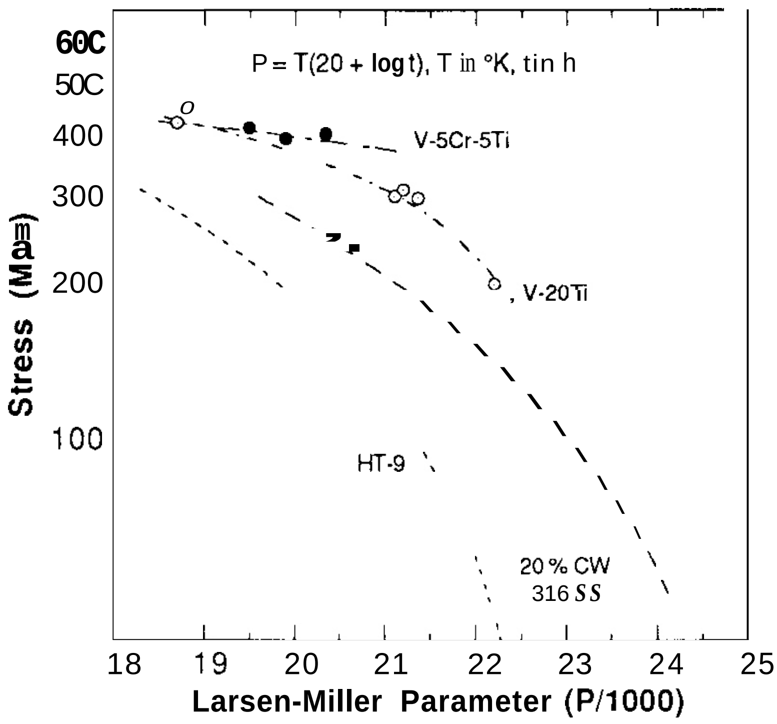

Figure 7. Larsen-Miller plots of creep strength of V-5Cr-5Ti and ferritic and austenitic steels

It has been reported that creep strength of binary V-Ti and ternary V-15Cr-Ti and V-3Cr-Ti alloys is maximum for 3 wt.% Ti.[7,8] Titanium content greater or less than ≈3 wt.% resulted in significantly decreased creep strength. Based on this observation, the creep strength of V-5Cr-3Ti is expected to be substantially higher than that of V-5Cr-5Ti. Increasing the Cr content to 7 wt.% is also expected to improve the creep strength of V-5Cr-5Ti. However, selection of optimal content of Cr (5-7 wt.%) and Ti (3-5 wt.%) must be tied closely to other important considerations, in particular, to the effects of neutron damage and helium generation on embrittlement and fracture toughness.

CONCLUSIONS

1. Stress-rupture life and steady-state creep rate of V-5Cr-5Ti and V-10Cr-5Ti have been determined at 600°C. Results of characterization of impurity contamination, hardness, phase structure, and dislocation and loop structures in the creep-tested specimens showed no unusual features that indicate an unacceptable effect of the environment on the measured creep rates. Impurity content of the tested specimens was comparable to that of a typical commercial vanadium-base alloy.

2. V-5Cr-5Ti exhibits a creep strength that is substantially superior to that of Type 316 stainless steel, HT-9, or V-20Ti, in particular, at higher Larsen-Miller parameters, i.e., at higher temperatures and/or longer service times.

3. Creep strength of V-10Cr-5Ti is similar to that of V-15Cr-5Ti and several times higher than that of V-5Cr-5Ti. However, if a creep strength higher than that of V-5Cr-5Ti is required. V-5Cr-3Ti or V-7Cr-5Ti appears to be a more attractive alternative than V-10Cr-5Ti from the point of view of irradiation-induced embrittlement.

FUTURE WORK

Stress-rupture tests on V-5Cr-5Ti and V-10Cr-5Ti will be extended to 650°C to obtain a larger number of data in a reasonable time period. Creep tests will be conducted on V-5Cr-3Ti, V-7Cr-5Ti, and V-3Ti-0.1Si alloys at 600 and 650°C, and an alloy that exhibits optimal creep properties will be identified.

REFERENCES

1. B. A. Loomis, A. B. Hull, and D. L. Smith, "Evaluation of Low-Activation Vanadium Alloys for Use as Structural Material in Fusion Reactors," J. Nucl. Mater., 179-181 (1991) 148-154.

2. B. A. Loomis and D. L. Smith, 'Vanadium Alloys for Structural Applications in Fusion Systems: A Review of Mechanical and Physical Properties," J. Nucl. Mater.. 191-194 (1992) 84-91.

3. H. M. Chung and D. L. Smith, "Correlation of Microstructure and Tensile and Swelling Behavior of Neutron-Irradiated Vanadium Alloys," J. Nucl. Mater. 191-194 (1992) 942-947.

4. H. M. Chung, B. A. Loomis, and D. L. Smith, "Irradiation-Induced Precipitation in Vanadium-Base Alloys Containing Titanium." Effects of Radiation on Materials: 16th International Symposium, ASTM STP 1175, A. S. Kumar, D. S. Gelles, R. K. Nanstad. and T. A. Little, eds., American Society for Testing and Materials, Philadelphia, 1993.

5. B. A. Loomis, L. J. Nowicki, and D. L. Smith, "Creep of V-5Cr-5Ti and V-10Cr-5Ti Alloys at 600°C," in Fusion Reactor Materials, Semiannual Progress Report for Period Ending September 30, 1992, DOE/ER-0313/13, U.S. Department of Energy, Office of Fusion Energy, in press.

6. B. A. Loomis, L. J. Nowicki, and D. L. Smith, "Tensile Properties of Vanadium and Vanadium-Base Alloys," in Fusion Reactor Materials, Semiannual Progress Report for Period Ending March 31, 1991, DOE/ER-0313/10, U.S. Department of Energy, Office of Fusion Energy, July 1991, pp. 145-155.

7. M. Schirra, "Das Zeitstandfestigkeits und Kriechverhalten von Vanad-Basis Legierungen," KfK-2440, April 1977, Karlsruhe Nuclear Research Center, Germany.

8. D. Harrod and R. Gold,"Mechanical Properties of Vanadium and Vanadium Base Alloys," Int. Met. Rev. 25 (1980) 163-221.

9. R. Bajaji and R. E. Gold, in Alloy Development for Irradiation Performance Semiannual Progress Report, DOE/ER0045/10, Oak Ridge National Laboratory, Oak Ridge, TN, 1983, p. 74.

DUCTILE-BRITTLE TRANSITION TEMPERATURES OF UNIRRADIATED VANADIUM ALLOYS, BASED ON CHARPY-IMPACT TESTING* - B. A. Loomis. L. J. Nowicki. J. Gazda, and D. L. Smith (Argonne National Laboratory).

OBJECTIVE

The objective of this research is to determine the composition of a vanadium-base alloy with the optimal combination of mechanical properties, corrosion resistance, fabricability, and weldability for use as a structural material in the environment of a magnetic fusion reactor.

SUMMARY

Ductile-brittle transition temperatures (DBTTs) were determined by Charpy-impact tests for dehydrogenated and hydrogenated V-3Ti, V-5Cr-3Ti, and V-5Cr-5Ti alloys. These DBTT data complement the data previously obtained by Loomis et al.[1-3] on Charpy-impact testing of unalloyed V, V-1Ti, V-3Ti-1Si, V-5Ti, V-10Ti, V-18Ti, V-4Cr-4Ti, V-8Cr-6Ti, V-9Cr-5Ti, V-10Cr-9Ti, V-14Cr-5Ti, V-15Cr-5Ti, V-7Cr-15Ti, and Vanstar-7 alloys. The results show that V alloys with Ti additions (0-18 wt.%) have a minimum DBTT (~-250°C) in an alloy containing 3-5 wt.% Ti, that addition of 4 to 15 wt.% Cr to V-(4-6)Ti alloy results in a substantial increase (25-215°C) of the DBTT, and that 0.5 and 1.0 wt.% Si additions to V-3Ti alloy result in a significant increase (~100°C) in DBTT. In addition, the results show that the presence of 400-1200 appm H in unalloyed V and V-base alloys causes a significant increase (~100°C) in DBTT. The results of these studies lead us to recommend the V-5Cr-5Ti alloy containing ~400 ppm O, ~200 ppm N, ~200 ppm C, and ~900 ppm Si for use as structural material in a fusion reactor.

PROGRESS AND STATUS

Introduction

The V-15Cr-5Ti alloy has been considered to be a reference alloy for the evaluation of vanadium-base alloys as structural material for a fusion reactor, based on this alloy's generally attractive mechanical, corrosion, and irradiation performance. However, recent data obtained from Charpy-impact tests and tensile tests on this alloy with and without neutron irradiation show that this alloy may be unacceptable as structural material for a fusion reactor because of its high DBTT (>250°C).[1-5] Loomis et al. have shown from Charpy-impact tests on unirradiated and irradiated vanadium alloys that a vanadium-base alloy containing Cr and/or Ti and Si alloying additions and intended for use as a structural material in a fusion reactor should contain 3-9 wt.% total alloying addition for maximum resistance to hydrogen- and/or irradiation-induced embrittlement.[2,3] In this report, we present data on the DBTTs for V-3Ti, V-5Cr-3Ti, and V-5Cr-5Ti alloys that tend to confirm the requirement of 3-9 wt.% combined Cr and/or Ti alloying addition to vanadium for a minimum DBTT. We also include DBTT data for unirradiated V and V-base alloys previously presented in Refs. 1-3.

Materials and Procedures

Vanadium-base alloys with the nominal compositions of V-3Ti, V-5Cr-3Ti, and V-5Cr-5Ti were obtained in sheet form with a 50% thickness reduction, i.e., cold work, resulting in a nominal thickness of 3.8 mm. The compositions of these materials and previously tested vanadium alloys

*Work supported by the Office of Fusion Energy, U.S. Department of Energy, under Contract W-31-109-Eng-38.

are listed in Table 1.[1-3]

Table 1. Compositions of V and V alloys.

Nominal Composition	ANL I.D.	Concentration (wt.%)			Concentration (ppm)			
		Cr	Ti	Fe	O	N	C	Si
V	BL 51				570	49	56	370
V-1Ti	BL 50		1.0		230	130	235	1050
V-3Ti	BL 62		3.1		320	86	109	660
V-3Ti-0.5Si	BL 42		3.1	0.02	580	190	140	5400
V-3Ti-1Si	BL 45		2.5	0.01	345	125	90	9900
V-5Ti	BL 46		4.6		300	53	85	160
V-10Ti	BL 12		9.8	0.63	1670	390	450	245
V-18Ti	BL 15		17.7	0.04	830	160	380	480
V-5Cr-3Ti	BL 54	5.1	3.0		480	82	133	655
V-4Cr-4Ti	BL 47	4.1	4.3		350	220	200	870
V-5Cr-5Ti	BL 63	4.6	5.1		440	28	73	310
V-8Cr-6Ti	BL 49	7.9	5.7		400	150	127	360
V-9Cr-5Ti	BL 43	9.2	4.9	0.02	230	31	100	340
V-14Cr-5Ti	BL 24	13.5	5.2	0.05	1190	360	500	390
V-15Cr-5Ti	BL 41	14.5	5.0	0.02	330	96	120	400
V-10Cr-9Ti	BL 44	9.9	9.2	0.04	300	87	150	270
V-7Cr-15Ti	BL 10	7.2	14.5	0.09	1110	250	400	400
Vanstar-7[a]	BL 28	9.7		*3.50*	280	520	640	

[a] Alloy contains 1.3% Zr.

Miniature Charpy-impact specimens were prepared for a determination of the temperature dependence of fracture behavior in the dehydrogenated and hydrogenated V-base alloys. The Charpy-test specimens had overall dimensions of 3.30 x 3.30 x 25.4 mm and a notch depth of 0.61 mm. Specimens were prepared with the notch orientation perpendicular to the rolling direction maintained during thickness reduction. Dehydrogenated Charpy-test specimens in the fully recrystallized condition were prepared from the 50% cold-worked materials by annealing for 1 h in a vacuum of 2×10^{-5} Pa.

The V-3Ti alloy specimens were annealed at 1050°C, and the V-5Cr-3Ti and V-5Cr-5Ti alloy specimens were annealed at 1125°C. In the case of the previously tested alloy specimens, the V-Cr-Ti specimens and the Vanstar-7 specimens were annealed at 1125°C. The V-18Ti and V-3Ti-Si alloy specimens were annealed at 1100 and 1050°C, respectively. These annealing conditions for the cold-worked materials resulted in average recrystallized grain diameters in the range of 0.02-0.04 mm. Hydrogen was introduced into Charpy-test specimens of the alloys by annealing the cold-worked specimens at the previously mentioned temperatures in argon-filled quartz tubes for 1 h and subsequently quenching the tubes and their contents, without rupture, in water. The hydrogen concentration in the specimens was adjusted by surface-finishing the specimens prior to the anneal."

The hydrogen concentration in the Charpy-test specimens was determined from the total partial pressure of hydrogen that was evolved on heating a specimen at 15°C/min from 25°C to 1000°C. This procedure is discussed in Ref. 6. In the case of the Charpy specimens annealed in vacuum (i.e., dehydrogenated), the hydrogen concentration was determined to be <30 appm. The hydrogen concentration in specimens annealed in quartz tubes (i.e., hydrogenated) ranged from 400 to 1200 appm.

The Charpy-impact tests were performed with an instrumented Dynatup Drop-Weight Impact Test machine. Impact velocity and load for these tests were 2.56 m/sec and 14.995 kg, respectively. Energy absorption was determined from applied load-time data that were acquired during impact. These data were analyzed and plotted with a GRC Model 730-I data acquisition and analysis system. The specimen temperature at the instant of impact was determined from a thermocouple that was spot-welded near the notch. Specimen temperatures during the Charpy tests were limited to -190 to 250°C. A curve for the energy absorbed during impact versus test temperature for V and V-base alloy specimens was fitted with a hyperbolic tangent equation to determine the curve inflection point; this curve point was used to define the DBTT. The DBTTs of the V-1Ti, V-3Ti, V-5Ti, V-10Ti, V-4Cr-4Ti, and V-5Cr-5Ti alloys were <-190°C since the alloy specimens on impact bent to an angle of 85" without complete fracture at temperatures ≥-190°C; and the DBTTs of these alloys were estimated from the temperature dependence of energy absorption during impact for test temperatures ≥-190°C.

The microstructures of annealed Charpy specimens, the appearance of fracture surfaces of tested specimens, and the temperature dependence of energy absorbed during the impact tests on some of the V-base alloys are described in Refs. 1 and 2.

Experimental Results

The DBTTs for dehydrogenated (<30 appm H) and hydrogenated (400-1200 appm H) V and V-base alloys are presented in Table 2.

1. Dependence of DBTT on Ti concentration

The DBTT dependence of dehydrogenated (i.e., <30 appm H) and hydrogenated (i.e., 400-1200 appm H) V-Ti alloys on Ti concentration is shown in Fig. 1. The DBTT of unalloyed V (-150°C for dehydrogenated V and -10°C for hydrogenated V) decreases as the Ti concentration increases to 3-5 wt.%, to yield the alloys with the minimum DBTTs, i.e., ≈-250°C for dehydrogenated alloy and -160°C for hydrogenated alloy. DBTTs for V-Ti alloys (dehydrogenated and hydrogenated) increase as Ti concentration increases from ~5 to ~18 wt.%. The DBTT values of the dehydrogenated and hydrogenated V-18Ti alloy were -40°C and 55°C, respectively.

As shown in Fig. 1, the presence of 400-1200 appm H in binary V-(0-18)Ti alloys causes a significant DBTT increase (60-200°C) in the dehydrogenated alloys. The differences between the DBTTs of dehydrogenated and hydrogenated unalloyed V and binary V-Ti alloys suggest that V-Ti alloys containing ≤5 wt.% Ti may be more susceptible to hydrogen embrittlement (see Fig. 1).

2. Dependence of DBTT on Cr concentration

The DBTT dependence of dehydrogenated and hydrogenated V-Cr-(4-6)Ti alloys on Cr concentration is shown in Fig. 2. The DBTTs of dehydrogenated and hydrogenated V-(4-6)Ti alloys, e.g., ≈-250°C and -160°C, respectively, for V-5Ti (BL 46), increase as the Cr concentration in these alloys rises to at least 15 wt.%. DBTT values of the dehydrogenated and hydrogenated V-15Cr-5Ti alloy (BL 41) were -10°C and 135°C, respectively. The presence of 400-1200 appm H in V-Cr-(4-6)Ti alloys causes a significant DBTT increase (60-145°C) in the dehydrogenated alloy (Fig. 2). The V-Cr-(4-6)Ti alloys containing < 10 wt.% Cr may be less susceptible to hydrogen embrittlement.

3. Dependence of DBTT on combined Cr and Ti concentration

The DBTT dependence of V and V-base alloys on combined Cr and Ti concentration is shown

Table 2. DBTTs of V and V-base alloys.

Nominal Composition	ANL I.D.	Hydrogen (appm)	DBTT (°C)
V	BL **51**	<30	-150
		700	-10
V-1Ti	BL *50*	<30	-225 [a]
		650	*-25*
V-3Ti	BL 62	<30	-255 [a]
		600	-175
V-3Ti-0.5Si	BL **42**	**<30**	-150
		520	-125
		970	-170
V-3Ti-1Si	BL 45	**<30**	-165
		990	**-30**
V-5Ti	BL **46**	<**30**	-250 [a]
		860	-160
V-10Ti	BL 12	<30	-190 [a]
		600	-130
V-18Ti	BL 15	<30	-40
		580	+55
V-5Cr-3Ti	BL 54	<30	***-85*** [b]
		600	**t65** [b]
V-4Cr-4Ti	BL 47	<30	*-225* [a]
		1200	-125
V-5Cr-5Ti	BL **63**	<30	-190 [a]
		600	-110
V-8Cr-6Ti	BL 49	<30	***-85***
		600	-5
V-9Cr-5Ti	BL **43**	**<30**	-60
		670	*+50*
V-14Cr-5Ti	BL 24	<30	-10
		590	+130
V-15Cr-5Ti	BL 41	<**30**	-10
		620	+135
V-10Cr-9Ti	BL 44	**<30**	+10
		1180	+155
V-7Cr-15Ti	BL 10	**<30**	+25
		400	+250
Vanstar-7	BL ***28***	<30	***-65***
		500	*-25*

"Lowest test temperature was -190°C. DBTT was estimated from the temperature dependence **of** energy absorption for test temperatures above -190°C.

[b]**DBTT was** anomalously high due to presence of **6-16** μm diameter precipitates on grain boundaries.

in Fig. **3.** (Note that the combined Cr and Ti concentration **is** $C_{Cr} + (C_{Ti})^{0.95}$. For the Vanstar-7 alloy, the Fe and Zr concentrations are treated as Cr and Ti concentrations, respectively. The DB'IT dependence on combined Cr and Ti concentration (Fig. **3)** is similar to the DBTT dependence on Ti concentration shown in Fig. 1, i.e., the minimum DBTT for dehydrogenated and hydrogenated V-base

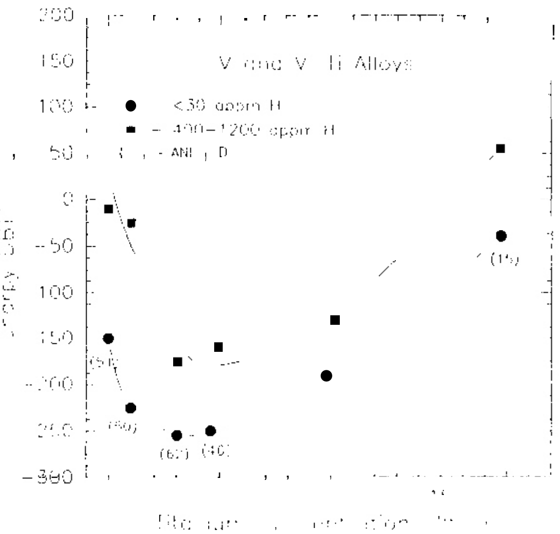

Fig. 1. V and V-Ti alloy dependence of DBTT on Ti concentration.

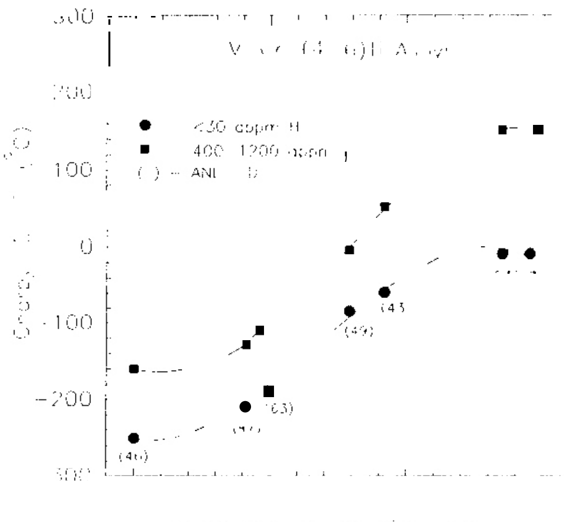

Fig. 2. V-Cr-(4-6)Ti alloy dependence of DBTT on Cr concentration.

alloys is seen when the combined Cr and Ti concentration is ~5 wt.%. The differences between DBTTs of dehydrogenated and hydrogenated unalloyed V and V-base alloys show that V-base alloys containing < 15 wt.% combined Cr and Ti concentration are less susceptible to hydrogen embrittlement (Fig. 3).

The DBTT data in Table 2 for the dehydrogenated and hydrogenated V-5Cr-3Ti alloy (BL 54) are not shown in Fig. 3, since these DBTTs are believed to be anomalously high (100-200°C) and do not conform with the general trend for dependence of the DBTT of V-base alloys on combined Cr and Ti concentration. The surfaces of fractured Charpy specimens of the V-5Cr-3Ti alloy were examined by observation with a JEOL JSM-50 scanning electron microscope (SEM). These observations showed the presence of precipitates with 6-16 μm diameter on grain boundaries (Fig. 4). These precipitates were non-uniformly distributed in the fracture surface with the highest number density of precipitates in some areas being ~300/mm^2 (e.g., see Fig. 4). The average grain size appeared to be significantly larger in areas of high precipitate number density. Precipitates with similar appearance and diameter (6-16 μm) were also observed in the fracture surface of the V-3Ti alloy (BL 62), but the precipitates were uniformly distributed with a number density of ~50/mm^2 (e.g., see Fig. 5). Analyses of the precipitates in the V-5Cr-3Ti and V-3Ti alloys using x-ray energy dispersive spectroscopy (EDX) showed that the precipitates were a vanadium compound containing K. Na, Cl, C. and O. It should be noted that these precipitates did not contain Ti. Precipitates with this composition, i.e., V(K, Na, Cl, C, O) were not observed in the other alloys.

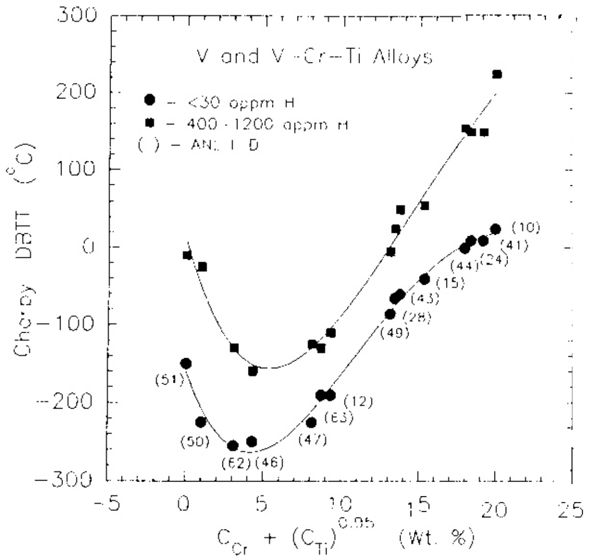

Fig. 3. V and V-base alloy dependence of DBTT on combined Cr and Ti concentration.

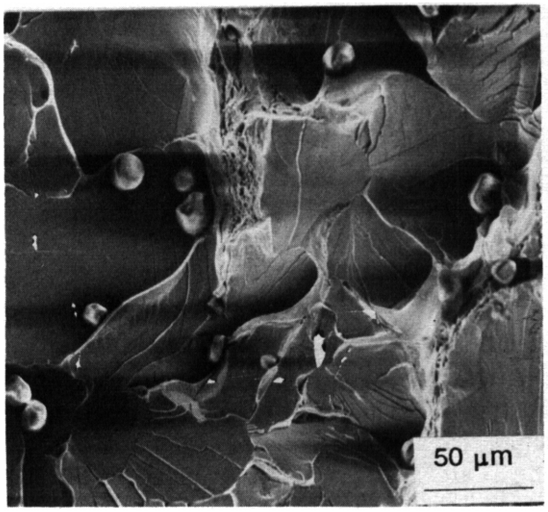

Fig. 4. Fracture surface of V-5Cr-3Ti alloy.

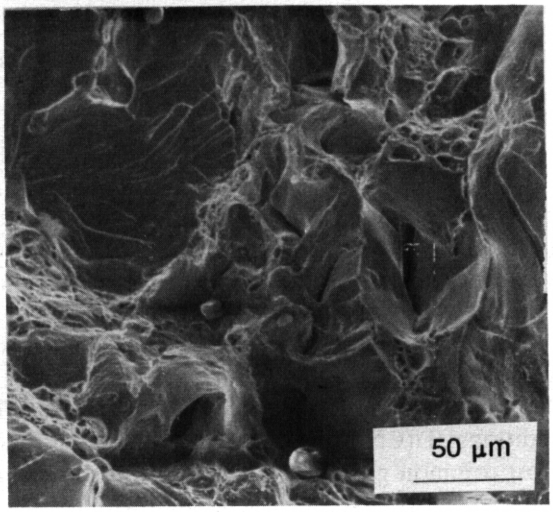

Fig. *5.* Fracture surface of V-3Ti alloy.

4. Dependence of DBTI **on** Si concentration

The DBTTs for V-3Ti (BL 62), V-3Ti-0.5Si (BL 42), and V-3Ti-1Si (BL 45) alloys are presented in Table 2 and in Fig. 6. These results suggest that the addition of 5400-9900 ppm Si to V-3Ti alloy results in ≈100°C increase of DB'IT in the dehydrogenated V-3Ti alloy. Hydrogenation (520-990 appm) of V-3Ti and V-3Ti-(0.5-1)Si alloys caused a 25-135°C increase of DBTI. The experimental results suggest that the presence of >0.5 wt.% Si in V-3Ti alloy causes this alloy to **be** more **susceptible** to embrittlement by hydrogen.

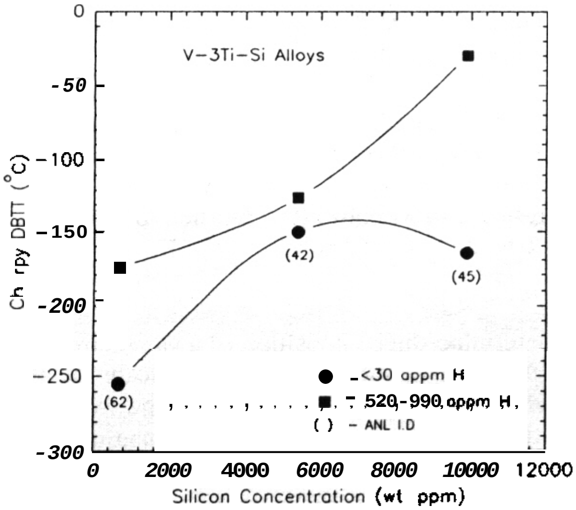

Fig. 6. V-3Ti alloy dependence of DBTT on Si concentration.

The effect of Si concentration on the DB'IT of V-Cr-Ti alloys has not been extensively investigated. However, comparison of the DB'IT for the V-4Cr-4Ti alloy (≈-225°C) containing 870 ppm Si and the V-5Cr-5Ti alloy (-190°C) containing 310 ppm Si suggests that the difference in DB'IT for these alloys is principally due to the higher Cr and Ti concentration, rather than the lower Si concentration, in the V-5Cr-5Ti alloy. With the exception of the V-3Ti-0.5Si (BL 42) and V-3Ti-1Si (BL 45) alloys, the Si concentration in the V-Ti and V-Cr-Ti alloys in Table **1** is in the range of 160 to 1050 ppm with the average Si concentration being 460 ppm. There **was no** significant effect of Si concentration **on** the DBTI (Table **1** and Figs. 1-3) of these alloys that could be attributed to variations of Si concentration in the range of 160-1050 ppm.

5. Dependence of DBIT on O, N, and *C* concentration

The O, **N,** and C concentrations in the V-Ti and V-Cr-Ti **alloys** in Table 1 are in the **ranges** of 230-1670, 28-390, and 73-500 ppm, respectively. There was no significant effect on the DB'IT (Table

2 and Figs. 1-3) of these alloys that could be attributed to these ranges of O, N, and C concentration.

DISCUSSION OF RESULTS

The results of this experimental study on V-Cr-Ti alloys utilizing Charpy-impact loading show that the DBTT of these alloys is lowest (≈-250°C) when the combined Cr and Ti concentration in the alloy is –5 wt.%. Also, the DB'IT of hydrogenated (400-1200 appm) V-Cr-Ti alloys is lowest (-160°C) when the the combined Cr and Ti concentration in the alloys is ≈5 wt.%.

A comprehensive analytical electron microscopy study of precipitates in the microstructures of unalloyed vanadium and V-1, 3, 5, 10, and 18 wt.% Ti alloys (Table 1) by Gazda has shown that (a) the unalloyed V and V-Ti alloys with 13 wt.% Ti contain VC precipitates with BCC structure and additional Ti(CNO) precipitates with unidentified structure that are coherent with the matrix, (b) the most common precipitates in all of the alloys containing Ti are $Ti(C_{1-x-y}N_xO_y)$ precipitates with FCC NaCl structure that are noncoherent with the matrix, (c) all of the precipitates in alloys with >3 wt.% Ti are noncoherent with the matrix, (d) the number density of all precipitates in these materials is maximum in the V-3Ti alloy, and (e) the size of precipitates in these materials is the minimum for alloys with 1-3 wt.% Ti.'' In comparison with the DBTTs for V-Ti alloys, we note that the tensile properties of V-(0-18)Ti alloys at 600°C are also significantly altered when the Ti concentration is –5 wt.% (see Figs. 7 and 15 in Ref. 7).

The dependence of DB1T for V-Ti alloys on Ti concentration (Fig. 1) is similar to the dependence of DBTT for V-Cr-Ti alloys on combined Cr and Ti concentration (Fig. 3). This similarity suggests that the minimum DBTT at –5 wt.% alloy concentration on Charpy-impact loading of V-Ti alloys, as well as V-Ti alloys with Cr additions, is due to the complex combination of Cr and Ti solid-solution strengthening effects and coherent and noncoherent precipitate-strengthening effects. The maximum number density and minimum size of precipitates in V-Ti alloys with –3 wt.% Ti are considered to be a manifestation of coherency and noncoherency of the precipitates.

The anomalously high (100-200°C) DB'IT for the V-5Cr-3Ti alloy is attributed primarily to the high number density of large V(K, Na, Cl, C, O) precipitates on the grain boundaries in this material. Although these precipitates were present in the V-3Ti alloy, their number density was relatively low and the precipitates were uniformly distributed which resulted in a minor effect on the DB'IT. These precipitates may have been the result of use of Ti that contained a relatively high Na, K, and Cl concentration in the alloy preparation?

The objective of this experimental program is to determine the composition of a vanadium-base alloy with the optimal combination of mechanical properties, corrosion resistance, fabricability, and weldability for use as a structural material in the environment of a fusion reactor. The following experimental results are considered in the selection of the optimal composition of the vanadium-base alloy. (1) The DB1T of a vanadium-base alloy can be expected to increase substantially (100-200°C, 41-44 dpa at 420°C) on neutron irradiation? (2) The swelling of V-Cr-Ti alloys on neutron irradiation is significantly reduced (<1% swelling, 36 dpa at 420°C) by the presence of ≥5 wt.% Ti in the alloy.'' (3) The long-term creep strength of V-Ti alloys is significantly increased by the addition of Cr.[11] (4) The tensile properties of V-(0-15)Cr-5Ti alloys with a tungsten/inert-gas weld zone are comparable to tensile properties of recrystallized alloys without a weld zone, but V-(0-15)Cr-5Ti alloys with Cr concentrations >5 wt.% have significantly reduced fracture toughness.'' These experimental results, together with the experimental results presented in this report, lead us to select the V-5Cr-5Ti alloy containing ≈400 ppm O, –200 ppm N, –200 ppm C, and ≈900 ppm Si for use as a structural material in a fusion reactor.

CONCLUSIONS

1. The V-5Cr-5Ti alloy containing ≈400 ppm O, –200 ppm N, –200 ppm C, and –900 ppm Si is recommended for use as a structural material in a fusion reactor.

FUTURE WORK

The effect of neutron irradiation on the DBT of V-3Ti-1Si, V-5Ti, and V-5Cr-5Ti alloys will be determined, and this will complement the DBTT data in Ref. 2 for irradiated V-base alloys.

REFERENCES

1. B. A. Loomis, B. J. Kestel, B. D. Edwards, and D. L. Smith, "Temperature Dependence of the Fracture Behavior and the DBT for Dehydrogenated and Hydrogenated Vanadium-Base Alloys," in: Fusion Reactor Materials, Semiannual Progress Report for Period Ending September 30, 1988, DOE/ER-0313/5, U.S. Department of Energy, Office of Fusion Energy, pp. 242-255.

2. B. A. Loomis, and D. L. Smith, "Response of Unirradiated and Neutron-Irradiated Vanadium Alloys to Charpy-Impact Loading," J. Nucl. Mater., 179-181, Part A (1991), pp. 783-786.

3. B. A. Loomis, L. J. Nowicki, and D. L. Smith, "The Effect of Hydrogen, Chromium, Titanium, and Silicon on the Ductile-Brittle Transition Temperature of Vanadium and Vanadium-Base Alloys," in: Fusion Reactor Materials, Semiannual Progress Report for Period Ending September 30, 1991, DOE/ER-0313/11, U.S. Department of Energy, Office of Fusion Energy, pp. 227-232.

4. N. S. Cannon, M. L. Hamilton, A. M. Ermi, D. S. Gelles, and W. L. Hu, "Influence of Neutron Irradiation on the Charpy Impact Properties of V-15Cr-5Ti," in: Fusion Reactor Materials, Semiannual Progress Report for Period Ending September 30,1987, DOE/ER-0313/3, U.S. Department of Energy, Office of Fusion Energy, pp. 239-245.

5. D. N. Braski, "The Tensile Properties of Several Vanadium Alloys after Irradiation to 90 DPA in FFTF," in: Fusion Reactor Materials, Semiannual Progress Report for Period Ending September 30, 1987, DOE/ER-0313/3, U.S. Department of Energy, Office of Fusion Energy, pp. 235-238. .

6. B. A. Loomis, A. B. Hull, O. K. Chopra, and D. L. Smith, "Hydrogen Concentration Distribution in Vanadium-Base Alloys after Surface Preparation and Exposure to Liquid Lithium," in: Fusion Reactor Materials, Semiannual Progress Report for Period Ending March 31,1988, DOE/ER-0313/4, U.S. Department of Energy, Office of Fusion Energy. pp. 160-167.

7. B. A. Loomis, L. J. Nowicki, and D. L. Smith, "Tensile Properties of Vanadium and Vanadium-Base Alloys," in: Fusion Reactor Materials, Semiannual Progress Report for Period Ending March 31, 1991, DOE-ER/0313/10, U.S. Department of Energy, Office of Fusion Energy, pp. 145-155.

8. J. Gazda, "Analytical Electron Microscopy Study of Vanadium and Vanadium-Base Alloys," University of Illinois at Chicago, 1993 (unpublished thesis for Master of Science in Metallurgy).

9. Communication from J. R. Peterson, Teledyne Wah Chang Albany, Albany, Oregon.

10. B. A. Loomis, D. L. Smith, and F. A. Garner, "Swelling of Neutron-Irradiated Vanadium Alloys," J. Nucl. Mater., 179-181, Part A (1991), pp. 771-774.

11. B. A. Loomis, L. J. Nowicki, and D. L. Smith, "Creep of V-5Cr-5Ti and V-10Cr-5Ti Alloys at 600°C," in: Fusion Reactor Materials, Semiannual Progress Report for Period Ending September 30, 1991, DOE/ER-0313/13, U.S. Department of Energy, Office of Fusion Energy.

12. B. A. Loomis, C. F. Konicek, L. J. Nowicki, and D. L. Smith, "Tensile Properties of Vanadium-Base Alloys with a Tungsten/Inert-Gas Weld Zone," in: Fusion Reactor Materials, Semiannual Progress Report for Period Ending March 31, 1992, DOE-ER/0313/12, U.S. Department of Energy, Office of Fusion Energy.

6.4 Copper Alloys

STATUS OF FATIGUE STUDIES ON IRRADIATED COPPER ALLOYS - F. A. Garner and M. L. Hamilton (Pacific Northwest Laboratory[a]), J. F. Stubbins and A. Singhal (University of Illinois) and B. N. Singh (Aisd National Laboratory)

OBJECTIVE

The objective of this effort is to provide fatigue life data for application of irradiated copper alloys to fusion high heat flux needs.

SUMMARY

Irradiation continuer in the EBR-II and OR-3 reactors of pure copper and GlidCop CuAl25 in the form of subsize tensile fatigue specimens. The first phase of the EBR-II irradiation sequence has been completed. A size effects experiment conducted on unirradiated CuAl25 fatigue specimens is nearing completion. Early results on the fatigue behavior of subsize specimens are presented in this report.

PROGRESS AND STATUS

Introduction

Pure copper and GlidCop CuAl25 are currently being considered as high heat flux structural components for the ITER divertor plate assembly. Data are required on the radiation performance of there materials and a variety of studies are in progress to provide data on void welling, tensile propertier and electrical conductivity.

One of the mort important properties far high heat flux applications. however, is the low cycle fatigue behavior, which is used to assess the mechanical strain contribution of thermal cycling on component lifetimes. A joint U.S./E.C. research program involving neutron irradiation of pure copper and GlidCop CuAl25 in the form of low cycle fatigue specimens is now in progress. The participants are the Risø National Laboratory in Denmark, Paciiic Nbrthwest Laboratory and the University of Illinois. The program is directed toward serving the goals of both the ITER (International Thermonuclear Experimental Reactor) and NET (Next European Torus) programs. The full program was described in an earlier report.[1]

Specimen Description

The specimens employed are not full-size tensile fatigue specimens as defined by ASTM standards but are typical of those employed in many fatigue studies. As shown in Figure 1 the specimens are 6 mm in maximum diameter by 50 mm long, with the gauge section 7 mm in length and 3.1 mm in diameter. The pure copper specimens were cut from OFHC copper and then fully annealed, while the CuAl25 Specimens were cut from the as-wrought condition as supplied to Risø National Laboratory by SCM Metals Products. all specimens were prepared at Risø to preserve uniformity between the various tests.

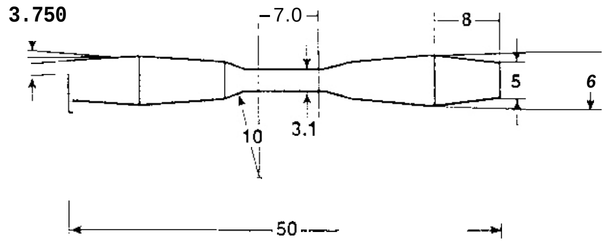

Fig. 1. Specimen dimensions of miniature tensile fatigue specimens. All dimensions are in mm.

Status of Neutron Irradiation Experiments

The first discharge from EBR-II of the COBRA IA subassembly has been accomplished after two reactor cycles. Fatigue specimens irradiated in COBRA IA at ~400°C are expected to be delivered to Pacific Northwest Laboratory in the second half of CY1993. The second ret of specimens will continue Irradiation in COBRA IA to a higher but yet unspecified exposure level

The lower exposure experiment currently being conducted in the DR-3 reactor at the RISØ Laboratory at 40. 100. 250, 350 and 450°C to ~0.4 dpa is nearing completion. Only the 450°C sequence remains to be irradiated. Fatigue testing of these specimens is scheduled to begin toward the end of CY 1993.

---

[a] Pacific Northwest Laboratory is operated for the U.S. Department of Energy by Battelle Memorial Institute under Constract DE-AC06-76RLO 1830.

Size Effects Comparison

Subsize specimens of GlidCop CuAl25 in the as-received condition have been tested to establish the fatigue durability of this alloy at room temperature. The tests were conducted as strain-controlled, fully-reversed cyclic fatigue to failure experiments. Testing Of full size specimens is now in progress. The results of the subsize tests are shown in Figure 2 and will be used to establish the influence of specimen size on fatigue durability, as well as to establish a baseline for the fatigue properties Of irradiated subsize specimens. The present data show no fatigue limit at least up to 10^6 cycles.

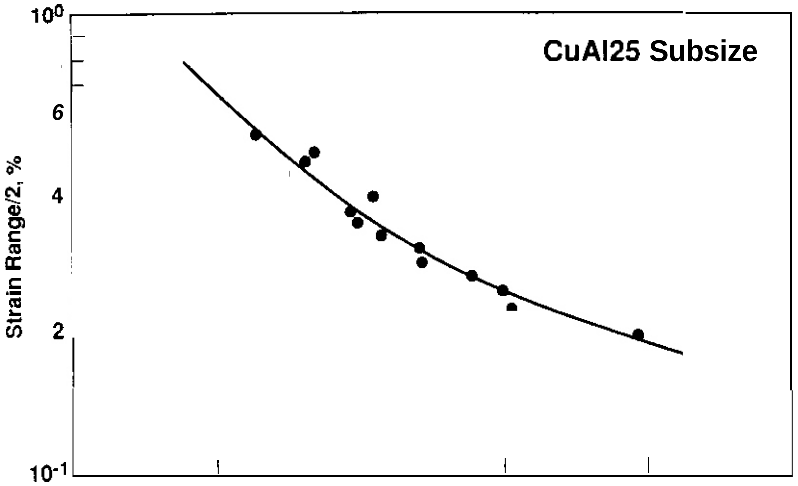

Fig. 2. Low cycle fatigue data obtained on subsize CuAl25 specimens tested at room temperature.

future Work

Testing of full size specimens of CuAl25 will continue. A similar set of tests will then proceed on pure copper.

Reference

1. F. A. Garner, B. N. Singh and J. F. Stubbins, "Status of Low Cycle Fatigue Studies on Irradiated Copper", Fusion Reactor Materials Semiannual Progress Report DOE/ER 0313/13 119931 pp. 265-266

2. F. A. Garner and M. L. Hamilton, COBRA 1A Experiment in EBR-II", ibid, pp. 255-257.

The Response of Dispersion-Strengthened Copper Alloys To High Fluence Neutron Irradiation at 415°C - D. J. Edwards. J. W. Newkirk. (U. of MO-Rolla), F. A. Garner, M. L. Hamilton. (Pacific Northwest Laboratory)[*], A. Nadkarni, and P. Samal, (SCM Metal Products)

OBJECTIVE

The objective of this effort is to supply irradiation data on copper alloys selected as candidates for high heat flux applications in fusion reactors.

SUMMARY

Various oxide-dispersion-strengthened copper alloys have been irradiated to 150 dpa at 415°C in the Fast Flux Test Facility [FFTF). The Al_2O_3-strengthened GlidCop™ alloys, followed closely by a HfO_2-strengthened alloy, displayed the best swelling *resistance*, electrical conductivity, and tensile properties. The Conductivity of the HfO_2-strengthened alloy reached a plateau at the higher levels of irradiation, instead of exhibiting the steady decrease in conductivity observed in the other alloys. A high initial oxygen content resulted in significantly higher swelling for a series of castable oxide-dispersion-strengthened alloys, while a Cr_2O_3-strengthened alloy showed poor resistance to radiation.

PROGRESS AND STATUS

Introduction

One of the most crucial components of the International Thermonuclear Experimental Reactor (ITER) is the divertor plate assembly, which will be subjected to a high heat flux (~25 MW/m^2) from the charged particles and thermal energy that escape the plasma, and to radiation damage from the 14 MeV neutrons and charged particles [1-5]. As a consequence of this severe irradiation environment, the divertor plate assembly must utilize structural materials that can maintain high strength and high thermal conductivity throughout *its* lifetime.

The high thermal conductivity requirement leads to the consideration of pure copper and its alloys. Pure copper, however, is not generally considered a structural material due to its low strength and low softening temperature. In addition, irradiation experiments [6-11] in the Fast Flux Test Facility (FFTF) have demonstrated that pure copper has little resistance to void swelling, which dramatically decreases the electrical conductivity. The thermal conductivity will also decrease since the two conductivities are directly proportional to each other. The FFTF experiments also revealed that oxide-dispersion-strengthened (ODS) copper alloys demonstrated the most promising behavior after irradiation to ~100 dpa, exhibiting excellent swelling resistance and good retention of electrical conductivity and strength. Transmutation of the copper produced enough nickel and zinc to lower the conductivity, an effect which becomes more noticeable as the fluence increases [12,13]

On the basis of electrical Conductivity and yield strength, the GlidCop™ alloys are considered a prime candidate material for current divertor plate designs, possibly being used for the heat sink and perhaps the tubing that carries the Coolant. Typical designs, shown in Fig. 1, call either for carbon fiber composite (CFC) tiles to be brazed Onto the plasma-facing surface of the copper heat sink, or for the divertor block to be made entirely of CFC with a metal coolant tube, possibly fabricated from dispersion-strengthened copper. The tiles act as an armor to prevent the thermal erosion of the copper and thus reduce the contamination of the plasma by high Z elements, and also allow higher temperatures to be obtained at the divertor surface without melting the copper [2,5]. Some of the problems associated with using copper alloys for the divertor include brazing difficulties due to mismatches in the thermal expansion coefficients of the copper and CFC's, and melting of the copper during a loss of cooling accident [2].

In this report the results of density measurements, tensile tests, fractography, and electrical conductivity measurements (used to estimate thermal conductivity) are presented for various dispersion-strengthened copper alloys irradiated to 104 and 150 dpa at 415°C in FFTF. Although these displacement levels are considerably higher than anticipated for ITER applications (~10 dpa), understanding the irradiation effects on the materials at these high displacement levels may be useful for commercial reactor applications

Experimental Results

The copper alloys irradiated in FFTF are listed in Table 1 along with their compositions and thermomechanical treatments. Although the three alloy classes are all dispersion-strengthened systems.

---

[*] Pacific Northwest Laboratory is operated for the *U.S. Department* of **Energy** ***by*** *Battelle Memorial* Institute under Contract DE-AC06-76RLO 1830.

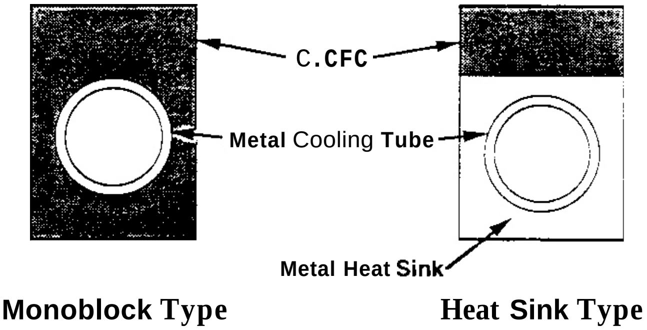

Fig. 1. Two possible designs for the ITER divertor block assembly utilizing dispersion-strengthened copper alloys [ref. 1].

each class was produced by a different method. The GlidCop™ alloys are produced by SCM Metal Products using an internal oxidation technique [14], which yields a very fine, uniform dispersion of Al_2O_3 particles, imparting high strength and yet allowing good electrical conductivity. The CuAl15 alloy contains ≤200 ppm boron, which was used as a deoxidant.

Table 1--ODS Copper Alloys Irradiated in FFTF at ~415°C

ALLOY	COMPOSITION (WT%)	THERMO-MECHANICAL PROCESSING
	GlidCop™ Alloys*	
CuAl15 + boron	0.15% Al as Al_2O_3, <200 ppm residual boron	Annealed, 900°C/0.5 hr/ air cooled (AC)
CuAl20	0.20% Al as Al_2O_3	20% cold worked (CW)
CuAl25	0.25% Al as Al_2O_3	50% CW
CuAl25 WELD	Same, laser welded	50% CW
	Mechanically Alloyed Copper**	
Cu-HfO_2	1.1 % Hf as HfO_2	20% CW, 450°C/0.5 hr/AC
Cu-Cr_2O_3	3.5% Cr as Cr_2O_3	20% CW, 450°C/0.5 hr/AC
	Castable Copper Alloys***	
ODS-1	0.25% Mg, 1% Al_2O_3	40% CW
ODS-1 WELD	Same, laser welded	40% CW
ODS-2	0.25% Mg, 1% Al_2O_3	40% CW
ODS-3	0.50% Mg, 1% ZrO_2	40% CW
ODS-4	0.50% Mg, 1% Al_2O_3	40% CW

*	Produced by SCM Metal Products
**	Supplied by Prof. N. Grant at Massachusetts Institute of Technology
***	Produced by Technical Research Associates, Inc., Salt Lake City, Utah

The second class of alloys studied were two mechanically alloyed copper alloys incorporating either Cr_2O_3 or HfO_2 as the strengthening particles. Dr. ti. Grant at the Massachusetts Institute of Technology supplied these alloys. The alloys were produced using powder metallurgy techniques involving the mixing of pure copper powder and the metal oxide powder and then extruding the final powder at 700°C using a 16:1 extrusion ratio.

The third class of alloys represented an attempt by Technical Research Associates. Inc. to produce a castable. oxide-dispersion-strengthened alloy. As will be shown later. this effort proved unsuccessful for an unexpected reason. The alloy was produced by adding oxide particles [coated with copper by a proprietary chemical coprecipitation method) to a melt of magnesium-bearing oxygen-free high conductivity (OFHC) copper, and then casting the melt. *The ODS-1 and ODS-2* alloys have the *same composition* but were produced from different melts. The ODS-3 and ODS-4 alloys contain more magnesium than the two previous alloys. but the ODS-3 alloy uses ZrO_2 as the oxide dispersion instead of the Al_2O_3 used in the other three alloys.

Both transmission electron *microscopy (TEM)* disks and miniature tensile specimens [15, 16] were punched from sheet stock of the various materials; only TEM disks were punched from the ODS-2 stock. Tensile specimens of CuAl25 and ODS-1 were also fabricated from strips of 0.25 mm thick sheet that had been cut and then joined together by laser welding. The tensile specimens were punched from the welded sheet so that the weld was centered in the gage length. TEM disks were also punched from the weld regions.

Density measurements were obtained at room temperature from TEM disks, using an immersion density technique accurate to ±0.16% density change. Electrical conductivity measurements were made at room temperature on both miniature tensile specimens and TEM disks using a four-point probe. DC potential drop method described by Anderson and coworkers [9]. The dimensions of the miniature tensile specimens are given in Fig. 2. Conductivity measurements on both types of specimens were in good agreement with each other. Tensile tests were performed after the conductivity measurements were completed. using a miniature tensile testing apparatus developed specifically for this specimen geometry [15,16]. Tensile tests were performed at room temperature with a free-running crosshead speed of 0.0025 mm s^{-1}, which yields an initial strain rate of 4.8 x 10^{-4} s^{-1}.

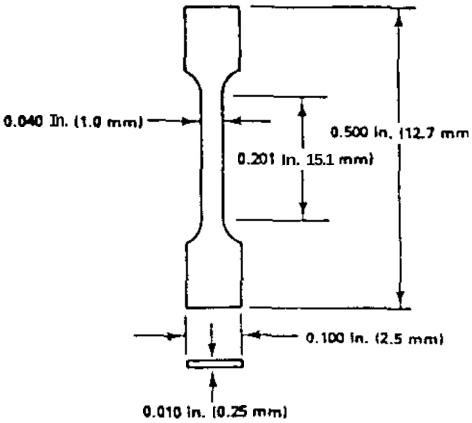

Fig. 2. Dimensions of the miniature tensile specimens irradiated in FFTF.

Fracture surfaces were examined in both a JEOL 840 scanning electron microscope and a JEOL JSH 35C. Oxidation of the surfaces can occur quickly and obscure details at magnifications higher than 1000x, so specimens were loaded into one of the microscopes Immediately after being tested.

Results

Castable ODS Alloys

Swelling data for the castable ODS alloys are presented in Fig. 3 along with data on pure copper for comparison. As a group. all four alloys exhibit poor swelling resistance, roughly paralleling the swelling behavior of pure copper, although significant differences are apparent for the various ODS alloys. The ODS-4 alloy exhibits considerably less swelling than pure copper and the other three alloys, however. The swelling resistance of the ZrO_2-strengthened ODS-3 alloy is the lowest. Laser welding obviously has an additional detrimental effect on the swelling of the ODS-1 alloy because the welded ODS-1 material displays the most swelling, greater than that of pure copper

Figure 4 shows that the electrical conductivity of the castable ODS alloys lies within a common band that steadily decreases with increasing Irradiation. Notice that the conductivity for the ODS-3 alloy lies near the bottom of the band, which is not unexpected since it exhibits the greatest swelling of the four alloys.

Conductivity for the laser welded ODS-1 alloy was not obtained because of surface irregularities caused by the weld zone developing considerably more swelling than that of the *surrounding unwelded* material. As a result. the probes could not make proper contact with the surface of the specimen. and no reliable reading could be obtained.

The ultimate tensile and yield strengths of the castable ODS alloys are presented in Fig. 5, and show that both measures of strength *decrease* dramatically after *exposure* to 50 *dpa*. The yield strengths of the ODS-1 and ODS-4 alloys decrease 50% or more after irradiation to 50 dpa. and then appear to level out. The data for the ODS-3 alloy, which are available only at 104 and 150 dpa. show that the strength of the ODS-3 alloy matches closely the strength of the ODS-1 and ODS-4 alloys. The welded ODS-1 specimens irradiated to 104 dpa and to 150 dpa both failed before reaching 0.2% strain. The specimen irradiated to 104 dpa failed in two different locations within the gage length. while the specimen irradiated to 150 dpa failed in the welded region of the gage length.

Mechanically Alloyed Cu-Cr_2O_3 and Cu-HfO_2

The two mechanically alloyed copper alloys exhibited different behavior, demonstrating the importance of the stability of the oxide used far the dispersion strengthening. Fig. 6 shows the swelling behavior of the Cu-Cr_2O_3 and the Cu-HfO_2 alloys. and clearly shows that a large difference exists. The Cu-HfO_2 alloy appears to swell slightly, although no voids were found in the specimens Irradiated to 50 dpa.

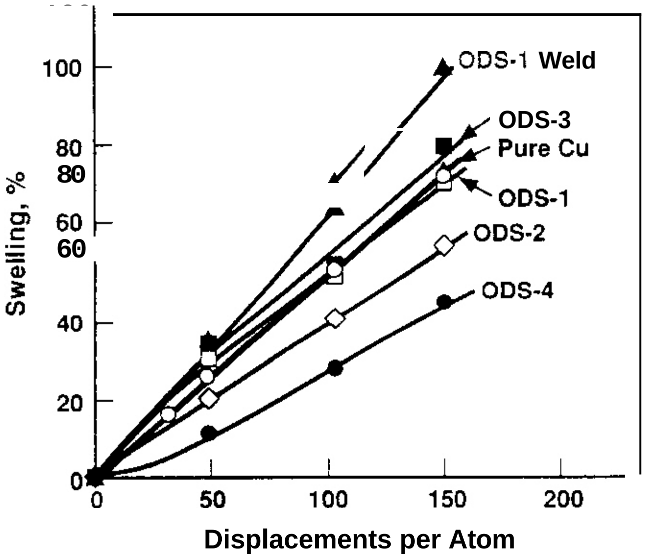

Fig. 3. Swelling of the castable ODS alloys irradiated to 150 dpa in FFTF at 415 C. Swelling data for pure copper are also presented for comparison.

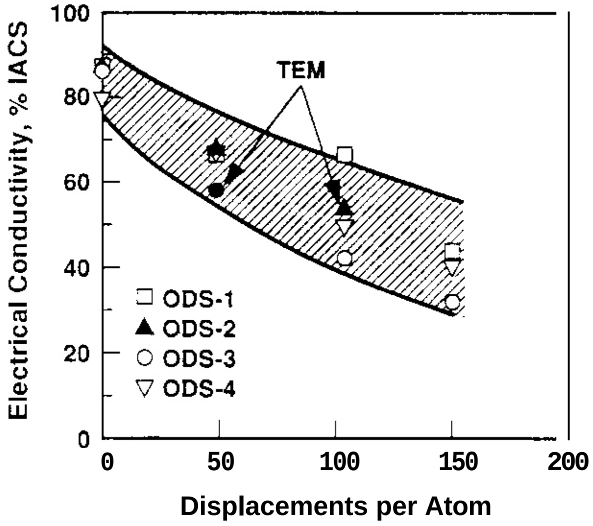

Fig. 4. Electrical conductivity behavior of the castable ODS alloys after irradiation to 150 dpa at 415 C in FFTF

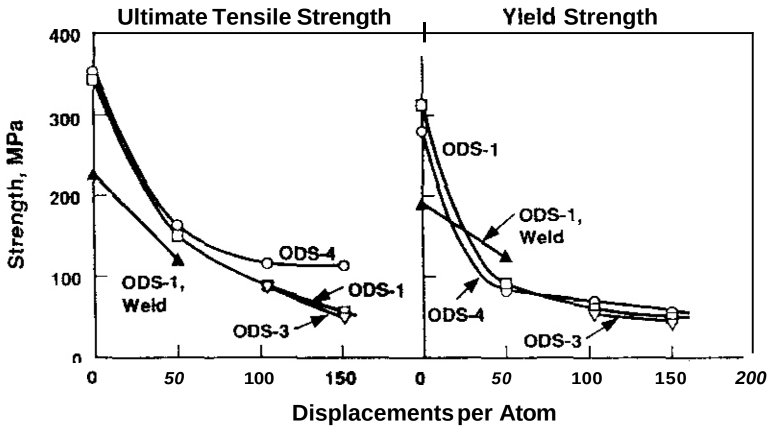

Fig. 5. Ultimate … 150 dpa in FFTF at 415°C.

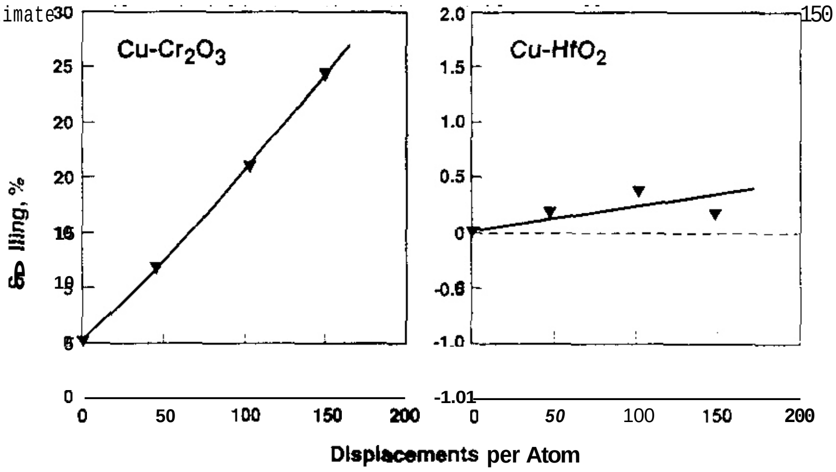

Fig. 6. Swelling behavior of the mechanically alloyed $Cu-Cr_2O_3$ and $Cu-HfO_2$ alloys irradiated to **150** dpa in FFTF **at** 415°C.

The electrical conductivity of the two alloys, **shown** in Fig. 7. further demonstrates the difference **between** the two alloys. The conductivity of the $Cu-HfO_2$ alloy shows an unusual plateau behavior not **seen** in any of the other alloys. **As** expected. the conductivity of the $Cu-Cr_2O_3$ alloy continuously **decreases** as expected in **response** to swelling and transmutation.

The strength behavior of the two **alloys** is shown in fig. 8. The strength of the $Cu-HfO_2$ alloy initially decreases but then **reaches** a **minimum** value and maintains that level throughout the rest of the irradiation. In comparison, the strength of the $Cu-Cr_2O_3$ alloy is lower in the unirradiated condition, and **decreases** steadily throughout the irradiation. *Tensile **curves** are presented later in the report (Fig. 14) comparing* the behavior of the $Cu-Cr_2O_3$ alloy with that of the CuAl25 alloy. fracture surfaces for the $Cu-Cr_2O_3$ alloy are shown in Fig. 9. and **reveal that the** failure mode involved microvoid **coalescence.**

GlidCop™ Alloys

The GlidCop™ alloys showed **the** best overall swelling resistance of any of the **three** classes of oxide-dispersion-strengthened alloys investigated in this study. **As shown** in Fig. 10. the CuAl20 **and** CuAl25 alloys actually densify at the higher dpa **levels.** in Contrast to the CuAl15 which swells throughout **the** irradiation. **Swelling** data far the laser-welded CuAl25 are quite variable. ranging from 19% to 43% at 104 dpa. **and** 8% to 20% at 150 dpa. This variability probably reflects a considerable heterogeneity in the welded zone **and** surrounding region.

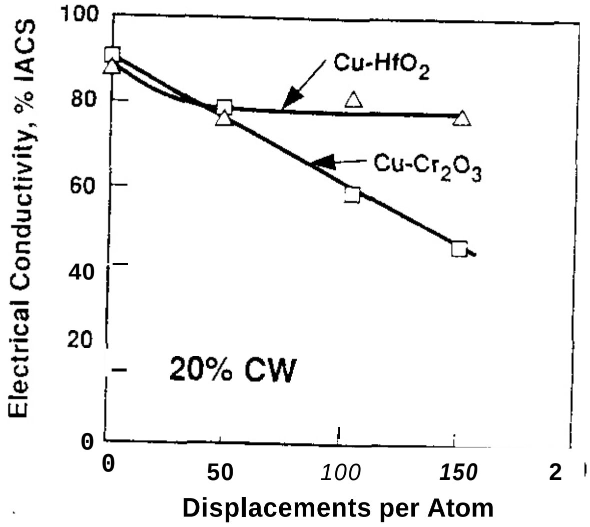

Fig. 7. Electrical conductivity of the mechanically alloyed Cu-Cr_2O_3 and Cu-HfO_2 alloys irradiated to 150 dpa in FFTF at 415°C.

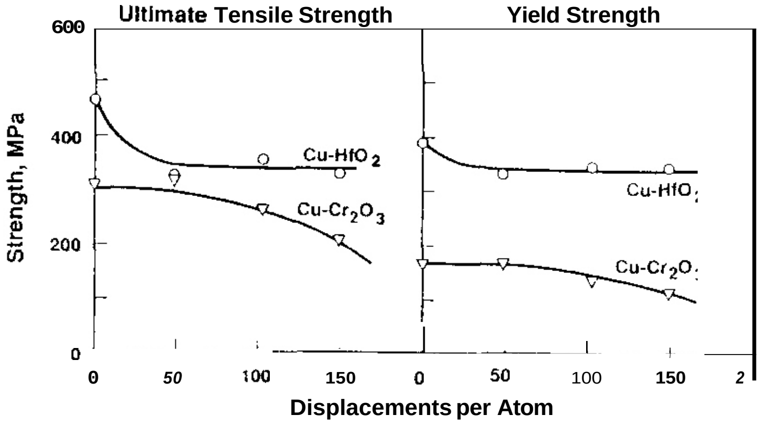

Fig. 8. Ultimate tensile and yield strength of the mechanically alloyed Cu-Cr_2O_3 and Cu-HfO_2 alloys irradiated to 150 dpa in FFTF at 415°C.

Fig. 11 demonstrates that the electrical conductivity of the various GlidCop™ alloys exhibits essentially the same behavior despite the differing levels of cold work and Al_2O_3 content, decreasing with increasing irradiation exposure. Note that laser welding lowers the conductivity both before and after irradiation.

The ultimate tensile and yield strength of the GlidCop™ alloys are shown in Fig. 12. As observed in Cu-HfO_2, the CuAl20 and CuAl25 show the same behavior, i.e. their strength decreases somewhat and then levels out. The strength of the GlidCop™ alloys, however, is higher than that of the Cu-HfO_2 alloy both before and after irradiation, demonstrating that the only advantage to using the Cu-HfO_2 instead of the GlidCop™ alloys is its surprising electrical conductivity behavior. The effect of laser welding on the strength of the CuAl25 is more dramatic compared to the castable ODS-I alloy, primarily because of the higher initial strength of the GlidCop™ alloys. The fracture surfaces for the CuAl25 alloy are shown in Fig. 13, revealing the failure mode as transgranular failure by microvoid coalescence. A comparison of the tensile curves for the CuAl25 alloy and the Cu-Cr_2O_3 alloy is presented in Fig. 14, demonstrating the dramatic differences in tensile behavior both before and after irradiation, most notably in the degree of strain hardening, total elongation, and reduction in area.

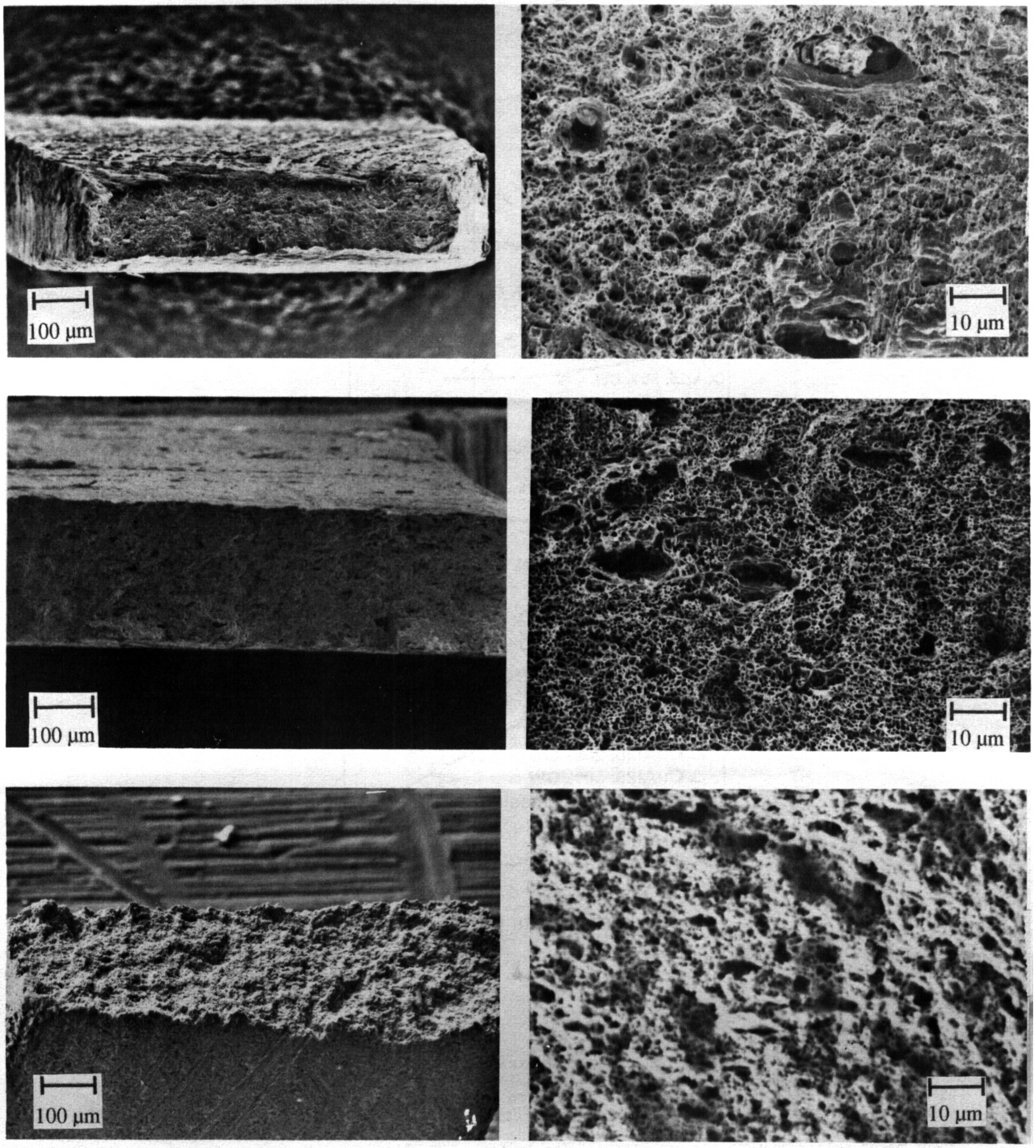

Fig. 9. Fracture surfaces of the Cu-Cr$_2$O alloy in the unirradiated condition (top), after irradiation to 50 dpa (middle) and after 150 dpa (bottom?. The entire fracture surface is shown on the left, and a higher magnification is shown on the right.

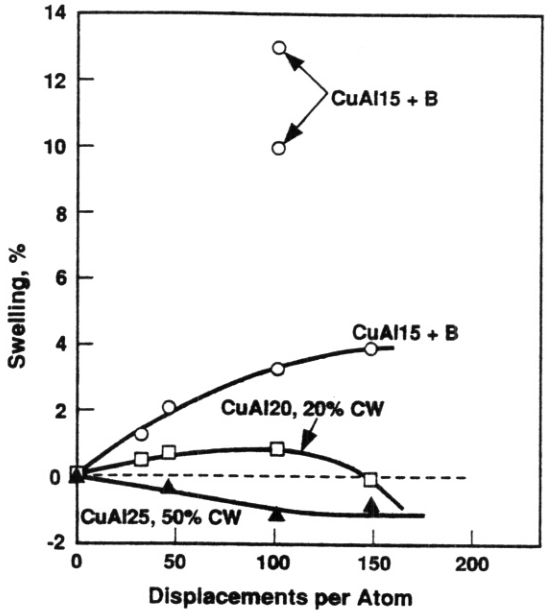

Fig. 10. Swelling behavior of the GlidCop™ alloys irradiated to 150 dpa in FFTF at 415°C.

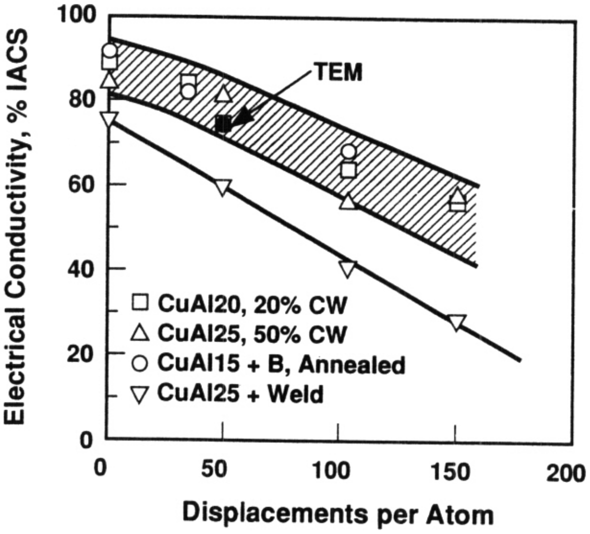

Fig. 11. Electrical conductivity of the GlidCop™ alloys irradiated to 150 dpa in FFTF at 415°C.

DISCUSSION

The results of this study showed that the GlidCop™ alloys exhibit the best overall retention of strength, electrical conductivity, and swelling resistance, followed closely by the Cu-HfO$_2$ alloy which actually demonstrates the best electrical conductivity behavior for very high fluence applications. The castable ODS alloys as a group have proven undesirable due to lack of swelling resistance, a problem also encountered with the Cu-Cr$_2$O$_3$ alloy. The overall retention of electrical conductivity and strength relates directly to the resistance of the alloy to swelling, allowing the alloys studied to be divided into two groups based solely on swelling resistance. The castable ODS alloys, the laser-welded specimens, and the Cu-Cr$_2$O$_3$ alloy form one group, whose lack of swelling resistance is comparable to that of pure copper, whereas the GlidCop™ alloys and the Cu-HfO$_2$ alloy demonstrate excellent swelling resistance.

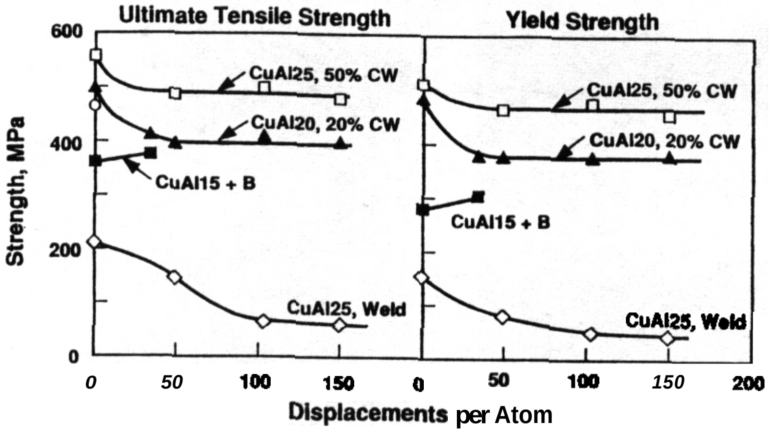

Fig. 12. Ultimate tensile and yield strength of the GlidCop™ alloys irradiated to 150 dpa in FFTF at 415°C.

In this study swelling was found to occur whenever the oxide dispersion was altered by either irradiation or laser welding. In two separate classes of alloys (GlidCops™ and castable ODS) laser welding has been shown to lead to a significant increase in swelling compared to the unwelded material. Dissolution of the Al_2O_3 dispersion in the weld zone is thought to have occurred and placed the aluminum and oxygen into solution. Both elements have been found to enhance the swelling of copper in two separate studies. Garner et al. [6,7] shared that a Cu-5Al alloy swelled more than pure copper, presumably due to the aluminum in solution. Zinkle and Lee [17] have shown significant enhancement of swelling under ion bombardment due to small concentrations of oxygen in solution. They attributed the enhancement to the oxygen stabilizing void formation by reducing the surface tension of the voids, making them more stable than dislocation loops and stacking fault tetrahedra. Other studies involving neutron irradiation of electrolytic tough pitch copper [18-20] demonstrated a swelling rate of –2.5% per dpa.

Laser welding of the CuAl25 provides a measure of just how detrimental the dissolution of the oxide can be to the electrical conductivity. Butterworth [21] reports that aluminum in solution increases the resistivity by 2.88 μΩ cm/wt% Al. Based on the assumption that the Al_2O_3 was completely dissolved, a preirradiation conductivity of 71% IACS (International Annealed Copper Standard) was calculated for the CuAl25 alloy compared to the measured value of 75.8% IACS. Similar calculations for the oxygen placed in solution lowers the preirradiation conductivity by an additional 3% IACS for a total reduction to 66% IACS. The fact that the measured conductivity is somewhat higher than the calculated value suggests that most but not all of the oxide was dissolved by the laser welding process.

The poor performance of the cartable ODS alloys in almost every respect provides additional information on the detrimental effect of dissolved oxygen. The alloys apparently picked up considerable oxygen during the casting process, which manifested itself as microporosity in the unirradiated bare alloy, forming planar arrays of bubbles along the rolling direction of the rolled sheet [22,23]. The lower swelling of the ODS-1 alloy may be due to the higher amount of magnesium added to promote the distribution of the oxide during casting. The ODS-3 alloy contains the same amount of magnesium as the ODS-4 alloy, however. The higher swelling of the ODS-3 alloy suggests that the ZrO_2 may not be as stable under irradiation as the Al_2O_3. The poor strength of the castable ODS alloys is due in part to poor thermal stability. as demonstrated by these alloys in ageing studies [23]. This instability in conjunction with the large swelling results in very poor tensile properties.

Another mechanism whereby oxygen and aluminum may be introduced into solution is recoil resolution of the oxide particles. Spitznagel and coworkers suggested this mechanism as a possible explanation for the dissolution and amorphization of the Al_2O_3 particles observed in an ion- irradiated CuAl60 GlidCop™ alloy [24]. Anderson and coworkers suggested that recoil resolution accounted for the apparent decrease in particle number density in the CuAl25 and CuAl20 alloys irradiated to 50 dpa [23]. The intensity of the oxide diffraction rings in electron diffraction patterns decreased with increasing irradiation, which led to the conclusion that the number density of the particles was smaller. and that radiation damage in the particles perhaps altered the oxide dispersion. The densification of the CuAl25 after irradiation in this study supports the supposition that the oxide is being dissolved, and its constituents placed in solution. The relatively low swelling of the CuAl25 and the CuAl20 indicates that if the Al_2O_3 dispersion indeed undergoes recoil resolution, then the oxygen and aluminum must be recombining on a smaller scale or their effect on swelling is being counteracted somehow by the operation of another mechanism.

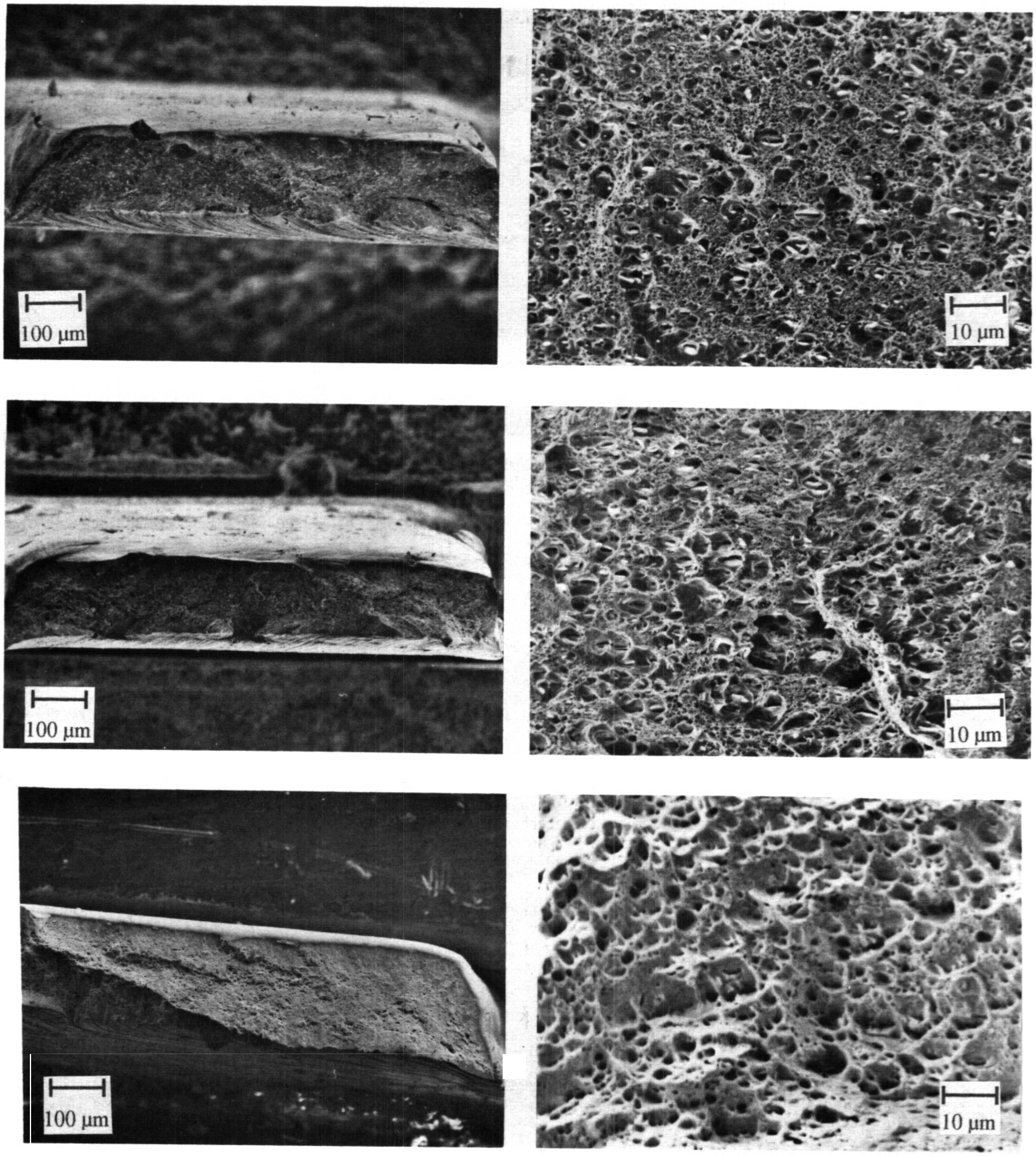

Fig. 13. Fracture surfaces of the CuAl25 alloy in the unirradiated condition (a), fracture surfaces of the CuAl25 alloy (b) after irradiation to 50 dpa, and (c) after irradiation to 150 dpa.

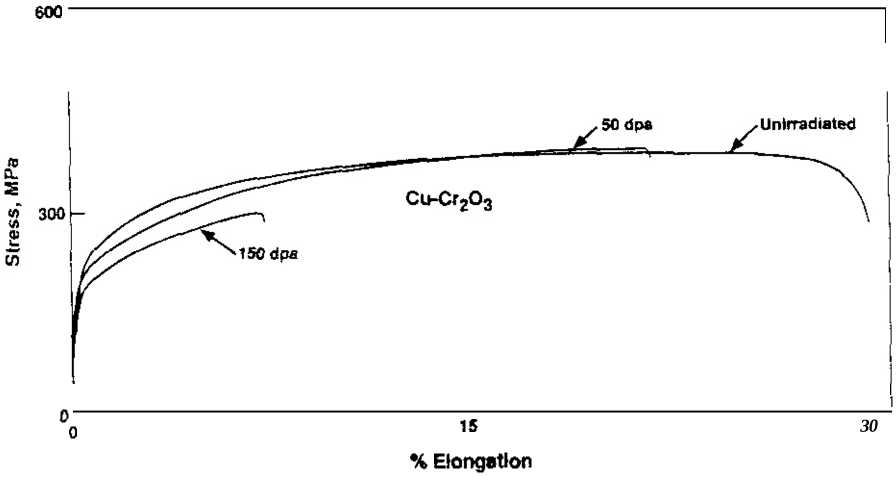

Fig. 14. Tensile curves of the CuAl25 alloy and the Cu-Cr$_2$O3 alloy. showing the effect of neutron irradiation and the importance of the type of dispersion.

It may well be that the aluminum and oxygen are being reprecipitated to form smaller oxide particles. Wanderka et al. [25] presented strong evidence that in CuAl25 irradiated to 30 dpa at 293 K by 300 keV copper ions, Al$_2$O$_3$ particles smaller than 10 nm were not stable under irradiation, and that larger particles fragmented to form smaller particles. The results of their work may not be directly-comparable to the present work because their study was conducted at room temperature. whereas the specimens in FFTF were Irradiated to much larger fluences and at ~0.5 of the melting temperature. allowing for a stronger role of diffusion in reforming the particles.

The results of the ion irradiation study lend some credibility to the idea of recoil resolution and reprecipitation of precipitates. particularly when the irradiation temperature is fairly high and taker place over a period of several years. A recent study by Zinkle and coworkers [26] showed a 20% decrease in average particle size (10 nm to 8 nm) far the same CuAl25 alloy examined in this study after irradiation by 750 MeV protons at 470 K to 2 dpa. It is unclear whether a steady-state particle distribution had been obtained at this low dpa level [25]. Thus it is possible that irradiation to higher displacement levels may result in a greater change in particle-size distribution.

Although no microscopy results are yet available in this study to directly answer the question of recoil resolution. the tensile test results of the CuAl25 and Cu-Cr$_2$O$_3$ provide additional evidence that the oxide dispersion was altered by the neutron irradiation. Fig. 13 shows the fracture surfaces from the CuAl25 miniature tensile specimens in the "" irradiated condition, and irradiated to 50 and 150 dpa. The made of failure throughout the entire series was microvoid coalescence, accompanied by a small amount of reduction in area in the irradiated specimens. Note that oxide particles are easily visible in the dimples of the unirradiated specimen's fracture surface. They are fewer in number in the specimen irradiated to 50 dpa, however, and completely absent in the 150 dpa specimen. Whether the oxide particles have been completely dissolved or simply redistributed into very small particles that cannot be easily imaged is not apparent from the SEM micrographs. Transmission electron microscopy is in progress to answer this question.

The tensile behavior of the CuAl25, CuAl20, and Cu-HfO$_2$ suggests that same form of dispersoid still exists at 104-150 dpa because their high strength is maintained. The decrease in the ultimate tensile strength (UTS) and yield strength of all three alloys is attributed to recovery and recrystallization. which reduces the initial dislocation density resulting from the pre-irradiation cold work. The apparent increase in strength of the CuAl15 alloy might be a result of void strengthening, but at this point this suggestion is just speculative. The tensile curve for the CuAl25 alloy is shown in Fig. 14, and demonstrates the behavior that is representative of the CuAl20 and Cu-HfO$_2$ alloys as well. Of great interest is the fact that after irradiation the amount of Strain hardening falls essentially to zero. with a slight drop in strength after yielding, reminiscent of a yield drop phenomenon. The tensile curve for the unirradiated CuAl25 alloy is characteristic of a material in the 50% cold-worked state. displaying only a limited ability to strain harden due to the high dislocation density already present from the 50% cold work. The lack of any significant Strain hardening in the irradiated specimens suggests that the dislocations are shearing through the particles, not bypassing them through the Orowan mechanism. Such behavior has been observed before in precipitation strengthened Al-Cu alloys [27] aged to form coherent Guiner-Preston (GP) zones. In this case the dislocations were able to cut through the GP zones. but only at a significantly higher stress than required for easy glide in either pure aluminum or solution strengthened aluminum. After Irradiation. the decreasing intensity of the oxide diffraction ring, the prominent lack of particles on the 150 dpa specimen's fracture surface. and the tensile behavior of the CuAl25 all point to redistribution of the oxide to smaller particle sizes. Microscopy is in process to determine if this is actually the case. however.

The decrease in strength of the CuAl20 alloy is due to complete recrystallization after 50 dpa [23]. Anderson et al. reported that the CuAl25 alloy still retained some of its prior cold worked structure even after irradiation to 50 dpa, mast likely due to the higher Al_2O_3 Content. The unexpected high swelling values noted for the CuAl15 at 104 dpa represent an unexplained breakdown in the swelling resistance, perhaps due to inhomogeneous distribution of the baron and/or the Al_2O_3. The CuAl25 and CuAl20 both exhibited a reasonable amount of reduction of area even after irradiation to 150 dpa. The total elongation increased significantly after irradiation to 50 dpa, most likely due to recovery and recrystallization of the cold work induced dislocation structure. Following further irradiation to 150 dpa, however, the total elongation decreased from ~12% to ~5%. The reason for this decrease in total elongation without swelling remains to be determined. The steady decrease in conductivity is easier to explain and is attributed to the formation of transmutation products, mainly nickel and zinc [12,13].

The strength behavior of the Cu-HfO_2 alloy following irradiation parallels that of the GlidCops™, presumably far the same reasons. The alloy was reported to be completely recovered and recrystallized after irradiation to 50 dpa [23], with the hafnia being redistributed to form smaller polygonal particles. The retention of room-temperature strength after irradiation suggests that the oxide dispersion still exists in some form to strengthen the alloy, just as in the GlidCops™. Also, the total elongation increased from 8.7% to 20.5% after irradiation to 50 dpa, and then remained constant through irradiation to 150 dpa. The reason for this behavior is not immediately obvious. The surprising electrical conductivity behavior of the Cu-HfO_2 alloy is probably caused by the transmutants and hafnia being redistributed or interacting in some manner that keeps the individual elements out of solution. One unfortunate drawback to using the Cu-HfO_2 alloy is the longer-lived radioactivity from ^{178m}Hf, making it somewhat less desirable for use as a structural material.

The strength of the Cu-Cr_2O_3 alloy, shown in Fig. 8, remains roughly the same after irradiation to 50 dpa, then decreases with further irradiation. One possible explanation for the strength retention lies in the redistribution of the Cr_2O_3 particles into smaller particles. The increased degree of Orowan strengthening possibly compensates for the expected strength decrease due to complete recrystallization. The tensile curves shown in Fig. 14 for the Cr_2O_3 alloy differ drastically from the curves of the CuAl25 alloy, showing a steady decrease in total elongation and a considerable decrease in the reduction of area.

The fracture surface of the unirradiated specimen shown in Fig. 9 contains large inclusions embedded in the surface, apparently introduced at some stage in the production of the powders. These large inclusions are no longer present at 150 dpa, presumably because they were dissolved during the irradiation. The fracture surface at 150 dpa clearly demonstrates the effect of the loss of the reduction in area, and the resultant inability to sustain even a small amount of localized deformation. The subsequent drop in strength after irradiation to 104 and 150 dpa suggests that the oxide dispersion may have coarsened during irradiation, but microscopy is needed to check this possibility. Though a gradual decrease in strength occurs, there remains a moderate amount of strain hardening, suggesting that there is still a small degree of Orowan strengthening occurring from the redistributed oxide. The higher swelling of this alloy compared to the Cu-HfO_2 and the GlidCops™ could be the result of oxygen being placed into solution by irradiation.

CONCLUSIONS

Irradiation of the several different oxide-dispersion-strengthened alloys at 415°C to 104 and 150 dpa revealed that the Al_2O_3-strengthened GlidCop™ alloys offered the best overall resistance to irradiation. A Cu-HfO_2 alloy also showed some potential despite having a higher level of longer-lived radioactivity, although pure copper becomes highly radioactive due to the formation of ^{60}Co. Both the GlidCops™ and the Cu-HfO_2 alloy exhibit similar tensile behavior, particularly with respect to the lack of strain hardening after irradiation. Despite the apparent alteration of the oxide dispersion, the three alloys still maintain a large fraction of their strength after exposure to high fluences. The retention of electrical conductivity after irradiation of the GlidCop™ alloys and the Cu-HfO_2 alloy was very good, particularly in comparison to the other alloys studied. The formation of transmutation products (Ni and Zn) is believed to be primarily responsible for the observed decrease in conductivity in the two GlidCop™ alloys. An interaction between the hafnium and the transmutation products may have removed some of the transmutation products from solution, thus leading to the unusual conductivity behavior of the Cu-HfO_2 alloy. This proposal has not yet been confirmed experimentally.

The castable ODS alloys exhibited poor swelling resistance, which had a very adverse effect on their electrical conductivity and mechanical properties. The high swelling that developed in the irradiated ODS alloys appears to be the result of oxygen contamination introduced during the casting process. The swelling appeared to dominate the mechanical property behavior of the castable ODS alloys, overshadowing any possible effect that the various compositional variations of the alloys might have had in determining the strength behavior.

The Cu-Cr$_2$O$_3$ alloy exhibited relatively poor swelling resistance compared to that of the GlidCops™ and the Cu-HfO$_2$ alloy, possibly due to the dissolution of the Cr$_2$O$_3$, which may have placed oxygen into solution. As observed in the cartable ODS alloys, void swelling was primarily responsible for the poor electrical conductivity and strength of the Cu-Cr$_2$O$_3$ alloy.

FUTURE WORK

Microscopy will be completed on the CuH$_2$O$_2$ and GlidCop alloys

REFERENCES

1. Conn, R.W., Chuyanov, V.A., Inoue, N.. and Sweetman, D.R., Scientific American, April 1992, p. 103.

2. Vieider, G., Cardella, A., Akiba. M.. Matera, R.. and Watson. R.. fusion Engineering and Design, Vol 16, 1991, pp. 23-34.

3. Zolti, E., Fusion Engineering and Design, Vol. 16, 1991. pp. 163-171.

4. Munz, D. and Diegele, E.. Fusion Engineering and Design, Vol. 16, 1991, pp. 45-57.

5. Akiba, M., Bolt, H.. Watson. R.. and Kneringer, G.. and Linke, J., Fusion Engineering and Design, Vol 16, 1991, pp. 111-125.

6. Garner, F. A., Brager, H. R... and Anderson. K. R., Journal of Nuclear Materials, Vol. 179-181, 1991, p. 250.

7. Garner, F. A. and Anderson. K. R.. Fusion Reactor Materials Semiannual Progress Report DOE/ER-0313/7, 1989, p. 220.

8. Brager, H. R.. Journal Nuclear Materials 141-143, 1986, p. 79, 163

9. Anderson, K. R., Garner. F. A., Hamilton. M. L.. and Stubbins, J. F.. fusion Reactor Materials Semiannual Progress Renort DOE/ER 0313/6, 1989, p. 357.

10. Garner, F. A,, Anderson, K. R.. and Shikama, I., Fusion Reactor Materials Semiannual Progress Report, DOE/ER-0313/9, 1990, p. 199.

11. Shikama. T., Garner, F. A.. Hamilton. El. L.. and Anderson. K. R.. Proceedings of the 15th International Symposium on Effects of Radiation on Materials, ASTM STP 1125. R. E. Stoller, 4. 5. Kumar and D. S. Gelles, Eds., American Society for Testing and Materials. Philadelphia, 1992, pp. 846-853.

12. Garner. F. A., Heinisch, H. t., Simons, R. L., and Mann, F. M., Radiation Effects and Defects in Solids, 1990, p. 229.

13. Garner, F. A., Hamilton, M. L.. Edwards. D J., Newkirk. J. W.. Stubbinr. J F.. and Mitchell. M. A this conference.

1?. GlidCop, SCM Metal Products, Inc.. 11000 Cedar Ave., Cleveland. Ohio. 44106, USA, 1988

15. Panayotou, N. F., Atkin, S. D., Puigh, R. J.. and Chin. B. A., ASTM STP 888. 1986. p. 201

16. Garner, F. A,, Hamilton. M. L., Heinisch, H. L., and Kumar, A. S., Proceedings of ASTM International Symposium on Small Test Techniques and Their Applications to Pressure Vessel Annealing and Plant Life Extension, New Orleans, Louisiana, January 29-30, 1992, [in press].

17. Zinkle, S. J., and Lee. E. H.. Metallurgical Transactions, Vol. 21A, May 1390. p. 1037.

18. Ames, M.. Kohse, G., Lee, T. S.. Grant, N. J.. and Harling, O. K.. Journal of Nuclear Materials, Vol 141-143, 1986, pp. 174-178.

19. tee, T. S., Hobbs. L. W.. Kohse. G.. Ames, M.. Harling, O. K.. and Grant, N. J.. Journal of Nuclear Materials, Vol. 141-143, 1986. pp. 179-183.

20. Harling. O. K., Grant. N. J., Kohse. G., Amer. G.. Lee. T. S., and Hobbs, L. W., Journal of Materials Research, Vol. 2, 1987, pp. 568-579.

?!. Butterworth, G. J., Journal of Nuclear Materials. Vol. 135, 1985, p. 160.

22. Anderson. K. R.. Doctoral Thesis, University of Illinois at Urbana-Champaign, 1990.

23. Anderson, K. R., Garner, F. A., Hamilton, M. L., and Stubbins, J. F., Proceedings of 15th International Symposium of Effects of Radiation on Materials, ASTM STP 1125, R. E. Stoller, A. S. Kumar and D. S. Gelles, Eds., American Society for Testing and Materials, Philadelphia, 1992, pp. 854-874.

24. Spitznagel, J. A., Doyle, N. J., Choyke, W. J., Greggi Jr., J. G., McGruer, J. N., and Davis, J. W., Nuclear Instruction and Methods in Physics Research, Vol. B16, 1986, p. 279.

25. Wanderka, N., Yuan, Y., Jiao, L., Wahi, R. P., and Wollenberger, H., Proceedings of the 5th International Conference of Fusion Reactor Materials, held in Florida, Nov. 1991, in press.

26. Zinkle, S. J., Horsewell, A., Singh, B. N., and Sommer, W. F., this conference

27. Greetham, G., and Honeycomb, R. W. K., Institute of Metals Journal, Vol. 89, 1960-1961, p. 13

Neutron-Induced Swelling Observed in Copper Alloys Irradiated in MOTA's 2A and 28 - F. A. Garner (Pacific Northwest Laboratory)[1], D. J. Edwards (University of Missouri - Rolla), B. N. Singh, (Risø National Laboratory) and H. Watanabe (Kyushu University)

OBJECTIVE

The objective of this effort is to provide data on the response of copper alloys being considered far application in fusion reactors.

SUMMARY

Density measurements have been completed an copper alloys irradiated in MOTA 2A and MOTA 28 at (375°C, 12.7 dpa and 21.2 dpa) and (423°C, 48.0 and 95.4 dpa). While most of the density changer observed are consistent With those of earlier studies, there were several surprises. Addition of 5% Ni appears to accelerate the swelling rate initially at 423°C, but depresses swelling at 375°C. The suppressing action of cold work on swelling of Cu-5Ni is relatively small, and Cu-5Mn resists swelling very strongly in both the annealed and cold-worked conditions.

PROGRESS AND STATUS

Introduction

In an earlier report (1) the status of on-going copper irradiation experiments was reviewed. One of the experiments discussed was a two-part FFTF irradiation sequence conducted in MOTA ZA and MOTA 2B at target temperatures of 373 and 418°C. Gamma heating raises the temperatures to 375 and 423°C. Both segments of this irradiation sequence have now been completed and measurements were made of the densities of the various specimens

Results

Each part of the irradiation sequence consisted of two TEH packets. The first MOTA 2A packet (OE01) operated at 375 ± 5C and reached 2.61 x 10^{22} n cm^{-2} (E>0.1MeV) which is 12.7 *dpa* (1.333 X 9.5 dpa for stainless steel) for copper. The second packet (OE02) operated at 423 ± 5°C, reaching 8.53 x 10^{22} n/cm^2 (E>0.1MeV), which is 48.0 dpa for copper (36.0 for stainless steel). The comparable copper dpa values for the MOTA 28 packets (OE03 and OE04) were 21.2 and 95.4 dpa, respectively.

The swelling values calculated from the density changes observed in both irradiation segments of this experiment are listed in Table 1.

Table I. Swelling of Copper Alloys from MOTA ZA

Alloy	Condition	Specimen Engraving Code	Swelling, %			
			375°C		423°C	
			12.7 dpa	21.2 dpa	48.0 dpa	95.4 dpa
Marz Cu	Annealed	1	4.7	7.0	24.4 (21.6)*	45.4 (43.5)
Cu-5Ni	Annealed	2	0.91	1.63	30.1	50.3 (46.6)
Cu-5Ni	40% CW	3	0.37	0.85	22.1	35.9 (38.8)
Cu-5Mn	Annealed	4	0.004	1.40	-0.04	2.4
Cu-5Mn	40% CW	5	-0.03	0.72	0.13	2.0

*Three specimens were measured. one at 21.5% and two at 24.4%. Any measurements without a separate value in parentheses represent the average of 3 identical specimens whose swelling values agreed within the convergence Criterium used. i.e. ±0.16%.

---

[1] Pacific Northwest Laboratory is operated for the U.S. Department of Energy by Battelle Memorial institute under Contract DE-AC06-76RLO 1830.

Discussion

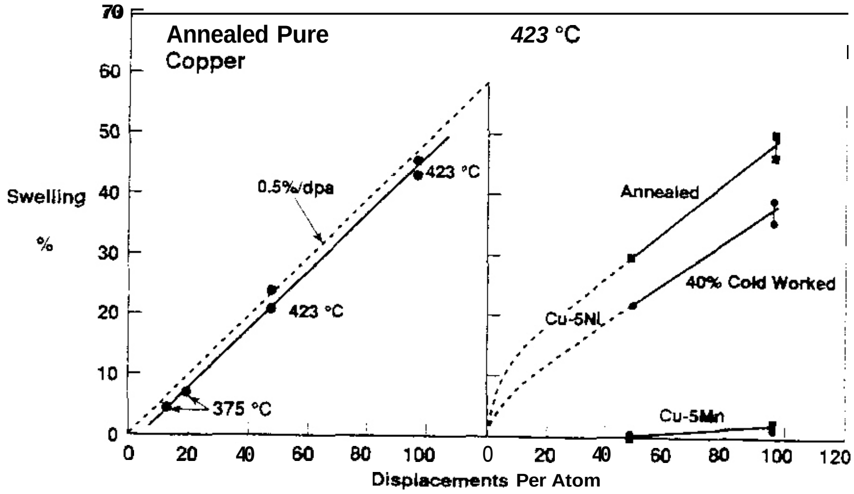

Fig. 1 Swelling of copper and capper alloys in MOTA's 2A and 2B

if we assume that the i75 and 423°C swelling data for annealed pure copper are independent of temperature, as shown in Figure 1a. the swelling appears to be consistent with the ~0.5%/dpa swelling rate usually observed for pure copper at ~400°C *(2)* An incubation period of ≤6 dpa is associated with this assumed behavior. however. Table 1 and Figure 16 show that nickel's Influence on swelling of copper is rather variable. however, increasing swelling at 423°C and decreasing It at 375°C, although the variability may reflect the impact of the order of magnitude difference in displacement rate associated with these two irradiation temperatures. Cold work appears to suppress swelling temporarily in both Cu-5Ni and Cu-5Mn. The suppressant effect of manganese on swelling persists to very high fluence. Swelling of Cu-5Mn appears to begin sooner at 375°C than at 423°C, however.

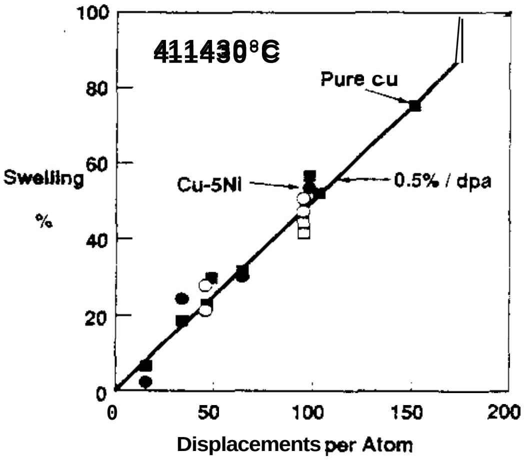

Fig. 2 Comparison of data from MOTA 2A and 2B with data from earlier experiments in FFTF designated Generation 1 and Generation 2.

Since these comparisons are based on side-by-side irradiations, it is felt that the conclusions drawn in the preceding paragraph are relatively valid. It is expected, however, that the onset of swelling in simple copper alloys is somewhat sensitive to a variety of environmental history variables. The range of data scatter shown in Figure 2 tends to obscure somewhat the effects of second order variables such as solute Composition, displacement rate and temperature history

FUTURE WORK

Microscopy on these alloys will proceed. The electrical conductivity of each alloy will also he measured.

REFERENCES

1. F. A. Garner. H. L. Hamilton, D. J. Edwards, B. N. Singh. J. F. Stubbins, T. Shikama, S. J. Zinkle and P. Samal, Fusion Reactor Materials Semiannual P-ogress Report DOE/ER-0313/10 (1991) pp. 186-191.

IRRADIATION OF COPPER ALLOYS IN THE SM-3 REACTOR - -

S.J. Zinkle (ORNL), F.A. Garner (PNL), V.R. Barabash (D.V. Efrcmov), **S.A.** Fahritsiev (D.V. Efremov) and **A.S.** Pokrovsky **(SRIAR)**

OBJECTIVE

This **report** summarizes the experimental matrix of copper specimens which have been prepared **for** irradiation in the SM-3 reactor.

SUMMARY

A total of 74 alloys of varying composition and thermomechanical condition have been prepared for a joint 17s-Russia irradiation experiment in the SM-3 reactor in Dimitrovgrad, Russia. The alloys will be irradiated in the form of TEM disks and sheet tensile specimens at temperatures of about 120, 250, and 340°C for one 45-day cycle in the core and Channel 2 irradiation positions. This will produce damage levels of about 7 and 1 dpa, respectively. Cadmium shielding will be used in the Channel 2 position to shield the thermal neutrons and thereby reduce the amount of solid transmutation products in copper.

INTRODUCTION

Accurate predictions of material lifetimes in a fusion reactor depend on irradiation data generated in fission reactors at fusion-relevant conditions. Although mixed spectrum fission reactors can achieve low irradiation temperatures that are of interest **for** near-term fusion reactors. the associated high thermal neutron fluxes induce large amounts ***of*** solid transmutation products in copper. These solid transmutation products cause a large decrease in the electrical and thermal conductivity of copper alloys. In addition, the amount of helium generated in a fission neutron spectrum is about an order of magnitude less than that produced in a fusion reactor. Helium production may have a strong influence on the resistance **of copper alloys** to swelling **and** high-temperature irradiation embrittlement.

In order **to** provide a closer simulation of the fusion neutron irradiation behavior of copper alloys, a spectrally tailored experiment has been designed **for** the **SM-3** mixed spectrum reactor. A cadmium sheet of 2-mm thickness will be used in the Channel 2 irradiation position to screen out the thermal neutrons. Specimens will also be irradiated without Cd shielding in the reactor core. Specimens will be irradiated with and without boron doping in order to study the effects of helium generation.

IRRADIATION CONDITIONS *AND* SPECIMEN MATRIX

The SM-3 reactor has recently been restarted after being shut down for about 2 years in order **to** replace the reactor core. The water-cooled SM-3 reactor operates at a power level of 100 MW_{th} and has a core height of about 40 cm. The present irradiation experiment will utilize space in the core and Channel 2 irradiation positions. Detailed characterization **of** the neutron spectrum for the new reactor core is still in progress.

Preliminary calculations of the neutron spectrum are summarized in Table 1 along wilh a general description **of** the core and Channel 2 irradiation positions. Irradiation for one 45-day cycle in the core and Channel 2 positions will produce approximately 7 dpa and 1 dpa, respectively in copper

Table 1. Char eristics of Irradiation Positions in e SM-3 reactor.

	Core	Channel 2
Neutron Flux (n/cm^2-s)		
E > 1 MeV	~1 x 10^{15}	-2 x 10^{14}
E > 0.1 MeV	-2 x 10^{15}	-3 x 10^{14}
E < 0.68 eV	-2 x 10^{14}	~1 x 10^{15}
Irradiation Cycle (days)	45	45
Fluence (n/cm^2, E>0.1 MeV)	-8 x 10^{21}	-1 x 10^{21}
Channel Diameter (cm)	1.0	6.0
Capsule Length (cm)	35	35
Coolant temperature (°C)	70	70

Three types of specimen geometries will be irradiated: Transmission electron microscopy (TEM) disks (3 mm dia x -0.25 mm thickness), and two types of sheet tensile specimens, "large tensile specimens" (LTS) and "small tensile specimens" (STS). The geometries for the LTS and STS specimens are shown in Fig. 1. The thickness of the STS specimens was increased **to** 1 mm in some cases such as annealed copper in order to ensure a minimum ***of*** 4 grains across the gage thickness. In addition to tensile properties, the electrical conductivity can be measured on either type of sheet tensile specimen.

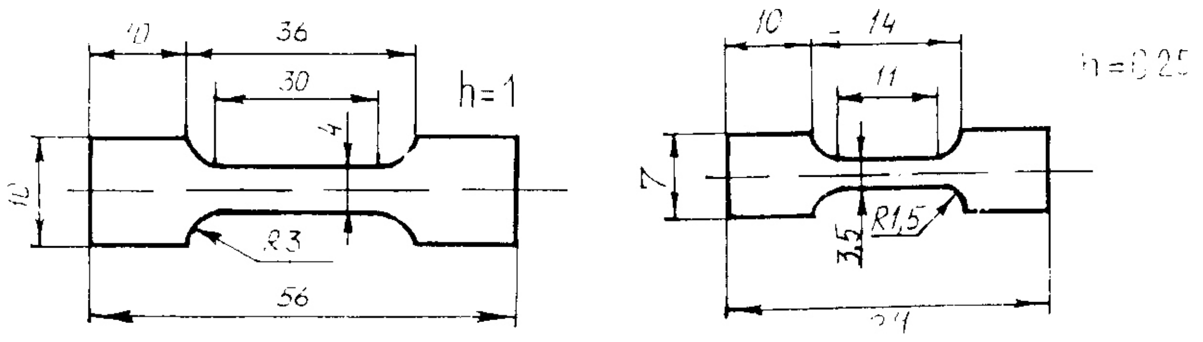

Fig 1. Types of **samples** being used for irradiation in the channel 2 (dimensions in mm)

A total of **3** capsules will he irradiated in the core positions for one cycle (45 days) to produce a damage level of about 7 dpa. The design temperatures for these 3 capsules are 100 **to** 120°C, 240 to 260°C, and 330 to 350°C. **A** total of 2 capsules will he irradiated in the Channel 2 positions to produce a damage level of **about** 1 dpa. These capsules are designed to he irradiated **at** 120 to 140°C and 240 **to** 260°C.

Approximately half of the length of the Channel 2 capsules will be surrounded with a 2 mm Cd shield to eliminate the thermal neutrons. All of the US-supplied specimens irradiated in the Channel 2 positions will be located in the Cd-shielded region of the capsules.

Tables 2 and 3 summarize the specimen matrix supplied by the US for the core and Channel 2 irradiation capsules, respectively. The US specimen matrix has a strong emphasis on two grades of oxide dispersion strengthened copper, GlidCop Al15 and Al25. The GlidCop Al25 specimens were supplied by B.N. Singh of Risø National Laboratory in Denmark as part of a collaborative investigation. The experimental matrix will allow the effects of cold work and He generation (from ^{10}B(n,α) reactions) to be independently studied. High-purity copper in various thermomechanical conditions (with and without B) has been included for comparison with the dispersion strengthened copper. The remainder of the specimen matrix is restricted to TEM disks. It includes some binary alloys, precipitation-strengthened Cu-Cr-Zr, and several different types of dispersion strengthened copper which will be compared with the GlidCop alloys. A prototypic heat of Cu-Al$_2$O$_3$ and several Cu-W and Cu-Mn alloys were supplied by T. Shikama, I. Smid, and Y. Shimomura, respectively as part of a collaborative study.

Table 2. Summary of US specimens in the core positions of the SM reactor.

Material	100 to 120°C		240 to 260°C		330 to 350°C	
(1) GlidCop Al25 (no B), as-wrought	2	3	2	2	2	2
(2) GlidCop Al25 + B, as-wrought	2	3	2	2	2	2
(3) GlidCop Al25 (no B), 20% CW	2	3	2	2	2	2
(4) GlidCop Al25 + B, 20% CW	2	3	2	2	2	2
(5) GlidCop Al15 + B, as-wrought	2	2	2	2	2	2
(6) GlidCop Al 15 + B, 20% CW		2	-	2		2
(7) GlidCop Al15 + B, 70% CW		1		1		1
(8) GlidCop Al15 + B, induction brazed	1	2	1	1	1	1
(9) 99.999% Cu, as-wrought		1		1		1
(10) 99.999% Cu, 80% CW	2	2	2	1	2	1
(11) 99.999% Cu, annealed 400°C, 1 h		2		1		1
(12) 99.999% Cu, annealed 550°C. 2 h	2	2	2	2	2	2
(13) 99.999% Cu, oxygenated (950°C, 0.5 h)		2		2		2
(14) Cu-100 ppm B, cold-rolled		1		1		1
(15) Cu-100 ppm B, annealed 550°C, 2 h		2		1		1
(16) Cu-Cr-Zr (MZC), solution ann. + aged		1		1		1
(17) Cu-Cr-Zr (MZC), CW + aged		1		1		1
(18) MAGT 0.05 (Technology 2)		2		1		1
(19) MAGT 0.2 (Technology 1)		3		2		2
(20) MAGT 0.2 (Technology 2)		3		2		2
(21) ULTRAM GOLDEN Cu-Al$_2$O$_3$		2		1		1
(22) Japanese Cu-Al$_2$O$_3$		2		1		1
(23) Cu-70 wt% W (Nippon Tungsten)		2		1		1
(24) Cu-70 wt% W (Plansee)		2		1		1
(25) Cu-0.5% Mn (as melted)		2		1		1
(26) Cu-1% Mn (as melted)		2		1		1
(27) Cu-1% Mn (remelted)		2		1		1
(28) Cu-5% Mn (as melted)		2		1		1
(29) Cu-5% Mn (remelted)		1		1		1
(30) MER Cu-graphite - Al$_2$O$_3$	-	2	-	1		1
(31) OFHC Cu, annealed (Risø)	-	1	-	1		1
Totals	15	61	15	41	15	41

Table 3. Summary of US specim in the Channel 2 posi n of the SM-3 reactor.

Material	Channel 2 (120 to 140°C) LTS	Channel 2 (120 to 140°C) STS	Channel 2 (120 to 140°C) TEM	Channel 2 (240 to 260°C) LTS	Channel 2 (240 to 260°C) STS	Channel 2 (240 to 260°C) TEM
(1) GlidCop Al25 (no B), as-wrought	3	3	3	3	3	3
(2) GlidCop Al25 + B, as-wrought	3	3	3	3	3	3
(3) GlidCop Al25 (no B), 20% CW	3	3	3	3	3	3
(4) GlidCop Al25 + B, 20% CW	3	3	3	3	3	3
(5) GlidCop Al15 + B, as-wrought	2	3	3	2	3	3
(6) GlidCop Al15 + B, 20% CW	1		3	1		3
(7) GlidCop Al15 + B, 70% CW	-	2	2		2	2
(8) GlidCop Al15 + B, induction brazed	3	2	2	3	2	2
(9) 99.999% Cu, as-wrought	3		2	3		2
10) 99.999% Cu, 80% CW	-	3	3		3	3
11) 99.999% Cu, annealed 400°C, 1 h	-	3	3		3	3
12) 99.999% Cu, annealed 550°C, 2 h	3	3	3	3	3	3
13) 99.999% Cu, oxygenated (950°C, 0.5 h)	-	3	2		3	2
14) Cu-100 ppm B, cold-rolled	-		1			1
15) Cu-100 ppm B. annealed 550°C, 2 h	-		2			2
16) Cu-Cr-Zr (MZC), solution ann. + aged	-		2			2
17) Cu-Cr-Zr (MZC), CW + aged	-		2			2
18) MAGT 0.05 (Technology 2)	-		3			3
19) MAGT 0.2 (Technology 1)	-		3			3
20) MAGT 0.2 (Technology 2)	-		3			3
21) ULTRAM GOLDEN Cu-Al_2O_3	-		3			3
22) Japanese Cu-Al_2O_3	-		2			2
23) Cu-70 wt% W (Nippon Tungsten)	-		2			2
24) Cu-70 wt% W (Plansee)	-		2			2
25) Cu-0.5% Mn (as melted)	-		2			2
26) Cu-1% Mn (as melted)	-		2			2
27) Cu-1% Mn (remelted)	-		2			2
28) Cu-5% Mn (as melted)	-		2			2
29) Cu-5% Mn (remelted)			2			2
30) MER Cu-graphite- Al_2O_3			3		2	3
31) OFHC Cu, annealed (Risø)			2			2
Totals	24	31	75	24	33	75

Table 4 summarizes the Russian specimens included in the SM-3 irradiation capsules. The Russian matrix includes specimens prepared by alternative techniques such as electron beam evaporation and condensation.

FUTURE WORK

The SM-3 irradiation is scheduled to begin in June 1993. Postirradiation testing of the mechanical and electrical properties of the specimens will be performed in Russia. The US TEM specimens will be shipped to the US for density measurements and microstructural analysis. Several Cu-B specimens will be analyzed for He content in the US and Russia as part of a round robin study.

Table 4. List of RF samples to be irradiated in the core and Channel 2 positions in SM-3.

1. Pure Cu(1), annealed 550°C, 1h	LTS	STS*	TEM
2. Pure Cu(1), 70% CW	LTS	STS	TEM
3. Pure Cu, annealed 550°C. 1h		STS*	TEM
4. Pure Cu(3) + H, 70% CW	LTS		TEM
5. Pure Cu(3) + H, annealed 550°C, 1h			TEM
6. Pure Cu(2), 70% CW			TEM
7. Cu-70 ppm B, annealed 550°C, 1h	LTS	STS*	TEM
8. Cu-70 ppm B, 70% CW		STS	TEM
9. Cu-300 ppm B, annealed 550°C, 1h	LTS	STS*	TEM
10. Cu-300 ppm B, 70% CW		STS	TEM
11. Cu-90 ppm B (e-beam), 70% CW		STS	TEM
12. Cu-90 ppm B (e-hem), ann. 550°C, Ih		STS	TEM
13. Cu-Mo (e-beam), 70% CW		STS	TEM
14. Cu-Mo (e-heam), annealed 550°C, 1h		STS	TEM
15. Cu-Mo-B (e-beam). 70% CW		STS	TEM
16. Cu-Mo-B (e-beam), annealed 550°C, 1h		STS	TEM
17. MAGT 0.2, as-wrought	LTS	STS	TEM
18. MAGT 0.2, annealed 550°C, 1 h	LTS	STS	TEM
19. MAGT 0.2. annealed 950°C, 1h		STS	TEM
20. MAGT 0.05, as-wrought	LTS	STS	TEM
21. MAGT 0.05, annealed 550°C, 1h		STS	TEM
22. Cu-70 ppm B, annealed 950°C. 1h		STS	TEM
23. Cu-300 ppm B, annealed 950°C. 1h		STS	TEM
24. Cu-90 ppm B (e-beam), ann. 950°C, 1h		STS	TEM
25. Cu-Be, aged	LTS	STS	TEM
26. Cu-Mo (type 3, e-beam). as wrought		STS	TEM
27. Cu-Mo (type 9, e-beam). as wrought		STS	TEM
28. Cu-Mo (type 11, e-hem), as wrought		STS	TEM
29. Cu-Cr, annealed 550°C, 1h		STS	TEM
30. Cu-Zr, annealed 550°C, 1 h		STS	TEM
31. Cu-Al, annealed 550°C, 1h		STS	TEM
32. Cu-Cr-Zr, aged	LTS	STS	TEM
33. Cu-Cr-Zr, annealed 550°C, 1h		STS	TEM
34. Cu-Cr-Zr-Mg, aged		STS	TEM
35. Cu-Cr-Zr-Mg, annealed 550°C, 1h		STS	TEM
36. Cu-NbC (e-beam), as wrought		STS	TEM
37. Cu-Al_2O_3 (e-beam), as wrought		STS	TEM
38. Stainless steel, annealed 550°C. 1h		STS	TEM
39. Stainless steel + ZrB_2, ann. 950°C, 1h		STS	TEM
40. High nickel alloy, annealed 950°C. 1h		STS	TEM
41. High nickel alloy (PH), aged			TEM
42. MAGT 0.2 + H, as wrought	LTS	STS	TEM
43. MAGT 0.2 + H, annealed 550°C, 1h		STS	TEM

STS thickness = 1 mm

EFFECT OF ION IRRADIATION ON THE STRUCTURAL STABILITY OF DISPERSION. STRENGTHENED COPPER ALLOYS*

S. J. Zinkle,[1] E. V. Nesterova,[2] V. R. Barabash,[3] V. V. Rybin,[2] and A. V. Naberenkov[3]

[1]Oak Ridge National Laboratory, P.O. Box 2008, Oak Ridge, TN 37831-6376, USA
[2]Central Research Institute for Structural Materials "Prometey," 193167 St. Petersburg, Russia
[3]D. V. Efremov Scientific Research Institute of Electrophysical Apparatus, 189631 St. Petersburg, Russia

OBJECTIVE

To investigate the effect of high dose ion irradiation on the microstructure of Russian and American dispersion strengthened copper alloys.

SUMMAKY

Transmission electron microscopy was used to compare die microstructure and particle distributions of two commercial oxide dispersion-strengthened copper alloys, GlidCop A125 and MAGT 0.2. Measurements were made on specimens in their as-wrought condition, after thermal annealing for 1 h at 900°C, and after 3 MeV Ar^+ ion irradiation at 180 and 350°C to damage levels of 20 to 30 displacements per atom (dpa). All of the annealed and ion-irradiated specimens were found to be resistant to recrystallization. In addition. void formation was not observed in any of the irradiated specimens. The GlidCop oxide particle geometry was transformed from triangular platelets to circular disks by the ion irradiation. The MAGT particle geometry consisted of circular disks and spheres before and after irradiation. The oxide particle edge length in the unirradiated GlidCop alloy was about 10 nm, whereas the mean diameter of the particles in the unirradiated MAGT alloy was about 6 nm. After irradiation, the mean particle diameter in both the MAGT and GlidCop alloys was about 6 nm.

PROGRESS AND STATUS

Introduction

Dispersion-strengthened copper alloys are being considered as a high heat flux structural material in fusion reactors due to their combination of high thermal conductivity with high mechanical strength. Unlike precipitation strengthened alloys, oxide dispersion strengthened copper is not susceptible to precipitate overaging and softening after high temperature annealing. This feature is important because high temperature braze cycles will likely be needed for joining high heat flux components. Recent ion [1,2] and fission neutron [3-5] studies have found that dispersion strengthened copper containing a high density of small Al_2O_3 particles is very resistant to radiation-induced softening and void swelling. One important issue that has not yet been completely resolved is the stability of these small oxide particles against ballistic dissolution during irradiation to high doses. Spitznagel et al. [1] reported evidence of particle fragmentation in oxide dispersion-strengthened copper after ion irradiation to 10 dpa at 250 to 350°C, but did not quantify the fraction of affected particles. Two recent studies [6,7] have found that energetic particle irradiation to damage levels of 2 to 3 dpa may cause a modest decrease in the size and density of Al_2O_3 particles in a dispersion-strengthened copper.

---

*Research sponsored in part by the Office of Fusion Energy, U.S. Department of Energy, under contract DE-AC05-84OR21400 with Marlin Marietta Energy Systems. Inc.

The purpose of the present study was to compare the effect of high-dose ion irradiation on the microstructure and particle size of two commercial oxide dispersion-strengthened alloys produced in Russia and the United States. These two alloys have slightly different panicle geometries and sizes in the as-fabricated condition due to differences in the manufacturing processes. The microstructural response of the two alloys to high temperature thermal annealing and highdose ion irradiation was investigated by transmission electron microscopy (TEM)

Experimental Procedure

The two alloys for this study were MAGT 0.2, produced by "Spetssplav," Moscow, Russia, and GlidCop Al25, produced by SCM Metal Products, Inc., Research Triangle Park, North Carolina, USA. The MAGT alloy contained 0.17 wt % AI, 0.05 wt % Hf, and 0.09 wt % Ti in the form of oxide particles, and the GlidCop alloy contained 0.25 wt % Al in the form of Al_2O_3. proprietary powder metallurgy and internal oxidation techniques were used to produce a uniform dispersion of small oxide particles in the alloys. The GlidCop alloy used in this study was cold worked 50% after fabrication.

Several specimens of each alloy were vacuum annealed at 900°C for 1 h. Some of the annealed and as-received specimens were subsequently irradiated with 3 MeV Ar^+ ions at the D. V. Efremov Institute to damage levels of 20 to 30 displacements per atom (dpa) at temperatures of 180 and 350°C. These calculated damage levels refer to a depth of 0.2 mm, which was the depth chosen for TEM observations in this study. The corresponding damage rate at thii depth was between 2 and 4 x 10^{-3} dpa/s. The as-received, annealed, and irradiated specimens were electrochemically thinned near room temperature and examined in a Philips EM400 electron microscope at CRISM Prometey. The TEM specimens were initially electropolished with an applied potential of 25V in a solution containing 133 ml CH3 COOH, 40 ml H_2O and 25 g CrO_3. The. final electropoliihig solution contained 440 ml H_3PO_4 and 60 g CrO_3.

The techniques used to examine the particle distribution in the alloys have been described previously [7]. Briefly, the analysis used weak-beam dark field micrographs taken on {002} copper matrix diffraction spots and centered dark field imaging using reflections from the {440} diffraction ring of the cubic Al_2O_3 particles. Carbon extraction replicas were prepared from unirradiated specimens by electropolishing at -30°C in a solution of 33% HNO_3/67% CH_3OH with an applied potential of 5V, evaporating a carbon film, and etching in a solution of 10% HCI in methanol. The chemical composition of individual particles in the extraction replicas was analyzed by energy dispersive X-ray spectroscopy (EDS) using a Philips 400T electron microscope. equipped with a field emission gun at ORNL.

Results

Both alloys initially contained a high density of dislocations ($>10^{14}/m^2$) due to their as-wrought cold-worked condition. Details of the dislocation and subgrain structure of the two alloys before and after thermal annealing or ion irradiation are described elsewhere [8]. The total panicle density observed in both the unirradiated MAGT and GlidCop alloys was about 4.5 x $10^{22}/m^3$. This included a low density ($<1 \times 10^{21}/m^3$) of large panicles with sizes ≥100nm. It was observed that the particle size in the two alloys was unaffected by annealing at 900°C. Figure 1 compares the microstructure of the MAGT and GlidCop alloys after annealiig at 900°C for 1 h.

Most of the oxide particles in the GlidCop alloy were found to be, triangular platelets (Fig. 1), with an average edge length of about 10 nm. The aspect ratio of the particles (edge length to thickness) in the GlidCop alloy was between 2 and 6, in agreement with previous measurements on Cu-Al_2O_3 alloys [7, 9, 10]. About 80 to 90% of the oxide particles in the MAGT alloy were spherical in shape. and the rest of the panicles were in the form of circular disks. The average particle diameter in the MAGT alloy was 6 nm. As discussed elsewhere [10], the round particle shape in the. MAGT alloy is due to the addition of Ti and Hf, which also acts to refine the particle size. Figure 2 shows the chemical composition of two small panicles extracted from the as-wrought MAGT alloy. Whereas the GlidCop alloy contained only aluminum oxide panicles, the MAGT alloy contained Al-, Ti-, and Hf-oxide particles. and mixed Al- and Ti-oxide particles of varying composition. For example, the Ti/Al atomic ratio for the particle in Fig. 2a was 0.21.

ORNL-PHOTO 6873-92

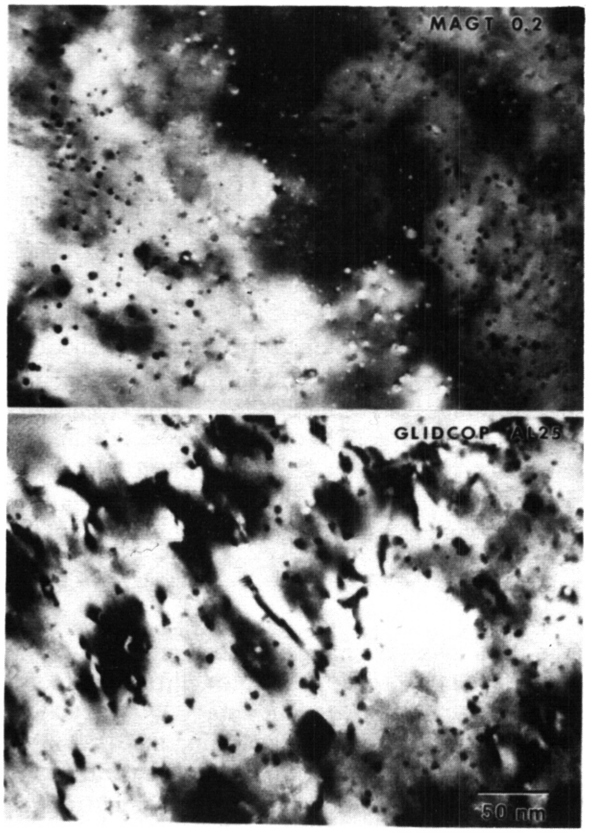

Fig. 1. Comparison of the oxide particle dispersions in MAGT 0.2 and GlidCop A125 copper alloys after annealing at 900°C for 1h.

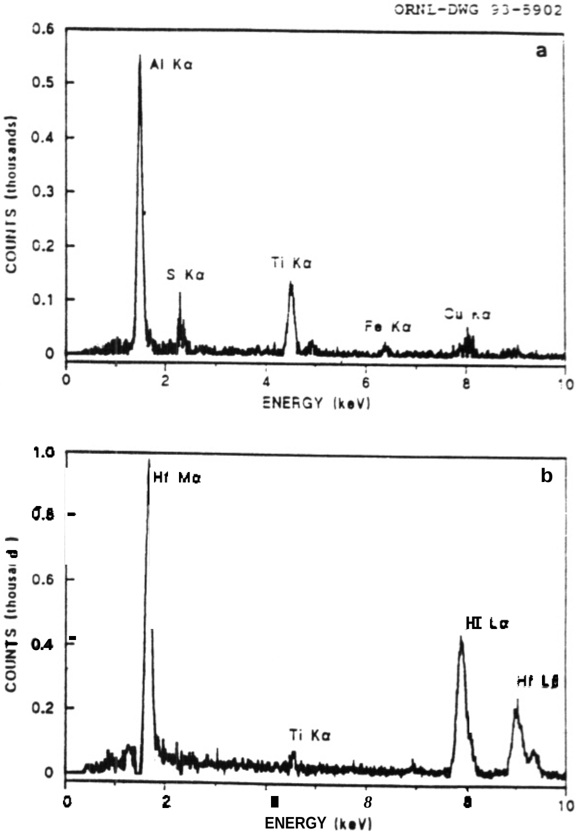

Fig. 2. EDS spectra (corrected for hole counts) obtained on two individual small oxide. particles extracted from the as-wrought MAGT 0.2 alloy. The sulfur peak visible in Fig. 2a is a contaminant present in the evaporated carbon.

Figure 3 compares the measured particle size distributions in the as-received MAGT and GlidCop alloys. A precise measurement of the particle size and density was hampered by heterogeneous variations of the particle distribution within the alloys. The dispersion strengthened alloys exhibited good resistance to recrystallization during annealing at 900°C (0.87 T_M) for 1 h. Several isolated regions in the MAGT 0.2 alloy recrystallized after this annealing treatment, whereas the GlidCop A125 alloy remained in its non-recrystallized state. The slightly superior resistance to recrystallization of GlidCop A125 compared MAGT 0.2 may be attributable to the larger average particle size in the GlidCop alloy (10 nm vs. 6 nm). As shown in Fig. 4, recrystallization in the MAGT alloy occurred heterogeneously in regions where the localized particle size was only about 4 nm. Recrystallization did not occur in the remaining volume of the MAGT alloy, where the mean particle diameter was about 6 nm. Vickers microhardness measurements for the annealed MAGT and GlidCop specimens were both comparable, which indicates that the limited recrystallized volume in the MAGT alloy did not seriously degrade its mechanical strength. The as-received and annealed microhardness for MAGT 0.2 was 167 and 145 VHN, respectively. The corresponding microhardness measured for the as-received and annealed GlidCop alloy was 137 and 134 VHN, respectively.

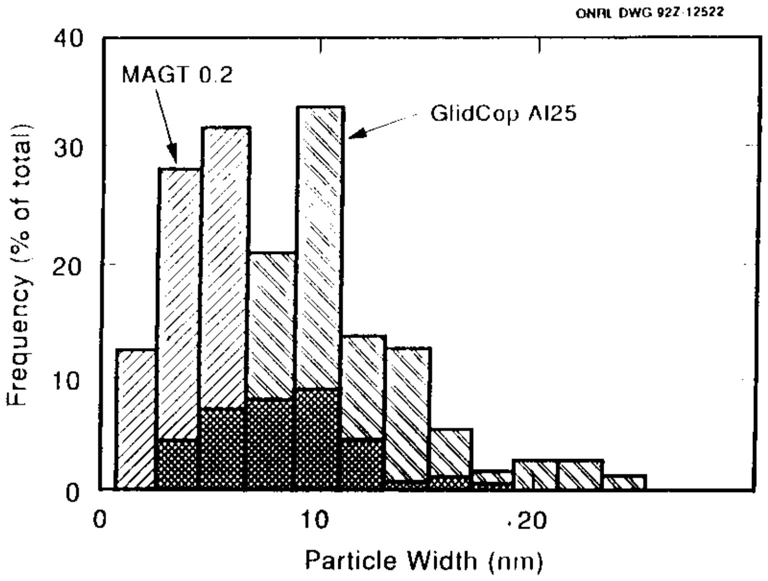

Fig. 3. Size distribution of oxide particles in the as-wrought MAGT 0.2 and 50% cold-worked GlidCop A125 copper alloys.

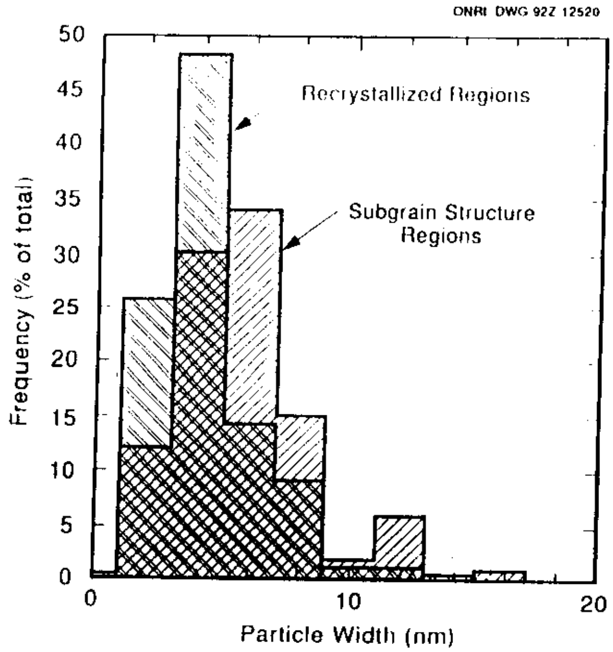

Fig. 4. Comparison of the oxide particle size distribution in recrystallized and nonrecrystallized regions of a MAGT 0.2 specimen that was annealed at 900°C for 1 h.

The general microstructure of the irradiated alloys was similar to their unirradiated state. The main effect of irradiation on the dislocation and subgrain structure was to induce dislocation recovery, which produced well-defined subgrains with a reduced dislocation density [8]. Cavity formation was not observed in either alloy for any of the irradiation conditions of this study. Figure 5 shows the microstructure of the GlidCop alloy after irradiation to 30 dpa at 180°C. A high density ($5 \times 10^{23}/m^3$) of defect clusters was ***created*** in the MAGT and GlidCop alloys **as** a result of **this** irradiation condition, with a mean size of 2 nm. Figure 6 shows the measured defect cluster size distribution in **the** GlidCop alloy irradiated at 180°C. About 80% of the defect clusters were identified **as** stacking fault tetrahedra (SFT) (visible **as** triangular-shaped defects in the lower photo **in** Fig. ***5).*** Irradiation at a temperature of 350°C produced a much lower defect cluster density of about $7 \times 10^{21}/m^3$ in both the MAGT and GlidCop alloys, with essentially all of the clusters in the form of SFT.

ORNL-PHOTO 6877-92

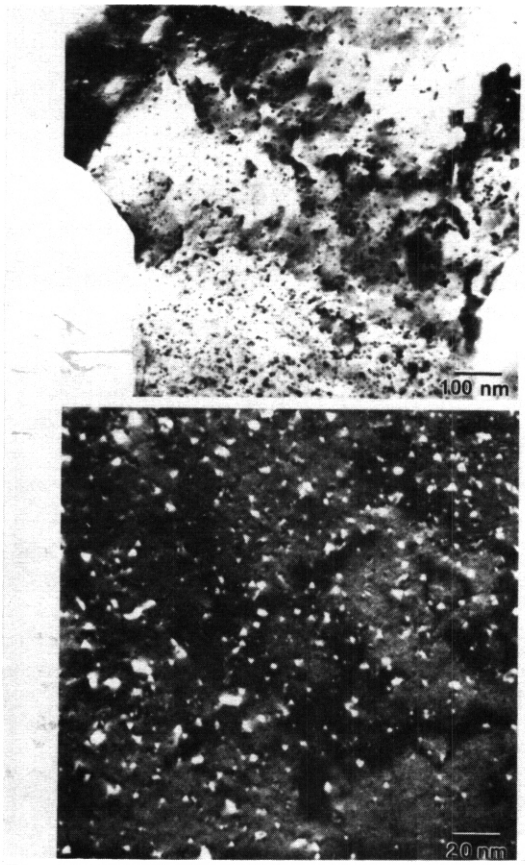

Fig. 5. Defect cluster formation in 50% cold-worked GlidCop A125 that was irradiated with 3 MeV Ar^+ ions to a damage level of 30 dpa at 180°C. Both micrographs were taken at a beam direction near <110> and a diffraction vector of <002>. The bottom photograph is a (g, 3g) weak **beam** micrograph showing triangular-shaped stacking fault tetrahedra.

Following ion irradiation to damage Levels greater than 20 dpa, the geometry of the oxide particles in the GlidCop alloy was transformed from predominantly triangular platelets to nearly circular platelets. This gradual change in particle geometry was apparently due to selective ballistic dissolution of the comers of the initially triangular oxide particles in GlidCop. The circular disk and spherical geometries of the MAGT alloy oxide particles was not changed even after high-dose irradiation. Figures 7 and ***8*** show the typical particle morphology in GlidCop Al25 following irradiation to 30 dpa at 180°C. The aspect ratio (diameter/thickness) of the oxide particles was about three in the irradiated GlidCop specimens, which is comparable to the unirradiated value of two to six. The small arrow in Fig. ***8*** points to an oxide particle that is close to an edge-on orientation. Measurements on particles in this orientation were used to determine the aspect ratio.

There was occasional evidence for complete ballistic fracturing of a **small** fraction of the oxide particles in the MAGT and GlidCop alloys after high dose irradiation. Figure 9 shows a fractured Al_2O_3 particle in a GlidCop Al25 specimen that was irradiated to 30 dpa. The percentage of fractured particles observed in the **inadiited** specimens was only about 1% of the total panicles, and we cannot exclude the possibility that these particles may have been fractured **as** a result of mechanical processing (cold rolling) prior to the irradiation.

Figure 10 compares the measured particle size distribution in nonirradiated and irradiated GlidCop Al25. These size distributions include measurements made on **both** as-received and annealed specimens. Irradiation to 30 dpa at 180°C caused a shift in the GlidCop particle distribution to smaller sizes. The most probable edge length of the predominantly triangular platelets present in nonirradiated GlidCop AI25 was 10 nm. After irradiation, the most probable diameter of the predominantly circular platelets was 6 nm. The corresponding mean particle sizes before and after irradiation were 10.5 nm and 7.1 nm. respectively.

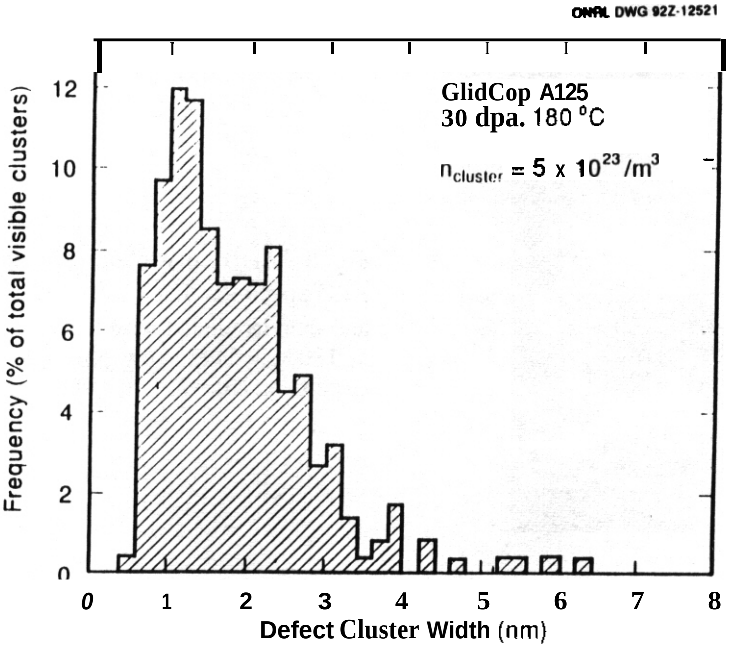

Fig. 6. Size distribution of radiation-induced defect clusters in 50% cold-worked GlidCop A125 after 3 MeV Ar^+ ion irradiation to 30 dpa at 180°C.

ORNL-PHOTO 6878-92

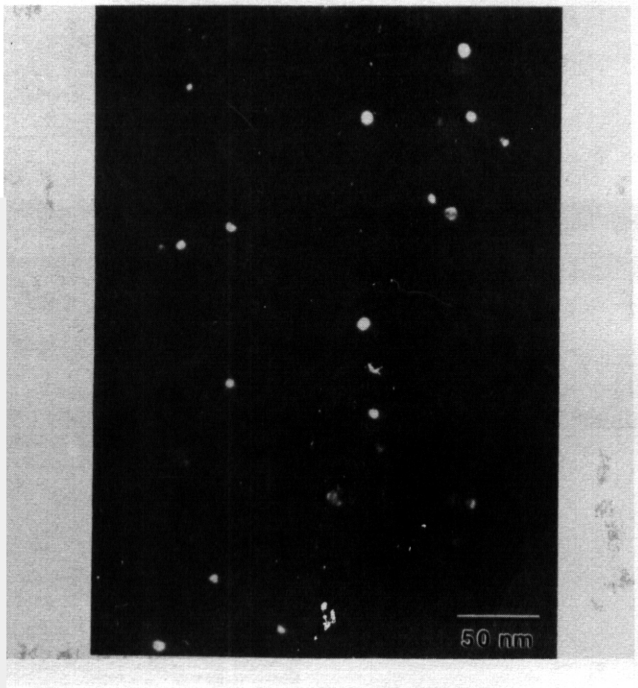

Fig. 7. Centered dark-field image of the Al_2O_3 particle morphology in annealed GlidCop A125 after 3 MeV Ar^+ ion irradiation to 30 dpa at 180°C.

ORNL-PHOTO 6874-92

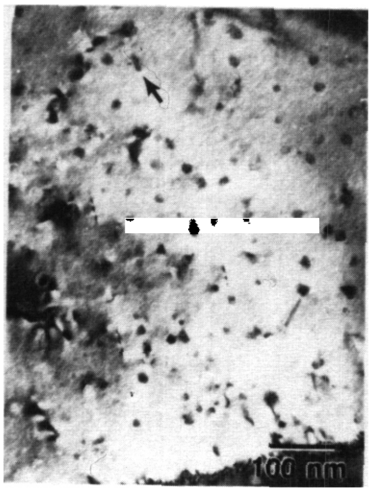

Fig. 8. Al_2O_3 particle morphology in a GlidCop A125 specimen that was annealed at 900°C for 1 h and then irradiated with 3 MeV Ar^+ ions to 30 dpa at 180°C. The arrow points to a particle that is close to an edge-on orientation.

OWL-PHOTO 6875-92

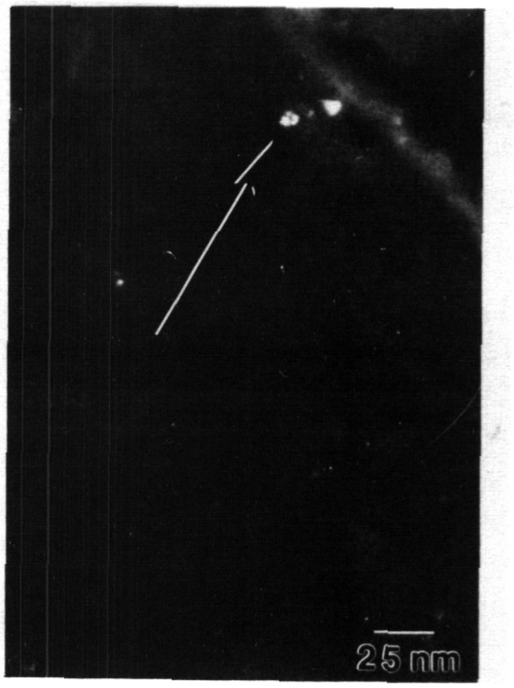

Fig. 9. Centered dark-field image of a fractured Al_2O_3 particle in a 50% cold-worked GlidCop A125 specimen that was irradiated to 30 dpa at 180°C.

ORNL DWG 92Z-12518

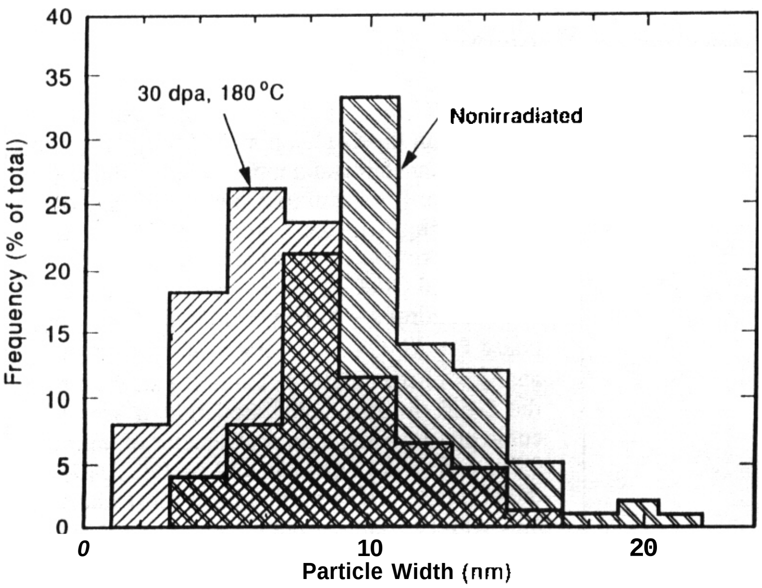

Fig. 10. Size distribution of Al_2O_3 particles in GlidCop A125 before and after ion irradiation to 30 **dpa** at 180°C.

Irradiation of GlidCop at a higher temperature and lower dose caused a somewhat smaller shift in the particle distribution. The most probable and mean particle sizes in GlidCop after irradiation to 20 dpa at 350°C were about **8** nm and **8.4** nm, respectively.

The average panicle density in GlidCop A125 was about **4.5** x $10^{22}/m^3$ before inadiation, with some regions containing particle densities as high as **8** x $10^{22}/m^3$ or as low as 2 x $10^{22}/m^3$. The measured oxide particle density in the GlidCop alloy after irradiation ranged between 1.3 x $10^{22}/m^3$ and *8.6* x $10^{22}/m^3$. Figure 11 shows an example of the large variability observed in the particle size and density for different regions in an irradiated GlidCop specimen.

As shown in Figure 12, the particle size distribution in the MAGT **0.2** alloy was essentially unaffected by irradiation to damage levels in excess of 20 dpa. The particle size and density in the MAGT alloy also exhibited significant (~50%) region-to-region variations, in a manner similar to that observed in the GlidCop specimens. Due to these heterogeneous variations in the particle size and density, it was not possible to quantitatively determine if the average particle density in the MAGT 0.2 alloy was altered by irradiation. However, in qualitative terms, the density was similar in the nonirradiated and irradiated specimens.

ORNL-PHOTO 6879-92

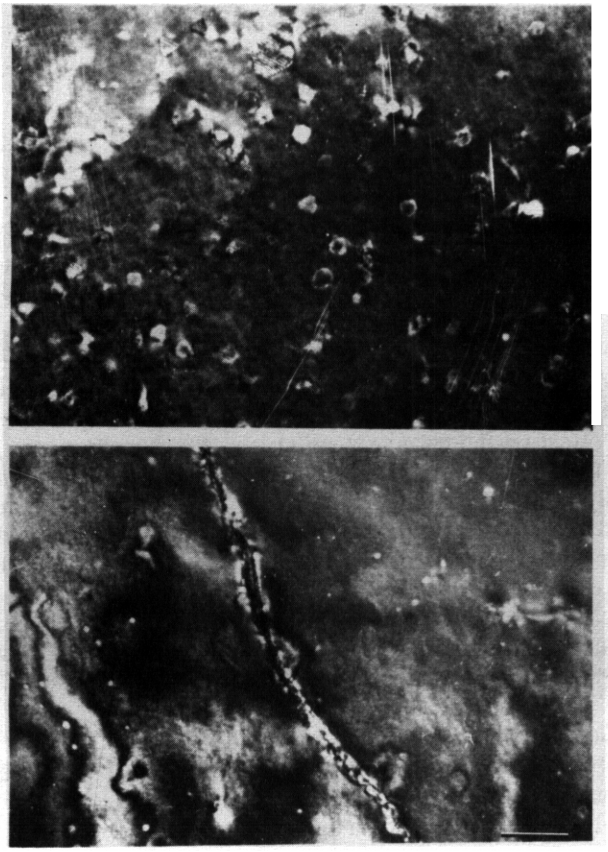

Fig. 11. Centered dark field micrographs showing the variability of the Al_2O_3 particle sizes in different regions of a GlidCop A125 specimen that **was annealed at 900°C and then irradiated** to 30 dpa **at 180°C.**

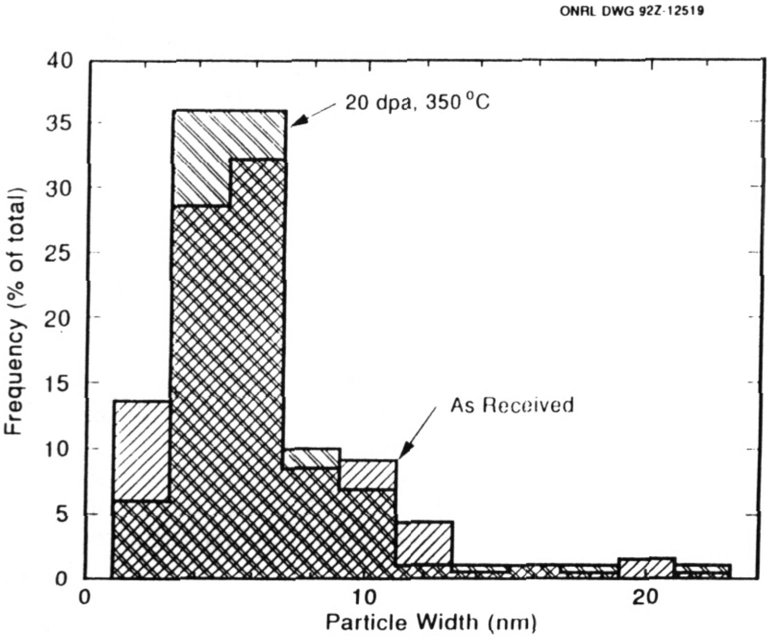

Fig. 12. Size distribution of oxide particles in as-wrought MAGT 0.2 before and after ion irradiation.

DISCUSSION

Several different types of oxide particles were observed in the GlidCop and MAGT alloys. Thermal annealing and ion irradiation did not produce any measurable compositional or phase changes in the oxide particles. The large particles (d >100 nm) in both the MAGT and GlidCop alloys were identifed as rhombohedral a - Al_2O_3, which is the stable phase for Al_2O_3 [11]. Electron diffraction analysis of the small (d ≤20 nm) particles in the GlidCop alloy indicated that it was a cubic phase with a lattice parameter of about 0.795 nm. As discussed by Ernst et al. [9], these small Al_2O_3 particles are most likely h¢ - Al_2O_3. The h¢ cubic spinel phase has essentially the same lattice parameter as the g - Al_2O_3 spinel transitional phase (0.790 to 0.797 nm) [9, 11], and can be considered to be a disordered form of g - Al_2O_3 due to slightly different coordination of the ions on the Al sublattice [9]. Characterization of the small particles in the MAGT 0.2 alloy was somewhat more complicated due to the presence of TiO_2 and HfO_2 particles in addition to Al_2O_3. In addition, EDS (Fig. 2a) indicated that at least some of the small Al-rich particles in MAGT 0.2 also contained Ti. Daneliya and Teplitskiy [10] reported that the mixed Al- and Ti-oxide particles in an alloy similar to MAGT 0.2 consisted of a cubic Al_2O_3 core and a Ti-rich shell. The structure of these mixed oxide particles was not investigated in the present study.

The particle size distributions summarized in Figures 10 and 12 indicate that the most probable oxide particle size after high dose irradiation with 3 MeV Ar^+ ions is between 5 and 6 nm for both the MAGT 0.2 and GlidCop Al25 alloys. Since the mean particle diameter in nonirradiated MAGT 0.2 was 6 nm (Fig. 3), ion irradiation to 30 dpa did not have a large effect on the particle distribution. On the other band, the particle size in GlidCop was reduced by about 40% (from 10 nm to 6 nm) as a result of the ion irradiation. This size reduction was accomplished primarily through the dissolution of the corners of the triangular-shaped oxide platelets in GlidCop, which caused the particle geometry to transform into nearly circular disks after high-dose irradiation (Figs. 7 and 8). From simple geometric considerations, the largest circle that can be inscribed inside of an equilateral triangle of edge length L is $D = L/+3 = 0.58$ L. This suggests that the observed 40% reduction in the GlidCop particle size can be directly accounted for by selective ballistic dissolution of the corners of the initially triangular particles. The oxide particles in MAGT 0.2 were initially in the form of spheres and circular disks, and their geometry was not changed during irradiition.

Previous microstructural studies of irradiated GlidCop alloys have not reported evidence for a transformation in the oxide particle geometry from triangular platelets to circular disks [1,3,6,7]. However, the dose for one of these studies [7] was only 2 dpa, and the high dose studies [1,3,6] apparently did not examine the morphology of the small (<10 nm) particles but instead concentrated on the larger (>10 nm) oxide particles, which may he less susceptible to ballistic dissolution effects. Spitznagel and coworkers [1] reported chat some of the Al_2O_3 particles were fracturcd by ballistic dissolution following high dose (>10 dpa) ion irradiation, but the fraction of affected panicles was not reported.

Since the oxide particles in MAGT 0.2 are relalively unaffected by high-dose ion irradiation, this suggests that the radiation stability **and** tensile propcrties should not be greatly changed after irradiation. Barabash and coworkers [2] have observed that the yield strength of MAGT 0.2 measured at **400°C** was essentially unchanged after fast neutron irradiation at 400°C to a dose of about 7 dpa. High-dose neutron irradiation studies performed on GlidCop A125 have round that its room temperature yield strength decreased by about 10% after irradiation at 415 to 430°C to a damage level of 16 dpa, and then remained constant **during** further irradiation up lo damage **levels** of 150 dpa [5,12]. This strength decrease after neutron irradiation to 16 dpa may be due to a slight decrease in the mean size of the Al_2O_3 particles associated with ballistic dissolution, in a manner similar to **our** observations on ion-irradiated GlidCop (Fig. 10). If the strength decrease in neutron-irradiated GlidCop is due to a dccreasc in the oxide-dispersion **size,** then the strength decrease mcasurcd at elevated temperatures (e.g., 400°C) would be proportionately greater, due to the increased importance **of** thermally activated bypassing of the oxide particles by dislocations for **small** particle sizes. Tensile tests performed at the irradiation temperature arc needed **to** quantitatively evaluate the strength decrease in GlidCop alloys associated with ncutron irradiation at elevated temperatures.

CONCLUSIONS

Microstructural examination of two commercial oxide dispersion-strengthened copper alloys after thermal annealing and ion irradiation revealed the following features:

1. MAGT 0.2 and GlidCop **A125** are both resistant to microstructural changes during annealing at high temperature and high-dose ion irradiation. GlidCop A125 is slightly more rcsistant to recrystallization than MAGT 0.2 during thermal annealing, apparently because of its slightly larger initial oxide particle **size** (10 nm **vs.** 6 nm).

2. The most probable particle size in GlidCop A125 was reduced fmm 10 nm to 6 nm after 3 MeV Ar^+ ion irradiation **to** damage levels greater than 20 dpa, and the oxide particle morphology changed from triangular platelets to circular disks. In contrast, the particle size in **MAGT** 0.2 was nearly unaffected **by** high-dose ion irradiation with **a** constant diameter near 6 nm. Radiation-induced changes in the particle density in the MAGT and GlidCop alloys were insignificant compared **to** grain-to-grain variations in the particle density (–50% variation) in the as-wrought material. The similarity of the particle size, density, and morphology in *the* MAGT and GlidCop alloys after high dose ion irradiation suggests that both alloys will exhibit similar mechanical properties alter irradiation.

ACKNOWLEDGEMENTS

The authors thank F. **A.** Gamer (Battelle Pacific Northwest Laboratory) **for** supplying the GlidCop A125 foil used for this study, and N. D. Evans for performing the EDS measurements.

REFERENCES

1. J. A. Spitznagel, N. J. Doyle, W. J. Choyke, J. *G.* Greggi, J. N. McGrucr, and J. W. Davis, ***Nucl. Instr. Methods B*** **16** (1986) 279.

2. V. R. Barabash, **A.** A. Gervash, **A.** V. Naherenkov, E. V. Nesterova, and S. A. Fabritsiev, ***Mar.*** *Sci.* ***Forum*** **97-99** (1992) **483.**

3. R. J. Livak, T. G. Zocco, and L. W. Hobbs, *J.* ***Nucl. Mater.*** **144** (1987) 121.

4. I. V. Gorynin, S. A. Fabritsiev, V. V. Rybin, V. A. Kasakov, **A.** S. Pokrovskii, **V.** R. Barabash, and Y. G. Prokofiev, *J.* ***Nucl. Mater.*** **191-194** (1992) **401.**

5. D. J. Edwards, K. R. Anderson, F. A. Gamer, M. L. Hamilton, J. F. Stubbins, and A. S. Kumar, *J. Nucl.* ***Mater.*** **191-194** (1992) 416.

6. N. Wanderka, Y. Yuan, L. Jiao, R. P. Wahi, and H. Wollenberger, ***J. Nucl. Mater.*** **191-194** (1992) 1356.

7. **S.** J. Zinkle. **A.** Horsewell, B. N. Singh, and W. F. Sommer, *J. Nucl.* ***Mater.*** **195** (1992) 11

8. E. V. Nesterova V. V. Rybin, S. J. Zinkle, V. R. Barabash, and A. V. Naberenkov, 2nd Conf. on the Effect of Irradiation on the Materials of Fusion Reactors, September 22-24, 1992, St. Petersburg, Russia, to be published in ***Plasma Devices and Operations*** (in press).

9. F. Ernst, P. Pirouz, and **A.** H. Heuer, ***Phil.*** Mag. **A** ***63*** (1991) 259.

10. Ye. P. Danceliya and M. D. Teplitskiy, ***Phys. Mer. Metallogr. (Fiz. Metal Metalloved.) 52,*** No. ***4*** (1981) 104.

11. K. Wefers and C. Misra, Oxides and Hydroxides of Aluminum, Alcoa Laboratories Technical Paper No. 19, revised (Alcoa Laboratories, 1987).

12. H. R. Bragcr, H. L. Heinisch, and F. A. Garner, *J.* ***Nucl.*** *Mater.* **133-134** (1985) ***676***

6.5 Environmental Effects in Structural Materials

MASS TRANSFER IN LITHIUM/STAINLESS STEEL TEST LOOP*

P. R. Luebbers and O. K. Chopra (Argonne National Laboratory)

OBJECTIVE

The objective of this program is to investigate the influence of a lithium environment on compatibility, corrosion, and mechanical properties of candidate vanadium alloys for first wall/blanket systems in fusion reactors.

SUMMARY

The plugged pipe removal from the cold-trap purification loop of the forced-circulation lithium system was examined to study mass transfer/deposition behavior and to establish the cause of plugging. Several intermetallic compounds were identified in residue collected from the plugged cold-trap pipe. Plugging was caused by deposition of calcium/zinc/nickel crystals in the pipe sections within the pump coil and flow-meter magnet. Addition of calcium as a getter to reduce the concentration of nitrogen in the lithium leads to formation of $(Ca,Zn)Ni_5$ crystals and subsequent plugging of the cold-trap loop. Deposits of manganese/iron/nickel globules and manganese/zinc/nickel dendrites, as well as Li_9CrN_5 and possibly Ca_3N_2, were also identified in the residue. These phases may have reduced flow through the cold-trap loop but were *not* abundant enough to plug the loop. The results indicate that the use of a dissolved getter, such as calcium, to reduce nitrogen content in an austenitic stainless steel loop may not be effective. Elements in the lithium from structural alloys (e.g., due to corrosion) and those added (e.g., calcium) to reduce the concentration of nonmetallic impurities (e.g., nitrogen) play an important role in the mass transfer/deposition behavior in circulating lithium systems.

PROGRESS AND STATUS

Compatibility of structural materials with liquid metals has a major influence on material selection and operating limitations for liquid-metal blankets. Corrosion in the form of uniform or selective dissolution, intergranular attack, and transfer of interstitial elements to and from the liquid metal can reduce the effective section thickness of structural components. Radioactive mass transfer/deposition of corrosion products may cause severe flow restrictions and excessive accumulation of radioactive material in unshielded regions. Corrosion/dissolution can reduce mechanical integrity, and mass transfer/deposition phenomena can increase pumping-power requirements, decrease energy conversion efficiency, and complicate system maintenance.

Mass transfer/deposition occurs in nonisothermal systems because of temperature and concentration gradients. Alloy elements dissolve in the hot regions of a liquid-metal loop because their concentrations in the liquid metal are lower than their solubilities, and they deposit in cold regions of the loop where their concentrations in the liquid metal are greater than their solubility limits. Severity of the corrosion and mass transfer varies with different combinations of containment material and liquid metal and depends on many variables. These include the liquid metal and its purity (i.e., concentrations of nitrogen, carbon, oxygen, etc.); composition and microstructure of the containment material; time and temperature of exposure; and system parameters such as flow velocity (including magnetohydrodynamic effects), AT (difference of temperature across the circulating system), surface area and temperature profile of the system, and material

---

* Work supported by Office of Fusion Energy, U.S. Department of Energy, under Contract W-31-109-Eng-38

combination (i.e., bimetallic or monometallic system). Several studies have been conducted to evaluate the influence of different material and system parameters on corrosion behavior of candidate structural materials in lithium.[1,2] Most studies have been conducted in circulating lithium systems such as thermal-convection or forced-circulation loops.

The present investigation was undertaken in an attempt to better understand the process of mass transfer/deposition in circulating lithium systems. Since 1981, corrosion/compatibility studies at Argonne National Laboratory have been conducted in a test facility consisting of a forced-circulation lithium loop and an MTS servohydraulic fatigue machine for performing mechanical tests in the liquid metal environment. A schematic diagram **of** the lithium loop is shown in Fig. 1. The lithium system, which is constructed of Type 304 stainless **steel,** consists of a primary loop with three test vessels and a secondary cold-trap purification loop. The quantity of lithium in the loop is $\approx$20 L which **is** circulated at –16 cm^3/s in the primary loop. The concentration of interstitial elements in the lithium is controlled by maintaining the cold-trap temperature at 200–220°C. In addition, the nitrogen level in the lithium is reduced to levels of <100 wppm by hot-trapping with Ti foils and by dissolved getters such as calcium. Nitrogen content is reduced by formation of TiN or Ca_3N_2, which are more stable than Li_3N. In the latter case, Ca_3N_2 is trapped in cooler regions of the loop, e.g., the cold trap.

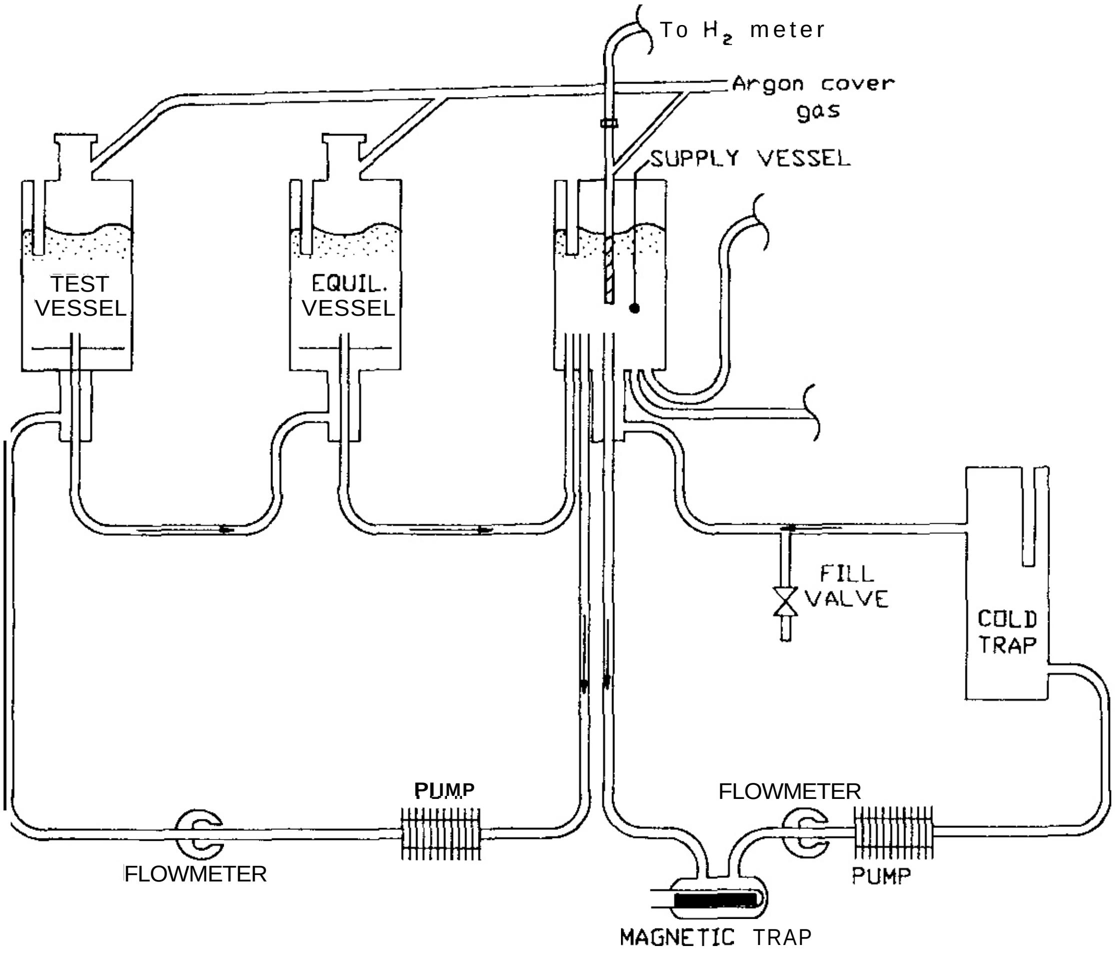

Figure 1. Schematic diagram of the lithium loop

During the initial six months of operation. the lithium system was shut down several times because of plugging of the flow meter and pump section of the cold–trap loop. Nitrogen concentration in the lithium during these early phases of operation increased to –1200 wppm due to contamination from the fixture used for performing mechanical tests. Examination of the plugged pipe sections indicated an accumulation of MnNi and $MnNi_3$ compounds, which are paramagnetic below 360°C, inside the pipe sections within the pump coil and flow–meter magnet? Panicles of pure iron and iron/nickel compounds were also detected in metallic residue collected from the plugged sections. Chromium was present as a ternary nitride (Li_9CrN_5) that decomposed into ammonia and lithium chromate when the lithium was dissolved in a solution of methyl alcohol and water. Subsequently, a magnetic trap (Fig. 1) was installed upstream of the flow meter and pump section of the cold–trap loop. The lithium loop has operated with few interruptions for ≈10 yr after installation of the magnetic trap.

At present. the lithium loop is being used to study the stability of various nitride and oxide coatings on vanadium–base alloys. Nitrogen content in the lithium has occasionally increased to >1000 wppm: consequently, calcium was added as dissolved getter to reduce the nitrogen concentration. The cold–trap loop plugged up within 24 h of the calcium addition. The magnetic trap, flow meter, and pump section of the cold–trap loop were removed for examination, and the results are presented in this report.

Results and Analysis

The plugged pipe removed from the cold–trap loop was cleaned by dissolving the lithium in a solution of methyl alcohol and water. The solution and residue collected from different sections of the pipe were examined to study mass transfer/deposition behavior and to establish the cause of plugging.

Cleaning solutions from those sections of pipes not within the pump coil or flow meter magnet. were relatively clean. Solutions collected after dissolving lithium from the center of these pipes had a milky–white appearance and were free of particulates. Solutions collected after cleaning the surfaces of these sections turned muddy gray or yellow and contained particulates. Cleaning solutions from inside the pipe sections within the pump coil or flow meter magnet formed a dark yellow or green sludge. A strong odor of ammonia was detected while cleaning these sections. Spectrographic analysis of the yellow/green solutions indicated a high concentration of chromium and small amounts of iron and calcium. These results indicate the presence of Li_9CrN_5 and possibly Ca_3N_2, both of which decompose in alcohol or water.

Several intermetallic compounds were identified in the residue of the cleaning solutions. Sludge collected from inside the pipe sections within the pump coil or flow meter magnet consists primarily of large rectangular plates of a calcium/zinc/nickel compound (Fig. 2).* Energy–dispersive X–ray (EDAX) analyses indicate that the crystals are most likely $(Ca,Zn)Ni_5$. The surface morphology of the panicles varies from a perfectly smooth surface to an etched and pitted appearance. depending on the composition. Other major constituents in the sludge were long dendritic crystals of a manganese/zinc/ nickel compound and small globular particles of a manganese/iron/nickel compound (shown in Fig. 3). The latter is most likely the cubic $(Mn,Fe)Ni_3$ phase that had been identified earlier in the particulate collected from plugged sections of the cold–trap loop?

---

* The source of zinc in the lithium is a Korloy (Zn–11Al) clamp that accidentally fell into the test vessel of the loop.

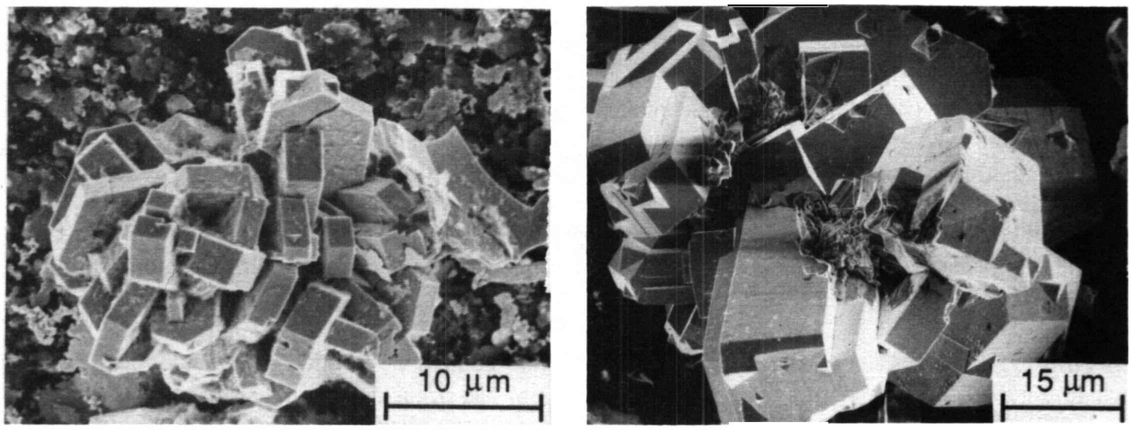

Figure 2. Photomicrographs of calcium/zinc/nickel compound collected from plugged flow meter and pump sections of cold–trap pipe

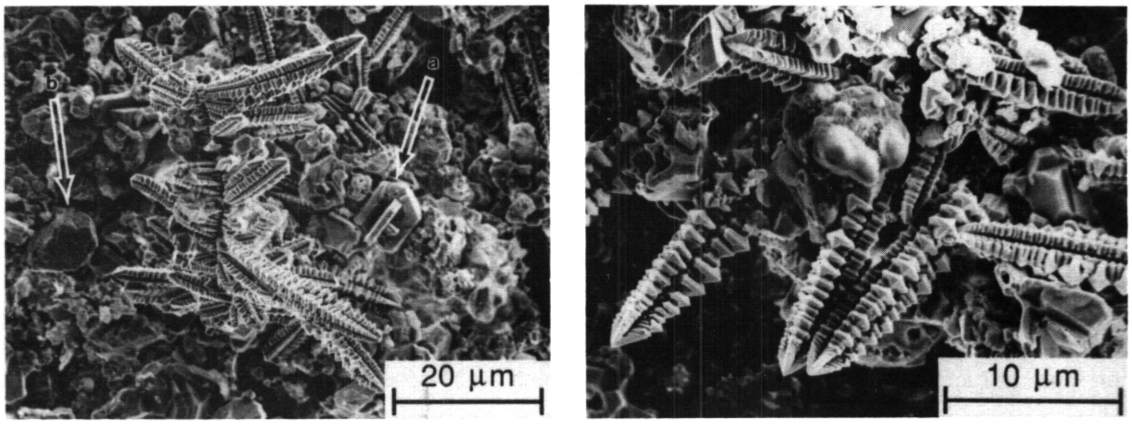

Figure **3.** *Photomicrographs of metallic residue collected from plugged flow meter and pump sections* ***of*** *cold–trap pipe. Phases at the* ***left*** *are (a)(Ca,Zn)Ni$_5$ and (b) (Mn,Fe)Ni$_3$.*

Large pieces of what appear to be broken ferrite layers were also detected in the residue. Austenitic stainless steels exposed to lithium develop a very porous ferrite layer because of preferential dissolution of nickel and, to some extent, chromium from the steel. The large metallic chunks are most likely spalled ferrite layer from the loop material.

A photomicrograph of the surface of the pipe section within the flow–meter magnet is shown in Fig. **4.** The surface has the etched appearance typical of austenitic stainless steels exposed to lithium and is covered with globular deposits that are enriched in nickel and manganese. **EDAX** analyses indicate that the deposits **are** globular particles of the manganese/iron/nickel compound shown in Fig. 3. The pipe surfaces do not show preferential dissolution of nickel or chromium from the steel; the composition of the pipe surface is the same **as** that of the base metal.

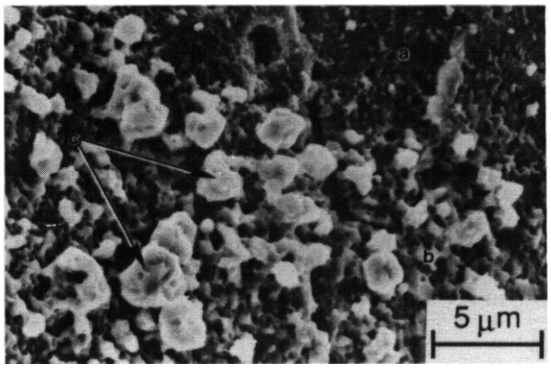

Figure 4.
Surface of pipe section within flowmeter magnet. Region (a) is pipe surface; Region (b) and (c) are globular particles of manganese/iron/nickel compound shown in Fig. 3.

CONCLUSIONS

Metallographic examination of the cold–trap pipe indicates that plugging was caused by napping of calcium/zinc/nickel crystals within the pump coil and flow–meter magnet sections of the pipe. The addition of dissolved calcium to reduce the nitrogen in the lithium leads to formation of $(Ca,Zn)Ni_5$ crystals and subsequent plugging of the cold–trap loop. Deposits of manganese/iron/nickel globules and manganese/zinc/nickel dendrites, as well as Li_9CrN_5 and possibly Ca_3N_2, were already present in the pipe sections prior to the calcium addition. These other phases may have reduced the flow through the cold–trap loop but were not abundant enough to plug the loop.

The results indicate that the use of a dissolved getter, such as calcium, to reduce the nitrogen content in an austenitic stainless steel loop may not be effective. The calcium may react with dissolved nickel in the lithium to form a calcium/nickel compound rather than Ca_3N_2. Elements in lithium from structural alloys (e.g., due to corrosion) and those added (e.g., calcium) to reduce the concentration of nonmetallic impurities (e.g., nitrogen) play an imponant role in the mass transfer/deposition behavior of circulating lithium systems.

FUTURE WORK

The contents of the magnetic trap removed from the cold–trap loop will be examined. X–ray diffraction and microprobe analyses will be used to identify the various phases.

REFERENCES

1. O. K. Chopra, D. L. Smith. P. F. Tortorelli, J. H. DeVan, and D. K. Sze, *Liquid–Metal Corrosion,* Fusion Technol., 8, 1956–1969 (1985).

2. O. K. Chopra and P. F. Tortorelli. *Compatibility of Materials for Use in Liquid–Metal Blankets of Fusion Reactors,* J. Nucl. Mater., 122 & 123, 1201–1212 (1984).

3. O. K. Chopra and D. L. Smith, *Corrosion of Ferrous Alloys in a Flowing Lithium Environment,* J. Nucl. Mater., 133 & 134, 861–866 (1985).

COMPATIBILITY OF CANDIDATE STRUCTURAL MATERIALS WITH STATIC GALLIUM*

P. R. Luebbers, W. F. Michaud, and O. K. Chopra (Argonne National Laboratory)

OBJECTIVE

Gallium has been considered as a possible heat transport liquid in the International Thennonuelcar Experimental Reactor (ITER). Gallium is attractive for such applications because the temperature range over which it remains liquid is wider than that of any other metal, i.e., from near room temperature (30°C) to 2300°C, and because it has good thermal conductivity and very low vapor pressure at high temperatures. However, gallium has high chemical reactivity with most metals. The objective of this study is to investigate the compatibility of gallium with candidate structural materials for ITER first-wall/blanket systems.

SUMMARY

Scoping tests were conducted on compatibility of gallium with candidate structural materials, e.g., Type 316 SS, Inconel 625, and Nb–5 Mo–1 Zr alloy, as well as Armco iron, Nickel 270. and pure chromium. Type 316 stainless steel is least resistant and Nb-5 Mo–1 Zr alloy is most resistant to corrosion in static gallium. At 400°C, corrosion rates are ≈4.0, 0.5, and 0.03 mm/y for Type 316 SS, Inconel 625, and Nb–5 Mo–1 Zr alloy, respectively. The pure metals react rapidly with gallium. In contrast to findings in earlier studies, pure iron shows greater corrosion than does nickel. The corrosion rates at 400°C are ≥90 and 17 mm/y, respectively, for Armco iron and Nickel 270. The results indicate that at temperatures up to 400°C, corrosion occurs primarily by dissolution accompanied by formation of metal/gallium intermetallic compounds.

PROGRESS AND STATUS

Gallium has a high affinity for most engineering metals and alloys. Pure metals such as aluminum, zinc, and tin disintegrate in liquid gallium at 30°C. The refractory metals and ceramics show the greatest stability in gallium. Gallium can be contained successfully in beryllium, tantalum. stabilized ZrO_2, or Pyrex glass at temperatures up to 450°C; in tungsten, rhenium, or graphite at temperatures up to 800°C; and in refractory oxides (such as sintered BeO or Al_2O_3) and vitreous quartz at 1000°C or higher.[1–3]

Corrosion occurs primarily by dissolution due to solubility of metals in gallium which results in metal recession and weight loss, and at higher temperatures also by diffusion into the metal. which leads to formation of surface scale and weight gain. For most metals, dissolution is accompanied by formation of metal/gallium intermetallic compounds from the saturated solution. The solubility and corrosion of pure metals in gallium have been investigated.[4–8] Figure 1 shows solubility of pure metals in gallium at 200–700°C. Unlike alkali metals, where solubility represents a saturated solution in equilibrium with pure metal, solubility in gallium is based on a saturated solution in equilibrium with an intermetallic compound. For most engineering metals, the intermetallic compound is of the form MGa_3 or MGa_4. Solubility data at a given temperature, e.g., 400°C, show a periodicity with atomic number similar to that observed in other low-melting metals, e.g., mercury, indium, tin, lead, bismuth, lithium, sodium, or potassium. Although the absolute value of solubility may vary for the various liquid metals, in all cases a minimum in solubility is observed for beryllium, boron, vanadium, niobium, molybdenum, tantalum, tungsten, rhenium, and osmium.[8]

---

* Work supported by Office of Fusion Energy, U.S. Department of Energy. under Contract W–31–109–Eng–38.

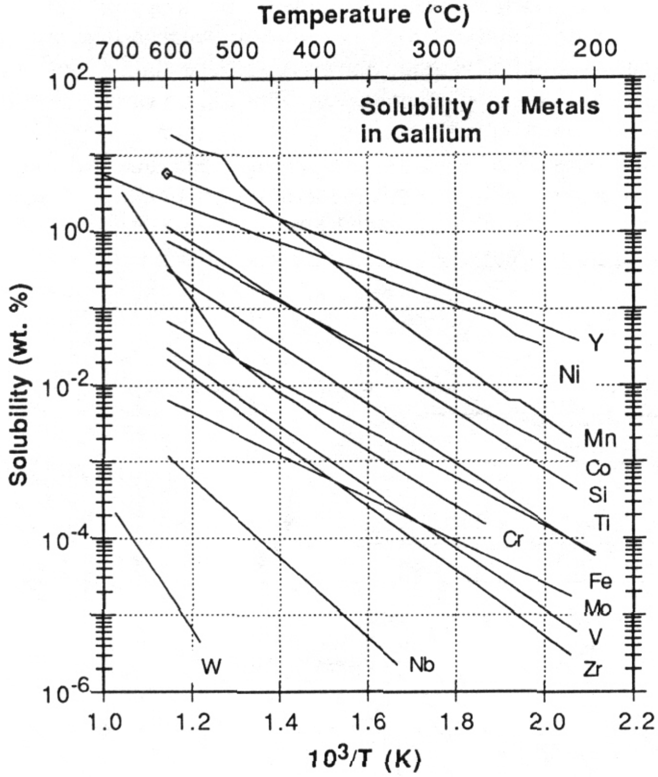

Figure 1. Solubility of pure metals in gallium at 200–700°C

Corrosion data correlate well with solubility, i.e., metals with high solubility show poor corrosion resistance. At 400°C, both solubility and corrosion of nickel in gallium are more than one order of magnitude greater than for iron.[7,9] Various high-alloy ferritic and martensitic steels and austenitic stainless steels (SSs) show fair resistance to corrosion in gallium at temperatures up to 400°C, i.e., a corrosion rate of ≤1 mm/y.[9] In general, corrosion rates of high-alloy steels decrease with increasing chromium content, while changes in nickel content have little or no effect on corrosion. Additions of aluminum to nickel–chromium steels increase corrosion rates, and titanium additions decrease corrosion rates in gallium.[9] This report presents results of scoping tests on compatibility of gallium with candidate structural materials for ITER first-wall/blanket systems, e.g., Type 316 SS, Inconel 625, and Nb-5 Mo-1 Zr alloy. Armco iron, Nickel 270, and pure chromium were also included in the study as reference materials.

Experimental Procedures

Corrosion tests were conducted in alumina capsules (≈11-mm inner diameter and 254-mm length) with a threaded metal fitting at the top end for sealing. The capsules were filled with ≈11 cm^3 (≈65 g) of gallium, capped, and sealed in a high-purity argon environment. The capsules were baked for 24 h at 425°C prior to the tests. Each capsule contained a single test specimen. An alumina rod (6.5-mm diameter and 150-mm length) was placed in each capsule to ensure that the corrosion coupon would remain immersed in gallium and to keep the specimen in place when the capsules were inverted during cooling. Corrosion coupons (≈10 x 20 x 0.4–1.1 mm) were prepared from Type 316 SS, Inconel 625, Nb-5 Mo-1 Zr alloy, Nickel 270, Armco iron, and pure chromium. The coupons were bent into a U shape to study the effect of cold work. Dimensions and weights of the specimens were recorded after degreasing and cleaning.

Corrosion tests were conducted at 300 and 400°C for times up to 3,000 h. In addition, the Type 316 SS specimens were also exposed at 200°C for up to 3,000 h. After testing, the capsules were inverted and the gallium drained from the specimens to prevent possible deposition of corrosion products on the specimen surface during cooling. Corrosion coupons were washed in a warm solution of soap and water to remove gallium. If needed, a rubber scrubber was used to scrape any gallium adhering to the surface. Specimen weight and dimensions were recorded after rinsing and drying. All specimens were examined metallographically to determine metal loss and thickness of the reaction layer. A schematic representation of the corrosion behavior is shown in Fig. 2. Metal loss for each surface was determined from the initial thickness of the corrosion coupon and sound metal remaining after the test.

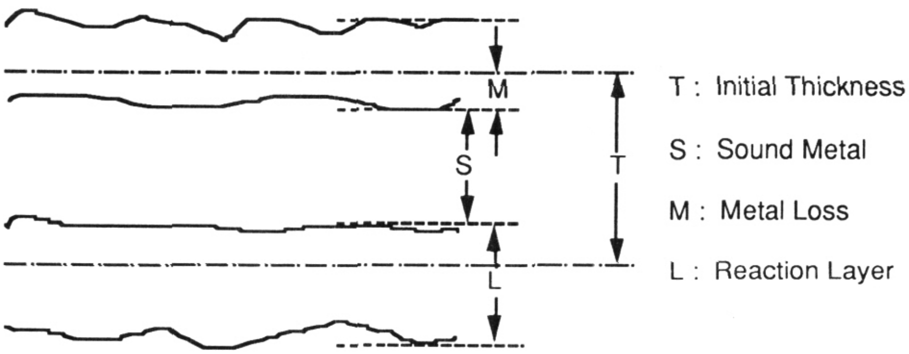

Figure 2. Schematic diagram showing typical measurements to determine corrosion behavior of materials

Results and Analysis

The corrosion test results for the various materials are given in Table 1. Nearly all corrosion coupons gained weight after exposure; only the Nb–5 Mo–1 Zr alloy exposed at 400°C for 300 and 1,076 h lost weight. The pure metals react rapidly with gallium at 400°C. An ≈0.5–mm–thick iron specimen reacted completely within 24 h, and ≈0.3–mm–thick chromium specimen disintegrated within 100 h. In contrast to earlier results,[9] pure iron shows higher corrosion than nickel. The corrosion rates at 400°C were estimated as ≥10 and 2 µm/h for Armco iron and Nickel 270, respectively. A corrosion rate for chromium cannot be estimated accurately because the chromium coupon was exposed only for 100 h (the 100–h result yielded a rate of ≥1.5 µm/h).

Armco iron shows significant corrosion even at 300°C; photomicrographs of the specimen exposed to gallium for 300 h at 300°C are shown in Fig. 3. The specimen develops a very porous and thick reaction layer that X–ray diffraction analysis reveals to be $FeGa_3$, with gallium metal present in the pores. A similar corrosion behavior is observed for Nickel 270; the reaction layer contains Ni_2Ga_3 and some $NiGa_4$ in the region in contact with gallium. Most likely, the latter formed during cooling. Metallographic examination of the reaction layers indicates that at the test temperatures, corrosion of nickel, chromium, and iron occurs entirely by dissolution accompanied by formation of metal/gallium intermetallic compounds from the saturated solution of gallium. Corrosion or dissolution can occur only with the growth of intermetallic compounds. The growth of these compounds may control the overall rate of corrosion of most metals and alloys. For nickel and iron, the reaction proceeds at the metal surface and an adherent but extremely porous reaction layer grows outward into the melt. The process continues as long as gallium can reach the reaction zone.

Table **1.** Corrosion behavior of materials exposed **with** gallium in ***sealed*** alumina capsules

Material and Specimen	Exposure Temp. (°C)	Exposure Time (h)	Before Exposure Weight (mg)	Before Exposure Thickness (mm)	Change After Exposure Weight (mg/cm^2)	Change After Exposure Thickness (µm)	Metal Loss[a] (µm)	Reaction Layer (µm)
Type 316 SS								
SS–4A	400	24	860.6	0.5405	31.2	137.8	21.3	90.2
SS–4F	400	48	854.1	0.5135	19.8	80.1	–3.0	37.1
SS–4B	400	100	900.1	0.5405	36.5	439.6	60.5	280.3
SS–4C	400	300	834.2	0.5675	362.6	980.4	130.0	620.2
SS–4E	400	1076	770.0	0.5675	394.5	1284.1	160.1	802.2
SS–3C–D	375	300	893.9	0.5135	169.3	451.8	48.3	274.2
ss–3c–c	350	**300**	931.3	0.5135	30.7	129.1	3.7	68.3
SS–3C–B	320	300	899.7	0.5135	2.1	23.2	–11.6	–
SS–3B	300	100	806.7	0.5135	2.7	22.7	–11.4	–
SS–3C–A	300	300	792.5	0.5405	0.3	–8.1	4.1	–
SS–3D	300	1008	845.5	0.5135	4.7	32.5	–7.4	8.9
SS–3E	300	3000	820.1	0.5405	8.4	27.3	9.6	23.3
SS–2C	200	300	743.2	0.5540	–	–17.9	9.0	–
SS–2D	200	1000	870.1	0.5135	–	27.7	–13.9	–
SS–2E	200	3000	742.0	0.5675	0.1	–23.0	11.5	–
SS–24C[b]	200	300	856.5	0.5540	61.5	160.4	32.8	113.0
SS–24D[b]	200	1008	928.6	0.5135	69.9	208.6	18.4	122.7
SS–24E[b]	200	3000	792.6	0.5540	59.1	176.1	34.4	122.4
Inconel 625								
IN–4A	400	24	2515.2	1.3696	17.4	23.7	–3.9	8.0
IN–4F	400	4R	2465.4	1.3825	2.9	11.6	3.8	9.6
IN–4B	400	100	2441.1	1.3825	4.1	8.9	6.6	11.0
IN–4C	400	300	2471.0	1.3696	27.9	83.3	14.3	56.0
IN–4E	400	1076	2508.0	1.3567	82.9	293.8	56.5	203.4
IN–3B	300	**100**	2114.5	1.3825	4.6	0.5	–0.3	–
IN–3C	300	300	2447.7	1.3825	0.0	–0.5	0.3	–
IN–3D	300	1008	2443.3	1.3825	1.8	–17.5	8.8	–
IN–3E	300	3000	2427.8	1.3825	1.0	11.5	–5.8	–
Nb–5 Mo–1 Zr Alloy								
NB–4F	400	24	1560.7	0.8602	**1.0**	10.6	**5.3**	–
NB–4B	400	**100**	1750.2	0.8602	3.9	–2.4	–1.2	–
NB–4C	400	300	1746.2	0.8736	–0.1	6.3	3.2	–
NB–4E	400	1076	1704.7	0.8602	–5.1	7.1	3.6	–
NB–3B	300	100	1550.7	0.8602	0.8	–5.8	2.9	–
NB–3C	300	300	1701.7	0.8602	3.1	1.8	–0.9	–
NB–3D	300	1008	1714.2	0.8602	1.2	–0.2	0.1	–
NB–3E	300	3000	1874.7	0.8602	0.6	12.4	–6.2	–
Armco Iron								
FE–4F	400	24	744.1	0.4594	reacted completely to form $FeGa_3$			
FE–3B	300	100	765.0	0.4594	150.9	406.4	47.1	250.3
FE–3C	300	300	758.2	0.4594	346.4	1167.9	129.5	713.5
FE–3D	300	1008	785.5	0.4594	reacted completely to form $FeGa_3$			
Nickel 270								
NI–4B	400	**100**	1320.3	0.7155	277.1	925.3	201.2	663.9
Pure Chromium								
CR–4B	400	100	488.6	0.2921	disintegrated completely into $CrGa_4$ crystals			

---

[a] Negative value represent an increase in thickness. Accuracy of measurements ±10 µm.

[b] Specimens exposed **at** 400°C for 24 h to ensure complete wetting prior to **the** exposure at 200°C

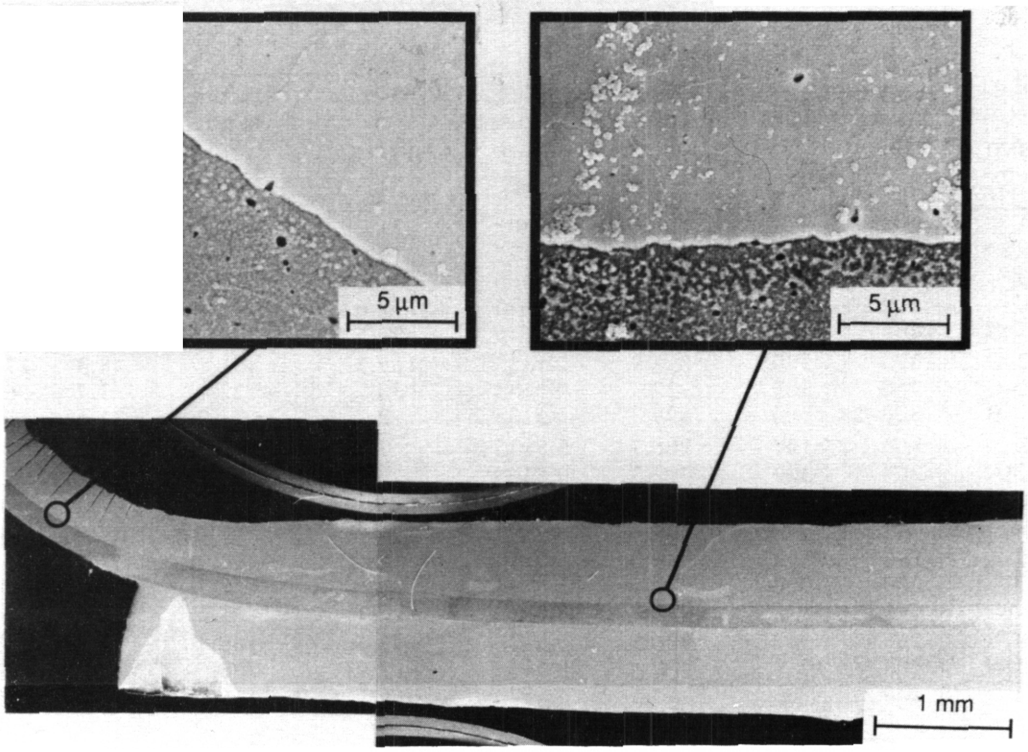

Figure 3. Cross section of Armco iron exposed to gallium at 300°C for 300 h

A somewhat different behavior is observed for chromium metal: the specimen disintegrated into small crystals. The crystals were identified as $CrGa_4$ by X–ray diffraction analyses. This indicates that the mechanism for corrosion of chromium is basically the same as that for nickel or iron, with the only difference that the $CrGa_4$ phase in equilibrium with the saturated solution of gallium does not adhere to the metal surface.

Type 316 SS and Inconel 625 specimens show significant corrosion at 400°C and little or no corrosion at 300°C. Once again, the iron–base Type 316 SS shows greater corrosion than did the nickel–base Inconel 625 alloy. At 400°C, the corrosion rate of Type 316 SS is nearly one order of magnitude greater than that of Inconel 625. The Nb–5 Mo–1 Zr alloy showed no measurable corrosion at 300 or 400°C. Metal loss for the various alloys and pure metals exposed to gallium at 300°C and 400°C is plotted as a function of time in Fig. 4. Only approximate values of corrosion rates could be obtained for the various alloys exposed at 300°C; long–term corrosion data are needed for accurate estimates of corrosion rates.

In most cases, metal loss increases linearly with time, and the corrosion rates may be represented by a single value. Corrosion rates for Type 316 SS exposed at 400°C, however, decrease with time. This behavior may be attributed to changes in the experimental conditions within the capsule. As discussed above. corrosion may slow or stop completely when the intermetallic compounds form. This may happen in several ways because of the limited quantity of gallium used in the experiments and also because of space restrictions. For example, corrosion on the inner surface of the U–shaped coupon will stop when the space between the two sides of the specimen fills with reaction layer. This behavior was observed for the Type 316 specimen exposed at 400°C for 1076 h. Consequently, only values of metal loss up to 300 h were used to determine the corrosion rate of Type 316 SS at 400°C. Short–term corrosion tests (300 h) were

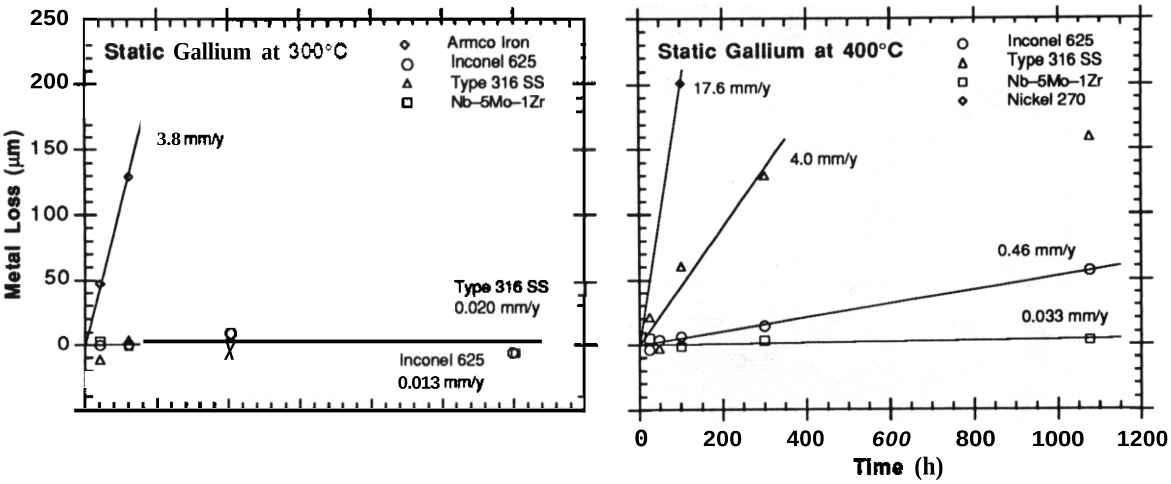

Figure 4. Metal loss for candidate structural alloys and pure metals exposed to gallium at 300 and 4009:

conducted at 375.350, and 320°C to better establish the temperature dependence of the corrosion rate of Type 316 SS. The results show excellent agreement with 3 W h tests at 400 and 300°C.

Photomicrographs of cross sections of Type 316 SS, Inconel 625, and Nb-5 Mo–1 Zr alloy exposed to gallium at 400°C are shown in Figs. 5-7. Type 316 SS and Inconel 625 develop a thick and porous reaction layer similar to those of pure iron or nickel specimens. The Nb-5 Mo–1 Zr alloy shows little or no reaction with gallium. The reaction layer on Type 316 SS consists primarily of $FeGa_3$ and gallium and also some $CrGa_4$ in the region next to the steel surface; nickel–gallium compounds were not detected. The reaction layer on Inconel 625 contains $CrGa_4$ and gallium across the entire thickness, and also Ni_2Ga_3 in the region next to the steel surface. The overall corrosion rate of these alloys is most likely controlled by the rate of formation of these compounds. Corrosion rates of the alloys are lower than those of pure metals because of differences in the morphology of reaction layer and/or differences in the rate of formation of these multicomponent compounds. Microprobe and X–ray diffraction analyses of the specimens are in progress to establish the mechanism of corrosion.

The results also indicate that cold work has no effect on corrosion of Type 316 SS and Inconel 625. However, cold–worked (i.e., bent) regions of Nb–5 Mo–1 Zr alloy show some corrosive attack at 400°C (Fig. 7). Entire grains seem to have broken from the surface. These are the only specimens that showed weight loss after exposure. Metallographic examination of the specimens indicate that weight loss is due to corrosive attack in cold–worked regions of the specimen.

An Arrhenius plot of the corrosion rates of various metals and alloys is shown in Fig. 8. In all cases, linear metal–loss behavior was assumed to determine the corrosion rates. These values may represent a conservative estimate of corrosion. Results for high–alloy steels Kh18N9T (Fe–18 Cr–9 Ni-0.6 Ti) and KhN77TYu (Ni–21 Cr–2.6 Ti-0.8 Al) exposed to gallium under dynamic conditions (0.15 m/s flow velocity) at 250 and 4 W C are also included in the figure? Corrosion rates of Inconel 625 and Type 316 SS at 400°C are comparable to those of Kh18N9T and KhN77TYu but show lower values at 250°C. The differences are most likely due to velocity effects.

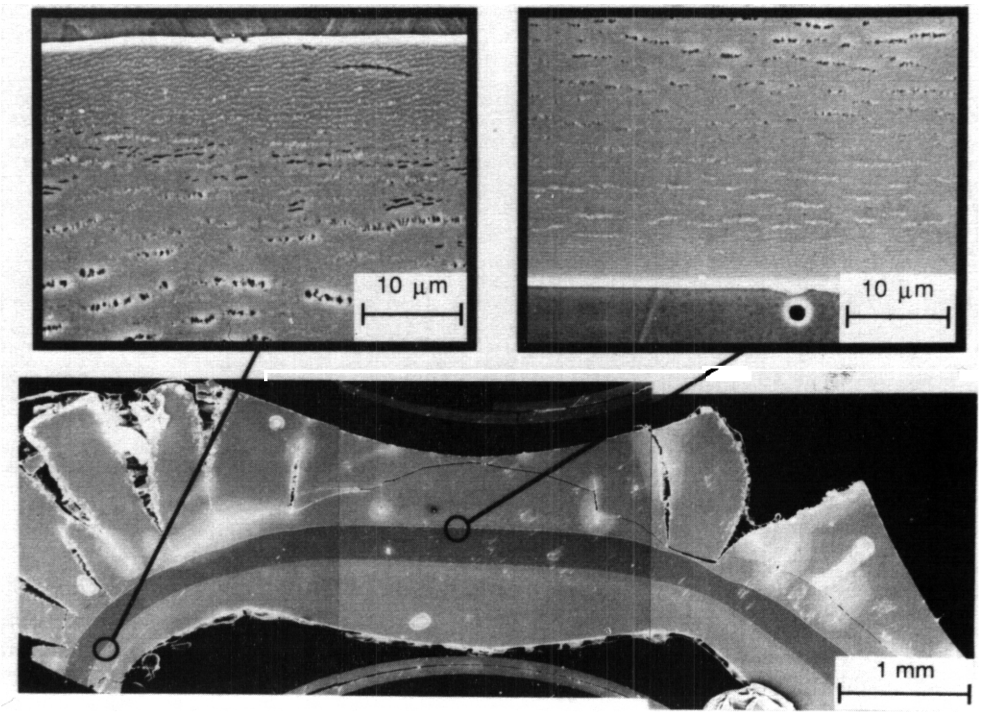

Figure 5. Cross section of Type 316 stainless steel exposed to gallium at 400°C for 300 h

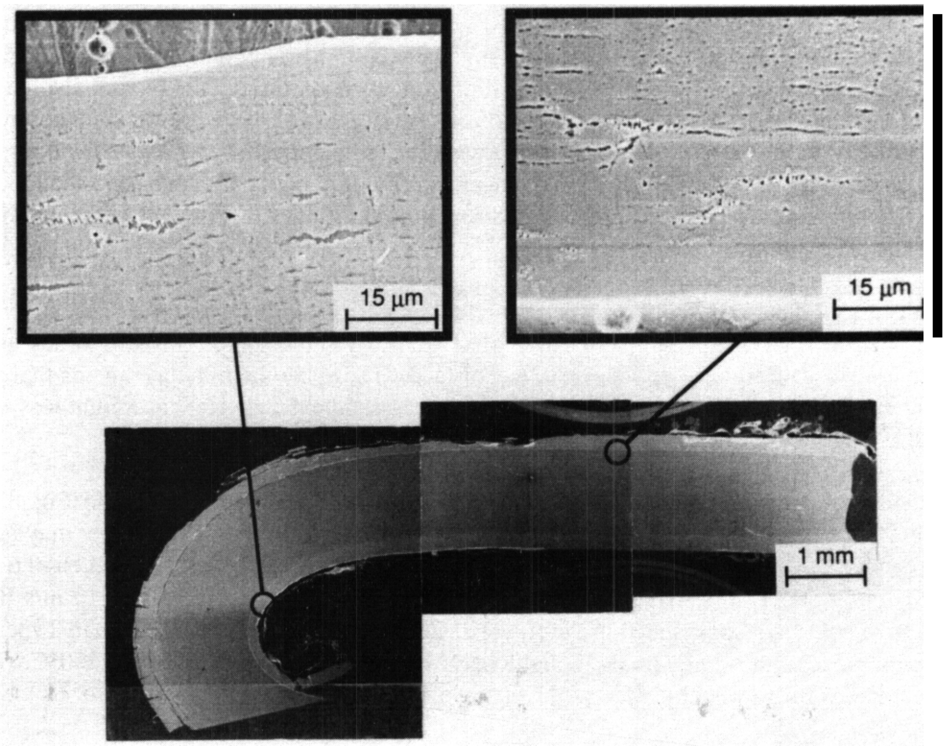

Figure 6. Cross section of Inconel 625 exposed to gallium at 400°C for 1076 h

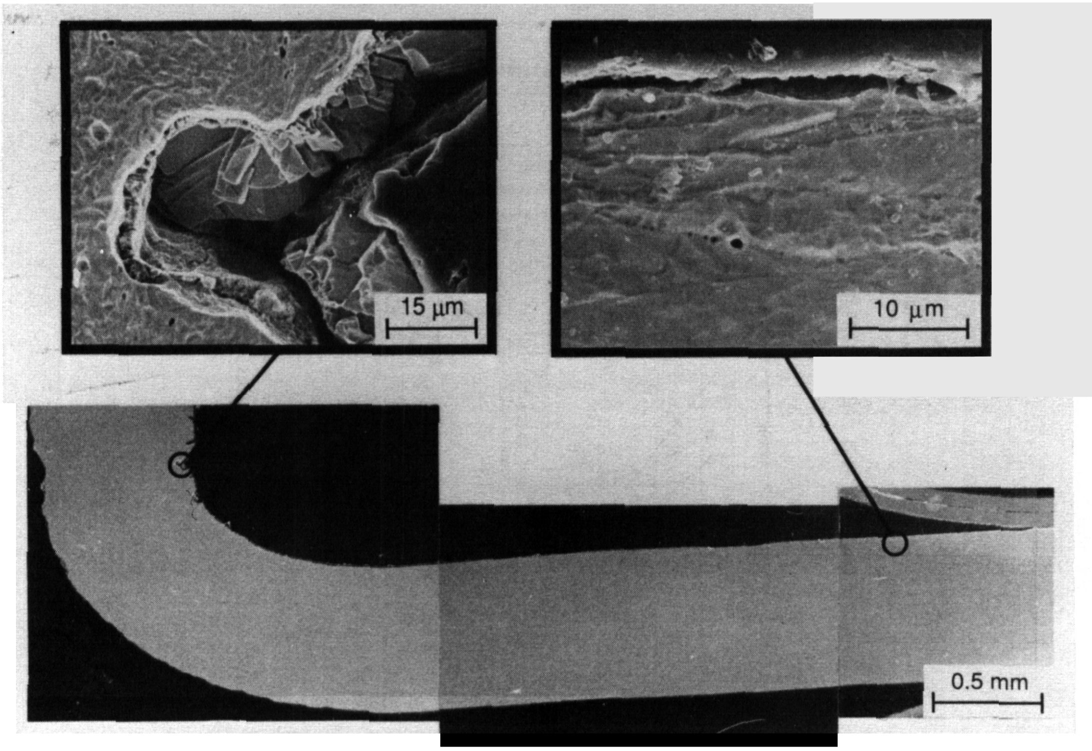

Figure 7. Cross section of Nb–5 Mo–1 Zr alloy exposed to gallium at 400°C for 1076 h

Figure 8 can be used to establish the maximum temperature limit for gallium/structural alloy systems. A maximum corrosion rate is first defined on the basis of either the allowable change in section thickness of the component or allowable mass transfer in the liquid metal system. The maximum operating temperature corresponding to the maximum corrosion rate is then obtained from Fig. 8 for a specific alloy/gallium system. For example, the maximum surface temperature of a Type 316 SS component must be <350°C to keep the conusion rates below 250 µm/y. The niobium alloy can operate at higher temperatures for the Same corrosion criterion. It should be noted that Fig. 8 does not include the effects of system variables such as velocity and AT on corrosion mass transfer.

CONCLUSIONS

Scoping tests have been conducted on the compatibility of gallium with candidate structural materials, e.g., Type 316 SS, Inconel 625, and Nb-5 Mo-1 Zr alloy, as well as Armco iron, Nickel 270, and pure chromium. The pure metals react rapidly with gallium. In contrast to earlier studies, pure iron shows greater corrosion than does nickel. The corrosion rates for Armco iron and Nickel 270 at 400°C are ≥90 and 17 mm/y, respectively. The results indicate that at temperatures up to 400°C. corrosion occurs primarily by dissolution accompanied by formation of metal/gallium intermetallic compounds. The growth of intermetallic compounds may control the overall rate of corrosion. Corrosion of iron–base Type 316 SS is greater than that of nickel–base Inconel 625. The Nt-5 Mo–1 Zr alloy is most resistant to corrosion in static gallium. At 400°C, corrosion rates are ≈4.0, 0.5, and 0.03 mm/y for Type 316 SS, Inconel 625, and Nb-5 Mo-1 Zr alloy, respectively.

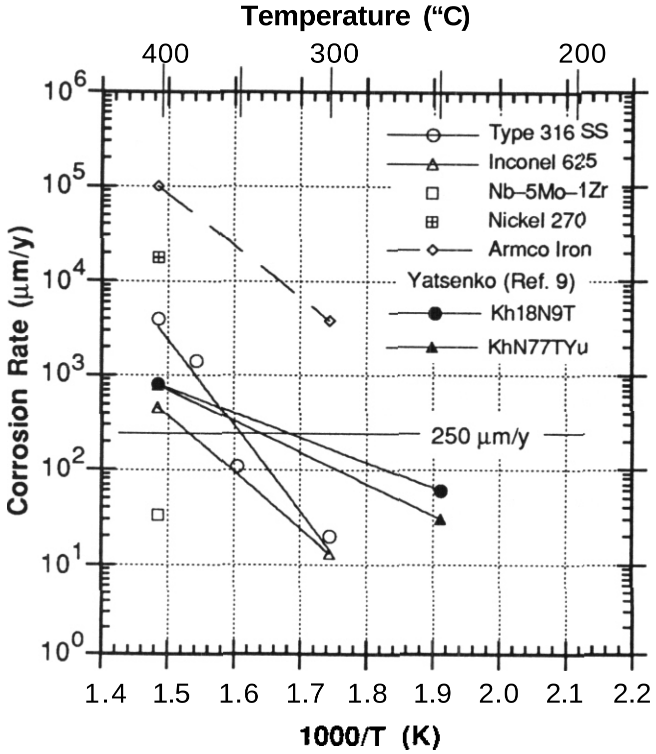

Figure 8. Corrosion rates of candidate alloys and pure metals in gallium

FUTURE WORK

Compatibility tests are in progress on preoxidized Type 316 SS specimens. Tests are also planned in an oxidizing environment to study the stability of oxide coatings in gallium.

ACKNOWLEDGMENTS

The authors thank C. Reed and P. Dombrowski for experimental contributions, B. Tani for performing X–ray diffraction analyses, and T. F. Kassner for helpful discussions.

REFERENCES

1. W. D. Wilkinson, *Effects of Gallium on Materials at Elevated Temperatures.* Argonne National Laboratory Report ANL–5027 (August 1953).

2. W. D. Wilkinson, *Effects of Gallium on Materials at Elevated Temperatures Supplementary Report,* Argonne National Laboratory Report ANL–4582 (August 1953).

3. L. R. Kelman, W. D. Wilkinson, and F. L. Yaggee, *Resistance of Materials to Attack by Liquid Metals*, Argonne National Laboratory Report ANI4417 (July 1950).

4. S. P. Yatsenko and Y. A. Anikin, *Solubility of Metals of the Fifth Period in Liquid Gallium.* Sov. Mat Sci., **6,** 333–337 (1970).

5. S. P. Yatsenko and Y. A. Anikin, *Solubility of Group IV Metals in Liquid Gallium,* Russ. Metall., **4,** 118–123 (1970).

6. S. P. Yatsenko, L. N. Rykova, Y. A. Anikin, and E. N. Dieva, *The Corrosion of Group VIII Metals in Liquid Gallium,* Sov. Mat. Sci., **8,** 310-313 (1972).

7. S. P. Yatsenko, *Correlation of Physical Properties of Pure Solid Metals with Their Resistance to Corrosion by Liquid B Metal,* Russ. J. Phy. Chem., **45,** (8). 1095–1098 (1971).

8. C. Guminski, *Solubility of Metals in Liquid Low-Melting Metals,* Z. Metallkd., **81,** (2), 105–110 (1990).

9. S. P. Yatsenko, *Gallium Interaction With Metals,* Nauka, Moscow (1974).

AQUEOUS STRESS CORROSION OF CANDIDATE AUSTENITIC STEELS FOR ITER STRUCTURAL APPLICATIONS[*]

– W. K. Soppet, D. M. French, and T. F. Kassner
(Argonne National Laboratory)

OBJECTIVE

Austenitic stainless steels are being considered as a structural material for first–wall/blanket systems in the International Thermonuclear Experimental Reactor (ITER).[1] Information on stress corrosion cracking (SCC) susceptibility of several candidate stainless steels under ITER-relevant conditions will help to identify an optimal combination of structural material, coolant chemistry, and operational conditions for ongoing ITER design work. The objective of this task is to provide baseline information on SCC susceptibility of candidate stainless steels in oxygenated water that simulates many important parameters anticipated in ITER first–wall/blanket systems. SCC tests will also be conducted under off–normal water chemistry conditions and at higher temperatures to establish the performance limits of the materials.

SUMMARY

Susceptibility of crevice–weldment specimens of Types 316L and 316NG stainless steel (SS) to SCC was investigated in slow–strain–rate–tensile (SSRT) tests in water that simulates important parameters anticipated in first–wall/blanket systems. The SSRT tests were performed in oxygenated water containing 0.06–10 ppm chloride at temperatures of 95 to 225°C to establish the effects of water purity and temperature on SCC resistance. These steels, including weldments, exhibit good resistance to SCC under crevice conditions at temperatures of <150°C in water containing ≤0.1 ppm chloride. It appears that Type 316NG SS is somewhat more resistant to SCC than Type 316L SS at temperatures >150°C in oxygenated water containing 0.1–10 ppm chloride. Most specimens fractured in the base metal, and several others fractured in the heat–affected zone (HAZ) of the weld, but none failed in the weld metal.

PROGRESS AND STATUS

The research and development needs[2] of the ITER with respect to aqueous corrosion include establishing a reliable data base on reference materials (viz., Types 316, 316L, and 316NG SS in the solution-annealed, cold–worked, and welded conditions). A nominal ITER water chemistry would most likely be high-purity water containing stable radiolysis/electrolysis products, e.g., dissolved O_2, H_2O_2, and H_2 at ppm levels, and ionic species at ppb levels, namely, soluble corrosion products and impurities in the makeup water and from release by ion–exchange resins in water purification systems. Higher concentrations of ionic impurities (e.g., Cl^-, SO_4^{2-}, H^+, etc.) in the coolant may be present during off–normal operating and extended lay–up conditions of the system.

Previous work[3,4] focused on developing criteria to define the simulated ITER water chemistry and establishing experimental methods for SSRT tests on noncrevice and crevice specimens. Results from experiments to evaluate SCC susceptibility from SSRT tests on Types 316NG, 316, and 304 SS have been reported previously.[5–10] No indication of SCC was observed in tests on noncrevice specimens of Type 316NG SS[8] in oxygenated water containing 0.1-1.0 ppm SO_4^{2-} at temperatures of 95 and 150°C and a strain rate of $3 \times 10^{-7}\ s^{-1}$. Crevice specimens were also resistant to SCC in oxygenated water containing 0.1 ppm SO_4^{2-} at temperatures ≤150°C.[9] Predominantly ductile fracture (with a minor amount of transgranular cracking, TGSCC) was observed in crevice specimens of Type 316NG SS at higher temperatures. Intergranular failure occurred in Type 304 SS crevice specimens heat treated to yield sensitization values of 2 and 20 $C \cdot cm^{-2}$ by electrochemical potentiokinetic reactivation.[8,9] Initial tests on

---

[*] Work supported by the U.S. Department of Energy, under Contract W-31-109-Eng-38.

temperatures. Intergranular failure occurred in Type 304 SS crevice specimens heat treated to yield sensitization values of 2 and 20 C·cm^{-2} by electrochemical potentiokinetic reactivation.[8,9] Initial tests on weldment specimens of Type 316L SS with matching filler metal, under crevice conditions in oxygenated water containing 0.06–6.0 ppm chloride at 150–225°C, revealed that most specimens fractured in the base metal and that several others fractured in the HAZ of the weld, but that none failed in the weld metal.[10] In this report, results from SSRT tests at 95 and 225°C on crevice–weldment specimens of Type 316NG SS in air and in water containing O_2, H_2O_2, and Cl^- are compared with similar data on weldment specimens of Type 316L SS.

Experimental Procedures

Cylindrical tensile specimens with a 6.35 mm diameter and a 36.0 mm gage length were fabricated from Types 316NG and 316L SS. The chemical composition of the materials used in these experiments is given in Table 1. The experimental methods have been described in previous papers.[6,8–10] Crevice–weldment specimens were created by drilling three small-diameter (≈0.8-0.9 mm) through holes in the gage section of the specimens. i.e., in the base metal, the HAZ of the weld (edge of the hole =1–2 mm from the fusion line), and in the weld metal, and placing austenitic SS pins in the holes to form tight crevices (Fig. 1). The location of the hole in the HAZ was selected on the basis of experimental measurements and model predictions of variations in degree of sensitization across this region in welds of 24–in.–diameter Type 304 and 316 SS pipe.[11] This location corresponds to maximum sensitization (i.e., Cr depletion and carbide precipitation at grain boundaries). Although sensitization does not occur in low–C grades of Types 316NG and 316L SS, this location may be synonymous with other thermal segregation processes involving alloying elements and impurities in the steel. The weldment specimens were tested in the as–received condition without any heat treatment. Tests were carried to failure at strain rates of 1×10^{-5} s^{-1} in air and 3×10^{-7} s^{-1} in water in small-diameter autoclaves with a once-through water system.

Water chemistry was established by bubbling a 20% O_2-80% N_2 gas mixture through deoxygenated/deionized feedwater (conductivity <0.2 μS·cm^{-1}) contained in a 130-liter SS tank to produce a dissolved-oxygen concentration of ≈8.0 ppm. H_2O_2 (5.0 to 8.0 ppm) and NaCl (0.06 to 10.0 ppm Cl^-) were added to the feedwater before sparging with the gas mixture to ensure adequate mixing. An external 0.1M KCl/AgCl/Ag reference electrode, a thermocouple, and Pt and Type 3W SS electrodes were located at the autoclave outlet to establish redox and open-circuit potential, respectively. The electrochemical potentials measured during the experiments were converted to the standard hydrogen electrode (SHE) scale by using thermocell and liquid-junction potentials.[12]

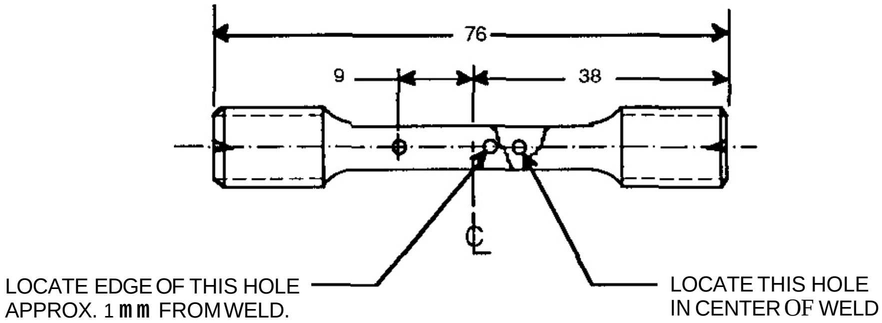

Figure 1. Weld specimen fabricated from gas–metal–arc–welded plate of Type 316L SS with matching filler metal. Crevices were formed by inserting tight–fitting SS pins into the holes.

The tests provide information on time-to-failure, total strain, maximum *stress*, and appearance of fracture surfaces. The load applied to each specimen was recorded continuously as a function of time, and an engineering-stress-versus-strain curve was produced for each specimen. Total elongation and reduction in area were determined from measurements on the fractured specimens. The fracture surfaces were examined by both optical microscopy and scanning electron microscopy (SEM) to determine the fractions of reduced cross-sectional areas with ductile, transgranular, and intergranular morphologies.[13]

Results and Analysis

Cracking susceptibility can be assessed from various parameters. Total elongation, reduction in area, and maximum stress are often used, as are fracture surface morphology and maximum crack length (either on the fracture surface or on the sectioned surface after test interruption). Because of the high SCC resistance of Type 316NG SS relative to that of sensitized Type 304 SS, it is difficult to quantify SCC behavior of Type 316NG SS in terms of crack growth rate[14] from SSRT test results. An alternative, employed here, is evaluation of SCC susceptibility in terms of the ratio of the strain at failure (e_{env}/e_{air}) from companion tests on identical specimens in water and in air. Values of the strain ratio <1.0 indicate environmentally assisted cracking.

Results of SSRT tests at temperatures of 60 to 289°C on crevice and noncrevice specimens of Types 316NG and 304 SS were presented previously.[6,8–10] The SSRT results in Tables 2 and 3 were obtained from the engineering–stress (based on a cross–sectional area without subtracting the area associated with the hole) versus engineering–strain curves in air and water on identical specimens. Although the air tests were performed at a higher strain rate (e.g., 1 x 10^{-5} s^{-1}), the yield and ultimate strengths, total elongation, reduction in area, and fracture morphology can be compared in the two environments to assess SCC susceptibility. Because the tests were performed at two strain rates, time–to–failure is not a useful parameter. Total elongation at failure appears to be the most promising measure of SCC susceptibility. Consequently, the data in Tables 2 and 3 were analyzed on the basis of a strain–ratio parameter, namely, $S_r = e_{env}/e_{air}$ at failure for identical specimen geometries. The strain ratios as a function of temperature and chloride concentration in oxygenated water are given in Tables 4 and 5 for Types 316L and 316NG SS, respectively.

It is well known that chloride concentration in oxygenated water significantly affects SCC and pitting of austenitic stainless steels.[15–21] Most available SCC data pertain to standard–grade steels (e.g., Types 316 and 304 in the sensitized and solution–annealed conditions) under noncrevice conditions. As temperature and chloride and/or dissolved–oxygen concentration in the water increase, these steels become susceptible to SCC, particularly in the sensitized condition. Types 316L and 316NG SS, both with low C content and the latter with a controlled N content (0.06–0.10%), are expected to be more resistant to SCC in oxygenated water containing low levels of chloride.

The effects of chloride concentration and temperature on the strain ratio at failure from SSRT tests on crevice–weldment specimens of Types 316L and 316NG SS are shown in Figs. 2 and 3. The results indicate that low–C–content Types 316L and 316NG SS are susceptible to TGSCC under crevice conditions in high–temperature oxygenated water containing chloride at low concentrations (<10 ppm). The curves in Fig. 2 indicate that as the temperature increases (from 95 to 225°C), the critical chloride concentration in water for the onset of SCC (a strain ratio of <1.0) is <0.1 ppm. The actual values at temperatures >150°C for Type 316L SS can only be approximated from the results in Fig. 2. However, for chloride concentrations >0.6 ppm in the bulk water, SCC is significant, as indicated by values of the strain ratio between ≈0.3 and 0.7. The curves for Type 316NG SS at 95 and 225°C reveal that this material is somewhat more resistant to SCC, e.g., at 225°C. the strain ratios are between ≈0.9 and 0.6, in contrast to between ≈0.5 and 0.3 for Type 316L SS. Strain ratios for Type 316NG SS were ≈1.0 at 95°C, which is indicative of no SCC in these environments. Figure 3 also illustrates the marked effect of temperature on SCC of the steels.

Table 1. Composition of austenitic stainless steels (wt.%)

Alloy	Heat No.	Cr	Ni	Mo	Mn	Si	Cu	N	C	P	S	Fe
316NG	NDE–28	17.79	13.58	2.59	1.77	0.52	0.10	0.110	0.014	0.020	0.002	Bal
316L	16650	16.50	10.39	2.09	1.78	0.43	0.19	0.054	0.018	0.026	0.013	Bal
316L[a]	4H3367	18.69	12.29	b	1.98	0.63	0.25	b	0.018	0.023	0.018	Bal

[a] Type 316L SS filler metal for weld specimens of Heat 16650.

[b] Not analyzed.

Table 2. SCC susceptibility of Type 316NG SS crevice–weldment specimens[a] strained to failure

			Strain	Feedwater Chemistry[b]					SSRT Parameters							Potentials	
Test	Heat	Temp.	Rate	H_2O_2	O_2	Cl^-	Cond.	pH at	Fail. Time	Yield Stress	Max. Stress	Total Elong.	Reduct. in Area	Failure Region[c]	Fracture	304 SS	Pt
100	NDE 28	95	1×10^{-5}	air test					5.0	339	567	18.1	72	B	1.0 D	—	—
101	NDE 28	95	3×10^{-7}	5.0	8.0	0.1	1.4	6.2	162	329	563	16.8	72	B	1.0 D	433	396
102	NDE 28	95	3×10^{-7}	5.0	8.5	1.0	4.2	6.3	172	348	570	18.3	69	B	1.0 D[d]	443	389
103	NDE 28	95	3×10^{-7}	5.0	8.0	10.0	34.5	6.5	171	327	568	18.1	54	HAZ	0.7 D, 0.3T	414	389
104	NDE 28	225	3×10^{-7}	5.5	8.0	0.1	0.9	6.2	139	260	497	14.9	63	B	1.0 D	290	305
105	NDE 28	225	3×10^{-7}	6.0	8.0	1.0	4.0	6.3	101	266	458	11.6	55	B	0.7 D, 0.3 T	295	320
106	NDE 28	225	3×10^{-7}	6.0	8.0	10.0	35.9	6.2	68	296	411	10.0	44	B	0.5 D, 0.5 T	273	325

[a] Crevice SSRT specimen from a gas–metal–arc weldment of Type 316NG SS 28–in.–diameter pipe (Heat No. NDE 28).

[b] Conductivity and pH were adjusted by addition of 0.1, 1.0, or 10.0 ppm Cl^- as NaCl.

[c] Specimen failed in the base metal (B), in the heat affected zone (HAZ), or in the weld (W).

[d] Specimen failed in the base metal but a crack was present in the HAZ.

Table 3. SCC susceptibility of Type 316L crevice–weldment specimens[a] strained to failure

			Strain	Feedwater Chemistry[b]					Fail.	Yield	Max.	Total	Reduct.	Failure		Potentials	
Test No.	Heat No.	Temp. (°C)	Rate (s^{-1})	H_2O_2 (ppm)	O_2 (ppm)	Cl^- (ppm)	Cond. ($\mu S \cdot cm^{-1}$)	pH at 25°C	Time (h)	Stress (MPa)	Stress (MPa)	Elong. (%)	in Area (%)	Region[c]	Fracture Morphology	304 SS (mV[SHE])	Pt
80	16650	150	1×10^{-5}	air test					4.4	296	497	15.7	66	B	1.0 D	—	—
82	16650	150	3×10^{-7}	7.0	8.0	0.06	1.5	6.01	152	281	498	16.2	65	B	0.9 D, 0.1 T	359	331
87	16650	150	3×10^{-7}	7.0	8.0	0.6	3.4	6.06	97	280	439	10.6	61	B	0.8 D, 0.2 T	359	367
83	16650	150	3×10^{-7}	7.0	8.0	6.0	23.0	5.95	96	291	456	10.4	52	HAZ	0.8 D, 0.2 T	—	—
84	16650	175	1×10^{-5}	air test					4.5	292	493	16.1	67	B	1.0 D	—	—
86	16650	175	3×10^{-7}	8.0	8.0	0.06	2.1	6.05	141	279	494	14.3	66	B	0.9 D, 0.1 T	333	349
85	16650	175	3×10^{-7}	6.0	8.0	0.6	3.6	5.80	89	281	434	9.2	52	B	0.8 D, 0.2 T	346	384
88	16650	200	1×10^{-5}	air test					4.4	279	485	16.1	65	B	1.0 D	—	—
90	16650	200	3×10^{-7}	8.0	8.0	0.06	2.0	6.17	>80	276	>431	>6	d	d		246	246
89	16650	200	3×10^{-7}	7.0	8.0	0.6	3.6	5.60	70	275	402	7.5	53	B	0.8 D, 0.2 T	280	287
91	16650	200	3×10^{-7}	8.0	8.0	6.0	21.6	6.02	61	247	338	6.6	39	HAZ	0.9 D, 0.1 T	295	346
92	16650	225	1×10^{-5}	air test					4.6	284	486	16.7	68	B	1.0 D	—	—
94	16650	225	3×10^{-7}	8.0	9.0	0.06	1.8	5.92	89	262	429	9.5	61	B	0.7 D, 0.3 T	284	307
93	16650	225	3×10^{-7}	8.0	8.0	0.6	4.0	5.86	58	270	388	5.9	54	B	0.6 D, 0.4 T	e	e

[a] Crevice SSRT specimen from a gas–metal–arc weldment of Type 316L SS plate (Heat No. 16650) and filler metal (Heat No. 4H3367).

[b] Conductivity and pH were adjusted by addition of 0.06, 0.6, or 6.0 ppm Cl^- as NaCl.

[c] Specimen failed in the base metal (B), in the heat affected zone (HAZ), or in the weld (W).

[d] Specimen did not fracture; test was terminated because of an equipment problem.

[e] Reference electrode failed; no values were measured.

Table 4. Influence of temperature on SCC susceptibility of Type 316L SS crevice-weldment specimens[a] in oxygenated water conraining various chloride concenrrarions. based on strain raiio ($\varepsilon_{env}/\varepsilon_{air}$) atfailure

Tcsi No.	Tcmp. (°C)	Cl^- (ppm)	Strain Ratio	Tcsi No.	Tcrnp. (°C)	Cl^- (ppm)	**Strain** Ratio
82/80	150	0.06	1.03	90/88	200	0.06	>0.4
87/80	150	0.6	0.68	89/88	200	0.6	0.47
83/80	150	6.0	0.66	91/88	200	6.0	0.41
86/84	175	0.06	0.89	94192	225	0.06	0.57
85/84	175	0.6	0.57	93/92	225	0.6	0.35

[a] Crevice SSKT **spcciincns** from a gas-metal-arc weldment of Type 316L SS plate (Heat **No.** 16650) and filler metal (Heat No. 4H3367).

Table 5. influence of temperature on SCC susceptibility of Type 316NG SS crevice-weldmeni specimens[a] in oxygenated water containing various chloride concenrrarions. based on sirain ratio ($\varepsilon_{env}/\varepsilon_{air}$) atfailure

Test No.	Tcmp. (°C)	Cl^- (ppm)	Strain Ratio	Test No.	Temp. (°C)	Cl^- (ppm)	Strain Ratio
101/100	95	0.1	0.93	104192	225	0.1	0.89
102/100	95	1.0	1.01	105/92	225	1.0	0.70
103/100	95	10.0	1.00	106192	225	10.0	0.60

[a] Crevice SSKT **spccimcns** from a weldment in a 28-in.-diameter Type 316NG SS pipe (Heat No. NDE 28).

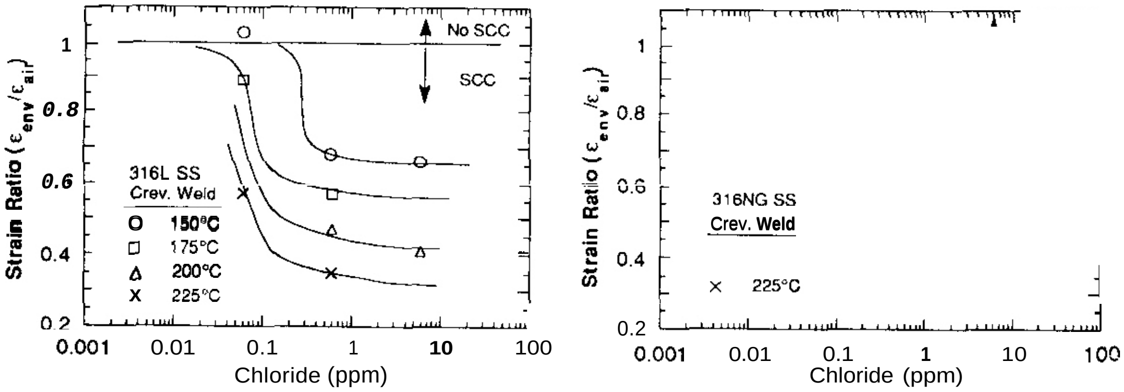

Figure 2. *Strain raiio atfailure vs. chloride concenrrarion in oxygenated waferat several temperatures for SSRT crevice-weldmenr specimens of Type 316L SS and Type 316NG SS*

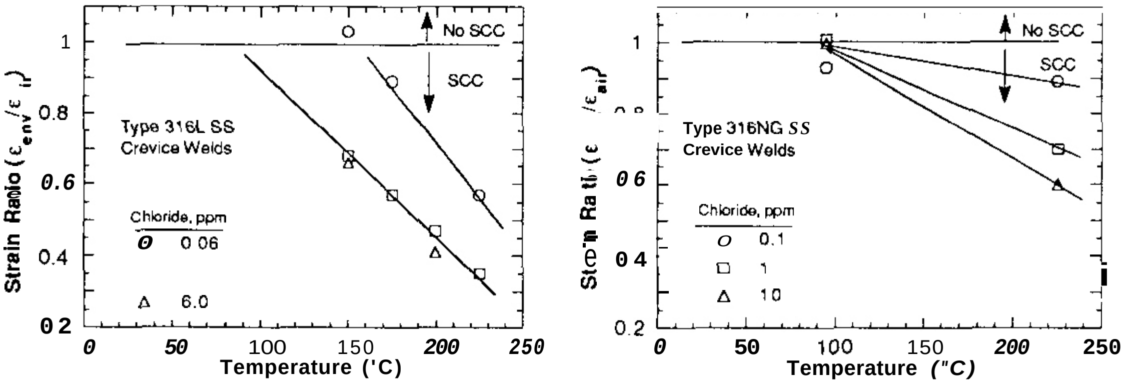

Figure 3. Strain ratio at failure vs. temperature for SSRT crevice-weldment specimens of Types 316L and 316NG SS in oxygenated water containing 0.06–10 ppm chloride

As indicated in Tables 2 and 3, most of the specimens failed in the base metal and three specimens failed in the HAZ of the weld, but no failures occurred in the weld metal. Fracture surfaces of the specimens have been examined by SEM to determine the mode of cracking and to establish whether the cracks initiated in the crevice as expected. Photomicrographs showed that the extent of TGSCC increased with temperature at a constant chloride level in the water and with chloride concentration at a constant temperature.

CONCLUSIONS

Types 316L and 316NG SS crevice–weldment specimens exhibit good resistance to SCC in SSRT tests in oxygenated water containing ≤ 0.1 ppm Cl^- at temperatures ≤ 150°C. This environment is representative of a nominal coolant chemistry for an ITER first wall/blanket system, except for short–lived radical species from radiolysis of water. Most of the Types 316L and 316NG SS crevice–weldment specimens fractured in the base metal rather than in the HAZ of the weld or in the weld metal. From the present results, it appears that the purity of bulk coolant water (e.g., Cl^- and SO_4^{2-} concentrations) will have to be maintained to a high standard to mitigate SCC of low–C grades of austenitic SSs, particularly at temperatures of >150°C. Present guidelines for the design and operation of water purification systems for light–water–cooled fission reactors can be employed to ensure that impurity levels in an ITER coolant are maintained at levels that will limit corrosion and SCC of system materials.

FUTURE WORK

Additional SSRT tests will be conducted on crevice–weldment specimens of Type 316NG SS in water containing dissolved O_2, H_2O_2, and Cl^- to define the critical chloride concentration in oxygenated water that is required for the onset of SCC. These data, when coupled with the present results, will be used to determine the regime of temperature and chloride concentration at which these materials are resistant to SCC under crevice conditions, and thereby establish the margin of performance of the material under off–normal or poor lay–up water chemistry conditions at temperatures of 95 to 225°C.

REFERENCES

1. R. W. Conn, V. A. Chuyanov, N. Inoue, and D. R. Sweetman, *The International Thermonuclear Experimental Reactor*, Scientific American, *226* (4) 1992.

2. D. L. Smith, *Aqueous Corrosion Task for ITER R&D*, U.S. Coordination Meeting, Argonne National Laboratory, August 6, 1990.

3. H. G. Khalak, *Computer Simulation of Water Coolant Chemistry in a Fusion Reactor.* Proc. 3rd National Conf. on Undergraduate Research, April 27-29, 1989, University of North Carolina, Asheville, p. 287.

4. H. Khalak, A. B. Hull, and T. F. Kassner, *Aqueous Stress Corrosion of Austenitic Steels*, 6th Fusion Reactor Materials Semiannual Progress Report for Period Ending March 31, 1989, DOE/ER-0313/6, Oak Ridge National Laboratory, p. 379.

5. A. Patel, A. B. Hull, and T. F. Kassner, *Aqueous Stress Corrosion of Structural Materials*, 7th Fusion Reactor Materials Semiannual Progress Report for Period Ending September 30, 1989, DOE/ER-0313/7, Oak Ridge National Laboratory. p. 250.

6. A. B. Hull, M. R. Fox, J. W. Pascoe, and T. F. Kassner, *Environmental Effects on Aqueous Stress Corrosion of Candidate Austenitic Steels for ITER Structural Applications*, 9th Fusion Reactor Materials Semiannual Progress Report for Period Ending September 30, 1990, DOE/ER-0313/9, Oak Ridge National Laboratory, p. 228.

7. A. B. Hull and T. F. Kassner, *Aqueous Stress Corrosion of Candidate Austenitic Steels for ITER Structural Applications*, 10th Fusion Reactor Materials Semiannual Progress Report for Period Ending March 31, 1991, DOE/ER-0313/10, Oak Ridge National Laboratory, p. 241.

8. M. R. Fox, A. B. Hull. and T. F. Kassner, *Stress Corrosion Cracking of Candidate Structural Materials under Simulated First-Wall/Aqueous Coolant Environments*, Fusion Technol.. **19**, 1619–1628 (1991).

9. A. B. Hull, P. R. Luebbers, M. R. Fox, W. K. Soppet, and T. F. Kassner, Aqueous *Stress Corrosion of Candidate Austenitic Steels for ITER Structural Applications.* 12th Fusion Reactor Materials Semiannual Progress Report for Period Ending March 31, 1992, DOE/ER-0313/12, Oak Ridge National Laboratory, p. 225.

10. D. M. French, W. K. Soppet, and T. F. Kassner, Aqueous *Stress Corrosion of Candidate Austenitic Steels for ITER Structural Applications*, 13th Fusion Reactor Materials Semiannual Progress Report for Period Ending September 30, 1992, DOE/ER-0313/13, Oak Ridge National Laboratory, p. 276.

11. S. M. Bruemmer. L. A. Charlot, and D. G. Atteridge, *Sensitization Development in Austenitic Stainless Steel—Measurement and Prediction of Thermomechanical History Effects*, Corrosion **44**, 427–442 (1988).

12. D. D. Macdonald, A. C. Scott, and P. Wentrcek, *External Reference Electrodes for Use in High Temperature Aqueous Systems*, I. Electrochem. Soc., **126**, 908–911 (1979).

13. H. D. Solomon, *Transgranular, Granulated. and Intergranular Stress Corrosion Cracking in AISI 304 SS*, Corrosion **40**, 493–506 (1984).

14. W. E. Ruther, W. K. Soppet, and T. F. Kassner, *Effect of Temperature and Ionic Impurities at Very Low Concentrations on Stress Corrosion Cracking of AISI 304 Stainless Steel*, Corrosion **44**, 791–799 (1988).

15. B. M. Gordon, *The Effect of Chloride and Oxygen on the Stress Corrosion Cracking of Stainless Steels: Review of Literature*, Materials Performance 19 (4), 29–37 (1980).

16. P. L. Andresen and D. J. Duquette, *The Effects of Dissolved Oxygen, Chloride Ion, and Applied Potential on the SCC Behavior of Type 304 Stainless Steel in 290°C Water*, Corrosion **36**, 409–415 (1980).

17. J. Congleton, H. C. Shih, T. Shoji, and R. N. Parkins, *The Stress Corrosion Cracking d Type 316 Stainless Steel in Oxygenated and Chlorinared lligh Temperature Water.* Corrosion Science ***25,*** 769–788 (1985).

18. **W.** M. M. Huijbregts, *Oxygen and Corrosion Potential* ***Effects*** *on Chloride Stress Corrosion Cracking,* Corrosion **42,** 456–462 (1986).

19. J.–H. Wang, C. C. Su, and Z. Szklarska-Smialowska, ***Effects*** *d* Cl^- *Concentration and Temperalure on Pitting of AISI 304 Stainless Steel,* Corrosion **44,** 732–737 (1988).

20. H. K. Juang and C. Altstctter, ***Effect*** *of pIl and Chloride Contents* ***on*** *Stress Corrosion Crocking of Ausreniric Stainless Steels at Room Temperature,* Corrosion **46,** 881–887 (1990).

21. H. M. G. Smets and W. F. L. Bogaerts, *SCC Analysis d Ausreniric Srainless* ***Steels*** *in Chloride Bearing Warer by Neural Nerwork Techniques,* Corrosion **48,** 618–623 (1992).

FORMATION OF ELECTRICALLY INSULATING COATINGS ON ALUMINIDED VANADIUM–BASE ALLOYS IN LIQUID LITHIUM. — J.-H. Park and G. Dragel (Argonne National Laboratory)

OBJECTIVE

The magnetohydrodynamic (MHD) force and its subsequent influence on thermal hydraulics are major concerns in the design of liquid–metal blankets for magnetic fusion reactors (MFRs). The objective of this study is to develop in–situ stable electrically insulating coatings at the liquid-metal/structural-material interface to prevent adverse MHD-generated currents from passing through the structural walls.[1-3]

SUMMARY

Aluminide coatings were produced on vanadium and vanadium–base alloys[4,5] by exposure of the materials to liquid lithium that contained 3-5 at.% dissolved aluminum in sealed capsules at temperatures between 775 and 880°C. Reaction of the aluminide layer with dissolved nitrogen in liquid lithium provides a means of developing an in–situ electrical insulator coating on the surface of the alloys. The electrical resistivity of AlN coatings on aluminided V and and V–20 wt.% Ti was determined in–situ.

INTRODUCTION

Corrosion resistance of structural materials, and the MHD force and its subsequent influence on thermal hydraulics, are major concerns in the design of liquid–metal cooling systems.[1-3] The objective of this study is to develop in–situ electrically insulating coatings at the liquid-metal/structural-material interface. The electrically insulating coatings should be capable of forming on various shapes such as the inside of tubes or on irregular shapes during operational conditions to prevent adverse MHD-generated currents from passing through the structural walls. The coatings could also improve general corrosion resistance and act as a diffusion barrier for hydrogen isotopes, viz., deuterium and tritium. Aluminide coatings on vanadium and vanadium–base alloys can react with nitrogen in lithium to form a thin electrically insulating AlN film.

COATING METHODS

Nitride coatings (e.g., AlN, TiN, etc.) on aluminide layers and Ti can be produced in an Li + Li_3N mixture, based on thermodynamic considerations[6] and the Li-Li_3N phase diagram. The melting points of Li and Li_3N are 180.6 and 815°C, respectively. The liquidus temperature increases monotonically as the nitrogen concentration increases? However, an Li–Li_3N mixture at a given temperature provides a means of establishing a fixed nitrogen partial pressure that corresponds to the thermodynamic equilibrium for the two–phase mixture.

EXPERIMENTAL PROCEDURE

A nitride coating (TiN) on Ti was produced in an Li–Li_3N mixture at temperatures between 200 and 807°C. Aluminized V and V-20%Ti capsules from previous experiments were tilled with liquid Li that was enriched in Al and N by adding Al powder and Li_3N. The capsules were heated to 700–850°C for 24–72 h.

• Work supported by the U.S. Department of Energy under Contract W-31-109-Eng-38.

The Al powder and Li_3N facilitated the formation of AlN on the aluminide surface layer on the capsules. Electrical resistivity of layers that formed was monitored as a function of time during the exposure.

RESULT AND DISCUSSION

Figure 1a is an SEM micrograph of a TiN layer on the surface of a Ti tube (1/4–in. outer diameter) that formed in liquid Li containing Li_3N. The TiN surface was bright in appearance after rinsing with water. EDS analyses were performed to determine the N concentration after exposure to Li.* Figure. 1b shows that a significant amount of N was detected in samples exposed to Li at temperatures ≥600°C.

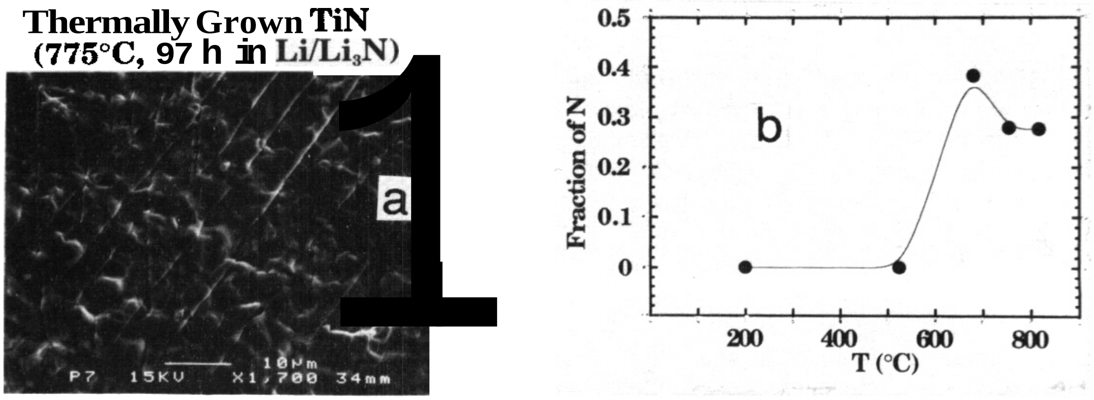

Figure *1*. (a) *SEM* photograph of surface of thermally grown layer of *TiN* on Ti in liquid lithium containing N. and *(b)* N content of surface layers as a function of exposure temperature

To determine the in–situ electrical conductivity of nitride layers, an aluminide coating was applied to the inside surface of V and V-20%Ti capsules, as described previously. The aluminide layer was then nitrided in an Li–Li_3N mixture in a system that also allowed measurement of electrical conductivity during formation of the AIN layer. Electrical resistance was determined from the slopes of potential drop vs. current curves when the current through the coating layers was passed in the positive and negative directions (Fig. 2). Because of the open–circuit potential across the coating layer (without supplying current), the ohmic resistance across the coating layer was determined by Ohm's law, i.e., $R(\Omega) = [\partial E(\mathrm{Volt})/\partial i(\mathrm{Amp})]$.

Results of in–situ electrical conductivity measurements are shown in Fig. 2, and the dependence of the ohmic resistance on temperature over the duration of the experiment is shown in Fig. 3. The coating area (surface of the tube in contact with liquid Li) was 20 cm^2. If we assume that the thickness of the AlN film is ≈1 mm, the electrical conductivity at 700°C is consistent with literature values[8] However, thermal cycling tends to decrease the resistivity, as shown in Fig. 3 for the second cycle. Ohmic resistance dropped from –1.5 to 0.43 Ω and remained constant after the temperature was increased to 800°C, where we expected that the reaction between the aluminide layer and N would proceed at a higher rate and thereby show an increase in resistance over the previous value of –1.5 Ω. This trend, if it had occurred, would indicate that nitriding of spalled regions or defects (e.g., cracks or open boundaries) in the film occurs rapidly. However, an ohmic resistance of ≈0.4 Ω may be adequate for an insulator coating in MFR applications.

---

* Because the positions of the Ti(l) and N(k) peaks are very close to one another. the N concentration was determined by subtraction of the Ti(l) peak area from the EDS spectrum of TiN.

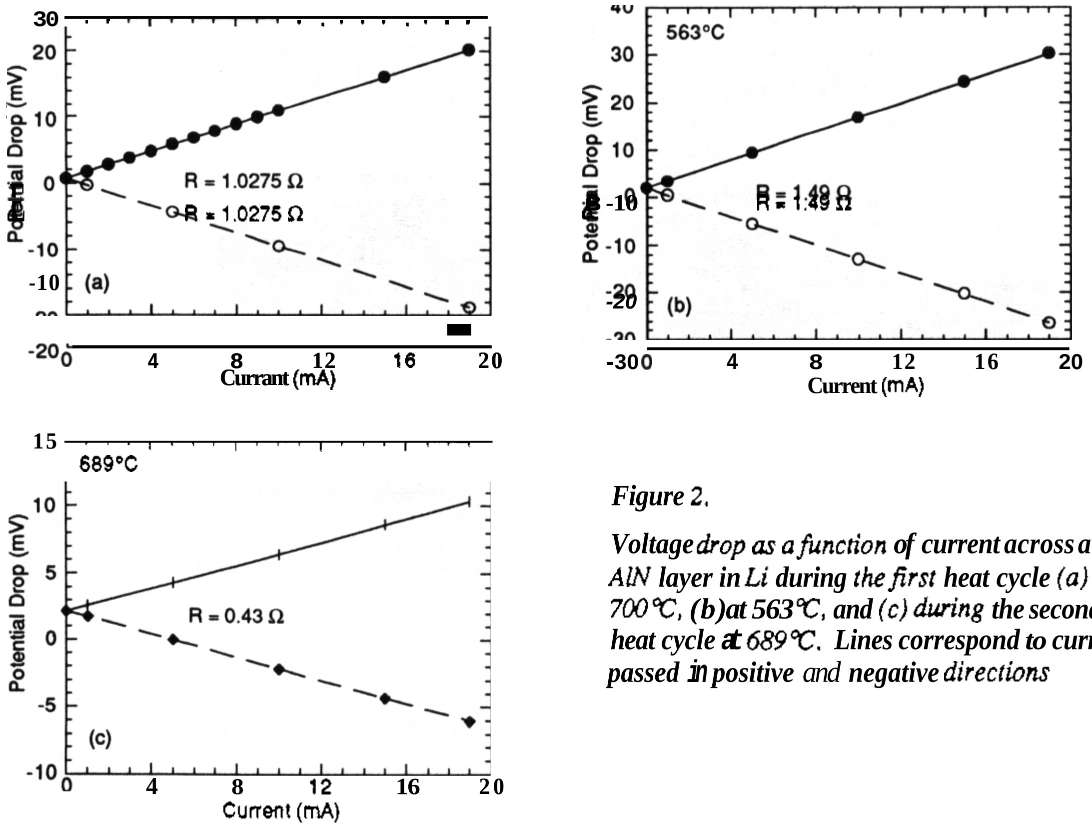

Figure 2.

Voltage drop as a function of current across an AlN layer in Li during the first heat cycle (a) at 700°C, (b) at 563°C, and (c) during the second heat cycle at 689°C. Lines correspond to current passed in positive and negative directions

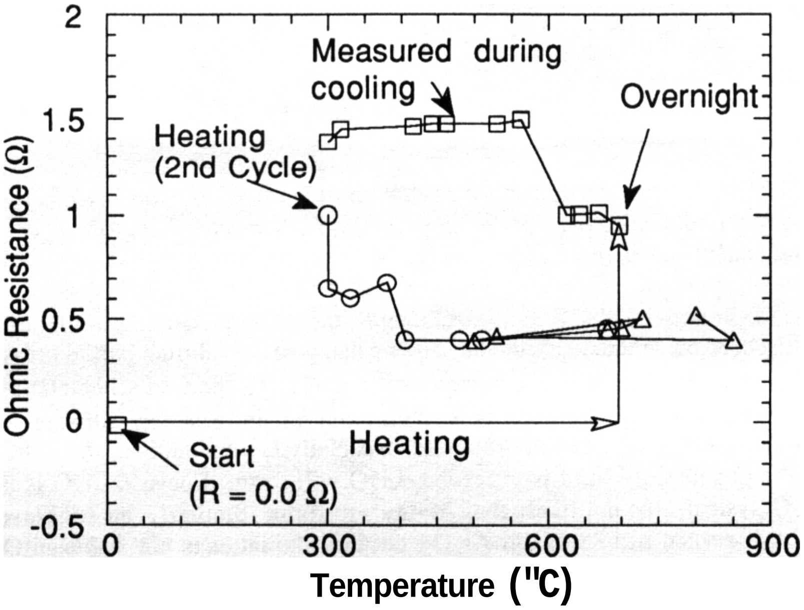

Figure 3. Ohmic resistance vs. temperature during heating cycles

Figure. **4** shows **SEM** micrographs of an AIN film and a spalled **area** on an aluminided surface of V–20%Ti, along with electron–energy–dispersive–spectroscopy **(EDS) spectra** from the two regions. The **EDS** results indicate a relatively high concentration of Al, N, and **O** in the coating compared ***to*** the spalled **area.** Electrical resistivity of the AIN film **was** measured at room temperature after the cell was dissembled. The ohmic resistance was $>10^{12}\ \Omega$, which indicates that it is a good electrical insulator.

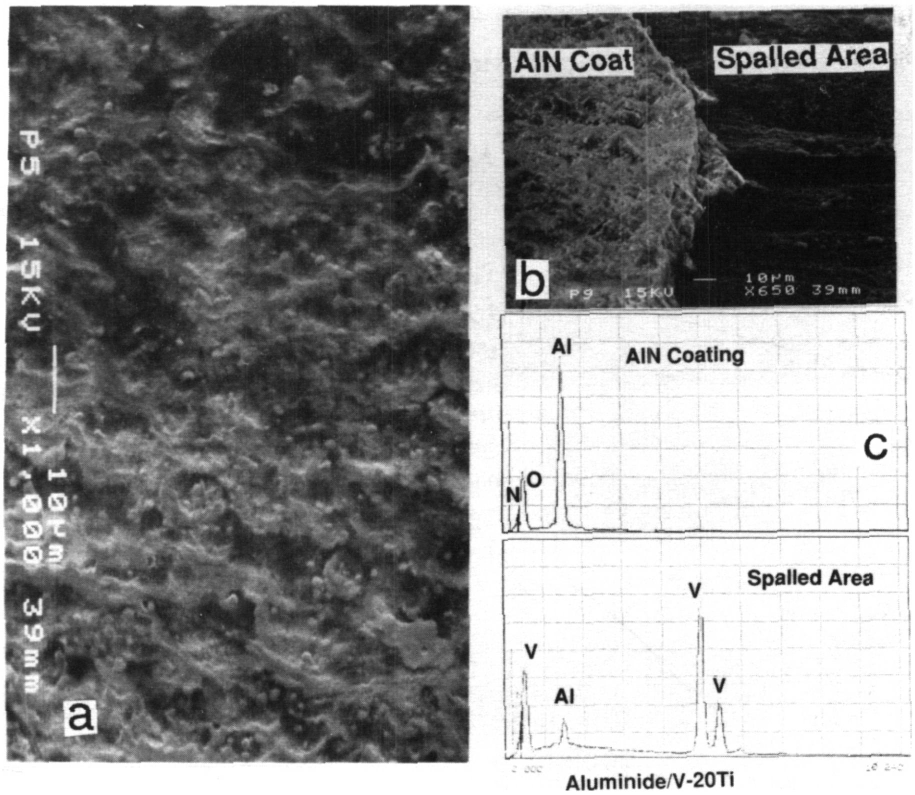

Figure 4. (a) SEM micrograph of surface of AIN on aluminide layer on V-20%Ti, (b) AlN and spalled area of coating, and (c) EDS spectra from AlN layer and spalled area in (b)

To rationalize the present conductivity measurements. the thermodynamic stability of several simple oxides and nitrides has been considered. Figure 5a shows calculated equilibrium partial pressures of O_2 and N_2 in the Li–AI–Y system **as** a function of temperature? and Fig. 5b shows a schematic thermochemical diagram for the M·N·O system, where **M** denotes Al, Li, and **Y.** In these experiments, it is difficult to exclude interactions with the gas–phase environment, especially O_2 contamination. When O_2 interacts with liquid Li and the **O** solubility limit is exceeded, Li_2O will form. Because Li_2O is the most stable oxide in the Li–Al–O system, it is not likely that Al_2O_3 will form. Similarly, an AIN layer is not likely to react with dissolved oxygen in Li to form Al_2O_3 because the latter is not stable in 0–saturated Li. Consequently, AIN can be a stable phase in liquid Li with a relatively high N_2 partial pressure. Figure 5a indicates that the stability of AIN is greater than that of Li_3N over a wide temperature range. ,

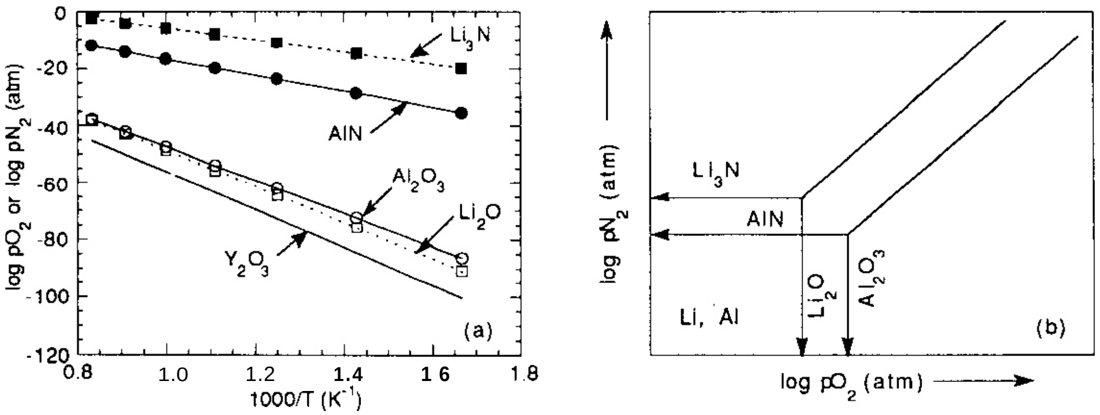

Figure **5.** *(a) Calculated equilibrium partial pressures of O_2 and N_2 in Li–Al–Y system and (b) schematic thermochemical diagram for M-N-O system, where M represents Al or Li*

Formation of an AlN film on an aluminide layer follows the reaction

$$Li_3N + Al = 3\,Li + AlN, \tag{1}$$

where the free–energy change, ΔG, is –25 kcal/mole at 500°C. If the AlN film cracks or spalls, the reaction (Eq. 1) should take place and repair the film, provided that N is present in Li and the Al activity in the alloy is sufficient for spontaneous reaction to occur. The main requirement is that the N level in Li be high enough. If this is not the case, we must also consider the possibility of dissolution of the AlN film based on the solubilities of Al and N in liquid Li, i.e.,

$$AlN = \underline{Al} + \underline{N} \text{ (in Li)}. \tag{2}$$

The ΔG for this reaction is +31.2 kcal/mole; therefore, the equilibrium constant K for the reaction at 500°C is

$$K = 2 \times 10^{-9} = a_{Al} a_N, \tag{3}$$

when the activities for Li and AlN are assumed to be unity. The typical impurity level for N in Li is ≈50–200 ppm. Therefore, the Al concentration in Li must be in the range of 40–10 ppm at 500°C to maintain the AW layer. In capsule experiments, it is relatively easy to meet these criteria for the formation and long–term stability of the AlN phase. In a forced–circulation loop under heat transfer conditions, the effect of the temperature gradient throughout the system on the concentrations of Al and N in Li must be considered so that the AlN film can be maintained at all temperature regions over long periods of time. This will be explored in future work after additional information on the stability and resistivity of insulator coatings is obtained in capsule tests. Subsequently, the results will be applied to an MFR system.

CONCLUSIONS

Surface modification via high-temperature liquid–phase deposition can provide intermetallic aluminide coatings on V–base alloys. This process is facilitated in liquid Li because surface contamination by O_2 or oxide films is virtually eliminated, and the process to produce homogeneous coatings on various surface shapes can be controlled by exposure time. temperature, and composition of the liquid metal. Conversion of aluminide layers to an electrically insulating coating (e.g., an AlN film) in liquid Li was demonstrated.

FUTURE STUDIES

Results of mechanical-property[10] and irradiation-damage[11,12] studies indicate that V-5%Cr-5%Ti is the most promising V-base alloy for MFR applications. Consequently, the insulator development study will focus on the V-5%Cr-5%Ti alloy.

REFERENCES

1. C. C. Baker et al., *Tokamak Power System Studies FY 1985*, Argonne National Laboratory Report ANL/FPP-85-2 (December 1985).
2. Y. Y. Liu and D. L. Smith, *Ceramic Electrical Insulators for Liquid Metal Blankets*, J. Nucl. Mater.. **141-143**, 38 (1986).
3. T. Kammash, *Fusion Reactor Physics*, Chapter 15, Ann Arbor Science Pub. Inc., Ann Arbor, MI (1975) pp. 405-439.
4. J.-H. Park and G. Dragel, *Development of In-Situ-Formed Electrical Insulator Coatings on High-Temperature Alloys in Lithium*, Fusion Reactor Materials Semiannual Progress Report for the Period Ending September 30, 1992.
5. J.-H. Park and G. Dragel. *Development of Aluminide Coatings on Vanadium-Base Alloys in Liquid Lithium*, Fusion Reactor Materials Semiannual Progress Report for the Period Ending March 31, 1993.
6. L. S. Darken and R. W. Gurry, *Physical Chemistry of Metals*, McGraw-Hill, New York (1953).
7. M. Hansen, *Constitution of Binary Alloys*, McGraw-Hill, New York (1958).
8. S. F. Palguev, R. P. Lesunova, and L. S. Karenina, Solid State Ionics **20**, 255-258 (1986).
9. F. A. Shunk, *Constitution of Binary Alloys, Second Supplement*, McGraw-Hill, New York (1969).
10. R. F. Mattas, B. A. Loomis. and D. L. Smith, *Vanadium Alloys for Fusion Reactor Applications*, JOM, **44**(8), 26 (1992).
11. H. M. Chung, L. J. Nowicki, and D. L. Smith, *Effect of Impurities and Doping Elements on Phase Structure of Vanadium-based Alloys Containing Titanium*, Fusion Reactor Materials Semiannual Progress Report for the Period Ending September 30, 1991, DOE/ER-0313/11, *Oak* Ridge National Laboratory. Oak Ridge, TN. pp. 215-226.
12. M. Salou and H. M. Chung, *Effect of Impurities and Doping Elements on Phase Structure of Vanadium-based Alloys Containing Titanium*, Fusion Reactor Materials Semiannual Progress Report for the Period Ending September 30, 1992, DOE/ER-0313/13, Oak Ridge National Laboratory. *Oak* Ridge, TN.

CORROSION FATIGUE OF CANDIDATE AUSTENITIC STEELS FOR ITER STRUCTURAL APPLICATIONS[*] – W. E. Ruther and T. F. Kassner (Argonne National Laboratory)

OBJECTIVE

Austenitic stainless steels are being considered as a structural material for first–wall/blanket systems in the International Thermonuclear Experimental Reactor (ITER).[1] Information on the corrosion fatigue properties of candidate stainless steels under ITER-relevant conditions will help to identify an optimal combination of structural material, coolant chemistry, and operational conditions for ongoing ITER design work. The objective of this task is to provide baseline information on corrosion fatigue of candidate stainless steels in oxygenated water that simulates many important parameters anticipated in ITER first–wall/blanket systems. Tests will also be conducted under off–normal water chemistry conditions and over a range of temperatures to establish the performance limits of the materials.

SUMMARY

Crack–growth–rate (CGR) tests were performed on 1–in.–thick (1T) compact–tension (CT) specimens of Types 316NG and 316L stainless steel (SS) in oxygenated water containing 0–5 ppm Cl^- at 150, 185, and 225°C. The results obtained under cyclic loading conditions at stress intensity factors of ≈27 to 39 $MPa{\cdot}m^{1/2}$ indicate that environmental enhancement of the rates increases with Cl^- concentrations >0.1 ppm at 150°C in comparison with calculated rates in air under the specific loading conditions. In contrast, at the higher temperatures the CGRs were not affected by Cl^- in oxygenated water but were greater than the predicted rates in air by one order of magnitude.

PROGRESS AND STATUS

Research and development needs[2] of the ITER with respect to aqueous corrosion include establishing a reliable data base on reference materials, viz., Types 316, 316L, and 316NG SS in the solution-annealed, cold–worked, and welded conditions. A nominal ITER water chemistry would most likely be high-purity (HP) water (a) containing stable radiolysis/electrolysis products, e.g., dissolved O_2, H_2O_2, and H_2 at ppm levels, and (b) ionic species at ppb levels, namely, soluble corrosion products and impurities in the makeup water and from release by ion–exchange resins in water purification systems. Higher concentrations of ionic impurities (e.g., Cl^-, SO_4^{2-}, H^+, etc.) in the coolant may be present during off–normal operating and extended lay–up conditions of the system.

Although the nominal ITER coolant operating temperature in an initial design was ≈60°C, periodic increases to 150°C and above were envisaged. Mechanical loads and temperature gradients across the first–wall structure will produce both static and cyclic stresses, which when coupled with residual tensile stresses associated with welds, can exceed the yield strength of the material. Tensile stresses that exceed the yield stress under ITER cyclic operation (≈10^4 cycles) are conducive to crack propagation under corrosion fatigue conditions.

Previous work focused on susceptibility of Types 316NG, 316L, and 304 SS to stress corrosion cracking (SCC) by slow–strain–rate–tensile (SSRT) tests.[3–7] No indication of SCC was observed in tests[3] on noncrevice specimens of Type 316NG SS in oxygenated water containing 0.1-1.0 ppm SO_4^{2-} at temperatures of 95 and 150°C and a strain rate of $3 \times 10^{-7}\ s^{-1}$. Crevice specimens were also resistant to SCC in oxygenated water containing 0.1 ppm SO_4^{2-} at ≤150°C.[3–5] Predominantly ductile fracture (a minor amount of transgranular cracking, or TGSCC) was observed in crevice specimens of Type 316NG SS

---

[*] Work supported by the U.S. Department of Energy under Contract W-31-109-Eng-38

at higher temperatures. Intergranular failure occurred in crevice specimens of sensitized Type 304 SS.[6,7] Results described in this report are from corrosion fatigue tests in water containing dissolved oxygen and Cl^- at 150, 185, and 225°C on fracture–mechanics specimens fabricated from Type 316L and two heats of Type 316NG SS.

Experimental Procedures

A large autoclave (=6 L) equipped with an MTS hydraulic test system was used for fracture–mechanics CGR tests on 1–in.–thick compact–tension (ITCT) specimens. The apparatus had a calibrated load cell and a crack–length monitoring system for in–situ measurement of the crack length of each specimen during the test. Crack lengths were determined by a DC potential–drop method. which can resolve length changes of 0.025 mm. Standard ITCT specimens (ASTM E–399) of the same heats of steel used in the SSRT tests,[3–7] viz., two specimens of Type 316NG and one specimen of Type 316L SS, all with machined side grooves, were loaded in series. All specimens were solution–annealed for 0.5 h and then heat treated at 650°C for 24 h, which simulates the material condition of a heat–affected zone in a typical weld. The composition of the steels is given in Table 1.

Table I. Composition of Types 316NG and 316L stainless steels (wt.%)

Alloy	Heat No.	Cr	Ni	Mo	Mn	Si	Cu	N	C	P	S	Fe
316NG	D440104	17.91	13.25	2.48	1.75	0.49	0.01	0.098	0.015	0.011	0.002	Bal
316NG	13198	16.51	10.70	2.08	1.63	0.64	0.20	0.085	0.021	0.022	0.017	Bal
316L	16650	16.50	10.39	2.09	1.78	0.43	0.19	0.054	0.018	0.026	0.013	Bal

The specimens were fatigue–precracked in air at room temperature to introduce a sharp starter crack. The tests were then conducted in water under a low-frequency cyclic-loading with a positive sawtooth waveform at a frequency of 0.09 Hz, an R ratio of 0.7 (where R is the ratio of the minimum load to the maximum load of 21.24 kN), and maximum stress intensity values, K_{max}, ranging from =27 to 39 MPa·m$^{1/2}$. Stress intensity values were computed with the expression in ASTM Standard E–399, together with compensation for the side grooves in the specimens. The electrochemical potential (ECP) of Type 303 SS and a platinum electrode was also monitored during the CGR tests, and optical and scanning electron microscopes were used to evaluate the fracture surface of the specimens and measure the final crack length.

Water chemistry was established by bubbling a 20% O_2-80% N_2 gas mixture through deoxygenated/deionized feedwater (conductivity <0.1 µS·cm^{-1}) contained in a 130–L SS tank to produce a dissolved-oxygen concentration of ≈8.0 ppm. NaCl (0 to 5.0 ppm Cl–) was added to the feedwater before sparging with the gas mixture to ensure adequate mixing. Influent and effluent water chemistry was monitored (pH, conductivity, and concentration of dissolved oxygen), and an electrochemical measurement system with an 0.1M KCl/AgCl/Ag external reference electrode for redox and corrosion potential measurements was located at the autoclave outlet. The measured ECP values were converted to the standard hydrogen electrode (SHE) scale by using thermocell and liquid–junction potentials.[8] The dissolved–oxygen concentrations in the feed– and effluent water were measured with an Orbisphere oxygen meter.

Results

CGR tests have been completed on one set of three 1TCT specimens of Types 316NG and 316L SS at 150, 185 and 225°C. The tests were conducted under low–frequency cyclic loading with a positive sawtooth waveform (rise time of 10 s and fall time of 1 s) at a load ratio ($R = K_{min}/K_{max}$) of 0.7. The water chemistry, loading conditions, and results of the CGR tests are given in Table 2. The CGRs encompass the range of -3×10^{-10} to 1×10^{-8} $m{\cdot}s^{-1}$ for the various test conditions. Figure 1 shows the dependence of the CGRs on Cl^- concentration at 150 and 225°C. At 150°C. the CGRs increase with Cl^- concentration >0.1 ppm in the oxygenated water; at 225°C the rates are quite high and are not dependent on either alloy composition or Cl^- concentration in water.

The dependence of the CGRs on temperature is shown in Fig. 2. The results indicate that rates increase more slowly as the temperature increases, and in water containing 5 ppm Cl^-, a broad maximum occurs at temperatures of −170−210°C. SSRT data by Ruther et al[9] and Ford[10] suggest that environmentally assisted CGRs of austenitic SSs peak at ≈200–225°C and that in HP water (conductivity <0.2 $\mu S{\cdot}cm^{-1}$), CGRs decrease at both higher and lower temperatures. In tests by Ruther et al[9] at higher impurity levels (conductivity >0.9 $\mu S{\cdot}cm^{-1}$), no decrease was observed at higher temperatures. Because the tests were performed only with H_2SO_4 additions, it is not known whether this effect was associated with specific chemical species or depends only on the overall impurity (conductivity) level. In fracture–mechanics CGR tests at R = 0.95. Ruther et al.[9] confirmed that in HP water, CGRs at 320°C were much lower than at 288°C. Andresen[*] found that CGRs in fracture–mechanics tests are typically 10–20 times higher at 200°C than at 288°C. His data also suggest a sharp drop in CGRs at temperatures of >300°C in HP water. At the end of the tests, the specimens were sectioned for metallographic examination. The crack paths and fracture surface morphologies of the specimens indicate a predominantly transgranular mode.

Most of the available data on corrosion fatigue of piping and pressure vessel steels in aqueous environments have been developed in support of light–water–reactor (LWR) technology in the United States and abroad. Because Section XI of the ASME Code currently provides only an in–air design curve, corrosion fatigue data in simulated boiling–water–reactor (BWR) environments, obtained at Argonne National Laboratory (ANL) and from the literature, have been analyzed to develop corrosion fatigue curves for SSs in aqueous environments.[11] The approach is basically an update of the work of Gilman et al.,[12] incorporating additional data that are now available. The modified equations from Section XI of the ASME Code for fatigue crack growth of Type 304 SS in air (ASME air curve) and crack growth curves in 289°C water[11] form a useful basis of comparison for our current results under specific loading conditions at lower temperatures.

The CGR, $\dot{a}$, in the environment is written as a superposition of a term representing the contribution of stress corrosion cracking (SCC), $\dot{a}_{SCC}$; a corrosion fatigue term, $\dot{a}_{env}$, representing the additional CGR under cyclic loading due to the environment; and a mechanical fatigue term $\dot{a}_{air}$, representing the fatigue crack growth in air:

$$\dot{a} = \dot{a}_{SCC} + \dot{a}_{env} + \dot{a}_{air}. \qquad (1)$$

---

[*] Private communication. Peter Andresen, General Electric Corporate R & D Center. to W. J. Shack, Argonne National Laboratory. May 1991

Table 2. Crack growth results for austenitic SS specimens[a] under cyclic loading in oxygenated water at 150, 185, and 225°C

			Water Chemistry			Potential[b]		Conditions[c]			Crack Growth Parameters for Several Heats of Type 316NG SS					
											Heat No. 13198		Heat No. 440104		Heat No. 16650	
Test No.	Test Time,[d] h	Temp., °C	Oxygen Conc., ppm	Cl⁻ Conc., ppm	Cond. at 25°C, µS·cm⁻¹	304 SS mV(SHE)	Pt mV(SHE)	Rise Time, s	Freq., Hz	Load Ratio	K_{max}[e], MPa·m$^{1/2}$	Growth Rate, 10^{-10} m·s^{-1}	K_{max}[e], MPa·m$^{1/2}$	Growth Rate, 10^{-10} m·s^{-1}	K_{max}[e], MPa·m$^{1/2}$	Growth Rate, 10^{-10} m·s^{-1}
5	120	150	9.3	0.1	0.47	–[f]	–[f]	10	0.09	0.7	27.6	3.2	27.3	2.5	27.5	3.3
6	140	150	8.9	1.0	3.67	–[f]	–[f]	10	0.09	0.7	28.3	7.5	27.6	2.4	28.3	8.9
7	120	150	7.8	5.0	17.4	–[f]	–[f]	10	0.09	0.7	29.5	17.2	28.1	7.5	29.7	18.1
8	28	225	8.1	5.0	17.4	–[f]	–[f]	10	0.09	0.7	30.3	50.1	28.9	54.5	31.3	69.5
9	28	225	8.9	1.0	3.67	–[f]	–[f]	10	0.09	0.7	31.0	39.1	29.8	46.8	32.7	65.3
10	24	225	8.1	0.1	0.47	220	350	10	0.09	0.7	32.0	56.1	30.8	63.4	34.1	76.3
11	24	225	9.3	0	0.10	210	370	10	0.09	0.7	33.1	59.4	32.2	73.0	36.4	97.1
12	29	185	8.7	0	0.10	252	337	10	0.09	0.7	34.1	38.6	33.1	42.3	36.7	8.6
13	24	185	8.6	5.0	17.4	265	390	10	0.09	0.7	35.6	82.2	34.1	54.5	38.9	105.0

[a] Compact tension specimens (1TCT) of Type 316NG SS (Heat No. 13198; Specimen No. 4), (Heat No. 440104; Specimen No. 3), and Type 316L SS (Heat No. 16650; Specimen No. 11) received the following heat treatment: solution–anneal at 1050°C for 0.5 h followed by 650°C for 24 h.

[b] Electrochemical potential of Type 304 SS and platinum at the test temperature corrected to the standard hydrogen electrode (SHE).

[c] Rise time, frequency, and load ratio for the positive sawtooth waveform.

[d] After the chloride concentration in water was either increased or decreased, the system operated for ≈48 h before load cycling began.

[e] Stress intensity, K_{max}, values at the end of the time period.

[f] Electrodes were shorted internally; problem was corrected at the beginning of Test No. 10.

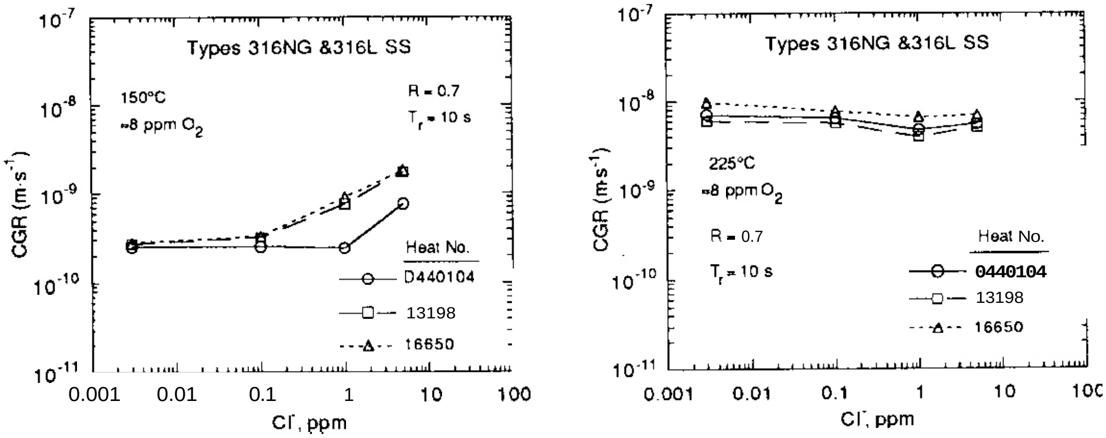

Figure 1. Dependence of cruck growrh rares of Types 316NG and 316L SS on Cl$^-$ concenrrution in oxygenated water at 150 and 225°C during high-R. low-frequency loading

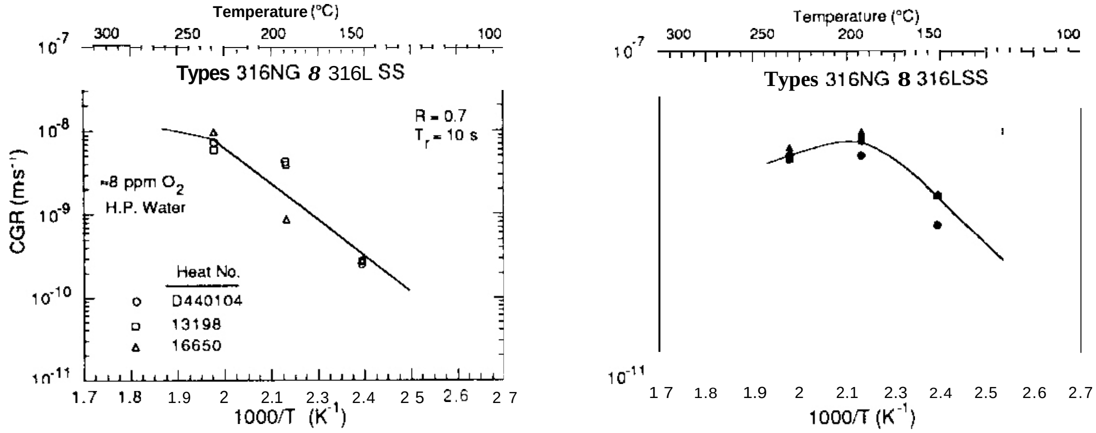

Figure 2. Dependence of crack growrh rates of Types 316NG und 316L SS on reciprocal temperature during high-R. low-frequency loading in HP oxygenated waler and oxygenated water conraining 5 ppm Cl$^-$

For the SCC term, the correlation given in the U.S. Nuclear Regulatory Commission Report NUREG-0313, Rev. 2, January 1988, is used for water chemistries with 8 ppm dissolved oxygen:

$$\dot{a}_{SCC} = 2.1 \times 10^{-13} K^{2.161} \ (\mathrm{m \cdot s^{-1}}). \qquad (2)$$

The air term is given by the current ASME Section XI correlation at 288°C, based on the work of James and Jones:[13]

$$\begin{aligned} \dot{a}_{air} &= 3.43 \times 10^{-12} S(R) \Delta K^{3.3} / T_R && (\mathrm{m \cdot s^{-1}}) \\ S(R) &= 1 + 1.18R && R \le 0.8 \\ &= 43.35 + 51.91R && R > 0.8 \end{aligned} \qquad (3)$$

where T_R is the rise time of the loading waveform. Following Shoji et al.[14] and Gilman et al.,[12] the corrosion fatigue term is assumed to be related to $\dot{a}_{air}$ through a power law,

$$\dot{a}_{env} = A\dot{a}_{air}^{m}. \tag{4}$$

The values of the coefficient A and the exponent **m** for water with 8 ppm dissolved oxygen at 288°C, obtained by an empirical power–law curve fit to the existing data for $R < 0.9$ (where cyclic loading dominates and the stress corrosion term in the superposition model Eq. 1, can be ignored). are

$$\begin{aligned} A &= 1.5 \times 10^{-4} \\ m &= 0.5, \end{aligned} \tag{5}$$

for CGRs in $m \cdot s^{-1}$ and K in $MPa \cdot m^{1/2}$.

The available experimental data for sensitized Type 3W SS in water with 8 ppm dissolved oxygen at 288°C are compared in Fig. 3 with correlations based on **Eqs.** 1–5. In most cases, the correlations were intended to be conservative but not necessarily upper bounds for all the data. The data from the ANL tests in simulated BWR environments are summarized in Ref. 15. The other data were obtained from the literature (Refs. 16–22). Although it is clear that nonsensitized steels such as Types 316NG, CF–3M, and solution–annealed 304 SS are much more resistant to SCC initiation. they show comparable environmentally enhanced CGRs under cyclic loading.

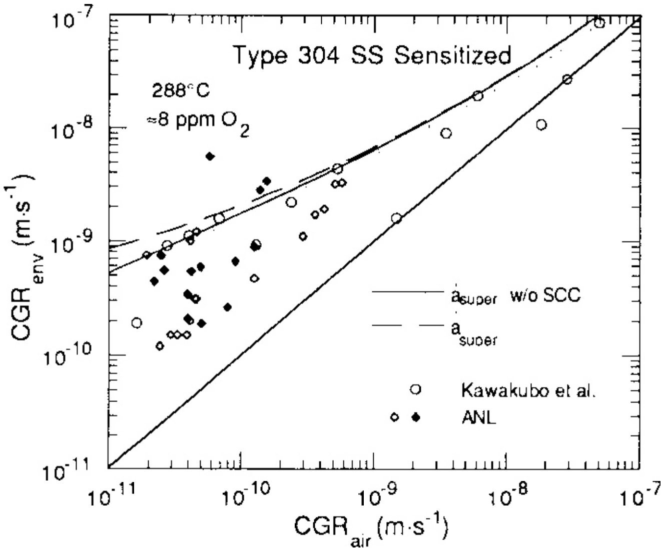

Figure 3. Corrosion fatigue data for sensitized Type 304 SS in water containing 8 ppm dissolved oxygen at 288°C compared with models. Diagonal line corresponds to crack growth in air.

The correlations (**Eqs.** 1–5) and data (Fig. 3) are based on tests at 288°C; relatively few data are available in the literature on corrosion fatigue CGRs at other temperatures. The CGRs in Table 2 were compared with those predicted by the modified ASME Section **XI** fatigue crack growth correlation for Type 304 SS in air (**Eq.** 3) under the loading conditions in the different tests. The results are plotted in

Figs. 4–6. Almost all of the data points in Fig. **4** and 5 fall above the diagonal line, i.e., the experimental CGR values in water are higher than the Code predictions in air by factors of ≈5 to 10. Under these loading conditions, the environmental contribution to crack growth is significant. The results **at** 150°C (Fig. 6) indicate that CGRs in water containing 1.0 and 0 ppm Cl^- are either consistent with or lower than the Code predictions (diagonal line), respectively, which implies that crack growth is dominated by mechanical fatigue. In oxygenated water containing 5 ppm Cl^- at 150°C. the environmental enhancement compared to air is small (greater by a factor of ≈2). Because the Code curve is drawn at a 95% confidence level, it is not surprising that in the absence of environmental effects, the Code predictions are somewhat conservative.

Although the present data (Figs. 4–6) are probably inadequate to completely quantify the effects of temperature on CGRs in water, the correlations[11] based on data at 288°C are consistent with results at 185 and 225°C, but are conservative for temperatures 5150°C.

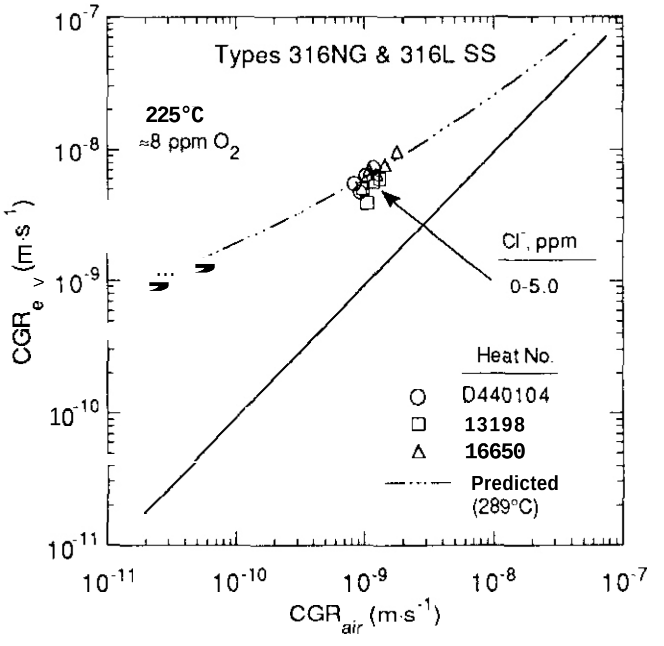

Figure 4. Corrosion fatigue data at 225% in water containing 8 ppm dissolved oxygen and 0–5 ppm Cl^- compared with model. Diagonal line corresponds to crack growth in air.

CONCLUSIONS

CGR *tests* were performed on a set of three ITCT specimens of Types 316NG and 316L *SS* in oxygenated water containing 0–5 ppm Cl^- at 150, 185, and 225°C. The results obtained at 225 and 185°C at and R value of 0.7, a frequency of 0.09 Hz, and stress intensity factors of **−27** ***to*** 39 $MPa \cdot m^{1/2}$ indicate environmental enhancement relative to calculated rates in air under the specific cyclic loading conditions. In contrast, the data obtained at 150°C were consistent with the predicted rates in air, particularly at lower Cl^- concentrations (i.e., <1 ppm). Predictions of a model (developed at ANL[11]) for corrosion fatigue of austenitic SSs in aqueous environments at 288°C are consistent with data obtained at 185 and 225°C in this study. The model must be modified to accurately predict CGRs at temperatures <170°C.

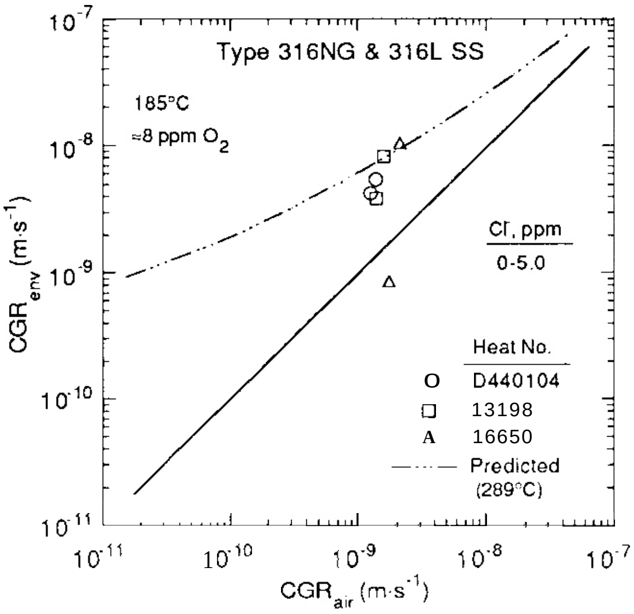

Figure 5. *Corrosionfatigue data at 185°C in water conruining 8 ppm dissolved oxygen und* ***0–5*** *ppm Cl^- compared with model. Diagonal line corresponds to crack growth in air.*

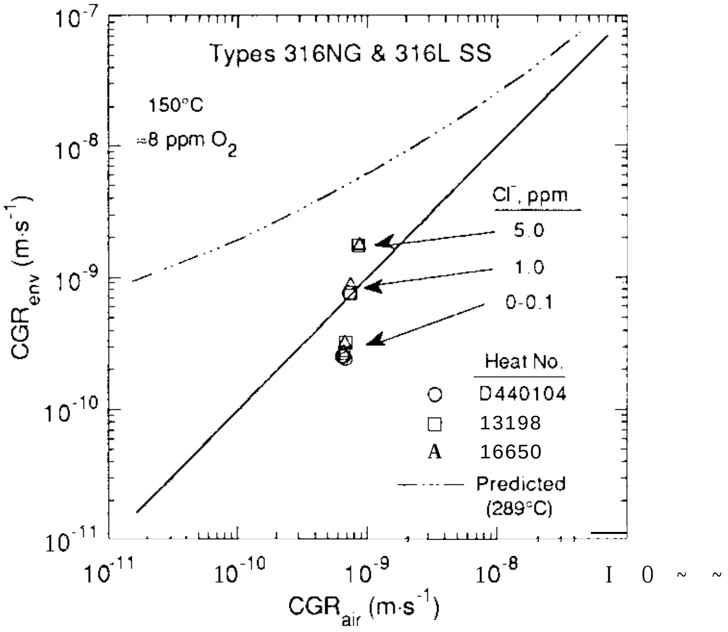

Figure 6. *Corrosionfurigue dara ai 150°C in wurer containing 8 ppm dissolved oxygen* ***iind*** *0–5 ppm C t compared with model. Diagonal line corresponds to crack growth in air.*

FUTURE WORK

Crack growth rate tests will be conducted on another set **of** 1TCT specimens from several heats **of** Type 316NG *SS* in simulated ITER water chemistries under cyclic loading conditions. The **tests** will be performed at higher load ratios and lower frequencies that are more typical of reactor loading conditions. The influence **of** temperalure on CGRs will also be investigated. This information will supplement the existing data base developed for BWRs, **as** well **as** the ASME Boiler and Pressure Vessel Code, ASTM Standards, and other consensus codes and standards. The tests will provide a technical basis for selection **of** appropriate crack growth curves for design and analysis, and will confirm that the chances of service–induced cracking **of** a candidate material for ITER first–wall/blanket systems are small.

REFERENCES

1. R. W. Conn, V. A. Chuyanov, N. Inoue, and D. R. Sweetman, *The International Ihermonuclear Experimental Reactor,* Scientific American, *226* (4) 1992.

2. D. L. Smith, *Aqueous Corrosion Task for ITER R&D*, U.S. Coordination Meeting, Argonne National Laboratory, August 6, 1990.

3. A. E. Hull, M. R. Fox, J. W. Pascoe, and T. F. Kassner, *Environmental Effects on Aqueous Stress Corrosion of Candidate Austenitic Steels for ITER Structural Applications,* 9th Fusion Reactor Materials Semiannual Progress Report for Period Ending September 30, 1990, DOE/ER-0313/9, *Oak* Ridge National Laboratory, p. 228.

4. A. B. **Hull** and T. F. Kassner, *Aqueous Stress Corrosion of Candidare Ausreniric Steels for ITER Structural Applicarions,* 10th Fusion Reactor Materials Semiannual Progress Report for Period Ending March 31, 1991, DOE/ER-0313/10, *Oak* Ridge National Laboratory, **p.** 241.

5. M. R. Fox, A. B. Hull, and T. F. Kassner, *Stress Corrosion Cracking of Candidate Structural Materials under Simulated First-Wall/Aqueous Coolant Environments*, Fusion Technol., **19,** 1619–1628 (1991).

6. A. B. Hull, P. R. Luebbers, M. R. Fox, W. K. Soppet, and T. F. Kassner, *Aqueous Stress* ***Corrosion of Candidate Austenitic Steels for ITER Structural Applicarions,*** **12th Fusion Reactor** Matcrials Semiannual Progress Report for Period Ending March 31. 1992. DOE/ER-0313/12, *Oak* Ridge National Laboratory, p. **225.**

7. D. M. French, W. K. **Soppet,** and T. F. Kassner, Aqueous *Stress Corrosion of Candidare Austenitic Steels for ITER Structural Applicarions,* **13th** Fusion Reactor Materials Semiannual Progress Report for Period Ending September 30, 1992, DOE/ER-0313/13, *Oak* Ridge National Laboratory.

8. D. D. Macdonald, A. C. Scott, and P. Wentreek, *Exrernal Reference Electrodes for Use in High Temperature* ***Aqueous*** *Systems.* J. Electrochem. Soc., **126,** 908–911 (1 979).

9. W. E. Ruther, W. K. Soppet, and T. F. Kassner, in *Environmenrally Assisted Cracking in Light Wafer Reacrors, Annual Reporr, October 1983—September 1984*, NUREG/CR–4287, ANL–85–33, pp. 93–1 13 (June 1985).

10. F. P. Ford, ***A*** *Mechanism* ***of*** *Environmentally–Controlled Crack Growth* ***of*** *Structural Steels in High–Temperature Water.* Proc. IAEA Specialists' Meeting on Subcritical Crack Growth, NUREG/CP–044 Vol. *2,* MEA–2014 Vol. *2* (May 1983).

11. W. J. Shack, in *Environmentally Assisted Cracking in Lighr Water Reactors Semiannual Report, October 1990 — March 1991,* NUREG/CR-4667 Vol. 12, ANL-91/24, pp. 31–37 (August 1991).

12. J. D. Gilman, R. Rungta, P. Hinds, and H. Mindlan, *Corrosion-Farigue Crack Growth Rates in Austenitic Stainless Steels in Light Warer Reactor Environmenrs,* Int. J. Pressure Vessel Piping 31, 55-68 (1988).

13. L. **A.** James **and** D. P. Jones, *Fatigue Crack Growth Correlation for Ausreniric Slainless Steels in Air,* Proc. Conf. on Predictive Capabilities in Environmentally-Assisted Cracking, R. Rungta, ed., PVP Vol. 99, American Society of Mechanical Engineers, **NY. pp.** 363–414 (1985).

14. T. Shoji, H. Takahashi. M. **Suzuki, and** T. Kondo, ***A** New Parameter for Characterizing Corrosion Fatigue Crack Growrh,* J. Eng. Mater. Tcchnol. 103, 298–304 (1981).

15. W. E. Rulher, W. J. Shack, T. F. Kassner, and W. K. Soppct, in *Environmentally Assisred Cracking in Light Water Reacrors Semiannual Reporr. April — September 1988,* NUREG/CR-4667 Vol. 7, ANL-89/40, **pp.** 3–14 (March 1990).

16. L. G. Ljungherg, D. Cubicciolti, and M. Trolle, *The Effect of Sulfate on Environmental Cracking in* **Boiling** *Wafer* ***Reactor.! under*** *Constant Loud or Fatigue,* Corrosion **46**, 641–652 (1990).

17. L. G. Ljungbcrg, D. Cubicciolti, and M. Trollc, *Effect of Water lmpurities in BWRs on Environmental Crack Growrh under Realistic Loud Conditions,* Proc. 4th Int. Symp. Environmental Degradation of Materials in Nuclcar Power Systems — Water Reactors. National Association of Corrosion Engineers, Houston, **pp.** 4–59 to 4–74 (1990).

in, L. G. Ljungbcrg, D. Cuhicciotti, and M. Trollc, *Effect of Wurer lmpurities in BWRs on Environmental Crack Growrh* ***in*** *Type* ***304*** *Stainless Steel,* NUREG/CP-0112 Vol. 2, ANL-90/22 Vol. 2, pp. 57–64 (August 1990).

19. J. Alexander et al., *Alternurive Alloys for BWR Pipe Applicurions,* EPRI NP-2671-LD, **pp.** 5–17 to 5–32, Electric Power Research Institute, Palo Alto, CA (October 1982).

20. C. W. Jewett and **A.** E. Pickett, *The Benefit of Hydrogen Addition to the Boiling Wurer Reuctor Environment on Srress Corrosion Cruck Initiation and Growth in Type* ***304*** *Stainless* ***Steel,*** J. Eng. Mater. Tcchnol. 108, 10–19 (1986).

21. P. L. Andresen, *Effects of Stress Intensity, R Vulue, and Environmental lmpuriries in 288°C Water* ***on*** *Crack Growrh Rate in Type 304 SS CT Specimens,* Corrosion 88, Paper No. 11, St. Louis, MO (March 1988).

22. T. Kawakuho. M. Hishida, K. Amano, and M. Katsuta, *Crack Growth Behavior of Type* ***304*** *Stainless Steel in Oxygenated* 290°C *Pure Water* **under** *Low Frequency Cyclic Loading,* Corrosion **36**, 638-647 (1980).

DEVELOPMENT OF ALUMINIDE COATINGS ON VANADIUM–BASE ALLOYS IN LIQUID LITHIUM'

—J.-H. Park and G. Dragel (Argonne National Laboratory)

OBJECTIVE

The corrosion resistance of structural materials and the magnetohydrodynamic (MHD) force and its subsequent influence on thermal hydraulics and corrosion are major concerns in the design of liquid–metal blankets for magnetic fusion reactors (MFRs). The objective of this study is to develop in–situ stable coatings at the liquid-metal/structural-material interface, with emphasis on coatings that can be converted to an electrically insulating film to prevent adverse MHD-generated currents from passing through the structural walls.[1-3]

SUMMARY

Aluminide coatings were produced on vanadium and vanadium–base alloy8 by exposure of the materials to liquid lithium that contained 3-5 at.% dissolved aluminum in sealed V and V-20 wt.% Ti capsules at temperatures between 775 and 880°C. After each test. the capsules were opened and the samples were examined by optical microscopy and scanning electron microscopy (SEM), and analyzed by electron–energy–dispersive spectroscopy (EDS) and X-ray diffraction. Hardness of the coating layers and bulk alloys was determined by microindentation techniques. The nature of the coatings, i.e., surface coverage, thickness, and composition, varied with exposure time and temperature, solute concentration in lithium, and alloy composition. Solute elements that yielded adherent coatings on various substrates can provide a means of developing in–situ electrical insulator coatings by reaction of the reactive layers with dissolved nitrogen in liquid lithium.

INTRODUCTION

The corrosion resistance of structural materials and the MHD force and its subsequent influence on thermal hydraulics are major concerns in the design of liquid–metal cooling systems.[1-3] This study focuses on the development of in–situ stable corrosion–resistant coatings at the liquid-metal/structural-material interface. The coatings should be capable of (a) forming on various shapes such as the inside of tubes or on irregular shapes during operational conditions, (b) improving general corrosion resistance, and (c) acting as a diffusion barrier for hydrogen isotopes, viz., deuterium and tritium.

COATING METHODS

Aluminide coatings that form on structural alloys during exposure to liquid Li that contain dissolved Al suggest a means for producing stable electrical insulator layers, such as AlN, by subsequent nitridation of the intermetallic layer in the liquid–metal environment? The formation of several aluminides (V_xAl_y) that contain >40–50 at.% of Al on V–base alloys can be predicted from the V-AI phase diagram5 The Al-Li phase diagram[5,6] indicates that AI is soluble in liquid Li, whereas V is not soluble in Li.[7] These phase. relations make up the underlying basis for the formation of aluminide coatings on V and its alloys in liquid Li. Aluminide coatings were produced on V and V–base alloys by exposure of the materials to liquid Li that contained 3–5 at.% AI in sealed V and V-20%Ti capsules? The nature of aluminide coatings formed on V, Ti, and V–base alloys containing Ti and Cr at 775–880°C is described in this report.

Work supported by the U.S. Department of Energy under Contract W-31-109-Eng-38.

EXPERIMENTAL PROCEDURE

Aluminide coatings were produced on V, Ti, and several V–base alloys (V-5%Ti, V-20%Ti, V-5%Cr-5%Ti, and V-15%Cr-5%Ti) by exposure of the materials to liquid Li containing Al at temperatures of 775, 800, 860, and 880°C. The specimens and liquid Li were contained in V-20%Ti and V capsules that were placed in a larger stainless steel container. An argon cover gas (99.999% pure) was maintained in the system to prevent oxidation of the V capsules and the Li. The whole assembly was placed in a vertical furnace. At the end of the test, the capsules were cut open above the Li level to remove the samples. The capsules were placed in a beaker of water to dissolve the small volume of Li and the samples were removed and cleaned ultrasonically in acetone and ethanol and dried in air. The samples were examined by optical microscopy and SEM, and analyzed by EDS and X-ray diffraction. Hardness of the coating layers and bulk alloys was determined by Vickers indentation measurements with a Leitz microhardness tester.

RESULT AND DISCUSSION

The effects of exposure time, temperature, environment above the Li, and capsule material (V and V–20%Ti) on the formation of aluminide coatings were explored. Degree of surface coverage and thickness of the layers varied considerably, depending on exposure time and temperature. At temperatures and exposure times of <800°C and <90 h, respectively, the aluminide layers were not uniform. Figure 1 shows the microstructures of aluminide coatings formed at 775°C for 87 h and 880°C for 48 h. At the lower temperature, small grains on the surface began to connect with neighboring grains by a grain–growth mechanism. At the higher temperature, the microstructure reveals that grain size is larger by at least one order of magnitude. Dependence of Al concentration at the coating surface on temperature is shown for several samples in Fig. 2. The EDS analysis of the coating surface was obtained over a region of 1,000 x 1,000 μm.

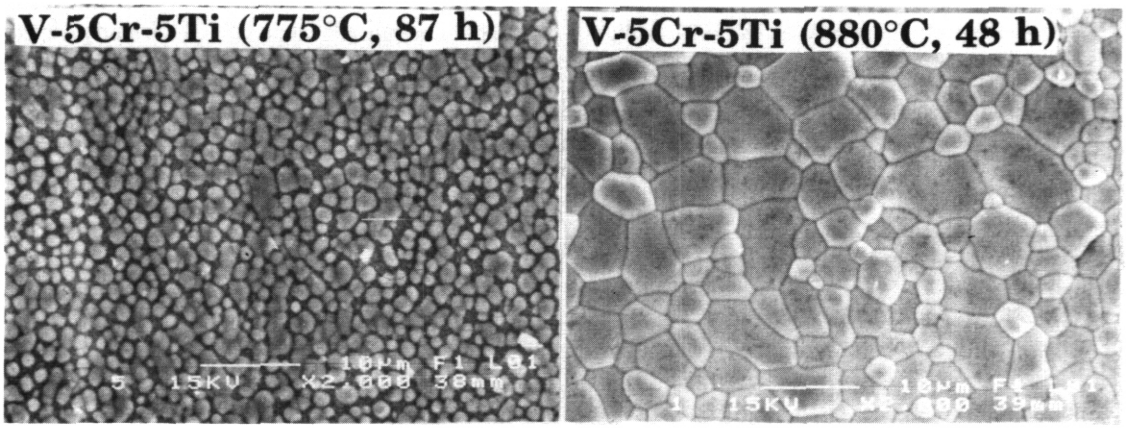
V-5Cr-5Ti (775°C, 87 h)

V-5Cr-5Ti (880°C, 48 h)

Figure 1. Typical aluminide surface formed on V-5%Cr-5%Ti at 775 and 880°C

A typical cross section of an aluminide coating layer is shown in Fig. 3. Based on these SEM photographs, the surface region is virtually defect–free, but an array of small defects is present beneath the compact layer. These defects may be clustered near a dislocation zone that is depleted in Al and rich in Li because of fast diffusion of Li via dislocations. Composition–vs.–depth profiles for the V and V-20%Ti specimens are shown in Fig. 4. The depth of Al interdiffusion in V-20%Ti is ≈3-4 times greater than in pure V at 860°C, which suggests a higher mobility of Al in V-20% Ti than in V.

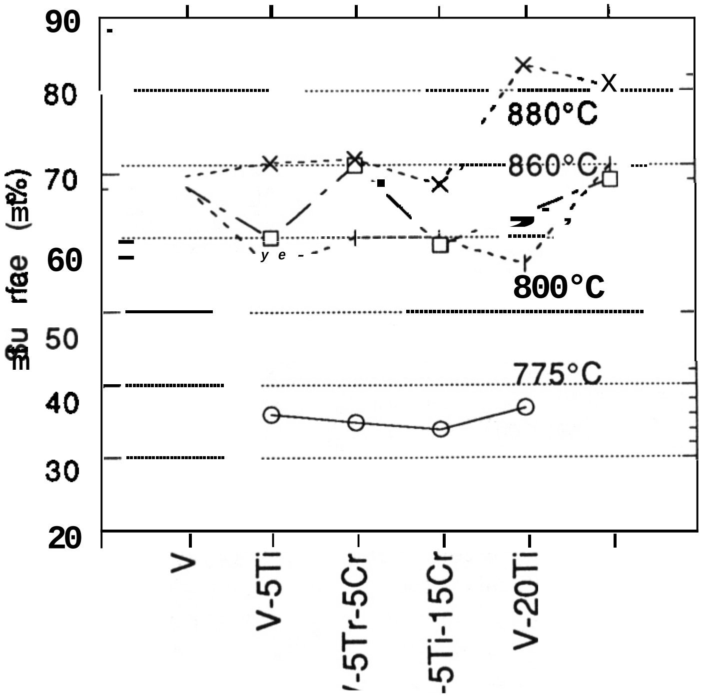

Figure 2. Aluminum content of aluminized surfaces formed on several V-base alloys and Ti at several temperatures between 775 and 880 °C

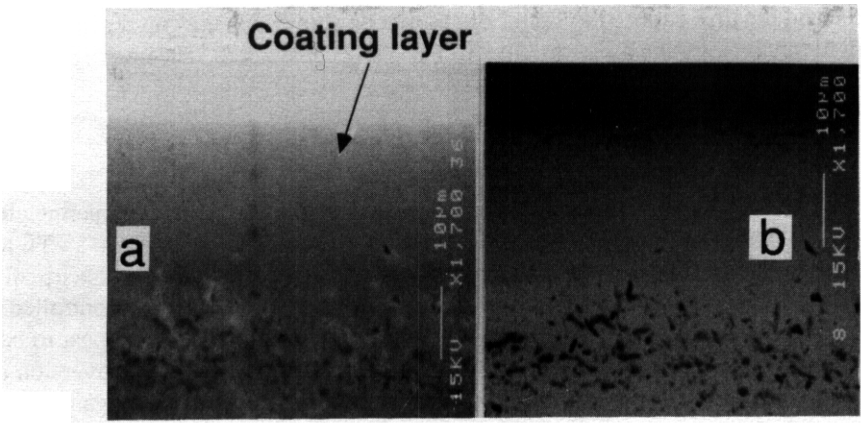

Figure 3. SEM photographs of a cross section of an aluminide layer on a V–20%Ti alloy specimen: (a) bright field and (b) back–scatter electron image

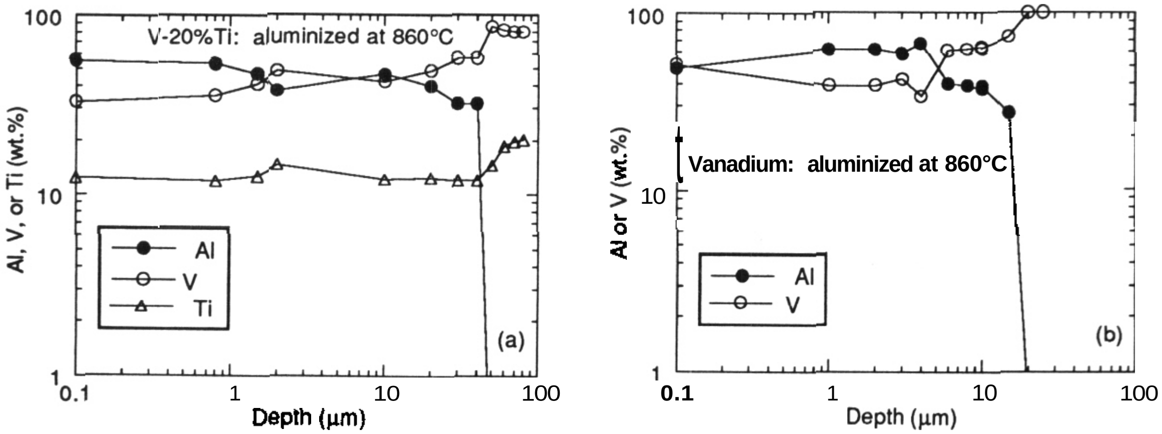

Figure 4. Chemical composition as afunction of depthfor aluminide layers on (a)V-20%Ti and (b) V

Vickers hardness measurements of the aluminide layers and the underlying V and V-20%Ti alloy were conducted at 25–and 50–g loads. The aluminide layers were harder than either V or V-20%Ti, which can be attributed to interstitial Al atoms in the cubic lattice of V. Because the distribution on nonmetallic elements (O, N, C, H) between V–base alloys and Li favors the Li, the alloys tend to become depleted in these constituents during exposure to high–temperature Li. Consequently, the hardness increase is most likely caused by diffusion of Al into V and V–20%Ti. Our experience indicates that V becomes more ductile after exposure to liquid Li.

Figure 5 illustrates the high degree of coverage of an aluminide layer on a weld joint between a V–20%Ti tube and a V disk, as well as in the crevice region where fusion did not occur. Figure 5a shows a cross section of the capsule containing the weld zone; it reveals shallow penetration and a crevice between the tube and the disc. Figure 5b shows this region in higher magnification. The aluminide coating is not only present on the surface of the tube and the face of the disk, but also penetrates the 1–μm space between the V-20%Ti tube and V disk. The thickness of the coating in this region is similar to that on the inner surface of the tube and the disk exposed to liquid Li. Figure 5c shows that the gap region between tube and the edge of the disk (denoted by the arrow in Fig. 5a) has also been coated. The coating behavior suggests that bulk diffusion is the main process.

CONCLUSIONS

Surface modification via high-temperature liquid–phase deposition can provide intermetallic aluminide coatings on various alloys, namely, V, V-5%Ti, V-20%Ti, V-5%Cr-5%Ti, V-15%Cr-5%Ti, and Ti. This process is facilitated in liquid Li because surface contamination by O_2 or oxide films is virtually eliminated and the process to produce homogeneous coatings on various surface shapes can be controlled by exposure time, temperature. and composition of the liquid metal. Coating integrity does not appear to be sensitive to defects (e.g., open pores, fissures, or microcracks) present in the alloy substrate. Conversion of aluminide layers to an electrical insulator coating (e.g., an AlN film) in liquid Li is being investigated.

FUTURE STUDIES

Results of mechanical-property[8] and irradiation–damage[9,10] studies indicate that V-5%Cr-5%Ti is the most promising V–base alloy for MFR applications. Consequently, the coating develdpment study will focus on the V-5%Cr-5%Ti alloy.

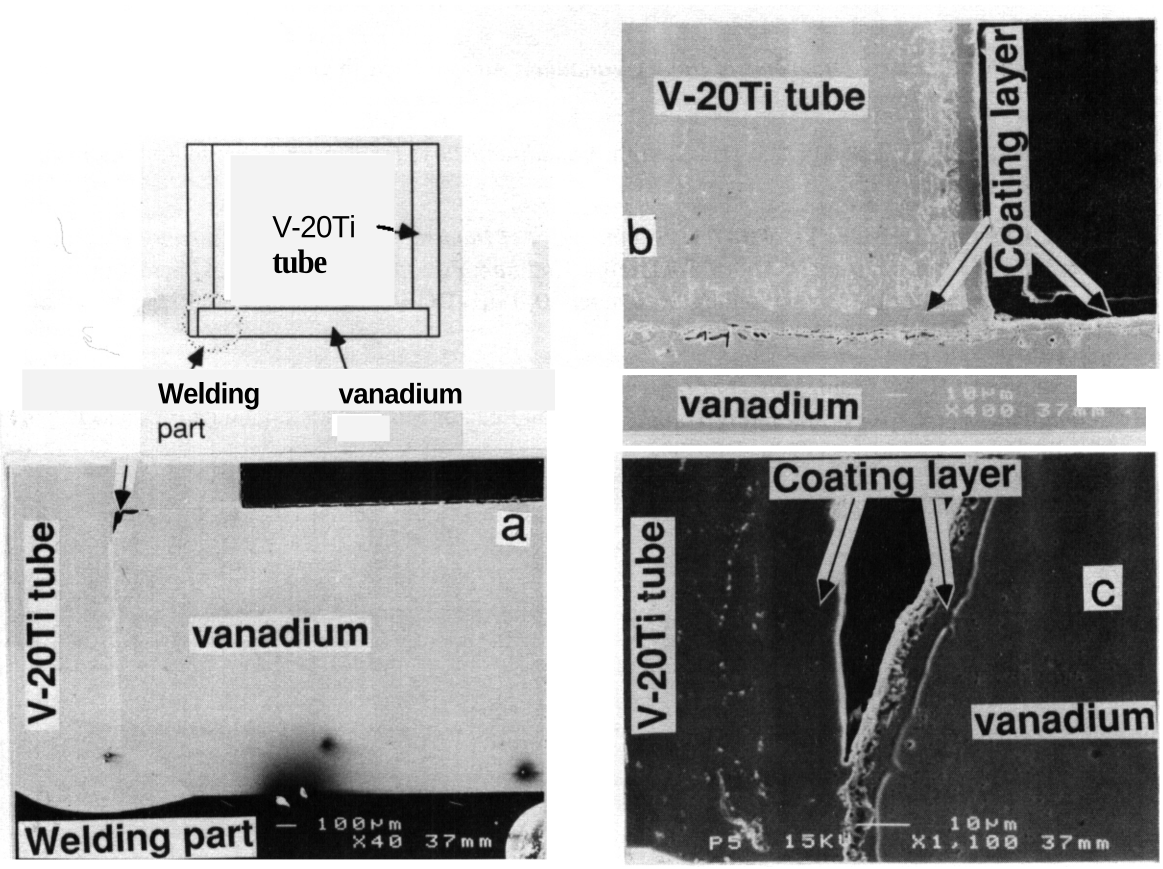

Figure **5.** *(a)Cross section of weld zone between V-20%Ti tube and* **V** *disk, (b) aluminide coating* **on** *surface of tube and disk and in crevice region between tube and disk, and (c) coating* **of** *gap region between tube and disk, denoted be arrow in (a)*

REFERENCES

1. **C. C. Baker et al.**, *Tokamak Power System Studies FY* ***1985,*** **Argonne National** Laboratory **Report ANL/FPP-85-2** (December 1985).

2. **Y. Y. Liu and D. L. Smith,** *Ceramic Electrical Insulatorsfor Liquid Metal Blankets, J.* **Nucl. Mater.. 141-143, 38 (1986).**

3. **T. Kammash,** *Fusion Reactor Physics.* Chapter 15, **Ann Arbor Science Pub. Inc., Ann Arbor. MI (1975)** pp. 405-439.

4. J.-H. Park **and G. Dragel,** *Development* ***of*** *In-Situ-Formed Electrical Insulator Coatings on High-Temperature Alloys in Lithium,* **Fusion** ***Reactor*** **Materials Semiannual Progress Report for the** Period **Ending September 30, 1992.**

5. **M. Hansen.** *Constitution of Binary Alloys.* McGraw-Hill **, New York** (1958).

6. **F. A. Shunk,** *Constitution of Binary Alloys, Second Supplement,* McGraw-Hill **, New York (1969).**

7. J. F. Smith, ed.. *Phase Diagrams of Binary Vanadium Alloys,* ASM International, Metals Park, OH (1989).

8. R. F. Mattas, B. A. Loomis, and D. L. Smith, *Vanadium Alloys for Fusion Reactor Applications*, JOM, 44(8), 26 (1992).

9. H. M. Chung, L. J. Nowicki. and D. L. Smith, *Effect of Impurities and Doping Elements on Phase Structure of Vanadium-based Alloys Containing Titanium,* Fusion Reactor Materials Semiannual Progress Report for the Period Ending September 30,1991, DOE/ER-0313/11, *Oak* Ridge National Laboratory. *Oak* Ridge, TN, pp. 215-226.

10. M. Satou and H. M. Chung, *Effect of Impurities and Doping Elements on Phase Structure of Vanadium-based Alloys Containing Titanium,* Fusion Reactor Materials Semiannual Progress Report for the Period Ending September 30,1992.

7.0 SOLID BREEDING MATERIALS AND BERYLLIUM

No contributions.

8.0 CERAMICS

CERAMICS RADIATION EFFECTS ISSUES FOR ITER--S. J. Zinkle *(Oak* Ridge National Laboratory)

OBJECTIVE

To review the key radiation effects issues associated with the use of ceramic insulators in near-term fusion reactors.

SUMMARY

The key radiation effects issues associated with the successful operation of ceramic materials in components of the planned International Thermonuclear Experimental Reactor (ITER) are discussed. Radiation-induced volume changes and degradation of the mechanical properties should not be a serious issue for the fluences planned for ITER. On the other hand, radiation-induced electrical degradation effects may severely limit the allowable exposure of ceramic insulators. Degradation of the loss tangent and thermal conductivity may also restrict the location of some components such as ICRH feedthrough insulators to positions far away from the first wall. In-situ measurements suggest that the degradation of physical properties in ceramics during irradiation is greater than that measured in postirradiation tests. Additional in-situ data during neutron irradiation are needed before engineering designs for ITER can be finalized.

INTRODUCTION

Ceramic insulators are integral parts of numerous components essential for the heating, control, and diagnostic measurement of fusion plasmas. The proposed International Thermonuclear Experimental Reactor (ITER) will be the first fusion plasma machine to receive significant amounts of radiation damage due to the anticipated extended periods of operation with a deuterium-tritium fuel mixture, which generates 14 MeV neutrons and intense ionizing radiation fields. As shown schematically in Figure 1, the anticipated radiation fields to be experienced by ceramic components in ITER range from ionizing and displacement damage fluxes of <1 Gy/s and $<10^{-10}$ dpa/s at the neutral beam insulators located several meters outside of the vacuum vessel to $\sim 10^4$ Gy/s and $\sim 10^{-6}$ dpa/s for diagnostic component insulators located near the **first wall** (Clinard 1979, Scott *et* al. 1985, Zinkle and Hodgson 1992). Most of these ceramic insulators will have moderate electric fields (10 to 1000 V/mm) applied during their operation. In addition to maintaining adequate dimensional stability and mechanical properties through their design lifetime, ceramic insulators must also maintain acceptable physical properties during irradiation. The physical properties of greatest interest for fusion applications are electrical conductivity (dc and ac), dielectric loss tangent at frequencies from 50 MHz to 200 GHz, and thermal conductivity.

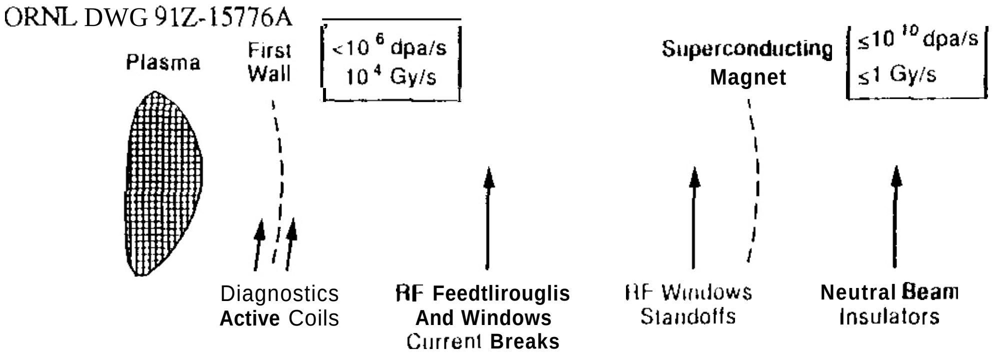

Fig. 1. Range of ionizing and displacive radiation fluxes anticipated for ceramic components in ITER

As discussed by Zinkle and Hodgson (1992), radiation-induced swelling and mechanical property degradation of ceramics typically become significant after damage levels greater than 1 dpa. This damage level is in excess of the anticipated lifetime dose of many of the ceramic components in ITER. Unfortunately, recent data suggests that significant degradation in the physical properties of ceramic insulators may occur during irradiation to doses much less than 1 dpa. **A** particularly important point regarding the experimental measurement of the physical properties **of** ceramics is that the value measured during irradiation can be significantly different from the postirradiation value (Zinkle and Hodgson 1992). This highlights the importance of obtaining data in-situ during irradiation, since the anticipated physical property changes that occur during operation are the relevant parameters for fusion design purposes. Unfortunately, with the exception of measurements of the transient radiation-induced electrical conductivity in ceramics (with little or no displacement damage), there has been only a handful of in-situ physical property measurements obtained on ceramics during irradiation. In the following sections, the available data on in-situ measurements **of** changes in the electrical conductivity. loss tangent, and thermal conductivity are summarized.

ELECTRICAL CONDUCTIVITY

Ionizing radiation excites bound electrons from the valence band of insulators into the conduction band. The resultant free electron-hole pairs are very mobile and can produce a large enhancement in the electrical conductivity of insulators. The electrical conductivity during irradiation is given by:

$$\sigma = \sigma_o + KR^{\delta} \qquad (1)$$

where σ_o is the conductivity in the absence **of** a radiation field (base conductivity), and the second term represents the radiation-induced conductivity (RIC) where R is the ionizing dose rate and K and δ are constants which depend on material and irradiation conditions (Rose 1955, van Lint et al. 1957, 1980, **Pells 1991b**). It is generally observed that the RIC is proportional to the ionizing radiation flux ($\delta = 1$), although the specific relation between RIC and flux depends on the details of electron-hole trapping and recombination (and hence on experimental variables such as temperature and impurity content). **Most** studies have found that the RIC is only weakly dependent on irradiation temperature (Zinkle and Hodgson 1992). Figure 2 summarizes some RIC data that has been obtained on high-purity oxide insulators during irradiation near **room** temperature (van **Lint** et al. 1968. Klaffky et al. 1980, Pells 1986, 1991b, Hodgson and Clement 1986). The room temperature conductivity in the absence of radiation was $<10^{-12}/\Omega$-m in

ORNL DWG 93M-5090R

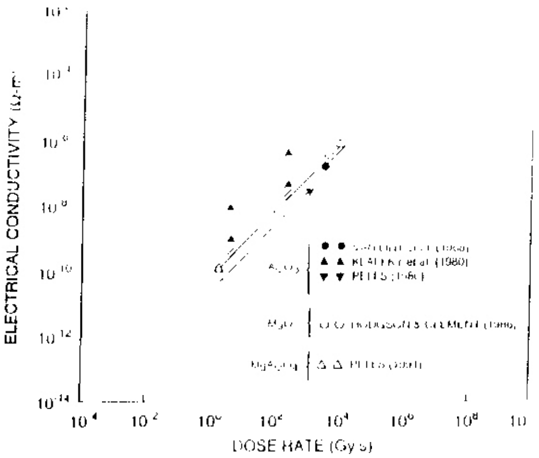

Fig. **2.** Radiation induced conductivity of pure oxide ceramics measured during irradiation near room temperature.

these materials. The RIC for the three oxides shown in Fig. 2 is directly proportional to the ionizing dose rate over a wide range (10 orders of magnitude) of flux. Since the maximum ionizing dose rate associated with a fusion reactor is ~10^4 Gy/s, Fig. 2 indicates that the associated maximum RIC expected in pure ceramic oxides in fusion reactor components would be ~10^{-6}/W-m. Although this conductivity is a significant increase compared to the nonirradiated room temperature value of <10^{-12}/W-m, it is too low to be of concern for fusion reactor insulator applications. The maximum conductivity allowable in fusion insulators ranges from ~10^{-4} to 1/W-m, depending on the application. Hence, based on prompt RIC measurements alone, one would anticipate that ceramic insulators should operate satisfactorily in a fusion irradiation environment.

Recent in-situ studies have determined that there is an additional, potentially more serious, degradation of the electrical resistivity of ceramic insulators that only occurs when displacement damage and an electric field are simultaneously present (along with ionizing radiation) during the irradiation (Ivanov et al. 1981, Hodgson 1989, 1991, 1992a, 1992b, Pells 1991a, Shikama et al. **1992).** Figure **3** shows the dose-dependent electrical conductivity of Al_2O_3 measured in-situ during **1.8** MeV electron irradiation at 450°C with an applied electric field of 130 V/mm (Hodgson 1989). The conductivity rapidly increased to a plateau regime at the beginning of the irradiation due to ionization-induced RIC effects. However, accumulated displacement damage in the presence of an applied electric field eventually caused the conductivity to increase above this plateau level. Hodgson (1989, 1991, 1992a, 1992b) has shown that the conductivity increase associated with accumulated displacement damage represents a <u>permanent</u> degradation in the base conductivity s_0 (Eq. 1) of the ceramic. As shown in Fig. **3,** the base conductivity measured in the absence of radiation (s_0) steadily increases with increasing dose and can become much larger than the RIC component. Of particular importance is that, unlike RIC, this radiation induced electrical degradation (KED) represents a permanent degradation of the electrical conductivity and cannot be recovered by thermal annealing (Pells 1991a). Permanent degradation in the electrical conductivity of A1203 and $MgAl_2O_4$ above 10^{-4}/W-m has been observed by Pells (1991a) after light ion irradiation.

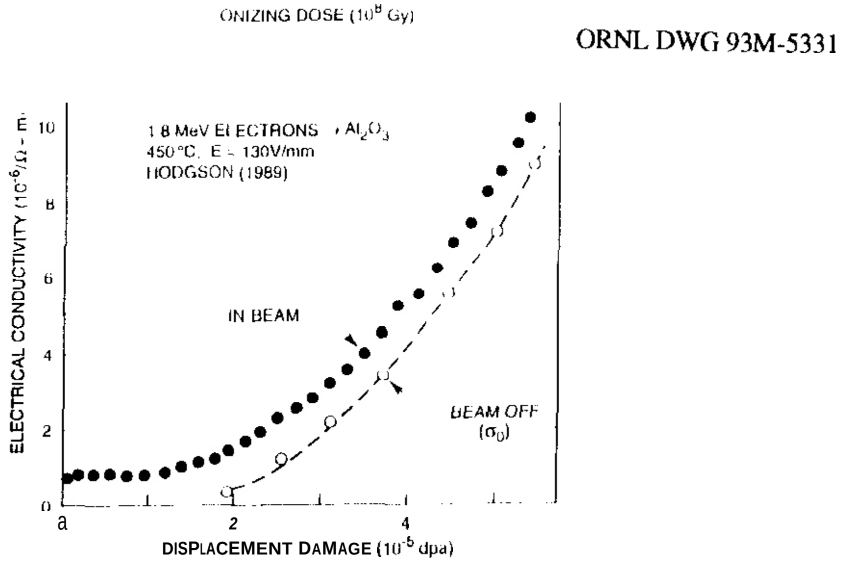

Fig. **3.** Fluence-dependent behavior of the electrical conductivity of Al_2O_3 measured in-situ **by** Hodgson (1989) during 1.8 MeV electron irradiation at 450°C with an applied dc electric field of 130 V/mm. The ionizing dose rate was 2800 Gy/s.

Complete quantification of the magnitude of RIED is hampered by a lack of **data** on the influence of electric field strength. temperature, and irradiation spectrum. In the absence of an applied electric field, permanent electrical degradation apparently does not occur in irradiated ceramics. Instead, several studies have shown that ceramics often become better insulators after irradiation if an electric field is not applied during the irradiation (Thatcher et al. 1964, Klaffky 1980, Zinkle and Hodgson 1992). As summarized by

Zinkle **and** Hodgson (1992), significant permanent electrical degradation can occur if an electric field ≥10 V/mm is applied during the irradiation, **and** the degradation process is accelerated if the electric field is greater than –60 V/mm. The degradation occurs for both dc and ac fields, up to at least 126 MHz (Hodgson 1992a). The electrical degradation process is apparently maximized at temperatures between 300 and 600°C (Zinkle and Hodgson 1992, Pells 1992a). This temperature dependence is consistent with suggestions (Hodgson 1991) that the RIED may be associated with the formation of metallic precipitates (colloids).

There are several indications that irradiation spectrum may have a significant influence on the kinetics of RIED. In particular, there is considerable evidence that the electrical degradation process is accelerated in radiation environments with a high ratio of ionizing to displacive radiation. Figure **4** compares the results of several recent RIED studies on Al_2O_3 that have been performed at temperatures of 450 to 530°C using

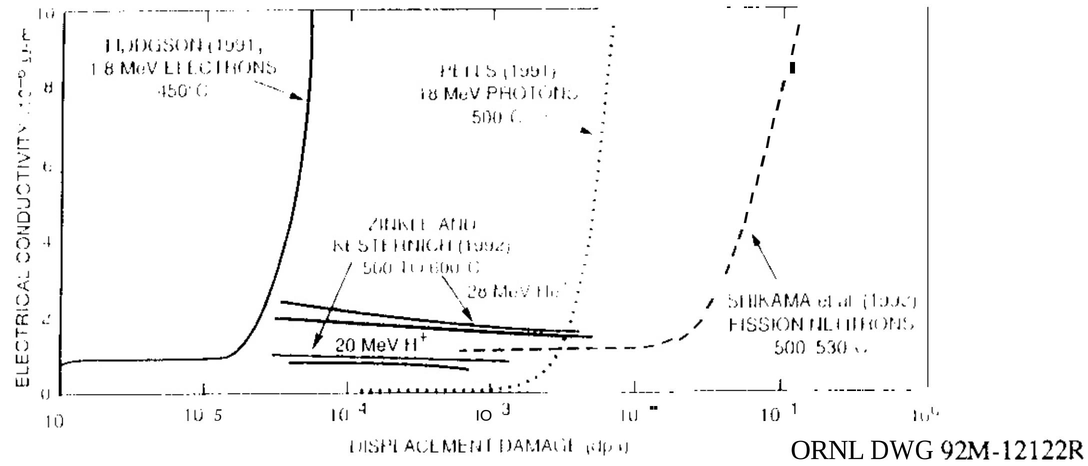

Fig. **4.** Effect of extended irradiation in different radiation fields on the electrical conductivity of Al_2O_3. The electric fields present during irradiation ranged from 130 V/mm (Hodgson 1991) to 500 V/mm (Pells 1991a and Shikama et al. 1992). The figure includes unpublished data by Zinkle **and** Kestemich obtained with an applied electric field of 500 V/mm.

electron, light ion, and fission reactor irradiation sources (Hodgson 1991, Pells 1991a, Shikama et al. 1992). It can be seen that the dose required to initiate significant permanent electrical degradation ($>1 \times 10^{-5}$/W-m) is $<10^{-4}$ dpa for electron irradiation, whereas >0.1 dpa is required to induce a similar amount of degradation during fission neutron irradiation. The accelerated degradation process found in highly ionizing environments such as electron irradiation may be due to the phenomenon of ionization-enhanced diffusion (**Zinkle** 1993). For ITER design applications, the fission neutron data shown in Fig. **4** is the closest match to the anticipated ionizing and displacement damage radiation fields in a fusion reactor first wall or blanket. However, additional data are needed over a wide range of temperature and dose in order to better **assess** the potential problems associated with RIED in ceramic insulators. In particular, extended in-situ neutron irradiation data are needed to determine if the RIED process causes the conductivity to significantly exceed 10^{-4}/W-m (the maximum allowable conductivity for some fusion insulator applications).

Due to the inherent difficulties associated with obtaining in-situ electrical conductivity **data,** there are only a few published studies that have monitored the performance of ceramic insulators during neutron irradiation with an applied electric field. As summarized by Thatcher et al. (1964). no permanent degradation was observed in ceramic insulators or capacitors after fission reactor irradiation at temperatures of *–250°C* to damage levels of about 2×10^{-3} dpa. In addition, little or no degradation occurred in Al_2O_3 or Y_2O_3 for neutron doses of 0.01 to 0.1 dpa at temperatures of 700 to 1100°C with an **applied** field of –40 V/mm (Grossman and Kaznoff 1966, Ranken and Veca 1988, Ranken 1991). Considering these **data** and other published RIED fission neutron studies (Gusekov and Sachkov 1959, Ivanov et al. 1981, Shikama 1992), it appears that RIED should not he a serious ITER design concern for damage levels less than 10^{-3} to 0.1 dpa, depending on the particular ceramic and irradiation temperature. Further study is clearly needed to improve the data base for ITER ceramic insulator engineering designs.

DIELECTRIC PROPERTIES AT RADIO FREQUENCIES

The power absorbed by a low-loss dielectric from an incident electromagnetic wave is given by

$$P = \omega \varepsilon' \tan\delta E^2 \qquad (2)$$

where w is the angular frequency of the ac electric field with root mean square amplitude E, ***e$*** is the dielectric permittivity, and tan d is the loss tangent (Kingery et al. 1976). For ITER applications, the dielectric **loss** factor, **c¢ tan** d, should he less than 10^{-2} for ion cyclotron (–100 MHz) heating applications and less than ahout 10^{-5} for electron cyclotron (–100 GHz) heating applications to avoid excessive heating in the dielectric. The dielectric permittivity of most ceramic insulators is approximately 10 e_0 over a wide range of temperature and frequency, where e_0 is the permittivity of free space. The value of tan **d** for low-loss dielectrics is dependent on temperature and frequency (Heidinger 1991). Typical unirradiated **loss** tangent values for a **low-loss** dielectric such as single crystal alumina at a frequency of 100 MHz are ~10^{-4} **at** room temperature and ~10^{-6} at 77 K.

Radiation-induced changes in the dielectric properties occur mainly in the **loss** tangent; most studies have found that the dielectric constant remains within 5% of its nonirradiated value (Zinkle and Hodgson 1992). The radiation-induced changes in the loss tangent can he described by two main components (Kingery et al. 1976, Pells and Hill 1986):

$$\tan\delta = \frac{\sigma}{\varepsilon' \omega} + \frac{\chi'' \varepsilon_o}{\varepsilon'} \qquad (3)$$

The first term represents electrical conductivity (s) joule heating losses associated with RIC and RIED. The second term represents polarization losses associated with the accumulation of displacement damage in the form of point defects or defect clusters, where c≤ is the imaginary part of the electric susceptibility. From **Eq.** (3) the **loss** tangent increase at a frequency of 100 MHz associated with RIC or RIED during irradiation **is** simply:

$$(\Delta \tan\delta)_e \cong 18\sigma \qquad (4)$$

where s is measured in units of $(\text{W-m})^{-1}$ and assuming a typical dielectric constant of **c¢/**e_0 = 10. It ***can*** be seen from Eq. **(4)** that an electrical conductivity of **-5** x10^{-5}/W-m in the dielectric produces an unacceptable loss tangent increase of 10^{-3} in ceramic components at frequencies relevant for ion cyclotron heating (100 MHz). Similarly, an unacceptable loss tangent increase of 10^{-6} also occurs at electron cyclotron heating frequencies (~100 GHz) for a ceramic electrical conductivity of **-5** x 10^{-5}/W-m. Hence, considerations of RIC and RIED are even more important for dielectrics in radio frequency heating components than for **dc** fusion insulator applications.

Postirradiation measurements have generally found that neutron doses in excess of 0.1 dpa are required to increase the room temperature loss tangent of low-loss ceramics to 10^{-3} (Heidinger 1991, Zinkle and Hodgson 1992). However, it should he recognized that these postirradiation measurements did not detect the electrical conductivity contribution associated with RIC or RIED (Eq. **4),** since an electric field was not applied during the irradiation. In-situ measurements during extended irradiation with an applied electric field must he performed to assess the magnitude of this component of the **loss** tangent degradation. In addition, Buckley and Agnew (1988) have shown that a significant amount of the loss tangent increase that is present immediately after irradiation is recovered by annealing at room temperature for several hours. Postirradiation measurements on neutron irradiated ceramic specimens are typically not performed until weeks or months after the end of the irradiation. Hence, much of the displacement-induced loss tangent degradation may have recovered prior to the measurements.

Figure 5 shows the loss tangent at 100 MHz measured in-situ for six different ceramic insulators during pulsed fission neutron irradiation **at** room temperature (Stoller et al. 1992, Goulding et al. 1993). **A** large transient increase in the loss tangent was observed in all six materials during the ~30 ms pulse length, and the loss tangent rapidly recovered to near the unirradiated value after the pulse. The in-situ loss tangent increases during the irradiation pulse were correlated with the ionizing radiation flux, and it was determined by Pb shielding experiments that the transient **loss** tangent increases were due to RIC effects, as described by Eq. **(4).** There was no correlation between the preirradiation (or post- irradiation) loss tangent and the loss tangent measured during the irradiation pulse, which underscores the importance of in-situ measurements for ITER design purposes. In a separate study, in-situ measurements made at higher frequencies (1 to 10 GHz) did not record any significant increase in the loss tangent of several ceramics during **pulsed** neutron irradiation above their nonirradiated room temperature values **of** ~10^{-4} (Edelson et al. 1969). The expected contribution of ionization-induced electrical conductivity (RIC) to the loss tangent at these higher frequencies is small (~10^{-5}) compared to the room temperature polarization losses (Eq. *3)*. However, prompt RIC effects could still be significant at these frequencies, since the maximum loss tangent that could be tolerated in a high power plasma heating system operating at 1 to 10 GHz (lower hybrid regime) would be ~10^{-5}, which corresponds to an RIC of 5×10^{-5}/W-m.

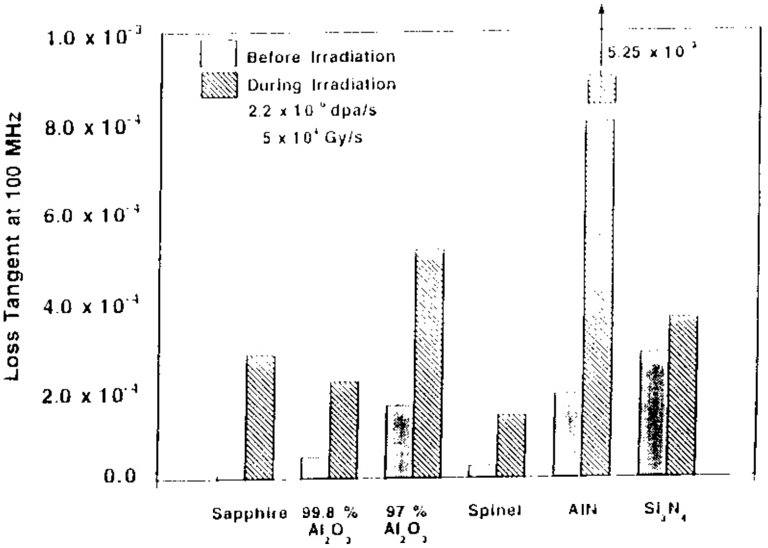

Fig. 5. Loss tangent of ceramic insulators measured in-situ before and during pulsed fission neutron irradiation at room temperature (Goulding et al. 1993).

There is only one known in-situ study that examined the effect of extended irradiation on the **loss** tangent. Buckley and Agnew (1991) found that the dielectric **loss** factor (ε' tan δ) of Al_2O_3 increased above an unacceptable level of 10^{-2} at 60 **MHz during room** temperature proton irradiation after a displacement dose of only ~10^{-3} dpa. An rf electric field of ~10 V/mm was applied during the irradiation. In view of the apparent strong influence of irradiation spectrum on the RIED measurements (Fig. 4), **it** appears essential for ITER design purposes that extended in-situ neutron irradiation experiments must be performed to confirm if a similar rapid degradation of the loss tangent occurs during neutron irradiation with a fusion-relevant applied rf field.

THERMAL CONDUCTIVITY

A high thermal conductivity is desirable to minimize thennal stresses that could lead to mechanical failure of ceramic components such as rf windows and insulating feedthroughs. Postirradiation measurements have found that the room temperature thermal conductivity of ceramics is reduced to 10 to 50% of the unirradiated value after neutron irradiation to doses of ~0.1 dpa, and that further irradiation produces an apparent saturation in the conductivity degradation (Wullaert et al. 1964, Wilks 1968, Sandakov et al. 1984, Rohde and Schulz 1990, Heidinger 1991, Yano and Iseki 1991). The rate of degradation of the thermal conductivity for ceramics irradiated or measured at cryogenic temperatures is proportionally much greater (Berman et al. 1955, McDonald 1963, Pryor et al. 1964, Salce and de Goer 1988).

These postirradiation results must he considered lower limits to the amount of thermal conductivity degradation that would occur during irradiation, since substantial annealing of point defects and small point defect clusters may occur at room temperature during the time interval between the end of the irradiation and the start of the postirradiation measurements (typically several months). The limitcd amount of published in-situ thermal conductivity data indicates that post- irradiation annealing at room temperature may induce a significant (>30%) recovery of the thennal conductivity degradation in some cases (McDonald 1963, Keilholtz et al. 1964. Davis 1966). Postirradiation annealing effects hecome insignificant for ceramics irradiated at temperatures well above room temperature.

In contrast to the electrical conductivity and loss tangent behavior, there does not appear to he any prompt degradation in the thcrmal conductivity of ceramics associated with ionizing radiation; no instantaneous changes in the thermal conductivity occurred during low flux (~1 Gy/s, ~10^{-10} dpa/s) fission reactor irradiations as the neutron source was turned on and off (McDonald 1963, Davis 1966). Figure 6 shows the calculated degradation in the thermal conductivity of Al_2O_3 at 400 K due to increased phonon-electron scattering associated with RIC (White 1993). It can he seen that RIC valucs as high as 10^{-2}/W-m produce a negligible (<0.1%) degradation in the thermal conductivity.

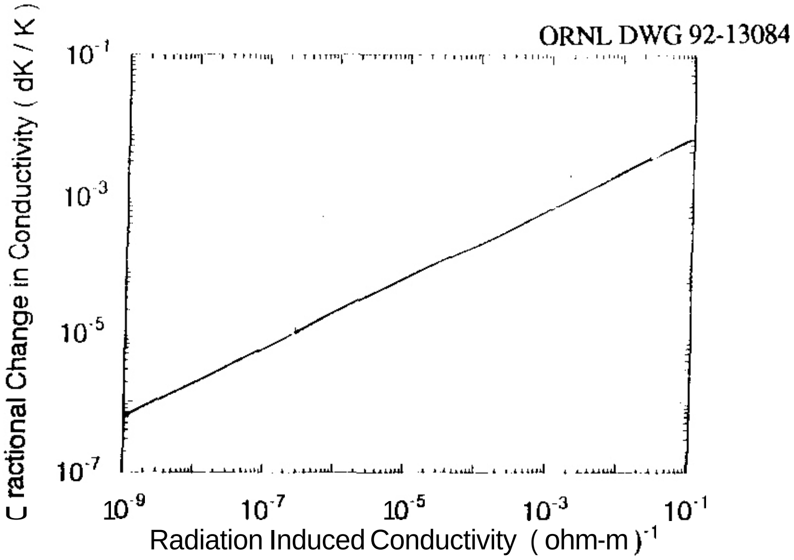

Fig. 6. Calculated fractional decrease in the thermal conductivity of Al_2O_3 due to radiation induced electrical conductivity (electron-phonon scattering) at 400 K.

Point defects and small defect clusters are effective phonon scatterers, and hence can cause large degradations in the thennal conductivity of ceramics (Klemens ct al. 1976, White 1993). Calculations by White (1993) indicate that a point defect concentration of 1 at. % can produce ~40% degradation in the thermal conductivity of Al_2O_3 at 400 K. Such point defect concentrations have been indirectly observed from lattice parameter and density measurements on ceramics after neutron irradiation near room temperature to damage levels of about 0.1 dpa (Wullaert et al. 1964, Thorne et al. 1967, Wilks 1968, Palentine 1980). Since point defects can recombine or coalesce during postirradiation annealing at room temperature, there is a strong need for in-situ thermal conductivity measurements to assess the amount of degradation that occurs during irradiation.

In-situ measurements are generally not needed for high temperature (>400°C) applications, since significant defect annealing will occur during the irradiation and subsequent postirradiation annealing at room temperature would be insignificant. However, it should be recognized that the amount at thermal conductivity degradation that occurs as the result of high-temperature irradiation (measured in-situ or postirradiation) will generally depend on the irradiation flux, due to defect annealing that occurs during the irradiation (Keilholtz et al. 1964). Hence, application of postirradiation thermal conductivity **data** must take into consideration the irradiation flux along with the accumulated amount of displacement damage.

A final concern is the possibility that different radiation-induced defect microstructures may develop in ceramics irradiated under fusion-relevant electric fields and mechanical stresses. In particular, the possible formation of colloids (metallic precipitates) in ceramics irradiated in the presence of an electric field would introduce an additional component to the thermal conductivity degradation since these colloids would be effective phonon scatterers (Klemens et al. 1976, White 1993).

DISCUSSION AND CONCISJSIONS

Due to their relative ease and lower cost, postirradiation measurements have been **used** almost exclusively over in-situ measurements in radiation effects studies on materials. Although a large amount of postirradiation physical property data has been accumulated on ceramic insulators, this data pool is not directly relevant for ITER design purposes since it is generally an improper measurement of the in-situ degradation. There are two reasons why in-situ measurements are needed for an accurate assessment of the potential performance of ceramic components in a radialion environment. First, in-situ measurements can detect transient property changes that occur during irradiation that either vanish quickly (e.g., RIC) or gradually recover (e.g., point defect annealing) after irradiation, and hence would not be fully detected in postirradiation measurements. Second, the recent discovery **of** new radiation-induced phenomena such as RIED demonstrates that the microstructural development during irradiation will, in general, depend strongly on the electro-mechanical environment in addition to the irradiation spectrum. This consideration requires that irradiations be performed with applied electric fields and mechanical stresses that are comparable to the intended fusion component operating condition. For example, the possibility that applied mechanical loads during irradiation might accelerate the mechanical property degradation of ceramics beyond that observed in conventional post- irradiation tests (due to radiation-enhanced crack initiation or stress corrosion cracking) should bc investigated.

It appears at the present time that the useful lifetime of ceramic iiisulators in fusion reactor components will be controlled by deterioration in their physical propcrties (e.g., electrical conduclivity or loss tangent) rather than by structural degradation (e.g., swelling or flexure strength). Unacceptable degradation in the physical properties of ceramic iiisulators may occur after damage lcvels as low as 10^{-3} dpa, depending on temperature, radiation spectrum, dose rate, and the elcctro-mechanical environment. This corresponds to less than one hour of full power operation in the first wall region of ITER.

In-situ studies at ITER-relevant radiation fluxes (ionizing and displacive) are urgently needed before the ITER engineering designs can be finalized. RIED effects associated with microstructural changes during irradiation with an applied electric field may cause unacceptable degradation in both the electrical resistivity and rf loss tangent of ceramic insulators at very low doses. There is some encouraging evidence from the limited number of published in-situ studies that operation of ceramic components at low (<200°C) or very high (>700°C) tempcratures may suppress the development of RIED. **A** comparison of in-situ **data** obtained from various irradiation sources suggests that highly ionizing radiation sources such as electrons or light ions produce an acceleration of the RIED process compared to neutron irradiation results (Fig, **4).** Ilowever, in recognition of the present lack of comprchensive in-situ neutron irradiation studies, the electron and ion irradiation results should he considered to he more appropriate for ITER design purposes than conventional postirradiation data obtained on neutron irradiated specimens.

ACKNOWLEDGMENTS

This work was supported hy the Office of Fusion Energy, U.S. Department of Energy, under contract DE-AC05-84OR21400 with Martin Marietta Energy Systems, lnc.

REFERENCES

Berman, R., Foster, E. L. and Rosenberg, H. M. (1955) in ***Report ofthe Bristol Conf. on Defects in Crystalline Solids,*** The Physical Society, London, p. 321.

Buckley, *S*. N. and Agnew, P. (1988) **J. *Nuclear Mater.*** 155-157,361

Buckley, *S*. N. and Agnew, **P**. (1991) in ***Microwave Processing of Materials I,*** W. B. Snyder **et** al., eds, MRS Symp. Proc. Vol. 189, Materials Research Soc., Pittsburgh, **p.** 503.

Clinard. F. W., **Jr**. (1979) J. ***Nucl.*** *Mater.* 85-86. 393.

Davis, M. V. (1966) in ***Proc. Conf. on Nuclear Applications of Nonfissionable Ceramics,*** A. **Boltax** and J. H. Handwerk. eds, American Nucl. Soc., Hinsdale, IL, p. **229.**

Edelson, D., Jaeger, R. E., and Williams, J. C. (1969) *J. Amer. Ceram. Soc.* ***52,*** **359.**

Goulding, R. H., Rasmussen, D. A., Stoller, R. E.. and Zinkle, S. J. (1993), "Transient Effects of Ionizing and Displacive Radiation on the Dielectric Properties of Ceramic Insulators," submitted to ***Phys. Rev, B.***

Grossman, L. N. and Kaznoff, **A.** I. (1955) in ***Proc. Conf. on Nuclear Applications of Nonfissionable Ceramics,*** A. Boltax and J. H. Handwerk, eds, American Nucl. Soc., Hinsdale, IL, **p. 421.**

Guskov, ***Yu.*** K. and Sachkov, V. F. (1959), *Sov. **J. Atomic Energy (Atomnaya Energ.) 6.204.***

Heidinger, R. (1991), *J.* ***Nucl. Mater.*** **179-181**, 64.

Hodgson, **E.** R. (1989), *Crys. Latt. Def. Amorphous* ***Mater.*** **18**, 169.

Hcdgson, E. R. (1991), **J.** ***Nucl. Mater.*** 179-181,383.

Hodgson. E. R. (1992a), ***Nucl. Instr. Methods B*** 65,298.

Hodgson, **E.** R. **(1992b)**, *J. Nucl.* ***Mater.*** 191-194, 552.

Hodgson, E. R. and Clement, S. **(1985)**, ***Rad. Effects*** 97,251

Ivanov, **V.** M.. Kalinin, ***G.*** M., Kuzovitkin, V. F., Sklizkov, S. P., Markina. N. V., Sarksyan, V. V., and **Skobeleva V. A. (1981)**, ***Inorganic Materials*** (Izv. Akad. Nauk **SSSR,** Neorgan. Mater.) 17, 1203.

Kingery, W. D., Bowen, H. K., and Uhlmann, D. R. (1976), ***Introduction*** *lo* ***Ceramics,*** 2nd Ed., Wilcy and Sons, New York, **p.** 913.

Klaffky, **R.** W. (1980) in *Special Purpose Materials Annual Progress Report,* DOE/ER-0048/1, U.S. Dept. **of** Energy. Washington, D.C., p. 19.

Klaffky, R. W., Rose, B. H., Goland, **A.** N., **and** Dienes, G. J. (1980), *Phys. **Rev.** B* **21, 3610.**

Klemens, P. G., Hurley, G. F., and Clinard, F. W. (1976), in *Proc. 2nd Topical Mtg. on the Technology of Controlled Nuclear **Fusion,** G.* L. Kulcinski **and** N. M. Burlcigh, eds, CONF760935, pp. 957-964.

McDonald. D. **L.** (1963), *Appl. Phys. Lett.* **2,** 175

Palentine, J. E. (1980), *J. Nucl. Muter* **92,** 43.

Pells, *G.* P. (1986), *Rad. Effects* **97,** 199.

Pells, G. P. (1991a), *J. Nucl. Mater* **184,** 177.

Pells, G. P. (1991b), J. *Nucl. Muter* 184, 183.

Pclls, G. P. and Hill, G. J. (1985), *J. Nucl. Muter.* **141-143,** 375

Pryor, **A.** W., **Tainsh, K.** J., aid White, G. K. (1964), *J. Nucl. Mater.* **14,** 208

Rankcn, W. **A.** (1991) in *Proc. DOE Workshop on Electrical Breakdown of Insulating Ceramics in a High Radiation Field,* CONF-9105175, National Technical Inform. Scrv., Springfield. VA, **p.** 433.

Ranken, W. **A.** and Veca, **A.** K. (1988) in *Space Nuclear Power Systems,* M.S. El-Genk **and** M. D. Hoover, eds, Orbit **Book** Co.. Malabar, FL, **p.** 329.

Rohdc, M. and Schulz. B. (1990), *J. Nucl. Mater.* **173,280**

Rose, **A.** (1955), *Phys. Rev.* Y7. 1538.

Salcc, B. **and** deGoer, **A.** M. (1988) in *Proc. Conf. Digest of the Int. Conf. on Defects in Insulating Materials,* Parma, **p.** 499.

Sandakov, **V.** S., Kostyukov, N. S., and Dubinin, G. V. (1984), *Irradiation Effects on the Ceramics Thermal Stress Resistance,* Research Inst. Atomic Reactors Report, RIAR-8 (620), Dimitrovgrad.

Scott, **I.** L., Clinard, F. W., Jr., and Wiffen, F. W. (1985), *J. Nucl. Muter.* **133 & 134, 156,**

Shikama, T., **Narui,** M.. Endo, **Y..** Sagawa, T., and Kayano, H. (1992), *J. Nucl. Mater.* **191-194**, 575

Stoller, R. E.. Goulding, R. H., and Zinkle, S. J. (1992), *J. Nucl. Muter.* **191-194**, 602.

Thatcher, R. K., et al. (1964), *The Effects of Nuclear Radiation on Electronic Components, including Semiconductors,* Battelle Memorial Institute Report REIC-36, Battelle Columbus Lab., Columbus, **OM.**

Thorne, R. P.. Howard, **V.** C., and Hope, B. (1967), *Proc. Brit. Ceram. Soc.* **7,** 449.

van Lint, V.A.J., Flanagan, T. M., Leadon, R. E., Nabor. J. A., and Rogers, V. C. (1980), *Mechanisms of Radiation Effects in Electronic Materials,* Vol. I, Wiley and Sons, New **York.**

van Lint, **V.A.J..** Harrity, J. W., and Flanagan, T. M. (1968), *IEEE Trans. on Nucl. Sci.*, **NS-15**, No. 6, 194.

White, D. **P.** (1993), *J. Applied Phys.* **73,2254.**

Wilks, R. S. (1968), *J. Nucl. Mater. 26,* 137.

Wullaert, R. **A.,** Burian, R. J., Melehan, J. B., Kangilaski, M., and Gates, J. E. (1964) in *Effects of Radiation on Materials and Components,* J. F. Kircher and R E Bowman, eds, Reinhold **Publ.** Corp., New York, pp. 277401.

Yano, T. and Iseki, T. (1991), *J. Nucl. Muter.,* **179-181,** 387

Zinkle, S. J. (1993), "Effectof Irradiation Spectrum on the Microstructural Evolution in Oxide Ceramics," this semiannual (DOE/ER-0313/14).

Zinkle, S. J. and Hodgson, E. R. (1992). J. *Nucl. Mater.* **191-194,** *58*

EFFECT OF IRRADIATION SPECTRUM ON THE MICROSTRUCTURAL EVOLUTION IN OXIDE CERAMICS -- **S.J.** Zinkle (*Oak* Ridge National Laboratory)

OBJECTIVE

To summarize recent microstructural evidence for ionization enhanced diffusion obtained on ion-irradiated oxide ceramics.

SUMMARY

Cross section transmission electron microscopy was utilized to examine the radiation-induced microstructural changes in oxide ceramics after irradiation with a wide variety of ion beams. The microstructure showed a strong dependence on ion mass and energy. The microstructural **results** have been correlated with the calculated depth-dependent partitioning between ionization and displacement damage. This correlation indicates that defect clusters do not form in $MgAl_2O_4$ if the ratio of energy deposited into electronic ionization to atomic displacements is greater than about 10. The corresponding ratio needed to suppress defect cluster formation in MgO and Al_2O_3 is 500 to 1000. Additional microstructural evidence obtained on the ion irradiated ceramic specimens suggests that the physical mechanism responsible for the lack of defect clusters in highly ionizing radiation environments is associated with ionization-enhanced diffusion (ED), which promotes annihilation of the point defects created by displacement damage during the irradiation. The most important parameter for IED is the ratio of ionizing to displacive radiation, since this is roughly proportional to the amount of ionization per dpa. However, the absolute magnitude of the ionizing radiation flux is also important.

INTRODUCTION

In a previous report [1], microstructural evidence was presented which showed that irradiation of oxide ceramics such as Al_2O_3 and $MgAl_2O_4$ with light ions caused a suppression in the nucleation of dislocation loops compared to heavy ion or neutron irradiation. It was proposed that the suppression in dislocation loop formation was associated with the high proportion **of** energy **lost** to electronic ionization events compared to displacement damage events during light ion irradiation. In the present report, additional microstructural evidence is presented which indicates that the suppression in dislocation loop nucleation is due to enhanced point defect diffusion (as opposed to a modification in the production of point defects).

EXPERIMENTAL PROCEDURE

Polycrystalline blocks **of** Al_2O_3 (GE Lucalox or Wesgo Al995), MgO (Ubc) and $MgAl_2O_4$ (Ceredyne) were sliced into foils of 0.5 mm thickness, and 3-mm-diameter TEM disks were cut from the foils. The disks were mechanically polished with 0.5 μm diamond paste, and then bombarded in a **3** x ***3*** array at room temperature or ***650°C*** in the triple ion beam accelerator facility [2] at *Oak* Ridge National Laboratory.

Table 1 lists the ion beam conditions which have been studied to date. The TRIM-90 [3] computer code was **used** to calculate the depth-dependent ionizing and displacive radiation doses for an Al_2O_3 target. **A** threshold displacement energy of 40 eV was used to calculate the displacements per atom (dpa) in Al_2O_3.

This displacement energy is intermediate between the measured [4] threshold displacement energies of 24 eV and 78 eV for the Al and O sublattices, respectively. The near-surface (0.5 µm depth) ionizing radiation dose **rate** ranged from 0.1 to 10 MGy/s, whereas the ionizing to displacive absorbed dose (IDAD) ratio

Table 1. Summary of Ion Beam Conditions

Ion **Beam**	Temp °C	**Flux** ($10^{16}/m^2$-s)	Fluence ($10^{20}/m^2$)	Dose at 0.5 µm depth (dpa)	Peak dose (dpa)	MGy/s @ 0.5 µm	IDAD @ 0.5 µm
1 MeV H^+	650	60	170	0.09	3.2	3	2000
	650	60	20	0.01	0.4	3	2000
	650	6	15	0.008	0.3	0.3	2000
	650	8	3	0.002	0.06	0.4	2000
1 MeV He^+	650	40	100	1	21	10	800
	650	40	10	0.1	2.1	10	800
	650	4	10	0.1	2.1	1	800
	650	4	1	0.01	0.2	1	800
3 MeV C^+	25	1.5	4	0.3	5	1	250
	25	1.5	0.4	0.03	0.5	1	250
	650	0.8	0.5	0.03	0.6	0.7	250
	650	0.2	0.3	0.02	0.4	0.1	250
	650	0.2	0.04	0.003	0.05	0.1	250
2.4 MeV Mg^+	25	20	22	14	54	14	20
	25	15	14	10	40	10	20
	650	15	14	10	40	10	20
2 MeV Al^+	25	11	30	30	90	7	13
	25	11	12	10	35	7	13
	650	11	40	30	100	7	13
	650	11	15	14	45	7	13
	650	11	5	4	14	7	13
4 MeV Zr^{3+}	25	0.3	2.2	20	34	0.3	2.4
	25	0.2	0.3	3	5	0.2	2.4
	25	0.2	0.1	1	1.5	0.2	2.4
	650	0.2	0.2	2	3	0.2	2.4
	650	0.2	0.02	0.2	0.3	0.2	2.4

ranged from 2.4 to 2000. Figure 1 shows the calculated depthdependent IDAD ratios for several of the ion **beams** used **in** this study. The IDAD ratio for ion irradiations is simply obtained from the depth-dependent ratio **of** the electronic stopping power to the nuclear **stopping** power.

Some of the C^+ ion irradiated specimens were coated with a thin layer ***of*** conductive carbon prior to irradiation to ensure that specimen charging did not occur. The microstructure of these carbon-coated specimens was found to be identical to that of uncoated specimens following irradiation.

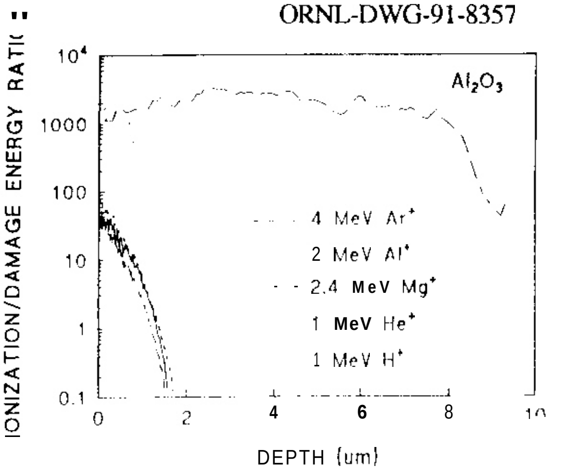

Fig. 1. **Depth** dependent ratio of ionizing to displacive absorbed dose (IDAD) for various ions incident in Al_2O_3.

Cross section transmission electron microscopy (TEM) specimens were prepared using techniques that are described elsewhere [5]. The microstructure of the cross section specimens was examined with a Philips CM-12 electron microscope. operating at 120 keV.

RESULTS

The dominant microstructural feature associated with ion irradiation of the three oxide ceramics was the formation of interstitial dislocation loops. The size and density of the **loops** was dependent on the damage level and irradiation spectrum (IDAD ratio). For a given dose, the size of the loops increased and the density of the loops decreased with increasing IDAD ratio. Most of the spectrum-dependent changes occurred near a sharp threshold IDAD value. The threshold IDAD ratio was about 10 for $MgAl_2O_4$, and 500 **to** 1000 for MgO and Al_2O_3.

Threshold Dose for Dislocation Loop Formation

Figure 2 shows the typical microstructure for $MgAl_2O_4$ irradiated with 4 MeV Zr^+ ions, which have a low IDAD ratio. A very high density **of** small dislocation loops were uniformly distributed throughout the irradiation region. Microstructural analysis of spinel specimens irradiated with Zr^+ ions at low doses, and analysis of spinel specimens irradiated with 4 MeV Ar^+ ions [6] indicates that the threshold dose for observable dislocation **loop** formation in $MgAl_2O_4$ is ≤ 0.1 dpa. This result is in agreement with observations on spinel irradiated with Xe^+ ions [7] and fission neutrons [8].

Figure 3 shows the cross section microstructure of Al_2O_3 after 3 MeV C^+ ion irradiation to a fluence of 3 x 10^{19} C^+/m^2. This produced a displacement damage level of about 0.4 dpa at the damage *peak* (2 µm depth) and a damage level of about 0.02 dpa at a depth of *0.5* µm. Small dislocation loops were observable between depths of about 0.5 µm and 2 µm, which suggests that the threshold dose for observable dislocation **loop** formation in Al_2O_3 is about 0.02 dpa.

In a previous study [9], the threshold dose for dislocation loop formation in MgO was determined to be less than –0.1 dpa for 2.4 MeV Mg^+ ion irradiation.

Effect *of* Irradiation Spectrum on Dislocation Loop Formation

Figure **4** shows the cross section microstructure of MgO following **1** MeV H^+ ion irradiation to a fluence of **1.7** x $10^{22}/m^2$, which produced a peak damage level of about **3** dpa. A high density of dislocation loops were present near the ion implantation region (11 µm depth), where the IDAD ratio approaches unity.

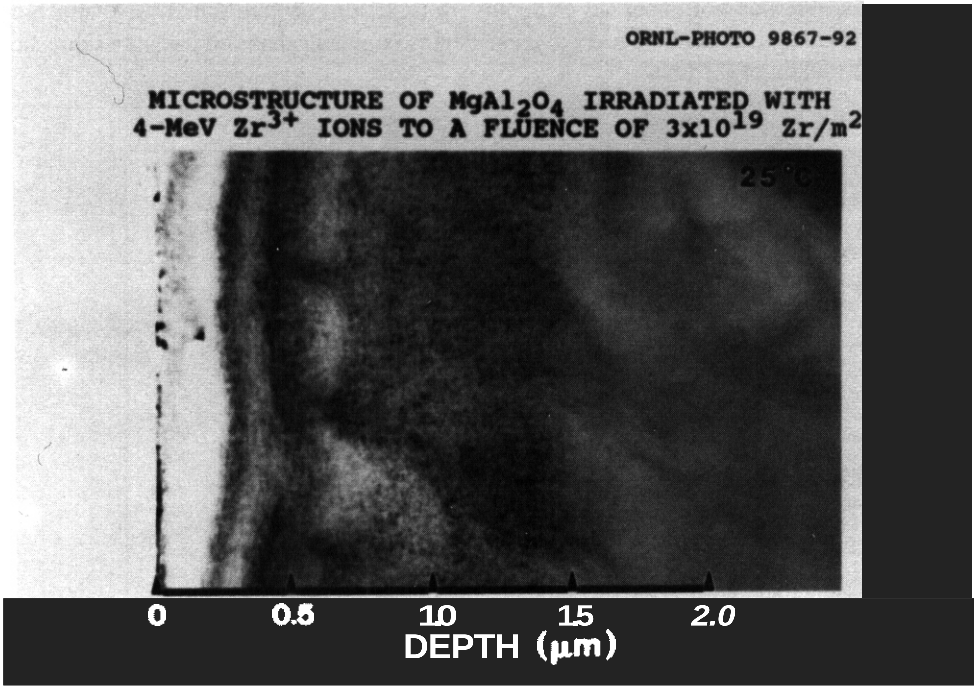

Fig. 2. Microstructure of MgAl$_2$O$_4$ after 4 MeV Zr^{3+} ion irradiation to a *peak* damage level of 5 dpa at 25°C.

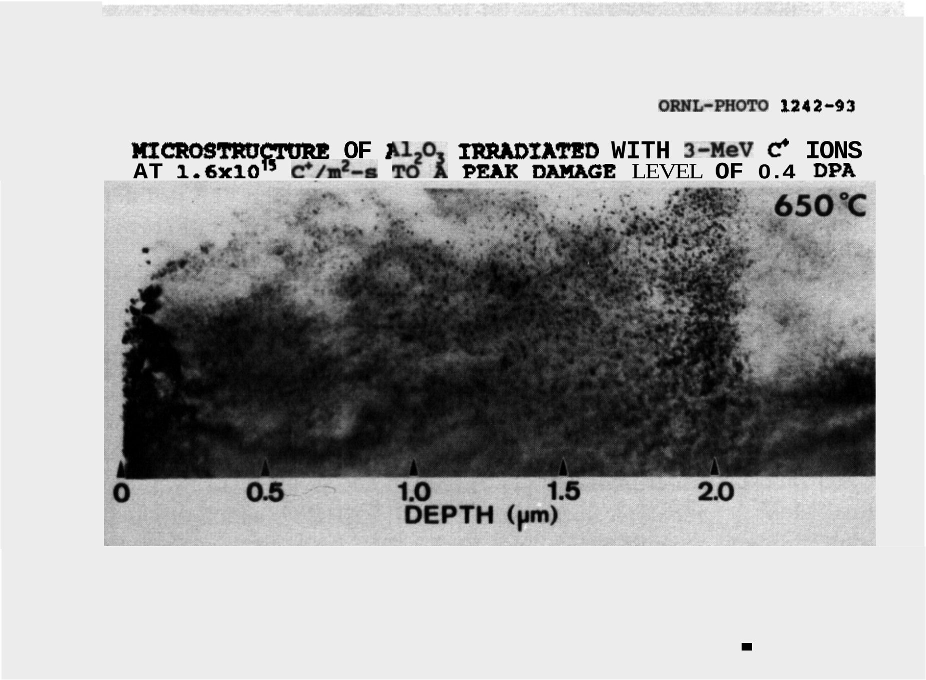

Fig. 3. Microstructure of Al$_2$O$_3$ irradiated with 3 MeV C$^+$ ions to a peak damage level of 0.4 dpa at 650°C.

Dislocation loop formation was not observed at depths up to 10 μm (where the IDAD ratio is >1000), despite the fact that the calculated damage level at these depths is greater than the measured threshold dose for dislocation loop formation of 0.1 dpa.

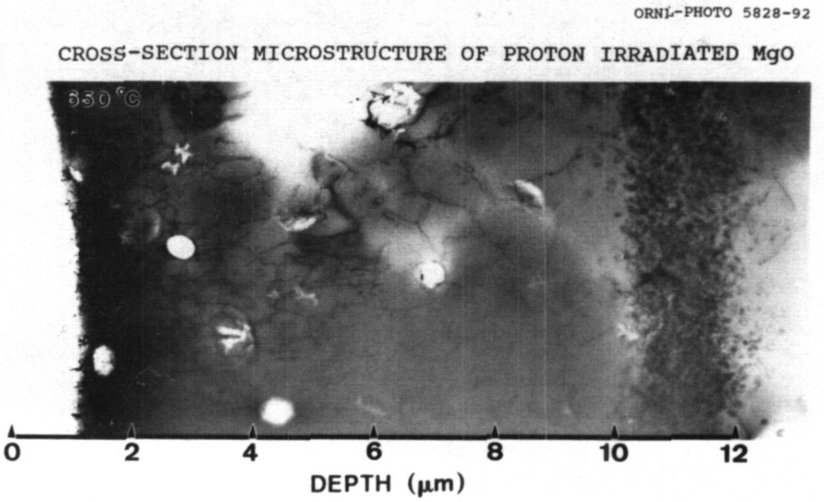

Fig. 4. Microstructure of MgO irradiated with 1 MeV H^+ ions to a peak damage level of 3 dpa at 650°C. Some sintering pores are visible in the micrograph.

Figure 5 shows the corresponding cross section microstructure of MgO following 1 MeV He^+ ion irradiation to a fluence of 1 x10 ^{22} He^+/m^2, which produced a peak damage level of about 21 dpa. Dislocation loop formation is pronounced near the ion implantation region (2.3 μm depth). A very low density of dislocation loops were observed at depths <1.8 μm, where the IDAD ratio is >500.

Spinel has been found to be particularly sensitive to irradiation spectrum variations. For example, Shaibani [10,11] was unable to observe any dislocation loop formation in stoichiometric spinel during 1 MeV electron irradiation (IDAD ratio ~10,000) up to very high damage levels. Stoichiometric spinel did not form any observable defect clusters after 3 MeV proton irradiation (IDAD ratio ~2500) at 600°C to a damage level of 0.1 dpa [12]. We have previously reported that dislocation loop formation in ion irradiated spinel is suppressed if the IDAD ratio is greater than ~10 [1]. Figure 6 shows the cross section microstructure of spinel irradiated with 2 MeV Al^+ ions to a fluence of 1.5 x 10^{21} Al^+/m^2, which produced a displacement damage level of about 14 dpa at a depth of 0.5 μm. Dislocation loops did not form in the near-surface region, and a defect-free region was also observed surrounding an internal defect sink. Large defect-free regions have also been observed adjacent to grain boundaries in Al^+-irradiated spinel [13]. These microstructural observations suggest that ionizing radiation is somehow effective in enhancing point defect diffusion in spinel.

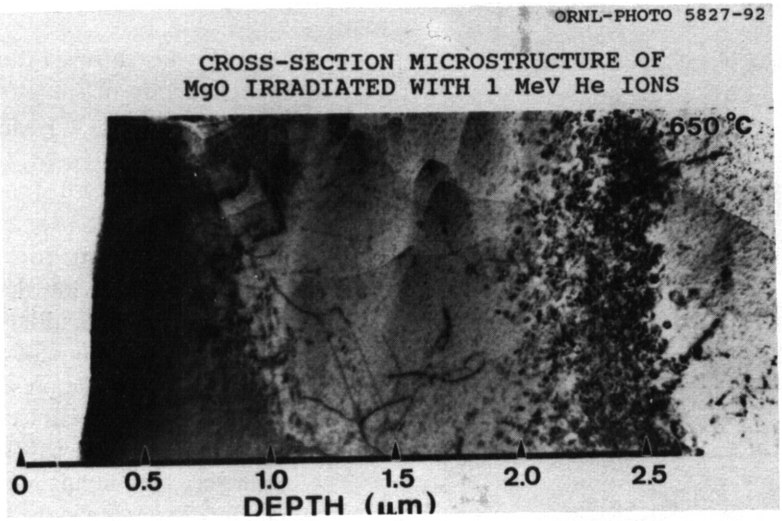

Fig. 5. Microstructure of MgO irradiated with 1 MeV He+ ions to a peak damage level of 21 dpa at 650°C.

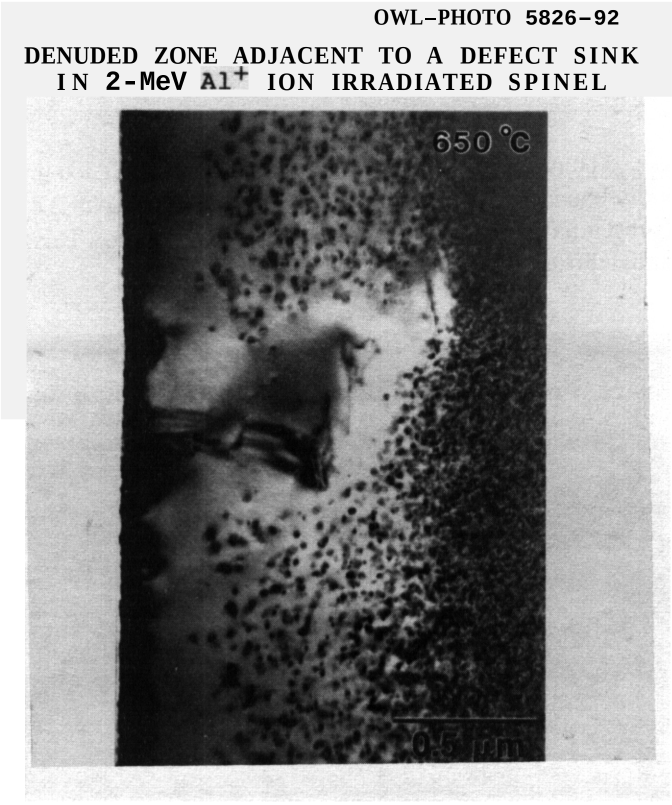

Fig. 6. Defect-free zones adjacent to the *surface* and an internal defect *sink* in MgAl$_2$O$_4$ irradiated with 2 MeV Al$^+$ ions to a fluence of 1.5×10^{21} Al$^+$/m^2 at 650°C.

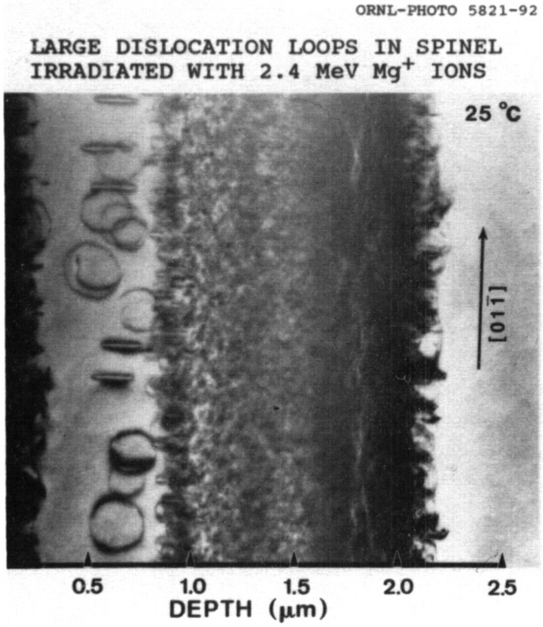

Fig. 7. Microstructure of $MgAl_2O_4$ irradiated with 2.4 MeV Mg^+ ions to a peak damage level of 54 dpa at 25°C.

Figure shows the cross-section microstru ıre of spinel irradiated at room temperatu with 2.4 MeV Mg^+ ions to a fluence of .2 x 10^{21} Mg^+/m^2 (peak damage level of 5 dpa). An abrupt transition in the microstru ıre occurs at a depth of about 0.8 µm (corr ponding to an IDAD ratio of about 10). A very low density of large (250 nm diam r) interstitial dislocation loops lying on { 0} planes are present in the near-surface re on. The presence of such a low density o large dislocation loops implies that the p int defect diffusivity must have been very igh in this region. The loop size rapidly de eases and the loop density rapidly increases t depths greater than 0.8 µm, which i plies that the point defect diffusivit is much lower in this region compared near the surface.

Further evidence of enhanced point defect diffusion in $MgAl_2O_4$ during lig ion irradiation is obtained from an examination of the grain boundaries. As shown in Fig. 8, irradiation th 2.4 MeV Mg^+ ions at room temperature produced substantial subsurface grain boundary cavitatior This implies that irradiation enhances not only interstitial diffusivities but also vacancy diffusivities.

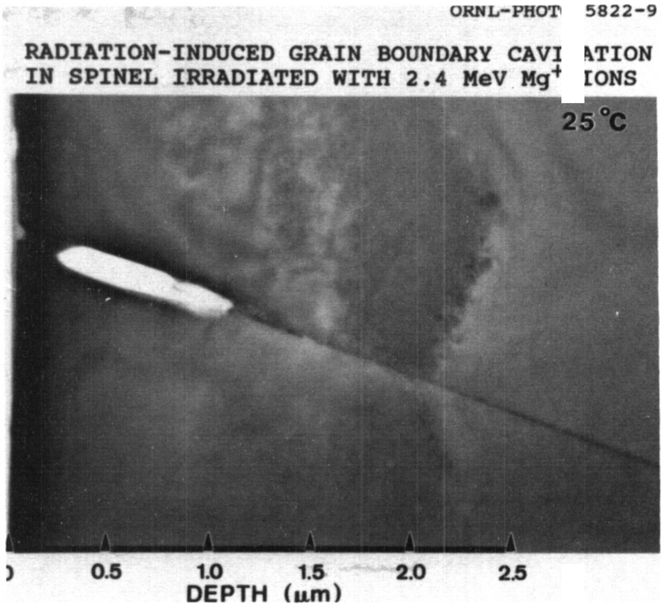

Fig. 8. Radiation-induced grain boundary cavitation in $MgAl_2O_4$ irradiat with 2.4 MeV Mg^+ ions to a peak damage level of 54 dpa at 25°C.

Effect of Ionizing Radiation Flux on Dislocation Loop Formation

A limited study of flux effects for a fixed ion mass and energy has been completed to date. The microstructural results indicate that the absolute magnitude of the ionizing flux can influence the size and density of dislocation loops. Figure 9 compares the cross section microstructure of 2 spinel specimens that were irradiated to comparable damage levels with 3 MeV C^+ ions at two different fluxes. Due to the high initial IDAD ratio of 3 MeV C^+ ions, dislocation loop formation only occurred near the ion implanted region (2.2 μm depth) where the IDAD ratio approached a value of 10. The dislocation loops in the "high flux" specimen were larger and of lower density compared to the "low flux" specimen. This implies that the point defect diffusivity was enhanced for the "high flux" irradiation condition.

Figure 10 compares the microstructure in Al_2O_3 following 1 MeV H^+ ion irradiation at two different fluxes. As noted previously [1], dislocation loops were not observed at intermediate depths in the "high flux" specimen (~3 x 10^6 Gy/s at a depth of 0.5 μm). However, irradiation at an order of magnitude lower flux (0.3 x 10^6 Gy/s at a depth of 0.5 μm) produced some observable dislocation loops despite the fact that the total accumulated dose was only 0.01 dpa, which was one-tenth of the "high flux" specimen. This observation is consistent with the proposed interpretation that high fluxes of ionizing radiation cause an enhancement in the point defect diffusivities.

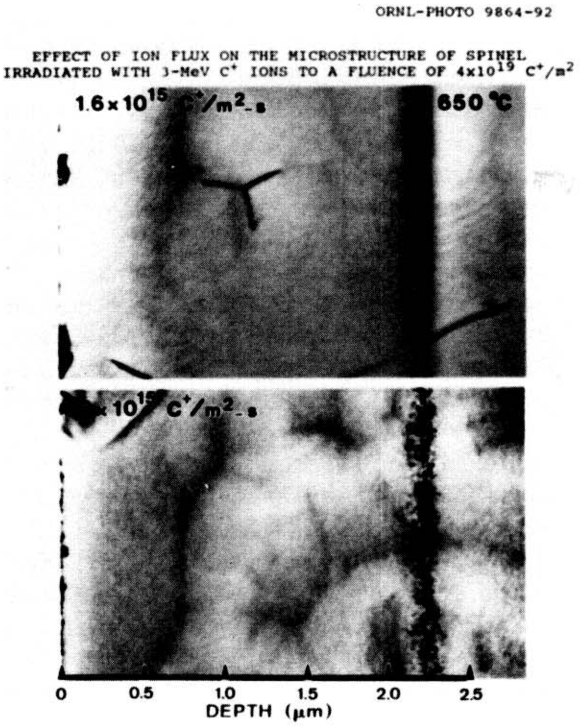

Fig. 9. Effect of ion flux on the microstructure of $MgAl_2O_4$ irradiated with 3 MeV C^+ ions to a peak damage level of about 0.5 dpa at 650°C.

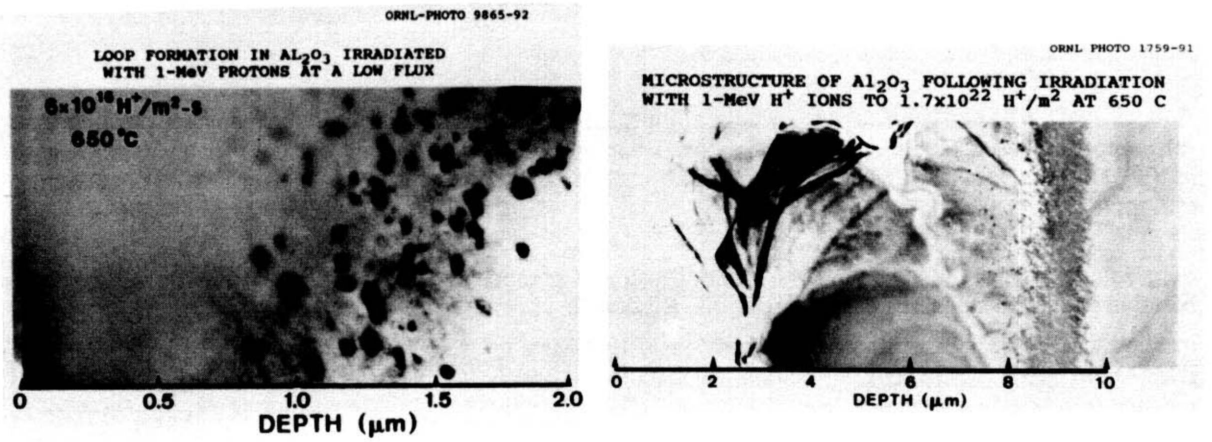

Fig. 10. Comparison of the microstructure of Al_2O_3 irradiated at two different fluxes with 1 MeV protons at 650°C. (a) 6 x 10^{17} H^+/m^2-s, (b) 6 x 10^{16} H^+/m^2-s.

DISCUSSION

The suppression of dislocation loop formation in oxide ceramics irradiated with light ions (high IDAD ratio) could in principle be due to two different effects; either a decrease in the defect production rate or an increase in the amount of point defect diffusion. It appears unlikely that the defect production rate was significantly reduced for the light ion irradiation case, since defect clusters were observed in Al_2O_3 irradiated with a low flux of protons after a dose of only ~0.01 dpa (Fig. 10). In addition, considerable growth occured in the few dislocation loops that were nucleated in regions with high IDAD ratios (e.g., Fig. 7). This suggests that the suppressed dislocation loop density is not associated with a reduction in defect production. Defect production measurements by Luera [14] on Al_2O_3 irradiated with low energy ions indicate that protons actually have a higher defect production rate (relative to the calculated displacement damage rate) than heavier ions such as N^+ or Xe^{++}. Buckley and Shaibani [11] observed that the lack of defect clusters in spinel irradiated with 1 MeV electrons (IDAD ratio ~10,000) was due to difficulties in loop nucleation rather than point defect production--preexisting dislocations climbed readily during electron irradiation, which is evidence for a significant concentration of point defects.

Several previous studies have found that the radiation-induced changes in oxide ceramics are dependent on the irradiation spectrum. The most extensive study to date on spectrum effects was performed by Eernisse, Arnold and coworkers on SiO_2 and Al_2O_3 [15-17]. Light ions such as H^+ and He^+ (which have a high IDAD ratio) produced less volume swelling per dpa in Al_2O_3 compared to heavier ions. In addition, the volume expansion induced by the heavy ion irradiation could be relieved by subsequent electron or H^+ ion irradiation. Walker [18] reported similar annealing of volumetric swelling for BeO that was irradiated with fission neutrons and subsequently irradiated with 1 MeV electrons. Irradiation of BeO with electrons alone did not produce any significant change in the lattice parameter. It was suggested that electron irradiation enhanced the mobility of point defects, which led to enhanced point defect recombination.

There is relatively little published information on radiation enhanced diffusion in ceramics [19,20]. Bourgoin and Corbett [19] have summarized a variety of physical mechanisms which could produce enhanced diffusion in semiconductors and insulators. Of direct interest is the phenomenon of ionization enhanced diffusion (IED). They discussed several mechanisms which could produce IED, including (1) reduced point defect migration energies due to an ionization-induced change in the charge state of the migrating defect, (2) Electro-striction enhanced diffusion, in which the presence of electrons and holes in the conduction or valence bands results in a change of the lattice constant, (3) the Bourgoin saddle point jump mechanism, and (4) multiple ionization of anions which would give an anion defect enough energy to cause migration. Irradiation studies performed on metals have determined that moderate levels of ionizing radiation promotes recombination of point defects [19,21-23].

Another ionization mechanism which would produce enhanced diffusion in insulators is defect creation by self trapped excitons [19,24]. This mechanism is important in alkalai halides and in other insulators such as SiO_2, but has not been found to produce significant amounts of displacement damage in MgO or Al_2O_3 [24-26].

Supporting evidence for ionization enhanced diffusion of point defects in irradiated oxide ceramics can be found in published studies of cavity formation. Resolvable cavities were present in Al_2O_3 after triple beam irradiation at room temperature with 2 MeV Al^+, 1.44 MeV O^+ and 200-400 keV He^+ ions (combined IDAD ratio ~100) [27]. Cavity formation is generally not observed in neutron-irradiated Al_2O_3 unless the irradiation temperature is well above room temperature. The presence of resolvable cavities at room temperature in the light ion irradiated specimens may be due to IED.

CONCLUSIONS

The microstructural changes in oxide ceramics induced by ion irradiation are dependent on the **mass** and energy of the incident ion. The microstructural evidence suggests that ionization enhanced diffusion (IED) promotes long range diffusion and recombination **of** point defects. The results are most closely correlated with the ratio of ionizing to displacive absorbed dose (IDAD). The absolute magnitude of the ionizing radiation flux is also an important parameter.

ACKNOWLEDGEMENTS

Most of the ion irradiations were performed by S.W. Cook. The cross section TEM specimens were prepared by A.M. Williams, J.W. Jones and J.M. Cole. **A** portion **of** the microscopy on the C^+ ion irradiated Al_2O_3 specimens was performed by Y. Katano (JAERI).

FUTURE WOKK

Specimens of Al_2O_3, $MgAl_2O_4$, and Si_3N_4 will be irradiatcd with varying dual-beam fluxes of 4 MeV Fe^{++} and 1 MeV He+ ions in order to further investigate the importance of the IDAD ratio, ionizing **flux,** and irradiation spectrum on microstructural evolution in insulating ceramics.

REFERENCES

1. S.J. Zinkle, Fusion Reactor Materials Semiann. Prog. Report for Period Ending March 31, 1991, WEER-0313110.

2. M.B. Lewis, W.R. Allen, R.A. Buhl. N.H. Packan, S.W. Cook, and L.K. Mansur, Nucl. Instr. Meth. **B 43 (1989) 243.**

3. J.F. Ziegler, J.P. Biersak, and U.L. Littmark, The Stopping and Range of Ions in Solids (Pcrgamon **Press,** New York, 1985).

4. P. Agnew. Phil. Mag. ***A*** 65 (1992) 355

5. S.J. Zinkle, C.P. Haltom, L.C. Jenkins, and C.K.H. DuBose, J. Electron Microscopy Techn. 19 (1991) **452.**

6. R. Yamada, S.J. Zinkle, and G.P. Pells, J. Nucl. Mater., submitted (1993).

7. **H. Abe,** C. Kinoshita, and K. Nakai. J. Nucl. Mater. 179-181 *(1991)* 917.

8. K. Nakai, K. *Fukumoto*, and C. *Kinoshita*, J. Nucl. Mater. 191-194 **(1992)** 630

9. S.J. Zinkle, in Structure-Property Relationships in Surface-Modified Ceramics, Eds. C.J. McHargue et al. (Kluwer Academic Publ., 1989) **p.** 219.

10. S.J. Shaibani, D. Phil. Thesis, Univ. Oxford, Oxford, UK, 1986

11. S.N. Buckley and S.J. Shaibani, Phil. Mag. Lett. 55 (1987) 15.

12. P.A. Knight, D. Phil. Thesis, Univ. Oxford, Oxford, UK, 1989.

13. S.J. Zinkle, in Effects of Radiation on Materials, ASTM STP 1125, Eds. R.E. Stoller, A.S. Kumar and D.S. Gelles (ASTM, Philadelphia, 1992) p. 749.

14. T.F. Luera, J. Appl. Phys. 51 (1980) 5792.

15. E.P. EerNisse, J. Appl. Phys. 45 (1974) 167.

16. G.W. Arnold, G.B. Krefft and C.B. Norris, Appl. Phys. Lett. 25 (1974) 540.

17. G.B. Kreffl and E.P. EerNisse, J. Appl. Phys. 49 (1978) 2725.

18. D.G. Walker, J. Nucl. Mater. 14 (1964) 195.

19. J.C. Bourgoin and J.W. Corbett, Rad. Effects 36 (1978) 157.

20. Hj. Matzke, Rad. Effects 64 (1982) 3.

21. A. Dunlop and D. Lesueur, Rad. Effects 117 (1991) 91.

22. A. Iwase, T. Iwata, S. Sasaki and T. Nihara, J. Phys. Soc. Jpn. 59 (1990) 1451.

23. I.P. Chemov et al., Rad. Effects 97 (1986) 155.

24. N. Itoh, Rad. Effects 110 (1989) 19.

25. C. Itoh, K. Tanimura, and N. Itoh, J. Phys. C 19 (1986) 6887

26. F. Jollet, J.P. Duraud and C. Noguera, Rad. Effects 110 (1989) 185

27. S.J. Zinkle and S. Kojima, J. Nucl. Mater. 179-181 (1991) 395.

ELECTRICAL CONDUCTIVITY OF CERAMIC INSULATORS DURING EXTENDED ION IRRADIATION WITH AN APPLIED ELECTRIC FIELD -- S.J. Zinkle (ORNL) and W. Kesternich (Forschungszentrum Juelich)

OBJECTIVE

The objective of this study is to examine whether ceramic insulators suffer radiation-induced electrical degradation (RIED) during irradiation with an applied electric field.

SUMMARY

The initial results are presented from a cyclotron ion irradiation program investigating radiation-induced conductivity (RIC) and radiation-induced electrical degradation (RIED) of ceramic insulators. Polycrystalline specimens of Al_2O_3, $MgAl_2O_4$, AlN and Si_3N_4 were irradiated with either **28** MeV He^{++} or **20** MeV H^+ ions at temperatures between 150 and 600°C with an applied dc electric field of 100 to 500 V/mm. **A** large prompt increase in the electrical conductivity **was** observed in **all** of the specimens during irradiation. However, there was no evidence for permanent electrical degradation in any of the specimens for damage levels **up** to about 5×10^{-3} displacements per atom.

INTRODUCTION

Insulating ceramics are essential for the successful operation of numerous components in a fusion reactor, including radiofrequency heating systems, the breeding blanket and first wall **(as** a current break), and numerous diagnostic systems [1-3]. It **has** long been known that the electrical properties of insulating materials are dramatically altered by energetic radiation, due to the excitation of valence electrons into the conduction band [4-7]. The high mobility and capture cross sections of electrons and holes in the conduction band generally results in recombination **of** the electron-hole pairs within $<10^{-9}$ s [7]. Hence, the magnitude of this radiation-induced conductivity (RIC) can only he determined by in-situ experiments conducted while the specimen is being irradiated. It has generally been ohserved that the electrical conductivity of the ceramic reverts to a value very near its preirradiation value immediately after the irradiation **source** is turned off [7,8]. One notable exception is the class of alkali halides, which can suffer permanent displacement damage associated with ionizing radiation alone [9].

Most studies have found that the increase in the electrical conductivity of insulating materials during irradiation is nearly proportional to the ionizing radiation dose rate [6,7,10-14]:

$$\sigma = \sigma_0 + K R^{\delta} \qquad (1)$$

where σ_0 is the conductivity in the absence of radiation, R **is** the ionizing radiation dose rate, K is a proportionality conslant, and δ is the dose rate exponent, which is on the order of 1.0.

According to fusion design studies, the maximum conductivity that is allowable in ceramic insulators during operation is between 10^{-4} S/m and 1 S/m, depending on the particular application [1]. Fortunately, the prompt RIC associated with fusion-relevant ionizing radiation levels (1 to 10^4 Gy/s) is generally less than 10^{-6} S/m in oxide ceramic insulators. Figure 1 shows the measured RIC in several oxide ceramic insulators as a function of ionizing dose rate [10-14]. It can be seen that the RIC is proportional to the ionizing dose rate over a very wide range of ionizing dose rates (10 orders of magnitude). Whereas the prompt RIC can be very significant at fusion-relevant ionizing dose rates compared to the typical nonirradiated room temperature conductivities of 10^{-12} S/m, the conductivity is still well below the practical upper limit for fusion insulator applications of 10^{-4} to 1 S/m

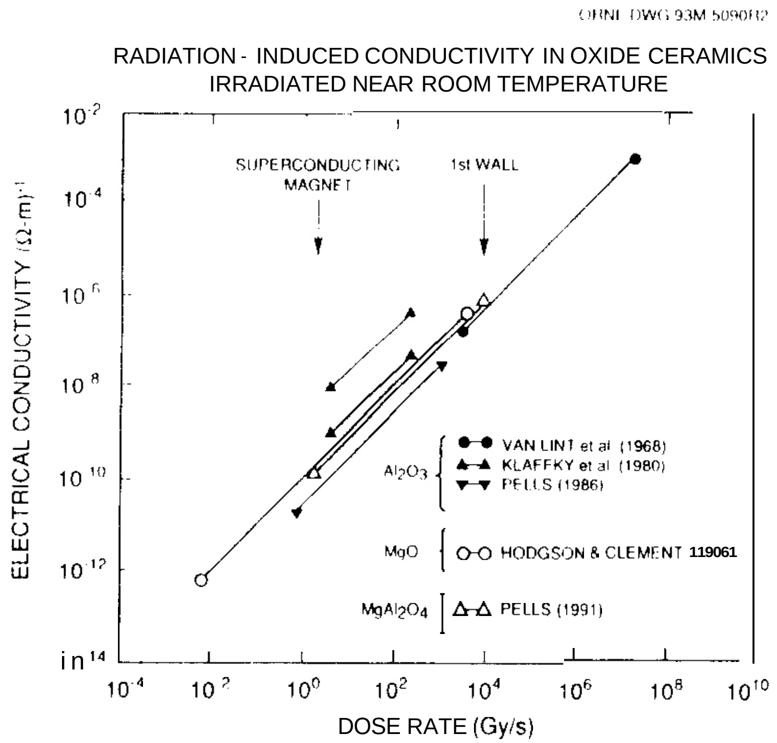

Fig. 1. Effect of ionizing dose rate on the electrical conductivity of oxide ceramics irradiated near room temperature [10-14]

Recently, several studies have found that severe permanent increases in the electrical conductivity of ceramic insulators may occur during extended irradiation if an electric field is applied during the irradiation [15-22]. Most of the data available on this new phenomenon are due to Hodgson [16-18,22], who used electron irradiation to show that radiation-induced electrical degradation (RIED) did not occur unless the radiation produced atomic displacements in addition to the ever-present ionizing radiation component. Hodgson also demonstrated that application of an electric field during the irradiation was necessary to produce RIED, and that the degradation stopped as soon as the electric field was turned off. On the other hand, irradiation without an applied electric field typically causes a slight improvement in the electrical resistivity of ceramics, due to an increase in the trap concentration associated with displacement damage [1,8,23]. RIED has been observed to occur for electric fields as small as ~20 V/mm [18]. This phenomenon is a more serious technological issue than the well-known RIC because the observed electrical degradation is permanent [16,17] (i.e., it is retained even after the specimen is removed from the radiation field). In addition, the degradation apparently cannot be removed by thermal annealing [19]. The magnitude of the permanent RIED observed to date has exceeded 10^{-4} S/m [19,21]. Permanent increases in the electrical conductivity of Al_2O_3 and $MgAl_2O_4$ above 10^{-5} S/m have been observed after exposure to damage levels of 0.001 to 0.1 dpa, and there is no definitive evidence of any saturation in the RIED [16-20]. There is limited evidence that the electrical degradation is maximized at irradiation temperatures near 450°C. with relatively little degradation occurring at temperatures $\leq$200°C or $\geq$650°C [1,18,19].

Observations of RIED reported to date have been limited to 3 oxide ceramics, Al_2O_3, MgO, and $MgAl_2O_4$ [15-22]. The microstructural alteration responsible for the large permanent increase in the electrical conductivity has not yet been identified, although there are several indications that it may he due to the formation of metallic precipitates (colloids). The evidence in support of colloid formation includes optical observation of large opaque features [22], reduction of the activation energy for conduction to values coparable to metals [1,19], and the temperature dependence of the RIED process [1,19].

The present study was initiated in order to generate additional data on this intriguing physical process, and to determine by postirradiation analytical electron microscopy whether colloid formation had occurred. Since materials with ionic bonding are generally thought to be more susceptible to colloid formation [9], two types of nitride ceramics with predominantly covalent bonds were included in the experimental matrix in order to assess the importance of bond type on RIED susceptibility.

EXPERIMENTAL PROCEDURE

Four commercial polycrystalline ceramics were used for this study: Al_2O_3 (Wesgo AL-995), $MgAl_2O_4$ (Ceredyne), AlN (Cercom), and Si_3N_4 (Kyocera SN733). Wafers of thickness 0.25 nun were cut from the hulk material using a low-speed diamond saw, and disks of 3 mm diameter were ultrasonically cut from the wafers. The 3-mm diameter disks were mounted on a steel stub with a low-melting wax and were precision ground on a diamond wheel to a final thickness of 0.15 to 0.16 mm with the aid of a commercial precision grinding tool. The final 15 µm of material was removed in 3 passes of 5 µm each.

Disks of the four ceramic materials were brazed to a nickel substrate. Pure nickel was chosen as the substrate material due to its relatively high thermal and electrical conductivity and also because its coefficient of thermal expansion was comparable to that of the four ceramics (which thereby minimized temperature-induced stresses on lhe thin ceramic disks). Attempts to diffusion bond the ceramic disks to a Ni substrate using a thin (10 µm) Au foil produced poor adhesion for the AlN and Si_3N_4 specimens. Satisfactory adhesion of all 4 ceramic TEM disks was achieved by brazing the specimens onto a 5-nun thick Ni base using a 60 µm thick Ag-19.5%Cu-5%In-3%Ti brazing foil. The braze cycle consisted of heating slowly to 820°C, holding at temperature for 20 minutes, then heating at 5°C per minute up to 920°C, holding for 5 minutes, then cooling at 10 to 20°C per minute to room temperature. The ceramic disks were precisely aligned on the Ni substrate during the brazing process with the aid of a ceramic alignment fixture. The brazed surface of the ceramic disks served as the back (ground) electrode, and ensured that there was good thermal contact between the ceramic disks and the Ni substrate. This latter feature was important because the specimen thermocouple was located in the Ni substrate approximately 2.5 mm beneath the specimens, and the high beam currents utilized in our irradiations would have produced an unacceptable temperature gradient between the specimens and the thermocouple if there was poor thermal contact. The specimen temperatures given in this paper have been corrected for the temperature gradient between the thermocouple and the specimens (<50°C for the highest flux irradiations).

The center and guard ring electrodes were attatched to the top of the brazed ceramic disks by sputter deposition. Sputterdeposited platinum did not have good adhesion to spinel or the nitride ceramics. Good adhesion of the electrodes to all of the specimens was obtained by first depositing 0.3 µm Ti and then 3 µm Pt using a 2-source vacuum sputter deposition system. The guard ring geometry was produced by attatching with silver paint a **small** steel ring of inner and outer diameter 1.6 mm and 2.0 mm, respectively, to the top surface of each ceramic disk prior to the sputter deposition. The steel ring was removed from the specimens after the Pt deposition by soaking in acetone, and the excess silver paint was removed **by** rubbing with a cotton tip applicator. Figure 2 shows the final geometry of the guarded specimens. The specimen geometry was in conformance with the applicable ASTM standards on 3-terminal volume resistivity measurements [28]. The resistance between the guard ring and the Ni base was typically very low (~ 1 Ω) after the brazing and electrode deposition processes **due** to the presence of a **thin** film of metallic impurities on the ceramic disk surfaces. This metallic film around the edges of the disks was removed by a small dental abrasive drill. The resismce between the center and guard-ring electrodes and the guard-ring and **base** electrodes was > 20 **M** Ω after this cleaning procedure.

CERAMIC SPECIMEN GEOMETRY FOR IN-SITU ELECTRICAL CONDUCTIVITY TESTS

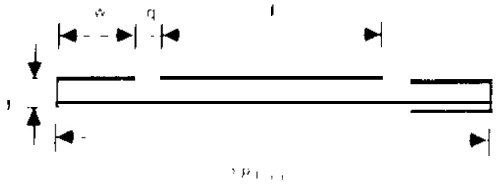

t = 0.16 mm
d = 1.6 mm
W = 0.4 mm
g = 0.2 mm

$d_{eff} = d + 0.58\,g = 1.7$ mm
Geometry factor $t/A_{eff} = 69/m$

ASTM Standard*	Present design
$W > 2t$	$W = 2.5\,t$
$d > 4t$	$d = 10\,t$
g t	$g = 1.25\,t$

* D257-78 (reapproved 1983) Standard Test Methods for D-C Resistance or Conductance of Insulating Materials

D150-87 Standard Test Methods for A-C Loss Characteristics and Permittivity (Dielectric Constant) of Solid Electrical Insulating Materials

Fig. 2 Specimen and electrode geometry **used** for the in-situ electrical conductivity measurements.

Figure 3 shows schematically how the electrical leads were attached to the center and guard ring surfaces. Initial attempts to attach 100 µm diameter Pt wires to the electrode surfaces with a parallel-electrode spot welding machine produced mixed results. Excellent wire adhesion was generally obtained for the Al_2O_3 specimens, but Pt wires could not be welded to the Si_3N_4 specimens. In addition, attempts to ultasonically bond thin Pt wires to the Pt electrodes were also unsuccessful. Satisfactory results were obtained by employing a spring-loaded tungsten wire contact system. The signal from the center electrode of each specimen was protected against leakage currents to ground by incorporating a guarded pedestal configuration for the W spring **supports,** as shown in Fig. 3.

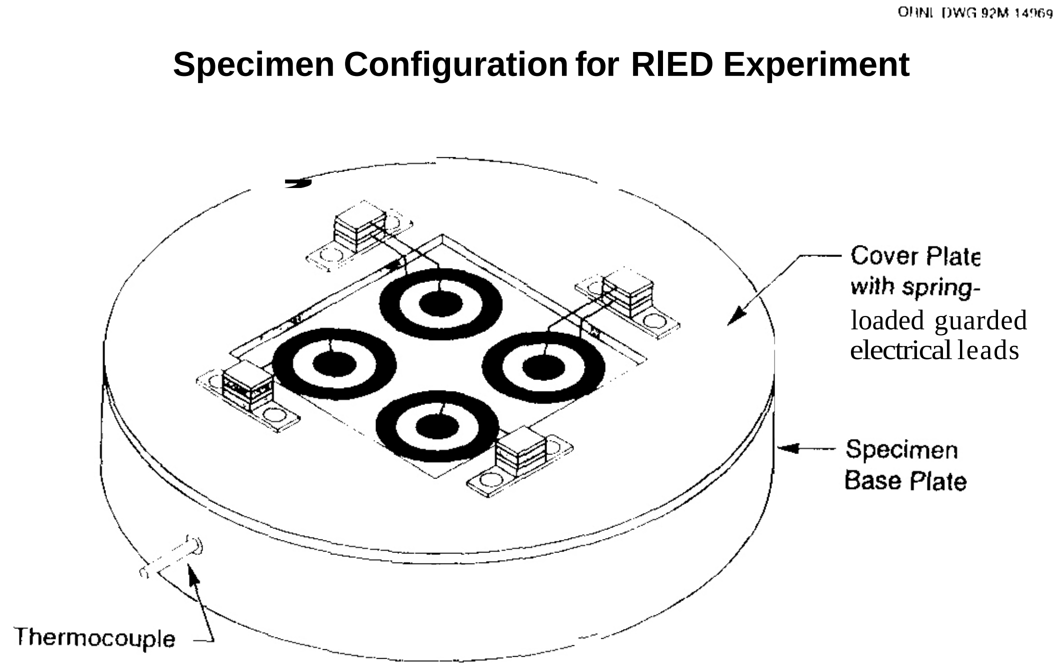

Fig. 3. Specimen configuration for the cyclotron in-situ conductivity measurements showing the spring-loaded W wire contacts and the guarded wire support pedestals.

The irradiations were performed using either 20 MeV H^+ ions or 28 MeV He^{++} ions at the Forschungszentrum Juelich compact cyclotron. The range of these ions in Al_2O_3 of ideal density is 0.21 mm and 1.3 mm. respectively, according to a TRIM-YO [24] calculation. The calculated displacement damage and ionizing dose rates at a depth of 0.08 mm for a beam current of 1 A/m^2 incident on an Al_2O_3 target are 1.21×10^{-6} dpds and 2.2×10^6 Gy/s for 20 MeV H^+ ions, and 6.7×10^{-6} dpds and 1.2×10^7 Gy/s for 28 MeV He^{++} ions, Typical fluxes maintained during the irradiation were 0.05 to 0.1 A/m^2. The TRIM calculations were performed using a binding energy of 2 eV and the measured [24,25] threshold displacement energies for Al_2O_3 of 20 eV and 78 eV for the aluminum and oxygen sublattices, respectively. Identical results for the nuclear and electronic stopping powers were obtained from TRIM calculations performed with a threshold displacement energy of 40 eV for both sublattices. The conversion from damage energy (nuclear stopping power) to NRT dpa [27] assumed an average displacement energy of 40 eV. Figure 4 shows the calculated displacement damage and ionizing radiation profiles for 20 MeV H^+ and 28 MeV He++ ions incident on Al_2O_3. The calculated variation in the damage rate between the front and back surfaces for an Al_2O_3 specimen of thickness 0.16 mm was $<5\%$ for the 20 MeV proton irradiations and –50% for the 28 MeV He^{++} ion irradiations.

A schematic of the target chamber used for the cyclotron irradiations is shown in Fig. 5. The target chamber was evacuated during the irradiations with a 270 l/s turbomolecular pump, which produced a base pressure of about 1×10^{-5} torr in the chamber. The specimen temperature was controlled with a cylindrical (5 mm diam.) mineral-insulated electrical resistance heater that was controlled by the specimen thermocouple. The target chamber was electrically isolated from the cyclotron beam line and target stand by

ORNL DWG 93M 6305

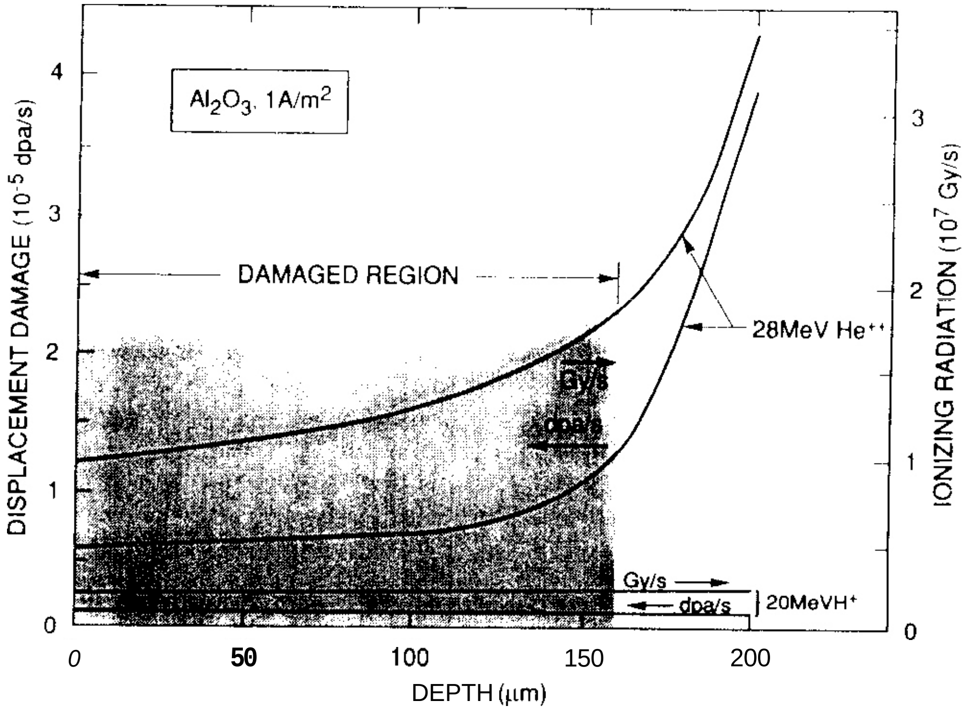

Fig. 4 Calculated [24] displacement damage **and** ionizing radiation profiles for ion-irradiated Al_2O_3.

ORNL DWG 92M 14971

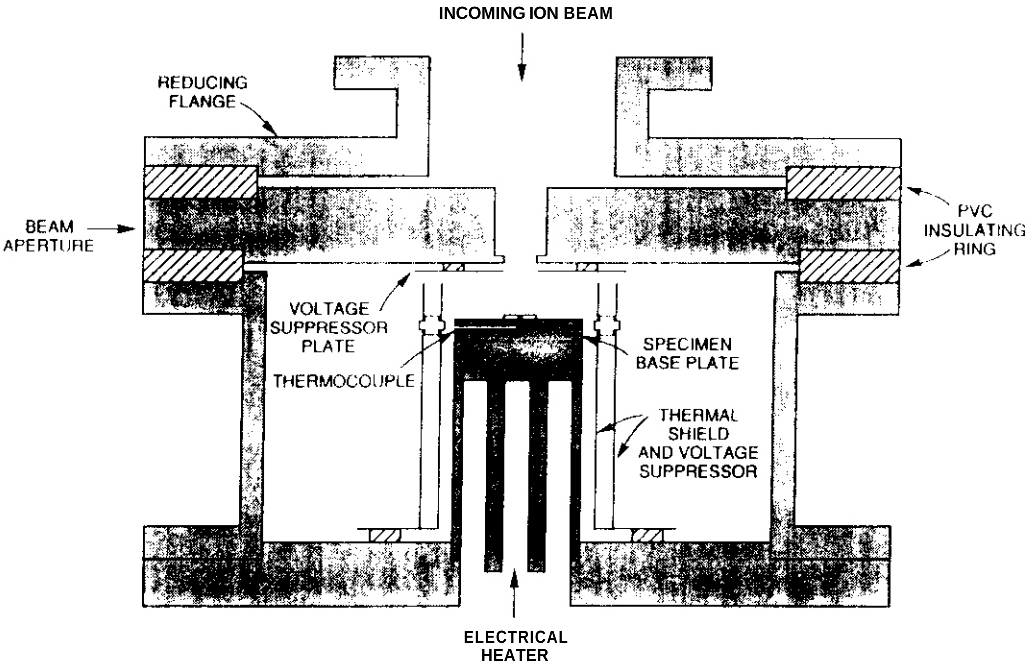

Fig. 5 Schematic of the target chamber used for the in-situ electrical conductivity measurements.

polyvinyl chloride insulation. A set of electrically isolated concentric cylindrical steel sheets surrounding the specimen pedestal served as both a heat shield and to suppress the emission of secondary electrons during the irradiation. The suppressor voltage was set at the same (negative) value as the voltage applied to the specimens during the irradiation. This feature effectively guarded the specimen leads as they passed through the steel heat shields inside of Macor ceramic-insulated feedthoughs. Floating coaxial vacuum feedthroughs and triaxial cables were used to connect the guard and center leads from the target chamber to the experimenters area outside of the irradiation target room.

A Keithley Model 480 picoammeter was used to measure the specimen currents. A dc potential of either 15 or 75 V was continuously applied during the irradiation. which produced an electric field of 100 and 500 V/mm, respectively. A switching circuit was built that allowed the current through each individual center electrode or guard ring circuit to be monitored one at a time, while continuously maintaining the potential on all 8 leads. Due to the small size of the specimens used in this study, the resolution limit for electrical conductivity changes was about 5 x $10^{-8}/\Omega$-m. In addition, the spinel specimens were generally found to have anomalously high leakage currents compared to the other specimens. It is believed that the low strength of the spinel caused it to be susceptable to microcracking during the specimen grinding on the diamond-impregnated metal platen. Improved performance has recently been observed in spinel specimens that were ground with diamond paste on a standard nylon polishing pad.

RESULTS AND DISCUSSION

Table 1 summarizes the irradiation conditions that have been studied to date on the 4 ceramic insulators. The electrical conductivity of all four ceramics was observed to increase immediately at the start of the irradiation. and then remained constant or decreased slightly as the irradiation proceeded. Typical RIC values observed during irradiation with 28 MeV He^{++} ions at 600°C at a beam current of 0.06 A/m^2 (0.7 MGy/s) ranged from 1 x 10^{-6} to 1 x $10^{-5}/\Omega$-m for the different ceramics. These prompt RIC measurements were in reasonable agreement with previous measurements (Fig. 1) reported for oxide ceramics. The ion beam was turned off at regular intervals of about 2 hours during the irradiation so that the conductivity in the absence of radiation could be measured. This "beam off' conductivity did not show any significant change compared to the nonirradiated values for any of the irradiation conditions studied so far. The present results indicate that significant amounts of RIED does not occur in any of the four ceramic materials during cyclotron irradiation with light ions for displacement damage levels up to about 5x10^{-3} dpa.

Figure 6 compares the results of several studies on the effect of electron. ion, or neutron irradiation at 450 to 530°C on the electrical conductivity of Al_2O_3 [1,16,17,19,20]. Irradiation with an applied electric field eventually produces significant RIED in all three types of irradiation spectra. However, the dose required to produce a significant permanent degradation in the electrical resistivity appears to vary considerably depending on the irradiation source. In particular. irradiation sources such as electrons which produce isolated point defects (low energy primary knock-on atoms, PKAs) and have high ionizing to displacive radiation ratios appear to exhibit accelerated NED kinetics compared to fission neutrons. A similar large dependence on irradiation spectrum is evident when the RIED results are plotted versus absorbed ionizing radiation dose (Gy). According to the results by Pells [19], significant RIED begins to occur in Al_2O_3 during light ion irradiation for displacement damage levels greater than about 5 x 10^{-3} dpa.

This is equal to the maximum dose obtained in our cyclotron studies so far, and may explain why we have not yet observed measureable amounts of NED.

Table 1. Irradiation conditions for the in-situ electrical conductivity experiments. The beam currents were maintained at 0.06 to 0.1 A/m^2 for all irradiations. Two of the 28 MeV He^{++} ion irradiations were performed using multiple temperatures and/or electric fields, as indicated.

Material	Ion	Electric Field	Temperatures	Dose
$MgAl_2O_4$	28 MeV He^{++}	100 V/mm	275°C +150°C	1 x 10^{-3} dpa +1 x 10^{-3} dpa
$MgAl_2O_4$, Al_2O_3, AlN, Si_3N_4	28 MeV He^{++}	100 V/mm	590°C	4 x 10^{-3} dpa
$MgAl_2O_4$, Al_2O_3, AlN, Si_3N_4	28 MeV He^{++}	100 V/mm +500 V/mm +500 V/mm	500°C +500°C +600°C	5 x 10^{-3} dpa +1 x 10^{-3} dpa +1 x 10^{-3} dpa
$MgAl_2O_4$, Al_2O_3, AlN, Si_3N_4	20 MeV H$^+$	500 V/mm	500°C	3 x 10^{-3} dpa

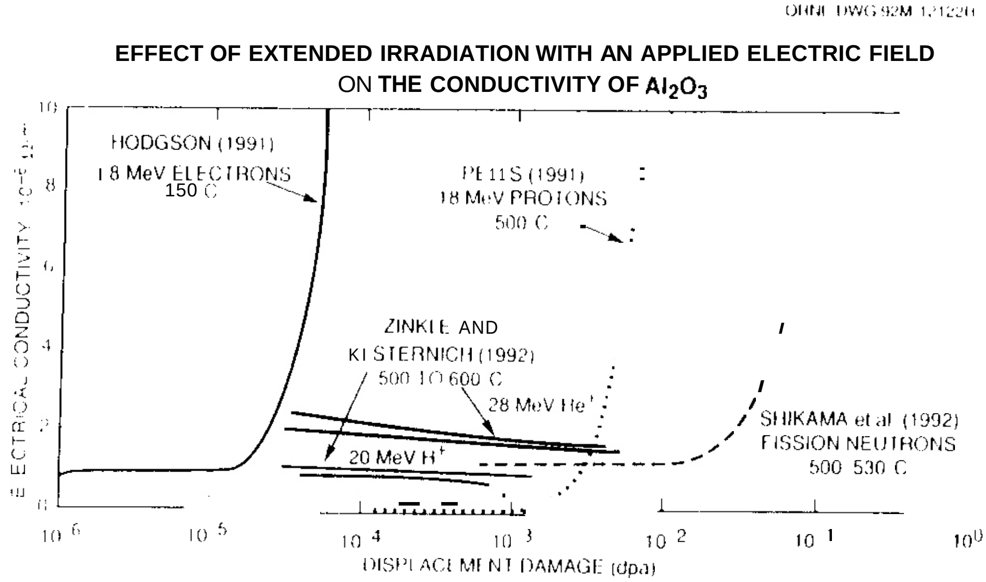

Fig. 6. Effect of extended irradiation with an applied electric field on the electrical conductivity of A1203 [1,16,17,19,20]. The data by Pells was obtained while the ion beam was turned off, whereas the data shown from the other studies was taken during irradiation.

Transmission electron microscopy was used to investigate the microstructure of one of the $MgAl_2O_4$ specimens irradiated with 28 MeV He$^+$ ions at 300°C to a damage level of about 1x10^{-3} dpa. There was no evidence of observable (>2 nm diameter) colloids or other defect clusters. We are planning to perform higher dose irradiations at the Juelich cyclotron to further investigate the RIED behavior of ceramics. Microstructural analysis of additional ceramic specimens irradiated with 28 MeV He^{++} ions to damage levels of ahout 5 x 10^{-3} dpa is in progress.

Recent microstructural observations on oxide ceramics irradiated with a wide range of different ions have found similar evidence for a strong spectral effect on the microstructural evolution [29]. A useful parameter for correlating the microstructural response with irradiation spectrum was found to be the ratio of ionizing to displacive radiation, S_e/S_d, where S_e is the electronic Component of the stopping power and S_d is the nuclear (atomic displacements) component of the stopping power. The microstructural observations indicate that highly ionizing radiation environments greatly enhance defect mobilities. This ionization enhanced diffusion mechanism may explain why irradiation sources such as electrons that have high ratios of S_e/S_d exhibit accelerated RIED kinetics compared to neutron irradiation sources. The ratio of S_e/S_d in Al_2O_3 is about 10,000 for 1.8 MeV electrons, 4000 for 20 MeV protons, and about 100 for mixed spectrum fission neutrons [30]. The calculated ratio of S_e/S_d appropriate for ceramics in a fusion reactor depends on their location. At the first wall, this ratio for Al_2O_3 is about 20. The corresponding ratio at depths further away from the plasma depends strongly on the particular choice of coolant and blanket/shielding material in a fusion reactor. Typical ratios of S_e/S_d for ceramics at the superconducting magnets vary from 40 to 350, depending on the coolant and blanket/shield material [30]

ACKNOWLEDGEMENTS

Experimental assistance for this project was provided by W Schmitz. H. Klein and J. Deutz at Forschungszentrum Jiilich.

FUTURE WORK

Specimens will be irradiated with 28 MeV He^{++} ions to damage levcls in excess of 0.01 dpa in an attempt to initiate RIED. This future work will be part of the thesis research of F. Scheuermann. The microstructure of the ceramic specimens will he analyzcd hy analytical electron microscopy to investigate the possibility of colloid formation.

REFERENCES

1. S.J. Zinkle and E.R. Hodgson. J. Nucl. Mater. **191-194 (1992)** 58.

2. F.W. Chard, Jr., J. Nucl. Mater. **85&86** (1979) 393.

3. J.L. Scott, F.W. Chard, Jr. and F.W. Wiffen, J. Nucl. Mater. **133&134 (1985) 156.**

4. W.C. Roentgen and A. Joffe, Ann. Physik **41 (1913)** 449; **64**(1921)1.

5. R. Hofstadter, Nucleonics **4 (1949)** 2.

6. **A.** Rose, Phys. Rev. 97 **(1955) 1538.**

7. V.A.J. van Lint, T.M. Flanagan, R.E. Leadon, J.A. Nabor, and V.C. Rogers, Mechanisms of Radiation Effects in Electronic Materials, Vol. **1** (Wiley and Sons, New York, 1980).

8. E.H. Famum, J.C. Kennedy, F.W. Clinard and H.M. Frost, J. Nucl. Mater. **191-194** (1992) **548,**

9. A.E. Hughes, Rad. Effects **74** (1983) 57.

10. R.W. Klaffky, B.H. Rose, A.N. Goland **and** G.J. Dienes, Phys. Rev. B **21** (1980) 3610.

11. E.R. Hodgson and **S.** Clement, Rad. Effects **97** (1986) 251.

12. G.P. Pells, Rad. Effects **97** (1986) 199.

13. V.A.J. van Lint, J.W. Harrity and T.M. Flanagan, IEEE Trans. on Nucl. Science. Vol. **NS-15,** No. 6 (1968) 19

14. G.P. Pells. J. Nucl. Matcr. **184** (1991) 183.

15. V.M. Ivanov, G.M. Kalinin, V.F. Kuzovitkin, S.P. Sklizkov, N.V. Markina, V.V. Sarksyan, and V.A. Skobeleva, Inorganic Mater. **17** (1981) 1203.

16. E.R. Hodgson, Cryst. Latt. Def. Amorph. Mater. **18** (1989) 169.

17. E.R. Hodgson, J. Nucl. Mater. **179-181** (1991) 383.

18. E.R. Hodgson, **I.** Nucl. Mater. 191-194 (1992) 552.

19. G.P. Pells, J. Nucl. Mater. **184** (1991) 177.

20. T. Shikama, M. Narui, Y. Endo, T. **Sagawa,** and H. Kayano, J. Nucl. Matcr. **191-194** (1992) 575.

21. E.H. Famum, private comm. (LASREF irradiation of Al_2O_3).

22. E.R. Hodgson, Rad. Eff. Dcf. Solids **119-121** (1991) 827.

23. R.W. Klaffky, in Special Purpose Materials Ann. Prog. Rep., DOE/ER-0048/1 (U.S. Dept. of Energy, Washington D.C., 1980) **p.** 19.

24. J.F. Ziegler, J.P. Biersack and U.L. Littmark, The Stopping and Range of Ions in Solids (Pergamon **Press,** New York, 1985).

25. G.P. Pells and A.Y. Stathopoulos, Rad. Effects **74** (1983) 181.

26. P. Agnew, Phil. Mag. ***A 65*** (1992) 355

27. M.J. Norgett, M.T. Robinson and I.M. Torrens, Nucl. Eng. Des. **33** (1975) 50.

28. ASTM Standard Test Methods for DC Resistance or Conductance of Insulating Materials, D-257-91.

29. S.J. Zinkle, Fusion Rcactor Materials Scmiann. Prog. Rep. ending March 31, 1993, DOE/ER-0313/14

30. S.J. Zinkle and L.R. Greenwood, Fusion Reactor Materials Semiann. Prog. Rep. ending March 31, 1993, DOE/ER-0313/14.

IRRADIATION OF $MgAl_2O_4$ SPINEL IN FFTF-MOTA - F. A. Garner and G. W. Hollenberg (Pacific Northwest Laboratory)*, C. A. Black and R. C. Bradt (University of Nevada-Reno)

OBJECTIVE

The objective of this effort is to determine the response of $MgAl_2O_4$ spinel to high fluence neutron irradiation at elevated temperatures.

SUMMARY

$MgAl_2O_4$ spinel specimens irradiated in FFTF-MOTA at temperatures between 385 and 750°C to fluences ranging from 2.2 to 24.9 x 10^{22} n cm^{-2} (E>0.1 MeV) darken significantly, but do not develop any loss in weight or change in dimensions. Measurements of knoop hardness and its dependence on crystalline orientation, neutron fluence and irradiation temperature are in progress. Measurements of elastic properties are also nearing completion.

STATUS AND ACCOMPLISHMENTS

Introduction

Magnesium aluminate spinel is an electrical insulator that has been considered as a potential fusion reactor candidate material for service as dielectric windows for radio frequency heating systems or as insulators for magnetic coils.[1] Previous irradiation studies have shown that the dimensional stability of this material is remarkably insensitive to neutron damage at exposures *up* to 2 x $10^{22} n/cm^2$.[2-5]

Since 1985, Pacific Northwest Laboratory has been conducting a collaborative project with Professor R. C Bradt (University of Nevada-Reno), involving irradiation in FFTF/MOTA of very high purity $MgAl_2O_4$ spinel (see Table 1). The various irradiation sequences are now complete and analysis of the specimens is in progress.

Experimental Details

Three specimen types and two specimen geometries are employed in this experiment. The three types are hot pressed (HP) polycrystals at 100% of theoretical density. (100)-oriented single crystals and (111)-oriented single crystals. Both of the latter are oriented with the specified crystalline direction in the axial or height direction of the specimen. Most of the specimens are in the form of ~0.19" (4.8 mm) diameter cylindrical pellets. The height of the pellets varies with specimen type. as shown in Figure 1. The heights were ~0.23" (5.8 mm) for HP. ~0.17" (4.3 mm) for (111) and ~0.11" (2.8 mm) for (100)-oriented specimens

The other specimen geometry is in the form of ~0.5" (12.7 mm) square plates with thicknesses comparable to those of the heights of the pellet specimens. The plates were produced by diamond parallel surface grinding, and the pellets by diamond core drilling of the plate material. Laser etching was employed to mark the circumference of the pellets and the side of the squares with an individual identification code.

Prior to irradiation the specimens were weighed and their dimensions measured to 0.0001 inches using a ZYGO 110 laser Telemetric System. Diameters of the pellets were measured using the average of three measurements at three orientations approximately 60° apart on the pellets. The height of the plates was determined by averaging six measurements across both diagonals of the square plates. The specimens were then ultrasonically washed in distilled water. air dried. ultrasonically washed in ethyl alcohol and then dried in air at 200°C for *24* hours before being sealed in a hermetic storage container to remove adsorbed water

The specimens were later removed from the storage container and placed in irradiation capsules filled with helium gas at 1 atm and room temperature. Each capsule was closed by electron beam welding under helium and then helium leak checked. The capsules were constructed of D9 titanium-modified steel. Each of the pellet-containing capsules contained a molybdenum spring and five specimens: specifically, one HP specimen and two each of the single crystal types. as shown in Figure 1.

---

* Pacific Northwest laboratory is operated for the U.S. Department of Energy by Battelle Memorial Institute under Contract DE-AC06-76RLO 1830.

Table 1 Chemical Composition* of Spinel Specimens (appm) Determined by Spectrographic Analysis

	100**	111	HP
Li	0.01	0.1	>50
B	0.3	<0.1	<0.1
Na	5	5	5
Si	600	<60	60
P	1	0.5	10
S	90	90	300
Cl	10	10	10
K	<10	<10	<10
Ca	10	40	10
Sc	10	10	30
Ti	10	10	40
V	3	3	8
Cr	4	10	4
Mn	5	<2	<2
Fe	80	30	30
Co	0.2	<0.2	0.2
Ni	1	1	1
Cu	3	1	<0.3
Ga	9	30	3
Ge	10	4	<4

*Major constituents determined by stoichiometry derived from x-ray diffraction to be 37.9 wt% aluminum, 45.0 wt% oxygen and 17.1 wt% magnesium

**Specimen type

The nominal irradiation conditions experienced by the pellets in the FFTF reactor were

385°C, 22.9 and 24.9 x 10[illegible] n/cm^2 (E > 0.1 MeV),

405°C, 5.3 x 10[illegible] n/cm^2,

750°C 5.6, 13.7 and 21.7 x 10[illegible] n/cm^2.

The emphasis on nominal irradiation conditions reflects the fact that these specimens started irradiation in MOTA-1D, in which the specimens experienced an overtemperature event in the middle of FFTF cycle 7 of ~50 minutes duration, followed by a prolonged and variable undertemperature history in cycle 8. Only the 750°C irradiation experienced a significant variation in temperature, however, reaching 934°C for 50 minutes and then running at a range of temperatures well below 750°C throughout cycle 8. For the second and third irradiation sequences conducted in FFTF cycles 9, 10, and 11 in MOTA-1E, 1F and 1G, respectively the temperatures were held to ±5°C of the target temperature.

The square plate specimens were irradiated in larger D-9 capsules placed in the below-core canister at 365°C and irradiated to 1.3, 2.2 and 4.6 x 10[illegible] n/cm^2 (E>0.1MeV). The spinel specimens were placed in the capsule with many other high heat flux specimens, some of which melted and/or decomposed during irradiation. The 1.8x10[illegible] n/cm^2 specimens were below the decomposed materials and did not survive the irradiation.

after irradiation. the specimens were removed from the capsules, cleaned, and their weights and dimensions measured using the same techniques employed prior to irradiation.

Results

Due to their high purity. the specimens were only mildly radioactive and could be easily handled. Prior to irradiation, the single crystal specimens were transparent and the hot-pressed specimens were white. In regular light the irradiated specimens all appear to be very dark, as shown in Figure 2, but placing them in front of a strong lamp showed that some light was transmitted, with colors ranging from yellow to dark red.

The weights of the specimens remained essentially unchanged, with all measurements ranging from 0.0 to ~0.2% loss in weight. The loss, if any, was always in the fourth significant figure and may be related either to different levels of adsorbed moisture before and after irradiation or to small chips lost during handling.

All post-irradiation measurements fell within ±1% of the preirradiation measurements, with most below ±0.5%. Combining the point-to-Point variations observed in thickness and the reproducibility of the measurements, it appears that the measured variations in preirradiation dimensions should be ≤1%. There were no discernible trends of these small differences with respect to orientation, irradiation temperature, neutron fluence or specimen type. The obvious conclusion is that no significant irradiation-induced changes occurred in the dimensions of these specimens.

Measurements at room temperature of the orientation dependence of microhardness on the irradiated specimens are proceeding for comparison with measurements made earlier on unirradiated specimens.' . In the unirradiated condition. the (100) plane exhibits a maximum microhardness in the [001] direction and a minimum in the [011] direction, consistent with a primary slip system of $\{111\}\langle 1\bar{1}0\rangle$. The microhardness of the (111) plane is independent of indenter orientation, also consistent with such a primary slip system. With increasing irradiation, the hardness increases somewhat and the orientation dependence tends to disappear, as the primary slip system becomes blocked.

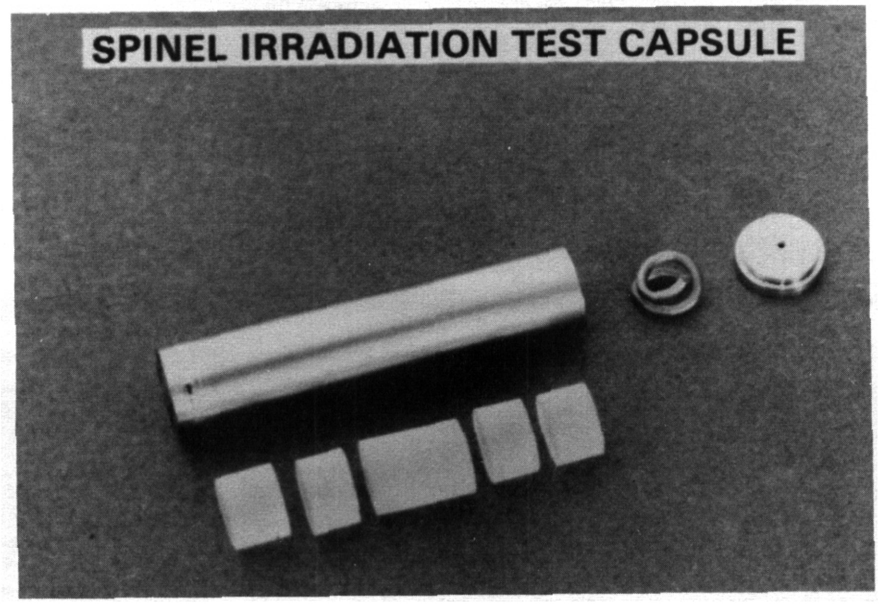

Fig. 1. Contents of typical irradiation capsule for pellet specimens.

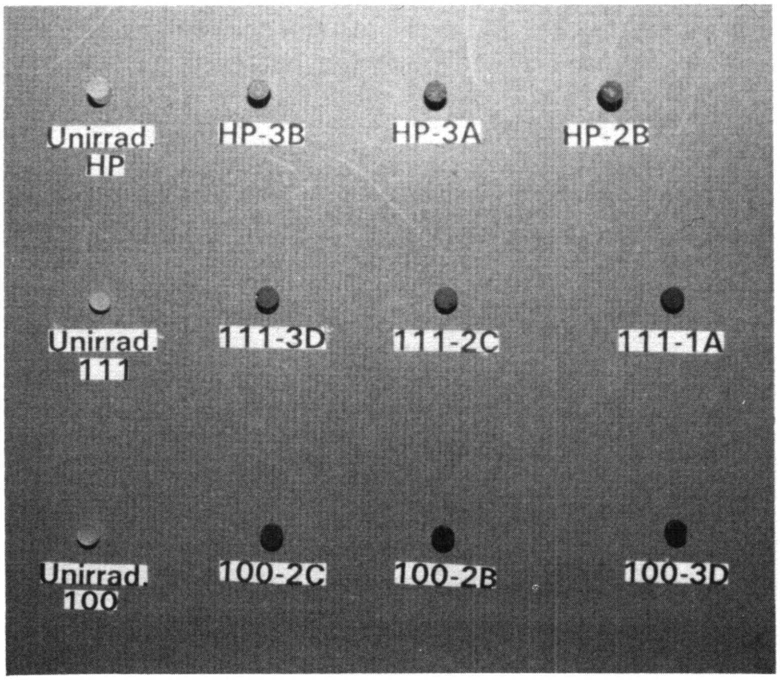

Fig. 2. Comparison of specimen appearance before and after irradiation at 750°C. Exposure levels increase from left to right (0, 5.6, 13.7 and 21.7 x 10^{22} n cm^{-2} (E>0.1 MeV).

Future Efforts

When hardness measurements are complete these specimens will be divided into a number of groups and shipped to other researchers for a variety of initially non-destructive and finally destructive measurements.

The types of examinations currently planned are as follows:

Nondestructive
- measurement of single crystal elastic constants (nearing completion)
- thermal diffusivity
- optical absorption spectra
- electrical and dielectric properties

Destructive
- transmission election microscopy
- thermal diffusivity during annealing
- electron paramagnetic resonance
- neutron diffraction
- thermally stimulated depolarization
- response to electric fields during reirradiation in LASREF

References

1) F.W. Clinard, Jr., G.F. Hurley and R.W. Klaffky, *Res. Mech.* 8 (1983) 207.
2) G.F. Hurley and J.M. Bunch, *Am. Ceram. Soc. Bull.* 59 (1980) 456.
3) F.W. Clinard, Jr., G.F. Hurley and L.W. Hobbs, *J. Nucl. Mater.* 108-109 (1982) 655.
4) Y. Fukushima, T. Yano, T. Maruyama and T. Iseki, *J. Nucl. Mater.* 175 (1990) 203
5) H. Suematsu, T. Iseki, T. Yano, Y. Saito, T. Suzuki and T. Mori, *J. Am. Ceram. Soc.* 75 (1992) 1742.
6) Y. Akimuni and R. C. Bradt, *J. Am. Cer. Soc.* 70 (1987) C84-C86.

HIGH-TEMPERATURE PROPERTIES OF SiC/SiC FOR FUSION APPLICATIONS - R. H. Jones and C. H. Henager, Jr (Pacific Northwest Laboratory)[a]

OBJECTIVE

The objective of this study is to evaluate the high-temperature mechanical properties of SiC/SiC composite materials for fusion structural applications.

SUMMARY

SiC/SiC composites exhibit novel mechanical properties relative to their monolithic counterparts. The crack velocity (da/dt) versus stress intensity (K) relationship for monolithic ceramics can be described by a simple power law relationship where SiC/SiC was found to exhibit a multi-stage da-dt versus K relationship similar to that for stress corrosion of metals. A K independent stage II was followed by a strongly K dependent stage III which paralleled the monolithic behavior. Experiments to determine the threshold K or stage I were not conducted; however, it is expected that they exist for these materials. There is also evidence that the fracture resistance of there materials is greater if cracks are produced by subcritical growth processes relative to machined notches. Oxygen was found to increase da/dt and decrease the K far the stage II to stage III transition while cyclic loads produced little damage at low K values but there was some evidence for increasing damage with increasing number of cycles and K.

PROGRESS AND STATUS

Experimental Procedures

Composites consisting of Nicalon fiber cloth (0°/90°) and CVI β-SiC with carbon (C) interfaces were tested. The composites are 8-ply material. 4 mm thick. fabricated by Refractory Composites. Inc. of Whittier, CA. Interfaces of 1.0 μm C were deposited on the Nicalon fibers before the β-SiC CVI fabrication step. Single-edge-notched bend bar (SENE) specimens with dimensions of 4 mm x 5.5 mm x SO mm were prepared. The SENE specimens were tested in 4-point bending using a fully articulated SiC bend fixture. Other test details have been discussed previously (1,2).

The subcritical crack growth (SCG) studies were performed using constant load tests for times up to 7 x 10^4 h. and using stepped load tests with load holding carried out at 1100°C in Ar and Ar plus varying PO_2. The specimens were typically loaded at an applied stress intensity of 7-8 MPa$\sqrt{m}$ to begin the test. The test continued until a load drop was observed. Specimens that were tested in Ar plus O_2 were brought up to temperature in pure Ar.

Each SCG test consisted of either a series of 1000-s constant-load tests or a long-term hold at constant load in 4-point bending at a constant temperature. The displacement-time curves for the 1000-s exposures at constant load in Ar indicate that the specimen displacement, and thus the crack opening displacement. undergoes a transient period of displacement that is logarithmic in time and does not achieve steady-state over the 1000-s hold time. The slope of the displacement-time curve over the final 600 s of the load step. however, was fairly linear and was taken as proportional to the crack velocity for each 1000-s period. The longer term hold displacement-time data were fit to polynomial functions and differentiated to give $\partial\delta/\partial t$.

Writing $\delta = P\,C(\alpha)$, where δ is the displacement, P is the load, C is the specimen mid-point compliance, and α is equal to a/W (normalized crack length) can be used to give

$$\frac{\partial\delta}{\partial t} = \frac{\partial}{\partial t}(PC(\alpha)) = P\frac{\partial C}{\partial\alpha}\frac{\partial\alpha}{\partial t} = \frac{P}{W}\frac{\partial C}{\partial\alpha}\frac{\partial a}{\partial t} \qquad (1)$$

which is then used to derive the following expression for $da/dt/V_c$.

$$\frac{da}{dt} = V_c = \frac{\frac{\partial\delta}{\partial t}W}{PC'(\alpha)} \qquad (2)$$

where V_c is the crack velocity and W is the specimen thickness. An expression was determined for the mid-point compliance of a SENE specimen in 4-point bending and was used to calculate crack length and $C'(\alpha)$ (2). The slope of the displacement-time curve at a given load is $\partial\delta/\partial t$.

Pacific Northwest Laboratory is operated for the U.S. Department of Energy by Battelle Memorial Institute under Contract DE-AC06-76RLO 1830.

Fatigue crack growth tests were performed similarly to the static load subcritical crack growth tests with the load cycled 5 or 25 times at each of the constant loads used for the static load tests. The load was held for 1000s between each load cycle and the load ratio, R, was 0.1. Tests were conducted in both Ar and Ar plus 2000 ppm O_2. The crack velocity was determined during each of the 1000s hold periods between load cycles and compared to the crack velocity obtained with the statically loaded samples

Experimental Results

The data for the C-interface materials, when plotted as crack velocity versus applied stress intensity (*V-K* curves), reveal a stage-II region here the crack velocity is essentially independent of the applied stress intensity (Figure 1) followed by a stage-III, or power-law crack growth region, at high stress intensities.

The power-law region exhibits a strong dependence, but the stage-II region exhibits a weak dependence, on the applied stress intensity. The data reveal a pronounced increase in stage-II crack velocity because of O_2 in the gar. The crack velocity increases with increasing O_2 content of the Ar (Figure 1). Also, the stress intensity required far the onset of stage-III is shifted to a lower value of the applied stress intensity.

When the crack velocity is plotted as a function of time (*V-t* curves), the effects of O_2 became more pronounced (figure 2). The time-dependence of V_c in Ar show a decreasing velocity with time while V_c in the varying P_{O_2} environments show either a constant V_c or increasing V_c with time. The curves for 10,000- and 20,000-ppm O_2 indicate that the crack velocity increases quite rapidly and that those tests were much shorter in duration than the 5000- and 2000-ppm O_2 tests.

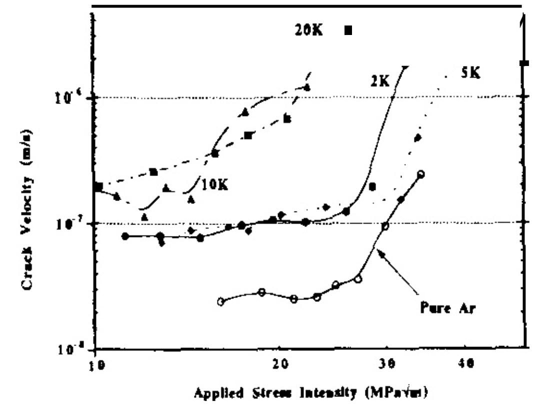

Fig. 1. V-K curves as a function of O_2 partial pressure and applied stress intensity. Curve labels indicate P_{O_2} in units of 10^3 ppm.

SCG data for monolithic ceramics that do not exhibit a large-scale bridging zone do not show stage-II behavior; rather, the crack velocity is observed to be a power-law function of applied stress intensity (K_a) (3-6). The observed stage-II region in the present data reveals a weak dependence on K_a. This behavior suggests that SCG in CMCs is controlled by crack-bridging by the continuous fibers in the crack wake. The bridging zone screens, or shields, the crack-tip from the applied stress intensity. Over the region of increasing K_a as a function of increasing crack length, a bridging zone is established for these materials, and it screens the crack-tip from K_a. A nearly constant crack-tip stress intensity, K_{tip}, is established as the bridging zone develops and R-curve behavior is observed. Eventually, the bridging zonesaturates and cannot continue to shield the crack-tip.

Discussion and Modeling of Results

The evidence for bridging zone domination of SCG is suggested from the experiments using Ar plus O_2 in comparison with pure Ar and also from a micromechanical model developed to rationalize SCG in CMC materials (1, 2). Adding O_2 to the 1100°C Ar environment increases the crack velocity in the stage-II regime and shifts the stage-II-to-stage-III transition to lower K_a values (Figure 1). The shift to lower K_a values for the transition to stage-III crack growth is consistent with a reduction in the closure forces imparted on the crack faces by the bridging fibers. Scanning electron photomicrographs (not shown here) of the CMCs exposed to the O_2 reveal the partial removal of the C-interfaces due to oxidation at 1100°C. Removing this interface material reduces the shear strength of the interface, reduces the ability of the matrix to transfer load to the fibers, and reduces the bridging zone effectiveness.

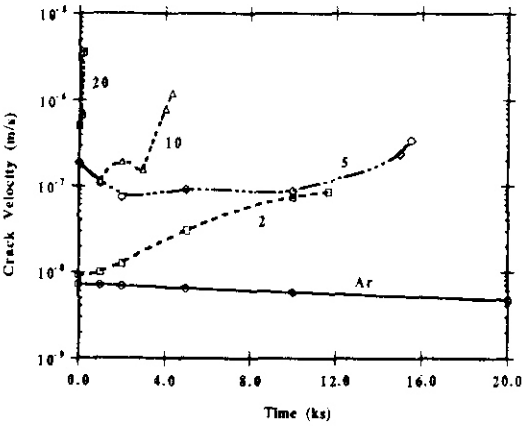

Fig. 2. Crack Velocity as a Function of Time in Pure Ar and in Varying O_2 Partial Pressures.

These effects are rationalized using a 2D-micromechanical model of a crack in a CMC material (1.2). The model places a semi-infinite crack in a linear-elastic body and simulates the bridging fibers by crack closure forces placed along the crack face. The forces applied by the fibers to the crack face are calculated using an explicit frictional bridging model that calculates the fiber load transfer as a function of distance from the crack-tip. A basic result of the model is to predict crack-tip screening over a range of crack extension (R-curve behavior) when high-strength fibers and weak interfaces are present (1,2).

The model is used to explore the time-dependence of crack growth by allowing the crack-closure forces to undergo time-dependent relaxation. Available creep data for Nicalon fibers at 1100°C in pure Ar (8) were used to construct a constitutive equation for the stress- and time-dependence of creep in Nicalon fiberr at 1100°C. Based on this approach, the discrete micromechanics model is used to calculate the crack velocity using a quasi-static approach (2)

Using a definition for the Stress intensity for an equilibrium bridging zone. an expression was derived for the velocity of a crack in a composite at equilibrium, which gives a quasi-static approximation to the crack velocity. For this approximation, it is assumed that the bridging zone is in equilibrium by virtue of a balance between crack advance and relaxation of bridging zone stresses. As the crack advancer. it bridges additional fibers. which retards its growth. As the stresses in the bridging zone relax. the crack-tip screening is reduced, and the crack tends to advance.

The quasi-static approximation assumes that K_{tip} is a constant, such that

$$K_{tip}(a,t) = C - dK_{tip} = 0 \tag{3}$$

Therefore, one can write the total differential of K_{tip} as

$$dK_{tip} = \frac{\partial K_{tip}}{\partial a}da + \frac{\partial K_{tip}}{\partial t}dt \tag{4}$$

which was used to derive an expression for crack velocity. V_c, as

$$V_c = \frac{da}{dt} = -\left(\frac{\dfrac{\partial K_{tip}}{\partial t}}{\dfrac{\partial K_{tip}}{\partial a}}\right) \tag{5}$$

where the crack velocity is expressed as the ratio between the tile-dependence of K_{tip} due to stress relaxation of bridging forces. $\partial K_{tip}/\partial t$, and the change in K_{tip} due to crack advance. $\partial K_{tip}/\partial a$. Reducing the crack-closure (fiber bridging) forces as a function of time. due to either stress relaxation in the fibers (figure 7) or removal of the interface. allows the crack to extend during the load step. The agreement of the predicted velocities. as well as the time-dependence, suggests that fiber creep is controlling SCG in the pure Ar environment at 1100°C. Other relaxation processes. such as interface removal. would be expected to occur in O_2. This relaxation process would be faster than for fiber creep alone because the fiber/matrix interface is simultaneously being removed by oxidation. This process would reduce the fiber/matrix interfacial shear strength as a function of time. A faster stress relaxation shifts the onset of accelerated cracking (stage-III) to lower K. values and increases the relative crack 'velocities in the stage-II region

The crack velocity-time data in O_2 (figure 2) indicates that velocities are increasing with time, which cannot be accounted for by using a logarithmic function fur $K_{tip}(t)$, such as that used for fiber creep. A linearly increasing $K_{tip}(t)$ will give a constant crack velocity, while a power-law function would be required to account for increasing velocities with time. Such a result would have to come from a model of interface removal and subsequent bridging zone relaxation. which remains to be accomplished

Fiber/matrix Interfaces with improved high-temperature stability relative to C are being developed by the CMC industry. Boron nitride is one such material being considered to improve the high-temperature stability. However. comparison between SiC/SiC with BN and C Interfaces. Figure 1 and 3 shows little Improvement. A BN interface is also rat a good choice for fusion applications because of neutron activation of nitrogen and helium generation from the B. Carbon interfaces could have suitable long-term stability in high-purity He or liquid lithium; however. reaction with H or F is a major concern. The suitability of SiC/SiC with a carbon interface for fusion applications must be evaluated in the presence of H. A test in He with variable H partial pressures would be one method of evaluating the stability of SiC/SiC rith C interfaces in H bearing environments

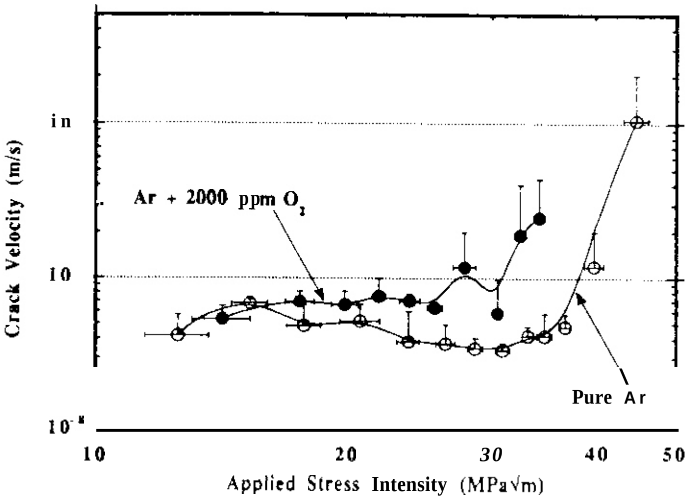

Fig. 3. Crack velocity as a function of applied stress intensity (V-K) data for BN-interface material at 1100°C in pure Ar and Ar plus 2000 ppm oxygen. Data is averaged from several specimens and single-sided error bars are shown.

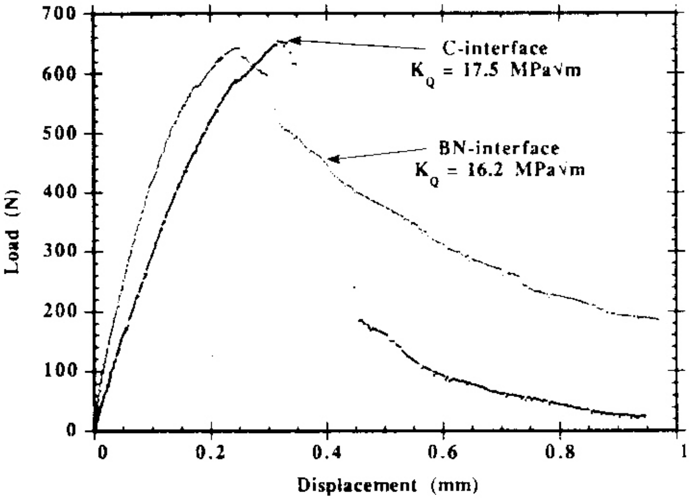

g. 4. Load-displacement curves at 1100 C in pure Ar for C- and BN-interface material. Peak load racture toughness values of 17.5 MPa√m and 16.2 MPa√m are calculated for these specimens, respectivel, The high-temperature mechanical properties of SiC reinforced with continuous SiC fibers exhibit novel properties relative to monolithic ceramics. The presence of the K independent stage II is one novel aspect of the CMC material. A second is the apparent shift in K for cracks produced by subcritical growth relative to machined notches. This effect is demonstrated by comparing the transition *from* stage II to stage III in Figures 1 and 3 to the fracture toughness curves shown in figure 4 for these materials. Comparison of the results in Ar show that the transition from stage II to stage III exceeds K by a factor of almost 2 increasing from about 15 MPa√m to 27 to 30 MPa√m. In most materials, this transition is less than K. Further experimental work is in progress to verify this effect.

Further examination of the creep/fatigue data for tests conducted on SiC/SiC with the C interface suggested that, contrary to our previous conclusion (7) that cyclic loads produced no damage, some damage may have accumulated with increasing cycles or stress-intensity. An example of this behavior is given in Figure 5 where it is evident that the difference in the crack velocity following the first cycle and the twentiefifth cycle decreases with increasing stress intensity. Comparison of the crack velocity versus applied stress intensity for static and cyclic tests conducted in Ar, Figure 6, may also provide evidence for fatigue damage. One cyclic test was terminated at the stage II to stage III transition while the second cyclic test was still in stage II when the test was terminated. The results from one test suggest that cyclic loads reduce the stage II to stage III transition while the other suggests no effect. Further experiments are in progress to further evaluate these effects.

FUTURE DIRECTION

Tests to determine the value of K following the growth of cracks at high-temperature will be completed. Also, further fatigue tests and modeling will be completed to determine whether tension-tension cyclic stresses induce damage in these materials. The temperature dependence and oxygen reaction kinetics will be measured to determine the activation energy for crack growth and to model the environmental contribution to crack growth rates, respectively.

ACKNOWLEDGEMENTS

The assistance of J. L. Humason in performing the crack growth experiments and Diane Forsyth for preparation of the manuscript are gratefully acknowledged. This work was supported by the Office of Fusion Energy and the Office of Basic Energy Sciences of the U.S. Department of Energy (under contract DE-AC06-76RLO 1830 with Battelle Memorial Institute which operates Pacific Northwest Laboratory for DOE.

REFERENCES

1. C. H. Henager, Jr. and R. H. Jones, "The Effects of an Aggressive Environment on the Subcritical Crack Growth of a Continuous-fiber Ceramic Composite," Ceramic Eng. Sci. Proc., 13 (7 8) (1992), 411-419.

2. C. H. Henager, Jr. and R. H. Jones, "High-Temperature Plasticity Effects In Bridged Cracks and Subcritical Crack Growth in Ceramic Composites' (Accepted for publication in Mater. Sci. and Engr.

3. J. L. Henshall, "The Mechanism and Mechanics of Subcritical Crack Propagation in Hot-Pressed SiC Above 1000°C," Advances in Fracture Research (Fracture 81), D. Francois, ed., Pergamon Press, NY (1981), 1541-1549.

4. H. Cao, B. J. Dalgleish, C. Hsueh, and A. G. Evans, "High Temperature Stress Corrosion Cracking in Ceramics," J. Am. Ceram. Soc., 70 (1987), 257-264.

5. C. H. Henager, Jr. and R. H. Jones, "Environmental Effects on Slow Crack Growth in Silicon Nitride," Ceramic Eng. Sci. Proc., 9 (9-10) (1988), 1525-1530.

6. C. H. Henager, Jr. and R. H. Jones, "Molten Salt Corrosion of Hot-Pressed Si_3N_4/SiC-Reinforced Composites and Effects of Molten Salt Exposure on Slow Crack Growth of Hot-Pressed Si_3N_4," in Corrosion and Corrosive Degradation of Ceramics, Ceramic Transactions, V. 10, R. E. Tressler and M. McNallen, eds., American Ceramics Society, Westerville, OH (1990), 197-210.

7. R. H. Jones and C. H. Henager, Jr., "Fatigue Crack Growth of SiC/SiC at 1100°C", in Fusion Reactor Materials Semiannual Progress Report for period ending September 30, 1992, DOE/ER-0313/13.

8. G. Simon and A. R. Bunsell, "Creep Behavior and Structural Characterization at High Temperatures of Nicalon SiC Fibres," J. Mater. Sci., 19 (1984), 3658-3670.

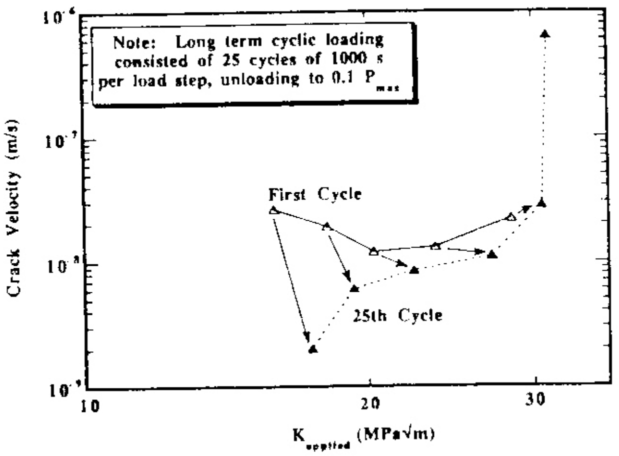

Fig. 5. Crack velocity versus stress intensity for cyclically loaded sample showing velocity after 1st and 25th cycle at each K.

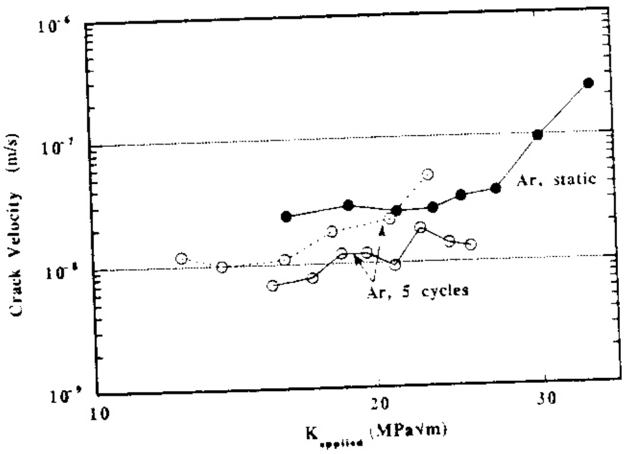

Fig. 6. Comparison of crack velocity-stress intensity relationships for static and cyclic loads.

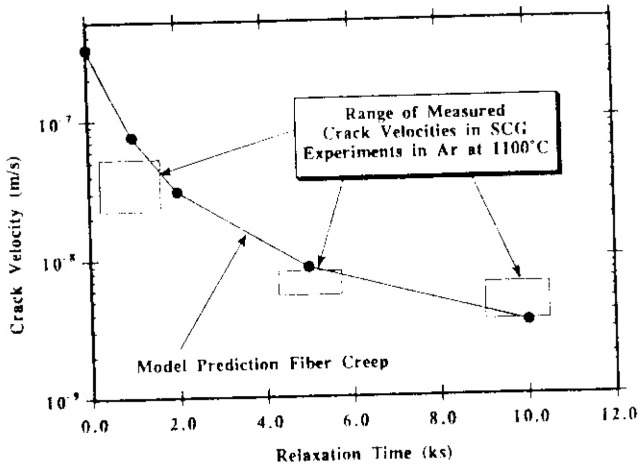

Fig. 7. Theoretical crack velocity as a function of time for the case of stress relaxation due to fiber creep.

MEASUREMENT OF DC ELECTRICAL CONDUCTIVITY OF ALUMINA DURING SPALLATION-NEUTRON IRRADIATION -- E. H. Farnum, F. W. Clinard Jr., J. C. Kennedy III, W. F. Sommer and M. D. Dammeyer (Los Alamos National Laboratory)

OBJECTIVE

The objective of this experiment is to determine the extent of degradation during neutron irradiation of electrical and optical properties of candidate dielectric materials. The goals are to identify promising dielectrics for ITER and other fusion machines for diagnostic applications and establish the basis for optimization of candidate materials.

SUMMARY

An irradiation experiment was carried out during the summer of 1W2 at the Los Alamos Spallation Radiation Effects Facility (LASREF). *In situ* measurements of electrical conductivity in alumina, sapphire and mineral-insulated electrical cables were made at 640 °C, 590 °C and 400 °C. Both DC and AC (100 Hz to 1 MHz) measurements were made to a fluence of approximately 3×10^{23} n/m^2. Optical absorption from 200 nm to 800 nm was measured in pure silica- and OH-doped silica-core optical fibers during the irradiation. A large number of passive samples were included in the irradiation. some at the furnace temperatures and some at ambient temperature. This report describes preliminary analysis of the DC conductivity measurements. The AC measurements are analyzed in the companion report. All samples are being recovered for post-irradiation examination as this report is being written in May, 1993. Final analysis of the conductivity data awaits the results of measured fluence from activation foils and will be published at ICFRM-6.

PROGRESS AND STATUS

The basic description of the experiment was reported in the last progress report (April 92 through September 92).

Furnace Temperature

Each furnace had three type K thermocouples. These were located near the top. center and bottom of the heated zone. The top and bottom thermocouples were located radially about half-way between the axis and wall. and the center thermocouple was located on the axis. The temperature was controlled (held at a constant set point) using the center thermocouple and the other two temperatures were recorded continuously during the experiment. Because of gamma and neutron heating. the furnace temperature profile changed slightly from the beam-on condition. in which most power was supplied by the radiation, and the beam-off condition, in which all the power was supplied by the furnace heater. Fig. 1 shows a two-dimensional furnace layout with the two AC capsules on the right and the DC capsule with layered samples on the left. The temperature of the three thermocouples for each of the three furnaces, A, B and C, are plotted versus axial furnace position. This furnace temperature profile was used to obtain a better estimate of the temperature of the samples. From this, our best-estimate temperature of the three DC conductivity capsules when the beam was on at high power was 655 °C, 615 °C and 395 °C, all ± 5 °C.

The furnace temperatures were initially set to 300 °C, 400 °C and 500 °C. Early in the experiment, when the beam power was low, these temperatures were held. However, when the beam power was increased. the temperatures increased to their final values and the control points were adjusted to maintain constant temperature (within 10 °C) with beam on and off. The temperature history of the furnaces during the early part of the experiment is shown in Fig. 2. Only the top thermocouple for the three furnaces is plotted in this figure. The fourth plot is a thermocouple in the temperature-uncontrolled capsule containing passive samples, labeled Clinard. The temperature of this capsule is directly related to neutron flux.

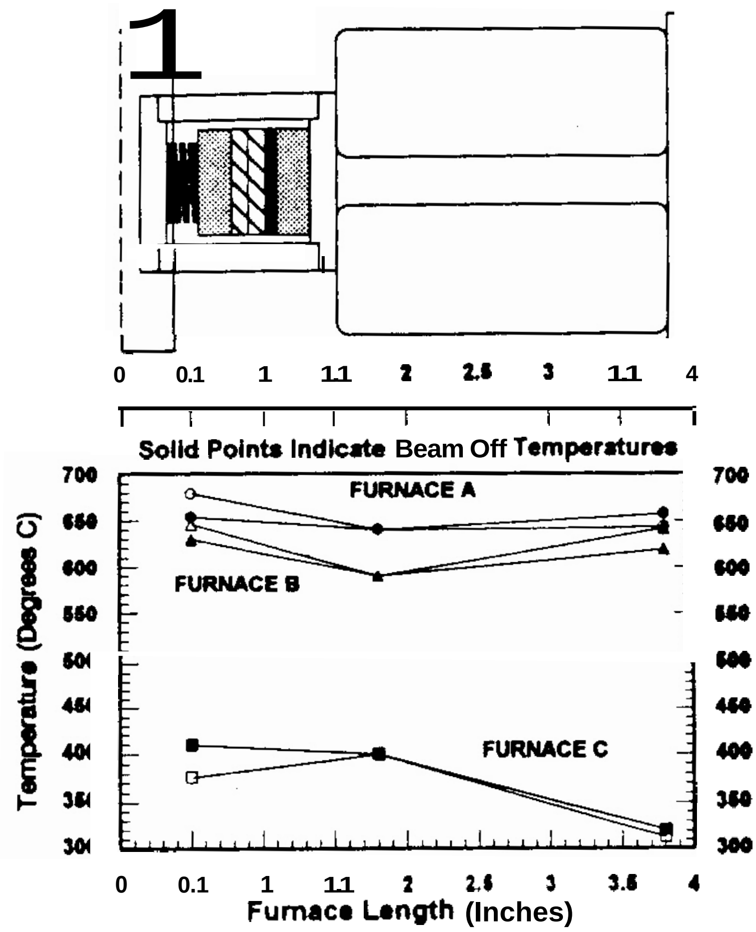

Figure 1. Temperature profiles of the three furnaces with proton-beam on and off. Double capsules on the right are AC, single capsule on the left is DC. The "top" end is on the right.

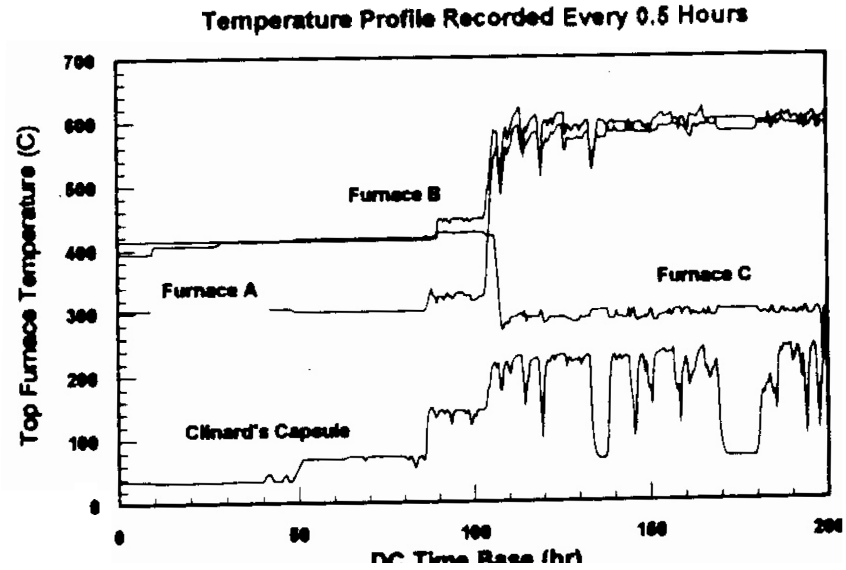

Figure 2. Temperature history of the top thermocouple in each furnace versus estimated fluence early in the experiment.

The DC electrical measurements

Each furnace held one DC capsule that was open to the argon furnace atmosphere. Each DC capsule contained two 1-mm-thick and two 3-mm-thick, 1.9-cm-diameter alumina disks. The disks were stacked with interleaved electrodes such that disks of equal thickness were electrically parallel. An applied DC voltage of 150 V caused an electric field of 500 V/cm on the thick disks and 1500 V/cm on the thin disks. This voltage was applied continuously during the experiment. The alumina disks are part of the IEA round-robin 99.5 Wesgo alumina purchased by R. Stoller at ORNL. Each DC capsule had four electrodes, the high-voltage input, a thin-disk output. a thick-disk output, and a "dummy" output that entered the capsule and hung down beside the samples but was not connected to any disks. The dummy electrode, placed closer to the high-voltage electrode than either of the other output electrodes, was intended to measure the maximum contribution to the sample current from gas and surface conduction. The three "output" electrodes and one MgO-insulated cable in each furnace were scanned continuously with a computer-controlled switch and pico-ammeter, and sample current, time and proton-beam current were, digitized and archived. Fig. 3 shows sample current versus estimated fluence for a sample electrode (furnace A thick samples) and a dummy electrode in the same furnace. Because of the small contribution. dummy electrode currents were not subtracted from sample currents in calculating conductivity.

During the experiment, the proton beam current was changed a number of times. This caused proportional changes in neutron flux, that in turn caused changes in the DC conductivity. The effect of these changes can be seen in Fig. 4. The DC conductivity is plotted versus estimated fluence for both proton-bean-on and beam-off condition. The flux was estimated from previous activation foil measurements and also from the temperature of the Clinard capsule as shown in Fig. 2. Using this flux data and assuming that the beam-on radiation-induced conductivity is directly proportional to the flux. we corrected the conductivity data for the flux changes by increasing the conductivity of the lower-flux regions by the ratio of maximum flux (in the fluence region between 0.5 and 13 x 10^{23} n/m^2) to flux in the corrected region.

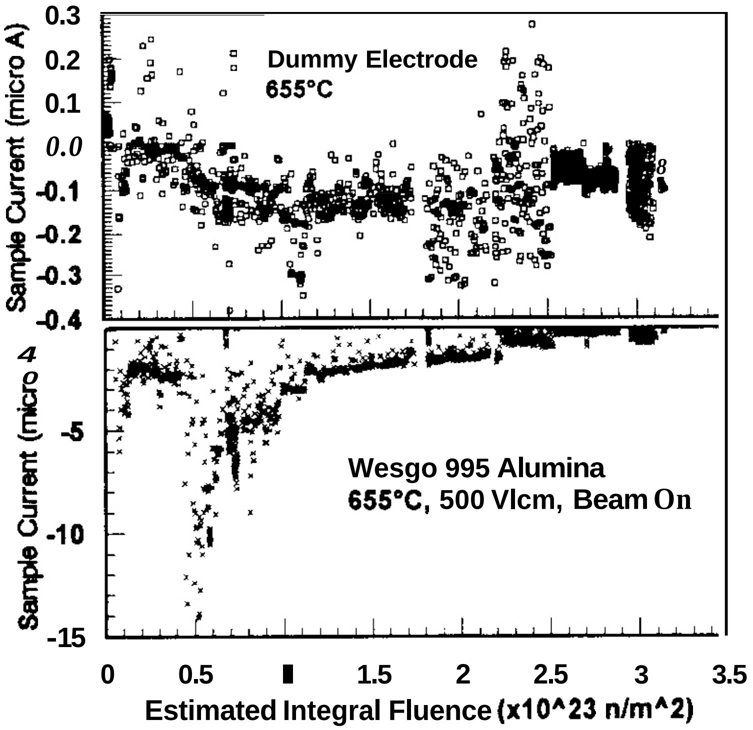

Figure 3. Comparison of the electrode current for a sample set at 655 °C and the dummy electrode in the same furnace.

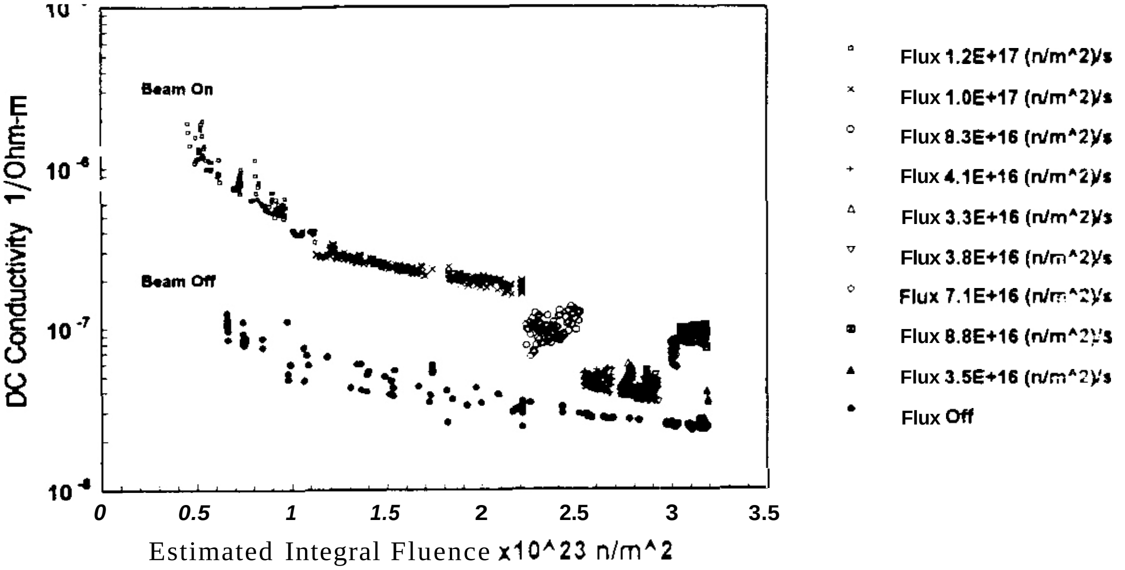

Figure 4. As measured conductivity in a sample set at 655 "C versus estimated fluence without correction for flux changes.

The flux-corrected data for three sample sets are shown in Fig. 5, a,b,c. The data taken prior to stabilization of the furnace temperatures at their final value is not shown because the analysis is not yet complete. The data for the highest temperature and highest voltage samples (655 "C, 1500 Vlcm) are not presented because we presently believe that they are erroneous and are waiting for post-irradiation measurements to verify these data The data for the lowest temperature samples are shown in Fig. 6. At this temperature, no changes were observed in either beam-on, bean-off or long-term conductivity. Therefore. no flux correction was applied to the Fig. 6 plot. The data for both the 500 Vlcm and 1500 Vlcm sample sets were similar at the lowest temperature. The data on DC conductivity of MgO-insulated cables have not yet been analyzed.

During the experiment, when the beam was off for a substantial period. we turned off the furnace power and measured electrical conductivity vs. temperature as the samples cooled, then again as they were reheated with power on. Fig. 7 is an Arrhenius plot of the conductivity taken with bean off at an estimated fluence of 0.67 x 10^{23} n/m^2. Heating and cooling data were identical. The observance of two activation energies is characteristic of an irradiated material.[1]

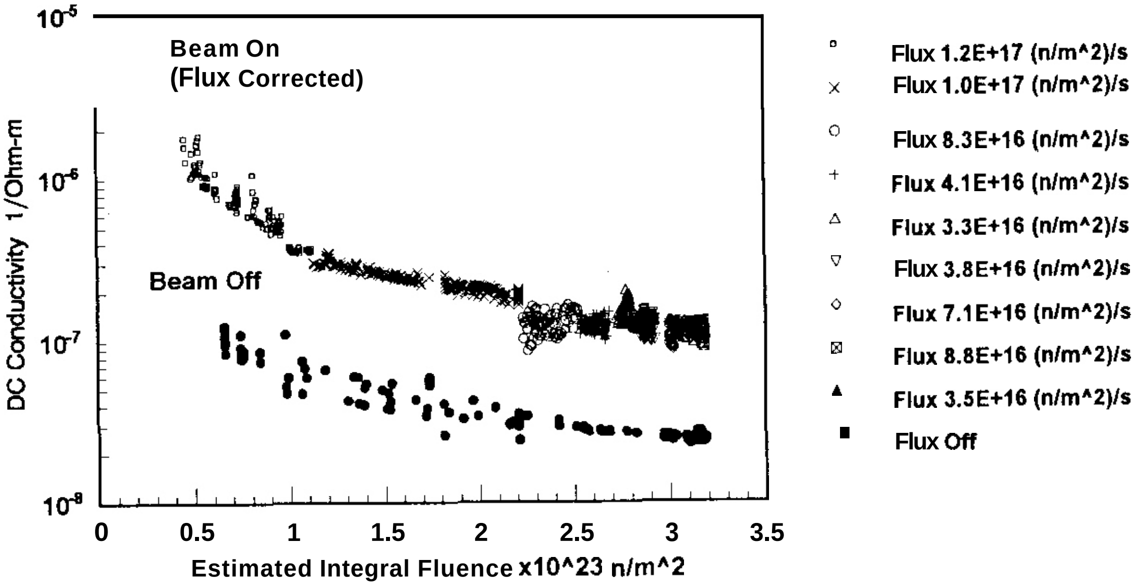

Figure 5a. Flux-corrected conductivily of the sample set at 665°C and 500 V/cm versus estimated fluence. Upper curve is bcam on, lower curve is beam off. Wesgo 995 Alumnia.

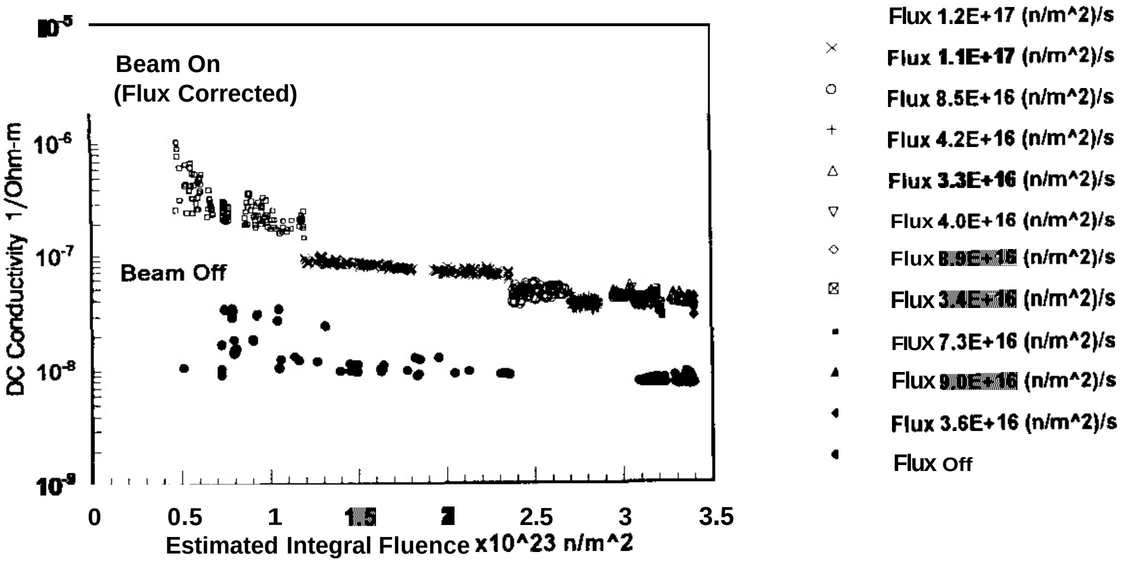

Figure 5b. Flux-corrected conductivity of the sample set at 615°C and 1500 V/cm versus estimated fluence. Upper curve is beam on, lower curve is beam off. Wesgo 995 Alumnia.

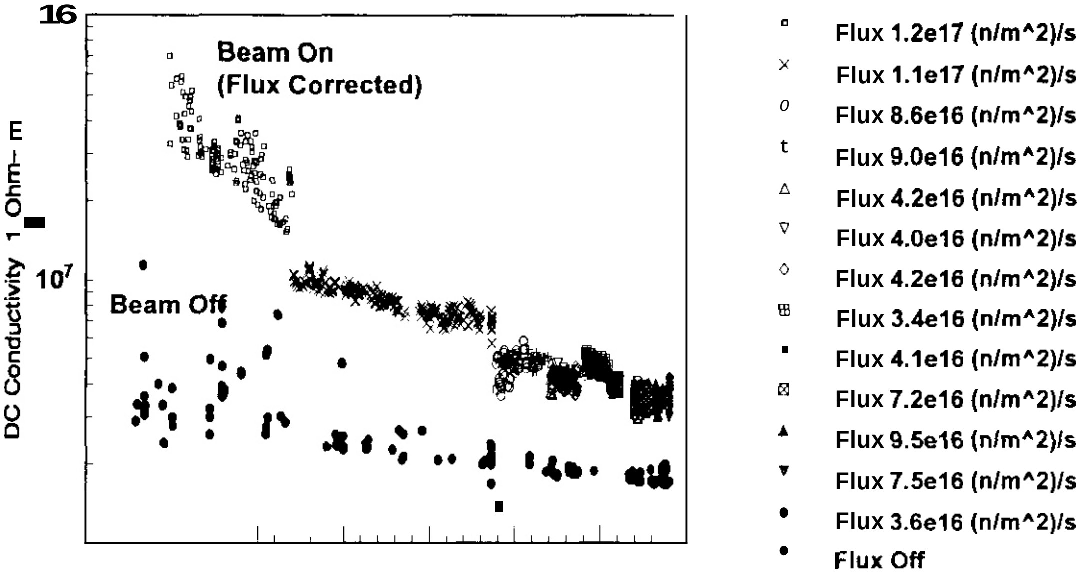

Figure 5c. Flux-corrected conductivity of the sample set at 615°C and 500 Vlcm versus estimated fluence Upper curve is beam on, lowcr curve is beam off. Wesgo 995 Alumina.

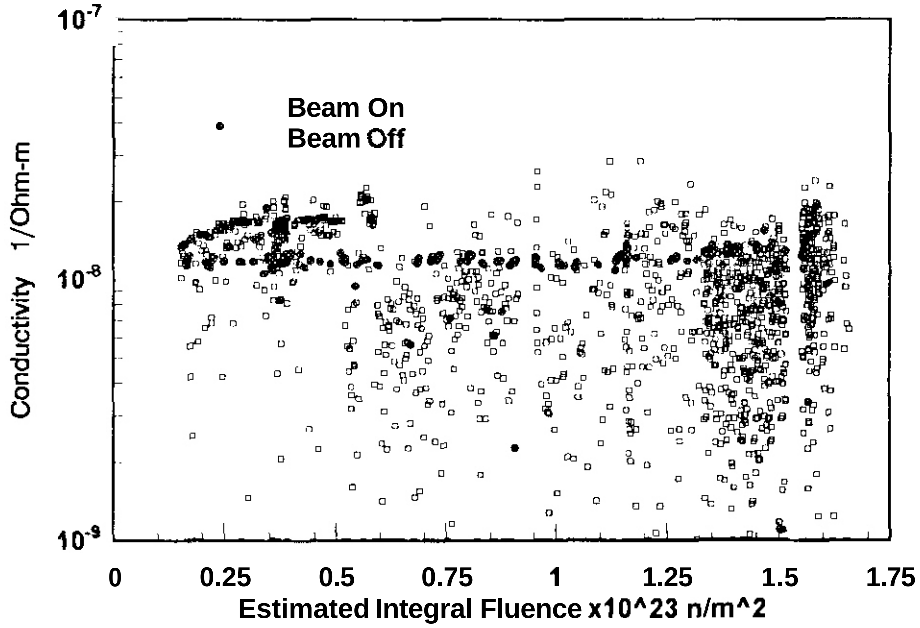

Figure 6. Conductivity of the sample set at 395°C and 500 V/cm versus estimated fluence. Wesgo 995 Alumina.

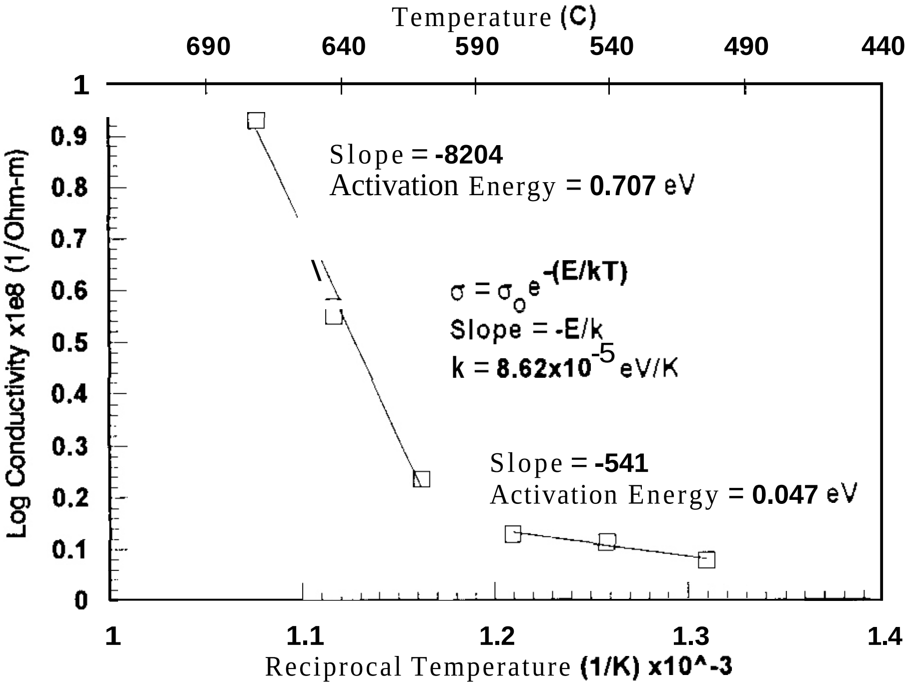

Figure 7. Logarithm of the conductivity versus reciprocal temperature for the sample set at 655° C and 500 V/cm. Fluence is constant at 6.65 x 10^{23} n/cm^2. Beam off.

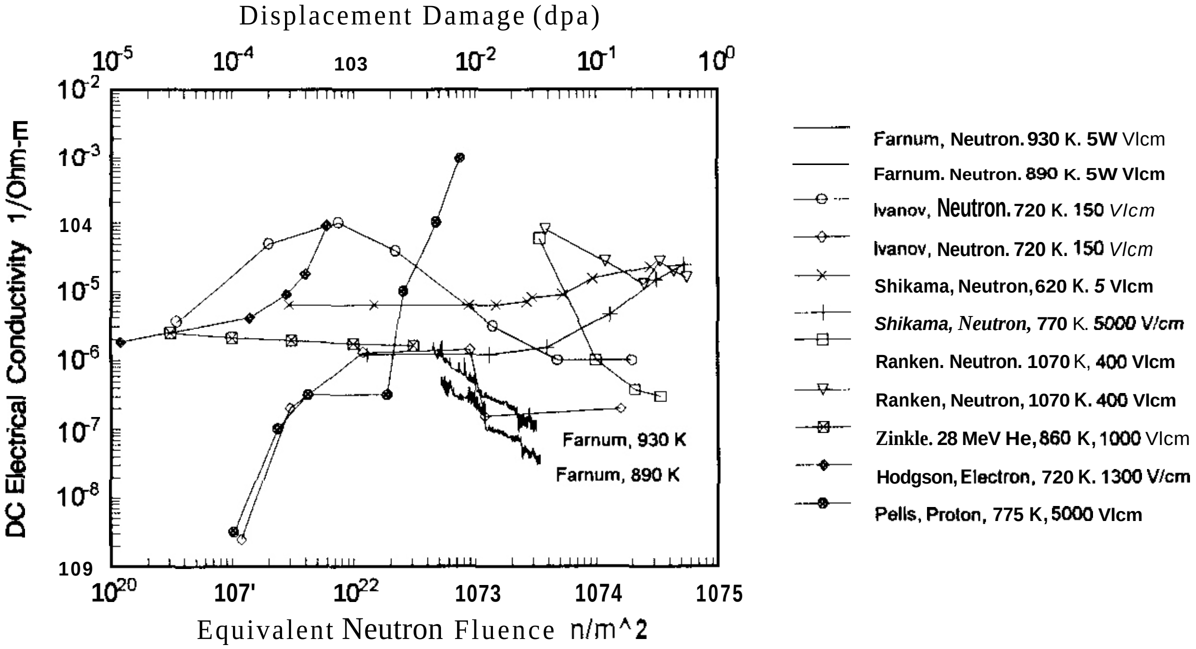

Figure 8. Compilation of data on RIED studies. Published data for electron, proton and neutron irradiation at various applied voltages and temperatures.

Summary

The DC data for most of the LASREF *in situ* irradiation experiment have been analyzed. No dramatic increases in conductivity were observed to the maximum estimated flux of 0.034 displacements per atom (dpa). Data from one DC sample set and the MI cables has yet to be fully analyzed and is waiting for post-irradiation measurements. The DC conductivity for two of our sample sets is compared to previous attempts to measure the RIED effect in Fig. 8. It should be noticed that no dramatic RIED effect bas yet been observed with DC measurements under neutron irradiation. Shikama's factor-of-three increase is. so far, the largest observed DC effect. These data would not indicate that RIED is a serious problem for fusion applications at least in the temperature, voltage. fluence ranges measured to date.

FUTURE WORK

The AC measurements we made at LASREF, described in the companion report, are dramatically different from the DC data described here. We do not yet have a plausible explanation for this difference. We are in the process of recovering the insert and samples and will begin post-irradiation examination in the third quarter. Post-irradiation electrical measurements will be compared between the DC and AC samples in an attempt to understand the differences in these two experiments. We will also conduct TEM examinations of both ac and dc samples to look for the onset of colloid formation. Steve Zinkle at ORNL will collaborate in these measurements.

Many passive samples were included in the LASREF experiment. These were contributed through our collaborations with researchers world wide. We will continue these collaborations, returning samples and making some post-irradiation measurements beginning in the third quarter.

References

1. G. P. Pells et. al., "Radiation Effects in Electrically Insulating Ceramics. Harwell Report AERE R 13222, September, 1988.

LAUR 93-2048

MEASUREMENT OF AC ELECTRICAL CONDUCTIVITY OF SINGLE CRYSTAL AL_2O_3 DURING SPALLATION-NEUTRON IRRADIATION

--, J. C. Kennedy III, E.H. Farnum, W F. Sommer and F. W. Clinard, Jr. (Los Alamos National Laboratory)

OBJECTIVE

The objective of this experiment is to determine the extent of electrical insulating degradation in Al_2O_3, a candidate dielectric material for fusion applications, during neutron irradiation and with an applied electric field.

SUMMARY

Samples of single crystal Al_2O_3, commonly known as sapphire, and polycrystalline Al_2O_3 were irradiated with spallation neutrons at the Los Alamos Spallation Radiation Effects Facility (LASREF) under various temperature conditions and with a continuously applied alternating electric field[1]. This paper describes the results of measurements on the sapphire samples. Neutron fluence and flux values are estimated values pending recovery and analysis of dosimetry packages. The conductivity increased approximately with the square root of the neutron flux at fluences less than 3×10^{19} n/m^2 and at fluxes less than 1×10^{16} n/m^2-sec. Conductivity initially decreased at low fluences with minimums near fluences of 1×10^{20} n/m^2. Incubation periods with a gradual increase in conductivity preceded the onset of an accelerated increase in conductivity beginning at fluences as low as 10^{21} n/m^2. The increase in conductivity reached saturation levels as high as 2×10^{-2} (ohm-m)$^{-1}$ at fluences as low as 2×10^{22} n/m^2. Frequency swept impedance measurements indicated a change in the electrical properties from capacitive to resistive behavior with increasing fluence.

PROGRESS AND STATUS

Introduction

The Fusion ceramics community has been concerned with the phenomenon of radiation-induced electrical degradation (RIED) in ceramic insulators ever since E.R. Hodgson[2-3] observed and reported the effect in single crystal Al_2O_3 during high energy electron irradiation.

RIED has been observed[2,4] only under conditions of concurrent ionizing radiation, displacement damage, moderately elevated temperatures, and applied electric fields. Degradation has been reported[2] for single crystal Al_2O_3 under both applied DC and AC fields up to 126 MHz. There is little or no frequency dependence of degradation behavior under AC applied fields but the onset of degradation has been reported to be delayed and the degradation rate reduced compared to DC applied fields[2]. Accelerated degradation has been observed[2] at fluences as low as 10^{-5} displacements per atom (dpa) with applied voltages above a threshold value of about 500 V/cm during 1.8Mev electron irradiation at a flux of 10^6 Gy/hr and a temperature of 450° C.

Studies of proton irradiated[4] polycrystalline $MgAl_2O_4$ and Al_2O_3 and electron irradiated[2] single crystal Al_2O_3 show degradation trends consisting of an incubation period during which conductivity is slowly increasing followed by the onset of a supralinear increase in conductivity. The incubation period has been found[2] to decrease with increasing dose rate and to increase with decreasing temperature.

Recently, Shikama et. al.[5] observed degradation in polycrystalline Al_2O_3 after irradiation with fission reactor neutrons near 500°C with a 5000 V/cm applied electric field.

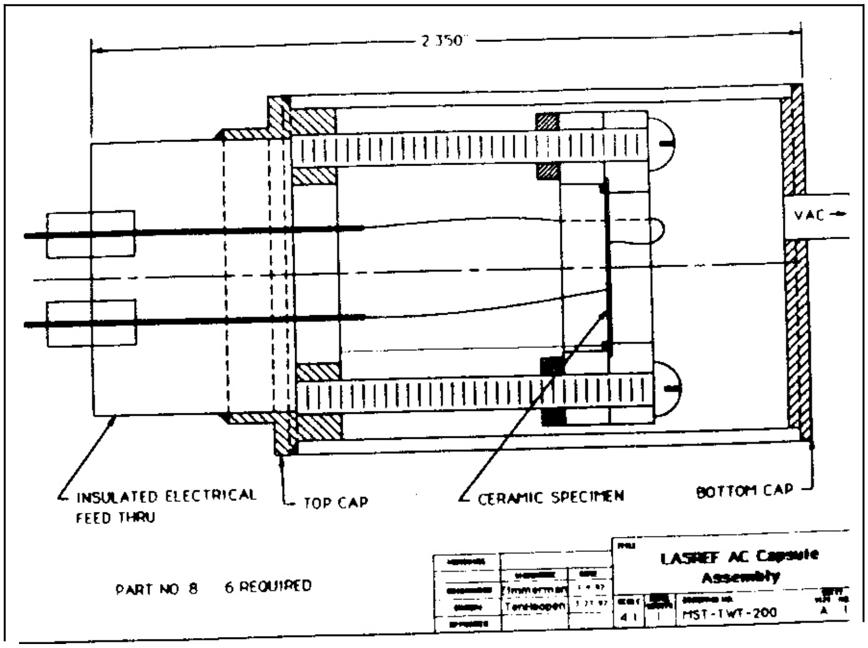

Fig. 1. Schematic diagram of **AC test capsule. Guard ring electrical lead is shown in contact** With **the capsule body or** electrical **ground.**

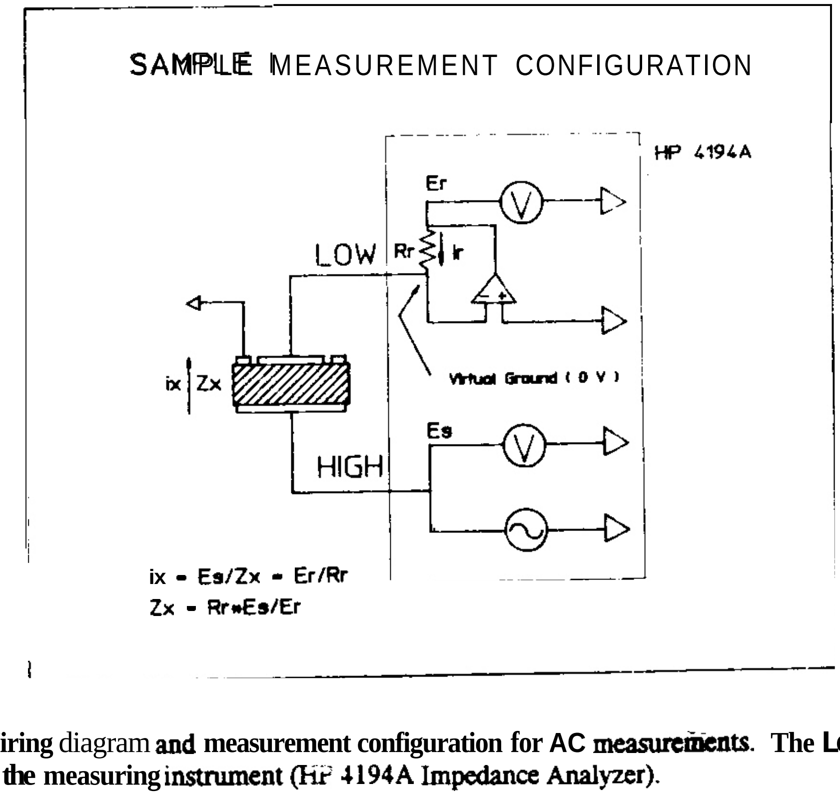

Fig 2. Wiring diagram **and measurement configuration for AC measurements. The Low side is driven** to **0 volts at the measuring instrument (HP 4194A Impedance Analyzer).**

A separate, but related, phenomenon is radiation induced conductivity (RIC) caused by the creation of excess charge carriers under ionizing radiation. RIC is a function of the ionization rate and the lifetime of excess charge carriers as determined by trapping and recombination processes.[6-9]. RIC is given by $\sigma=\sigma_0 + KR^{\delta}$, where σ_0 is the conductivity in the absence of ionizing radiation and R is the ionizing **flux** Studies[9-11] of Al_2O_3 under various types of ionizing radiation have generally reported flux-dependent δ values between 0.5 and 1.5 In addition, δ can have a complicated temperature dependence determined by the defect or doping state[10,11].

Experimental Method

The irradiation was carried out at LASREF near the beam stop of LAMPF. LAMPF is an **800** MeV linear proton accelerator that generally operates with an average beam current of 0.75 mA and a neutron **flux** near experimental stations of **3.8 x** 10^{17} **n/m^2-s-mA**[12,13] for neutron energies greater than 0.1 MeV. Calculated[13] gamma **flux** is approximately 1.4 x 10^{17} **/m^2-s-mA**. The proton beam is pulsed every **8.3** ms with the beam on for a period of 0.5 to 0.8 ms. Interaction of the protons with a copper beam stop produces spallation neutrons with an energy distribution corresponding to a moderated fission spectrum plus a high energy tail.

Although accurate determinations of neutron fluxes and fluences during our experiment must await recovery of dosimetry foils, it is estimated that the maximum average neutron **flux** (E > 0.1 MeV) at the samples ranged from 5.5 **x** 10^{16} to 1.0**x** 10^{17} n/m^2-sec. Total neutron fluences (E > 0.1 MeV) are estimated to range between 1.2 and **2.2** x 10^{23} **n/m^2**.

Samples were individually encapsulated in stainless steel capsules [Figure 1]. Based on measurements outside the capsules, it is estimated the single crystal sample capsules were evacuated to less than 10^{-4} torr . Two sample capsules, one with single crystal and one with polycrystalline Al_2O_3, were contained in each of three separately controlled and DC powered furnaces. The details of the furnace construction has been previously reported[1]. The furnaces were continuously supplied with argon at atmospheric pressure. Approximately 5m of MgO-insulated cables with stainless steel sheaths and nickel center conductors provided electrical leads from the capsules out of the high radiation area. Another 25m of polymer insulated coaxial cable carried the electrical signals to the instruments.

The single crystal sample capsules had ceramic insulated electrical feed-throughs with nickel leads. Platinum leads 0.005 inches in diameter were thermosonically bonded to the sample electrodes and **spot**-welded to the nickel leads. The sample electrodes were sputter deposited with 100 Angstroms of titanium followed by 2500 Angstroms of platinum. A guard ring configuration **as** specified in ASTM Standard D150 was applied using photolithography masking techniques. Samples were single crystal Al_2O_3 supplied by Crystal Systems, Inc. with face orientation $(11\bar{2}0)$. Major impurities were 8 ppm Fe and 6 ppm ***Ce.*** Sample dimensions were 0.216 mm thick **x 12.7** mm in diameter. The guarded electrode diameter was 7.65 mm.

The polycrystalline samples and sample capsules were supplied by Dr. Tatsuo Shikama of Tohoku University, Japan. The capsules were similar in construction to those reported by him **as** a 'second subcapsule design' in a separate irradiation experiment[14]. The samples were manufactured by Kyocera Co. Ltd., and had nominal dimensions of 0.15 mm thick **x 8** mm in diameter. Sample electrodes were similar to those for the single crystal samples.

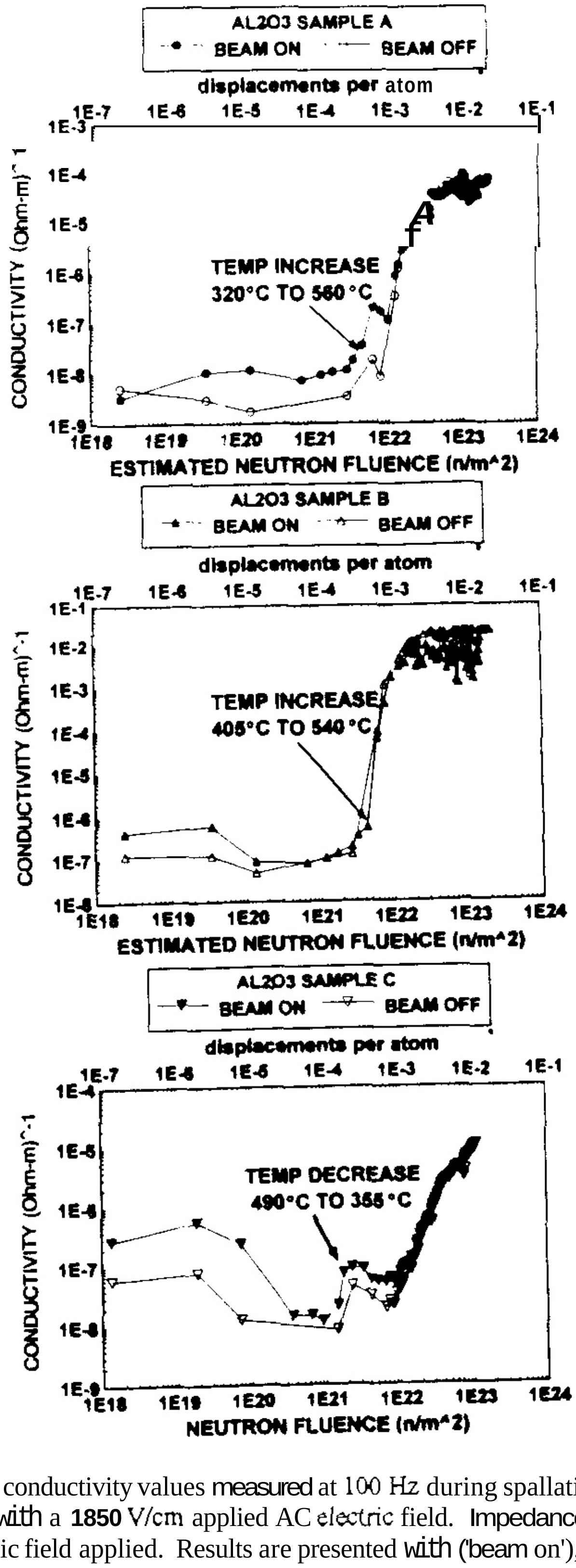

Fig's 3a-c. Averaged conductivity values measured at 100 Hz during spallation neutron irradiation of single crystal Al_2O_3 with a 1850 V/cm applied AC electric field. Impedance measurements were made without the AC electric field applied. Results are presented with ('beam on'), and without ('beam off), neutron flux present.

The samples were supplied with a 10 kHz voltage with a peak-to-peak amplitude of 80 volts. The applied electric field had a peak value of 1850 V/cm and an rms value of 1310 V/cm. The field was continuously applied to the samples during the irradiation except for periods of 30 to 60 seconds every 1 to 2 hours to allow frequency swept impedance measurements to be made.

Electrical measurements were made with a HP 4194A impedance analyzer which uses an auto-balancing bridge technique. Measurements were made over the frequency range of 100 Hz to 1 MHz. A three terminal configuration was used as shown in Figure 2. The impedance analyzer drives the low side of the circuit to 0 volts leaving the guard and guarded electrodes at the same potential. Measurement signal voltages are a maximum of 1 volt at high impedances with a compliance of 20 mA. Since the source voltage applied to the sample depends only on the impedance of the sample, any leakage current on the high side has minimal effect on the accuracy of the measurement as long as the total current is within instrument specifications. Separate measurements of MgO-insulated cables during irradiation with an applied electric field peak strength of 1750 V/cm did not reveal any degradation in cable insulation.

Results

This progress report concerns data collected from the single crystal samples. Analysis of the polycrystalline samples is not yet complete and is being done in collaboration with Dr. Tatsuo Shikama.

The irradiation initially began with Sample A (Furnace A) at 300°C, Sample B (Furnace B) at 375°C and Sample C (Furnace C) at 480°C. Early in the irradiation an increase in flux-induced heating caused us to reverse the low and high temperature furnaces and to increase the controlling temperature levels. All furnaces increased in temperature at 66 hours into the irradiation coincident with a factor of two flux increase. Another factor of two flux increase and coincident temperature increase at 85 hours resulted in the changes in furnace controlling levels referred to above.

Sample A increased from 300°C to 320 C at 66 hours and from 320°C to 560°C at 85 hours. Sample A averaged 580°C ± 20° C over the period of rapid degradation. Sample B increased from 375°C to 405°C at 66 hours and from 405°C to 540°C at 85 hours. The temperature increase in Sample B at 85 hours, unlike Sample A, precipitated a rapid, and nearly immediate, rise in conductivity of about two orders of magnitude. Sample B averaged 550°C ± 10 C over the rapid degradation period. Sample C increased from 480°C to 490°C at 66 hours and was lowered from 490°C to 355°C at 85 hours. The temperature was thereafter increased to 380° C and Sample C averaged 380°C ± 10°C over the degradation that continued throughout the irradiation cycle. The temperature profiles are further described in a companion progress report on DC conductivity measurements.

Figures 3 a-c show conductivity measured at 100 Hz versus estimated fluence in n/m^2 and dpa (1×10^{25} n/m^2 is estimated to induce one displacement per atom). Conductivity was calculated from the measured values of impedance modulus |Z| (ohms) and phase angle Θ (theta degrees). The AC conductivity is given by $\sigma=\omega k\varepsilon_o\tan\delta$; where ω is the angular frequency, k is the real part of the relative dielectric constant, ε_o is the permittivity of free space and $\tan\delta$ is given by the equivalent series resistance Rs ($|Z|\cos\Theta$) divided by the equivalent series reactance Xs ($|Z|\sin\Theta$). k is given by $Cp\, d/\varepsilon_o A$, where Cp is the parallel capacitance, d is the sample thickness, and A is the guarded electrode area. Cp is given by $1/\omega\, Rp \tan\delta$, where Rp is the parallel resistance. The conductivity can therefore be calculated from the expression, $\sigma=d/Rp\, A$, where the parallel resistance, Rp, is given by $Rp=Rs[(1+\tan^2\delta)/\tan^2\delta]$.

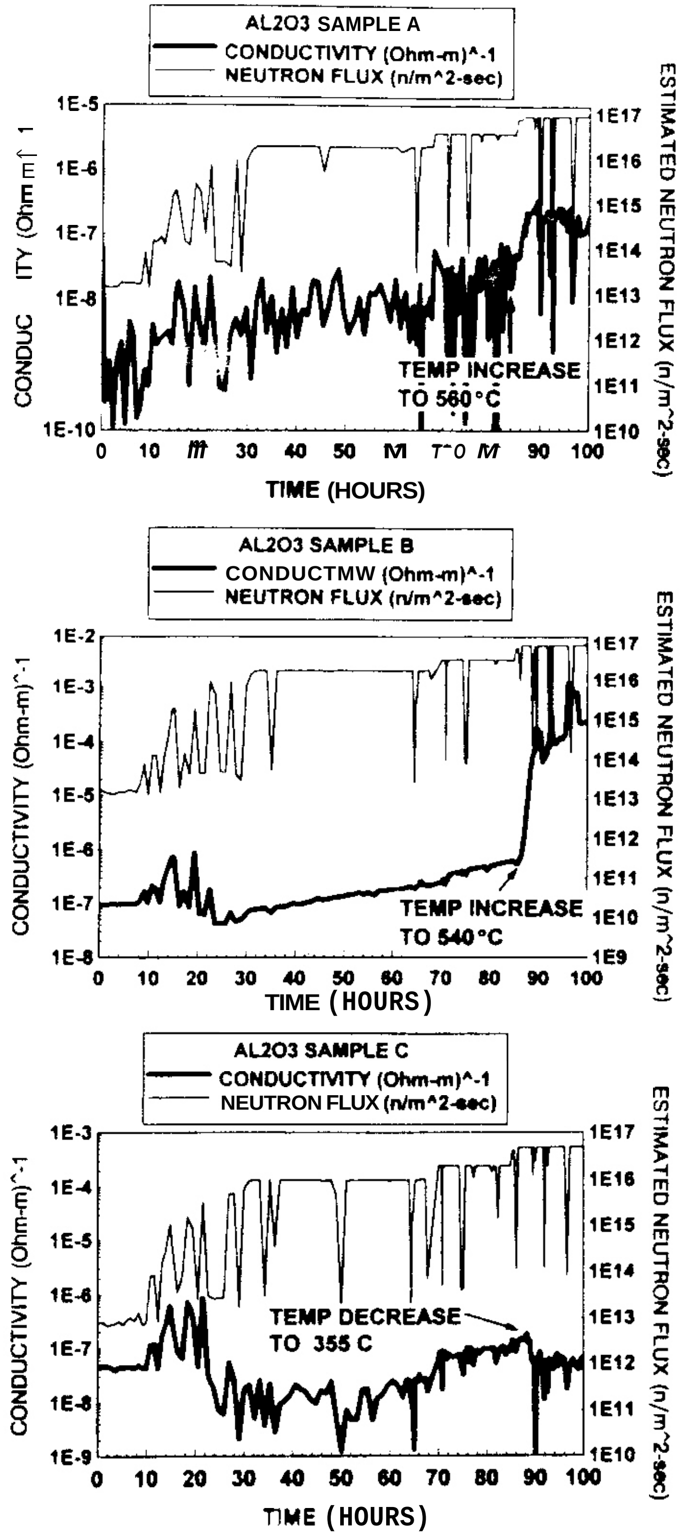

Fig's 4a-c. Conductivity of single crystal Al_2O_3 measured at 100 Hz early in the irradiation cycle. Neutron flux, in the upper part of the figure, is contrasted with conductivity, shown in the lower part of the figure. Increases in flux are seen at 66 and 85 hours. Temperature changes are indicated at 85 hours.

Conductivity values are initially presented here at 100 Hz since they are they are the lowest frequency measured and are more closely comparable to DC measurements. Conductivity trends for higher frequencies are similar and will be presented in a future publication with further analysis of frequency dependent behavior.

Conductivity results presented in Figures 3 a-c represent the averages of several conductivity measurements taken over eight hour periods **of** irradiation. The proton beam at LAMPF was off periodically during the irradiation for periods of a few minutes to several hours. Measurements were made with the proton beam both on and off. Conductivity with the proton beam on is contrasted with beam-off values in Figures **3** a-c.

Figures 4 a-c show unaveraged conductivity measurements and cslimated neutron flux. The neutron flux was calculated from beam current measurements taken before and after frequency swept impedance measurements. Early in the irradiation, increases in conductivity correspond to increases in neutron flux. Figure 5 shows conductivity as a function of neutron flux at low fluences ($<3 \times 10^{19}$ n/m^2) before any measurable change in the base conductivity. RIC increases as approximately the square root of the neutron flux.

The conductivity for all samples in Figures 3a-c shows a slight decrease in the base conductivity early in the irradiation. Decreases in radiation induced conductivity (RIC) for Samples B and C were also observed in this region. The conductivity response to flux and fluence can be seen in more detail in Figures 4 a-c. The base conductivity in all samples reaches a minimum value at about 10^{20} n/m^2. ***RIC*** appears to decrease relative to the base conductivity in all samples before the onset of degradation.

Sample B, initially irradiated at 375°C, shows an immediate and dramatic response with the fastest degradation rate after a temperature increase from 405°C to 550°C. Sample **A,** initially irradiated at 300° C, and with a large temperature increase from 320°C to 560°C, shows a much slower response to temperature change and a slower degradation rate. Sample C initially irradiated at 480°C and subsequently lowered in temperature from 490°C to 355°C, shows the beginning of rapid degradation which then appears to he retarded by the decrease in temperature and proceeds at a much slower rate thereafter.

Sample B reached the **highest** saturated conductivity with a value of 2×10^{-2} (ohm-m)$^{-1}$ at a fluence near 2×10^{22} n/m^2. Sample **A** degraded to a saturated conductivity of about 6×10^{-5} (ohm-m)$^{-1}$ at a fluence of about 5×10^{22} n/m^2 . The degradation in Sample C did not reach saturation, but had a conductivity of 1×10^{-5} (ohm-m)$^{-1}$ at the end of the irradiation cycle at a fluence of about 1×10^{23} n/m^2. Sample B, and to a lesser extent Sample **A,** show very noisy signals beginning near saturation, with the 'beam-on' condition resulting in decreased conductivity (an inverse ***RIC).***

Figures 6a-c show the measured impedance modulus and phase angle values **as** a function of frequency **at** fluences corresponding to the unirradiated condition, approximately half way (logarithmically) to saturation , and near saturation. Sample C , not having reached saturation, is shown at the highest fluence at the end of the irradiation cycle. Changes in the impedance behavior over the frequency spectrum indicate the general trend of a change from capacitive to resistive behavior with increasing fluence . **A** spike seen in some of the plots at 10 kHz is caused by interference from the applied electric field present on the samples not being measured.

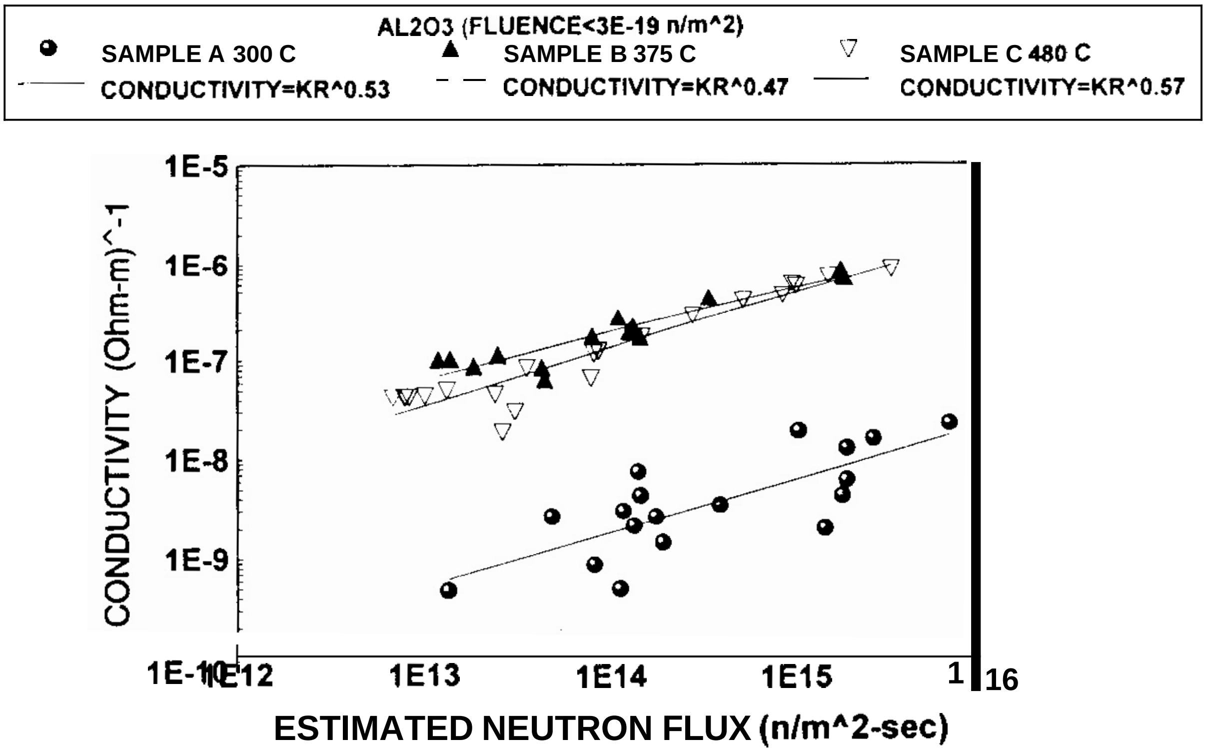

Fig. 5. Variation of radiation-induced conductivity with **estimated neutron flux in single crystal Al_2O_3 at 100 Hz prior to any changes in the base conductivity. Data were taken at fluences < 3 x 10^{-19} n/m^2.**

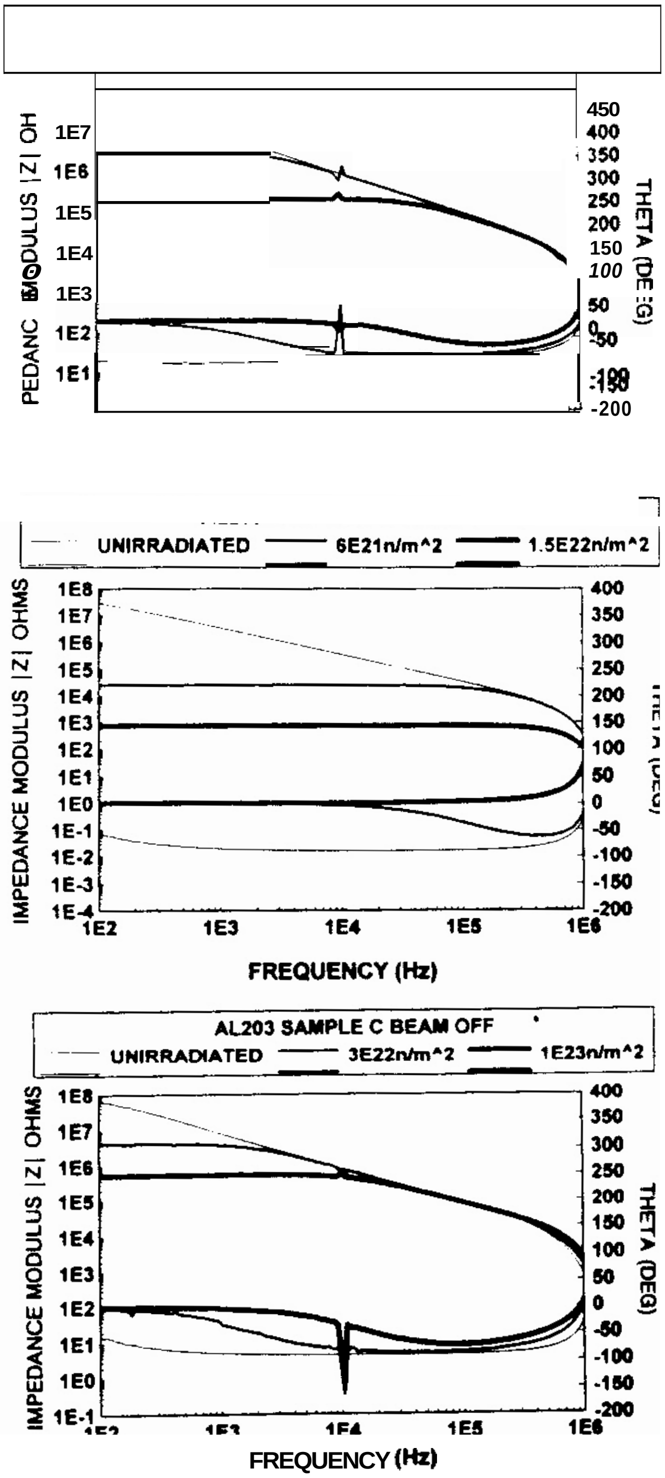

Fig's 6a-c. Impedance modulus |Z| (ohms) and phase angle, theta (deg), from 100 Hz to 1 MHz measured in the unirradiated condition, approximately half way to conductivity saturation on a logarithmic scale, and near saturation. See Fig's 3a-c. The spike at 10^4 Hz is caused by interference from the bias AC voltage.

Discussion

The AC data reported here differ dramatically from the DC conductivity data reported in the companion progress report on polycrystalline alumina. We do not yet have a plausible explanation for these differences. The extremely rapid rise in conductivity of Sample B and very noisy signals with an unexpected response to the 'beam-on' condition beginning near saturation are reasons for further analysis. Further analysis is also needed with respect to possible synergistic effects caused by coincidental changes in flux and temperature. It is expected that some of the present uncertainties will be addressed in the near future with the recovery of dosimetry packages and post-irradiation measurements.

REFERENCES

1. E.H. Farnum, F.W. Clinard Jr., J.C. Kennedy III, and W.F. Sommer, Semiann. Prog. Rep. on Fusion Reactor Materials for the period ending September 30, 1992, in press.

2. E.R. Hodgson, Cryst. Latt. Def. and Amorph. Mater. 18 (1989) 169

3. E.R. Hodgson, J. Nucl. Mater. 179-181 (1991) 383-386

4. **G.P** Pells, J. Nucl. Mater. 184 (1991) **177-182**

5. T. Shikama, M. Nami, Y. Endo, T. Sagawa and H. Kayano, J. Nucl. Mater. 191-194 (1992) 575.
6. A. Rose, RCA Review 12, No. 3, (1951) 363.

7. A. Rose, Concepts in Photoconductivity and Allied Problems, in: Interscience Tracts on Physics and Astronomy, No. 19 (Interscience Publishers **1963).**

8. **V.A.J.** vanLint et. al., Mechanisms of Radiation effects in Electronic Materials, Vol. 1 (Wiley & Sons, New York, 1980).

9. **V.A.J.** vanLint, J.W. Harrity, and T.M. Flanagan, IEEE Trans. Nucl. Sci. NS-15, No. 6, (1968) 194.

10. R.W. Klaffky, B.H. Rose, **A.N.** Goland. and G.J Dienes, Phys. Rev. B 21 **(1980) 3610.**

11. G.P. Pells and G.J. Hill, J. Nucl. Mater. 141-143 (1986) 375

12. D.R. Davidson. W.F. Sommer, J.N. Bradbury, R.E. Prael, and R.C. Little, J. Nucl. Mater. 122-123 (1984) **989.**

13. D.R. Davidson, PHD Dissertation, Neutron and Proton Dosimetry at the LAMFF 800-MeV Proton Accelerator, Iowa State University, 1990.

14. M. Nami, T. Shikama, Y. Endo, T. Sagawa, and H. Kayono, J. Nucl. Mater. 191-194 (1992) 592

IRRADIATION EFFECTS IN CERAMICS: TRANSITION FROM LOW TO HIGH DOSE BEHAVIOR - -

F. W. Chard, Jr. and E. H. Famum (Los Alamos National Laboratory)

OBJECTIVE

The objective of this work is to assess the changes that occur in various types of ceramics as irradiation doses progress from low to high levels, and to interpret those changes in terms of our present understanding of damage effects[1].

SUMMARY

Ceramics subjected to irradiation show a wide variety of damage responses, depending on composition, nature of bonding, crystal structure, impurity levels, starting microstructure. number of phases, and type of bombarding particle. As doses reach high levels (a condition that varies in magnitude from one material to another) major changes in physical properties can occur, and atomic arrangements may even change from crystalline to disordered. However, some ceramics show marked resistance to damage, and some properties may improve. More work is needed to fully understand these phenomena, but it is currently possible in many cases to predict at least qualitatively both microstructural damage response and observed property changes.

PROGRESS AND STATUS

Introduction

At low damage levels, physical property changes in ceramics are for the most part small in magnitude. The primary damage state and effects of low-dose damage comprise the first topic discussed here.

As damage accumulates and larger defect aggregates are formed, major changes in physical properties (not always deleterious) can be expected. Nevertheless, in many ceramics the constituent ions are for the most part not permanently displaced, and so the damage can be characterized as isolated. High-dose isolated damage is the next topic addressed.

Ceramics with primarily covalent bonding *can*, at moderate damage levels (e.g., one displacement per atom) become globally disordered. This condition, which is sometimes referred to as the amorphous or metamict state, is considered next

Engineering materials are often made up of two or more phases. Since each phase will demonstrate a characteristic response to irradiation, the combined damage state can be complex. The unusual swelling behavior of such a material is the last topic discussed.

The Primary Damage State and Low-Dose Behavior

With respect to neutron irradiation, ***primary*** damage ***effects*** are usually Visualized in terms of cascade formation and post-cascade defect content. Damage cascades have been extensively studied in metals, but little work has been done on ceramics. Issues that are especially important to ceramics include:

-- The possibility of forming anti-site defects, e.g., Al ions on O ion sites in alumina or N ions on O sites in aluminum oxynitride;

-- The consequence of unequal numbers of cation and anion displacements;

-- Amorphicity in cascades and as the permanent, bulk damage condition;

-- Direct observation of cascades

At low damage levels, ceramics accommodate permanent displacement damage in the form of cation and anion vacancies and interstitials, as well as small clusters. Insight as to defect species present and their charge states can be obtained by employing various experimental techniques, among which the most commonly used is optical absorption. An example of the use of this technique is the work of Atobe et al. [2], in which various point defects and small aggregates were identified in neutron-irradiated Al_2O_3.

Isolated High-Dose Damage

Many ceramics will, after irradiation to damage levels on the order of one displacement per atom (about 1×10^{25} n/m^2) exhibit a population of defect aggregates such as cavities and interstitial dislocation loops. These aggregates, and other defects such as isolated vacancies, can have a profound effect on physical properties. For example, Al_2O_3 swells 4 vol. % at 1100 K (Fig. 1) as a result of the formation of 9 nm dia. cavities [3]. Fracture toughness of this material has doubled, apparently as a result of the interaction of cracks with the cavity population [4]. Room temperature thermal diffusivity is significantly reduced, an effect attributed to phonon scattering both from the cavities and from point defects or fine aggregates too small to be detected in conventional transmission electron microscopy [5].

Figure 1 also shows swelling data for $MgAl_2O_4$ spinel after elevated temperature neutron irradiation [3]. It can be seen that this material is highly resistant to dimensional changes, at least in single-crystal form. The microstructure of irradiated spinel exhibits only faulted interstitial dislocation loops [3], with the absence of cavities indicating that vacancies either remain in the dispersed state or for the most part recombine with interstitials. The lack of degradation of thermal diffusivity in single-crystal spinel [5] implies that most of the point defects have in fact recombined. Measurements carried out on $MgAl_2O_4$ after irradiation to 680 and 815 K show that this material is markedly strengthened by irradiation to a fluence of 2×10^{26} n/m^2 [6]. Such strengthening may result from the interaction of propagating cracks with strain fields around the interstitial loops.

Ceramics with non-cubic crystal structures are subject to anisotropic swelling, which can result in high intergranular stresses that markedly reduce mechanical properties. This effect can best be seen in the data of Hickman on the hexagonal ceramic BeO [7]. Here it was found that beyond a fluence of 1×10^{25} n/m^2 at 348-373 K the polycrystalline form of this ceramic loses more that 90% of its strength.

Electrical conductivity of insulating ceramics is usually not greatly affected by prior displacement damage. However, this property has been shown by Klaffky et al. [8] to be strongly dependent on rate of absorption of ionizing energy during irradiation, with conductivity of Al_2O_3 exhibiting increases of several orders of magnitude. A potentially more serious problem has been identified by Hodgson [9]: when deposition of ionizing energy and displacement damage occur concurrently with application of an electric field, conductivity of Al_2O_3 over time shows an additional increase beyond that caused by flux effects. This phenomenon appears to be related to microstructural changes in the material.

Of particular importance to the use of ceramics in fusion reactors is the role of transmutation products. Calculations by Rovner and Hopkins [10] indicate that after ten years at the first wall of a 2 MW/m^2 reactor, impurity levels of gaseous and metallic transmutation products can reach concentrations on the order of 1 atomic percent. The effects of such high impurity concentrations have not been investigated, but are expected to be significant.

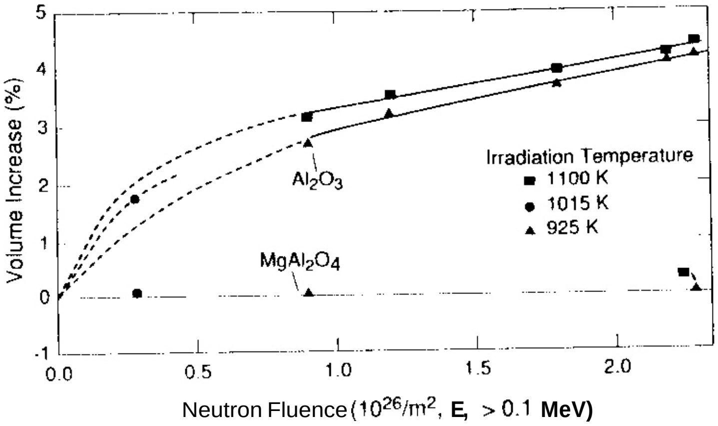

Fig. 1. Swelling of single-crystal Al_2O_3 and $MgAl_2O_4$ as a function of neutron fluence for three irradiation temperatures [3]

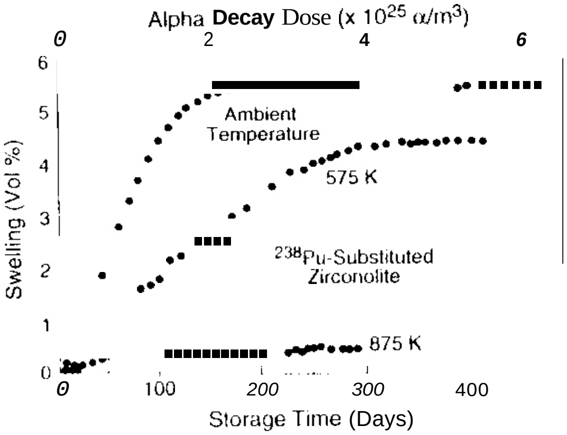

Fig. 2. **Bulk** swelling of $CaPuTi_2O_7$ as a function of temperature, damage dose, and storage time. Ambient temperature was aproximately 350 K. [11].

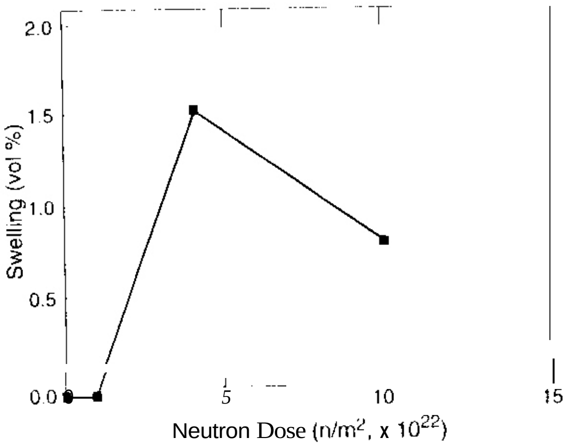

Fig. 3. Swelling of Macor at room temperature **as** a function **of** fluence **of** 14 MeV neutrons [14].

Amorphization

Some ceramics, especially those with primarily covalent bonding, accommodate displacement damage by formation of localized microvolumes of disordered (variously referred to as amorphous, aperiodic, or metamict) material. With a sufficiently large damage dose, the ceramic can become completely amorphous.

An example of such irradiation behavior is the response of the simulated nuclear waste form $CaPuTi_2O_7$ to self-damage resulting from alpha decay of ^{238}Pu [11]. Here, most of the damage results from recoil of the ~100 keV ^{234}U ion. As can be seen from Fig. 2, this material exhibits significant swelling near room temperature, with saturation being reached at a damage level of about 1 dpa. If the material is held at 575 K during self-irradiation, a less-disordered condition is achieved and swelling is reduced. Aging at 875 K results in retention of the crystalline state, as damage is recovered concurrently with its formation.

With respect to fusion applications, silicate-based insulators, which are specified for use in diagnostic applications, are most likely to undergo a crystalline-to-amorphous transformation. For example. crystalline quartz (SiO_2) has been shown to convert to an amorphous condition and undergo swelling of 14 vol % when irradiated near room temperature to a fluence of $2x10^{24}$ n/m^2 [12]. Such a dose, although modest for ceramics such as A1203 and $MgAl_2O_4$, must be thought of as "high" for quartz.

Response of a Multiphase Ceramic

Each phase of a multiphase materials system will have its own characteristic damage response under irradiation. It can be anticipated that some multiphase materials will perform less well than would each phase separately, as relative changes in some properties (e.g., density) may not easily be accommodated. An example of such a system is Macor, a machinable glass-ceramic [13]. This material consists of two silicate phases, one crystalline and one amorphous; the microstructure is made up of 1 to 10 micron platelets of crystalline mica dispersed in a borosilicate glass matrix, with each phase comprising approximately 50 vol % of the glass-ceramic.

Irradiation of Macor to a fluence of $1x10^{23}$ n/m^2 at room temperature results in the unusual swelling behavior shown in Fig. 3 [14]: after an incubation period swelling rises to 1.5 vol %, but is then halved at a higher fluence. This behavior has been interpreted [14] by use of a model based on information in the literature on the swelling behavior of crystalline and amorphous silicates, along with the experimental data of Fig. 3. The model assumes that each phase begins to change in density after an incubation period, and swells or densifies exponentially with fluence to a steady-state value. Making use of data showing densification of amorphous SiO_2 [12] and swelling of mica [15], it was possible to fit the experimental swelling curve for Macor with fair accuracy and to predict a saturation swelling value for the glass-ceramic of less than 0.5 vol % [14]. However, it should be recognized that this reasonably good dimensional stability may, because of differential swelling, be accompanied by high internal strains, microcracking, and significant strength loss.

FUTURE WORK

Irradiation behavior of ceramics as fluence is increased from low to high doses cannot easily be generalized, because of the variety of damage responses that can occur. Future materials and reactor design studies should take into account (1) the major changes that can occur in ceramics which retain their crystallinity at high fluences, (2) the possibility that Some ceramics may become amorphous under irradiation at relatively low doses, and (3) the likelihood that multiphase ceramics will suffer degradation of physical properties primarily because of differences in damage response between each phase rather than from intrinsic damage effects in the separate phases.

REFERENCES

1. This report is an abbreviated version of a paper that will **appear** in the Journal of Nuclear Materials

2. K, Atobe, N. Nishimoto **and** M. Nakagawa, Phys. Stat. **Sol.** 89 (1985) 155.

3. F. W. Chard, Jr., L. W. Hobbs and G. F. Hurley, J. Nucl. Mater. 108&109 (1982) 655.

4. F. W. Chard, Jr.. *G.* F. Hurley, R. A. Youngman and L. W. Hobbs, J. Nucl. Mater. 133&134 (1985) 701.

5. F. **W.** Clinard, Jr. **and** I.. W. **Hobbs,** in: Physics of Radiation Effects in **Crystals,** eds. R. **A.** Johnson and A. N. Orlov (North Holland. Amsterdam, 1986) **p.** 387.

6. F. **W.** Chard, Jr., G. F. Hurley, L. W. Hobbs, D. L. Rohr and R. **A.** Youngman, J. Nucl. Mater *122&123 (1984) 1386.*

7. B. S. Hickman, Radiation Effects in Beryllium and Beryllium Oxide, in: Studies in Radiation Effects, Series **A,** Physical and Chemical, **Vol.** 1, ed. G. J. Dienes (Gordon **and** Breach, New **York,** 1966) p. 72.

8. R. W Klaffky, B. **H.** Rose, **A.** N. Goland and G. J. Dienes, Phys. Rev. B21 (1980) 3610.

9. E. R Hodgson, J. Nucl. Mater. 191-194 (1992) 552.

10. L. H. Rovner and G. R. Hopkins, Nucl. Technol. 29 (1976) 274.

11. W. A. Coghlan and F. W. Chard, Jr., J. Less-Common Metals 140 (1988) 255.

12. M. Wittels and F. A. *Sherill,* Phys. Rev. 93 (1954) **1117.**

13. Macor is a product of Corning Glass **Works,** Coming, NY.

14. W. **A.** Coghlan **and** F. **W.** Chard, Jr., J. Nucl. Mater. 179-181 (1991) 391.

15. C. D. Bopp, O. Sisman and R. L. Towns, The Effect of Irradiation on the Thermal Stability of Muscovite Mica, *Oak* Ridge National Laboratory Report ORNL-3017 **(1960).**

THE EFFECT OF RADIATION INDUCED ELECTRICAL CONDUCTIVITY (RIC) ON THE THERMAL CONDUCTIVITY OF SAPPHIRE AT 77 K – D.P. White (Oak Ridge National Laboratory)

OBJECTIVE

This work is intended to provide information on the changes expected in the thermal conductivity of sapphire due to the scattering of phonons by conduction band electrons, which are present due to the RIC.

SUMMARY

Microwave heating of plasmas in fusion reactors requires the development of microwave windows through which the microwaves can pass without great losses. The degradation of the thermal conductivity of alumina in a radiation environment is an important consideration in reliability studies of these microwave windows. Several recent papers [1,2,3] have addressed this question at higher temperatures and at low temperatures [4]. The current paper extends the low temperature calculations to determine the effect of phonon-electron scattering on the thermal conductivity at 77 K due to RIC. These low temperature calculations are of interest because the successful application of high power (>1 MW) windows for electron cyclotron heating systems in fusion reactors will most likely require cryogenic cooling to take advantage of the low loss tangent and higher thermal conductivity of candidate window materials at these temperatures.

PROGRESS AND STATUS

Introduction

The lattice thermal conductivity is calculated using the Callaway [5] formulation of the thermal conductivity integral given in Ref. 4. In order to calculate the thermal conductivity using this formulation it is necessary to have functional forms for the relaxation times for the various phonon scattering mechanisms. As in Ref. 4 the normal process relaxation time, the umklapp phonon relaxation time, the boundary scattering relaxation time, and the intrinsic point defect scattering relaxation time used are those obtained by de Goer [6] for a cylindrical sapphire sample 50mm long and 5mm in diameter (de Goer's sample 5).

In order to determine the effect of phonon-electron scattering on the thermal conductivity the phonon-electron relaxation time must be included as a resistive phonon scattering process in the Callaway formulation. The phonon-electron relaxation time may be obtained though a momentum balance argument [3] and is of the form:

$$\frac{1}{\tau_{p-e}} = \frac{3v^2}{\mu^2}\frac{\sigma}{CT} \tag{1}$$

where v is the phonon velocity, μ is the electron mobility, C is the phonon specific heat of those phonons which are allowed to interact with the conduction band electrons (due to energy and wave-vector conservation considerations), σ is the electrical conductivity, and T is the temperature.

Calculation

The relaxation time given in Eq. 1 must be evaluated in order to use it in the thermal conductivity integral. Klaffky et.al. [7] found evidence of a temperature independent mobility for $T < 300$ K, and Hughes [8] reported a temperature independent mobility of $(3 \pm 1) \times 10^{-4} m^2/V - s$ for an undoped aluminum sample between 100 and 350 K. In the calculations presented here it is assumed that, this constant mobility holds to 77 K.

The specific heat, C, of those phonons up to a cut off frequency of $\omega_c = \frac{2v}{\hbar}(2mk_BT)^{1/2}$ is given, in the Debye approximation, by:

$$C = 9nk_B \left(\frac{T}{\Theta_D}\right)^3 \int_0^{\Theta_c/T} \frac{x^4 \exp x}{(\exp x - 1)^2} dx \tag{2}$$

In these expressions, m is the electron mass, k_B is the Boltzmann constant, n is the number of unit cells per unit volume, Θ_D is the Debye temperature, Θ_c is the phonon-electron cut off temperature given by $\Theta_c = \hbar\omega_c/k_B$, $x = \hbar\omega/k_BT$, where $\hbar$ is Plank's constant divided by 2π, and w is the phonon angular frequency. The expression given in Eq. 2 may be evaluated by numerical integration for any particular temperature and then this value may be used in the relaxation time of Eq. 1. The value of the phonon velocity is $v = 7 \times 10^3 m/s$.

It is possible to calculate the changes in the thermal conductivity due to changes in σ by numerically evaluating the Callaway thermal conductivity integral for different values of σ in the phonon-electron relaxation time.

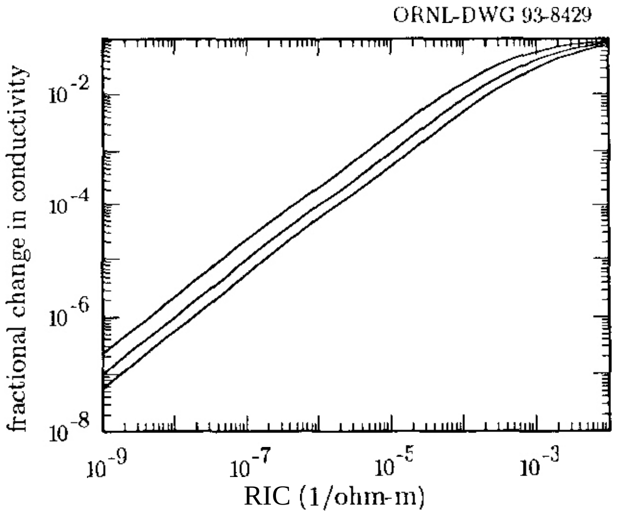

Figure 1: Fractional change in the lattice thermal conductivity versus RIC at 77 K. Each curve corresponds to a different value of the electron mobility, covering the range of uncertainty in the mobility $(3 \pm 1) \times 10^{-4} \mathrm{m}^2/\mathrm{V} - \mathrm{s}$. The upper curve corresponds to $\mu = 2 \times 10^{-4} \mathrm{m}^2/\mathrm{V} - \mathrm{s}$, the center curve to $\mu = 3 \times 10^{-4} m^2/V - s$, and the lower curve to $\mu = 4 \times 10^{-4} \mathrm{m}^2/\mathrm{V} - \mathrm{s}$.

Results of Calculations

The results of the thermal conductivity calculations are given in Fig. 1. In this figure the fractional change in the thermal conductivity versus RIC is plotted. The three different curves correspond to different values of the electron mobility, covering the range of uncertainty in the electron mobility. The upper curve corresponds to $\mu = 2 \times 10^{-4} m^2/V - s$, the middle curve corresponds to $\mu = 3 \times 10^{-4} m^2/V - s$, and the lower curve corresponds to $\mu = 4 \times 10^{-4} m^2/V - s$. From this plot it can be seen that at the highest values of the RIC plotted, the change in the thermal conductivity approaches a maximum of about 9%. This value corresponds to the case of all phonons below the cut off frequency being strongly scattered, and thus is the limiting value of the reduction in the thermal conductivity which can occur at this temperature due to phonon-electron scattering.

DISCUSSION AND CONCLUSIONS

The maximum of the range of prompt RIC values in sapphire in a fusion environment is expected to be on the order of $10^{-5}(\Omega - m)^{-1}$. Using this value for the RIC the corresponding range for the fractional change in the thermal conductivity is from 0.05% to 0.2% at 77 K. It was found [1,3] that at 300 K the expected fractional change in the conductivity at this value of the RIC was about 0.01%. Thus the effect of phonon-electron scattering on the thermal conductivity is larger at low temperatures but these are very small changes in the thermal conductivity and are not expected to be of importance in the design of microwave windows. Even in the extreme case of very large values of the RIC the maximum effect the phonon-electron interaction can have on the thermal conductivity is about 9%, as pointed out in the previous section. It should also be noted that there is essentially no change in the thermal conductivity due to the small electronic component added by the RIC, as pointed out in Ref. 3.

These changes are particularly insignificant when the temperature dependence of the thermal conductivity at low temperatures is considered. In this low temperature region the thermal conductivity is strongly temperature dependent; for example, in the region around 77 K calculations show that a 1% change in the temperature leads to a 4% change in the thermal conductivity. Thus the effects of temperature fluctuations on the thermal conductivity are expected to be at least as important as any effects due to phonon-electron scattering.

The small changes expected in the thermal conductivity due to phonon-electron scattering suggest that there is no need for *in-situ* thermal conductivity measurements in order to study this effect. However this does not rule out the need for performing *in-situ* cryogenic thermal conductivity tests in order to study the effects of thermally unstable radiation produced defects.

FUTURE WORK

It is planned to further investigate phonon-electron scattering effects in the presence of radiation induced vacancies. This will be of interest because as the point defect concentration is increased, the thermal conductivity at low temperatures is a much shallower function of temperature [9,10] and it can be reduced on the order of 90% [4]. Because point defects and electrons scatter phonons on opposite ends of the phonon spectrum the phonon-electron effect may become significant at high point defect concentrations for these reasons.

Surface preparation Effects in Near Surface Modulus Measurement for CVD SiC —

M. C. Osborne (Rensselaer Polytechnic Institute), L. L. Snead (Oak Ridge National Laboratory), and D. Steiner (Rensselaer Polytechnic Institute)

OBJECTIVE

This study was performed to determine *the* variation in the measured modulus resulting from the use of various polishing grits on CVD SiC when taking shallow indents (20 nm) on a SiC/Nicalon^{TM} composite sample. When ion bombarding the SiC composite, the ion penetration is only a few microns. To measure the **modulus** as a function **of** the damage level, Nanoindenter^{TM} indents are made on the material in cross-section at various depths below *the* surface presented to the incoming ions.[1,2] The purpose of making shallow indents is to minimize the volume sampled at a given depth, which leads to a more accurate determination of the modulus at any damage level.

SUMMARY

Surface preparation has an observable effect on the data obtained from *the* Nanoindenter for shallow (20 nm) indents on CVD SiC when polished with Syton^{TM}. This observed effect is significantly less for 1/2 micron diamond polished CVD SiC and for deep (160 nm) indents. These effects were manifested by the relative variations in the experimental modulus and hardness data. **An** analytical analysis of the anticipated variation in the modulus and hardness is performed and shown to correlate well **with** *the* observed **trends.** The observed variations appear to be the result of SiC material properties. as well as surface preparation, since the predicted variations are much smaller than the observed variations.

PROGRESS and STATUS

Introduction

In this study, variations in experimental modulus and hardness data are compared to modulus and hardness variations predicted semi-theoretically considering surface roughness as the only variable. **A** load controlled Nanoindenter is employed to experimentally determine modulus and hardness values for CVD SiC and Nicalon. Modulus and hardness variations **are** defined as relative variations given **by:**

$$\frac{\Delta E}{E} = \frac{E_S - E_C}{E_S} \qquad (1)$$

$$\frac{\Delta H}{H} = \frac{H_S - H_C}{H_S} \qquad (2)$$

where E_S **and** H_S are either (1) *the* average modulus **or** hardness determined by the Nanoindenter (experimental) or (2) a calculated modulus or hardness for a flat **(smooth)** surface. E_C **and** H_C are either (1) the average plus one **standard** deviation of the modulus or hardness determined by *the* Nanoindenter (experimental) or (2) a calculated modulus or hardness for a curved (rough) surface.

The Nanoindenter determines the sample modulus, E. by the following equation:[3]

$$E = \frac{1}{2}\frac{dP}{2dh}\left(\frac{\pi}{A(h_p)}\right)^{1/2} \qquad (3)$$

where $A(h_p)$ is the cross-sectional area of the indenter associated with the contact area projected onto the plane of the surface. The area $[A(h_p)]$ is determined as a function of the plastic depth (h_p). This contact area is calculated by the Nanoindenter software assuming ideal Berkovich indenter tip geometry. The stiffness. dP/dh, is the slope of the unloading ponion of the load-displacement curve generated by a load-displacement experiment as shown schematically in Fig. 1.[4] The point at which the tangent line intersects the displacement axis is the plastic depth.

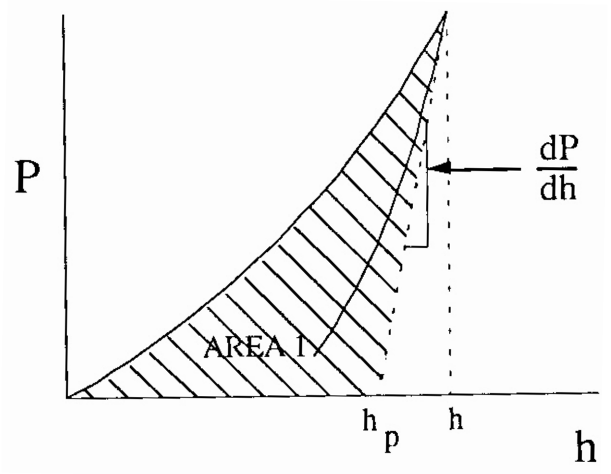

Figure 1. Indenter Load-Displacement Curve

The hardness, H, is determined by the Nanoindenter from the following equation:

$$H = \frac{P}{A(h_p)} \qquad (4)$$

where P is the *peak* load.

Equations 1 through 4 are also used to predict theoretical variations in modulus and hardness for either a flat (smooth) or curved (rough) surface. The calculational approaches for obtaining dP/dh, P, and $A(h_p)$ are outlined below.

We first consider the evaluation of dP/dh, which *can* he expressed as:

$$\frac{dP}{dh} = \frac{P}{(h - h_p)} \qquad (5)$$

where h is the indenter depth. To determine P, h, and h_p, a knowledge of the volume of material plastically deformed by the indentation is required. For a flat surface, this plastically deformed volume is hemispherical, with an assumed radius of about 10 h from the indenter tip when the indenter is at the desired depth.[1,6] When the indent is made on a curved surface rather than a flat surface. a volume of material is/is not deformed by the indenter, depending on the indent location, as shown in Fig. 2.

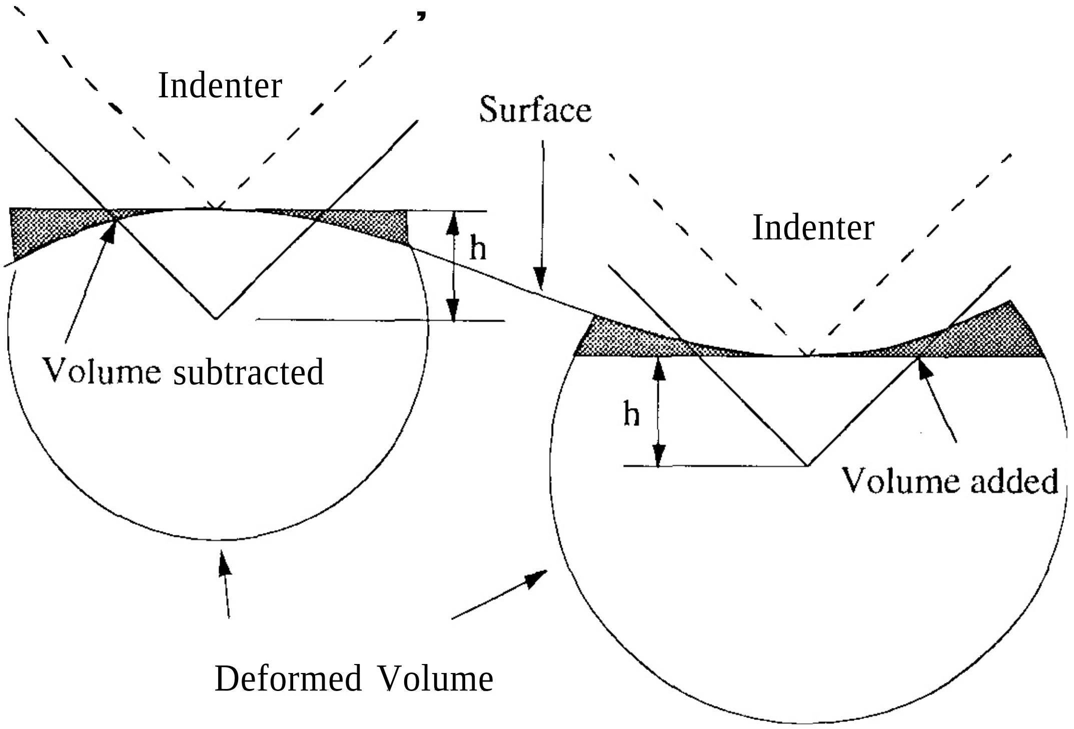

Figure 2 . Indent Cross-section Profile

Referring to Fig. 1, Area 1 represents the work done on the material due to plastic deformation and is proportional to the product of P and h_p. Assuming that the plastic strain energy per unit volume is approximately constant, since relatively little plastic deformation occurs in SiC, the plastic work is also proportional to the volume of material plastically deformed. Therefore, the loads (P), plastic depths (h_p), and volumes of plastically deformed material for flat and curved surfaces are related as follows:

$$\left(\frac{Ph_p}{V_{deformed}}\right)_{flat} = \left(\frac{Ph_p}{V_{deformed}}\right)_{curved} \qquad (6)$$

In the schematic of Fig. 2 (showing the cross-section of the indenter and sample) there is some volume of material that is added or subtracted depending on the indent location. The actual volume of material deformed by the indenter on a curved surface would equal the volume deformed when indenting on a flat surface plus/minus the volume between the true surface and the projected cross-section of the deformed volume onto a flat surface. Thus,

$$V_{deformed\ actual} = V_{deformed\ flat} \pm V_{surface\ difference} \qquad (7)$$

The deformed volume for a flat surface is related to the indent depth, h, and can be estimated by:

$$V_{deformed\ flat} = \frac{1}{2}\frac{4\pi(10\,h)^3}{3} + \pi(10\,h)^2\,h \qquad (8)$$

example, if the sample had been Syton polished, was the second sample of the group, and was subjected to a second set of indents on the sample. then it would be labeled Syton 2,2. Table 1 gives the results for the 20 nm indents and Table 2 gives the result. for the 160 nm indents.

Table 1 Modulus and hardness for CVD SiC at an indent depth of 20 nm

Sample Syton polished CVD SiC	Average modulus (GPa)	Relative variation	Hardness	Relative variation
1.1	509	0.0585	45.6	0.087
2.1	456	0.0822	44.0	0.097
2.2	478	0.0674	46.4	0.101
2.3	474	0.160	43.7	0.192
3.1	434	0.0624	34.9	0.074
4.1	542	0.119	55.3	0.161
Averages	482	0.0916	45.0	0.11
1/2 micron diamond polished CVD SiC				
1.1	461	0.0555	39.7	0.075
1.2	477	0.0413	45.6	0.065
2.1	440	0.0665	34.9	0.065
Averages	459	0.0544	40.1	0.069
3 micron diamond polished CVD SiC				
1.1	473	0.129	48.2	0.158
1.2	457	0.128	48.1	0.158

Table 2. Modulus and hardness for CVD SiC at an indent depth of 160 nm

Sample Syton polished CVD SiC	Average modulus (GPa)	Relative variation	Hardness	Relative variation
1.1	513	0.0337	41.7	0.0360
2.1	469	0.0356	43.1	0.0510
2.2	474	0.0344	44.5	0.0449
2.3	445	0.0454	40.9	0.0636
3.1	371	0.0383	20.2	0.0297
4.1	480	0.0340	43.7	0.0389
Averages	459	0.0369	39.0	0.440
1/2 micron diamond polished CVD SiC				
1.1	481	0.0170	37.2	0.0323
1.2	449	0.0274	35.9	0.0418
2.1	350	0.0251	23.9	0.0251
Averages	427	0.0232	32.3	0.0331
3 micron diamond polished CVD SiC				
1.1	466	0.0539	42.8	0.0678
1.2	474	0.0521	43.7	0.0641

The Nicalon fibers were also indented. Only one sample for each polish grit was indented for the fibers. The results for Nicalon fibers are shown in Table 3.

Table 3. Modulus and hardness of Nicalon fiber, at indent depths of 20 nm and 160 nm

Polish	Average modulus (GPa)	Relative variation	Hardness	Relative variation
indent (20 nm)				
Syton	191	0.0445	20.2	0.0743
1/2 micron	217	0.106	25.4	0.177
3 micron	216	0.206	23.9	0.247
indent (150 nm)				
Syton	176	0.0256	18.3	0.0273
1/2 micron	185	0.0438	20.8	0.0338
3 micron	190	0.0721	21.7	0.0691

A 1/2 micron and a Syton sample were inspected using an atomic force microscope (AFM) to resolve the surface roughness. The surface profiles allowed the determination of the peak to valley height for the different polishes. Typical micrographs are shown in Figure 3. Figure 3a shows the surface profile of a Syton polished composite sample. It is obvious from the micrograph that the CVD SiC matrix has a rougher surface than the Nicalon fiber. Because the Syton is a very fine (–0.05 micron) polish of silica, preferential removal of the matrix can take place. Figure 3a shows a radial ridge typical of the radially grown CVD SiC grains. The individual grains are polished at different rates and are therefore exposed along with the growth boundaries. Figure 3b shows an AFM image of an indent taken on the Syton polished CVD SiC demonstrating that the ridge structure is on a scale which is significant as compared to the indent. Because the Nicalon fiber is made up of very fine SiC crystallites (–10 nm) in an amorphous matrix of glass, no preferential polishing takes place, leaving a relatively smooth surface (Fig. 3a).

Figure 3c shows a micrograph of diamond indents taken on a 1/2 micron polished CVD surface at about half the magnification shown in 3b. It can be seen from this micrograph that the diamond polish has not left behind the fine ridge structure caused by Syton polishing. This is to be expected, as the diamond polishing media is harder than the CVD SiC and is also on the order of size of the grains.

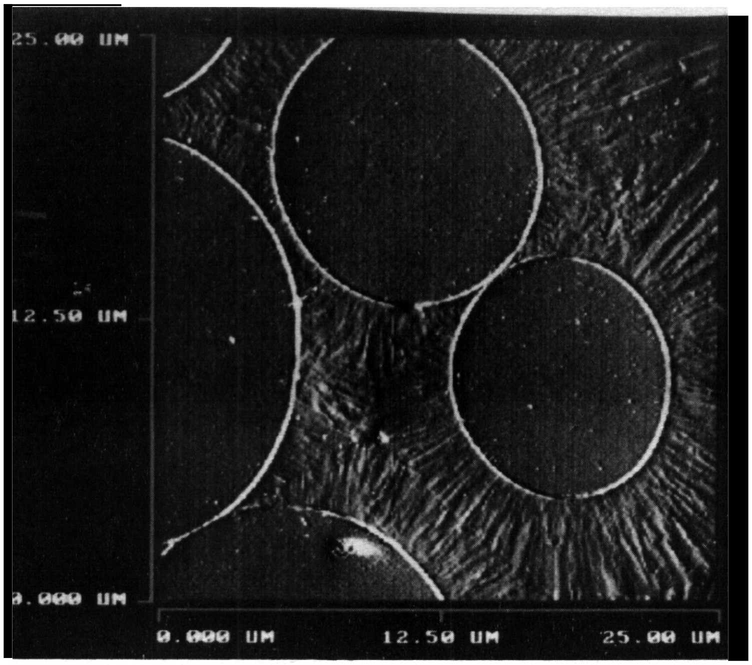

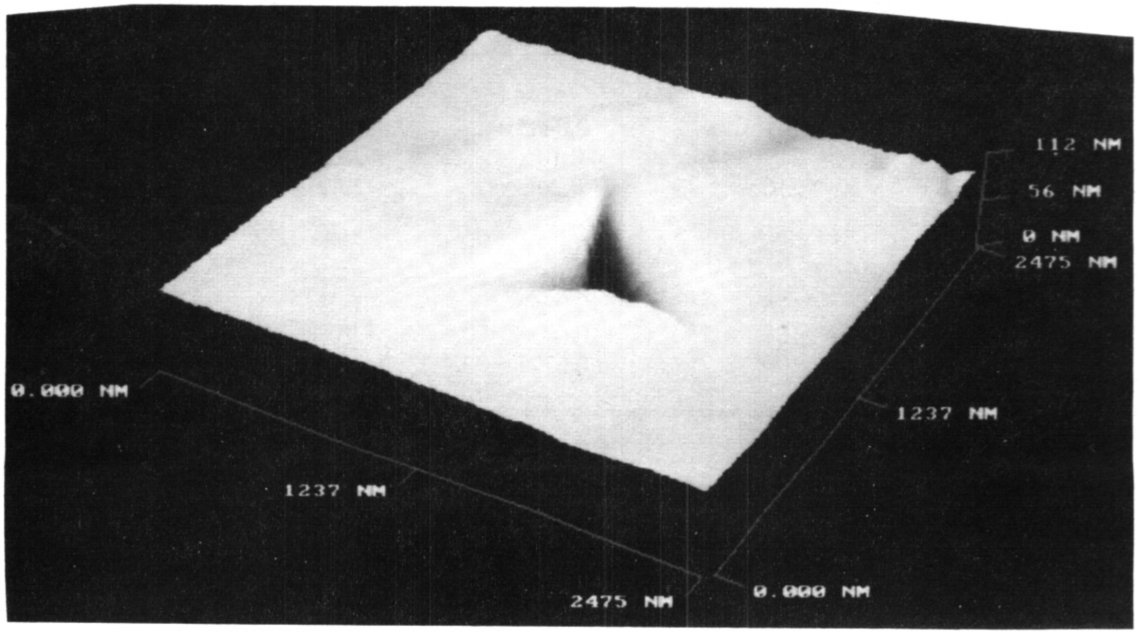

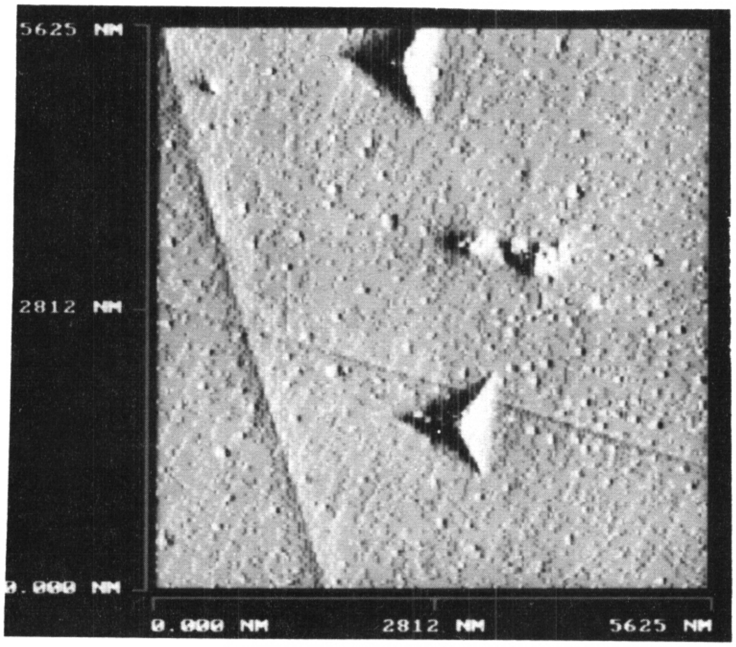

Figure 3. AFM Images on CVD SiC Matrix: (a) 1/2 micron diamond polish with two indents, (b) Syton polish (c) micrograph of diamond indents taken on a 1/2 micron polished CVD surface at about half the magnification shown in 3b.

The AFM was able to show the surface contour of the CVD matrix for the Syton and 1/2 micron polishes, as well as for the Syton polished fiber. Sample contours of each case are shown in Figure **4.**

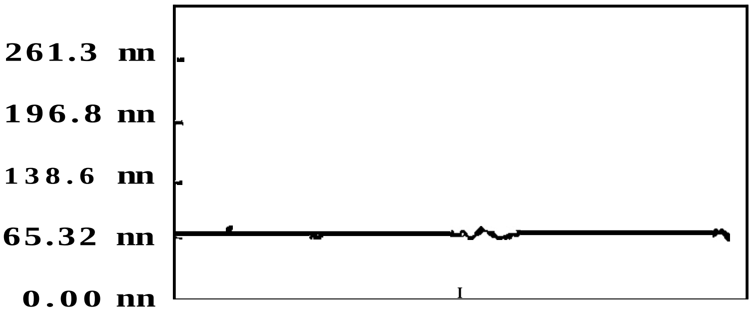

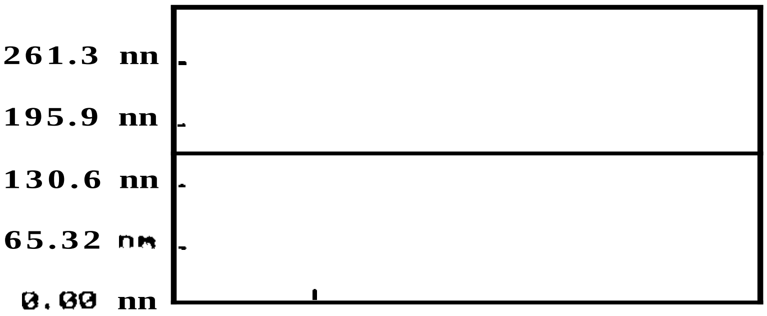

(b)

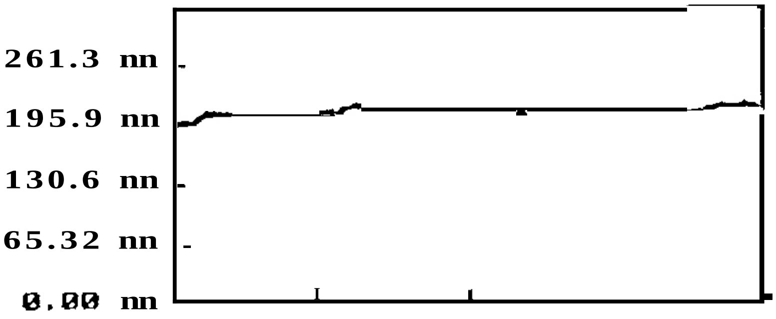

DISCUSSION

For the Nicalon fiber, the relative variations in modulus and hardness decrease for the finer polishes. This result was expected because the Nicalon has very small b-SiC crystals (order of a few nanometers) and **has** amorphous regions? This makes the material softer (lower in hardness **and** modulus than the CVD SiC) and, therefore, easily ground and polished to *make* the fiber approach a flat surface profile. **Also,** for the deeper indents (160 nm **vs.** 20 nm), there is **less** relative variation in the modulus and hardness. This result was expected for the deeper indents because of the larger volume sampled. The small (relatively) surface variations have less of an effect for the deep indents than for the shallow indents.

As shown in Table 1, there is greater variation for the Syton polished CVD SiC than for the 1/2 micron polish. This result was not expected because the finer polish should produce a flatter smoother surface, but for the CVD SiC it did not. The variation increases for the 3 micron polished samples. This result is expected because the 3 micron diamond leaves scratches on the surface that can lead to large surface variations.

As discussed earlier, the volume of material displaced varies with elevation change on the sample surface. Assuming the sample surface has a sinusoidal variation, the relative modulus and hardness variations can be estimated. For the assumed sinusoidal surface, the peak to valley height was chosen **as** the average *height* plus one standard deviation. This choice of height is expected to account for most of the height variation on the sample surface. The peak to valley average heights were calculated from contours similar to the ones shown in Figure 4. The peak to valley heights **used** were 20 nm for Syton and 5 nm for 1/2 micron diamond polished CVD SiC. The wavelength associated with the idealized sinusoidal surface was estimated to be 300 nm. From these values, relative moduli and hardness variations were calculated **for** 20 nm and 160 nm indents and *are* shown in Table 4. The plastic depths for flat surfaces were calculated to be 12.29 nm and 123.00 nm, respectively, using c as .75, E **as** 400 GPa, P_{max} as .4 mN (20 nm indents), and 15 mN (160 nm indents).

Table 4. Analytically determined modulus and hardness variations

Polish	Indent in peak ΔE/E	ΔH/H	Indent in valley ΔE/E	ΔH/H
<u>indent depth (20 nm)</u>				
Syton	0.0632	-0.00046	-0.0650	0.000577
1/2 micron diamond	0.0162	0.00074	-0.0163	-0.0000753
<u>indent depth (160 nm)</u>				
Syton	0.0145	0.00009	-0.0152	0.000037
112 micron diamond	0.0047	-0.00192	-0.0038	-0.000047

The results shown in Table 4 are consistent with the data fur the 20 nm indents, since there is a larger variation in the modulus for the Syton results than for the 1/2 micron diamond results. The calculations **are** also consistent with the results when comparing the 20 nm and **160** nm indents, since the variations **are** lower for 160 nm than for 20 nm indents.

These analytical results suggest that the surface preparation has a several percent effect on the 20 nm Syton polished samples. while for all the other calculated indentations, the effect was about 1.5% or **less.** Thus, the calculated variations in modulus for 20 nm indents on Syton polished **CVD** SiC are at least four times greater than the other calculated variations. **Also,** the calculated variations for the 1/2 micron diamond polished and the 160 nm indents are much lower than their corresponding experimental values.

Therefore, it is reasonable to assume that there are other effects causing the variations, especially in the case of the 20 nm, 1/2 micron diamond polished CVD SiC.

In comparing the data of Tables 1 and 2, the variation in modulus decreases when going from 20 nm and 160 nm. This result is expected, since a larger volume **of** material is sampled for the 160 nm indents than for the 20 nm indents, making the effects of small volume changes on the surface insignificant. These results are consistent with Table **4.**

Comparing Tables 1 and 2, the overall average moduli dropped by about 20 GPa when comparing 160 nm and **20** nm indents. This effect is also expected and discussed in Reference **5.** The overall average moduli dropped another 20 GPa when comparing Syton and 1/2 micron diamond polishes. This observation suggests that there is also **a** material effect, possibly grain size (sensing only one grain for shallow indents and many grains for the deeper indents) or slight plastic deformation **of the** polished surface from the diamond polish affecting the indentation.

When comparing the calculated hardness variations of Table **4,** these variations are much smaller than the modulus variations and show that there **is** not much of a surface effect on hardness **values.** Any differences in the magnitude or sign of the calculated hardness variations probably arise from rounding off errors in *the* calculations.

The two trends discussed above were not observed for the 3 micron diamond polish. It **is** suggested that some other material property is coming into play. There could be some slight plastic deformation of the surface due to the **3** micron grains, or the many scratches caused by the polish might be causing an averaging of the material properties.

CONCLUSIONS AND FUTURE WORK

The surface preparation has a **small** effect on the CVD SiC modulus and hardness measurement. There is greater variation in the data surface profile changes due to SiC grain exposure by the Syton polish than in the 1/2 micron polish for indents at 20 nm. The surface variation **results** from the line SiO_2 particles exposing the CVD SiC grains, unlike the 1/2 micron diamond polish. which removes a layer in the same plane.

The calculations confirm the trends of **the** experimental observations. **hut** the calculated variations are, for most cases. Smaller than the experimental varialions. These calculations **do not** completely explain the scatter in the experimental results. Further research should examine SiC grain morphology and its effect on making shallow indents in order **for** this technique to be a useful tool in the measurement of CVD **SiC** properties after ion bombardment. **Also,** in future work, indentation should be performed on a known hard flat surface to determine if machine noise accounts for any experimental variation.

ACKNOWLEDGMENTS

The authors would like to **thank** D. N. Braski for the AFM analysis and W. C. Oliver for use of the Nanoindenter.

REFERENCES

1. L. **L.** Snead, S. J. Zinkle, D. Steiner, "Cross Sectional Measurement of Elastic Modulus for Ion Beam Damaged Silicon Carbide," Fusion Reactor Materials, DOE/ER-0313/10, pp. **320-327** (1991).

2. **S.** J. Zinkle and W. C. Oliver, "Mechanical Property Measurements on Ion-Irradiated Metals," ORNL/TM-10126, (August 1986). Metals and Ceramics Division.

3. L. L. Snead, Ph.D. Thesis, 1992, Rensselaer Polytechnic Institute, Troy, New **York.**

4. W. C. Oliver **and** G. Pharr, "An Improved Technique for Determining Hardness **and** Elastic Modulus Using Load and Displacement Sensing Indentation Experiments" J. Mater. Res., Vol 7 (6), (June 1992), pp. 1564-1583.

5. I. J. McColm, "Ceramic Hardness," New **York** (1990), Plenum Press, p 7.

6. L. E. Samuels and T. O.Mulhearn, "An Experimental Investigation of the Deformed Zone Associated with Indentation Hardness Impressions." J. Mech. and Physics of Solids, Vol. 5, pp. 125-131 (1957).

7. L Sawyer, "Microstructure of Ceramic Fibers," Fiber Reinforced Ceramic Composites, ed. K. S Mazdiyazni, Noyes Publication, Park Ridge, NJ (1990) pp. 141-180.

8. W. C. Oliver **and** G. M. Pharr, "An Improved Technique For Determining Hardness And Elastic Modulus Using Load And Displacement Sensing Indentation Experiments," J. Mater. Res, Vol. 7, pp. 1564-1583 (1992).

MICROMECHANICS OF FIBER PULLOUT AND CRACK BRIDGING IN SCSG **SiC- CVD SiC COMPOSITE SYSTEM AT HIGH-TEMPERATURE'** A.El-Azab and N.M. Ghoniem, University of California, Los Angeles

OBJECTIVE

The purpose of this work is to develop a micro mechanical model to study the process of fiber pull-out and crack bridging in Sic-Sic composites at high temperature, where fiber creep dominates the time evolution of the matrix crack mechanics. Crack growth and failure of Sic-Sic composites in fusion are determined by considerations of the micro mechanical model.

SUMMARY

A micro mechanical model is developed to study fiber pull-out and crack bridging in fiber reinforced Sic-Sic composites with time dependent thermal creep. By analyzing the creep data for monolithic CVD SiC (matrix) and the SCS-6 SiC fibers in the temperature range 900-1250°C, it is found that the matrix creep rates can be ignored in comparison to those of fibers. Two important relationships are obtained: (1) a time dependent relation between the pull-out stress and the relative sliding distance between the fiber and matrix for the purpose of analyzing pull-out experiments, and (2) the relation between the bridging stress and the crack opening displacement to be used in studying the mechanics and stability of matrix crack bridged by fibers at high tenmperatures. The present analysis can be also applied to Kicalon-reinforced CVD SiC matrix system since the Nicalon fibers exhibit creep characteristics similar to those of the SCSG fibers.

PROGRESS AND STATUS

Introduction

Ceramic matrix fiber reinforced materials have recently received significant attention because of their excellent performance at elevated temperature, and their high strength-to-weight ratio. It has been experimentally shown that appropriate micro structural design of such materials influences their toughening and crack propagation characteristics. In this context, relevant micro mechanical modeling helps in understanding the fundamental mechanical behavior, on the one hand, and further improving the micro structural design, on the other. An important toughening mechanism in ceramic matrix composites is achieved when fibers are embedded in the matrix, leading to what **is** known as *bridging* of matrix cracks. It has been experimentally shown that such bridging can lead to impedance of propagation of matrix cracks. and thus higher loads can be withstood without catastrophic failure (MARSHALL and EVANS, 1985; LUN and EVANS, 1987; SUZUKI, SATO and SAKAI, 1992).

Several micro mechanical models have been recently developed to analyze crack bridging (GAO, MAI and COTTEREL, 1988; SHETTY, 1988; HSUEH, 1988; SIGL and EVANS, 1989; HUTCHINSON and JENSEN, 1990; LIANG and HUTCHINSON, 1993) , and were coupled with push-out and pull-out experiments (MARSHALL, SHAW and MORRIS, 1992; MARSHALL, 1992; ZHOU, KIM and MAI, 1992; FU, ZHOU, CHEN, XU, HE, and LUNG 1993; JIANG and PENN, 1992). Mostly, these models are based on a composite (fiber/matrix) cylinder which represents the local mechanical response. These micro-models are then incorporated in global representations of the overall macro mechanical behavior of the composite. The relevance to crack bridging and ceramic matrix composite toughening is manifested in:

'This **material is** based **upon work supported by the** U. S. **Department of Energy under** ***award number*** DE-FG03-**91ER54115 at UCLA.**

1. Establishing a relationship between the bridging stress and the crack opening displacement within the bridged zone in a matrix crack so that bridged crack mechanics problems can be solved. Such a relationship is known as the traction law.
2. Studying the dependence of crack propagation on debonding and frictional pull-out of fibers (SIGL and EVANS, 1989; THOULESS and EVANS, 1988).

The development of a traction law was first considered by MARSHALL, COX and EVANS(1985) in their study of crack mechanics with fiber bridging. SIGL and EVANS(1989) and HUTCHINSON and JENSEN(1990) derived more elaborate form of that relationship for different fiber/matrix interface conditions. NAIR, JAKUS and LARDNER(1991) developed a time dependent traction law. They considered fiber pull-out of the matrix with a viscous interface layer which softens at high temperature.

Advanced ceramic composites, such as SiC-SiC systems, are developed for high-temperature structural applications (e. g. in fusion reactor first walls and blankets, rocket nozzles, heat exchangers, and special aerospace components). In these applications inelastic phenomena such as thermal creep, irradiation-induced creep and irradiation swelling are critical. For example, fiber creep within the bridged zone of a matrix crack is anticipated to relax the bridging traction and drive a time dependent evolution of the overall crack field. Under thermal creep conditions, the relevant mechanisms become significant above a threshold temperature. Irradiation creep, however, occurs over a wide range of temperatures and is kinetically possible once the material is subjected to a combined mechanical and irradiation loading. Another example is the build-up of internal stresses by irradiation swelling. Such evolution of internal stress affects the pull-out characteristics of the fiber. This may enhance or degrade the toughness of the composite while in service.

Regarding the SiC-SiC composite system, creep experiments have been performed on both CVD SiC fibers (1100 – 1450°C) (DICARLO, 1986) and on monolithic CVD SiC material (1650°C) (CARTER and DAVIS, 1984) at comparable stress levels. The CVD SiC fibers are commercially known as SCSG fibers. These fibers are about 140 micron in diameter and are produced by chemical vapor deposition of SiC on a carbon core. The creep in these fibers is explained in terms of grain boundary sliding due to free silicon. It is observed that fiber creep is anelastic or recoverable and occurs at temperatures where dislocation motion is negligible. Because of that, significant creep strains can be obtained at relatively small loads. For CVD monolithic SiC, the creep mechanism is determined to be a dislocation mechanism which requires certain threshold stress and temperature. By analyzing the creep data from the last two cited references it is concluded that the creep rate of monolithic CVD-SiC is negligible compared to that of fibers up to $\sim 1500°C$.

In the present work, a model is developed to study high-temperature micro mechanics relevant to fiber pull-out and crack bridging in SCS-6 SiC - CVD SiC composites. Only thermal creep of fibers is considered . This model includes development of the relationship between the applied stress at the fiber end and the relative sliding distance between the fiber and matrix ends. This distance may then be related to the crack opening displacement, within the bridging zone in a matrix crack. Such a relationship is timedependent since fiber creep at high-temperature drives a stress relaxation process. The relaxation modulus of SCSG fibers is obtained from creep compliance data by the method of Laplace transform. The elastic-viscoelastic correspondence principle is used to obtain the viscoelastic (time-dependent) solution from the elastic one. The model accounts for residual thermal mismatch stresses.

Composite cylinder model : Elastic Solution

The composite cylinder model depicted in Fig. 1 is taken to represent a composite reinforced with a volume fraction, $f = (R_f/R_o)^2$, of aligned continuous fibers. The analysis accounts for composite systems which have residual mismatch stresses normal to the fiber-matrix interface. A Coulomb friction type is assumed over the length of permissible relative sliding between fibers and matrix, L,.

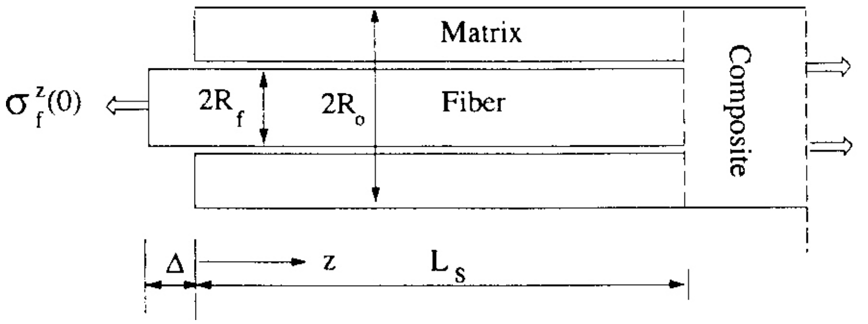

Figure 1: Composite cylinder model

The model presented here neglects shear gradients compared with gradients in normal stresses. The outer cylinder surfaces are taken to be traction *free*. These approximations have been considered and justified by many authors [e. g. SIGL and EVANS, 1989; GAO, MAI and COTTERELL, 1988). In this case, the stresses in the fiber and matrix *are* given in terms of the interface normal stress q (which is negative) by the following relations

$$
\begin{aligned}
\sigma_r^f &= q, \\
\sigma_\theta^f &= q, \\
\sigma_r^m &= \frac{q}{(1-f)}\left[\left(\frac{R_f}{r}\right)^2 - f\right], \\
\sigma_\theta^m &= \frac{-q}{(1-f)}\left[\left(\frac{R_f}{r}\right)^2 + f\right]
\end{aligned} \tag{1}
$$

where the superscripts f and m refer to the fiber and matrix, respectively, r is the distance from the fiber center, and R_f is the fiber radius The elasticity solutions for this system are well developed, and the corresponding strains are given by

$$
\begin{aligned}
\epsilon_r^f &= \epsilon_{in}^f + \frac{1}{E_f}\left[q(1-\nu_f) - \nu_f\sigma_z^f\right], \\
\epsilon_\theta^f &= \epsilon_r^f, \\
\epsilon_z^f &= \epsilon_{in}^f + \frac{1}{E_f}\left[\sigma_z^f - 2\nu_f q\right], \\
\epsilon_r^m &= \epsilon_{in}^m + \frac{1}{E_m}\left(\frac{q}{(1-f)}\left[\left(\frac{R_f}{r}\right)^2(1+\nu_m) - f(1-\nu_m)\right] - \nu_m\sigma_z^m\right)
\end{aligned}
$$

$$\epsilon_\theta^m = \epsilon_{in}^m - \frac{1}{E_m}\left(\frac{q}{(1-f)}\left[\left(\frac{R_f}{r}\right)^2(1+\nu_m)+f(1-\nu_m)\right]-\nu_m\sigma_z^m\right),$$
$$\epsilon_z^m = \epsilon_{in}^m + \frac{1}{E_m}\left(\sigma_z^m + \frac{2\nu_m f q}{(1-f)}\right) \qquad (2)$$

where $\epsilon_{in}^f = \alpha_f \Delta T$ and $\epsilon_{in}^m = \alpha_m \Delta T$ are thermal inelastic strain components in fibers and the matrix, respectively. Such a model **was** used by SIGL and EVANS(1989) for similar fiber and matrix properties. ***AT*** is a temperature change from the stressfree temperature. Due to the ax-symmetry of the problem, the tangential strains in fibers and matrix consist of the radial displacements u_r divided by the radial coordinate r. While relative sliding in the axial direction is permissible. the continuity of the radial displacements at the fiber-matrix interface implies that

$$\epsilon_\theta^f(R_f) = \epsilon_\theta^m(R_f) \qquad (3)$$

which yields

$$q(1-\nu_f) - \nu_f\sigma_z^f = E_f\Delta\epsilon_{in}$$
$$\frac{f}{E_m}\left(\frac{f}{(1-f)}\left[(1+\nu_m)+f(1-\nu_m)\right]-\nu_m\sigma_m^z \qquad \mathbf{f4}$$

where $\Delta\epsilon_{in} = \epsilon_{in}^m - \epsilon_{in}^f$. The axial equilibrium of fibers and matrix can be described by

$$\frac{d\sigma_z^f}{dz} = \frac{-2\tau}{R_f} = -\left(\frac{1-f}{f}\right)\frac{d\sigma_z^m}{dz} \qquad (5)$$

where the interfacial shear stress τ **is** related to the interface pressure q by

$$\tau = -\mu q \qquad (6)$$

in which μ is the friction coefficient. Differentiating equation **(4)** with respect to z, **results** in a relationship between the axial gradients of q, σ_z^f and σ_z^m. By further using equations (5) and (6). the following first order differential equation is obtained for the interface pressure q

$$\frac{dq}{dz} = \frac{2\mu c}{R_f}q \qquad (7)$$

where

$$c = \frac{E_m(1-f)\nu_f - E_f f \nu_m}{E_m(1-f)(1-\nu_f) + E_f\left[(1+\nu_m)+f(1-\nu_m)\right]} \qquad (8)$$

The solution to (7) is obtained as

$$q = q(o)\exp\left(\frac{2\mu c}{R_f}z\right) \qquad (9)$$

where $q(o)$ is the value of Q at $z = 0$. In the particular case $c = 0$, $q(z) = q(0)$ which is **a** constant Consequently, the axial stresses in the fiber and matrix vary linearly along the z direction.

Expression for $q(0)$ in terms of $\sigma_z^f(0)$ and $\sigma_z^m(0)$ can be obtained using equation **(4).** The latters are given by

$$\sigma_z^f(0) = \sigma_b + \sigma_R^f$$
$$\sigma_z^m(0) = \sigma_e \qquad (10)$$

where σ_R^f is the initial axial stress in the fiber, σ_b is the externally imposed stress at the fiber end, and σ_e is the external applied stress at the matrix end. The addition of σ_R^f to σ_b depends on the situation. In a pull-out experiment, where and external tensile load is applied **only** at the fiber end, no initial stresses are considered. In this case, $\sigma_z^f(0) = \sigma_b$ and $\sigma_z^m(0) = 0$. In the case of crack bridging, however, an initial axial compressive stress in fibers develops such that the bridging stress at the fiber end is modified by the amount σ_R^f. On the other hand, the matrix end would still be traction free, i. e., $\sigma_z^m(0) = 0$. The component σ_R^f depends on the axial residual stresses in the fibers and matrix prior to crack initiation, i. e., on the initial strain mismatch. However, the formulation of $q(0)$ considers a non-zero stress at the matrix's end for a few more steps. Appendix **A** contains a solution for the initial axial stresses σ_R^f. Using equation **(4)** at $z = 0$ results in the following expression for $q(0)$

$$q(0) = \frac{a_1\sigma_z^f(0) + a_2\sigma_z^m(0) + a_3\Delta\epsilon_{in}}{a_4} \tag{11}$$

where the constants a_{1-4} depend on the elastic constants of the composite system and the fiber volume fraction. These constants are given by

$$\begin{aligned} a_1 &= E_m(1-f)\nu_f \\ a_2 &= E_f(1-f)\nu_m \\ a_3 &= E_m(1-f)E_f \\ a_4 &= E_m(1-f)(1-\nu_f) + E_f\left[(1+\nu_m) + f(1-\nu_m)\right] \end{aligned} \tag{12}$$

Using equations (5), *(6)* and (9), expression. for the axial stresses in fiber and matrix are obtained as follows

$$\begin{aligned} \sigma_z^f(z) &= \sigma_z^f(0) + \frac{q(0)}{c}\left[\exp\left(\frac{2\mu c}{R_f}z\right) - 1\right] \\ \sigma_z^m(z) &= \sigma_z^m(0) - \left(\frac{f}{1-f}\right)\frac{q(0)}{c}\left[\exp\left(\frac{2\mu c}{R_f}z\right) - 1\right] \end{aligned} \tag{13}$$

In the special case of $c = 0$, expression for $\sigma_z^f(z)$ and $\sigma_z^m(z)$ can **bc** written as

$$\begin{aligned} \sigma_z^f(z) &= \sigma_z^f(0) + \frac{2\mu q(o)}{R_f}z \\ \sigma_z^m(z) &= \sigma_z^m(0) - \left(\frac{f}{1-f}\right)\frac{2\mu q(o)}{R_f}z \end{aligned} \tag{14}$$

The free end condition for the matrix, which will be considered from now and on, leads to dropping the terms containing $\sigma_z^m(0)$.

The solution given by equations (9) through **(14)** is valid over a certain range $z \in [o, L_s]$, where L_s is the length over which relative sliding between the fiber and matrix in the axial direction is permissible. Beyond that length, axial displacements, and subsequently axial strains, in both fiber and matrix are equal ***(compatibility).*** Therefore the solution for $z \geq L_s$ must account for the continuity of radial and axial displacements at the fiber-matrix interface, at the same time. However, for the purpose of finding the sliding length, L_s, it is only needed to equate the expressions for the axial strains (or displacements) from equations **(2)** along with the use of (9) for the interface pressure q and **(13)** or **(14)** for the axial stresses, at $z = L_s$. Implementing this procedure results in the following expression for the sliding length

$$\frac{L_s}{R_f} = \frac{1}{2\mu c} \log_e \left[\frac{b_4 - b_1 + b_2 q(0)}{(b_2 - b_3) q(0)} \right] \tag{15}$$

where the wnstants b_{1-4} have the following expressions

$$\begin{aligned} b_1 &= \sigma_z^f(0) - \frac{E_f}{E_m} \sigma_z^m(0) \\ b_2 &= \left[1 + \frac{f E_f}{(1-f) E_m} \right] / c \\ b_3 &= 2\nu_f + \left(\frac{2\nu_f f}{1-f} \right) \frac{E_f}{E_m} \\ b_4 &= E_f \Delta\epsilon_{in} \end{aligned} \tag{16}$$

SIGL and EVANS (1989) have used a different approach to determine the sliding length. They considered the global equilibrium of fiber over the sliding length such that the fiber load at its end is balanced by the resultant friction forces. Other authors (HSUEH, 1988; HSUEH, 1990), however, have used the more rigorous approach presented here to satisfy the compatibility condition in the axial direction at the end of sliding zone to determine the sliding length. The axial displacements $u_z^f(0)$ and $u_z^m(0)$ at the fiber end, $z = 0$, for fiber and matrix are given in term of the respective axial displacements at $z = L_s$, by the following equations

$$\begin{aligned} u_z^f(L_s) - u_z^f(0) &= \int_o^{L_s} \epsilon_z^f(z) dz = \left[\sigma_z^f(0) - \frac{q(0)}{c} \right] \frac{L_s}{E_f} + \epsilon_{in}^f L_s \\ &+ \frac{q(0) R_f}{2\mu c^2 E_f} \left[\exp\left(\frac{2\mu c}{R_f} L_s \right) - 1 \right] - \frac{\nu_f q(0) R_f}{\mu c E_f} \left[\exp\left(\frac{2\mu c}{R_f} L_s \right) - 1 \right] \\ u_z^m(L_s) - u_z^m(0) &= \int_o^{L_s} \epsilon_z^m(z) dz = \left[\sigma_z^m(0) + \frac{f q(0)}{(1-f)c} \right] \frac{L_s}{E_m} \\ &+ \epsilon_{in}^m L_s - \frac{f q(0) R_f}{2(1-f)\mu c^2 E_m} \left[\exp\left(\frac{2\mu c}{R_f} L_s \right) - 1 \right] \\ &+ \frac{\nu_m f q(0) R_f}{(1-f)\mu c E_m} \left[\exp\left(\frac{2\mu c}{R_f} L_s \right) - 1 \right] \end{aligned} \tag{17}$$

where $u_z^f(L_s) = u_z^m(L_s)$. The relative sliding distance **A** at the fiber end is then given by

$$\begin{aligned} \Delta &= \int_o^{L_s} \left[\epsilon_z^f - \epsilon_z^m \right] dz \\ &= u_z^m(0) - u_z^f(0) \end{aligned} \tag{18}$$

In presenting the results, the fiber volume fraction is taken to be 0.3. The fiber and matrix propenies used are those for a CVD SiC matrix with SCS-6 fibers. These are given by: $E_f = 420$ GPa (DICARLO, 1986), $E_m = 380$ GPa (GULDEN, 1969), $\nu_f = 0.3$ (HSUEH,1989), and $\nu_m = 0.2$. The friction coefficient μ usually varies depending on the manufacturing condition of the composite as well as on the interface. A value of $\mu = 0.2$ is chosen in the present work as a reference point, based on the existing literature of similar composite system (e. g. HSEUH, 1989). However. the friction coefficient is varied to show its effect on the relative sliding between fibers and matrix when necessary. The differential thermal strain mismatch $\Delta\epsilon_{in}$ is taken to be 0.05%. This corresponds to $\alpha_m - \alpha_f = 10^{-6}$ K^{-1} and a temperature cooling of 500K. This choice can be justified based on

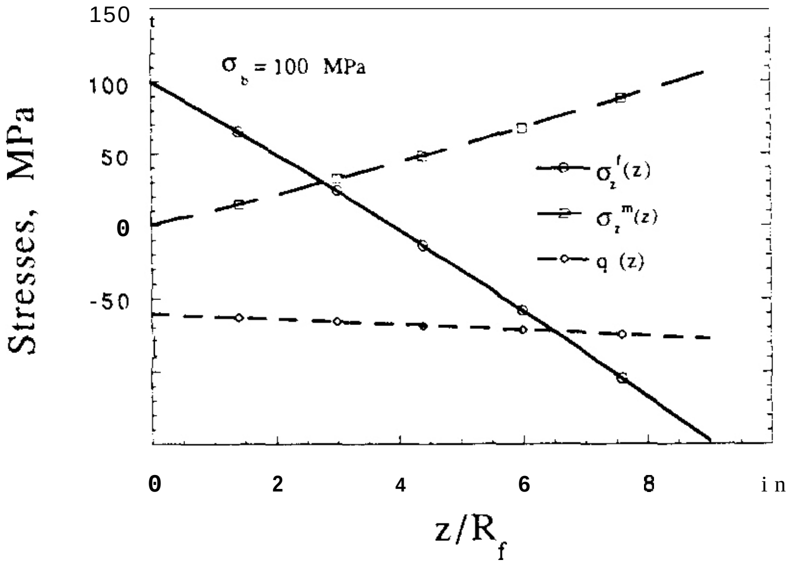

Figure 2: Axial variation of σ_z^f, σ_z^m and $q(z)$

the fact that the existing data on the coefficient of thermal expansion for CVD SiC fibers represent a wide scatter. CARROLL and DHARANI (1992) reported values of $\alpha_f = (2.6 - 3.25) \times 10^{-6}K^{-1}$, BRUN and BOROM (1989) reported values of $\alpha_f = (4.5 - 5) \times 10^{-6}K^{-1}$, which is similar to those reported by DICARLO (1966). In this case, values of the thermal strain mismatch, rather than the difference in thermal expansion coefficients and cooling temperature, are important.

In Fig.2 the axial stresses in the fiber and matrix are shown for a partial pull-out test. The results are in general agreement with the existing literature (e. g., HSUEH, 1968). The compressive fiber stress over a large part of the sliding length is caused by large values of the mismatch strain. In that particular example, the residual axial compression in the fiber, away from its end, is $\sigma_R^f = -187$ MPa. This shows the effect of the applied stress in releasing some of that compression over L_s. Fig. 3 shows the variation of A with the applied stress σ_b for pull-out test versus crack bridging problem. The fact that A is smaller in the case of bridging can be attributed to the effect of the residual compressive stress, σ_R^f, which modifies the stress at the fiber end. In Fig. 4, L_s versus σ_b is shown. and the difference, again, can be interpreted the same way.

The present work is conducted to investigate the micro mechanics relevant to crack bridging and fiber pull-out in a SiC-SiC composite system, where fibers are under thermal creep conditions. A time-dependent solution is therefore required. Before getting to that step, a summary of the creep characteristics of SCS-6 SiC fibers is given.

Analysis of creep of SCS-6 SiC fibers

As mentioned before, creep experiments on SCS-6 SiC fibers have been carried out in the temperature range 1100-1450 "C (DICARLO, 1964; DICARLO and MORSCHER, 1991). Creep strain is observed to increase logarithmically with time, monotonically with temperature, and linearly with the applied stress. Fiber creep is found to be totally viscoelastic, which allowed a simple predictive method to be developed for describing the fiber total deformation as function of time, temperature and stress. The fiber viscoelastic behavior is explained in terms of grain boundary sliding due to free silicon. The total fiber strain ϵ is written in terms of the applied stress σ_a as follows

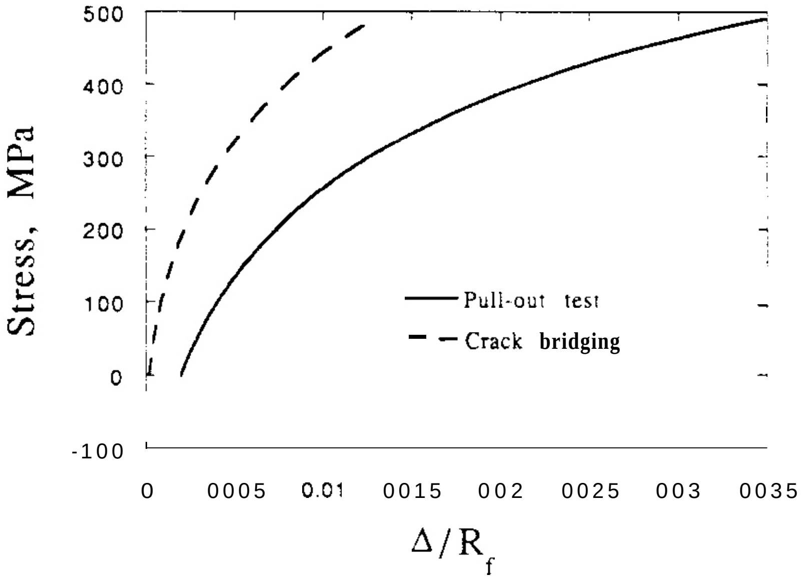

Figure 3: Variation of σ_b versus **A**

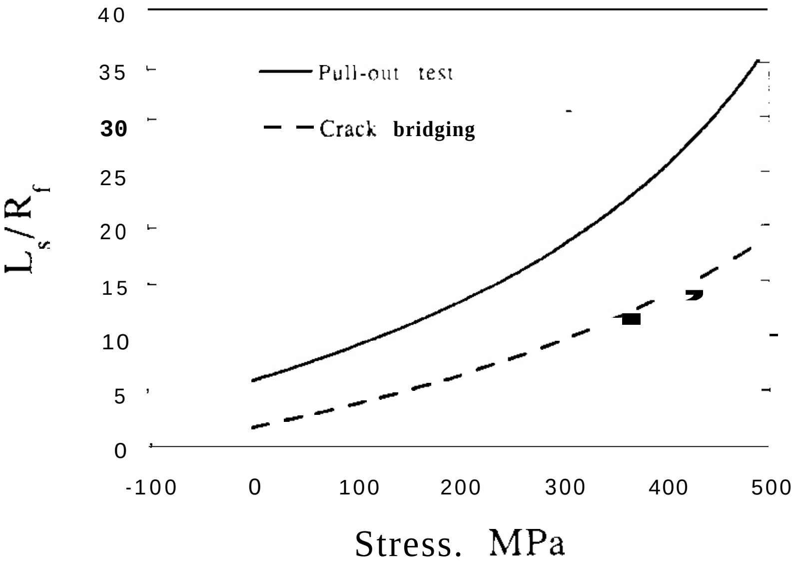

Figure 4: Varaition of L_s versus σ_b

$$\epsilon = \frac{\sigma_a}{E_f(0)} + J_c(\gamma)\sigma_a = J_f(\gamma)\sigma_a \tag{19}$$

where the first term represents the prompt (elastic) component of the total strain, and the second term is the strain due to fiber creep. $J_f(\gamma)$ is the total compliance of the fiber and will be simply denoted as the creep compliance $J_f(t)$. The parameter γ is written in terms of time, t, and the absolute temperature, T, as follows

$$\gamma = \ln(t) - Q/RT = \ln(t) - 57700/T \tag{20}$$

where Q is the activation energy. The following empirical correlation of J_c to time and temperature was obtained

$$J_c(t,T) = J_c(\gamma_o)\exp\left[-p(Q/RT + \gamma_o)\right]t^p = C(T)t^p \tag{21}$$

where the parameters $p = 0.36$, $\gamma_o = -35$ and $J_c(\gamma_o) = 10^{-3}$ $(\mathrm{GPa})^{-1}$ are measured by fitting the experimental data to formula (21). Details of this analysis are given by DICARLO and MORSCHER (1991). In the present work we extend the analysis to obtain relaxation information from creep data.

The relaxation modulus $E_f(t)$ is defined by a relation similar to (19), and written as

$$\sigma = E_f(t)\epsilon_a \tag{22}$$

in which ϵ_a is the applied strain. The relations (19) and (22) yield the strain and stress in creep and relaxation tests, respectively. By manipulating these two relations, the relaxation modulus can be related to the one dimensional tensile creep compliance $J_f(t)$ by the following convolution integral (PIPKIN, 1986; GOLDEN and GRAHAM, 1988)

$$\int_0^t E_f(t-t')J_f(t')dt' = \int_0^t E_f(t')J_f(t-t')dt' = t \tag{23}$$

The Laplace transforms of these two functions are therefore related by

$$\hat{E}_f(s)\hat{J}_f(s) = \frac{1}{s^2} \tag{24}$$

which is used to obtain $E_f(t)$ from $J_f(t)$. It can be shown that the Laplace transformed compliance function is given by

$$\hat{J}_f(s) = \frac{1}{sE_f(0)} + C(T)\frac{\Gamma(1+p)}{s^{p+1}} \tag{25}$$

where $\Gamma(1+p)$ is the gamma function. The last relation yields the following expression for the Laplace transformed relaxation modulus

$$\hat{E}_f(s) = \frac{E_f(0)}{s + C(T)E_f(0)\Gamma(1+p)s^{1-p}} \tag{26}$$

There is no direct inversion formula for the expression (26). However, a widely used approximate inversion method, which proved to be highly accurate for the purpose of obtaining timedependent solutions in the theory of linear viscoelasticity, is used in the present work. This formula is due to SCHAPERY(1962) . The statement of that inversion formula is as follows; if $\psi(s)$ is the Laplace transform, which is known, for the function $\psi(t)$, then the latter is approximately given by

$$\psi(t) \simeq \left[s\hat{\psi}(s)\right]_{s=\frac{0.5}{t}} \tag{27}$$

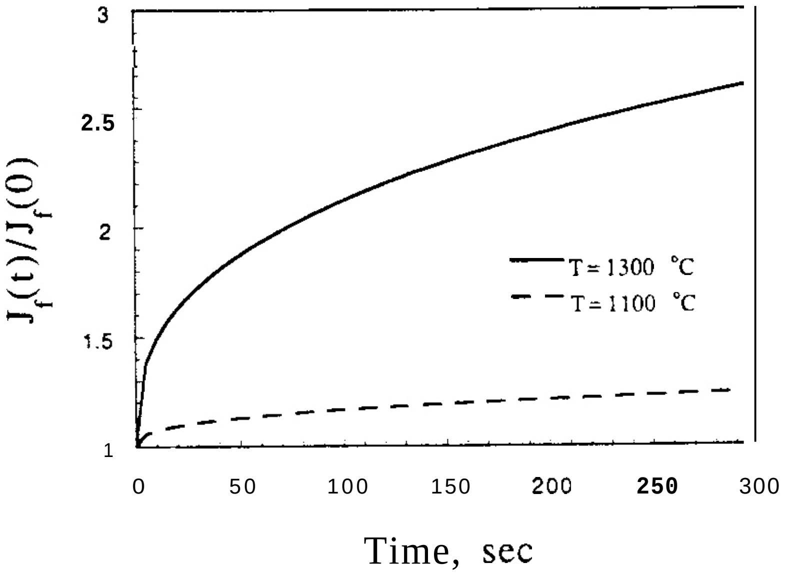

Figure 5: Creep compliance of SCS-6 fibers

In some cases, this inversion method is found to be more accurate than other numerical techniques of inversion such as the collocation method. Besides, little computational effort is required in using this method. Details of comparison of this method with exact and collocation methods are found in (SCIIAPERY, 1962). Figs. 5 and 6 show the creep compliance and the relaxation modulus of SCS-6 fibers, where SCHAPERY's method is used to calculate the latter.

Viscoelastic solution: Pull-out experiments

The quantities $q(z)$, $\sigma_z^f(z)$ and $\sigma_z^m(z)$ are linearly related to the applied external stress σ_b and the thermal strain mismatch **Ae,,** through their linear dependence on $\sigma_z^f(o)$ and $q(0)$. This linearity is important in formaulating a timedependent solution for an arbitrary time history of these externally imposed mechanical and thermal mismatch conditions. In the present work , however, we consider only the time variation of the applied stress at the fiber end and formulate an isothermal solution. Moreover, $\sigma_z^m(0)$ is taken to be zero, i. e., the matrix end is traction free. The solution to a step stress input is first obtained. Then, by virtue of the linearity property of σ_z^f, σ_z^m and q with respect to the applied stress at the fiber end, the solution corresponding to an arbitrarily time-varying stress is obtained using the convolution theory.

Let $R(t - t')$ be a response to a differential step input $d\sigma(t')$ imposed at time t'. Then, the response $\mathcal{R}(t)$ due to some varying stress history $\sigma(t)$ is given by

$$\mathcal{R}(t) = \int_{-\infty}^{t} R(t-t')d\sigma(t') \qquad \textbf{(28)}$$

Therefore it is important first to establish the response to the step input.

Step input solution

In obtaining the response to a step input, the elastic-viscoelastic correspondence principle is used. The developed elastic solution can be used to obtain the Laplace transformed viscoelastic solution by replacing the boundary conditions (externally imposed conditions, $\sigma_z^f(0)$ and **Ae,,)** by their

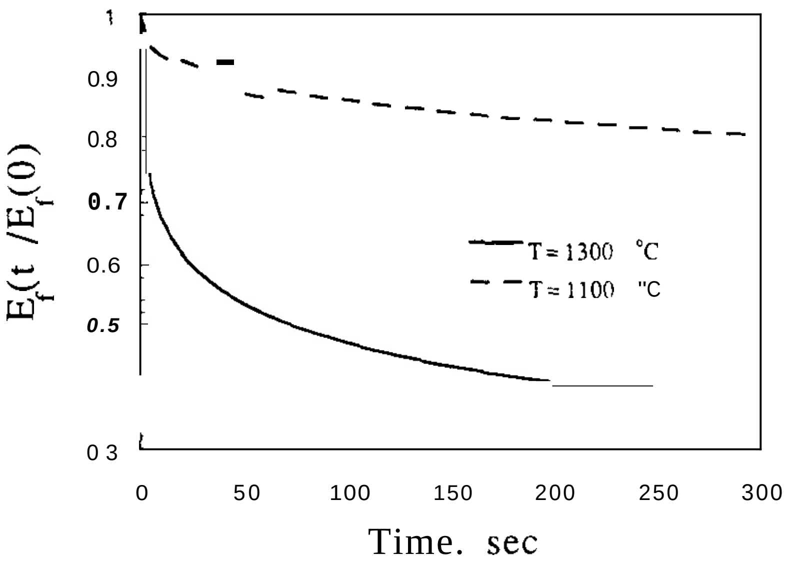

Figure *6:* Relaxation modulus of SCS-6 fibers.

respective Laplace transforms in the elastic solution. Also the elastic constants are replaced by their s-multiplied Laplace transforms, mainly, $E_f \rightarrow s\hat{E}_f(s)$ and $\nu_f \rightarrow s\hat{\nu}_f(s)$. The quantities a_{1-4} given in equation (11) contain E_f and ν_f. In the Laplace transformed viscoelastic solution, these quantities can be represented as functions of the Laplace parameter s as $\hat{a}_{1-4}(s)$. Similarly, the constant c appearing in equation(8) transforms to $\hat{c}(s)$. Having done that, the rest of the work will be just inverting the Laplace transformed viscoelastic solution to get the solution in the time domain. In performing the inversion step, Schapery's rule is used.

The following expression can be obtained for the interface pressure in the Laplace domain

$$\hat{q}(z,s) = \hat{q}(0,s)\exp\left(\frac{2\mu\hat{c}(s)}{R_f}z\right) \tag{29}$$

where $\hat{q}(0,s)$ is given by

$$\hat{q}(0,s) = \frac{\hat{a}_1(s)\sigma_z^f(0) + \hat{a}_3(s)\Delta\epsilon_{in}}{s\hat{a}_4(s)} \tag{30}$$

in which $\sigma_z^f(0)$ is given by equation (10) where the initial stress component σ_R^f is not considered. By applying Schapery's method to (29) and (30), the following expression for $q(z,t)$ can be obtained

$$q(z,t) = q(0,t)\exp\left(\frac{2\mu c(t)}{R_f}z\right) \tag{31}$$

where $q(0,t)$ is given by

$$q(0,t) = \frac{a_1(t)\sigma_z^f(0) + a_3(t)\Delta\epsilon_{in}}{a_4(t)} \tag{32}$$

where application of Scharery's inversion method results only in replacing the constants $\hat{a}_{1-4}(s)$ and $\hat{c}(s)$, which contain $s\hat{E}_f(s)$ and $s\hat{\nu}_f$, with the time-dependent parameters $a_{1-4}(t)$ and $c(t)$. These time-dependent parameters are still given by equations (12), for a_{1-4}, and (8), for c, with replacing the elastic constants E_f and ν_f by the time dependent relaxation modulus $E_f(t)$ and the time dependent poisson's ratio $\nu_f(t)$. **A** similar methodology can be implemented to obtain expressions for $\sigma_z^f(z,t)$ and $\sigma_z^m(z,t)$, which can be shown to take the form

$$\begin{aligned}\sigma_z^f(z,t) &= \sigma_z^f(0) + \frac{a_1(t)\sigma_z^f(0) + a_3(t)\Delta\epsilon_{in}}{a_4(t)c(t)}\left[exp\left(\frac{2\mu c(t)}{R_f}z\right) - 1\right]\\ \sigma_z^m(z,t) &= -\frac{a_1(t)\sigma_z^f(0) + a_3(t)\Delta\epsilon_{in}}{a_4(t)c(t)}\frac{f}{(1-f)}\left[exp\left(\frac{2\mu c(t)}{R_f}z\right) - 1\right] \qquad (33)\end{aligned}$$

The distance L_s can be found by numerical matching of the instantaneous axial strains in the fiber and matrix. The distance A is then found by integrating the differential axial strain over that distance. This is explained in the following section.

Response to arbitrarily time-varying stress

In obtaining the solution for an arbitrary applied stress, equation (28) is utilized. Since At,, is assumed constant, the terms containing that quantity remain unchanged. Therefore, convolution integrals are considered only with term? containing $\sigma_z^f(0)$. In doing so, $\sigma_z^f(0)$ in equations (31) through **(33)** is replaced by $d\sigma_z^f(0,t')$ **and** the integrals are carried out. The expression for the interface pressure $q(z,t)$ is written as

$$\begin{aligned}q(z,t) = &\frac{a_3(t)\Delta\epsilon_{in}}{a_4(t)}exp\left(\frac{2\mu c(t)}{R_f}z\right)\\ &+ \int_{-\infty}^{t}\frac{a_1(t-t')}{a_4(t-t')}exp\left(\frac{2\mu c(t-t')}{R_f}z\right)d\sigma_z^f(0,t') \qquad \mathbf{(34)}\end{aligned}$$

which can be rewritten as

$$\begin{aligned}q(z,t) = &\frac{a_3(t)\Delta\epsilon_{in}}{a_4(t)}exp\left(\frac{2\mu c(t)}{R_f}z\right) + \frac{a_1(t)\sigma_z^f(0,0)}{a_4(t)}exp\left(\frac{2\mu c(t)}{R_f}z\right)\\ &+ \int_{0}^{t}\frac{a_1(t-t')}{a_4(t-t')}exp\left(\frac{2\mu c(t-t')}{R_f}z\right)\dot{\sigma}_z^f(0,t')dt' \qquad (35)\end{aligned}$$

The first two terms in the expression for $q(z,t)$ represent the response due to the initial application of $\sigma_z^f(0,0)$ and At,,. It can **bc** shown that these terms decrease in time due to the behavior of the parameters $a_{1,3,4}$ and c. An alternative expression for $q(z,t)$ can be written as

$$\begin{aligned}q(z,t) = &\frac{a_3(t)\Delta\epsilon_{in}}{a_4(t)}exp\left(\frac{2\mu c(t)}{R_f}z\right) + \frac{a_1(0)\sigma_z^f(0,t)}{a_4(0)}exp\left(\frac{2\mu c(0)}{R_f}z\right)\\ &+ \int_{0}^{t}\sigma_z^f(0,t-t')\frac{d}{dt'}\left(\frac{a_1(t')}{a_4(t')}exp\left(\frac{2\mu c(t')}{R_f}z\right)\right)dt' \qquad (36)\end{aligned}$$

In this expression, it is clear that the second term represents the prompt change in $q(z,t)$ due to varying the applied stress. However, because of the complexity of the integrand, expression (35) is easier to **use** for further manipulation of the equations. **A** similar argument can be applied to obtain expressions for the axial stresses in the fiber and matrix, which can be written as

$$\sigma_z^f(z,t) = \frac{a_3(t)\Delta\epsilon_{in}}{a_4(t)c(t)}\left[exp\left(\frac{2\mu c(t)}{R_f}z\right) - 1\right]$$

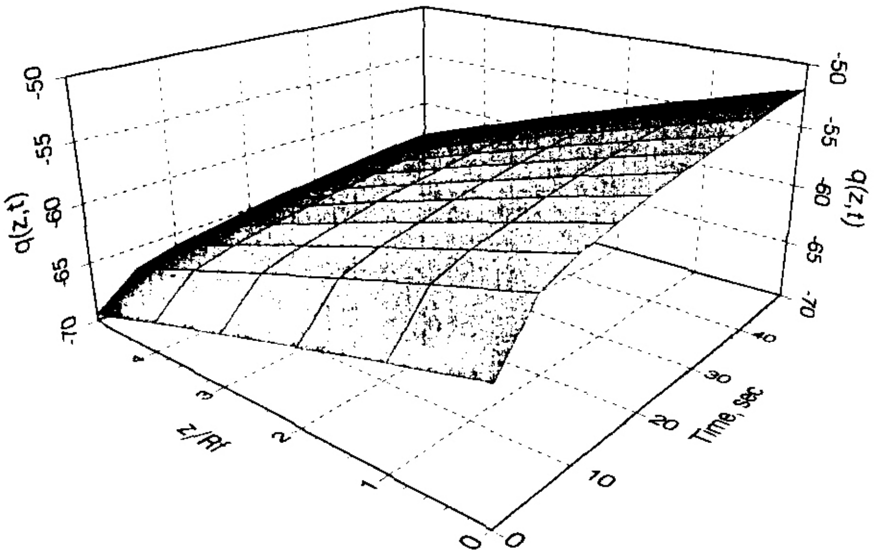

Figure 7: Relaxation of the interface pressure, $q(z,t)$

$$
\begin{aligned}
&+\sigma_z^f(0,0)\left(1+\frac{a_1(t)}{a_4(t)c(t)}\left[exp\left(\frac{2\mu c(t)}{R_f}z\right)-1\right]\right)\\
&+\int_0^t\left(1+\frac{a_1(t-t')}{a_4(t-t')c(t-t')}\left[exp\left(\frac{2\mu c(t-t')}{R_f}z\right)-1\right]\right)\dot{\sigma}_z^f(o,t')dt'
\end{aligned}
\qquad (37)
$$

and

$$
\begin{aligned}
\sigma_z^m(z,t)= &-\frac{a_3(t)\Delta c_{in}}{a_4(t)c(t)}\frac{f}{(1-f)}\left[exp\left(\frac{2\mu c(t)}{R_f}z\right)-1\right]\\
&-\sigma_z^f(0,0)\frac{f}{(1-f)}\frac{a_1(t)}{a_4(t)c(t)}\left[exp\left(\frac{2\mu c(t)}{R_f}z\right)-1\right]\\
&-\frac{f}{(1-f)}\int_0^t\frac{a_1(t-t')}{a_4(t-t')c(t-t')}\left[exp\left(\frac{2\mu c(t-t')}{R_f}z\right)-1\right]\dot{\sigma}_z^f(o,t')dt'
\end{aligned}
$$

In calculating the interface pressure and the axial stresses in the fiber/matrix system the convolution integrals in equations **(35)** through **(38)** are evaluated numerically. The Poisson's ratio of the fiber is assumed constant (time-independent) since there is no experimental data available on the fiber's shear compliance, which would have been combined with the uniaxial creep data to obtain $\nu_f(t)$. According to (GOLDEN and GRAHAM, 1988), for most viscoelastic problems, the assumption of time-independent Poisson's ratio ($\nu = 0.35-0.41$) is practical. In the present study a value of $\nu_f = 0.35$ is used in the viscoelastic analysis. Figs. 7 and 8 show the time evolution of $q(z,t)$ and $\sigma_z^f(z,t)$ along a portion of the fiber. These results are calculated for a value of $\sigma_b = 100MPa$ applied at the fiber end, and a temperature of 1200°C.

For the purpose of finding the instantaneous sliding length $L_s(t)$, a local matching of the instantaneous axial strains in the fiber and matrix, at $z = L_s$, is considered. For the matrix, the constitutive relations are elastic, and the axial strain is written in terms of the interface pressure q and the axial matrix stress as

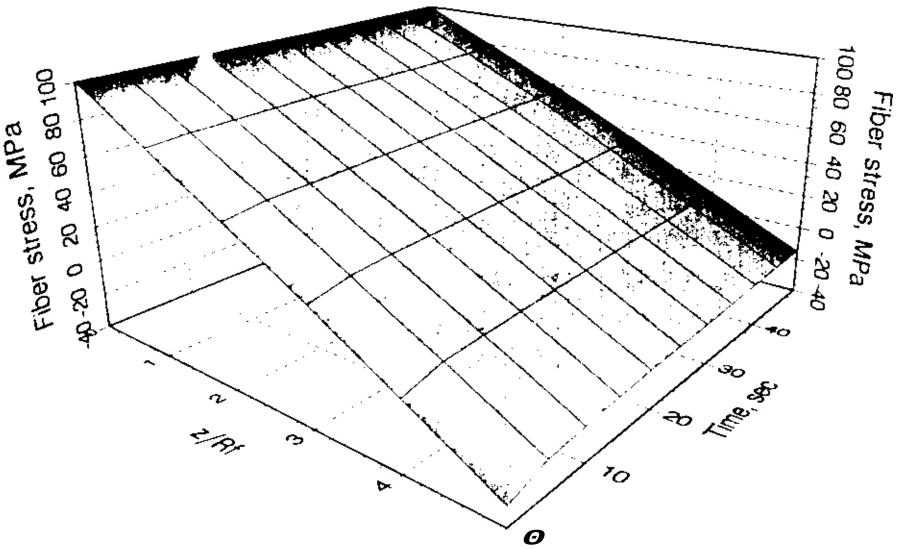

Figure 8: Relaxation of the axial fiber stress, $\sigma_z^f(z,t)$

$$\epsilon_z^m(z,t) = \epsilon_{in}^m + \frac{1}{E_m}\left(\sigma_z^m(z,t) + \frac{2\nu_m f q(z,t)}{(1-f)}\right) \tag{39}$$

For fibers. which behave viscoelastically, the axial strain is related to the interface pressure and the axial stress by

$$\begin{aligned}\epsilon_z^f(z,t) = \epsilon_{in}^f &+ \frac{\sigma_z^f(z,t) - 2\nu_f q(z,t)}{E_f(0)} \\ &+ \int_0^t \left(\sigma_z^f(z,t-t') - 2\nu_f q(z,t-t')\right) \dot{J}_f(t')dt'\end{aligned} \tag{40}$$

The relative sliding distance $\Delta(t)$ at the fiber end $z = 0$ is then given by equation (18). Carrying out the integral of differential axial strain with respect to z over the sliding length L_s the following expression is obtained for $\Delta(t)$

$$\begin{aligned}\Delta(t) = & -\Delta\epsilon_{in}L_s + \frac{1}{E_f(0)}\int_0^{L_s} \sigma_z^f(z,t)dz - \frac{1}{E_m}\int_0^{L_s} \sigma_z^m(z,t)dz \\ & -2\left[\frac{\nu_f}{E_f(0)} + \frac{\nu_m f}{E_m(1-f)}\right]\int_0^{L_s} q(z,t)dz \\ & + \int_0^t dt'\dot{J}_f(t')\int_0^{L_s}\left(\sigma_z^f(z,t-t') - 2\nu_f q(z,t-t')\right)dz\end{aligned} \tag{41}$$

where the z−dependence of the quantities σ_z^f, σ_z^m and q is depicted in equations (35) through (38). Some representative results for the distance L_s and **A** are shown in Figs. 9 through 14. for step and ramp stresses applied at the fiber's end. It can be shown that high values of the friction coefficient μ may severely impede the pull-out of fibers, and in turn, lower the composite toughness (Figs. 11 and 12). The decrease of the L_s with time for a step applied stress, Figs. 9, represents a localization of

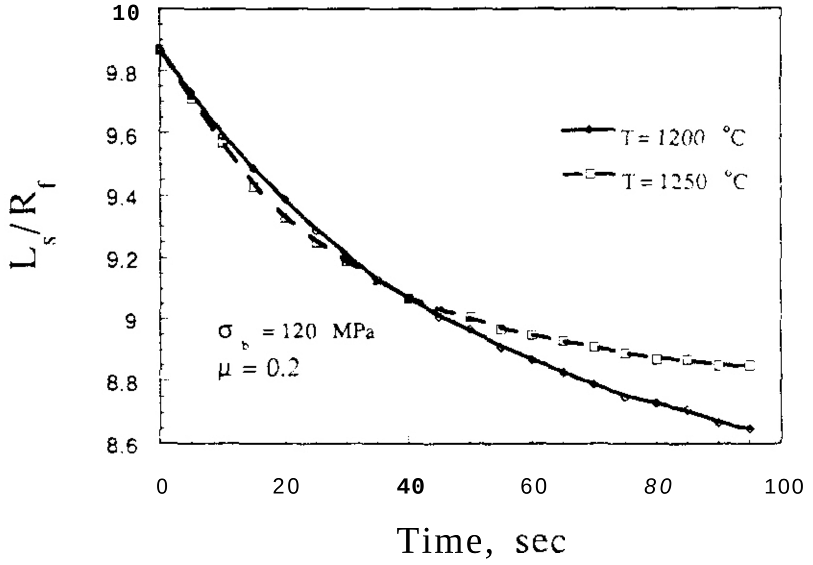

Figure 9: Evolution of the sliding length, L_s, for a step input (Pull-out)

creep strain in the portion of the fiber close to the fiber's end. For an applied stress that is increasing in time, the initial decrease in L_s due to strain localization is recovered (Fig. 13). It can be also noted that the faster the ramping of the applied stress the faster the recovery of L_s. It is highly probable that fibers would fail at sections which accumulate the highest amount of creep strains (e. g. between the two faces of a matrix crack rather than in the matrix). In this case, the frictional energy dissipation due to total pull-out of broken fibers is essentially negligible. This might have a serious effect on the energy dissipation by friction and, in turn, on the high-temperature fracture toughness of the composite. Therefore. the micro structure must be designed so as to consume more energy by viscoelastic dissipation to counterbalance that effect

So far. the problem of finding the stresses $\sigma_z^f(z,t)$ and $\sigma_z^m(z,t)$ and the interface pressure $q(z,t)$, the sliding length $L_s(t)$ and the relative sliding distance, corresponding to an arbitrary stress history is solved. Caution must be taken in implementing this methodology in case of a decreasing applied stress. It must be guaranteed at all times that the relative sliding velocity between fiber and matrix does not change its direction during the course of changing the applied stress. This is implied by the fact that the sign of the interfacial shear stress, which is responsible for load transfer between the fiber and matrix, must be the same at all times. In other words, the consistency between the fiber sliding direction and the axial equilibrium condition of fiber and matrix (Eqs. (5) and (6)) must be kept.

Viscoelastic solution: Crack bridging

In crack bridging analysis. the relationship of the bridging stress σ_b and the crack-opening displacement 6 is usually required . The latter can be related to the relative sliding distance A at the fiber's end. The crack opening displacement must be defined such that $f\sigma_b(t)d\delta/dt$, where f is the fiber volume fraction, is equal to the instantaneous rate of extra work, per unit area of crack surface, which occurs due to dissipation of energy by frictional sliding and viscoelastic straining of the fibers. Our interest in this article, however, is to find the bridging stress history $\sigma_b(t)$ due to an arbitrarily increasing **A** (or δ) such that a time dependent crack bridging mechanics problem can be formulated.

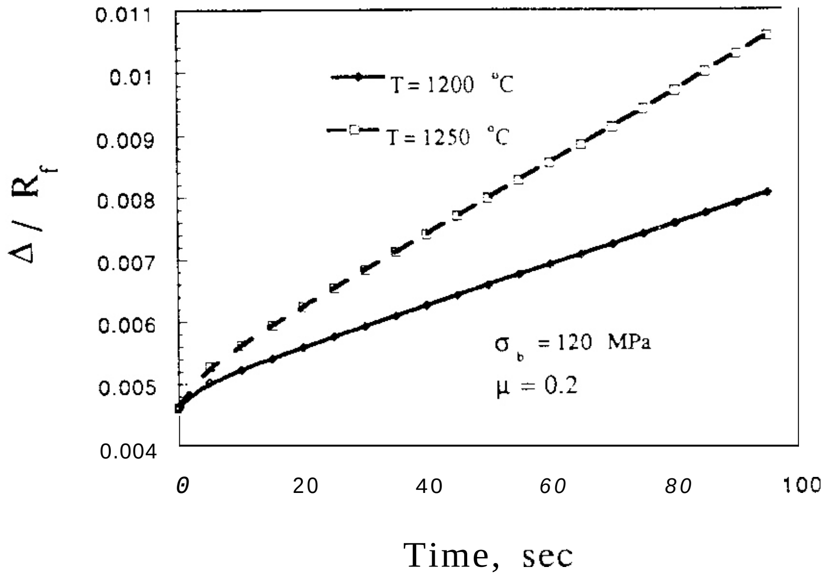

Figure 10: Evolution of the relative sliding distance, Δ for a step input (Pull-nul)

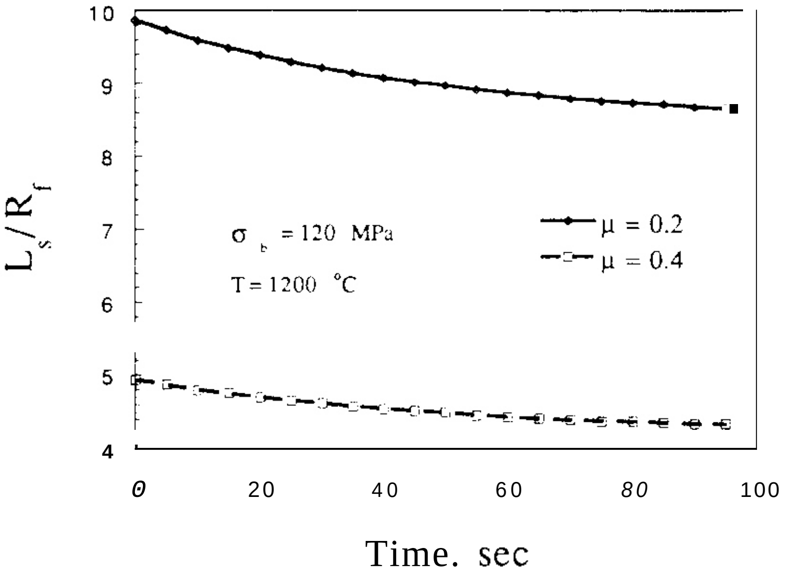

Figure 11: Effect of μ on evolution of L_s lor a step input (Pull-out).

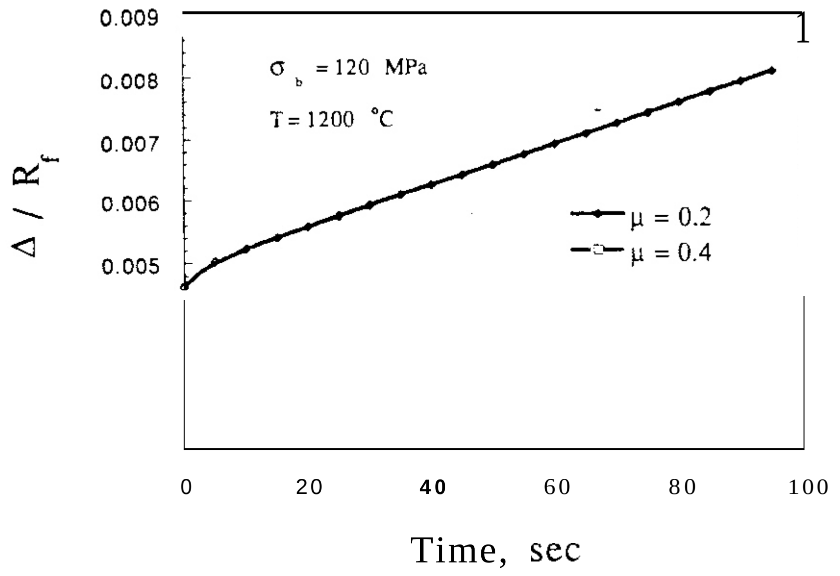

Figure 12: Effect of μ on evolution of **A** for a step input (Pull-out).

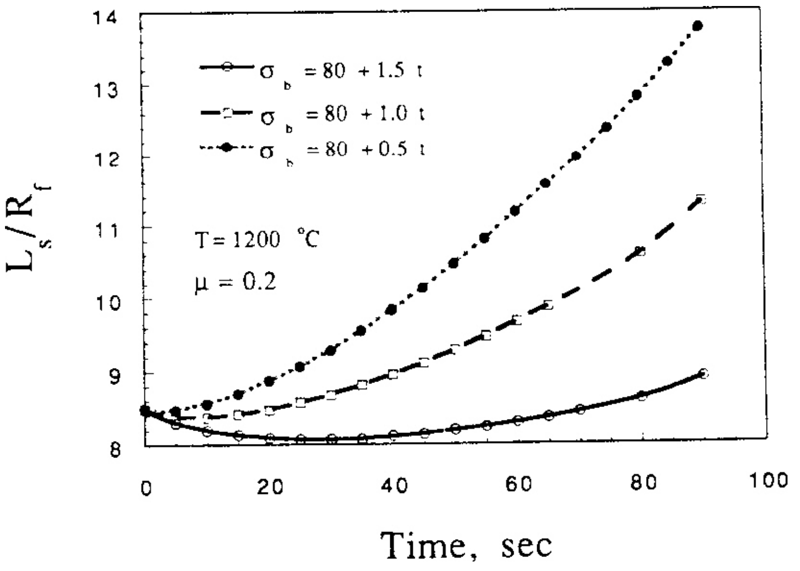

Figure **13:** Effect of ramping of σ_b on evolution of the sliding length, L_s (Pull-out)

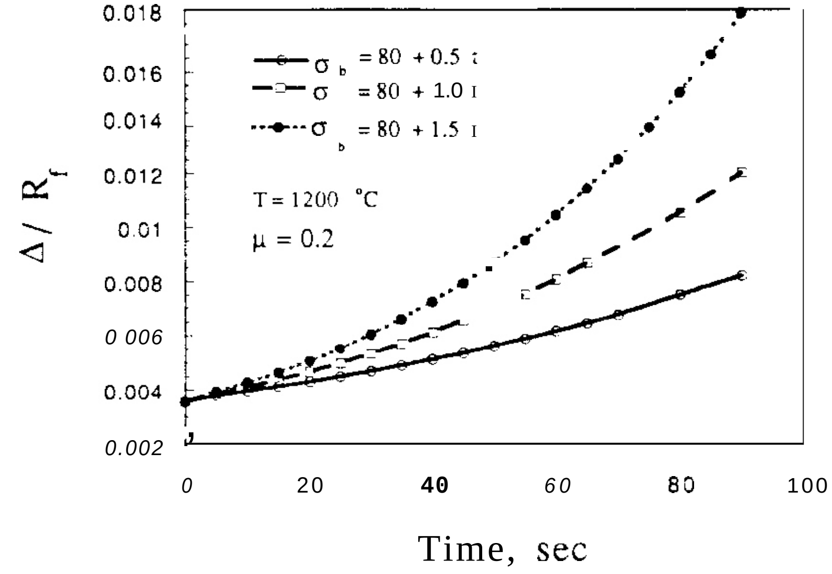

Figure 14: Effect of ramping of σ_b on evolution of the relative sliding distance, Δ (Pull-out;

The elastic and viscoelastic relationships developed for pull-out problem give the distance Δ in terms of the applied stress. In case of elastic solution such a relationship works both ways. i. e.. if Δ is given in terms of the bridging stress σ_b, then the latter can be represented in terms of Δ using the developed relation. Under fiber creep condition, however, this is difficult due to two factors: First, the hereditary integrals involved in that relation, and second, the relationship is non-linear because the sliding length shows a logarithmic dependence on the applied stress. It is therefore needed to solve the new problem of finding bridging stress history due to a relative displacement history at the fiber end.

Although. in principle, the solution to this new problem can be formally obtained starting with the basic equilibrium conditions and the viscoelastic constitutive relations of fibers, the solution can be greatly simplified if we assume a constant sliding length (creeping length) for fibers. This assumption is consistent with the physical situation in case of an initially bonded fiber/matrix interface. which debonds over a certain distance L_d upon the first application of load at the fiber's end. The solution for L_d can be totally elastic. Analytical approximate methods for finding the debond length in terms of the applied load are presented by SIGL and EVANS (1989) and HUTCHINSON and JESSES (1990), which can be coupled with the present analysis. If this is the case, it is possible to make use of the developed elastic solution as follows. In the $\Delta - \sigma_z^f(0)$ **(Eqs.** (17) and (18)), L_s can be replaced by L_d which is a constant. The rest of the terms included in that relation show linear dependence on $\sigma_z^f(0)$. With this in hand. the same relationship can be solved for $\sigma_z^f(0)$, in the elastic case in terms of Δ. This yields the following linear relation

$$\sigma_z^f(0) = f_1(f, E_f, E_m, \nu_f, \nu_m)\Delta\epsilon_{in} + f_2(f, E_f, E_m, \nu_f, \nu_m)\Delta \qquad (42)$$

where expressions for f_1 and f_2 are included in Appendix B. The bridging traction σ_b is then found, using equation (10), as

$$\sigma_b = -\sigma_R^f + f_1\Delta\epsilon_{in} + f_2\Delta \qquad (43)$$

The above developed elastic solution can be used to formulate the Laplace transformed viscoelastic solution for a step input Δ as shown below

$$\hat{\sigma}_b(s) = -\hat{\sigma}^f_R(s) + \hat{f}_1(s)\frac{\Delta\epsilon_{in}}{s} + \hat{f}_2(s)\frac{\Delta}{s} \tag{44}$$

In which $\hat{f}_1(s)$ and $\hat{f}_2(s)$ are obtained by replacing E_f and ν_f by their s– multiplied transforms in the original expressions for f_1 and f_2. The solution in the time domain is then given by

$$\sigma_b(t) = -\sigma^f_R(t) + f_1(t)\Delta\epsilon_{in} + f_2(t)\Delta \tag{45}$$

In inverting equation (44), Schapery's method is used. In obtaining the solution for arbitrary history $\Delta(t)$, the last term in (45) is replaced by a convolution integral. The final form of the solution can be written as

$$\begin{aligned}\sigma_b(t) = -\sigma^f_R(t) &+ f_1(t)\Delta\epsilon_{in} + f_2(t)\Delta(0) \\ &+ \int_0^t f_2(t-t')\dot{\Delta}(t')dt'\end{aligned} \tag{46}$$

or alternatively by

$$\begin{aligned}\sigma_b(t) = -\sigma^f_R(t) &+ f_1(t)\Delta\epsilon_{in} + f_2(0)\Delta(t) \\ &+ \int_0^t \dot{f}_2(t')\Delta(t-t')dt'\end{aligned} \tag{47}$$

The relaxation of the bridging stress is shown in Figs. 15 and 16 for time dependent **A**, which represents a time dependent crack opening displacement. The parameter **A** is linearly related to the crack opening displacement (HUTCHINSON and JENSEN, 1990). In Fig. 15 the effect of the fiber creeping length, L_d, is shown. That length, which is considered as a debond length, depends on the initial applied stress (or initial crack opening displacement) and the energy release rate of the fiber/matrix interface. The latter depends on the initial manufacturing conditions. It can be shown that while shorter L_d maintain higher bridging stress, the localization of the fiber creep between the faces of the matrix leads to a faster thinning of the bare fibers in that zone and, in turn, laster failure of the bridging. The stability of a bridged matrix crack, however, may require bridging stresses that are maintained for longer times. The question of stability can only be resolved by incorporating the present micro mechanical model into a formal stability study of bridged matrix cracks. The effect of the initial thermal strain mismatch is dipected in Fig. 17, where a comparison of the relaxation of the stress in a bridging fiber is compared to that of a bare fiber of the same length and subjected to the same displacement condition. It can be shown that at times greater than a 100 seconds the stresses in both fibers aproach the same value, which means that the matrix clamping effect, due to the initial strain mismatch, is greatly reduced.

Concluding remarks

It has been previously demonstrated that the residual thermal mismatch stresses and the fiber-matrix interface frictional characteristics are two important factors which impact the low temperature toughness of ceramic matrix composites. At high temperatures, however, creep and/or stress relaxation in one or more of the composite phases may control the toughening behavior. In this work we have explored only the effect of fiber creep on the fiber pull-out and crack bridging relaxation. The results, however, give some insight into composite behavior under conditions where other inelastic effects are present (e. g. irradiation creep and swelling). However, based on the results presented here, the following specific conclusions are derived:

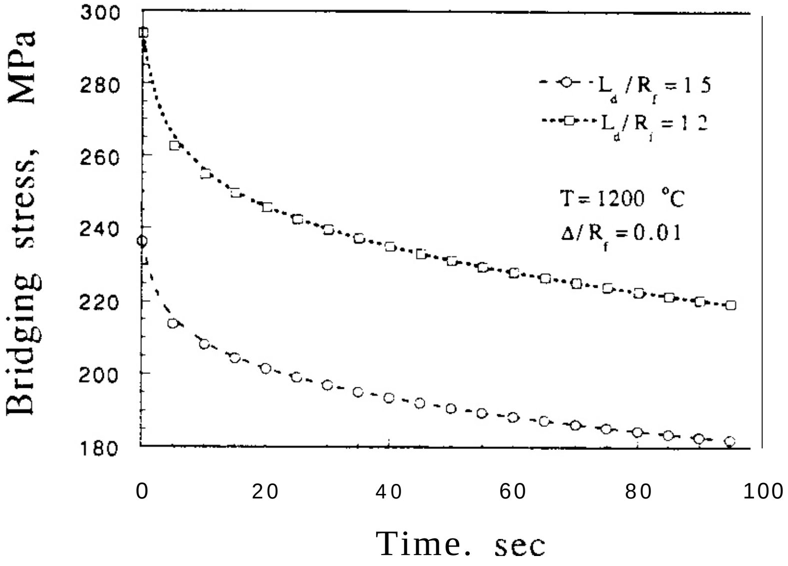

Figure 15: Relaxation of the bridging stress, σ_b, for a step crack opening.

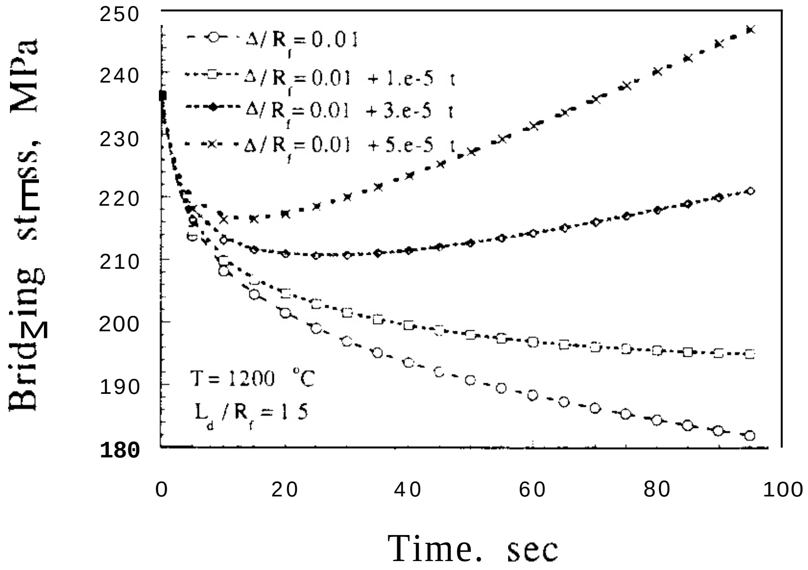

Figure 16: Relaxation of the bridging stress, σ_b, for a ramp crack opening.

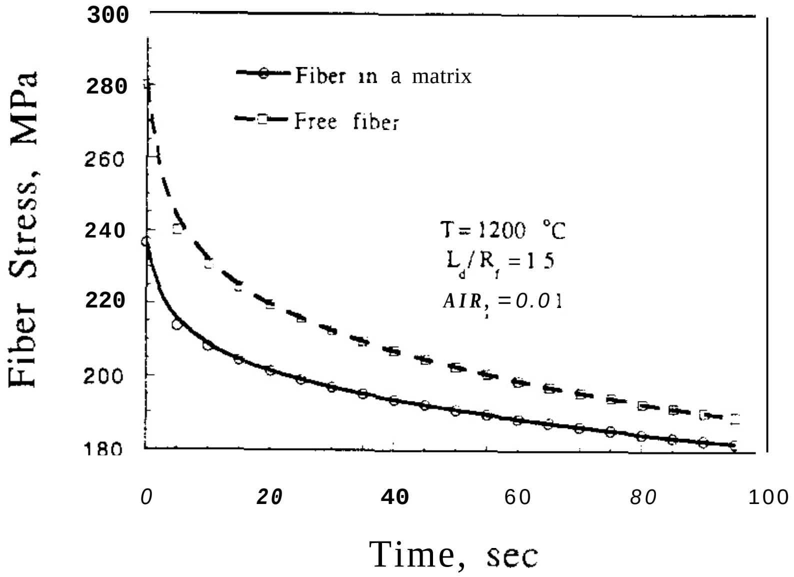

Figure 17: Relaxation of the bridging stress, σ_b, in comparison to bare fiber subjected to the same displacement condition.

1. The fiber-matrix interface friction coefficient, μ, is a primary factor which influences the high-temperature fiber pull-out and crack bridging. This conclusion is based on the results presented in Figs. 11 and 12, where it is clearly shown that for higher values of the friction coefficient the sliding length L_s is dramatically reduced. Under creep condition, this may lead to accumulating the fiber creep over smaller distances close to the matrix crack surface. hence, to a faster fiber failure in such zones.
2. From the composite toughness point. of view. there exists an optimum thermal strain mismatch, which maximizes *the* matrix cracking stress and the toughness of the composite. However, at elevated temperatures where creep of one or more of the composite phases is operable, such a thermal mismatch may not be important since it relaxes in time(Fig. 17). The time scale for such a relaxation process is controlled by the operating temperature (Figs. 5, 6). Therefore, in designing the micro structure for optimum toughness other means of optimization may need to be investigated.
3. At low temperatures. energy dissipation be frictional pull-out of failed fibers is a key term in the composite toughness. Under fiber creep conditions, the localization of creep strain close to the matrix crack surface may lead to failure of fibers close to the matrix surface. If this is the case, frictional energy dissipation by total pull-out of failed fibers may be negligible. Therefore, at high temperature, such a dissipation mechanism may be only important if the fibers remain intact for longer times, which allows a continuous frictional dissipation of energy before fiber failure.
4. **A** new factor, which may highly influence the composite toughness at elevated temperature, is the **energy** dissipation by viscoelastic straining of fibers. Significant amounts of energy may **be** dissipated in this way if the composite micro structure allows fiber survival for long times.

Some of the important features of the present model can also be summarized as follows:

1. The developed model can be utilized in designing and analyzing high-temperature fiber pull-out experiments in composite systems, where time-dependent inelastic effects dominate the composite behavior.

2. The model can be applied to solving problems of mechanics of bridged cracks at high-temperature. as well as studying the stability and growth of crack bridging.
3. The model can be used to optimize the micro structure of the composite system for maximum toughness by systematically exploring the effects of different parameters such as the friction coefficient, the initial inelastic strain mismatch, viscoelastic straining of fibers, and the effect of fiber sliding length on energy dissipation by frictional sliding and viscoelastic straining of fibers.

FUTURE WORK

The developed micro mechanical model will be used to optimize the micro structural design of SiC-SiC composite systems for maximum toughness under conditions relevant to fusion applications. This will be accomplished by systematically exploring the effects of different parameters (e. g. the friction coefficient, the residual stresses, and fiber creeping length) on the energy of fracture of these composite systems. The model will also be used to study the mechanics of matrix cracks bridged by fibers, at high temperatures. and determine the stability of crack bridging processes in Sic-Sic composite systems.

Appendices

Appendix A: Residual axial stress in fibers

To find σ_R^f, an infinite copmosite cylinder is considered, which is cooled down from the initial stress-free temperature. Three conditions are used to determine σ_R^f, the initial interface pressure q_R, and the axial matrix stress in the intact matrix σ_R^m(only σ_R^f is important in analyzing crack bridging problems). These conditions are:

1. Continuity of radial displacement at fiber matrix interface:

$$\epsilon_\theta^f(R_f) = \epsilon_\theta^m(R_f) \tag{48}$$

2. Continuity of the axial displacement:

$$\epsilon_z^f = \epsilon_z^m \tag{49}$$

which is a uniform strain component along the composite cylinder.

3. Self-equilibrium condition for the composite cylinder:

$$f\sigma_R^f + (1-f)\sigma_R^m = 0 \tag{50}$$

The first two conditions make use the strain-stress relations (2) given in Section 2, along with replacing σ_z^f by σ_R^f, σ_z^m by σ_R^m, and 9 by q_R. The third condition is used to eliminate σ_R^m in the first two conditions. The final form of the solution can be written as

$$\begin{aligned}
\sigma_R^f &= E_f E_m (1-f)\Delta\epsilon_{in}\left(\frac{d_2 - d_1}{c_1 d_2 - c_2 d_1}\right) \\
q_R &= E_f E_m (1-f)\Delta\epsilon_{in}\left(\frac{c_1 - c_2}{c_1 d_2 - c_2 d_1}\right) \\
\sigma_R^m &= \left(\frac{-f}{1-f}\right)\sigma_R^f
\end{aligned} \tag{51}$$

where

$$\begin{aligned} c_1 &= fE_f + (1-f)E_m \\ c_2 &= f\nu_m E_f - (1-f)\nu_f E_m \\ d_1 &= -2\left[(1-f)\nu_f E_m + f\nu_m E_f\right] \\ d_2 &= (1-f)E_m(1-nu_f) + E_f\left[1+\nu_m + f(1-\nu_m)\right] \end{aligned} \tag{52}$$

Appendix B: Expressions for f_1 and f_2

This appendix contains expressions for the constants f_1 and f_2 appearing in equation(42). The derivation starts by considering equations (17) and (18) and replacing L_s by L_d.

$$\begin{aligned} e &= \exp\left(\frac{2\mu c L_d}{R_f}\right) - 1 \\ e_1 &= \left[\frac{1}{E_f} - \frac{a_1}{a_4 c E_f} - \frac{a_1}{a_4 c E_m}\left(\frac{f}{1-f}\right)\right] L_d \\ e_2 &= \frac{a_1 R_f}{\mu c a_4}\left[\frac{1}{2cE_f} - \frac{\nu_f}{E_f} + \frac{f}{2c(1-f)E_m} - \frac{\nu_m f}{(1-f)E_m}\right] e \\ e_3 &= -\left[1 + \frac{a_3}{a_4 c E_f} + \frac{a_3}{a_4 c E_m}\left(\frac{f}{1-f}\right)\right] L_d \\ e_4 &= \frac{a_3 R_f}{\mu c a_4}\left[\frac{1}{2cE_f} - \frac{\nu_f}{E_f} + \frac{f}{2c(1-f)E_m} - \frac{\nu_m f}{(1-f)E_m}\right] e \end{aligned} \tag{53}$$

Expressions for f_1 and f_2 are then written as

$$\begin{aligned} f_1 &= -\left(\frac{e_3 + e_4}{e_1 + e_2}\right) \\ f_2 &= \left(\frac{1}{e_1 + e_2}\right) \end{aligned} \tag{54}$$

References

[1] BRUN, MILIVOJ . K. and BOROM, MARCUS. P. (1989) *J. Am. Ceram. Soc.* **72** No. **10**, 1993-1996.

[2] CARTER, C. H. and DAVIS, R. F. (1984) *J. Am. Cemm. Soc.* ***67*** No. **11**, 732-740.

[3] CARROLL, DOUGLAS R. and DHARANI, L. R. (1992) *J. Am. Cemm. Soc.* ***75*** **No. 4**, ***78C*** 794.

[4] DICARLO, JAMES **A.** (1986) *J. Mater. Sci.* **21**, 217-224.

[5] DICARLO, JAMES A. and MORCHER, GREGORY N. (1991) *Failure Mechanisms* ***of High*** *Temperature Composite Materials,* **pp.** 15-22 AD-Vol.22 -AMD-Vol.122, The American Society **pf** Mechanical Engineers.

[6] FU, ***S. Y.***, ZHOU, B. L., CHES, X., HE, G. H. and LUNG, C. W. (1993) *Composites* **24 No. 1**, 5-11.

[7] FU, S. Y., ZHOU, B. I.., CHEN, X., HE, G. H. and LUNG, C. W. (1993) *Composites* **24** No. **1**, 13-17.

[8] GAO, YU-CHEN, MAI, YUI-WING and COTTERELL, BRIAN (1988) *J. Appl. Math. Phys.***39**, 550-572.

[9] GOLDEN, J. M. and GRAHAM, G. A. C (1988) *Boundary Value Problems in Linear Viscoelasticity*, Springer-Verlag.

[10] GULDEN, T. G. (1969) *J. Am. Ceram. Soc.* **52 No. 11**, 585-590.

[11] HSUEH, CHUN-HWAY (1988) *J. Mat. Sci. Letters* **7**, 497-500.

[12] HSUEH, CHUN-HWAY, FERBER, MATTISON K. and BECHER, PAUL, F. (1988) *J. Mater Res.* **4 No. 6**, 1529-1537.

[13] HSUEH, CHUN-HWAY (1990) *J. Mat. Sci.* **25**, 811-817.

[14] HUTCHINSON, JOHN. W. and JENSEN, HENRIK M. (1990) *Mechanics of Materials* **9**, 139-163.

[15] JIANG, K. R. and PENN, L. S. (1992) *Composites Sci. Tech.* **45**, 89-103.

[16] LIANG, C. and HUTCHINSON, J. W. (1993) *Mechanics of Materials* **14**, 207-221.

[17] LUH, ELLICE Y. and EVANS, A. G. (1987) *J. Am. Ceram. Soc.* **70 No. 7**, 466-469.

[18] MARSHALL, D. B. and EVANS, A. G (1985) *J. Am. Ceram. Soc.* **68 No. 5**, 225-231.

[19] MARSHALL, D. B., COX, B. N. and EVANS, A. G. (1985) *Acta Metall.* **33 No. 11**, 2013-2021.

[20] MARSHALL, D. B., SHAW, M. C. and MORRIS, W. L. (1992) *Acta Metall. Mater.* **40 No. 3**, 443-454.

[21] MARSHALL, D. B. (1992) *Acta Metall. Mater.* **40 No. 3**, 427-441.

[22] NAIR, S. V., JAKUS, K. and LARDNER, T. J. (1991) *Mechanics of Materials* **12**, 229-244.

[23] PIPKIN, A. C. (1986) *Lectures on Viscoelasticity Theory*, Applied Mathematical Sciences-Vol.7, Springer-Verlag.

[24] SIGL, L. S. and EVANS, A. G. (1989) *Mechanics of Materials* **8**, 1-12.

[25] SUZUKI, TAKAYUKI, SATO, MASAHIRO and SAKAI, MOTOTSUGU (1992) *J. Mater. Res.* **7 No. 10**, 2869-2875.

[26] SHAPERY, R. A. (1962) *Proceedings of the Fourth U. S. National Congress of Applied Mechanics*, pp. 1075-1085.

[27] SHETTY, DINESH K. (1988) *J. Am. Ceram. Soc.* **71 No. 2**, C-107 - C-109.

[28] THOULESS, M. D. and EVANS, A. G. (1988) *Acta Metall.* **36 No. 3**, 517-522.

[29] ZHOU, LI-MIN, KIM, JANG-KYO and MAI, YU-WING (1992) *Composites Sci. Tech.***45**, 153-160.

Distribution

1-16. Argonne National Laboratory, 9700 South Cass Avenue, Argonne, IL 60439
M. C. Billone
O. K. Chopra
H. M. Chung
D. R. Diercks
R. Erck
A. K. Fisher
Y. Gohar
A. B. Hull
C. E. Johnson
F. Kassner
B. A. Loomis
R. F. Mattas
L. A. Niemark
J. H. Park
D. L. Smith
S. W. Tam
H. C. Tsai
H. Wiedersich

17-18. Argonne National Laboratory, EBR-II Division. P.O. Box 2528, Idaho Falls, ID 83403-2528
H. P. Planchon
D. L. Porter

19. Auburn University, Department of Mechanical Engineering. 201 Ross Hall, Auburn, AL 36849
B. A. Chin

20-33. Battelle-Pacific Northwest Laboratory, P.O. Box 999, Richland, WA 99352
J. L. Ethridge
F. A. Garner (5)
D. S. Gelles
L. R. Greenwood
M. L. Hamilton
H. L. Heinisch
G. W. Hollenberg
R. H. Jones
W. W. Laity
O. D. Slagle

34. Carnegie Institute of Technology, Carnegie-Mellon University, Schenley Park, Pittsburgh, PA 15213
W. M. Garrison, Jr.

35-36. EG&G Idaho, Inc., Fusion Safety Program, P.O. Box 1625. Idaho Falls, ID 83415-3523
D. F. Holland
S. J. Piet

37. GE Astrospace Division, San Jose Operations, 6834 via Deloro, P.O. Box 530954, San Jose, CA 95153-5354
Mike Kangilaski

38-41. General Atomics, P.O. Box 85608. San Diego, CA 92138
T. A. Lechtenberg
D. I. Roberts
K. R. Schultz
C. Wong

42. General Dynamics Corp., 5001 Kearny Villa Rd., San Diego, CA 92138
T. L. Cookson

43. Georgia Institute of Technology, Fusion Research Center, 0225. Atlanta, GA 30332
W. M. Stacey

44. Grand Canyon University, Department of Natural Science, 3300 W. Camelback Rd., Phoenix, AZ 85017
W. A. Coghlan

45-47. Lawrence Livermore National Laboratory, P.O. Box 808, Livermore, CA 94550
E.C.N. Dalder
M. Guinan
J. Perkins

48-55. Los Alamos National Laboratory. P.O. Box 1663, Los Alamos, NM 87545
J. L. Anderson
F. W. Clinard
E. H. Farnum
H. M. Frost
J. C. Kennedy
R. E. Siemon
W. F. Sommer
K. E. Sickafus

56. Manlabs, Inc., 231 Eric Street, Canbridge, MA 02139
D. Tognarelli

57-59. Massachusetts Institute of Technology, Department of Metallurgy and Materials Science, Cambridge, MA 02139
L. W. Hobbs
N. J. Grant
K. C. Russell

60-61. Massachusette Institute of Technology, Plasma Fusion Center Headquarters, Cambridge, MA 02139
H. D. Becker
D. B. Montgomery

62. McDonnell-Douglas Missile Systems Company, Mail Code 306 4204, P.O. Box 516, St Louis, MO 63166
J. W. Davis

63-65. National Institute of Standards and Technology, Boulder, CO 80302
I:. 11. Fickett
H. I. McHenry
R. 1. Reed

66. National Materials Advisory Board, 2101 Constitution Avenue, Washington, DC 20418
K. M. Zwilsky

67-68. Naval Research Laboratory, Code 6506, Washington, DC 20375
D. L. Gibson
J. A. Sprague

69-109. Oak Ridge National Laboratory, P.O. Box 2008, Oak Ridge, TN 37831
Central Research Library
Document Reference Section
Laboratory Records Department (2)
Laboratory Records-RC
Patent Section
D. J. Alexander
C. C. Baker
J. Bentley
E. E. Bloom
T. D. Burchell
J. H. DeVan
R. H. Goulding
M. L. Grossbeck
E. A. Kenik
R. L. Klueh
E. H. Lee
A. W. Longest
L. K. Mansur
P. J. Maziasz
J. E. Pawel
T. C. Reuther
T. K. Roche
A. F. Rowcliffe (9)
R. L. Senn
J. Sheffield
L. L. Snead
R. E. Stoller
K. R. Thoms
P. F. Tortorelli
C. A. Wang
D. P. White
S. J. Zinkle

110. Oregon Graduate Institute, Dept. of Materials Science & Engineering, 19600 N.W. Von Neumann Drive, Beaverton, OR 97006
J. M. McCarthy

111-113. Princeton University, Princeton Plasma Physics Laboratory, P.O. Box 451, Princeton, NJ 08540
C. Bushnell
H. Furth
Long-Poe Ku

114. Reactor Materials Technology, 272 Baywood Avenue, Pittsburgh, PA 15228
A. Boltax

115-116. Rensselaer Polytechnic Institute, Troy, NY 12181
D. Steiner
David Duquette

117. Rockwell International Corporation, NA02, Rocketdyne Division, 6633 Canoga Avenue, Canoga Park, CA 91304
D. W. Kneff

I 18-120. Sandia National Laboratories, Fusion Technology Dept., Dept. No 6531, P.O. Box 5800, Albuquerque, **NM** 87185-5800
M. J. Davis
W. B. Gauster
R. D. Watson

121-122. Sandia National Laboratories, Livermore Division 8316, Livermore. CA 94550
W. Bauer
W. G. Wolfer

123. San Diego State University, Mechanical Engineering Dept., San Diego, CA 92182-0191
L. D. Thompsoii

124. TSI Research, 225 Stevens Ave., #110, Solana Beach, CA 92075
E. T. Cheng

125-126. University of California, Dept. of Chemical and Nuclear Engineering, Santa Barbara, CA 93106
G. E. **Lucas**
G. R. Odette

127-129. University of California, Dept. of Chemical, Nuclear, and Thermal Engineering, Los Angeles, CA 90024
M. **A.** Abdou
R. W. Conn
N. M. Ghonicm

130. University of California, IPFR, 405 Hilgard Avenue, Los Angeles, CA 90024-1600
S. Sharafat

131. University of Michigan, Dept. of Nuclear Engineering, Ann **Arbor,** MI 48109
T. Kammash

132. University of Missouri, Department of Nuclear Engineering, Rolla, MO 65401
A. Kumar

133- 134. University of Wisconsin, Nuclear Engineering Dept., 1600 Johnson Drive, Madison, WI 53706
J. B. Blanchard
G. L. Kulcinski

135. Washington Stale University-Tri-Cities, 6012 W. Ridgecrest Drive, Spokane, WA 99208
D. *G.* Doran

136-139. Westinghouse Hanford Company, P.O. Box 1970, Richland, WA 99352
R. E. Bauer
A. M. Ermi
F. M. Mann
R. J. Puigh

140-142. Hokkaido University, Faculty of Engineering, Kita 13. Nishi 8, Kita-ku, **Sapporo** *060,* Japan
Heischichiro Takahashi
Somei Ohnuki
Akiia **Okada**

143-144. Japan Atomic Energy Research Institute. Tokai Research Establishment, Tokai-mura, Naka-gun, Iharaki-ken 319-11, Japan
Tatsuo Kondo
Akiiichi Hishinuma (3)

145. Kyushu University, Dept. of Nuclear Engineering, Faculty of Engineering, Kyushu University 36, **Hakozaki,** Fukuoka 812, Japan
C. Kinoshita

146. Kyushu University, Research Institute of Applied Mechanics, 6-1, Kasuga-Koen, Kasuga-Shi, Fukuoka-Ken 816, Japan
Takeo Muroga

147-148. Muroran Institute of Technology, Dept. of Metallurgical Engineering, 27-1 Mizumoto-cho,
Mororan 050, Japan
Toshihei Misawa Akiiiko Kimura

149. Nagoya University, Dept. of Nuclear Engineering, Furo-Cho, Chikusa-ku, Nagoya 464-01, Japan
Michio Kiritani

150-152. National Institute **for** Fusion Science, Furosho, Chikusa-ku, Nagoya 464-01, Japan
Osamu Motojima Chusei Namba Nohuaki Noda

153-155. National Research Institute for Metals, Tsukuha Branch, Sengen, Tsukuba-shi,
Ibaraki-ken, 305, Japan
Fujio Abe Josei Nagakawa Haruki Shiraishi

156. *Osaka* University. Dept. of Nuclear Engineering, **2-1** Yamadaoka, **Suita**, Osaka 565, Japan
Tetuo Tanabe

157. PNC Oarai, 4002 Narita, Oarai, Ibaraki 311-13, Japan
Itaru Shibasaki

158. Science University of **Tokyo,** Dept. **of** Materials Science & Technology, 2641 Yamazaki
Noda City, Chiba Prefecture 278, Japan
Naohira Igata

159. Teikyo University, Otsuka, Hachioji, Tokyo 192-03, Japan
Akiia Miyahara

160. Tohoku University, Institute for Materials Research, Katahira 2-2-1, Sendai 980, Japan
Hideki Matsui

161-162. Tohoku University. Institute for Materials Research, Oarai Branch, Oarai, Ibaraki 311-13, Japan
Tatsuo Shikama Hideo Kayono

163. Tohoku University, Dept. of Nuclear Engineering, Tohoku University, Aoba, Aramaki,
Sendai 980, Japan
Katsunori **Abe**

164-166. University of Tokyo, Dept. of Nuclear Engineering, 3-1, Hongo 7-Chome, Bunkyo-Ku,
Tokyo 113, Japan
Shiori Ishino **(2)** Naoto **Sekimura**

167-168. University of Tokyo, Dept. of Materials Science, **3-1,** Hongo 7-Chome, Bunkyo-ku,
Tokyo 1 13, Japan
Akii Kohyama Yutaka Kohno

169. Commission of European Communities, Directorate-General for Research Science and
Education, Fusion Programme RUE De La Loi 200. B-1049 Brussels, Belgium
J. Darvas

170-171 Chalk River Nuclear Laboratories, Atomic Energy **of** Canada, Ltd., Chalk River,
Ontario KOJ 1J0, Canada
I. J. Hastings D. P. Jackson

Southwestern Institute **of** Physics, P.O. Box 432, Chenedu 610041, Sichuan, P.R. China
J. **P.** Qian

173. Institute of Atomic Energy, Academia Sinica, P.O. Box 275-51, Beijing. P.R. China
J. Yu

174 **Riso** National Laboratory, Materials Dept., P.O. Box 49, DK-4000, Roskilde, Denmark
B. N. Singh

175. Centre d'Etudes Nucleaires, Saclay, DLPC/SMCM, Commissariat a l'Energie Atomique,
91191 Gif-Sur-Yvette, Cedex, France
N. Roux

176. Commission for European Communities, Joint Research Centre, I.A.M. lspra Establishment
21020 Ispra (Varese). Italy
P. Schiller

177. EURATOM/CIEMAT Fusion Association. Avenida Complutense 22,28040, Madrid, Spain
E. R. Hcdgson

178. Paul Scherrer Institute, CH-5232 Villigen, Wuerenlingen **PSI,** Switzerland
M. Victoria

179. Harwell Laboratory, B393, Radiation Damage Dept., Oxfordshire, OX11 ORA, United Kingdom
C. A. English

180. Metallurgical **and** Nuclear Consultant, 9A Cumnor Rise Road, Cumnor Hili, Oxford OX2 9HD,
United Kingdom
D. R. Harries

181. Culham Laboratory, **U.K.** Atomic Encrgy Authority, D5/117, Abingdon, Oxon OX14 3DB,
United Kingdom
G. J. Butterworth

182. Hahn-Meitner-Institut **fur** Kcmforschung Berlin, Glienicker Str. 100, D-1000 Berlin 39, Germany
H. J. Wollenberger

183. Institut **fur** Festkorperforschung der Kernforschungsanlage, **D-5**170 Julich 1,
Postfach 1913, Germany
H. Ullmaier

184-185. Kernforschungszentrum Karlsruhe, Postfach 3640, 75 Karlsruhe 1, Germany
M. Dalle-Donne (INR) K. Erlich (IMF-II)

186. A. A. Baikov Institute **of** Metallurgy, USSR Academy **of** Sciences, Leninsky Prospect 49,
Moscow, Russia
L. I. Ivanov

187. CRISM "Prometey," Naberezhnava r. Monastyrick 1, 193167, St. Petersburg, Russia
V. V. Rybin

188. D. V. Efremov Institute **of** Electro-Physical Apparatus, 189631, St. Petersburg, Russia
Yu. G. Prokofiev

189. Institute **of** Power Engineering, 218 M. Krasnosel's Kaji St., 107113 Moscow, Russia
G. M. Kalinin

190. Kharkov Physical-Technical Institute of Atomic Reactors, Kharkov, Academishen, 1,
Moscow, Russia
I. M. Neckludov

191. V. I. Lenin Research Institute of Atomic Reactors, 433510 Dimitrovgrad-10, Ulyanovsk Region, Ukraine
V. K. Shamardin

192. Department of Energy, DOE *Oak* Ridge Field Office, P.O. Box 2008,
Oak Ridge, TN 37831-6269
Assistant Manager for Energy Research and Development

193. Department of Energy, DOE *Oak* Ridge Field Office, P.O. Box 2008,
Oak Ridge, TN 37831-6269
S. D. Frey

194. Department of Energy, Office of Basic Energy Sciences. Washington, D.C. 20585
J. B. Darby

195-202. Department of Energy, Office of Fusion Energy, Washington. D.C. *20585*
S. E. Berk
M. M. Cohen
D. H. Crandall
N. **A.** Davies
W. F. Dove
T. R. James
R. E. Price
F. W. Wiffen

203. Department of Energy, Richland Operations Office, Federal Bldg., MS-A590,
Richland, WA 99352
D. Segna

204-253. Department of Energy. Office of Scientific **and** Technical Information, Office of Information Services, P.O. Box 62. *Oak* Ridge, **TN** 37831
For distribution as shown in DOE/TIC-4500, Distribution Categories UC-423 (Magnetic Fusion Reactor Materials) and UC-424 (Magnetic Fusion Energy Systems)